Soil-pile interaction for bored cast-in-situ piles in stiff clays

Jannie Knudsen

Soil-pile interaction for bored cast-in-situ piles in stiff clays

PhD Thesis

Jannie Knudsen

November 2024

Thesis submitted:	November 2024
PhD Supervisor:	Professor (Docent) Kenny Kataoka Sørensen Department of Civil and Architectural Engineering, Aarhus University
Company main supervisor:	Technical Director, Professor Jørgen S. Steenfelt Department 7104.008**,** COWI A/S, Kgs. Lyngby
Company co. supervisor:	Leading specialist Helle Trankjær Department 7104.002**,** COWI A/S, Aarhus
PhD Committee:	Professor Ken Gavin Department of Geoscience and Engineering, TU Delft
	Paul Morrison Director, Arup
	Associate professor Min Wu Department of Civil and Architectural Engineering, Aarhus University
PhD Series:	Faculty of Technical Sciences, Aarhus University
ISBN: DOI:	978-87-7507-585-0 10.7146/au.569

© 2024 Copyright by Jannie Knudsen

Abstract

Bored cast-in-situ piles are increasingly utilized as a foundation method in Denmark. Previously, driven precast concrete piles were the prevalent choice and are still widely applied. However, due to the construction of buildings in geotechnically challenging regions, the need to minimize noise and vibration in populated areas, and the construction of taller and more intricate structures with substantial loads, there is a gradual transition towards the use of bored cast-in-situ piles.

As the Danish construction industry has primarily relied on driven precast concrete piles, and the Danish National Annex to Eurocode 7 imposes restrictions on the shaft resistance for bored piles, it is necessary to expand the existing knowledge regarding the intricate interaction between the soil and the bored piles along their entire length.

Prior research conducted on bored piles in stiff clay has indicated that the interaction between the soil and the pile along the pile shaft is affected by the installation process, resulting in "locked-in" shear stresses on the pile shaft, also referred to as residual stresses. Furthermore, prior research indicates that the ultimate shaft resistance for bored piles can be predicted through a total stress analysis called the α method and that there is a linkage between the ultimate unit shaft resistance and the undrained shear strength.

The aim of this thesis is to examine the intricate soil-pile interaction along the entire length of bored piles in Danish Eocene clay, which is characterized as a stiff, over-consolidated, and highly plastic clay. The investigation takes place at a designated test site situated in Hinge, Jutland, Denmark. The research focuses on a field-test program involving eight bored piles, with a specific emphasis on understanding the effects of the pile installation process, particularly the residual stresses, and their impact on the mobilization of shaft resistance.

Additionally, the study explores the relationship between the ultimate shaft resistance and undrained shear strength, using the empirical adhesion coefficient known as α, and examines its compliance with the limitations presented in the Danish National Annex to Eurocode 7. The empirical adhesion coefficient, α, was found to be approximately 2.3 to 3.3 times higher than the value specified in the Danish National Annex to Eurocode 7. This indicates that the empirical adhesion coefficient provided in the Danish National Annex to Eurocode 7 may not accurately capture the behaviour of bored piles, emphasizing the need for further consideration and evaluation of this parameter in geotechnical engineering practices.

Lastly, the influence of time on the pile capacity is investigated to gain insight into the behaviour and performance of the piles over extended periods. The axial pile capacity was found to increase with approximately 12 % per log change in time. However, the trend is weak with an R^2 value of 0.48 indicating that additional data at various intervals after installation is required to improve the ability to predict the time evolution of pile capacity.

By analysing the results obtained from the static pile loading tests conducted during the study, an analytical model has been developed to determine the distribution of displacements and forces along the shaft of bored piles. This model can accommodate the consideration of residual stresses or exclude them, depending on the specific requirements of the analysis.

Furthermore, based on the soil properties observed in the Eocene clay at the designated test site in Hinge, a method for predicting the mobilised shaft resistance (known as load transfer functions) has been derived. These load transfer functions serve as a valuable tool in everyday practical geotechnical engineering, as they enable engineers to make initial estimations of the distribution of displacements and forces along the shaft of bored piles. This aids in the design and evaluation processes, providing crucial insights for geotechnical engineering projects.

The analysis of the test data obtained from the static pile loading tests revealed that residual stresses have an impact on the response of the piles to loading, specifically influencing the mobilised shaft resistance. Therefore, it is essential to consider these residual stresses when modifying the length, diameter, or other parameters of the piles.

It is worth noting that the residual stresses, although influential in the mobilization of the shaft resistance along the pile, do not impact the overall resistance of bored piles as demonstrated in a pile loading test. These stresses primarily affect the distribution and behaviour of the shaft resistance along the length of the pile.

Resumé

I Danmark er der en stigende tendens til at anvende borede in-situ støbte pæle som et alternativ til traditionelle rammede pæle. Selvom rammede pæle stadig anvendes i stor udstrækning, er der en øget anvendelse af borede pæle som følge af udnyttelse af geoteknisk mere udfordrende områder, behovet for at kunne reducere støj og vibrationer i bebyggede områder samt imødekomme kravene til stivheden af fundamenter under højere og mere komplekse bygninger med høje laster.

Dansk konstruktionspraksis har hidtil primært været baseret på rammede pæle, og det danske nationale anneks til Eurocode 7 begrænser overflademodstanden for borede pæle sammenlignet med rammede pæle. Derfor er det nødvendigt at udvide den eksisterende viden om den komplekse interaktion mellem jord og pæl langs borede pæle.

Tidligere studier har påvist, at interaktionen mellem jord og pæl langs borede pæle påvirkes af "fastlåste" forskydningsspændinger (også kendt som residuale spændinger), der opstår under installationen af pælene. Desuden viser studier, at den maksimale overflademodstand kan beregnes ved hjælp af α-metoden, som er en metode baseret på total spændingsanalyse. Her ser det ud til, at der er en sammenhæng mellem maksimal overflademodstand og udrænet forskydningsstyrke.

I denne afhandling bliver den komplekse interaktion mellem jord og pæl langs borede pæle i dansk eocen ler undersøgt. Testområdet er beliggende i Hinge, Jylland, Danmark, hvor leret karakteriseres som stift, overkonsolideret og meget fed. Der tages udgangspunkt i et fuldskalaforsøgsprogram bestående af otte borede pæle. Effekten af installationen af pælene, herunder de residuale spændinger, bliver undersøgt med særlig fokus på deres indflydelse på den mobiliserede overflademodstand.

Sammenhængen mellem overflademodstand og udrænet forskydningsstyrke, repræsenteret ved den empiriske adhæsionskoefficient α, undersøges. Resultaterne bliver relateret til det danske nationale anneks til Eurocode 7. Den empiriske adhæsionskoefficient α er blevet bestemt til at være mellem 2,2 og 3,3 gange højere end værdierne angivet i det danske nationale anneks til Eurocode 7 for de otte borede pæle i testområdet i Hinge. Dette indikerer, at den empiriske adhæsionskoefficient α, der er angivet i det danske nationale anneks til Eurocode 7, muligvis ikke afspejler borede pæles opførsel korrekt, hvilket understreger behovet for fortsat forskning og udvikling på dette område for at opnå mere præcise og robuste metoder inden for geoteknisk projektering.

Slutteligt undersøges, hvorvidt kapaciteten af borede pæle øges med tiden. Den aksiale pælebæreevne for borede pæle er blevet bestemt til at øges med 12 % per tidsdekade. Tendensen er dog svag med en R^2 værdi på 0.48. Dette indikerer, at der er behov for yderligere data bestemt på forskellige tidspunkter efter installation for at forbedre evnen til at kunne forudsige udviklingen at den aksiale pælebæreevne over tid.

Måledata fra de statiske belastningsforsøg på de otte borede pæle i testområdet i Hinge er blevet anvendt til at udvikle en analytisk model, der kan bestemme fordelingen af flytninger og laster langs overfladen af de borede pæle. Den analytiske model har fleksibilitet til at inkludere eller udelukke virkningen af residuale spændinger, alt efter behov.

Derudover er der blevet udviklet en metode til at estimere mobiliseringen af overflademodstanden, repræsenteret ved last-flytningskurver, baseret på egenskaberne af den danske Eocæne ler fra Hinge-testområdet. Dette værktøj er nyttigt i praksis til en indledende vurdering af, hvordan flytningsfordelingen og lasterne fordeler sig langs overfladen af borede pæle.

Baseret på de udførte forsøg er det blevet observeret, at de residuale spændinger har en betydelig indflydelse på den mobiliserede overflademodstand langs borede pæle. Derfor er det vigtigt at tage højde for residuale spændinger, når der foretages ændringer såsom at afkorte, forlænge eller ændre pælediameteren af borede pæle, baseret på den mobiliserede overflademodstand i de enkelte jordlag.

Det skal dog bemærkes, at residuale spændinger ikke påvirker den samlede overflademodstand for borede pæle.

Thesis details

Thesis title: Soil-pile interaction for bored cast-in-situ piles in stiff clays

PhD student: Jannie Knudsen

Supervisors: Professor (Docent) Kenny Kataoka Sørensen, Aarhus university
Technical Director, Professor Jørgen S. Steenfelt, COWI A/S, Kgs. Lyngby
Leading specialist Helle Trankjær, COWI A/S, Aarhus

This thesis has been submitted as part of the requirements for the completion of a PhD degree. It is structured as a monograph, but some specific aspects related to the historical background and preliminary results have been published as separate papers. These papers can be found in the "Published papers" section of the thesis.

The PhD student interpreted and presented results obtained from pile loading tests in tension conducted on bored test piles. The PhD student investigated the application and performance of Rayleigh-based fibre optic strain cables and provided insights into the lessons learned from this analysis. Additionally, the student performed an in-depth analysis of the field test results to gain a comprehensive understanding of the behaviour and performance of bored piles, particularly in relation to residual stresses and their implications for design considerations. Moreover, the PhD student proposed an analytical model that considers relevant factors such as soil characteristics and residual stresses, providing a framework for determining the distribution of displacements and forces along the shaft of bored piles.

The following collection of scientific papers have been published by the PhD student in collaboration with co-authors:

- Knudsen et al., 2019. " Design of bored piles in Denmark - a historical perspective" In ECSMGE 2019 Reykjavik. *Proceedings of the XVII European Conference on Soil Mechanics and Geotechnical Engineering – Geotechnical Engineering foundation of the future.* ISBN: 978-9935-9436-1-3. doi: 10.32075/17ECSMGE-2019-0732.
- Knudsen et al., 2019. " Tension tests on bored instrumented piles installed in marine Eocene clay" In NGM 2020 Helsinki (on-line conference). *Proceedings of the 18th Nordic geotechnical Meeting – IOP Conf. Series: Earth and Environmental Science.* doi: 10.1088/1755-1315/710/1/012034.

As part of the assessment, co-author statements have been made available to the assessment committee and are also available at the faculty. The published papers are discussed in the thesis along with other results obtained during the PhD project.

The thesis is based on an extensive field-test program conducted at a designated test site in Hinge, Jutland, Denmark. The research involved planning and collection of data from the field tests as well as subsequent analysis of the obtained data. Due to the large amount of data, Excel was found to be unstable and unsuitable for data analysis. Instead, the student utilized Spyder (Python) for programming and data analysis purposes. The scripts used for the analysis can be obtained by contacting the author via email: jahs@cowi.com.

During the field-test programme the PhD student actively planned, executed and supervised according to the following descriptions:

- Planning of all geotechnical investigations, laboratory tests and pile loading tests.
- Supervision of geotechnical ground investigations consisting of three geotechnical boreholes with field vane test and intact B-tubes, six adjacent boreholes for collecting intact samples in A-tubes (Shelby type) for advanced laboratory testing as well as four Cone Penetration Tests (CPTu) performed by Aarsleff A/S.
- Continuous measurements of ground water tables.
- Supervision of geological description of samples and preparation of geotechnical borehole profiles performed by COWI.
- Geotechnical classification tests on B tubes in terms of water content and unit weight.
- Specifications for advanced laboratory testing on A tubes in terms of oedometer tests (IL), triaxial compression (CIU) tests, Atterberg limits, calcite content and particle density performed by GEO.
- Learned to operate the fibre optic analyser (ODiSI) and switch.
- Instrumented the reinforcement cage with tell-tales, strain gauges and fibre optic cables.
- Provided specifications for development and installation of a flat jack under two of the test piles performed by Aarsleff A/S
- Supervised the installation of the test piles performed by Aarsleff A/S.
- Continuous measurement of strain gauges and fibre optic cables before installation of the test piles, during installation and casting of the concrete and after installation, while the concrete cured.
- Continuous measurements of tell-tales, strain gauges and fibre optic cables before, during and after the static pile loading tests.

Furthermore, the PhD student had assistance according to the description below:

- COWI designed the reinforcement and concrete for the test piles and performed a theoretical calculation of the axial pile stiffness.
- DMT GmbH, Germany performed static pile loading test in tension on the test piles.

Preface

This thesis represents the culmination of the industrial PhD project titled "Soil-pile interaction for bored cast-in-situ piles in stiff clays." The project was carried out from June 2018 to November 2024 (extended due to sick leave) in collaboration between Aarhus University, Department of Civil and Architectural Engineering, and COWI A/S. The successful completion of this work would not have been possible without the assistance and support of numerous individuals.

I would like to express my gratitude to my supervisors, Professor (Docent) Kenny Kataoka Sørensen from Aarhus University, Department of Civil and Architectural Engineering, Technical Director Jørgen S. Steenfelt and Leading Specialist Helle Trankjær from COWI A/S. Their support, technical discussions, and guidance over the past six years have been invaluable.

Special thanks are also due to my managers at COWI, Vice Presidents Michael Grøne Andersson (-2020), Helle Bøhl-Møller (2020), Vibeke Poulsen (2020-2024), and the Heads of Sections David Ross Alvin (-2021), Bjørn Staghøj Roesen (2021-2024) and Søren Madsen (2024-), for granting me the opportunity to pursue a PhD degree. Additionally, I am grateful to Carsten Sandgaard Christensen for his assistance in managing the time schedule for the PhD project.

In addition to the acknowledgements already mentioned, I would like to express appreciation to Innovation Fund Denmark and COWIfonden for providing partial funding for the project. Their support has been invaluable.

Special thanks are also due to Aarsleff A/S for funding and conducting geotechnical ground investigations, test piles, and static pile loading tests (performed by DMT). I am grateful to Leca Denmark A/S for generously making the designated test site in Hinge, Jutland, Denmark available throughout the entire duration of the PhD project.

I would like to extend my gratitude to Dr. Fellenius for taking the time to correspond with me and provide valuable insights on data analysis of the field test results.

I am indebted to my fellow PhD students at Aarhus University and my colleagues at COWI in Aarhus for creating a stimulating work environment filled with productive discussions and valuable input. Special thanks go to MSc students Camilla Gillibrand and Victor Kirchberg Hvoldal Nielsen for their assistance in the field during instrumentation and/or static pile loading tests on the test piles.

I would like to express gratitude to my family and friends for their unwavering support and encouragement throughout the past six years. Lastly, I want to dedicate this thesis to my husband Jimmy and my two children, Silje and Noah, for their immense love and support during the entire duration of my PhD project.

Jannie Knudsen, Vejle, November 15th, 2024

Contents

Abstract ii

Resumé iv

Thesis details vi

Preface viii

Contents ix

Nomenclature xii

1 Introduction 1

1.1 Aims of study 1
1.2 Methodology 3
1.3 Thesis Outline 5

2 Soil-pile interaction for bored piles in stiff clay 8

2.1 Installation effects and residual stresses 9
2.2 Prediction of ultimate shaft resistance 16
2.3 Linking α with undrained shear strength 21
2.4 Time effects on pile capacity 29
2.5 Load-movement response 36
2.6 Main findings of the published literature 52

3 Test site and soil characterization 55

3.1 Test site 55
3.2 Geology 56
3.3 Geotechnical investigations 57
3.4 Ground conditions 59
3.5 Index parameters for Søvind Marl 61
3.6 Total strength parameters for Søvind Marl 64
3.7 Effective strength parameters for Søvind Marl 67

3.8 Deformation properties for Søvind Marl 70
3.9 Groundwater conditions 73
3.10 Soil parameter overview for Søvind Marl 74

4 Methodology for field tests 76

4.1 Test programme 77
4.2 Test pile specifications 78
4.3 Instrumentation of test piles 79
4.4 Test setup 80
4.5 Loading procedures 81

5 Post-processing of data 84

5.1 Failure load definition 84
5.2 Data interpretation from tell-tales 85
5.3 Data interpretation of measured strains from strain gauges 85
5.4 Data interpretation of measured strains from fibre optic cables 87
5.5 Unit shaft resistance 88
5.6 Elastic lengthening of test piles 90
5.7 Shear stiffness 91

6 Results from field tension tests on bored piles 92

6.1 Temperature measurements 92
6.2 Observed behaviour from static pile loading tests 97
6.3 Mobilisation of shaft resistance 114

7 Rayleigh based fibre optic distributed line sensors 138

7.1 Application of distributed fibre optic sensing systems 138
7.2 Fibre optic sensing system 144
7.3 Validation of fibre optic temperature cables 149
7.4 Performance of Rayleigh based fibre optic strain cables 160
7.5 Lessons learned 190

8 Analysis of field test results 192

8.1 Residual stresses 192
8.2 Influence of residual stresses on load transfer curves 211
8.3 Influence of time 219

8.4 Linking unit shaft resistance with undrained shear strength 225

9 Analytical model for bored piles in stiff clays 237

9.1 Overview 238
9.2 Hyperbolic non-linear loading model (HN model) 240
9.3 Hyperbolic non-linear loading model incl. residual stresses (HNr model) 248
9.4 Prediction of load transfer curves based on soil properties 256

10 Conclusion and future works 265

10.1 Distributed fibre optic sensing systems 265
10.2 Residual stresses 266
10.3 Development of axial pile capacity with time 268
10.4 Determination of empirical adhesion coefficient using the field vane strength 269
10.5 Hyperbolic non-linear loading models 271
10.6 Prediction of load transfer curves 272
10.7 Future works 273

Bibliography 275

Published papers 286

Nomenclature

Definitions

$BODTA$	Brillouin Optical Time Domain Analysis
$BODTR$	Brillouin Optical Time Domain Reflectometer
CE	Extremely High Plasticity Clay
CFA	Continuous Flight Auger
CH	High Plasticity Clay
CID	Isotropic consolidated drained triaxial compression test
CIU	Isotropic consolidated undrained triaxial compression test
CL	Low Plasticity Clay
CM	Medium Plasticity Clay
CPT	Cone Penetration Test
$CPTu$	Cone Penetration Test with porewater pressure measurement
CRP	Constant Rate of Penetration. Test method used for field testing of bored piles, where a constant rate of penetration is achieved
CRU	Constant Rate of Uplift. Test method used for field testing of bored piles, where a constant rate of uplift of the pile top is achieved
CS	Super High Plasticity Clay
CV	Very High Plasticity Clay
DFOS	Distributed Fibre Optic Sensing
FOC	Fibre Optic Cables
FOS	Fibre Optic Switch
FOSA	Fibre Optic Spectrum Analyser
FOSC	Fibre Optic Strain Cables
FOTC	Fibre Optic Temperature Cables
HD	High-Definition
IU	Interrogation Unit
LAE	Low Air Entry
ML	Maintained Load. Test method used for field testing of bored piles, where the load is applied in incremental steps and maintained for a given period

$OFDR$	Optical Frequency Domain Reflectometry
$SCPTu$	Seismic Cone Penetration Test with porewater pressure measurement
SEM	Scanning Electron Microscopy
SG	Strain Gauges
TT	Tell-Tales
UC	Unconfined Compression test
USCS	Unified Soil Classification System
UU	Unconsolidated Undrained triaxial test
VWSG	Vibrating Wire Strain Gauges

Roman symbols

a	Slope of a straight line from the tangent method
a_c	Cone area ratio
A_b	Pile base area
A_p	Cross-sectional area of pile
A_s	Shaft surface area of pile
A_t	Rate coefficient depending on soil type related to increase of pile capacity with time
b	Y-intercept of a straight line from the tangent method
B_q	Pore pressure ratio
$B\ units$	Linear digits from datalogger (frequency squared divided by 1000)
c	Slope of a straight line from the direct secant method
c'	Apparent effective cohesion from the Mohr Coulomb strength equation
c_{fv}	Field vane strength
c_k	Consolidation coefficient (Danish terminology; internationally c_v)
c_u	Undrained shear strength
c_u^{CIU}	Undrained shear strength determined by isotropic consolidated undrained triaxial compression (CIU) test
$c_{u,a}$	Average undrained shear strength along the length of a pile
$c_{u,intact}$	Intact undrained shear strength

d	Y-intercept of a straight line from the direct secant method
d_s	Sample depth
D_p	Pile diameter
e_0	Void ratio
E_{oed}	Oedometer modulus
E_p	Young's modulus
E_pA_p	Axial pile stiffness
E_sA	Secant modulus (Axial secant stiffness)
E_tA	Tangent modulus (Axial tangent stiffness)
f	Frequency
F	Axial force (either back calculated or determined by the load transfer method)
F_c	Compressive pile load
$F_{measured}$	Axial force back calculated from the measured data
F_{model}	Axial force determined by the load transfer method
F_{res}	Residual load
F_t	Tensile pile load
G	Secant shear modulus
G^*	Normalised secant shear modulus
G_0	Initial linear elastic shear modulus / small-strain shear modulus
G_{pile}	Shear modulus of the pile-load response
G_s	Particle density
$\overline{G_{si}}$	Average shear modulus of the soil element
G_{shaft}	Shear modulus of the load transfer function
h_p	Pressure height
i	Indicator for pile element/soil layer no. E.g., R_{si} is the shaft resistance from pile element no. i or c_{ui} is the undrained shear strength for the i'th soil layer.
I_p	Plasticity index
k	Reduction factor (0.3 for bored piles)
k_p	Coefficient of permeability

k_s	Rate of creep
K_b	Axial spring stiffness representing the soil-pile interaction at pile base
K_0	Coefficient of earth pressure at rest
K_s	Axial spring stiffness representing the soil-pile interaction along the pile shaft
K_{sv}	Ratio of σ_s' / $\sigma_{v,0}'$
L_f	Length of fibre optic cable
L_p	Pile length
m	Material factor (1.0 for concrete)
M	Inclination of the failure envelope in the p'-q plot
M_w	Mass of water
M_s	Mass of solids
N	Indicator for strain gauge level no. E.g., F_N is the axial force (back calculated) at strain gauge level no. N
N_{kt}	Cone tip reduction factor
N_{kt}^{cfv}	Cone tip reduction factor in relation to measured field vane strength
OCR	Over consolidation ratio
p'	Mean effective stress
p_a	Atmospheric pressure (~101.3 kPa)
p'_{sat}	Isotropic effective stress during saturation
q	Deviator stress
q_0	Failure envelopes intersection with the y-axis in the p'-q plot
q_c	Cone resistance
q_{net}	Net cone resistance
q_t	Corrected cone resistance
Q	Load applied during pile loading test
Q_{max}	Maximum load applied during pile loading test
Q_t	Axial pile capacity at time t
Q_0	Axial pile capacity at time t_0
Q_{30}	Axial pile capacity after 30 days (1 month)

r	Distance from the centre of the pile
r_m	Maximum distance beyond which settlements are negligible
r_{peak}	Unit shaft resistance (peak value)
r_r	Regeneration factor due to remoulding of clay (0.4)
r_s	Unit shaft resistance
$r_{s,a}$	Average unit shaft resistance along the length of a pile
$r_{s,o}$	Observed unit shaft resistance
$r_{s,t}$	"True" unit shaft resistance
r_t	Unit shaft resistance at time t
r_0	Unit shaft resistance at time t_0
R_b	Base resistance
$R_{b,k}$	Characteristic value of base resistance
R_c	Pile resistance under compressive loads
$R_{c,d}$	Design value of pile resistance under compressive loads
$R_{c,k}$	Characteristic value of pile resistance under compressive loads
R_f	Friction ratio
R_{peak}	Shaft resistance (peak value)
R_s	Shaft resistance
$R_{s,k}$	Characteristic value of shaft resistance
R_t	Pile resistance under tensile loads
R_{target}	Shaft resistance (target value)
$R_{t,d}$	Design value of pile resistance under tensile loads
$R_{t,k}$	Characteristic value of pile resistance under tensile loads
s	Settlement of soil
s_s	Settlement of soil at the pile shaft
s_{cal}	Linear calibration factor for strain gauges in (micro) strain / digit
t	Time
t_0	Empirical initial time value
t_{90}	Time to 90 % dissipation in hydration temperatures

t_{peak}	Time to peak temperature, where the initial set of concrete is assumed to be complete
T	Temperature
T_{peak}	Peak temperature, where the initial set of concrete is assumed to be complete
T_{si}	The force along the length of the pile shaft that results in a specific settlement of soil at the pile shaft
u	Porewater pressure
u_2	Porewater pressure measured on the cone shoulder
V	Volume of a soil sample
V_s	Shear wave velocity
w_l	Liquid limit
w_{nat}	Natural water content
w_{pl}	Plastic limit
W	Weight of soil sample
W_p	Weight of pile
z	Distance from pile top
z_d	Depth below ground level
z_w	Depth of groundwater table below ground level

Greek symbols

Δ	Operator indicating change of a value. E.g., ΔT is change in temperature
α	Empirical adhesion coefficient
α_{cfv}	Empirical adhesion coefficient with field vane strength, c_{fv}, as reference
α^{CIU}	Empirical adhesion coefficient derived from undrained shear strength determined by isotropic consolidated undrained triaxial compression (CIU) test
α_{intact}	Empirical adhesion coefficient with intact undrained shear strength, $c_{u,intact}$, as reference
α_L	Linear coefficient of thermal expansion
α_{LCPC}	Empirical reduction factor
β	Semi-empirical adhesion coefficient
β_S	(Semi-logarithmic) rate parameter in shearing

β_{1D}	(Semi-logarithmic) rate parameter in 1D compression
γ	Shear strain or bulk unit weight
$\dot{\gamma}$	Shear strain rate
γ_b	Partial safety factor valid for base resistance
γ_c	Bulk unit weight of concrete
γ_f	Shear strain at failure (paired with τ_f)
$\gamma_{M=2}$	Reference strain to half the mobilisation
γ_{ref}	Reference shear strain
γ_s	Partial safety factor valid for shaft resistance (compressive loads)
$\gamma_{s,t}$	Partial safety factor valid for shaft resistance (tensile loads)
γ_w	Bulk unit weight of water
δ	Vertical displacement at pile top or tell-tale level
δ_c	Vertical displacement at pile top, where the shaft resistance is fully developed
$\dot{\delta}_{creep}$	Displacement rate during creep
$\delta_{measured}$	Displacement paired with $F_{measured}$
δ_{model}	Displacement paired with F_{model}
δ_{peak}	Displacement paired with R_{peak} or r_{peak}
$\delta_{pile,e}$	Elastic lengthening of the test pile
$\delta_{pile,soil}$	Relative vertical displacement between pile and soil
δ_{target}	Displacement paired with R_{target}
$\dot{\delta}_{uplift}$	Pile uplift rate
ε	Axial strain
$\dot{\varepsilon}$	Strain rate
ε_a	Average axial strain between two locations
ε_{mech}	Mechanical strain (also referred to as measured strains corrected for thermal influence, ε_t)
ε_{pseudo}	Pseudo strain (displacements normalised relative to the pile diameter)
ε_r	Measured strain (raw data)
$\varepsilon_{r,a}$	Average value of the measured strain (raw data)

ε_t	Measured strain corrected for thermal influence
$\varepsilon_{t,a}$	Average value of the measured strain corrected for thermal influence from two strain gauges/fibre optic cables on either side of the neutral axis
$\varepsilon_{thermal}$	Thermal induced strain
ε_{total}	Total strain (also referred to as measured strains, ε_r, from raw data)
k	Strain conversion factor (strain/frequency)
k_T	Temperature conversion factor (°C/frequency)
λ	Pile length factor
μ	Correlation factor, ratio of c_u^{CIU} / c_{fv}
ν_S	Spectrum in a fibre optic strain cable
ν_T	Spectrum in a fibre optic temperature cable
ξ	Correlation coefficient cf. DS/EN_1997-1_DK_NA (2021)
ρ	Soil mass density
σ	Stress
σ_f'	Effective normal stress at failure
σ_h'	Effective horizontal stress
$\sigma_{h,0}$	Pre-existing total horizontal stress (in situ stress)
$\sigma_{h,0}'$	Pre-existing effective horizontal stress (in situ stress)
σ'_{pc}	Effective pre consolidation stress
σ_s'	Radial effective stress
σ_v'	Effective vertical stress
σ_{vm}'	Mean vertical effective stress over the depth of the pile
$\sigma_{v,0}$	Pre-existing total vertical stress (in situ stress)
$\sigma_{v,0}'$	Pre-existing effective vertical stress (in situ stress)
τ	Shear stress
$\bar{\tau}$	Average shear stress
$\bar{\tau_0}$	Average shear stress at the pile shaft
τ_f	Shear strength at failure
τ_{mob}	Mobilised shear strength

φ'	Effective angle of shearing resistance
$tan(\delta)$	Effective coefficient of friction between pile shaft and clay

Function coefficients

α_c	Function coefficients (curvature parameter) for the Vardanega and Bolton method to estimate non-linear shear stiffness
a, b, c	Function coefficients for the Zhang function
A, B	Function coefficients for the Vardanega and Bolton shear strength mobilisation function
A_0, B_0, V	Function coefficient for the Vijayvergiya function
C_1, C_2	Function coefficients for the Hansen 80 % function
F, M	Function coefficients for the Rahman function

1 Introduction

In Denmark, there is a growing trend towards the increased usage of bored cast-in-situ piles as a foundation method. These piles are also referred to as bored piles, cast-in-situ piles, drilled shafts, or drilled piers. While driven precast concrete piles have traditionally been widely utilized and continue to be used extensively, there is a shift towards a more frequent adoption of bored cast-in-situ piles in construction projects. This change is driven by various factors, including the need to address the challenges posed by geotechnically demanding areas, requirements to minimize noise and vibration in populated regions, as well as the construction of taller and more complex buildings with larger loads and stricter demands on foundation stiffness. For consistency and convenience, the term "bored piles" will be used throughout this thesis.

1.1 Aims of study

The primary objective of this PhD project is to enhance the existing understanding of the complex soil-pile interaction along the length of bored piles, specifically focusing on the shaft resistance in stiff clays, in connection with installation, set-up, and during and after the pile loading tests. The overall research aims of this study are summarized in the following research questions:

- Can detailed and accurate measurements be obtained to enhance the reliability of the findings by utilizing fibre optic based distributed line sensors embedded in bored piles? Fibre optic sensors have the potential to provide high-resolution measurements along the length of the pile, allowing for a more comprehensive understanding of the soil-pile interaction behaviour. Using fibre optic sensors, it is anticipated that a deeper insight into the behaviour of bored piles can be achieved, leading to more reliable findings and improved understanding of the soil-pile interaction mechanisms.

- How is the soil-pile interaction along the shaft of bored piles influenced by pile installation, specifically examining whether it leads to the development of "locked-in" shear stresses on the pile shaft, which are commonly referred to as residual stresses? Understanding the presence and effects of residual stresses is crucial for accurate analysis and design of bored piles. They can impact the load distribution, mobilised shaft resistance, and overall behaviour of the pile under different loading conditions. By exploring these influences, this research aims to provide insights into the significance of residual stresses and their role in the soil-pile interaction along the shaft of bored piles.

- How is the pile capacity influenced by the time from installation to testing, commonly referred to as setup? Setup refers to the phenomenon where the pile's capacity increases over time after installation. Understanding the behaviour and magnitude of setup is crucial for accurately estimating the long-term load-carrying capacity of bored piles. By examining the time-dependent increase in pile capacity, this research aims to provide insights into the mechanisms and

contributing factors of setup, as well as its influence on the overall performance and behaviour of bored piles over time.

- Is there a linkage between the shaft resistance of bored piles and the undrained shear strength of the surrounding soil? Understanding the relationship between the undrained shear strength and the shaft resistance of bored piles is crucial for accurate design and assessment of pile foundations. This analysis will help evaluate the appropriateness and reliability of the current design guidelines, allowing for potential improvements or adjustments to design practices if needed.

- Is it possible to develop an analytical modelling of the distributions of displacements and forces along the shaft of bored piles? This modelling aims to provide insights into the behaviour and response of the piles under different loading conditions. The research will examine how the inclusion of residual stresses affects the predictions of the analytical models, such as changes in the distribution of displacements and forces along the pile shaft. This analysis will help evaluate the significance of residual stresses and their role in influencing the overall behaviour of bored piles.

- Can the load transfer functions for the analytical model be predicted based on soil properties? Load transfer functions describe the relationship between the applied load and the resulting forces and displacements along the shaft of bored piles. These functions are crucial for analysing the behaviour and response of the piles under different loading conditions. The research aims to develop methodologies or empirical relationships to predict load transfer functions for bored piles based on the available soil properties. This allows for a more accurate and reliable representation of the behaviour and response of bored piles in relation to applied loads. By establishing these predictions, engineers can make informed decisions regarding the design and evaluation of bored pile foundations, considering the specific soil characteristics at a given site.

Due to complications encountered during the field-testing program, two studies were omitted from the research:

- The first study, regarding pile capacity confirmation, aimed to utilize a flat jack applied at the base of the pile to verify its capacity. This method involves applying hydraulic pressure to the flat jack to induce stresses on the pile base, allowing for engaging of the shaft resistance in the opposite direction compared to the static pile loading test conducted in tension However, due to the complications encountered, this study could not be performed as originally intended.

- The second study, focusing on post-construction stressing, aimed to engage the base resistance of the pile to limit settlement or help compact loose or remoulded material at the pile base. Unfortunately, this study was also omitted due to the encountered complications.

Furthermore, two additional studies were initially planned but did not take place as the project's focus shifted towards the analysis of field test results and the development of the analytical soil-pile interaction model:

- The first planned study aimed to analyse the strain-rate-dependent stress-strain behaviour during a pile loading test. This study intended to assess how the chosen rate of penetration or uplift during the test affected the mobilised shaft resistance of the pile. Unfortunately, this study could not be carried out as originally intended.

- The second planned study involved conducting numerical finite element calculations in Plaxis, specifically in the 2D axisymmetric mode. The purpose of this study was to compare the results obtained from the analytical model with those from the numerical finite element analysis. However, due to the project's revised focus, this study was not undertaken.

1.2 Methodology

The field-test program consisted of conducting full-scale pile loading tests on eight bored piles in Eocene clay, which is a stiff over consolidated and very high plasticity clay. The objective was to investigate the complex soil-pile interaction along the length of the bored piles, specifically focusing on the shaft resistance. The test site was in Hinge, Jutland, Denmark.

To capture the soil-pile interaction behaviour, the eight test piles were instrumented with various measuring devices, including tell-tales, strain gauges, and fibre optic cables. This instrumentation allowed for continuous monitoring of the behaviour of the bored piles throughout the entire process, from boring to the casting and curing of the concrete, as well as before, during, and after the pile loading tests.

The purpose of this comprehensive monitoring was to document and analyse the complex soil-pile interaction along the shaft of the bored piles. The data collected during the field-test program provide valuable insights into the soil-pile interaction under different loading conditions.

To capture and document the soil-pile interaction, a range of specific instruments and equipment were utilized during the field-test program:

- Implenia 3 MN circular load cells were employed to measure the applied loads on the bored piles.
- HBM WA100-T displacement transducers were used to measure the movement of the pile top and the tell-tales.
- RST instruments data loggers with DT logger host software utilized in conjunction with Geosense VWS-4000 series vibrating wire sister bars, were employed to measure strains.
- LUNA fibre optic switch and optical distributed sensor interrogator, model ODiSI-B were used to manually read the data from the fibre optic strain and temperature cables.

By utilizing these instruments and equipment, the field-test program was able to capture critical data on applied loads, displacements, strains, and temperatures, facilitating the documentation and analysis of the complex soil-pile interaction.

The pile loading tests carried out as part of the field-test program were conducted as static pile loading tests in tension. This loading configuration was chosen to effectively isolate and assess the shaft resistance of the piles separately from the base resistance. By loading the piles in tension, the focus was specifically on investigating the behaviour and response of the pile shaft. The measurement and analysis of the shaft resistance were based on the results obtained from the static pile loading tests performed in tension.

In order to confirm the consistency of the shaft resistance derived from the static pile loading tests in tension, two of the test piles were equipped with a special flat jack installed at the pile base. By applying pressure to the base of the pile, the direction of the force reversed from pull at the pile top to pressure at the pile base in a manner similar to an O-cell test. The objective was to compare the results of the shaft resistance obtained from the flat jack test with those obtained from the static pile loading test in tension. This comparison was intended to validate and ensure consistency in the determination of the shaft resistance of the bored piles.

However, due to unforeseen circumstances, the flat jack test could not be carried out as planned. The test encountered issues shortly after the initiation of the pile loading test. As a result, the two test piles that were prepared for the flat jack test were instead subjected to static pile loading tests in tension, similar to the other test piles in the program.

The test piles were subjected to static pile loading tests in tension after different periods of rest, as part of the research program. The first two test piles were tested after a minimum of one month to ensure sufficient strength for the pile loading test. The remaining test piles were tested in pairs of three after six months and three years, respectively. By conducting the static pile loading tests at different intervals, the project was able to examine the behaviour and performance of the piles over time. This prolonged observation allowed for a more comprehensive understanding of the long-term capacity and response of the bored piles in the research study.

To characterize the soil and examine the relationship between the shaft resistance of the test piles and the undrained shear strength of the Eocene clay at the designated test site in Hinge, a comprehensive ground investigation was conducted. The ground investigation included Cone Penetration Tests (CPTu), geotechnical boreholes, field vane tests as well as both intact B-tube and A-tube (Shelby type) sampling for laboratory testing.

By combining the results of the ground investigations, groundwater measurements, and laboratory tests, the characterization of the soil and its properties, such as undrained shear strength, were established. This information played a crucial role in evaluating the current design practices for bored

piles in Denmark, allowing potential improvements or adjustments to be identified based on the specific soil conditions at the test site.

An analytical model for determining the distribution of displacements and forces along the shaft of bored piles was derived using Spyder IDE 5.4.3 with Python 3.8.10 64-bit | Qt 5.15.2 | PyQt5 5.15.9 on a Windows 10 operating system. The model was designed to incorporate the effects of residual stresses, if necessary, but it is limited to minor negative residual stresses resulting from downward movement of the pile.

The model is primarily based on data obtained from static pile loading tests performed in tension, as no static pile loading test in compression was conducted. Consequently, the unloading path of the compression phase is unknown. To address this limitation, the model assumes that the unloading path can be approximated as equal to the initial shear stiffness of the load transfer curves.

The derived analytical model allows for calculations of displacements and forces along the pile shaft, providing valuable insights into the behaviour and response of bored piles subjected to loading. However, it is essential to consider the limitations and assumptions inherent in the model, particularly regarding the inclusion of residual stresses and the compressive phase of the loading.

Two methods for predicting load transfer functions based on soil properties were investigated for Eocene clay at the designated test site in Hinge. These load transfer functions are integral components of the derived analytical model. The ability to predict load transfer functions using easily obtainable soil properties would provide a valuable tool for making initial estimates of displacement and force distribution along the shaft of bored piles in practical geotechnical engineering applications.

To validate and evaluate the findings, a literature review of previous studies on bored piles in stiff clays was conducted. This review served to compare the results obtained from the Eocene clay at the designated test site with existing knowledge and research in the field. By assessing the credibility and consistency of the findings, the review contributed to a comprehensive understanding of the behaviour and characteristics specific to the Eocene clay within the context of bored pile analysis and design.

1.3 Thesis Outline

The thesis is organized in the following manner:

- Chapter 2 examines previous research on soil-pile interaction concerning bored piles in stiff clay. It places special emphasis on Danish Søvind Marl, Danish Eocene clay, and London clay, in that specific order. This section introduces various methods that are subsequently applied for the analysis of the test data obtained from the designated test site in Hinge.
- Chapter 3 concentrates on the comprehensive field-test program conducted at the designated test site in Hinge. This chapter encompasses the thorough characterization of the site and soil,

including the stratification and geological description, index parameters, total strength parameters, effective strength parameters, and deformation properties. The aim is to provide a detailed understanding of the site conditions and soil properties relevant to the study.

- Chapter 4 presents the methodology utilized for the field tests, encompassing the test program, specifications and instrumentation of the test piles, test setup, and the loading procedures adopted. This chapter provide a comprehensive description of the approach and procedures employed to conduct the field tests, ensuring accurate and reliable data collection for further analysis and interpretation.
- Chapter 5 presents the post-processing of the measured test data obtained from tell-tales, strain gauges, and fibre optic strain cables. This chapter demonstrates the methodology used to determine various parameters, including axial pile stiffness, unit shaft resistance, elastic lengthening of the test piles, and shear stiffness.
- Chapter 6 presents the results obtained from the field tension tests conducted on the bored test piles. This chapter includes observations related to temperature, behaviour observed during the static pile loading tests, and the mobilization of shaft resistance along the length of the test piles. The findings and analysis presented in this chapter provide valuable insights into the behaviour and properties of the tested piles, contributing to a better understanding of their performance and interaction with the surrounding soil.
- Chapter 7 focuses on the utilization of Rayleigh-based fibre optic cables. This chapter delves into the state of the art regarding fibre optic sensing systems, details the specific fibre optic sensing system employed in the research, validates the functionality of the fibre optic temperature cables, assesses the performance of the fibre optic strain cables, and highlights the lessons learned throughout the study. By exploring these aspects, Chapter 7 provide a comprehensive understanding of the application and performance of Rayleigh-based fibre optic strain cables in the context of the research.
- Chapter 8 focuses on the analysis of the field test results obtained from the study. This chapter explores the evidence of residual stresses and their effects on the mobilised shaft resistance of the test piles. It also investigates the influence of time on the long-term pile capacity. Furthermore, the relationship between the shaft resistance of the test piles and the undrained shear strength of the Eocene clay from the designated test site in Hinge is established, and the evaluation is aligned with the current design practices for bored piles in Denmark. By examining these aspects, Chapter 8 contributes to a deeper understanding of the behaviour and performance of bored piles in relation to residual stresses and their implications for design considerations.
- Chapter 9 introduces the proposed analytical model for determining the distribution of displacements and forces along the shaft of bored piles. This model allows for the inclusion or exclusion of the effects of residual stresses as needed. Additionally, this chapter presents methods for predicting load transfer functions based on soil properties, specifically focusing on the Eocene clay from the designated test site in Hinge. The aim is to provide a framework for analysing and

predicting the behaviour of bored piles, considering relevant factors such as residual stresses and soil characteristics.

- Chapter 10 serves as a summary and conclusion of the present PhD project. This chapter provide a concise overview of the key findings, contributions, and implications of the research conducted. It highlights the main conclusions drawn from the study and offers recommendations for further research to build upon the current findings. The objective is to provide a comprehensive wrap-up of the PhD project, emphasizing its significance and suggesting potential paths for future investigations.

Reference list and published papers are located at the end of the thesis. Additional data and results of performed analyses are included in a separate Appendix.

2 Soil-pile interaction for bored piles in stiff clay

Soil-pile interaction has been a subject of intensive study for over a century, encompassing various aspects such as soil conditions, pile types, dimensions, installation methods, pile loading test methods, and interpretation methods. In the current study, the specific emphasis is on comprehending the intricate nature of soil-pile interaction along the shaft of straight shafted bored cast-in-situ piles that are installed in stiff clays. By focusing on this specific context, the research aims to enhance the understanding of the behaviour and performance of such piles within the complex soil conditions encountered in stiff clay formations.

A comprehensive literature review of previous studies has been conducted and is outlined in this section. The selected topics chosen are considered relevant for the analysis of the results presented in the subsequent sections of this thesis. The following topics have been selected and discussed:

- *Installation effects and residual stresses*
- *Prediction of ultimate shaft resistance*
- *Linking the empirical adhesion coefficient, α, with undrained shear strength,* c_u
- *Time effects on pile capacity*
- *Load-movement response*

In the literature review of previous studies, preference is given to studies originating from actual pile loading tests rather than laboratory tests. However, when applicable and relevant, studies based on laboratory tests are also included.

Comparable soil conditions are sought in the literature review, and they are prioritized in the following preferred order:

- *Søvind Marl from the actual test site (Hinge)*
- *Danish Søvind Marl*
- *Danish Eocene clay*
- *London clay (shares great resemblance with the Danish Eocene clay)*
- *Stiff and high plasticity clays in general*
- *Fine-grained soils in general*
- *Coarse-grained soils*

The focus is on finding studies that specifically investigate soil-pile interaction under similar soil conditions, which align with the Søvind Marl from the actual test site (Hinge) in the preferred order. This approach ensures that the literature review captures relevant research findings that directly relate to the soil conditions encountered in the present study.

When relevant, references are made to driven precast concrete piles, as the current design of bored piles in Denmark refers to the design principles and guidelines used for driven precast concrete piles.

By reviewing and discussing these selected topics, the thesis builds upon the existing knowledge and provide a solid foundation for the analysis and interpretation of the results presented in the subsequent sections.

2.1 Installation effects and residual stresses

During the installation of both driven and bored piles, the interaction between the pile and the soil can lead to the development of "locked-in" shear stresses, commonly referred to as residual shear stresses, acting on the pile shaft Fellenius (2002b).

In the case of driven piles, residual loads result from shear stresses developed between the pile and the soil as a result of driving due to the small downward soil movement relative to the pile particular in soft soil (i.e. negative skin friction) and the elastic rebound from the last impact particular in stiff soil. Residual shear stresses from driven precast piles manifest as positive shaft resistance in the upper part of the pile, which is counteracted by negative shaft resistance in the lower part of the pile, as well as some toe resistance. Additionally, the pile also exhibits a transition zone along an intermediate length. This transition zone encompasses the boundary between the positive shaft resistance above the neutral plane and the negative shaft resistance below the neutral plane (Fellenius, 2002a, Fellenius, 2002b, Fellenius, 2002c). This mechanism resembles the accumulation of dragload in a pile. The presence and importance of residual stresses are documented in several tests conducted on driven piles, e.g. Hunter et al. (1969), Hanna and Tan (1973), Holloway et al. (1978) and Fellenius (2002a).

For bored piles, residual loads result from pile installation and swelling or shrinkage of the concrete during curing (Hayes and Simmonds, 2002). During swelling (increase of pile volume) pile upwards movement and positive shaft resistance are generated in the upper part of the piles, while pile downwards movement and negative shaft resistance are generated in the lower part of the piles. During shrinkage (decrease of pile volume) the direction of pile movement and shear distribution is reversed (Mascarucci et al., 2013).

Unlike driven piles, the existence and significance of residual stresses are not as well-known or widely recognized for bored piles. One of the main reasons for this is the difficulty in discerning whether the measured strain in the bored pile originates from internal concrete processes or from the external processes of shear stresses developed between the pile and the surrounding soil. This ambiguity makes it challenging to attribute the measured strains solely to the effects of residual stresses (Flynn and McCabe, 2022a). Furthermore, the measurement of changes in soil and porewater pressure is not effective in supporting the interpretation of residual stresses. The narrow zone of disturbed soil surrounding bored piles (Meyerhof and Murdock, 1953) presents significant challenges, as the measurement process itself can introduce disturbances that impact the measurement results.

These challenges in directly measuring and attributing strains to the effects of residual stresses have limited the understanding of residual stress behaviour in bored piles. As a result, the mechanisms and magnitudes of residual stresses in bored piles are less well-understood and studied compared to driven precast concrete piles. The knowledge base surrounding the presence and behaviour of residual stresses in bored piles is limited, and only one experimental study was found that have confirmed their existence (Fellenius, 2002a).

The following sections provide a detailed account of how the soil-pile interaction along the shaft of bored piles is influenced by the pile installation process. It highlights the factors and mechanisms that come into play during installation and their effects on the interaction between the pile and the surrounding soil. Furthermore, three distinct methods for the interpretation of residual stresses are presented and their relevance in understanding the behaviour of the soil-pile system is considered. The subsequent discussions in these sections delve into how these residual stresses impact the load transfer curves along the pile shaft, shedding light on their significance in interpreting the load transfer mechanism.

2.1.1 Installation effects

During the installation of bored piles, various soil changes occur at different stages of the process. These processes can be described using cavity expansion and contraction theory as the stress relaxation during the excavation of a hole is analogous to a cylindrical cavity contraction (unloading) problem and subsequent concrete placement and axial loading resemble a cavity re-loading (i.e. expansion) problem (Lukose and Thiyyakkandi, 2022). The following is a description of the stress sequences involved for bored piles installed in stiff over consolidated and very high plasticity clay presented by Vardanega et al. (2012b):

a) Initial Stresses: Prior to the initiation of pile installation, there exist initial stresses at a depth, z_d, below the ground surface. The groundwater table is located at a depth, $z_d = z_w$.

b) Undrained Cavity Contraction: The borehole undergoes undrained cavity contraction from initial total radial stress, $\sigma_{h,0}$, to the mud pressure if drilled with bentonite fluid (or the pressure in the loosened soil around the installed casing). A reduction in total radial stress will set up negative excess porewater pressure in the soil around the pile.

c) Local Swelling and Softening: The installation process and the presence of the borehole lead to swelling and softening of the soil in the vicinity of the bored pile. This is a result of dissipation of negative excess porewater pressure and thereby reduction in radial effective stress, $\sigma'_{h,0}$.

d) Undrained Cavity Expansion: After the concrete is poured and the casing is removed, there is an expansion of the undrained cavity due to the pressure from the wet concrete, $\sigma_c = \gamma_c \cdot z$. An increase in total radial stress will lead to an increase in positive excess porewater pressure.

e) Reconsolidation: Radial transient flow occurs in the soil to restore the initial porewater pressure, u, in the soil. As time progresses, the dissipation of positive excess porewater will induce an increase in the effective radial stresses.

Uncertainties arise from variations in radial stress referred above, especially regarding the duration of softening during stress relief in the loosened soil around the installed casing and the subsequent time available for concrete hardening under wet concrete pressure.

In addition, it is important to note that bored piles, unlike driven precast concrete piles, undergo a curing process within the ground. During this curing process, chemical reactions take place within the concrete, resulting in volume changes. The extent of these volume changes is influenced by external environmental conditions such as soil and groundwater conditions, as well as the type of cement used (Flynn and McCabe, 2022a).

Typical cavity pressure (contraction / expansion) response during the different stages of construction and subsequent pile loading is presented in Figure 1.

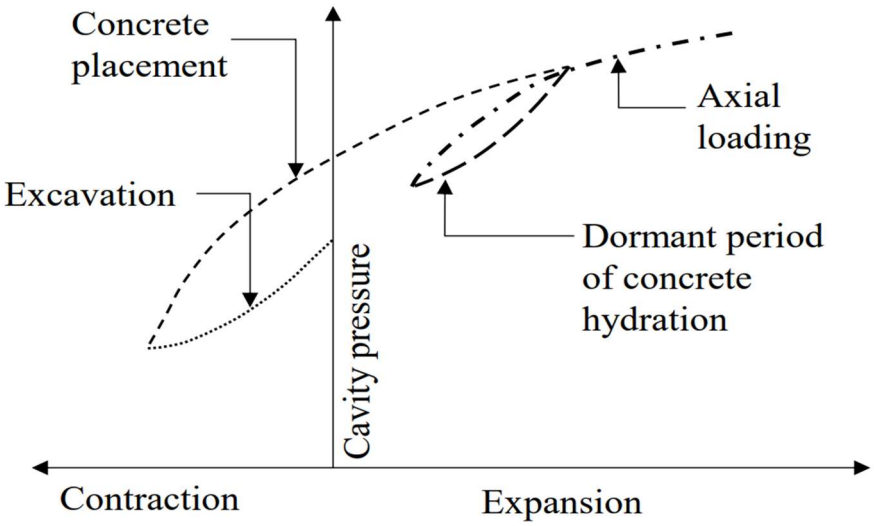

Figure 1: Cavity contraction / expansion analogy for pile construction and loading (Lukose and Thiyyakkandi, 2022).

Bored piles can be regarded as stress-free in their initial state, right after being cast, while the concrete is still in a fluid state and incapable of transferring shear stresses. Consequently, there are no shear stresses applied at the interface between the soil and the pile. Instead, the primary factor contributing to early soil-pile interaction is the shrinkage or swelling occurring during the curing process of the concrete, which induces a displacement field in both the radial and vertical directions.

Specifically, the displacement field in the radial direction originates from an increase (swelling) or reduction (shrinkage) of the pile's diameter:

An increase in pile diameter will lead to an increase in total radial stress, which will lead to an increase in positive excess porewater pressure in undrained conditions. As time progresses, the dissipation of

positive excess porewater will induce an increase in the effective radial stresses. In semi-drained conditions, an increase in the effective radial stresses will occur.

A reduction of the pile diameter will lead to a reduction in total radial stress and thereby negative excess porewater pressure will set up in the soil around the pile in undrained conditions. Consequently, local swelling and softening will develop in the soil around the bored pile over time as the negative excess porewater pressure dissipates and the effective radial stresses decreases. In semi-drained conditions, a decrease in the effective radial stresses will occur.

Additionally, the displacement field in the vertical direction, resulting from swelling or shrinkage of the concrete during curing, generates shear stresses on the pile shaft along its length. Due to the absence of any applied load on the pile during the curing process, these shear stress variations are balanced out in the vertical direction at a specific depth known as the neutral depth. Only limited literature is available on this subject, and reference is made to a numerical axial symmetric analysis dealing with single floating piles embedded in sandy silty soils and subjected to axial loading by Mascarucci et al. (2013), see Figure 2.

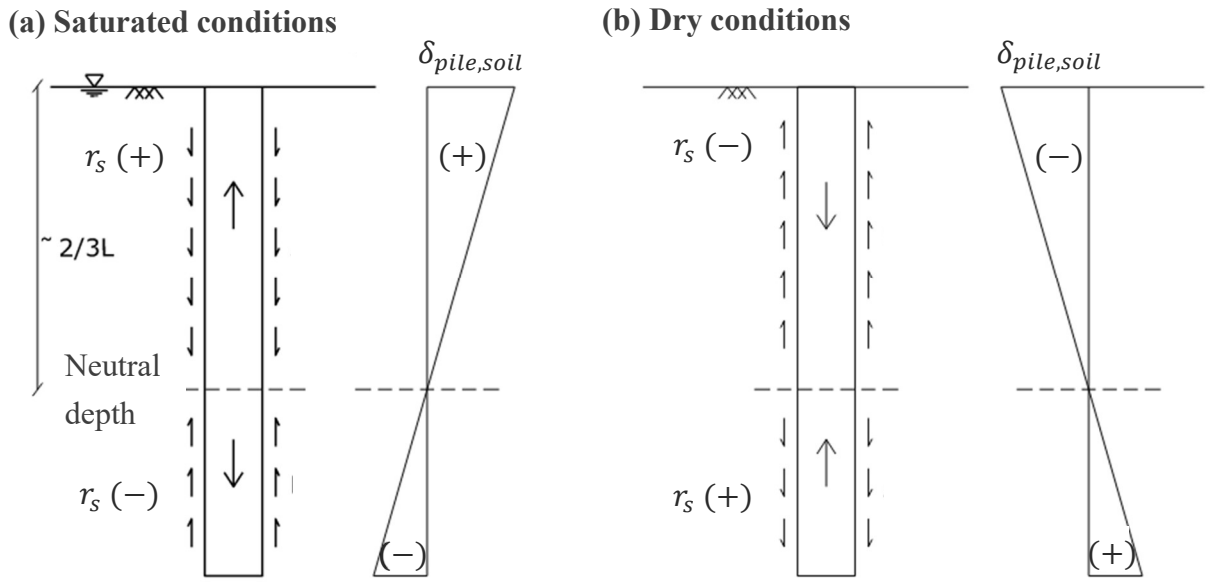

Figure 2: Effects of concrete curing on a floating pile in (a) saturated and (b) dry conditions modified after Mascarucci et al. (2013).

From Figure 2 it is seen, that when the surrounding soils are saturated, the curing process causes the concrete to swell, resulting in upward movement of the upper part of the piles (above the neutral depth) and downward movement of the lower part of the piles (below the neutral depth). Conversely, when the soils are dry, the curing process causes the concrete to shrink, leading to a reversed shear distribution.

Clearly, the issue being addressed is highly intricate and is influenced by various factors. The resulting effects can be substantially altered by different boundary conditions, such as the soil properties and groundwater conditions. It is worth noting that the presence of end-bearing piles

introduces a significant modification of the neutral depth. This adjustment occurs because the shaft resistance is balanced by the pile base, effectively shifting the neutral depth closer to the base of the pile.

Moreover, the position of the groundwater table plays a crucial role in determining whether the concrete undergoes shrinkage or swelling during the curing process. Additionally, the existence of low permeability clay can restrict the availability of water needed for swelling, even below the groundwater table.

2.1.2 Residual stresses

The incorporation of residual stresses into the analysis of pile response is a non-trivial aspect that deserves careful consideration. During a pile loading test, it is customary to reset all measurement values to zero just before initiating the test. However, a drawback of this practice is that residual stresses already exist prior to the pile loading test. Hence, in order to accurately account for residual stresses, it is imperative to commence measurements prior to the installation of bored piles and consistently carry out measurements throughout the entire installation and curing process.

Given that bored piles are cast in-situ, it is challenging to install strain measuring equipment directly at the pile-soil interface to obtain direct measurements of residual stresses. Consequently, the interpretation of residual stresses is based on internal strain measurements within the bored piles, where inverse analysis techniques is used to determine the corresponding residual stresses. Nevertheless, it is important to acknowledge that the interaction between the pile and surrounding soil is intricate, making it difficult to differentiate from the concrete-related processes that impact the internal pile strains during this period (Flynn et al., 2012, Flynn and McCabe, 2022a).

Generally, the concrete-related processes exhibit a predominant influence on the strain distribution during the initial stages after casting. This is attributed to the concrete setting, which leads to internal pile strain caused by phenomena like micro cracking due to temperature fluctuations, and chemical reactions within the concrete. On the other hand, long-term strain variations primarily occur due to moisture absorption and release by the pile shaft as the concrete cures. This causes the concrete to swell or shrink, consequently creating residual stresses along the length of the pile shaft. Furthermore, the long-term changes in strain are influenced by the recovery of the soil, encompassing both the set-up phenomenon and ageing effects, which occurs independently of and in parallel with the internal processes of the concrete (Flynn et al., 2012).

Methods for interpretation of residual stresses

In the literature, only a limited number of methods were found for determining and interpreting residual stresses for bored piles. Three of those methods, which include measurements prior to pile loading test, are presented below:

Method 1: Simplified method

The simplified method makes the assumption that the total change in strain occurring between concrete casting and the execution of a pile loading test is solely attributed to residual stresses (Kim et al., 2004). Therefore, strain gauge readings are only necessary immediately after concrete casting and before conducting the pile loading test. However, a limitation of this method is its inability to distinguish between internal pile strain from concrete setting, concrete curing (which produces residual stresses), and residual strains resulting from external forces like the recovery of the soil acting on the pile shaft.

Method 2: Pennington (1995)

The bored piles are assumed to be stress-free shortly after casting, specifically during the initial set at peak temperature. This assumption allows for the estimation of residual stresses by equating them to the change in strain between the peak temperature and the pile loading test (Pennington, 1995). Therefore, temperature measurements are required to identify the occurrence of the initial set and facilitate the determination of residual stresses.

Method 3: Siegel and McGillivray (2009)

The correction procedure is based on the assumption that residual loads can be considered negligible at or in close proximity to the top of the pile (Siegel and McGillivray, 2009, Kim et al., 2011). To obtain a strain profile that is independent of residual load effects, a set of strain gauges is placed at a designated reference level. This reference level allows for the comparison of strain profiles with the profiles measured at other levels of strain gauges. The point at which a strain profile deviates from the strain profile at the reference level indicates the onset of residual loads. The strain gauge at reference level then serves as a reference point for zero external load, even as internal stresses change to maintain equilibrium.

Comparison of interpretation methods

In a study conducted by Flynn et al. (2012), a comparison of different interpretation methods for derived residual loads in a driven cast-in-situ (DCIS) pile in mixed ground conditions was performed. The construction process of the pile involved top driving a hollow steel tube with a sacrificial driving shoe at the base. Following this, concrete was cast inside the tube, and reinforcement was subsequently installed to ensure the protection of the strain gauge instrumentation.

The development of residual stresses is depicted in Figure 3 is and is expected to be a combination of those resulting from a driven precast pile and a bored pile. Residual loads are anticipated to arise from shear stresses generated between the pile and the soil during the driving process of the hollow steel tube. Additionally, internal pile strains are expected due to the concrete setting and curing. However, residual loads are not anticipated to result from concrete swelling or shrinkage during the curing process, as the pile was cast inside a driven hollow steel tube.

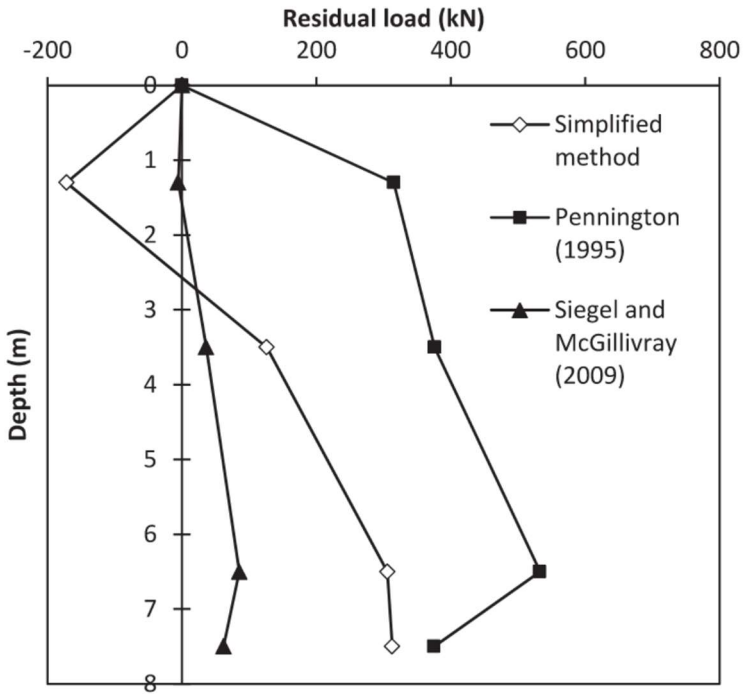

Figure 3: Comparison of derived residual loads using the interpretation methods given above for a driven cast-in-situ (DCIS) pile (Flynn et al., 2012).

It was found that the method proposed by Siegel and McGillivray (2009) produced the most realistic results. The derived residual load distribution from this method closely matched the drag load expected to develop due to development of negative skin friction resulting from consolidation in the silty clay and peat.

A similar study conducted by Flynn and McCabe (2022b) focused on two driven cast-in-situ (DCIS) piles in different soil conditions such as uniform sand and layered soils (clay, peat, sand and gravel). The study also concluded that the method proposed by Siegel and McGillivray (2009) provided the most realistic results in terms of derived residual loads.

Regrettably, a comparative analysis of the three interpretation methods for bored piles could not be located within the existing literature. Hence, it would be beneficial to explore and apply these methods specifically to bored piles to expand the understanding and improve the ability to interpret residual stresses in bored piles.

2.1.3 Effect of residual stresses on piles response to loading

Residual stresses exert a significant influence on the pile's response to loading, and addressing this issue requires careful consideration due to its complexity. This phenomenon can be addressed using load transfer curves ((Mascarucci et al., 2013, Fellenius, 2015).

The impact of residual stresses on load transfer curves, specifically the relationship between unit shaft resistance, r_s, and the relative vertical displacement between the pile and the soil, $\delta_{pile,soil}$, is visually demonstrated in Figure 4.

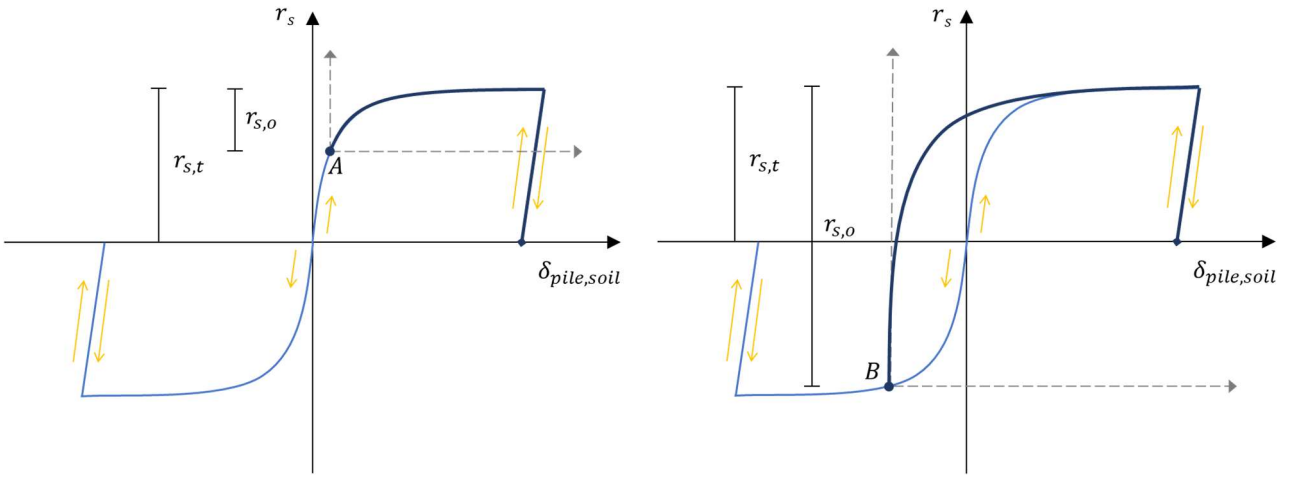

Figure 4: Effect of residual stresses on load transfer curves. Observed load transfer curves displayed with dotted grey axes and "true" load transfer curves displayed with solid black axes.

The "observed" load transfer curve in Figure 4 represents the load transfer curve derived directly from measured data, such as strain measurements during pile loading test. In this case, all strain measurements are reset to zero immediately before initiating the pile loading test.

On the other hand, the "true" load transfer curve represents the load transfer curve that would be observed in an ideal scenario, where all residual stresses acting on the pile at the start of the pile loading is accounted for. Hence, the residual stresses correspond to a point (A or B) on the "true" load transfer curves.

Point A represents a condition with positive residual stresses (upward pile movement), where the "observed" unit shaft resistance, $r_{s,o}$, is smaller than the "true" unit shaft resistance, $r_{s,t}$ ($r_{s,o} < r_{s,t}$).

Point B represents a condition with negative residual stresses (downward pile movement), where the "observed" unit shaft resistance, $r_{s,o}$, is larger than the "true" unit shaft resistance, $r_{s,t}$ ($r_{s,o} > r_{s,t}$).

2.2 Prediction of ultimate shaft resistance

The design of shaft resistance for bored piles in relation to the ultimate limit state is based on the bearing-capacity theory. In this theory, the shaft resistance for piles in clay can be calculated by multiplying the average adhesion along the pile shaft by the shaft surface area (Terzaghi, 1943).

The determination of shaft resistance can be done using either a total stress analysis, an effective stress analysis or a combination of the two. There are several specific methods commonly used for this purpose, including the α method, the β method, the λ method, and the Cone Penetration Test (CPT) method. These methods are presented in the following section.

In Denmark, the design of bored piles follows specific guidelines and regulations. These are presented subsequent, to determine whether the current design practices of bored piles in Denmark align with the shaft resistance determined from field tests.

2.2.1 Total stress analysis and effective stress analysis

The subsequent section details how the total stress analysis, the effective stress analysis or a combination of the two can be further specified into specific methods such as the α method, the β method, the λ method, and the Cone Penetration Test (CPT) method

α method

In conventional practice, the design of shaft resistance for bored piles typically relies on a total stress analysis approach. This method involves determining the average adhesion along the pile shaft by applying an empirical adhesion coefficient to the undrained shear strength profile. The term "α" was introduced by Skempton (1959) to represent the empirical adhesion coefficient for bored piles. Consequently, this approach is commonly known as the α method in present-day references:

$$R_s = \sum \alpha \cdot c_u \cdot A_s \tag{1}$$

Here, R_s is the shaft resistance, α is an empirical adhesion coefficient, c_u is the undrained shear strength and A_s is the shaft surface area.

The empirical adhesion coefficient, α, is determined as the relationship between the average unit shaft resistance, $r_{s,a}$, and the average undrained shear strength along the length of the pile, $c_{u,a}$.

β method

Alternatively, the design of shaft resistance for bored piles can be based on an effective stress analysis approach, which relies on the established principles of soil mechanics. In this method, the determination of the average adhesion along the pile shaft is related to the angle of soil-pile interface friction and the effective radial stress acting on the pile. This approach, commonly referred to as the β method, considers the effective stress distribution and the interaction between the pile and the surrounding soil:

$$R_s = \sum \beta \cdot \sigma'_{v,0} \cdot A_s \tag{2}$$

Here, R_s is the shaft resistance, β is a semi-empirical adhesion coefficient, $\sigma'_{v,0}$ is the pre-existing effective vertical stress and A_S is the shaft surface area.

Various approaches to the effective stress analysis have been proposed, and among them Burland (1973), Meyerhof (1976) and Burland and Twine (1988) have all presented a straightforward and similar formulation known as the β method. In this method, the parameter β is defined as $\beta = K_{sv} \cdot \tan(\delta)$, where K_{sv} represents the ratio of the radial effective stress, σ'_s, acting on the shaft to the pre-existing effective vertical stress, $\sigma'_{v,0}$, while $\tan(\delta)$ represents the effective coefficient of friction between the pile shaft and the clay. This unified formulation simplifies the determination of the average adhesion along the pile shaft when using an effective stress analysis

λ method

The determination of shaft resistance for bored piles can also be done using an empirical combination of both total stress analysis and effective stress analysis. This approach, commonly referred to as the λ method, incorporates elements from both analysis methods. It was introduced by Focht and Vijayvergiya (1972) and offers a practical way to estimate the shaft resistance for bored piles:

$$R_s = \sum \lambda \cdot (\sigma'_{v,0} + 2 \cdot c_u) \cdot A_s \quad (3)$$

Here, R_s is the shaft resistance, λ is a pile length factor, $\sigma'_{v,0}$ is the pre-existing effective vertical stress, c_u is the undrained shear strength and A_s is the shaft surface area.

The pile length factor, λ, is determined based on the length of the pile, L_p. The value of λ varies with different pile lengths, starting at $= 0.5$ for a pile length of $L_p = 0\text{m}$ and progressively decreasing to $\lambda = 0.2$ for $L_p = 15\text{m}$, $\lambda = 0.165$ for $L_p = 30\text{m}$ and $\lambda = 0.12$ for $L_p = 60\text{m}$. It is important to note that the pile length factor, λ, is derived from a database of driven pile data. However, there is no extensive research available in the literature regarding the specific validity of this factor for bored piles. Further investigation is necessary to determine its applicability in the context of bored piles

CPT method

The determination of shaft resistance for bored piles can also be carried out by utilizing the Cone Penetration Test (CPT) data. The CPT method has been widely used and applied for estimating the shaft resistance of bored piles. Among the various versions of the CPT method, one of the prominent approaches is the LCPC method as presented by Bustamante and Gianeselli (1982). This method provide a framework for evaluating the shaft resistance of bored piles using CPT data:

$$R_s = \sum q_c / \alpha_{LCPC} \cdot A_s \quad (4)$$

Here, R_s is the shaft resistance, q_c is the cone resistance, α_{LCPC} is an empirical reduction factor and A_S is the shaft surface area.

Selection of method

The α method is a conventional approach commonly employed to determine the ultimate shaft resistance of bored piles. This method is relatively straightforward and relies on information regarding the undrained shear strength profile. However, one of the limitations of the α method is its reliance on the empirical adhesion coefficient, α, which can vary depending on factors such as soil conditions, pile types, pile dimensions, installation methods, pile loading test methods, and methods of interpretation. These variations introduce uncertainties when used in new or untested situations.

The β method involves estimating the effective contact stresses at the interface between the soil and the pile. However, since significant shear deformation occurs primarily in a relatively thin zone surrounding the pile shaft, it becomes practically impossible to directly measure the detailed behaviour and distribution of normal and shear stresses around a bored pile (Meyerhof and Murdock, 1953, Clayton and Mililitsky, 1983). Consequently, the β method becomes just as empirical as the α method, as it relies on empirical relationships and assumptions due to the difficulty in obtaining precise measurements of these parameter.

A comprehensive comparison study by Chen et al. (2011) conducted on a large database comprising 78 bored piles found the λ method to be less reliable compared to both the α and β methods. This suggests that the α and β methods are more robust and preferable for estimating shaft resistance in such cases.

The CPT method generally considers the shaft resistance as a fraction of the cone resistance, q_c. Since the cone resistance, q_c, is correlated to the undrained shear strength, c_u, the CPT method can be viewed as a slightly modified version of the α method. However, it is worth noting that CPT profiles are not as commonly available as undrained shear strength profiles in everyday engineering practice.

In conclusion, considering the merits and limitations of the different methods, the conventional α method appears to be the most applicable for bored piles. As a result, the β, λ and CPT methods are not further considered in this thesis.

2.2.2 Design of bored piles in Denmark

The current design practice for bored piles in Denmark is outlined in DS/EN_1997-1 (2007) and DS/EN_1997-1_DK_NA (2021), specifically in Annex L. The design guidelines specified in these documents provide comprehensive information on the design requirements and procedures for bored piles in Denmark as presented below:

For piles under **compressive** loads, F_c, the pile resistance must be determined by:

$$R_c = R_s + R_b \tag{5}$$

Here, R_c is the pile resistance under compressive loads, R_s is the shaft resistance and R_b is the base resistance.

For piles under **tensile** loads, F_t, the pile resistance must be determined by:

$$R_t = R_s \tag{6}$$

Here, R_t is the pile resistance under tensile loads and R_s is the shaft resistance.

Axially loaded piles, subjected to either compressive or tensile loads, is illustrated in Figure 5.

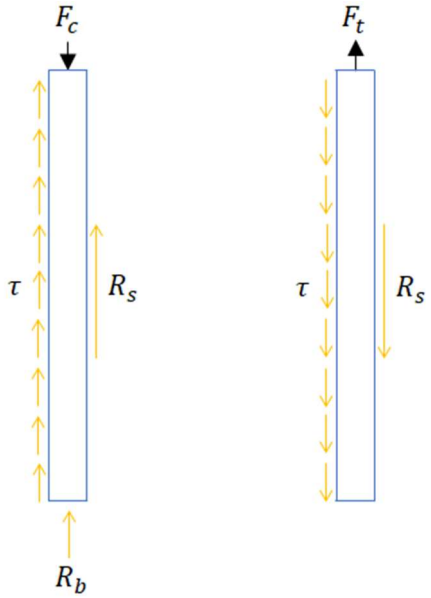

Figure 5: Illustration of pile under compressive and tensile load, respectively.

Shaft resistance

For fine grained soil, the shaft resistance, R_s, must be determined from ground test results as:

$$R_s = \sum_{i=1}^{n} k \cdot m \cdot r_r \cdot c_{ui} \cdot A_{si} \tag{7}$$

Here, R_s is the shaft resistance, $k = 0.3$ is a reduction factor specific to bored piles ($k = 1$ for driven piles), $m = 1.0$ is a material factor applicable to concrete, $r_r = 0.4$ represents a regeneration factor, accounting for the strength reduction of clay due to remoulding, valid for $c_u \leq= 500$ kPa, c_{ui} refers to the undrained shear strength for the i'th soil layer, often assumed to be equal to the measured field vane strength, c_{fv}, and A_{si} represents the shaft surface area of the i'th soil layer.

The multiplication of k, m and r_r $(i.e., \alpha = k \cdot m \cdot r_r = 0.3 \cdot 1.0 \cdot 0.4 = 0.12)$ gives rise to the empirical adhesion coefficient for bored piles in Denmark.

Base resistance

For fine grained soil, the base resistance, R_b, must be determined from ground test results as:

$$R_b = 9 \cdot c_u \cdot A_b \tag{8}$$

Here, R_b is the base resistance, c_u is the undrained shear strength and A_b is the area of the pile base.

In Danish tradition, if fissures are present in fine-grained soils, it is common practice to reduce the undrained shear strength, c_u, to one-third (1/3) of its original value. This adjustment accounts for the potential weakening effect of fissures on the soil's strength properties.

Ultimate design resistance

The ultimate design resistance of axially loaded piles, whether experiencing compressive or tensile loads, is obtained by utilizing equations (9) and (10):

$$R_{c,d} = \frac{R_{b,k}}{\gamma_b} + \frac{R_{s,k}}{\gamma_s} \tag{9}$$

$$R_{t,d} = \frac{R_{s,k}}{\gamma_{s,t}} \tag{10}$$

Here, $R_{c.d}$ is the design value of the pile resistance under compressive loads, $R_{t.d}$ is the design value of the pile resistance under tensile loads, $R_{b,k}$ is the characteristic value of pile base resistance, $R_{s,k}$ is the characteristic value of pile shaft resistance and $\gamma_b, \gamma_s, \gamma_{s,t}$ is partial safety factors.

The characteristic values must be obtained using correlation coefficients:

$$R_{c,k} = \frac{R_c}{\xi} \tag{11}$$

$$R_{t,k} = \frac{R_t}{\xi} \tag{12}$$

Here, $R_{c.k}$ is the characteristic value of the pile resistance under compressive loads, $R_{t.k}$ is the characteristic value of the pile resistance under tensile loads, R_c is the calculated value of pile resistance under compressive loads cf. equation (5), R_t is the calculated value of pile resistance under tensile loads cf. equation (6) and ξ is a correlation coefficient.

The values of partial safety factors ($\gamma_b, \gamma_s, \gamma_{s,t}$) and correlation coefficients (ξ) can be found in DS/EN_1997-1_DK_NA (2021) and will not be further analysed in this PhD project, as the overall safety index of bored piles lies outside the scope of the study.

2.3 Linking α with undrained shear strength

Initially, it was generally believed that the empirical adhesion coefficient, α, was primarily associated with the absolute value of the undrained shear strength, c_u, as illustrated by works such as Skempton (1959) and Kulhawy and Jackson (1989). However, further investigations revealed that the empirical adhesion coefficient, α, is intricately linked to the mean vertical effective stress throughout the pile depth, σ'_{vm} (Goh et al., 2005, Chen et al., 2011). This demonstrates that the relationship between α and the soil's characteristics is more complex and involves factors beyond just the undrained shear strength.

In the case of driven precast concrete piles, it is common to use the normalized strength $c_u/\sigma'_{v,0}$ as a basis for determining the empirical adhesion coefficient, α (Randolph and Murphy, 1985). It has been

demonstrated that the value of α decreases as the degree of overconsolidation (OCR) and pile slenderness (pile length over diameter ratio) increase (Kolk and der Velde, 1996). Additionally, the empirical adhesion coefficient, α, is influenced by the plasticity index, I_p, especially for soft clays with medium or low plasticity under normally consolidated conditions (Karlsrud et al., 2005).

The subsequent section provide details regarding the relationship between the empirical adhesion coefficient, α, and the undrained shear strength, c_u, based on databases found in the literature. These databases cover fine-grained soils in general but also specifically for London clay and Danish Eocene clay. However, it is important to note that not enough information is available in the literature to explore other relationships mentioned earlier.

Please note, that when investigating previous studies of the soil properties influence on the empirical adhesion coefficient, α, it is important to be aware that older databases often might be relatively uncontrolled. The values of shaft resistance, R_s, and undrained shear strength, c_u, are typically presented "as reported" by the original authors. In many cases, the methods used to obtain these values or whether tests or correlations were employed in the original sources are not even known. This situation is common due to the limited availability of guidelines for interpreting pile loading tests, resulting in minimal or incomplete reported strength data, often consisting solely of boring logs and Standard Penetration Test (SPT) data (Kulhawy, 2008).

2.3.1 General databases for fine-grained soils

Two recent databases on pile loading tests have been documented in the literature by Kulhawy and Phoon (1993), Chen and Kulhawy (1994) and Kulhawy and Chen (2003) as well as Chen et al. (2011). In both databases, the L1-L2 method by Hirany and Kulhawy (1988), Hirany and Kulhawy (1989) and Hirany and Kulhawy (2002) has been utilized to determine the shaft resistance, R_s, for both compression and tension. The L1-L2 method utilizes a graphical approach, simplifying the load-displacement curves into three distinct regions: the initial linear region, the transition region, and the final linear region, as depicted in Figure 6.

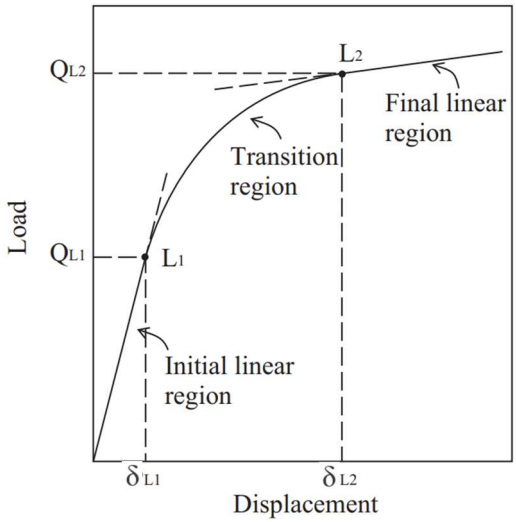

Figure 6: Load displacement curve, concepts of the L1-L2 method (Chen et al., 2011).

In order to establish a standardized relationship between the empirical adhesion coefficient, α, and the undrained shear strength, c_u, both databases selected the isotropically consolidated undrained triaxial compression (CIU) test as the appropriate reference for the undrained shear strength, c_u^{CIU}. In cases where unconsolidated undrained triaxial (UU) tests or unconfined compression (UC) tests were conducted instead, they were converted to "equivalent" undrained shear strength values, c_u^{CIU}, using the conversion method outlined in Chen and Kulhawy (1993) and Chen and Kulhawy (1994). Limited information is available regarding the specific soil conditions; however, it is stated that the data is applicable to bored piles in fine-grained soils, most likely referring to clay with low or medium plasticity as classified by the Casagrande plasticity chart (Casagrande, 1932).

Database A

The first database, used in studies by Kulhawy and Phoon (1993), Chen and Kulhawy (1994) and Kulhawy and Chen (2003), was examined. Although the original papers could not be accessed, the data points from Kulhawy and Phoon (1993) were conveniently reprinted by Knappett and Craig (2012), as shown in Figure 7.

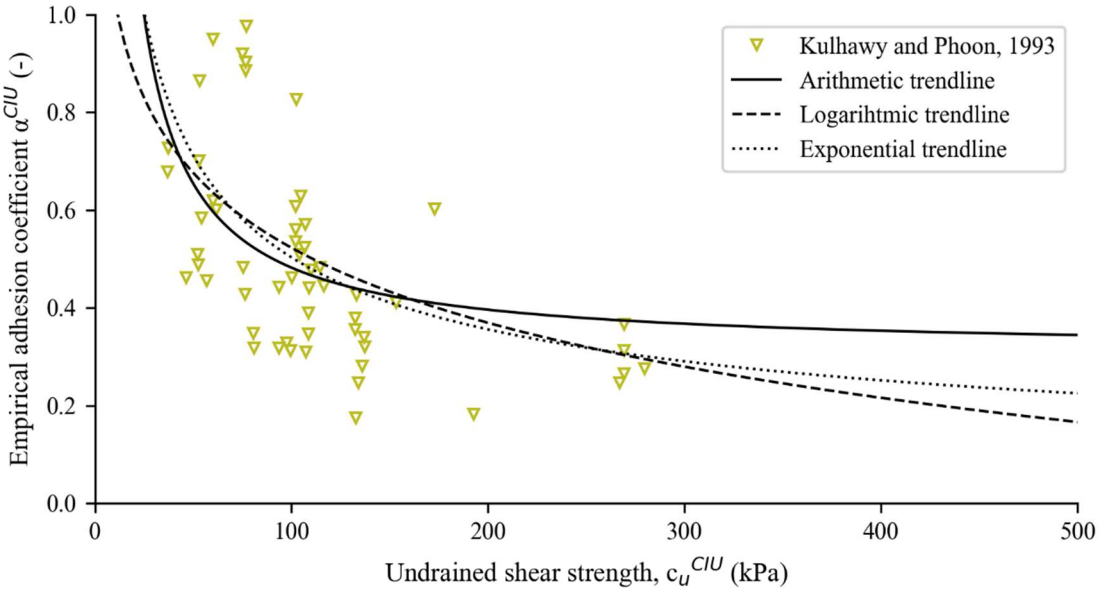

Figure 7: Correlation between empirical adhesion coefficient, α^{CIU}, and undrained shear strength, c_u^{CIU}, from database A modified after Knappett and Craig (2012).

The trendlines shown in Figure 7, which represent the best fit of the data, are derived from the original papers and summarized by Kulhawy (2008). These trendlines provide a concise representation of the relationship between the empirical adhesion coefficient and the undrained shear strength:

Arithmetic trendline:

$$\alpha^{\mathrm{CIU}} = 0.31 + \frac{0.17}{c_u^{CIU}/p_a} \tag{13}$$

Logarithmic trendline:

$$\alpha^{\mathrm{CIU}} = 0.52 - 0.51 * log_{10}(c_u^{CIU}/p_a) \tag{14}$$

Exponential trendline:

$$\alpha^{\mathrm{CIU}} = \frac{0.5}{(c_u^{CIU}/p_a)^{0.5}} \tag{15}$$

Here, α^{CIU} is the empirical adhesion coefficient, c_u^{CIU} is the undrained shear strength determined by isotropic consolidated undrained triaxial compression (CIU) tests and p_a is the atmospheric pressure (∼101.3 kPa).

Database B

The second database comprises pile loading test data collected from published literature and pile loading test reports, as documented by Chen et al. (2011). The dataset is categorized into drained and undrained loading conditions, with Figure 8 specifically presenting the data from undrained loading:

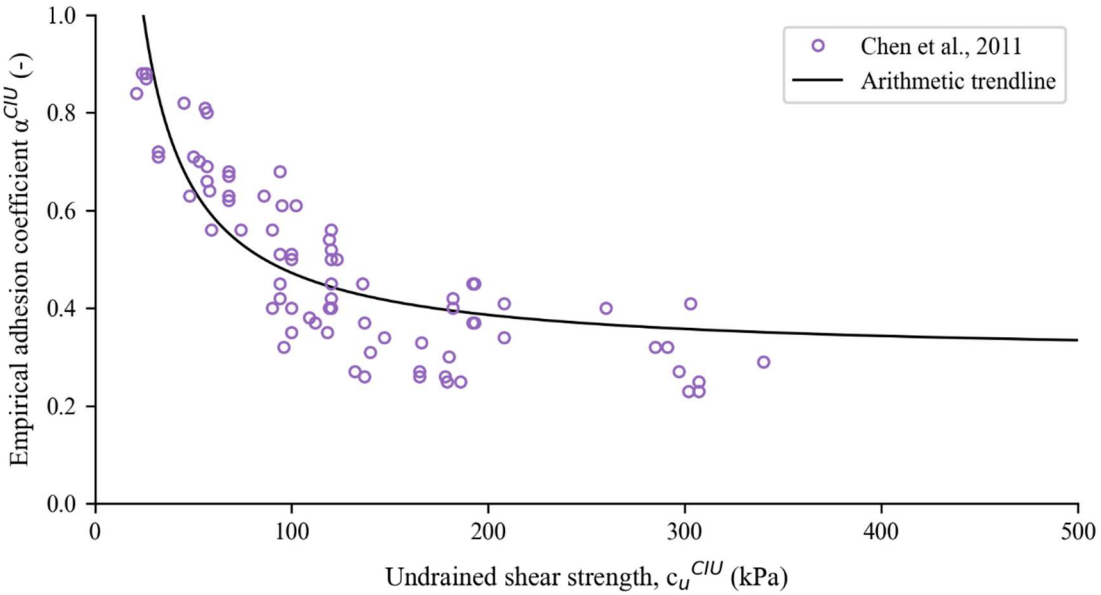

Figure 8: Correlation between empirical adhesion coefficient, α^{CIU}, and undrained shear strength, c_u^{CIU}, from database B modified after Chen et al. (2011).

The arithmetic trendline, representing the best fit of the data, shown in Figure 8, was determined by Chen et al. (2011) and is presented as:

$$\alpha^{\mathrm{CIU}} = 0.30 + \frac{0.17}{c_u^{CIU}/p_a} \tag{16}$$

2.3.2 London clay (UK)

This section presents representative examples found in the literature regarding pile loading tests conducted in London clay, a stiff and fissured marine sedimentary clay that shares similarities with Danish marine Eocene clay. One significant contribution to the determination of the empirical

adhesion coefficient, α, for London clay is the Skempton (1959) paper. This study involved examining records of pile loading tests on bored piles from ten different sites. The findings revealed that the empirical adhesion coefficient, α, for London clay typically ranged around 0.45, with values varying between 0.3 and 0.6. Unfortunately, no information regarding the methods employed in determining the shaft resistance, R_s, and the undrained shear strength, c_u, was provided in the literature.

However, the empirical adhesion coefficient, α, has traditionally been determined by comparing the results of pile loading tests to those of undrained triaxial compression tests on undisturbed specimens in the UK. In Skempton's study, the undrained shear strength, c_u, was obtained from triaxial compression tests conducted on 38 mm diameter specimens (Clayton and Milititsky, 1983). It is important to note that this approach implies that the empirical adhesion coefficient, α, will be significantly influenced by the presence of fissures (Skempton et al., 1969, Gasparre et al., 2007). As a result, it may not be directly comparable to an empirical adhesion coefficient, α, based on intact undisturbed undrained shear strength, $c_{u,intact}$, which can be determined through in-situ testing methods like the Danish field vane test.

In Marsland's study (1972), the average ratio between the undrained shear strength, c_u obtained from triaxial tests on 38 mm diameter specimens, and the intact strength determined from penetration tests was found to be approximately 0.46 for London clay, with values ranging between 0.37 and 0.55. This ratio is comparable to Danish experience, where the field vane strength is typically around two to three times the undrained shear strength (c_{fv}~2 á 3 · c_u). Consequently, the empirical adhesion coefficients, α, obtained in Skempton's study (1969), are converted based on the findings presented in Marsland (1972). These converted α coefficients are plotted relative to the converted intact undisturbed undrained shear strength, $c_{u,intact}$, as shown in Figure 9.

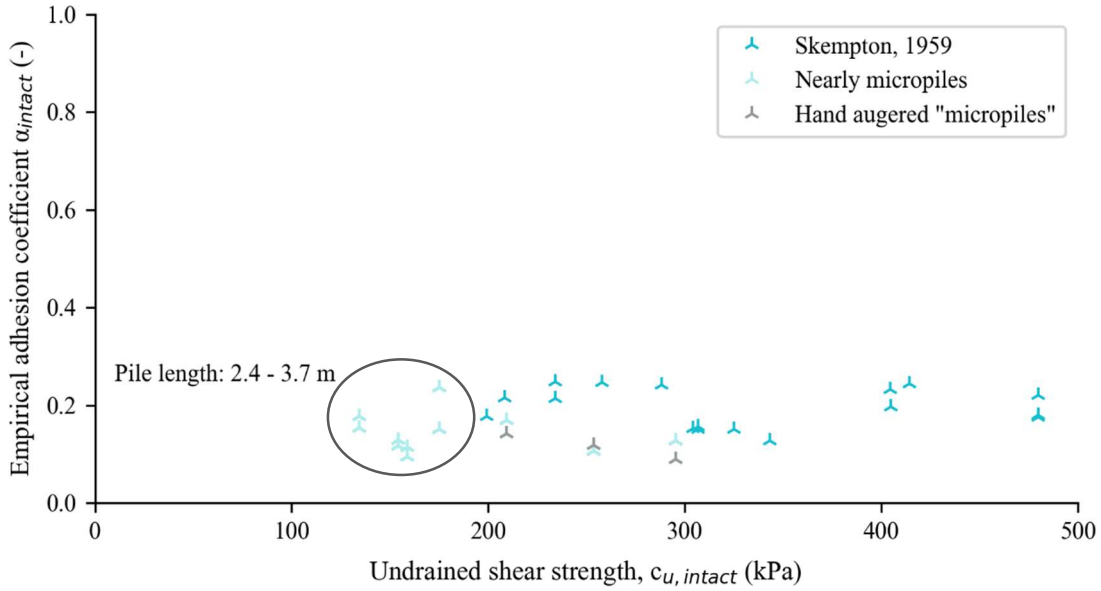

Figure 9: Empirical adhesion coefficients, $\alpha_{\,intact}$, for London clay.

Out of the 34 pile loading tests conducted on bored piles in the Skempton study (1969), it was determined that 3 of them were actually micropiles with a pile diameter smaller than 300 mm (DS/EN_14199, 2015). Hence, these 3 tests were excluded from the analysis. The remaining pile loading tests on bored piles consist of 14 nearly micropiles, characterized by pile diameters of either 305 or 356 mm. These “micropiles” are highlighted in light turquoise or light grey colour (Figure 9).

Among the "micropiles" under consideration, 8 of them have relatively shorter pile lengths ranging from 2.4 to 3.7 m. These shorter pile lengths imply that these piles are located in the upper layers of the London clay, where weathering and significant fissuring are commonly observed. Furthermore, out of the remaining 6 "micropiles", 3 of them were drilled using a hand auger (shown in light grey). The use of a hand auger introduces multiple days of exposure, which can result in a reduction of shear strength before the pile is installed.

Based on the aforementioned observations, it appears inappropriate to include the "micropiles" from Skempton's study (1969) when evaluating the adhesion coefficient, α. This exclusion is justified since these “micropiles” do not represent typical scenarios encountered in normal construction practices for bored piles.

2.3.3 Eocene clay (DK)

This section presents representative examples from the literature concerning pile loading tests conducted in Danish Eocene clay. Danish Eocene clay is characterized as a very high plasticity, stiff, and fissured marine sedimentary clay. The examples considered include a recent paper by Morrison et al. (2012) and unpublished work by Lyse et al. (2020) involving data from three different sites. In all three cases, the determination of shaft resistance, R_s, was based on a creep criterion or a substitute estimate of a creep criterium. The critical creep load was defined as the load beyond which the rate of axial displacement under constant load exhibits a noticeably increased increment, as illustrated in Figure 10.

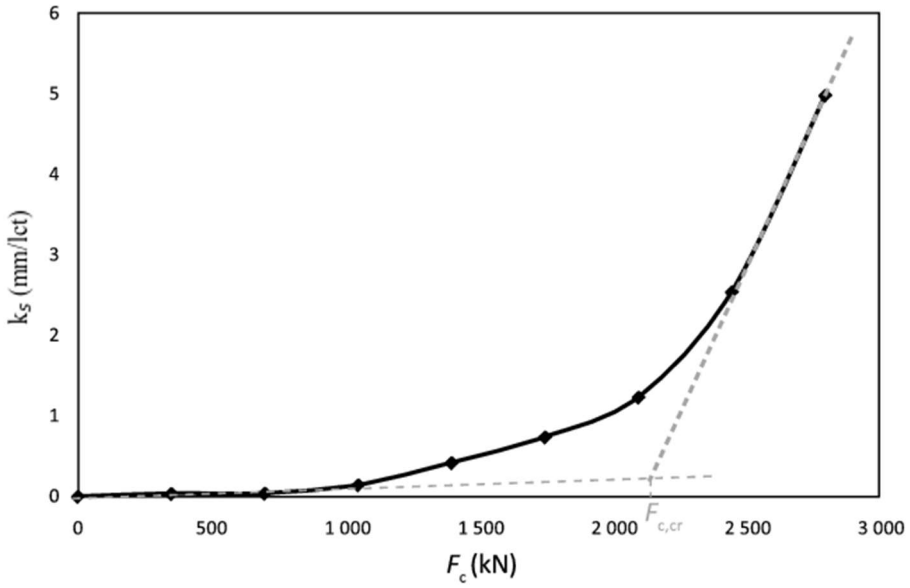

Figure 10: Concepts of the creep criterium in compression cf. DS/EN_ISO_22477-1 (2018).

In order to establish a standardized relationship between the empirical adhesion coefficient, α, and the undrained shear strength, c_u, two different approaches were employed for Danish Eocene clay. Firstly, Lyse et al. (2020) utilized the Danish field vane test as the appropriate reference, equating the undrained shear strength to the field vane strength ($c_u = c_{fv}$). Secondly, Morrison et al. (2012) established a site-wide correlation between undrained shear strength, c_u, and Cone Penetration Test (CPT) results ($c_u = q_{net}/N_{kt}$), employing a specific N_{kt} value of 25.5, indicating a correlation with undrained shear strength determined through triaxial testing.

To ensure compatibility, the α-c_u relation was subsequently converted to "equivalent" undrained shear strength values with the Danish field vane test as reference using $c_{fv} = 3 \cdot c_u$ (Christensen and Hansen, 1959, Grønbech, 2015). This conversion allowed for a consistent basis for development of the α-c_u relation. Figure 11 provide a visual representation of the α-c_u relation:

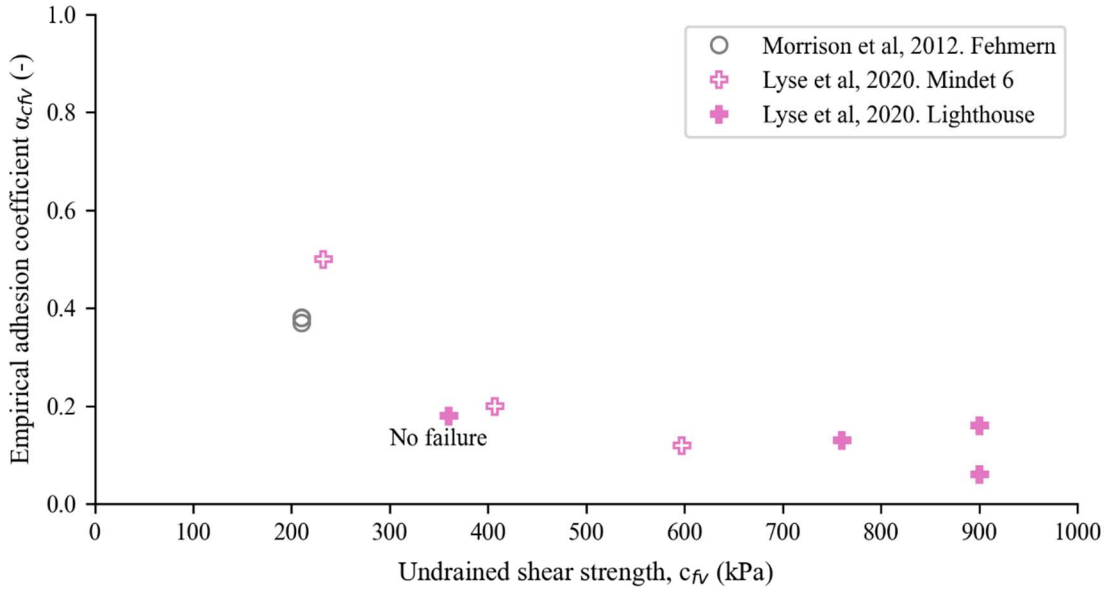

Figure 11: Empirical adhesion coefficients, α_{cfv} for Danish Eocene clay.

In order to err on the side of caution, a conservative estimation of the undrained shear strength, c_u, was employed to derive an empirical adhesion coefficient, α, according to Morrison et al. (2012) and Lyse et al. (2020). Additional details regarding the three test sites are provided below:

Fehmern

The dataset includes information from 4 bored piles, each consisting of a casing with an outer diameter of Ø610 mm and a diameter below the casing of Ø500 mm. These piles were installed offshore in a water depth of 10 m. Static pile loading tests were conducted, specifically in tension, over a period of 1 year. The loading was applied at a quasi-continuous rate.

To prevent any softening of the borehole walls, the bored piles were constructed with the use of a temporary casing. This casing was installed from above the sea level down to a depth of 10 m below the seabed. Below this temporary casing, the piles were bored without any additional support.

The subsurface conditions in the area comprise a layer of postglacial marine sediments with a thickness of less than two meters. Below this layer, there is a heavily folded clay deposit known as the Røsnæs unit (Eocene clay), which exhibits high plasticity. It is expected that fissures are present within the Røsnæs clay (Galsgaard et al., 2021).

The undrained shear strength profile of the clay layer has been determined using Cone Penetration Test (CPT) correlation. The undrained shear strength ranges from 10 kPa at the seabed level to 130 kPa at a depth of 25 meters below the seabed level, which corresponds to the base of the pile.

During the initial loading phase, the empirical adhesion coefficient, α, was determined to range between 1.10 and 1.15 (converted to 0.37 and 0.38 in Figure 11). However, with repeated loading and cumulative displacement, the α coefficient was observed to decrease to 0.75 (converted to 0.25) and potentially even lower. This behavior indicates a strain-softening response exhibited by the clay material.

Mindet

The dataset includes information from a single bored pile with a diameter of Ø1180mm. The pile was tested using the Osterberg load cell method, and the shaft resistance was measured at four strain gauge levels located above the O-cell, which was positioned 34.8 meters below the ground surface. During the construction of the bored pile, a temporary casing was utilized, extending to the full depth of 49 meters below the ground level. This temporary casing provided support and stability during the construction process.

In the region above the O-cell, where the shaft resistance was determined, the ground conditions comprise Søvind Marl. The undrained shear strength, determined as field vane strength, exhibits variability within the Søvind Marl deposit. In the uppermost region of the deposit, the undrained shear strength ranges between 100 and 200 kPa. However, at greater depths, the undrained shear strength exceeds 702 kPa.

Light house

The dataset includes information from a single bored pile with a diameter of Ø1860mm. The pile was tested using the Osterberg load cell method, and the shaft resistance was measured at five strain gauge levels located above the O-cell, positioned 49.9 meters below the ground surface. During the construction of the bored pile, a temporary casing was used, extending to a depth of 20 meters below the ground level. Below this point, the pile bore was supported by bentonite slurry, ensuring stability, until it reached the full depth of 70 meters below the ground surface

In the region above the O-cell, where the shaft resistance was determined, the ground conditions comprise Søvind Marl. The undrained shear strength, determined as field vane strength, exhibits variability within the Søvind Marl deposit. In the uppermost region of the deposit, the undrained shear strength ranges between 100 and 200 kPa. However, at greater depths, the undrained shear strength exceeds 702 kPa.

2.4 Time effects on pile capacity

The time elapsed between pile installation and the pile loading test has a direct impact on the pile capacity. Generally, the pile capacity for driven piles is expected to increase over time as the soil undergoes a recovery process (Skov and Denver, 1988, Clausen and Aas, 2000, Bullock et al., 2005a, Bullock et al., 2005b, Augustesen et al., 2006). During installation, the soil is displaced and disturbed with an increase in total horizontal stress, resulting in positive excess porewater pressure. As time passes, this excess porewater pressure dissipates, allowing for an increase in the effective stress as the soil consolidates (set-up). The set-up rate correspond to the rate of excess porewater pressure dissipation (Komurka et al., 2003). This set-up rate can be divided into two distinctive subphases:

1. Logarithmically nonlinear rate: This phase occurs immediately after installation and is characterized by a non-linear relationship between the dissipation of positive excess porewater pressure and time. During this phase, the excess porewater pressure dissipates rapidly and the set-up rate is high.

2. Logarithmically linear rate: This phase follows the logarithmically nonlinear rate and is characterized by a linear relationship between the dissipation of positive excess porewater pressure and time. In this phase, the excess porewater pressure continues to dissipate, albeit at a slower rate compared to the initial phase.

It can be observed that the majority of soil disturbance, excess porewater pressure generation, and dissipation predominantly occur along the pile shaft. As a result, the phenomenon of set-up is primarily attributed to an increase in shaft resistance (Skov and Denver, 1988, Axelson, 2002).

After the initial dissipation of positive excess porewater pressure, the pile capacity can continue to increase due to a phenomenon known as ageing (Schmertmann, 1991). Ageing refers to the time-dependent changes in soil properties at a constant effective stress and has a mechanical and frictional cause. As the soil gradually recovers and adjusts over time, the pile capacity can further improve in a third phase:

3. Ageing: The set-up process related to excess porewater pressure dissipation is essentially completed at a certain time after pile installation, as the set-up rate becomes significantly slow and negligible. However, even after the dissipation of positive excess porewater pressures, the pile capacity continues to increase and is instead attributed to the phenomenon of ageing.

Bored piles and driven piles differ primarily in their installation methods. Driven piles (full displacement piles) typically result in positive excess porewater pressure due to the increase in total horizontal stress caused by the significant displacement. On the other hand, bored piles are installed more cautiously, causing minimal displacement (non-displacement piles). As a result, bored piles experience smaller positive excess porewater pressures that typically leads to minor increases in pile capacity over time in comparison to driven piles (Li et al., 2019).

Extensive research has been conducted on the time-dependent increase in pile resistance for driven piles (Skov and Denver, 1988, Clausen and Aas, 2000, Bullock et al., 2005a, Bullock et al., 2005b, Augustesen et al., 2006). However, there is limited available information specifically addressing this phenomenon for bored piles (Bach and van Gelder, 2014).

This scarcity of information can partially be attributed to the fact that the zone with disturbed soil surrounding bored piles in clay is typically less than 0.5 pile radii (Meyerhof and Murdock, 1953). The narrow zone of disturbed soil around the bored pile makes it practically challenging to measure changes in soil and porewater pressure without the installation of measuring equipment affecting the capacity of the bored piles. In contrast, the disturbed zone in clay for driven piles extends to approximately 20 pile radii (Randolph et al., 1979), allowing for the measurement of changes in soil and porewater pressure without impacting the capacity of the driven piles. Further research is needed to better understand the time-dependent behaviour of bored piles and their resistance over time.

2.4.1 Pile set-up phenomenon and ageing effects

This section delves into a more detailed explanation of the pile set-up phenomenon and the ageing effects. Since there is limited information specifically focused on bored piles, the description relies on an extensive survey of published and unpublished literature on driven piles carried out by Komurka et al. (2003). The following is a summary of the findings.

Phase 1: Logarithmically nonlinear rate

During the first phase of set-up, the rate of dissipation of positive excess porewater pressure is not linear with respect to the log of time for some period after installation due to the highly disturbed state of the soil. The set-up rate corresponds to the rate of dissipation and is therefore also not linear with respect to the log of time for some period after installation. During this phase of logarithmically non-linear rate of dissipation of positive excess porewater pressure, the affected soil experiences an increase in effective horizontal stress, consolidates, and gains strength in a manner which is not well understood and is difficult to model/predict.

The duration of the logarithmically nonlinear rate of excess porewater pressure dissipation is a function of soil (type, permeability, and sensitivity) and pile properties (type, permeability, and size). The less permeable the soil and pile and the greater the volume of soil disturbed by the installation of the pile, the longer the duration of the logarithmically nonlinear rate of dissipation. The rate of dissipation may become linear almost immediately after installation of the pile for coarse grained soils, while the rate of dissipation may remain nonlinear for several days in fine-grained soils.

Phase 2: Logarithmically linear rate

During the second phase of set-up, the rate of positive excess porewater pressure dissipation becomes linear with respect to the log of time. The set-up rate still corresponds to the rate of dissipation and thus, becomes linear with respect to the log of time. During this phase of logarithmically linear rate of dissipation of positive excess porewater pressure, the affected soil experiences an increase in

effective horizontal stress, consolidates, and gains strength according to conventional consolidation theory (primary consolidation).

The duration of the logarithmically linear rate of excess porewater pressure dissipation is, as with the first phase, a function of soil (type, permeability, and sensitivity) and pile properties (type, permeability, and size). The less permeable the soil and pile and the greater the volume of soil disturbed by the installation of the pile, the longer the duration of the logarithmically linear rate of dissipation. The logarithmically linear rate of dissipation may be complete almost immediately or after a couple of hours after installation of the pile for coarse grained soils, while it may continue several weeks, several months or even years in fine-grained soils.

Phase 3: Ageing

The set-up process related to positive excess porewater pressure dissipation is essentially completed at a certain time after pile installation, as the set-up rate becomes significantly slow and negligible. However, even after the dissipation of positive excess porewater pressures, the pile capacity continues to increase (like secondary compression following primary consolidation). In this third phase, the increase in pile capacity becomes independent of the effective stress and is instead attributed to the phenomenon of ageing. Ageing refers to a time dependent change in soil properties at a constant effective stress and has a frictional and mechanical cause. Ageing results in an increased friction angle at the soil/pile interface and increases the soils shear modulus, stiffness and dilatancy and reduce the soils compressibility.

The three phases of set-up are shown idealized in Figure 12.

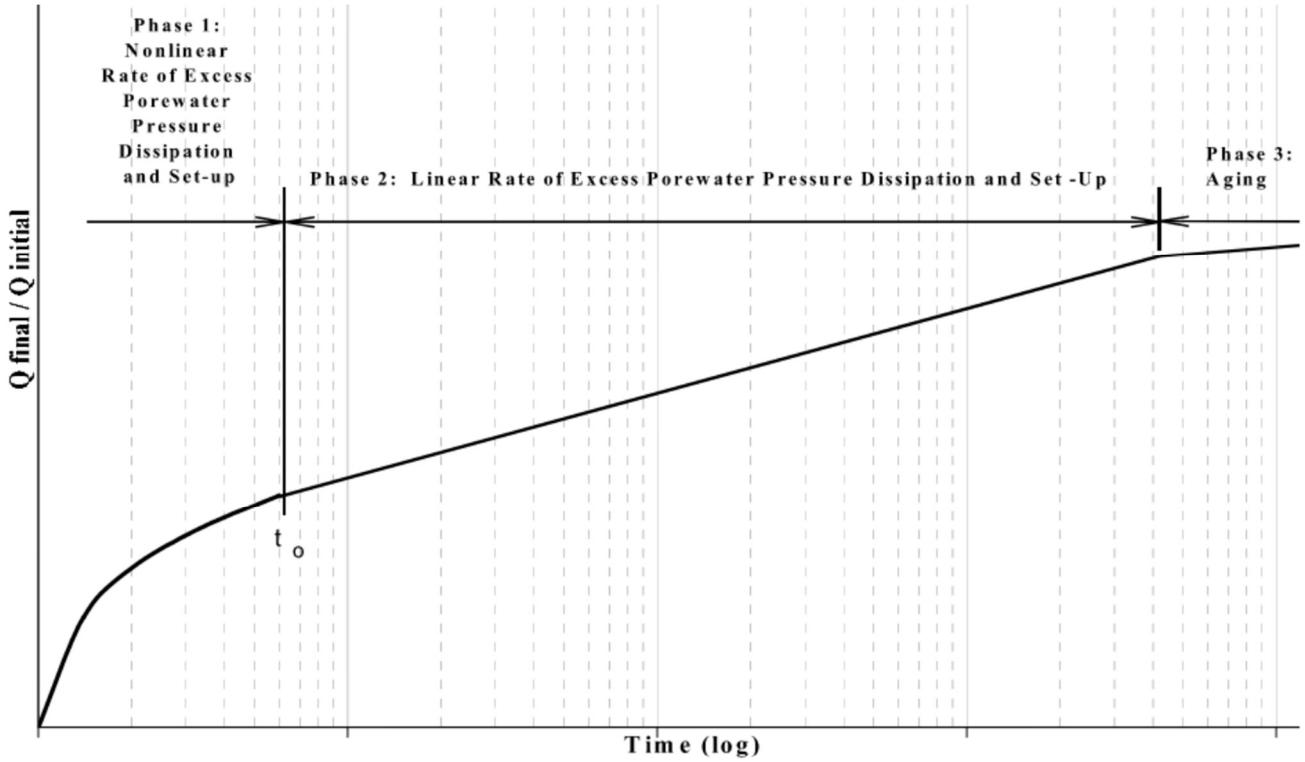

Figure 12: Idealized schematic of pile set-up (Komurka et al., 2003).

Bored piles

The differences in mechanisms and expected behaviour for bored and driven piles is presented below for each of the three phases of pile set-up and ageing effects:

For driven piles in phase 1, the rate of dissipation of positive excess porewater pressure is not linear with respect to the log of time for some period after installation during this phase (Komurka et al., 2003). This non-linearity arises due to the highly disturbed state of the soil including degradation of soil structure in fine-grained soils.

In the case of bored piles, where the state of the soil is considerably less disturbed compared to driven piles, this phase is expected to be less significant, and it may even be absent. This expectation is supported by Karlsrud et al. (2005), who found driven closed-ended piles generally exhibit greater shaft resistance than driven open-ended piles, as driven open-ended piles tend to cause less soil disturbance compared to their closed-ended counterparts.

Conducting pile loading tests to investigate the rate of set-up is infeasible for bored piles due to the time required for the fresh concrete to attain sufficient strength for testing, which typically takes around 30 days. In the case of driven piles, the emphasis on documented cases does not typically involve extensive testing within the initial few days, as this data is insignificant for practical geotechnical engineering purposes.

For driven piles in phase 2, the rate of excess porewater pressure dissipation becomes linear with respect to the log of time. During this phase, the soil affected by the pile experiences an increase in effective horizontal stress, consolidation, and a subsequent gain in strength (Komurka et al., 2003).

On the other hand, in the case of bored piles, where the state of the soil is less disturbed compared to driven piles, this phase is expected to have less significance. As a consequence, bored piles typically exhibit smaller positive excess porewater pressures, resulting in minor increases in pile capacity over time compared to driven piles. This expectation is supported in a numerical study by Li et al. (2019), who found pre-boring for driven piles to reduce the total horizontal stresses of pile installation, which propagate to the subsequent consolidation and loading phases. This results in minor increases of pile capacity over time compared to driven piles.

For bored piles in phase 3, the presence of excess porewater pressures after installation can be anticipated to be insignificant when compared to driven piles. As a result, the time-effects on pile capacity after installation are more likely to be dominated by the influences of ageing rather than the dissipation of excess porewater pressures. The transition from phase two to phase three is expected to occur gradually.

2.4.2 Time dependent increase in pile capacity

After conducting an extensive review of the literature, no scientific evidence was found regarding the time-dependent increase in pile capacity for bored piles. Therefore, reference is made to semi-logarithmic relationships that are applicable to the increase in pile capacity over time for driven piles.

A comprehensive study conducted by Augustesen et al. (2006) provided statistical evidence supporting the use of the time function proposed by Skov and Denver (1988) as the best fit for phase 2 compared to other set-up models found in the literature (Bullock et al., 2005a, Bullock et al., 2005b, Clausen and Aas, 2000). The study by Augustesen et al. (2006) was based on the analysis of 88 static pile loading tests on driven piles, which included a wide range of fine-grained soils and pile diameters ranging from approximately 0.1 to 1.4 m.

This study investigates whether the empirical relationship proposed by Skov and Denver (1988) also can be used to describe the development of bearing capacity for a bored pile:

$$\frac{Q_t}{Q_0} = 1 + \mathrm{A}_t \cdot log_{10}\left(\frac{t}{t_0}\right) \tag{17}$$

Here, Q_t is the axial pile capacity at time t after installation, Q_0 is the axial pile capacity at time t_0, A_t is a rate coefficient depending on soil type and t_0 is an empirical initial time value.

The empirical relationship expressed by equation (17) indicates a logarithmic-linear relationship between the axial pile capacity, Q_t, and the time elapsed since installation, t. Consequently, when normalizing with a reference pile capacity, Q_0, then the same relative rate coefficient, A_t, is achieved.

The axial pile capacity, Q_0, at time t_0 depends on the pile geometry (length and diameter), the surface of the pile shaft (smooth or rough) and the strength of the soil surrounding the pile. The rate coefficient, A_t, describes the relative increase in pile capacity with time (set-up) for each decade in log scale time and depends on soil properties (type, permeability, and sensitivity) as well as pile properties (type, permeability, and size) cf. Camp and Parmar (1999) and Svinkin and Skov (2000).

The empirical initial time value, t_0, represents the time at which the dissipation rate of excess porewater pressure starts to exhibit a linear relationship with the logarithm of time. The value of t_0 depends on soil type and pile size. It has been observed that a larger pile diameter corresponds to a higher value of t_0 (Camp and Parmar, 1999). In practice, multiple closely timed capacity determinations are required to define t_0. However, obtaining such measurements is often challenging. As a result, the empirical initial time value, t_0, must be assumed, estimated through back calculations using field data, or gleaned from empirical relationships documented in the existing literature.

The empirical initial time value, t_0, and rate coefficient, A_t, depending on soil type was given by Skov and Denver (1988) according to Table 1.

Table 1: Empirical initial time value, t_0, and rate coefficient, A_t, depending on soil type.

Soil type	t_0 [days]	A_t
Coarse grained soils	0.5	0.2
Fine grained soils	1	0.6
Chalk	5	5.0

The rate coefficient, A_t for fine grained soils was determined based on the analysis of six 19 m long and one 21 m long precast concrete pile. These piles had a cross-sectional area of 25x25=625cm^2. The installation site was located in Aalborg, Denmark, and consisted of fill, sand, and Yoldia clay. The piles underwent various testing methods, including static and dynamic loading tests, as well as CAPWAP analysis, to determine their performance and behaviour.

For comparison, the empirical initial time value, t_0, and rate coefficient, A_t, for fine grained soils was given by Augustesen et al. (2006) according to Table 2.

Table 2: Empirical initial time value, t_0, and rate coefficient, A_t, depending on loading type.

Loading type	t_0 [days]	A_t
Staged loading	1	0.46
Unstaged loading	1	0.18

Here, staged loading refers to pre-shearing effects. Thus, if the pile has been tested more than once, previous loading tests may have an effect on the capacity. A correction ratio to account for the transition from staged loading to unstaged loading is found from Table 2 to $0.46/0.18 = 0.39$. This recommendation aligns well with the suggestion of 0.4 presented by Bullock et al. (2005b).

The data utilized by Skov and Denver (1988) was re-examined in this study, as the rate coefficient, A_t, for fine-grained soils and staged loading in the study by Augustesen et al. (2006) is slightly lower than the corresponding value presented by Skov and Denver (1988) for fine grained soils.

Despite indicating an initial time value, t_0, of 1 day in the paper, it was found that the rate coefficient, A_t, for fine-grained soils was primarily determined based on an initial time value, t_0, of 0 days. Consequently, the rate coefficient, A_t, provided in their study as 0.60 is likely to be overestimated.

The comprehensive study by Augustesen et al. (2006) also focused on analysing whether the magnitude of set-up is related to the properties of the surrounding soil. However, it was found that neither the undrained shear strength, the plasticity index or the over consolidation ratio had a significant influence on the set-up.

The increase in pile capacity over time presented above is based on driven piles. For bored piles, a minor increase in pile capacity over time is expected compared to driven piles (Li et al., 2019).

During the literature review, two distinct cases involving bored piles installed in stiff, high plasticity clay were identified. These cases presented an opportunity to investigate the increase in pile capacity

over time further. The tests were conducted at different time points after the installation of the piles (unstaged loading).

The first case is 0.94 m diameter piles with a length of 12.5 m in London clay (Whitaker and Cooke, 1966). The second case is 0.61 m diameter piles in 10 m casing above seabed and 0.5 m diameter piles below seabed installed 25 m into Danish Eocene clay at Fehmern (Morrison et al., 2012). For both cases, the bored piles were tested in tension and represents the increase of shaft resistance with time. The variation in axial pile capacities over time for these cases is demonstrated in Figure 13.

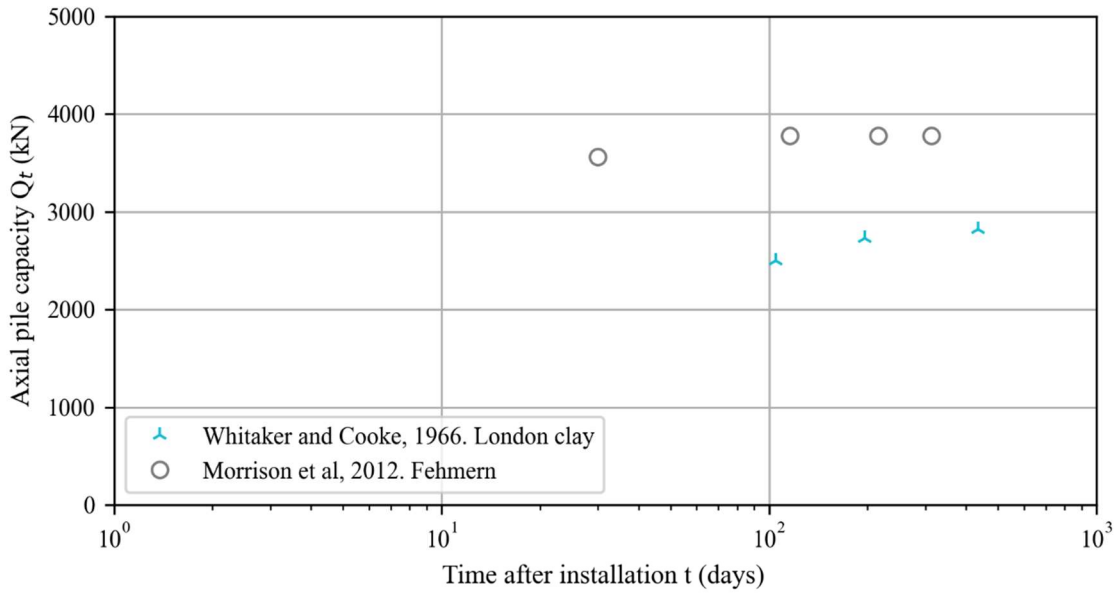

Figure 13: Development of pile capacity (shaft resistance) with time, Q_t, for bored piles in London clay (Whitaker and Cooke, 1966) and Danish Eocene clay (Morrison et al., 2012).

In the first case reported by Whitaker and Cooke (1966), the findings indicate a minor increase in pile capacity (specifically, shaft resistance) with time. However, it is important to acknowledge that drawing a definitive trend based on only three data points that do not cover a full decade of time intervals is not entirely reliable.

In the second case described by Morrison et al. (2012), the data presented does not exhibit a clear trend indicating an increasing pile capacity (specifically, shaft resistance) with time. It is important to note that except for the first data point, which is slightly lower, the remaining data points show relatively consistent pile capacities.

The limited data available makes it challenging to establish a conclusive pattern or trend in the development of pile capacity over time. Further research covering a wider time range would be necessary to provide a more comprehensive understanding of the time-dependent behaviour of bored piles installed in stiff, high plasticity clay.

2.5 Load-movement response

When modelling the interaction between soil and piles, three widely recognized methods are commonly employed or mentioned in the literature. These methods were initially developed for assessing soil-pile interaction in compression scenarios.

The first method is known as the **Load transfer method** (Seed and Reese, 1957, Reese, 1964, Coyle and Reese, 1966), where the pile is split up into a number of discrete sections to which a spring representing the soil-pile interaction is attached. The set of differential equations can be solved iteratively using a finite-difference approach. The method is also referred to as the t-z method.

The second method is the **Randolph and Wroth method** (Randolph and Wroth, 1978), which assumes the soil to behave elastically and the pile to be axially rigid in comparison. The methods enable simple closed form solutions to be derived from which the displacement under a given load can be determined.

The third method is the **hyperbolic method** (Fleming, 1992) and is based on the observation that by combining the pile shaft and base resistance described by hyperbolic functions and adding pile shortening by a simple procedure, an accurate model is obtained. The method is also referred to as a Semset/Cemsolve analysis.

The utilization of the hyperbolic method is disregarded due to the observed occurrence of strain-softening behaviour in the soil-pile response during pile loading tests, as detailed in section 6.2.2. The Randolph and Wroth method is not applicable for cases involving compressible piles. Despite the improvements made in the solution proposed by Randolph and Wroth (1979) to incorporate pile compressibility, this specific case and more intricate scenarios are typically more efficiently solved by employing numerical techniques, such as the load transfer method using a finite difference approach. Hence, for modelling soil-pile interaction, the load transfer method, specifically employing a finite difference approach, is adopted.

2.5.1 Load transfer method

The load transfer method was originally introduced in terms of conceptually explaining the mechanism of interaction between piles and soil during axial loading of a pile by Seed and Reese (1957). Subsequently, the actual load transfer method was developed by Reese (1964) and Coyle and Reese (1966).

The load transfer method is an iterative technique that solves a set of differential equations, which represents the pile behaviour using the finite-difference approach. The pile is split up into a number of discrete sections, to each of which a spring representing the soil-pile interaction is attached. The aim of the analysis is to determine the unknown distributions of displacements, Δz_i, and forces, F_i, along the pile.

The load transfer method is commonly used to describe the interaction between pile and soil for axial loading of piles under compressive and tensile loads, respectively e.g. Vijayvergiya (1977), O'Neil and Reese (1999), Knappett and Craig (2012), Zhang and Zhang (2012), Zhang et al. (2015), Cheng et al. (2018) and Cui et al. (2020). The load transfer method, as applied to piles subjected to tensile loads, is illustrated in Figure 14, outlining the underlying concept.

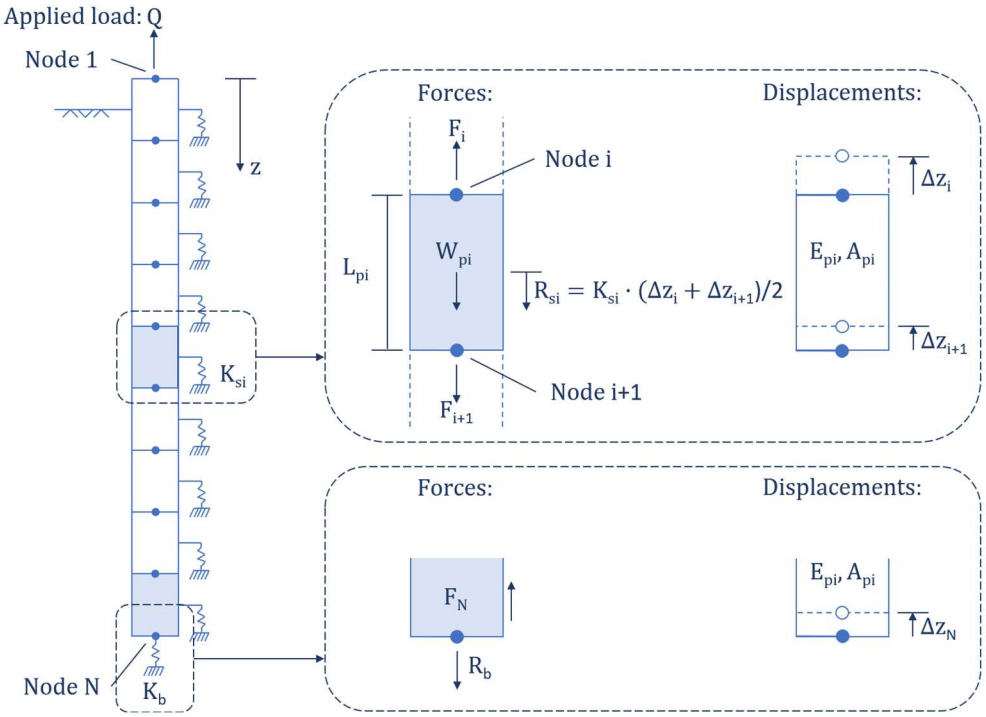

Figure 14: Load transfer method for piles under tensile loads modified after Knappett and Craig (2012).

The pile is divided into n-1 elements, and the i'th element is loaded by the force transmitted from the sections of pile above, F_i. Under this load, the pile element extends by an amount $(\Delta z_i - \Delta z_{i+1})$, also known as the pile slenderness effect. The average vertical movement of the pile element relative to the surrounding soil $(½ \cdot (\Delta z_i + \Delta z_{i+1}))$ generates a resistive force, R_{si}, in the spring (representative of shaft resistance). This force, plus the force from the element below, F_{i+1} and the dead-weight of the pile element, W_{pi}, act to resist, F_i. If the pile has not reached failure, then it must be in a state of equilibrium cf. equation (18).

$$F_i = F_{i+1} + W_{pi} + R_{si} \tag{18}$$

The resistive force, R_{si}, (shaft resistance) is expressed cf. equation (19):

$$R_{si} = K_{si}\left(\frac{\Delta z_i + \Delta z_{i+1}}{2}\right) \tag{19}$$

Here K_{si} is the stiffness of the spring and $(\Delta z_i + \Delta z_{i+1})/2$ is the average vertical movement of the pile element relative to the surrounding soil.

The pile is assumed to be linear elastic with Young's modulus, E_{pi}, cross-sectional area, A_{pi}, and length, L_{pi}. The displacements in equation (19) are related to each other through the elastic lengthening of the pile element under the average force in the element cf. equation (20).

$$\Delta z_i - \Delta z_{i+1} = \frac{L_{pi}}{E_{pi} \cdot A_{pi}} \left(\frac{F_i + F_{i+1}}{2} \right) \tag{20}$$

When determining the unknown distributions of displacements, Δz_i, and forces, F_i, along the length of the pile, an initial guess of the settlement at pile top (node 1) is made. The displacements of the nodes below (along the length of the pile) can then be found using equation (20).

For piles under tensile loads the resistive force, R_b, (representative of base resistance) at the pile base (node N) is balancing the forces acting on the pile before initiating the pile loading test and diminishes to between zero and the largest possible suction force ($A_b \cdot 1\ atm$) during failure. Hereafter, the known force for each node above is found using equation (18).

Unless the correct settlement was guessed initially, the pile load calculated for the pile top (node 1) does not corresponds to the applied load. Hence, an iterative technique is required to find the settlement at pile top that corresponds to the applied load as the displacements, Δz_i, and forces, F_i, depends on each other.

The key parameter, when using the load transfer method, is determining the appropriate resistive forces, R_{si} (shaft resistance) and R_b (base resistance) in the springs. This is often described by load transfer functions, which can simulate the interaction between the pile and the soil during axial pile loading. Load transfer functions are also known as t-z functions for shaft resistance and q-z functions for base resistance (Fellenius, 2023). As the load transfer method here is presented for piles under tensile loads, only load transfer functions (t-z functions) for shaft resistance are considered in the following.

2.5.2 Linear load transfer function

The resistive force, R_{si}, in the springs (shaft resistance) can be determined analytically using an elastic model. In this model, the soil is assumed to exhibit a linear elastic response until failure, as depicted in Figure 15. Given that linear load transfer functions rely on the properties of both the pile and the soil, the Randolph and Wroth method (Randolph and Wroth, 1978) can be employed to calculate the equivalent spring stiffness, K_{si}, and subsequently determine the resistive force, R_{si}, in the springs (shaft resistance). In the upcoming section, the Randolph and Wroth method is elaborated, specifically regarding the shaft resistance, R_s, and its implementation and utilization for determining the spring stiffness, K_{si}, as well as the resultant resistive force, R_{si}, in the spring (shaft resistance) is outlined.

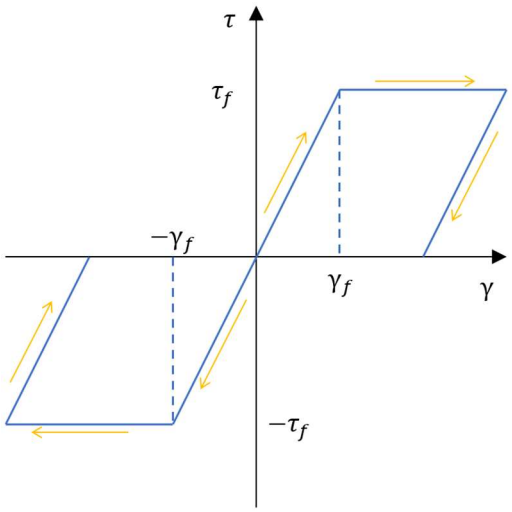

Figure 15: Principles of a linear elastic, perfectly plastic model.

Randolph and Wroth method

The Randolph and Wroth method was initially devised to analyse the behaviour of a pile subjected to axial compression. It was formulated on the basis of a two-layered soil model with a layer interface situated at the base of the pile. The method entailed evaluating the load-settlement response independently for the shaft resistance, R_s, and base resistance, R_b.

The fundamental assumption was that the soil behaved in an elastically idealized manner, while the pile was regarded as axially rigid in comparison. The deformation of the soil surrounding the pile shaft was represented as shearing of concentric cylinders, as illustrated in Figure 16.

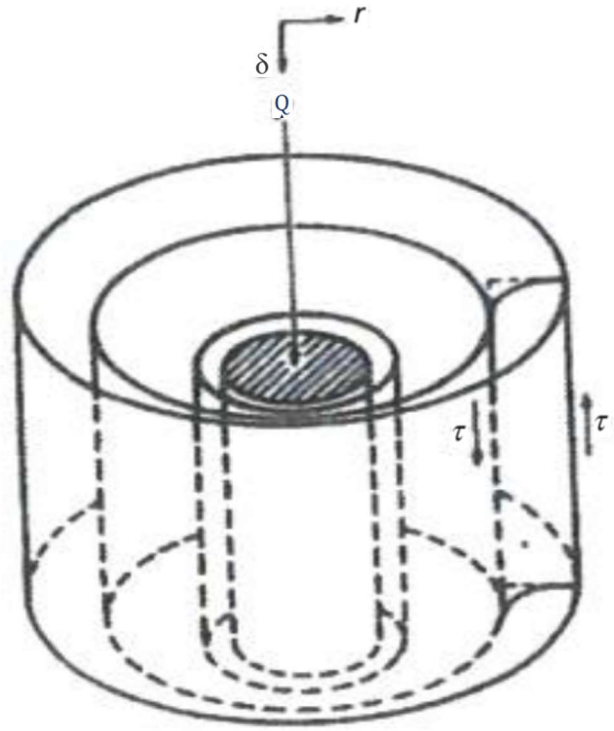

Figure 16: Mode of deformation for a pile shaft (Randolph and Wroth, 1978).

Under the influence of the applied load, Q, a vertical displacement, δ, occurs at the top of the pile, resulting in shear stresses, τ, within the surrounding soil. These shear stresses, τ, are dependent on the distance, r, from the centre of the pile.

The pile was considered to induce a shear mode of deformation within the surrounding soil as long as the shaft resistance along the pile shaft was not surpassed at the pile-soil interface, as depicted in Figure 17.

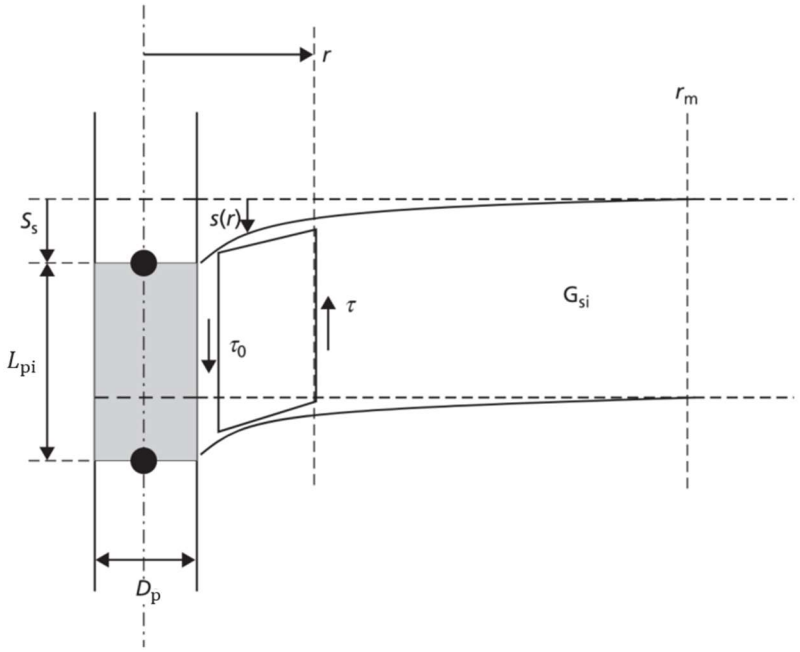

Figure 17: Equilibrium of soil around a settling pile shaft (Knappett and Craig, 2012).

For the soil annuli to be in vertical equilibrium, equation (21) was applied:

$$\left(2 \cdot \pi \cdot r \cdot L_{pi}\right) \cdot \bar{\tau} = \left(2 \cdot \pi \cdot \frac{D_p}{2} \cdot L_{pi}\right) \cdot \bar{\tau_0}; \therefore \bar{\tau} = \left(\frac{D_p}{2 \cdot r}\right) \cdot \bar{\tau_0} \tag{21}$$

Here $\bar{\tau_0}$ is the average shear stress at the pile shaft acting over the element length, L_{pi}, $\bar{\tau}$ is the average shear stress at the distance, r, from the centre of the pile and D_p is the pile diameter.

The shear strain, γ, in the soil annuli was approximated by $\gamma = ds/dr$ and was expressed as $\gamma = \bar{\tau}/G_{si}$ for linear elastic behaviour. Thus:

$$\frac{ds}{dr} = \left(\frac{D_p \cdot \bar{\tau_0}}{2 \cdot \overline{G_{si}}}\right) \cdot \frac{1}{r} \tag{22}$$

Here $\overline{G_{si}}$ is the average shear modulus of the soil element.

Equation (22) was integrated from a settlement, $s = 0$, at a distance from the pile ($r = \infty$) to the settlement, $s = s_s$, at the pile shaft ($r = D_p/2$) see equation (23) and (24). For practical purposes, a maximum distance, r_m, was defined beyond which settlements were negligible.

$$\int_{s_s}^{0} ds = \left(\frac{D_p \cdot \bar{\tau_0}}{2 \cdot \overline{G_{si}}}\right) \cdot \int_{D_p/2}^{r_m} \frac{1}{r} dr \tag{23}$$

$$s_s = \left(\frac{D_p \cdot \bar{\tau_0}}{2 \cdot \overline{G_{si}}}\right) \cdot \ln\left(\frac{2 \cdot r_m}{D_p}\right) \tag{24}$$

The force, T_{si}, along the length of the pile shaft that results in s_s was determined as:

$$T_{si} = \pi \cdot D_p \cdot L_{pi} \cdot \bar{\tau_0} \tag{25}$$

Thus, the stiffness of the spring, K_{si}, was determined by dividing equation (25) with equation (24):

$$K_{si} = \frac{T_{si}}{s_s} = \frac{2 \cdot \pi \cdot L_{pi} \cdot G_{si}}{\ln\left(\frac{2 \cdot r_m}{D_p}\right)} \tag{26}$$

The resistive force, R_{si}, in the spring can then be determined cf. section 2.5.1 as:

$$R_{si} = K_{si}\left(\frac{\Delta z_i + \Delta z_{i+1}}{2}\right) \tag{27}$$

Here $((\Delta z_i + \Delta z_{i+1})/2)$ is the average vertical movement of the pile element relative to the surrounding soil and K_{si} is the stiffness of the spring.

However, it is worth noting that soils exhibit apparent linear elastic behaviour only at low levels of applied load. As the load magnitude increases, a transition occurs, and the soil's response shifts towards a nonlinear elastic-plastic behaviour. Consequently, for enhanced accuracy, the determination of the resistive force, R_{si}, in the spring can be determined more accurately using nonlinear load transfer functions.

2.5.3 Nonlinear load transfer functions

The nonlinear elastic-plastic behaviour of soils, characterized by a hyperbolic curve, was initially described by Kondner (1963), as depicted in Figure 18. This representation captures the change in soil response as the applied load increases and provide a more accurate representation of the actual behaviour of soils under varying load conditions.

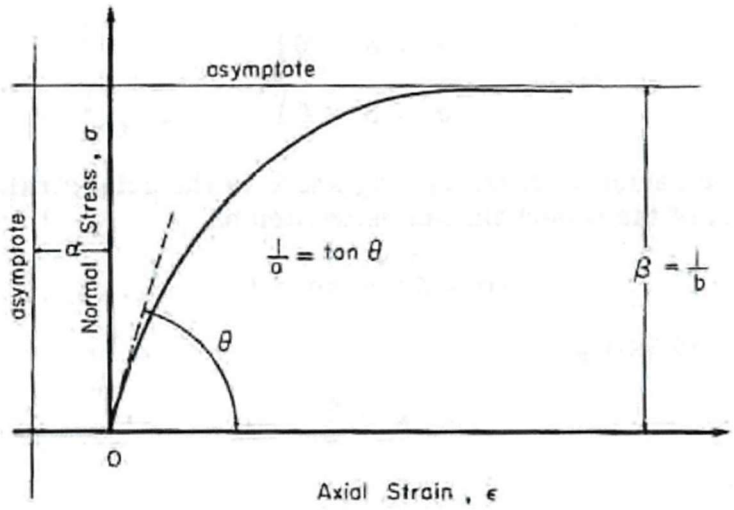

Figure 18: Rectangular hyperbolic representation of stress-strain (Kondner, 1963).

A number of different approaches have subsequently been developed to estimate nonlinear load transfer functions (t-z functions) with some relaying solely on empirical data from laboratory and field experiments and others based mainly on analytical framework (Stanton et al., 2015).

The nonlinear load transfer functions is often presented in terms of shear stiffness degradation curves (G/G_0), where G is the secant shear modulus and G_0 is the initial linear elastic shear modulus, versus the logarithm of shear strain, γ, e.g. Vardanega and Bolton (2011a) and Niazi and Mayne (2019).

However, in practical everyday geotechnical engineering the initial linear elastic shear modulus, G_0, is rarely known and the focus in generally on the undrained shear strength, c_u. Therefore, the nonlinear load transfer functions can alternatively be presented in terms of shear strength mobilisation based on the undrained shear strength, c_u, e.g. Vardanega and Bolton (2011b).

Two selected functions to predict the nonlinear load transfer functions, one based on shear stiffness degeneration curves (G/G_0) by Vardanega and Bolton (2011a), and one based on the undrained shear strength, c_u, by Vardanega and Bolton (2011b) are presented below. The selection of these functions is primarily motivated by their frequent citation in the literature, along with their origins in highly influential works. Furthermore, the authors who have employed these functions have consistently focused on bored piles, fine-grained soils, and, more specifically, London Clay.

The Vardanega and Bolton method to estimate non-linear shear stiffness

The Vardanega and Bolton method to estimate non-linear shear stiffness (Vardanega and Bolton, 2011a) is based on simple soil parameters from a database on fine grained soils found in published literature. The samples derive from various countries and were tested in a variety of conditions from normally consolidated to heavily over consolidated, in various laboratories and shear testing devices.

The modified hyperbola similarly presented by Darendeli (2001) and Zhang et al. (2005) was adopted:

$$\frac{G}{G_0} = \frac{1}{1 + \left(\frac{\gamma}{\gamma_{ref}}\right)^{\alpha_c}} \tag{28}$$

Here, G_0 is the initial linear elastic shear modulus, G is the secant shear modulus, γ is the shear strain, γ_{ref} is the reference strain and α_c is a function coefficient (curvature parameter).

All stiffness data was normalised to a standard test rate of 10^{-6} s^{-1} to represent a carefully conducted undrained triaxial test achieving peak strength at an axial strain of about 2 % (and therefore shear strain of approximately 3 %) after 8 hours as they focused on stiffness at moderate strains. A strain rate effect of 5 % per $\log_{10}$ cycle was adopted ($G^* = G + 0.05 \cdot log_{10}(10^6 \dot{\gamma})$) according to the findings of Lo Presti et al. (1997) and d'Onofrio et al. (1999), see Figure 19.

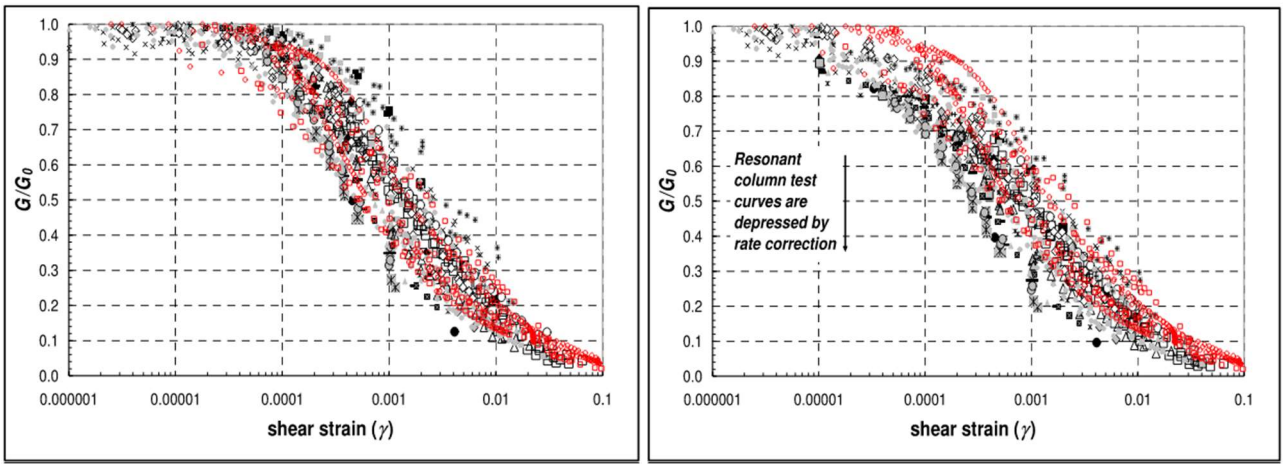

Figure 19: G/G_0 versus shear strain, γ, for raw and rate corrected data (Vardanega and Bolton, 2011a).

Figure 20 presents the normalized data from Vardanega and Bolton (2011a). They found that the modified hyperbola provided a good fit to the data.

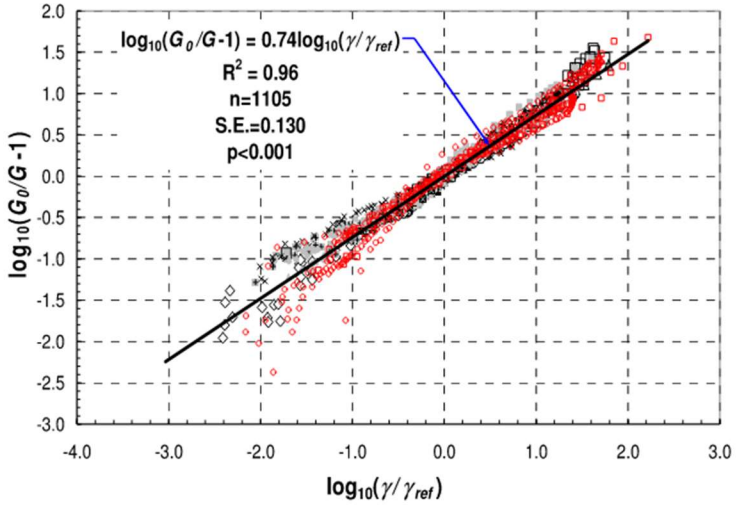

Figure 20: $Log_{10}(G_0/G - 1)$ versus $log_{10}(\gamma/\gamma_{ref})$ rate corrected data (Vardanega and Bolton, 2011a).

Therefore, the modified hyperbola was expressed as:

$$\frac{G}{G_0} = \frac{1}{1 + \left(\frac{\gamma}{\gamma_{ref}}\right)^{0.74}} \tag{29}$$

The reference strain, γ_{ref}, was defined as the shear strain, where the secant shear stiffness (G/G_0) reduces to half its maximum value. The following equations were provided for prediction of the reference strain, γ_{ref}, using plasticity index, I_p, liquid limit, w_l, plastic limit, w_{pl}, and void ratio, e_0:

$$\gamma_{ref} = 2.17 \cdot I_p/1000 \tag{30}$$

$$\gamma_{ref} = 1.25 \cdot w_l/1000 \tag{31}$$

$$\gamma_{ref} = 2.73 \cdot w_{pl}/1000 \tag{32}$$

$$\gamma_{ref} = 0.56 \cdot e_0/1000 \tag{33}$$

Reasonable coefficients of determination were obtained by linear regression for these correlations, except for five of the London Clay tests that were deemed outliers of the trend. (This may be caused by the presence of fissures in the clay). See Figure 21.

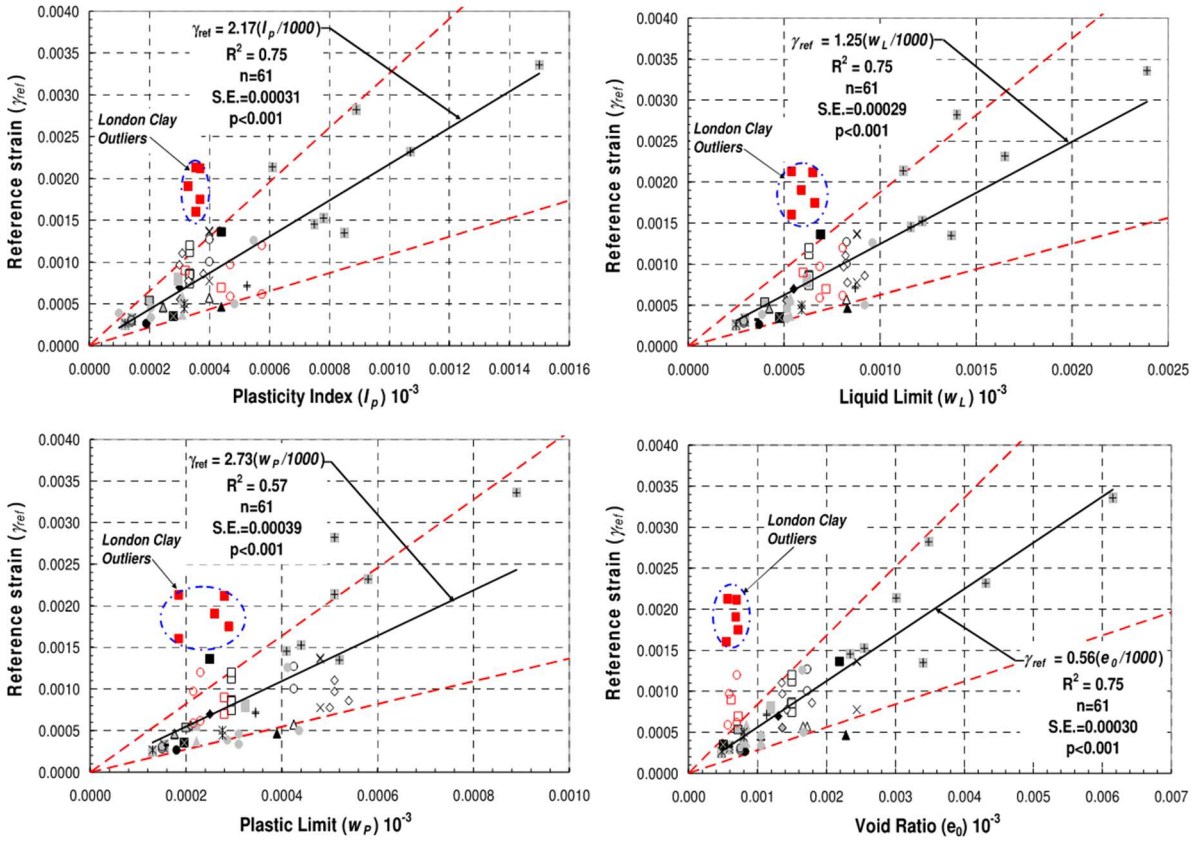

Figure 21: Reference strain, γ_{ref}, versus plasticity index, I_p,, liquid limit, w_l, plastic limit, w_{pl}, and void ratio, e_0, (Vardanega and Bolton, 2011a).

The liquid limit, w_l, relation was favoured, as the fall cone test is semi-automated and would require much less judgement from the operator than the plastic limit, w_{pl}. A correlation with plasticity index ($I_p = w_l - w_{pl}$) would require both tests to be performed. Void ratio would require undisturbed samples to minimize water migration but provided no statistical improvement. Hence, the liquid limit, w_l, was favoured.

Figure 22 presents the accuracy of the model based on liquid limit, w_l, cf. Vardanega and Bolton (2011a) for measured values of the secant shear stiffness (G/G_0) plotted against predicted values determined by equation (29) and (31):

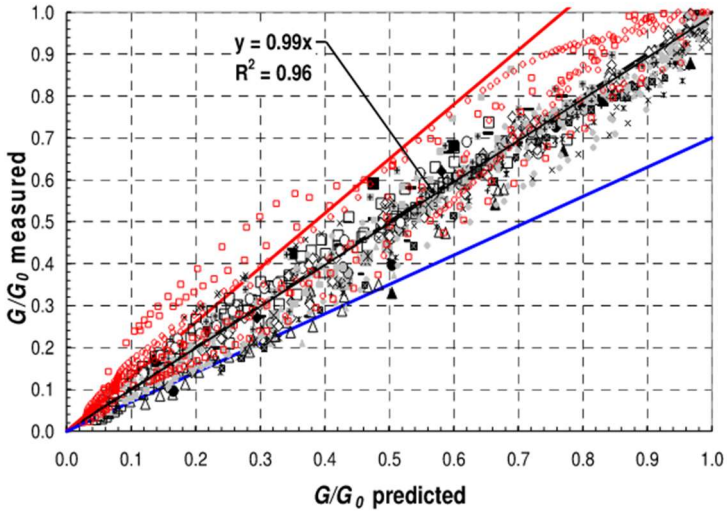

Figure 22: Measured values vs. predicted values of G/G_0 (Vardanega and Bolton, 2011a).

Hence, the Vardanega and Bolton methods to estimate the non-linear shear stiffness is generally able to predict values of G/G_0 within ± 30 %.

The Vardanega and Bolton shear strength mobilisation function

The shear strength mobilisation in fine grained soils is characterised by a power law within the moderate strain region cf. Vardanega and Bolton (2011b):

$$\frac{\tau_{mob}}{c_u} = A \cdot \gamma^B \tag{34}$$

Here, c_u is the undrained shear strength, τ_{mob} is the mobilised shear strength, γ is the shear strain and A, B is function coefficients.

The strain to half mobilisation was used to normalise the strain axis:

$$\frac{\tau_{mob}}{c_u} = 0.5 \cdot \left(\frac{\gamma}{\gamma_{M=2}}\right)^B \tag{35}$$

Here, $\gamma_{M=2}$ is the reference strain to half the mobilisation.

A database of London clay triaxial test data was used to determine the function coefficients A and B for London clay by Vardanega and Bolton (2011c).

They replotted the raw triaxial data, where the shear strain, γ, was taken as 1.5 times the axial strain, ε, and the mobilised shear strength, τ_{mob}, was taken as the product of the secant shear modulus, G, and shear strain, γ, see Figure 23.

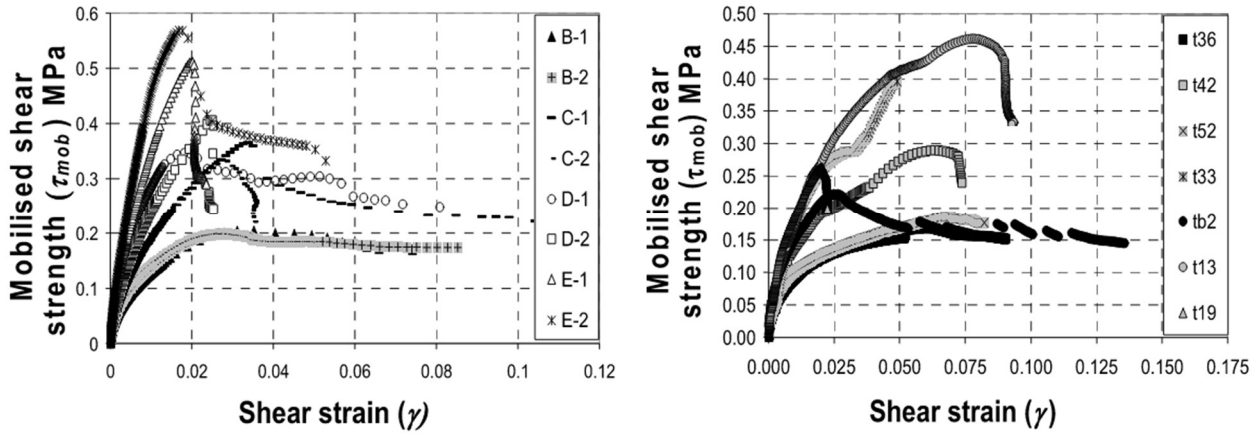

Figure 23: Original London clay triaxial test data replotted by Vardanega and Bolton (2011c).

Figure 24 presents the design stress-strain curve for London clay from Vardanega and Bolton (2011c). They found the weighted average exponent B to be 0.58.

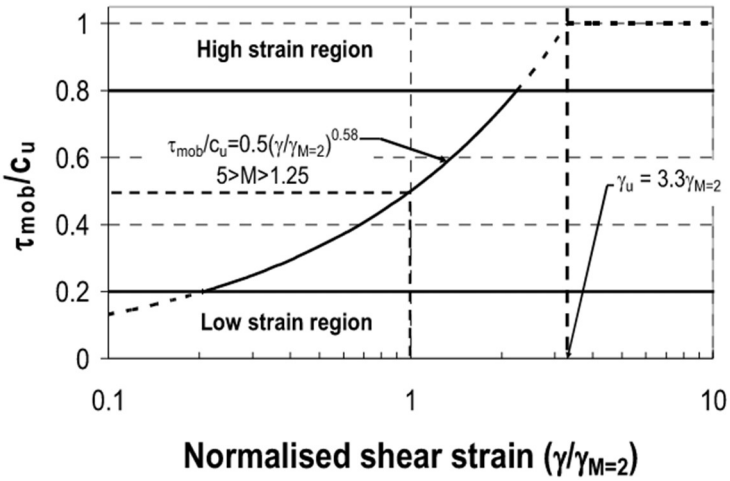

Figure 24: Design stress-strain curve for London clay (Vardanega and Bolton, 2011c).

A linear regression of data was performed by Vardanega and Bolton (2011c) and they provided a single power equation that represents the response of the London Clay soil deposit:

$$\frac{\tau_{mob}}{c_u} = 0.485 \cdot \left(\frac{\gamma}{\gamma_{M=2}}\right)^{0.58} \tag{36}$$

Figure 25 presents the accuracy of the model cf. Vardanega and Bolton (2011c) for measured values of τ_{mob}/c_u plotted against the predicted values determined by equation (35) with an exponent $B = 0.58$.

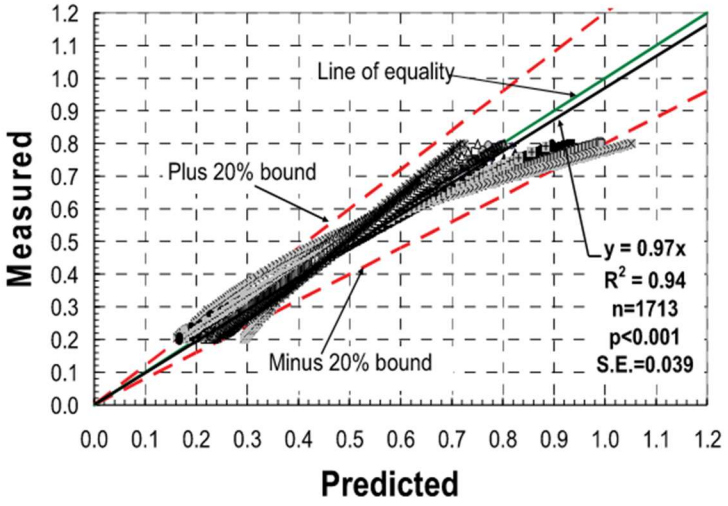

Figure 25: Measured values vs. predicted values of τ_{mob}/c_u (Vardanega and Bolton, 2011c).

Hence, the Vardanega and Bolton shear strength mobilisation function is generally able to predict values of τ_{mob}/c_u within $\pm 20\,\%$ at any strain level within the moderate strain region ($0.2 \leq \tau_{mob}/c_u \leq 0.8$).

The reference strain, $\gamma_{M=2}$, was defined in relation to the sample depth:

$$1000\gamma_{M=2} = -2.84\ln(d_s) + 15.42 \tag{37}$$

Here, d_s is the sample depth.

However, the determined coefficient of determination was only moderately significant and could simply arise from random fluctuation and small number of sites and samples, see Figure 26.

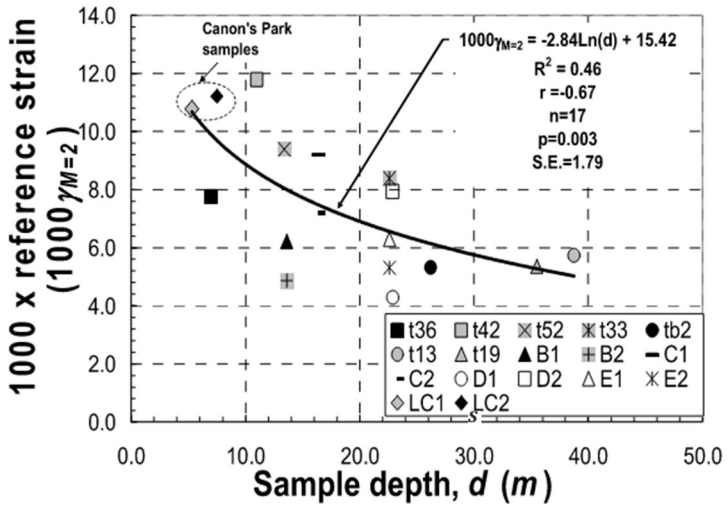

Figure 26: Reference strain, $\gamma_{M=2}$, vs. sample depth, d_s, (Vardanega and Bolton, 2011c).

2.5.4 Back-analysis of pile loading test results

Load transfer functions can also be obtained by back-analysis of pile loading test results, where the shaft resistance, R_s, of a pile to the applied load, Q, during pile loading test is a function of the relative displacement between pile and soil, $\delta_{pile,soil}$ (Randolph, 2003, Fellenius, 2023). The purpose of back-analysis of pile loading test results is to obtain the best possible description of this behaviour for a specific pile.

Four selected load transfer functions (t-z functions) are presented below. The functions are selected because they are commonly cited in the literature, and they display a strain softening response as expected for Danish Eocene clay (Morrison et al., 2012) and found during the data analysis, see section 6.2.2. The t-z functions below are governed by a known (selected) target shaft resistance, the displacement paired with it and additional function coefficients particular to the considered t-z function. The target values can be but is not necessary the peak values.

The Hansen 80 % function

The following strain-softening t-z function was proposed by Hansen (1963):

$$R_s = \frac{\sqrt{\delta_{pile,soil}}}{C_1 \cdot \delta_{pile,soil} + C_2} \tag{38}$$

Here, R_s is the shaft resistance, $\delta_{pile,soil}$ is the relative vertical displacement between pile and soil and C_1, C_2 is function coefficients.

To ease back-analysis, the function coefficients can be expressed as $C_1 = 1/(2 \cdot R_{peak} \cdot \sqrt{\delta_{peak}})$ and $C_2 = \sqrt{\delta_{peak}}/(2 \cdot R_{peak})$ making it depend directly on the peak values (Fellenius, 2023).

The Hansen 80 % function is shown in Figure 27:

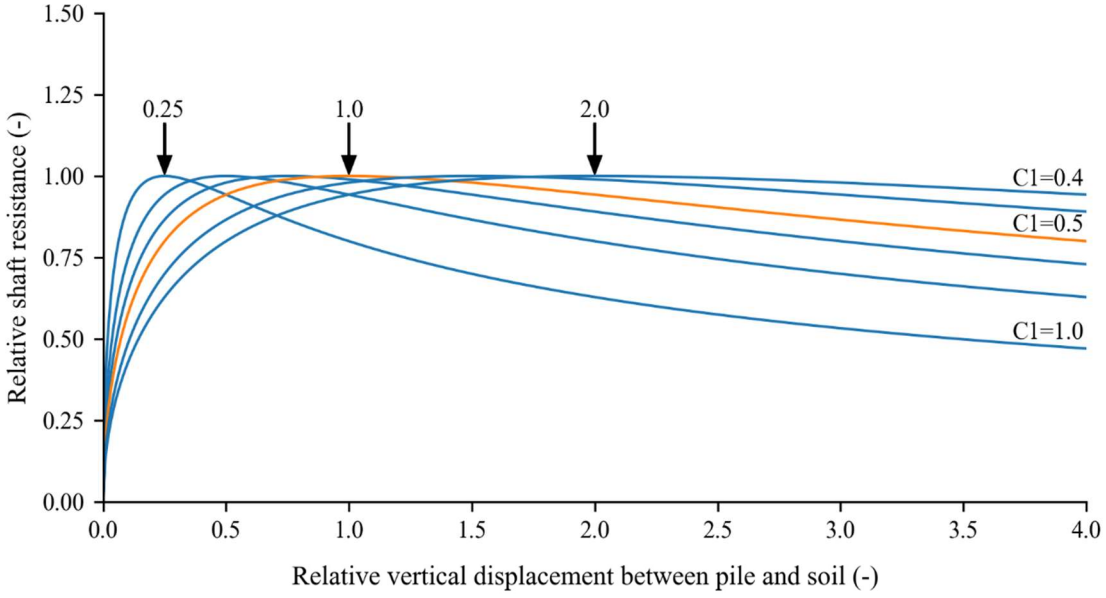

Figure 27: The Hansen 80 % strain softening t-z function.

The Hansen 80 % function will always have the peak value at 1.0 relative shaft resistance, and the function coefficient C1 controls the shape of the curve and the magnitude of vertical displacement between pile and soil for the peak value of shaft resistance.

The Zhang function

The following strain-softening t-z function was proposed by Zhang and Zhang (2012):

$$R_s = \frac{\delta_{pile,soil} \cdot (a + c \cdot \delta_{pile,soil})}{(a + b \cdot \delta_{pile,soil})^2} \tag{39}$$

Here, R_s is the shaft resistance, $\delta_{pile,soil}$ is the relative vertical displacement between pile and soil and a, b, c is function coefficients.

The peak values are defined by: $R_{peak} = 1/(4(b-c))$ and $\delta_{peak} = a/(b-2c)$.

To ease the back-analysis b and c can be expressed as $\mathrm{b} = 1/(2 \cdot R_{peak}) - a/(\delta_{peak})$ and $\mathrm{c} = 1/(4 \cdot R_{peak}) - a/(\delta_{peak})$ making it depend directly on the peak values and the function coefficient a.

The Zhang function always goes through the peak value, and the function coefficient, a controls the shape of the curve. If the peak value is known, the Zhang function provide more flexibility when fitting the shape of curve before and after the peak value, than the Hansen 80 % function.

The Zhang function is shown in Figure 28.

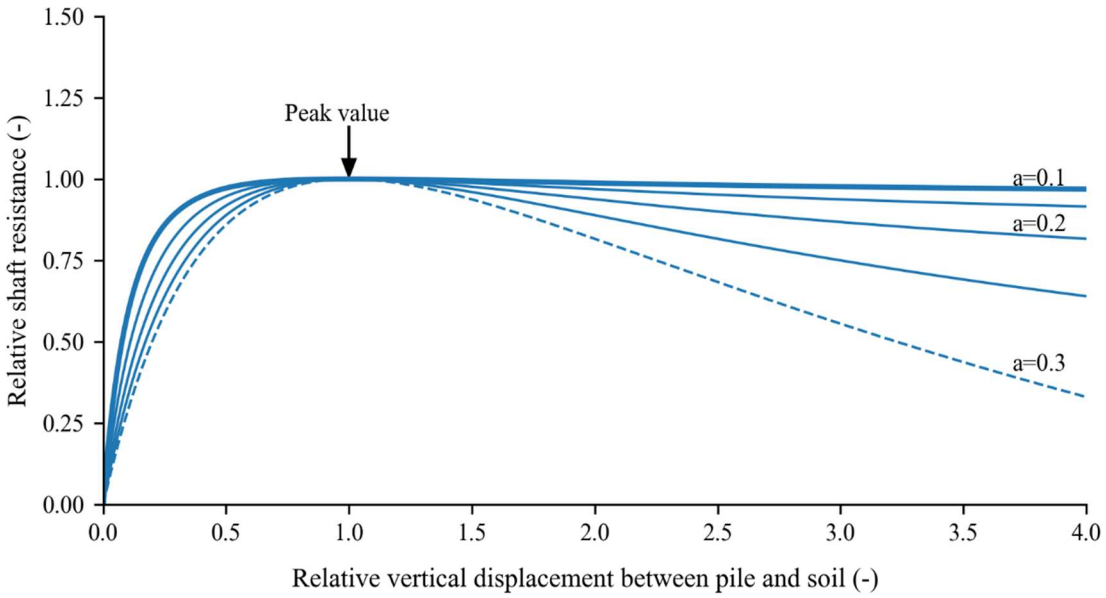

Figure 28: The Zhang strain softening t-z function.

The Rahman function

The following strain-softening t-z function was proposed by Fellenius and Rahman (2019):

$$R_s = R_{peak}\left(\frac{\delta_{peak}\delta_{pile,soil}^{F-1} + \delta_{peak}^{F-1}\delta_{pile,soil}}{\delta_{peak}^{F} + \delta_{pile,soil}^{F}}\right)^{\frac{1}{M}} \quad (40)$$

Here, R_s is the shaft resistance, $\delta_{pile,soil}$ is the relative vertical displacement between pile and soil, R_{peak} is the peak value of shaft resistance, δ_{peak} is the displacement paired with R_{peak} and F, M is function coefficients.

The Rahmann function has two separate function coefficients, M and F. Therefore, the influence of each function coefficient is illustated separately. The Rahmann function always goes through the peak value, R_{peak}, and both function coefficient controls the shape of the curve.

The Rahmann function is shown in Figure 29 and Figure 30.

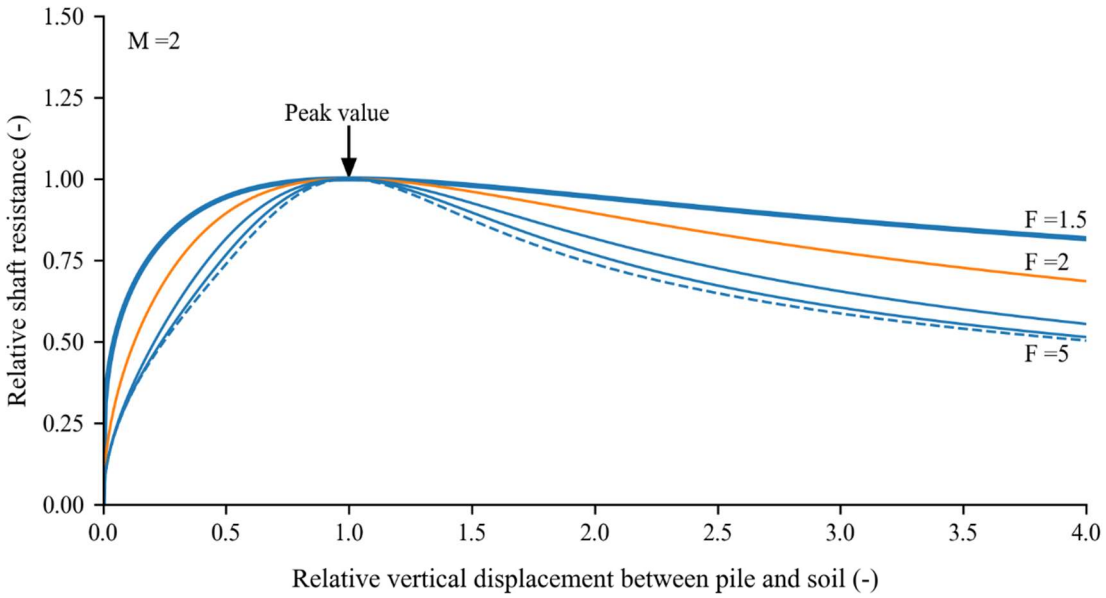

Figure 29: The Rahmann strain softening t-z function with fixed M=2 function coefficient.

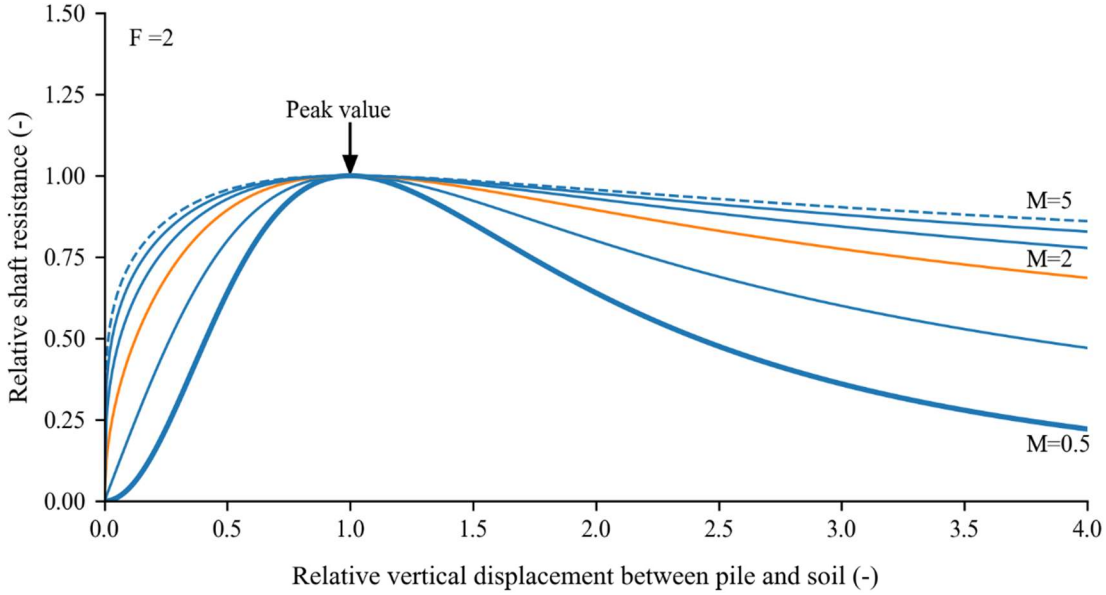

Figure 30: The Rahmann strain softening t-z function with fixed F=2 function coefficient.

The Vijayvergiya function

The following strain-softening t-z function was proposed by Vijayvergiya (1977):

$$R_s = R_{target}(A_0 \cdot \sqrt{\frac{\delta_{pile,soil}}{\delta_{target}}} - B_0 \cdot \frac{\delta_{pile,soil}}{\delta_{target}}) \quad (41)$$

Here, R_s is the shaft resistance, $\delta_{pile,soil}$ is the relative vertical displacement between pile and soil, R_{target} is the target value of shaft resistance, δ_{target} is the displacement paired with R_{target} and A_0, B_0 is function coefficients.

To ease back-analysis, the function coefficients A_0 and B_0 can be expressed as $A_0 = V$ and $B_0 = (V - 1)$ making it depend directly on the peak values and only one function coefficient, V, as A_0 and B_0 are generally found to be 2 and 1 for clays, respectively (Fellenius, 2023).

For the Vijayvergia function, the target values become the peak values for $V = 2$. If the function coefficient, $V > 2$, the curves reach a peak value that is higher than the target value and occurs before the vertical displacement between pile and soil, $\delta_{pile,soil}$, corresponding to the target value of shaft resistance, R_{target}. If the function coefficient, $V < 2$, the curves also reach a peak value that is higher than the target value, but it occurs after the vertical displacement between pile and soil, $\delta_{pile,soil}$, corresponding to the target value of shaft resistance, R_{target}. Thus, making the Vijayvergiya function capable of modelling an apparent strain-hardening behaviour as the peak values are shifted towards larger values.

The Vijayvergia function is shown in Figure 31.

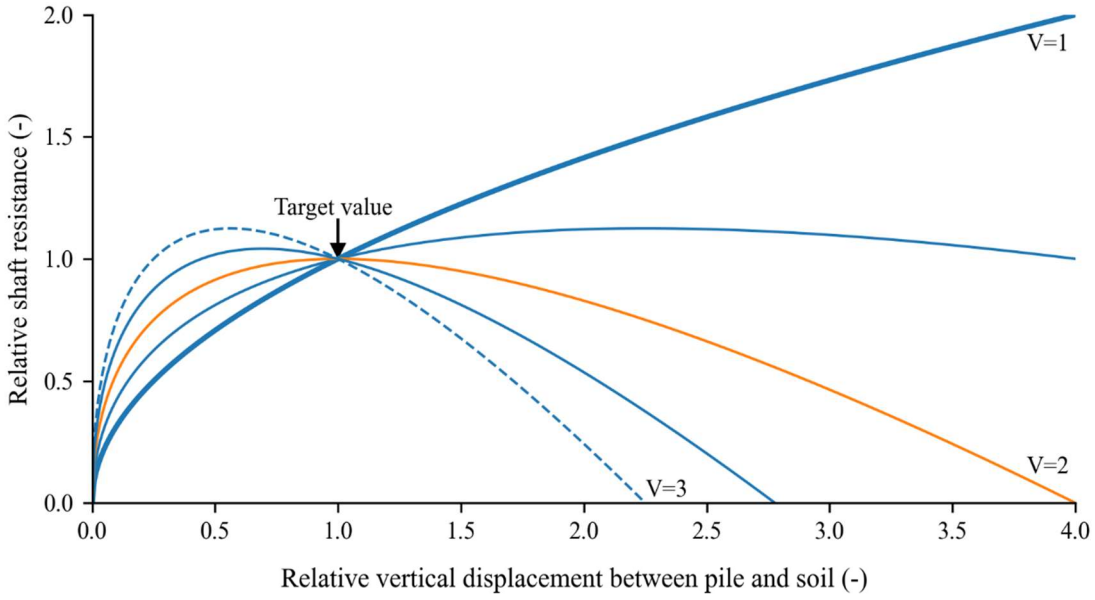

Figure 31: The Vijayvergia strain softening t-z function.

2.6 Main findings of the published literature

Residual stresses are associated with movement of the soil relative to the pile and the difference in stiffness between the pile and the soil. During the installation of both driven and bored piles, the interaction between the pile and the soil can lead to the development of "locked-in" shear stresses, commonly referred to as residual shear stresses, acting on the pile shaft. These residual stresses arise due to the displacement and disturbance of the soil during the installation process. For bored piles, residual loads also result from swelling or shrinkage of the concrete during curing. This results in residual stresses along the length of the pile shaft.

The incorporation of residual stresses into the analysis of pile response is a non-trivial aspect that deserves careful consideration. Given that bored piles are cast in-situ, it is challenging to install strain measuring equipment directly at the pile-soil interface to obtain direct measurements of residual stresses. Consequently, the interpretation of residual stresses is based on internal strain measurements within the bored piles, where inverse analysis techniques are used to determine the corresponding residual stresses.

Three different methods for interpretation of residual stresses are presented by Kim et al. (2004), Pennington (1995) and Siegel and McGillivray (2009), respectively. Flynn et al. (2012) and Flynn and McCabe (2022b) found the method proposed by Siegel and McGillivray (2009) to provide the most realistic results for driven cast-in-situ (DCIS) piles, which essentially is a combination of a driven and a bored pile. Regrettably, a comparative analysis of the three interpretation methods for bored piles could not be located within the existing literature. Hence, it would be beneficial to explore and apply these methods to bored piles.

The determination of shaft resistance can be done using either a total stress analysis, an effective stress analysis or a combination of the two. There are several specific methods commonly used for this purpose, including the α method, the β method, the λ method, and the Cone Penetration Test (CPT) method. The total stress analysis, also known as the α method, seems to be the most applicable for bored piles.

The α method is a conventional approach commonly employed to determine the ultimate shaft resistance of bored piles. This method is relatively straightforward and relies on information regarding the undrained shear strength profile. However, one of the limitations of the α method is its reliance on the empirical adhesion coefficient, α, which can vary depending on factors such as soil conditions, pile types, pile dimensions, installation methods, pile loading test methods, and methods of interpretation. These variations introduce uncertainties when used in new or untested situations. Today, the empirical adhesion coefficient $\alpha = 0.12$ for bored piles in Denmark cf. DS/EN_1997-1 (2007) and DS/EN_1997-1_DK_NA (2021), Annex L.

The relation between the empirical adhesion coefficient, α, and undrained shear strength, c_u, is commonly presented in the literature as either arithmetic, logarithmic, or exponential. However, it is

worth noting that the empirical adhesion coefficient, α, often surpasses the value of 0.12 determined according to the Danish National Annex to Eurocode 7, Annex L (DS/EN_1997-1_DK_NA, 2021), particularly for low values of undrained shear strength, c_u.

The time elapsed between pile installation and the pile loading test has a direct impact on the pile capacity. For driven piles, it is generally anticipated that the pile capacity will increase over time as the soil undergoes a recovery process. In contrast, bored piles, which are installed more cautiously, causing minimal displacement (non-displacement piles), exhibit different behaviour. In the case of bored piles, the increases in pile capacity over time are typically slight compared to driven piles (full displacement piles). Furthermore, under specific conditions like heavily overconsolidated clay, bored piles may even experience a reduction in pile capacity over time.

Two distinct cases involving bored piles installed in stiff, high plasticity clay were identified. In the first case reported by Whitaker and Cooke (1966), the findings indicate a minor increase in pile capacity (specifically, shaft resistance) with time. In the second case described by Morrison et al. (2012), the data presented does not exhibit a clear trend indicating an increasing pile capacity (specifically, shaft resistance) with time. The limited data available makes it challenging to establish a conclusive pattern or trend in the development of pile capacity over time. Further research covering a wider time range would be necessary to provide a more comprehensive understanding of the time-dependent behaviour of bored piles installed in stiff, high plasticity clay.

When modelling the interaction between soil and piles, the load transfer method by Seed and Reese (1957), Reese (1964) and Coyle and Reese (1966) is preferred as more intricate scenarios typically are more efficiently solved by employing numerical techniques, such as the load transfer method. When using the load transfer method, the pile is split up into a number of discrete sections to which a spring representing the soil-pile interaction is attached. The set of differential equations can be solved iteratively using a finite-difference approach.

The load transfer functions, also known as t-z functions, which characterize the interaction between the pile and the soil during axial loading, can be classified into two categories: linear load transfer functions and nonlinear load transfer functions. Nonlinear load transfer functions consider the nonlinear elastic-plastic behaviour that arises with increasing load levels, providing a more realistic representation of the soil-pile interaction.

The nonlinear load transfer functions are often presented in the form of shear stiffness degradation curves (G/G_0) as demonstrated by Vardanega and Bolton (2011a). Another approach, presented by Vardanega and Bolton (2011b), involves expressing the load transfer functions in terms of shear strength mobilization based on the undrained shear strength, c_u, This approach is more practical and widely applicable in everyday geotechnical engineering practice.

In addition to the previously mentioned methods, load transfer functions can be determined through the back-analysis of pile loading test results. The shaft resistance, R_s, of a pile subjected to an applied load, Q, during a pile loading test, can be represented as a function of the relative displacement, $\delta_{pile,soil}$ between the pile and the surrounding soil.

To capture the strain softening behaviour commonly observed in bored piles in stiff clay, four specific strain softening load transfer functions from the literature are presented for back-analysis of pile loading test results. These functions are derived from the works of Hansen (1963), Zhang and Zhang (2012), Fellenius and Rahman (2019) and Vijayvergiya (1977). By utilizing these strain-softening load transfer functions, the analysis of pile loading tests can provide valuable insight into the behaviour and capacity of bored piles in stiff clay.

3 Test site and soil characterization

The test piles were installed at a designated site in Hinge, where the soil primarily consisted of Eocene clay. Extensive characterization of the soil at the test site was conducted through various investigations, including ground investigations, groundwater measurements, and laboratory testing. The ground investigations involved three geotechnical boreholes, which included field vane tests and intact B-tubes, as well as six adjacent boreholes that collected intact samples using A-tubes (Shelby type) for advanced laboratory testing. Four Cone Penetration Tests (CPTu) were also performed.

In addition, previous ground investigations conducted by Simonsen (2018) were incorporated, as described in section 3.3. Laboratory testing was carried out on both remoulded and intact specimens extracted from the A- and B-tubes. This testing encompassed identification and description of the soil, classification tests, chemical tests, and advanced strength and deformation tests. The section provide an overview of the test site in Hinge and provide a detailed characterization of the soil, with particular emphasis on the Eocene clay. This clay is classified as a stiff, over consolidated, and very high plastic clay (Søvind Marl).

3.1 Test site

The designated test site in Hinge is presented in Figure 32.

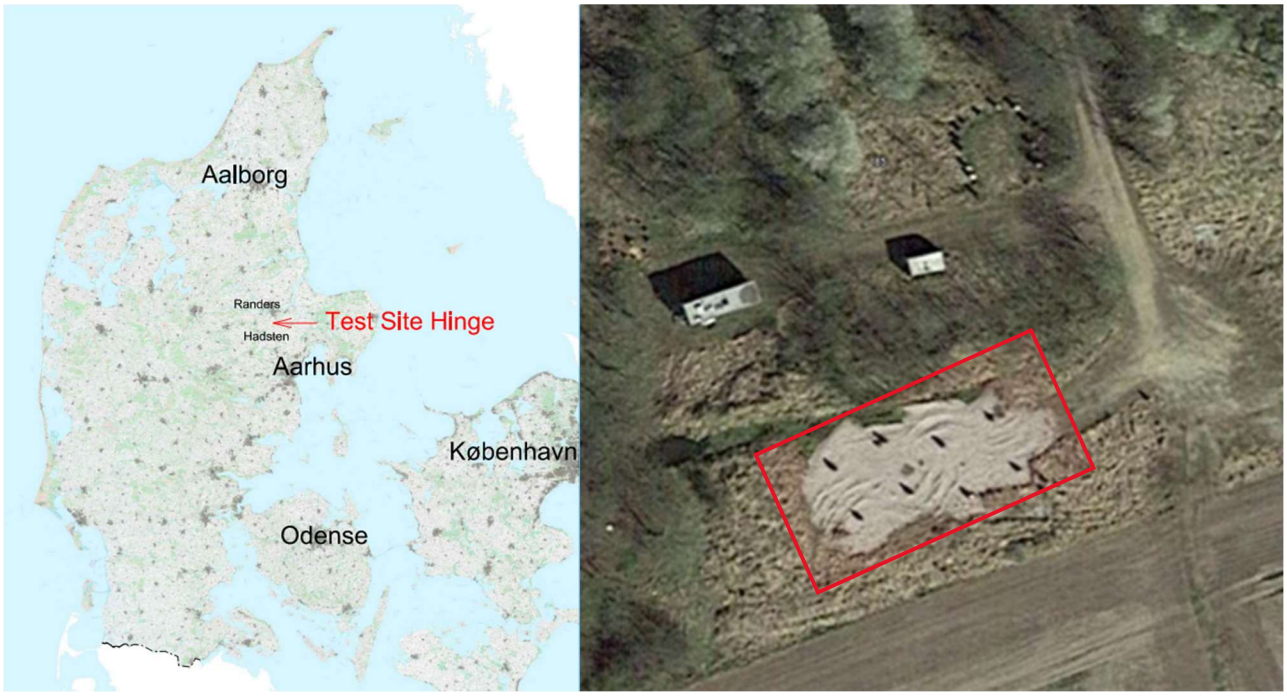

Figure 32: Location of test site Hinge in Jutland, Denmark.

The field test programme was carried out at a designated test site located in Hinge in the eastern part of Jutland, Denmark. The location of the test site provide uniform soil conditions in terms of very high plasticity clays used for production of LECA (Light Expanded Clay Aggregates) nearby as well as the opportunity to work undisturbed for the duration of the entire test programme.

3.2 Geology

In Denmark, very high plasticity clays are normally from the Paleogene period that spans from approximately 23 to 65 million years ago. The Paleogene period is divided into three eras known as the Oligocene era (23-34 million years ago), the Eocene era (34-56 million years ago) and the Paleocene era (56-65 million years ago).

During the Eocene era the deposit are of marine origin from a deep shelf environment and the marine clays deposited include the finest-grained deposits known from the North Sea Basin (Heilmann-Clausen et al., 1985). Normally, the Eocene clay is found at great depths, but most likely glacial activities during the Quaternary period have eroded younger soil strata, and the Eocene clay is found right below the Quaternary deposits within an area stretching from the north-western part of Jutland to the western part of Funen, see Figure 33.

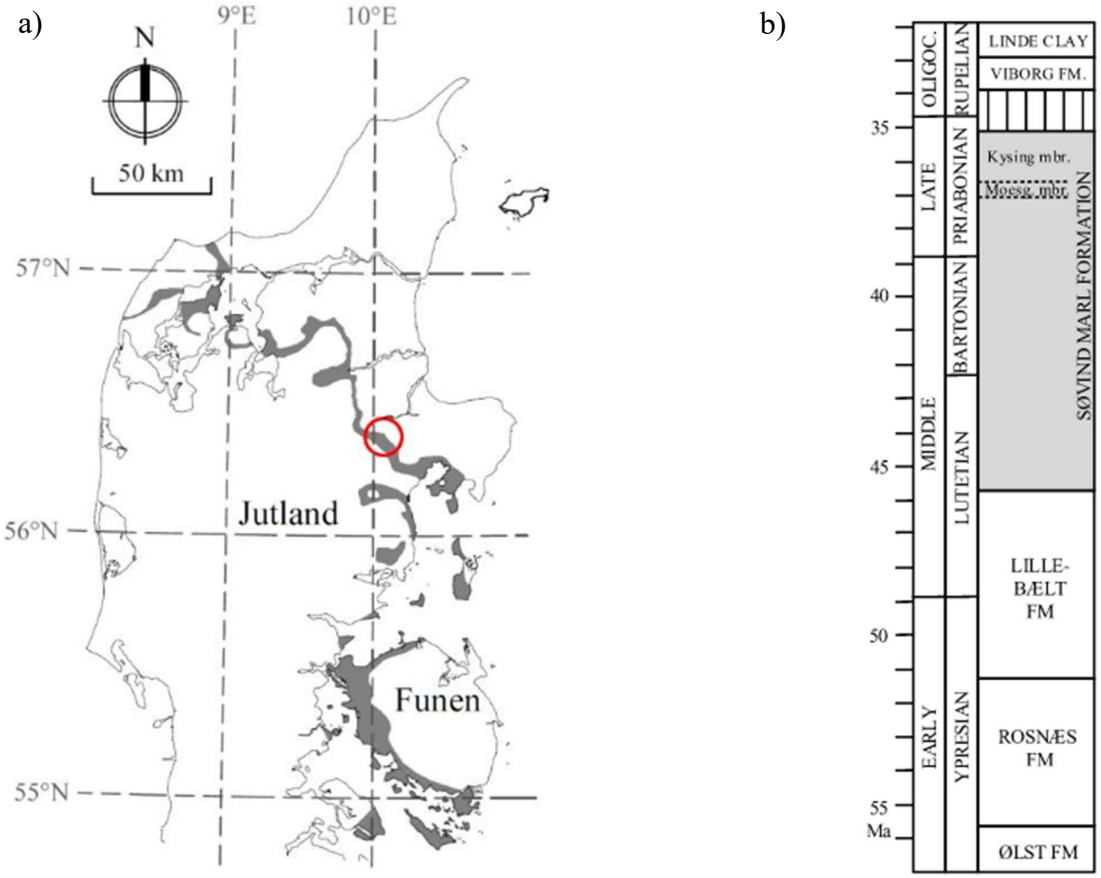

Figure 33: (a) Grey bands indicate areas where the Eocene clays are found right beneath the Quaternary deposits. Test site is marked with red circle; (b) Eocene succession in the Danish Basin with Søvind Marl formation marked grey (Simonsen, 2018).

Rather uniform ground conditions were found within the area of the test site and in immediate proximity of the test site that generally consists of approximately 3 m of clay till with a sharp boundary to the underlaying high plasticity clay from the Søvind Marl foundation (Simonsen, 2018). The Søvind Marl was found to extend to at least 15 meters below terrain with highly glauconitic horizons within the Søvind Marl layers. However, local deposits of the older Ølst formation with frequent ash layers were found in an area just east of the test site indicating glacial disturbance.

Søvind Marl is a stiff over consolidated very high plasticity and calcite rich clay with colours varying from almost white to dark (greenish) grey depending on the calcite content (Galsgaard et al., 2021). The highly varying calcite content (0-70 %) reflect the local climate and ocean currents during deposition, where the lighter marl with high calcite content is deposited during periods of warm and dry climate and the darker clay with lower calcite content is deposited during cooler and more humid climate (Sand-Jensen and Binderup, 2006). Søvind Marl is a very fine grained clay with a clay fraction between 70 and 95 % (Heilmann-Clausen et al., 1985, Grønbech, 2015) and is homogeneous in general, but contains glauconitic layers (Galsgaard et al., 2021).

3.2.1 Clay mineralogy

The clay mineral distribution of smectite, illite and kaolinite in Søvind Marl was determined a few kilometres from the test site in Ølst by Heilmann-Clausen et al. (1985), see Table 3. The large content of smectite minerals (61%) is normally offered as an explanation for the difference in behaviour between high plasticity Eocene clays and other clays.

Table 3: Clay mineral distribution in Søvind Marl in Ølst, near test site.

Location	Smectite (%)	Illite (%)	Kaolinite (%)
Ølst	61	17	22

3.3 Geotechnical investigations

3.3.1 Field investigations

At test site Hinge three geotechnical boreholes (TSH.B1-A, TSH.B2-A and TSH.B3-A) with Danish field vane test and intact B-tubes as well as four Cone Penetration Tests (TSH.CPT1-TSH.CPT4) were performed. The mutual location of the geotechnical investigation points and the bored test piles, Test pile 1 – Test pile 8, are illustrated in Figure 34.

Intact samples collected in A-tubes (Shelby type) for advanced laboratory testing were recovered from six adjacent boreholes (TSH B1-B&C, TSH B2-B&C and TSH B3-B&C) to obtain a more detailed knowledge of the ground characteristics. Due to malfunction of the laboratory fridge, unfortunately the intact samples in A-tubes from the TSH B1-B, TSH B2-B and TSH B3-B boreholes were exposed to frost and therefore discarded. New intact samples in A-tubes were collected from the TSH B1-C, TSH B2-C and TSH B3-C boreholes. For further information see the borehole profiles in Appendix A.

During the span of this PhD project, GEO was given permission to perform geotechnical investigations for a COWIfonden project about characterization of the test site in Hinge and in return two CPTu soundings (1B and BP_1.8m), two seismic CPTu (SCPT1 and SCPT2) soundings and two DMT profiles (DMT1 and DMT2) at the test site were handed over for use in this PhD project.

The test site was also previously used by former PhD student, Thomas Rye Simonsen during his PhD project on porewater pressure response and heave of Palaeogene clays in connection to deep excavation and pile driving (Simonsen, 2018). Borehole logs, CPTu soundings, swell tests and oedometer tests have been made available as well as still functioning piezometers already installed in the ground. Geotechnical investigations located in immediate proximity of the test piles (Test pile 1 – Test pile 8) is included in the present thesis. The mutual location of the geotechnical investigation points and Test pile 1 – Test pile 8 are illustrated in Figure 34.

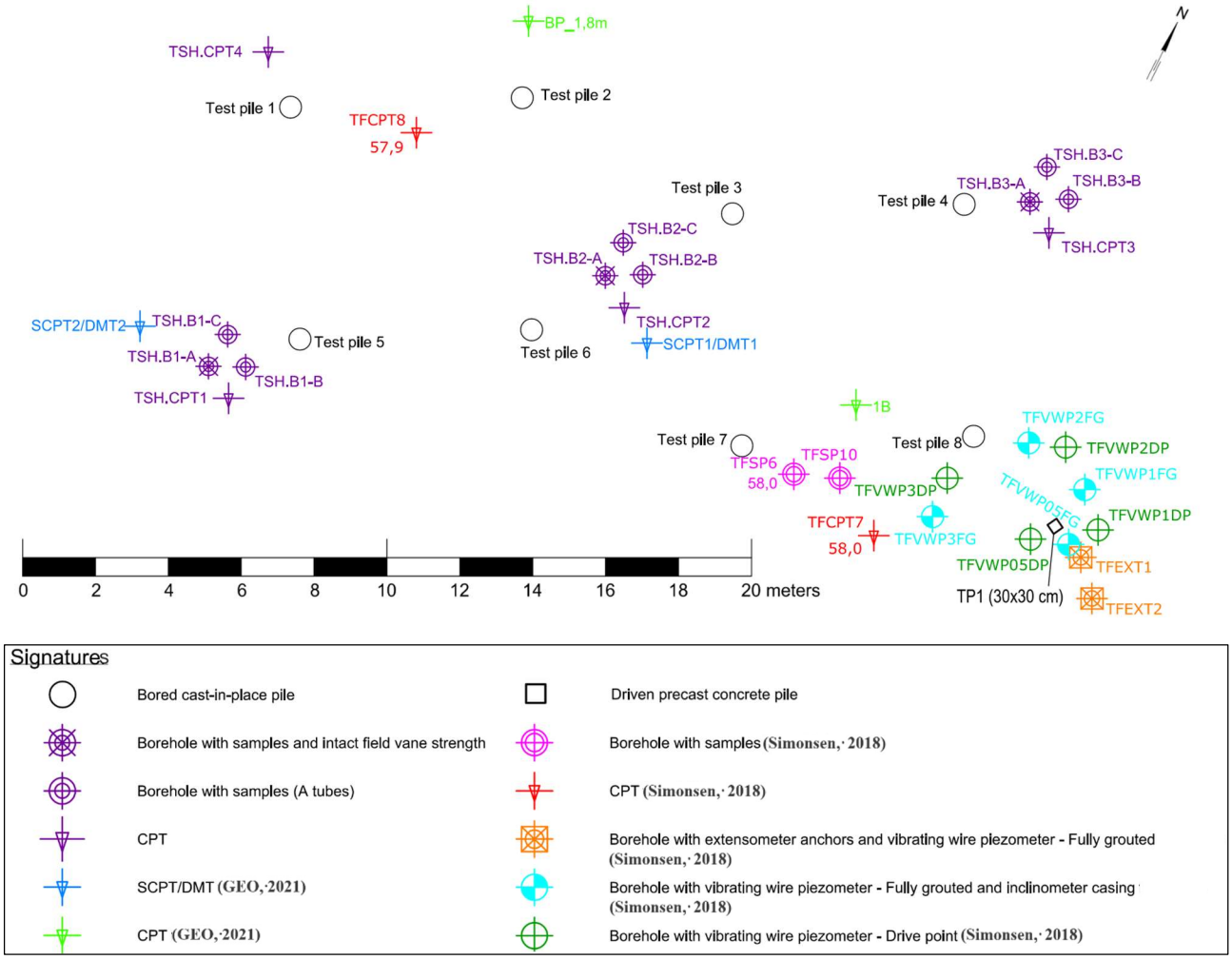

Figure 34: Locations of geotechnical investigations and test piles at test site Hinge.

3.3.2 Laboratory tests

In the present PhD project classification tests and advanced laboratory testing on the A tubes in terms of oedometer tests (IL), triaxial compression (CIU) tests, Atterberg limits, calcite content and particle density, were performed.

Several master students have performed laboratory testing on A-tubes from the geotechnical investigations from the present PhD project and Thomas Rye Simonsen's PhD project. The results from intact specimens are included were applicable.

An overview of the laboratory tests carried out on A-tubes from test site Hinge is shown in Table 4.

Table 4: Overview of laboratory testing performed on A-tubes from test site Hinge.

Borehole	Sample	Depth	Salinity	Ip	Calcite	Particle density	Swell	Oed	Triax
TSH.B1	7AA	3.5		x	x	x			CIU
	10AA	4.9		x	x				CIU
	14AA	7.0		x	x			x	CIU
	17AA	8.5		x	x				CIU
TSH.B2	*[1]11AA	5.4		x	x	x			CID
	*[1]14AA	7.0		x	x	x			CIU
	*[1]17AA	8.6		x	x	x		x	
	17AA	8.5		x	x			x	CIU
TSH.B3	10AA	5.1		x	x				CIU
	13AA	6.3		x	x				CIU
	17AA	8.4		x		x			CIU
	*[2]17A	8.3			x				CIU
TFVWP05DP	*[3]1A	5.5					x		
	*[3]4A	8.5					x		
TFVWP05FG	*[3]3A	11.5					x		
	*[3]4A	12.5					x		
TFSP6	*[3]21C	9.7						x	
	*[3]21D	9.6						x	
	*[3]25D	11.6						x	
TFVWP2FG	*[4]1	6	x						
	*[4]4	8.4							CIU
	*[4]4	8.5							CIU
	*[4]7	10.4							CIU
	*[4]10	12	x						
	*[4]13	14	x						
TFVWP2DP	*[4]?	7	x						

*[1] (Mikkelsen and Nielsen, 2023) *[2] (Gillibrand, 2020) *[3](Simonsen, 2018) *[4](Madsen and Christoffersen, 2018)

3.4 Ground conditions

3.4.1 Stratification and geological description

From ground level at approximately +58.0 m DVR90 (Danish Vertical Reference 1990) above mean sea level, the three geotechnical boreholes were performed to a depth of 10 m. The recorded stratification and the geological description of the extracted samples, is shown on the borehole profiles for TSH.B1-A to TSH-B3-A in Appendix A.

The top of the geotechnical boreholes TSH.B1-A and TSH.B2-A indicate 0.8 to 1.8 m clay fill, whilst the top of geotechnical borehole TSH.B3-A indicate 0.4 m topsoil (clay).

This is underlain by 0.4 to 0.8 m late glacial deposits of solifluction clay and 1.2 to 2.1 m glacial deposit of clay till down to the top of the Eocene clay 2.8 to 3.4 m below ground. The clay till

varies from low plasticity in the top of the layer to high plasticity in the bottom of the layer due to the underlying high plasticity Eocene clay. The clay till in the bottom of the layer is tertiary printed.

The Eocene clay is geologically described as glacially disturbed Lillebælt Clay (Member L6 and L5) on the borehole profiles in Appendix A. The signs of the glacial disturbance are, among other things, that there are elements of clay (f. e. “dusky yellow clay inclusions” and “light olive grey clay”) that do not belong in the geological sequence.

3.4.2 Ground conditions at test piles

Prior to installation of the bored piles the uppermost 0.4 m of soil was replaced by base course and steel mats to create a stable working platform for the piling rig, and subsequently replaced by gravel to minimize settlements in the upper layer during loading test.

At each pile location the top 3.4 m of soil was predrilled (Ø1000 mm diameter) and replaced by sand (poorly graded medium sand) at each pile location. This was done to minimize contributions from the upper soil layers to the shaft resistance and thereby making it easier to deduce contributions from the underlying layers of marine Eocene clay. However, surprisingly high ultimate values of mobilised unit shaft resistance are determined in the sand layers cf. section 6.3.4 indicating that another solution should have been chosen. In hindsight, a solution with double casing above the marine Eocene clay layer, leaving air in between the two, would have been preferable despite sacrificing the casings.

The soil profiles are illustrated in Figure 35.

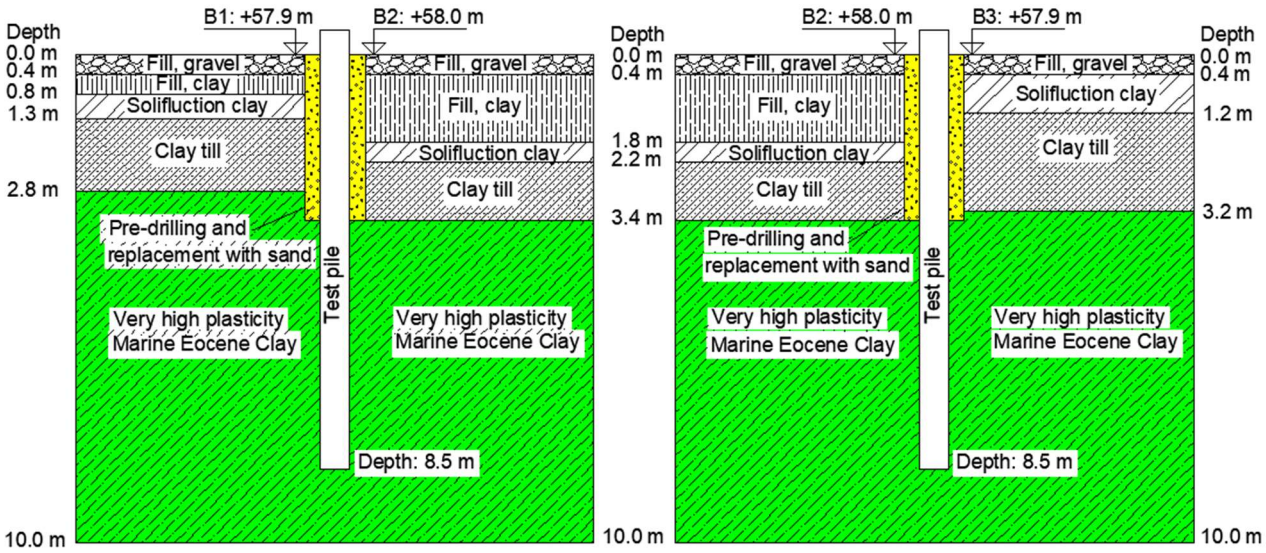

Figure 35: Soil profiles around the test piles (test pile 1-8) at test site Hinge.

3.4.3 Geological age of Eocene clay

It is well known that the Eocene sequence in the area has been glacial disturbed. The geological description at the borehole profiles states the marine Eocene clay as Lillebælt Clay, while Simonsen (2018) refers to the Marine Eocene clay as Søvind Marl. The boundary between the Lillebælt Clay and the Søvind Marl formation can be extremely hard to determine based on a geological

description and there is a gradual transition between Lillebælt Clay and Søvind Marl (Galsgaard et al., 2021).

Scanning Electron Microscopy (SEM) was performed on an intact subsample from TSH.B2, sample no. 11AA to determine the correct formation (Mikkelsen and Nielsen, 2023). Coccoliths are clearly visible on the scans, which can be seen in Figure 36.

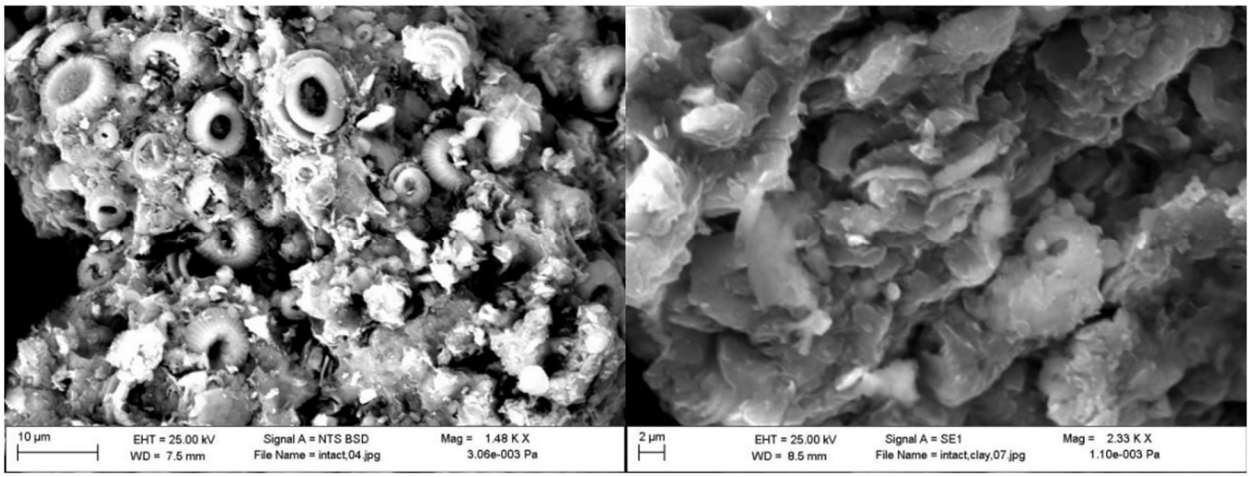

Figure 36: SEM scan of intact Marine Eocene clay cf. (Mikkelsen and Nielsen, 2023).

The SEM images were assessed by geologist Thomsen (2022) who stated that "no stratigraphical "important" species were found on the scan, but a rather large (approx. 12-13 µm) oval coccolith is seen from underneath, which is most likely the "Reticulofenestra umbilica" and thus, this makes the Marine Eocene clay likely to be from coccolith zone NP 15". Both the Lillebælt Clay (Member L6) and the Søvind Marl in the Ølst area (a few kilometers from Hinge) are from coccolith zone NP 15 (Heilmann-Clausen, 2022).

The calcite content at Ølst is around 10 % in the Lillebælt Clay and around 20 % in the Søvind Marl (Heilmann-Clausen et al., 1985). Most of the calcite contents determined at the test site in Hinge are at 20 % or higher (cf. section 3.5), indicating that the marine Eocene clay is more likely Søvind Marl although it is not possible to make a definite determination of the formation. Although the borehole profiles are indicated with member L5 and L6, the Marine Eocene clay is referred to as Søvind Marl throughout this thesis.

3.5 Index parameters for Søvind Marl

Bulk unit weight, γ, Atterberg limits (w_{nat}, w_{pl}, w_l) and calcite content of Søvind Marl are determined (Appendix B.2, B.3, B.4 and B.5) and presented in Figure 37. The bulk unit weight, γ, was determined from intact samples extracted in B tubes, while Atterberg limits (w_{nat}, w_{pl}, w_l) and calcite content were determined from intact samples in A tubes retrieved during borehole drilling. Procedures for laboratory tests are given in Appendix B.1.

The bulk unit weight, γ, is 16.6 kN/m^3 in average, which is relatively low and caused by the high natural water content. The particle density, G_s, is on the other hand found to be relatively high and determined as 2.77 and 2.78 for TSH.B1, sample 7AA and TSH.B3, sample 17AA (Appendix B.6). This is consistent with the findings of Grønbech et al. (2015), where a bulk unit weight, γ, between 16.7 and 18.1 kN/m^3 and a particle density, G_s, between 2.7 and 2.8 were found for Søvind Marl.

Søvind Marl encountered at the test site has a natural water content, w_{nat}, ranging from 46 to 62 % and a plasticity index ($I_p = w_l - w_{pl}$), ranging from 84 to 203 %, where w_l is the liquid limit (determined by fall cone method) and w_{pl} is the plastic limit. The measured calcite content (determined by titration) for specimens of Søvind Marl varies between 4 and 36 %.

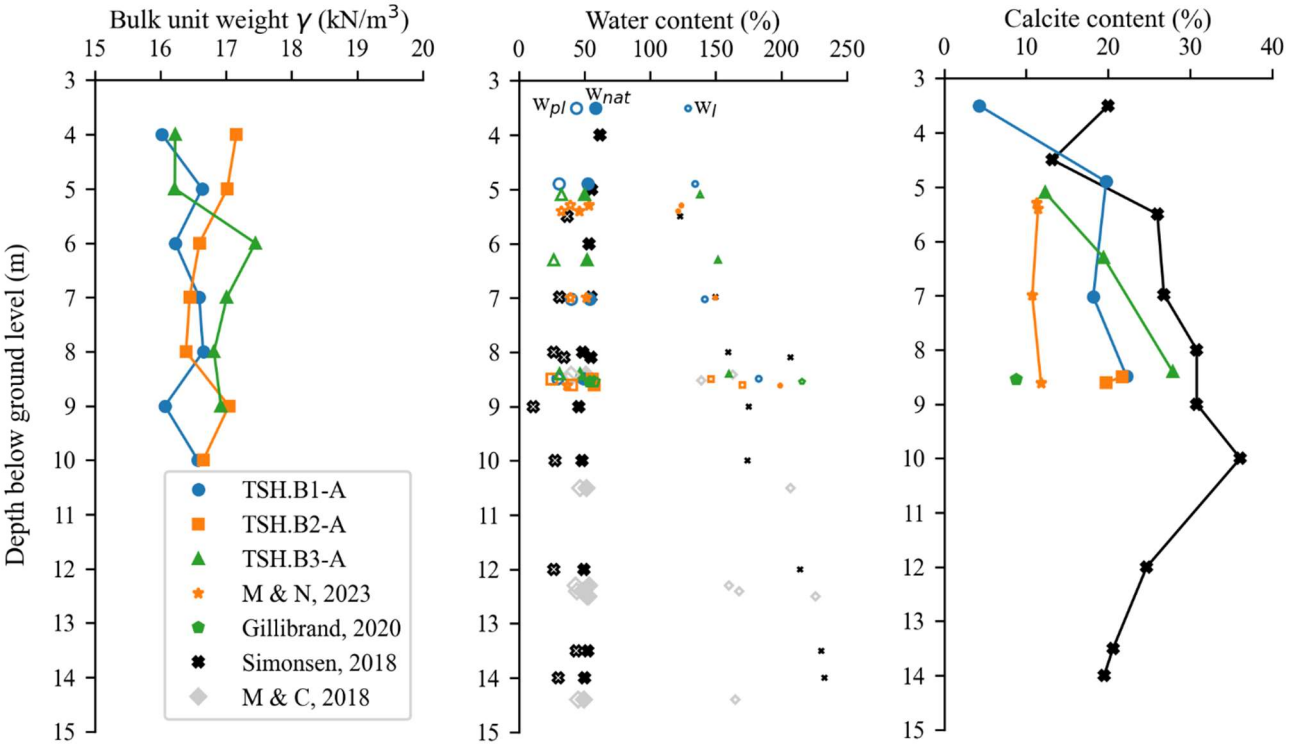

Figure 37: Bulk unit weight, water content, Atterberg limits and calcite content for specimens of Søvind Marl at the test site in Hinge. (Mikkelsen and Nielsen, 2023);(Gillibrand, 2020);(Simonsen, 2018);(Madsen and Christoffersen, 2018).

The Casagrande plasticity chart (Casagrande, 1932) for the samples is presented in Figure 38. Because of the high liquid limits of the Søvind Marl, and Danish Eocene clays in general, the data points plot outside the normal boundaries of the Unified Soil Classification System (USCS), which covers liquid limits up to 100 %. Grønbech et al. (2011) introduced two additional categories CS (Super High Plasticity Clay) and CE (Extremely High Plasticity Clay) to extend the USCS to cover clays with liquid limits up to 350 % and these have been added to the Casagrande chart.

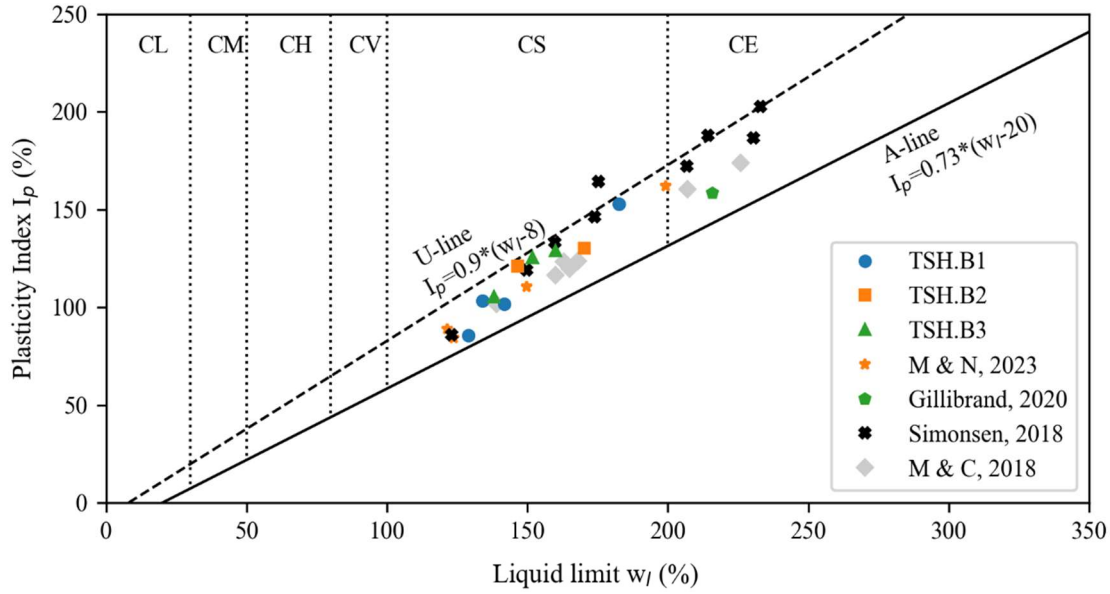

Figure 38: Extended Casagrande chart for specimens of Søvind Marl at the test site in Hinge. (Mikkelsen and Nielsen, 2023);(Gillibrand, 2020);(Simonsen, 2018);(Madsen and Christoffersen, 2018).

All data points lie above the A-line which generally separates inorganic clays from inorganic silts and organic clays and all but one beneath the U-line, also known as the Upper limit line, that indicates an error if data points lie above this line cf. Holtz and Kovacs (1981).

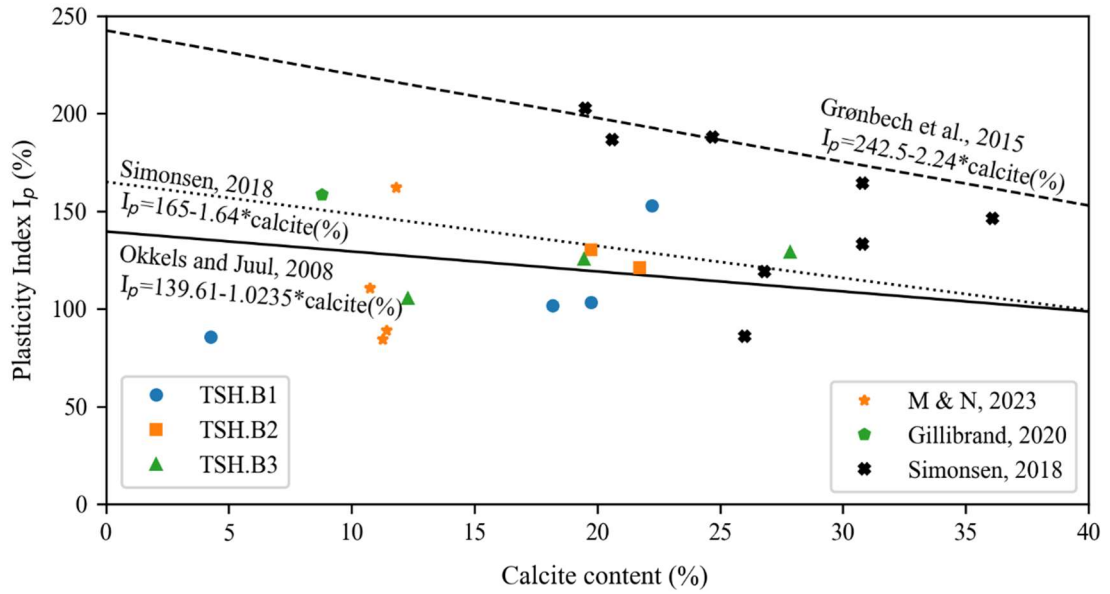

Figure 39: Relationship between plasticity index, I_p and calcite content for Søvind Marl at the test site shown with inverse correlations. (Mikkelsen and Nielsen, 2023);(Gillibrand, 2020);(Simonsen, 2018).

The plasticity index, I_p, is inversely correlated with the calcite content for Søvind Marl (Okkels and Juul, 2008, Grønbech et al., 2015, Simonsen, 2018). However, the Søvind Marl at the test site in Hinge is not well correlated and the plasticity index, I_p, seems more likely to be governed mainly by the clay mineralogy, see Figure 39.

3.6 Total strength parameters for Søvind Marl

Relatively uniform soil conditions are found in the Søvind marl at the test site in Hinge from the CPTu soundings performed across the entire test site. Figure 40 shows the corrected cone resistance, q_t, friction ratio, R_f, and porewater pressure, u_2, measured at the test site. The cone resistance is corrected due to "the unequal area effect" cf. Lunne et al. (2002):

$$q_t = q_c + u_2 \cdot (1 - a_c) \tag{42}$$

Here q_t is the corrected cone resistance, q_c is the cone resistance, u_2 is the porewater pressure measured on the cone shoulder and a_c is the cone area ratio.

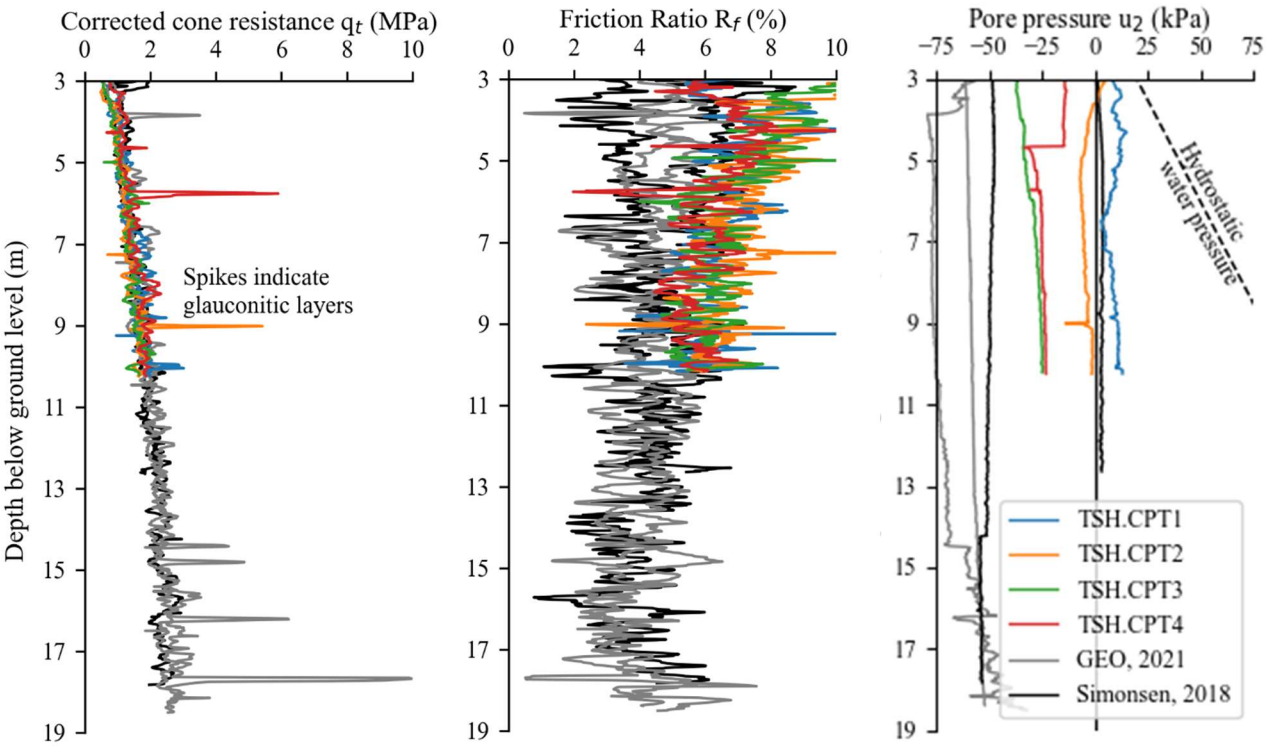

Figure 40: Corrected cone resistance, q_t, friction ratio, R_f, and porewater pressure, u_2, for Søvind Marl at the Hinge test site.

The CPTu soundings are very similar with exception of some spikes originating from high content of glauconitic layers. The porewater pressure is very close to zero, which is a typical response in heavily over consolidated clays (Lunne et al., 2002, Mayne et al., 1990). It is not recommended to use CPT classification charts as they are commonly based on either pore pressure ratio, B_q, and corrected cone resistance, q_t, or friction ratio, R_f, and corrected cone resistance, q_t. They do not take into account the high degree of over consolidation and thus, misclassify Søvind Marl and other highly over consolidated clays (Grønbech et al., 2015).

The undrained shear strength of Søvind Marl at the test site is evaluated by CPTu soundings, field vane tests and isotropic consolidated undrained triaxial compression (CIU) tests, see Figure 41.

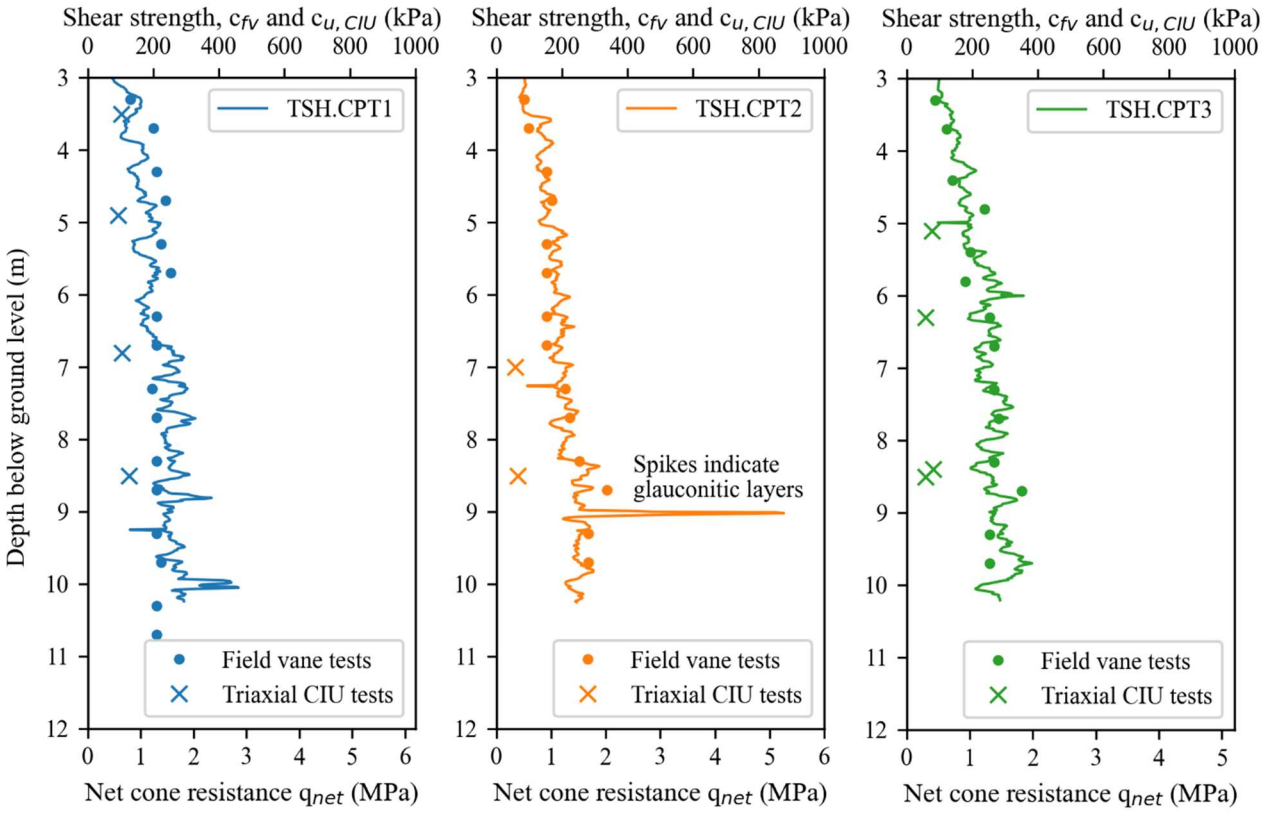

Figure 41: Measured field vane strength, c_{fv}, and undrained shear strength from isotropic consolidated undrained triaxial compression tests, c_u^{CIU}, for borehole TSH.B1 – TSH.B3 and net cone resistance, q_{net}, from nearby CPTu soundings TSH.CPT1- TSH.CPT3.

Measured field vane strength, c_{fv}, and net cone resistance, q_{net}, from CPTu soundings is observed to increase with depth for Søvind Marl at the test site cf. Figure 41, except from the measured field vane strength, c_{fv}, for borehole TSH.B1 that appears to be constant with depth.

The fissured and slicken sided structure of the Søvind Marl causes the undrained shear strength, c_u^{CIU}, determined by isotropic consolidated triaxial undrained compression (CIU) tests to be significantly reduced compared to the intact field vane strength, c_{fv}, measured by the Danish field vane tests (fast field vane test, approximately 1 round per minute). The strength is correlated by a factor μ:

$$c_u^{CIU} = \mu \cdot c_{fv} \tag{43}$$

Here c_u^{CIU} is the undrained shear strength determined by isotropic consolidated triaxial undrained compression (CIU) test and c_{fv} is the measured field vane strength.

The correlation factor μ varies between 0.26 and 0.79 for Søvind Marl at the test site in Hinge. Only the uppermost isotropic consolidated triaxial undrained compression (CIU) test on sample 7AA in borehole TSH.B1 provide a high correlation factor ($\mu = 0.79$), while the correlation factor μ varies between 0.26 and 0.59 for the rest of the isotropic consolidated triaxial undrained compression (CIU) tests. All the triaxial tested specimens present a barrel shaped failure mode with varying degree of

fissuring after failure, see an example of a fissured specimen in Figure 42 with a low correlation factor ($\mu = 0.26$).

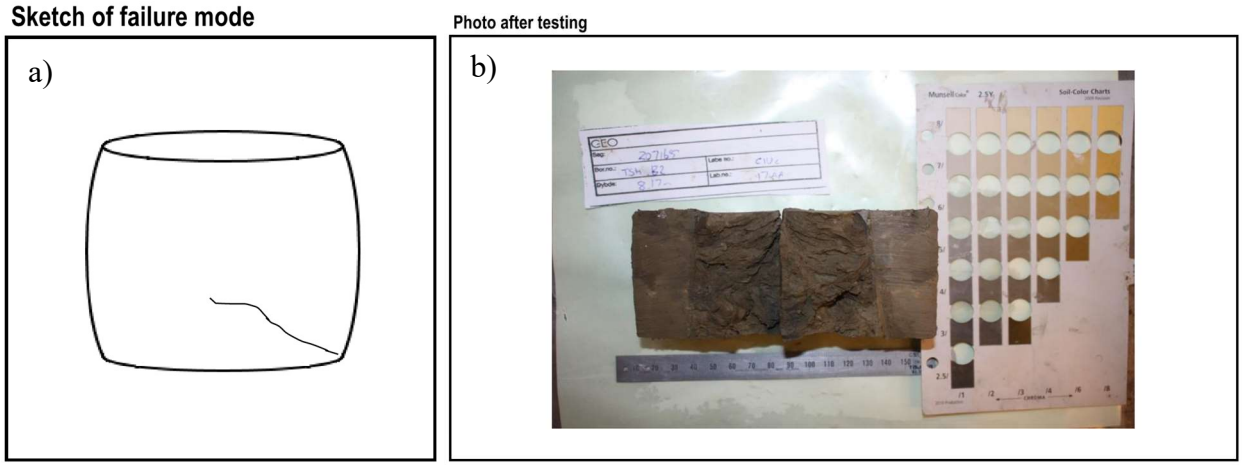

Figure 42: Triaxial test (CIU) on sample 17AA in TSH.B2 ($\mu = 0.26$). a) Sketch of specimen after failure (barrel shaped with fissures) and b) Photo of specimen after failure (with fissures).

For the isotropic consolidated triaxial undrained compression (CIU) tests on the upper Søvind Marl sample 7AA in borehole TSH.B1 the correlation factor was high ($\mu = 0.79$). This may be due to the fact that no visible fissures were observed after failure, and the Søvind Marl might have been glacially disturbed by the overlying clay till in immediate proximity of the tested specimen.

The variation of the correlation factor is found to be otherwise random ($\mu = 0.26 - 0.59$) with an average value of 0.36. This is consistent with the findings of Grønbech (2015), where the correlation factor μ varies between approximately 0.18 and 0.83 with an average value between 0.3 and 0.4 in the upper 10 m of Søvind Marl. Furthermore, an average value of 0.33 was found on Skive Septarian clay (a Danish highly fissured over consolidated clay) by Christensen and Hansen (1959).

Alternatively, the undrained shear strength, c_u^{CIU}, determined by isotropic consolidated triaxial undrained compression (CIU) tests can be related to the intact strength from CPTu soundings cf. Lunne et al. (2002), using the cone tip factor N_{kt}:

$$N_{kt} = \frac{q_t - \sigma_{v,0}}{c_u^{CIU}} \tag{44}$$

Here c_u^{CIU} is the undrained shear strength determined by isotropic consolidated triaxial undrained compression (CIU) test, q_t is the corrected cone resistance and $\sigma_{v,0}$ is the total vertical stress. $(q_t - \sigma_{v,0})$ is also referred to as the net cone resistance, q_{net}.

Due to the undrained shear strength, c_u^{CIU}, determined by isotropic consolidated triaxial undrained compression (CIU) test being highly affected by the fissure strength and the extend of fissures in the tested specimen, see Figure 41, the cone tip factor N_{kt}^{cfv} is alternative determined in relation to the field vane strength, c_{fv}, for a more firm and regular reference:

$$N_{kt}^{cfv} = \frac{q_t - \sigma_{v0}}{c_{fv}} \tag{45}$$

The cone tip factor N_{kt}^{cfv} is determined to 6.2, 6.0 and 5.2 respectively for geotechnical borehole TSH.B1, TSH.B2 and TSH.B3 by equalizing the best fit equations for the intact strength from CPTu soundings and the measured field vane strength, c_{fv}, in the middle of the observed Søvind Marl. The cone tip factor N_{kt}^{cfv} is seen to be increasing with depth.

The porewater pressures measured on the cone shoulder in the CPTu soundings in Figure 40 are seen to be negative or close to zero, which is commonly observed in stiff heavily over consolidated clays with low hydraulic conductivity. It is of course not a measure of the actual porewater pressure in the clay, this can only be observed if the pressure transducer is left in place for longer time. The shearing and cavity expansion in the clay around the cone tend to generate negative porewater pressures as it is heavily over consolidated.

Søvind Marl at the test site in Hinge will in the following analyses be considered as a uniform site-specific soil, as it is not possible to identify any significant differences between the three geotechnical boreholes.

3.7 Effective strength parameters for Søvind Marl

Generally, it is accepted that the effective strength of uncemented saturated clays is frictional, and the strength envelope is nonlinear. Hence, the true effective cohesion, $c' = 0$ kPa as the strength envelope passes through origin (Burland, 1990). However, the effective peak strength can, within a limited interval of stress, be approximated by a linear relationship between the effective normal stress at failure, σ'_f, and the shear strength at failure, τ_f, using the Mohr-Coulomb failure criterium:

$$\tau_f = \sigma'_f \cdot \tan\varphi' + c' \tag{46}$$

Here φ' is the effective angle of shearing resistance and c' is the apparent effective cohesion.

For specimens of very high plasticity clay it is important to prevent swelling by avoiding the effective stress to reduce below the in-situ stresses, as it otherwise may lead to destructuration of the micro-structure (Leroueil and Vaughan, 1990) and thus influence (reduce) the strength parameters.

The stress path from 12 isotropic consolidated triaxial undrained compression (CIU) tests and 1 isotropic consolidated triaxial drained compression (CID) test cf. section 3.3 are shown in a p'- q plot in Figure 43. The isotropic consolidated triaxial undrained compression (CIU) tests from TSH.B1, TSH.B2 and TSH.B3 are presented in Appendix B.8.

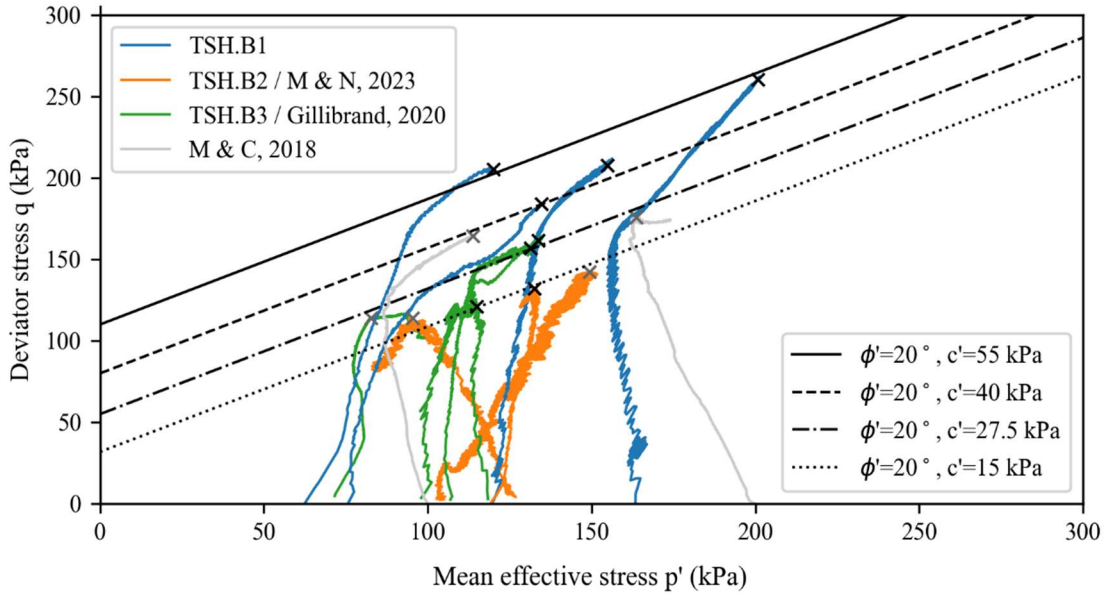

Figure 43: Stress path followed in 12 isotropic consolidated triaxial undrained compression (CIU) tests and 1 isotropic consolidated triaxial drained compression (CID) test with indication of failure points. (Mikkelsen and Nielsen, 2023);(Gillibrand, 2020);(Madsen and Christoffersen, 2018).

No unambiguously strength envelope appears for Søvind Marl from Figure 43, which is most likely because stiff over consolidated clays may fail along preexisting fissures and the strength is therefore governed by the fissure strength and the extend of fissures in the tested specimen.

The triaxial compression tests performed for this PhD project were performed with a height:diameter ratio of 1:1 (70 mm) and smooth end plates according to Danish tradition, while the master students all performed the triaxial compression tests with a height:diameter ratio of 2:1 (100 mm/50 mm) and rough end plates in accordance with DS/EN_ISO_17892-9 (2018). All specimens tested by the master students had either developed shear band or were heavily fissured after finalization of the triaxial compression tests, indicating that the Danish tradition with a height:diameter ratio of 1:1 and smooth end plates is more suitable for triaxial compression tests on stiff over consolidated clays.

In triaxial tests with "single specimen hight" and smooth end plates, there will be homogeneous stress-strain state in the specimen, while the stress-strain state will be inhomogeneous in specimen with double height, as failure often will develop in a narrow failure zone that separates two rigid soil bodies.

Furthermore, the effective angle of shearing resistance, φ', and the plasticity index, I_p, is inversely correlated and thus, specimens with different plasticity index, I_p, will not follow the exact same strength envelope. A best estimate of the effective angle of shearing resistance (peak values) for over consolidated soils are given by Sorensen and Okkels (2013) for $50\% \leq I_p < 150\%$:

$$\varphi' = 26 - 3 \cdot \log I_p \tag{47}$$

Here φ' is the effective angle of shearing resistance and I_p is the plasticity index.

With a variation of plasticity index, I_p, in the range 86% to 161% for the triaxial test specimens of Søvind Marl, the effective angle of shearing resistance can be estimated to vary between 19.4° and 20.2°. An average value of the effective angle of shearing resistance, $\varphi' = 20°$ is used and the failure envelopes with four different values of apparent effective cohesion, c', are shown in Figure 43.

In the p' – q plot the Mohr-Coulomb failure criterion is defined cf. Schofield and Wroth (1968):

$$q = \frac{6 \cdot \sin \varphi'}{3 - \cos \varphi'} \cdot (p' + c' \cdot \cot \varphi') \tag{48}$$

Here φ' is the effective angle of shearing resistance and c' is the apparent effective cohesion.

The inclination of the failure envelope in the p'-q plot, M, is defined by means of the effective angle of shearing resistance (φ' = 20°) to:

$$M = \frac{q}{p'} = \frac{6 \cdot \sin \varphi'}{3 - \sin \varphi'} \tag{49}$$

Here M is the inclination of the failure envelope in the p'-q plot and φ' is the effective angle of shearing resistance.

And based on the failure envelopes intersection with the q-axis in the p'-q plot, q_0, the apparent effective cohesion, can be given as:

$$c' = \frac{3 - \sin \varphi'}{6 \cdot \cos \varphi'} \cdot q_0 \tag{50}$$

Here c' is the apparent effective cohesion of the Mohr-Coulomb failure criterium, φ' is the effective angle of shearing resistance and q_0 is the failure envelopes intersection with the y-axis (p'-q plot).

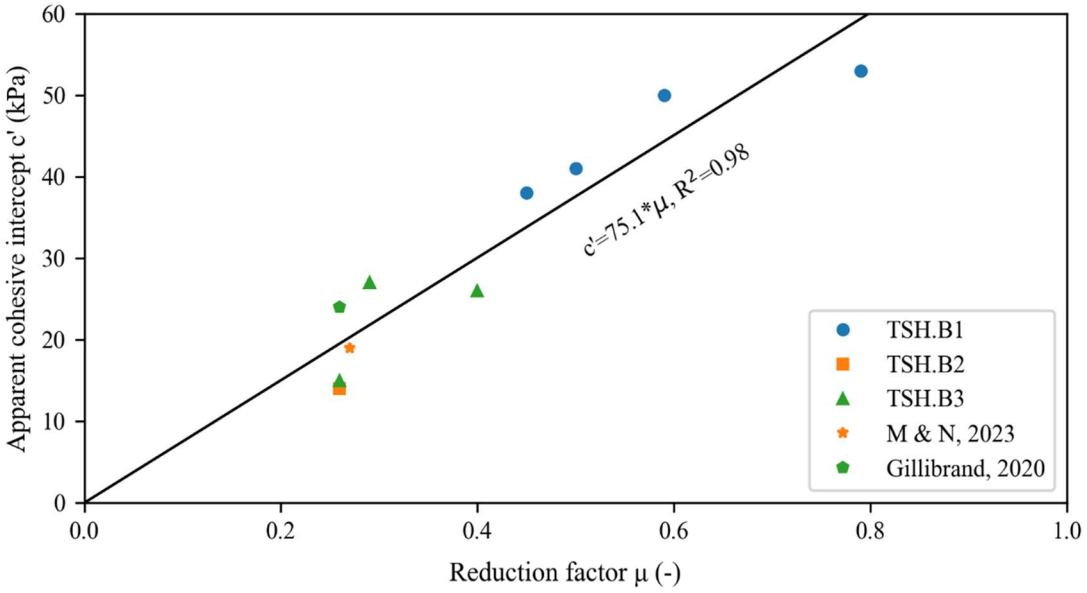

Figure 44: Effect of fissuring on the apparent effective cohesion, c', vs. the correlation factor, $\mu = c_u^{CIU} / c_{fv}$.

The apparent effective cohesion, c', from the Mohr-Coulomb failure criterium can then be perceived as an expression on how fissured and destructured the tested specimen is, see Figure 44. The lower apparent effective cohesion, the more fissured and destructured specimen and the higher apparent effective cohesion, the more intact specimen.

For unloading (excavation and active earth pressure) in fissured clay and clay with slickensides, the apparent effective cohesion must be disregarded (c' = 0) cf. the Danish National Annex to Eurocode 7, Annex K (DS/EN_1997-1_DK_NA, 2021).

3.8 Deformation properties for Søvind Marl

3.8.1 Preconsolidation stress

For Søvind Marl, and other heavily over consolidated clays, the determination of yield and pre consolidation stresses from oedometer tests have been discussed thoroughly because of the appearance of two apparent yield stresses (a low and a high). The high yield stress is believed to represent the geological pre consolidation pressure but might occur at such high stress levels that it is outside the range of conventional oedometer tests (Okkels and Hansen, 2016). The low yield stress is often described a "loss of memory" due to swelling or debonding (Krogsbøll et al., 2012), closure of fissures (Grønbech, 2015) or side friction beside specimen and oedometer ring (Okkels and Hansen, 2016).

The over consolidation ratio (high yield stress) has not been determined, but the Søvind Marl is likely to have an OCR of at least 20 (heavily over consolidated) at the test site, because of the very complex stress history with the erosion of several hundred meters of younger layers (Heilmann-Clausen and Rasmussen, 2010) and the weight of numerous glaciers during the Quaternary period.

The first oedometer test on Søvind Marl (see Appendix B.7) was performed for determination of the pre consolidation stress on TSH.B1, sample 14AA, and the pre consolidation stress was determined to $\sigma'_{pc} = 400 - 500$ kPa by the methods of Akai (Akai, 1960), Becker (Becker et al., 1987), Casagrande (Casagrande, 1936) and Janbu (Janbu et al., 1981). The over consolidation ratio (low yield stress) can be determined as $OCR = \sigma'_{pc}/\sigma'_{v,0}$ and hence, OCR = 7 á 9.

3.8.2 Earth pressure at rest

The coefficient of earth pressure at rest, K_0, is estimated from the 8 isotropic consolidated triaxial undrained compression (CIU) tests performed on TSH.B1, sample no. 7AA, 10AA, 14AA and 17AA, TSH.B2, sample no. 17AA and TSH.B3, sample no. 10AA, 13AA and 17AA, see Appendix B.8.

It is assumed that the swelling pressure of the specimen will be controlled by the mean effective stress in-situ. To prevent the specimens from swelling during saturation the isotropic stress applied, p'_{sat}, should approximately be equal to the swelling pressure. Hence, the effective horizontal in situ stress can be determined:

$$p'_{sat} = \frac{\sigma'_{v,0} + 2 \cdot \sigma'_{h,0}}{3} \leftrightarrow \sigma'_{h,0} = \frac{3 \cdot p'_{sat} - \sigma'_{v,0}}{2} \quad (51)$$

Here $\sigma'_{v,0}$ is the effective vertical in situ stress and $\sigma'_{h,0}$ is the effective horizontal in situ stress.

The coefficient of earth pressure at rest, K_0, is then determined as:

$$K_0 = \frac{\sigma'_{h,0}}{\sigma'_{v,0}} \quad (52)$$

The coefficient of earth pressure at rest, K_0, for the Søvind Marl at the test site was estimated to 1.8 á 2.9 (1.0 for TSH.B3, 13AA) and only for TSH.B1, sample no. 17AA swell unintentionally was observed, see Table 5 . This is reasonably consistent with the findings of Simonsen (2018) that estimated the coefficient of earth pressure at rest, K_0, at the test site to 2.5 á 3.0 from four swell test.

Table 5: Estimated coefficient of earth pressure at rest, K_0, based on results of triaxial tests (CIU).

Borehole	TSH.B1				TSH.B2	TSH.B3		
Sample	7AA	10AA	14AA	17AA	17AA	10AA	13AA	17AA
K_0	1.8	2.0	2.4	2.9*	1.8	2.6	1.0	1.9

*Swell observed in initial loading

The coefficient of earth pressure at rest, K_0, is dependent on correct determination of the effective vertical in situ stress, $\sigma'_{v,0}$. Uncertainty in the effective vertical stress may arise due to uncertainty in the unit weight of the soil and the groundwater level.

3.8.3 Small-strain stiffness

The small-strain shear modulus, G_0, have been determined based on the shear wave velocity, V_s, from two SCPTu soundings at the test site (GEO, 2021), see Figure 45.

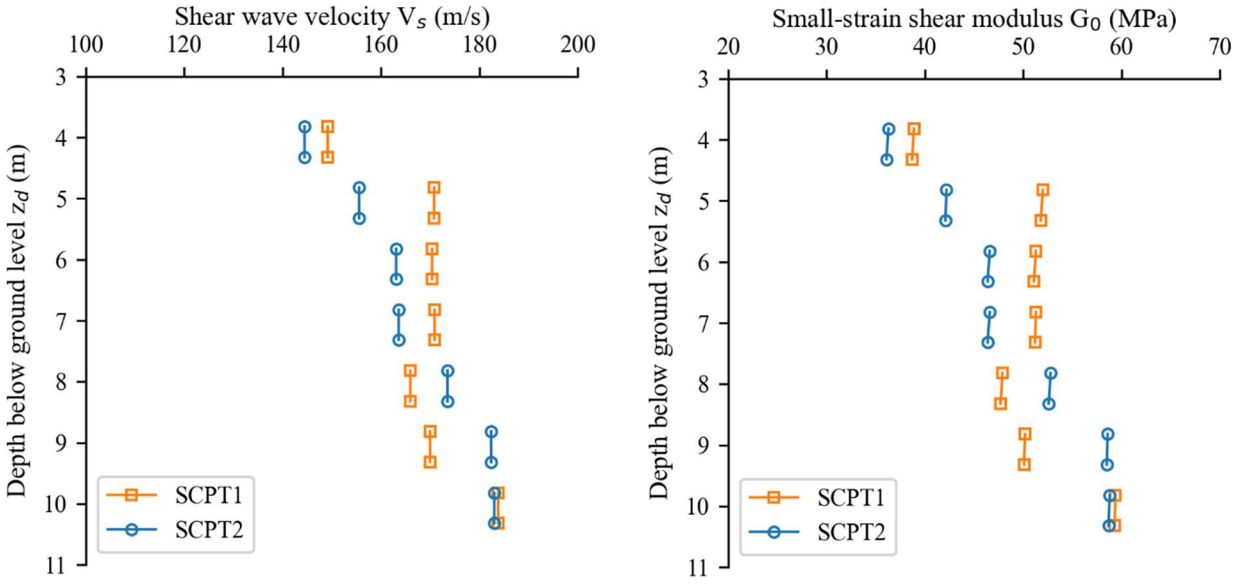

Figure 45: Shear wave velocity, V_s, and small-strain shear modulus, G_0, for the test site.

The small-strain shear modulus, G_0, increases (linearly) with depth and seem to correlate well with the CPTu soundings. The small-strain shear modulus, G_0, was determined cf. Lunne et al. (2002):

$$G_0 = \rho \cdot V_s^2 \tag{53}$$

Here G_0 is the small-strain shear modulus, ρ is the soil mass density (unit weight divided by the acceleration of gravity) and V_s is the shear wave velocity. A unit weight between 17.0 and 17.5 kPa has been used (GEO, 2021).

3.8.4 Large strain stiffness

Two oedometer tests were performed with two unloading, reloading loops to determine the mean oedometer modulus (in reloading) dependency of the stress level, see Appendix B.7. The results are presented together with the oedometer modulus for Søvind Marl at Aarhus Harbour cf. COWI (2023), see Figure 46.

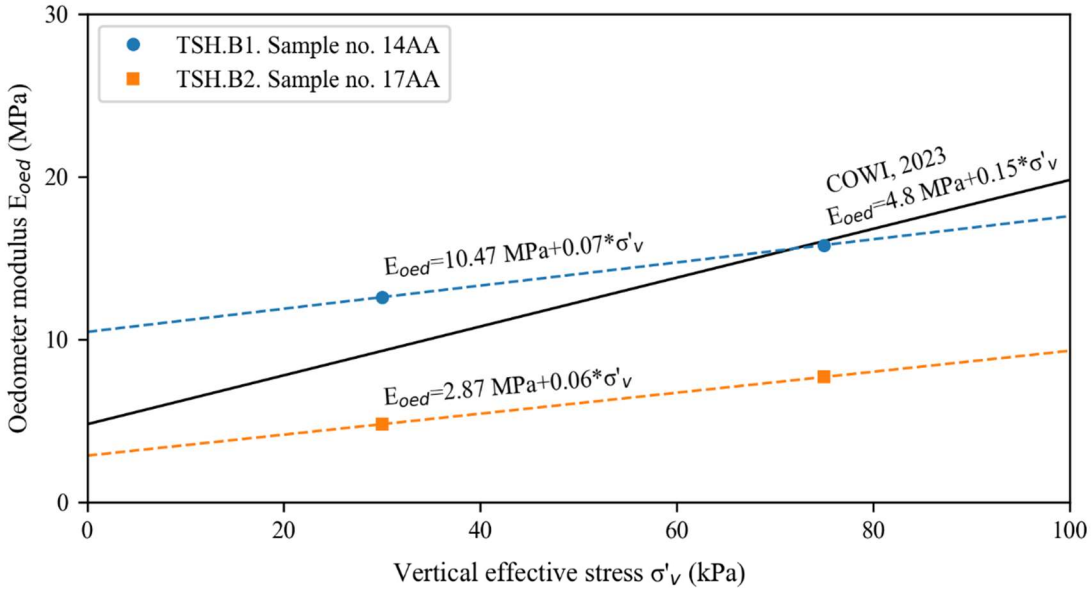

Figure 46: Oedometer modulus dependency of lowest vertical effective stress to which the clay has been exposed.

The determined oedometer modulus for specimens of Søvind Marl from the test site at Hinge are generally consistent with the parameters obtained from test on specimens of Søvind Marl from Aarhus Harbour. The oedometer modulus ranges from approximately 5 MPa in the upper part of the Søvind Marl (~3 m below ground level) to around 17 MPa at the bottom of the boreholes (~10 m below ground level). The determined range of oedometer modulus is consistent with the findings of Simonsen (2018), who estimated the oedometer modulus to around 8 MPa.

3.8.5 Permeability

Based on the three oedometer tests carried out on specimens from the test site (Appendix B.7), the consolidation coefficient, c_k, is in the laboratory (22° C) determined by classical consolidation theory for the individual load steps.

The coefficient of permeability, k_p, is subsequently determined by the following equation:

$$k_p = \frac{c_k \cdot \gamma_w}{E_{oed}} \tag{54}$$

Here c_k is the consolidation coefficient, γ_w is the bulk unit weight of water (9.816 kN/m^3) and E_{oed} is the secant oedometer modulus.

By indirect measurement, the coefficient of permeability of the Søvind Marl yields values in the interval $1 \cdot 10^{-12}$ m/s to $3 \cdot 10^{-11}$ m/s. It agrees well with the results of similar laboratory determination of Simonsen (2018) that estimated the coefficient of permeability, k_p, of the Søvind Marl at test site to be between $9 \cdot 10^{-12}$ m/s and $3 \cdot 10^{-1}$ m/s.

3.9 Groundwater conditions

3.9.1 Groundwater measurements

The filters were positioned in the Søvind Marl from 8.0 to 10.0 m below ground and in the overlying soil (clay fill, solifluction clay and clay till) from 1.5 to 3.5 m below ground. All standpipes were dry immediately after construction. However, the two groundwater levels were measured at various occasions during execution of the full-scale test programme. One groundwater level in the Søvind Marl and one in the overlying soil. The measured groundwater levels vary between level +55.0 and +57.9 m (from 3 m below ground level to ground level) and the variation can be seen on Figure 47.

The measured water levels are seen to vary approximately 1 m throughout the year, with the water levels being highest in the early spring and lowest in the autumn. The groundwater levels measured in the Søvind Marl for TSH.B1-A seem to be approximately 1 m below the other measurements of ground water levels at the test site in Hinge. This is expected to be caused by a downwards slope of the terrain approximately 25 meters west of TSH.B1-A.

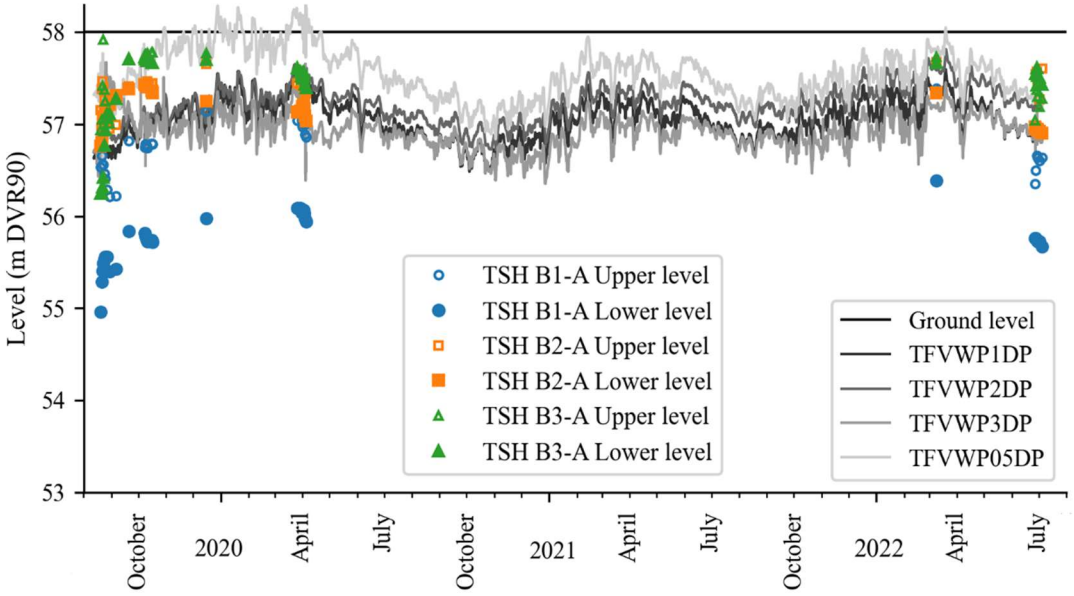

Figure 47: Groundwater levels measured during installation and execution of full-scale pile loading test.

The grey water levels denoted TFVWP1DP, TFVWP2DP, TFVWP3DP and TFVWP05DP are deduced from porewater pressure measurements by LAE (Low Air Entry) drive point piezometers (vibrating wire) already installed in the ground by Simonsen (2018). The piezometers were installed 10 m below ground level and the porewater pressure is assumed to be hydrostatic. No corrections are made for barometric pressure variations. The following equation is used to convert porewater pressure measurements (outliers removed) to water levels:

$$u = \gamma_w \cdot h_p \leftrightarrow h_p = u/\gamma_w \tag{55}$$

Here u is the porewater pressure, γ_w is the bulk unit weight of water (9.816 kN/m^3) and h_p is the pressure height.

3.9.2 Porewater salinity

Porewater salinity at the test site in Hinge was measured by major ion determination of the 6 major ions: Chloride (Cl^-), Sodium (Na^+), Sulfate (SO_4^{2-}), Magnesium (Mg^{2+}), Calcium (Ca^{2+}) and Potassium (K^+) by Madsen and Christoffersen (2018), see Table 6.

Table 6: Major ion concentrations of porewater at test site Hinge.

Test depth	Chloride (Cl^-)	Sodium (Na^+)	Sulfate (SO_4^{2-})	Magnesium (Mg^{2+})	Calcium (Ca^{2+})	Potassium (K^+)	Total
	mg/L	mg/L	mg/L	mg/L	mg/L	mg/L	mg/L
6 m	99	658	1393	60	88	47	**2345**
7 m	113	344	576	8	14	17	**1072**
12 m	149	548	951	6	6	14	**1674**
14 m	174	531	797	5	7	13	**1527**

The porewater salinity ranges between 0.11% and 0.23% with an average value of 0.17%. Classification and deformation parameters are both significantly influenced by porewater salinity for specimens with high smectite content (Lodahl, 2017). However, the influence of porewater salinity on the liquid limit determined on specimens from the test site in Hinge is found to change by 2% points from deionised water to 0.1% salinity water (Mikkelsen and Nielsen, 2023) and as the porewater salinity determined above for the test site in Hinge exhibit such low salinities, it is insignificant and either deionised water or tap water can be used for laboratory testing.

3.10 Soil parameter overview for Søvind Marl

This section contains an overview of the soil parameters determined in the previous sections for the Søvind Marl encountered at the designated test site.

Table 7: Soil parameters for Søvind Marl at the test site in Hinge.

Parameter.	Range
Bulk unit weight, γ (kN/m³)	16.0-17.4
Particle density, G_s (-)	2.77-2.78
Natural water content, w_{nat} (%)	46-62
Liquid limit, w_l (%)	121-233
Plastic limit, w_{pl} (%)	11-57
Plasticity index, I_p (%)	84-203
Calcite content (%)	4-36
Field vane strength, c_{fv} (kPa)*	100-300
Undrained shear strength, c_u^{CIU} (kPa)	60-130
Angle of shearing resistance, φ' (°)	~20°
Apparent effective cohesion, c' (kPa)	15-55
Preconsolidation pressure, σ'_{pc} (kPa)	400-500
Over consolidation ratio, OCR (-)	7-9
Coefficient of earth pressure at rest, K_0 (-)	1.8-2.9
Coefficient of permeability, k_p (m/s)	$1 \cdot 10^{-12}$-$3 \cdot 10^{-11}$
Small-strain shear modulus, G_0 (MPa)	35-60
Oedometer modulus, E_{oed} (MPa)	5-17

*The development of the site wide field vane strength, c_{fv}, with depth below ground level, z_d, is presented in Figure 48 and can be estimated based on the following linear relationship:

$$c_{fv} = 96.7 + 17.1 \cdot z_d \tag{56}$$

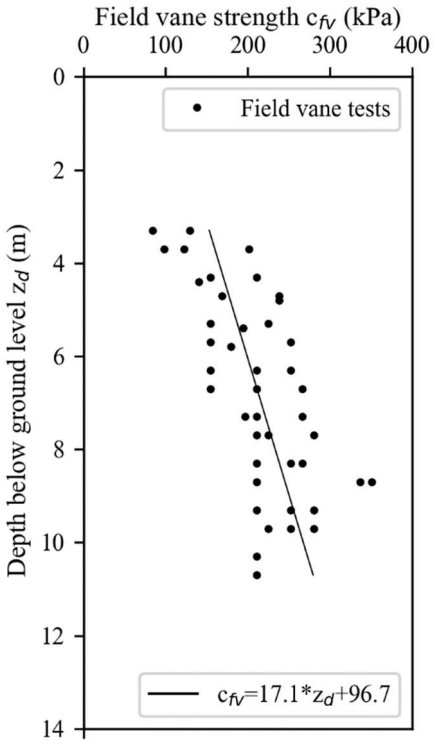

Figure 48: Site wide field vane strength, c_{fv}, at the test site in Hinge from borehole TSH.B1 – TSH.B3.

4 Methodology for field tests

A field-testing program was conducted to evaluate the performance of eight bored piles. These test piles were equipped with tell-tales, strain gauges, and fibre optic cables for instrumentation. The purpose of the structural monitoring was to enhance the understanding of the complex interaction between the soil and the piles during installation, pile loading tests, and post-testing of the bored piles. To examine the potential time effects (pile setup), the bored piles were tested at different time intervals after installation corresponding to approximately 1.5 months, 7 months, and 3 years.

Typically, two methods are used for testing bored piles: static pile loading tests or O-cell tests. The high cost involved in conducting O-cell tests ruled it out as an option for this PhD project, leading to the selection of static pile loading tests.

When performing static pile loading tests, the piles are subjected to compressive loads, which develop both shaft and base resistance. However, distinguishing the shaft resistance from the base resistance is challenging because the load-vertical displacement curve for shaft resistance significantly differs from that of the base resistance (refer to Figure 49).

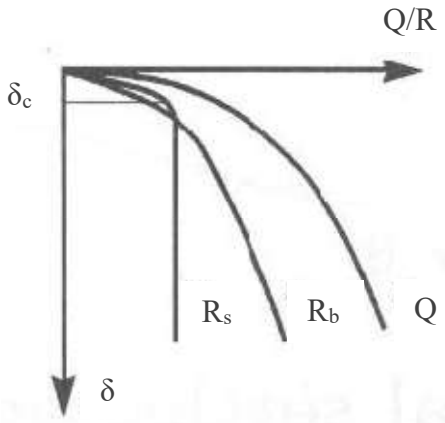

Figure 49: Load/resistance-vertical displacement curve modified after Gwizdala and Jacobsen (1992).

Here, Q is the applied load (equal to the total resistance), R_s is the shaft resistance, R_b is the base resistance and δ is the vertical displacement at pile top.

According to Figure 49, it can be observed that the shaft resistance reaches its maximum value once the vertical displacement at the top of the pile surpasses δ_c. However, the base resistance continues to increase. To obtain the most accurate determination of the shaft resistance, it was decided to conduct the static pile loading tests as tension tests. In tension tests, the contribution of base resistance to the overall resistance of the test piles is eliminated. The assumption is made that the shaft resistance determined by static pile loading tests in tension is equal to that of static pile loading tests in compression, as noted by Mohan and Chandra (1961).

This section provide an overview of the methodology followed during the field test program in this PhD project. For more detailed procedures, please refer to Appendix C.

4.1 Test programme

A full-scale test program involving eight instrumented bored piles was conducted. The installation of these piles took place from August 20th to August 23rd, 2019. In order to prevent any potential structural failure of the test piles, the initial two pile loading tests were delayed by approximately 1.5 months after the concrete was poured into the piles. This delay allowed the fresh concrete to gain sufficient strength and stiffness. To examine the potential effects of set-up on the shaft resistance, the remaining piles were tested in groups of three, roughly 7 months and 3 years after their installation.

An overview of the test programme is given in Table 8.

Table 8: Overview of the test programme at test site Hinge

Test pile	Installation date	Test date	Period of rest		Test method	
[no.]	[dd-mm-yyyy]	[dd-mm-yyyy]	months	days	ML	CRU
1	20-08-2019	10-10-2019	1	20	X	
7	21-08-2019	08-10-2019	1	17	X	
3	22-08-2019	02-04-2020	7	11	X	X
5	20-08-2019	31-03-2020	7	11	X	X
8	23-08-2019	04-04-2020	7	12	X	X
2	21-08-2019	28-06-2022	34	7	X	X
4	23-08-2019	02-07-2022	34	9	X	X
6	22-08-2019	30-06-2022	34	8	X	X

To determine the shaft resistance of the test piles, static pile loading tests were performed in tension. The chosen test method was the Maintained Load (ML) test, which involves progressively increasing the tensile load in steps until failure is reached. The ML test method is widely recognized and established for proof loading tests on working piles, as described in references such as CIRIA_Report_PG7 (1980), ASTM_D3689/D3689M (2013), Tomlinson and Woodward (2015) and ICE (2017). Two load phases were conducted to load the test piles to failure. The first load phase served to ensure system compliance, check instruments were working satisfyingly and examine the elastic behaviour of the test piles.

To obtain a more precise determination of the ultimate load of the test piles, a modification was made to the test method after the initial two pile loading tests. While the maintained load (ML) test was still utilized, a switch to the Constant Rate of Uplift (CRU) test was implemented when the test piles exhibited signs of imminent failure. After failure, the test piles were unloaded and subsequently reloaded using the CRU test method. The purpose of reloading the test piles was to investigate their residual strength.

This mixed test method is based on the principles recommended by CIRIA_Report_PG7 (1980) and Tomlinson and Woodward (2015) for static pile loading tests in compression. The CRU test involves progressively increasing the tensile load at a constant rate, causing the pile to be uplifted from the soil until failure occurs. By eliminating the time for consolidation or creep displacement of the ground, a more accurate interpretation of the load-displacement curve becomes possible.

4.2 Test pile specifications

To ensure that the applied tensile load represents the axial static tensile capacity of the test piles, a conservative dimensioning approach was employed. This dimensioning process aimed to prevent the applied tensile load from exceeding the structural strength of the piles. For more details, please refer to Appendix D.1.

The test piles have a diameter of 0.62 m and a total length of 9 m, including a 0.5 m section above ground level. The concrete used in the piles is A35 MPa, and each test pile is reinforced with eight Y32 bars, along with Y14/190 mm shear reinforcement. Table 9 provide an overview of the specifications for the test piles.

Table 9: Overview of test pile specifications.

Test pile	Pile length			Concrete	Reinforcement	
[no.]	Total	Above ground	Below ground		Length	Shear
1 - 8	9 m	0.5 m	8.5 m	A35 MPa	8 pcs. Y32	Y14/190 mm

At the request of DMT, a pair of Ø63.5 mm GEWI PLUS bars were implemented in each test pile to facilitate the transfer of force from the hydraulic jacks during static pile loading tests in tension. These GEWI bars were installed at a depth of 6.5 m within each test pile.

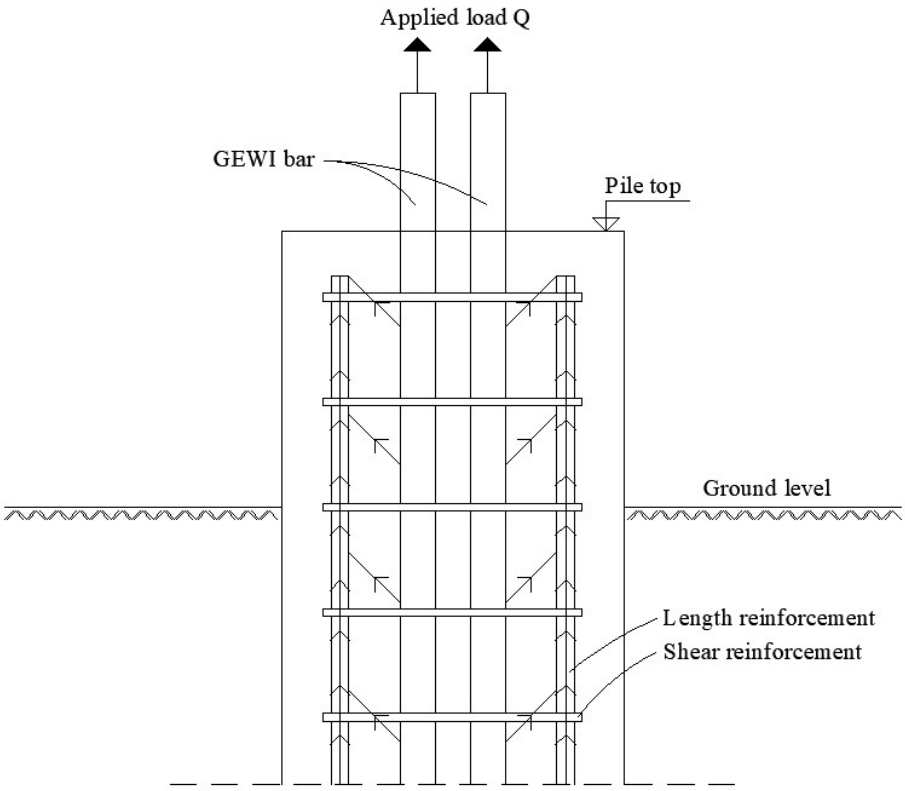

Figure 50: Details of transfer from GEWI PLUS bars to length reinforcement.

The presumption is that the force exerted by the hydraulic jacks is transmitted through the GEWI bars, which in turn distribute the load to the length reinforcement within the test piles. This transfer mechanism is illustrated in Figure 50.

4.3 Instrumentation of test piles

Bored piles experience significant shear distortion in a relatively thin zone around the pile shaft during loading and failure (Meyerhof and Murdock, 1953, Clayton and Milititsky, 1983). This makes it extremely difficult to directly measure normal and shear stresses, their distribution along the pile length, and excess porewater pressure in the surrounding soil. Therefore, the distribution of shaft resistance during pile loading tests is determined by analysing the measured displacements and strains inside the test piles at specific predetermined locations using tell-tales, strain gauges, and distributed fibre optic sensors.

In order to measure displacements within the test piles originating from the clay layer, four tell-tales (specifically one pair at two different levels) were strategically positioned near the pile base (tell-tale level 2) and at the interface between the clay and sand layers (tell-tale level 1), as shown in Figure 51.

To measure strains within the test piles, a total of 10 strain gauges were utilized. These strain gauges were strategically positioned in pairs at five different levels to obtain accurate measurements. The first level of strain gauges was placed at ground level (strain gauge level 1), while the second level was positioned in the middle of the sand layer (strain gauge level 2). Additionally, strain gauges were located at the interface between the clay and sand layers (strain gauge level 3) to separate strains derived from each layer. To further enhance the precision of strain measurements and refine the distribution of shaft resistance, strain gauges were also installed in the middle of the clay layer (strain gauge level 4) and as close to the pile base as possible (strain gauge level 5). Refer to Figure 51 for visual representation.

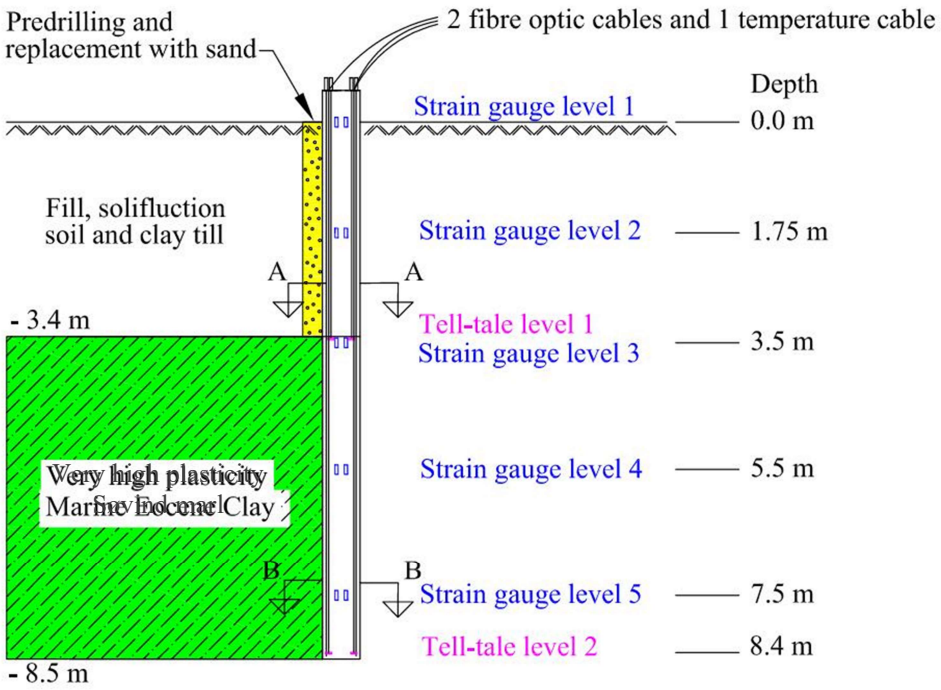

Figure 51: Details of test pile instrumentation. Levels relative to ground level.

In order to achieve highly precise measurements of strain distribution and shaft resistance along the length of the test piles, three cables were installed extending from the pile base to the pile top. These cables included two distributed fibre optic strain cables (FOSC) and one distributed fibre optic temperature cable (FOTC). This setup ensured accurate and comprehensive data collection. For a visual representation, please refer to Figure 51.

For proper separation of bending moments from axial loads, all monitoring equipment was installed in pairs on opposite sides of the neutral axis within the structure. This arrangement is depicted in Figure 52 for cross sections A-A and B-B.

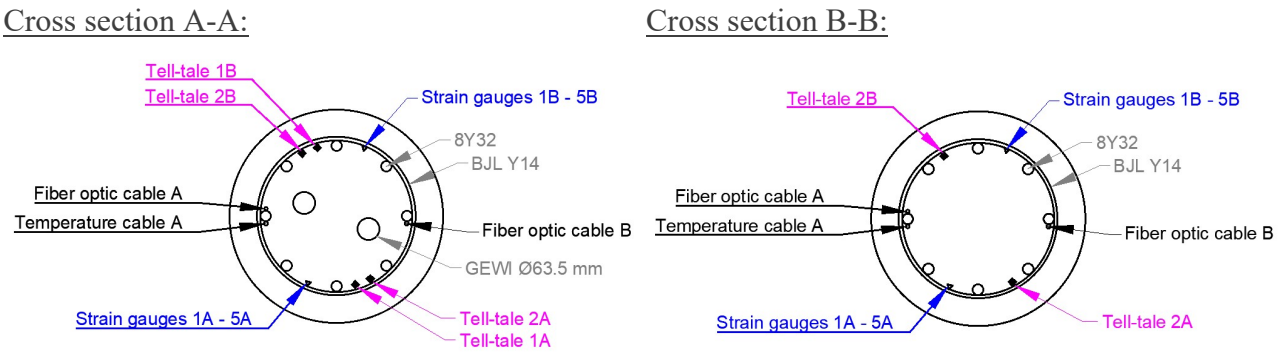

Figure 52: Upper cross section A-A and lower cross section B-B in test piles.

The strain gauges are labelled as strain gauge 1A and 1B for those at level 1, 2A and 2B for those at level 2, and so on. The same labelling system, denoting 1A, 1B, 2A, 2B, etc., is also used for the tell-tales.

4.4 Test setup

The steel traverse system was constructed around each test pile one day prior to the static pile loading test in tension. Cribbing was positioned on both sides of the test pile, maintaining a clearance of approximately 2.5 meters from the test pile. It is worth noting that recommendations in literature suggest a clearance between the test pile and cribbing ranging from 3 to 5 times the pile diameter, with a minimum clearance of 2 to 2.5 meters, as referenced in ASTM_D3689/D3689M (2013) and Tomlinson and Woodward (2015).

To support the load distribution, a set of HE300B load distribution beams, each measuring 4 meters in length, were placed on top of the cribbing. These beams provided support for the two HE800B main beams, which were 10 meters long. Additionally, above the main beams, two pairs of HE400B beams, each 4 meters in length, were positioned in a crosswise manner to distribute the load evenly on both main beams and to provide support for the load application system. Please refer to Figure 53 and Figure 54 for visual representation.

The load application system consisted of a load application frame equipped with four hydraulic jacks. Positioned centrally along the pile axis, each hydraulic jack had a capacity of 300 tons and a stroke of 250 mm. The load exerted was measured by 3 MN load cells situated on top of each hydraulic

jack. In order to transfer the force from the load application system to the test pile, a coupler steel plate with a GEWI PLUS 75 mm bar was attached to two GEWI PLUS 63.5 mm bars that were anchored into each test pile. Please refer again to Figure 53 and Figure 54 for clarity.

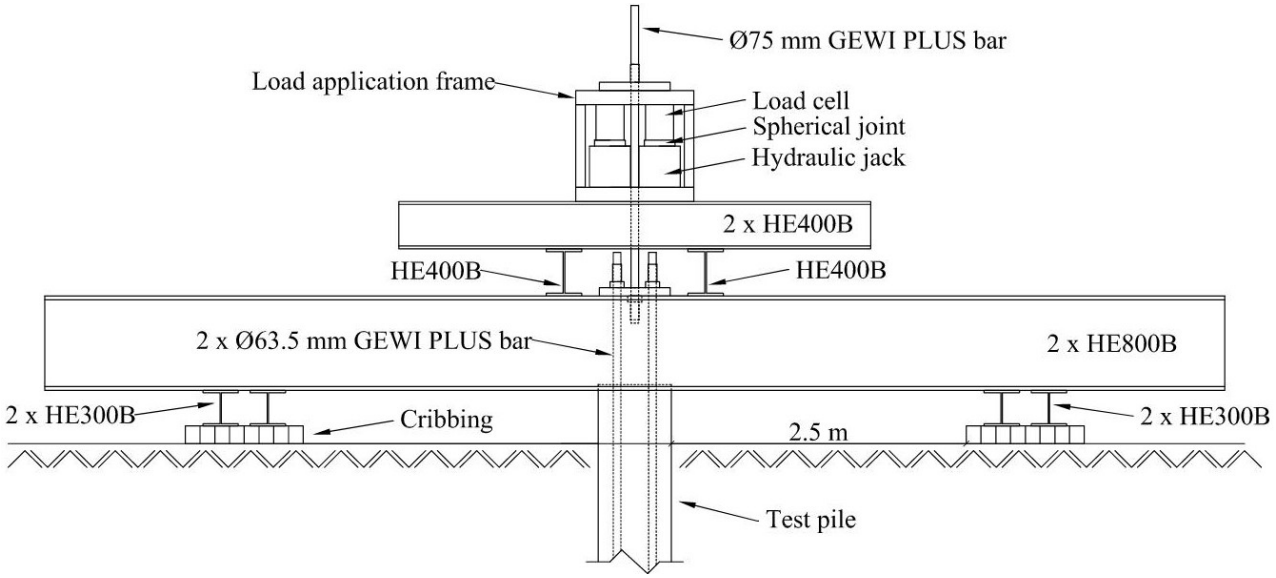

Figure 53: Illustration of steel traverse system for static pile loading test in tension seen from the side.

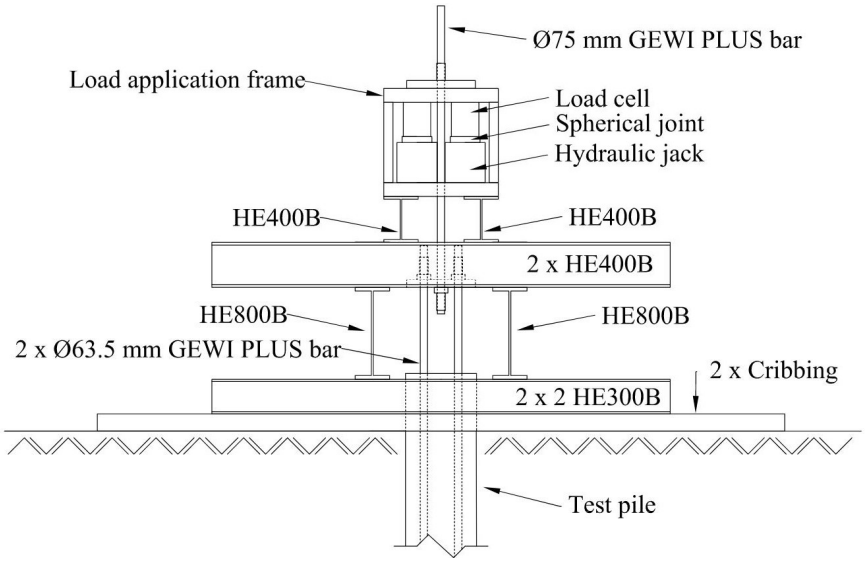

Figure 54: Illustration of steel traverse system for static pile loading test (tension) seen from the end.

4.5 Loading procedures

This chapter outlines the loading procedures for the two types of tests: the maintained load (ML) test and the constant rate of uplift (CRU) test (refer to section 4.1). In this context, the term CRU test refers to a static pile loading test that initially begins as a ML test. However, when the test piles exhibit indications of imminent failure, the testing method is modified to the CRU test.

Maintained load (ML) test

The test piles were subjected to failure by gradually increasing the tensile load in incremental steps. To prevent shocks and vibrations, the tensile load was continuously adjusted, either increased or decreased, over a period of approximately 3 minutes for each new load step. During each load step, efforts were made to maintain the load as constant as possible. The loading procedure for the ML test is depicted in Figure 55.

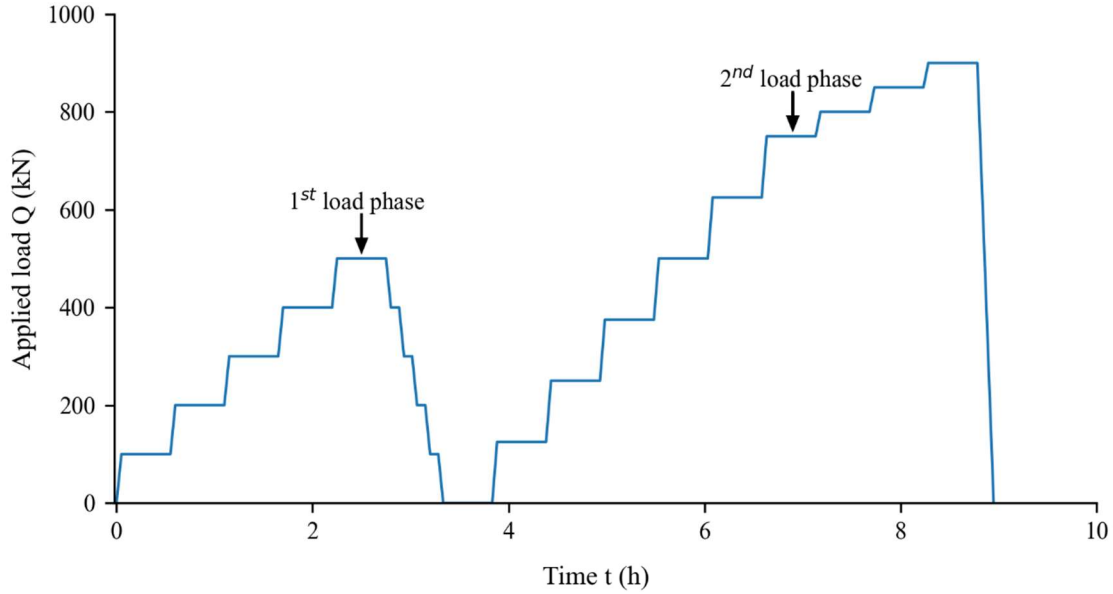

Figure 55: Illustration of loading procedure for maintained load (ML) test.

During the 1st load phase, the tensile load was applied in 5 incremental steps of 100 kN, resulting in a total load of 500 kN. Each load increment was sustained until the rate of creep either stabilized or decreased. The minimum observation period for each load increment was set at 30 minutes. Subsequently, the test pile was unloaded in 100 kN steps, with a 5-minute observation period at each step, followed by a 30-minute observation period before the commencement of the 2nd load phase.

In the 2nd load phase, the tensile load was applied in 125 kN increments. When the test pile indicated signs of imminent failure, the load increments were reduced to 50 kN steps. The load was maintained at each increment until the rate of creep became stable or decreased. Similar to the 1st load phase, a minimum observation period of 30 minutes was allocated for each load increment. The tensile load was increased until the test pile ultimately failed.

Constant rate of uplift (CRU) test

Initially, the ML test procedure was employed for the test pile until indications of imminent failure became apparent. At that point, the tensile load was systematically increased, causing the pile to be uplifted from the soil at a consistent rate until failure took place. Following failure, the test piles were unloaded and subsequently reloaded at a constant rate of pile uplift to examine the residual strength of the piles. The loading procedure for the CRU test is illustrated in Figure 56.

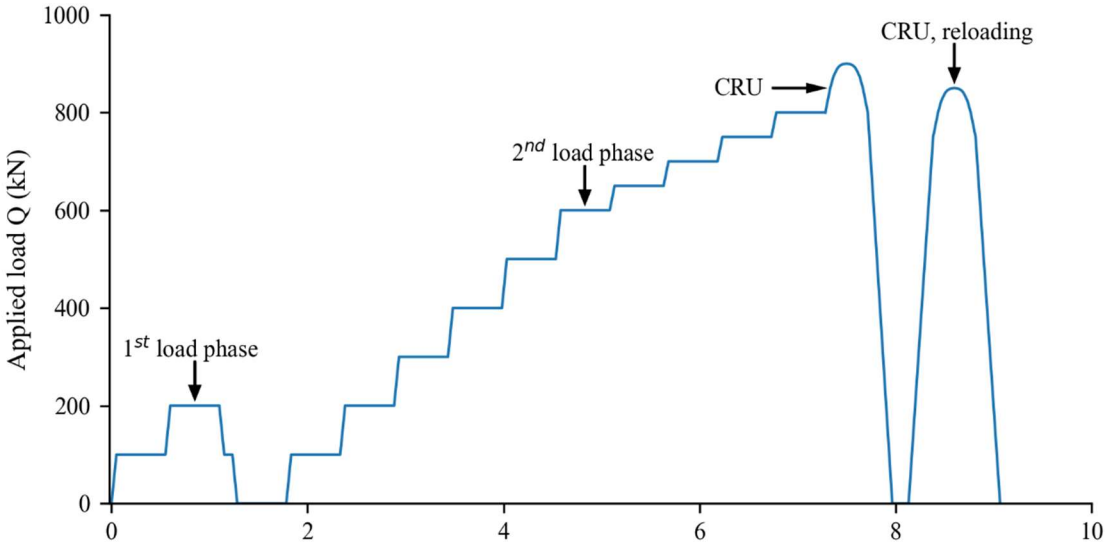

Figure 56: Illustration of loading procedure for constant rate of uplift (CRU) test.

During the 1st load phase, the load was applied in 2 increments of 100 kN, resulting in a total load of 200 kN. Each load increment was sustained until the rate of creep became stable or decreased. The minimum observation period for each load increment was set at 30 minutes. The test pile was then unloaded in steps of 100 kN, with a 5-minute observation period at each load step, followed by a 30-minute observation period before the commencement of the 2nd load phase.

In the 2nd load phase, the load was applied in 6 increments of 100 kN initially. Subsequently, the load increments were reduced to 50 kN steps until the test pile exhibited signs of imminent failure. Similar to the 1st load phase, each load increment was maintained until the rate of creep became stable or decreased. The minimum observation period of 30 minutes was allocated for each load increment.

The static pile loading test was then continued with a constant pile uplift rate. Once the peak value was reached, the test pile was unloaded and subsequently reloaded at a constant pile uplift rate. Finally, immediately after reaching the peak value for the reloading, the test pile was unloaded once again.

5 Post-processing of data

To determine the pile load response and the distribution of shaft resistance along the length of the test piles, various measurements are utilized. These include measured loads, displacements from pile top, displacements from tell-tales (TT), and strains from vibrating wire strain gauges (VWSG) and fibre optic strain cables (FOSC). The subsequent sections describe how the failure load is defined for the test piles and outline the processing of measured loads, displacements, and strains.

5.1 Failure load definition

The definition of failure varies depending on the selected test method. In the constant rate of uplift (CRU) test, failure is determined by the peak value attained at a specific pile uplift rate. On the other hand, for the maintained load (ML) test, failure is identified by a criterion that indicates a complete cessation of movement.

Constant rate of uplift (CRU) test

The literature provide limited recommendations for the pile uplift rate in the CRU test. According to ASTM_D3689/D3689M (2013), a constant pile uplift rate ranging from 0.5 to 1.0 mm/min, equivalent to 30-60 mm/h, is suggested. Generally, lower values of pile uplift rates are applicable for piles that primarily derive their bearing capacity from shaft surface resistance in fine grained soils. Considering the surrounding soil is primarily high plasticity clay, a constant pile uplift rate of 20 mm/h was chosen to represent the undrained behaviour during static pile loading test in tension.

Maintained load (ML) test

In the literature, there were limited recommendations regarding the criteria for cessation of movement in each load step for the ML test in tension. Typically, this criterion consists of a maximum allowable rate of axial movement and a minimum observation period. The maximum allowable rate of axial movement ranges from 0.1 to 0.25 mm/h according to ASTM_D3689/D3689M (2013) and ICE (2017). However, this linear consideration of axial movement criteria is likely derived from the ML test in compression and may result in misinterpretation of whether the axial movement has truly ceased.

Static pile loading tests in tension bear similarities to the testing of grouted anchors, where the criteria for cessation of movement is determined by a rate of creep as mentioned in DS/EN_ISO_22477-1 (2018). For acceptance and suitability tests, a permitted rate of creep of 2 mm/lct is used, while for investigation tests, failure occurs when there is a vertical asymptote in the load-rate of creep graph or when the rate of creep exceeds 5 mm/lct as mentioned in DS/EN_1997-1_DK_NA (2021).

Considering these observations, the cessation of movement criteria for the ML test was determined to have a rate of creep higher than 2 mm/lct for imminent failure and either a vertical asymptote in the rate of creep-load graph or a rate of creep higher than 5 mm/lct for failure.

5.1.1 Determination of rate of creep

The rate of creep, k_s, is calculated during the final 10 minutes of each maintained load step. This approach is adopted because the soil consists of a very high plasticity clay with low permeability, which requires some time before initiating creep displacements. Additionally, multiple measurements were taken during this 10-minute period, with a frequency of one measurement per second. The rate of creep, k_s, is determined using equation (57).

$$k_s = \frac{\delta_2 - \delta_1}{log_{10}(t_2/t_1)} \tag{57}$$

Here $\delta_2 - \delta_1$ is the vertical displacement at pile top from time t_1 to t_2 at a maintained load.

In the case of the ML tests, the final load step (failure) was not calculated during the final 10 minutes of the load step because it is practically impossible to sustain the load during the occurrence of failure. For test pile 1, the final load step was calculated after 16 minutes and 6 seconds, with a displacement of approximately 18.4 mm. Similarly, for test pile 7, the final load step was calculated after 14 minutes and 20 seconds, with a displacement of approximately 13.6 mm. To determine the rate of creep during failure, the last 1 minute of these final load steps was considered, as it provide a more reasonable representation of the creep rate during this stage.

5.2 Data interpretation from tell-tales

Vertical displacements were measured at the sand-clay interface and the pile base using tell-tales. In addition to providing information about the vertical displacement, the average axial strains can be calculated between two specific locations using a linear calculation method, as outlined below:

$$\varepsilon_a = \frac{\Delta z_N - \Delta z_{N+1}}{L_p} \tag{58}$$

Here ε_a is the average axial strain between two tell-tale locations, $(\Delta z_N - \Delta z_{N+1})$ is change in vertical displacement from one location to the other (extension or abbreviation) and L_p is length of pile between those two locations.

Regrettably, the measurements of vertical displacements obtained from the tell-tales are not considered useful for this PhD project, despite their generally reliable nature. The discrepancies in the measurements and a potential explanation for these discrepancies are detailed in Appendix G.

5.3 Data interpretation of measured strains from strain gauges

Vibrating wire strain gauges were utilized to measure strains inside the test piles, and an automatic data acquisition system (datalogger) was employed to record the data. Data acquisition took place at intervals of one minute.

The strain gauges generate a frequency, f, and the datalogger is responsible for exciting and measuring the system's response. The measured responses are presented as linear digits, known as B units. B units are defined as the frequency squared and divided by 1000 to reduce their scale. In order to obtain strains, ε_r, the B units are converted using the following linear calculation:

$$\varepsilon_r = s_{cal} \cdot (B\ unit_{current\ reading} - B\ unit_{site\ zero\ reading}) \tag{59}$$

Here ε_r is the measured strains (raw data) and s_{cal} is a linear calibration factor used to convert the raw data from B units to strains. Positive values of ε_r indicate tensile strain and negative values of ε_r indicate compressive strain.

The measurements are always referenced to an initial state of strain (and temperature) known as the site zero readings.

Thermal influence

In addition to strain measurements, temperatures inside the test piles were also recorded using vibrating wire strain gauges. The thermistors utilized had a resistance of 3k ohms at 25°C. Temperature is a crucial factor to consider because it affects not only the strain gauges but also the actual test piles to which the gauges are attached. To estimate the thermal-induced strain, ε_{therm} , equation (60) is employed. In this equation, α_L represents the linear coefficient of thermal expansion, and ΔT represents the change in temperature.

$$\varepsilon_{thermal} = \alpha_L \cdot \Delta T \tag{60}$$

Temperature changes during the static pile loading test impact both the strain gauges and the actual test piles. This phenomenon has two implications. Firstly, when the temperature rises and the strain gauges expand, they do not accurately measure the strain equivalent to the expansion, resulting in an underestimated strain measurement. Secondly, the actual test piles also expand due to the temperature change. The strain gauges include these expansion-related strains in their measurements, leading to an overestimate of the strain.

To account for these thermal influences and obtain accurate mechanical strain measurements, the measured strains corrected for thermal influence can be calculated using equation (61).

$$\varepsilon_t = \varepsilon_r + (\alpha_{L,strain\ gauge} \cdot \Delta T - \alpha_{L,test\ pile} \cdot \Delta T) \tag{61}$$

Here ε_t is the measured strains corrected for thermal influence, ΔT is the change in temperature ($T_{current\ reading} - T_{site\ zero\ reading}$) and $\alpha_{L,strain\ gauge}$, $\alpha_{L,test\ pile}$ is the linear coefficient of thermal expansion for the strain gauges and test piles, respectively.

The manufacturer (Geosense) specified the linear coefficient of thermal expansion for the strain gauges as $\alpha_{L,strain\ gauge} = 12 \cdot 10^{-6}/°C$. Meanwhile, the linear coefficient of thermal expansion

for the actual test piles was determined as $\alpha_{L,test\ pile} = 10 \cdot 10^{-6}/°C$ according to DS/EN_1991-1-5 (2007) and DS/EN_1991-1-5_DK_NA (2012), Annex C for composite structures (reinforced concrete).

As a result, there is a positive change in strain of $\Delta\varepsilon = 2\mu\varepsilon$ for each temperature change of 1°C, as illustrated by equation (62):

$$\varepsilon_t = \varepsilon_r + (12 \cdot 10^{-6}/°C \cdot 1°C - 10 \cdot 10^{-6}/°C \cdot 1°C) \rightarrow \varepsilon_t = \varepsilon_r + 2\mu\varepsilon \quad (62)$$

Average values

To differentiate between bending moments and axial loads, all strain gauges were installed in pairs within the structure, positioned on opposite sides of the neutral axis. The average value of the measured strains, corrected for thermal influence, $\varepsilon_{t,a}$, is determined by considering two strain gauges (ε_{t1} and ε_{t2}) located on the same level but on opposite sides of the neutral axis within the test piles. This calculation is performed according to equation (63).

$$\varepsilon_{t,a} = \frac{1}{2} \cdot (\varepsilon_{t1} + \varepsilon_{t2}) \quad (63)$$

5.4 Data interpretation of measured strains from fibre optic cables

Strains inside the test piles were measured using Rayleigh-based fibre optic strain cables (FOSC), and the data was acquired using a fibre optic spectrum analyser known as the LUNA ODiSI-B system. This advanced technology utilizes light scattering along an optical fibre, as outlined by Culshaw and Kersey (2008). The system consists of an interrogation unit, a standoff cable, and a remote module. The interrogation unit employs swept-wavelength interferometry to measure the spectral shift in the Rayleigh backscatter (LUNA, 2017). To ensure minimal back reflection of the fibre optic strain cable, the termination of the fibre-end was manufactured commercially by FIBRAIN in Poland. Data acquisition was carried out manually.

All measurements are referenced to an initial state of strain (and temperature), referred to as the site zero readings.

Thermal influence

Fibre optic temperature cables (FOTC) were employed to measure temperatures inside the test piles. The FOSC used in the measurements are sensitive to both strain and temperature changes, as noted by Kreger et al. (2006). Therefore, to obtain mechanically induced strains from the measured strains (raw data), it is necessary to perform thermal compensation in the event of temperature changes. Since the stiffness of the materials constituting the FOSC is significantly lower than the stiffness of the actual test piles (host structure), it can be assumed that the FOSC experience the same thermal expansion as the test piles, as stated by Kechavarzi et al. (2016).

Nevertheless, it is important to note that temperature changes still cause a shift in the spectrum of light scattered within the FOSC, as described by LUNA (2014). Therefore, to obtain thermally compensated strains, it is necessary to consider both the temperature effects on the scattered light within the FOSC and the thermal expansion of the test piles. The measured strains, corrected for thermal influence (also referred to as mechanical strains), can be calculated using equation (64) as specified by LUNA (2014).

$$\varepsilon_t = \Delta\nu_S \cdot k \ - (0.95 \cdot \Delta\nu_T \cdot k \ + \Delta\nu_T \cdot k_T \cdot \alpha_{L,test\ pile}) \tag{64}$$

Here ε_t is the measured strains corrected for thermal influence, $\Delta\nu_S$ is the spectral shift in a fibre optic strain cable, $\Delta\nu_T$ is the spectral shift in a fibre optic temperature cable, k is the strain conversion factor (strain/frequency) , k_T is the temperature conversion factor (°C/frequency) and $\alpha_{L,test\ pile}$ is the linear coefficient of thermal expansion for the test piles cf. section 5.3.

The strain conversion factor, k , is determined to be -6.67 με/GHz, while the temperature conversion factor, k_T, is determined as -0.638 °C/GHz according to LUNA (2014). This leads to a negative change in strain, where $\Delta\varepsilon$ equals -19.93$\mu\varepsilon$ for every 1°C temperature change, as indicated by equation (65):

$$\varepsilon_t = \varepsilon_r - \left(0.95 \cdot 1°C \cdot \frac{-6.67\,\frac{\mu\varepsilon}{\mathrm{GHz}}}{-0.638\,\frac{°\mathrm{C}}{\mathrm{GHz}}} + 1°C \cdot 10 \cdot \frac{10^{-6}}{°C}\right) \rightarrow \varepsilon_t = \varepsilon_r - 19.93\mu\varepsilon \tag{65}$$

Average values

To differentiate between bending moments and axial loads, all FOSC were installed in pairs within the structure, positioned on opposite sides of the neutral axis. The average value of the measured strains, corrected for thermal influence, $\varepsilon_{t,a}$, is determined by considering two FOSC (ε_{t1} and ε_{t2}) located on either side of the neutral axis within the test piles. This calculation is performed according to section 5.3, in line with equation (63).

5.5 Unit shaft resistance

The axial load within the test piles does not remain constant with depth; instead, it decreases proportionally in relation to the shaft resistance along the length of the test piles. As a result, the axial force, F, is determined through back calculation using the average value of the measured strains, corrected for thermal influence, $\varepsilon_{t,a}$, at each strain gauge level. This back calculation is performed using equation (66).

$$F = E_p \cdot A_p \cdot \varepsilon_{t,a} \tag{66}$$

Here E_p is Young's modulus and A_p is the cross-sectional area of the test pile, and E_pA_p denotes the axial stiffness of the test pile.

The distribution of the unit shaft resistance, r_s, in-between strain gauge levels is then correlated to the back calculated axial force, F_N, at each strain gauge level using equation (67).

$$r_s = \frac{F_N - F_{N+1}}{A_s} \tag{67}$$

Here A_s is the shaft surface area of the test pile in-between two strain gauge levels.

5.5.1 Determination of axial pile stiffness

Determining the axial stiffness, E_pA_p, of the test piles is a complex task due to several factors. Firstly, the relationship between the applied load, Q, and the resulting strains, $\varepsilon_{t,a}$, is not linear because the axial load in the test piles decreases proportionally with depth, corresponding to the shaft resistance along the length of the piles.

Furthermore, the elastic modulus of concrete is not constant but varies as a function of the applied load (or strain more correctly), decreasing with increasing strains. The difference between the initial and final elastic moduli can be significant, and this non-linearity must be considered.

Additionally, in the case of bored piles, the actual cross-sectional area may differ from the nominal area, introducing further complexity in calculating the axial stiffness.

Theoretical calculation

Initially, COWI provided a theoretical calculation to estimate the axial stiffness, E_pA_p, of the test piles. It is assumed that at low levels of stress, both the concrete and reinforcement experience tensile stresses. The Young's modulus of the concrete is assumed to be equal to the initial modulus of elasticity at the tensile strength. The contribution of the reinforcement's Young's modulus is considered by incorporating a weighted area of the reinforcement. The cross-sectional area is assumed to be equal to the nominal area.

Based on these assumptions, the initial estimation of the axial stiffness for the upper part of the test piles with GEWI bars is 14.5 GN, while for the lower part of the test piles without GEWI bars, the estimation is 13.2 GN. Further details can be found in Appendix D.2.

Determination from test records

An alternative approach to determine the axial stiffness is by directly analysing the test records, as proposed by Fellenius (1989). The axial stiffness, not the applied load, typically exhibits a linear relationship to the imposed strains, $\varepsilon_{t,a}$. In this method, the Young's modulus of the test piles is assumed to be equal to the secant modulus.

The tangent stiffness method establishes a relationship between the tangent modulus (or tangent axial stiffness) derived from the stress-strain (or load-strain) curve and the secant modulus (or

secant axial stiffness). As a result, the tangent axial stiffness, E_tA, and the secant axial stiffness, E_sA, can be calculated using equation (68) and (69) respectively.

$$E_tA = a \cdot \varepsilon_{t,a} + b \tag{68}$$

$$E_sA = 0.5 \cdot a \cdot \varepsilon_{t,a} + b \tag{69}$$

Here $\varepsilon_{t,a}$ is the average value of the measured strains corrected for thermal influence, a is the slope of the tangent axial stiffness line and b is the Y-intercept (initial tangent axial stiffness).

In addition, the direct secant method can be employed to determine the axial stiffness, but it is applicable only to strain gauges positioned either above or immediately below the ground level, as outlined by Fellenius (2023). Consequently, the secant axial stiffness, E_sA, can be directly calculated using equation (70).

$$E_sA = c \cdot \varepsilon_{t,a} + d \tag{70}$$

Here $\varepsilon_{t,a}$ is the average value of the measured strains corrected for thermal influence, c is the slope of the secant axial stiffness line and d is the Y-intercept (initial secant axial stiffness).

The expressions above represent a straight line and not a constant, as the test piles does not exhibit a linear stress-strain (or load-strain) behaviour when loaded, because Young's modulus of concrete reduces with the applied load.

It is important to note that the expressions provided in equation (70) represent a straight line and not a constant, as the test piles do not exhibit linear stress-strain (or load-strain) behaviour during loading. This is due to the fact that the Young's modulus of concrete decreases as the applied load increases. For more details on how to determine the axial stiffness from the test records, please refer to section 6.3.2.

5.6 Elastic lengthening of test piles

The strain measurements from the strain gauges installed in each test pile were used to determine the elastic lengthening, $\delta_{pile,e}$, of the test piles according to equation (71). It is assumed that there is a linear distribution of strain between each strain gauge level. The elastic lengthening, $\delta_{pile,e}$ of the test piles depends on the actual load, so it was calculated for each maintained load step and at the peak value of the applied load, Q, specifically for test piles 2-6 and 8 during the initial constant rate of uplift portion of the static pile loading test.

$$\delta_{pile,e} = \int_{L_p=0}^{9m} \varepsilon_{t,a}\, dL_p \tag{71}$$

Here $\varepsilon_{t,a}$ is the average value of the measured strain corrected for thermal influence and L_p is the pile length.

To calculate the elastic lengthening of the test piles, the average value of the measured strains corrected for thermal influence, $\varepsilon_{t,a}$, were used, averaged over each maintained load step. It is assumed that the creep displacement in the soil-pile interface does not affect the elastic lengthening.

During the initial constant rate of uplift portion of the static pile loading test for test piles 2-6 and 8, the average value of the measured strains corrected for thermal influence, $\varepsilon_{t,a}$, corresponding to the peak value of the applied load, Q, was utilized.

For test pile 1, strain gauge level 3 is disregarded due to malfunction. Instead, a linear distribution was assumed between strain gauge level 2 and 4. As a general linear tendency between strain gauge level 2 through 5 is observed, it is considered insignificant.

Additionally, the strain was assumed to be zero at the pile top and pile base, and to have a linear distribution to the nearest strain gauge level 1 or 5, respectively.

5.7 Shear stiffness

The shear stiffness of the pile load response was determined by finding the tangent slope between two adjacent data points, namely number N and N+1:

$$G_{pile} = \frac{Q_{N+1} - Q_N}{\delta_{N+1} - \delta_N} \tag{72}$$

Here G_{pile} is the shear modulus of the pile-load response, Q is the load applied during pile loading test and δ is the vertical displacement at pile top.

The shear stiffness of load transfer function for the individual soil layers was determined by differentiating the equation of the load transfer curves:

$$G_{shaft}(\delta_{pile,soil}) = r_s{}'(\delta_{pile,soil}) \tag{73}$$

Here G_{shaft} is the shear modulus of the load transfer function, r_s is the unit shaft resistance and $\delta_{pile,soil}$ is the vertical displacement between pile and soil (vertical displacement at pile top corrected for elastic lengthening cf. section 5.6).

6 Results from field tension tests on bored piles

In this section, the results of the static pile loadings test are presented. These results are derived from the pile test data, which includes measured loads and displacements from the pile top. The analysis also incorporates temperature and strain data from the vibrating wire strain gauges (VWSG), focusing on measured temperatures, observed pile behaviour during static pile loading tests, and the mobilisation of shaft resistance.

Section 7 of this thesis highlights the utilization of Rayleigh-based fibre optic distributed line sensors. These sensors were installed within the bored test piles to provide more comprehensive and detailed measurements of temperature and strain along the entire length of the test piles. The section will provide an overview of the findings and insights obtained from these fibre optic cables (FOC).

6.1 Temperature measurements

In the upcoming section, the temperature development over time is presented, starting from installation and leading up to the static pile loading test. The section also includes the temperature observations specifically recorded during the day of the static pile loadings test for the eight test piles located in the Hinge test site.

6.1.1 Temperature development with time

This section documents the observed temperature development over time, specifically focusing on the thermistors in the vibrating wire strain gauges (VWSG thermistor). The analysis pays special attention to test piles 4 and 8, as the measurements were conducted for an extended period after casting. Temperature measurements were taken by the VWSG thermistor for approximately 4 months and 7.5 months for test piles 4 and 8, respectively. Figure 57 and Figure 58 showcase the temperature development over time for test pile 8, which had the longest measurement duration. The temperature development for test pile 4 can be found in Appendix F.1.

The initial high temperatures depicted in Figure 57 are a result of the initial concrete set, hydration, and subsequent curing of the test pile. Once the test piles are constructed (including concrete placement and casing removal), the combination of cement binder and water initiates an exothermic reaction. The magnitude of heat generated during this reaction varies depending on the properties of the binder and the conditions present in the external environment (such as soil and groundwater conditions). For bored piles, this process is prolonged due to the superior insulation properties of the surrounding soil compared to air. As the reaction progresses, the hydration temperatures continue to rise for several hours after casting, while the concrete gradually hardens and sets during this period. The completion of the initial set is assumed to occur at the peak temperature, T_{peak} (Neville and Brooks, 1987).

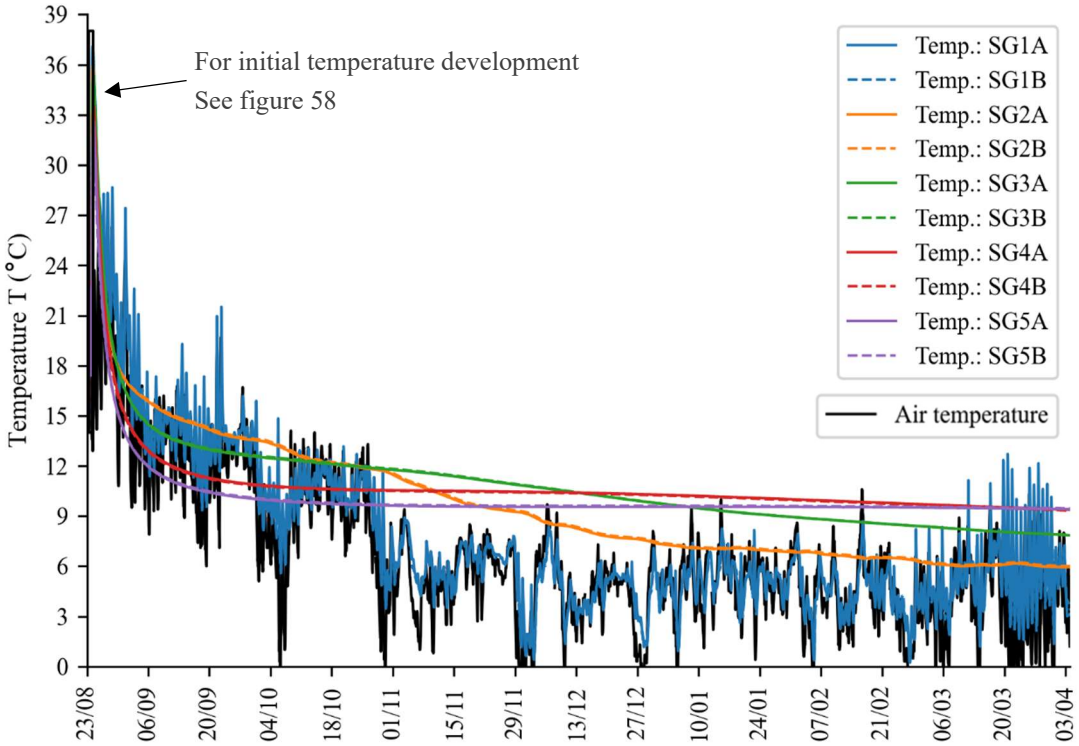

Figure 57: Measured temperatures in test pile 8 from installation of the test pile on the 23rd of August 2019 and throughout the following 225 days (~7½ months).

Based on the information shown in Figure 58, it is observed that the temperatures initially decrease slightly after the casing is withdrawn. This temperature reduction is due to the surrounding external environment conditions (such as soil and groundwater) being cooler than the temperature of the wet concrete. However, temperatures start to rise again after 4-10 hours when the exothermic reaction occurs. Once the hydration temperatures peak, the test piles experience a gradual decrease in temperature over time.

After approximately 48 hours, the initial high temperatures dissipate. However, the temperature at the upper strain gauge level (indicated by blue lines) situated at ground level is influenced by short-term temperature fluctuations on a daily basis, as depicted in Figure 57. The impact of temperature changes diminishes with increasing depth, transitioning from seasonal changes (represented by orange, green, and red lines) to nearly negligible changes at the lower strain gauge level (illustrated by purple lines) located approximately 7.5 meters below ground level, which aligns with expectations (Alberdi-Pagola, 2018).

The annual mean temperature recorded in Randers (the closest measuring point) was 8.9°C in 2019 and 9.4°C in 2020, based on data from DMI weather archive. These temperature measurements are consistent with the recorded temperatures at the lower strain gauge level (purple lines), with the lowest temperature observed being 9.5°C.

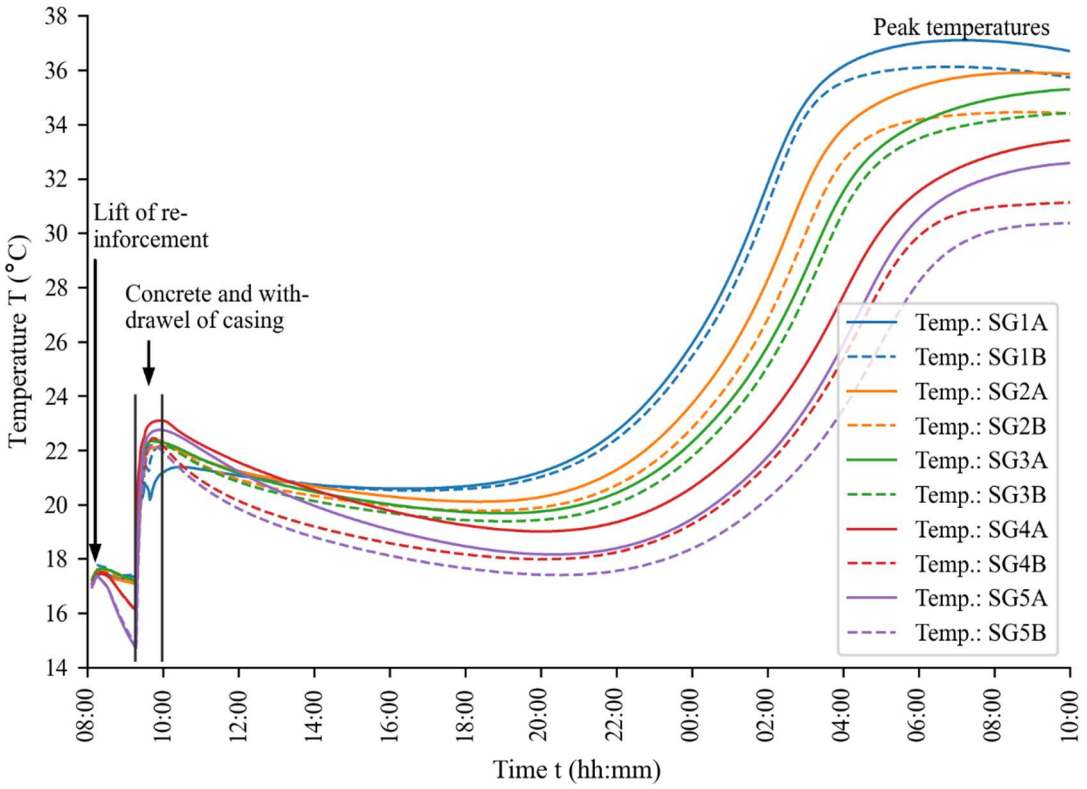

Figure 58: Measured temperatures in test pile 8 during installation of the test pile on the 23rd of August 2019 through the 24th of August 2019.

The temperature measurements obtained from the VWSG thermistors offers reliable data. It is observed that the temperatures at the upper strain gauge level located at ground level are influenced by short-term temperature fluctuations on a daily basis. However, as the depth increases below ground level, the impact of temperature changes decreases, transitioning to seasonal variations. Ultimately, at the lower strain gauge level (level 5) approximately 7.5 meters below ground level, nearly negligible changes in temperature are observed.

6.1.2 Temperature development during static pile loading test

The measurements obtained from the VWSG thermistors are showcased and compared with the air temperature data in Randers from the DMI weather archive during the static pile loading tests. An example is provided below for test pile 8, as depicted in Figure 59 and Figure 60. For detailed temperature observations of all the test piles, refer to Appendix F.2.

As depicted in Figure 59, it is observed that the temperature response curve for the upper SG level exhibits a slight delay compared to the air temperature recorded in Randers from the DMI weather archive. This delay is expected since an embedded thermistor monitored by a VWSG typically responds more slowly to changes in air temperature. Additionally, the air temperature demonstrates larger temperature variations on an hourly basis compared to the temperature curve for the upper SG level. However, the temperature curve for the upper SG level remains within a deviation of less than 6°C. It is worth noting that the temperature remains relatively constant during the static pile loading

test for the other four SG levels (SG level 2-5). Figure 60 presents the temperature development along the length of the test pile.

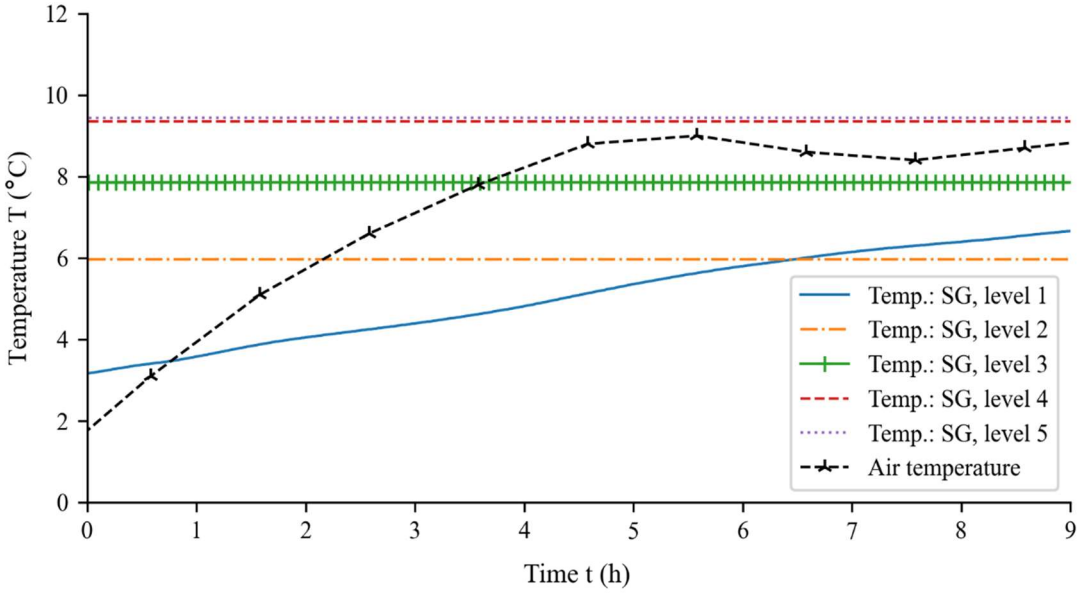

Figure 59: Temperatures at each strain gauge level for test pile 8 during static pile loading test. The time indications are established as zero at the beginning of the static pile loading tests.

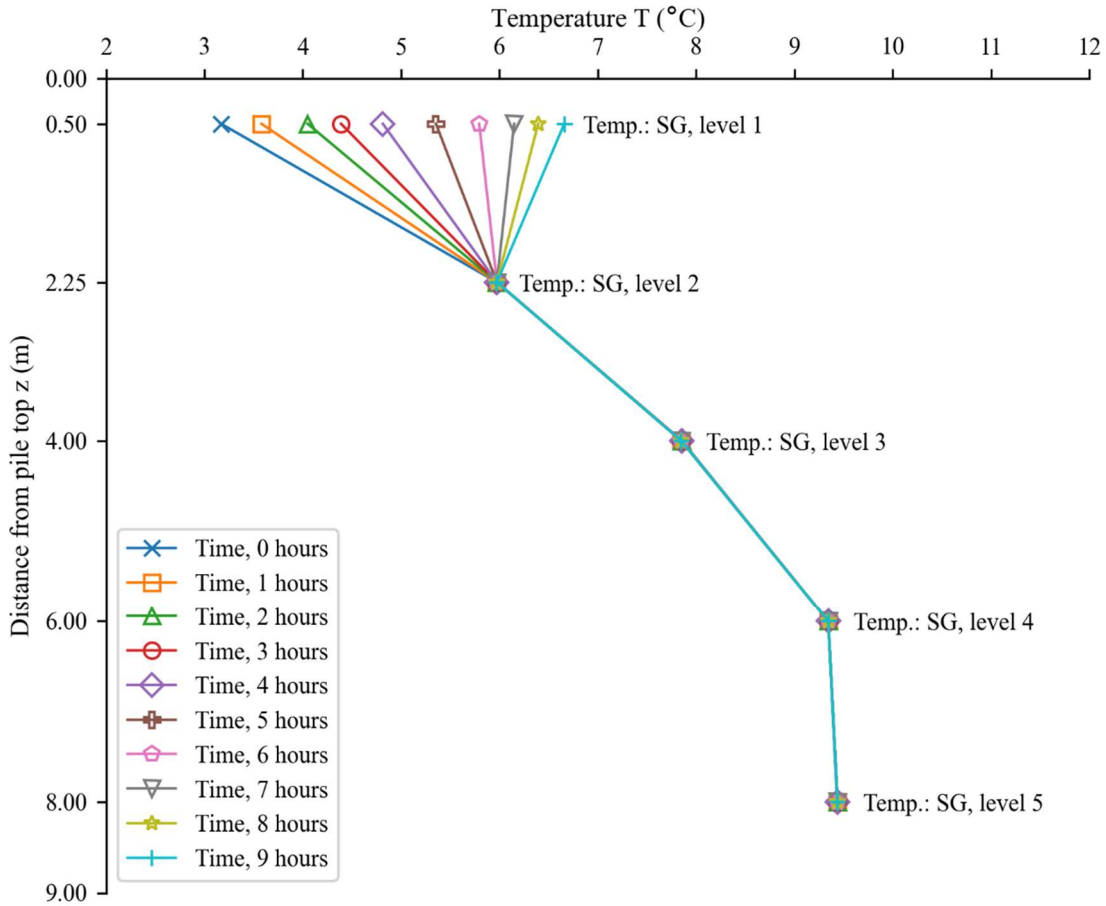

Figure 60: Temperature development along the length of test pile 8 during static pile loading test. The time indications are established as zero at the beginning of the static pile loading tests.

During the short-term static pile loading tests, it was observed that temperature changes primarily affected the upper strain gauge level at ground level. This observation aligns with expectations, as temperatures below approximately 1-2 meters below ground level are anticipated to remain relatively constant over shorter time periods, such as a single day.

6.2 Observed behaviour from static pile loading tests

The loading procedures outlined in section 4.5 were followed for the static pile loading tests, for both the maintained load (ML) test and the constant rate of uplift (CRU) test. Details of the actual loading process for each test pile, as well as any minor deviations observed during the tests, can be found in Appendix E.1 and E.3.

In this section, the primary focus is to examine the behaviour of the test piles during the static pile loading tests. This analysis includes validating the maintained load at each load step, assessing the mobilised pile capacity and shaft resistance, examining the effects of creep rate on shaft resistance, investigating the impact of CRU on shaft resistance, studying the virgin pile load response, and analysing the degradation of shear stiffness for the pile-load response, as well as the initial loading, unloading, and reloading shear stiffness.

6.2.1 Maintained load

The validation of the maintained load at each load step needs to be performed due to manual control of the applied load. To define each maintained load step, the first data point is identified when the applied load reaches or surpasses the target load for the first time. If the target load is not fully reached, the first data point is identified when the applied load decreases (or increases during unloading of the first load phase) for the first time.

The final data point for each maintained load step is determined when the load increases (or decreases during unloading of the first load phase) at a rate of more than 0.1 kN/s without any subsequent decrease (or increase for unloading) before the next load step. Additionally, the load must be above (or below for unloading) the target load at the final data point.

The predefined target load and the achieved average value for test piles 1-8 at each individual load step can be found in Appendix E.2. Table 10 provide an overview of the maximum deviation from the target load across all load steps for test piles 1-8.

Table 10: Maximum deviations from target loads for test pile 1-8.

Test pile [no.]	Maximum deviation	
	Positive deviation (%)	Negative deviation (%)
1	+6.4	-3.1
2	+0.8	-0.1
3	+5.8	-
4	+0.1	-1.4
5	+6.7	-
6	+5.0	-0.4
7	+8.6	-0.5
8	+4.3	-

Kindly take note that the high percentage deviations primarily occur in load steps with smaller loads (refer to Appendix E.2). For instance, a deviation of 1 kN corresponds to a 1% deviation in a load step of 100 kN, but it is only a 0.2% deviation in a load step of 500 kN.

The achieved average value shows a maximum deviation of +8.6% / -3.1% from the predefined target loads. The majority (86%) of the achieved average values deviate by less than +/- 2%. This deviation is considered insignificant as it is comparable to choosing a slightly different target load and data point for modelling the piles' response to loading. An example highlighting the predefined target load and achieved average value can be seen in Figure 61, specifically for test pile 7 in load step 5.

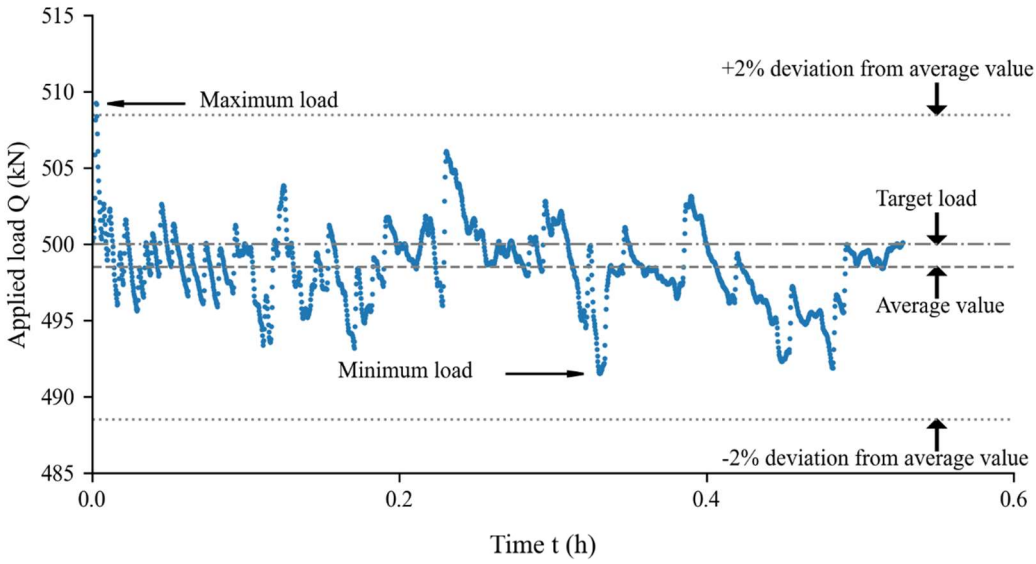

Figure 61: Deviation in load for load step 5 during static pile loading test of test pile 7, showcasing both the predefined target load and achieved average value for test pile 7 in load step 5.

In addition to assessing the deviation from the predefined target load to the achieved average value, it is crucial to consider the deviation of each data point from the achieved average value. This provide insight into whether the applied load can be deemed maintained at the specified load level. Appendix E.2 provide information on the determination of the maximum and minimum load for test piles 1-8 in each load step, along with the corresponding deviation from the achieved average value.

These maximum and minimum load values represent the upper and lower bounds for each load step, as depicted in Figure 61 for the example on load step 5 during static pile loading test of test pile 7. It is worth noting that the majority of data points are in immediate proximity to the achieved average value.

Table 11 provide an overview of the deviation between the achieved average value and the determined maximum and minimum load across all load steps for test piles 1-8.

Table 11: Deviations from average value to the determined maximum and minimum loads.

Test pile [no.]	Deviation from average value	
	Maximum load (%)	Minimum load (%)
1	+3.1	-4.9
2	+1.1	-2.1
3	+4.1	-4.5
4	+7.1	-3.6
5	+4.8	-5.3
6	+1.7	-4.2
7	+5.4	-7.5
8	+2.3	-4.3

The maximum deviation from the achieved average value to the determined maximum and minimum load for all load steps in test piles 1-8 is +7.1%/-7.5% respectively. The majority of data points (80% and 72% respectively) deviate by less than +/- 2%, and most data points are in close proximity to the achieved average value. This observation is satisfactory for a manually applied maintained load.

Furthermore, considering that the soil conditions primarily consist of a very high plasticity marine Eocene clay, which has a delayed response to minor load deviations, the manually applied load at each maintained load step can be regarded as a maintained load and not a cyclic load.

6.2.2 Mobilised pile capacities and shaft resistance

The shaft resistance, R_s, of the test piles is equivalent to the total bearing capacity obtained from the static pile loading tests conducted as tension tests. The total bearing capacity and thereby the shaft resistance, R_s, is determined from the load-displacement curves in Figure 62 and Figure 63. The load-displacement curves are based on data from the displacement transducers on pile top, and no correction are made relative to the surveyor's level.

An overview of the determined shaft resistance, R_s, is given in Table 12.

Table 12: Shaft resistance determined by static pile loading tests in tension.

Test pile	Period of rest		Test method		Shaft resistance
[no.]	months	days	ML	CRU	R_s (kN)
1	1	20	X		824
7	1	17	X		748
3	7	11	X	X	884
5	7	11	X	X	881
8	7	12	X	X	913
2	34	7	X	X	837
4	34	9	X	X	909
6	34	8	X	X	955

Maintained load (ML) test

The initial section of the load-displacement curves during the first load phase (500 kN) for test piles 1 and 7 exhibits an almost straight-line behaviour, accompanied by a minor plastic deformation of 0.5-1.1 mm after the initial unloading. This indicates an elasto-plastic response of the piles under load. As the test piles approach failure, the pile load response becomes predominantly plastic, as evident from the significant plastic deformation of 39.2-43.3 mm after the final unloading, as illustrated in Figure 62.

Test pile 1 fails under a sustained load of 824 kN, while test pile 7 fails under a sustained load of 748 kN,

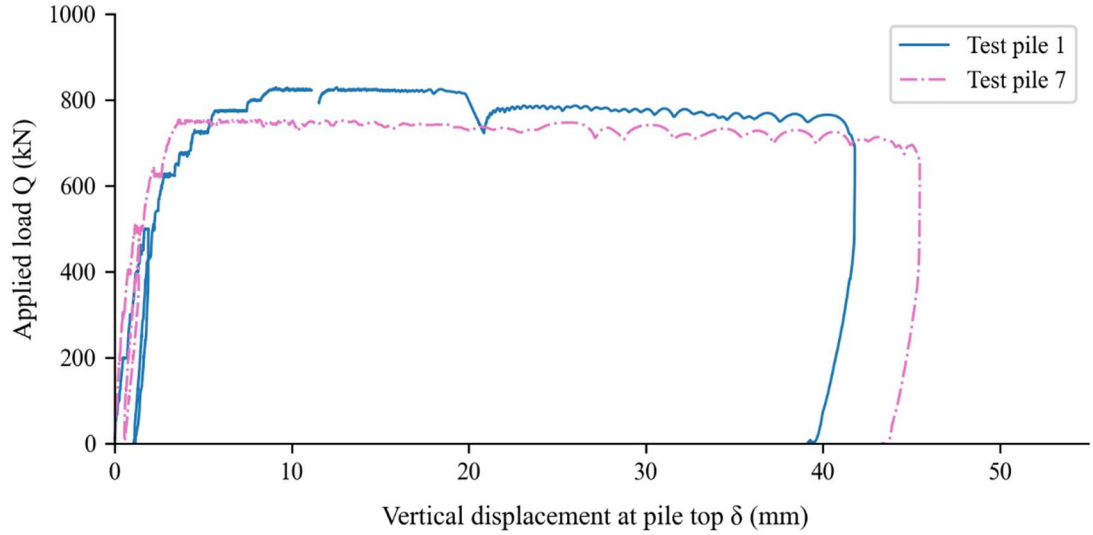

Figure 62: Load-displacements curves from the maintained load (ML) tests.

Constant rate of uplift (CRU) test

The initial section of the load-displacement curves for the first load phase (200 kN) indicate an elastic pile load response for test piles 2-6 and 8, with minimal plastic deformation after the first unloading. As the load increases, the pile load response is likely to transition from elastic to elasto-plastic, as observed in the ML test. Near failure, the pile load response becomes plastic, and the test piles exhibit significant plastic deformation (ranging from 5.6 to 13.4 mm) after unloading. When reloaded and then unloaded with a constant rate of uplift, the plastic deformation increases further to a range of 6.8 to 21.2 mm, as illustrated in Figure 63.

Test pile 2 reaches failure at a peak load of 837 kN during the CRU phase of the pile loading tests. Similarly, test piles 3-6 and 8 exhibit failure during the CRU phase with peak loads ranging between 881 kN and 955 kN.

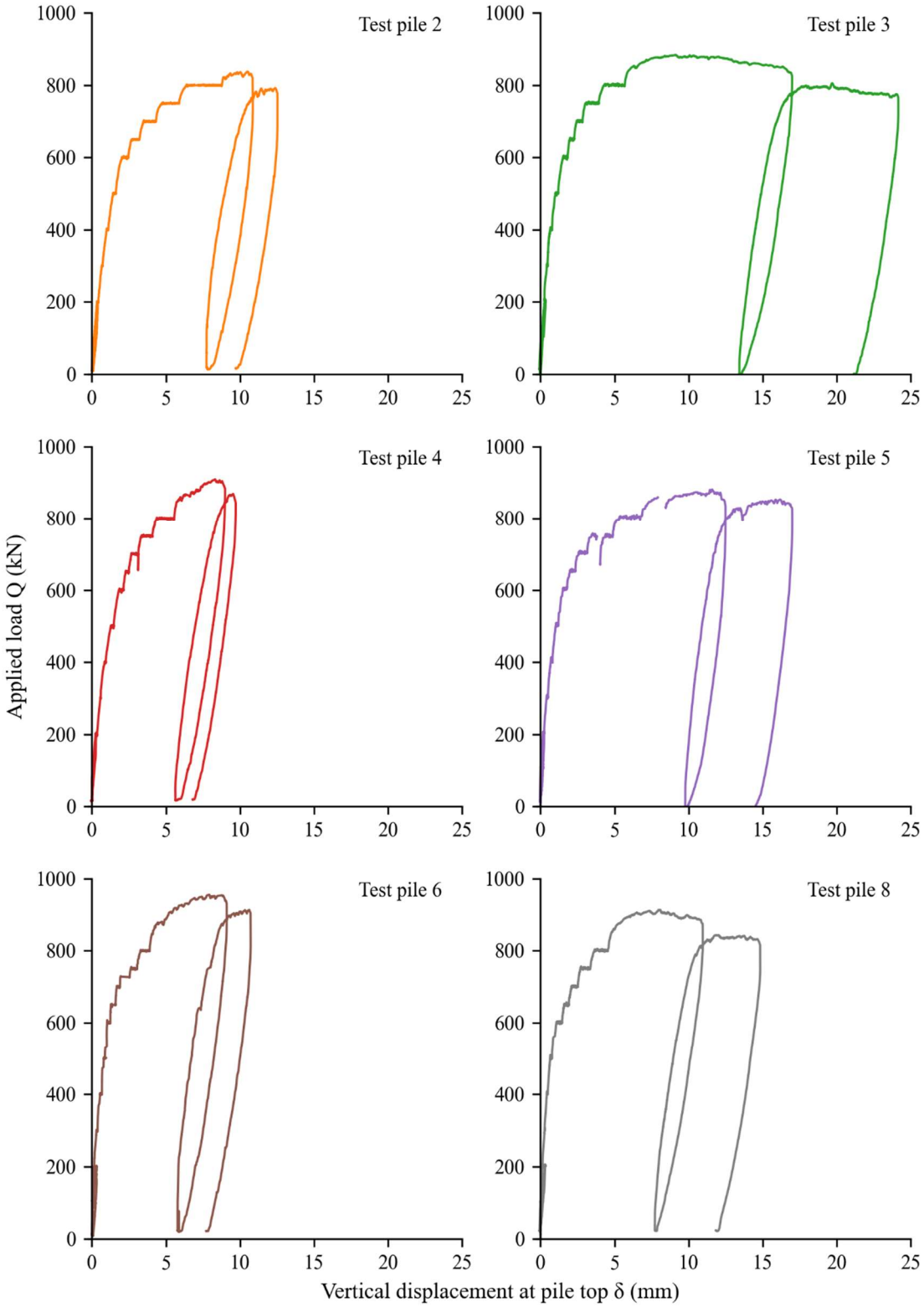

Figure 63: Load-displacements curves from the constant rate of uplift (CRU) tests.

6.2.3 Influence of rate of creep on shaft resistance

The precise determination of the total bearing capacity and thereby the shaft resistance, R_s, in a static pile loading test, especially through the ML test method, is challenging. This is because the final bearing capacity of the test pile depends on the selected load increments as well as the duration of each increment. Opting for smaller load increments improves the accuracy of determining the total bearing capacity. However, it is worth noting that the piles may also experience creep failure if sufficient time is allowed for creep after each load increment.

Maintained load (ML) test

To gain a deeper understanding of the impact of creep rate on the shaft resistance, R_s, the development of the rate of creep, k_s, for test pile 1 and 7 is depicted in Figure 64. Only the rate of creep determined during the second load phase is included in the figure, as the applied loads in the first load phase is nowhere near failure. The rate of creep for all load steps are given in Appendix E.4 and E.5.

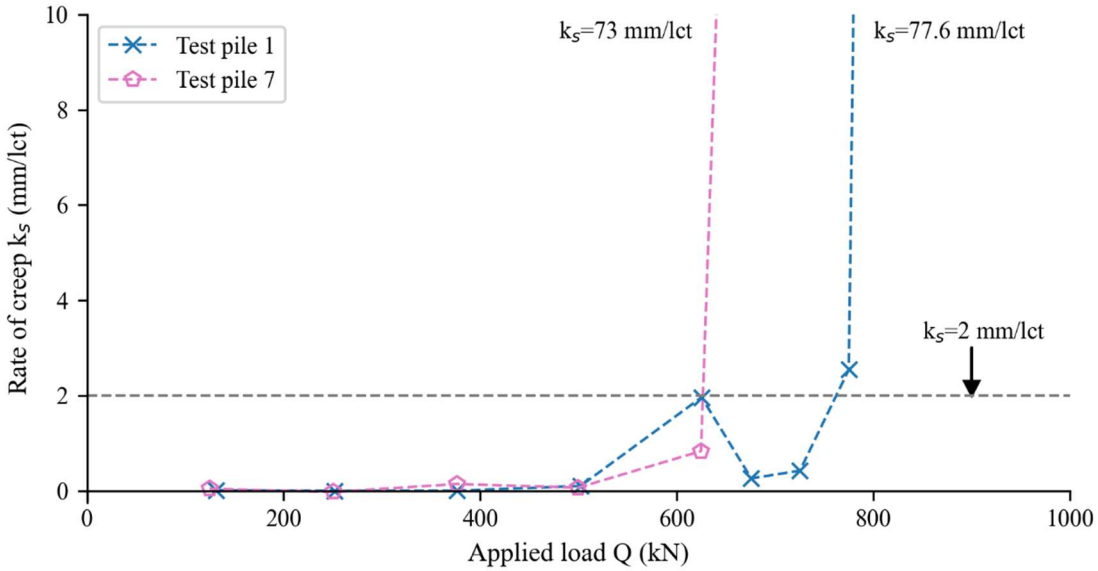

Figure 64: Development of rate of creep in load phase 2 for the maintained load (ML) tests.

Test pile 7, being the initial pile subjected to testing, exhibited an unexpected failure at the final load step (750 kN), despite having a rate of creep that remained well below the criteria for imminent failure (2 mm/lct) up until the second-to-last load increment (625 kN). However, at the last load step, the rate of creep sharply increased to 73 mm/lct, indicating a clear vertical asymptote and thus, failure for test pile 7.

Following the testing of Test pile 7, Test pile 1 was subsequently tested with some modifications. After reaching load step 15 (625 kN), the load steps were reduced to 50 kN. This adjustment was based on the insights gained from Test pile 7 and the observation of the rate of creep approaching the defined criteria for imminent failure, which is a cessation of movement criteria of 2 mm/lct. As the applied load increased further, the rate of creep decreased steadily. However, there was a slight increase in the rate of creep just above the defined criteria for imminent failure at the second-to-last

load step. The failure of Test pile 1 occurred at the last load step (825 kN), where the rate of creep sharply rose to 77.6 mm/lct, indicating a vertical asymptote and thus, failure.

Figure 65 illustrates the displacement rate during creep, $\dot{\delta}_{creep}$, for the final two load steps of test pile 1 and test pile 7. This aims to investigate whether the test piles experienced creep failure on the second-to-last load step. The displacement rate during creep is determined through a moving average calculation over a period of 2 minutes.

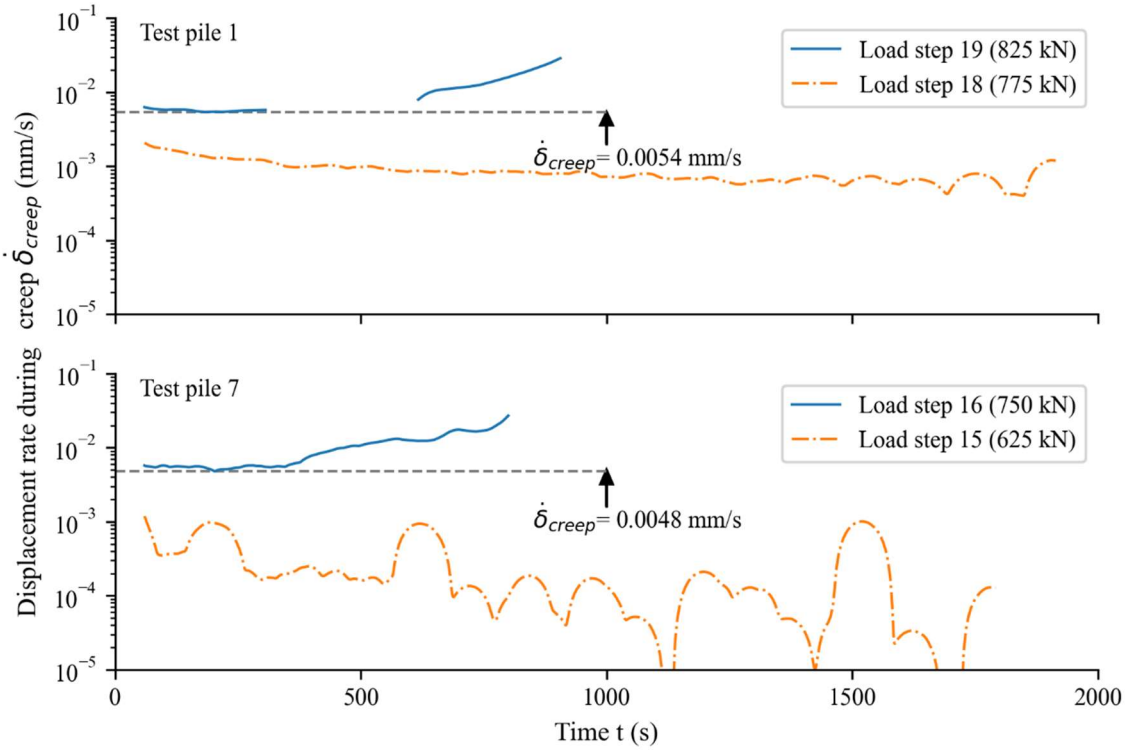

Figure 65: Displacement rate during creep for the final two load steps of test pile 1 and 7.

During the final two load steps (775 kN and 825 kN) of test pile 1, the rate of creep, k_s, is determined to be 2.5 mm/lct and 77.6 mm/lct, respectively. In load step 19 at 825 kN, the displacement rate during creep, $\dot{\delta}_{creep}$, initially showed a slight reduction. However, once the rate reached approximately 0.0054 mm/s (19.4 mm/h), the displacement rate during creep, $\dot{\delta}_{creep}$, accelerated, indicating the occurrence of creep failure in the pile. Considering the minimal load difference of only 50 kN between the two last load steps, it is likely that if sufficient time for creep had been allowed, the pile would have eventually experienced creep failure even at the previous load step 18 at 775 kN

During the final two load steps (625 kN and 750 kN) of test pile 7, the rate of creep, k_s, was determined to be 0.8 mm/lct and 73 mm/lct, respectively. In load step 16 at 750 kN, the displacement rate during creep, $\dot{\delta}_{creep}$, initially showed a slight reduction. However, once the rate reached approximately 0.0048 mm/s (17.3 mm/h), the displacement rate during creep accelerated, indicating the occurrence of creep failure in the pile. In the previous load step 15 at 625 kN, the displacement rate during creep, $\dot{\delta}_{creep}$, reduced approximately linearly with time, and there were no signs of

imminent failure. However, it is possible that test pile 7 could have experienced failure earlier if smaller load increments had been employed.

The determination of the ultimate shaft resistance, R_s, presents challenges due to its dependence on the selected load steps and the corresponding time allocated for creep after each load increment in static pile loading tests. This variability affects the total bearing capacity and, subsequently, the accurate determination of the shaft resistance, R_s.

Constant rate of uplift (CRU) test

To ensure the static pile loading tests were transitioned from the ML test into a CRU test when signs of imminent failure occurred cf. section 4.1, the development of the rate of creep, k_s, for test pile 2-6 and 8 is depicted in Figure 65. This aims to examine the development of the rate of creep, k_s in order to document that the test piles approached but did not surpass the cessation of movement criteria of 2 mm/lct for imminent failure cf. section 5.1. Only the rate of creep determined during the second load phase is included in the figure, as the applied loads in the first load phase is significantly below "near failure" thresholds. The rate of creep observed during the first load phase can be found in Appendix E.4 and E.5.

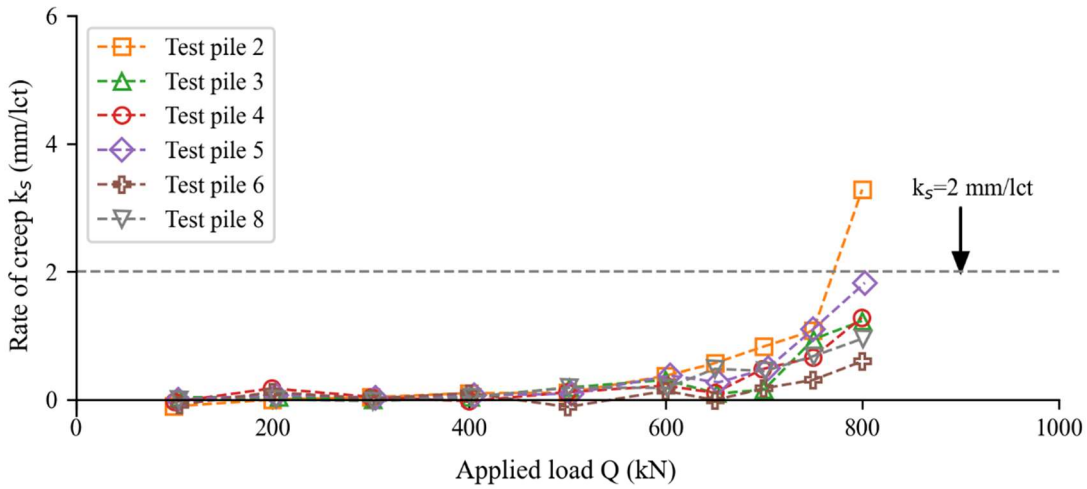

Figure 66: Development of rate of creep in load phase 2 for the constant rate of uplift (CRU) tests.

Throughout the ML portion of the pile loading tests, the rate of creep remains below the designated cessation of movement criteria of 2 mm/lct, except for the final load step (800 kN) before the CRU phase for test pile 2. This observation suggests that the failure of the test piles occurs during the CRU phase of the test.

In the case of test pile 2, the fact that it exceeds the cessation of movement criteria supports the selected value of 2 mm/lct. Test pile 2 fails at a peak load of 837 kN during the CRU phase, which is close to the final ML step of 800 kN. In contrast, test piles 3-6 and 8 fail at higher peak loads ranging from 881 kN to 955 kN.

6.2.4 Influence of constant rate of uplift (CRU) rate on shaft resistance

The prescribed pile uplift rate, $\dot{\delta}_{uplift}$, of 20 mm/h was maintained during both the initial loading phase in the CRU portion of the pile loading tests and the subsequent reloading phase. The investigation into the pile uplift rate aims to provide an understanding of its influence on the shaft resistance, R_s, of the test piles, see Figure 67.

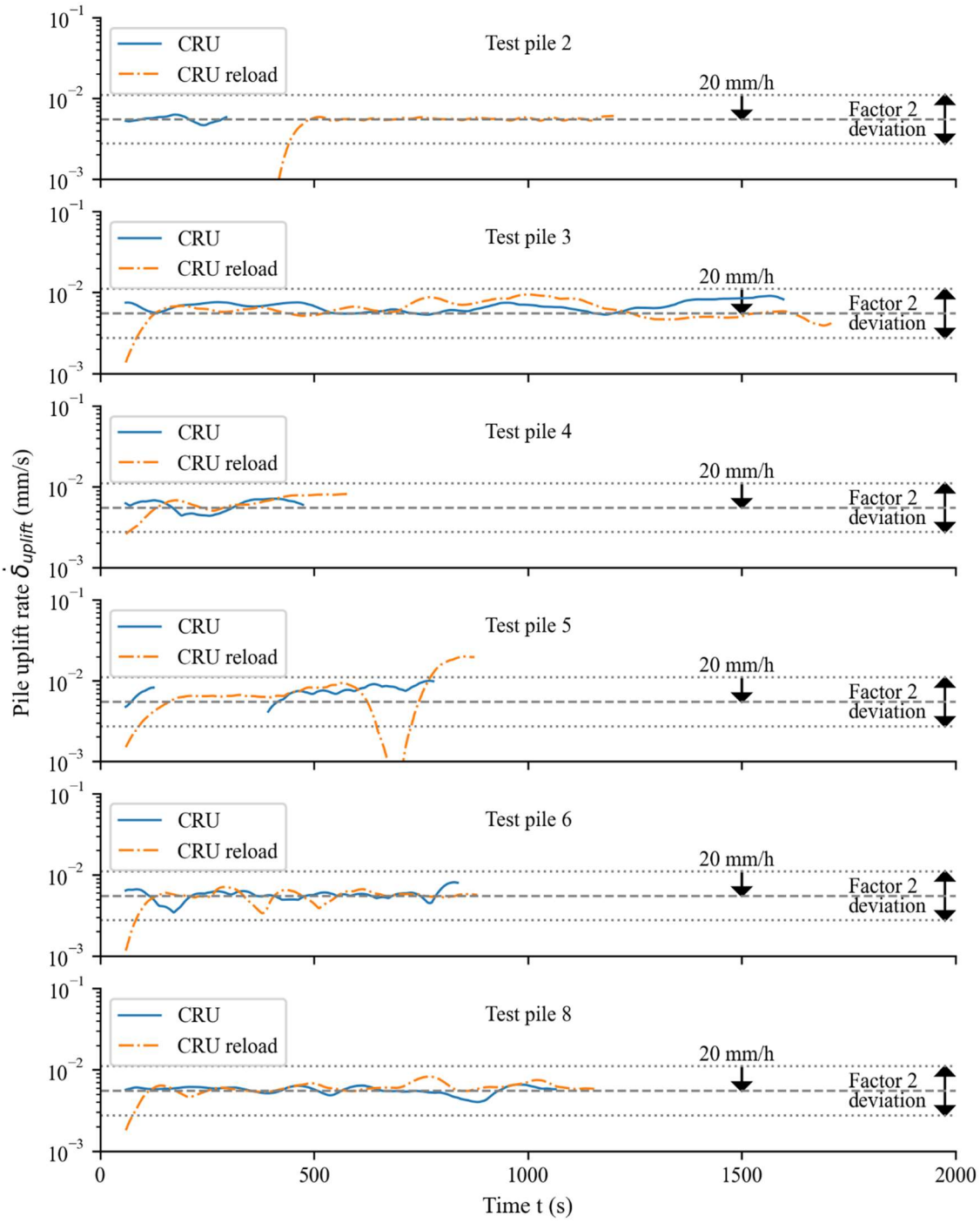

Figure 67: Pile uplift rate for initial loading and reloading of the constant pile uplift rate portion.

Figure 67 presents the progression of the pile uplift rate, $\dot{\delta}_{uplift}$, over time for test piles 2 to 6 and 8. The figure encompasses both the initial loading phase in the CRU portion of the pile loading tests and the reloading phase. The pile uplift rate is determined by calculating a moving average over a period of 2 minutes.

To ensure consistency, a factor of 2 deviation was applied to the prescribed pile uplift rate, $\dot{\delta}_{uplift}$, of 20 mm/h for both the initial loading phase (the blue solid lines) and the reloading phase (the orange dashed lines) in the constant pile uplift rate portion of the pile loading tests. Based on prior experience, this deviation introduces a minor deviation of approximately 2% in the results, which is of negligible significance.

During the reloading phase of the static pile loading test, specifically for test pile 2, the pile uplift rate, $\dot{\delta}_{uplift}$, initially deviated significantly from 20 mm/h in the early part of the reloading path (the orange dashed line) until approximately 500 seconds. However, as the load reached approximately 150 kN, the pile uplift rate gradually approached 20 mm/h, and thus the impact on the achieved peak value of 792 kN during reloading was negligible.

For test pile 5, an interruption occurred during the initial constant rate of uplift portion of the static pile loading test, resulting in minor data loss, indicated by the missing part of the blue solid line. During the reloading phase of the test, the pile uplift rate (the orange dashed line) exhibited greater deviations towards the end. Overall, the pile uplift rate, $\dot{\delta}_{uplift}$, for test pile 5 depicted a slightly increasing trend over time.

6.2.5 Virgin pile-load response

This section presents the response of the test piles to loading in the context of the virgin load curves. The virgin pile-load response includes load steps 1-5 and load steps 15 until failure for the ML test conducted on test piles 1 and 7. However, due to the nature of the ML test method and the absence of a constant rate of uplift, it is challenging to determine the overall behaviour of the test piles' response to loading, see Figure 68.

For the CRU test, the virgin pile-load response incorporates load steps 1-2 and load steps 7 until failure. In general, the response of the test piles to loading exhibits a strain softening behaviour after reaching the peak value in the CRU tests, see Figure 69.

Maintained load (ML) test

The virgin pile-load response for the maintained load test includes load steps 1-5 and from load step 15 until failure. This encompasses the initial loading phase ranging from 0 to 500 kN in the first load phase, as well as from 625 kN to failure in the second load phase. Since the first load step in the second load phase surpasses the final load step from the first load phase by 25%, it is determined that the unloading and reloading phases have negligible impact on the virgin pile-load response.

To exclude any influence from creep displacement, data points for the virgin load curves are determined as the first data point at each maintained load step. This is illustrated in Figure 68.

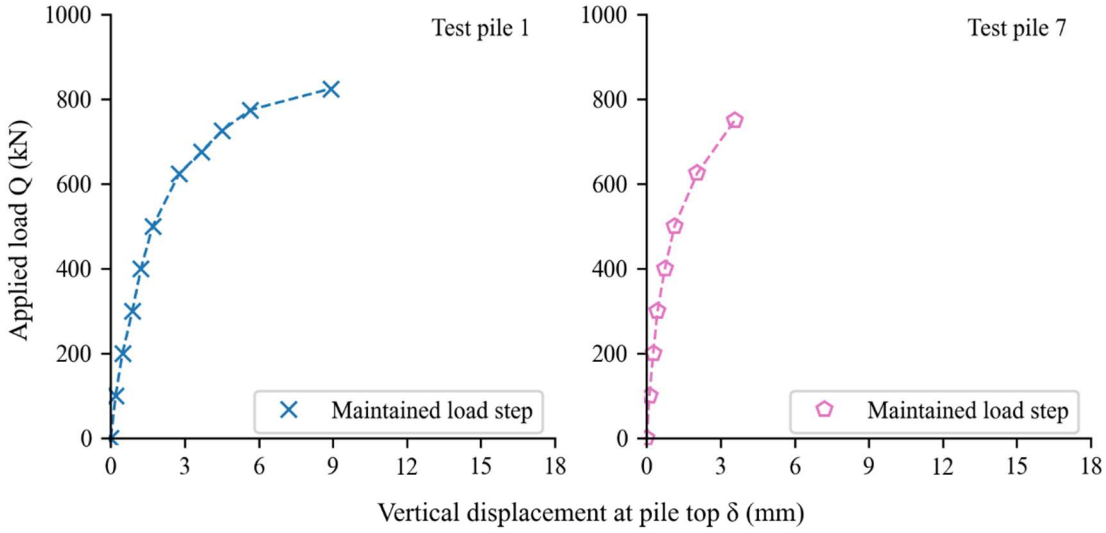

Figure 68: Virgin load curves for test pile 1 and 7.

Constant rate of uplift (CRU) test

The virgin pile-load response for the CRU test includes load steps 1-2 and from load step 7 until failure. This corresponds to the initial loading from 0 to 200 kN in the first load phase and from 300 kN to failure in the second load phase. Since the initial load step in the second load phase exceeds the final load step from the first load phase by 50%, it is determined that the unloading and reloading phases have no significant effect on the virgin pile-load response.

To exclude any influence from creep displacement, data points for the virgin load curves are established as the first data point at each maintained load step. In the initial constant rate of uplift portion of the static pile loading test, the peak value of the applied load, Q, and the corresponding vertical displacement at the pile top, δ, are used as data points for test piles 2-6 and 8.

Moreover, all data points from the initial CRU portion of the static pile loading test are presented to visually support the selection of the theoretical model for curve fitting, as shown in Figure 69. However, it is important to note that the first part of the data points in this portion of the test is expected to be too low, as the pile-load response needs to cover the transition from the end of the last maintained load step (after creep displacement) to the virgin load curve.

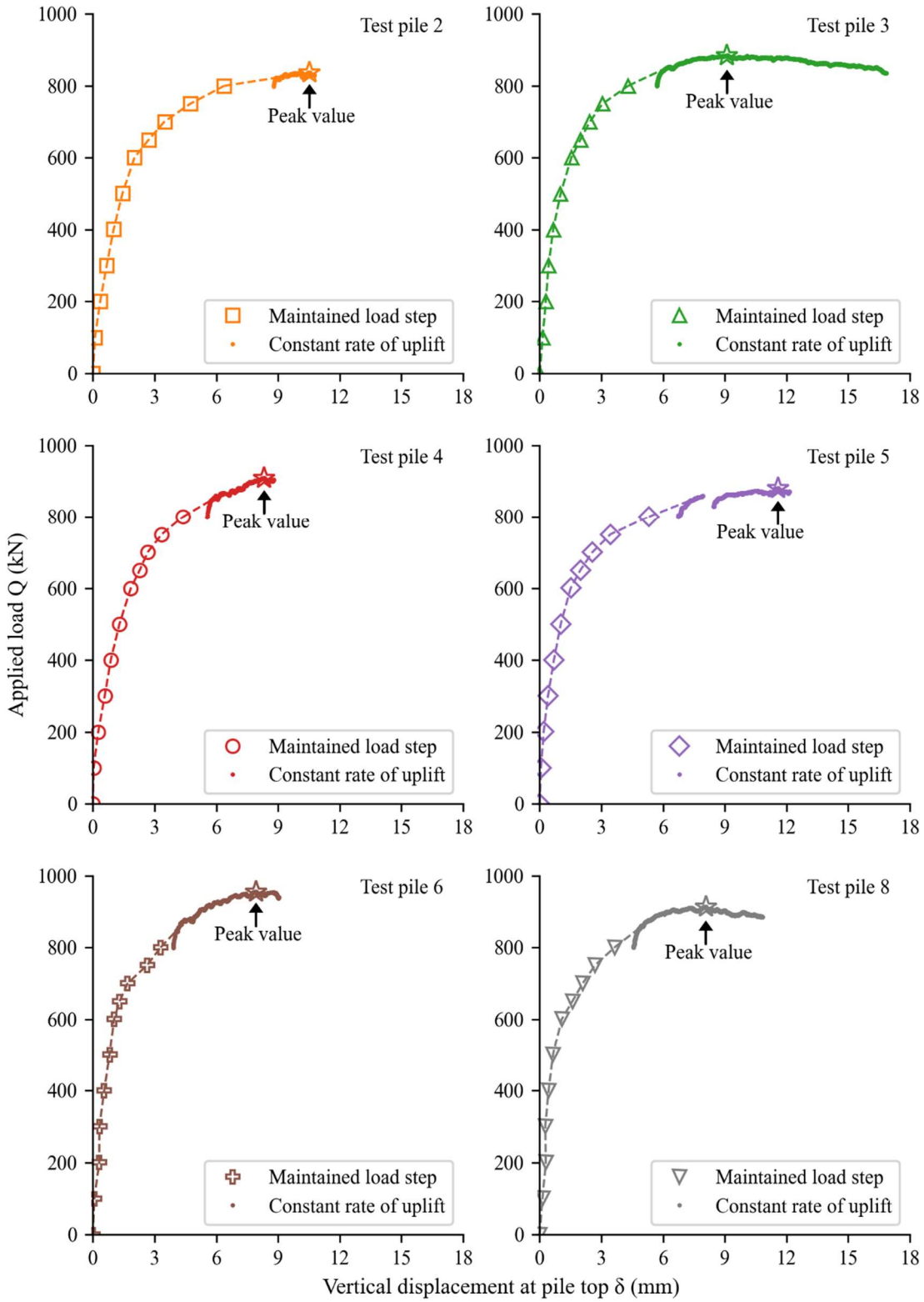

Figure 69: Virgin load curves for test pile 2-6 and 8.

6.2.6 Shear stiffness degradation for virgin pile-load response

Shear stiffness degradation refers to the variation of the shear modulus, G_{pile}, determined from the virgin pile-load response described in section 6.2.5, relative to the vertical displacement at the pile top, δ. The shear modulus, G_{pile}, is calculated as the tangent slope between two adjacent data points on the virgin load curve, as outlined in section 5.7. The vertical displacement at the pile top, δ, is obtained as an average value of the two adjacent data points.

The shear stiffness degradation curves are derived directly from the measured data. For the CRU portion of the shear stiffness degradation curves for test piles 2-6 and 8, a moving average over 120 readings (2 minutes) is utilized. However, the first 60 readings (1 minute) of the CRU portion are excluded. This is because the constant rate of uplift portion is initiated after a period of creep and not directly on the virgin load curve.

Figure 70 illustrates an example of the shear stiffness degradation curve for test pile 3. The shear stiffness degradation curves for test piles 1 and 7, based on the ML test, and test piles 2-6 and 8, from the CRU test, are provided in Appendix E.6.

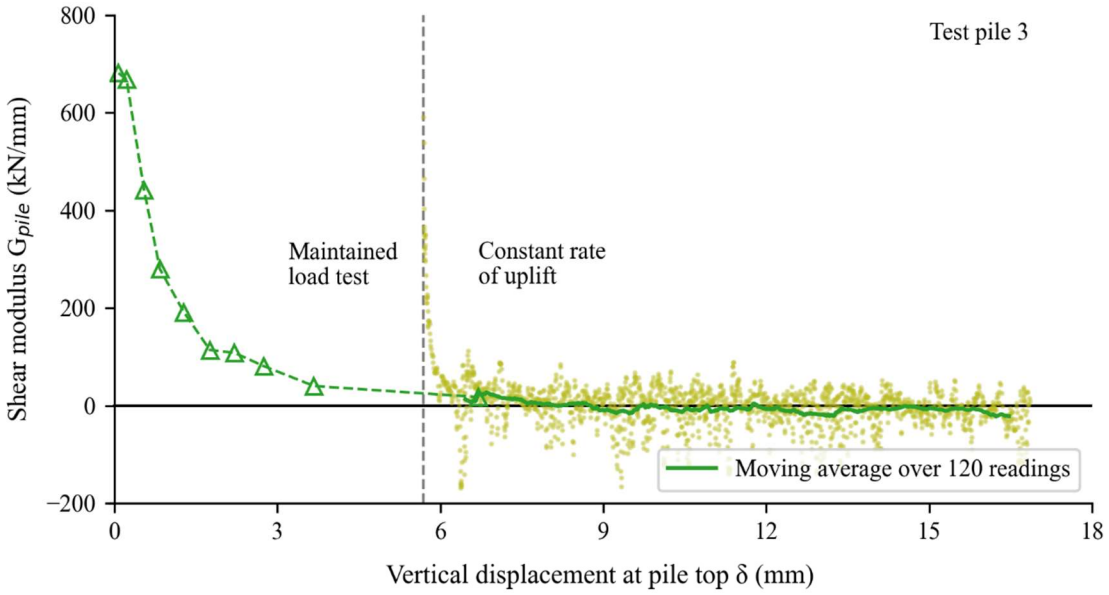

Figure 70: Example of shear stiffness degradation curve for test pile 3.

The shear stiffness values at the maintained load steps during the transition from load phase 1 to load phase 2 are omitted for the CRU tests conducted on test piles 2-6 and 8. This is due to the influence of unloading and reloading on the test piles' behaviour. However, for the ML tests performed on test piles 1 and 7, the shear stiffness during the transition from load phase 1 to load phase 2 appears to be unaffected by the unloading and reloading. This could be attributed to the unloading and reloading being performed at a higher load (500 kN instead of 200 kN) in these specific tests.

Figure 71 showcases the shear stiffness degradation curves for all test piles (1-8) in the static pile loading tests. The curves include both the shear stiffness degradation at the ML steps and the moving average over 120 readings (2 minutes) specifically for the CRU portion of the tests.

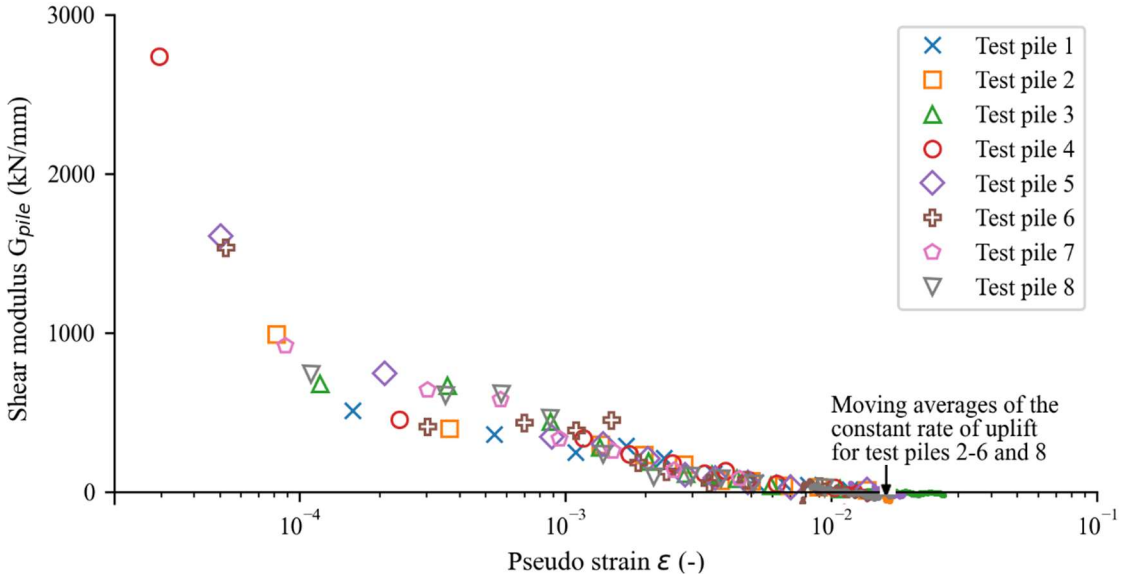

Figure 71: Shear stiffness degradation curves for test piles 1-8.

The shear stiffness degradation curves are displayed using a semilogarithmic scale on the x-axis. In this representation, the vertical displacement at the pile top, δ, is expressed as a pseudo strain, ε, through division by the pile diameter, D_p. It should be noted that for test piles 2-6 and 8 in the CRU portion of the static pile loading tests, the shear modulus, G_{pile}, may appear to become negative. However, this is not actually the case. Instead, it is a consequence of the momentarily decreasing manually applied load, Q, during loading, as well as the strain softening behaviour of the pile load response after reaching the peak value

The shear stiffness degradation curves tend to exhibit a trend towards infinite stiffness as the vertical displacement approaches zero, while approaching zero stiffness at failure (for high vertical displacement). Interestingly, it is observed that piles with higher initial stiffness values at the first ML step tend to have lower pseudo strain, ε, values. This suggests that the variation in stiffness is dependent on the choice of pseudo strain (ε) or vertical displacement at the pile top (δ) at which the shear stiffness is determined.

Additionally, there is no consistent trend indicating that certain piles possess generally higher shear stiffness degradation curves compared to others. This implies that the initial stiffness is not directly linked to the mobilised pile capacity of the individual test piles.

6.2.7 Initial loading, unloading, and reloading shear stiffness

The shear modulus, G_{pile}, is determined during the initial loading (ML + CRU portion) as well as the unloading and reloading stages of the CRU tests for test piles 2-6 and 8. The vertical displacement at the top of each pile, δ, is reset to zero at the start of the initial loading, unloading, and reloading,

respectively. This allows for the investigation of the relationship between these stages, as shown in Figure 72.

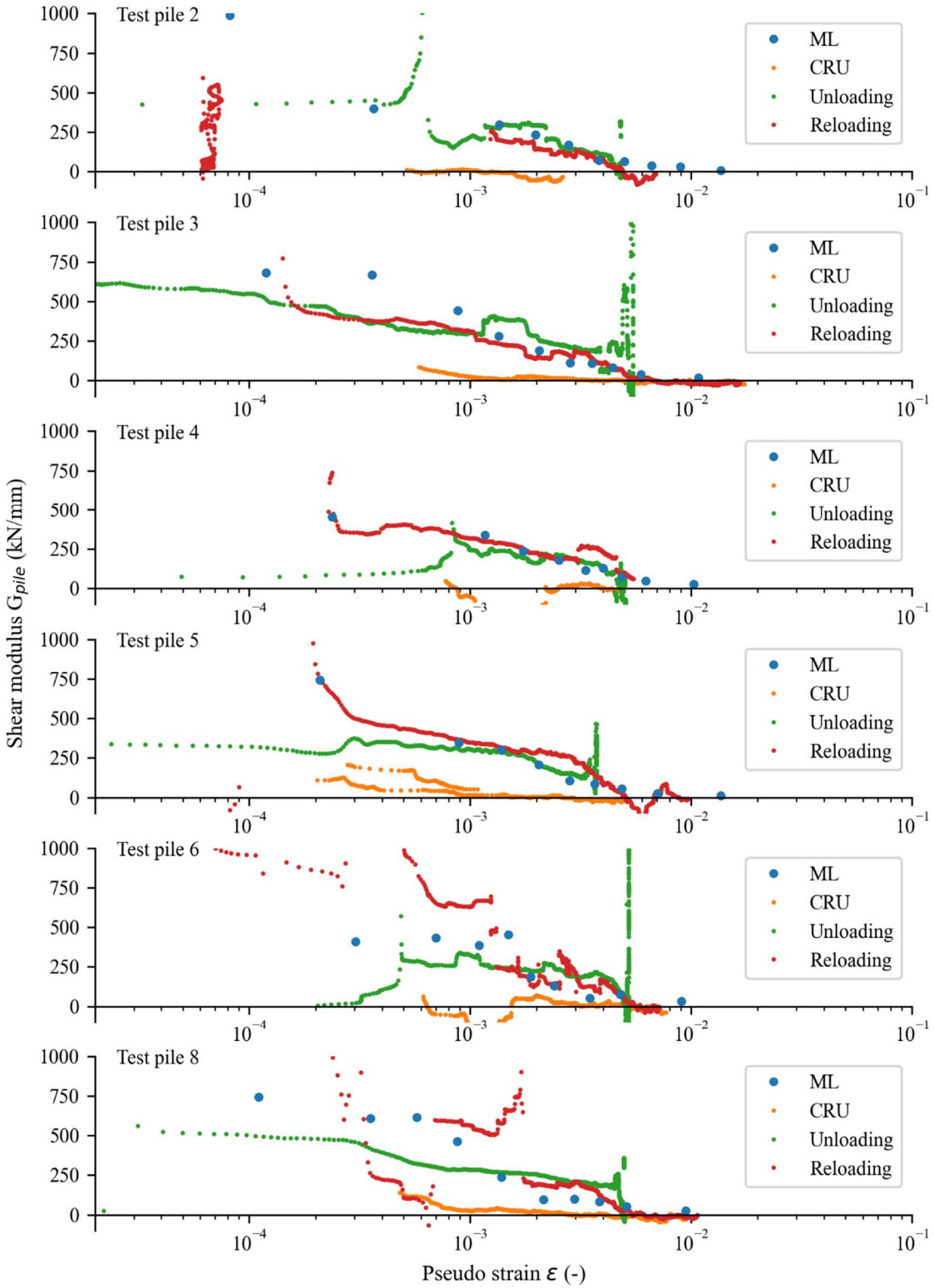

Figure 72: Shear modulus for initial loading for the maintained load (ML) and constant rate of uplift (CRU) portion as well as the unloading and reloading stages of the CRU tests for test piles 2-6 and 8.

The shear modulus, G_{pile}, is calculated as the tangent slope between two adjacent data points, and a moving average over 120 readings (2 minutes) is used for the CRU portion of the initial loading, unloading, and reloading. The shear modulus, G_{pile}, is plotted on a semi-logarithmic scale of the x-axis, where the vertical displacement at the top of the pile, δ, is expressed as a pseudo strain, ε, by dividing it by the pile diameter, D_p. To ensure meaningful results, the lower bound of the x-axis is set at $2 \cdot 10^{-5}$ pseudo strain, ε, which approximately corresponds to the displacement transducers precision of 0.01 mm. Additionally, the upper bound of the y-axis is set at 1000 kN/mm² as most of the previously determined shear modulus values fall below this range, as shown in Figure 71.

Although it may appear that the shear modulus, G_{pile}, becomes negative during the constant rate of uplift portion of the static pile loading tests for test piles 2-6 and 8, this is not actually the case. The apparent negative values are a result of momentary decreases in the manually applied load, Q, during loading and reloading, or momentary increases during unloading. Additionally, because the pile load responses exhibit strain softening behaviour after reaching the peak value. Furthermore, during unloading, the displacement transducers may get momentarily stuck, leading to unrealistic measurements.

In general, there is good agreement in the shear modulus, G_{pile} between pseudo strains, ε, ranging from 10^{-3} to 10^{-2} for the initial loading (ML portion), unloading, and reloading stages. This indicates that the initial shear modulus, G_{pile}, during these stages are similar in magnitude. During the initial loading (CRU portion), the shear modulus, G_{pile}, tends to be significantly lower. However, this is merely a change in loading rate (from creep to a constant rate of uplift), and it does not represent a new initial shear stiffness. It is worth noting that immediately after initiating the CRU portion of the initial loading, the shear modulus, G_{pile}, initially appears relatively high, as observed in Figure 70. However, it quickly diminishes and is not particularly pronounced when considering a moving average over 120 readings (2 minutes), as shown in Figure 72.

Shear stiffness determined from unloading-reloading loop

In addition, the shear modulus, G_{pile}, is determined by calculating the average inclination of the unloading-reloading hysteresis curve from the lowest value of the applied load Q, to the point of intersection within the hysteresis. The concept for determining the shear modulus, G_{pile}, is demonstrated for test pile 3 in Figure 73. The shear modules, G_{pile}, for test piles 1 and 7, based on the ML test, and test piles 2-6 and 8, from the CRU test, are provided in Appendix E.7.

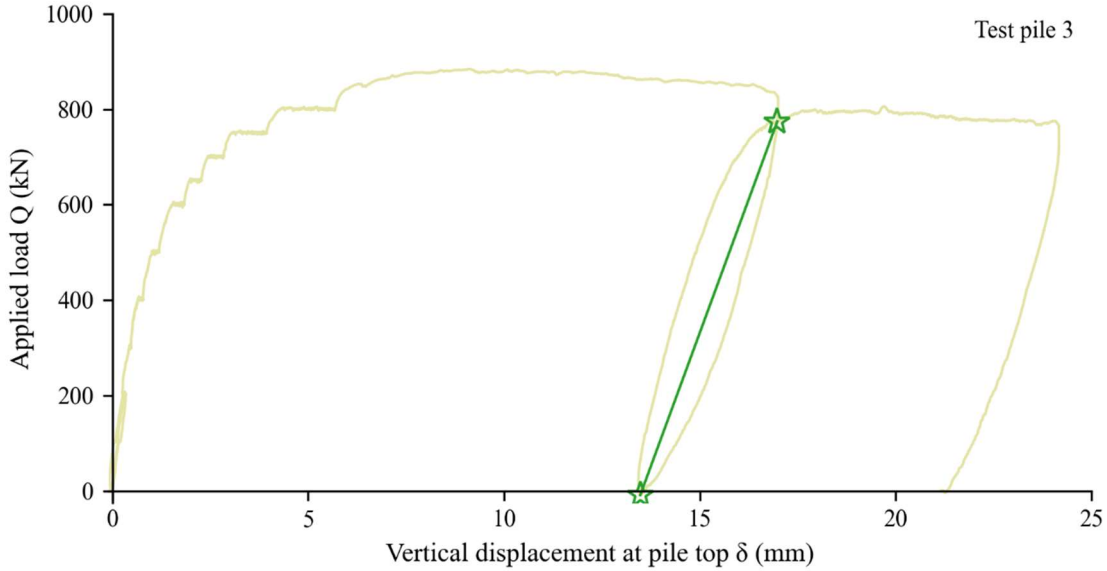

Figure 73: Illustration of the determination of the shear modulus, G_{pile}, as the average value of the inclination of the unloading-reloading hysteresis for test pile 3.

The shear modulus, G_{pile}, obtained from the average inclination of the unloading-reloading hysteresis, is presented in Table 13 for test piles 2-6 and 8.

Table 13: Unloading-reloading shear modulus, G_{pile}.

Test pile [no.]	**Unloading/reloading shear modulus (kN/mm)**
2	247
3	224
4	253
5	303
6	269
8	256

The unloading-reloading shear stiffness ranges from 224 kN/mm to 303 kN/mm, which generally aligns with the shear stiffness determined during initial loading, unloading, and reloading at a pseudo strain, ε, of approximately $2 \cdot 10^{-3}$.

6.3 Mobilisation of shaft resistance

The static pile loading tests in tension are conducted to determine the overall shaft resistance of the test piles. However, in order to assess the distribution of shaft resistance along the length of the piles, additional information is necessary. This information is obtained by installing vibrating wire strain gauges (VWSG) at five different locations along the length of the test piles, which provide data on strain and temperature.

Focus is on the internal strain profiles of the test piles, the determination of axial pile stiffness, the load distribution within the test piles, and the unit shaft resistance determined along the length of test piles 1-8 at the Hinge test site. This is interpreted based on strains and temperatures measured from the VWSG that is calculated in accordance with section 5.3.

To interpret the data from the VWSG, site zero readings for strains, temperatures, and applied loads are established at 6 o'clock in the morning of the static pile loading tests for each test pile. It is important to note that for test pile 4, the site zero readings are reset at 8.26 o'clock, and for test pile 8, they are reset at 7 o'clock in the morning. This reset is required due to data loss from the VWSG.

Furthermore, the site zero readings for pile top movement are reset at the beginning of the static pile loading test.

6.3.1 Internal strain profiles of the test piles

The internal strain profiles of the test piles are determined using measurements from the VWSG at each strain gauge level (strain gauge level 1-5). To assess the development of internal strain along the length of the test piles, the VWSG at each strain gauge level, and at each load step, are utilized. For each maintained load (ML) step, an average value is calculated from the measurements obtained by the VWSG. This approach enables accurate determination of the internal strain development along the length of the test piles since the test piles are typically not subjected to creep. Only for test piles 1 and 4, the uppermost strain gauges (strain gauge level 1) experience creep, as illustrated in Appendix H.3. However, this does not impact the subsequent analysis, as the applied load, Q, is directly used as described in section 6.3.3.

The measured raw strains, ε_r, can be found in Appendix H.1, while the measured temperatures are shown in Appendix F.2. The significance of thermal influence is demonstrated in Appendix H.2, where the average values of the measured raw strains, $\varepsilon_{r,a}$, and the average values of the measured strains corrected for thermal influence, $\varepsilon_{t,a}$, (also known as mechanical strains) are presented. Typically, only the upper strain gauges at level 1 (ground level) are affected by changes in temperature.

All subsequent data displayed are average values of measured strains corrected for thermal influence, $\varepsilon_{t,a}$, (mechanical strains) obtained from the strain gauge pairs installed on diametrically opposite

sides to separate bending moments from axial loads, as explained in section 5.3. It is worth noting that positive values of ε indicate tensile strain, while negative values of ε indicate compressive strain.

For test piles 1-3 and 5-7, a manual adjustment of 1 minute is required due to the observed drift in the datalogger over time, from its installation to the static pile loading test. However, for test pile 4, a manual adjustment of 6 minutes is necessary for the same reason.

In addition to the initial manual adjustments, further adjustments are needed during the static pile loading test for test piles 1, 3, and 5. These adjustments are necessary due to breakdowns that occurred and were not properly synchronized in terms of time. Specifically, test pile 1 is adjusted at 6 and 9 minutes after the first and second breakdowns, respectively, while test piles 3 and 5 require adjustments of no more than 2 minutes.

During the constant rate of uplift (CRU) portion of the static pile loading test for test piles 2-6 and 8, the peak values of the applied load, Q, and the corresponding strain, $\varepsilon_{t,a}$, are utilized.

Following these adjustments, representative internal strain profiles are provided for both ML test and the CRU test.

Maintained load (ML) test

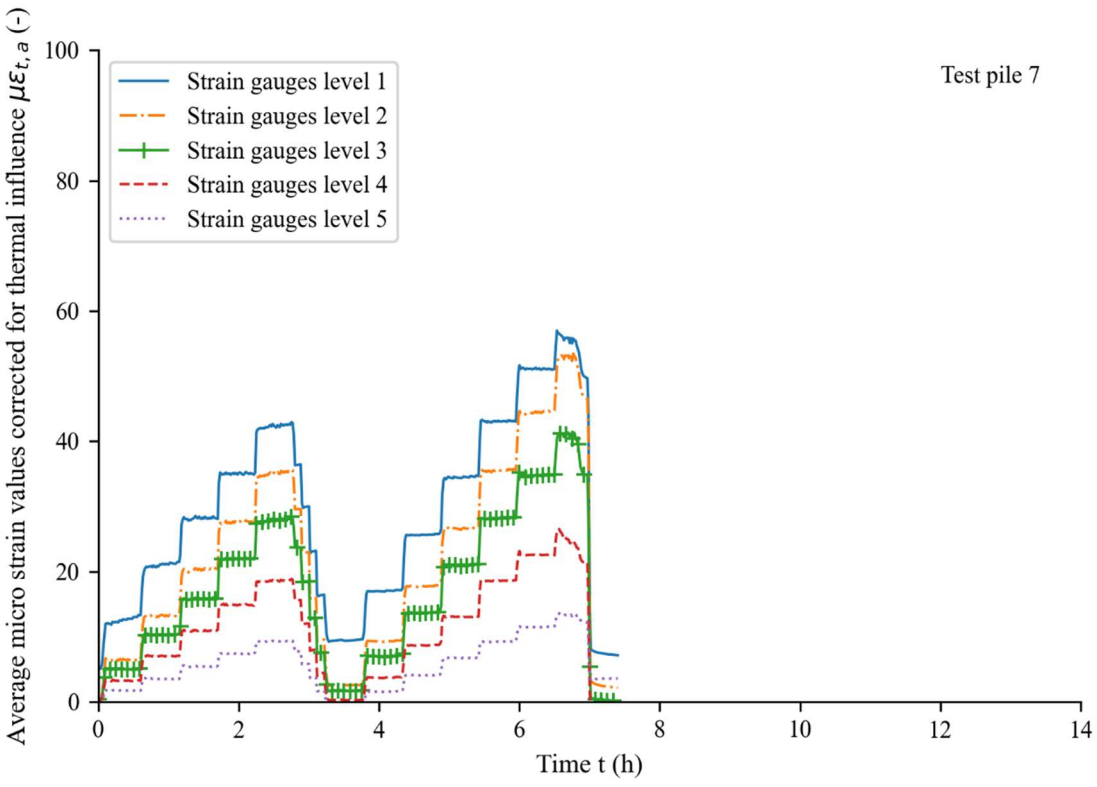

Figure 74: Average values of measured strains corrected for thermal influence for test pile 7.

The internal strain profiles for test piles 1 and 7 reveal that all strains exhibit tensile loading, as indicated by the positive values of strain. Additionally, the strains are highest at the upper strain gauge

level (strain gauge level 1) and decrease progressively as the measurements move further down the length of the test piles. This observation provide evidence that the test piles are experiencing tension. Figure 74 displays the time-strain curves for test pile 7, while Figure 75 and Figure 76 illustrate the strain development along the length of test pile 7 during load phases 1 and 2, respectively. The time-strain curves, and the strain development along the length of test pile 1, can be found in Appendix H.3 and Appendix H.4, respectively.

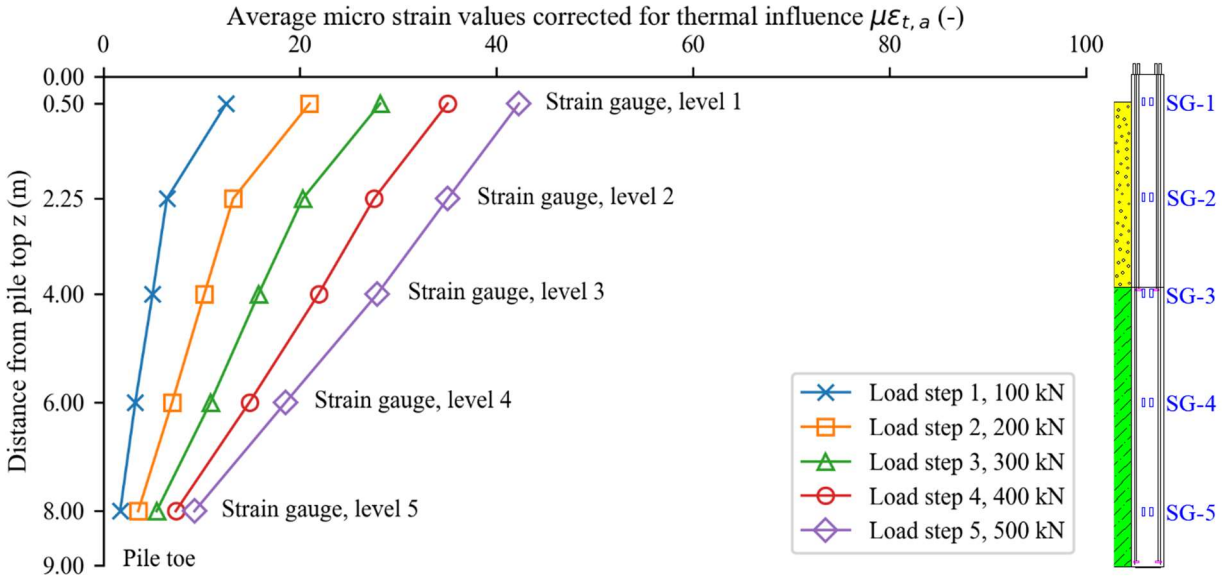

Figure 75: Strain development along the length of test pile 7 in load phase 1.

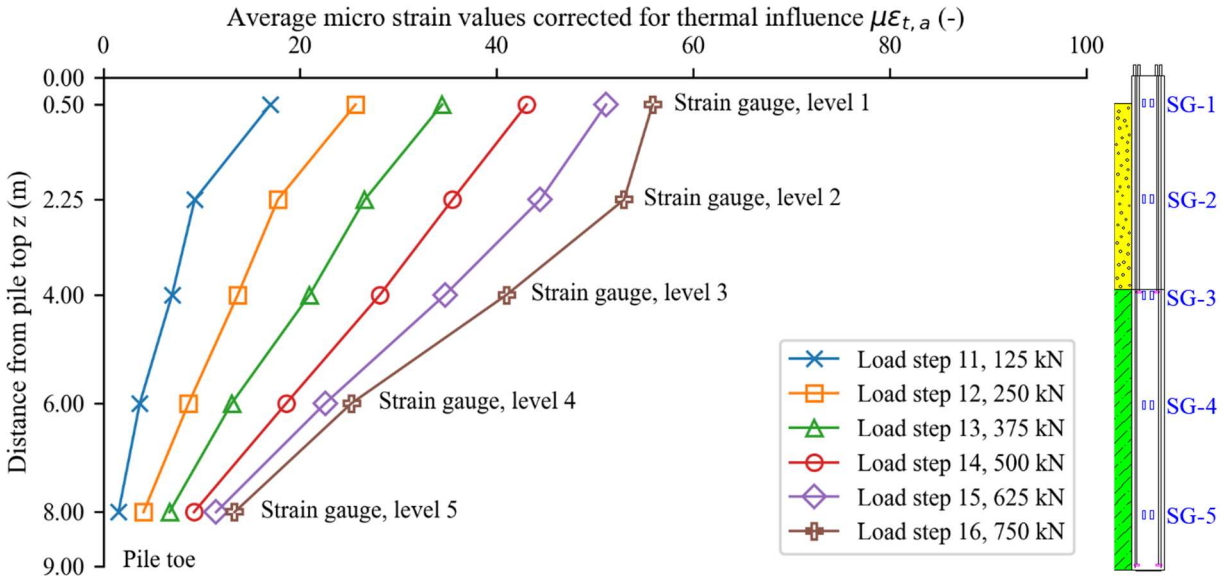

Figure 76: Strain development along the length of test pile 7 in load phase 2.

Test pile 1 demonstrates a similar trend to test pile 7 but with a few notable exceptions:

Overall, the measured strains appear to be higher in comparison to any other test pile, regardless of the selected test method. Specifically, at strain gauge level 1, the strains reach approximately 91 $\mu\varepsilon$, indicating significantly higher values.

Data obtained from strain gauge level 3 is based on estimation due to a partially defective strain gauge. To obtain reliable data fragments, the available data from strain gauge level 1 is reduced to 49% and compared to the data from the defective strain gauge at level 3. This approach allows for selecting the most reliable data. Notably, data from maintained load steps 11-15 and 18 exhibit acceptable consistency, while load steps 16 and 17 are interpolated, and load step 19 is extrapolated. This roughly corresponds to the second load phase, and all remaining data from strain gauge level 3 is discarded.

Moreover, temperature correction for strain gauge level 5 (5A and 5B) was conducted using only the temperature data from 5B, as data loss occurred from 5A. Since the strain gauges at level 5 are located at a depth of 7.5 m below ground level where the temperature remains relatively constant and consistent on both sides of the pile, it is evaluated that this loss of data has no significant impact.

Constant rate of uplift (CRU) test

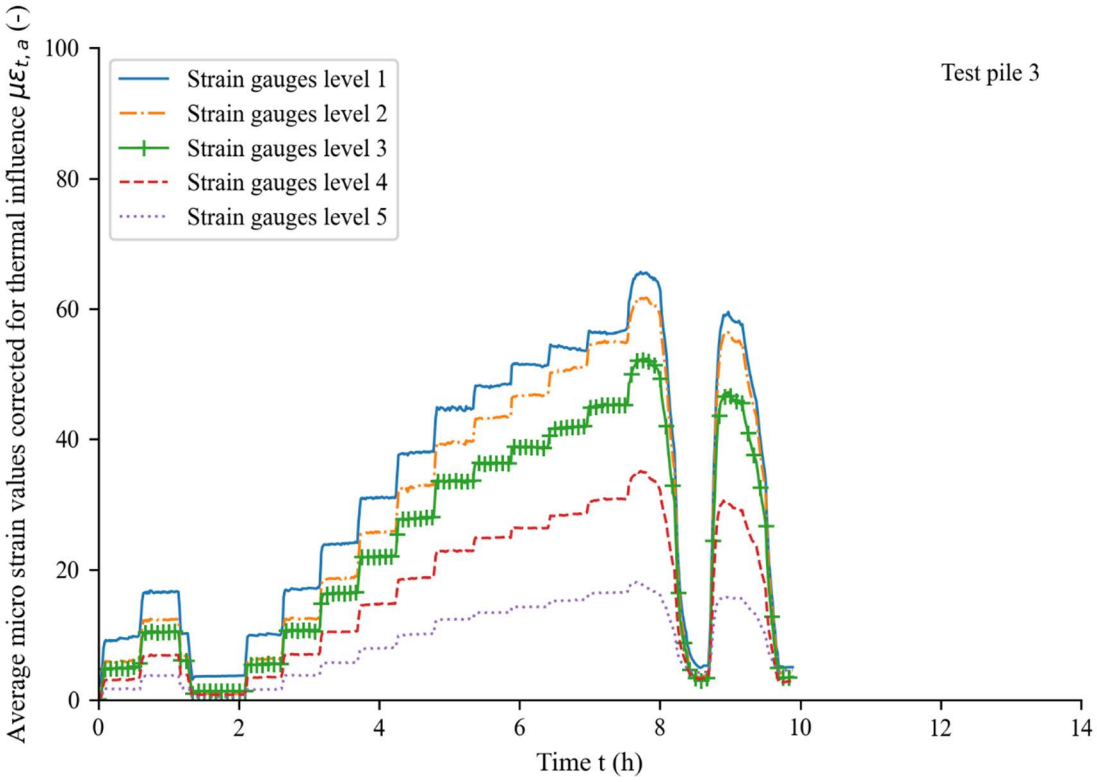

Figure 77: Average values of measured strains corrected for thermal influence for test pile 3.

The internal strain profiles for test piles 2-6 and 8 confirm that all strains exhibit tensile loading, as indicated by the positive values of strain. Additionally, the strains are highest at the upper strain gauge level (strain gauge level 1) and decrease progressively as the measurements move further down the length of the test piles. This observation supports the understanding that the test piles experience tension. Figure 77 depicts the time-strain curves for test pile 3, while Figure 78 and Figure 79 illustrate the strain development along the length of test pile 3 during load phases 1 and 2, respectively. The

time-strain curves, and the strain development along the length of test pile 2,4-6 and 8, can be found in Appendix H.3 and Appendix H.4, respectively.

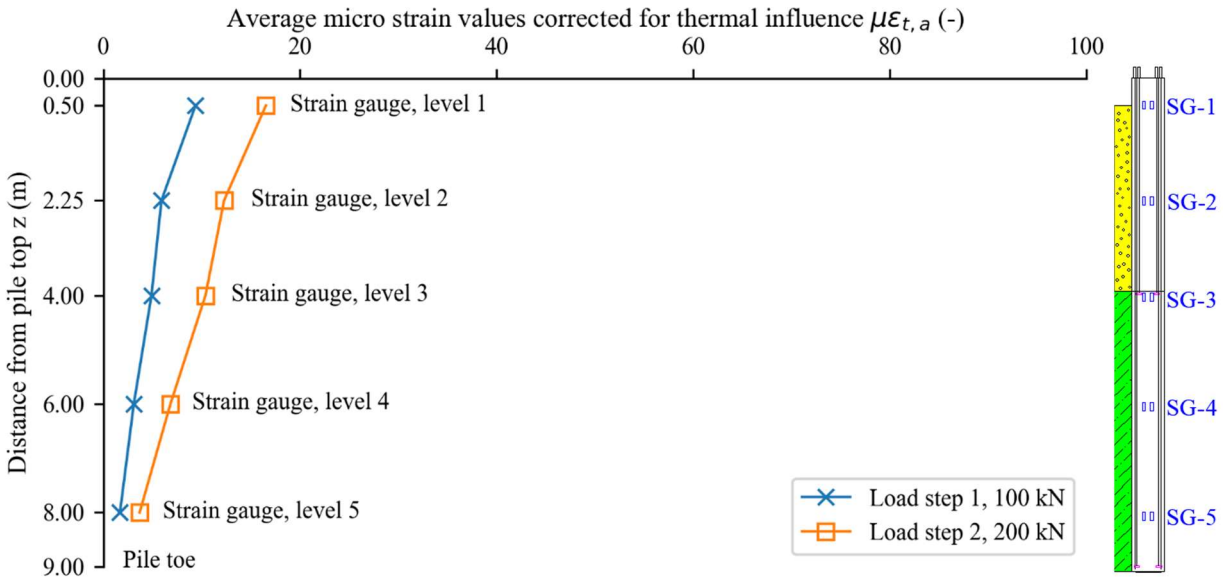

Figure 78: Strain development along the length of test pile 3 in load phase 1.

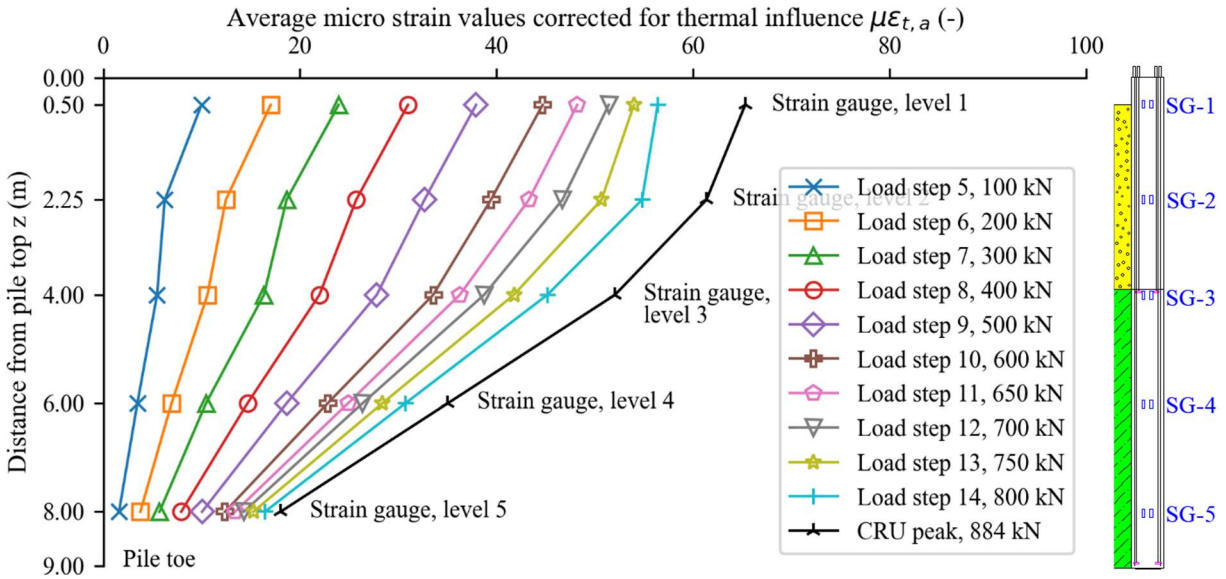

Figure 79: Strain development along the length of test pile 3 in load phase 2.

Test piles 2, 4-6, and 8 exhibit a development pattern similar to test pile 3, but with a few exceptions:

In the CRU portion of the static pile loading test, for test piles 2, 5, and 8, the strains at strain gauge level 1 either become equal to or slightly smaller compared to strain gauge level 2. However, for test piles 4 and 6, the strains at strain gauge level 1 become significantly higher than those at strain gauge level 2 as the test approaches failure.

For test pile 5, only data from after approximately 1 hour and 42 minutes, as stated in Appendix E.1, was considered for load step 13 (750 kN). This was due to data loss experienced during that period.

As for test pile 6, the strains from strain gauge 5A were adjusted to zero based on the measurements from strain gauge 5B. This adjustment was necessary to correct for an erroneous offset in the strain gauge measurements.

6.3.2 Determination of axial pile stiffness

If the test piles were free-standing columns, the slope of the load-strain curve would indicate the axial stiffness of the piles. However, in the case of bored piles, the axial load does not remain constant with depth but diminishes in proportion to the shaft resistance along the length of the piles. To determine the axial stiffness of the test piles from the test records, the load-strain curves, as well as the tangent axial stiffness and secant axial stiffness in relation to strain, are analysed using the methods described in section 5.5 and clarified below.

The strain gauge level situated at ground level (strain gauge level 1) is not affected by the shaft resistance, allowing the slope of the load-strain curve to represent the axial stiffness of the test pile's cross-section, assuming the applied load is fully transferred from the GEWI bars to the pile at the location of the strain gauge. Therefore, the axial stiffness of the test piles can be determined using either the tangent stiffness method or the direct secant method.

For strain gauges located further down the test piles, the initial load increments are reduced by the shaft resistance above the strain gauge's position. As a result, it is not possible to determine the true axial stiffness of the test piles using these strains. The axial stiffness of the test piles appears falsely higher, making it unsuitable to apply the direct secant method for strain gauges further down the test piles.

However, the tangent stiffness method can still be employed. Initially, the tangent axial stiffness will be greater than the true axial stiffness. However, as the shaft resistance mobilizes along the length of the test piles, the strain increments become larger, causing the tangent axial stiffness to decrease. When all the shaft resistance above a strain gauge level is mobilised, the tangent axial stiffness determined represents the true axial stiffness of the test piles. It is important to note that the tangent stiffness method can only be used for strain gauge readings affected by shaft resistance if the shaft resistance is in a plastic state, as explained in Fellenius (2023).

Figure 80 and Figure 81 display the applied load-strain curves for test piles 1-8. The axial pile stiffness can be determined by calculating the slope of the applied load-strain curves using either the tangent stiffness method or the direct secant method.

Maintained load (ML) test

For test pile 1, the applied load-strain curves from strain gauge level 3 exhibit a linear behaviour during load steps 15-19, where the applied load increases from approximately 625 kN. However, it is important to note that this behaviour is falsely induced as a result of employing interpolation and extrapolation to determine the internal strain profiles, as described in section 6.3.1.

Furthermore, in the middle part of load step 19 (825 kN), the load and strain data are not included due to a minor power loss encountered after around 11 hours and 40 minutes. It should be noted that the power loss experienced earlier, between load step 4 and 5 after approximately 3 hours, is of no significance. For a comprehensive description of the deviations observed during the static pile loading test of pile 1, please refer to Appendix E.1.

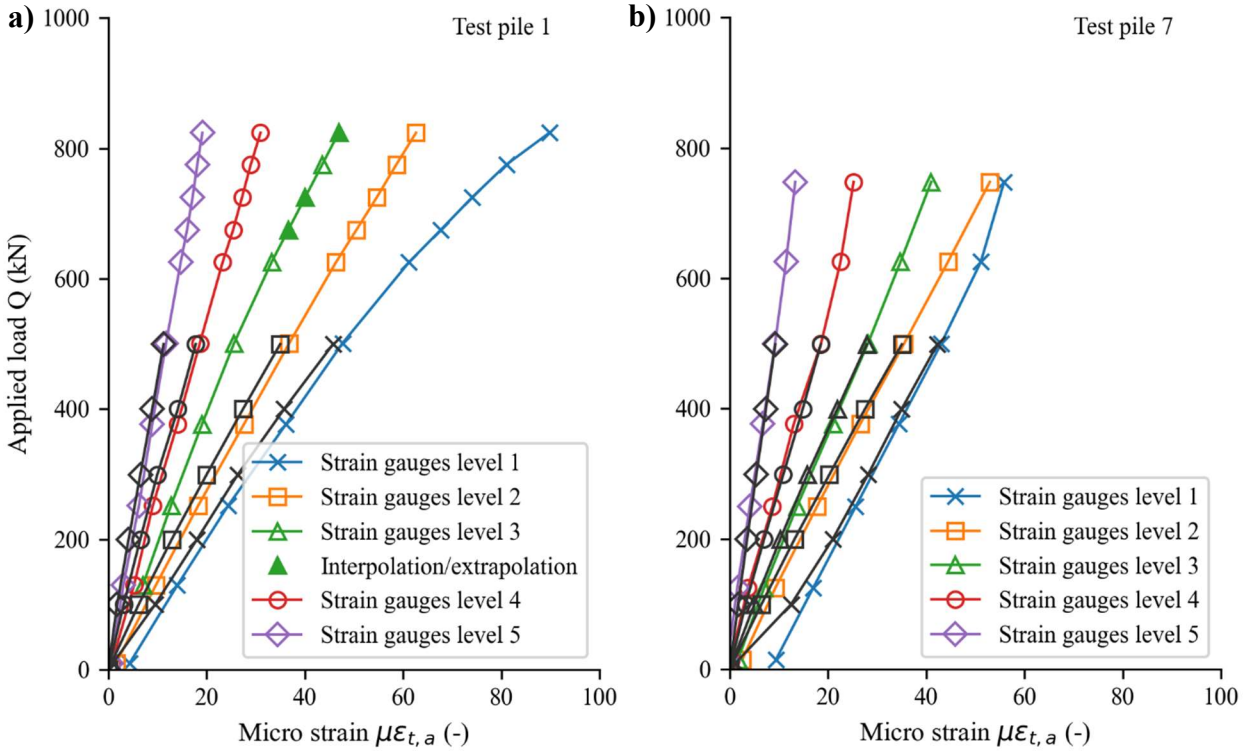

Figure 80: Average micro strain values corrected for thermal influence (mechanical strains) in relation to applied load for strain gauges level 1-5 in test pile (a) 1 and (b) 7. Load phase 1 is presented in black.

Constant rate of uplift (CRU) test

For test pile 3, the data from the middle part of load step 4, which occurred between the 1st and 2nd load phase, is not included due to a loss of load data lasting approximately 31 minutes. However, it is important to note that this loss only applies to the load values since the pile was already unloaded between the two load phases, making the strain values to be considered reliable. For a detailed description of the deviations observed during the static pile loading test of pile 3, please refer to Appendix E.1.

In the case of test piles 2, 3, 5, 7, and 8, the applied load-strain curves for the two uppermost strain gauge levels (strain gauge level 1 located at ground level and strain gauge level 2 located 1.75 m below ground) exhibit an immediate linear and parallel relationship. This is expected for the uppermost strain gauge at ground level, as it is not influenced by shaft resistance. The close agreement between strain gauge level 1 and 2 (parallel load-strain curves) suggests that only minor shaft resistance is mobilised within the upper sand fill.

However, the applied load-strain curve for strain gauge level 1 indicates a lower pile stiffness initially, between the zero reference and the first load step in load phase 1. This can possibly be attributed to the test piles' limited ability to evenly distribute the applied load across the cross-section initially, as the load is transferred through two GEWI PLUS bars, as noted in section 4.2.

Furthermore, an unexpected increase in the applied load-strain curve for strain gauge level 1 is observed at approximately 600 kN, indicating a false rise in pile stiffness. This can be attributed to the test piles' ability (or lack thereof) to effectively transfer the applied load from the two GEWI PLUS bars to the uppermost strain gauge level, located 0.5 m below the pile top.

Under favourable conditions with good adhesion between the GEWI PLUS bars/reinforcement and concrete, the two GEWI PLUS bars can transfer approximately 1980 kN/m of load, while the eight Y32 mm length reinforcements have a capacity of approximately 1150 kN/m, as detailed in section 4.2 and Appendix D.1. In this case, the lower value determines the pile's capacity, amounting to approximately 1150 kN/m or 575 kN at strain gauge level 1. This consistency with the observed unexpected increase in the applied load-strain curves above supports this explanation.

The remaining portion of the applied load is transferred from the GEWI bars to the test piles below strain gauge level 1. For all the test piles, this transfer is fully completed before reaching strain gauge level 2.

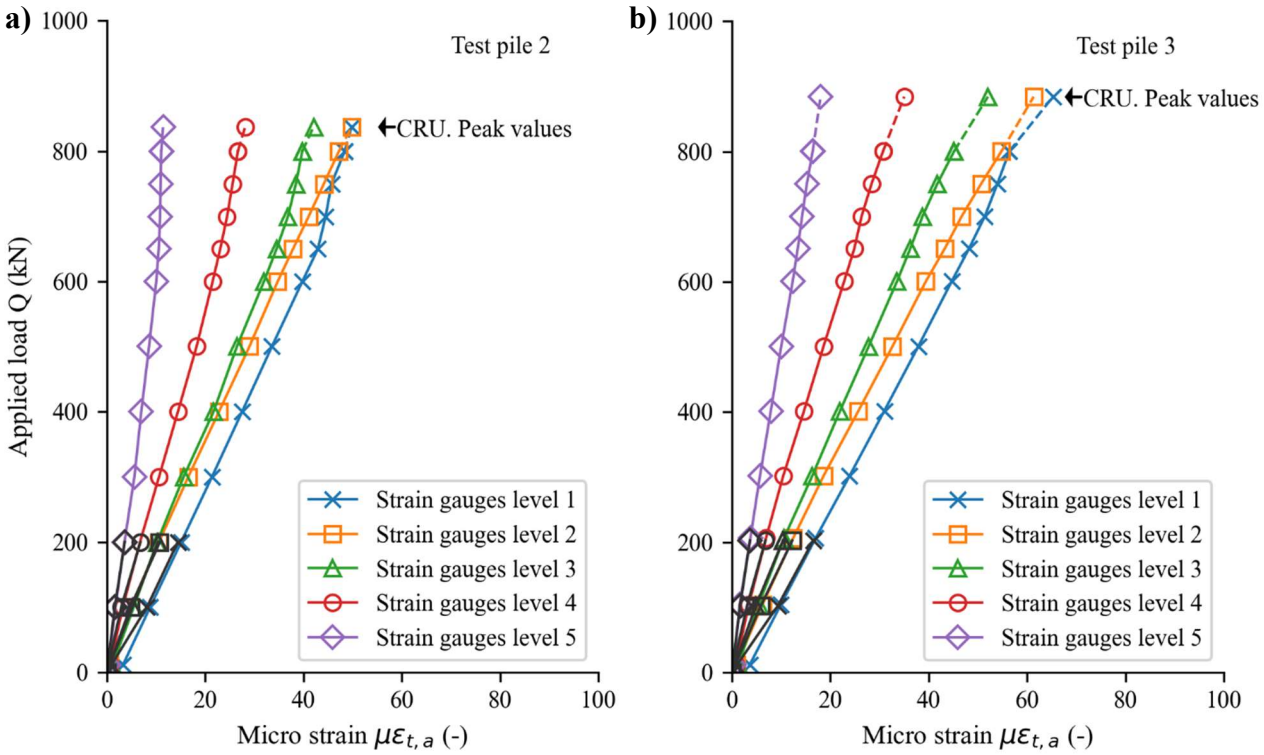

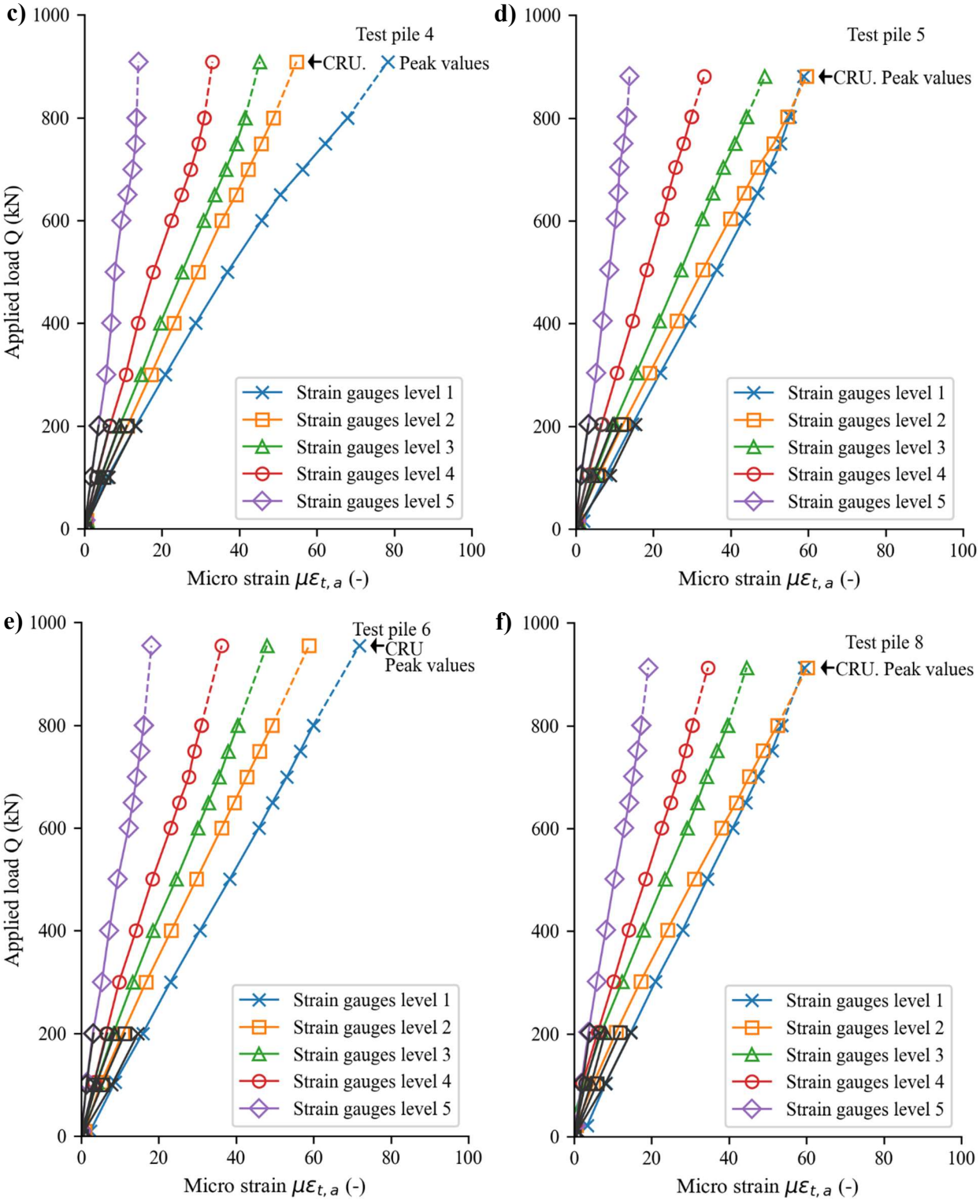

Figure 81: Average micro strain values corrected for thermal influence in relation to applied load for strain gauges level 1-5 in test pile (a) 2, (b) 3, (c) 4, (d) 5, (e) 6 and (f) 8. Load phase 1 is presented in black.

In the case of test piles 1 and 4, the applied load-strain curves for the uppermost strain gauge level (strain gauge level 1 located at ground level) display a softening behaviour as the load increases. This unexpected softening is surprising for the uppermost strain gauge at ground level since it is not influenced by shaft resistance. However, it is worth considering that strain gauge level 1 is positioned near the boundary of the respective test piles, typically at a distance of 0.5 m or less than one pile

diameter from the pile top. This proximity to the pile boundary introduces boundary effects, where plane surfaces need to remain plane in bending for the basic stress-strain relations to hold.

Additionally, the observed strain softening behaviour might be attributed to the creep phenomenon observed in the uppermost strain gauge level for test piles 1 and 4, as detailed in Appendix H.3. Creep effects are not supposed to be included when determining the axial pile stiffness and, therefore, should be excluded in this analysis.

Tangent stiffness method

If the applied load on the test piles is transferred gradually along the pile shaft by mobilizing the shaft resistance, it would be expected that the applied load-strain curves in Figure 80 and Figure 81 for the lower strain gauge levels (strain gauge level 3-5) would initially rise and then become linear and parallel with the applied load-strain curves for the uppermost strain gauges (strain gauge level 1 and 2) when the shaft resistance is fully mobilised above each strain gauge location.

However, this expected behaviour is not observed, and this can potentially be explained by the conservative design of the test piles to ensure that the applied tensile load does not exceed the axial structural strength of the piles, as described in section 4.2. As a result, the stiffness of the piles is significantly greater than the stiffness of the soil (approximately 5,000 - 10,000 times greater). Consequently, the shaft resistance is activated simultaneously along the entire length of the test piles rather than through gradual mobilization.

As a result, the tangent stiffness method cannot be applied to the lower strain gauges (strain gauge level 3-5) as the full mobilization of the shaft resistance does not occur until the failure of the static pile loading test. Therefore, the slope of the linear part of the applied load-strain curves for strain gauge level 1 and 2 represents the tangent axial stiffness

Maintained load (ML) test

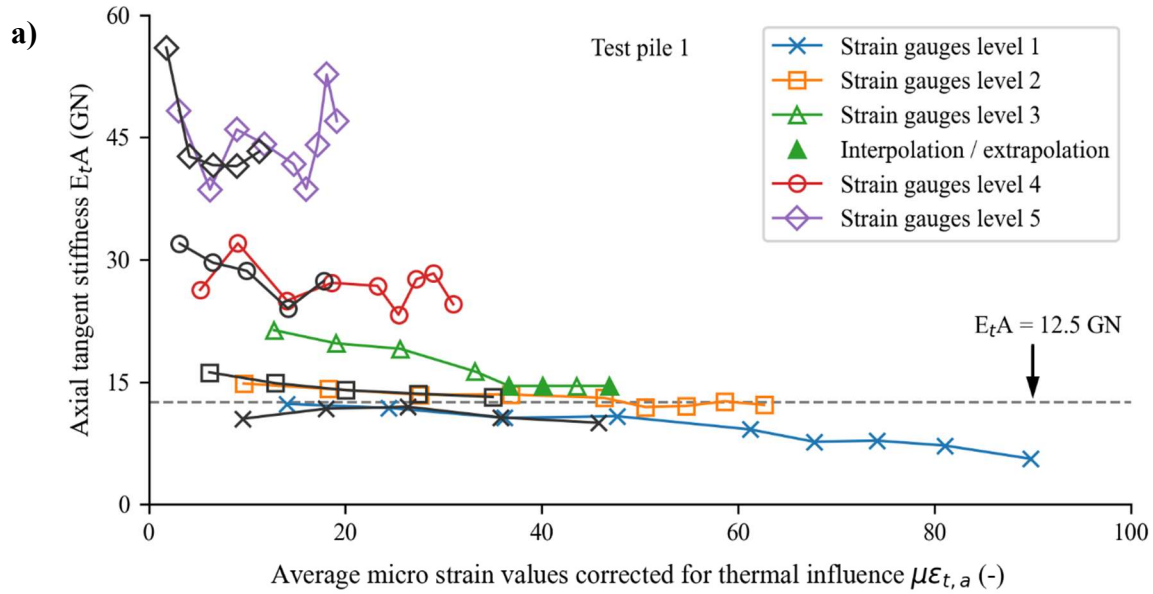

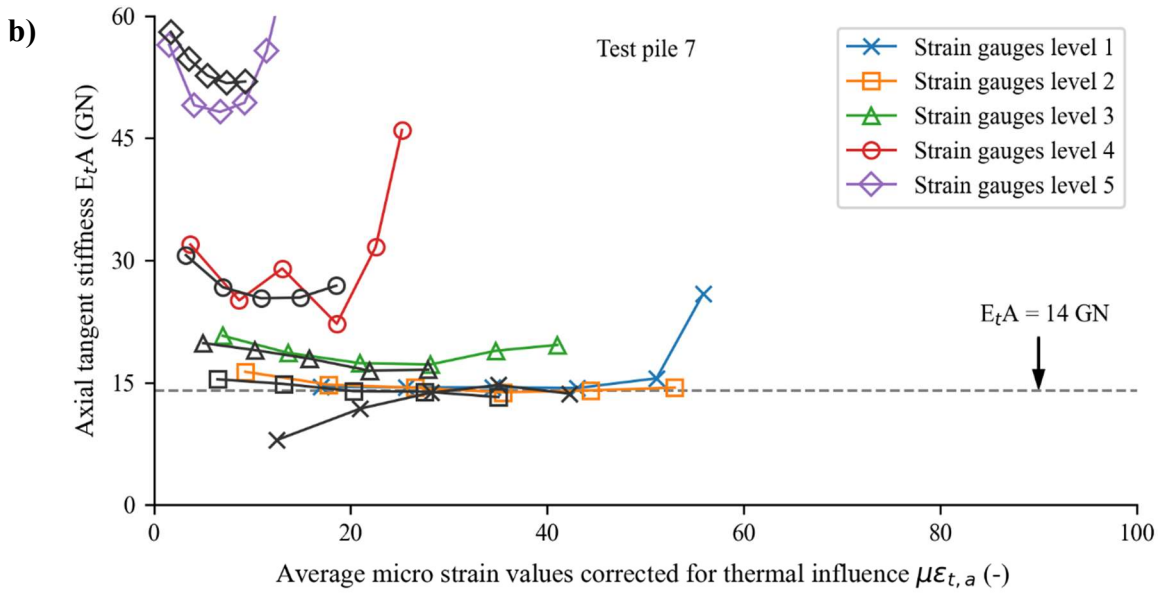

Figure 82: Axial stiffness determined by the tangent method for strain gauges level 1-5 in test pile (a) 1 and (b) 7. Load phase 1 is presented in black.

Constant rate of uplift (CRU) test

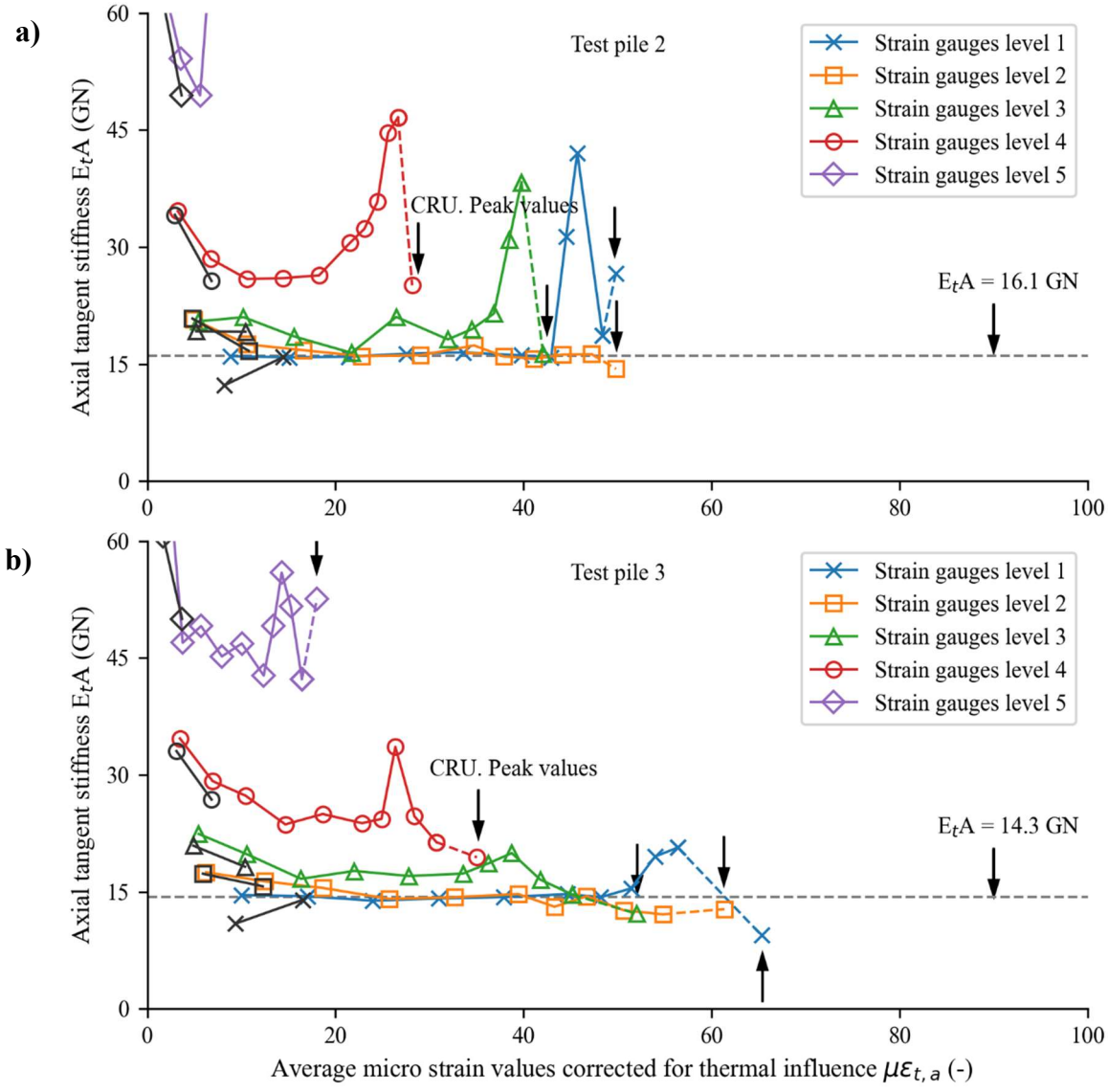

c)

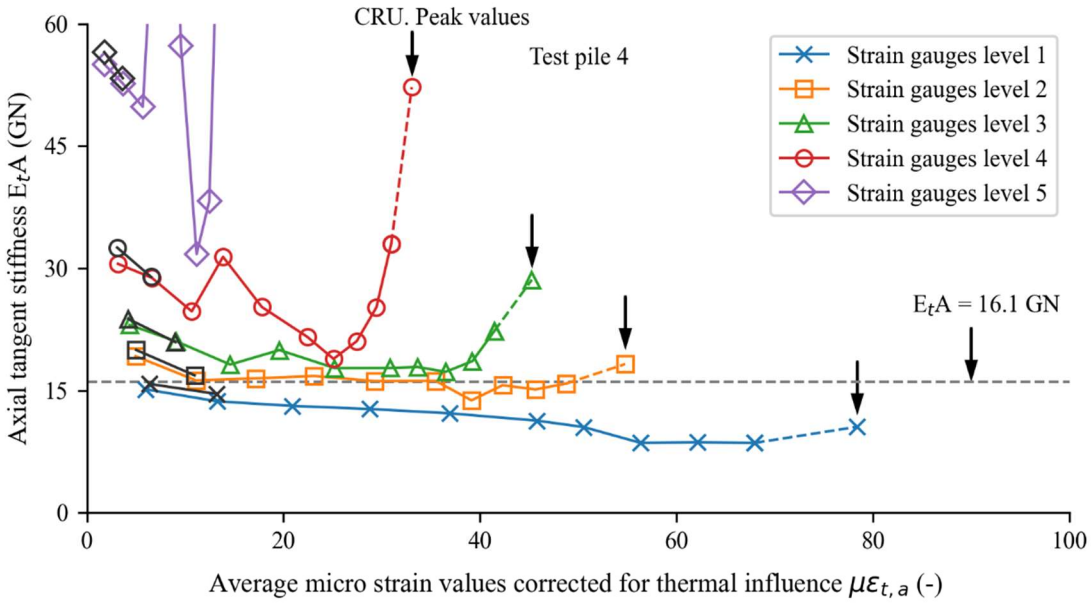
CRU. Peak values
Test pile 4
Strain gauges level 1
Strain gauges level 2
Strain gauges level 3
Strain gauges level 4
Strain gauges level 5
E_tA = 16.1 GN
Axial tangent stiffness E_tA (GN)
Average micro strain values corrected for thermal influence $\mu\varepsilon_{t,a}$ (-)

d)

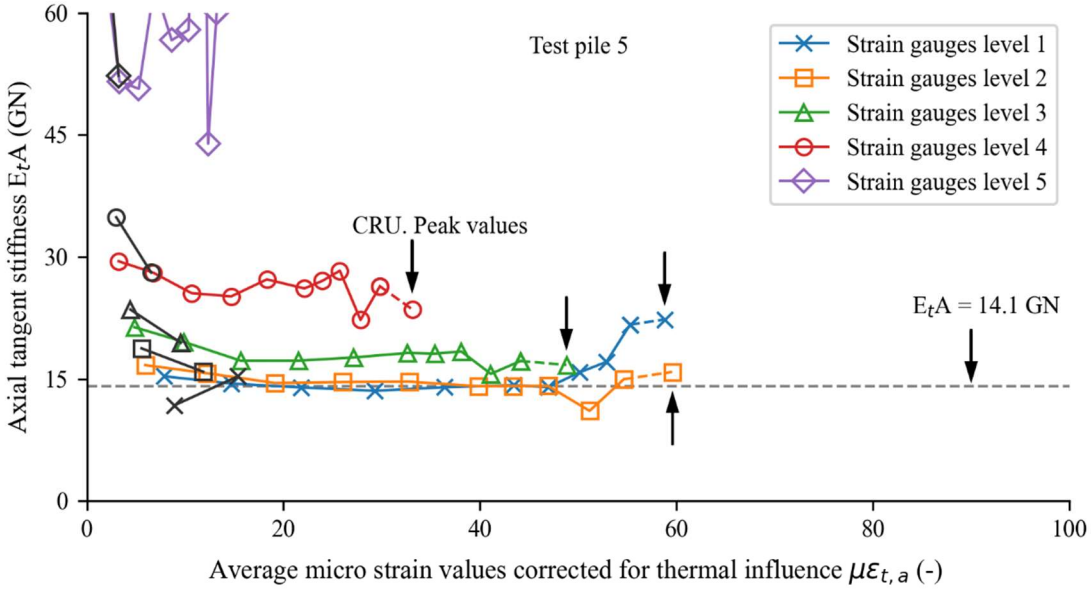
Test pile 5
Strain gauges level 1
Strain gauges level 2
Strain gauges level 3
Strain gauges level 4
Strain gauges level 5
CRU. Peak values
E_tA = 14.1 GN
Axial tangent stiffness E_tA (GN)
Average micro strain values corrected for thermal influence $\mu\varepsilon_{t,a}$ (-)

e)

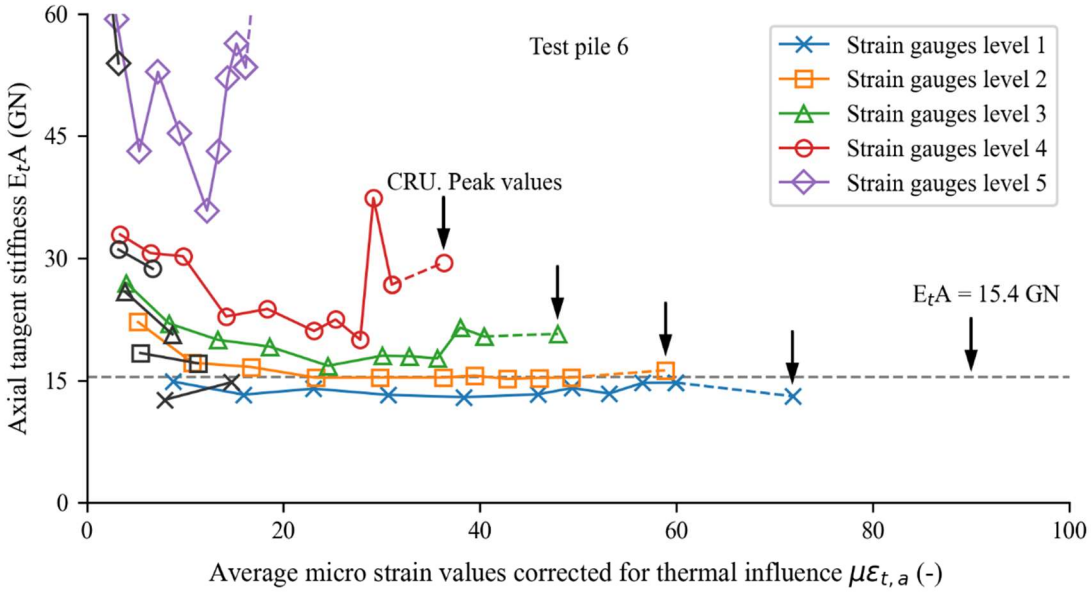
Test pile 6
Strain gauges level 1
Strain gauges level 2
Strain gauges level 3
Strain gauges level 4
Strain gauges level 5
CRU. Peak values
E_tA = 15.4 GN
Axial tangent stiffness E_tA (GN)
Average micro strain values corrected for thermal influence $\mu\varepsilon_{t,a}$ (-)

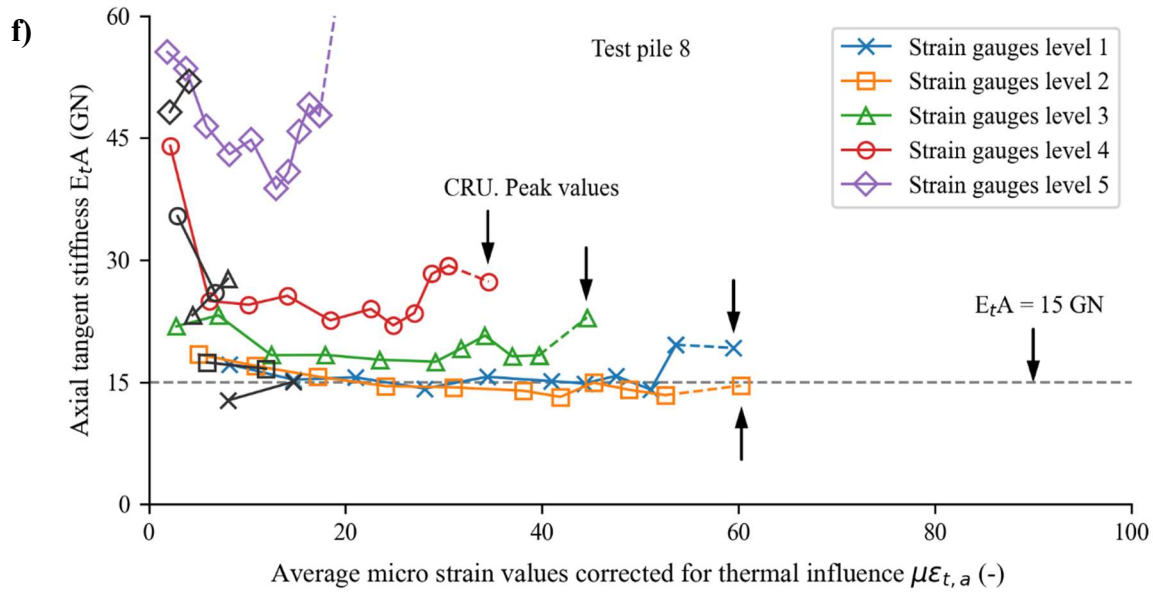

Figure 83: Axial stiffness determined by the tangent method for strain gauges level 1-5 in test piles (a) 2, (b) 3, (c) 4, (d) 5, (e) 6 and (f) 8. Load phase 1 is presented in black.

For test piles 2, 3, 5, 7, and 8, the axial stiffness values displayed in Figure 82 and Figure 83, determined through the tangent stiffness method, support the observations made from the corresponding applied load-strain curves in Figure 80 and Figure 81 for strain gauge level 1. These observations include a lower stiffness between the zero reference and the first load step during load phase 1, along with an unexpected increase suggesting a false increase in pile stiffness at around 600 kN.

Likewise, for test piles 1 and 4, the axial stiffness values presented in Figure 82 and Figure 83, determined using the tangent stiffness method, align with the observations made from the applied load-strain curves in Figure 80 and Figure 81 for strain gauge level 1. Specifically, these observations pertain to the softening behaviour observed as the load increases.

Under normal circumstances, it is expected that the tangent axial stiffness decreases linearly with increasing strain, as Young's modulus of concrete tends to decrease with applied load. However, as evident from the tangent axial stiffness-strain curves provided above, the tangent axial stiffness can be considered constant within the limited range of strain (0-60 $\mu\varepsilon$). As a result, the tangent axial stiffness and secant axial stiffness can be approximated as equal and used to estimate the axial pile stiffness, as outlined in Table 14.

Table 14: Axial pile stiffness determined by the tangent stiffness method.

	Test pile no.							
	TP1	TP2	TP3	TP4	TP5	TP6	TP7	TP8
Pile axial stiffness (GN)	12.5	16.1	14.3	16.1	14.1	15.4	14.0	15.0

The tangent stiffness method assumes a plastic response of the pile in relation to the surrounding soil, and the axial stiffness obtained from this method can be influenced by the strain-hardening or strain-softening behaviour of the soil, as explained in Fellenius (2023). However, as the axial tangent

stiffness is determined primarily based on strain gauge levels 1 and 2, which are minimally affected by shaft resistance, the significance is limited.

Additionally, it is important in the tangent stiffness method to have equal size load increments, equal load-holding increments, and no unloading-reloading cycles, as these factors can strongly impact the interpretation of the test records and, consequently, the axial stiffness determined using this method, as noted in Fellenius (2023). However, given that the test piles are expected to exhibit an elastic behaviour within the limited range of strain (0-60 $\mu\varepsilon$) and the determination of axial stiffness using the tangent stiffness method in Figure 80 and Figure 81 shows good correlation between the first and second load phases, it appears that these factors do not significantly affect the interpretation of the test records for the test piles at the Hinge test site.

Direct secant method

In addition to the requirements of equal size load increments, equal load-holding increments, and no unloading-reloading sequences as stated in the tangent stiffness method, the direct secant method also requires a correct zero reference for the load and essentially no shaft resistance between the hydraulic jack and the strain gauge levels, as described in Fellenius (2023).

For strain gauge level 1, there is no presence of shaft resistance between the hydraulic jack and the strain gauge because the strain gauge is situated at ground level. Similarly, for strain gauge level 2, there is minimal shaft resistance according to the applied load-strain curves presented in Figure 80 and Figure 81, as the surrounding soil has been replaced with poorly graded medium sand, as detailed in section 3.4.

However, the direct secant method cannot be applied to strain gauge levels 3-5 due to the significant presence of shaft resistance above these strain gauge levels, which obstructs the accurate determination of the secant axial stiffness using this method.

Regarding the correct zero reference, strain gauge level 1 appears to be influenced by the test piles' limited ability to evenly distribute the applied load across the cross-section initially due to the load being transferred through two GEWI PLUS bars, as explained in section 4.2. This effect is observed in Figure 80 and Figure 81, where the applied load-strain curves for strain gauge level 1 during load phase 1 start with lower values in the first load step and then increase to become linear and parallel with the applied load-strain curves for strain gauge level 2. Consequently, this can falsely lower the determined axial secant stiffness for strain gauge level 1.

However, for all test piles, it is evident that using the direct secant method for strain gauge level 2 to determine the axial stiffness yields results that align with those obtained from the tangent stiffness method. The direct secant method provide a smoother axial stiffness-strain curve compared to the tangent stiffness method, but this is expected due to the nature of a secant compared to a tangent.

An example of the axial secant stiffness-strain curves is shown in Figure 84 specifically for test pile 7 and are presented in Appendix H.5 for all test piles at the Hinge test site.

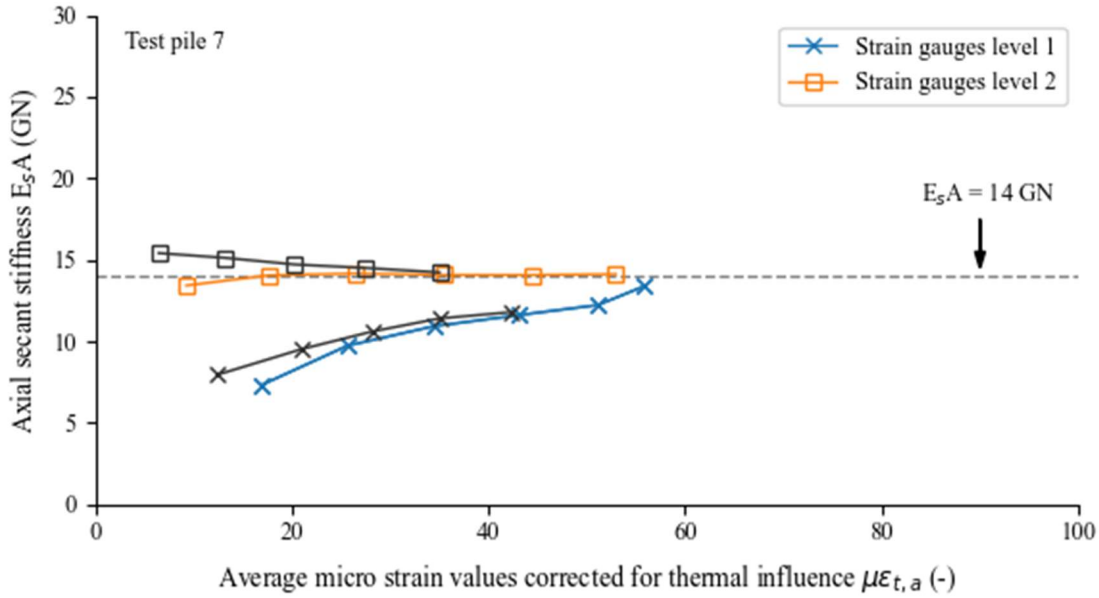

Figure 84: Axial stiffness determined by direct secant method for strain gauges level 1-2 in test pile 7. Load phase 1 is presented in black.

6.3.3 Load distribution in test piles

The load distribution is determined by converting the measured strain according to section 5.5. This is done using the previously determined axial pile stiffness from section 6.3.2, assuming it is valid for the upper 6.5 m of the test piles. To account for the reduced pile stiffness at the bottom 2.5 m of the test piles (due to the lack of GEWI bars), the axial pile stiffness at strain gauge level 5 is reduced to 91% of the determined axial pile stiffness in section 6.3.2, as indicated in the theoretical calculations in section 5.5.1. The reduced axial pile stiffness is observable in the data from the fibre optic strain cables (FOSC), as presented in section 7.4.4.

Additionally, it should be noted that the axial pile stiffness can vary throughout the length of the test piles. This is due to variations in pressure during the curing process as well as different external environmental factors such as temperature, soil conditions, and groundwater conditions. A slower curing process usually leads to increased strength and therefore greater stiffness. However, please note that providing a detailed analysis of the axial pile stiffness along the entire length of the test piles falls outside the scope of this PhD project.

For the strain gauges located at the uppermost level (strain gauge level 1), the applied load is used directly. This is because the measured strains in this region are influenced by several factors: the inability of the test piles to distribute the load evenly across the cross-section initially, the limited capacity of the test piles to transfer loads above approximately 575kN from the two GEWI PLUS bars to the uppermost strain gauge level (which is located 0.5 m below the pile top), and the boundary effects caused by the proximity of strain gauge level 1 to the pile top. For the test piles in Hinge, it is

not possible to absorb the load anywhere between the pile top and strain gauge level 1, so the applied load can be considered directly.

Figure 85 and Figure 86 depict the back-calculated axial force, F, along the length of test piles 1-8 for load phase 1 and 2, respectively.

Maintained load (ML) test

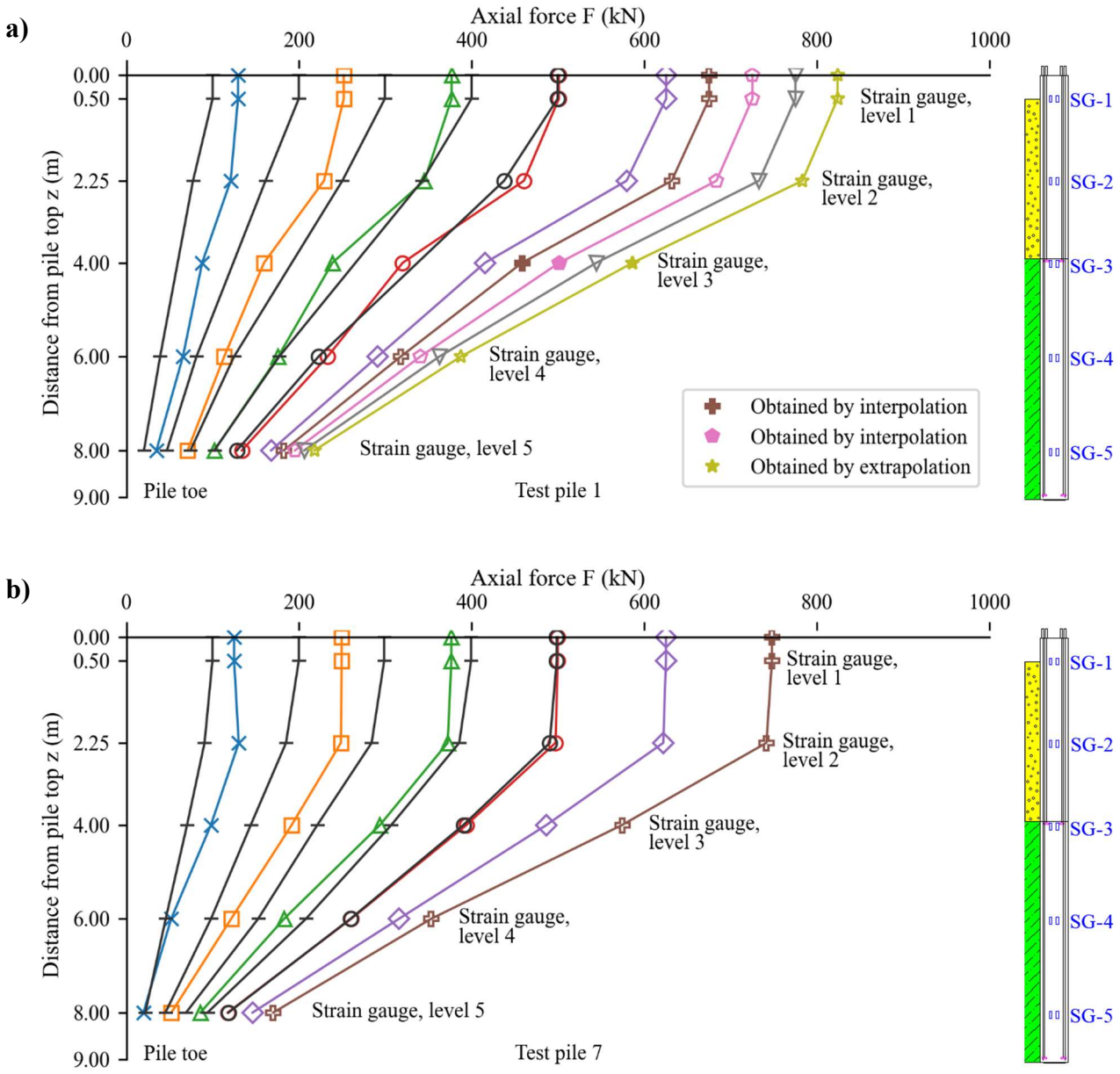

Figure 85: Back calculated axial force along the length of test pile (a) 1 and (b) 7. Load phase 1 is presented in black.

In the case of test piles 1 and 7 (ML tests), there is a discrepancy between the load steps used in the first load phase and the initial load steps in the second load phase. This difference results in a natural variation in the back-calculated axial force curves depicted in Figure 85. During load phase 1, the load steps are set at 100, 200, 300, 400, and 500 kN. While, for load phase 2, the initial load steps are adjusted to 125, 250, 375, and 500 kN.

Observing test pile 1 and 7, the load distribution lines between strain gauge level 2 and 5 exhibit an approximately linear trend and gradually rotate as the load increases. This suggests that the mobilised unit shaft resistance remains relatively constant with depth and is activated simultaneously along the pile below strain gauge level 2.

Constant rate of uplift (CRU) test

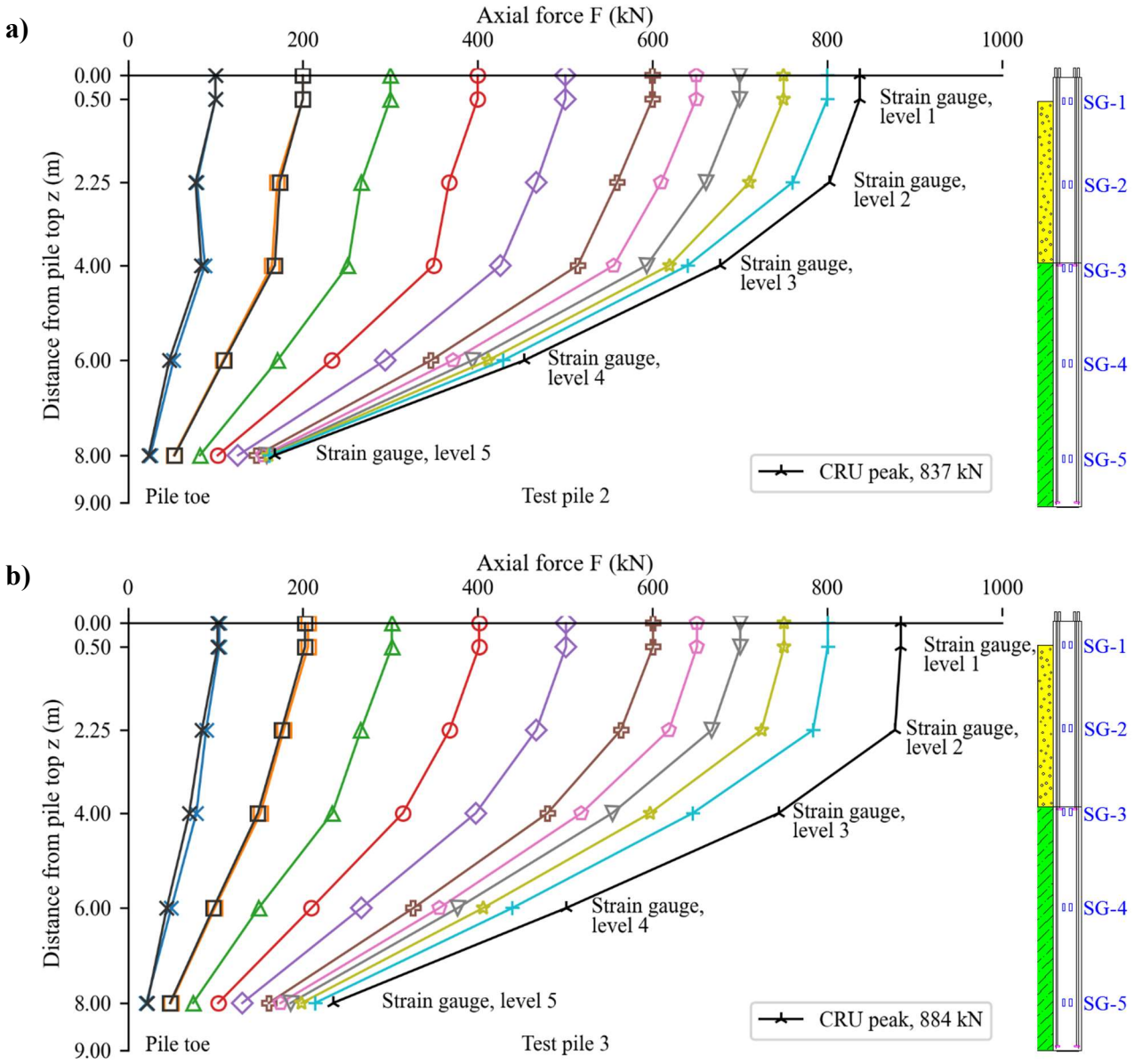

c)

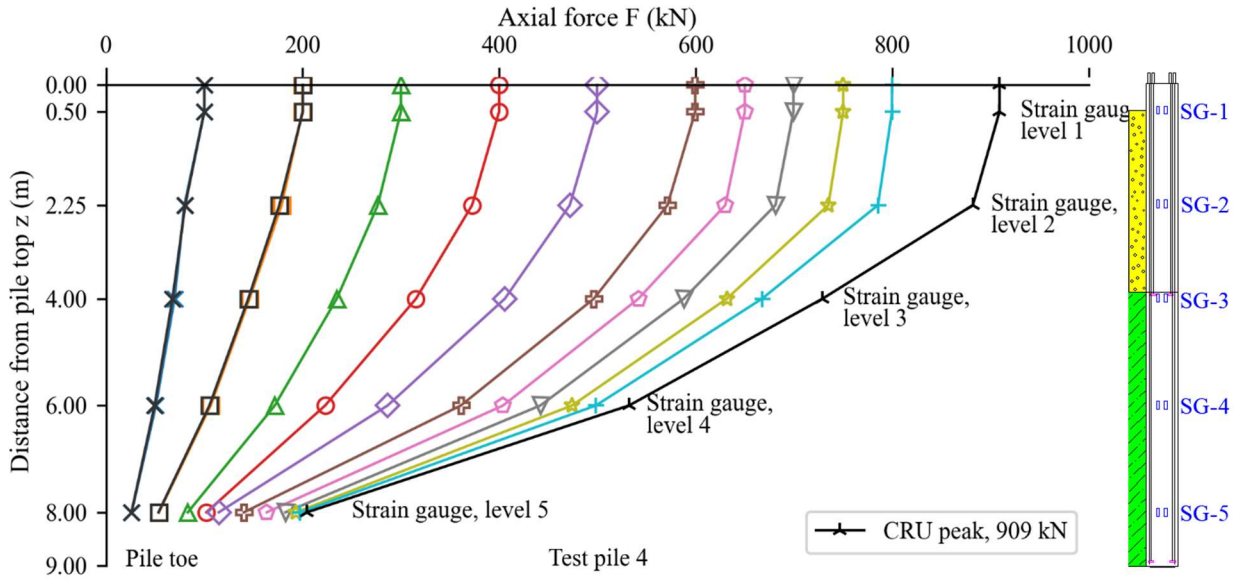
Axial force F (kN)
0
200
400
600
800
1000
Distance from pile top z (m)
0.00
0.50
2.25
4.00
6.00
8.00
9.00
Strain gauge, level 1
Strain gauge, level 2
Strain gauge, level 3
Strain gauge, level 4
Strain gauge, level 5
Pile toe
Test pile 4
CRU peak, 909 kN
SG-1
SG-2
SG-3
SG-4
SG-5

d)

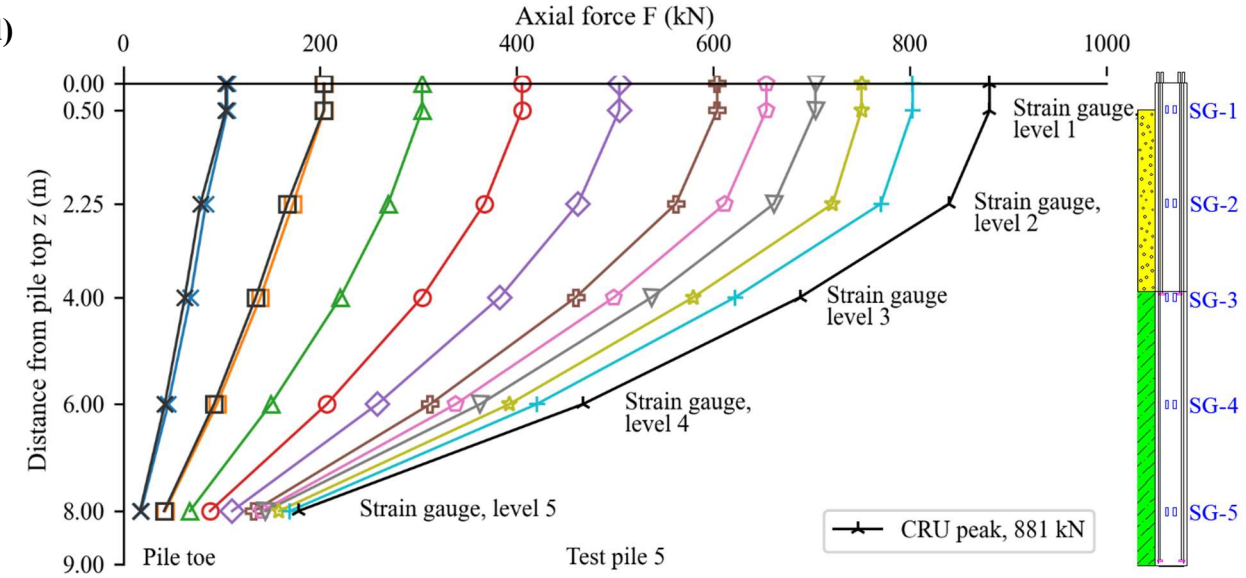
Axial force F (kN)
0
200
400
600
800
1000
Distance from pile top z (m)
0.00
0.50
2.25
4.00
6.00
8.00
9.00
Strain gauge, level 1
Strain gauge, level 2
Strain gauge level 3
Strain gauge, level 4
Strain gauge, level 5
Pile toe
Test pile 5
CRU peak, 881 kN
SG-1
SG-2
SG-3
SG-4
SG-5

e)

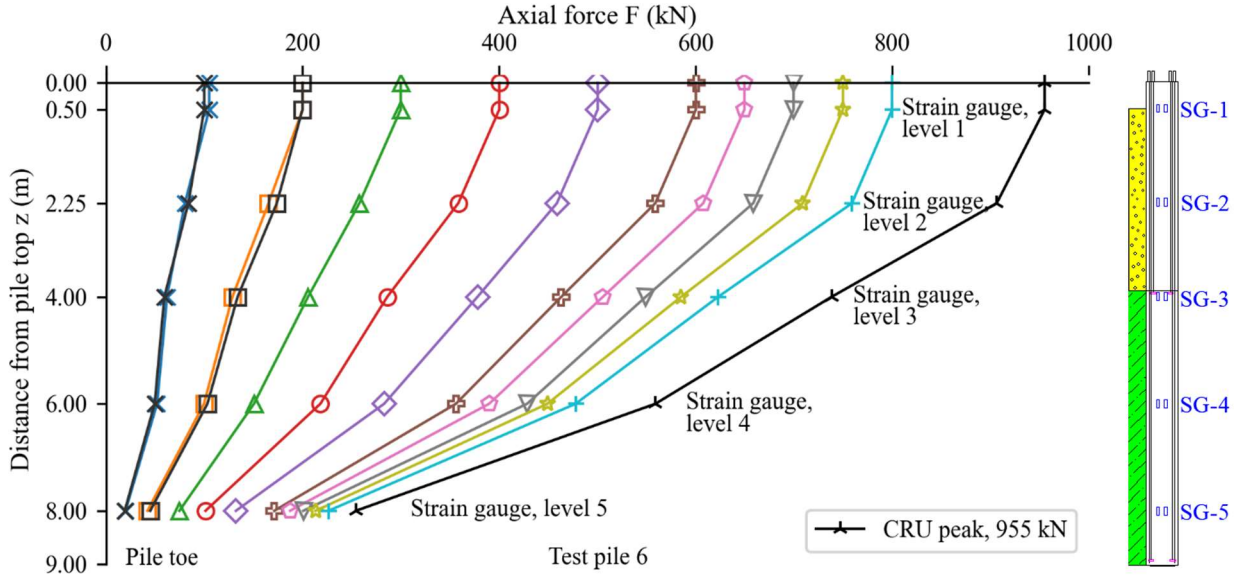
Axial force F (kN)
0
200
400
600
800
1000
Distance from pile top z (m)
0.00
0.50
2.25
4.00
6.00
8.00
9.00
Strain gauge, level 1
Strain gauge level 2
Strain gauge, level 3
Strain gauge, level 4
Strain gauge, level 5
Pile toe
Test pile 6
CRU peak, 955 kN
SG-1
SG-2
SG-3
SG-4
SG-5

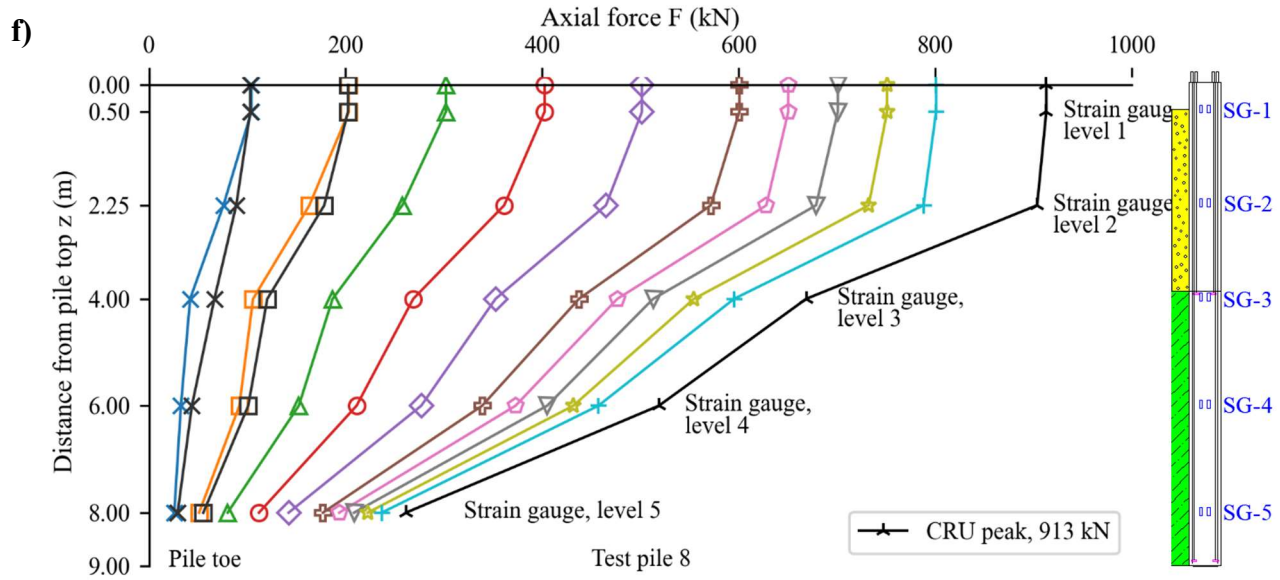

Figure 86: Back calculated axial force along the length of test piles (a) 2, (b) 3, (c) 4, (d) 5, (e) 6 and (f) 8. Load phase 1 is presented in black.

In the case of test piles 1-2 and 4-6, the load distribution lines between strain gauge level 1 and 2 exhibit a steep slope. This suggests a relatively low shaft resistance in the upper sand layer. Furthermore, for test piles 3, 7, and 8, the load distribution lines in the same region are practically vertical. This indicates a lack of shaft resistance in the upper sand layer.

For test piles 2 and 5, the load distribution lines between strain gauge level 2 and 5 gradually rotate as the load increases and rise from the pile base towards the pile top. This implies that the mobilised unit shaft resistance is activated simultaneously along the pile below strain gauge level 2. Furthermore, the shaft resistance is highest at the bottom of the pile in the lower clay layer (between strain gauge level 4 and 5) and gradually decreases towards the lower sand layer (between strain gauge level 2 and 3).

When considering test pile 3, the load distribution lines between strain gauge level 3 and 5 show an approximately linear pattern and gradually rotate as the load increases. Additionally, the slope of these load distribution lines becomes steeper above strain gauge level 3, indicating a lower shaft resistance in the lower sand layer (between strain gauge level 2 and 3).

As for test piles 4 and 6, the load distribution lines between strain gauge level 2 and 4 exhibit a relatively linear trend and gradually rotate with increasing load. However, the slope of these load distribution lines decreases below strain gauge level 4, indicating a higher shaft resistance in the lower clay layer (between strain gauge level 4 and 5).

In the case of test pile 8, the load distribution lines between strain gauge level 2 and 5 display an approximately linear trend and gradually rotate with increasing load. However, there is interference in the straight portion of the lines between strain gauge level 3 and 4, indicating a lower shaft resistance in the upper clay layer.

It is worth noting that for all test piles (test piles 1-8), if the load distribution lines are extended from strain gauge level 5 to the pile base, assuming the same slope as observed between strain gauge level 4 and 5, the lines do not reach either zero or the maximum possible suction force ($A_b \cdot 1\ atm \sim 30kN$) during failure at the pile base. This would be expected for a static pile loading test in tension and the deviation suggests that residual stresses have an impact on the behaviour of the test piles.

6.3.4 Unit shaft resistance

The observed mobilised unit shaft resistance, $r_{s,o}$, for each strain gauge level is obtained using the methodology described in section 5.5. These values are then plotted against the vertical displacement between the pile and soil, $\delta_{pile,soil}$, using data points from the virgin load curves. The vertical displacement between the pile and soil is determined by subtracting the elastic lengthening, $\delta_{pile,e}$, between two adjacent strain gauges, as outlined in section 5.6, from the corresponding vertical displacement at the pile top, δ, for each of the test piles.

In order to fit the obtained data by back-analysis, the four strain softening load transfer functions mentioned in section 2.5.4 are utilized. The Hansen 80% function and the Zhang function was originally derived based on pile loading test in sand. The Zhang function (Zhang and Zhang, 2012) is selected for the sand layers, as this provide more flexibility to accurately represent the shape of the curve before and after the peak value, than the Hansen 80 % function.

On the other hand, the Vijayvergiya function (Vijayvergiya, 1977), originally derived from pile loading tests conducted in clay, is chosen for the clay layers. This function offers a high level of versatility as it can model both strain softening and apparent strain hardening behaviour. This allows for greater flexibility in fitting the shape of the curve before and after the peak value, providing more accurate representation for the clay layers. The mobilised unit shaft resistance, r_s, is illustrated in Figure 87 and Figure 88.

Maintained load (ML) test

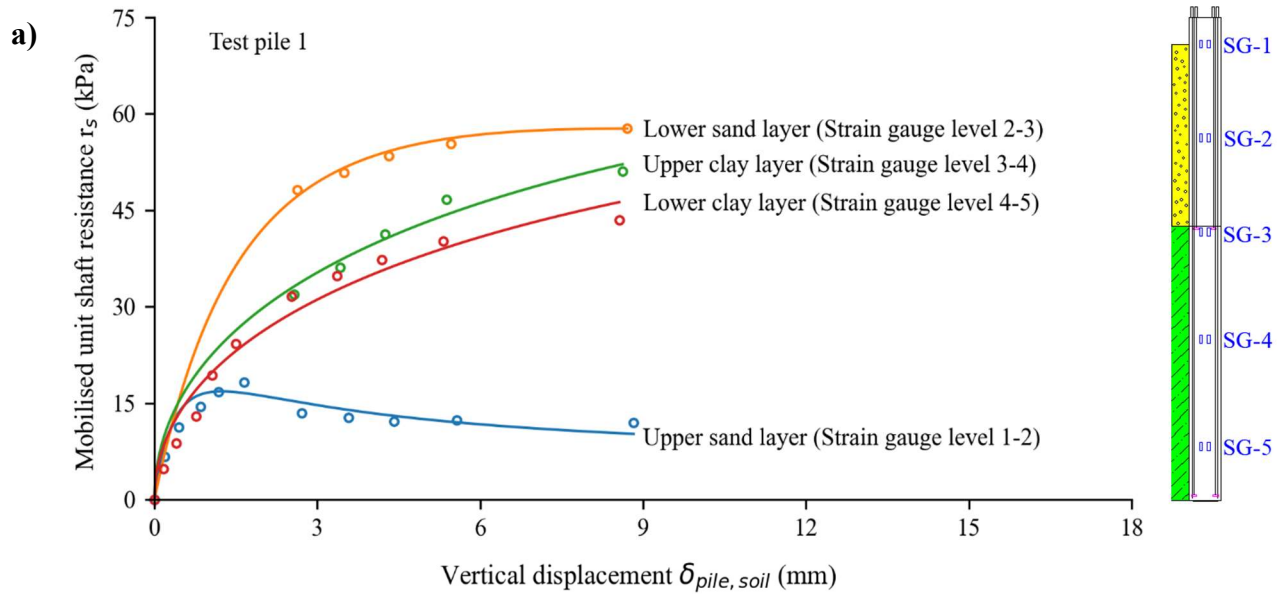

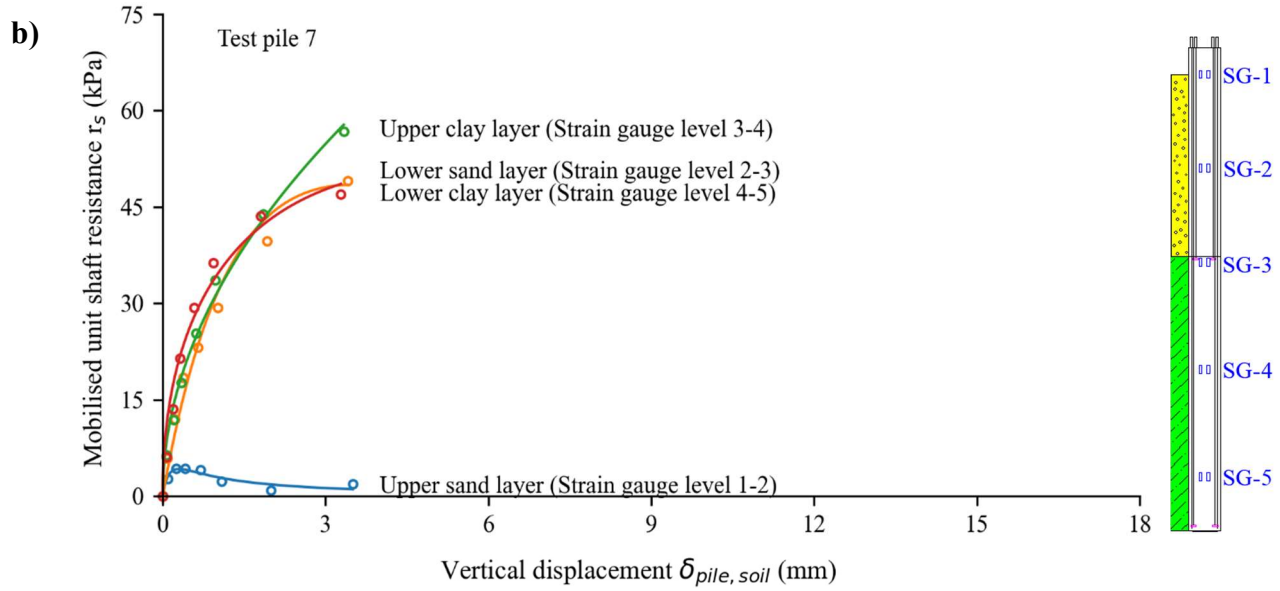

Figure 87: Mobilised unit shaft resistance based on the virgin load curves for test pile (a) 1 and (b) 7.

Constant rate of uplift (CRU) test

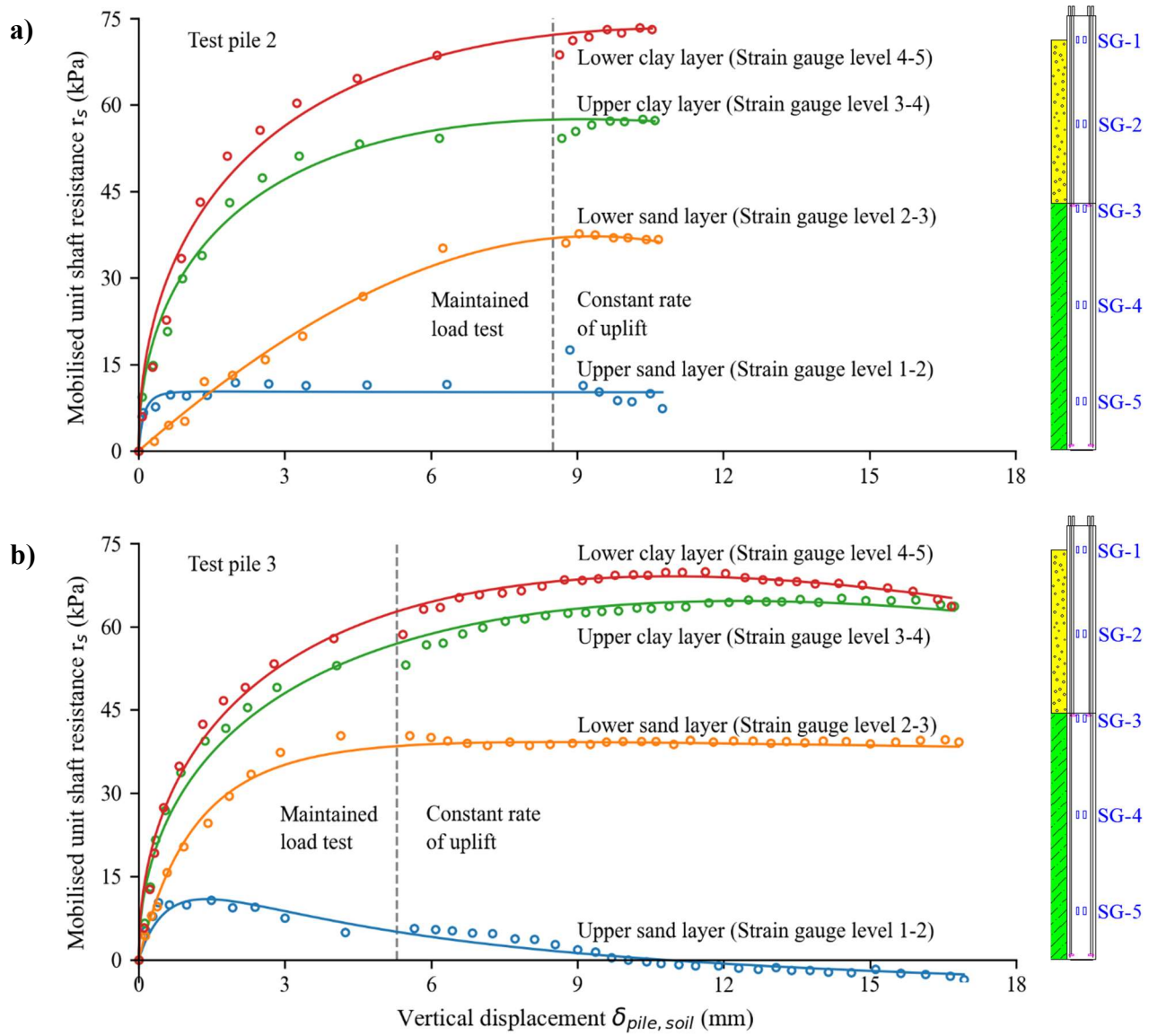

c)

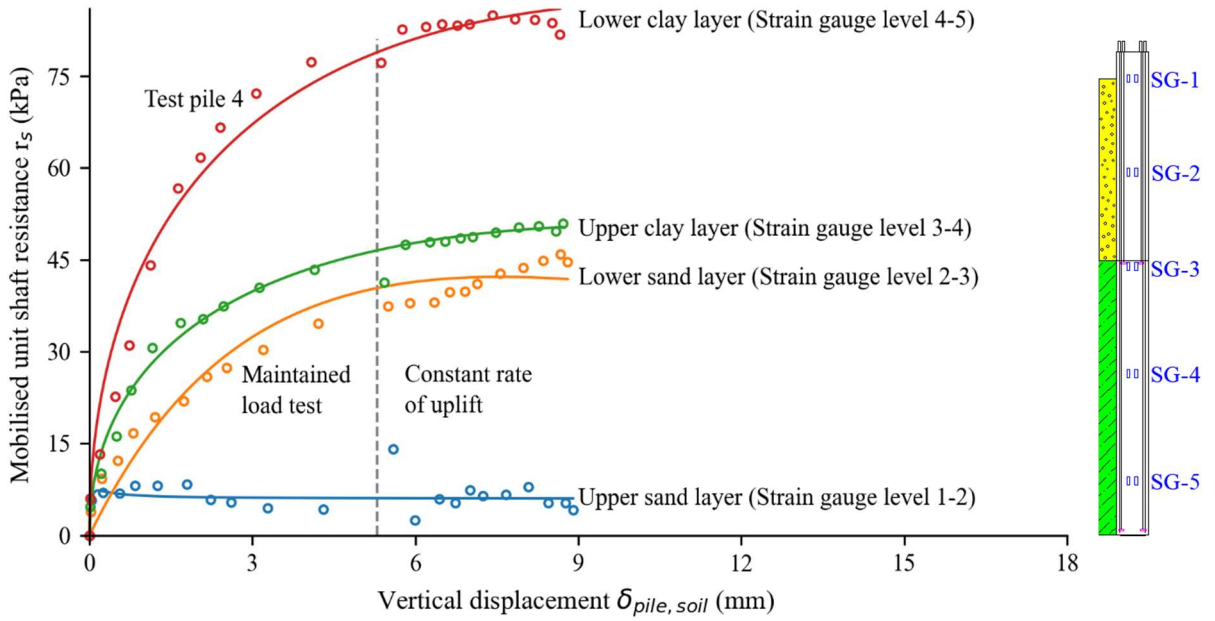
Test pile 4
Lower clay layer (Strain gauge level 4-5)
Upper clay layer (Strain gauge level 3-4)
Lower sand layer (Strain gauge level 2-3)
Upper sand layer (Strain gauge level 1-2)
Maintained load test
Constant rate of uplift
Mobilised unit shaft resistance r_s (kPa)
Vertical displacement $\delta_{pile,\,soil}$ (mm)
SG-1
SG-2
SG-3
SG-4
SG-5

d)

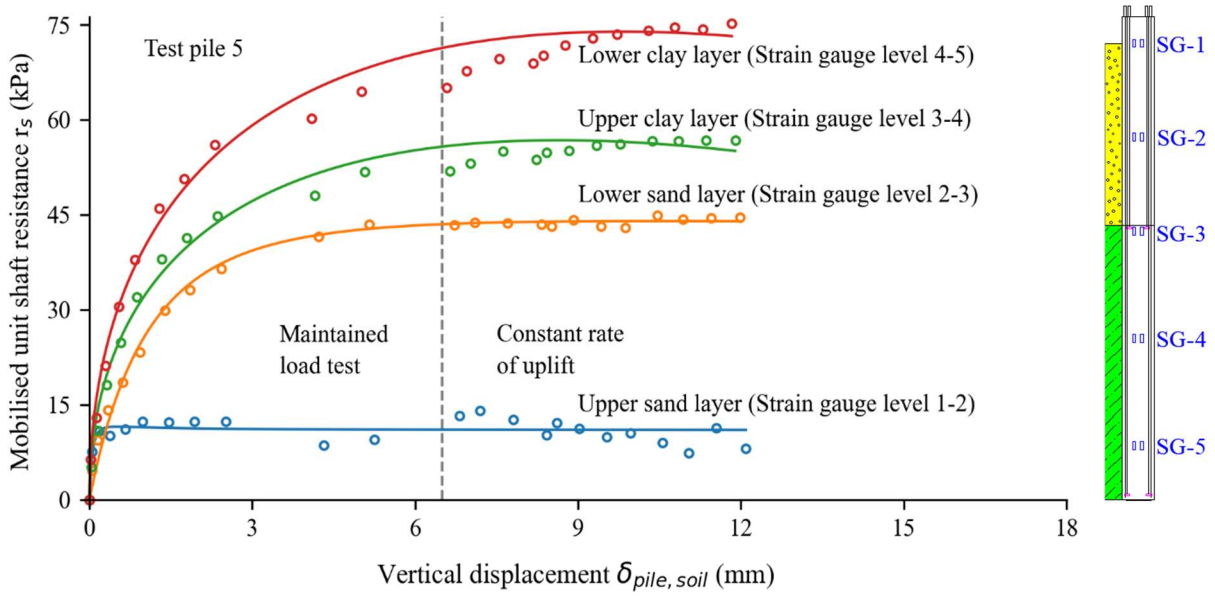
Test pile 5
Lower clay layer (Strain gauge level 4-5)
Upper clay layer (Strain gauge level 3-4)
Lower sand layer (Strain gauge level 2-3)
Upper sand layer (Strain gauge level 1-2)
Maintained load test
Constant rate of uplift
Mobilised unit shaft resistance r_s (kPa)
Vertical displacement $\delta_{pile,\,soil}$ (mm)
SG-1
SG-2
SG-3
SG-4
SG-5

e)

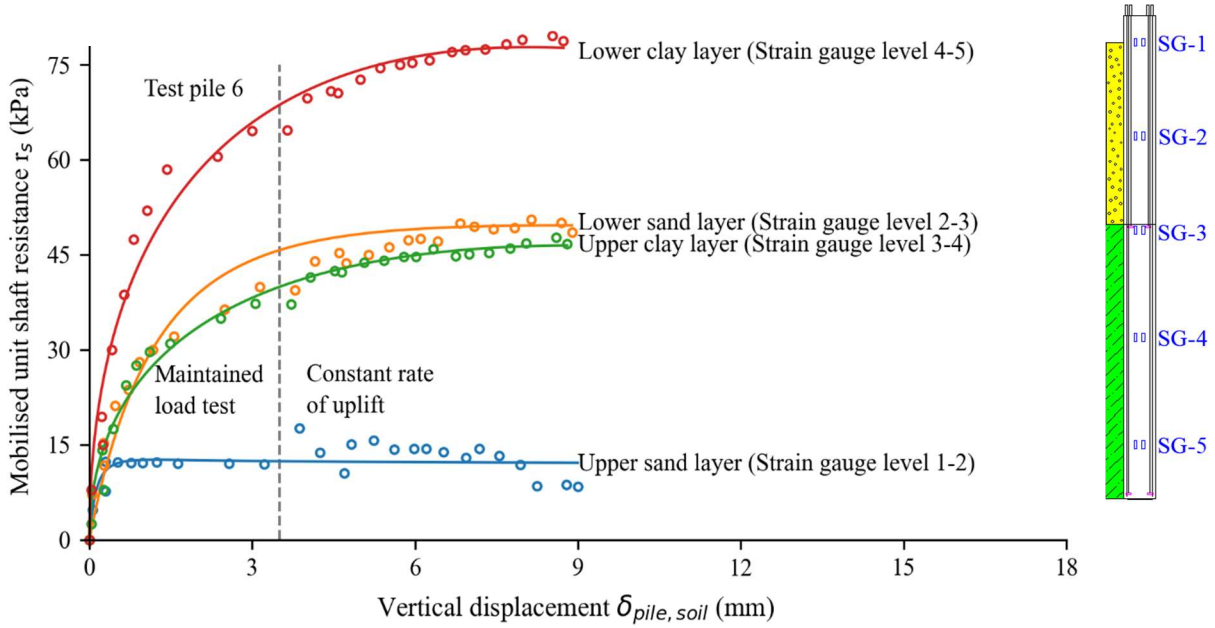
Test pile 6
Lower clay layer (Strain gauge level 4-5)
Lower sand layer (Strain gauge level 2-3)
Upper clay layer (Strain gauge level 3-4)
Upper sand layer (Strain gauge level 1-2)
Maintained load test
Constant rate of uplift
Mobilised unit shaft resistance r_s (kPa)
Vertical displacement $\delta_{pile,\,soil}$ (mm)
SG-1
SG-2
SG-3
SG-4
SG-5

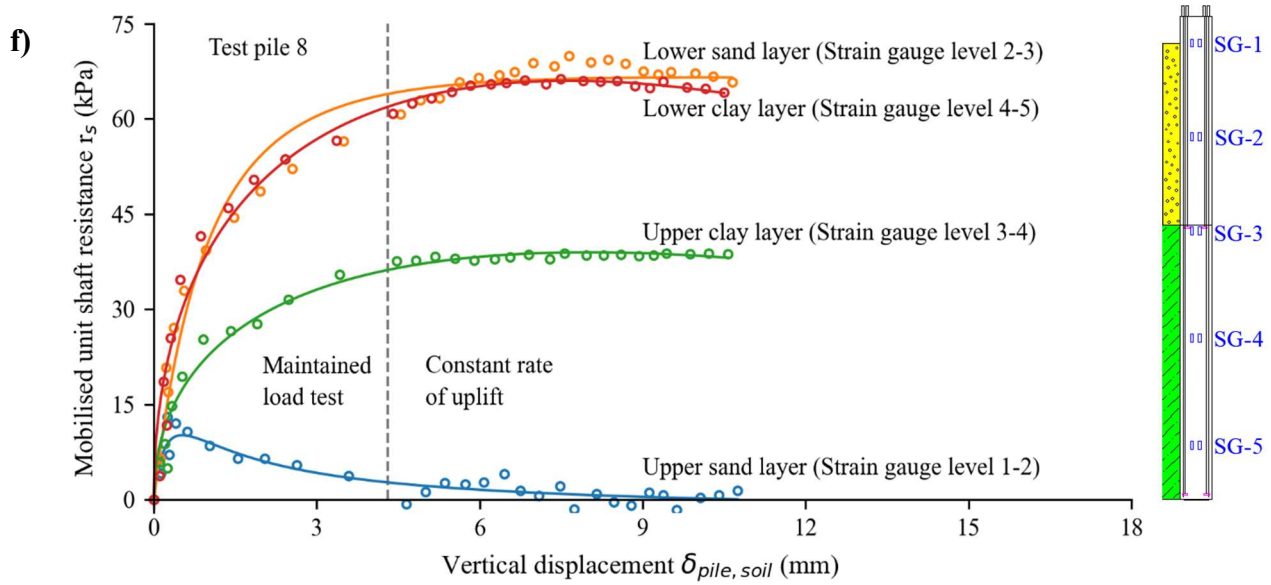

Figure 88: Mobilised unit shaft resistance based on the virgin load curves for test piles (a) 2, (b) 3, (c) 4, (d) 5, (e) 6 and (f) 8.

The observed mobilised unit shaft resistance, $r_{s,o}$, exhibits a gradual increase as the pile moves relative to the soil. The ultimate values of the mobilised unit shaft resistance are found to be up to 18 kPa for the upper sand layer, 70 kPa for the lower sand layer, 65 kPa for the upper clay layer, and 85 kPa for the lower clay layer, as shown in Table 15.

Table 15: Ultimate mobilised unit shaft resistance from the observed load transfer curves.

Soil layer	Ultimate mobilised unit shaft resistance [kPa]							
	TP1	TP2	TP3	TP4	TP5	TP6	TP7	TP8
Upper sand layer	18	12	11	8	12	16	4	12
Lower sand layer	58	38	40	46	45	51	49	70
Upper clay layer	51	58	65	51	57	48	57	39
Lower clay layer	44	73	70	85	75	80	47	66

The upper sand layers (strain gauge level 1-2) yield small ultimate values for the observed mobilised unit shaft resistance, $r_{s,o}$, as expected. The range of ultimate values varies from 4 kPa for test pile 7 to 18 kPa for test pile 1, with an average value of approximately 12 kPa.

Surprisingly, the lower sand layers (strain gauge level 2-3) demonstrate high ultimate values for the observed mobilised unit shaft resistance, $r_{s,o}$. The variation in these values is unexpectedly high, ranging from 38 kPa for test pile 2 to 70 kPa for test pile 8. This is particularly surprising considering the fact that the soil was replaced with uniform sand before pile installation, as described in section 3.4. This discrepancy suggests the presence of residual stresses that affect the behaviour of the test piles.

In the upper clay layers (strain gauge level 3-4), the ultimate values of the observed mobilised unit shaft resistance, $r_{s,o}$, range from 39 kPa to 65 kPa, with an average value of 53 kPa. In the lower clay

layers (strain gauge level 4-5), the ultimate values of the observed mobilised unit shaft resistance range from 44 kPa to 85 kPa, with an average value of 68 kPa.

It is expected that the ultimate values of the observed mobilised unit shaft resistance would be similar for the clay layers at similar levels across the test piles, owing to the uniform ground conditions of Søvind Marl at the test site in Hinge, as described in section 3.6. However, there is variation in the ultimate values within both the upper clay layers (strain gauge level 3-4) with up to 26 percentage points difference from the average value and the lower clay layers (strain gauge level 4-5) with up to 35 percentage points difference from the average value.

The average value of the observed mobilised unit shaft resistance, $r_{s,o}$, shows an increase of approximately 28% from the upper clay layers (strain gauge level 3-4) to the lower clay layers (strain gauge level 4-5). This increase is slightly higher than expected based on the increase in field vane strength, c_{fv}, with depth. The field vane strength increases by about 20% from the middle of the upper clay layers (4.5 m below ground level) to the lower clay layers (6.5 m below ground level), as summarised in section 3.10.

In the case of test piles 2-6 and 8, the observed mobilised shaft resistance exhibits strain softening behaviour after reaching ultimate values. This behaviour becomes more evident after a vertical displacement at the pile top, δ, of approximately 10 mm. Since the test piles were immediately unloaded after reaching peak values, this strain softening behaviour can be observed more clearly during reloading with the constant pile uplift rate, as depicted in Appendix H.6. However, no strain softening behaviour is observed for test piles 1 and 7. This discrepancy is likely due to the chosen method of pile loading test (ML step and absence of a CRU portion) and does not accurately reflect the behaviour of the mobilised shaft resistance.

7 Rayleigh based fibre optic distributed line sensors

In this section, focus is on the analysis of Rayleigh-based fibre optic distributed line sensors. These sensors were strategically embedded in the bored test piles to enhance the accuracy and reliability of the measurements. While the vibrating wire strain gauges (VWSG) offer selected point measurement, the fibre optic cables (FOC) provide more comprehensive and detailed measurements along the entire length of the test piles.

7.1 Application of distributed fibre optic sensing systems

The concept of using optical fibre technology for sensing purposes originated from its initial application in communication. However, a modified version of optical fibres can be fabricated and utilized specifically for sensing. The potential of using optical fibres as a means of sensing and measuring was first recognized over 50 years ago, with the patenting of the Fotonic sensor in the mid-1960s.

Initially, the focus of fibre optic sensing was primarily on point measurements. However, over time, the idea gradually emerged that if it is possible to influence the transmission of an optical fibre through external parameters, then it might also be possible to measure theses parameters as a function of position along the optical fibre. These measurements, often referred to as distributed measurements, have become a vital characteristic of fibre sensor technology. The ability to facilitate distributed measurements over distances of several tens of kilometres is unique to fibre optics (Culshaw and Kersey, 2008).

7.1.1 Basic principles

Fibre optic sensors can generally be classified into two categories: extrinsic sensors and intrinsic sensors. Extrinsic sensors are primarily utilized in commercial applications for chemical and biomedical measurements, while intrinsic sensors are typically applied for physical measurements.

One of the main advantages of using fibre optic sensing (FOS) for physical measurements, compared to other sensing technologies, is its intrinsic immunity to external physical fields. Additionally, FOS offers flexibility, cost-effective operation, and low cost for the sensing element. An impressive characteristic of FOS is its ability to be easily multiplexed, enabling measurements over long distances and/or with a large number of sensing points. This makes FOS well-suited for applications that require extensive spatial coverage and/or a high number of sensing points. Distributed fibre optic sensors (DFOS), a specific class of FOS, excel in providing measurements of physical fields distributed along the entire length of the fibre optic cable (FOC). However, it's important to note that DFOS is associated with the drawback of a higher cost for the reading unit.

7.1.2 Distributed fibre optical measurements

The DFOS are based on a scattering process that originate from the interaction between light and matter. When the fibre is probed with an optical signal, each of these scattering processes generates

a back propagating light that is used to interpret the local properties of the fibre and to collect information on the surrounding environment. Three different scattering processes may take place in an optical fibre, namely Rayleigh, Raman and Brillouin, where Raman scattering is sensitive only to temperature and Brillouin and Rayleigh scattering is sensitive to both temperature and strain. However, there is a big difference in the basic mechanism of Raman and Brillouin scattering on one side and Rayleigh scattering on the other.

Raman and Brillouin scattering

Basics mechanism of Raman and stimulated Brillouin scatter is given in Figure 89.

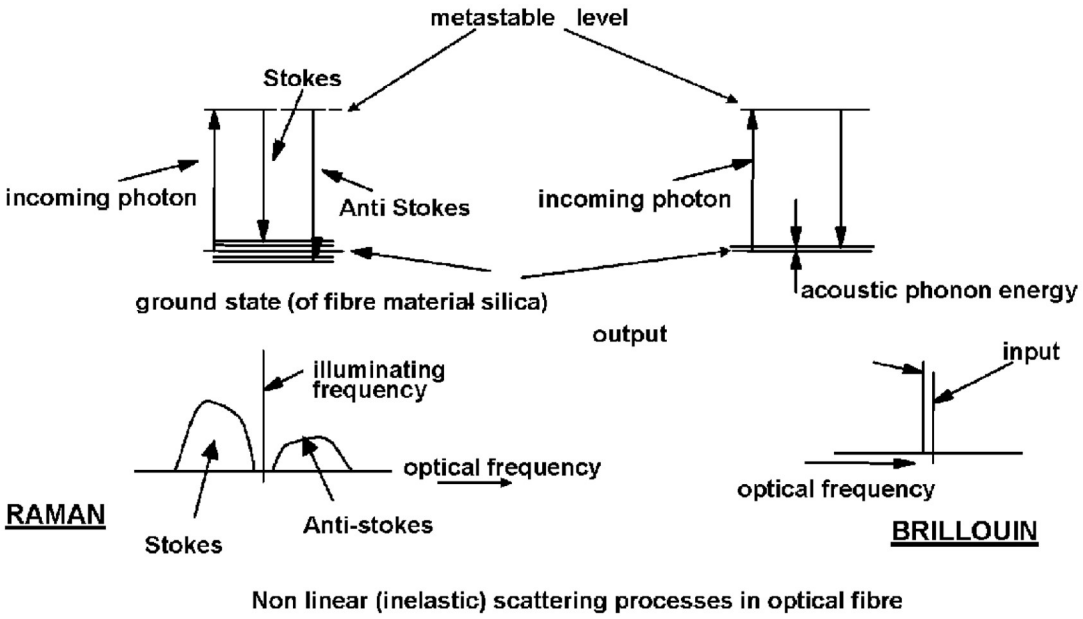

Figure 89: Basic mechanism of Raman and stimulated Brillouin scatter cf. Culshaw and Kersey (2008).

The intensity of Raman scattering (anti-Stokes) in the fibre has an intrinsic dependency of the temperature, which has been effectively utilized in the development of distributed temperature sensors (Culshaw and Kersey, 2008). Similarly, the frequency of Brillouin scattering is intrinsically dependent of the fibre density, which is affected by temperature and strain. Therefore, with adequate understanding of temperature variations, it is possible to detect varying strain fields using Brillouin scattering (Culshaw and Kersey, 2008). Both Raman and Brillouin scatter have the benefit that they do not require either measuring or modulating optical loss from the fibre. This characteristic makes them well-suited for applications over extremely long distances.

Rayleigh scattering

Rayleigh scattering can be explained as a random Bragg grating in which the fibre is divided into short sections, each of which is considered as a weak random fibre Bragg grating. Despite its randomness, the fibre Bragg grating remains stable over time. Similar to the analysis of standard fibre Bragg gratings, the reflected spectrum of this system shifts with changes in temperature and strain, as shown in Figure 90.

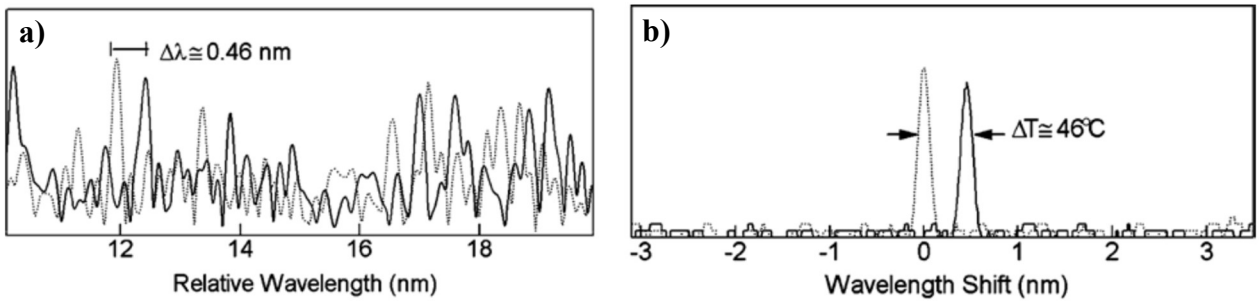

Figure 90: Spectral shift induced by thermal variation in an equivalent fibre Bragg grating made by a 5 mm long section of fibre cf. Palmieri and Schenato (2013). a) Spectral response of the fibre section before (grey) and after (black) heating. b) Auto-correlation of the spectral response before heating (grey) and cross-correlation between the two spectra after heating (black).

Rayleigh scattering in optical fibre is per se independent of almost any external physical fields, and its purpose is solely to track and reveal propagation effects, which is the actual sensing mechanism. These propagation effects encompass attenuation, gain, phase interference, and polarization changes. Phase interference is the underlying physical phenomenon in the well-known "fibre fingerprint" and is the only commercially successful distributed fibre optic system. This system is highly sensitive to variations in temperature and strain and can be categorized into two classes based on whether the fibre is probed in the frequency domain or time domain. Although the physical effect remains the same in both cases, the substantial difference in spatial resolution and measurement speed between the two approaches result in significantly different applications (Palmieri and Schenato, 2013).

Measurement range and spatial resolution

Distributed fibre optic sensors are characterized by two primary parameters: measurement range and spatial resolution. The measurement range refers to the maximum length of the sensing fibre and can vary from under one meter to over 100 kilometres, depending on the specific physical field being monitored and the sensing method employed. Spatial resolution, on the other hand, represents the level of spatial accuracy at which the physical field can be mapped and can range from millimetres to some meters.

There is a trade-off between measurement range and spatial resolution, as achieving a higher spatial resolution requires using probe light with a wider bandwidth, which introduces more noise and makes it challenging to detect and propagate over long distances without distortion. This compromise, determined by the ratio between measurement range and spatial resolution, corresponds to the number of point sensors provided by a distributed fibre optic sensor. In some cases, this can be as high as tens of thousands of individual point sensors

By utilizing Raman or Brillouin scattering, it is possible to achieve a spatial resolution of approximately 0.5-1.0 meters over an extensive measurement range spanning many tens of kilometres. On the other hand, with Rayleigh scattering, it is possible to achieve an impressive spatial resolution of just a few millimetres, albeit with a reduced measurement range of only tens of meters.

7.1.3 State of the art

The use of distributed fibre optic sensing systems for bored piles is rather recent and most of the available studies are based on measurements from distributed fibre optic sensing systems based on Brillouin scattering. Only a few studies have focused on Rayleigh scattering.

The first use of Brillouin scatter for distributed fibre optic sensing systems for bored piles was presented nearly 20 years ago (Klar et al., 2006). Since then, the installation and testing procedures was further developed through axially loaded large, bored piles (Mohamad et al., 2009, Ouyang et al., 2015, de Battista et al., 2016a, Pelecanos et al., 2017, Pelecanos et al., 2018, Kechavarzi et al., 2019), including continuous flight auger, CFA (de Battista et al., 2016b) and tension piles (Pelecanos et al., 2016).

These early studies were based on spontaneous Brillouin scatter and the use of Brillouin optical time-domain reflectometer (BOTDR) for distributed fibre optic sensing systems for bored piles. The typical sampling resolution for BODTR is around 0.1 m with a spatial resolution of 1.0 m, the strain precision is as best around $\mp 15 \mu\varepsilon$ and the temperature precision is around $\mp 1°C$.

Later, studies were applied based on stimulated Brillouin scatter and the use of Brillouin optical time-domain analysis (BOTDA) for distributed fibre optic sensing systems for bored piles (Mohamad et al., 2017, Xu et al., 2018, Pei et al., 2019). The advantage of using BOTDA is an improved strain precision of optimally $\mp 4 \mu\varepsilon$ and a temperature precision of $\mp 0.2°C$ for a typical sampling resolution of 0.05 m with a spatial resolution of 0.5 m.

The advantage of using Rayleigh scatter and optical frequency domain reflectometry (OFDR) for distributed fibre optic sensing systems is the impressive sampling resolution of 2.6 mm based on a spatial resolution of only 5.2 mm, which enables measurements of localised strains. The use of OFDR for bored piles has only been reported in a couple of studies (Bersan et al., 2018, Kania and Sørensen, 2018) for continuous flight auger, CFA installed in sand or a mixture of sand, silt, silty clay and gravel.

In order to assess the reliability of fibre optic strain cables (FOSC), the measurements can be compared with the measurements obtained using conventional Vibrating Wire Strain Gauges (VWSG). In a study conducted by Kania and Sørensen (2018), it was observed that the FOSC provided strain measurements that aligned well with those obtained from conventional VWSG. Furthermore, the FOSC were found to offer detailed information about the stress and strain distribution along the entire length of a bored pile, as depicted in Figure 91.

The test pile used by Kania and Sørensen (2018) was a Ø630 mm CFA pile installed in sand and incrementally loaded in two phases as part of a static pile loading test in compression. The test pile was equipped with 2 VWSG, 4 FOSC, and 2 fibre optic temperature cables (FOTC).

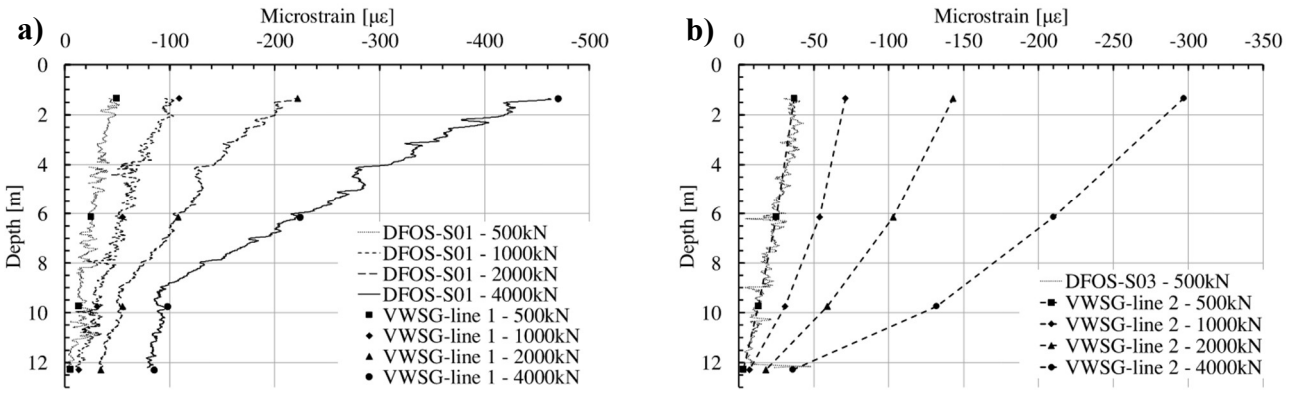

Figure 91:Measured strain distribution from the test pile by Kania and Sørensen (2018) for (a) VWSG-line 1 and DFOS-S01 and (b) VWSG-line 2 and DFOS-S03.

The availability of detailed stress and strain distribution data along the entire length of a bored pile allows for an investigation into the impact of non-uniform pile stiffness. Kania et al. (2020) observed, that there was a local reduction in strain at the specific location of the 6x60 mm stiffening rings. These rings were positioned at regular intervals of 0.97 m along the reinforcement cage, as illustrated in Figure 92 (a).

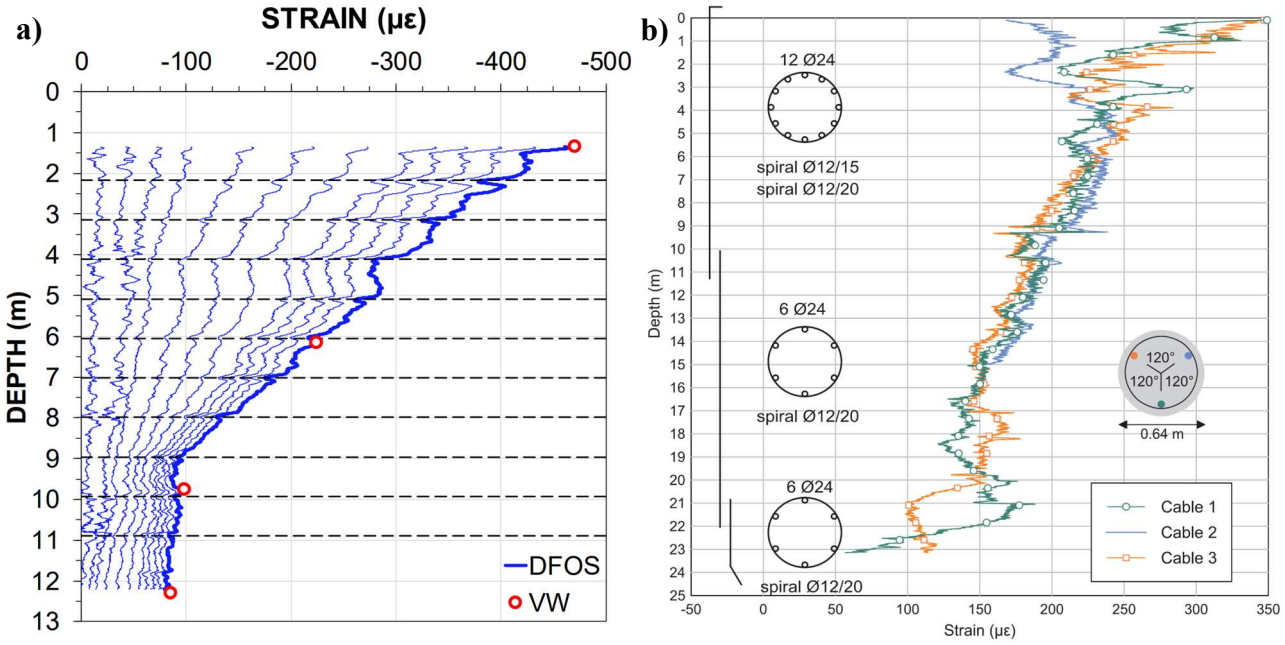

Figure 92: Strain measurements obtained from fibre optic strain cables (FOSC) by (a) Kania et al. (2020) with location of stiffening rings and (b) Bersan et al. (2018) with sketch of the reinforcement cage to the left.

In a similar study conducted by Bersan et al. (2018), a distinct localized reduction in strain was observed, as depicted in Figure 92 (b). Notably, a sharp decrease in strain was identified at a depth ranging between 9 and 10 m. This reduction was attributed to an increase in pile stiffness resulting from the superposition of two sections of the reinforcement cage. However, upon aligning the drawing of the reinforcement cage with the strain profiles, a discrepancy of approximately 1 m was noted between the zones of rebar superposition and the areas of strain decrease.

Furthermore, a similar pattern was observed in fibre 1 at a depth between 20 and 21 m, while this was not observed for strain cable 3. Highly localised, very small reductions of strain are visible for cable 1 and partly for cable 2 and 3 that were attributed to be a consequence of the increase in pile stiffness produced by the inner rings of the reinforcement cage.

While these localized strain variations can be accurately identified, they can also lead to erroneous interpretations of strain data concerning the behaviour of the soil-pile interface if not fully comprehended. Due to the limited available data on this subject, there is a need for further studies in relation to FOSC used for traditional bored piles installed in fine grained soils.

Mechanical strains were also found to have an impact on the FOTC for a driven steel pile (Kania et al., 2020). No similar studies were found for the FOTC in bored piles and there is a need to investigate this matter.

7.2 Fibre optic sensing system

In addition to traditional vibrating wire strain gauges (VWSG) and tell-tales (TT), a Rayleigh-based distributed fibre optic sensing system utilizing optical frequency domain reflectometry (OFDR) was implemented for measuring temperature and strain in the test piles. This distributed fibre optic sensing system consisted of two primary components: a fibre optic spectrum analyser (FOSA) and either a fibre optic temperature cable (FOTC) or a fibre optic strain cable (FOSC)

For the test piles, the FOSA utilized a LUNA optical distributed sensor interrogation unit (IU), model ODiSI-B, which operated with the ODiSI-B software. It was applied in combination with a standoff cable, a remote module, and the LUNA fibre optic switch (FOS). Please refer to Figure 93 for a visual representation.

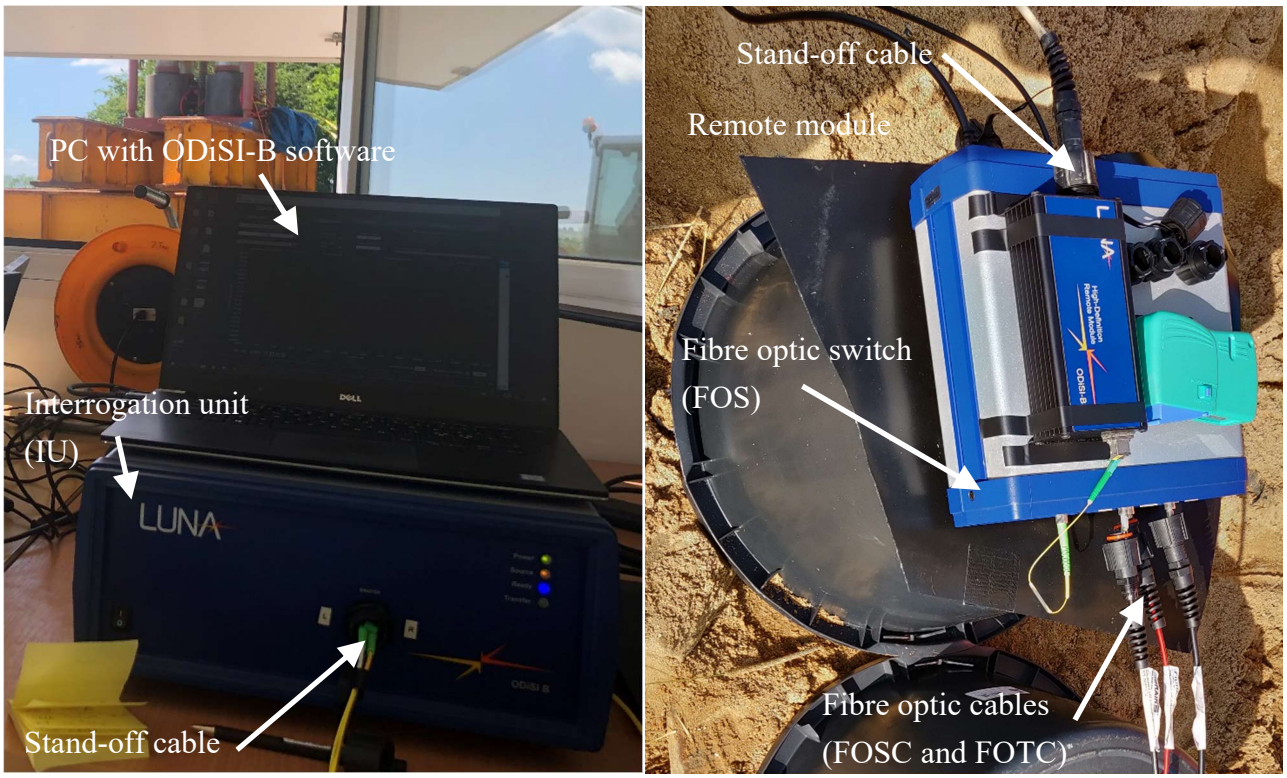

Figure 93: ODiSI-B measurement system used on test site Hinge.

The IU employs swept-wavelength interferometry to measure the spectral shift in Rayleigh backscatter. The spatial resolution, which is the length over which the IU calculates a single strain, is 5.2 mm, and the sampling resolution, the distance between two data points, is 2.6 mm (LUNA, 2017).

In the case of the test piles in Hinge, the maximum sensing length for the system is 20 m, but due to the use of FOS, it is reduced to 18 m. The FOTC and FOSC used were commercially available BRUsens temperature 85 °C cables (red) and BRUsens V9 strain cables (blue) from BRUGG cables, respectively. To avoid any complications related to the system's recognition of individual FOSC, given their highly sensitive nature, the first approximately 4 m of the FOSC (the section between the test pile and the FOS) is substituted with a passive cable (black). Figure 94 illustrates an idealized representation of the embedded FOTC and FOSC in the test piles.

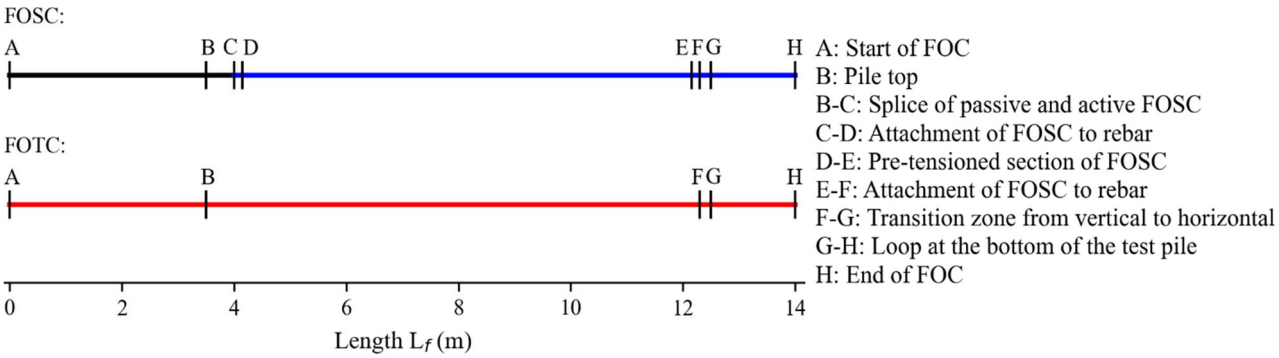

Figure 94: Illustration of fibre optic temperature cable (FOTC) and fibre optic strain cable (FOSC) embedded in the test piles.

The precise positioning of the FOTC and FOSC components within the test piles is illustrated in Figure 95:

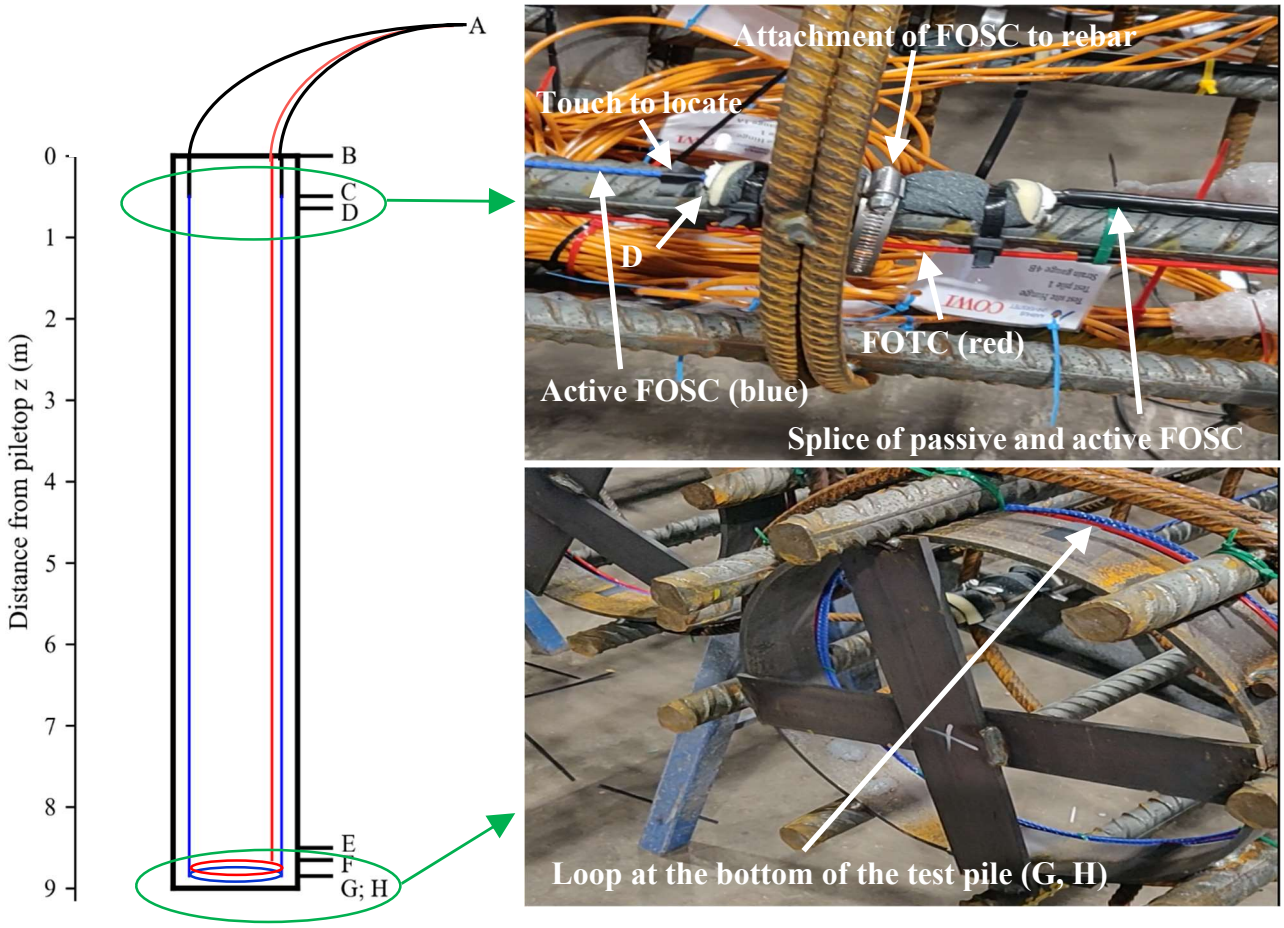

Figure 95: Precise positioning of fibre optic temperature cable (FOTC) and fibre optic strain cable (FOSC) within the test piles, with reference to Figure 94.

7.2.1 Influence of multi-channel switch

The process of measurement with the FOSA requires careful handling, and the FOS facilitates the ability to measure at smaller intervals between different FOTC and FOSC components. All the cables under consideration are connected to the FOS, allowing for direct selection of a specific cable using the ODiSI-B software without the need for physically changing cables between measurements.

However, Kania and Sørensen (2018) discovered that the signal quality, indicated by increased scattering, was affected when the FOS was utilized. As the use of the FOS is optional, this section investigates the impact on the measured strain data. To address this, two Luna high-definition (HD) strain sensors were employed. These low-profile and flexible sensors are specifically designed for use with the ODiSI measurement system. Moreover, they are supplied with NIST-traceable calibration coefficients and each HD strain sensor has a unique key ID ("fibre fingerprint"), allowing for plug-and-play identification and operation.

The two Luna high-definition (HD) strain sensors were positioned flat and naturally curled up on the ground, without any external factors influencing them. The test setup when the FOS is employed follows the description provided in section 7.2. Conversely, the test setup without the FOS involves directly connecting the FOC to the remote module. The strain measurements along the length of HD strain sensor 1 are depicted in Figure 96 and Figure 97, showcasing measurements taken over a 5-second period at a frequency of 1 Hz (i.e., 5 measurements).

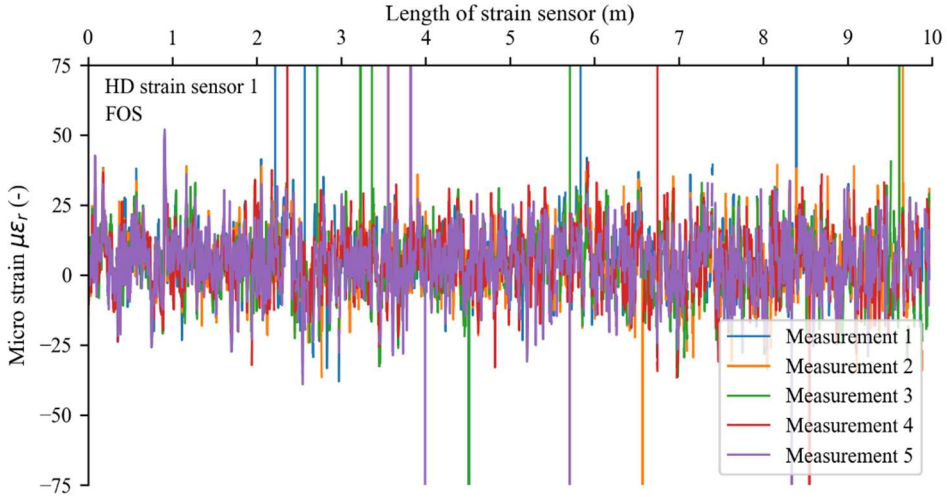

Figure 96: Development of strain along the length of high-definition (HD) strain sensor 1 using the fibre optic switch (FOS).

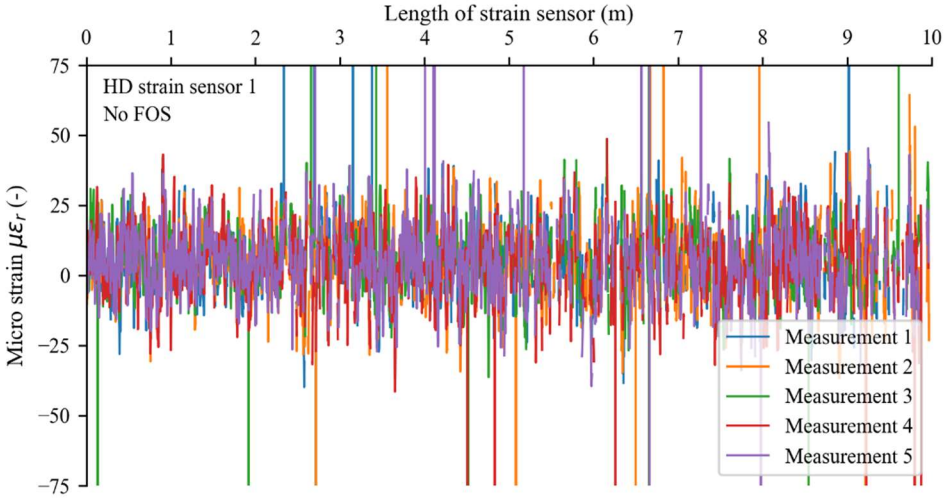

Figure 97: Development of strain along the length of high-definition (HD) strain sensor 1 without using the fibre optic switch (FOS).

Based on the observations in Figure 96 and Figure 97, it is evident that both figures display a similar level of scattering, irrespective of the usage of the FOS. Furthermore, it appears that the measurements fall within the ±25 $\mu\varepsilon$ accuracy range specified by the manufacturer (LUNA, 2017). To provide further clarification, the mean value, 5th percentile, 95th percentile, and standard deviation are calculated for all five measurements conducted with and without the FOS. The results are summarized in Table 16.

Table 16: High-definition (HD) strain sensor 1: Mean (arithmetic), 5th percentile, 95th percentile and standard deviation for all 5 measurements individually with and without fibre optic switch (FOS).

HD strain sensor 1	**Mean [$\mu\varepsilon$]**	**5th percentile [$\mu\varepsilon$]**	**95th percentile [$\mu\varepsilon$]**	**Standard deviation [$\mu\varepsilon$]**
FOS				
Measurement 1	6.50	-12.70	22.60	585
Measurement 2	16.93	-12.78	22.30	674
Measurement 3	18.25	-13.90	21.68	685
Measurement 4	12.62	-12.67	21.30	355
Measurement 5	12.43	-12.92	21.16	581
No FOS				
Measurement 1	28.67	-13.56	24.79	702
Measurement 2	-9.50	-14.39	23.49	768
Measurement 3	-11.85	-13.00	23.14	1086
Measurement 4	3.59	-15.03	21.59	762
Measurement 5	68.21	-15.05	24.58	1142

From examining Table 16, it becomes apparent that the measurements conducted without the FOS exhibit significant variation in mean values, occasionally exceeding the boundaries of the 5th and 95th percentiles. These measurements also demonstrate high standard deviations ranging from 702 $\mu\varepsilon$ to 1142 $\mu\varepsilon$, suggesting the presence of several extreme outliers in the collected data.

Conversely, the strain measurements obtained with the FOS yield more reasonable mean values, all of which fall within the boundaries of the 5th and 95th percentiles. Additionally, these measurements exhibit lower standard deviations spanning from 355 $\mu\varepsilon$ to 685 $\mu\varepsilon$. However, it is important to note that the standard deviations remain relatively high, likely due to the presence of multiple outliers.

Consequently, Figure 98 displays the measured strain along HD strain sensor 1, incorporating an average value of the five measurements obtained with and without the FOS. Outliers exceeding $\pm 75\mu\varepsilon$ have been removed during the representation.

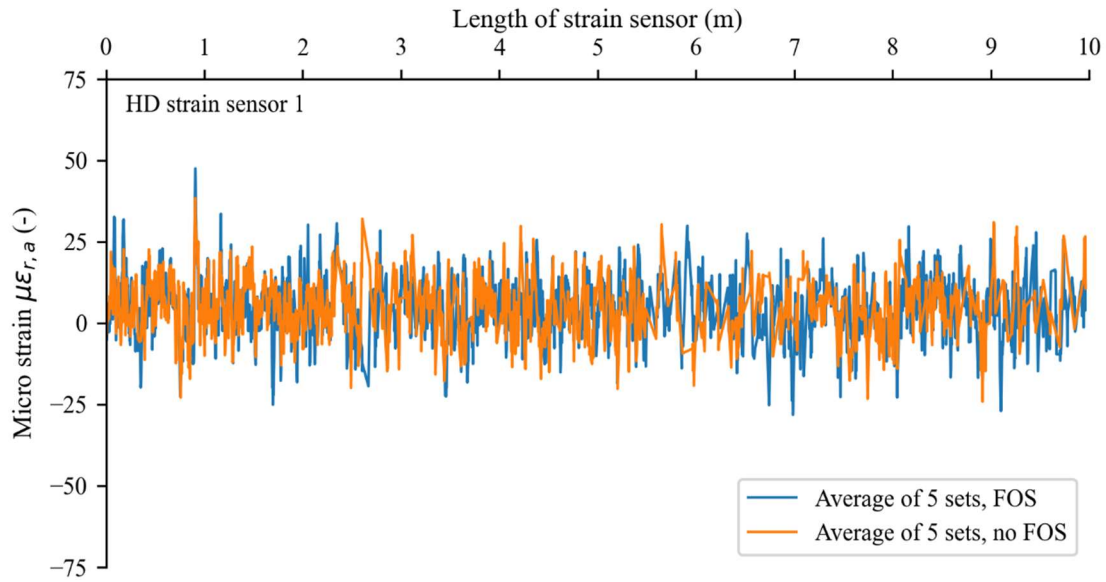

Figure 98: Development of strain along the length of high-definition (HD) strain sensor 1 for an average value of 5 measurements with and without the use of fibre optic switch (FOS).

Despite the difference in the use of the FOS, both strain measurements show a similar pattern. Therefore, the mean value, 5th percentile, 95th percentile, and standard deviation are calculated for both scenarios— with and without the use of the FOS. Please refer to Table 17 for these calculated values.

Table 17: High-definition (HD) strain sensor 1: Mean (arithmetic), 5th percentile, 95th percentile and standard deviation for an average value of all 5 measurements with and without fibre optic switch (FOS).

HD strain sensor 1	Mean [$\mu\varepsilon$]	5th percentile [$\mu\varepsilon$]	95th percentile [$\mu\varepsilon$]	Standard deviation [$\mu\varepsilon$]
FOS	4.46	-11.00	19.88	9.4
No FOS	4.63	-11.47	20.34	9.7

The analysis reveals that there is a negligible difference between the mean value, 5th percentile, and 95th percentile within 0.5 $\mu\varepsilon$, with only a 0.3 $\mu\varepsilon$ deviation in standard deviation for measurements conducted with and without the FOS for HD strain sensor 1. This evaluation was subsequently repeated for HD strain sensor 2, and the results can be found in Appendix I.1. For HD strain sensor 2, there is a discrepancy of 5.5 $\mu\varepsilon$ in mean value, 5th percentile, and 95th percentile, and a 3 $\mu\varepsilon$ difference in standard deviation between measurements conducted with and without the FOS. This disparity is caused by a peak in measured strain occurring at approximately 1 meter along the length of HD strain sensor 2 in measurements performed without the FOS

Considering these findings, no evidence supports the claim that the signal quality is poorer when employing the FOS. As a result, the FOS will be utilized throughout this PhD project.

7.3 Validation of fibre optic temperature cables

The primary emphasis of this section is on the fibre optic temperature cables (FOTC) due to the discovery in a previous study by Kania et al. (2020), that mechanical strains have an impact on FOTC. However, this aspect was not included in this PhD project as the test piles were promptly planned, ordered, and installed to maximize the rest period. Additionally, the article was completed and published the year following the installation of the test piles.

Ensuring accurate measurement of temperature changes is crucial because the measured strains are influenced by fluctuations in temperature, as indicated by equation (74):

$$\varepsilon_{total} = \varepsilon_{mech} + \varepsilon_{thermal} \tag{74}$$

Here, ε_{total} is the total strain (also referred to as measured strains ε_r from the raw data), ε_{mech} is the mechanical strain (also referred to as the measured strains corrected for thermal influence ε_t) and ε_{therm} is the thermal induced strain.

To assess the impact of temperature changes on the measured strains and axial pile capacity of the test piles in Hinge, the following example is considered:

Assuming the axial pile stiffness of the test piles in Hinge is 15 GN (as stated in section 6.3.2) , a 1°C temperature change results in a thermal-induced strain, ε_{therm} , of $-2\mu\varepsilon$ for the VWSG (as described in section 5.3). This leads to an underestimation of the axial load by approximately 30 kN. Conversely, for the FOSC (as mentioned in section 5.4) , a 1°C temperature change causes a thermal-induced strain, $\varepsilon_{thermal}$, of $20\mu\varepsilon$, resulting in an overestimation of the axial load by approximately 300 kN.

From the given example, it is evident that the fibre optic strain cable (FOSC) is significantly more sensitive to temperature changes compared to the vibrating wire strain gauges (VWSG). Nonetheless, it is essential to correct for thermal-induced strain irrespective of whether VWSG or FOSC is utilized.

7.3.1 Filtering and smoothing of data from FOTC

Unlike the thermistors in the vibrating wire strain gauges (VWSG thermistors), the FOTC are susceptible to internal signal disturbance such as scatter caused by wear and tear, cracks, and sharp bending of the cables. Additionally, they are also influenced by external environmental conditions like dust, wind, and vibration. As a result, it is necessary to employ filtering and smoothing techniques to enhance the quality of the FOTC data. Consequently, data obtained from the reinforcement cage to test pile 8 is utilized to illustrate the process of filtering and smoothing the FOTC data.

The procedure is demonstrated using temperature measurements taken shortly after installing the FOTC on the reinforcement cage in an indoor storage facility. During this period, the reinforcement cage remains flat, and the FOTC's measurements are solely influenced by temperature and not affected by any other factors

Initially, the FOTC data is subjected to a filtering process to eliminate any NaN (Not a Number) values present in the raw data. These NaN values are easily identifiable and subsequently removed from the dataset, as shown in Figure 99.

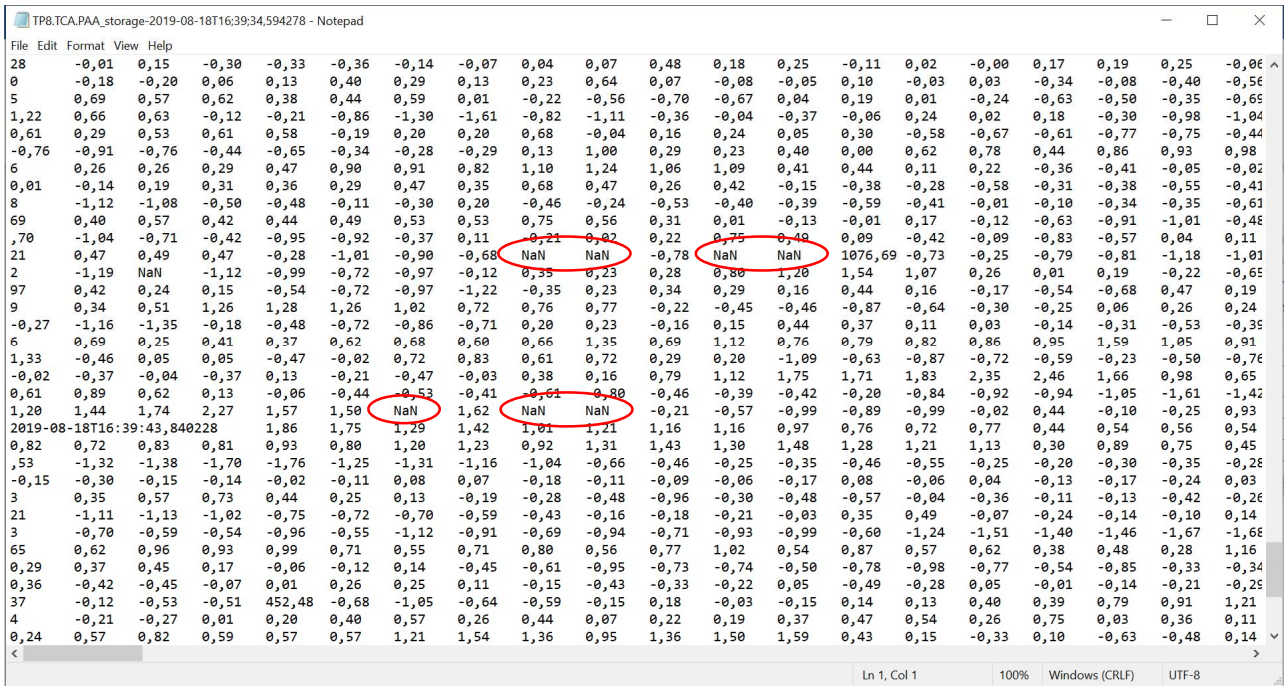

Figure 99: Example of identification of NaN (Not a Number) values in raw data from fibre optic temperature cables (FOTC).

Since FOTC can only measure temperature changes between two points in time and not absolute temperatures, a reference temperature profile was employed. This reference profile was derived from temperature data obtained during storage at the indoor AU laboratory. The reference temperature was determined by averaging the temperatures recorded by all 10 thermistors of the VWSG for each test pile. More details can be found in Table 18.

Table 18: Reference temperature from storage at the AU laboratory.

	Test pile no.							
	1	2	3	4	5	6	7	8
$T_{ref.}$ [°C]	22.8	22.8	22.8	22.8	22.7	22.6	22.4	22.2

After converting the FOTC data to actual temperatures, the next step involves filtering the data to remove outliers. These outliers can be easily identified as they exhibit significantly larger or smaller values compared to the actual temperature measurements.

For instance, in the example depicted in Figure 100, representing the reinforcement cage data from test pile 8, the actual temperatures range between approximately 20°C and 25°C, while the outliers present negative values ranging from -530°C to -1530°C and positive values from 190°C to 1580°C. These outlier temperatures are completely unrealistic and, therefore, all data below e.g. 15°C and above 30°C is discarded.

Additionally, to obtain an average temperature value, the filtered data from FOTC is computed based on measurements taken over a period of 5 seconds, with a frequency of 1 Hz. This corresponds to taking an average of 5 measurements, as indicated by the light grey line in Figure 100 (a).

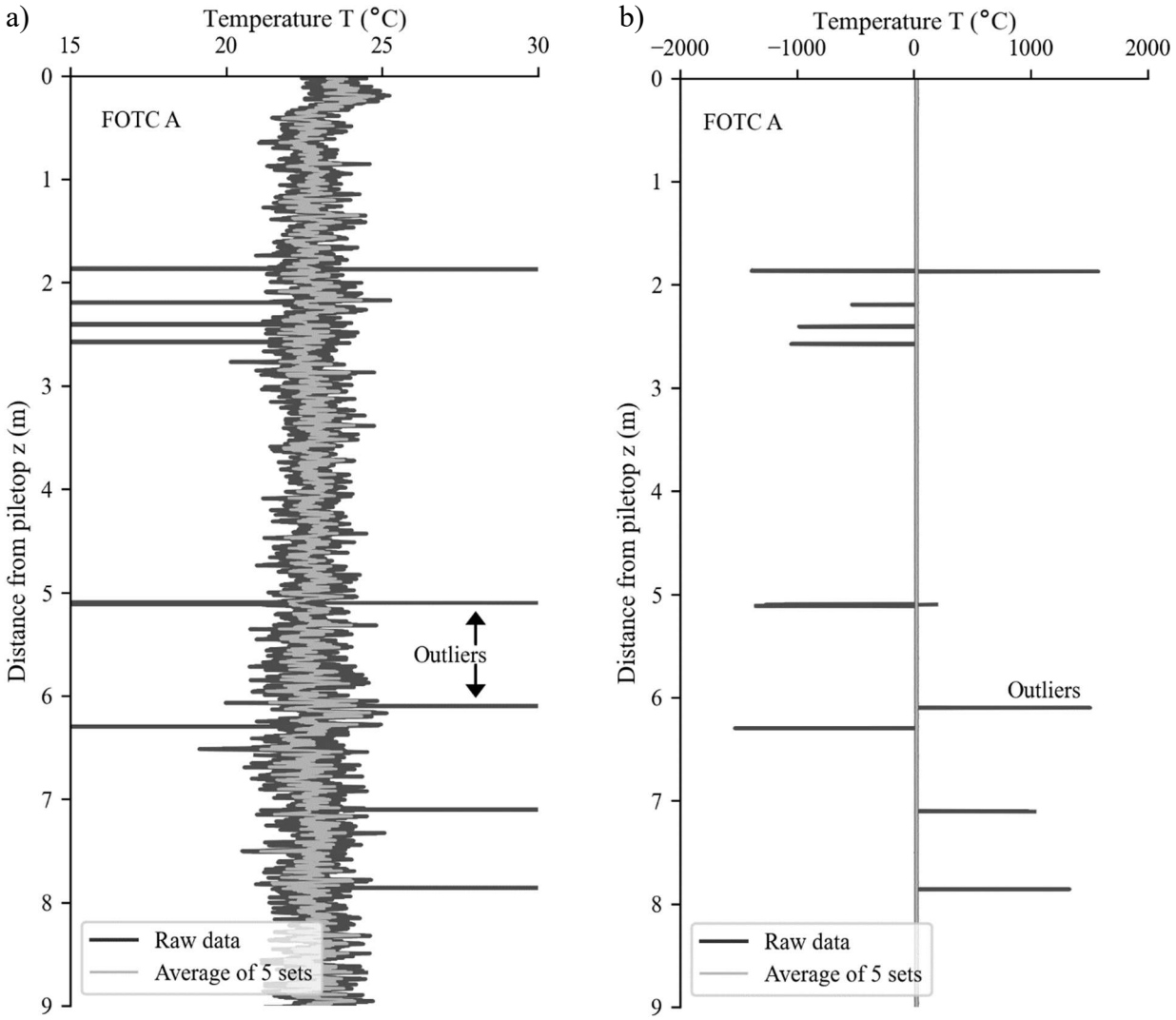

Figure 100: Temperature measurements conducted along the reinforcement cage of test pile 8 at an indoor storage facility shown for the temperature intervals of (a) 15°C to 30°C and (b) -2000°C to 2000°C.

To smoothen the data obtained from the FOTC, a moving average approach is employed along the length of the test piles. The selection of an appropriate moving average length involves examining the temperature data with moving averages of 50, 100, and 200 readings, as illustrated in Figure 101.

The determination of the most suitable moving average length relies on engineering judgment based on the visual smoothness of the line. After analysing Figure 101, it is evident that a moving average of 200 readings or approximately 0.52 m is suitable for smoothing the temperature data. This chosen moving average length will be consistently applied in this section.

It is important to note that the moving average length of the FOTC may correspond to the moving average length of the FOSC for determining mechanical strain. Ensuring the length of the moving average from the FOTC matches that of the FOSC is critical for accurate comparison and analysis.

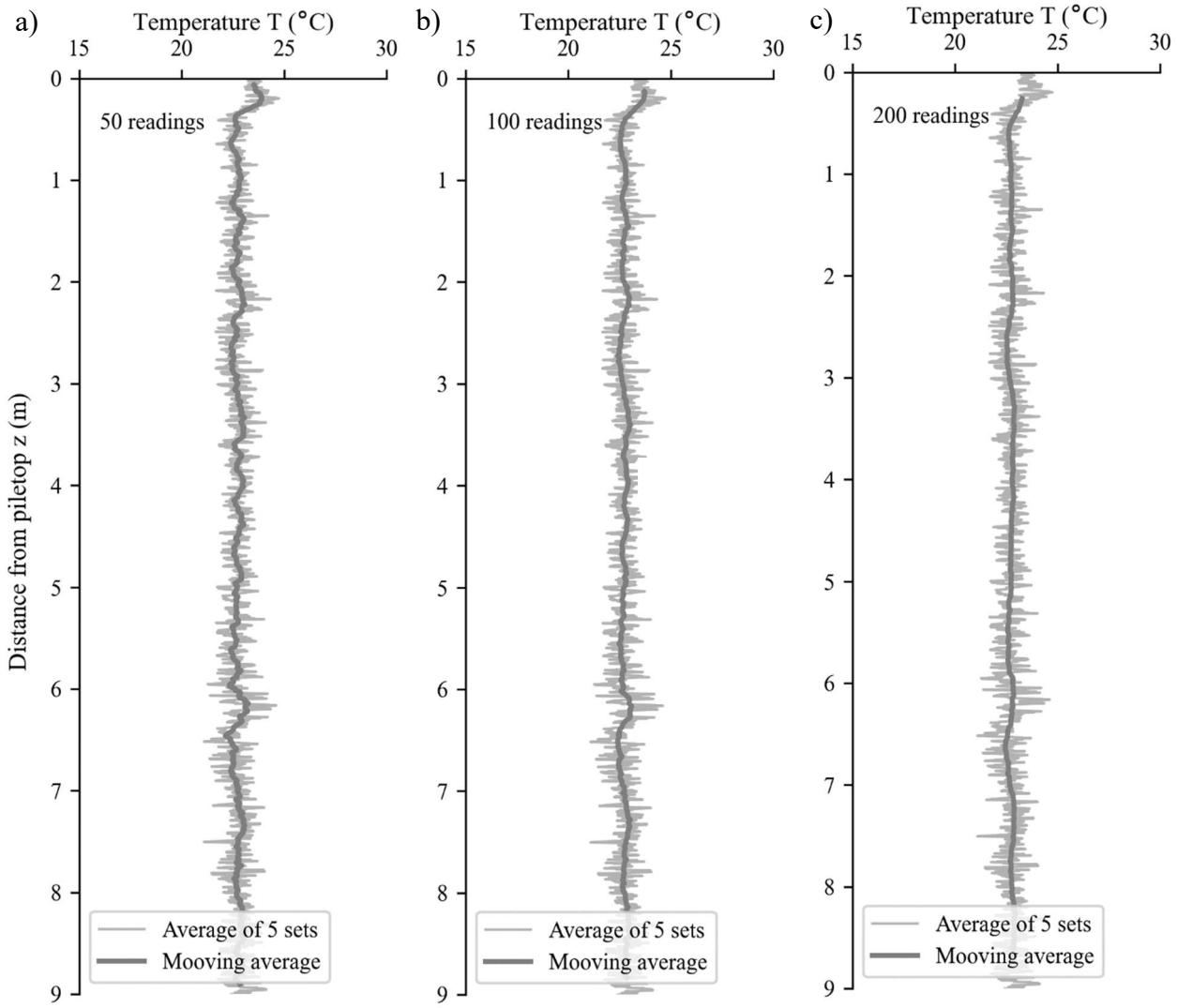

Figure 101: The temperature data along the reinforcement cage of test pile 8 at an indoor storage facility is displayed with a moving average of (a) 50, (b) 100 and (c) 200 readings.

7.3.2 Reliability of temperature measurements

Temperature and strain are the primary physical fields that directly impact distributed fibre optic sensing (DFOS) utilizing Rayleigh scattering. However, due to their joint sensitivity, DFOS sensors are unable to discern between strain and temperature. Therefore, either one of the parameters must be assumed constant (such as by loosely installing the fibre to decouple it from structural strain) or measured independently using another sensor.

In this PhD project, commercially available BRUsens temperature cables from BRUGG cables, capable of withstanding temperatures up to 85 °C and featuring a loose tube inside the FOTC, were utilized. Furthermore, the FOTC were loosely attached without pre-tension to ensure their ability to function independently of the strain in the structure.

This section primarily focuses on assessing the reliability of temperature measurements obtained from the FOTC compared to the WVSG thermistors. The verification process involves comparing measurements from the VWSG thermistors and FOTC in two different scenarios: one where the test piles are free from any external strain influence and another where the test piles are subjected to strain.

Temperature observations from strain free piles

The temperatures observed from both the VWSG thermistors and the FOTC were recorded while the reinforcement cages for the test piles were stored in an indoor facility with a relatively constant temperature (referred to as Day 0). During these measurements, the reinforcement cages were placed flat on the ground, ensuring that there was no strain applied to them.

Additionally, the observed temperatures were compared to infrared temperature measurements for validation purposes. After a period of 2-5 days, the temperature measurements were conducted again while the reinforcement cages remained strain-free, this time on the outdoor test site in Hinge.

To provide an example, the observed temperatures for the reinforcement cage of test pile 1, which exhibited the highest cross-sectional temperature variation on the Hinge test site, are illustrated in Figure 102. Further details regarding the observed temperatures for all reinforcement cages can be found in Appendix F.3.

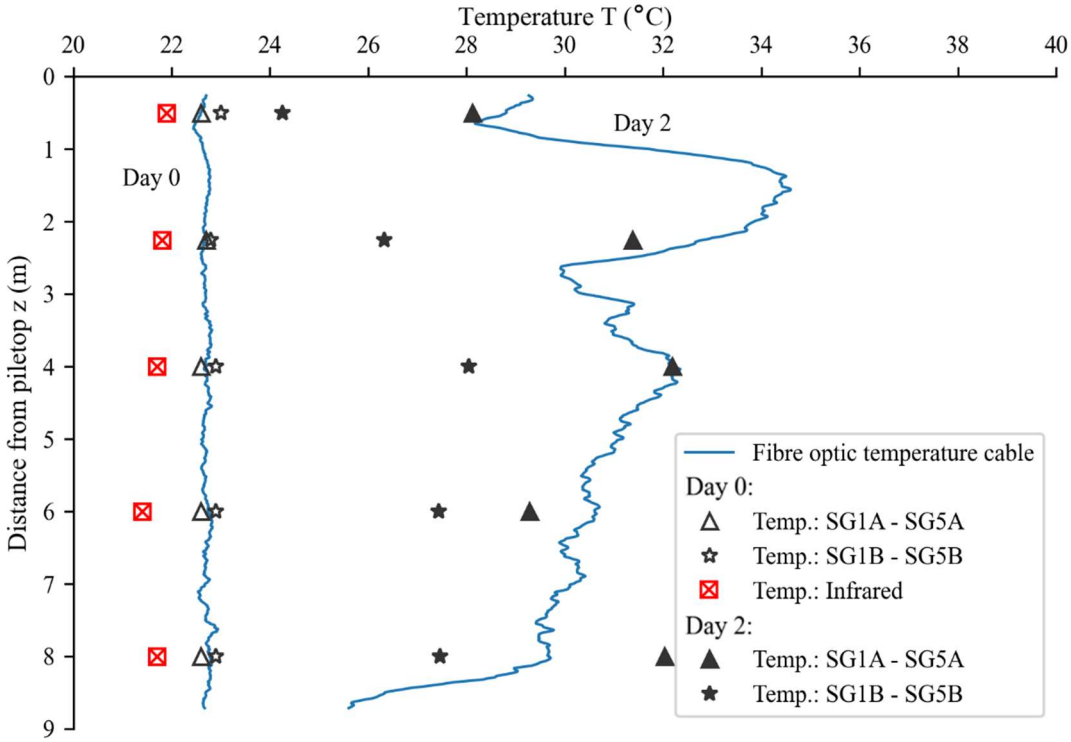

Figure 102: Temperature measurements collected along the reinforcement cage connected to test pile 1 for Day 0: with the reinforcement cage stored indoors at a facility with a relatively constant temperature and Day 2: with the reinforcement cage positioned on the ground on the outdoor test site in Hinge. Blue lines represent the fibre optic temperature cables (FOTC), and symbols represent the thermistors in the vibrating wire strain gauges (VWSG thermistor).

The measured temperatures from both the VWSG thermistors and the FOTC along the reinforcement cages at the indoor storage facility on Day 0 exhibit a similar trend. However, the temperatures recorded via infrared measurements are slightly lower, ranging between 0.6°C and 1.6°C. This variance is reasonable because the infrared temperature measurements are taken on the surface of the reinforcement, which can be influenced by cooling effects from wind breezes. Therefore, it is expected that the infrared measurements would not precisely match the temperatures recorded by the VWSG thermistors, which are protected by surrounding materials.

It is worth noting that the FOTC solely measures changes in temperature and is expected to align with the temperatures measured by the VWSG thermistors. The VWSG thermistors are utilized to establish the reference temperature profiles for the FOTC, as explained in section 7.3.1.

During the period when the reinforcement cages were positioned on the ground (outdoors) at the test site in Hinge, uneven temperatures were observed across the cross-section and along the length of the test piles. This variation in temperature along the cross-section and length of the test piles occurred between Days 2 and 5 before the actual installation process for each test pile commenced.

The weather conditions during this four-day period were generally sunny with partial cloud cover. The temperatures ranged between 15-20 °C, and there was either no wind or only a slight breeze. Additionally, there was minimal rainfall, with just a few drops on the first day.

The observed uneven temperatures can be attributed to the lack of shading available for the reinforcement cages. Consequently, the measured temperatures were influenced by direct exposure to sunlight, as well as partial shading caused by tufts of grass, sand, and other factors present around the test site.

Temperatures in test piles 6, 7, and 8 were measured between 8 a.m. and 9 a.m., during which the lowest measured temperatures were primarily between 15 and 17 °C. Temperatures in test piles 2-5 were measured between 10.40 a.m. and 11.40 a.m., showing measured temperatures primarily between 22 and 26 °C. Temperatures in test pile 1, on the other hand, was measured around 13.37 p.m., displaying the highest measured temperatures between 24 and 34 °C. These observations align with expectations, as temperatures tend to be lowest in the morning and increase throughout the day. More details can be found in Appendix F.3.

Based on the findings, the FOTC demonstrate reliability in providing temperature measurements when the reinforcement cages were lying flat and strain-free in an indoor facility on Day 0. The measured temperatures align well with the reference temperature interval, with a close match between the measured range of 22.0 °C to 23.1 °C and the reference temperatures falling in the range of 22.2 °C to 22.8 °C.

However, when the reinforcement cages were placed on the ground (outdoors) at the test site in Hinge from Days 2 to 5, uneven temperatures were observed across the cross-section. This uneven

temperature distribution can be attributed to the absence of shading available for the reinforcement cages. As a result, it becomes challenging to evaluate the reliability of the FOTC measurements in this specific outdoor scenario.

In order to comprehensively investigate the impact of temperature changes on the FOTC while ensuring no influence of strains, it would have been necessary to conduct FOTC measurements at multiple time points. Regrettably, such measurements were not carried out as part of this PhD project.

Temperature observations from piles influenced by strain

In order to determine whether the temperature measurements obtained from the FOTC are affected by mechanical strains, the observed temperature data during the static pile loading test in tension is analysed and compared to the temperature measurements from the VWSG thermistors. This analysis aims to assess any potential correlation between temperature variations and mechanical strain during the static pile loading test. An example of this comparison is provided for test pile 8, as illustrated in Figure 103. Furthermore, information regarding the temperature development along the length of all test piles can be found in Appendix F.4.

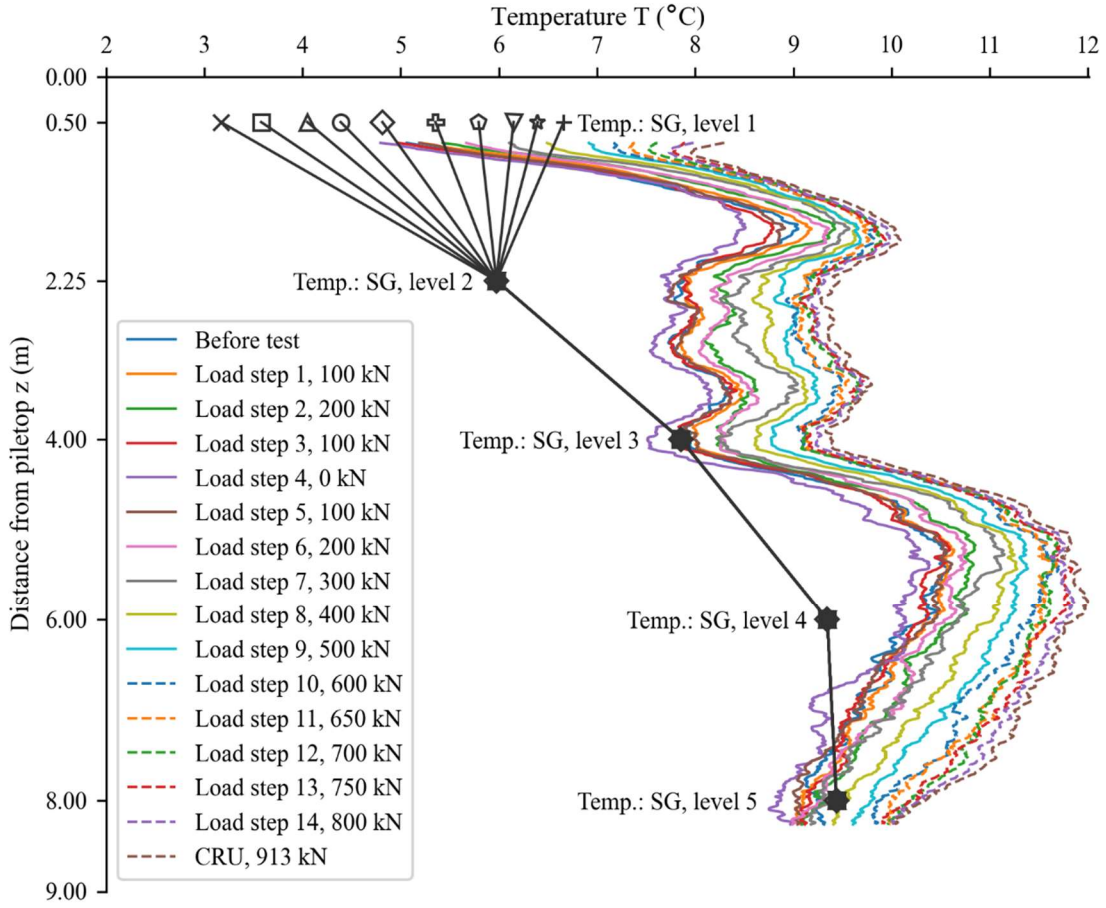

Figure 103: Temperature development along the length of test pile 8 at the inception of each load step during the static pile loading test, focusing on the data obtained from the fibre optic temperature cables (FOTC). Load phase 1 and 2 is shown with solid lines, smaller load steps in phase 2 is shown with dotted lines. Additionally, the temperature development recorded by the thermistors in the vibrating wire strain gauges (VWSG thermistors) is represented by the black lines.

Figure 103 provide insights into the temperature variations along the length of test pile 8 during different load steps of the static pile loading test. During the load testing, it is observed that the temperatures measured by the FOTC exhibit a rise in temperature with increasing load during load phase 1 (load step 0-2). Conversely, the temperatures decrease with decreasing load in the unloading phase of load phase 1 (load step 2-4). Subsequently, the temperatures rise again with increasing load during load phase 2 (load step 4-14 and CRU). These temperature variations indicate that the FOTC measurements are influenced by the mechanical strain experienced by the test piles.

The change in temperature between load steps appears to be relatively constant with depth, which does not indicate a direct influence of mechanical strain as it would typically decrease with depth. There seems to be a consistent offset for a given load level, except at the top and bottom. However, this is believed to be due to the presence of a loose gel-filled core inside the FOTC, which is designed to eliminate the effects of strain and thus only experiences an average impact along the cable.

As a result, the temperatures measured by the FOTC are considered invalid and unsuitable for temperature correction of the raw strain data measured by the FOSC. Consequently, the temperature data obtained from the VWSG thermistors is used instead to determine the mechanical strains, accounting for thermal influence, from the raw strain data measured by the FOSC. This is achieved by employing linear interpolation between different strain gauge levels.

7.3.3 Validation of cross-sectional temperature variation during installation and curing

In this section, the temperature variation across the cross-sectional areas is examined to investigate the feasibility of using linear interpolation between the average temperatures measured by the VWSG thermistors to determine the mechanical strains, accounting for thermal influence, from the raw strain data measured by the FOSC during installation and curing.

The concern arises from the fact that the VWSG thermistors are not located at the same cross-sectional positions as the FOSC, which can significantly impact the accuracy of the corrections made. This is particularly important as even a small temperature change of 1°C can lead to a correction of the axial load by approximately 300 kN, as explained in section 7.3. Therefore, it is vital to evaluate the potential errors that could arise from using linear interpolation across different cross-sectional locations to correct for thermal influence.

Dataloggers were used to record temperature measurements from the VWSG thermistors, which were attached to the reinforcement cages placed on the ground at the outdoor test site in Hinge. These measurements were initiated and continued throughout the installation of the reinforcement cages and the casting of the test piles.

The temperature measurements from the FOTC were carried out in the same setting. The FOTC measurements were performed with the reinforcement cages positioned on the ground, suspended in the borehole, and resting on the bottom of the borehole. It is important to note that the reinforcement

cages were not completely free hanging in the borehole, as the guide bars attached to them made contact with the casings.

As an example, the temperature measurements for test pile 1, which exhibit the highest cross-sectional temperature variation at the Hinge test site, are presented in Figure 104 and Figure 105. More detailed temperature measurements for all test piles can be found in Appendix F.5.

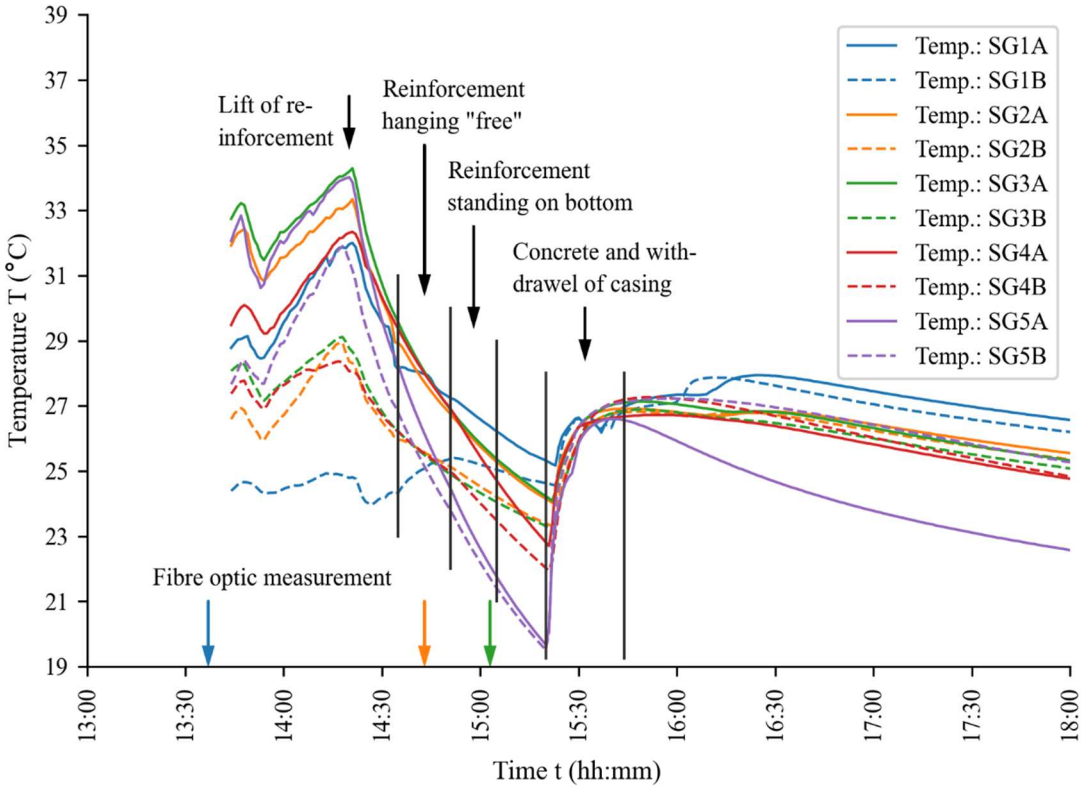

Figure 104: Temperatures recorded by the thermistors in the vibrating wire strain gauges (VWSG thermistors) during the installation of the reinforcement cage in the borehole for test pile 1 on the 20th of August 2019.

Figure 104 demonstrates that the temperatures exhibit a drop as the reinforcement cage is lifted from the ground. This decline can be attributed to the cooling effect from the surrounding ambient air temperature. As the reinforcement cage is then lowered into the relatively cooler and shady borehole, the temperatures continue to decrease. However, once the concrete is poured into the borehole, the temperatures begin to rise due to the influence of the higher temperature of the wet concrete.

It is worth noting that the temperature drop is most significant for test pile 1. This test pile had its reinforcement cage installed in the afternoon when the temperature was at its highest, ranging between 24 and 34 °C (as indicated in section 7.3.2) before the installation took place. In contrast, test piles 2-5 were installed around noon, with temperatures between 22 and 26 °C prior to the installation, while test piles 6-8 were installed in the morning and subjected to the lowest temperatures between 15 and 17 °C. Concerning the last group of test piles, the measured temperatures exhibit a more even distribution during the installation of the reinforcement cage into the borehole

Previously, it was observed that the cross-sectional temperatures and temperature variations along the length of the test piles were uneven when the reinforcement cages were placed on the ground at the outdoor test site in Hinge. This unevenness was primarily due to the absence of shading for the test piles, resulting in direct exposure to sunlight and partial shading by objects like tufts of grass or sand (as mentioned in section 7.3.2).

As the reinforcement cages were lowered into the borehole, the uneven temperature distribution across the cross-section and along the length of the test piles started to reduce. However, due to insufficient time for temperature equalization, some degree of unevenness persisted during the installation of the test piles. This can be observed in Figure 105.

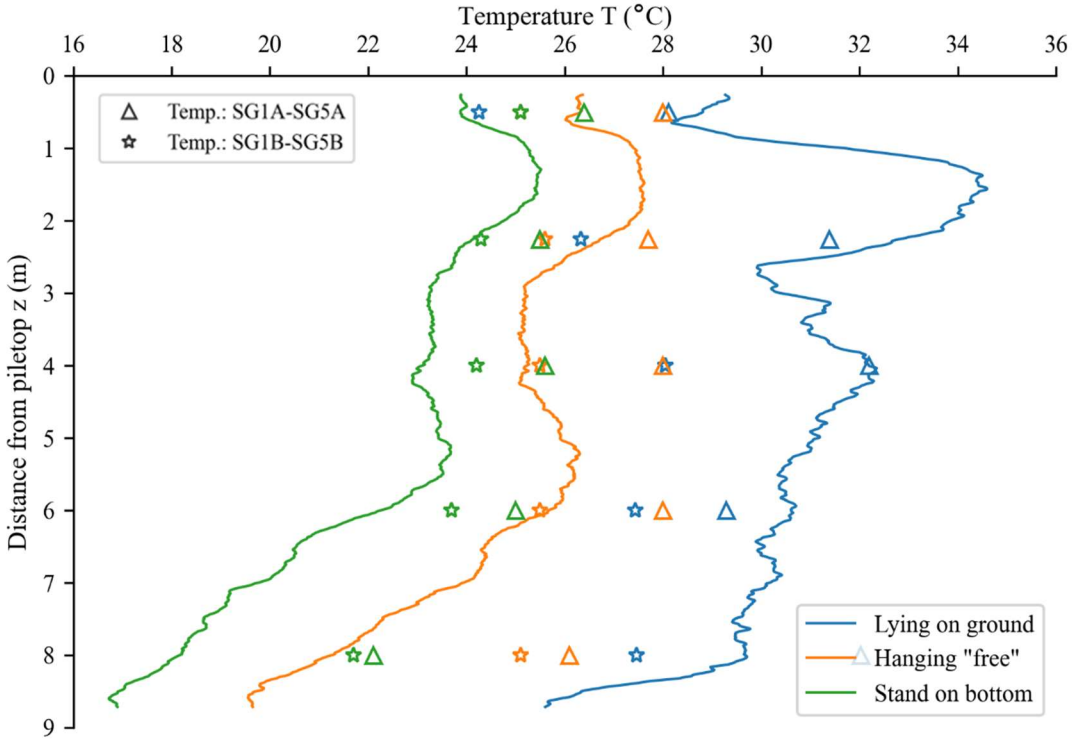

Figure 105: Temperatures recorded by the fibre optic temperature cables (FOTC) and the thermistors in the vibrating wire strain gauges (VWSG thermistors) during the installation of the reinforcement cage in the borehole for test pile 1 on the 20th of August 2019. Solid lines (blue, orange and green) represent the fibre optic temperature cable (FOTC), and symbols represent the thermistors in the vibrating wire strain gauges (VWSG thermistor).

Based on the observations, it can be concluded that a linear interpolation between average temperatures measured by the VWSG thermistors is not appropriate for determining the mechanical strains, accounting for thermal influence, from the raw strain data measured by the FOSC during installation and the early stages of curing. This is because the temperatures have not yet equalized throughout the cross-sectional area, rendering the linear interpolation method unsuitable for accurate corrections.

Regrettably, due to the lack of temperature equalization during installation and the early stages of curing, it is not possible to make accurate corrections for temperature effects during this period.

7.3.4 Main observations from temperature measurements

The temperature measurements obtained from the fibre optic temperature cables (FOTC) show a correlation between increasing load and rising temperatures, as well as decreasing load and falling temperatures. This relationship indicates that the temperature measurements are influenced by mechanical strain in the test piles.

Therefore, the temperatures measured by the FOTC are deemed invalid and unsuitable for accurately correcting the strain data measured by the fibre optic strain cables (FOSC). Consequently, the temperature data obtained from the vibrating wire strain gauges (VWSG) is used instead to determine the mechanical strains, accounting for thermal influence, from the raw strain data measured by the FOSC. This is achieved by employing linear interpolation between different strain gauge levels.

Utilizing a linear interpolation between the average temperatures measured from the thermistors in the vibrating wire strain gauges (VWSG thermistors) will yield more accurate results compared to not correcting the raw strain data for temperature or using temperature measurements affected by mechanical strain for temperature correction. However, it is important to acknowledge that linear interpolation is an estimation, and determining the precise level of zero thermal induced strain between the strain gauge levels can be challenging.

It is crucial to note that during the installation of the test piles, it is not possible to determine the mechanical strains, accounting for thermal influence, from the raw strain data measured by the FOSC. This is primarily due to the observed uneven temperatures across the cross-section and the fact that the FOSC are not located at the same cross-sectional positions as the VWSG.

7.4 Performance of Rayleigh based fibre optic strain cables

In this section, the focus is on analysing the performance of the Rayleigh-based fibre optic strain cables (FOSC). The credibility of the FOSC is evaluated by comparing the average strain measurements obtained from two different methods: the vibrating wire strain gauges (VWSG) and the FOSC.

Additionally, an investigation is conducted to assess the non-uniform pile stiffness of the test piles and examine the cross-sectional distribution of strains. These analyses provide insights into the variations in stiffness along the pile length and whether the applied load is vertical or if the load on the test piles is biased.

Furthermore, the axial pile stiffness, axial load distribution, and unit shaft resistance are determined using data from the FOSC. These results are then compared to the values obtained from the VWSG and the cone penetration test (CPT) profiles obtained from the test site in Hinge. This comparison allows for an assessment of the consistency and accuracy of the FOSC measurements.

7.4.1 Pre-tensioning

According to good practice recommended by Kechavarzi et al. (2016), it is advisable to pre-tension the FOSC to an amount exceeding the expected compressive strain. However, in the case of the test piles, which were subjected to static pile loading tests in tension, there was no anticipated compressive strain.

Nevertheless, to keep the option open for potential future compressive testing on the test piles, the FOSC were pre-tensioned to approximately 1000 $\mu\varepsilon$. This pre-tensioning between two known locations along the test pile also serves to align the FOSC relative to the length of the test piles. The specific locations of the FOSC relative to the test pile can be determined after attaching the FOSC to the reinforcement cage by applying pressure, heating, or cooling to the desired location while simultaneously recording the signal from the FOSC.

An example of the pre-tensioning process is provided in Figure 106 and Figure 107, showcasing FOSC A and FOSC B from test pile 8, respectively.

In the case of test pile 8, it was observed that the pre-tensioning slightly loosened within the first 6 hours, during which strain measurements were conducted at the indoor storage facility. However, it is challenging to accurately determine the extent of the pre-tensioning when the reinforcement cages were placed on the ground at the test site in Hinge (day 5 on site). The uneven temperatures across the cross-section and along the length of the test piles make temperature correction unreliable, as mentioned in section 7.3.3.

These observations regarding the pre-tensioning and the challenges in temperature correction apply not only to test pile 8 but also to the remaining test piles (test pile 1-7), as outlined in Appendix I.2.

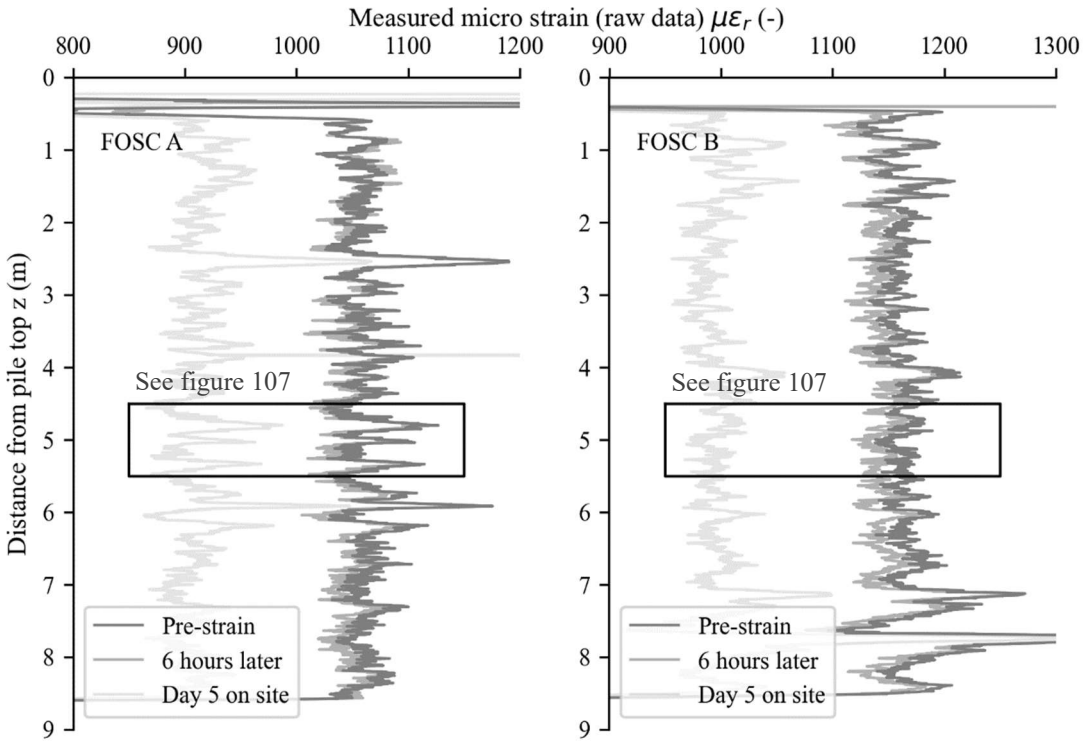

Figure 106: Development of pre-tensioning within the first 6 hours at the indoor storage facility as well as with the reinforcement cage on the ground at the test site in Hinge (day 5 on site).

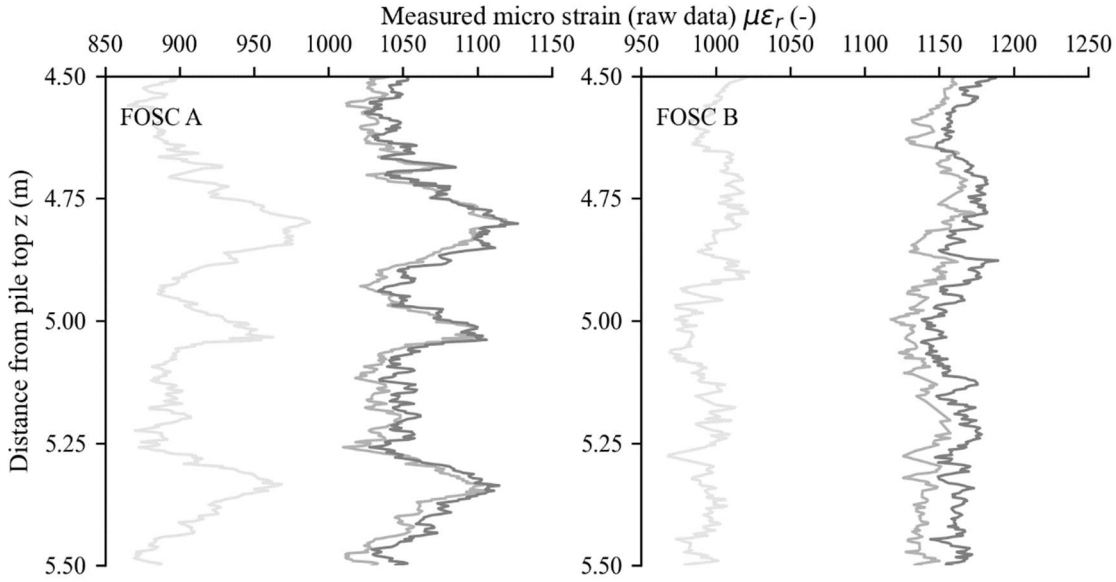

Figure 107: Closer examination of the strain development along the length of test pile 8, as measured by the fibre optic strain cables (FOSC), reveals that the pre-tensioning experiences a slight loosening within the initial 6-hour period. However, it should be noted that the subsequent strain measurements with the reinforcement cage on the ground at the test site in Hinge (day 5 on site) are influenced by irregular temperature changes across the cross-section and along the length of test pile 8. For an explanation of signatures, refer to Figure 106.

The slight loosening of the pre-tensioning over time could potentially impact strain measurements taken during the early stages until the concrete has fully cured. However, it is difficult to ascertain the exact effect due to the presence of uneven temperatures across the cross-section and along the length of the test piles, which makes temperature correction unreliable.

Nonetheless, it should be noted that strain measurements obtained during static pile loading tests, where the measurements are zeroed immediately before initiating the tests, will not be affected by the loosening of the pre-tensioning. These measurements can be considered reliable as they are not subject to the uncertainties associated with temperature correction.

7.4.2 Filtering and smoothing of data from FOSC

The initial step in processing the data from the FOSC involves filtering by removing any NaN (Not a Number) values found in the raw data, as described in section 7.3.1 for the fibre optic temperature cables (FOTC). Following this, the data is further filtered to remove outliers. Outliers can be easily identified as they have significantly larger or smaller values compared to the actual strain measurements. For instance, FOSC A from test pile 8, load step 14, is examined in Figure 108 to illustrate this process.

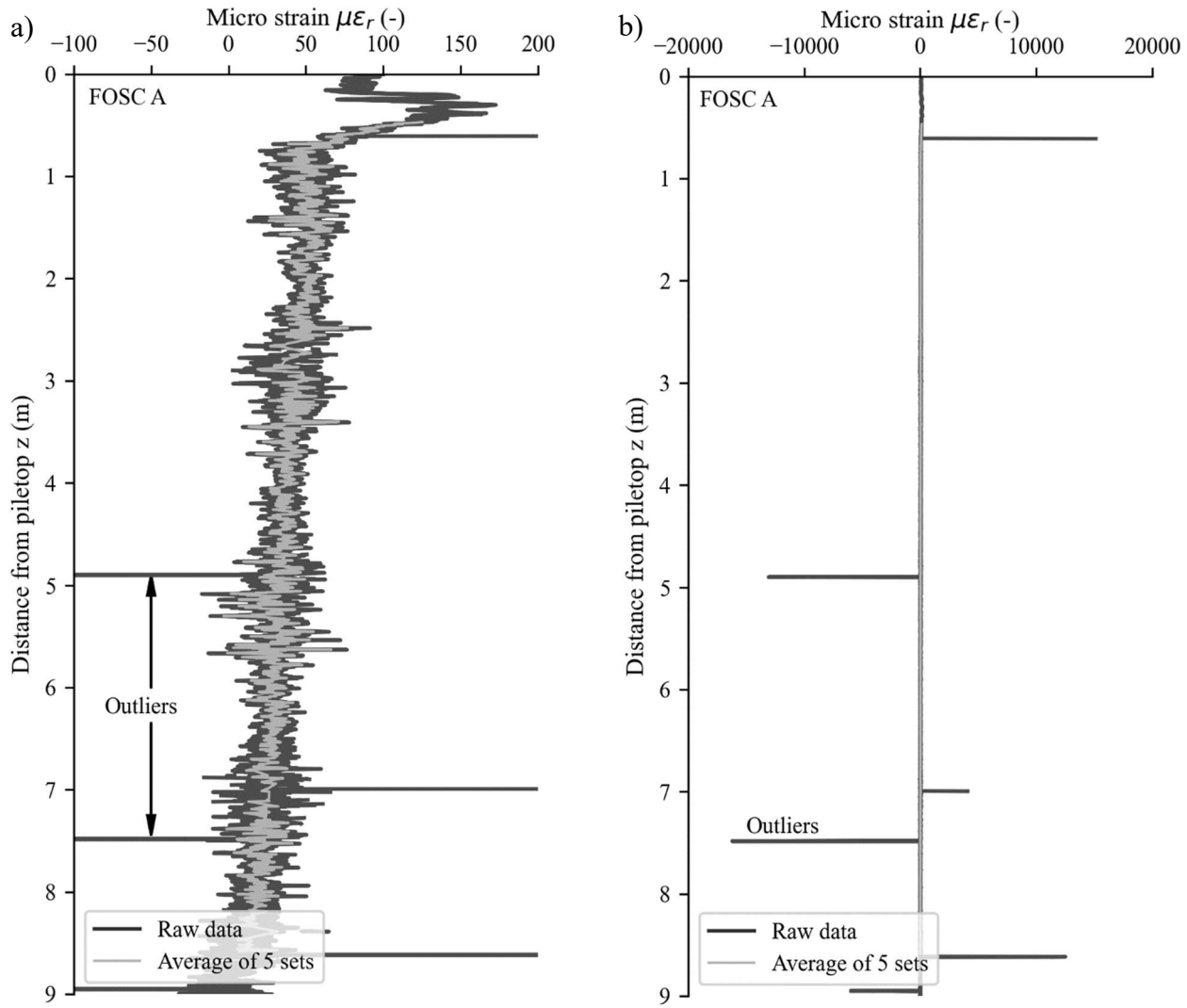

Figure 108: Strain measurements along the length of test pile 8 during load step 14, focusing on strain intervals of (a) -100με to 200με and (b) -20,000με to 20,000με.

In the example presented in Figure 108, the actual strains are observed to range approximately from -50 $\mu\varepsilon$ to 175 $\mu\varepsilon$. Conversely, the outliers exhibit negative values between -6000 $\mu\varepsilon$ and -16000 $\mu\varepsilon$, as well as positive values between 4000 $\mu\varepsilon$ and 15000 $\mu\varepsilon$. These outlier strain values are clearly unrealistic and are therefore removed by discarding all data below -100 $\mu\varepsilon$ and above 200 $\mu\varepsilon$. This filtering process helps to ensure that only reliable and valid strain data is used for further analysis.

In addition, the average value of the filtered data obtained from FOSC A is determined over a duration of 5 seconds, with a frequency of 1 Hz. This corresponds to taking an average of 5 measurements, and the results are represented by the light grey line in Figure 108 (a).

The average value is specifically calculated for the pre-tensioned section of FOSC A, which is located approximately 0.5 m from the top and bottom of the test pile, respectively. It is important to note that additional data from the upper 0.5 m of the test piles cannot be included in the analysis due to the attachment (sanding pad) used for pre-tensioning the FOSC as well as the embedded passive cable, as shown in Figure 109 (a). The embedment of the passive cable serves to protect the splice between the passive and active cables.

Furthermore, it is not feasible to incorporate additional data for the lower 0.5 m of the test piles. This limitation arises because the attachment (sanding pad) used for pre-tensioning the FOSC is embedded in the test piles. This embedded attachment is followed by a transition zone that transforms the direction from vertical to horizontal, facilitating the establishment of a loop at the bottom of the test pile. Please refer to Figure 109 (b) for a visual representation of this configuration.

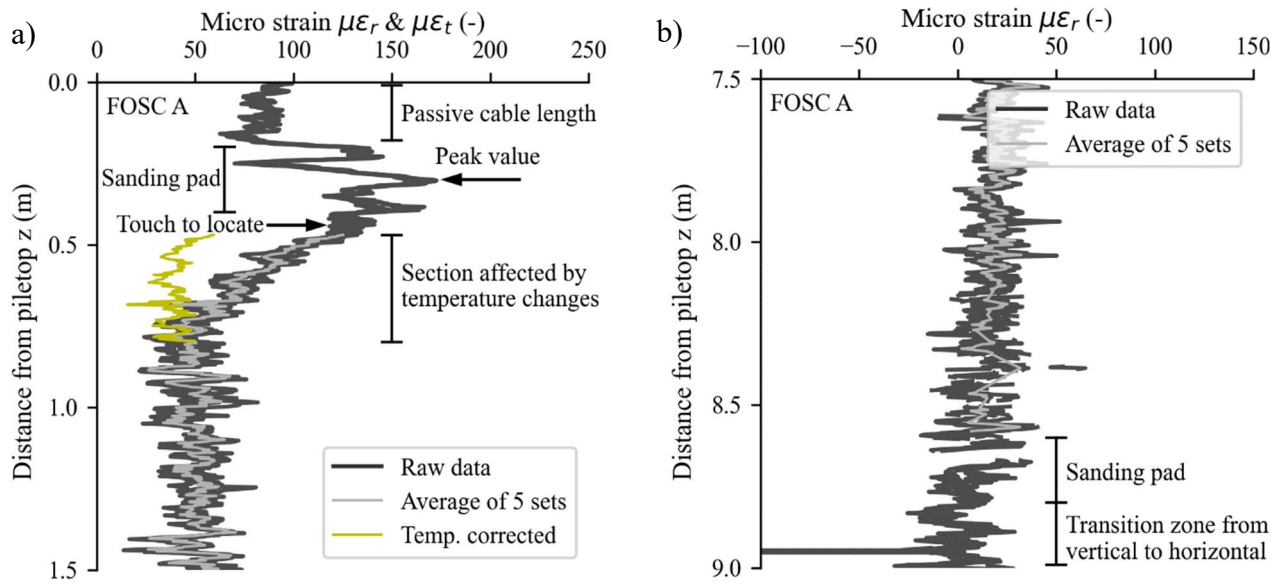

Figure 109: Strains from FOSC A in the (a) upper and (b) lower part of test pile 8 during load step 14.

Observing Figure 109 (a), it is evident that a significant peak in strain values is observed in the upper part of the test pile. This peak corresponds to the location of the sanding pad used for attaching the pre-tensioned FOSC. Considering the position of the sanding pads and the observed peak values, it is likely that these peak values are a result of the attachment process of the pre-tensioned FOSC.

However, the section immediately below the sanding pad still displays heightened strain values. This continued elevation in strain values is likely due to temperature changes. Visually assessing the affected section, it is estimated to be around 0.8 m (0.3 m below ground level). In the calculation of thermally compensated strains (mechanical strains) measured by the FOSC, temperature data from the VWSG are utilized. Linear interpolation is performed between VWSG level 1 and the level of zero thermal induced strain between VWSG level 1 and 2, as explained in section 7.3.4.

In Figure 109 (b), there is no apparent peak value observed near the pile base. This absence of a peak value is likely attributed to the fact that the test piles were subjected to static pile loading tests in tension. As a result, it is expected that the load at the pile base is zero and significantly diminished within a distance of less than 0.5 m from the pile base. Therefore, no significant strain peaks are observed in close proximity to the pile base in this scenario.

In order to ultimately focus on the unit shaft resistance in the soil-pile interface, it is necessary to smooth the data and eliminate the impacts caused by the fibre/concrete interaction. Although the FOSC provide valuable information regarding concrete strains and can help identify issues such as concrete cracks, the main objective of this study is to analyse the unit shaft resistance. Therefore, data smoothing is crucial to eliminate any confounding effects originating from the fibre/concrete interaction.

To smooth the data obtained from the FOSC for analysis, a moving average technique is applied along the length of the test piles. The smoothing process, while effective in reducing noise and improving the readability of the data, has the drawback of removing some of the fine details at the top and bottom of the pile. This loss of data is due to the nature of the smoothing algorithm, which uses neighbouring data points to calculate the average values.

In order to determine the appropriate length for the moving average, the strain data is presented using different moving average lengths of 100, 200, and 400 readings for FOSC A from test pile 8, specifically during load step 14 of the static pile loading test. The results of these moving averages are visualized in Figure 110 and can be examined to identify the most suitable length for achieving the desired level of smoothing in the strain data.

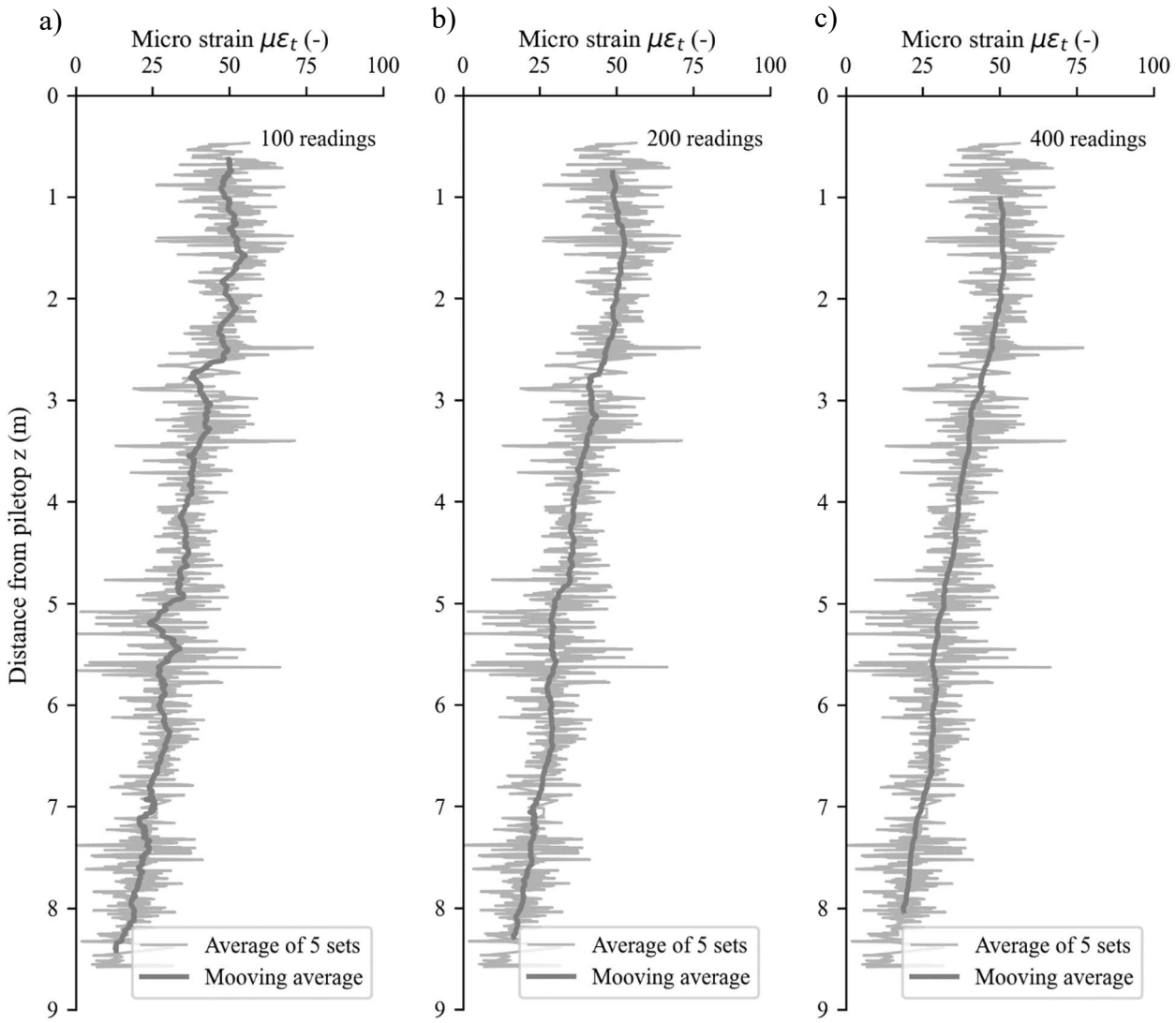

Figure 110: Thermally compensated (mechanical) strain data presented with a moving average of (a) 100, (b) 200 and (c) 400 readings for FOSC A from test pile 8, load step 14 during static pile loading test.

Figure 110 indicates that a moving average of either 100, 200 or 400 readings is effective in smoothing the strain data. However, it should be noted that as the smoothed strain data is used for determining axial loads along the length of the test piles, irregularities become more prominent, as depicted in Figure 111. The trade-off between smoothing the data and preserving the fine details becomes more apparent when the strain data is utilized for analysis purposes such as determining axial loads.

Based on Figure 111, it is evident that a moving average of 400 readings or approximately 1.04 m is suitable for smoothing the strain data. This finding aligns with the results reported by Kania et al. (2020) for Rayleigh-based FOSC used in bored piles. Unfortunately, a direct comparison with moving averages used for Brillouin-based FOSC is not feasible. This is due to the significantly different spatial resolution, which is at least 0.5 - 1.0 m for Brillouin-based FOSC, as opposed to the finer resolution of 5.2 mm utilized for Rayleigh-based FOSC in this PhD project and by Kania et al. (2020).

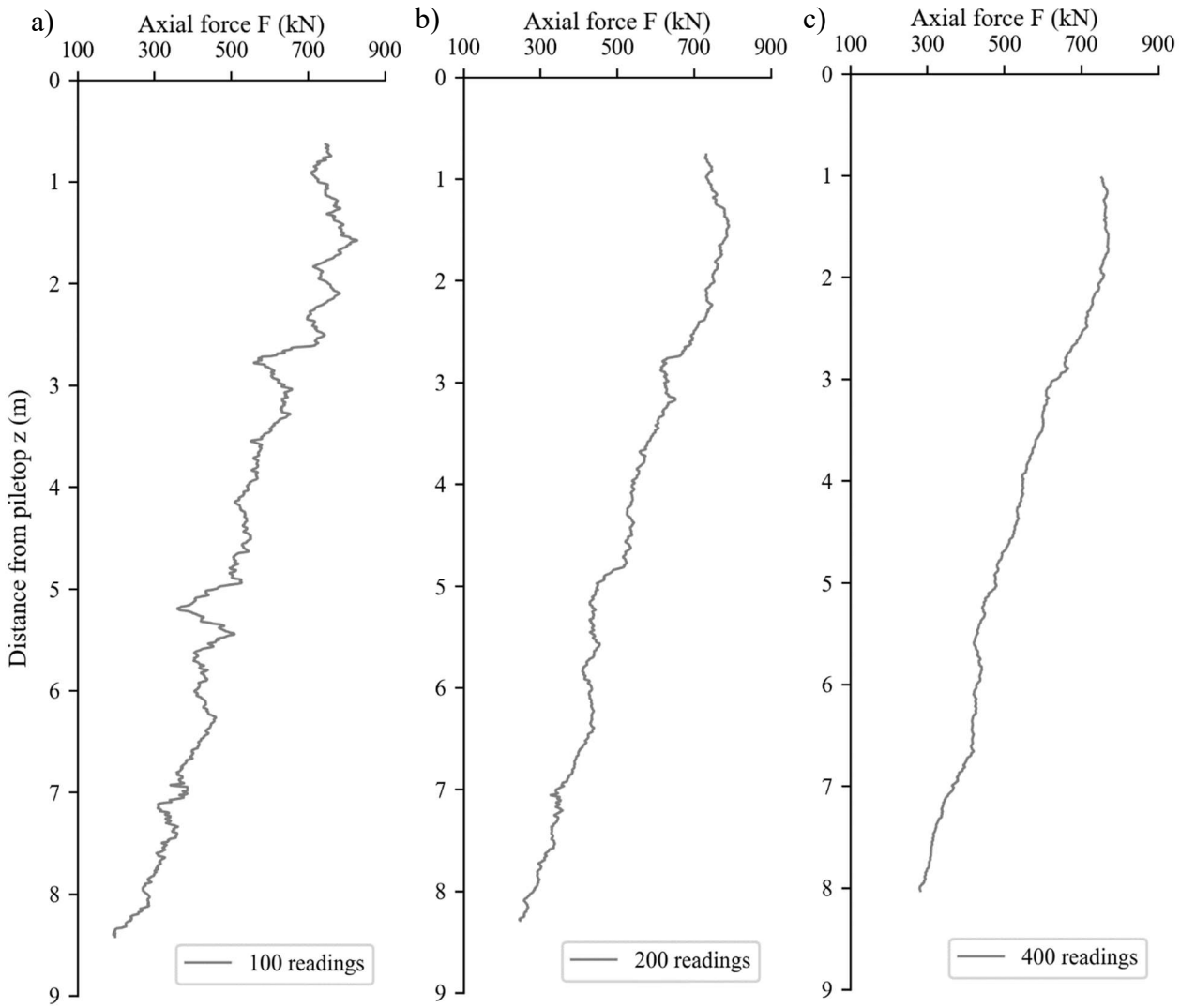

Figure 111: Axial load along test pile 8 during load step 14 in the static pile loading test with a moving average of (a) 100, (b) 200 and (c) 400 readings.

7.4.3 Comparison of strain measurements from FOSC with VWSG

The strain measurements of opposing strain sensors from FOSC are compared with VWSG by utilizing the internal strain profile of the test piles obtained during the static pile loading tests. The measured strains are then interpreted and adjusted for thermal effects, as outlined in sections 5.3 and 5.4. Positive values of ε represent tensile strain, while negative values indicate compressive strain.

To determine the internal strain development along the length of the test piles, the average value at each strain gauge level (SG, level 1-5) is used for the VWSG over the duration of each maintained load step. For the FOSC, a manual measurement is taken immediately after reaching each maintained load step. Creep is only observed at the upper strain gauge level (SG, level 1) for the VWSG in test pile 1 and 4, as indicated in Appendix H.3. Furthermore, creep is not expected for the FOSC. This is verified during the final maintained load step of the static pile loading tests, as shown in Appendix I.3.

Please refer to Figure 112 - Figure 119 for the internal strain profiles during load phases 1 and 2.

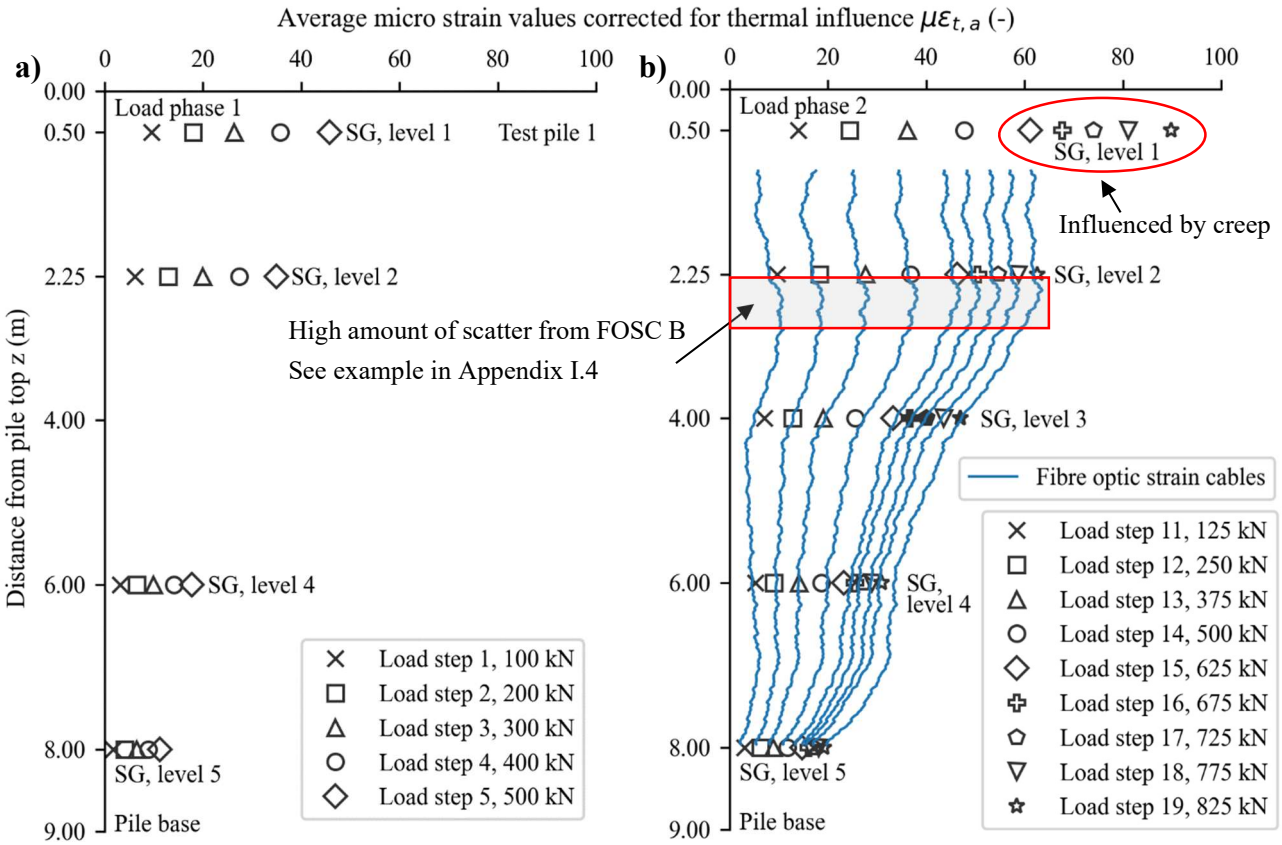

Figure 112: Strain development along the length of test pile 1 in (a) load phase 1 and (b) load phase 2.

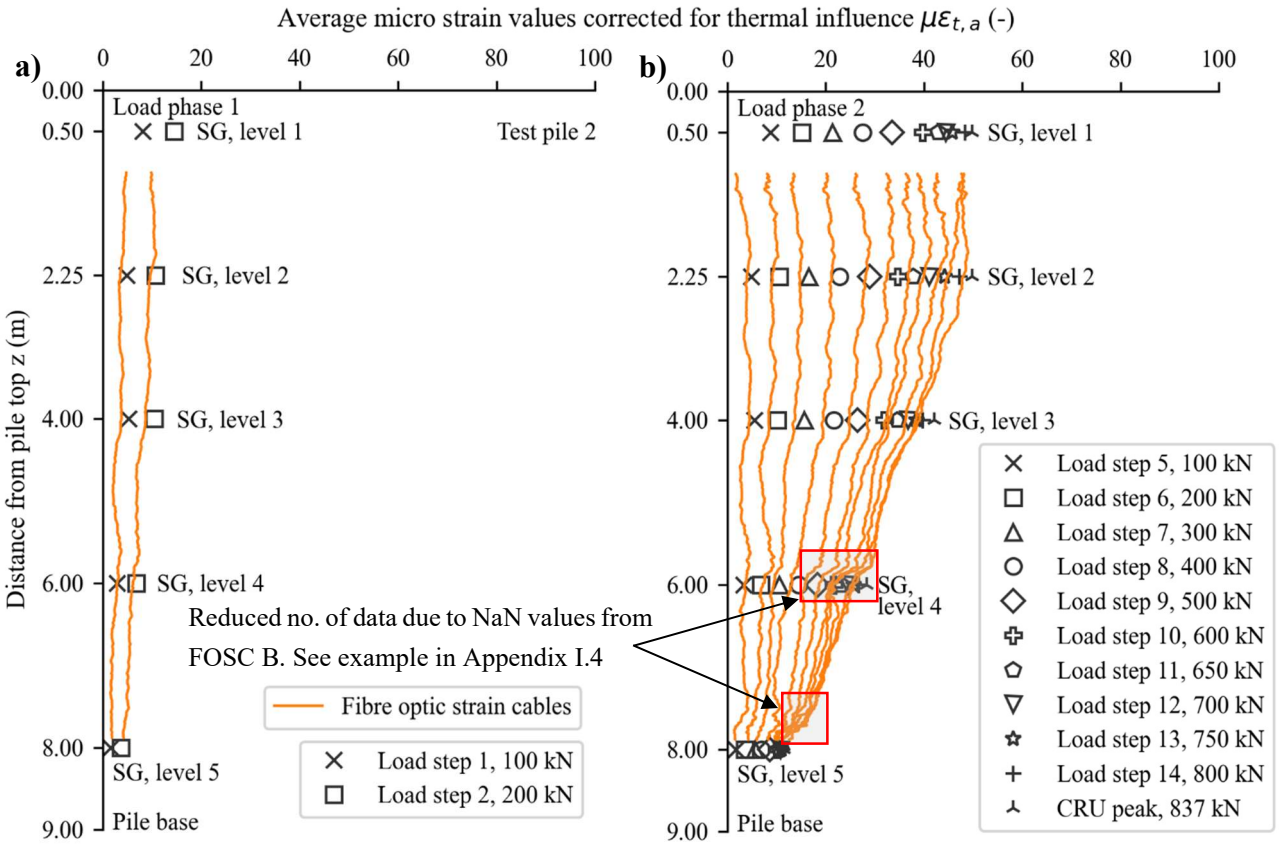

Figure 113: Strain development along the length of test pile 2 in (a) load phase 1 and (b) load phase 2.

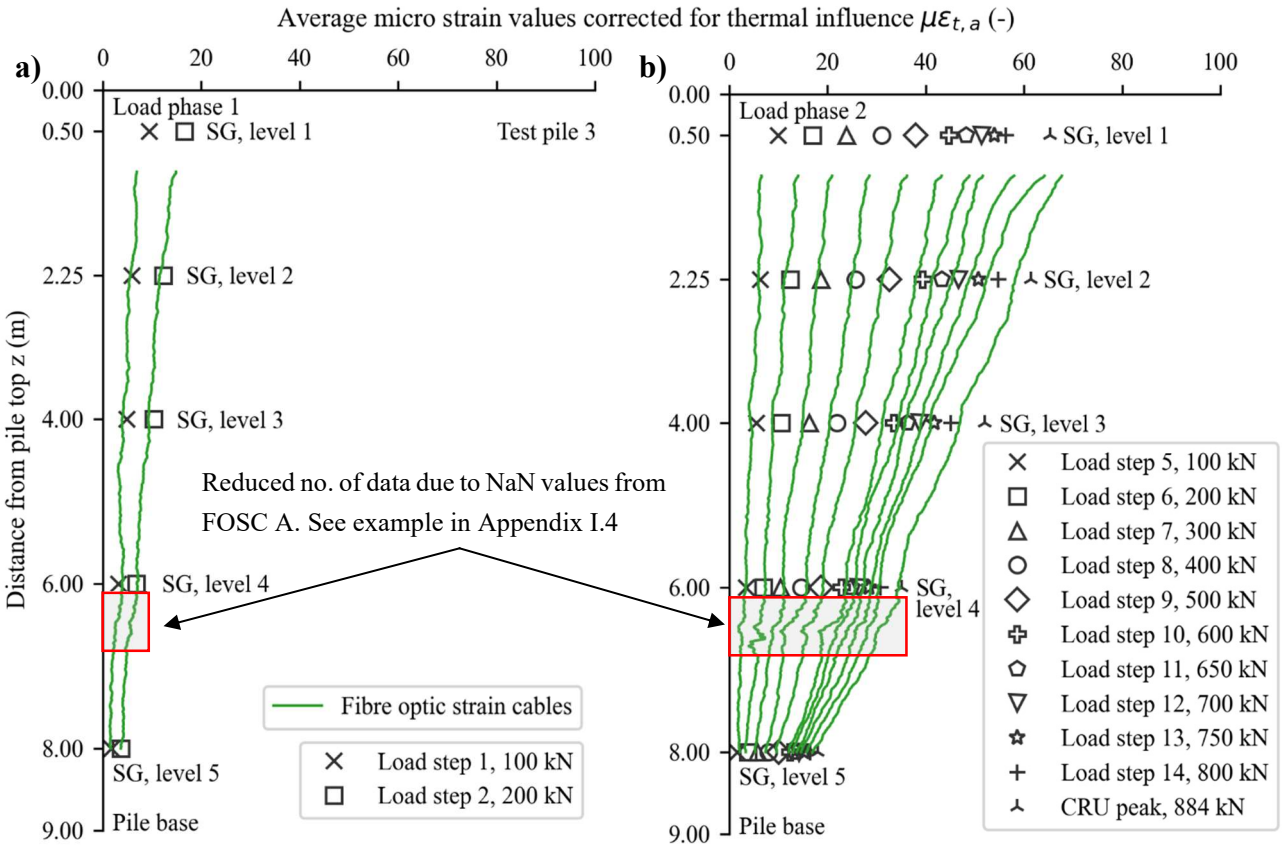

Figure 114: Strain development along the length of test pile 3 in (a) load phase 1 and (b) load phase 2.

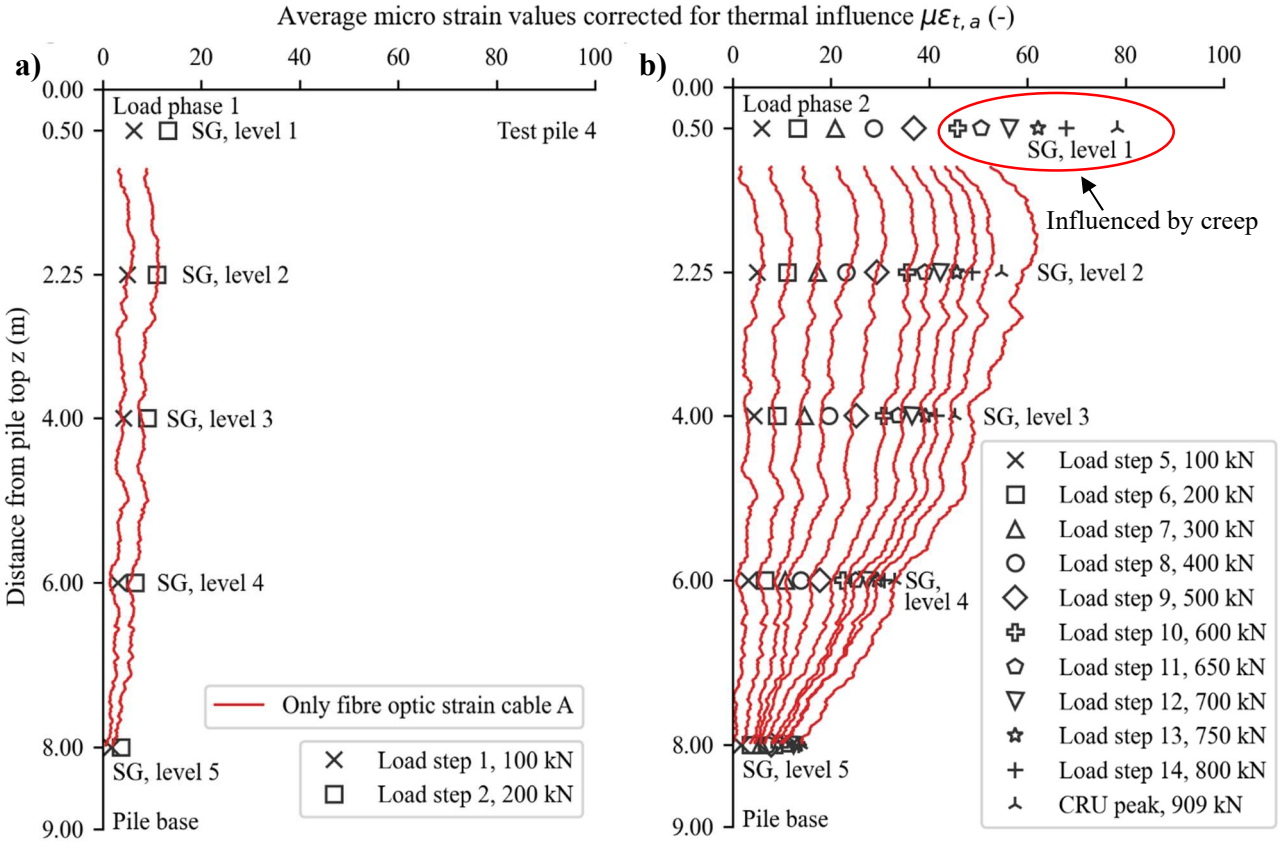

Figure 115: Strain development along the length of test pile 4 in (a) load phase 1 and (b) load phase 2.

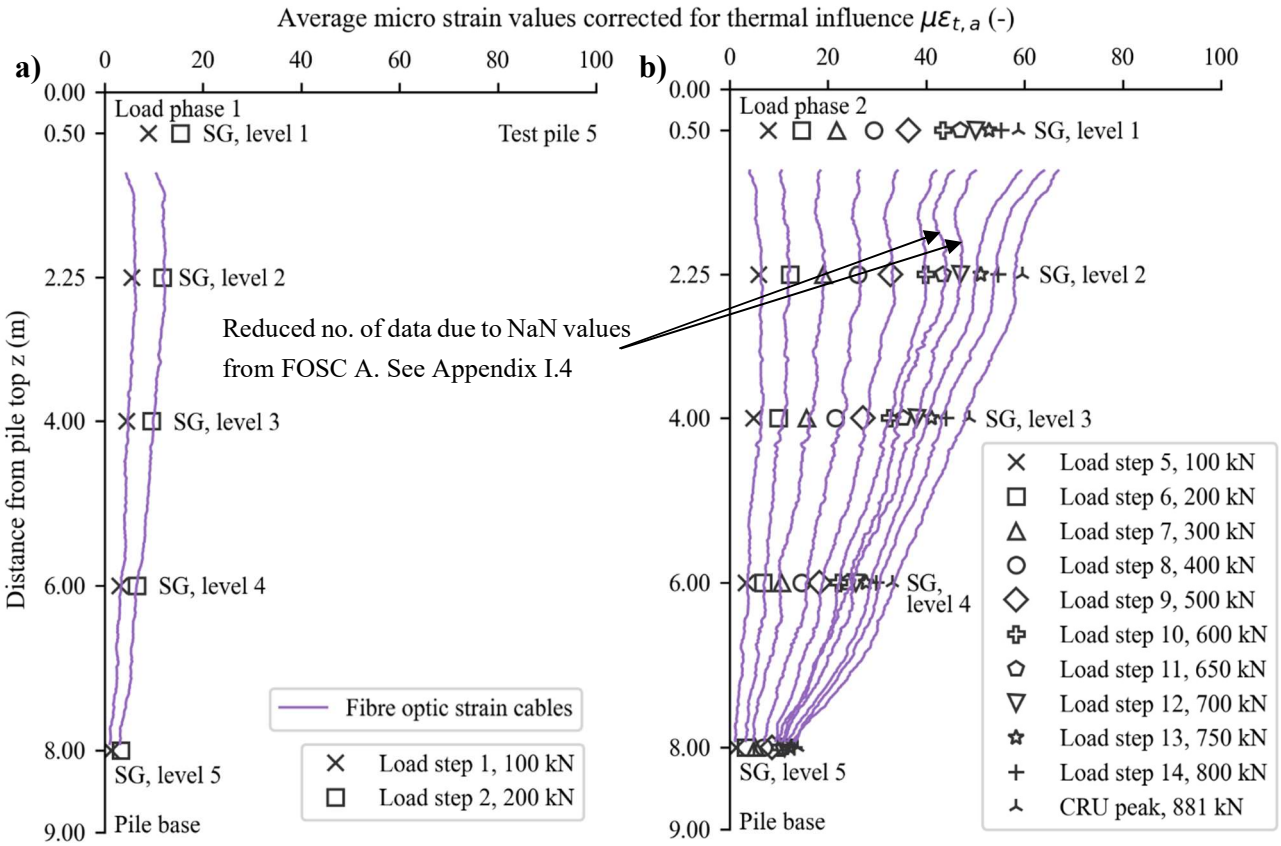

Figure 116: Strain development along the length of test pile 5 in (a) load phase 1 and (b) load phase 2.

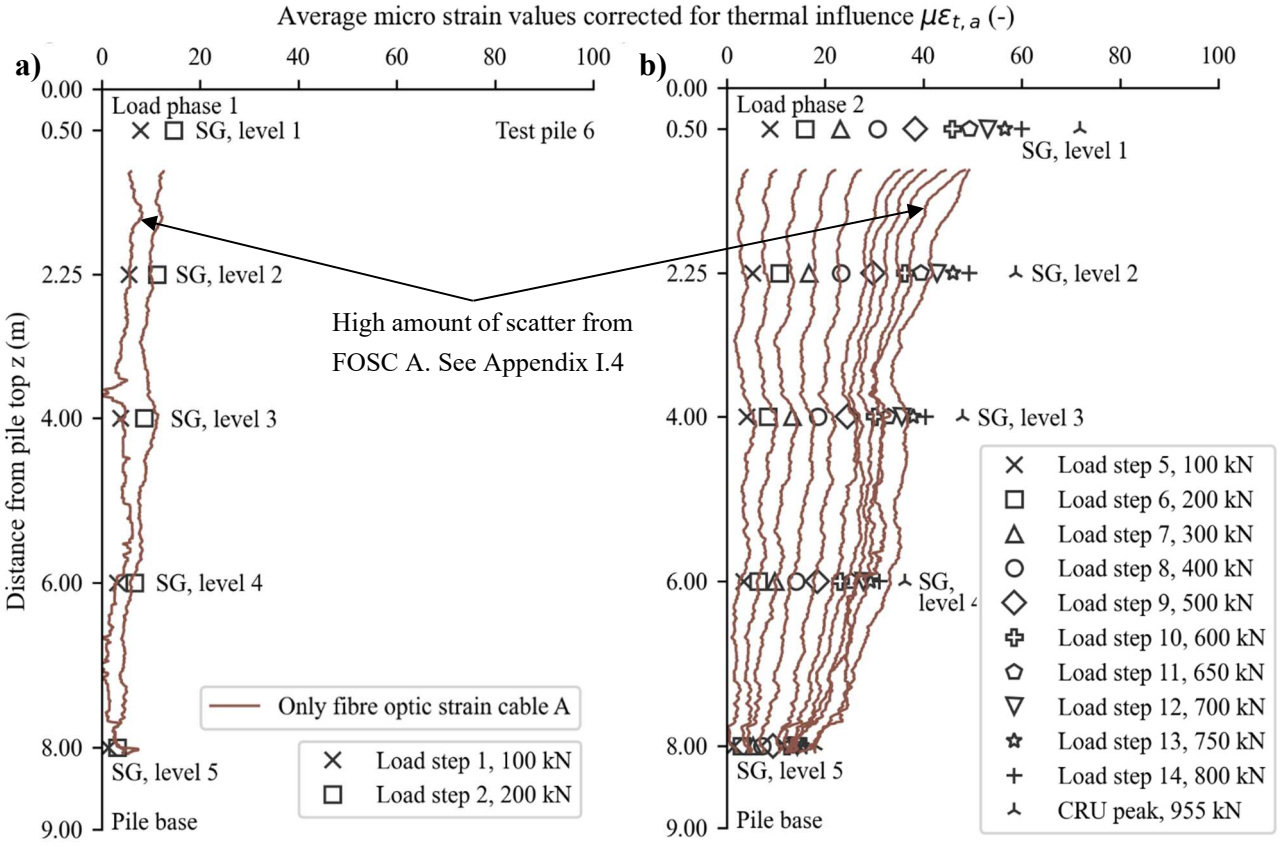

Figure 117: Strain development along the length of test pile 6 in (a) load phase 1 and (b) load phase 2.

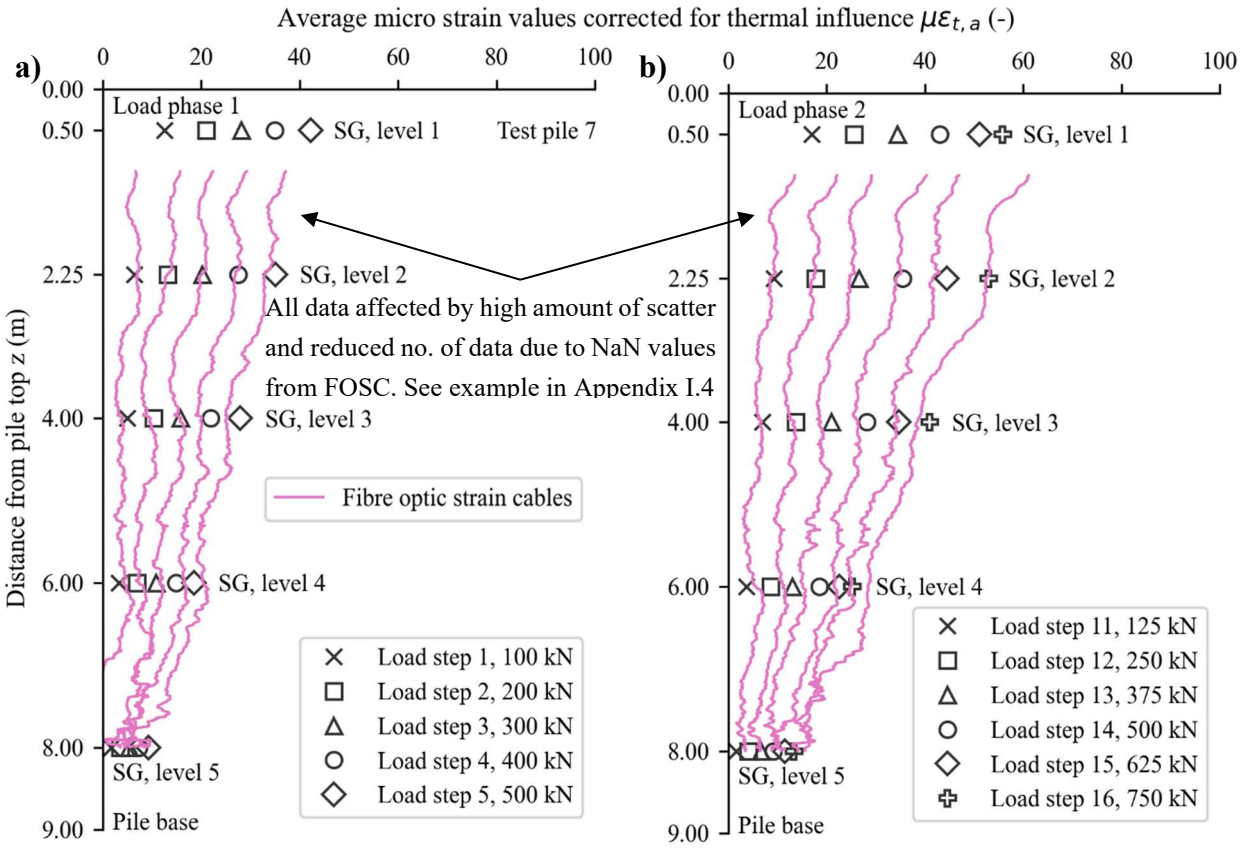

Figure 118: Strain development along the length of test pile 7 in (a) load phase 1 and (b) load phase 2.

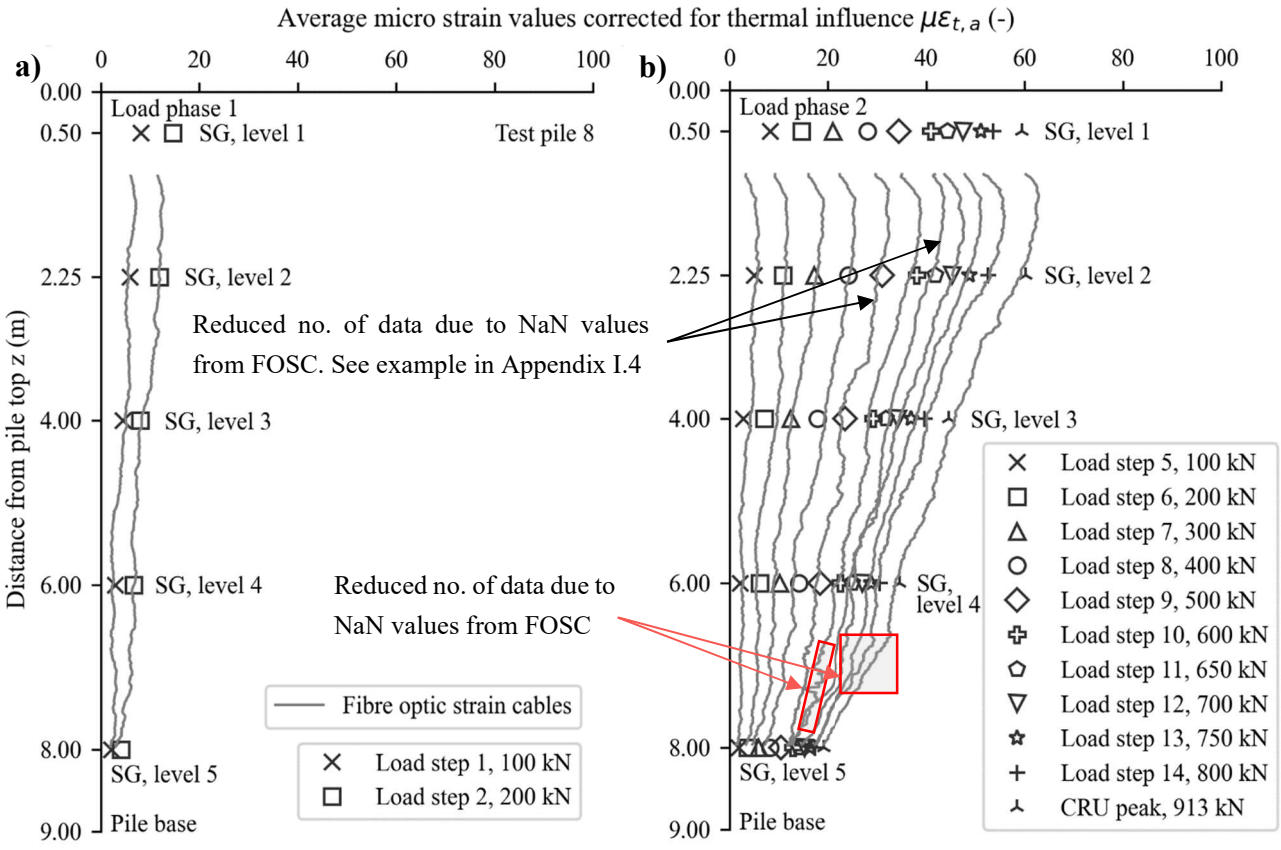

Figure 119: Strain development along the length of test pile 8 in (a) load phase 1 and (b) load phase 2.

In general, the strain measurements obtained from the FOSC demonstrate a linear relationship between the VWSG measurements. As the load increases, the inclination of the lines representing the average strain measurements with depth decreases. This observation is consistent with the notion that higher loads are being absorbed along the shaft.

During the static pile loading test for test pile 4 and 6, only fibre optic strain cable A was functional. As a result, it is not possible to determine the average strain measurements of opposing strain sensors from the FOSC for these piles. Hence, test pile 4 and 6 are excluded from further analysis in the following sections.

For test piles 1, 2, 3, and 8, a local deviation from the approximately linear relationship between the VWSG is observed. This can be attributed to either a reduced number of data points due to NaN (Not a Number) values or high levels of scatter, as illustrated in Figure 112-Figure 114 and Figure 119. The measured strains from the FOSC are affected within a range of 0.5 m above and below the corresponding section due to the use of a moving average. Additionally, a more widespread occurrence of either a reduced number of data points due to NaN values or high levels of scatter is observed along the length of test piles 5 (load step 11 + 12), test pile 6 (load step 1 + 14), and test pile 8 (load step 9 + 11), as shown in Figure 116, Figure 117 and Figure 119.

In the case of test pile 7, the stand-off cable suffered from wear and tear, resulting in strain measurements from the FOSC with significant scatter. This made it impossible to determine an average value over a period of 5 seconds with a frequency of 1 Hz (i.e., 5 measurements), as stated in section 7.4.2. As a result, the average value was determined from the 5 measurements with the highest number of data points collected during manual readings lasting 8 to 14 seconds. For fibre optic cable B, load steps 4, 5, and 6 were based on an average over 3 readings, while load step 8 was based on a single reading due to the presence of scatter. Nevertheless, there are still instances of reduced data availability due to NaN values and noticeable scatter, as depicted in Figure 118.

In test piles 1, 5, and 8, the lines representing the average strain measurements from the FOSC exhibit a nearly vertical trend between approximately 6.0 m and 7.0 m below the pile top. This specific depth coincides with the termination point of the GEWI bars and will be further examined in section 7.4.4.

Figure 120 provide an overall evaluation of the average strain measurements for SG level 2-5 of opposing strain sensors from the FOSC and the VWSG, based on the internal strain profile of test piles 1-3, 5, 7, and 8 during both load phases 1 and 2 in the static pile loading tests. The comparison between the FOSC and the VWSG is conducted by employing an approximately 1.04 m moving average along the FOSC data. It is worth noting that the length of the sister bar, to which the VWSG is attached, is 1.4 m. Considering the influence of boundary effects on the sister bars, this methodology seems to enable a fair and equitable comparison between the two measurement techniques.

However, it is not possible to compare the strain measurements of opposing strain sensors from the VWSG and the FOSC at SG level 1 due to several reasons. Firstly, no strain measurements from the FOSC are available at SG level 1 since the passive cable is embedded in the test piles to safeguard the splice between the passive and active cables, as well as the attachment of the FOSC during pre-tensioning, as described in section 7.4.2. Secondly, a moving average is applied along the length of the test piles for smoothing the FOSC data, causing the upper data point to be lower (the data point represents the midpoint of the observed section). Lastly, the strain measurements from the VWSG at SG level 1 are influenced by boundary effects and creep, as outlined in section 6.3.3 and Appendix H.3.

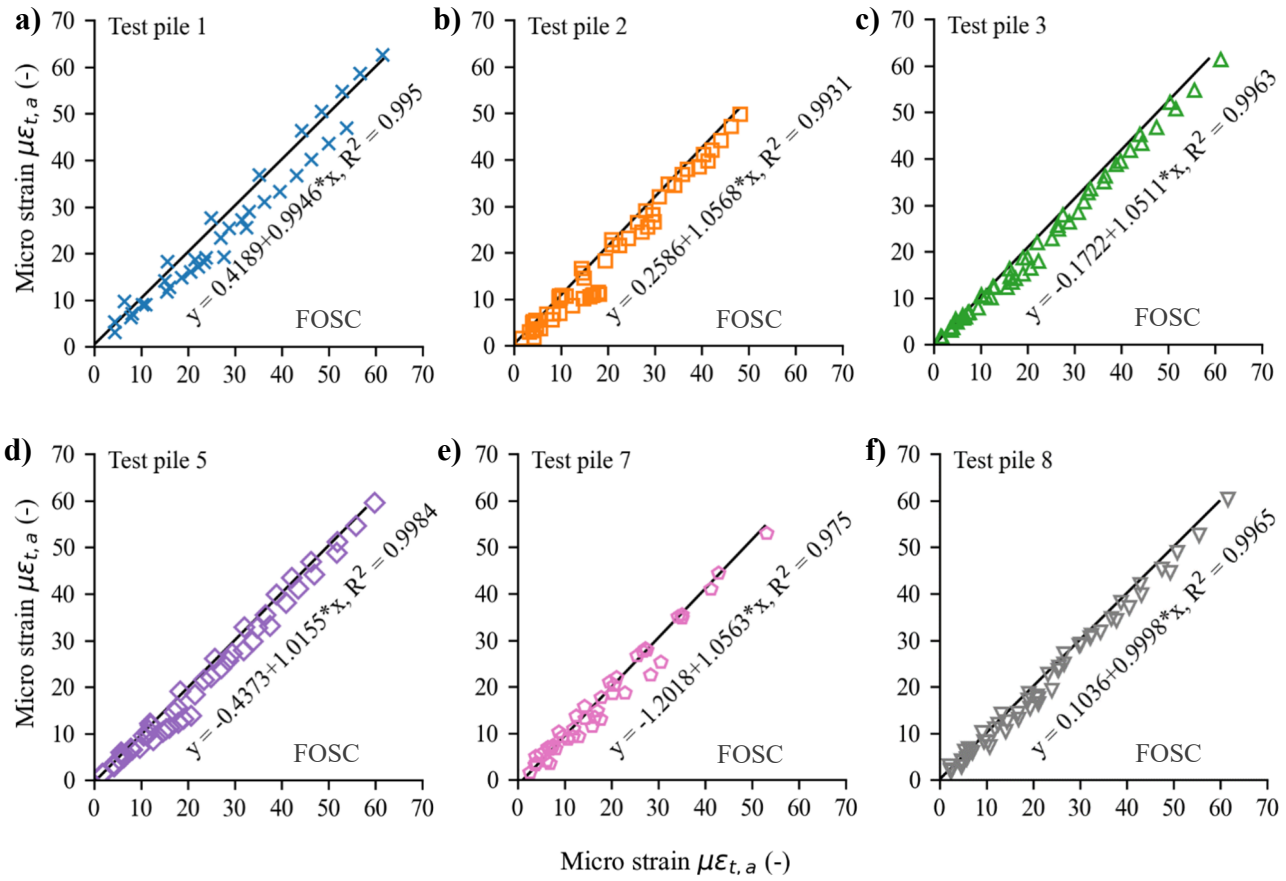

Figure 120: Average strain measurements of opposing strain sensors from the FOSC, relative to the VWSG, for test piles (a-c) 1-3, (d) 5, (e) 7, and (f) 8 during the static pile loading tests.

The average strain measurements of opposing strain sensors from the VWSG and the FOSC demonstrate a high level of agreement for test piles 1-3, 5, 7, and 8. This is evident in Figure 120, where the average strain measurements of opposing strain sensors from VWSG and FOSC are closely aligned, with R2 values ranging from 0.9931 to 0.9984 (0.975 for test pile 7, which has reduced data availability due to NaN values and significant scatter).

Therefore, it is observed that two strain sensors from either the VWSG pairs or the FOSC, installed in diametrically opposite sides, effectively differentiate between bending moments and axial loads while providing a reliable average value. Consequently, the installation of four strain sensors (two

pairs of opposing strain sensors) does not seem to significantly enhance the determination of a reliable average value.

Nevertheless, it is recommended to install four strain sensors (two pairs of opposing strain sensors) as a precautionary measure, considering the possibility of the VWSG or the FOSC breaking, which would render the data from a single sensor unusable. The additional cost of incorporating extra sensors is minimal compared to the expenses associated with conducting additional tests.

However, the utilization of the FOSC, in comparison to the VWSG, has the potential to offer more comprehensive and detailed information regarding the strain distribution along the length of the test piles. This aspect will be further explored and examined in the following sections.

7.4.4 Influence of non-uniform pile stiffness

In the case of bored piles, the presence of non-uniform pile stiffness is often attributed to variations in the amount of reinforcement steel along the length of the piles. In test pile 1, 5, and 8, a notable observation is made where the lines representing the average strain from FOSC display an almost vertical trend between approximately 6.0 m and 7.0 m below the pile top. Significantly, this aligns with the end of the 2 Ø63.5 mm GEWI PLUS bars located 6.5 m below the pile top. These GEWI bars serve the purpose of transferring the force from the hydraulic jacks to the test piles.

To effectively visualize the impact of non-uniform pile stiffness, the average strain from the FOSC is normalized at a depth of 6.5 m below the pile top, coinciding with the termination point of the 2 Ø63.5 mm GEWI PLUS bars. This normalisation is performed for the internal strain profile of test pile 1, 5 and 8 during load phase 1 and 2 in the static pile loading tests. Please refer to Figure 121 for a graphical representation of this normalization.

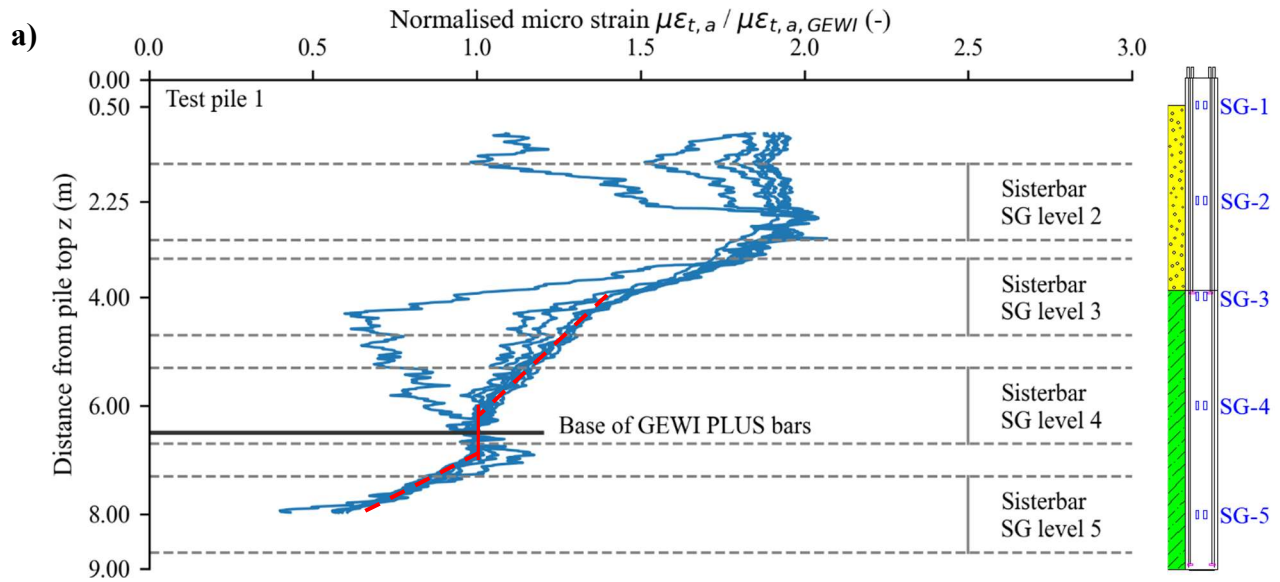

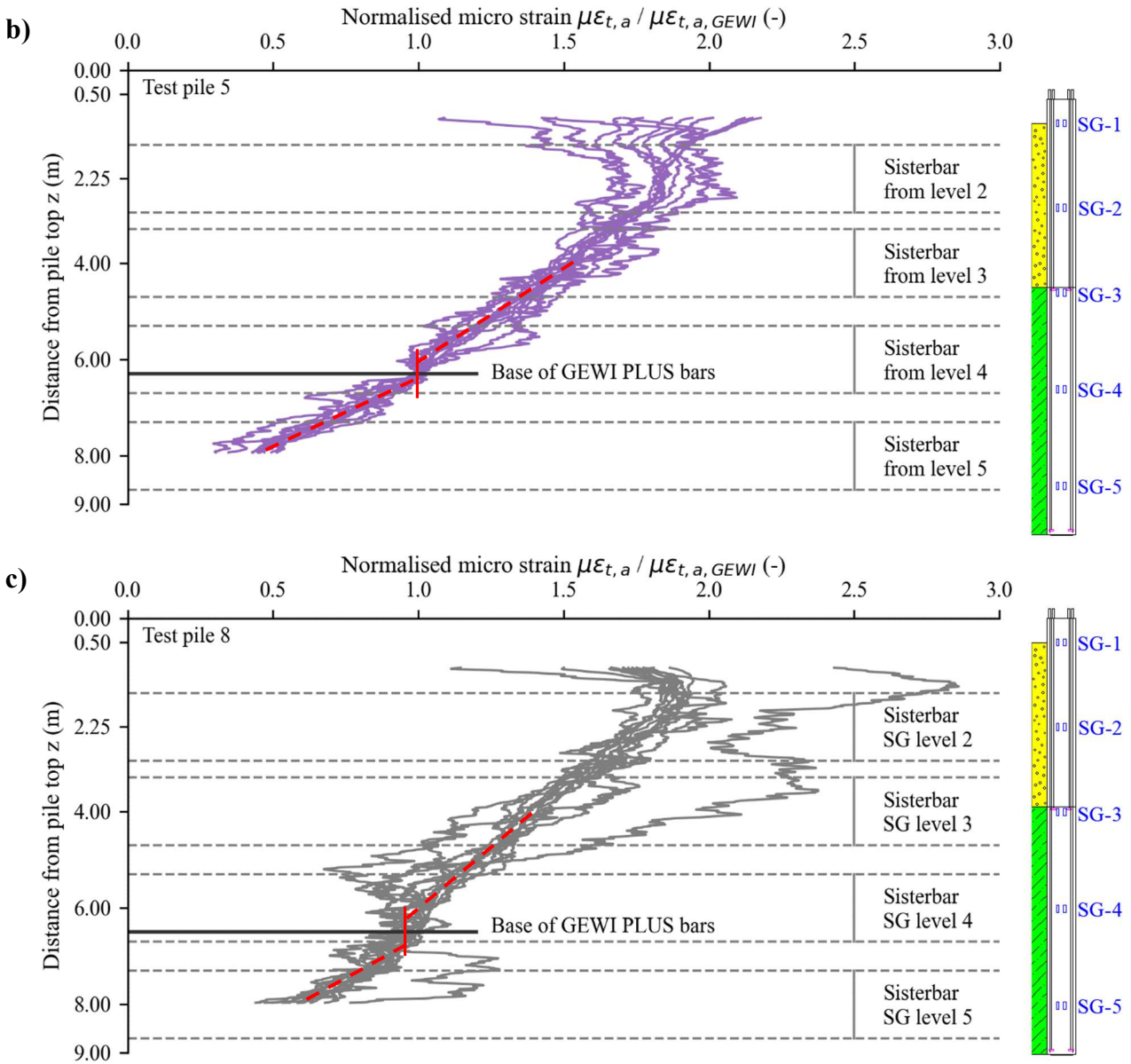

Figure 121: Influence of non-uniform pile stiffness on test pile (a) 1, (b) 5 and (c) 8. Dashed, grey lines indicate top and base of the approximately 1.4 m long sister bars used for the vibrating wire strain gauges (VWSG) measurements. Black line indicates base of the GEWI PLUS bars employed for transferring the force from the hydraulic jacks to the test piles during the static pile loading tests.

In Figure 121, the red vertical solid lines represent the length of the moving average, approximately 1.04 m for 400 readings, which also corresponds to the section affected by changes in reinforcement or axial pile stiffness. Notably, there is a significant increase in strain observed at the base of the GEWI PLUS bars, indicating a lower pile stiffness in the lower part of the test piles as expected due to the reduction in reinforcement.

However, due to the overall scatter present in the FOSC measurements, it is challenging to accurately identify non-uniform pile stiffness in relation to sister bars for the VWSG, stiffening rings, and space bars on the reinforcement.

Similarly, in a study conducted by Bersan et al. (2018), a sharp localized decrease in strain was observed for a CFA pile. This phenomenon was interpreted as an indication of an increase in pile stiffness resulting from the overlapping sections of the reinforcement cage. Regrettably, no specific explanation was identified for the observed shift of approximately 1 m between the zones of rebar overlap and the zones of strain decrease.

Furthermore, in the study conducted by Bersan et al. (2018), highly localized and very small reductions in strain were observed in one cable and partially in two other cables. These reductions were attributed to the increase in axial stiffness caused by the inner rings of a reinforcement cage. These findings align with the observations made by Kania et al. (2020), who also noted localized strain reductions in the 6x60 mm stiffening rings of a reinforcement cage for a CFA pile.

Regrettably, test piles 2 and 3 exhibit a limited number of data points due to the presence of NaN values at the same locations, specifically at the base of the GEWI PLUS bars. For test pile 7, on the other hand, all data points are affected either by a reduced number of data due to NaN values or by significant scatter. Consequently, it becomes impossible to accurately identify non-uniform pile stiffness for these piles. For further details, please refer to Appendix I.5.

7.4.5 Cross-sectional variation in strain

The strain profiles within the cross-sectional area of the test piles can vary significantly depending on the location of the specific strain sensor. The mechanical strain measured by two opposing FOSC can be utilized to calculate parameters such as curvature, gradient (change in curvature), lateral displacement, bending moment, and shear force (Kania et al., 2020). However, since the observed test piles are only subjected to vertical forces (axial tension), these parameters are theoretically expected to be zero.

Nevertheless, the variation in strain across the cross-section can help determine if the vertical force is truly vertical or if there is a bias in the load acting on the test piles. The assessment of cross-sectional strain variation is primarily based on the final maintained load step in the static pile loading tests, where the vertical loads (axial tension) are at their highest and exert the most influence on the cross-sectional strain distribution. However, for test pile 1, the strain data from the second to last load step was used, as a partially defective strain gauge resulted in the need to extrapolate some of the strain data for the final load step.

In the case of the constant rate of uplift (CRU) test, the strain data from the last maintained load step is preferred over the peak load since no matching strain data is collected during the constant rate of uplift phase of the test. Practical limitations also restrict the ability to measure more than one Fibre Optic Cable (FOC) at a time, resulting in some time required for switching between the three different FOCs for strain and temperature measurements.

Figure 122 - Figure 124 illustrate the cross-sectional variation of strain obtained from both the VWSG and the FOSC for test piles 1-3, 5, 7, and 8. The cross-sectional distribution is presented at four (or five) different levels beneath the pile top (corresponding to strain gauge levels) and along the length of the test piles.

In subfigures (a) and (b), the dashed lines depict the distribution of strain across the cross-section of the test piles at different levels beneath the pile top. The circles represent strain gauge levels, with larger circles indicating higher levels and smaller circles indicating lower levels due to the tension test conducted. When the axial load is perfectly vertical, the circles in the cross-section are perfectly centred. However, if there is a slight inclination in the load application, the introduction of moments causes the circles to shift away from the centre.

In subfigures (c) and (d), the strain measurements from opposing strain sensors of the VWSG and the FOSC are expected to show a consistent and uniform pattern along the length of the test piles, if the axial load is perfectly vertical. However, if there is a slight inclination in the load, variations between the lines can be anticipated. It is practically impossible to achieve a completely vertical application of axial loads, which leads to smaller variations across the cross-section and length of the test piles.

In Figure 122 - Figure 124, the strain distributions across the cross-sections, as measured by the VWSG and the FOSC, are slightly uncentred and exhibit minor variations with depth, as anticipated. At the lowest strain gauge levels, the circles appear elliptical, which is attributed to uncertainties in the measurements that become significant, when the applied loads are small at the end of the pile. However, overall, the circles in the cross-section are almost centred and demonstrate a reasonably vertical application of the axial load.

Nevertheless, the non-uniformity is notably significant for test pile 1, which also exhibits the highest amount of creep, see Appendix H.3. This may be attributed to the steel traverse system on one end of test pile 1 being situated in close proximity to a ditch and thereby, being more compliant to the applied load and potentially introducing bias into the system.

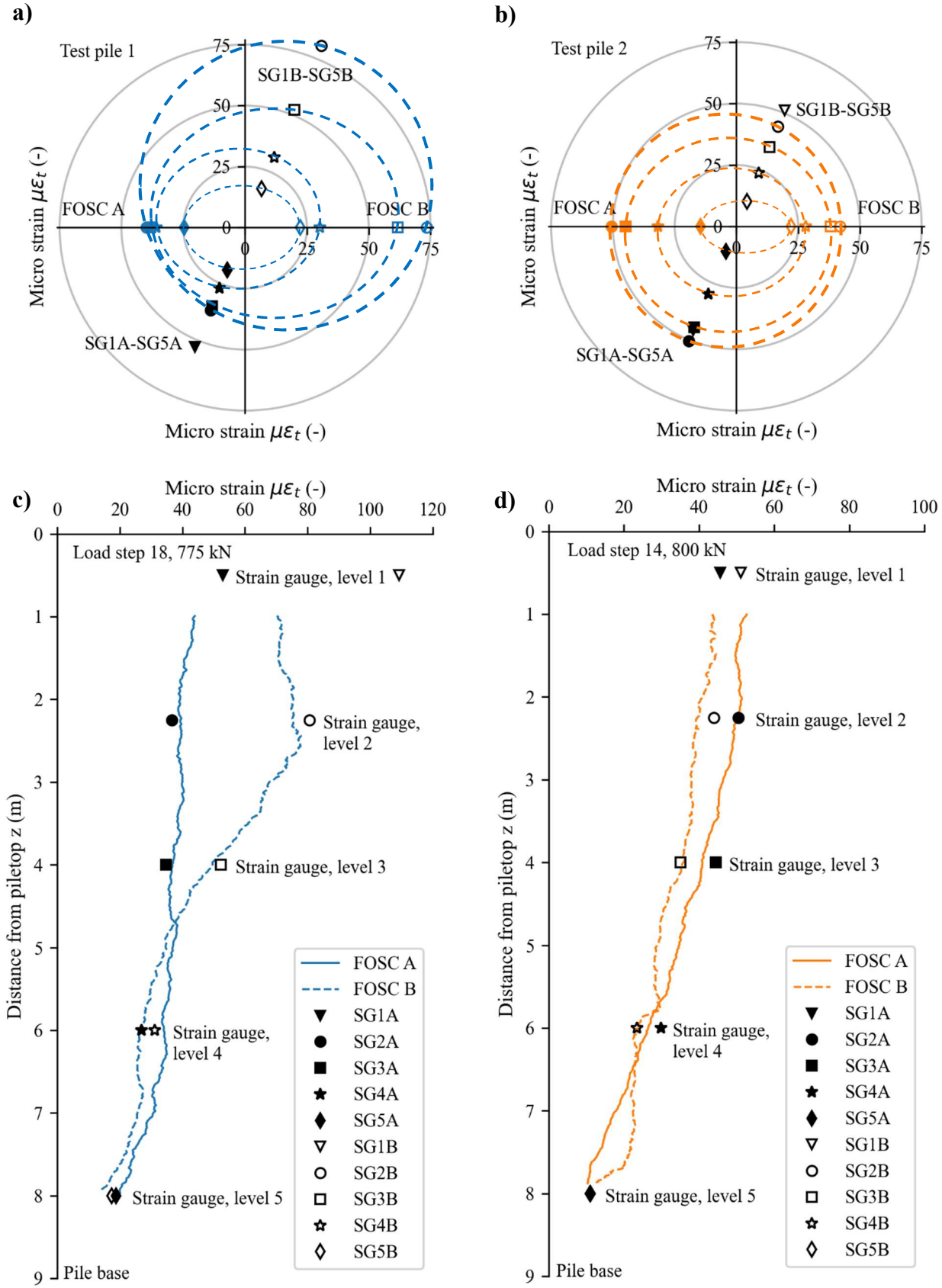

Figure 122: Cross-sectional variation of measured strain for test pile 1 and 2 as (a + c) cross-sectional distribution at 4 (5) different levels under pile head and (b + d) along the length of the test piles. Data from vibrating wire strain gauges (VWSG) shown in black and data from fibre optic strain cables (FOSC) shown in blue for test pile 1 and orange for test pile 2.

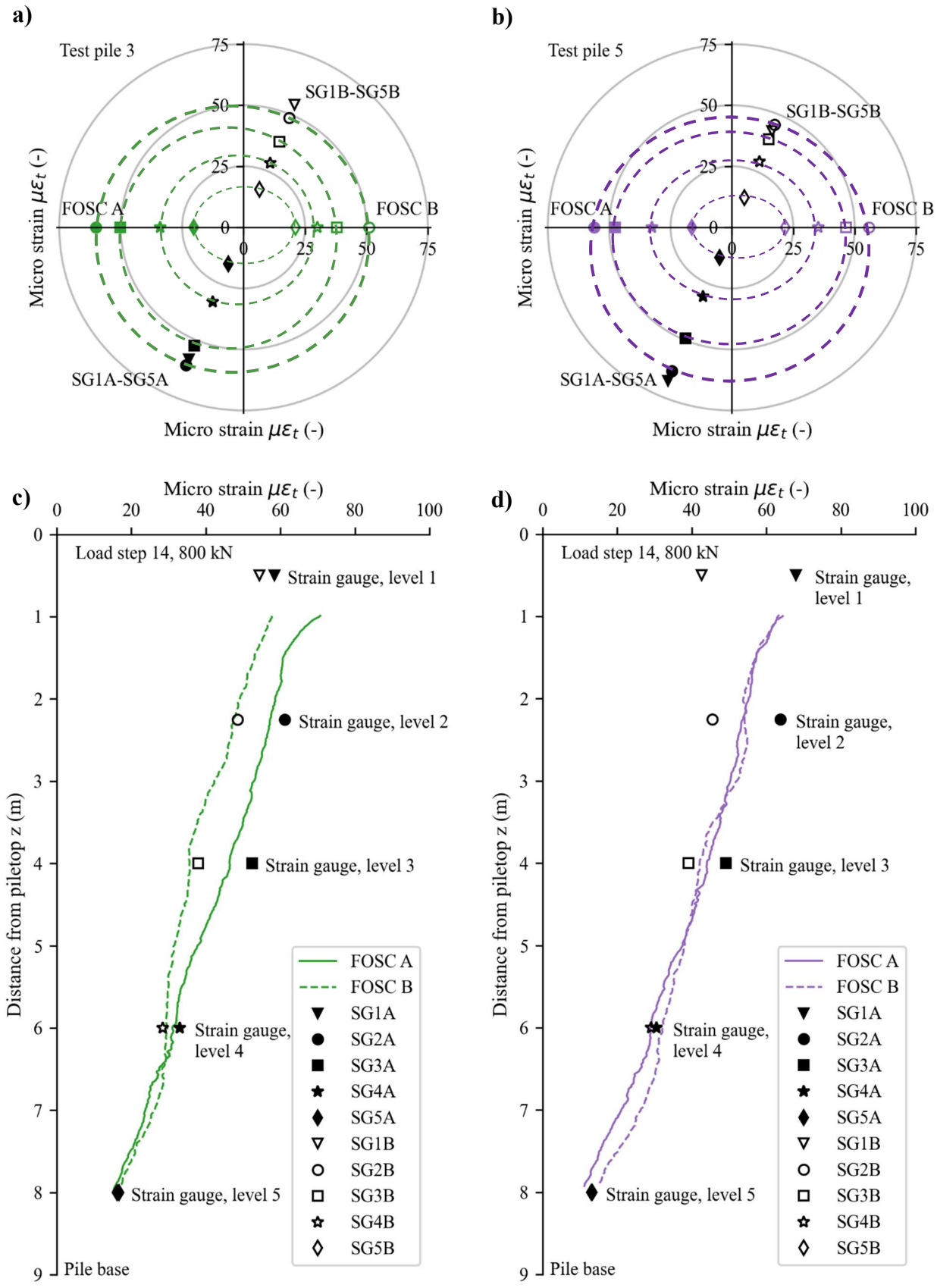

Figure 123: Cross-sectional variation of measured strain for test pile 3 and 5 as (a + c) cross-sectional distribution at 4 (5) different levels under pile head and (b + d) along the length of the test piles. Data from vibrating wire strain gauges (VWSG) shown in black and data from fibre optic strain cables (FOSC) shown in green for test pile 3 and purple for test pile 5.

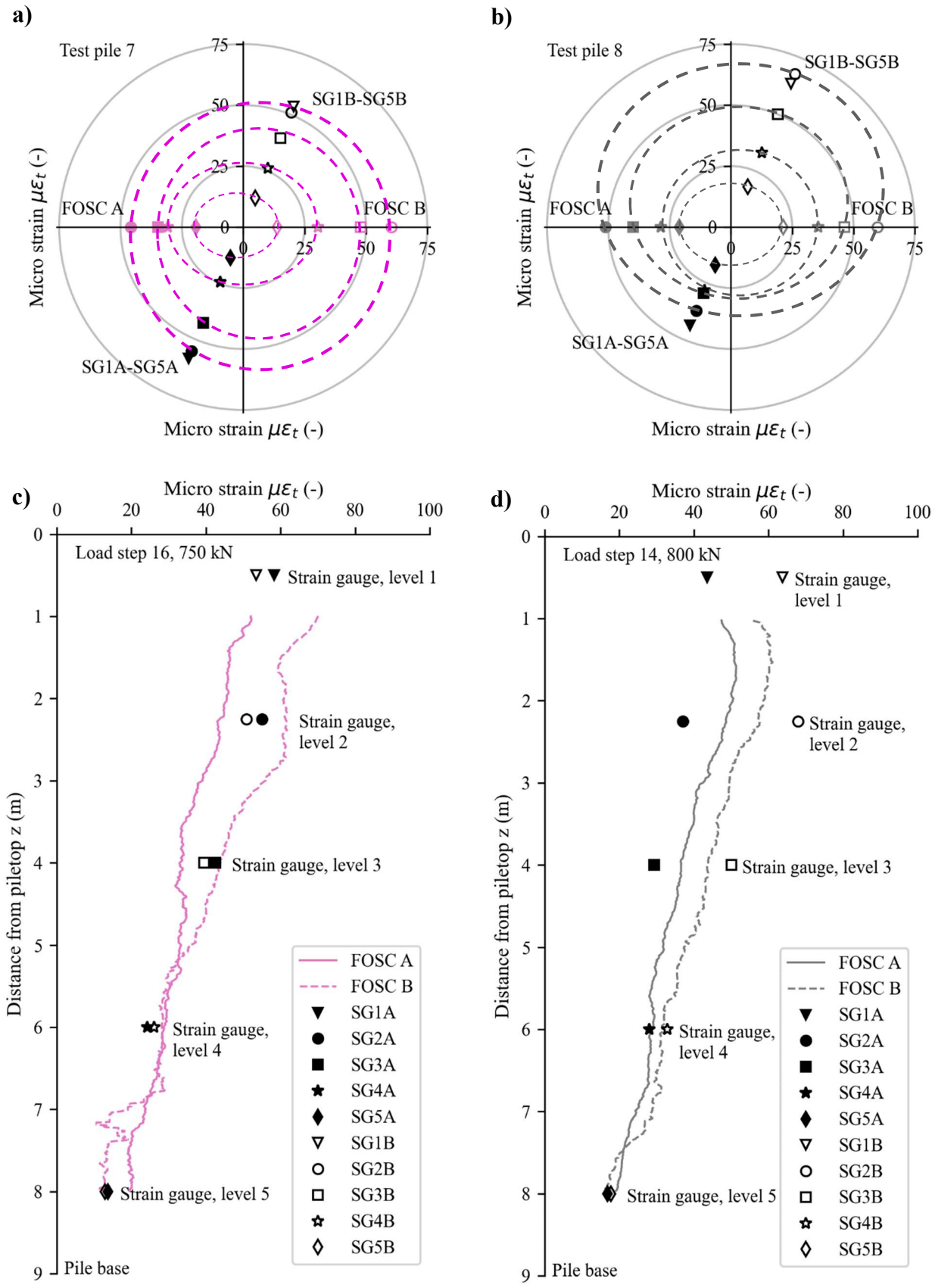

Figure 124: Cross-sectional variation of measured strain for test pile 7 and 8 as (a + c) cross-sectional distribution at 4 (5) different levels under pile head and (b + d) along the length of the test piles. Data from vibrating wire strain gauges (VWSG) shown in black and data from fibre optic strain cables (FOSC) shown in pink for test pile 7 and grey for test pile 8.

7.4.6 Axial pile stiffness determined from FOSC

The axial stiffness of the pile is calculated using the tangent stiffness method (refer to section 5.5.1) based on the FOSC. The obtained results are then compared with the axial pile stiffness calculated from the VWSG (refer to section 6.3.2). However, it is not possible to directly compare the determined axial pile stiffness at SG level 1 due to factors such as the embedded passive cable length, attachment of the FOSC, and the use of a moving average. Therefore, the axial pile stiffness from the FOSC is determined and compared at SG level 2 during load phase 2 in the static pile loading test as depicted in Figure 125.

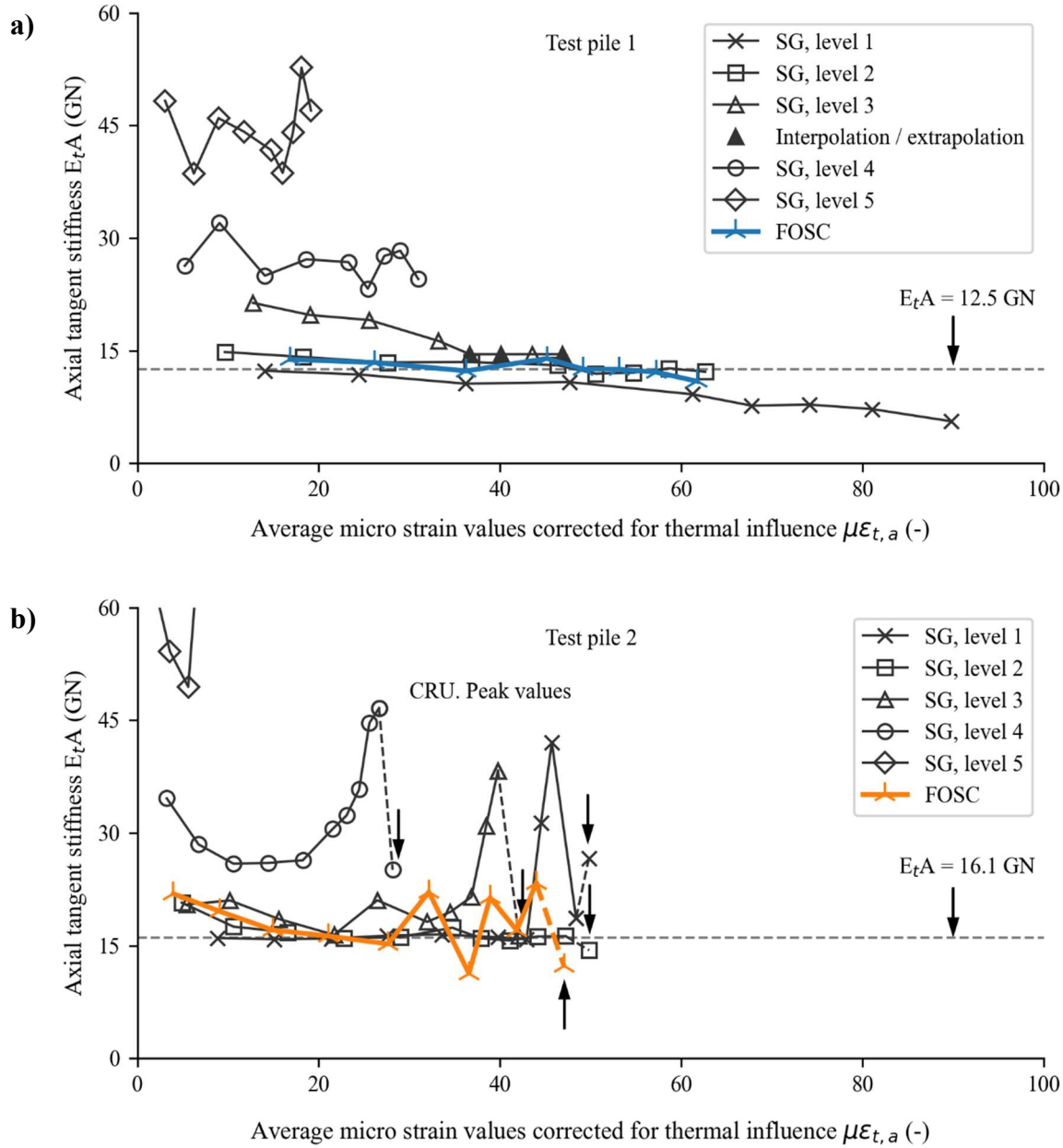

c)

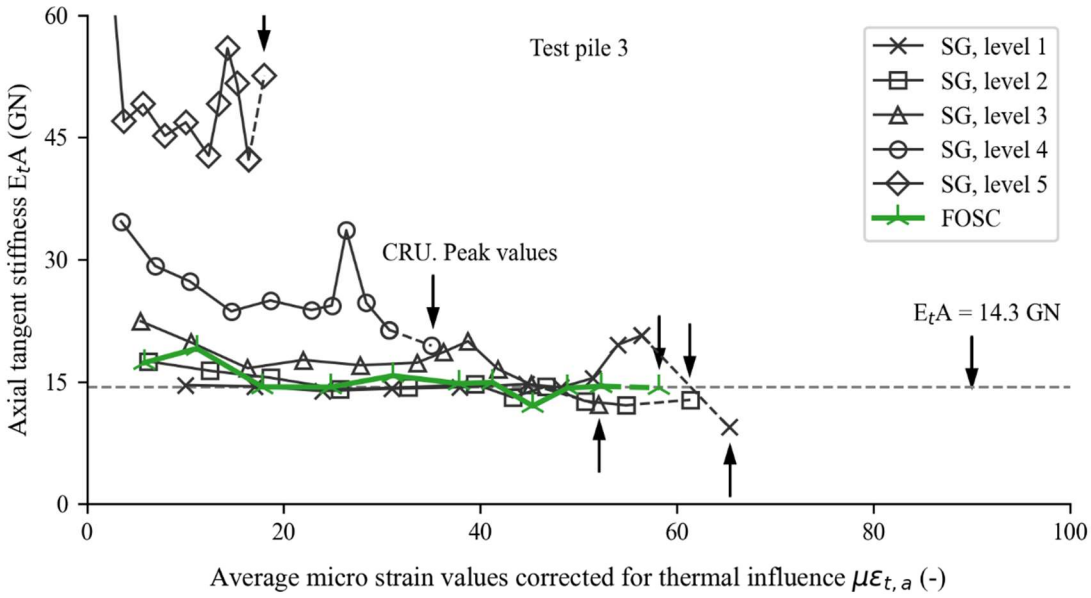
Test pile 3
SG, level 1
SG, level 2
SG, level 3
SG, level 4
SG, level 5
FOSC
CRU. Peak values
EtA = 14.3 GN
Axial tangent stiffness EtA (GN)
Average micro strain values corrected for thermal influence με t, a (-)

d)

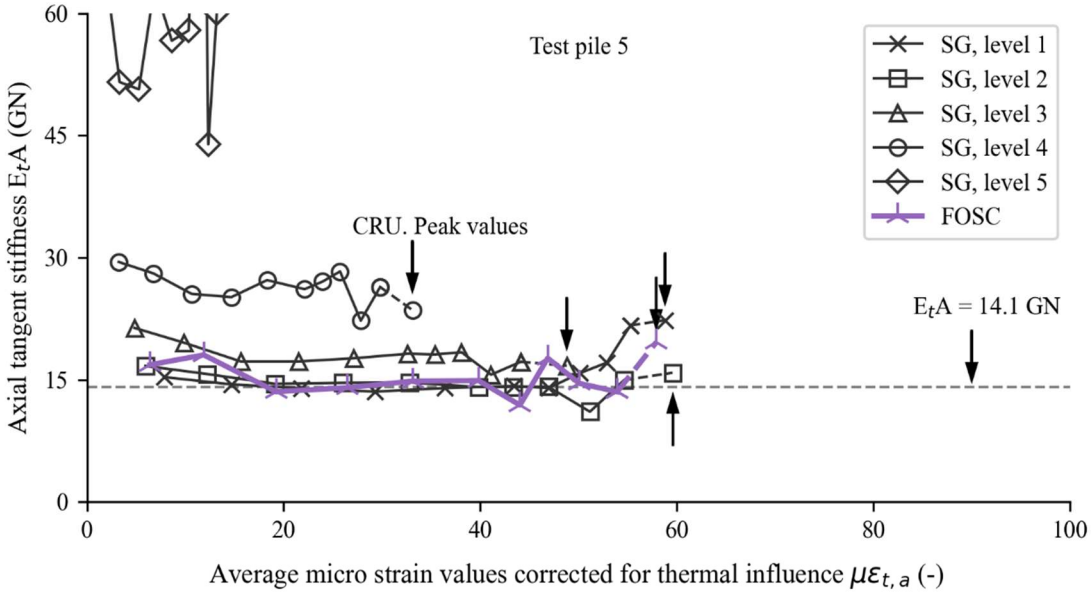
Test pile 5
SG, level 1
SG, level 2
SG, level 3
SG, level 4
SG, level 5
FOSC
CRU. Peak values
EtA = 14.1 GN
Axial tangent stiffness EtA (GN)
Average micro strain values corrected for thermal influence με t, a (-)

e)

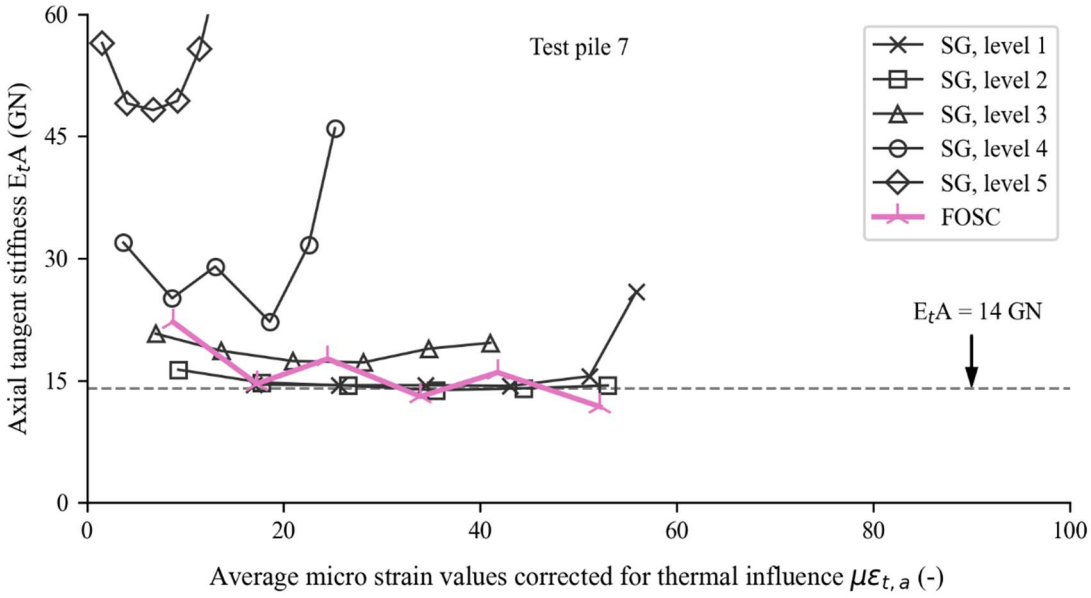
Test pile 7
SG, level 1
SG, level 2
SG, level 3
SG, level 4
SG, level 5
FOSC
EtA = 14 GN
Axial tangent stiffness EtA (GN)
Average micro strain values corrected for thermal influence με t, a (-)

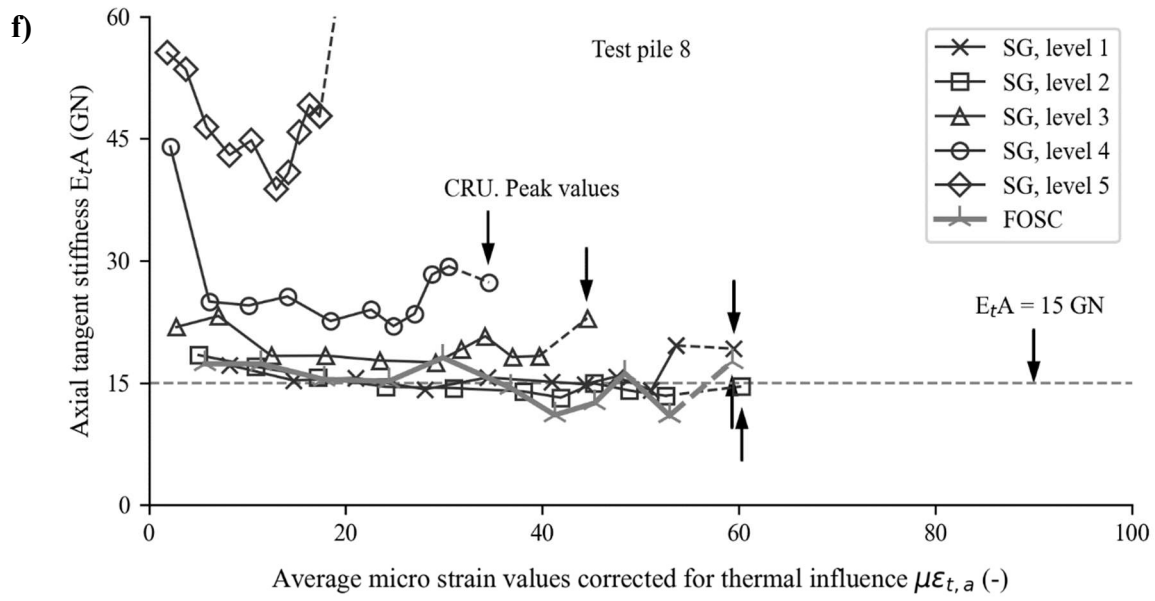

Figure 125: Axial pile stiffness determined by the tangent method for fibre optic strain cables (FOCS) at SG level 2. Axial stiffness determined from vibrating wire strain gauges (VWSG) shown in black. Determined during load phase 2 in the static pile loading test for test piles (a-c) 1-3, (d) 5, (e) 7 and (f) 8.

The axial pile stiffness determined from the FOSC at SG level 2 shows agreement with the axial pile stiffness determined from the VWSG at SG level 2, although it exhibits slightly more variability. Thus, it can be assumed that the tangent axial stiffness is equivalent to the value determined in section 6.3.2, Table 14.

However, it is important to consider the influence of non-uniform pile stiffness, as discussed in section 7.4.4. Since better information is lacking, the theoretical difference in axial pile stiffness as mentioned in section 5.5.1, is used for piles with and without the 2 Ø63.5 mm GEWI PLUS bars. Consequently, the axial pile stiffness below the 2 Ø63.5 mm GEWI PLUS bars is assumed to be 91% of the axial pile stiffness determined by the tangent method for the test piles above the bars. Unfortunately, any potential boundary effects related to the presence of the 2 Ø63.5 mm GEWI PLUS bars have not been accounted for.

7.4.7 Load distribution from FOSC

The load distribution is determined through back calculation, as explained in section 5.5, using the FOSC. This is then compared with the load distribution determined from the VWSG, as discussed in section 6.3.3. However, for the uppermost strain gauges (SG level 1), the directly applied load is used instead of relying on measured strains. This is because the measured strains are influenced by boundary effects, as mentioned in section 6.3.3. Since it is not possible for the load to diminish between the pile top and SG level 1, the applied load is used directly.

When determining the load distribution from the FOSC, the difference in axial pile stiffness below the 2 Ø63.5 mm GEWI PLUS bars is assumed to be 91% of the axial pile stiffness determined by the tangent method for the test piles above the bars, as indicated in section 7.4.6 The load distribution can be seen in Figure 126.

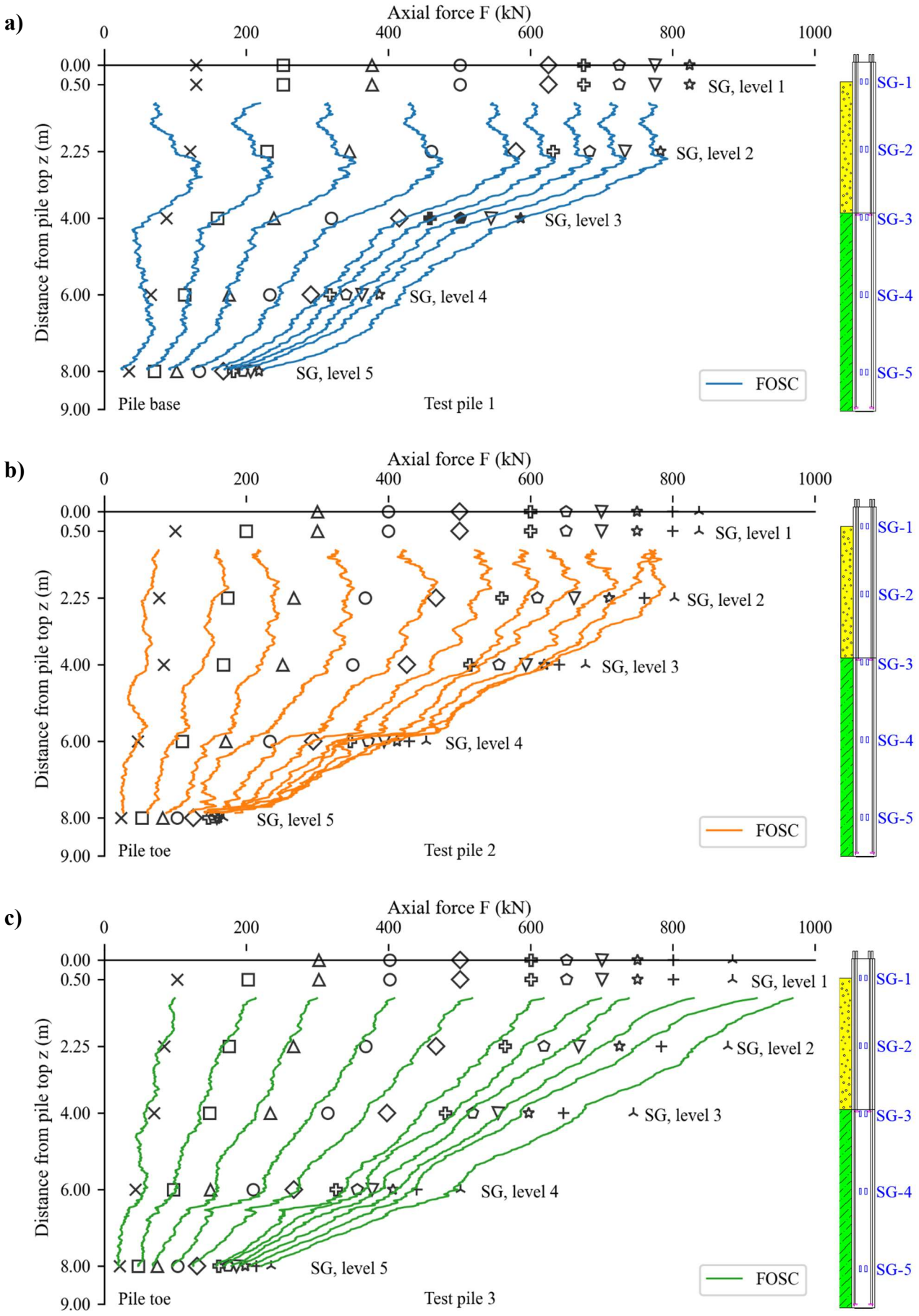
a)
Axial force F (kN)
0
200
400
600
800
1000
0.00
0.50
2.25
4.00
6.00
8.00
9.00
Distance from pile top z (m)
SG, level 1
SG, level 2
SG, level 3
SG, level 4
SG, level 5
Pile base
Test pile 1
FOSC
SG-1
SG-2
SG-3
SG-4
SG-5
b)
Axial force F (kN)
0
200
400
600
800
1000
0.00
0.50
2.25
4.00
6.00
8.00
9.00
Distance from pile top z (m)
SG, level 1
SG, level 2
SG, level 3
SG, level 4
SG, level 5
Pile toe
Test pile 2
FOSC
SG-1
SG-2
SG-3
SG-4
SG-5
c)
Axial force F (kN)
0
200
400
600
800
1000
0.00
0.50
2.25
4.00
6.00
8.00
9.00
Distance from pile top z (m)
SG, level 1
SG, level 2
SG, level 3
SG, level 4
SG, level 5
Pile toe
Test pile 3
FOSC
SG-1
SG-2
SG-3
SG-4
SG-5

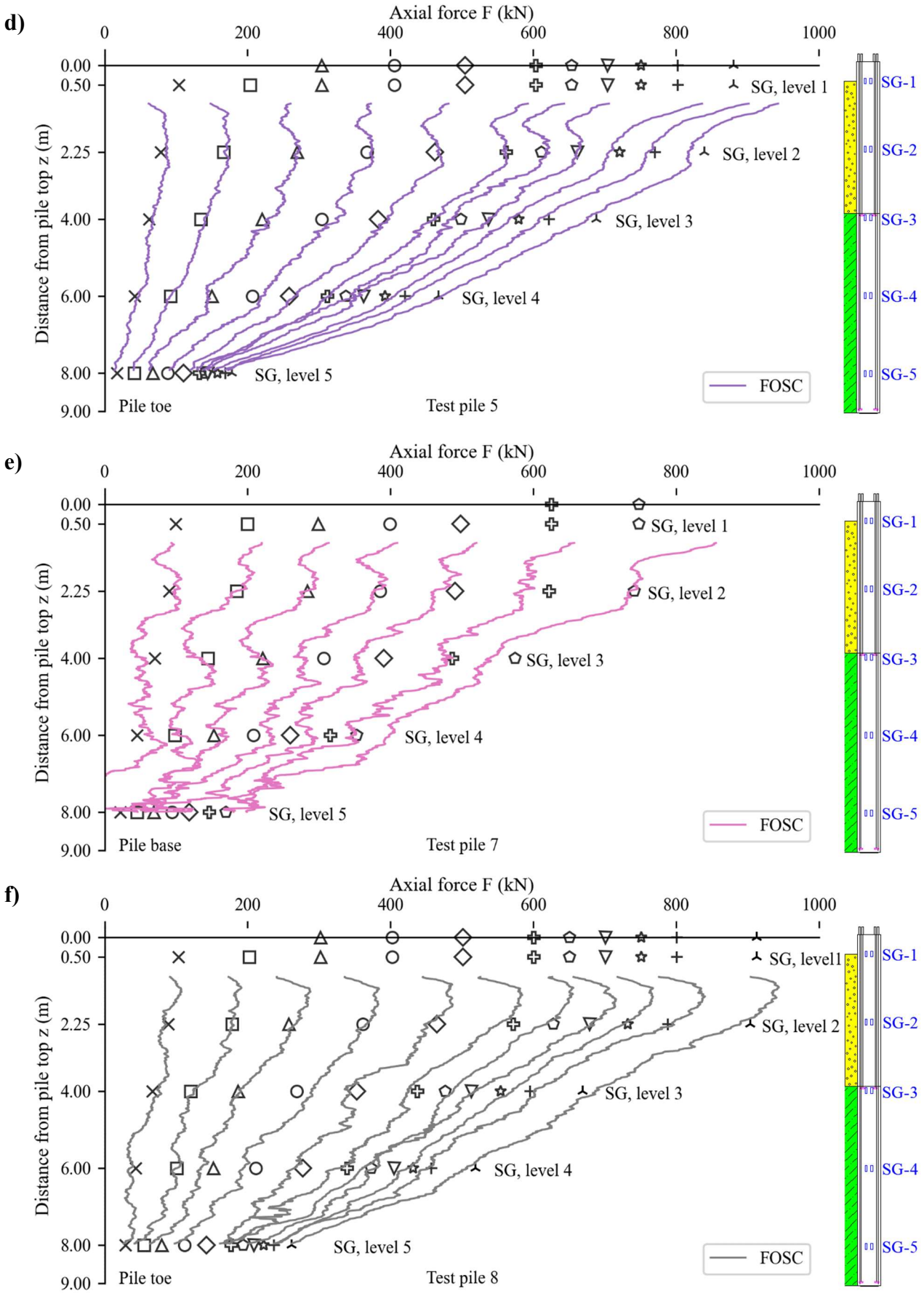

Figure 126: Load distribution for test piles 1-3, 5, 7, and 8 determined using fibre optic strain cables (FOSC). The load distribution is determined in load phase 2 for test pile (a) 1 and for the virgin load curves

of test piles (b) 2, (c) 3, (d) 5, (e) 7, and (f) 8. The load distribution determined by vibrating wire strain gauges (VWSG) is presented in black.

In general, the load distribution obtained from the FOSC shows an approximate linear trend between the VWSG. The inclination of the lines representing the average strain measurements decreases as the load increases, indicating an increase in load transfer along the shaft, which is expected.

Near the pile top, fluctuations can be observed in Figure 126. These fluctuations are likely caused by a combination of boundary effects, as discussed in section 6.3.3, and temperature effects, despite temperature corrections being applied. The FOSC is sensitive to temperature changes, and even a slight temperature variation of 0.2°C can lead to a deviation in the axial load of approximately 60 kN, as explained in section 7.3.

For detailed information regarding the local deviations from the approximately linear trend observed between the VWSG, please refer to section 7.4.3. It should be noted that the back calculated load distribution is derived by multiplying the strain distribution obtained from the FOSC by a constant factor representing the axial pile stiffness.

The shift in inclination observed approximately 6.5 meters below the pile top can be attributed to the end of the 2 Ø63.5 mm GEWI PLUS bars used to transfer the force from the hydraulic jacks to the test piles. Further details on this can be found in the referenced section 7.4.4.

To confirm the linear relationship in between the VWSG, the measured field vane strength, c_{fv}, and net cone resistance, q_{net}, from CPTu soundings is observed. They are seen to generally increase linear with depth for the Søvind Marl at the test site, except from the measured field vane strength, c_{fv}, for borehole TSH.B1 that appears to be constant with depth, see Figure 41.

If soil strength increases with depth, the inclination of the lines in Figure 126 is expected to decrease. However, if the increase in soil strength is limited and the VWSG locations are close together, they may appear visually linear in between the VWSG. Additionally, if soil strength is constant with depth, a linear trend is expected. Consequently, no abrupt deviations between the VWSG along the length of the test piles is anticipated.

7.4.8 Unit shaft resistance from FOSC

The most challenging part is determining the unit shaft resistance by differentiating the load data. While the VWSG method provide discrete data, the FOSC method offers continuous data along the length of the test piles, although not entirely smooth. Even after applying a moving average over approximately 1 m, it is still not enough to accurately infer a continuous unit shaft resistance throughout the length of the test piles. Figure 127 and Figure 128 illustrate this discontinuity for the upper and lower clay layers in test pile 8.

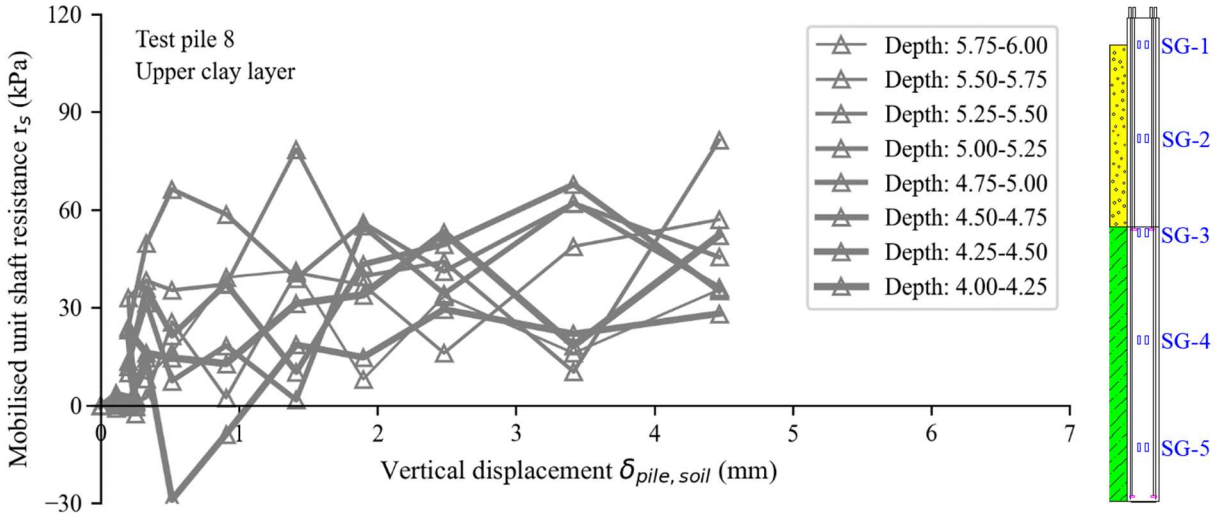

Figure 127: Mobilised unit shaft resistance along the length of the upper clay layer in test piles 8 determined using fibre optic strain cables (FOSC). The upper clay layer is divided into 8 sublayers, each with a thickness of 0.25 meters.

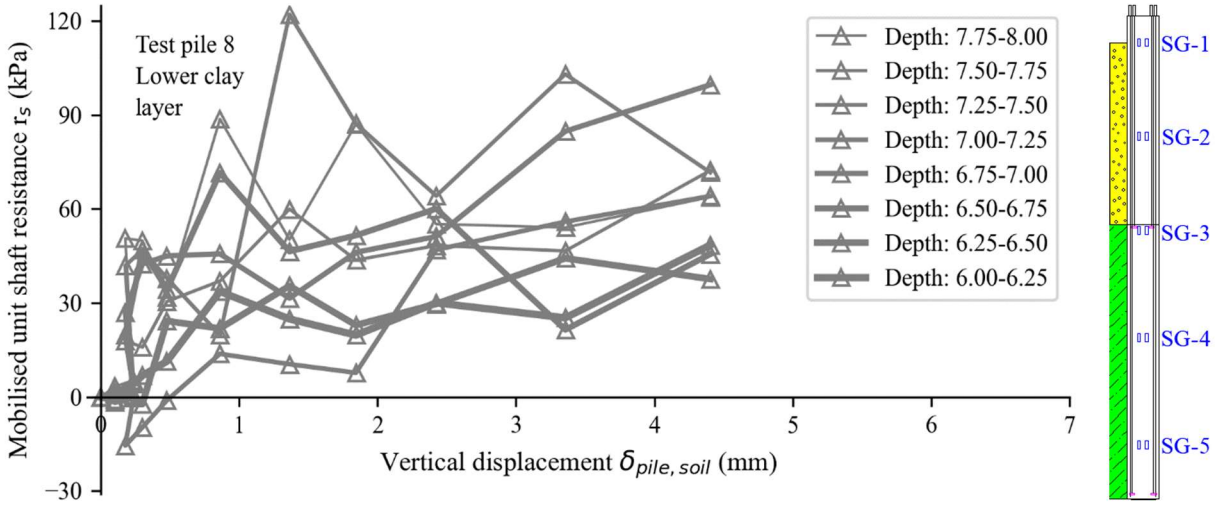

Figure 128: Mobilised unit shaft resistance along the length of the lower clay layer in test piles 8 determined using fibre optic strain cables (FOSC). The lower clay layer is divided into 8 sublayers, each with a thickness of 0.25 meters.

Assuming that soil strength increases with depth, an increase in the mobilised unit shaft resistance is anticipated as well. Similarly, if the soil strength remains constant throughout the depth, a relatively consistent mobilised unit shaft resistance is expected. However, neither of these patterns is observed in Figure 127 and Figure 128. This observation confirms that the significant local deviations from the approximately linear trend observed between the VWSG prevents inferring a continuous unit shaft resistance along the entire length of the test piles.

As a result, the unit shaft resistance is determined between each SG level, using the strains corresponding to the applied load for the uppermost strain gauges (SG level 1), as shown in Figure 129.

a)

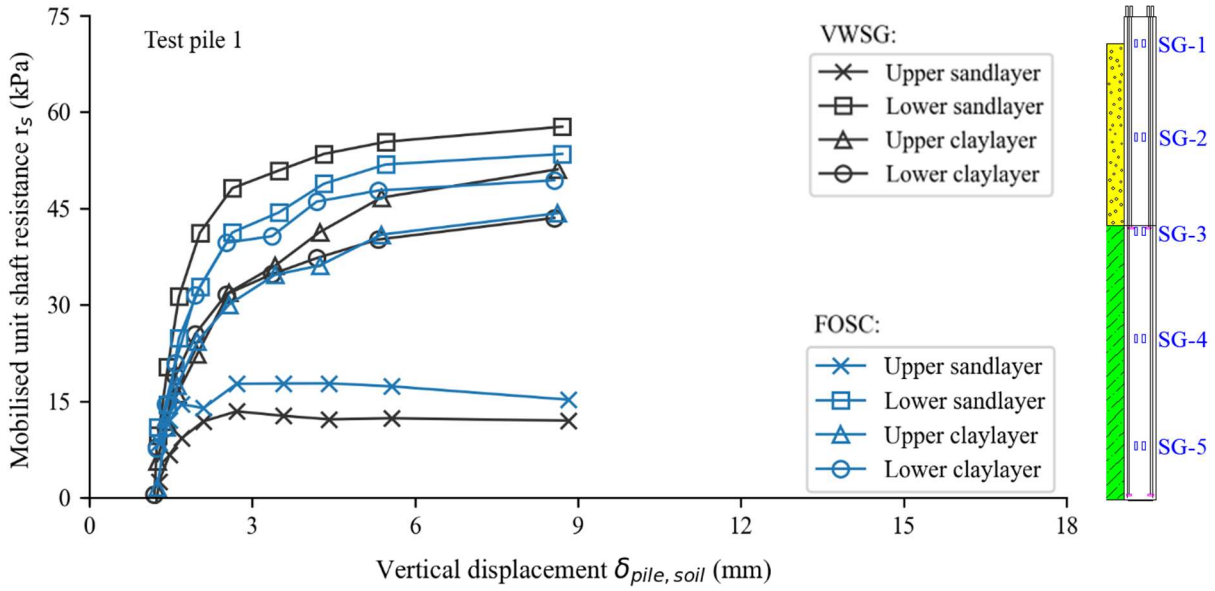
Test pile 1
Mobilised unit shaft resistance r_s (kPa)
Vertical displacement $\delta_{pile,soil}$ (mm)
VWSG:
Upper sandlayer
Lower sandlayer
Upper claylayer
Lower claylayer
FOSC:
Upper sandlayer
Lower sandlayer
Upper claylayer
Lower claylayer
SG-1
SG-2
SG-3
SG-4
SG-5

b)

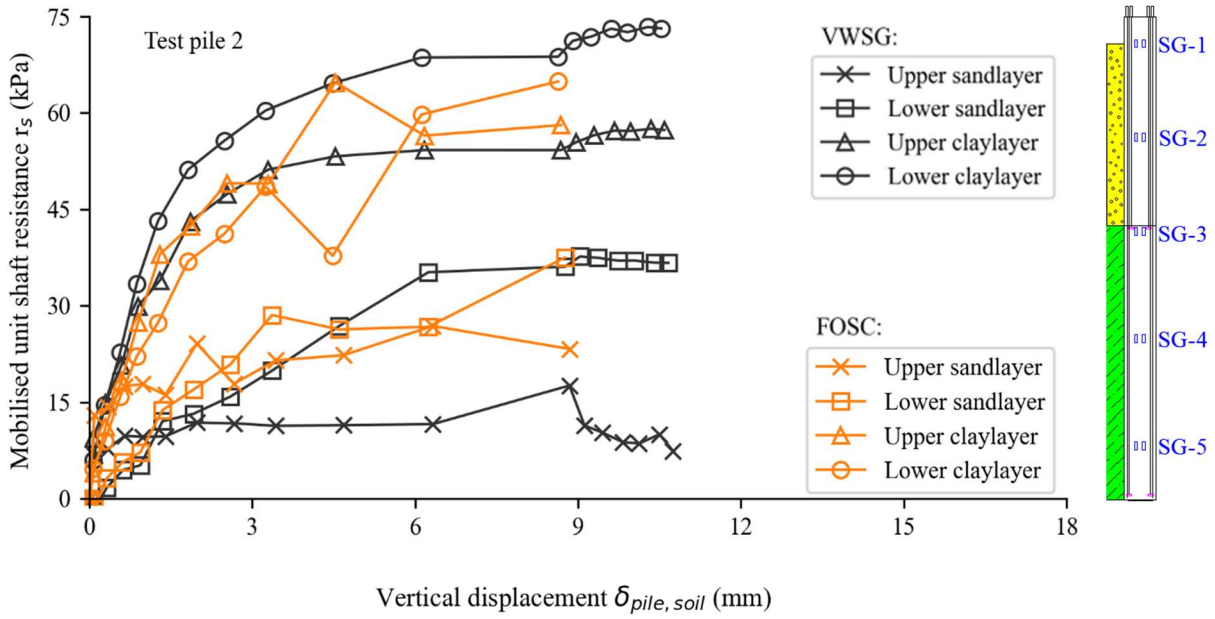
Test pile 2
Mobilised unit shaft resistance r_s (kPa)
Vertical displacement $\delta_{pile,soil}$ (mm)
VWSG:
Upper sandlayer
Lower sandlayer
Upper claylayer
Lower claylayer
FOSC:
Upper sandlayer
Lower sandlayer
Upper claylayer
Lower claylayer
SG-1
SG-2
SG-3
SG-4
SG-5

c)

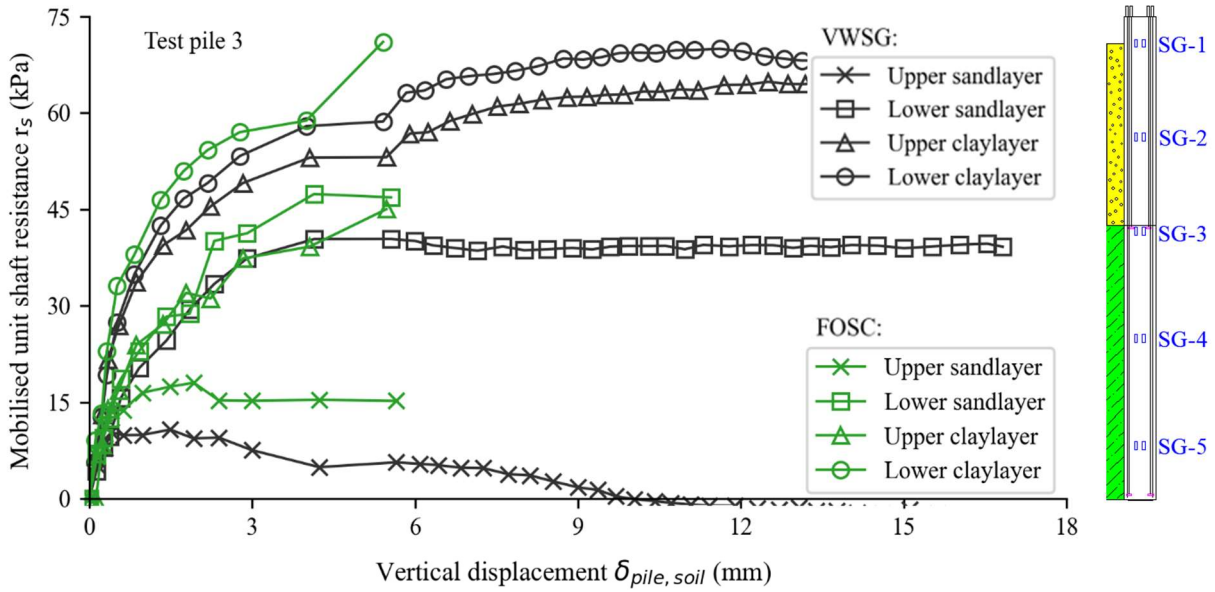
Test pile 3
Mobilised unit shaft resistance r_s (kPa)
Vertical displacement $\delta_{pile,soil}$ (mm)
VWSG:
Upper sandlayer
Lower sandlayer
Upper claylayer
Lower claylayer
FOSC:
Upper sandlayer
Lower sandlayer
Upper claylayer
Lower claylayer
SG-1
SG-2
SG-3
SG-4
SG-5

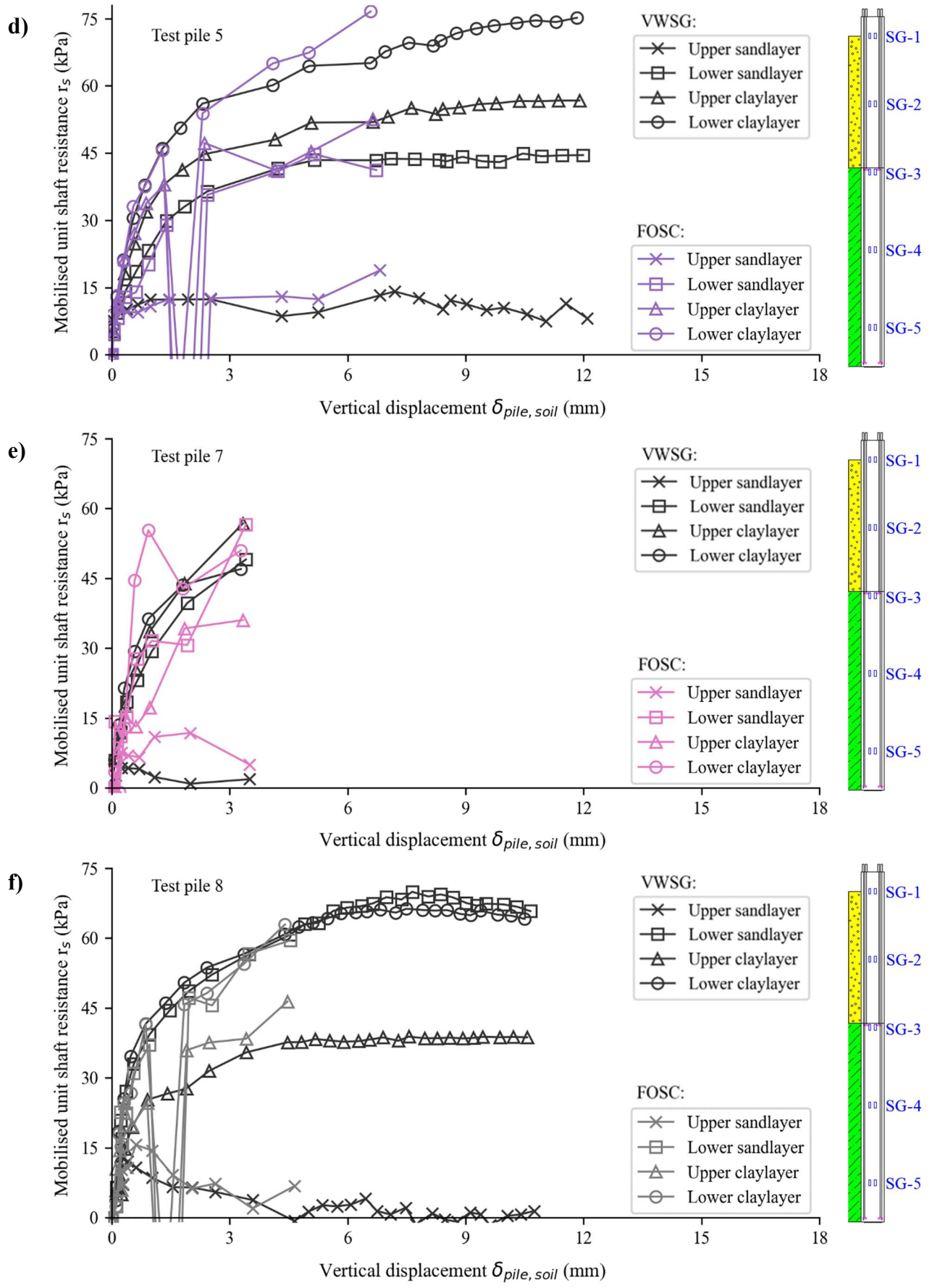

Figure 129: Mobilised unit shaft resistance along the length of the test piles 1-3, 5, 7, and 8 determined using fibre optic strain cables (FOSC). The mobilised unit shaft resistance is determined in load phase 2 for

test pile (a) 1 and for the virgin load curves of test piles (b) 2, (c) 3, (d) 5, (e) 7, and (f) 8. The mobilised unit shaft resistance determined by vibrating wire strain gauges (VWSG) is presented in black.

By examining Figure 127, Figure 128 and Figure 129, it becomes apparent that the uncertainty resulting from multiple NaN values, considerable scatter, possible local concrete cracks, variations in cross-sectional area, and pile stiffness is too significant to utilize the FOSC for anything beyond confirming the trend observed from the VWSG.

Thus, Rayleigh based FOSC can provide continuous strain profiling that enables identification of local defects that can affect the pile capacity by quantifying local strain variations with great accuracy, but also at the same time can lead to erroneous interpretation of strain data in terms of soil-pile interface behaviour, if not fully understood. A similar conclusion was drawn by Bersan et al. (2018) and despite Kania and Sørensen (2018) and Kania et al. (2020) not encountering this bias, the PhD student found out via personal communication that Jakub Kania experienced it subsequently in a commercial project.

7.5 Lessons learned

In this section, the insights gained from utilizing distributed fibre optic sensors (DFOS) as compared to traditional vibrating wire strain gauges (VWSG) for monitoring test piles are presented. The DFOS offers continuous data along the length of the piles, measured manually at specific intervals, while the VWSG provide discrete data that are more convenient for automating ongoing measurements over an extended period of time.

- The first and most obvious lesson learned is that fibre optic strain cables (FOSC) offer highly detailed strain measurements along the length of the test piles, surpassing what is achievable with the vibrating wire strain gauges (VWSG). However, it is important to note that these FOSC measurements do not provide consistent data over time, as they are obtained manually at specific selected times. Consequently, the FOSC is not suitable for detecting changes in strain over time, and the timing and execution of relevant measurements need to be carefully planned and executed.
- The fibre optic temperature cable (FOTC) was found to be influenced by mechanical strains. Unfortunately, this knowledge was not implemented into this PhD project as the test piles had to be rapidly planned, ordered, and installed, allowing for as long a period of rest as possible. The urgency of the process led to defective measurements of temperature from the FOTC, which could potentially have been avoided. It would have been beneficial to conduct tests on methods to make the FOTC immune to mechanical strains, such as installing it within a small tube or protecting it with a flexible material to shield it from strain-related influences.
- It would have been beneficial to provide shading for the reinforcement cages placed outdoors on the Hinge test site. This is because uneven temperatures were observed across the cross section and along the length of the test piles due to the absence of shading. Direct sunlight and partial shading from surrounding grass or sand had an impact on the measured temperatures. As the reinforcement cages were lowered into the boreholes, the uneven temperatures tended to decrease. However, sufficient time was not provided to allow the temperatures to align properly. As a result, during the installation and initial curing of the test piles, uneven temperatures persisted. An alternative approach would have been to acquire accurate temperature measurements at the precise locations where the strain measurements were taken, rather than relying on average values. However, shading remains the preferred solution as temperature corrections often introduce inaccuracies.
- To facilitate the conversion from strains to axial loads in the test piles, it would have been preferable to install the GEWI PLUS bars to the pile base. The stiffness of the piles decreases approximately 6.5 meters below the pile top, which is where the 2 Ø63.5 mm GEWI PLUS bars, responsible for transferring force from the hydraulic jacks to the test piles, come to an end. This reduction in stiffness is evident as a significant increase in strain at the base of the GEWI PLUS bars, indicating a lower pile stiffness in the lowermost part of the test piles. However, differentiating the reduction in pile stiffness from general scatter and noise can be challenging, which complicates the accurate conversion from strains to axial loads in the test piles.

- In order to effectively interpret strain data from the FOSC, it is essential to conduct thorough geotechnical investigations. These investigations provide valuable insights and understanding of the soil conditions, which are crucial in accurately interpreting the strain data obtained from the FOSC.
- Applying FOSC in bored piles presents unique challenges compared to steel piles. The FOSC measurements in bored piles can be affected by local factors such as cracks and changes in pile stiffness. Consequently, it is necessary to use a wide moving average span (>1m) along the length of the test piles. It is important to note that the usage of a wide moving average span in the FOSC measurements has the potential to mask minor changes in strain. This is due to the fact that each data point per 2.6 mm represents a moving average over a considerable length. As a result, subtle variations in strain may be less apparent in the measurements.
- The LUNA equipment utilized during this PhD project is better suited for conducting measurements within controlled environments like a laboratory. However, deploying the equipment in field settings presents challenges due to its high accuracy and sensitivity. This requires constant efforts to maintain functionality and protect it against various factors such as machinery, shocks, sharp bends, weather elements (wind, rain, heat), dust, animals, and even people on the site. As a result, automating these delicate and time-consuming measurements from the DFOS has not been feasible. Nonetheless, ongoing advancements in technology are focused on developing more robust solutions for the equipment, holding the promise of easier automation for DFOS measurements in field settings in the future.
- Incorporating DFOS data into the analysis poses additional challenges due to the large volume of data generated. In the case of VWSG, logging was conducted every minute for 75 hours (across test piles 1-8) for both temperature and strain, resulting in approximately 45,000 data points during the static pile loading tests. In contrast, for DFOS, there were a total of 615 load steps (across test piles 1-8) with three manual measurements (taken after 0, 10, and 20 minutes) at each load step for three FOC (one temperature and two strain) with approximately 5,384 data points along each FOC (considering a 14-meter cable with a sampling resolution of 2.6 mm). Each manual measurement was taken for a minimum of 5 seconds at a frequency of 1 Hz, resulting in over 150 million data points during the static pile loading tests. The sheer volume of data quickly surpasses the memory limitations of Excel, necessitating a shift to processing all data in Python for this PhD project.

8 Analysis of field test results

Field test results are analysed with respect to residual stresses using the methods presented in the literature review in section 2.2.1 and a new method presented in section 8.1.4. In the new method, residual stresses are documented based on post pile loading test data, making it advantageous as it relies on practical everyday geotechnical engineering information. This is in contrast to the methods discussed in section 2.1.2, which depend on data measurements starting from the casting of the bored pile until the initiation of the pile loading test.

Additionally, the development of pile capacity over time is analysed by considering the logarithmic linear rate of excess pore water pressure dissipation from the second phase of setup. The data is compared to the information found in the literature review in section 2.4.2. The bored piles were tested after different periods of rest as described in section 4.1. The first two piles were tested approximately 1.5 months after installation, while the remaining piles were tested (3 at a time) around 7 months and 3 years after the pile installation, respectively.

Furthermore, the empirical adhesion coefficient, α, is determined according to section 2.2.1 using the field vane strength, c_{fv}, as reference for the undrained shear strength, c_u. This reference is commonly used in practical everyday geotechnical engineering in Denmark. The α-c_u relationship is analysed based on the data obtained during the literature review in section 2.3, and the best fit, lower bound, and upper bound envelopes for the α -c_u relationship is derived.

8.1 Residual stresses

This section focuses on residual stresses, including the expected size and distribution of these residual stresses. Additionally, evidence of the existing of residual stresses is presented from test piles 1-8 at the test site in Hinge.

To interpret residual stresses, three different methods based on vibrating wire strain gauges (VWSG) data from the casting of the bored pile until the initiation of the pile loading test are employed for test piles 4 and 8. However, these existing methods presented in the literature review in section 2.2.1 are not suitable for correcting residual stresses on the test piles as described in section 8.1.3. Hence, a new method is proposed for interpreting residual stresses.

The method proposed in this study takes advantage of post static pile loading test data, which is beneficial as it relies on practical everyday geotechnical engineering information. This approach offers practical applicability and relevance.

Additionally, the actual size and distribution of both the residual loads and the axial load distribution along the length of the test piles is presented. This provide valuable insights into the behaviour and characteristics of the piles under varying loading conditions.

8.1.1 Expected size and distribution of residual stresses

The residual stresses can build up to fully mobilised negative or positive unit shaft resistance making the observed load transfer curve cf. section 2.1.3 either reflect the ultimate unit shaft resistance twice or leave the impression that there is no mobilised unit shaft resistance along the length of the pile.

For driven piles, the unit shaft resistance is often fully mobilised in the upper and lower lengths of the pile with a transition zone along an in-between length, embracing the boundary between unit shaft resistance in positive direction above and negative direction below the neutral plane. The distribution of residual stresses for driven piles is governed by the small downward soil movement relative to the pile particular in soft soil (i.e. negative skin friction) and the elastic rebound of the pile after driving particular in stiff soil. These phenomena always occurring after construction of a pile induce positive unit shaft resistance along the upper length of the pile. The down drag is resisted by negative unit shaft resistance along the lower length of the pile and the pile base (Fellenius, 2015).

In the case of bored piles, it is expected that the residual stresses would be smaller compared to driven piles, mainly because the soil undergoes less disturbance during the installation process. Additionally, bored piles often have minimal residual base resistance, limited to the weight of the fluid concrete and the effects of concrete curing (Fellenius, 2015). Furthermore, bored piles can have layers of softened soil immediately below the pile base that has to be compressed before a residual base resistance can develop. Consequently, the downward drag is primarily resisted by negative unit shaft resistance along the lower portion of the pile until sufficient movement at the pile base occurs to engage the pile base resistance.

In addition, bored piles are susceptible to internal strains caused by concrete setting and curing, which cannot reliably be differentiated from mechanical strains originating from external forces such as negative skin friction acting on the shaft of the pile, see Figure 130.

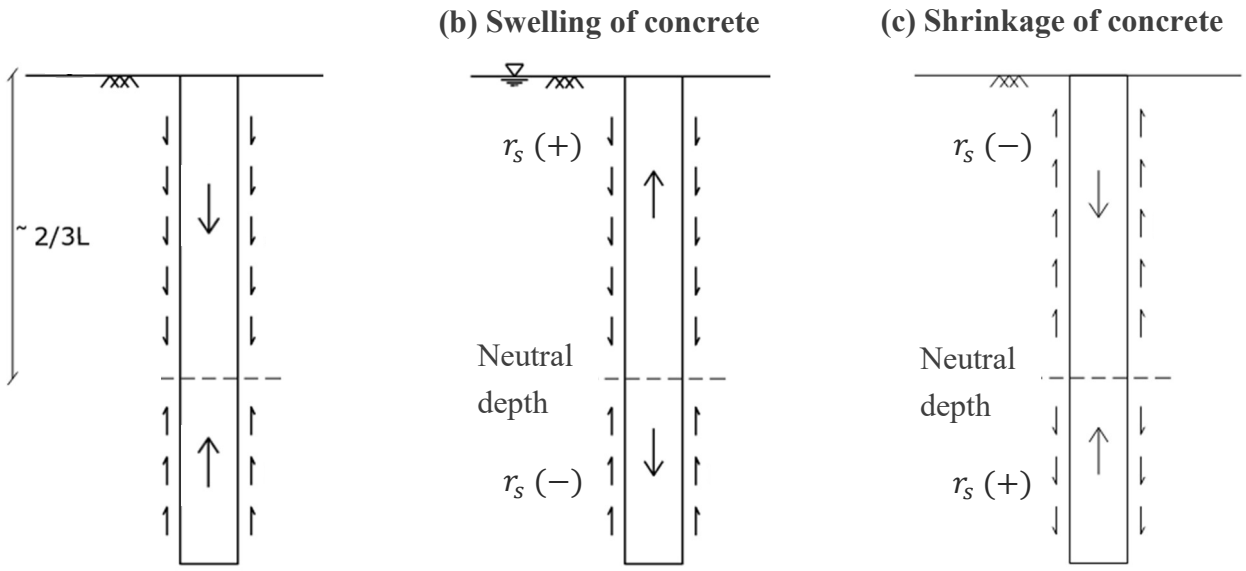

Figure 130: Effects of (a) down drag from soft soil layers and concrete curing in terms of (b) swelling and (c) shrinkage of concrete.

From Figure 130 it is seen, that a long term compressive force in the pile can either be a result of down drag on the pile (a) or shrinkage of the concrete during curing (c) leading to unit shaft resistance working in opposite directions on the pile shaft. Hence, measuring only internal pile strains can easily lead to misinterpretation of unit shaft resistances on the pile shaft. For example, if internal compressive forces are measured in a pile and they originate from both down drag and shrinkage of concrete during curing, they could potentially balance each other out leaving no unit shaft resistance on the pile shaft and be interpreted incorrectly as working in either of two opposing directions.

8.1.2 Evidence of residual stresses

During static pile loading tests conducted in tension, the resistive force, R_b, at the pile base can either be zero or reach the maximum suction force ($A_b \cdot 1\ atm \sim 31\text{kN}$) during failure. To determine whether the axial force at the pile base is zero or equal to the maximum suction force, the load distribution along the length of the test piles is investigated during failure.

The load distribution along the length of the test piles during failure can be found in section 6.3.3. As the static pile loading tests were conducted in tension, it is important to account for the weight of the test piles. The weight of the concrete is determined using the total unit weight instead of the effective unit weight. This choice is made because the concrete is considered impermeable compared to the surrounding soils.

In order to accurately analyse the load distribution, the weight of the test piles is subtracted from the axial load distribution. This adjustment is essential because before the tension load is transferred as shaft resistance, the weight of the test piles need to be counteracted. The axial force at the pile base level during failure for test piles 2-8, after compensating for the weight of the test piles, is provided in Table 19:

Table 19:Axial force at pile base level for test piles 2-8 after compensating for the weight of the test piles.

Level	Axial force F [kN]							
	TP1	TP2	TP3	TP4	TP5	TP6	TP7	TP8
Pile base	-	-43	33	-27	-34	34	11	65

The deviation of the axial force at the pile base level during failure from the expected values of either zero or the maximum suction force indicates the existence of residual stresses prior to initiating the pile loading tests. Notably, test pile 3 and 6 demonstrate axial forces at the pile base that are close to the given maximum suction force ($A_b \cdot 1\ atm \sim 31\text{kN}$).

In contrast, test pile 2 and 8 exhibit the largest deviations in the opposite direction from the anticipated values of axial force at the pile base (-43 kN in compressive force and 65 kN in tension). The load distribution along the length of test piles 2 and 8, adjusted for the weight of the test piles, is depicted in Figure 131 and Figure 132. Additionally, the load distribution along the length of all test piles (test pile 2-8), taking into account the weight of the test piles, can be found in Appendix J.1.

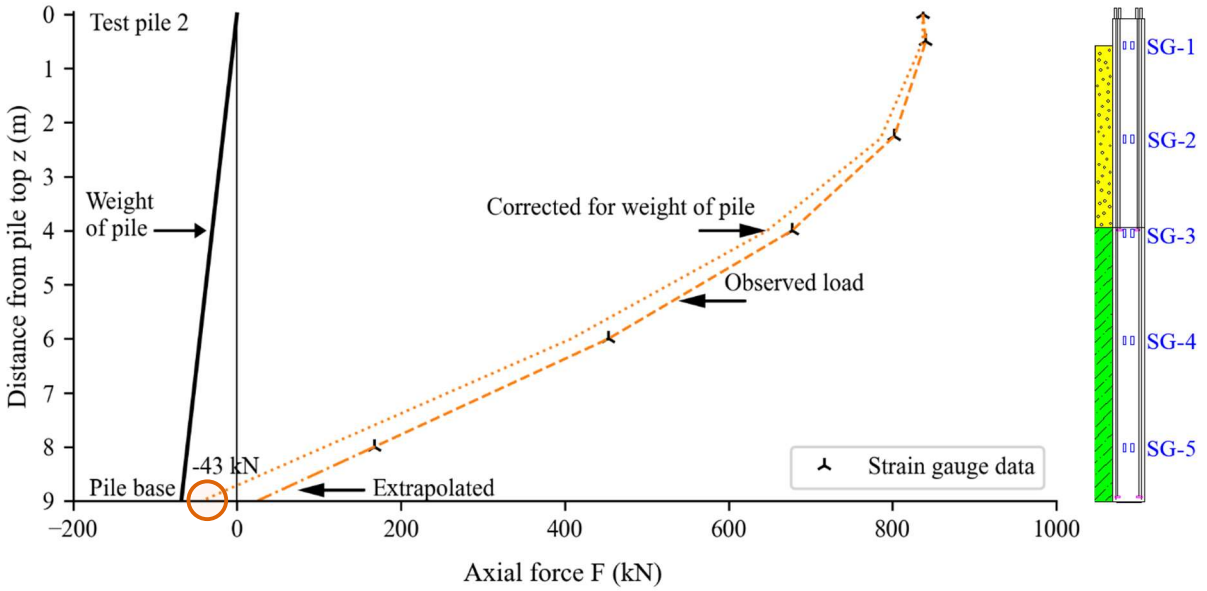

Figure 131: Axial load distribution along the length of test pile 2 based on vibrating wire strain gauge (VWSG) data, which corrected for weight of the test pile has -43 kN in compressive force at pile base.

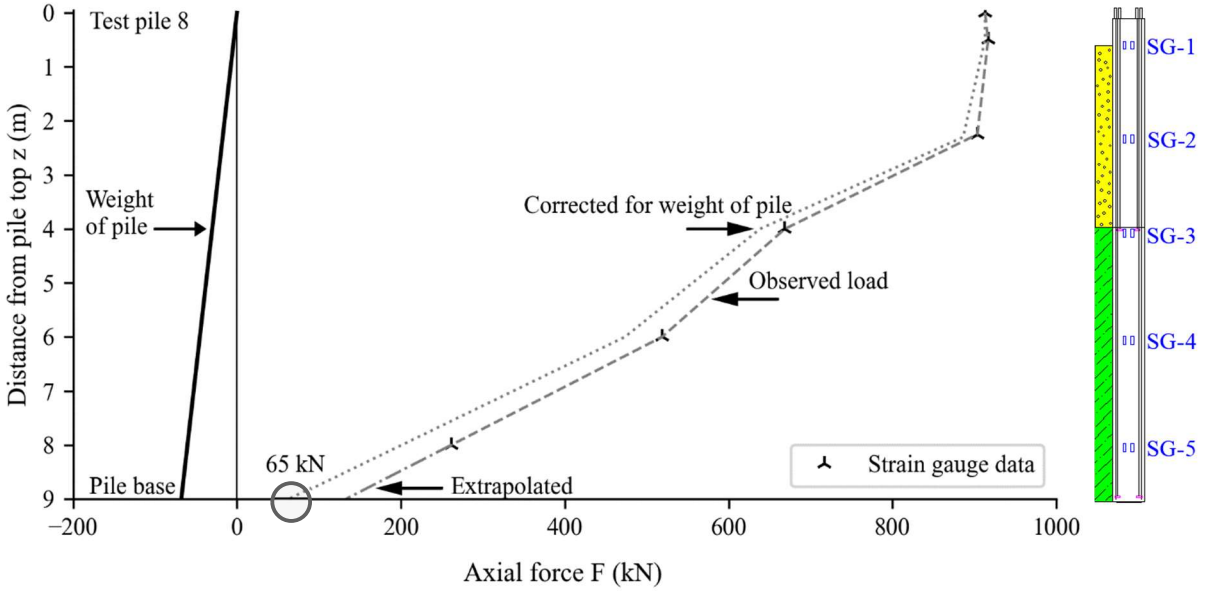

Figure 132: Axial load distribution along the length of test pile 8 based on vibrating wire strain gauge (VWSG) data, which corrected for weight of the test pile has 65 kN in tension at pile base.

8.1.3 Methods for interpretation of residual stresses

To study the development of residual stresses, dataloggers for the VWSG were connected to test piles 4 and 8 for an extended period after installation. The dataloggers were attached for 16 weeks for test pile 4 and 32 weeks for test pile 8, with strain and temperature measurements recorded at intervals of 1 minute for the first 2 days, 10 minutes for the following 5 days, and hourly intervals thereafter. Test pile 4 was tested after approximately 149 weeks or 3 years, while test pile 8 was tested after 32 weeks.

The interpretation of residual stresses is carried out using three methods outlined in section 2.1.2. The residual stresses are determined based on internal pile strains corrected for thermal influence

(mechanical strains), contrary to the suggestion by Flynn and McCabe (2022b) that methods 1 and 3 should utilize total strains (raw data). The correction of total strains for thermal influence is performed to accommodate the disparity in thermal expansion between the VWSG and the test piles caused by temperature variations. It is important to note that this discrepancy is not believed to have any impact on the residual stresses that act on the interface between the pile and the shaft. Therefore, the strain data is adjusted for thermal influence to accurately represent the actual extension or compression of the test pile.

It should be noted that there are no soft soil layers surrounding the test piles in Hinge, and thus, there is no basis for the development of negative skin friction. However, there may be downward drag due to the compression of loosely consolidated sand surrounding the top 3.4 meters of the test piles caused by rain or water seepage. Additionally, compression might occur due to the upper 0.4 meters of sand being replaced with gravel, as described in section 3.4.2.

If long-term internal pile strains are present, reduction of mechanical strain indicates compression of the VWSG and consequent shrinkage of the concrete during curing. Conversely, increase of mechanical strain indicates extension of the VWSG and subsequent swelling of the concrete during curing. The application of the methods is demonstrated in Figure 133 and Figure 134 for test pile 8 and in Appendix J.2 for test pile 4.

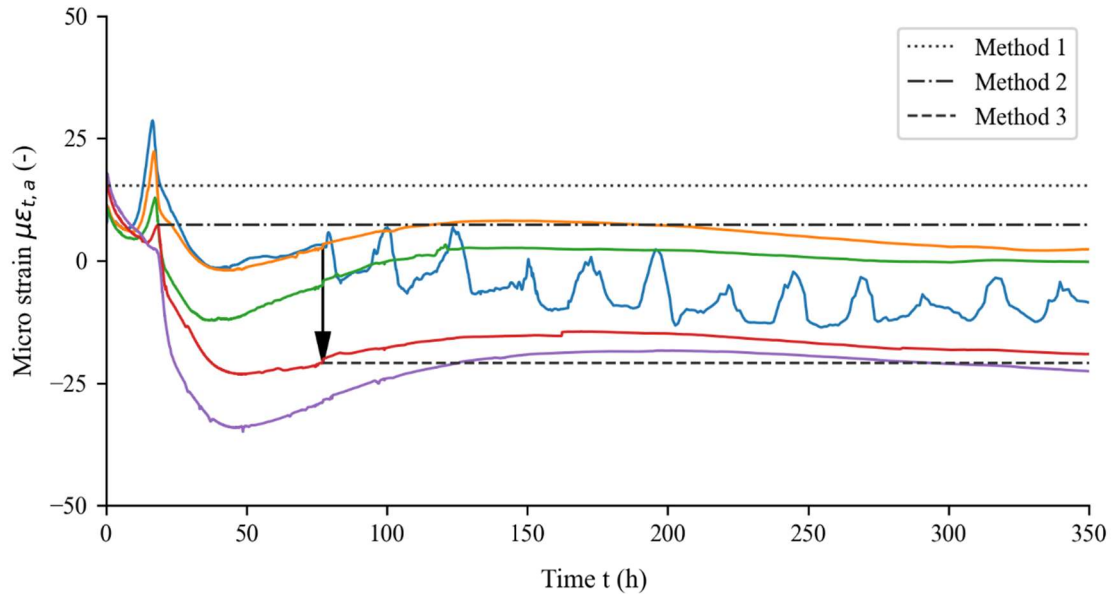

Figure 133: Development of residual stresses in the initial 350 hours after installation of test pile 8 cf. Method 1; Simplified method; Method 2; Pennington (1995) and Method 3; Siegel and McGillivray (2009).

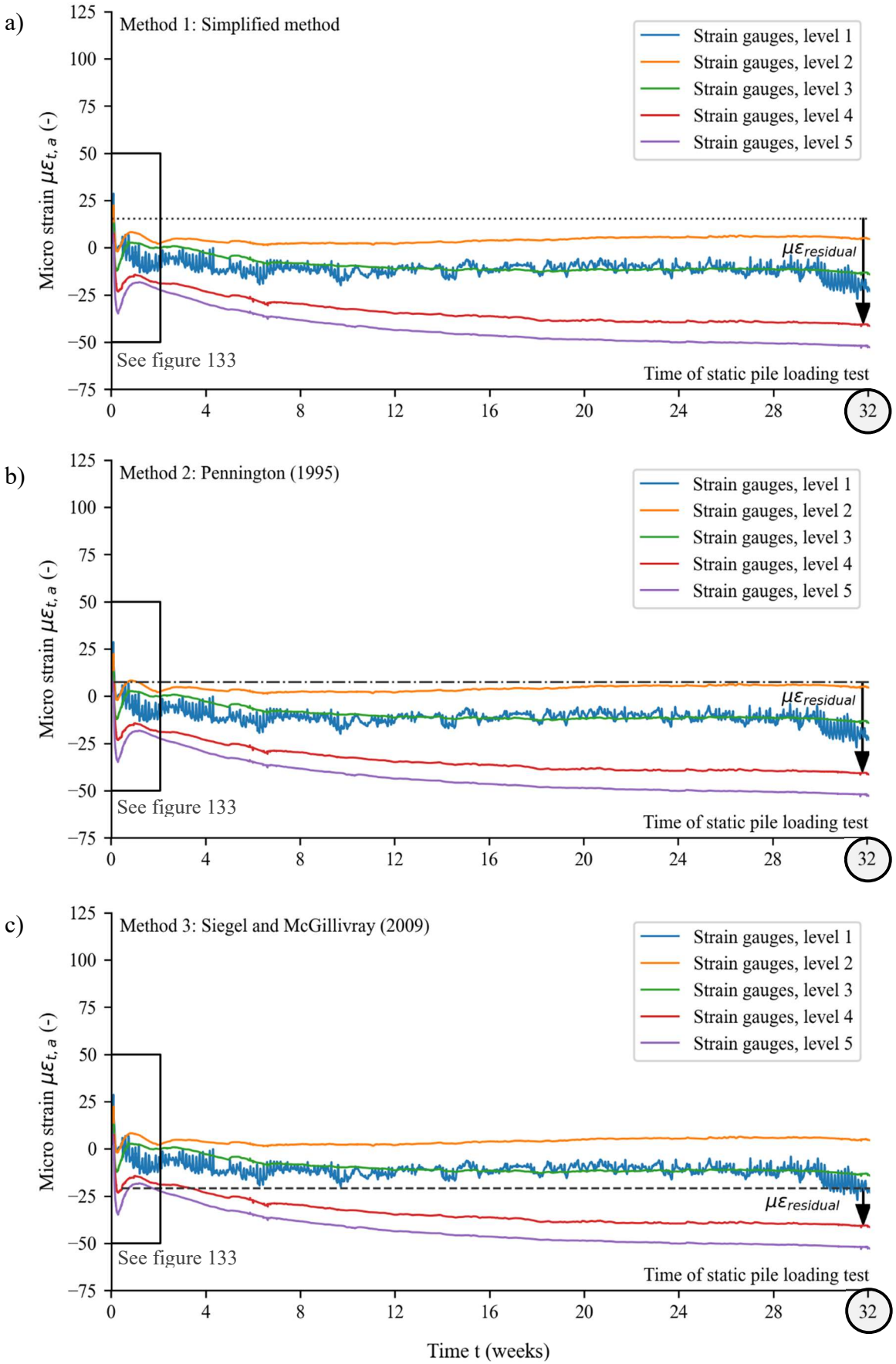

Figure 134: Interpretation of residual strains cf. (a) Method 1; Simplified method; (b) Method 2; Pennington (1995) and (c) Method 3; Siegel and McGillivray (2009) for test pile 8.

By analysing Figure 133 and Figure 134, it becomes evident that the residual strains exhibit a reduction in mechanical strain at all levels of the VWSG. This reduction suggests internal compression of the test piles, with the exception of variations observed during the initial approximately 150 hours. This compression can be attributed to either down drag or concrete shrinkage during the curing process.

It is important to highlight that the most significant reduction in strain is observed at VWSG level 1. According to Method 3 proposed by Siegel and McGillivray (2009), it is assumed that residual loads are considered negligible at or near the top of the pile, which corresponds to the uppermost VWSG level in this case (level 1). Therefore, to determine the actual residual strain, the changes in strain from all other VWSG levels must be subtracted from the strain reduction observed at VWSG level 1.

Since all other VWSG levels exhibit a smaller strain reduction compared to level 1, this reveals an increase in residual strain for these additional VWSG levels (level 2-5). This increase indicates an apparent extension of the VWSG and subsequent swelling of the concrete during the curing process.

The expectation of shrinkage during curing applies to piles in dry or semi-dry conditions, where the surrounding soils are unable to supply sufficient free water to the concrete for swelling. In the case of the lower section of the test piles at the Hinge site, this is likely due to the presence of low-permeability, high-plasticity Eocene clay (Søvind Marl), as described in section 3.8.5. However, it should be noted that the sand layers in the upper section of the test piles are surrounded predominantly by clay till and clayey fill, which could potentially retain water and provide sufficient free water for the concrete to undergo swelling during the curing process (as described in section 3.4.2).

Another observation made from Figure 133 and Figure 134 is that the strain development in the upper VWSG level is still influenced by temperature fluctuations, despite being corrected for thermal influence. This discrepancy can be attributed to a combination of errors during temperature correction and the difference in thermal expansion between the test piles and the surrounding soils.

Figure 135 illustrates the distribution of residual loads along the length of test pile 4 and 8. This distribution is determined based on the assumption that the axial pile stiffness is equal to the value derived from the tangent stiffness method utilized during the static pile loading tests, as discussed in section 6.3.2.

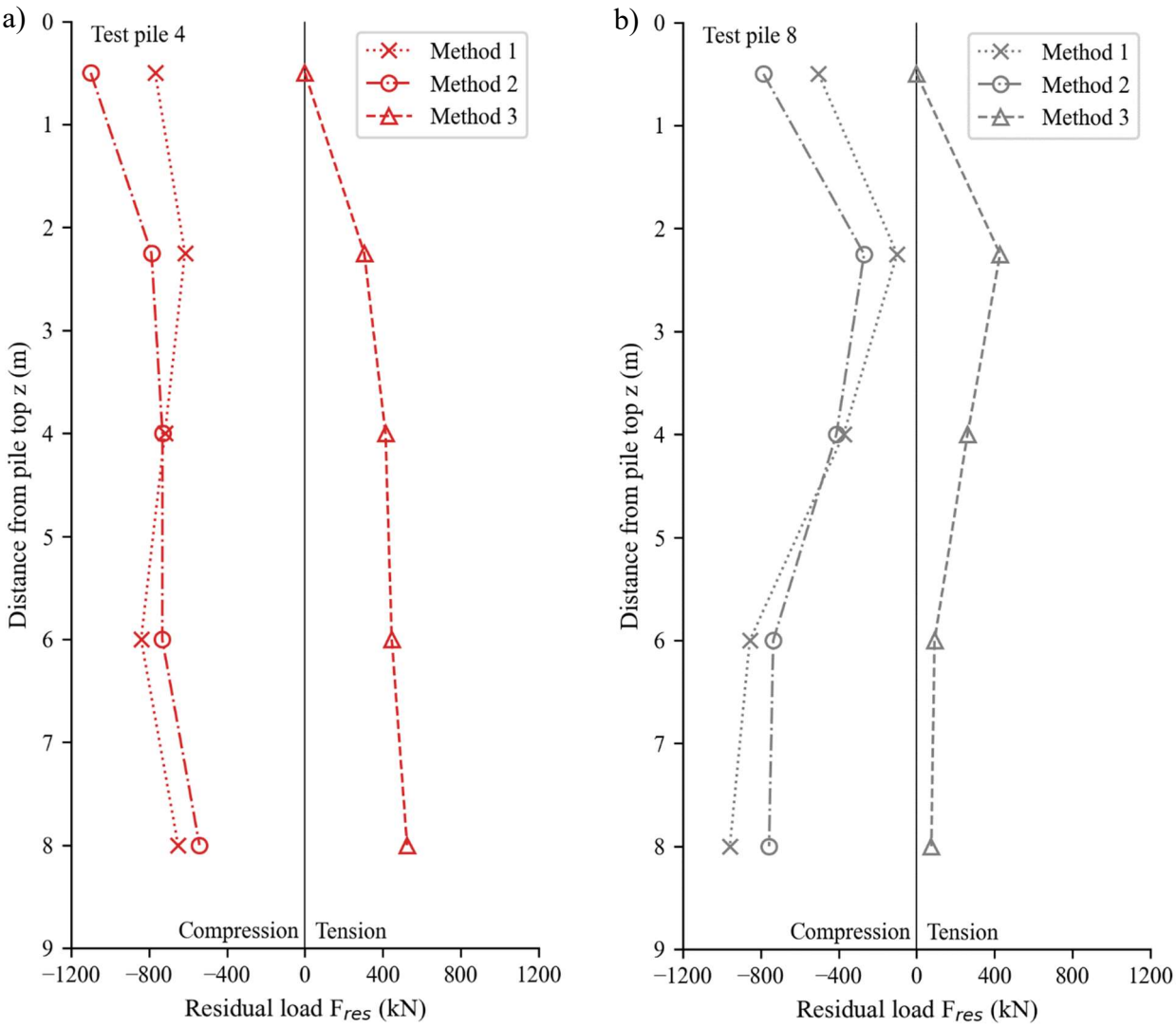

Figure 135: Distribution of residual loads along the length of test pile (a) 4 and (b) 8 cf. Method 1: Simplified method, Method 2: Pennington (1995) and Method 3: Siegel and McGillivray (2009).

Figure 135 clearly demonstrates the contrasting distribution of residual load among the three interpretation methods (Method 1, Method 2, and Method 3). Method 1, the Simplified method, and Method 2 based on Pennington (1995) indicate excessive compressive forces at the pile base, with values of -651 kN and -541 kN for test pile 4, and -959 kN and -758 kN for test pile 8, respectively. Method 3 proposed by Siegel and McGillivray (2009) also appears excessive, with an unrealistic tension force of 525 kN for test pile 4 and a more reasonable tension force of 75 kN for test pile 8.

Additionally, uncertainties exist regarding the distribution of residual loads along the length of test pile 4 and 8. One factor contributing to these uncertainties is the significant variation in axial pile stiffness throughout the concrete curing process and along the length of the test piles. These variations could potentially have a substantial impact on the interpretation of residual loads.

Moreover, it is important to note that in the initial phase when the concrete is in a fluid state, bored piles are incapable of transferring internal pile strains to the surrounding soils.

Figure 136 and Figure 137 illustrate the outcomes when employing Method 1, 2, and 3 to adjust the load distribution along the length of test piles 4 and 8.

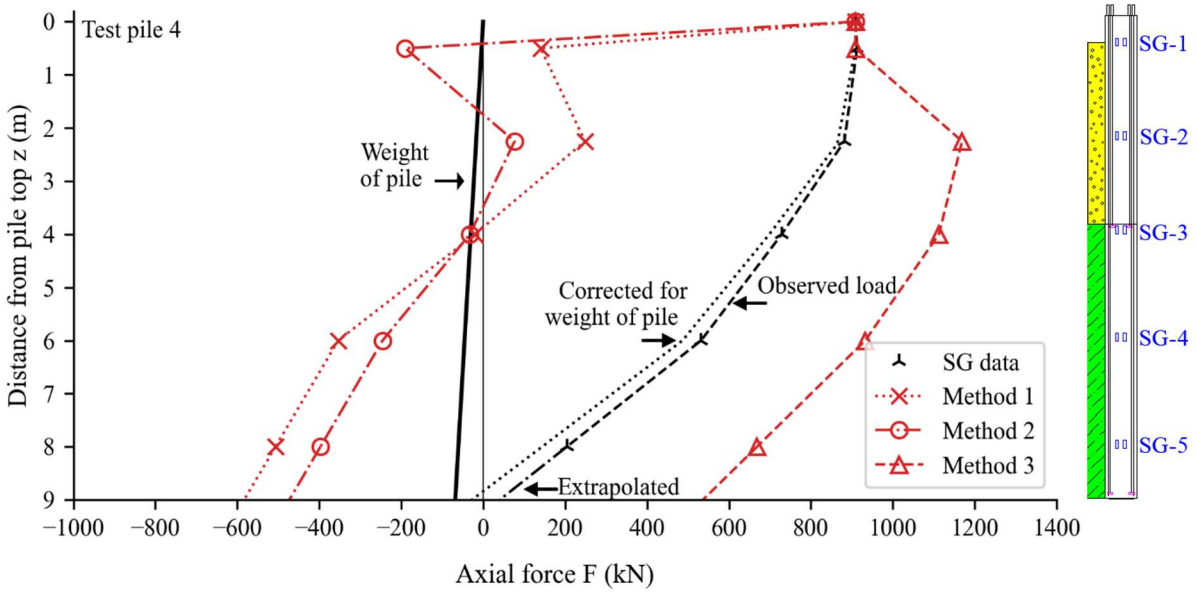

Figure 136: Load distribution along the length of test pile 4 with correction of residual stresses based on Method 1: Simplified method, Method 2: Pennington (1995) and Method 3: Siegel and McGillivray (2009).

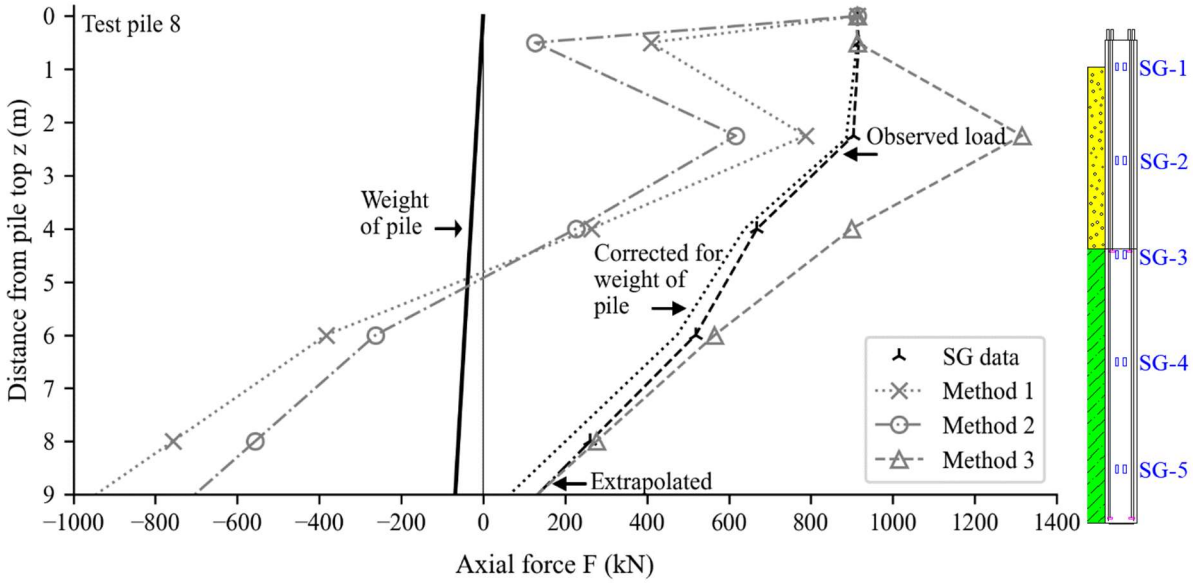

Figure 137: Load distribution along the length of test pile 8 with correction of residual stresses based on Method 1: Simplified method, Method 2: Pennington (1995) and Method 3: Siegel and McGillivray (2009).

The analysis in Figure 136 and Figure 137 reveals that the interpretation methods, namely Method 1: Simplified method and Method 2: Pennington (1995), exhibit unrealistic load distribution along the length of test piles 4 and 8. This is evident from the axial load reaching compression values ranging from approximately -473 kN to -945 kN at the base of the pile, which is unrealistic for a pile tested in tension.

In addition, Method 3: Siegel and McGillivray (2009) yield axial loads between 132 kN and 537 kN in tension at the base of test piles 4 and 8. The expected axial load should either be zero or the maximum suction force ($A_b \cdot 1\ atm \sim 31\text{kN}$) during failure. Consequently, the existing methods from the literature are inadequate for rectifying residual stresses in the test piles.

The primary issue with these methods for correcting residual stresses lies in the difficulty of accurately quantifying and distinguishing internal pile strains resulting from concrete setting and curing, from mechanical strains originating from external forces on the pile shaft (such as down drag). Thus, a new method is proposed for interpreting residual stresses

8.1.4 New method for interpretation of residual stresses

Residual stresses are documented using a new method based on post pile loading data, making it advantageous as it does not require supplementary, long-term measurements. In the new method, the remaining unit shaft resistance is assessed after unloading the test piles. It assumes that the shaft resistance is entirely mobilised along the length of the test piles during the failure stage of the pile loading test and considers the pile to be "stress-free" post-unloading as depicted in Figure 138 (a) and (b).

The latter assumption is most likely not correct, as residual forces may also remain after unloading due to difference in elastic pile strains and soil stiffnesses along the length of the pile. It would require that the stiffness of the soil increased with depth to balance the reducing elastic strains with depth for the pile to be stress free after unloading.

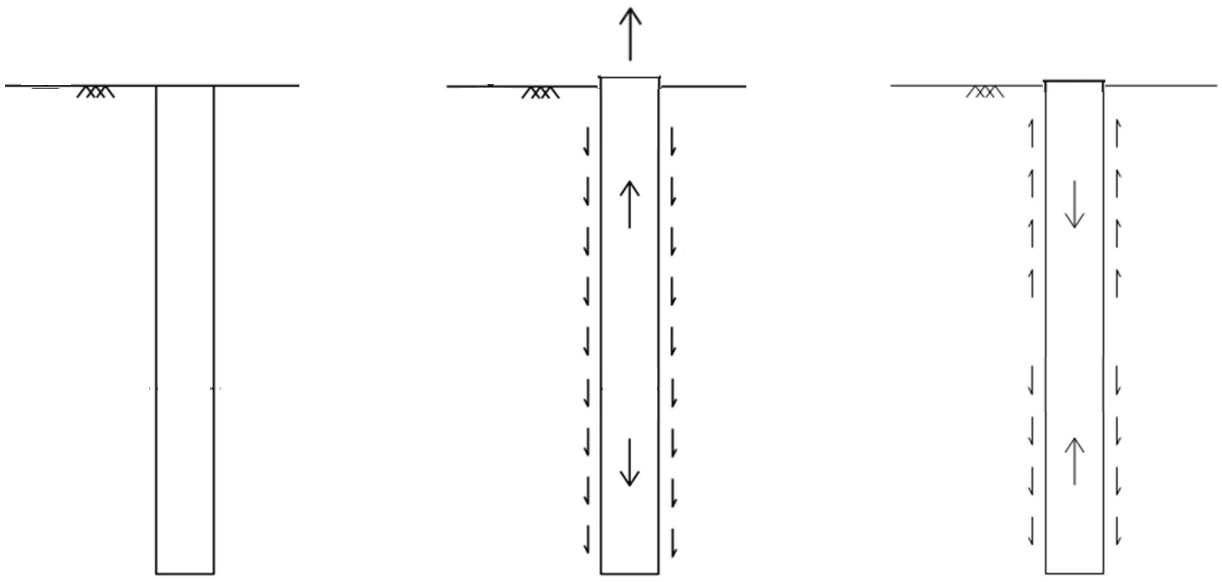

Figure 138: Distribution of residual stresses in (a) the stress-free state, (b) the failure stage and (c) after unloading the test piles.

Most likely the distribution of residual stresses after unloading is governed by the small downward pile movement relative to the soil from the elastic rebound of the pile after the static pile loading test in tension. This induce negative unit shaft resistance along the upper length of the pile that is resisted by positive unit shaft resistance along the lower length of the pile as depicted in Figure 138 (c).

The elastic rebound is defined as the maximum elastic lengthening, $\delta_{pile,e}$, of the piles. At the test site in Hinge, the elastic rebound is determined cf. section 5.6 to be between 0.3 and 0.4 mm for test piles 1-8. By analysing the mobilised unit shaft resistance curves provided in section 6.3.4, it becomes evident that the maximum error, when assuming a stress-free state after unloading, remains below 10 kPa for all soil layers. This minor error is considered to be a representation of the uncertainties associated with the utilization of the new method.

Upon analysis of the mobilised unit shaft resistance, particularly the unloading path, it becomes apparent that the upper sand layer likely experiences tensile failure during loading and compressive failure during unloading (due to the elastic rebound). This is demonstrated by the example shown in Figure 139 for test pile 5, where the vertical displacement exhibits a horizontal segment in both the loading and unloading path, indicating soil failure (black dashed lines). If the mobilised unit shaft resistance is numerically similar in both the loading and unloading path, and if equal ultimate unit shaft resistance in tension and compression for the sand layer is assumed, it can be inferred that no residual stresses are present in the upper sand layer. While this is not entirely accurate, the upper sand layer is considered to be a close representation of the "true" unit shaft resistance. The same observation applies to the other test piles in Hinge, as shown in Appendix H.6.

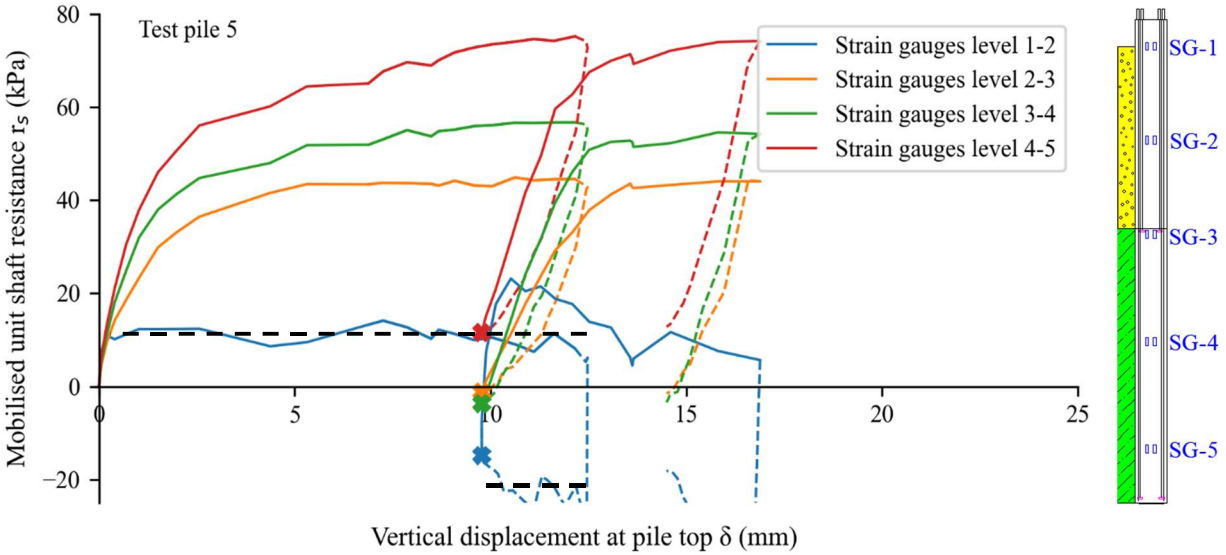

Figure 139: Mobilised unit shaft resistance for test piles 5. Residual stresses marked with a cross.

Figure 139 illustrates the mobilised unit shaft resistance for test pile 5, which might indicate that this particular pile was not influenced by residual stresses prior to the pile loading test. The negative unit shaft resistance observed in the upper sand layer (strain gauge level 1-2) is attributed to the elastic rebound of the test piles, counteracted by the positive unit shaft resistance of the lower clay layer

(strain gauge level 4-5). However, these observations do not hold true for the other test piles, indicating the presence of residual stresses before the static pile loading test, see Appendix H.6.

In the following analysis the residual stresses after unloading are assumed to be "stress-free" post-unloading despite the potential error (<10 kPa) on the mobilised unit shaft resistance introduced by disregarding the presence of residual stresses after unloading due to elastic rebound of the test piles.

The determination of residual stresses, represented by the remaining unit shaft resistance after unloading of the test piles, is provided and shown for test pile 4 and 8 in Figure 140-Figure 141 and in Appendix H.6 for all test piles (test pile 1-8). However, for test pile 1, there is no separate measurement of post pile loading data available in the lower sand layer and upper clay layer due to an error in strain gauge level 3. Therefore, only an average value spanning from the middle of the sand layer (strain gauge level 2) to the middle of the clay layer (strain gauge level 4) can be obtained. Consequently, test pile 1 is excluded from the following sections of this thesis since adjustments for residual stresses cannot be made.

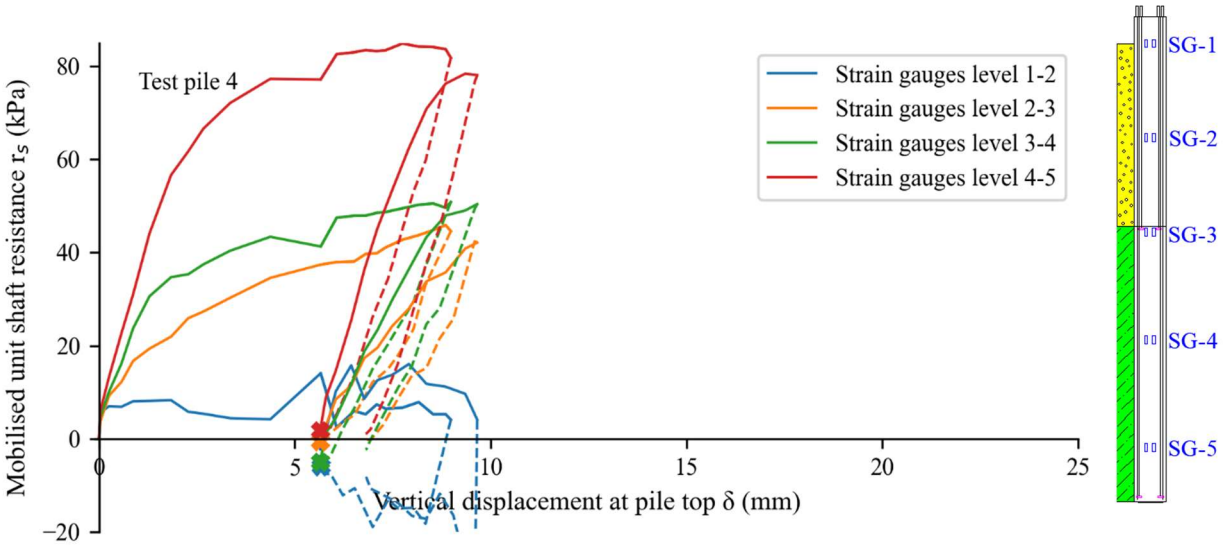

Figure 140: Mobilised unit shaft resistance for test pile 4. Residual stresses marked with a cross.

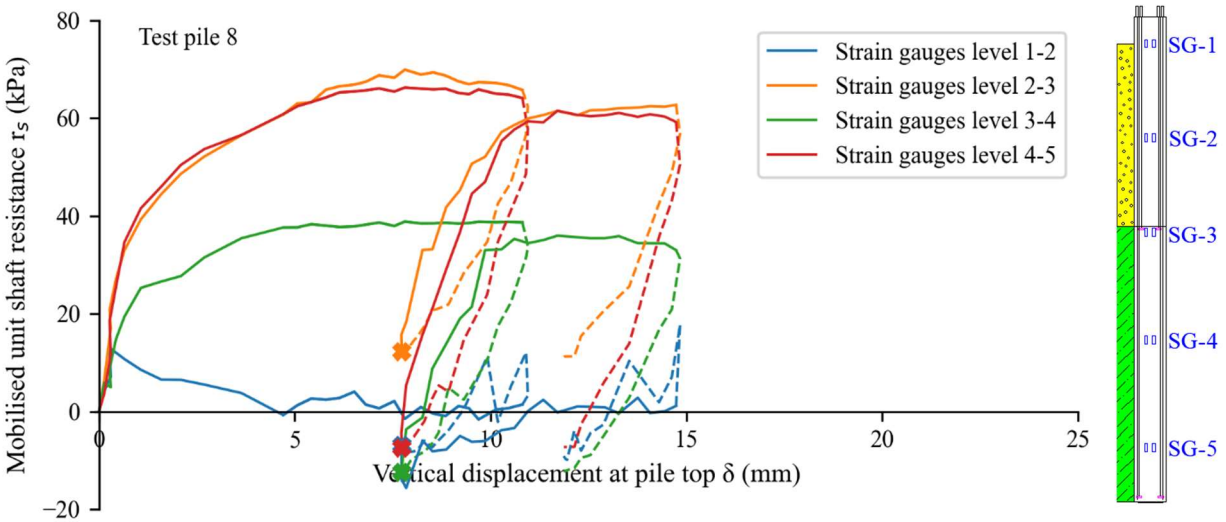

Figure 141: Mobilised unit shaft resistance for test pile 8. Residual stresses marked with a cross.

When the remaining unit shaft resistance after unloading of the test piles is negative, it indicates that positive residual stresses had developed prior to the pile loading test. Consequently, the ultimate unit shaft resistance determined from the observed load transfer curves is smaller than that from the "true" load transfer curves. Conversely, when the remaining unit shaft resistance after unloading of the test piles is positive, it signifies that negative residual stresses had developed prior to the pile loading test. Therefore, the ultimate unit shaft resistance determined from the observed load transfer curves is larger than that from the "true" load transfer curves. The magnitude of residual stresses in the upper sand layer, lower sand layer, upper clay layer, and lower clay layer are presented in Table 20 for test piles 2-8.

Table 20: Residual stresses determined from unit shaft resistance remaining after unloading of test piles 2-8.

Soil layer	Residual stresses [kPa]							
	TP1	TP2	TP3	TP4	TP5	TP6	TP7	TP8
Upper sand layer	-	3.3	15.0	5.8	14.8	5.3	10.6	6.9
Lower sand layer	-	1.7	-1.5	0.6	1.2	3.4	-9.0	-12.2
Upper clay layer	-	-2.9	0.4	5.0	3.6	11.2	-8.9	12.4
Lower clay layer	-	-3.9	1.7	-1.8	-11.7	-4.8	19.3	7.4

Remaining unit shaft resistance after unloading of the test piles in the upper length of the test piles (upper sand layer, strain gauge level 1-2) are all negative indicating positive residual stresses was developed prior to pile loading test and thus, the "true" load transfer curves are between 3.3 and 15.0 kPa higher than seen from the observed load transfer curves.

For the lower sand layer (strain gauge level 2-3) the remaining unit shaft resistance after unloading of the test piles range from -3.4 kPa to 12.2 kPa indicating both positive and negative residual stresses was developed prior to pile loading test and thus, the "true" load transfer curves are between 3.4 kPa higher to 12.2 kPa lower than seen from the observed load transfer curves.

For the upper clay layer (strain gauge level 3-4) the remaining unit shaft resistance after unloading of the test piles range from -12.4 kPa to 8.9 kPa indicating both positive and negative residual stresses was developed prior to pile loading test and thus, the "true" load transfer curves are between 12.4 kPa higher to 8.9 kPa lower than seen from the observed load transfer curves.

And finally, for the lower clay layer (strain gauge level 4-5) the remaining unit shaft resistance after unloading of the test piles range from -19.3 kPa to 11.7 kPa indicating both positive and negative residual stresses was developed prior to pile loading test and thus, the "true" load transfer curves are between 19.3 kPa higher to 11.7 kPa lower than seen from the observed load transfer curves.

8.1.5 Actual size and distribution of residual loads

To determine the size and distribution of residual loads, F_{res}, the residual stresses determined by the new method are summarized along the length of test piles 2-8. These values are then compared with those determined using Method 1: Simplified method, Method 2: Pennington (1995), and Method 3:

Siegel and McGillivray (2009) for test piles 4 and 8. Figure 142 displays the comparison between the different methods.

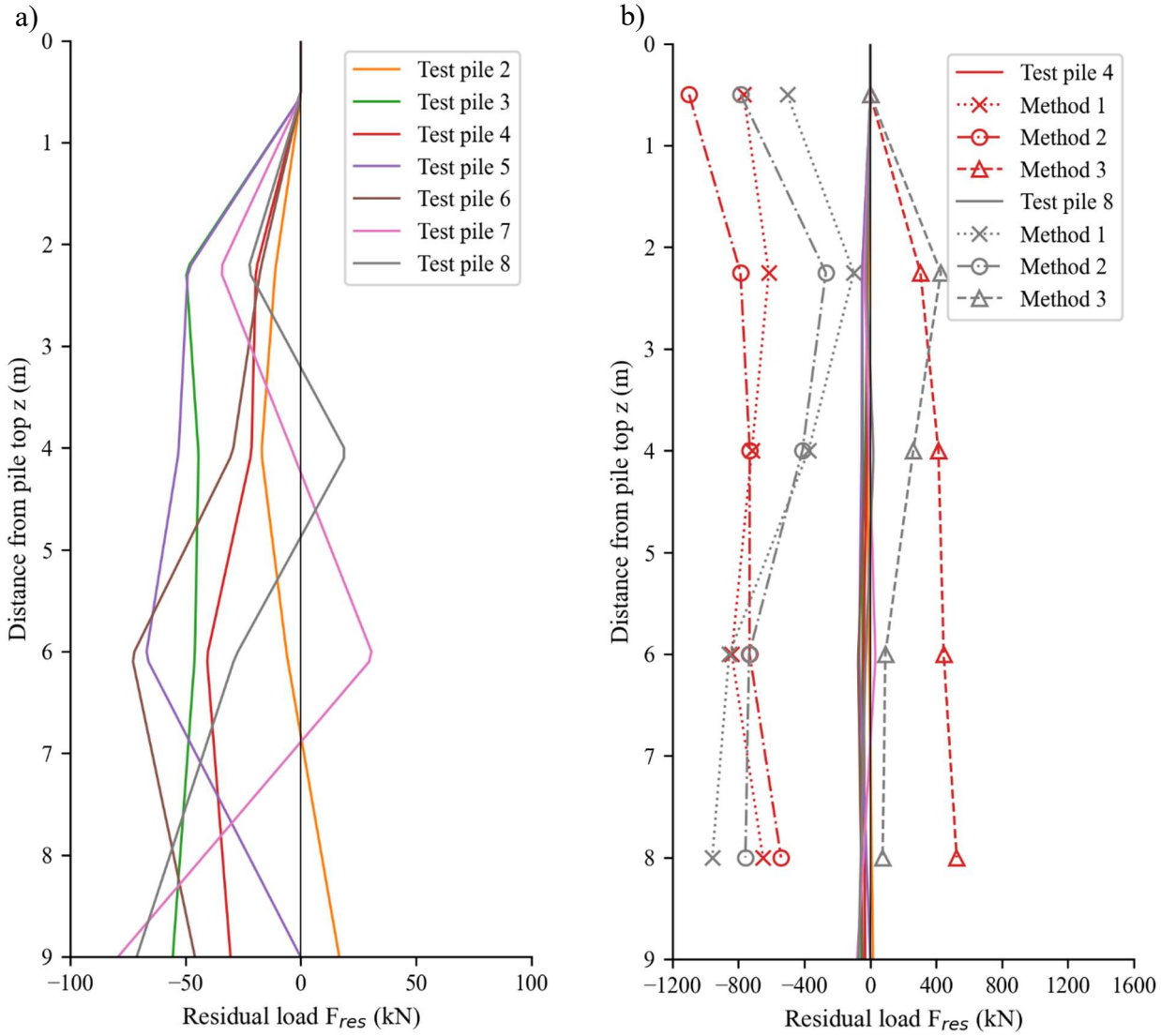

Figure 142: Residual loads, F_{res}, (a) obtained from the residual stresses in test piles 2-8 and (b) compared to the residual loads derived using Method 1: Simplified method; Method 2: Pennington (1995) and Method 3: Siegel and McGillivray (2009) for test pile 4 and 8.

At first glance (cf. Figure 142 (a)), the residual loads, F_{res}, for test piles 2-8 appear to exhibit random variations. However, when compared to the residual loads determined from Method 1: Simplified method, Method 2: Pennington (1995), and Method 3: Siegel and McGillivray (2009) for test piles 4 and 8 (as shown in Figure 142 (b)), it becomes evident that the residual loads determined by the new method are of similar magnitudes, despite variations along the length of the test piles.

The residual loads at the pile base range from -75 kN in axial compression to 25 kN in axial tension. These values are reasonable and can be resisted as either base resistance, calculated as $R_b = 9 \cdot 1/3 \cdot c_u \cdot A_b = 9 \cdot 1/3 \cdot 242\text{kPa} \cdot 0.31\text{m}^2 = 226\text{kN}$, or as suction force ($A_b \cdot 1\ atm \sim 31\text{kN}$) beneath the pile base.

Test piles 2, 4, 5, and 6 exhibit a behaviour where positive induced residual stresses are observed along the upper length of the piles, while negative induced residual stresses are observed along the lower length of the piles. This behaviour can be attributed to down drag effects caused by the compression of loosely built sand in the top 3.4 m of the test piles due to rainwater seepage and/or the replacement of sand and base course with gravel in the upper 0.4 m before conducting pile loading tests. Refer to Figure 143 (a) for visual representation.

On the other hand, test piles 3, 7, and 8 display a different pattern where positive induced residual stresses are observed along both the upper and lower length of the piles, with negative induced residual stresses in between. This behaviour could be attributed to internal strains within the piles resulting from concrete setting and curing, causing swelling in the sand layer at the upper section of the test pile and shrinkage in the low permeable, high plasticity Eocene clay (Søvind Marl) at the lower section. Refer to Figure 143 (b) for visual representation.

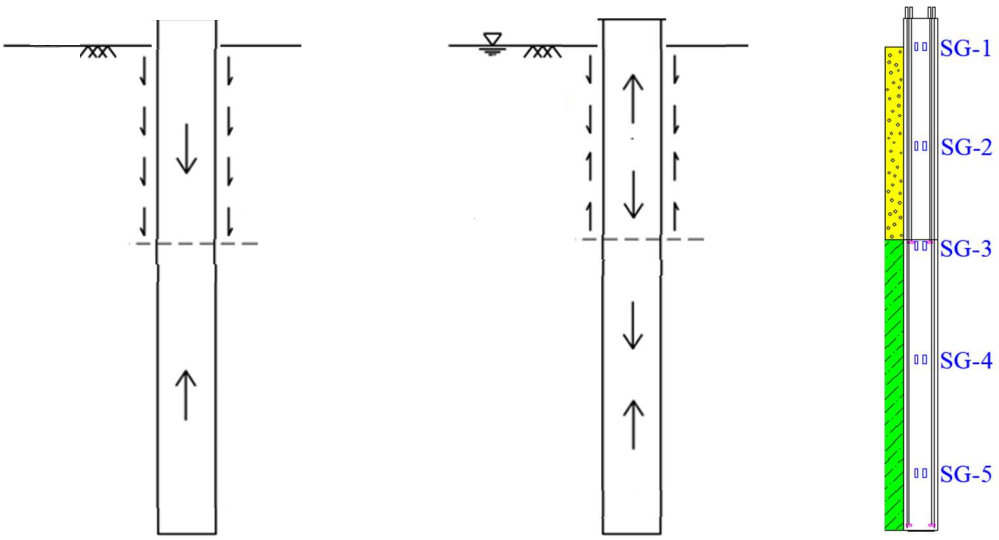

Figure 143: Effects of (a) down drag and (b) concrete curing in terms of swelling and shrinkage of concrete.

In reality, the variation along the length of the test piles in terms of residual stresses is likely influenced by a combination of external strains from down drag, internal pile strains resulting from concrete setting and curing, as well as available residual base resistance. However, it is challenging to accurately quantify or provide a detailed explanation for these variations.

Ideally, the fibre optic strain cables (FOSC) could have been utilized to further investigate and define the neutral depths where the direction of the residual stresses shifts. Unfortunately, due to the presence of multiple NaN (Not a Number) values, high levels of scatter, local concrete cracks, changes in cross-sectional area, and pile stiffness, the uncertainty associated with the FOSC measurements is too significant. As a result, the FOSC data can only be used to confirm the trend observed from the VWSG, as presented in section 7.4.

The effects of utilizing residual loads for adjusting the load distribution along the length of test piles 2-8 are depicted in Figure 144 and Figure 145.

Maintained load (ML) test

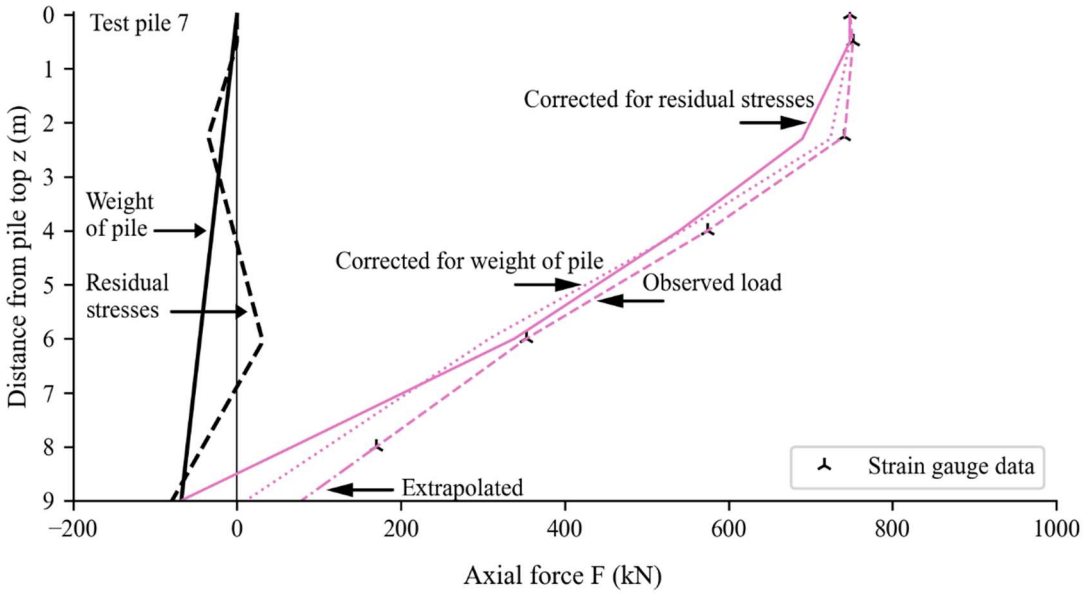

Figure 144: Load distribution along the length of test pile 7 based on vibrating wire strain gauge (VWSG) data corrected for weight of the test pile and residual stresses determined by the new method.

Constant rate of uplift (CRU) test

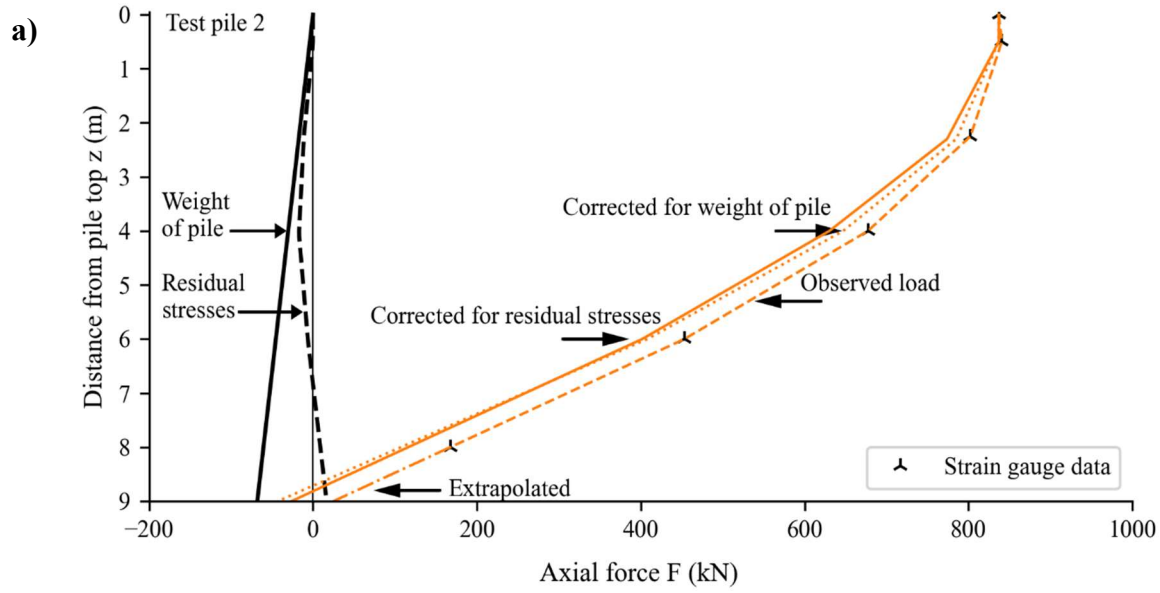

b

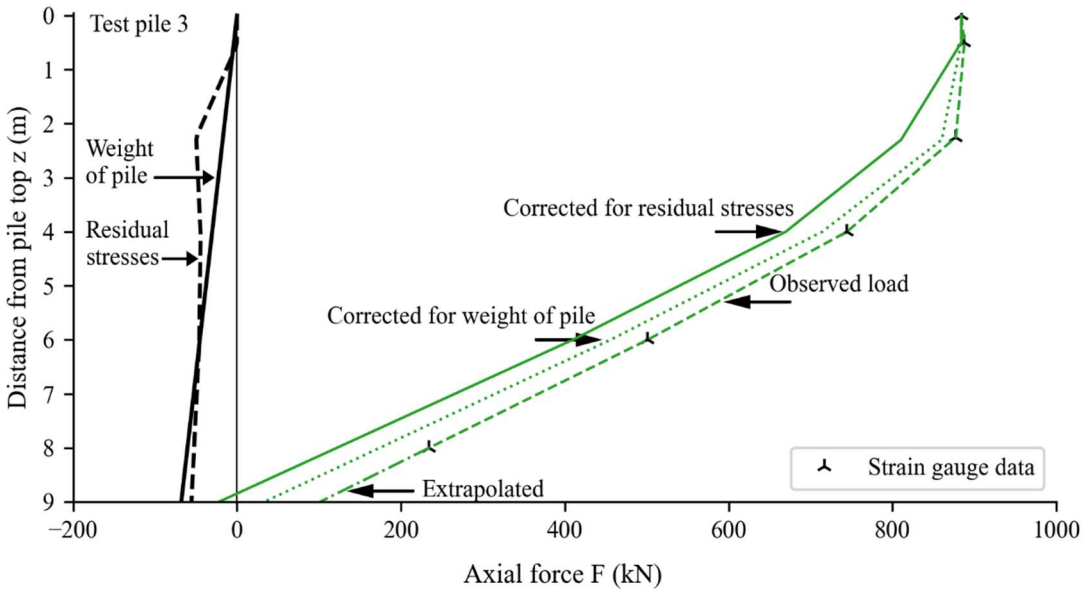
Test pile 3
Weight of pile
Residual stresses
Corrected for residual stresses
Observed load
Corrected for weight of pile
Extrapolated
Strain gauge data
Distance from pile top z (m)
Axial force F (kN)
0
1
2
3
4
5
6
7
8
9
−200
0
200
400
600
800
1000

c)

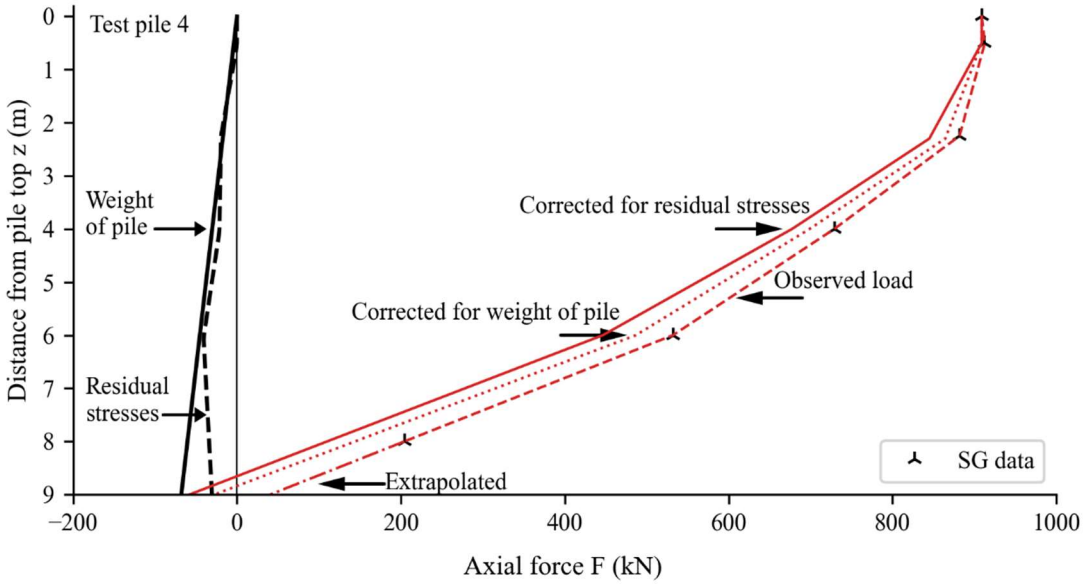
Test pile 4
Weight of pile
Residual stresses
Corrected for residual stresses
Observed load
Corrected for weight of pile
Extrapolated
SG data
Distance from pile top z (m)
Axial force F (kN)
0
1
2
3
4
5
6
7
8
9
−200
0
200
400
600
800
1000

d

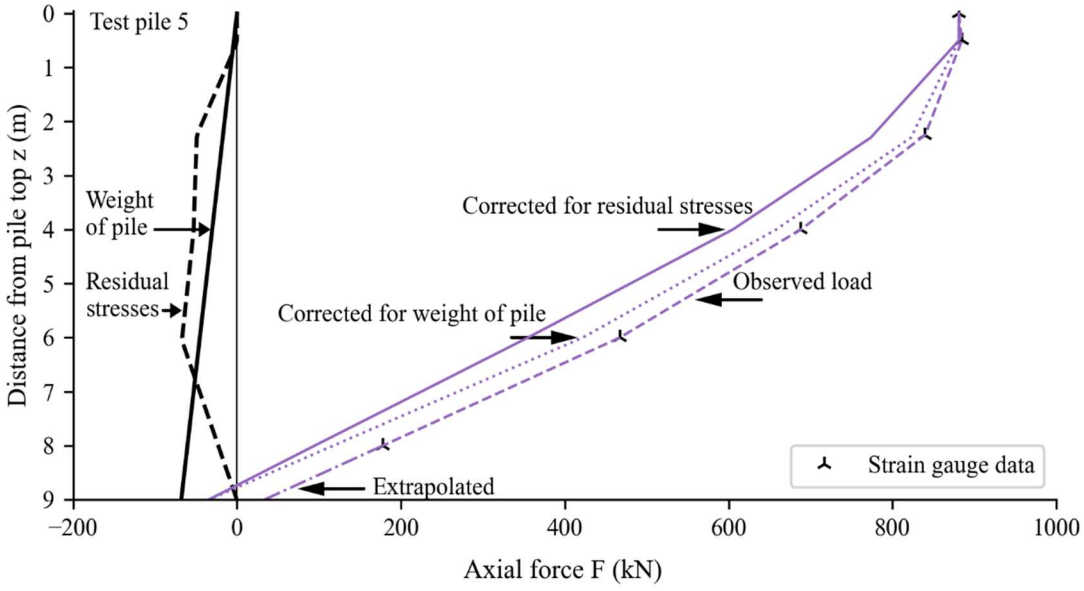
Test pile 5
Weight of pile
Residual stresses
Corrected for residual stresses
Observed load
Corrected for weight of pile
Extrapolated
Strain gauge data
Distance from pile top z (m)
Axial force F (kN)
0
1
2
3
4
5
6
7
8
9
−200
0
200
400
600
800
1000

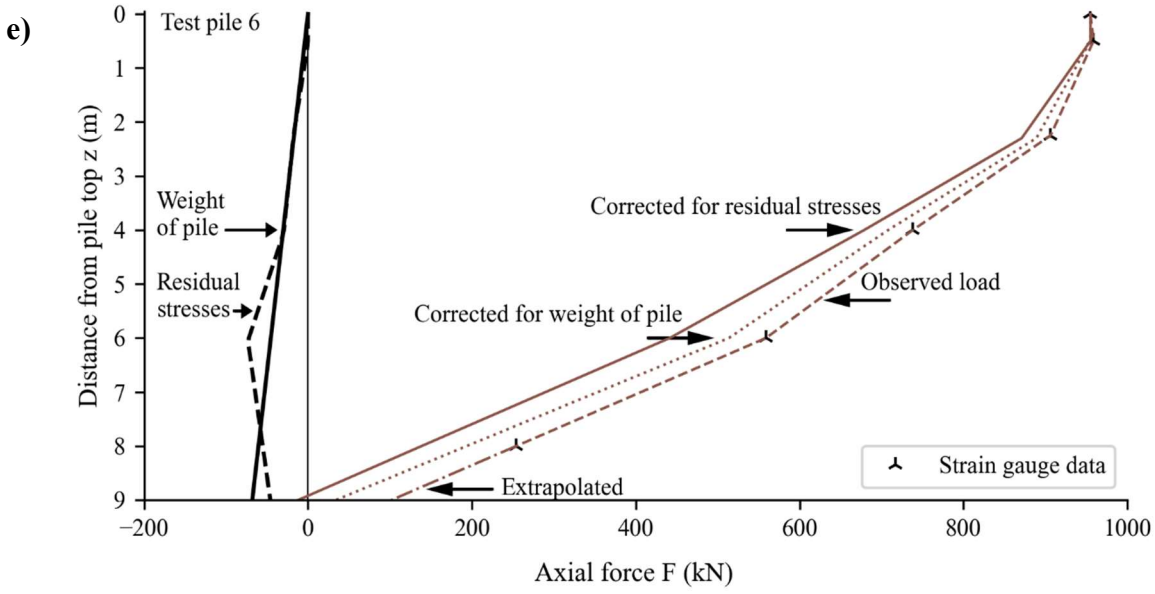

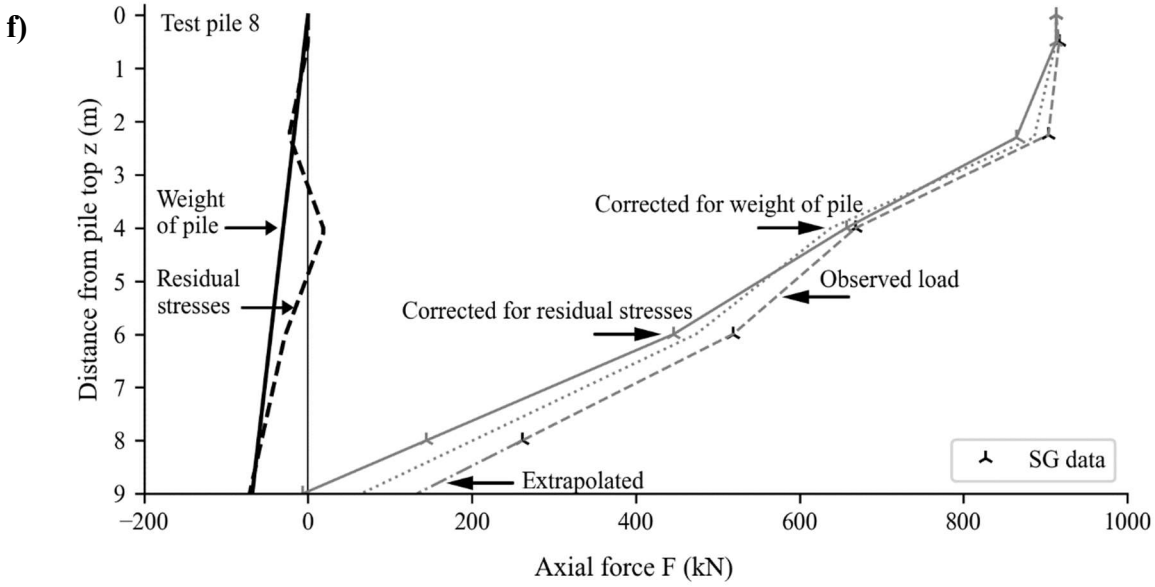

Figure 145: Load distribution along the length of test pile (a) 2, (b) 3, (c) 4, (d) 5, (e) 6 and (f) 8 based on vibrating wire strain gauge (VWSG) data corrected for weight of the test piles and residual stresses determined by the new method.

Table 21 provide the axial force at the pile base level during failure for test piles 2-8, after adjusting for the weight of the test pile and accounting for residual loads determined using the new method.

Table 21:Axial force at pile base level during failure for test piles 2-8 after adjusting for the weight of the test pile and residual stresses determined using the new method.

Level	Axial force F [kN]							
	TP1	TP2	TP3	TP4	TP5	TP6	TP7	TP8
Pile base	-	-26	-22	-58	-34	-12	-69	-6

After correction for residual loads, the axial force at the pile base level during failure for test piles 2, 3, 6, and 8 shows reduced deviations from zero, compared to the values before correction. However, for test piles 4 and 7, the deviation slightly increases. The axial force at the pile base level during

failure before correction can be found in Table 19 The deviations correspond to errors ranging from 0.7% to 9.2% of the ultimate shaft resistance.

The new method for interpreting residual loads has not yet been tested on other piles. However, Fellenius (2015) observed apparent tension after the unloading of a static pile loading test in compression, which was attributed to the release of residual load - supporting the rationale behind the new method. This observation was similar to the fully mobilised residual load at the start of the test determined by Fellenius's direct method (Fellenius, 2002a, Fellenius, 2002b, Fellenius, 2002c).

The pile in question was a 45-meter-long, concrete-filled, closed-toe steel pipe pile with a diameter of 400 mm, driven into sand and soft clay. During failure, the shaft resistance was fully mobilised along the length of the test pile (see Figure 146).

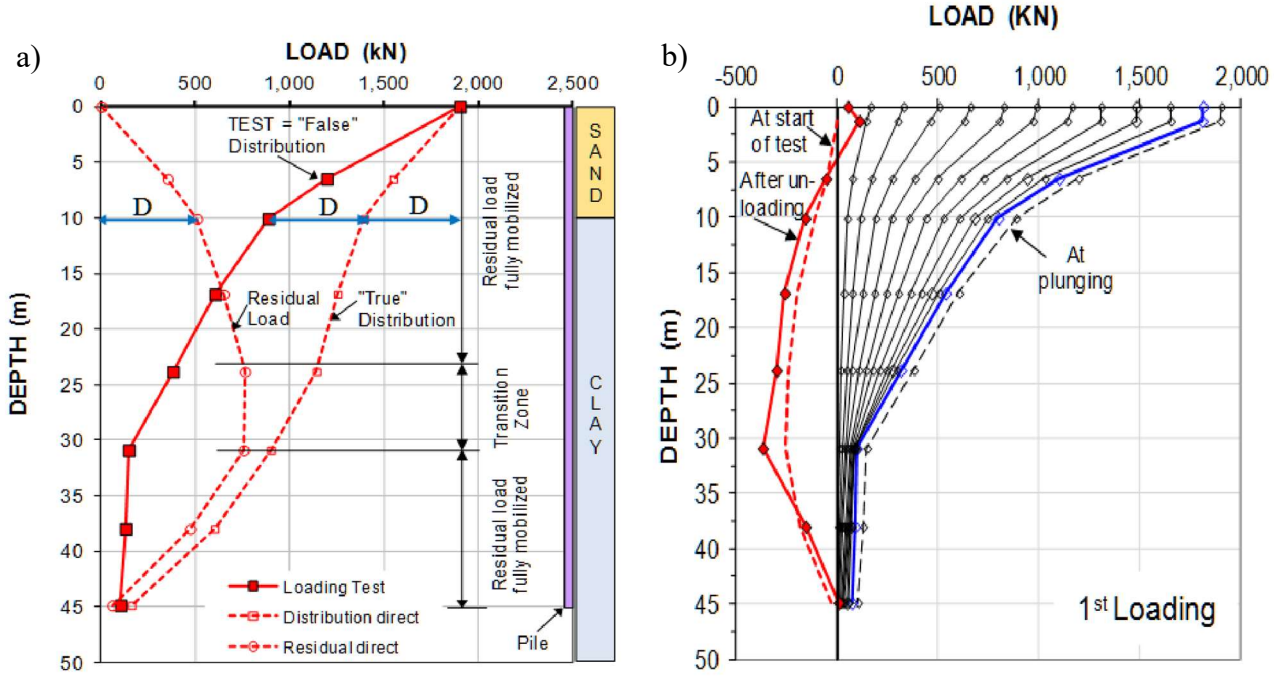

Figure 146: (a) "False", "True" and Residual load distribution cf. Fellenius direct method (Fellenius, 2002a, Fellenius, 2002b, Fellenius, 2002c) and (b) Residual load distribution after unloading of a static pile loading test compared to at the start of the test determined by Fellenius direct method.

Given the relatively small size of the residual stresses, it becomes challenging to establish a clear demonstration of their influence on the pile loading test data. Hence, in addition to the observations presented above, an assessment is made as to whether the ultimate unit shaft resistances align better with the expected values before or after correcting for the effects of residual stresses.

The ultimate unit shaft resistance is anticipated to exhibit lower values in the upper sand layer, gradually increasing along the length of the test piles through the lower sand layer, upper clay layer, and lower clay layer cf. section 3.4.2 and 3.6. Please refer to section 8.2. for further details.

8.2 Influence of residual stresses on load transfer curves

In this section, it is assessed whether the ultimate unit shaft resistances align better with expectations before or after accounting for residual stresses. This assessment is conducted by examining the "true" load transfer curves in comparison to the observed load transfer curves. It is analysed whether the magnitude of ultimate unit shaft resistance in the sand and clay layers follows the expected order and whether the magnitude of ultimate unit shaft resistance is plausible.

Additionally, the influence of residual stresses on the ultimate mobilised observed unit shaft resistance is considered, taking into account the size and distribution of residual stresses outlined in section 8.1.4 and 8.1.5.

8.2.1 "True" load transfer curves

The determination of the "true" load transfer curves involves adjusting the observed load transfer curves based on the residual stresses provided in Table 20 and the relative vertical displacement between the pile and soil, $\Delta\delta_{pile,soil}$. It is assumed that during pile unloading after failure, the behaviour follows a linear elastic pattern with a shear stiffness equivalent to the initial linear elastic shear stiffness of the observed load transfer curve. While this assumption is an approximation, it has been found to be reasonably accurate in section 6.2.7.

However, it should be noted that the process of determining the "true" load transfer curves by adjusting the observed load transfer curves with the aforementioned assumptions is only valid for minor negative residual stresses, or downward movement of the pile. The method described above cannot be applied to situations involving major negative residual stresses due to the absence of compression pile loading tests. Consequently, the unloading path from point B in Figure 142 remains unknown in such cases.

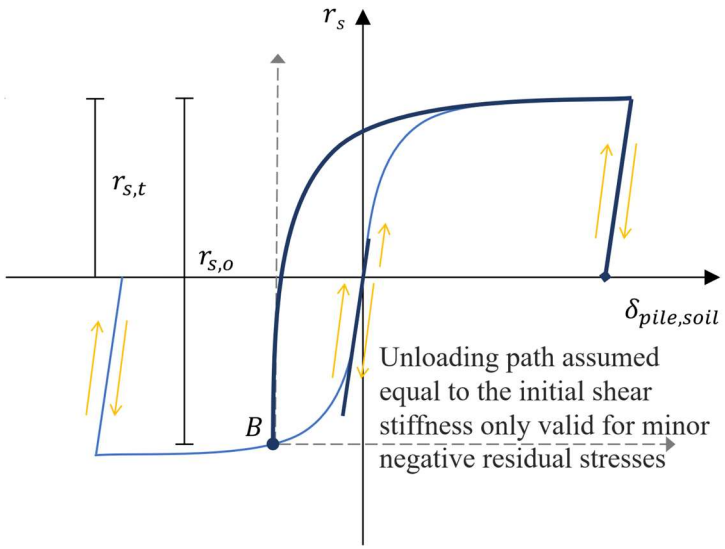

Figure 147: Assumed unloading path on load transfer curves. Observed load transfer curves displayed with dotted grey axes and "true" load transfer curves displayed with solid black axes.

Adjustment of the relative vertical displacement between pile and soil, $\Delta\delta_{pile,soil}$, is based on the residual stresses given in Table 20 and the initial linear elastic shear modulus, G_0, of the shear stiffness degradation curves presented in Appendix H.7. The initial linear elastic shear modulus, G_0, is determined at a pseudo strain of 10^{-4} corresponding to 0.062 mm vertical displacement between pile and soil, $\delta_{pile,soil}$, and presented in Table 22.

Table 22: Initial linear elastic shear modulus, G_0 determined at a pseudo strain of 10^{-4}.

Soil layer	Initial shear modulus [kPa/mm]							
	TP1	TP2	TP3	TP4	TP5	TP6	TP7	TP8
Upper sand layer	-	48.0	23.6	27.3	59.5	57.3	25.3	48.0
Lower sand layer	-	7.3	33.2	17.8	40.1	41.1	45.1	66.1
Upper clay layer	-	70.2	68.6	58.2	70.9	57.1	63.5	50.4
Lower clay layer	-	81.6	77.7	97.3	87.1	100.2	78.6	87.2

Therefore, the vertical displacement between pile and soil, $\delta_{pile,soil}$, is adjusted cf. Table 23.

Table 23: Adjustment of vertical displacement between pile and soil, $\Delta\delta_{pile,soil}$.

Soil layer	Vertical displacement between pile and soil [mm]							
	TP1	TP2	TP3	TP4	TP5	TP6	TP7	TP8
Upper sand layer	-	-0.07	-0.64	-0.18	-0.25	-0.09	-0.42	-0.14
Lower sand layer	-	-0.23	0.05	-0.03	-0.03	-0.08	0.20	0.18
Upper clay layer	-	0.04	-0.01	-0.09	-0.05	-0.20	0.14	-0.25
Lower clay layer	-	0.05	-0.02	0.02	0.13	0.05	-0.25	-0.08

The "true" load transfer curves and origin of the observed load transfer curves can be seen in Figure 148 and Figure 149 for test piles 2-8 with indication of ultimate observed unit shaft resistance, $r_{s,o}$ and ultimate "true" unit shaft resistance, $r_{s,t}$ for strain gauge level 1-2 (upper sand layer).

Maintained load (ML) test

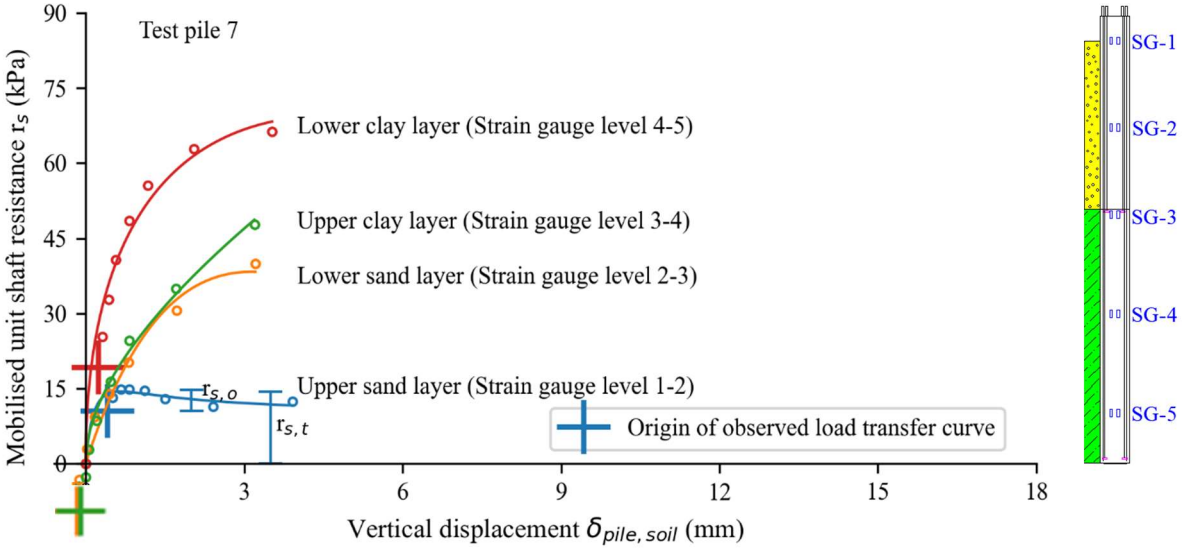

Figure 148: Mobilised unit shaft resistance corrected for residual stresses for test piles 7.

Constant rate of uplift (CRU) test

a)

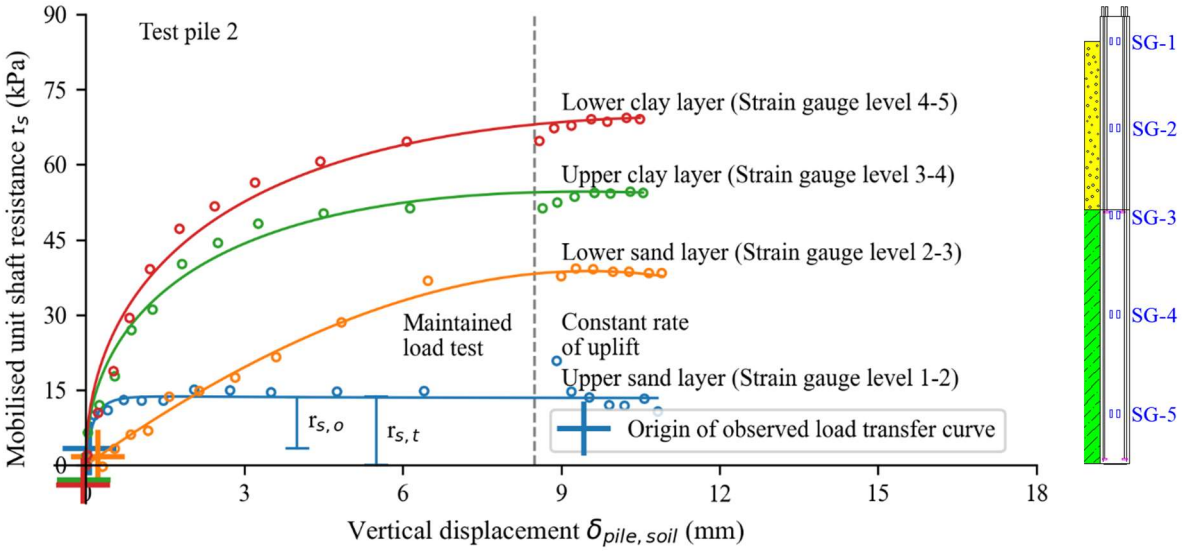

b)

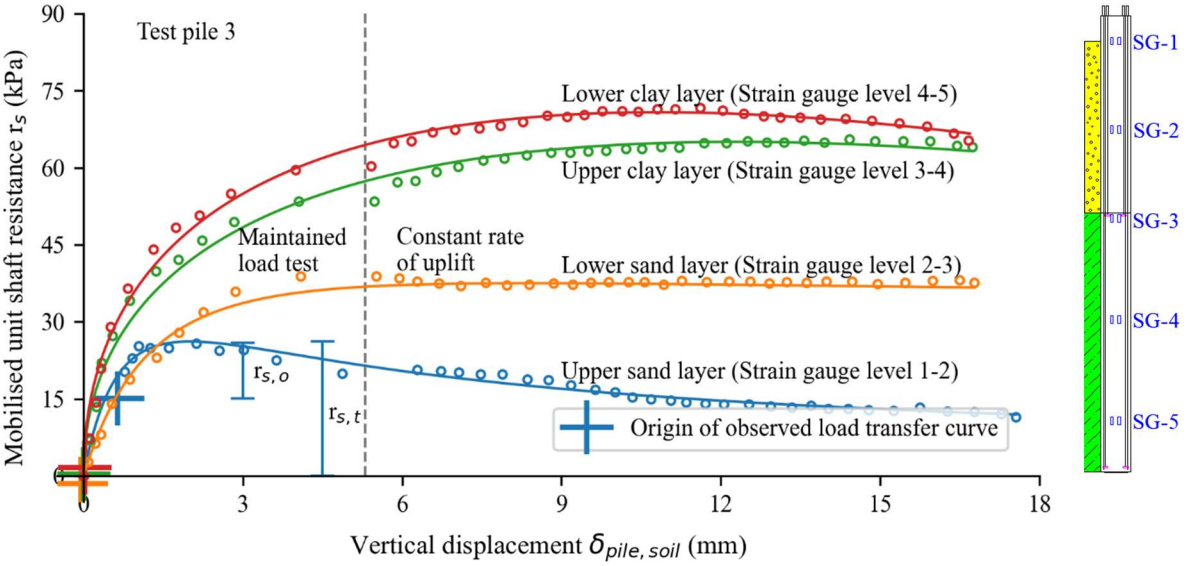

c)

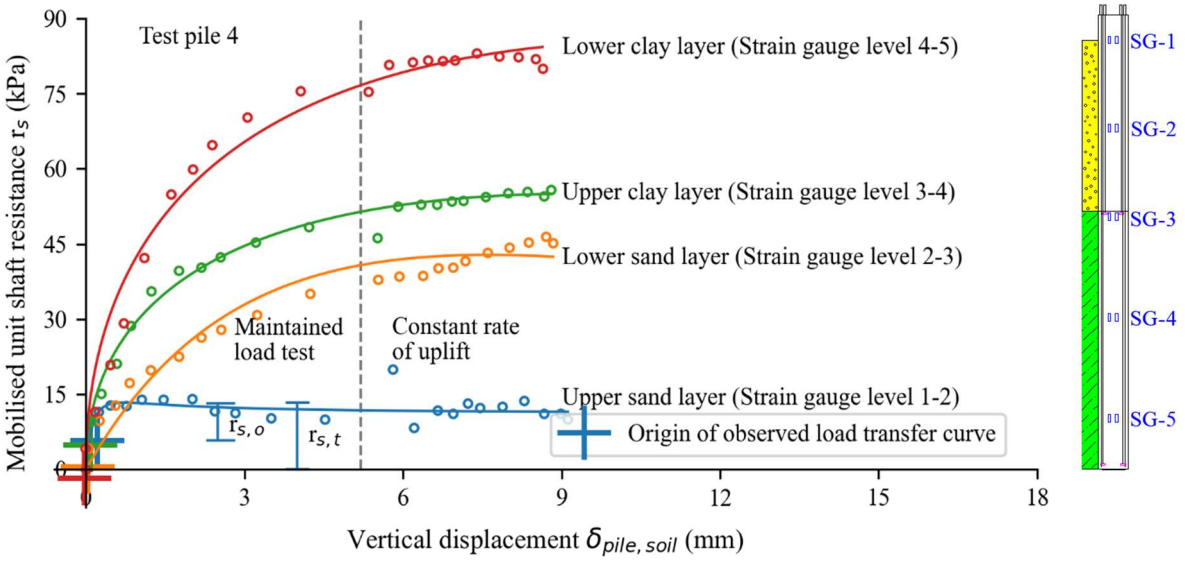

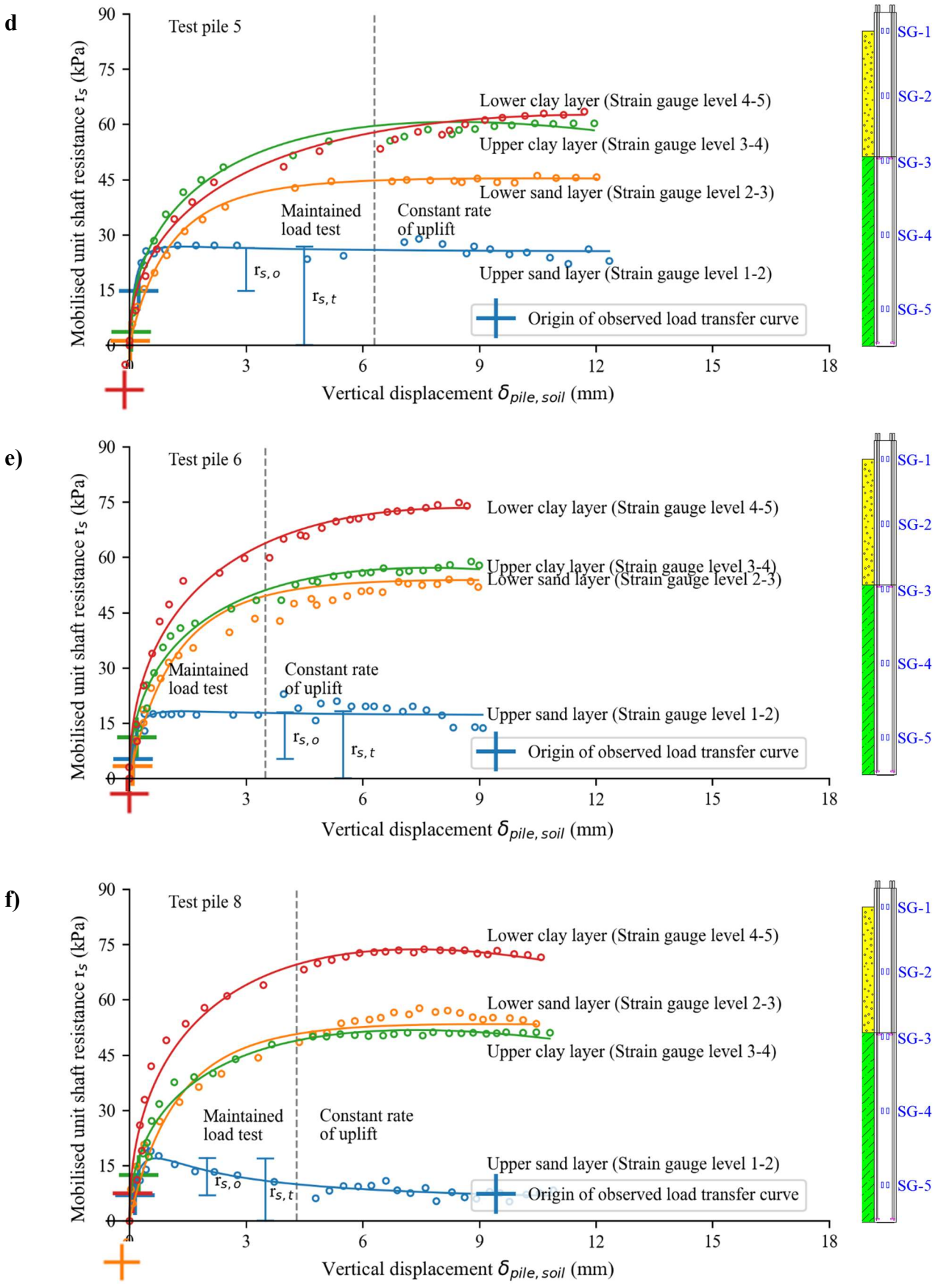

Figure 149: Mobilised unit shaft resistance corrected for residual stresses for test piles (a) 2, (b) 3, (c) 4, (d) 5, (e) 6 and (f) 8.

The unit shaft resistance is seen to increase gradually as the pile is moving upwards relative to the soil. The ultimate values of unit shaft resistance are 27 kPa for the upper sand layer, 58 kPa for the lower sand layer, 66 kPa for the upper clay layer, and 83 kPa for the lower clay layer cf. Table 24.

Table 24: Ultimate mobilised unit shaft resistance from the "true" load transfer curves.

Soil layer	Mobilised unit shaft resistance [kPa]							
	TP1	TP2	TP3	TP4	TP5	TP6	TP7	TP8
Upper sand layer	-	15	26	14	27	21	15	20
Lower sand layer	-	39	39	47	46	54	40	58
Upper clay layer	-	55	66	56	60	59	48	51
Lower clay layer	-	70	72	83	64	75	66	74

The ultimate unit shaft resistances derived from the "true" load transfer curves demonstrate better alignment with expectations compared to the observed load transfer curves presented in Table 15 of section 6.3.4. The magnitude of the ultimate unit shaft resistance follows the anticipated pattern, with the lowest values in the upper sand layer and increasing along the length of the test piles through the lower sand layer, upper clay layer and lower clay layer. However, it is worth noting an exception with test pile 8, where the ultimate unit shaft resistance in the lower sand layer is slightly higher than the ultimate unit shaft resistances observed in the upper clay layer.

8.2.2 Ultimate values of unit shaft resistance in the sand layers

The ultimate values of the "true" mobilised unit shaft resistance in the upper sand layers (strain gauge level 1-2) are determined to be between 14 kPa and 27 kPa, with an average value of 20 kPa. Similarly, the ultimate values of the "true" mobilised unit shaft resistance in the lower sand layers (strain gauge level 2-3) range from 39 kPa to 58 kPa, with an average value of 46 kPa.

Contrary to expectations, the ultimate values of "true" mobilised unit shaft resistance in the sand layers are very high and can potentially be explained by the following factors:

The mobilised unit shaft resistance is a function of the density of the sand and the horizontal stress. In this case, the sand surrounding the test piles are not compacted and thus loose immediately after being replaced. These sand layers are then enclosed by the overlying layer of gravel and road plates, which do not allow vertical deformations.

Compaction of the sand layers occurs subsequently due to the vibrations from installation (drilling) of the test piles, leading to an increase in the density of the sand layers. Moreover, during the casting of the test piles, the fluid pressure exerted by the wet concrete surpasses the horizontal stresses present in the sand layers. This causes the diameter of the test piles to enlarge and reduces the available volume for the surrounding sand. Ultimately, this process increases the density of the sand layers.

While curing, the test piles are exposed to free-standing groundwater, which causes the diameter of the test piles to increase. Consequently, the volume available for the sand surrounding the test piles decreases, leading to an increase in the density of the sand layers.

The sand layers are enclosed due to the coefficient of earth pressure at rest, K_0, in the surrounding preloaded clay till being greater than, K_0, in the loose sand surrounding the test piles. As a result, when the moraine clay gradually expands over time, the available volume for the sand surrounding the test piles is further reduced. This expansion causes an increase in the density of the sand layers.

During casting of the test piles, the sand surrounding them becomes enclosed. As a result, the effective horizontal stresses, σ_h', in the sand will rise to a level that corresponds to the fluid pressure in the wet concrete ($\gamma_c = 24\ \mathrm{kN/m^3}$). This can be calculated, for instance, in the middle of the lower sand layer, approximately 2.63 m below ground level (with the water table at 1.0 m below ground level):

$$\sigma_h' = 24\ \mathrm{kN/m^3} \cdot 1\ \mathrm{m} + 14\ \mathrm{kN/m^3} \cdot 1.63\ \mathrm{m} = 46.8\ \mathrm{kN/m^2} \tag{75}$$

The ultimate value of unit shaft resistance, r_s, on the test piles can be estimated by multiplying the effective horizontal stresses, σ_h', with $\tan(\varphi')$, where φ' is the effective angle of shearing resistance of the sand layers.

Assuming that the sand has been densified from a loose to a dense state with a 10% volume reduction, the angle of shearing resistance, φ', can be estimated as 38°. As a result, the ultimate value of unit shaft resistance can be calculated as $46.8\ \mathrm{kN/m^2} \cdot \tan(38°) = 36.6\ \mathrm{kN/m^2}$.

A theoretical value of the ultimate unit shaft resistance is then determined by assuming a 10% reduction in the volume of the sand, corresponding to an increase in the pile diameter by approximately 14%. Therefore, the ultimate value of unit shaft resistance can be calculated as $(36.6\ \mathrm{kN/m^2}/0.63\ \mathrm{m}) \cdot 1.14 \cdot 0.63\ \mathrm{m} = 42\ \mathrm{kN/m^2}$.

For comparison, the determined ultimate unit shaft resistance in the lower sand layer is 46 kN/m² in average, i.e., in the same order of magnitude.

8.2.3 Ultimate values of unit shaft resistance in the clay layers

The upper clay layers (strain gauge level 3-4) exhibit ultimate values of "true" mobilised unit shaft resistance ranging from 48 kPa to 66 kPa, with an average value of 56 kPa. The lower clay layers (strain gauge level 4-5) display ultimate values of "true" mobilised unit shaft resistance between 64 kPa and 83 kPa, with an average value of 72 kPa.

The ultimate values of "true" mobilised unit shaft resistance are anticipated to be comparable for clay layers at corresponding levels between the test piles due to the uniform ground conditions of Søvind Marl at the test site in Hinge, as described in section 3.6. In the upper clay layers (strain gauge level 3-4), the ultimate values of "true" mobilised unit shaft resistance for each test piles deviate by less

than 18% from the average value determined for piles 2-8. Likewise, in the lower clay layers (strain gauge level 4-5), the ultimate values of "true" mobilised unit shaft resistance for each test piles vary by less than 14% from the average value determined for piles 2-8. Although the variation is slightly higher than expected, it is still significantly better than the observed ultimate values of mobilised unit shaft resistance, as stated in section 6.3.4.

The average value of "true" mobilised unit shaft resistance demonstrates an approximate increase of 29% from the upper clay layers (strain gauge level 3-4) to the lower clay layers (strain gauge level 4-5). This increment is slightly higher than expected based on the increase in field vane strength, c_{fv}, with depth. The field vane strength increases by approximately 20% from the middle of the upper clay layers (4.5 m below ground level) to the lower clay layers (6.5 m below ground level), as presented in section 3.10.

The observed deviations between the individual test piles, and from the upper to the lower clay layer, may be attributed to the following factors. Firstly, it is possible that incorrect correction of residual stresses has played a role. Secondly, there could be variation in the degradation of clay structure caused by pile installation and the curing process of concrete, leading to variation in effective stresses.

8.2.4 Influence of residual stresses on the ultimate mobilised observed unit shaft resistance

The impact of residual stresses on the ultimate mobilised unit shaft resistance can be demonstrated by comparing the observed load transfer curves to the "true" load transfer curves. Figure 148 and Figure 149, along with Table 25, illustrate this relationship.

Table 25: Percentage of the "true" ultimate mobilised unit shaft resistance displayed by the observed load transfer curves for test piles 2-8 at the test site in Hinge.

Soil layer	Observed amount of "true" unit shaft resistance [%]							
	TP1	TP2	TP3	TP4	TP5	TP6	TP7	TP8
Upper sand layer	-	80	42	57	44	76	27	60
Lower sand layer	-	97	103	98	98	94	123	121
Upper clay layer	-	105	98	91	95	81	119	76
Lower clay layer	-	104	97	102	117	107	71	89

Due to the influence of residual stresses, the ultimate mobilised unit shaft resistance derived from the observed load transfer curves is found to vary between 27% and 127% of the ultimate mobilised unit shaft resistance obtained from the "true" load transfer curves. Specifically, between 27% and 80% in the upper sand layer, between 94% and 123% in the lower sand layer, between 76% and 119% in the upper clay layer, and between 71% and 117% in the lower clay layer.

Consequently, the ultimate mobilised unit shaft resistance values obtained from the observed load transfer curves align with expectations of either the expected ultimate unit shaft resistance twice or the impression that there is no mobilised unit shaft resistance along the length of the pile, as described

in section 8.1.1. It is important to note that these results also indicate that the development of residual stresses is not fully developed for the test piles.

Although it is challenging to establish the influence of residual loads on pile loading test data, especially for bored piles, it is crucial to take residual stresses into account. Quantifying the effects of these residual stresses is even more difficult. However, the method described above, where residual stresses are documented based on post pile loading test data, demonstrates that the ultimate unit shaft resistances presented by the "true" load transfer curves, after correcting for residual stresses, align more closely with expectations compared to the observed load transfer curves.

8.3 Influence of time

This section focuses on analysing the impact of time on the pile capacity for bored piles. The analysis is conducted using the empirical relationship presented by Skov and Denver (1988), which was originally developed for the second phase of set-up for driven piles (refer to section 2.4.2). The objective of this study is to examine whether the empirical relationship proposed by Skov and Denver (1988) can also be applied to characterize the development of bearing capacity for a bored pile. This investigation is centred around test pile 2-8 from the Hinge test site, along with available data obtained from the literature review on time effects in section 2.4.

The initial phase of set-up, characterized by non-linear dissipation of excess porewater pressure, is observed for a period of less than one week after installation. This phenomenon is due to the highly disturbed state of the soil (structure degradation of clay). However, static pile loading tests are not conducted during this phase, as freshly cast concrete requires approximately one month to attain sufficient strength. Therefore, the initial phase of set-up is excluded from the subsequent observations.

The analysis focuses on the remaining two phases of set-up: the second phase characterized by linear dissipation of excess porewater pressure, and the third phase known as ageing. In the case of bored piles, the presence of excess porewater pressures after installation is expected to be negligible compared to driven piles. Therefore, the post-installation time-effects on pile capacity are primarily influenced by ageing rather than the dissipation of excess porewater pressures. The transition from phase two to phase three is expected to occur gradually. In this study, it is assumed that the same log-linear evolution of pile capacity can be applied during this transition.

8.3.1 Development of axial pile capacity with time

The bored test piles in Hinge were subjected to testing after varying periods of rest, as indicated in section 4.1. Specifically, the first two piles were tested after approximately 1.5 months, while the remaining piles were tested (three at a time) approximately 7 months and 3 years after installation, respectively. Figure 150 illustrates the progression of pile capacity over time, based on static pile loading tests conducted on test piles 1-8 at the Hinge test site.

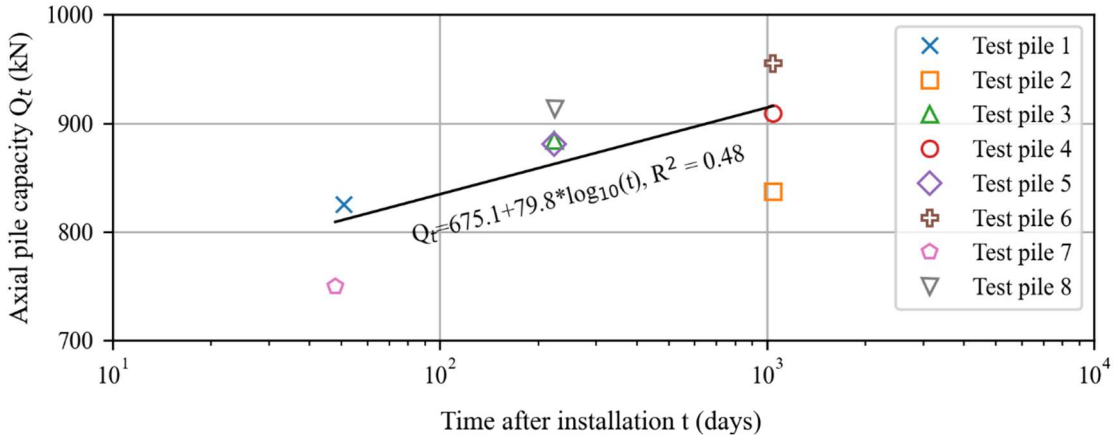

Figure 150: Development of axial pile capacity, Q_t, with time, t, for test piles 1-8 at the test site in Hinge.

As anticipated, the pile capacity of test piles 1-8 at the Hinge test site shows a slight increase over time, from the initial installation of the test piles to the subsequent static pile loading tests. This increase in capacity can be attributed to the dissipation of positive excess porewater pressures and the onset of ageing effects. It is important to note that test piles 1-8 is subjected to unstaged loading during static pile loading tests, which eliminates the need to account for reloading effects.

In order to investigate the applicability of the empirical relationship proposed by Skov and Denver (1988) in characterizing the development of bearing capacity with time for the test piles in Hinge, the estimation of the pile capacity with respect to time, Q_t, is derived:

$$Q_t = 675.1 + 79.8 \cdot log_{10}(t) \tag{76}$$

Here Q_t is the axial pile capacity and t is time after installation.

Thus, the axial pile capacity of the test piles increases with approximately 80 kN for each decade of time. However, the trend is weak with an R2 value of 0.48 and a noticeable scatter of the results.

In this context, it is assumed that the pile geometry (length and diameter) as well as the surface condition of the pile shaft (smooth or rough) are practically identical and have no significant influence on the observed scatter.

However, the observed scatter in the data could be attributed to variations in the axial pile capacities, Q_0, at time t_0. These variations may arise from minor differences in the strength of the soil surrounding the test piles. Despite the relatively small test area with relatively uniform ground conditions, it is important to note that the Søvind Marl, being potentially glacially disturbed, exhibits minor variations in soil strength as indicated by the field vane strengths, c_{fv}, shown in Figure 48 in section 3.10. It is challenging to attribute these variations to specific test piles since only three geotechnical boreholes were conducted across the test area, without a direct correlation to each of the eight test piles as depicted in Figure 34 (refer to section 3.3.1).

Moreover, it should be acknowledged that the permeability of the Søvind Marl could vary significantly. This is due to the presence of highly glauconitic horizons within the Søvind Marl layers, which might affect the dissipation of excess porewater pressure. Consequently, this variation in porewater pressure dissipation can influence the increase in effective horizontal stress, consolidation, and the overall strength gain of the soil.

The analysis examines the impact of time on pile capacity in relation to both the second phase of set-up, which follows a logarithmically linear rate of excess porewater pressure dissipation and the third phase, characterized by ageing effects. However, the empirical relationship proposed by Skov and Denver (1988) may not accurately represent the transition from phase two to phase three for bored piles by the same log-linear evolution of pile capacity.

The narrow zone of disturbed soil around the bored pile makes it practically challenging to measure changes in soil and porewater pressure without the installation of measuring equipment affecting the capacity of the bored piles. As a result, it is challenging to determine if and when each pile reaches the third phase of set-up (ageing). Considering the significant range of time elapsed, it is likely that ageing has begun.

8.3.2 Development of unit shaft resistance with time

This section focuses on evaluating the development of bearing capacity with time, specifically within the Søvind Marl. Figure 151 illustrates the progression over time, specifically in terms of unit shaft resistance, for the upper and lower clay layers (Søvind Marl). The data is obtained from strain gauge measurements at levels 3-4 and 4-5 of test piles 2-8 at the test site in Hinge.

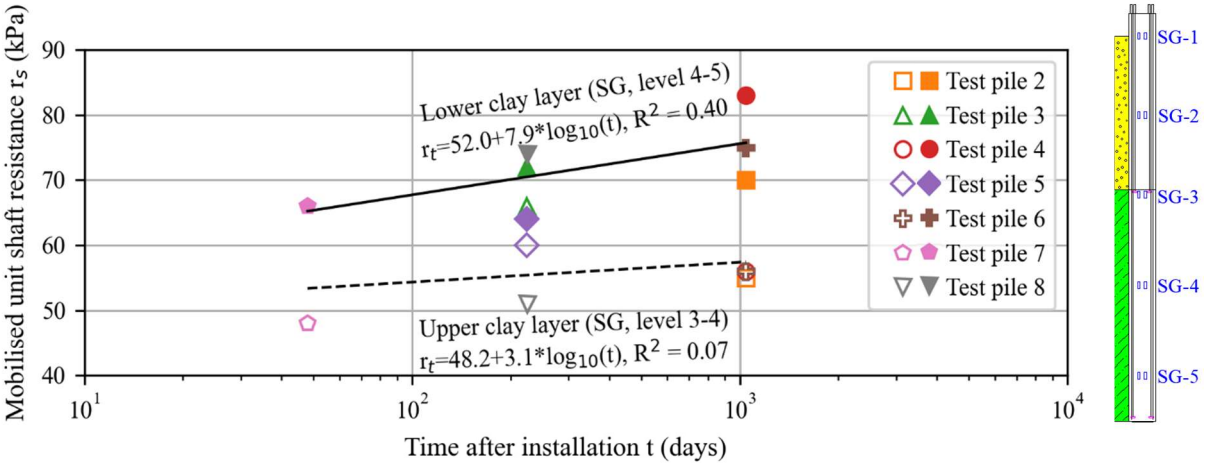

Figure 151: Development of unit shaft resistance over time in the Søvind Marl for test piles 2-8, categorized into the upper clay layer (strain gauge level 3-4) and the lower clay layer (strain gauge level 4-5). Open signatures represent the upper clay layer, while closed signatures represent the lower clay layer.

To examine the applicability of the empirical relationship proposed by Skov and Denver (1988) in describing the evolution of unit shaft resistance over time for both the upper and lower clay layers in the test piles at the Hinge site, the estimation of unit shaft resistance with respect to time, r_s, is derived:

Upper clay layer (SG, level 3-4):

$$r_s = 48.2 + 3.1 \cdot log_{10}(t) \quad (77)$$

Lower clay layer (SG, level 4-5):

$$r_s = 52.0 + 7.9 \cdot log_{10}(t) \quad (78)$$

Here, r_s is the unit shaft resistance and t is time after installation in days.

Thus, the unit shaft resistance increases with approximately 3 and 8 kPa respectively for each decade of time. However, the trend is weak with R2 values of 0.07 and 0.40 and a noticeable scatter of the results.

The presence of scatter in the empirical relationships presented above is surprising, considering that the Søvind Marl in the clay layers is generally perceived as relatively consistent. However, it should be acknowledged that this uniformity may be influenced by glacial disturbance and variations in soil strength, as indicated by the site-wide field vane strengths, c_{fv}, shown in Figure 48 in section 3.10. Therefore, the observed scatter could be attributed to different axial pile capacities, Q_0, at time t_0 originating from variations in the soil strength surrounding the test piles.

Variation in structure degradation of clay due to the pile installation and thereby variation in effective stresses after installation might also affect the set-up with respect to the logarithmically linear rate of excess porewater pressure dissipation in the second phase of set-up. Additionally, the differing soil permeability resulting from the presence of highly glauconitic horizons within the Søvind Marl may also influence the dissipation of excess porewater pressure in phase 2 and thereby contribute to the observed scatter.

The initiation of ageing effects from the third phase of set-up and the transition from phase two to phase three for bored piles, as discussed in section 8.3.1, may also contribute to the scatter observed in the results.

Lastly, it is important to consider that the observed scatter may be attributed to potential inaccuracies in correcting residual stresses for certain test piles or specific clay layers.

8.3.3 Comparison with data from existing case studies in high plasticity clay

The development of axial pile capacity over time for test piles 1-8 at the Hinge test site is compared with data from relevant case studies on high plasticity clay documented in the literature, as discussed in section 2.4.2. Please refer to Figure 152 for a visual representation of these comparisons.

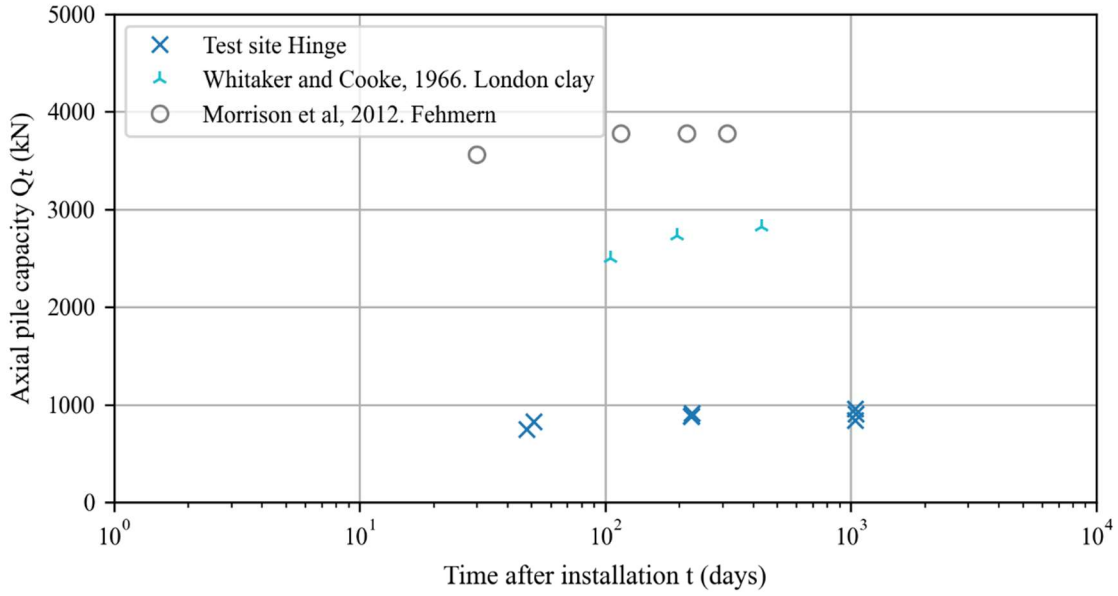

Figure 152: Development of axial pile capacity with time, Q_t, for test piles 1-8 at the test site in Hinge compared with data from relevant case studies on high plasticity clay documented in the literature.

In Figure 152, the trend observed in all three cases indicates a relatively higher rate of evolution in pile capacity during the initial 100-200 days. After this initial period, the logarithmic rate of pile increase appears to decrease or even cease as in the Fehmern case. To facilitate a meaningful comparison of the development of pile capacity with time, Q_t, between the test piles in Hinge and existing case studies on high plasticity clay, the axial pile capacity is normalized relative to the axial pile capacity, Q_0, after one month (t_0=30 days). The selected normalization relative to the strength at 30 days is specifically chosen for bored piles, as freshly cast concrete typically requires around one month to achieve the necessary strength prior to conducting pile loading tests. Please refer to Figure 153 for a visual representation of this normalized comparison.

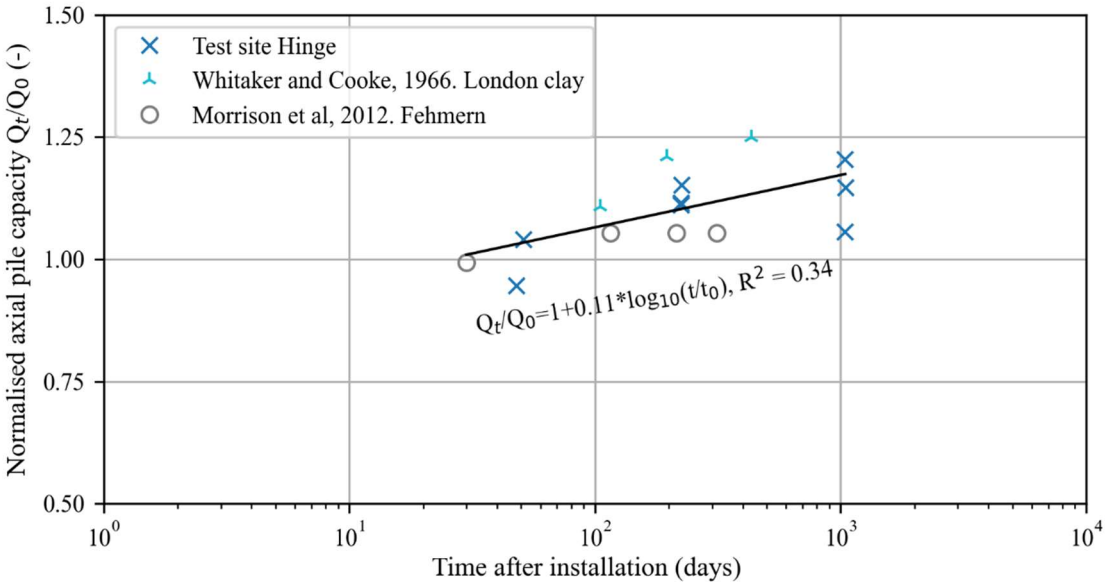

Figure 153: Development of axial pile capacity with time, Q_t, normalized to the axial pile capacity, Q_0, one month after pile installation (t_0=30 days).

Additional data at various intervals after installation is required to improve the ability to predict the time evolution of pile capacity. This also enables the determination of whether the observed decrease or cessation in the logarithmic rate of pile increase after the initial 100-200 days is a result of the transition from the second phase, characterized by linear dissipation of excess porewater pressure, to the third phase, known as ageing. The respective phases of pile set-up are presented in section 2.4.1.

Currently, the progression of bearing capacity over time for the test piles depicted in Figure 153 is characterized by utilizing the empirical relationship introduced by Skov and Denver (1988). As a result, the normalized log-linear relationship for the development of axial pile capacity with respect to time, Q_t, can be expressed as follows:

$$\frac{Q_t}{Q_0} = 1 + 0.11 \cdot log_{10}\left(\frac{t}{t_0}\right) \tag{79}$$

Here, Q_t is the axial pile capacity at time t, Q_0 is the axial pile capacity at time t_0, where t is time after installation and t_0 is an empirical initial time value.

The axial pile capacity increases with approximately 11 % per log change in time, which is slightly lower than the axial pile capacity increase of 14 % per log change in time (t_0=30 days) found for driven piles by Augustesen et al. (2006). However, the trend is weak with an R^2 value of 0.34.

In light of the weak trend observed in the previous analysis, the development of pile capacity with respect to time, Q_t, is assessed individually for each case study conducted in high plasticity clay. Please refer to Table 26 for a detailed overview of the specific findings for each case study.

Table 26: Case study overview of coefficient depending on soil type, A_t and R^2 values.

Case study	Pile diameter	Pile length	t_0 [days]	A_t	R^2
Hinge	0.63 m	8.5 m	30	0.12	0.48
London clay	0.94 m	12.5 m	30	0.34	0.91
Femern	0.50 m	25.0 m	30	0.07	0.84
Combined	-	-	**30**	**0.11**	**0.34**

The analysis reveals that the axial pile capacity for the bored piles in Hinge increases by approximately 12% for each logarithmic change in time. This figure closely aligns with the combined axial pile capacity increase averaging 11% per logarithmic change in time across the three case studies conducted in high plasticity clay. However, it is important to note that the eight test piles in Hinge are installed through a layer of sand measuring 3.4 m, undoubtedly affecting both the axial pile capacity and its development over time.

In the case of bored piles at Fehmern, the lowest increase in axial pile capacity is observed, with approximately a 7% increase per logarithmic change in time. These bored piles are installed 25 meters into Danish Eocene clay beneath the seabed, fully submerged underwater. It is expected to have a lower average rate compared to the test piles at the Hinge test site, as there is a cessation in the logarithmic rate of pile increase after the initial 100-200 days in the Fehmern case.

On the other hand, the bored piles in London clay exhibit the highest increase in axial pile capacity, with an approximate 34% increase per logarithmic change in time. However, it is important to note that this trend is based on only three data points, making the results tentative and subject to further investigation.

In light of the weak trend observed in the previous analysis, the development of pile capacity with respect to time, Q_t, utilized by the empirical relationship introduced by Skov and Denver (1988) is not ideal to use combined over presumably the second and third phase of set-up of bored piles in high plasticity clay. Thus, additional data at various intervals after installation is required to improve the ability to predict the time evolution of pile capacity. This also enables the determination of whether the observed decrease or cessation in the logarithmic rate of pile increase after the initial 100-200 days is a result of the transition from the second phase, characterized by linear dissipation of excess porewater pressure, to the third phase, known as ageing.

.

8.4 Linking unit shaft resistance with undrained shear strength

The mobilised unit shaft resistance, r_s, from the "true" load transfer curves is connected to the undrained shear strength, c_u, through the empirical adhesion coefficient, α, as discussed in section 2.2. This section outlines the process of selecting a reference value for undrained shear strength, c_u, as well as determining the empirical adhesion coefficient, α. It also includes the creation of best-fit, lower bound, and upper bound envelopes to depict the α-c_u relationship and compares them with the specification in the Danish National Annex to Eurocode 7, Annex L (DS/EN_1997-1_DK_NA, 2021). Additionally, the robustness of transitioning from mass strength to intact strength, which serves as the selected reference for undrained shear strength, is thoroughly evaluated.

8.4.1 Selection of reference for undrained shear strength

The selection of a reference value for undrained shear strength, c_u, is often influenced by national geotechnical engineering traditions and personal experience in practical applications. However, this choice becomes particularly critical when dealing with fissured and slicken-sided structured clays, such as the Søvind Marl. In such cases, the undrained shear strength, c_u^{CIU}, obtained from isotropic consolidated undrained triaxial compression (CIU) test, is significantly lower compared to other measurements like the intact field vane strength, c_{fv}, determined through Danish field vane tests. This divergence can be attributed to differences in failure mechanisms, as illustrated in Figure 154.

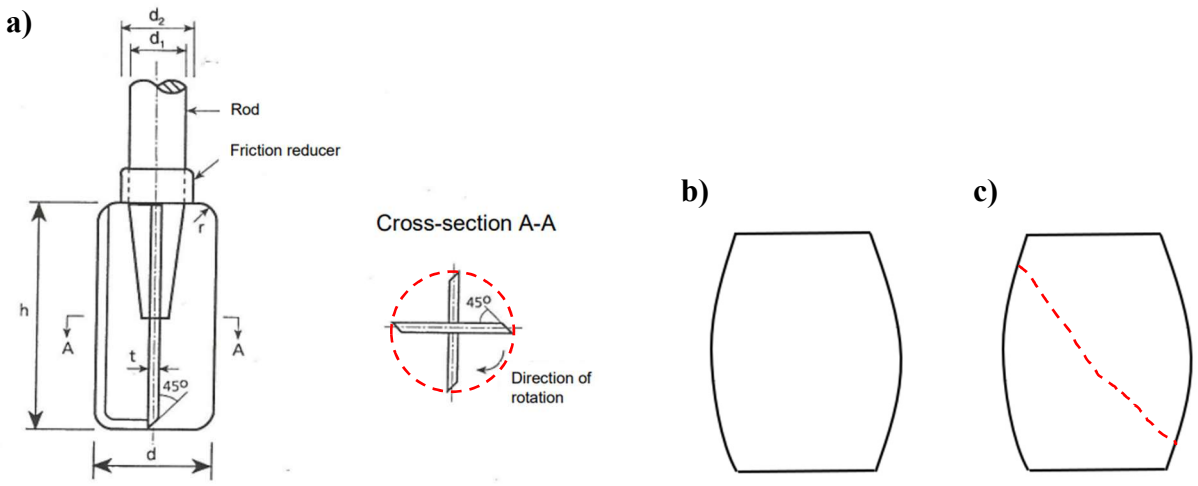

Figure 154: Failure mechanism for (a) Danish field vane test and isotropic consolidated undrained triaxial compression (CIU) test as either (b) barrel shaped failure mode or (c) failure along a fissure.

In general, the Danish field vane test (shown in Figure 154 (a)) induces failure along the vane's edge during rotation, representing the intact undrained shear strength, $c_{u,intact}$, if $c_{fv} = c_{u,intact}$ is assumed.

On the other hand, an isotropic consolidated undrained triaxial compression (CIU) test on a soil mass exhibits a barrel-shaped failure mode (shown in Figure 154 (b)), representing the intact undrained shear strength , $c_{u,intact}$, if $c_u^{CIU} = c_{u,intact}$ is assumed.

However, in the case of the Søvind Marl, which is fissured and slicken-sided, an isotropic consolidated undrained triaxial compression (CIU) test will predominantly induce failure along a fissure (as shown in Figure 154 (c)). This failure mode represents a fissured undrained shear strength, $c_{u,fissured}$, if $c_u^{CIU} = c_{u,fissured}$ is assumed.

Based on studies in section 3.6 and Grønbech (2015), the fissured undrained shear strength, c_u^{CIU}, from the isotropic consolidated undrained triaxial compression (CIU) test is found to range between approximately 20% and 80% of the intact undrained shear strength, c_{fv}, obtained from the Danish field vane test. This variation depends on the degree of fissuring present in the tested specimen. The advantages and disadvantages of using these two different testing methods are presented below:

Danish field vane test

The intact undrained shear strength obtained from the Danish field vane test, c_{fv}, serves as a reliable and commonly employed reference in practical geotechnical engineering in Denmark. It is not influenced by the local degree of fissuring or slicken sides, and it offers ease of use and cost-effectiveness while providing consistent results.

However, the Danish field vane test does not provide information about the potential disturbance caused by pile installation in the surrounding soil, including horizontal or vertical soil movements. It also does not account for the generation of excess porewater pressure or stress changes resulting from the curing process of bored piles, which can affect both normal and shear stresses at the soil-pile interface. Further details can be found in the literature study in section 2.1.

Isotropic consolidated undrained triaxial compression (CIU) test

The fissured undrained shear strength, represented by the mass strength, obtained from the isotropic consolidated undrained triaxial compression (CIU) test, c_u^{CIU}, serves as a reference that varies depending on the extent of fissures present in the tested specimen. This testing method is relatively expensive and time-consuming to perform and often yields inconsistent results due to variations among individual test specimens.

In the case of over consolidated soil like the Søvind Marl at the Hinge test site (with an over consolidation ratio of 7 to 9 cf. section 3.8.1), it is possible to evaluate the residual strength of the soil, taking into account the reduction in strength after reaching the peak failure. Furthermore, it could potentially provide a more comprehensive understanding of the soil's behaviour and allow for consideration of the installation disturbances and the curing effects on the surrounding soils from the bored pile. These considerations can be studied by testing specimens in different states like e.g. a remoulded, reconstituted, or fully softened state.

However, the remoulded specimen eliminates the effect of fissures in the specimen, but also removes the clay structure and the effect of over consolidation. The effect of over consolidation can be artificially reinstated, also known as a reconstituted specimen, but the effects of clay structure is not

included. The fully soften specimen is allowed to absorb free water and thereby for the clay to fully soften, leading to degradation of clay structure. Hence, there are pros and cons using the two different testing methods and neither of them are found to give an exact representation of the failure strength for bored piles.

Experience from effective strength (β method)

For London clay, Burland (1973) pointed out that the fully softened values of φ' ($\sim 21.5°$) represents an upper theoretical limit for bored piles entirely embedded in clay. The fully softened value was deduced from the coefficient of earth pressure at rest, K_0, determined in laboratory test by Skempton (1961) and Bishop et al. (1965).

Furthermore, Burland and Twine (1988) found the approximate residual values of φ' ($\sim 12°$) to represent a lower theoretical limit for bored piles assuming hydrostatic conditions below top of clay. The residual strength characteristic was studied by (Bishop et al., 1971) using a ring shear apparatus. The peak strength at 24° was achieved at a displacement of 2.5 mm and fell to 12° at a displacement of 25 mm. Continued shearing resulted in a residual value of 9.4° beyond a displacement of 380 mm. Using a ring shear apparatus will force the failure line between the upper and lower section of the apparatus resulting in an intact residual strength not affected by fissures. The above behaviour relates to the formation of residual shear surfaces within the mass of clay.

Please note, that it is assumed that $\delta' = \varphi'$ in the section above.

Selection of reference

The undrained shear strength is primarily an empirical index value that relies on historical sampling and laboratory test methods, along with the back analysis of pile test data. It is not considered a fundamental soil parameter in itself. The chosen method of installation and the duration of softening before casting bored piles are believed to have significant impacts on the ultimate shaft resistance of the piles.

To ensure optimal results, it is advisable to avoid using water during the installation process. The presence of free water can cause the soil to soften, leading to a significant reduction in ultimate shaft resistance, particularly for bored piles installed in over consolidated high-plasticity, fine-grained soils like Søvind Marl. The smectite minerals present in the Søvind Marl tend to swell when free water is available, disrupting the structure of the clay and causing it to approach a fully softened state.

For bored piles, the capacity is primarily derived from shaft friction, with base resistance not significantly mobilised under working loads. Even for compressive piles, as the design is primarily focused on meeting the deformation requirements of the structure. Shaft failure occurs when shearing takes place across a substantial soil volume along the length of the bored piles and such large, interconnected fracture systems are unrealistic. Therefore, it is more favourable to consider the intact undrained shear strength, $c_{u,intact}$, rather than the fissured undrained shear strength, $c_{u,fissured}$, as

the representative value for shaft failure. The fissured undrained shear strength, $c_{u,fissured}$, is more applicable for determining base failure, as it involves a smaller volume of soil influenced by existing fissures.

Furthermore, the field vane test is relatively straightforward and cost-effective, making it a commonly employed practice in practical geotechnical engineering in Denmark. By using this widely accepted reference, a substantial amount of data can be accumulated in the near future, further advancing the knowledge of the α-c_u relationship.

8.4.2 Determination of empirical adhesion coefficient

The determination of the empirical adhesion coefficient, α, for test piles 2-8 utilizes the undrained shear strength, c_u, which is calculated by correlating the field vane strength, c_{fv}, in the middle of the soil layers being considered. This correlation is site-wide and is explained in section 3.10. Specifically, the undrained shear strength, c_u, for the upper clay layer (strain gauge level 3-4) is determined as c_{fv}=174 kPa at a depth of 4.5 m below ground level. Similarly, the undrained shear strength, c_u, for the lower clay layer (strain gauge level 4-5) is determined as c_{fv}=208 kPa at a depth of 6.5 m below ground level. The empirical adhesion coefficient, α_{cfv}, is illustrated in Figure 155.

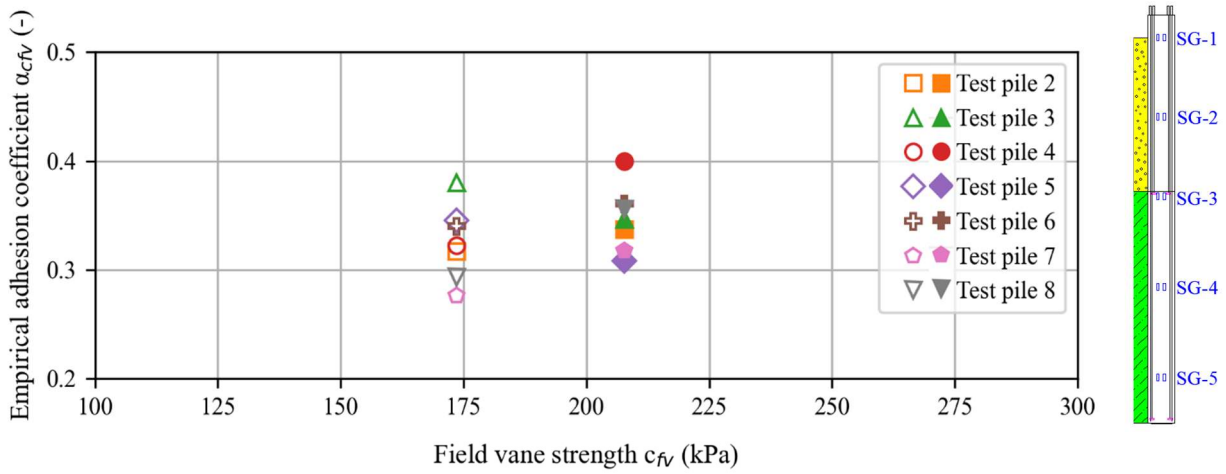

Figure 155: Empirical adhesion coefficients, α_{cfv}, for Søvind Marl determined for test piles 2-8, categorized into the upper clay layer (strain gauge level 3-4) and the lower clay layer (strain gauge level 4-5). Open signatures represent the upper clay layer, while closed signatures represent the lower clay layer.

The observed empirical adhesion coefficient, α_{cfv}, exhibits a range of variation between 0.28 and 0.38 for the upper clay layer (strain gauge level 3-4), and between 0.31 and 0.40 for the lower clay layer (strain gauge level 4-5). Consequently, the empirical adhesion coefficient, α_{cfv}, is approximately 2.3 to 3.3 times greater than the empirical adhesion coefficient $\alpha = 0.12$ specified for bored piles in Denmark, as mentioned in section 2.2.2.

The variability observed in the data could potentially arise from different factors. Firstly, it may stem from the incorrect adjustment of residual stresses as discussed in section 8.1 and 8.2, Secondly, variations in the degradation of the clay structure during pile installation, which leads to variations in

effective stresses and potentially impact the effective strength parameters after installation. Thirdly, the development of unit shaft resistance over time, as described in section 8.3, could also contribute to the scatter. This is further analysed in the following.

The changes in the empirical adhesion coefficient, α_{cfv}, over time are depicted in Figure 156.

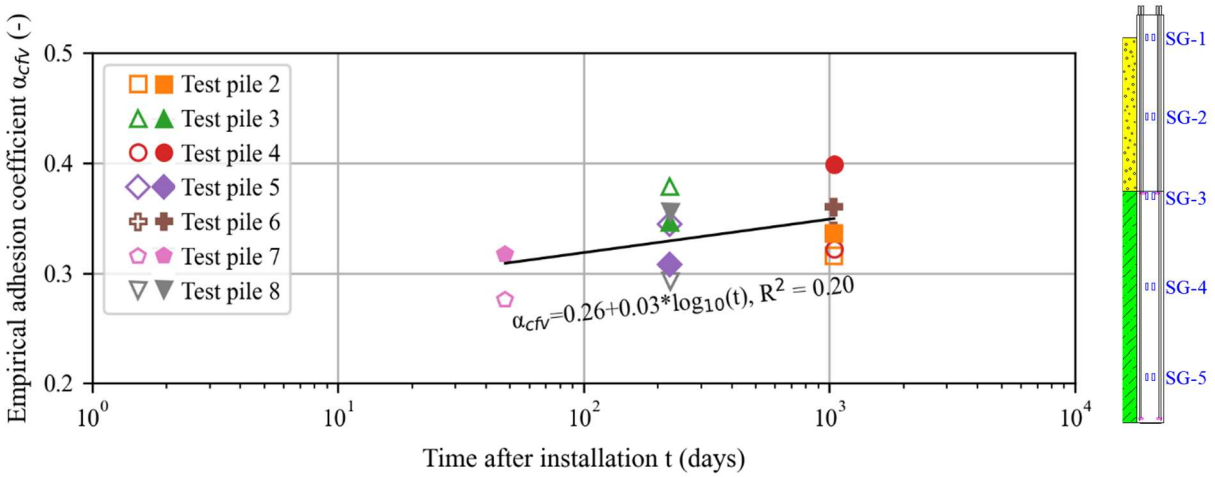

Figure 156: Development of empirical adhesion coefficients, α_{cfv}, with time for Søvind Marl determined for test piles 2-8, categorized into the upper clay layer (strain gauge level 3-4) and the lower clay layer (strain gauge level 4-5). Open signatures represent the upper clay layer, while closed signatures represent the lower clay layer.

An estimation of the empirical adhesion coefficient, α_{cfv}, as it evolves over time, can be derived using the following log linear relationship:

$$\alpha_{cfv} = 0.26 + 0.03 \cdot log_{10}(t) \quad (80)$$

Here α_{cfv} is the empirical adhesion coefficient and t is time after installation in days.

Thus, the empirical adhesion coefficient, α_{cfv}, increases slightly with approximately 0.03 for each decade of time. However, the trend is weak with an R2 value of 0.20 and a noticeable scatter of the results.

The variation observed in the data could be attributed to slight discrepancies in the strength and permeability of the soil surrounding the test piles, as explained in the context of the scatter observed in the progression of axial pile capacity over time (refer to section 8.3.1).

The empirical adhesion coefficients, α_{cfv}, obtained are recalibrated to represent a period of one month (30 days) after the installation of the piles. The recalibration is performed using the log linear relationship presented above in equation (80). These recalibrated coefficients are then compared with the findings from the literature review in section 2.4.2 to establish the best fit, lower bound, and upper bound envelopes for the relationship between α and c_u.

The decision to determine the empirical adhesion coefficients, α_{cfv}, at the 30-day mark is specifically made for bored piles. This time frame allows for freshly cast concrete to attain the required strength before conducting pile loading tests. The literature review findings are assumed to correspond to a 30-day strength, and thus the recalibration is performed to align the data for subsequent analysis in the following section.

8.4.3 Best fit, lower bound and upper bound envelopes for the α-c_u relationship

Despite the considerable scatter resulting from the empirical adhesion coefficient α's dependence on various factors such as soil conditions, pile types, dimensions, installation methods, pile loading test methods, and interpretation techniques, it appears feasible to establish a best fit, lower bound, and upper bound envelope for the α-c_u relationship based on a comprehensive literature review (refer to section 2.3).

To determine these envelopes for fine-grained soils and high plasticity clay, relevant databases from the literature were included, including those pertaining to fine-grained soils in general, as well as specific soils such as London clay and Danish Eocene clay. However, it is essential for the α-c_u relationship to account for an equivalent intact undrained shear strength, $c_{u,intact}$, as the empirical adhesion coefficient α is heavily influenced by the choice of reference for undrained shear strength, c_u.

General databases for fine grained soils:

The relationship between α and c_u from the general databases for fine-grained soils, as discussed in section 2.3.1, is directly incorporated. This data is believed to primarily originate from clay with low or medium plasticity. Therefore, the undrained shear strength, c_u^{CIU}, determined through isotropic consolidated undrained triaxial compression (CIU) tests, is assumed to represent an intact undrained shear strength, $c_{u,intact}$.

In cases where unconsolidated undrained triaxial (UU) tests or unconfined compression (UC) tests were performed, they were converted to an "equivalent" undrained shear strength, c_u^{CIU}, as described by Chen and Kulhawy (1993) and Chen and Kulhawy (1994).

London clay (UK):

In section 2.3.2, the α-c_u relationship for the London clay is adjusted to reflect the intact undrained shear strength, $c_{u,intact}$. This adjustment involves utilizing the ratio between the undrained shear strength, c_u, obtained from triaxial tests on 38 mm diameter specimens, and the intact strength determined through penetration tests. For the London clay, this ratio was found to average around 0.46, ranging between 0.37 and 0.55, as reported by Marsland (1972). Notably, this ratio aligns with Danish experience, where c_{fv} is typically 2 to 3 times greater than c_u.

Eocene clay (DK):

In the case of Danish Eocene clay, the α-c_u relationship is directly included from the works of Lyse et al. (2020). This relationship is based on the intact field vane strength c_{fv} measured through Danish field vane tests, which is used as the reference for the intact undrained shear strength ($c_{u,intact} = c_{fv}$).

Additionally, in section 2.3.3, the α-c_u relationship from Morrison et al. (2012) is adjusted to represent the intact undrained shear strength, $c_{u,intact}$. In the original paper, a site-wide correlation between the undrained shear strength, c_u, and the cone penetration test (CPT) value was employed ($c_u = q_{net}/N_{kt}$). The applied N_{kt} value of 25.5 indicates a correlation with undrained shear strength determined through triaxial testing. Therefore, the α-c_u relationship is converted to "equivalent" undrained shear strength values obtained through the Danish field vane test, using the relationship $c_{fv} = 3 \cdot c_u$, as described by Christensen and Hansen (1959) and Grønbech (2015).

Historical cases (DK):

It is of particular interest for geotechnical engineers in Denmark to consider pile loading tests on bored piles conducted prior to the late 1970s. Although only seven cases have been discovered, all of which are undocumented and unpublished, they provide valuable insights. Among these cases, six are related to clay till, while one case pertains to high plasticity, fissured Paleogene clays, specifically Septarieler and Søvind Marl (Balstrup, 1972, Knudsen, Undated, Bennick, 1975). Supplementary information concerning soil conditions, pile types, dimensions, installation methods, and pile loading test methods can be found in the published paper by Knudsen et al. (2019), which is included at the end of the thesis.

Fine grained soils

The α-c_u relationship for fine-grained soils in general is illustrated in Figure 157, and it includes the determination of best fit, lower bound, and upper bound envelopes for the α-c_u relationship. The best fit envelope is established by fitting a power function to the entire dataset. The lower and upper bounds, on the other hand, are determined by fitting power functions to the 5th and 95th percentiles for smaller sections of around 50 kPa each. The length of these sections increases in pace with the reduction in the number of data points for higher values of the undrained shear strength, c_u.

The empirical adhesion coefficients, α_{cfv}, obtained from test piles 2-8 at the Hinge test site for Søvind Marl, are considered to represent the intact undrained shear strength, $c_{u,intact}$. These adhesion coefficients are observed to reasonably align with the best fit envelope and fall within the lower and upper bound envelopes for the α-c_u relationship.

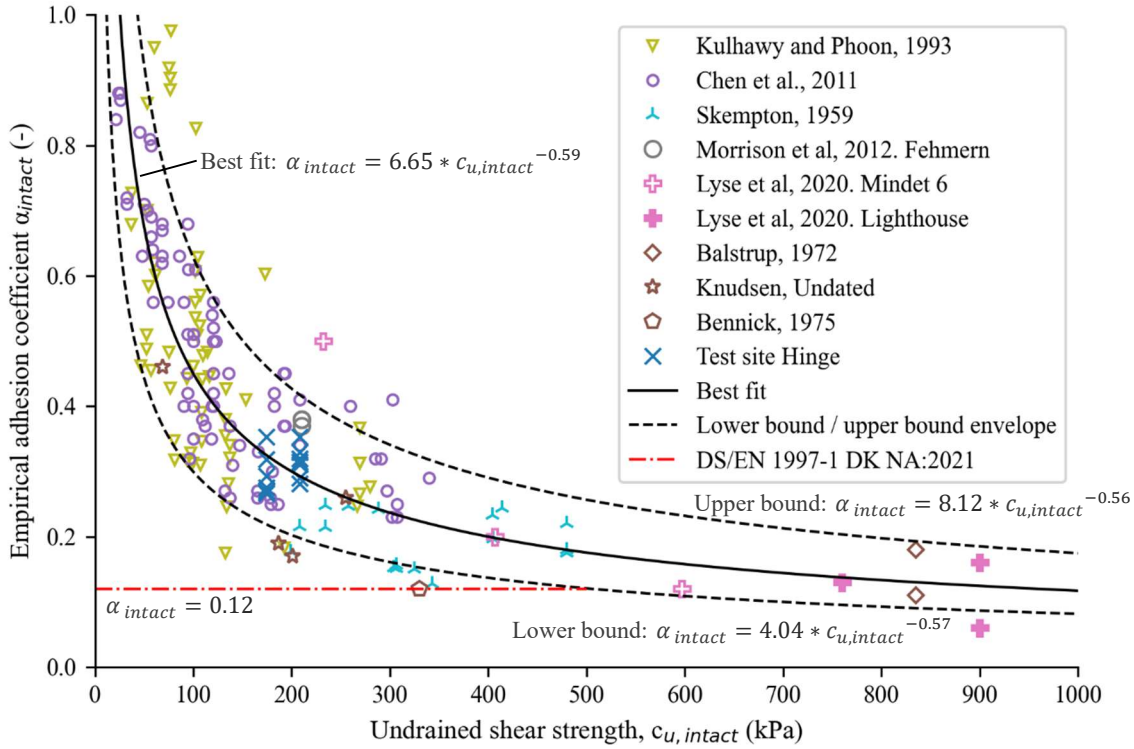

Figure 157: Relation between empirical adhesion coefficients, α_{intact}, and the intact undrained shear strength, $c_{u,intact}$, for fine-grained soils, characterized by best fit, lower bound and upper bound envelopes for the α-c_u relationship.

Notably, even the lower bound envelope exceeds the empirical adhesion coefficient $\alpha = 0.12$, as specified in the Danish National Annex to Eurocode 7, Annex L (DS/EN_1997-1_DK_NA, 2021). For instance, the lower limit envelope surpasses the empirical adhesion coefficient $\alpha = 0.12$ specified for bored piles in Denmark by 2.4 times when the undrained shear strength is 100 kPa. Similarly, it exceeds the empirical adhesion coefficient $\alpha = 0.12$ by 1.6 times for an undrained shear strength of 200 kPa. This Danish specification, described in section 2.2.2 and depicted as a red dashed-dot line in Figure 157, pertains to an undrained shear strength c_u of 500 kPa or lower.

Equation (81) represents the best-fit envelope, while equations (82) and (83) correspond to the upper and lower bound envelopes of the α-c_u relationship.

Best fit:

$$\alpha_{intact} = 6.65 * c_{u,intact}^{-0.59} \quad (81)$$

Upper bound (95th percentile):

$$\alpha_{intact} = 8.12 * c_{u,intact}^{-0.56} \quad (82)$$

Lower bound (5th percentile):

$$\alpha_{intact} = 4.04 * c_{u,intact}^{-0.57} \quad (83)$$

Here, α_{intact} is the empirical adhesion coefficient and $c_{u,intact}$ is the intact undrained shear strength or the equivalent intact undrained shear strength for fissured clays.

In Figure 157, the distribution of data points is uneven, with a majority of them falling within the lower range of intact undrained shear strength ($c_{u,intact} \leq 300$ kPa). It would be beneficial to have a greater number of data points, especially for values of intact undrained shear strength above 500 kPa.

There is no available information regarding residual stresses considered in the determination of the provided empirical adhesion coefficients, α. It is important to note that neglecting residual stresses can greatly influence the α-c_u relationship, potentially leading to inaccuracies that are considerably larger than those resulting from the transition of undrained shear strength, c_u^{CIU}, from mass strength to intact strength cf. section 8.4.1 and the changes in the empirical adhesion coefficient, α_{cfv}, over time cf. section 8.4.2. The misinterpretation of the empirical adhesion coefficient, α, may range from appearing as zero to being double the actual empirical adhesion coefficient due to the misinterpreted ultimate unit shaft resistance, as discussed in section 8.1.1.

High plasticity clay

In order to assess if the α-c_u relationship for stiff and highly plastic clays differs from the trend observed in fine-grained soils in general, Figure 158 presents the α-c_u relationship specifically for the London clay (section 2.3.2), the Danish Eocene clay (section 2.3.3), and the Søvind Marl derived from test piles 2-8 at the Hinge test site. The figure also showcases the best-fit, lower bound, and upper bound envelopes for the α-c_u relationship specific to these clays, determined using the same principles as outlined above for fine grained soils.

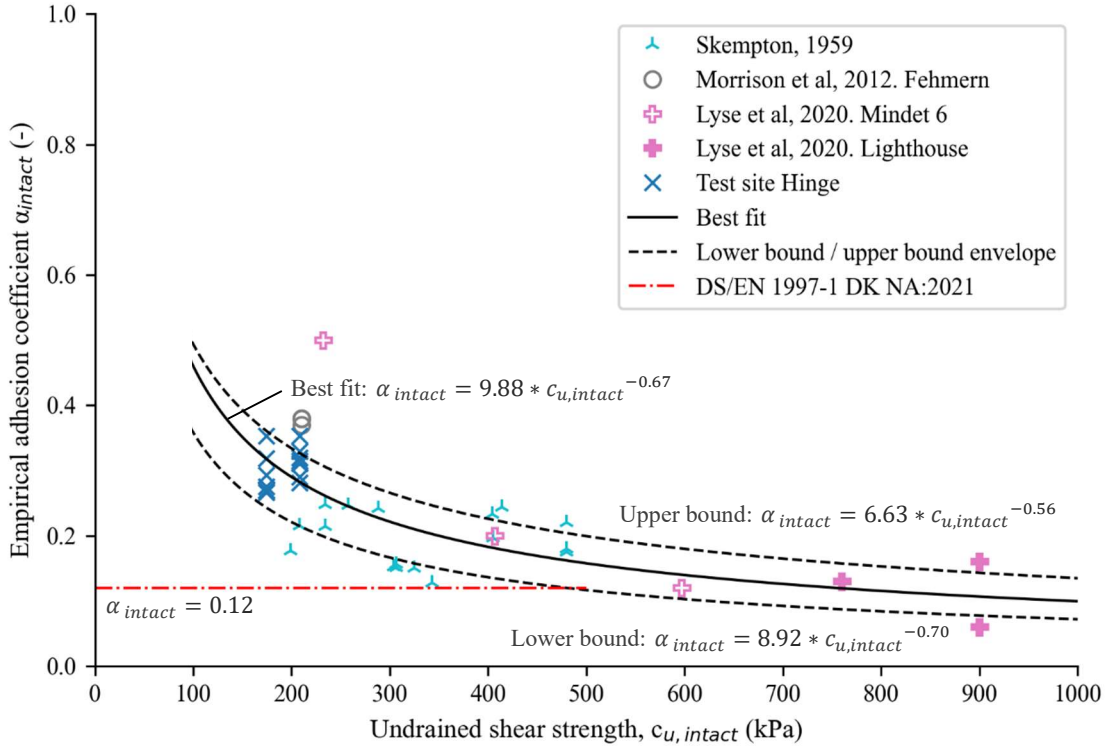

Figure 158: Relation between empirical adhesion coefficients, α_{intact}, and the intact undrained shear strength, $c_{u,intact}$, for stiff and high plasticity clays , characterized by best fit, lower bound and upper bound envelopes for the α-c_u relationship.

The empirical adhesion coefficients, α_{cfv}, obtained for Søvind Marl from test piles 2-8 at the Hinge test site are observed to be reasonably positioned around the best-fit envelope. However, they exceed the upper bound envelopes for the α-c_u relationship, suggesting a potential underprediction. Equations (84), (85), and (86) present the best-fit, lower bound, and upper bound envelopes for the α-c_u relationship exclusively for the high plasticity clays:

Best fit:

$$\alpha_{intact} = 9.88 * c_{u,intact}^{-0.67} \quad (84)$$

Upper bound (95th percentile):

$$\alpha_{intact} = 6.63 * c_{u,intact}^{-0.56} \quad (85)$$

Lower bound (5th percentile):

$$\alpha_{intact} = 8.92 * c_{u,intact}^{-0.70} \quad (86)$$

Here, α_{intact} is the empirical adhesion coefficient and $c_{u,intact}$ is the intact undrained shear strength or the equivalent intact undrained shear strength for fissured clays.

The α-c_u relationship for stiff and highly plastic clays exhibits the same power functions as the α-c_u relationship for fine-grained soils in general. Some minor deviations are noticed, particularly for the upper bound envelope, but these discrepancies are likely due to the altered (reduced) number of data points rather than any other factor. Hence, the best-fit, lower bound, and upper bound envelopes provided for fine-grained soils in general are preferred.

8.4.4 Robustness of change from fissured mass strength to intact strength

The purpose of the best-fit, lower bound, and upper bound envelopes for the α-c_u relationship is not initially for the design of bored piles, but rather as a tool for geotechnical engineers during the design and planning of test piles. The rationale behind this is explained below:

In practical geotechnical engineering, the empirical adhesion coefficient, α, is often considered less important in the design of bored piles since the design primarily focuses on the structure's deformation requirements. Therefore, the design is mainly based on test piles. While this approach is technically correct, the lack of emphasis on the empirical adhesion coefficient, α, is often the reason why test piles fail to reach failure. This can occur due to inadequate test equipment, undersized test piles, or failure occurring in the "wrong" direction during O-cell tests.

This situation is unfortunate because it leads to overly conservative designs that are uneconomical and environmentally burdensome. If the best-fit, lower bound, and upper bound envelopes for the α-c_u relationship presented in section 8.4.3 are intelligently utilized in practical geotechnical engineering, they can provide supplementary test data and enhance our understanding of the α-c_u

relationship. This, in turn, can lead to improved designs and a better knowledge of the interaction between the adhesion coefficient, α, and the undrained shear strength, c_u.

Regrettably, there was insufficient available data to establish the best-fit, lower bound, and upper bound envelopes for the α-c_u relationship for neither fine-grained soils in general nor fissured high plasticity clay concerning the intact field vane strength, c_{fv}, as measured by Danish field vane tests. As a result, databases from the literature have been utilized to determine the best-fit, lower bound, and upper bound envelopes that includes undrained shear strength, c_u determined by other methods. These databases primarily pertain to fine-grained soils in general, as well as specifically for the London clay and Danish Eocene clay, as discussed in section 2.3.

In this study, the field vane strength, c_{fv}, serves as a reference for the undrained shear strength, c_u, and it is assumed to represent an intact undrained shear strength, $c_{u,intact}$. Therefore, the databases sourced from the literature have been adapted to reflect an intact undrained shear strength, $c_{u,intact}$. Typically, it is advisable to apply a conservative transformation when converting the undrained shear strength, c_u^{CIU}, from fissured mass strength to intact strength. However, due to the linear relationship between fissured mass strength and intact strength (e.g. $c_{fv} = 3 \cdot c_u$) and the non-linear nature of the α-c_u relationship (power function), it is not always feasible to consistently choose the safer side for the transformation. Consequently, a best estimate is provided to capture this uncertainty. The impact of this transformation is demonstrated in Figure 159:

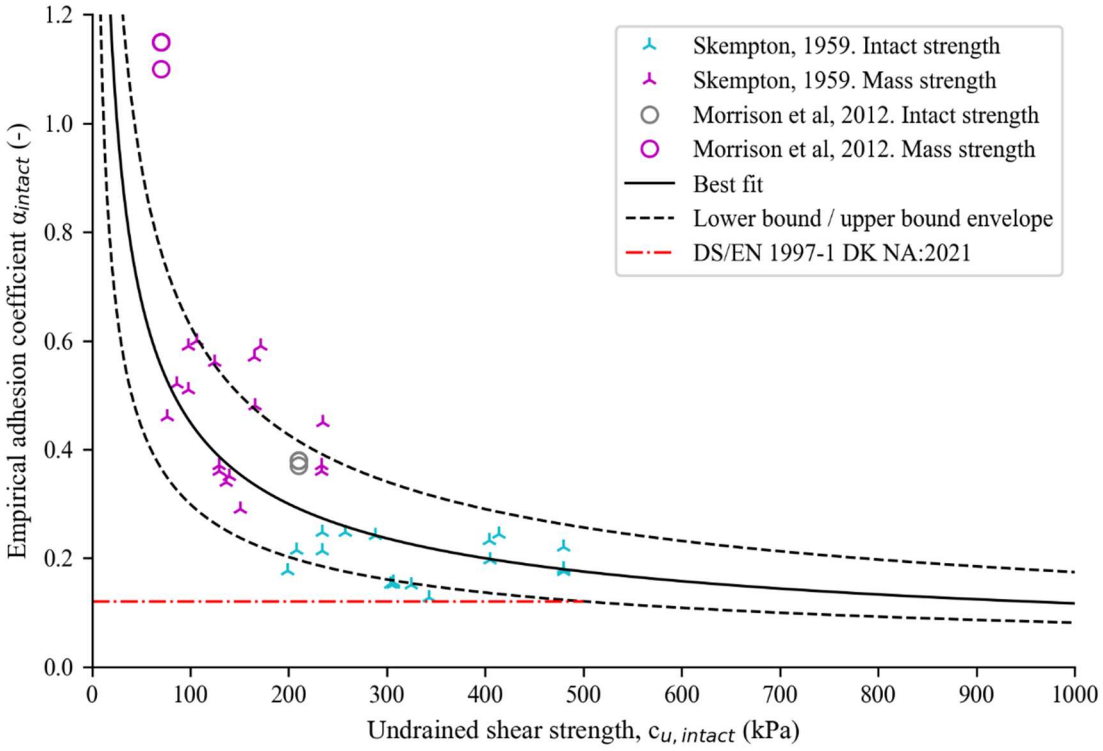

Figure 159: Relation between empirical adhesion coefficients, α_{intact}, and the intact undrained shear strength, $c_{u,intact}$, with best fit, lower bound and upper bound envelopes for fine-grained soils. Data points in red represent the original determined mass strength for comparison relative to the determined envelopes.

Figure 159 clearly demonstrates the robustness of the transformation used in the analysis. The magenta data point represents the original fissured mass strength values obtained from Skempton (1959) and Morrison et al. (2012). These data points are positioned higher in comparison to the determined best-fit, lower bound, and upper bound envelopes for the α-c_u relationship. Consequently, if the originally determined fissured mass strengths were used, it would force the envelopes to be positioned higher, which would be on the unsafe side.

Moreover, it is worth noting that Morrison et al. (2012) reported empirical adhesion coefficients, α, that exceed 1, which is quite illogical. This suggests the expectation of the clay to regenerate to a strength higher than its original strength, which is not a realistic scenario.

9 Analytical model for bored piles in stiff clays

Two analytical models, the hyperbolic non-linear loading model (HN model) and the hyperbolic non-linear loading model including residual stresses (HNr model), have been developed for bored piles in stiff clays using the load transfer method. These models are based on previous works by Seed and Reese (1957), Reese (1964) and Coyle and Reese (1966).

The objective of developing these two analytical models is twofold. Firstly, it aims to investigate the impact of residual stresses on the analytical model, allowing for a better understanding of their influence. Secondly, these models provide a reliable tool for the analysis of bored piles specifically in stiff clay soils.

The load transfer method employs an iterative approach to solve a set of differential equations that represent the behaviour of the pile using the finite-difference technique. To incorporate the soil-pile interaction, the pile is divided into discrete sections, with each section connected to a spring representing the soil-pile interaction. The objective of this analysis is to determine the unknown distributions of displacements, Δz_i, and forces, F_i, along the pile, as explained in section 2.5.1.

The developed analytical models rely on load transfer functions to describe the soil-pile interaction in individual soil layers. These load transfer functions are derived from earlier research, such as Vijayvergiya (1977) and Zhang and Zhang (2012). However, in practical engineering practice, it is uncommon for the load transfer functions to be readily available at the beginning of a new project. Therefore, the prediction of load transfer functions based on soil properties becomes necessary, and two methods for predicting these load transfer functions are presented.

The first method is a simple approach that relies on the load transfer function proposed by Vijayvergiya (1977) and the field vane strength, c_{fv}, determined through Danish field vane tests. This method is often employed when limited information is available at the start of a new project. Note that the field vane strength, c_{fv}, can be substituted with any other representation of the intact undrained shear strength, c_u, such as the CPTu sounding.

The second method requires additional data obtained from triaxial tests to better describe shear strength mobilization, τ_{mob}. This method, as described by Vardanega and Bolton (2011b), utilizes shear strain, γ, and the Randolph and Wroth method, detailed in section 2.5.2, to determine the mobilised shear strength, τ_{mob}. In this approach, the mobilised shear strength, τ_{mob}, is linked to displacements, $\delta_{pile,soil}$, rather than shear strain, γ, thereby enabling its use as a load transfer function.

9.1 Overview

This section provide an overview of the hyperbolic non-linear loading model (HN model) and the hyperbolic non-linear loading model including residual stress (HNr model). The underlying concept of these models is depicted in Figure 160.

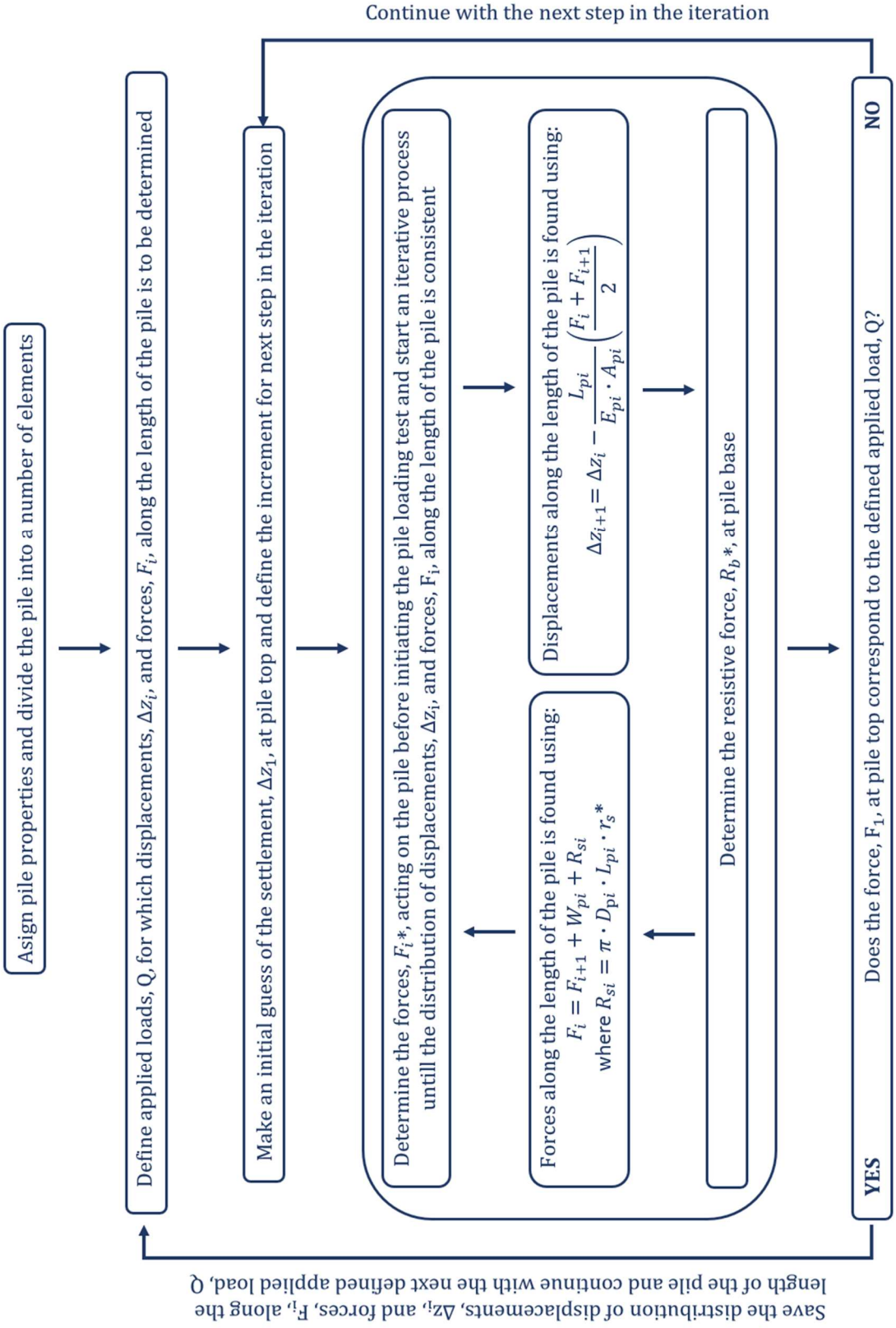

Figure 160: Principal construction of the analytical models (HN model/HNr model) in Spyder IDE 5.4.3.

* Input parameters that change depending on whether the analytical model is used as a hyperbolic non-linear loading model (HN model) or a hyperbolic non-linear loading model incl. residual stresses (HNr model) cf. section 9.2 and 9.3.

The two analytical models presented in this study are specifically developed for bored piles in stiff clays using the load transfer method. The load transfer method utilizes an iterative technique to solve a set of differential equations that represent the behaviour of the pile, employing the finite-difference approach. The automation of this iterative process is facilitated using the Spyder IDE 5.4.3 (Python 3.8.10 64-bit | Qt 5.15.2 | PyQt5 5.15.9 | Windows 10).

To provide a practical example of the HN model and HNr model, the corresponding script is provided in Appendix K.3, specifically focusing on test pile 3.

9.2 Hyperbolic non-linear loading model (HN model)

The hyperbolic non-linear loading model (HN model) is evaluated by comparing with the measured data from the static pile loading test from test piles 2-8. The following input parameters are applied:

- Diameter, $D_{pi} = 0.62$ m, Cross sectional area, $A_{pi} = 0.30$ m² and a circumference of 1.95 m.
- The 9 m long piles are divided into 90 elements, each with a length of $L_{pi} = 10$ cm
- The forces, F_i*, acting on the piles before initiating the pile loading tests is determined as the cumulative weight of the piles along the length of the piles, where weight of the piles (reinforced concrete) is considered with hydrostatic water pressure (uplift) beneath the pile base (the piles are assumed impermeable). Thus, bulk weight = 25 kN/m³.
- The axial stiffness ($E_{pi} \cdot A_{pi}$) of the pile is considered equal to14.0 á 16.1 GN cf. section 6.3.2.
- The force, R_b*, at the pile base is considered equal to the total weight of the pile before initiating the pile loading test and is assumed to diminish linear to zero during failure.
- The resistive force in the spring, R_{si}, is determined directly from the measured data as $R_{si} = \pi \cdot D_{pi} \cdot L_{pi} \cdot r_s$ for each element, where the unit shaft resistance r_s* is derived from measured data.
- The mobilised unit shaft resistance, r_s*, in the sand layers is determined by a hyperbolic strain softening t-z function (Zhang and Zhang, 2012) fitted to measured data from strain gauge level 1-2 and 2-3, respectively. See section 6.3.4.
- The mobilised unit shaft resistance, r_s*, in the clay layers is determined by a hyperbolic strain softening t-z function (Vijayvergiya, 1977) fitted to measured data from strain gauge level 3-4 and 4-5, respectively. Furthermore, the mobilised unit shaft resistance, r_s*, in the clay layers below strain gauge level 5 is assumed equal to the measured mobilised unit shaft resistance from strain gauge level 4-5. See section 6.3.4.

The analytical model of the axial force, F, and the vertical displacement, $\delta_{pile,soil}$, is plotted along the length of the test piles and compared with the data obtained from pile loading tests. These comparisons are made separately for each load step on the virgin load curves and for the peak value from the constant rate of uplift portion of the pile loading test.

To ensure accuracy, the measured data is corrected for the weight of the pile. This correction is necessary because the strain gauges only measure changes in strain and not the actual strain values. The weight of the pile remains constant before and after the pile loading test, and it is not accounted for by the strain gauges.

9.2.1 Distribution of axial force along the length of the test piles

Figure 161 and Figure 162 illustrate the axial force, *F*, distribution along the length of test piles 2-8 as determined by the hyperbolic non-linear loading model (HN model) alongside the corresponding measured data. The signatures in the figures represent the measured data for each load step, while the solid lines represent the distribution of axial force, F, as predicted by the hyperbolic non-linear loading model (HN model).

Maintained load (ML) test

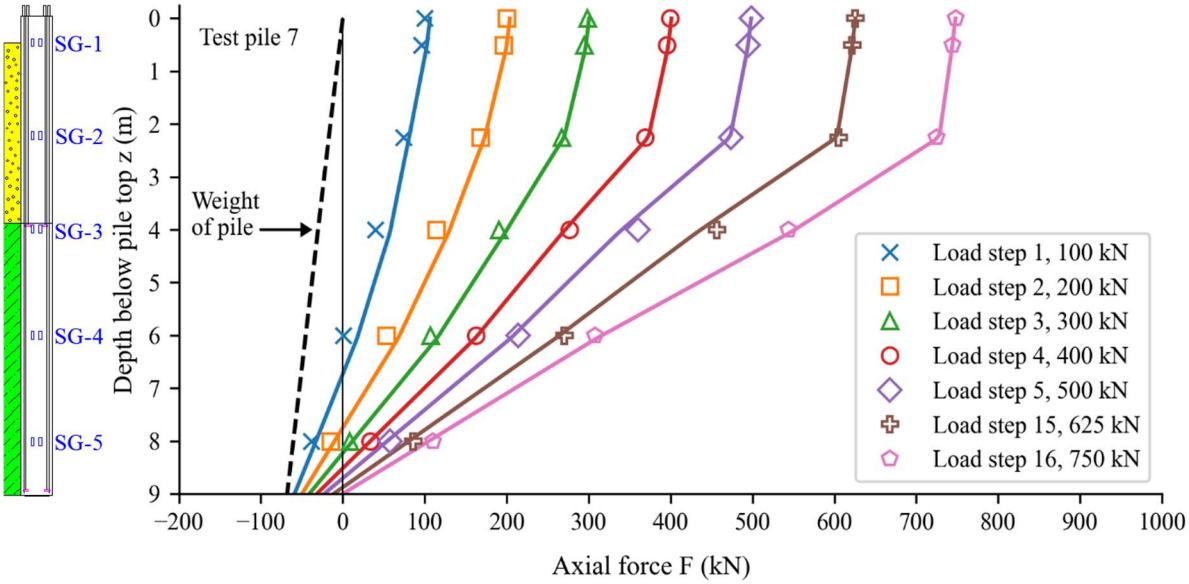

Figure 161: Hyperbolic non-linear loading model (HN model) for test pile 7.

Constant rate of uplift (CRU) test

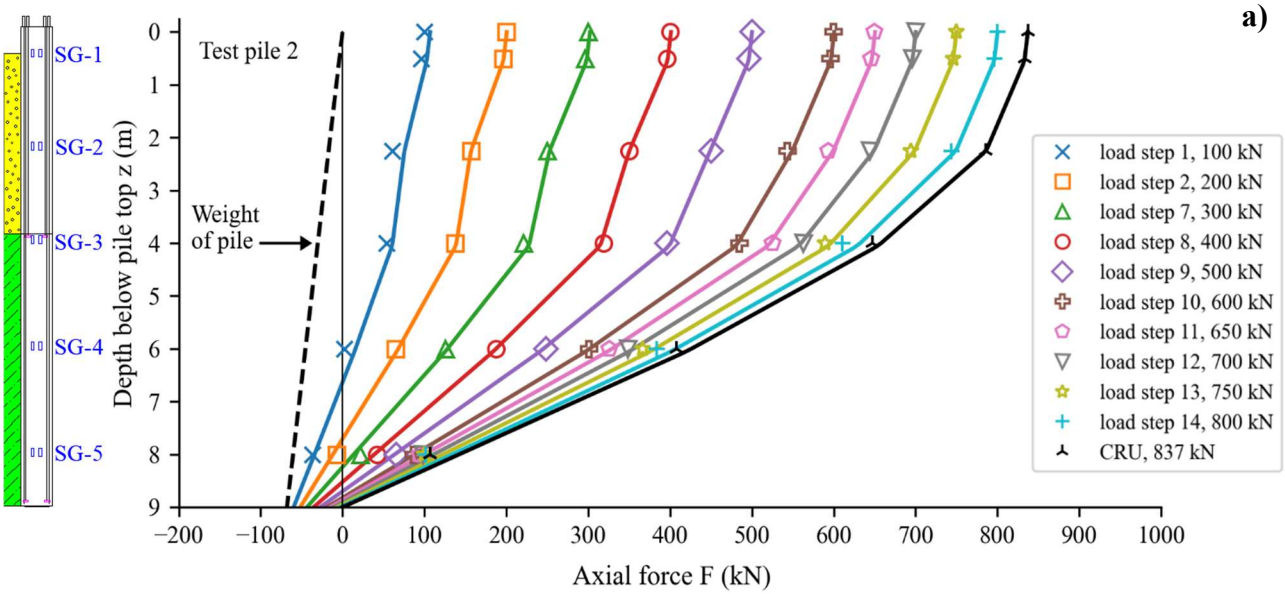

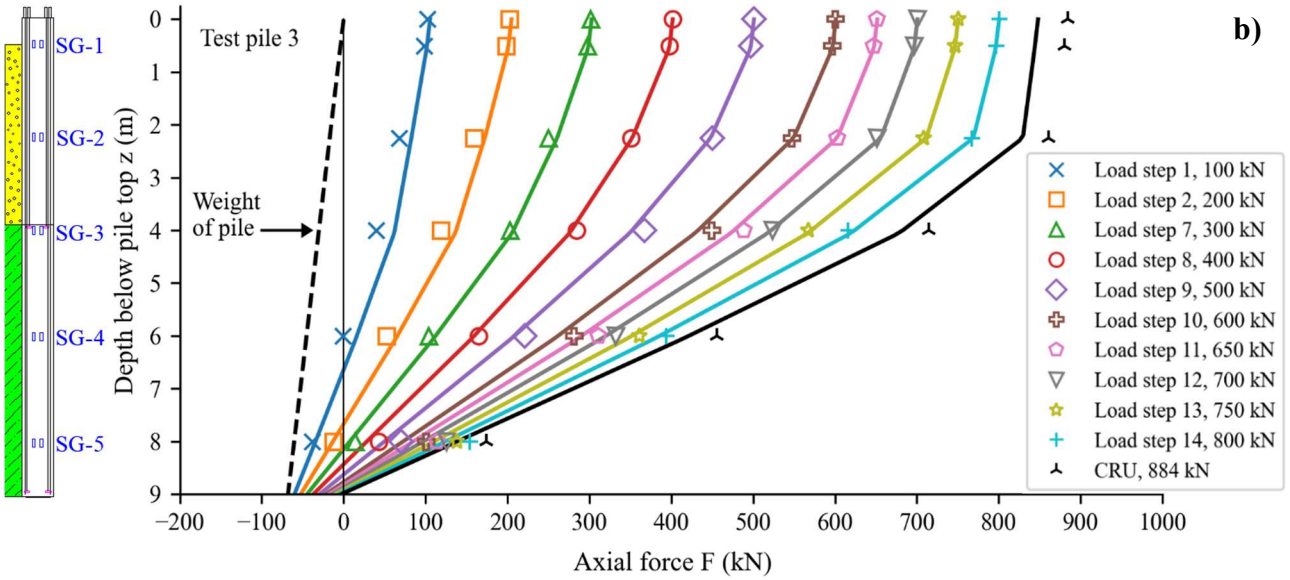
b)
Test pile 3
SG-1
SG-2
SG-3
SG-4
SG-5
Weight of pile
Depth below pile top z (m)
Axial force F (kN)
Load step 1, 100 kN
Load step 2, 200 kN
Load step 7, 300 kN
Load step 8, 400 kN
Load step 9, 500 kN
Load step 10, 600 kN
Load step 11, 650 kN
Load step 12, 700 kN
Load step 13, 750 kN
Load step 14, 800 kN
CRU, 884 kN

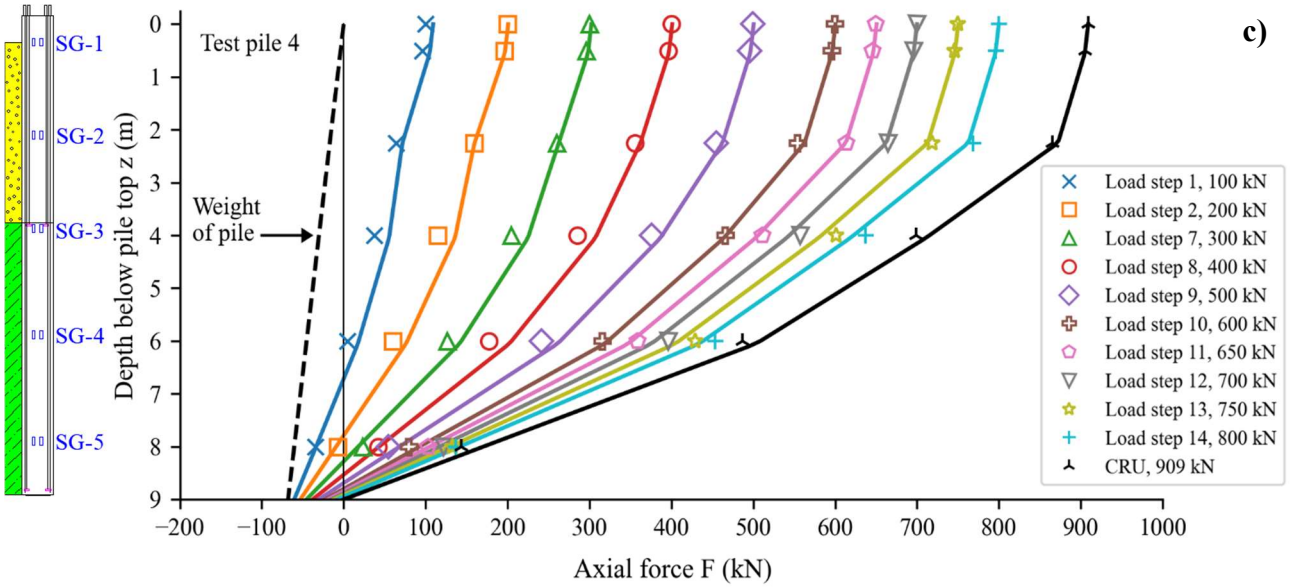
c)
Test pile 4
SG-1
SG-2
SG-3
SG-4
SG-5
Weight of pile
Depth below pile top z (m)
Axial force F (kN)
Load step 1, 100 kN
Load step 2, 200 kN
Load step 7, 300 kN
Load step 8, 400 kN
Load step 9, 500 kN
Load step 10, 600 kN
Load step 11, 650 kN
Load step 12, 700 kN
Load step 13, 750 kN
Load step 14, 800 kN
CRU, 909 kN

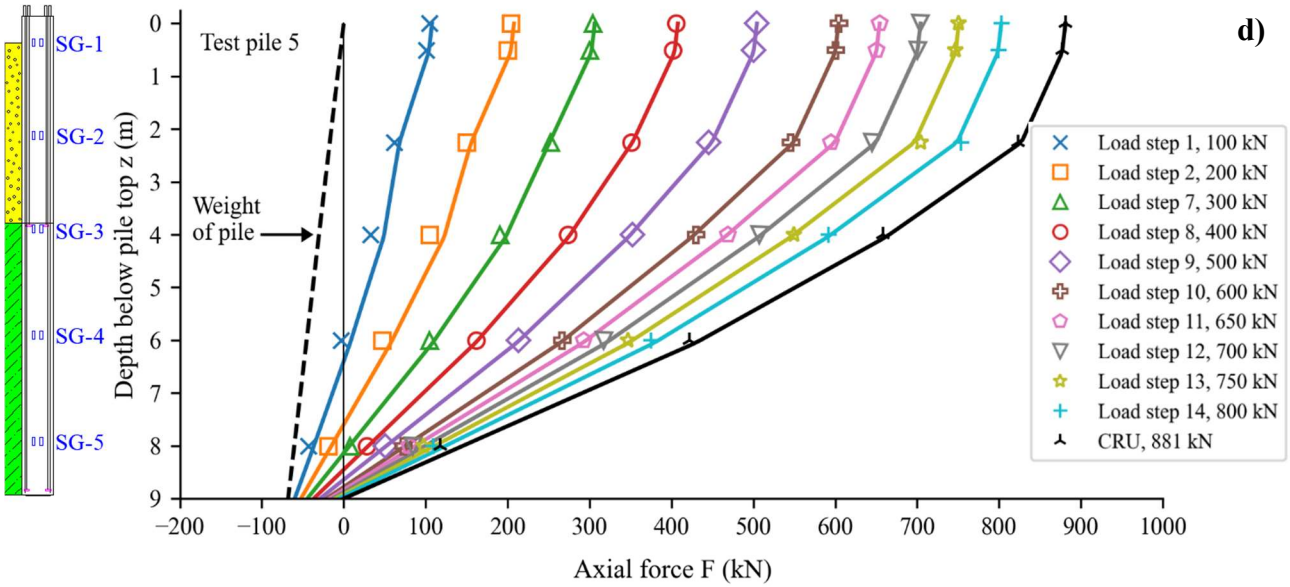
d)
Test pile 5
SG-1
SG-2
SG-3
SG-4
SG-5
Weight of pile
Depth below pile top z (m)
Axial force F (kN)
Load step 1, 100 kN
Load step 2, 200 kN
Load step 7, 300 kN
Load step 8, 400 kN
Load step 9, 500 kN
Load step 10, 600 kN
Load step 11, 650 kN
Load step 12, 700 kN
Load step 13, 750 kN
Load step 14, 800 kN
CRU, 881 kN

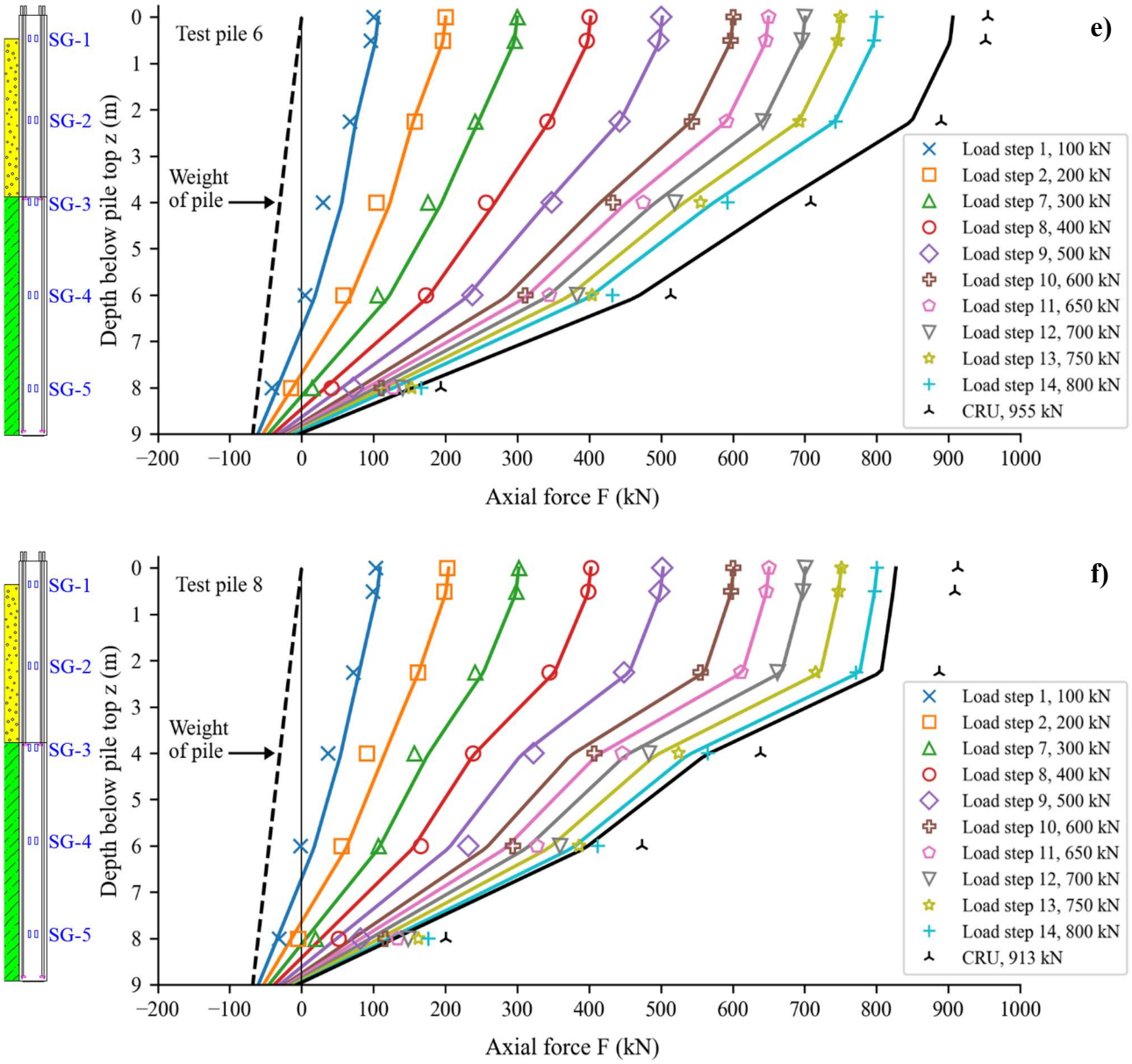

Figure 162: Hyperbolic non-linear loading model (HN model) for test piles (a) 2, (b) 3, (c) 4, (d) 5, (e) 6 and (f) 8.

In general, the hyperbolic non-linear loading model (HN model) demonstrates a good overall fit to the measured data for test piles 2-8. However, there are certain observations to note. For test piles 3, 6, and 8, the HN model is unable to accurately capture the ultimate values obtained during the constant rate of uplift portion of the static pile loading test. Additionally, for test piles 3, 6, and 8, the HN model underpredicts the axial forces, F, in the lower strain gauge levels (strain gauge level 4-5) as the applied load, Q, increases. On the other hand, for test piles 2, 4, and 5, the HN model slightly overpredicts the axial forces, F, at the lowest strain gauge level (strain gauge level 5) with increasing applied load, Q.

These discrepancies could potentially be attributed to the neglect of residual stresses and the utilization of observed load transfer curves instead of "true" load transfer curves. By using observed load transfer curves, there is a possibility that the ultimate unit shaft resistance, r_s, may be either

overrated or underrated, thereby impacting the distribution of axial forces, F, along the length of the test piles.

9.2.2 Accuracy of the HN model on the distribution of axial forces

The measured data, $F_{measured}$, for each load step is plotted against the corresponding HN model values of axial forces, F_{model}, along the length of each individual test pile. These plots can be found in Appendix K.1. Linear equations that pass through the origin (0,0) and the corresponding R^2 values are provided in Table 27.

Table 27: Linear equations and R^2 values for each individual test pile using the HN model.

Test pile	TP1	TP2	TP3	TP4	TP5	TP6	TP7	TP8
Linear equation	-	1.0068x	0.9883x	1.0022x	1.0042x	0.9791x	1.0008x	0.9672x
R^2 values	-	0.9988	0.9969	0.9982	0.9993	0.9952	0.9986	0.9884

The HN model demonstrates high accuracy in modelling the axial forces, F, with R^2 values ranging between 0.9952 and 0.9993. This indicates a strong correlation between the measured data and the HN model values, making the HN model highly reliable.

An overall evaluation of the HN model is presented in Figure 163. This plot showcases the comparison between the measured data, $F_{measured}$, and the HN model values of axial forces, F_{model}, along the length of all test piles (test piles 2-8) at the Hinge test site. The evaluation includes data from all levels of strain gauges (strain gauge levels 1-5) and for each load step on the virgin load curves and for the peak value from the constant rate of uplift portion of the pile loading test, as depicted in Figure 161 and Figure 162 (refer to section 9.2.1).

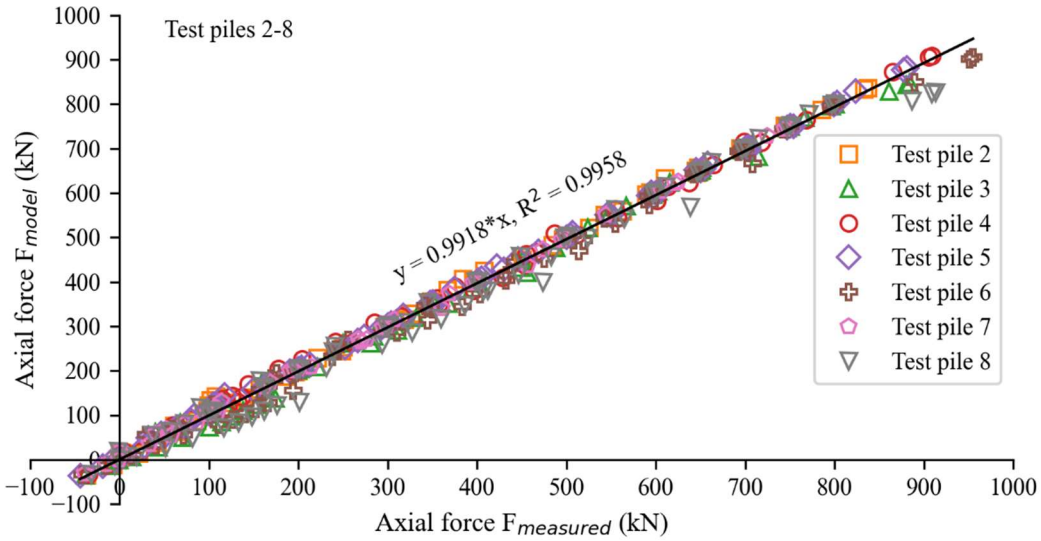

Figure 163: Measured data vs. HN model values of axial forces for test piles 2-8 at the Hinge test site.

The HN model is generally able to model values of axial forces, F, with a R^2 value of 0.9958.

9.2.3 Vertical displacement between pile and soil along the length of the test piles

Figure 164 and Figure 165 present the comparison between the vertical displacement between pile and soil along the length of test piles 2-8 as determined by the hyperbolic non-linear loading model (HN model), δ_{model}, and the corresponding measured data, $\delta_{measured}$, for each applied load step on the virgin load curves and for the peak value from the constant rate of uplift portion of the pile loading test.

In these figures, an average value for all levels of strain gauges (strain gauge levels 1-5) is plotted using a blue circle for each applied load step. Additionally, the upper and lower values are indicated by a blue vertical line, offering a visual representation of the range of values, as shown in Figure 164 and Figure 165.

Maintained load (ML) test

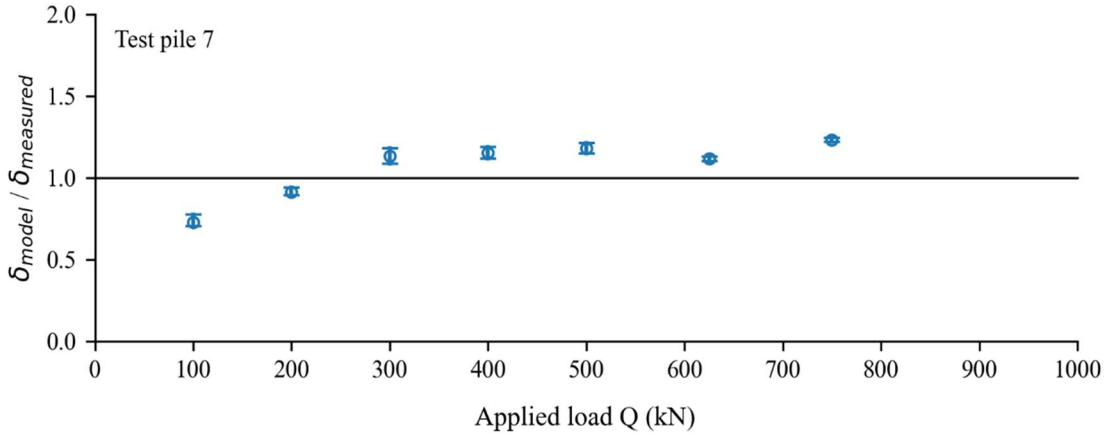

Figure 164: Vertical displacement ratio between hyperbolic non-linear loading model (HN model), δ_{model}, and measured data, $\delta_{measured}$, for test pile 7.

Constant rate of uplift (CRU) test

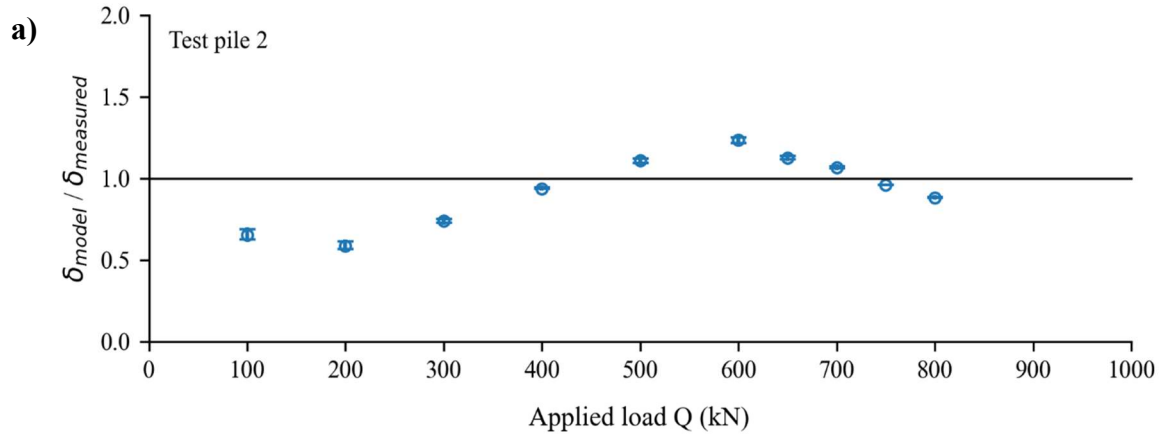

b)

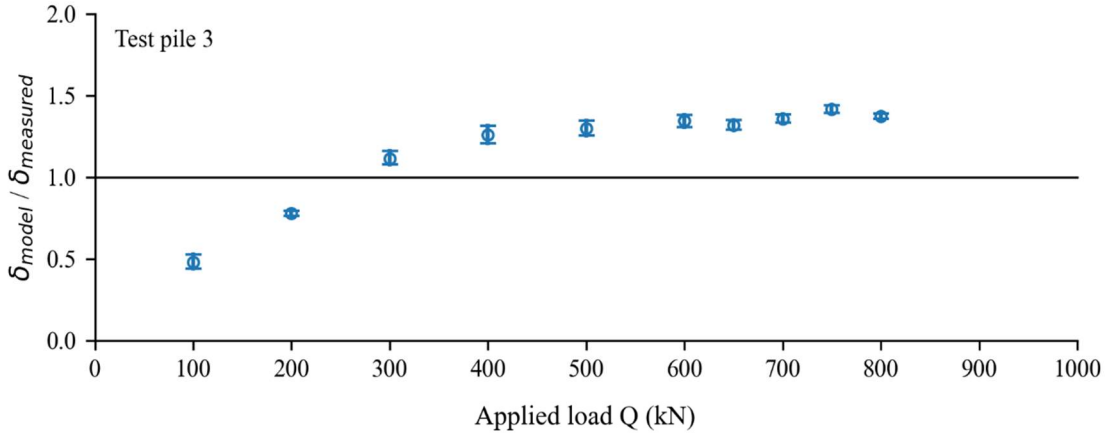
Test pile 3
$\delta_{model} / \delta_{measured}$
2.0
1.5
1.0
0.5
0.0
0
100
200
300
400
500
600
700
800
900
1000
Applied load Q (kN)

c)

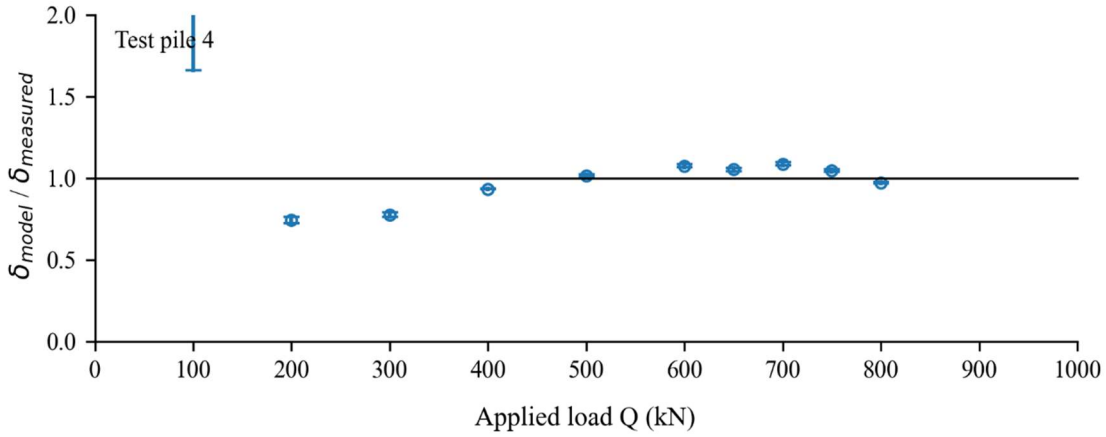
Test pile 4
$\delta_{model} / \delta_{measured}$
2.0
1.5
1.0
0.5
0.0
0
100
200
300
400
500
600
700
800
900
1000
Applied load Q (kN)

d)

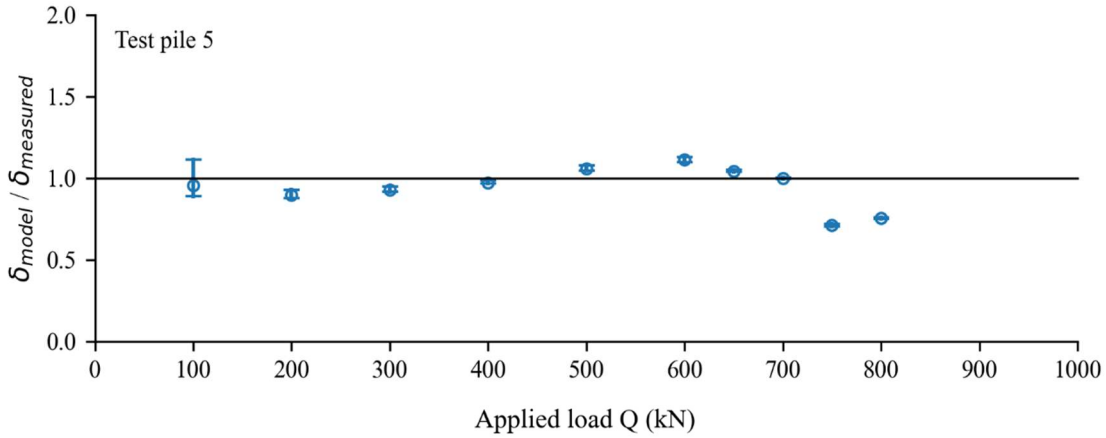
Test pile 5
$\delta_{model} / \delta_{measured}$
2.0
1.5
1.0
0.5
0.0
0
100
200
300
400
500
600
700
800
900
1000
Applied load Q (kN)

e)

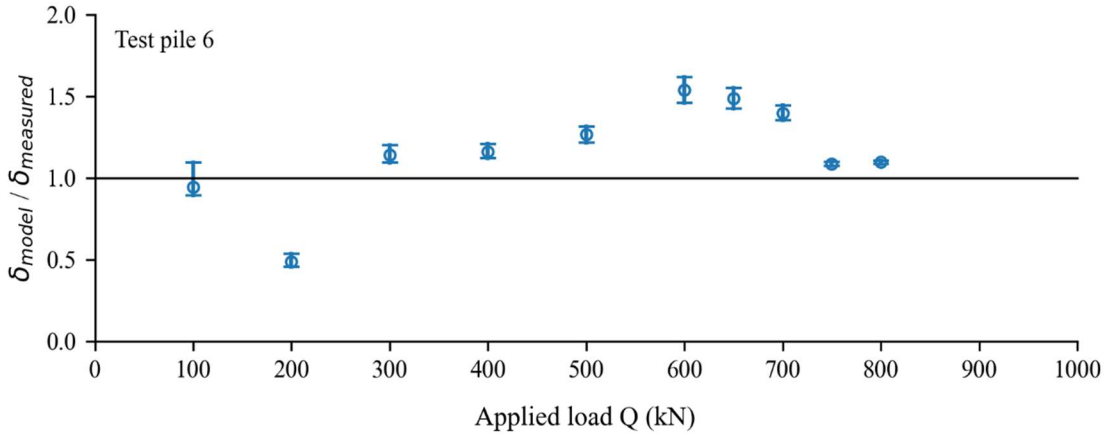
Test pile 6
$\delta_{model} / \delta_{measured}$
2.0
1.5
1.0
0.5
0.0
0
100
200
300
400
500
600
700
800
900
1000
Applied load Q (kN)

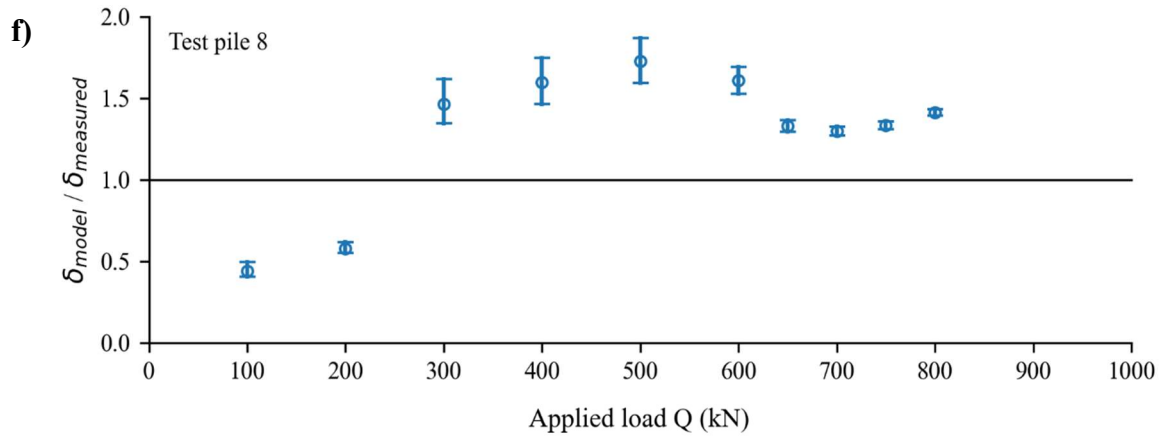

Figure 165: Vertical displacement ratio between hyperbolic non-linear loading model (HN model), δ_{model}, and measured data, $\delta_{measured}$, for test piles (a) 2, (b) 3, (c) 4, (d) 5, (e) 6 and (f) 8.

The hyperbolic non-linear loading model (HN model) models the vertical displacements, $\delta_{pile,soil}$, between the pile and soil along the length of test piles 2-8. The average vertical displacement ratio varies from 0.44 to 1.73 for each load step on the virgin load curves and for the peak value from the constant rate of uplift portion of the pile loading test. However, there is an exception for test pile 4, load step 1 (applied load Q = 100 kN), where the vertical displacement ratio exhibits greater variability ranging from 1.66 to 7.32 with an average of 3.37.

9.3 Hyperbolic non-linear loading model incl. residual stresses (HNr model)

The hyperbolic non-linear loading model incl. residual stresses (HNr model) is evaluated by comparing with the measured data from the static pile loading test from test piles 2-8. The following input parameters are applied:

- Diameter, $D_{pi} = 0.62$ m, Cross sectional area, $A_{pi} = 0.30$ m² and a circumference of 1.95 m.
- The 9 m long piles are divided into 90 elements, each with a length of $L_{pi} = 10$ cm
- The forces, F_i*, acting on the piles before initiating the pile loading tests is determined as the cumulative weight of the piles along the length of the piles, where weight of the piles (reinforced concrete) is considered with hydrostatic water pressure (uplift) beneath the pile base (the piles are assumed impermeable). Thus, bulk weight = 25 kN/m³.
- The residual stresses are determined based on post pile loading data as the unit shaft resistance remaining after unloading of the test piles cf. section 0.
- The axial stiffness ($E_{pi} \cdot A_{pi}$) of the pile is considered equal to14.0 á 16.1 GN cf. section 6.3.2.
- The force, R_b*, at the pile base is considered equal to the total weight of the pile before initiating the pile loading test and is assumed to diminish linear to zero during failure.
- The resistive force in the spring, R_{si} is determined directly from the measured data as $R_{si} = \pi \cdot D_{pi} \cdot L_{pi} \cdot r_s$ for each element, where the unit shaft resistance r_s* is derived from measured data.
- The mobilised unit shaft resistance, r_s*, in the sand layers is determined by a hyperbolic strain softening t-z function (Zhang and Zhang, 2012) fitted to measured data from strain gauge level 1-2 and 2-3, respectively. See section 8.2.1.
- The mobilised unit shaft resistance, r_s*, in the clay layers is determined by a hyperbolic strain softening t-z function (Vijayvergiya, 1977) fitted to measured data from strain gauge level 3-4 and 4-5, respectively. Furthermore, the mobilised unit shaft resistance, r_s*, in the clay layers below strain gauge level 5 is assumed equal to the measured mobilised unit shaft resistance from strain gauge level 4-5. See section 8.2.1.

The analytical model of the axial force, F, and the vertical displacement, $\delta_{pile,soil}$, is plotted along the length of the test piles and compared with the data obtained from pile loading tests. These comparisons are made separately for each load step on the virgin load curves and for the peak value from the constant rate of uplift portion of the pile loading test.

To ensure accuracy, the measured data is corrected for the weight of the pile. This correction is necessary because the strain gauges only measure changes in strain and not the actual strain values. The weight of the pile remains constant before and after the pile loading test, and it is not accounted for by the strain gauges.

9.3.1 Distribution of axial force along the length of the test piles

Figure 166 and Figure 167 illustrate the axial force, F, distribution along the length of test piles 2-8 as determined by the hyperbolic non-linear loading model (HNr model) alongside the corresponding measured data. The signatures in the figures represent the measured data for each load step, while the solid lines represent the distribution of axial force, F, as predicted by the hyperbolic non-linear loading model (HN model).

Maintained load (ML) test

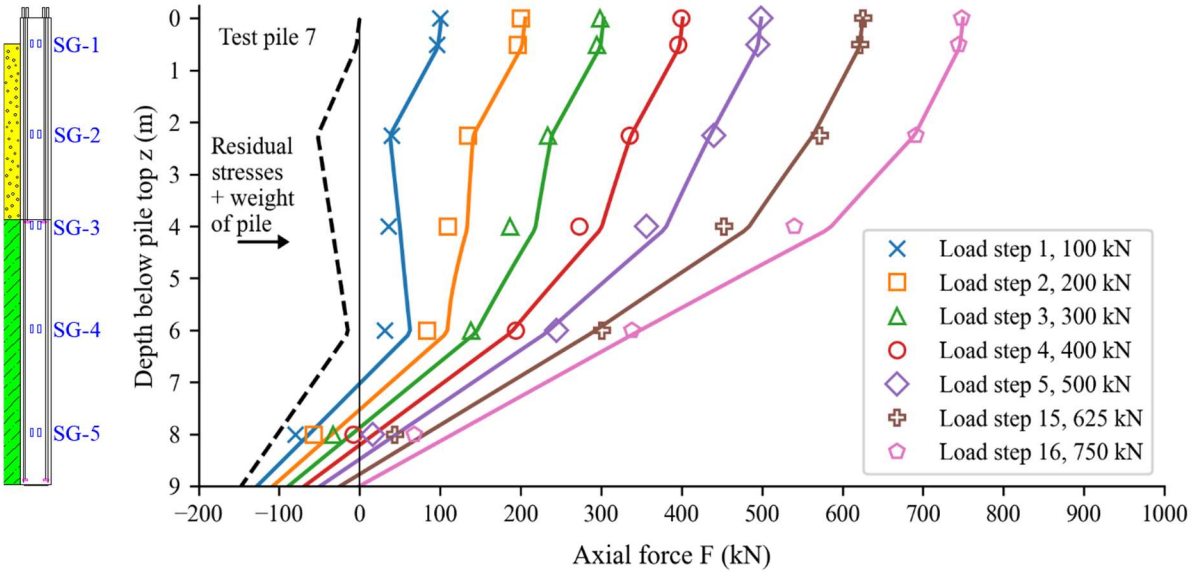

Figure 166: Hyperbolic non-linear loading model incl. residual stresses (HNr model) for test pile 7.

Constant rate of uplift (CRU) test

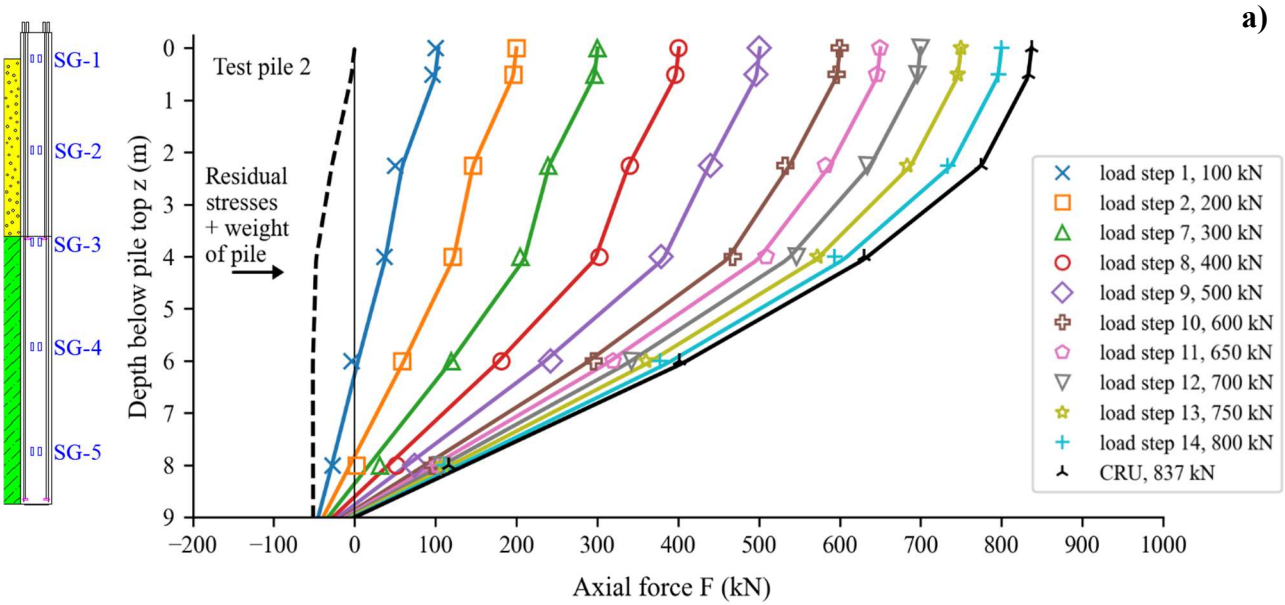

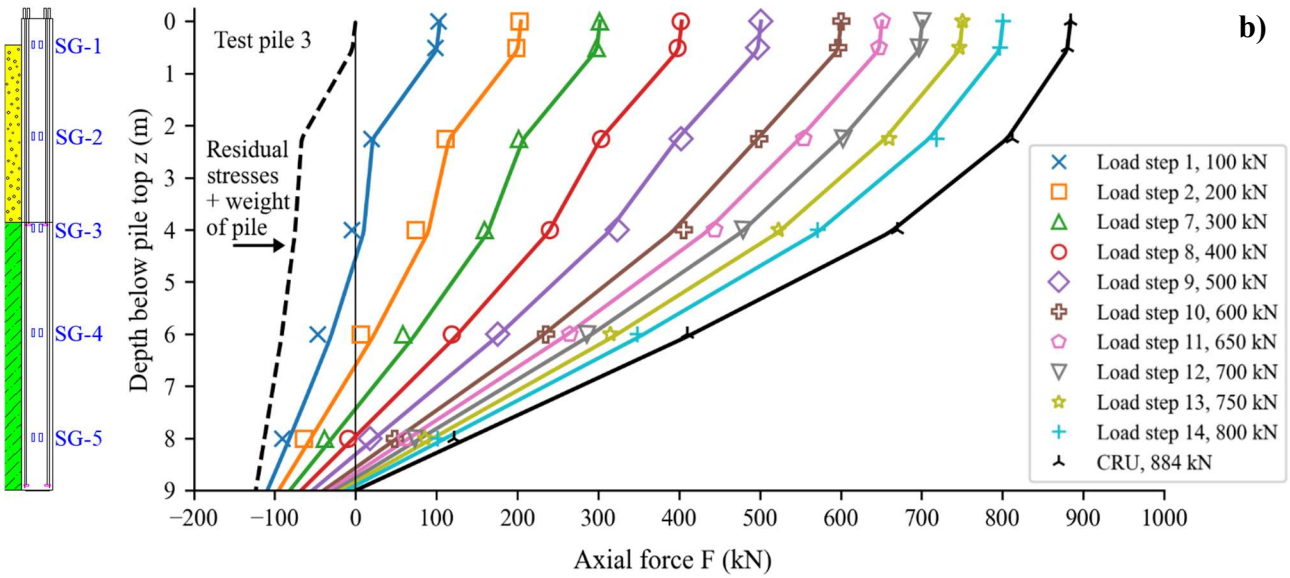
b)
Test pile 3
Residual stresses + weight of pile
SG-1
SG-2
SG-3
SG-4
SG-5
Depth below pile top z (m)
Axial force F (kN)
Load step 1, 100 kN
Load step 2, 200 kN
Load step 7, 300 kN
Load step 8, 400 kN
Load step 9, 500 kN
Load step 10, 600 kN
Load step 11, 650 kN
Load step 12, 700 kN
Load step 13, 750 kN
Load step 14, 800 kN
CRU, 884 kN

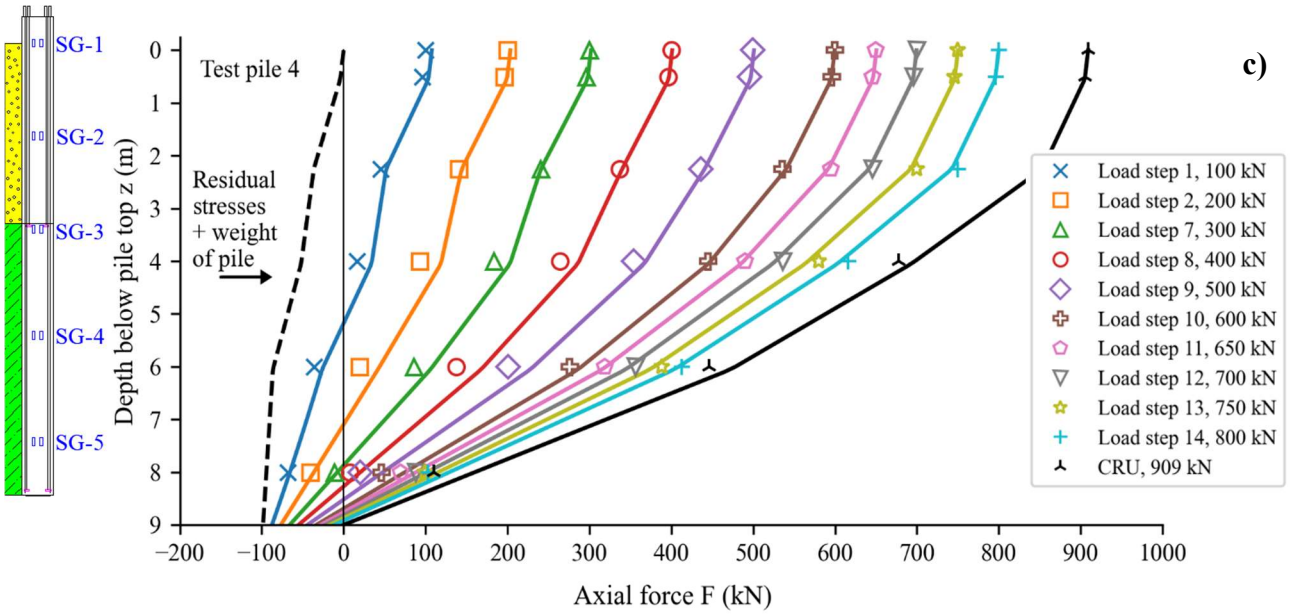
c)
Test pile 4
Residual stresses + weight of pile
SG-1
SG-2
SG-3
SG-4
SG-5
Depth below pile top z (m)
Axial force F (kN)
Load step 1, 100 kN
Load step 2, 200 kN
Load step 7, 300 kN
Load step 8, 400 kN
Load step 9, 500 kN
Load step 10, 600 kN
Load step 11, 650 kN
Load step 12, 700 kN
Load step 13, 750 kN
Load step 14, 800 kN
CRU, 909 kN

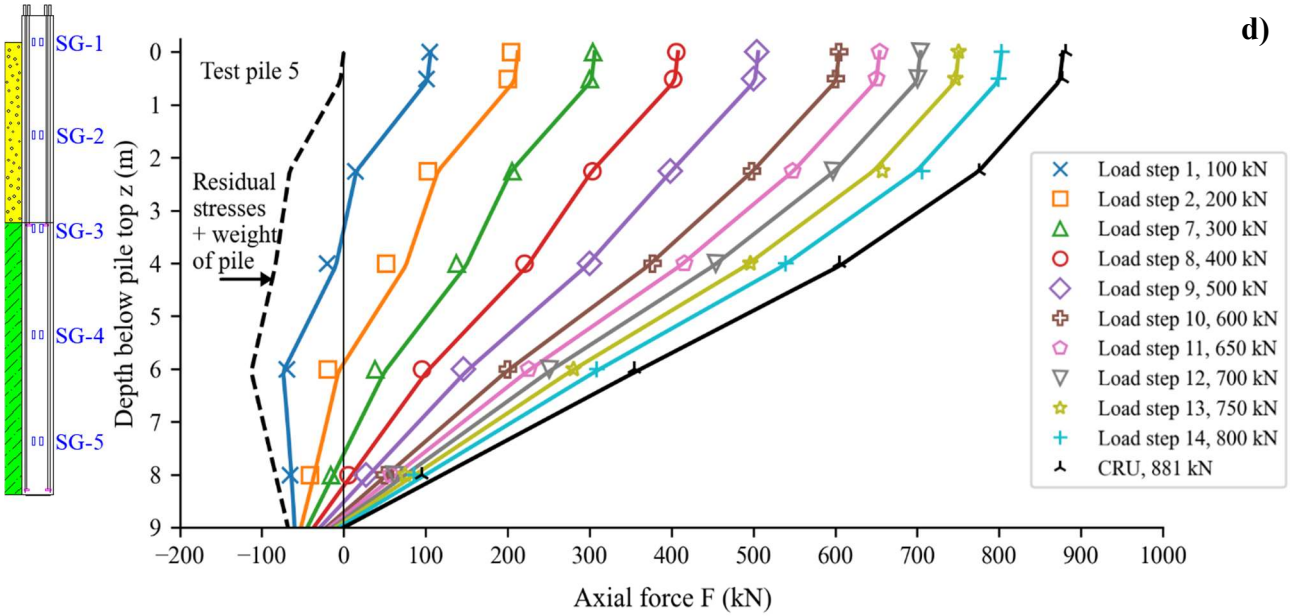
d)
Test pile 5
Residual stresses + weight of pile
SG-1
SG-2
SG-3
SG-4
SG-5
Depth below pile top z (m)
Axial force F (kN)
Load step 1, 100 kN
Load step 2, 200 kN
Load step 7, 300 kN
Load step 8, 400 kN
Load step 9, 500 kN
Load step 10, 600 kN
Load step 11, 650 kN
Load step 12, 700 kN
Load step 13, 750 kN
Load step 14, 800 kN
CRU, 881 kN

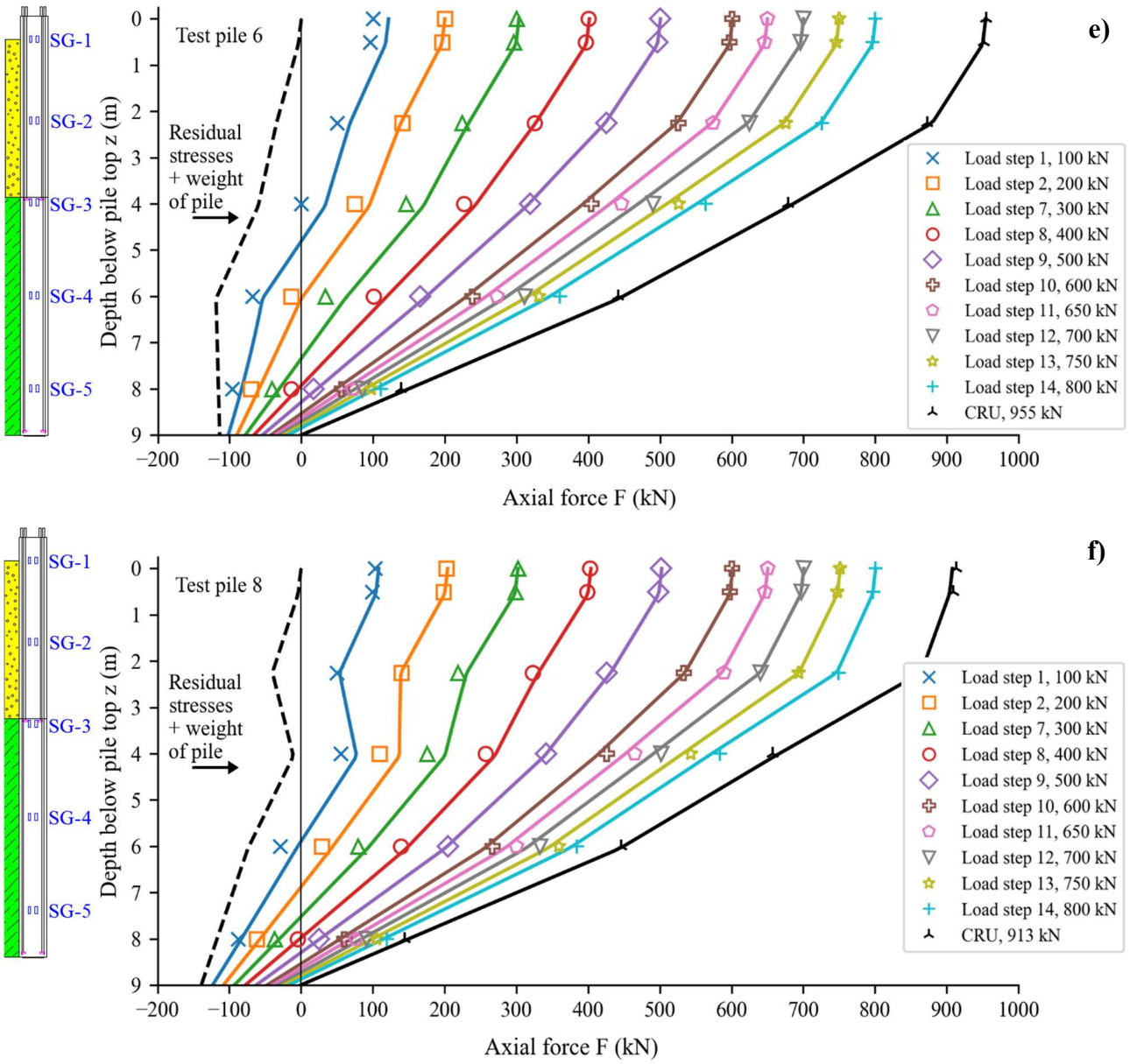

Figure 167: Hyperbolic non-linear loading model incl. residual stresses (HNr model) for test piles (a) 2, (b) 3, (c) 4, (d) 5, (e) 6 and (f) 8.

The hyperbolic non-linear loading model, which includes residual stresses (HNr model), is found to accurately fit the measured data for test piles 2-8. Kindly be advised, there is an issue with the HN model discussed in section 9.2, as it is unable to accurately model the ultimate values achieved during the constant rate of uplift phase of the static pile loading test for test piles 3, 6, and 8. Furthermore, the HN model underestimates the axial forces, F, at lower strain gauge levels (specifically, strain gauge level 4-5) as the applied load, Q, increases for test piles 3, 6, and 8.

This issue is resolved by implementing the HNr model instead. However, similar to the HN model, the HNr model slightly overestimates the axial forces, F, at the lowest strain gauge level (strain gauge level 5) as the applied load, Q, increases for test piles 2, 4, and 5.

9.3.2 Accuracy of the HN model on the distribution of axial forces

The measured data, $F_{measured}$, for each load step is plotted against the corresponding HNr model values of axial forces, F_{model}, along the length of each individual test pile. These plots can be found in Appendix K.2. Linear equations that pass through the origin (0,0) and the corresponding R^2 values are provided in Table 28.

Table 28: Linear equations and R^2 values for each individual test pile using the HNr model.

Test pile	TP1	TP2	TP3	TP4	TP5	TP6	TP7	TP8
Linear equation	-	1.0034x	1.0004x	1.0049x	1.0028x	0.9984x	1.0153x	0.9990x
R^2 values	-	0.9994	0.9993	0.9971	0.9993	0.9981	0.9931	0.9988

The HNr model demonstrates high accuracy in modelling the axial forces, F, with R^2 values ranging between 0.9931 and 0.9994. This indicates a strong correlation between the measured data and the HNr model values, making the HNr model highly reliable.

An overall evaluation of the HNr model is presented in Figure 168. This plot showcases the comparison between the measured data, $F_{measured}$, and the HNr model values of axial forces, F_{model}, along the length of all test piles (test piles 2-8) at the Hinge test site. The evaluation includes data from all levels of strain gauges (strain gauge levels 1-5) and for each load step on the virgin load curves and for the peak value from the constant rate of uplift portion of the pile loading test, as depicted in Figure 166 and Figure 167 (refer to section 9.3.1).

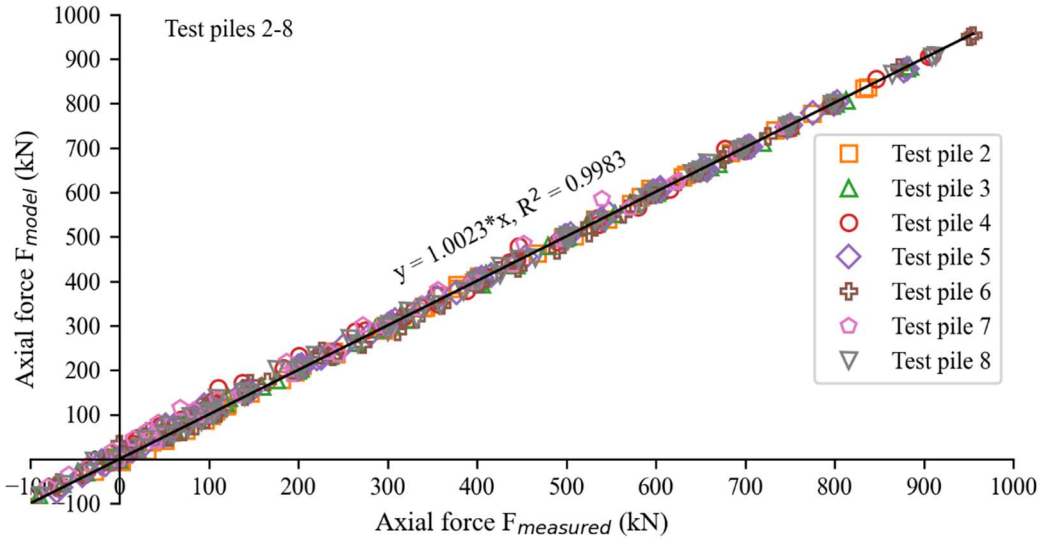

Figure 168: Measured data vs. HNr model values of axial forces for test piles 2-8 at the Hinge test site.

The HNr model demonstrates overall effectiveness in modelling the values of axial forces, F, exhibiting a slightly higher R^2 value of 0.9983 compared to the HN model's R^2 value of 0.9958.

9.3.3 Vertical displacement between pile and soil along the length of the test piles

Figure 169 and Figure 170 present the comparison between the vertical displacement between pile and soil along the length of test piles 2-8 as determined by the hyperbolic non-linear loading model (HNr model), δ_{model}, and the corresponding measured data, $\delta_{measured}$, for each applied load step on the virgin load curves and for the peak value from the constant rate of uplift portion of the pile loading test.

In these figures, an average value for all levels of strain gauges (strain gauge levels 1-5) is plotted using a blue circle for each applied load step. Additionally, the upper and lower values are indicated by a blue vertical line, offering a visual representation of the range of values, as shown in Figure 169 and Figure 170.

Maintained load (ML) test

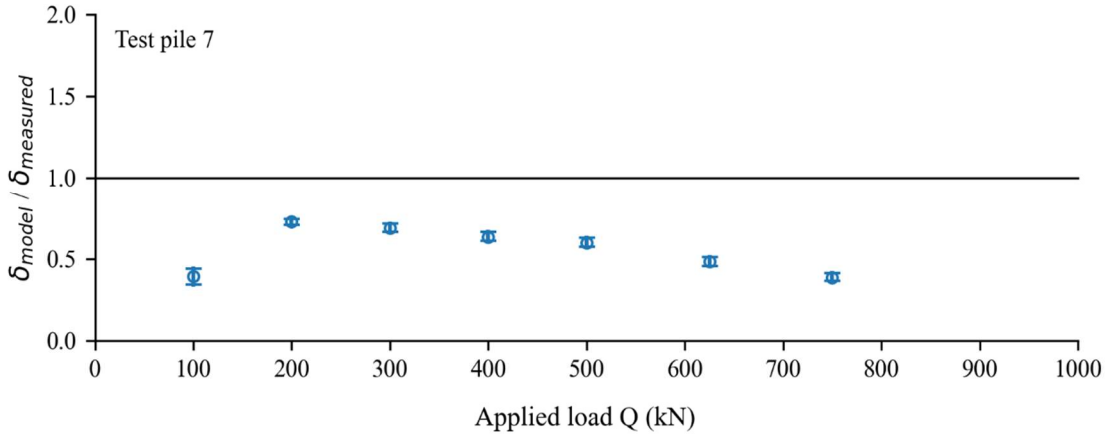

Figure 169: Vertical displacement ratio between hyperbolic non-linear loading model incl. residual stresses (HNr model), δ_{model}, and measured data, $\delta_{measured}$, for test pile 7.

Constant rate of uplift (CRU) test

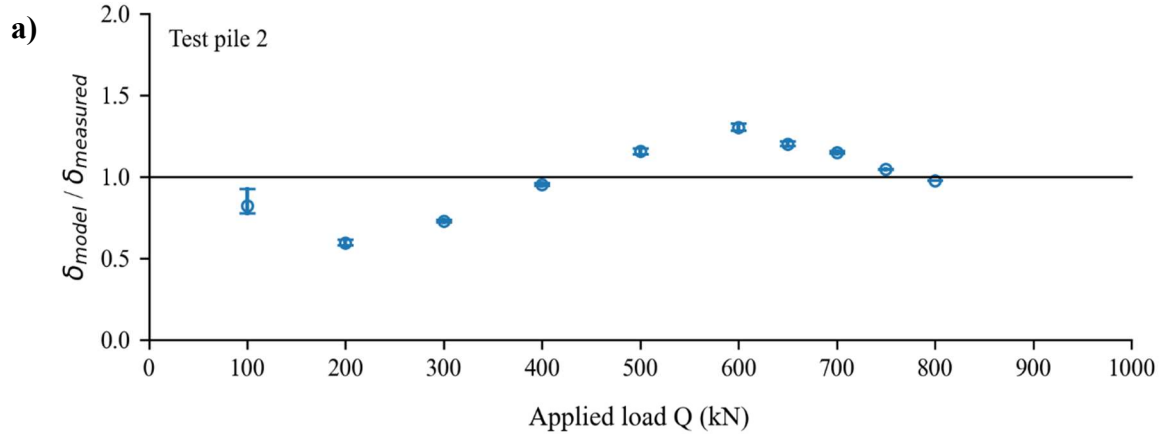

b)

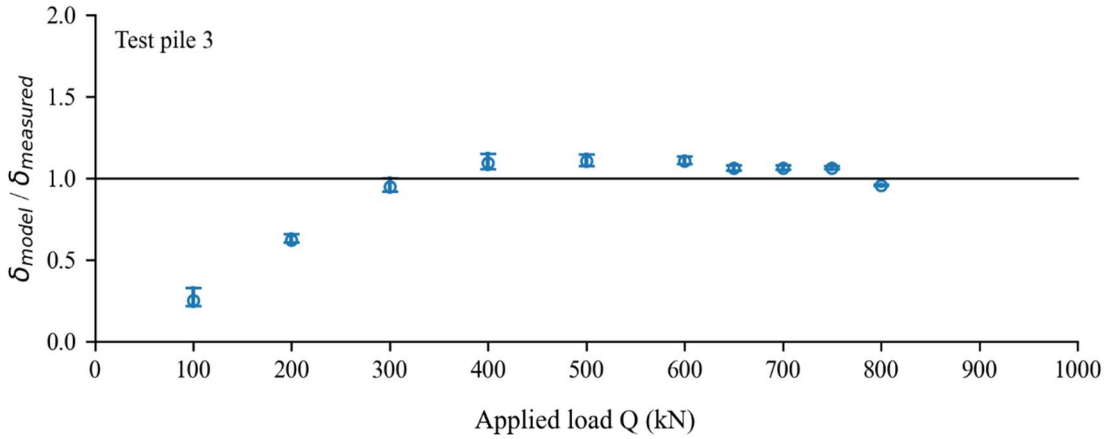
Test pile 3
$\delta_{model} / \delta_{measured}$
2.0
1.5
1.0
0.5
0.0
0
100
200
300
400
500
600
700
800
900
1000
Applied load Q (kN)

c)

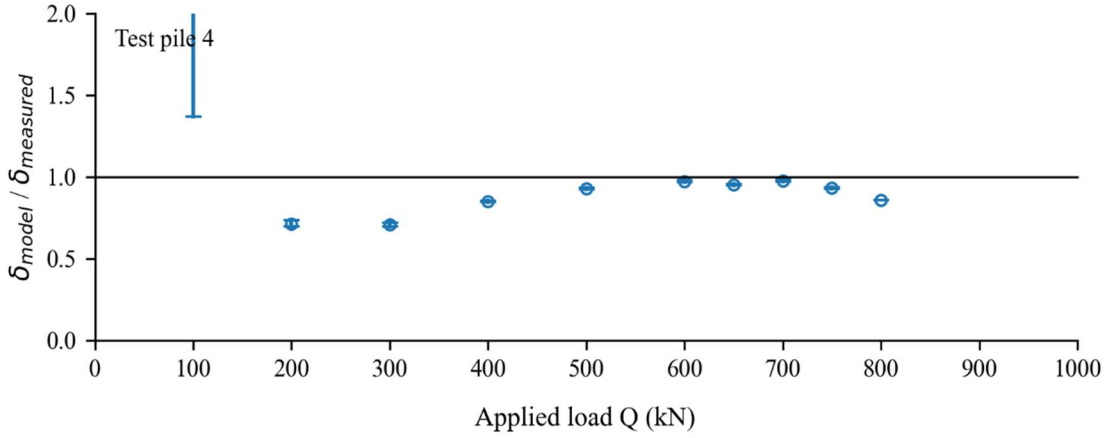
Test pile 4
$\delta_{model} / \delta_{measured}$
2.0
1.5
1.0
0.5
0.0
0
100
200
300
400
500
600
700
800
900
1000
Applied load Q (kN)

d

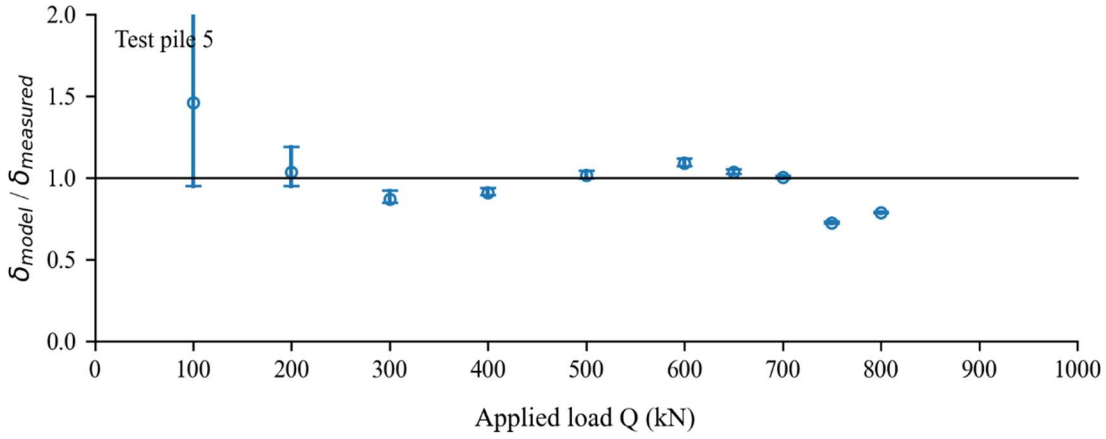
Test pile 5
$\delta_{model} / \delta_{measured}$
2.0
1.5
1.0
0.5
0.0
0
100
200
300
400
500
600
700
800
900
1000
Applied load Q (kN)

e)

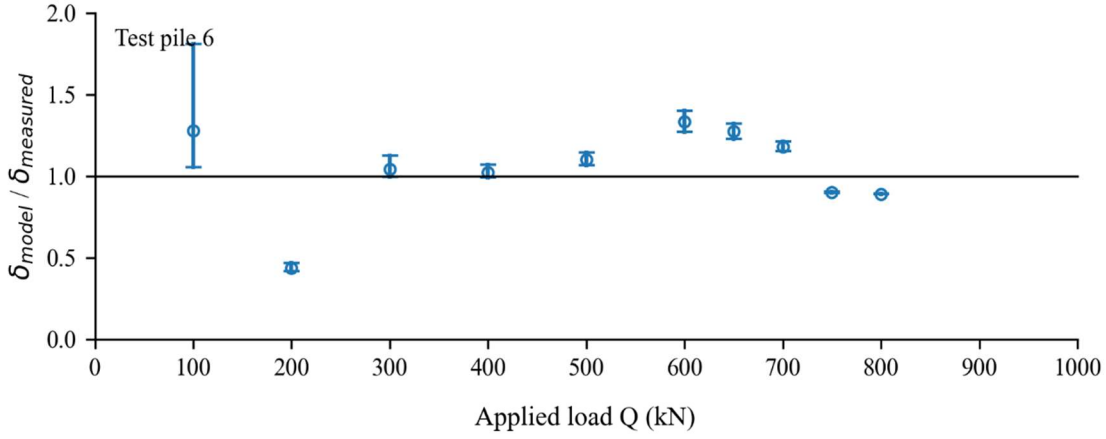
Test pile 6
$\delta_{model} / \delta_{measured}$
2.0
1.5
1.0
0.5
0.0
0
100
200
300
400
500
600
700
800
900
1000
Applied load Q (kN)

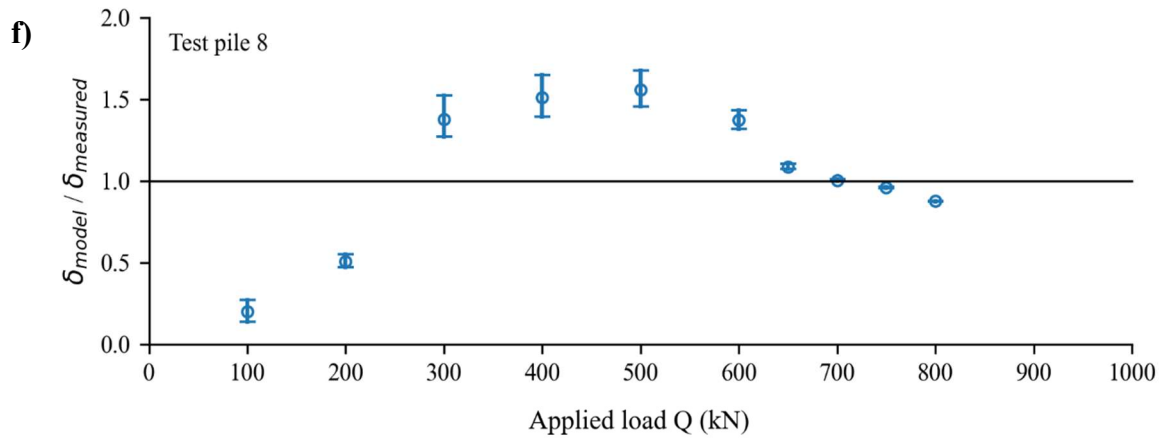

Figure 170: Vertical displacement ratio between hyperbolic non-linear loading model incl. residual stresses (HNr model), δ_{model}, and measured data, $\delta_{measured}$, for test piles (a) 2, (b) 3, (c) 4, (d) 5, (e) 6 and (f) 8.

The hyperbolic non-linear loading model (HNr model) models the vertical displacements, $\delta_{pile,soil}$, between the pile and soil along the length of test piles 2-8. The average vertical displacement ratio varies from 0.20 to 1.56 for each load step on the virgin load curves and for the peak value from the constant rate of uplift portion of the pile loading test. However, there is an exception for test pile 4, load step 1 (applied load Q = 100 kN), where the vertical displacement ratio exhibits greater variability ranging from 1.37 to 7.73 with an average of 3.19.

9.4 Prediction of load transfer curves based on soil properties

In situations where load transfer functions are unknown, it becomes necessary to predict these functions based on soil properties. In practical geotechnical engineering, it is often valuable to make an initial estimation of load transfer curves using limited information available at the project's outset. For fine-grained soils, one commonly available parameter is the field vane strength, c_{fv}, determined through the Danish field vane test.

To model the load transfer function for the Søvind Marl surrounding the test piles in Hinge, the strain-softening load transfer function proposed by Vijayvergiya (1977) has been successfully used in previous back analyses of static pile loading test results in both the upper and lower clay layers (refer to section 6.3.4). Thus, the strain-softening load transfer function by Vijayvergiya (1977) is selected for predicting load transfer functions based on soil properties.

Additionally, the Vardanega and Bolton shear strength mobilisation function (Vardanega and Bolton, 2011b) is also chosen for predicting load transfer functions based on soil properties. This method characterizes shear strength mobilisation in fine-grained soils using a power law within the moderate strain region, with the strain to half mobilisation serving to normalize the strain axis (refer to section 2.5.3). The Vardanega and Bolton shear strength mobilisation function requires both triaxial test data and information on field vane strength, c_{fv}, obtained through the Danish field vane test to determine shear strength mobilisation.

9.4.1 Prediction based on Danish field vane test

The strain-softening load transfer function for fine-grained soils, proposed by Vijayvergiya (1977), is outlined below with function coefficients A_0 and B_0 assigned values of 2 and 1, respectively (Vijayvergiya, 1977).

The strain-softening load transfer function by Vijayvergiya (1977) is presented below with function coefficients A_0 and B_0 equal to 2 and 1, respectively valid for fine-grained soils:

$$\frac{r_s}{r_{peak}} = 2 \cdot \sqrt{\frac{\delta_{pile,soil}}{\delta_{peak}}} - \frac{\delta_{pile,soil}}{\delta_{peak}} \tag{87}$$

Here, r_s is the mobilised unit shaft resistance, $\delta_{pile,soil}$ is the displacement paired with, r_{peak} is the ultimate unit shaft resistance, δ_{peak} is the displacement paired with r_{peak}.

In order to forecast the load transfer function accurately, it becomes essential to ascertain the ultimate unit shaft resistance, r_{peak}, as well as the corresponding displacement, δ_{peak}, The pairing between the ultimate unit shaft resistance, r_{peak}, and the displacement, δ_{peak}, is elucidated in the subsequent section.

Displacement paired with ultimate unit shaft resistance

The load transfer functions obtained for the upper and lower clay layers are normalised with respect to the ultimate unit shaft resistance, r_{peak}. The corresponding displacement, δ_{peak}, paired with r_{peak}, is determined to be 8.7 mm for the Søvind Marl at the Hinge test site.

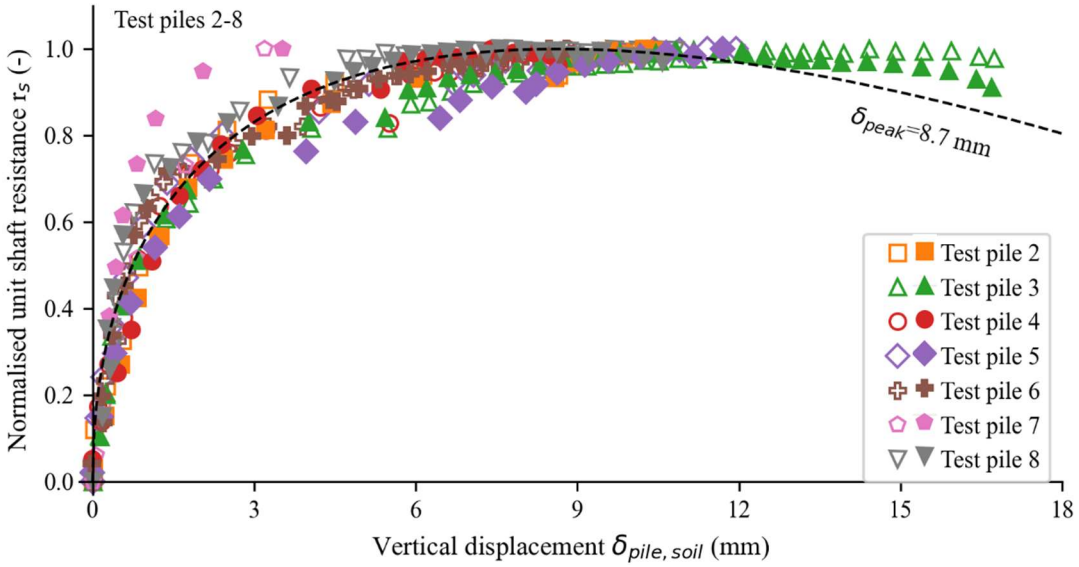

Figure 171: Normalized load transfer functions derived from the static pile loading tests conducted on test piles 2-8 for both the upper and lower clay layers at the Hinge test site. Open signatures represent the upper clay layer, while closed signatures represent the lower clay layer.

The displacement, δ_{peak}, corresponding to the ultimate unit shaft resistance, r_{peak}, is anticipated to fall within the range of 5-10 mm (Vijayvergiya, 1977, Kulhawy, 1985), which aligns well with the determined value of 8.7 mm for the Søvind Marl at the Hinge test site. In cases where no previous knowledge of pile load tests under similar ground conditions and pile dimensions is available, it is recommended to utilize the mean value of the displacement, δ_{peak} within the provided range.

Ultimate unit shaft resistance

The determination of the ultimate unit shaft resistance, r_{peak}, follows the α method explained in section 2.2.1. It assumes that the undrained shear strength, c_u, is equivalent to the field vane strength, c_{fv}, at the middle of the considered soil layer, as described in equation (56) in section 3.10 (where $c_{fv} = 96.7 + 17.1 \cdot z_d$). The empirical adhesion factor, $\alpha_{c_{fv}}$, is obtained from the best-fit envelope for the α-c_u relationship mentioned in equation (81) in section 8.4.3, representing fine-grained soils in general ($\alpha_{c_{fv}} = 6.65 * {c_{u,c_{fv}}}^{-0.59}$). A similar approach is employed for high plasticity clay, using the best-fit envelope given by equation (84) in section 8.4.3 ($\alpha_{c_{fv}} = 9.88 * {c_{u,c_{fv}}}^{-0.67}$).

For the upper clay layer (strain gauge level 3-4), the undrained shear strength, c_u, is determined as the field vane strength, $c_{fv} = 174$ kPa, at the middle of the layer (4.5 m below ground level). Likewise, for the lower clay layer (strain gauge level 4-5), the undrained shear strength is derived from the field vane strength, $c_{fv} = 208$ kPa, at the middle of the layer (6.5 m below ground level).

The empirical adhesion factor, α, is determined as $\alpha_{c_{fv}} = 0.32$ for the upper clay layer (strain gauge level 3-4) and $\alpha_{c_{fv}} = 0.29$ for the lower clay layer (strain gauge level 4-5).

Predicted load transfer functions

The predicted load transfer functions are showcased in relation to the measured unit shaft resistance, r_s, obtained from the static pile loading tests conducted on test piles 2-8 in both the upper and lower clay layers at the Hinge test site. These load transfer functions are illustrated in Figure 172 and Figure 173, considering a displacement of $\delta_{peak} = 8.7$ mm as determined earlier through fitting analysis of the performed pile load test.

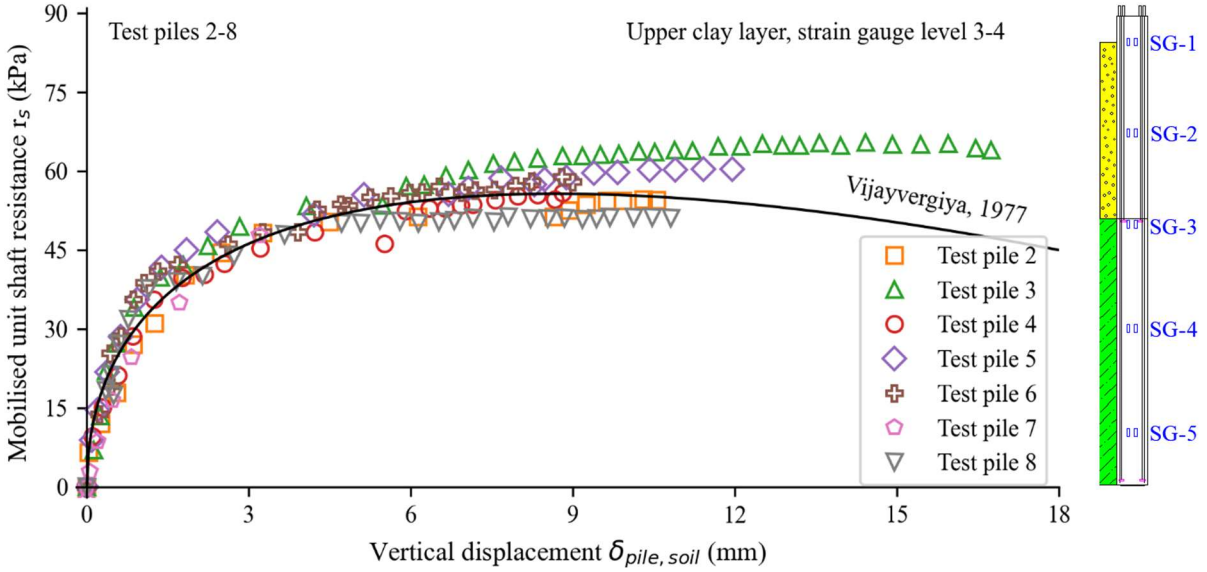

Figure 172: Predicted load transfer functions cf. Vijayvergiya (1977) and unit shaft resistance obtained from the static pile loading tests conducted on test piles 2-8 in the upper clay layer (strain gauge level 3-4) at the Hinge test site.

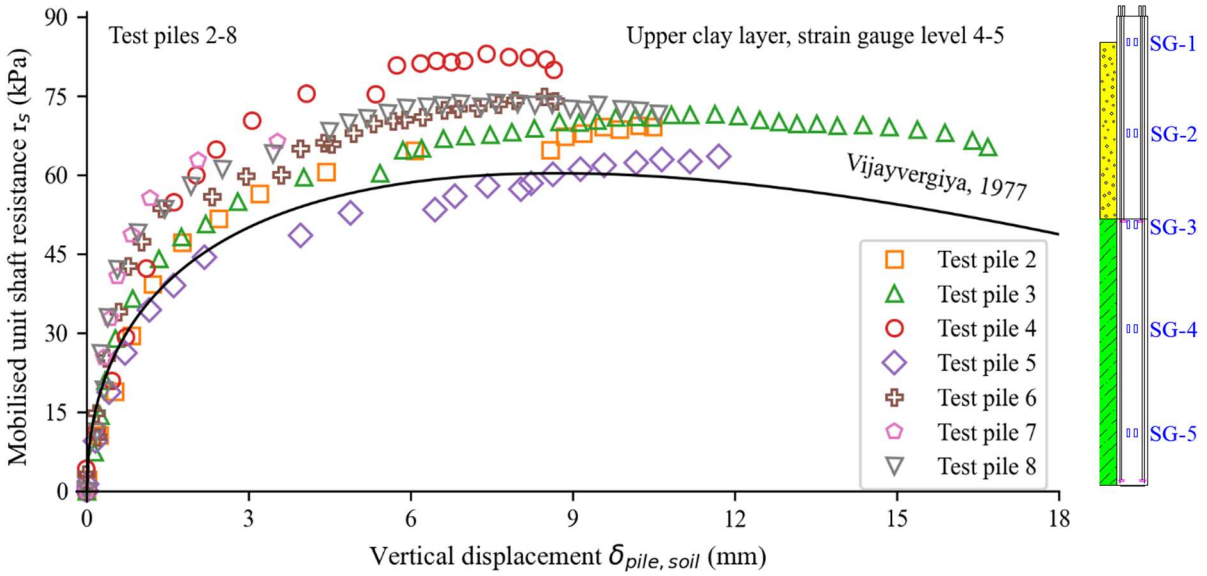

Figure 173: Predicted load transfer functions cf. Vijayvergiya (1977) and unit shaft resistance obtained from the static pile loading tests conducted on test piles 2-8 in the lower clay layer (strain gauge level 4-5) at the Hinge test site.

The predicted load transfer functions demonstrate a satisfactory representation of the measured unit shaft resistance, r_s, obtained from the static pile loading tests conducted on test piles 2-8 in the upper clay layer. However, the accuracy is slightly reduced in the lower clay layer. This discrepancy can be attributed to the empirical adhesion factor, α, derived from the best-fit envelope for fine-grained soils in general, which underestimates the ultimate unit shaft resistance, r_{peak}, determined from the static pile loading tests. It is important to note that this discrepancy is not due to an inaccurate determination of the displacement, δ_{peak}, corresponding to the ultimate unit shaft resistance, r_{peak}.

Nevertheless, the predicted load transfer functions do effectively represent the lower 50% of the measured unit shaft resistance, which is the pertinent range commonly utilized in practical everyday geotechnical engineering.

Accuracy of the predicted load transfer functions

The load transfer functions predicted above, utilizing the Vijayvergiya function, have the capability to predict the mobilised unit shaft resistance within a satisfactory ±30% margin up to the peak value, as illustrated in Figure 174.

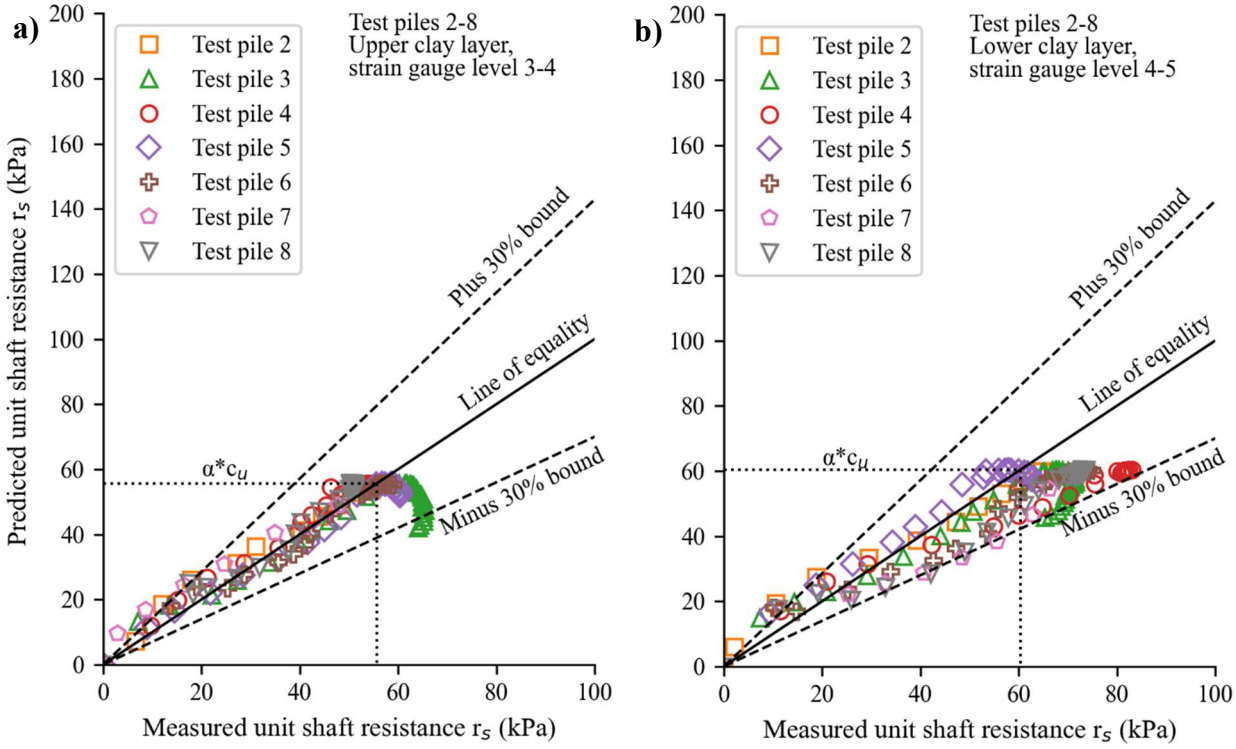

Figure 174:Measured vs. predicted values of unit shaft resistance for (a) the upper clay layer (strain gauge level 3-4) and (b) the lower clay layer (strain gauge level 4-5).

It is important to note that the predicted load transfer functions have only been applied to a limited number of test piles in the Søvind Marl at the Hinge test site. The undrained shear strength, c_u, is assumed to be equal to the field vane strength, c_{fv}, with values of 174 in the middle of the upper clay layer (4.5 m below ground level) and 208 kPa in the middle of the lower clay layer (6.5 m below

ground level). Therefore, further validation of these load transfer functions is required by testing multiple piles in various types of fine-grained soils, considering different undrained shear strengths, c_u. This validation process will help ensure the reliability and applicability of the predicted load transfer functions in a broader range of scenarios.

9.4.2 Vardanega and Bolton shear strength mobilisation function

The Vardanega and Bolton shear strength mobilisation function (Vardanega and Bolton, 2011b), as outlined in equation (35) in section 2.5.3, proposes that shear strength mobilisation in fine-grained soils can be represented by a power law relationship within the moderate strain range. This function normalizes the strain axis using the shear strain required for half mobilisation:

$$\frac{\tau_{mob}}{c_u} = 0.5 \cdot \left(\frac{\gamma}{\gamma_{M=2}}\right)^B \tag{88}$$

Here c_u is the undrained shear strength, τ_{mob} is the mobilised shear strength, γ is the shear strain, $\gamma_{M=2}$ is the reference strain to half the mobilisation and B is a function coefficient.

For London clay, the function coefficient, B, was determined as 0.58 based on a database of triaxial test (Vardanega and Bolton, 2011c). However, this does not conform with Søvind Marl, where the function coefficient, B, is estimated to 0.22 based on the 8 isotropic consolidated triaxial undrained compression (CIU) tests performed on TSH.B1, TSH.B2 and TSH.B3, see Appendix B.8.

The shear strain to half mobilisation, $\gamma_{M=2}$, is found to be 0.6% in average assuming the shear strain is equal to $\gamma = 1.5 \cdot \varepsilon$ (Vardanega and Bolton, 2011b), where ε is the axial strain. The shear phase of the isotropic consolidated triaxial undrained compression (CIU) tests show a strain-hardening behaviour and failure is defined at 10% additional axial strain (15% shear strain) and thus:

$$1 = 0.5 \cdot \left(\frac{0.15}{0.006}\right)^B \leftrightarrow B = \frac{log_{10}(1/0.5)}{log_{10}(0.15/0.006)} = 0.22 \tag{89}$$

Conversion from shear strain to vertical displacements between pile and soil

As the Vardanega and Bolton shear strength mobilisation function focuses on shear strain rather than displacements between the pile and soil, the Randolph and Wroth method, described in section 2.5.2, is employed to determine the mobilised shear strength, τ_{mob}, as a function of displacements. This process begins by isolating the shear strain in equation (88):

$$\gamma = \gamma_{M=2} \cdot \left(\frac{1}{0.5}\right)^{1/0.22} \cdot \left(\frac{\tau_{mob}}{c_u}\right)^{1/0.22} \tag{90}$$

Randolph's equation of vertical equilibrium at any given radius (Fleming et al., 2009) gives:

$$\tau = \left(\frac{\tau_0 \cdot r_0}{r}\right) \tag{91}$$

Here τ is the mobilised shear strength at a distance, r, from the pile centre and τ_0 is the mobilised shear strength at a distance, r_0 $(D_p/2)$, from the pile centre. Hence:

$$\gamma = \gamma_{M=2} \cdot \left(\frac{1}{0.5}\right)^{1/0.22} \cdot \left(\frac{\tau_0 \cdot r_0}{r \cdot c_u}\right)^{1/0.22} \tag{92}$$

The shear strain, γ, in the soil annuli is approximated by $\gamma = ds/dr$:

$$\int_{s_s}^{0} ds = \int_{r_0}^{r_m} \gamma \, dr \tag{93}$$

$$s_s = \gamma_{M=2} \cdot \left(\frac{1}{0.5}\right)^{1/0.22} \cdot \left(\frac{\tau_0 \cdot r_0}{c_u}\right)^{1/0.22} \cdot \int_{r_0}^{r_m} \mathrm{r}^{-1/0.22} \, dr \tag{94}$$

Here s_s is the settlement of the soil at the pile shaft, r_0 is the distance from pile centre to pile shaft $(D_p/2)$ and r_m is the maximum distance from the pile centre beyond which settlements are negligible.

The mobilised shear strength, τ_0, at the pile shaft $(r_0 = D_p/2)$ is isolated in equation (94):

$$\tau_0 = \frac{0.5 \cdot {s_s}^{0.22} \cdot c_u}{{\gamma_{M=2}}^{0.22} \cdot r_0 \cdot \left(\int_{r_0}^{r_m} \mathrm{r}^{-1/0.22} \, dr\right)^{0.22}} \tag{95}$$

If the maximum distance, r_m, from the pile centre beyond which settlements are negligible is assumed equal to the pile length, L_p, (Knappett and Craig, 2012) then the definite integral can be solved:

$$\int_{r_0}^{r_m} \mathrm{r}^{-1/0.22} \, dr = -0.28 \cdot {r_m}^{-1/0.28} + 0.28 \cdot {r_0}^{-1/0.28} = 18.35 \tag{96}$$

Undrained shear strength

In the Vardanega and Bolton shear strength mobilisation function, the undrained shear strength, c_u, is substituted with the ultimate unit shaft resistance, r_{peak} to ascertain the response corresponding to static pile loading tests. The determination of the ultimate unit shaft resistance, r_{peak}, follows the α method as described in section 2.2.1. This method assumes that the undrained shear strength, c_u, is equal to the field vane strength, c_{fv}, at the middle of the considered soil layer, as defined in equation (56) in section 3.10 (where $c_{fv} = 96.7 + 17.1 \cdot z_d$). The empirical adhesion factor, α, is determined based on the best-fit envelope given in equation (81) in section 8.4.3, representing fine-grained soils

in general ($\alpha = 6.65 * {c_u}^{-0.59}$). A similar approach is used for high plasticity clay, utilizing the best-fit envelope provided by equation (84) in section 8.4.3 ($= 9.88 * {c_u}^{-0.67}$).
The undrained shear strength, c_u, for the upper clay layer (strain gauge level 3-4) is determined as the field vane strength, $c_{fv} = 174$ kPa, at the middle of the layer (4.5 m below ground level). Similarly, the undrained shear strength, c_u, for the lower clay layer (strain gauge level 4-5) is obtained from the field vane strength, $c_{fv} = 208$ kPa, at the middle of the layer (6.5 m below ground level).

The empirical adhesion factor, α, is calculated as $\alpha = 0.32$ for the upper clay layer (strain gauge level 3-4) and $\alpha = 0.29$ for the lower clay layer (strain gauge level 4-5).

Predicted load transfer functions

The load transfer functions predicted using the Vardanega and Bolton shear strength mobilisation function are presented in relation to the measured unit shaft resistance, r_s, obtained from the static pile loading tests conducted on test piles 2-8 in both the upper and lower clay layers at the Hinge test site. These predicted load transfer functions are depicted in Figure 175 and Figure 176.

The Vardanega and Bolton shear strength mobilisation function does not predict the load transfer function well, which might be caused by the fact, that a power law function is not ideal for modelling measured load transfer functions presenting a hyperbolic shape.

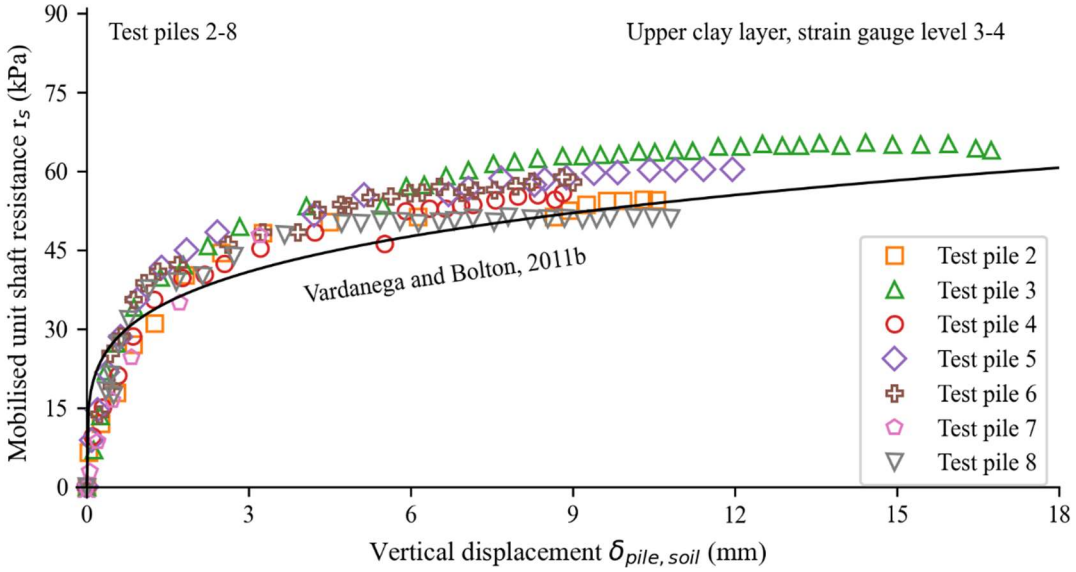

Figure 175: Predicted load transfer functions cf. Vardanega and Bolton (2011b) and unit shaft resistance obtained from the static pile loading tests conducted on test piles 2-8 in the upper clay layer (strain gauge level 3-4) at the Hinge test site.

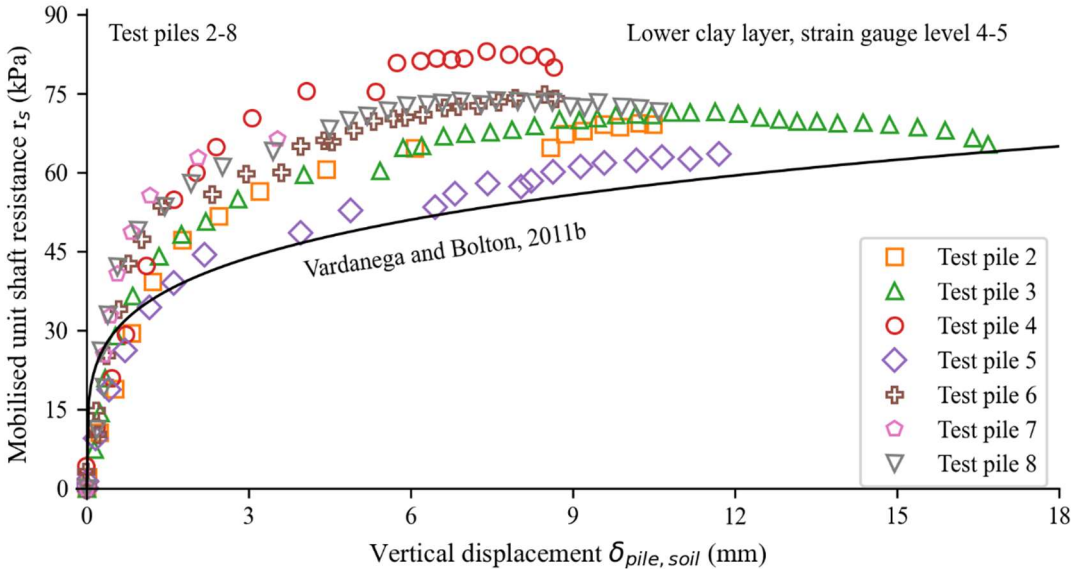

Figure 176: Predicted load transfer functions cf. Vardanega and Bolton (2011b) and unit shaft resistance obtained from the static pile loading tests conducted on test piles 2-8 in the lower clay layer (strain gauge level 4-5) at the Hinge test site.

Accuracy of the predicted load transfer functions

Figure 177 illustrates the comparison between the measured values of mobilised unit shaft resistance and the corresponding predicted values for both the upper clay layers (strain gauge levels 3-4) and the lower clay layers (strain gauge levels 4-5), respectively.

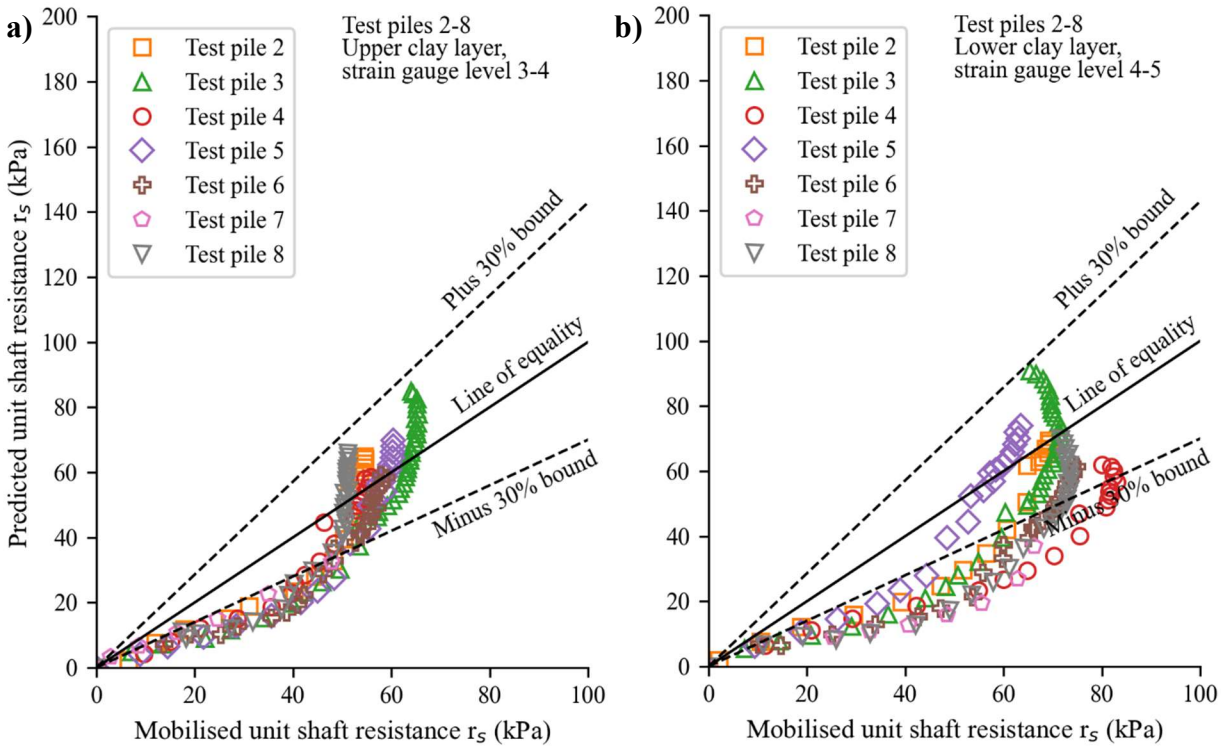

Figure 177: Measured vs. predicted values of unit shaft resistance for (a) the upper clay layer (strain gauge level 3-4) and (b) the lower clay layer (strain gauge level 4-5).

The predicted load transfer functions do not adequately represent the measured unit shaft resistance, r_s, obtained from the static pile loading tests conducted on test piles 2-8 in either of the clay layers. The majority of the values lie outside the ±30% bounds, indicating poor agreement between the predicted and measured values. Therefore, based on this analysis, the method is not recommended for predicting load transfer curves based on soil parameters.

10 Conclusion and future works

This section provide a summary of the key findings from the PhD-project titled "Soil-pile interaction for bored cast-in-situ piles in stiff clays". The objective of this project is to enhance the understanding of the intricate soil-pile interaction that takes place along the length of bored piles (specifically the shaft resistance) in various stages, including installation, setup, pile loading tests, and post-testing of bored piles in stiff clays. Additionally, the section offers recommendations for future research on the complex soil-pile interaction along the length of bored piles (shaft resistance).

10.1 Distributed fibre optic sensing systems

Rayleigh-based fibre optic distributed line sensors were strategically embedded in the bored test piles to enhance the accuracy and reliability of the measurements. While the vibrating wire strain gauges (VWSG) offer selected point measurement, the fibre optic cables (FOC) provide more comprehensive and detailed measurements along the entire length of the test piles.

The temperature measurements obtained from the fibre optic temperature cables (FOTC) show a correlation between increasing load and rising temperatures, as well as decreasing load and falling temperatures. This relationship indicates that the temperature measurements are influenced by mechanical strain in the test piles. Therefore, the temperatures measured by the FOTC are deemed invalid and unsuitable for accurately correcting the strain data measured by the fibre optic strain cables (FOSC).

Consequently, the temperature data obtained from the VWSG is used instead to determine the mechanical strains, accounting for thermal influence, from the raw strain data measured by the FOSC. This is achieved by employing linear interpolation between different strain gauge levels. However, it is important to acknowledge that linear interpolation is an estimation, and determining the precise level of zero thermal induced strain between the strain gauge levels can be challenging.

The strain measurements of opposing strain sensors from FOSC are compared with VWSG by utilizing the internal strain profile of the test piles obtained during the static pile loading tests. The measured strains are then interpreted and adjusted for thermal effects, as outlined above. It is observed that two strain sensors from either the VWSG pairs or the FOSC, installed in diametrically opposite sides, effectively differentiate between bending moments and axial loads while providing a reliable average value. Consequently, the installation of four strain sensors (two pairs of opposing strain sensors) does not seem to significantly enhance the determination of a reliable average value.

Nevertheless, it is recommended to install four strain sensors (two pairs of opposing strain sensors) as a precautionary measure, considering the possibility of the VWSG or the FOSC breaking, which would render the data from a single sensor unusable. The additional cost of incorporating extra sensors is minimal compared to the expenses associated with conducting additional tests.

The utilization of the FOSC, in comparison to the VWSG, has the potential to offer more comprehensive and detailed information regarding the strain distribution along the length of the test piles like e.g. non-uniform pile stiffness.

In the case of bored piles, the presence of non-uniform pile stiffness is often attributed to variations in the amount of reinforcement steel along the length of the piles. For test pile 1, 5, and 8, there is a significant increase in strain observed at the base of the GEWI PLUS bars, indicating a lower pile stiffness in the lower part of the test piles as expected due to the reduction in reinforcement.

However, due to the overall scatter present in the FOSC measurements, it is challenging to accurately identify non-uniform pile stiffness in relation to sister bars for the VWSG, stiffening rings, and space bars on the reinforcement.

Moreover, the application of FOSC presents an opportunity to obtain continuous strain profiles, enabling a more accurate assessment of axial pile stiffness, load distribution, and unit shaft resistance along the entire length of bored piles. Unfortunately, the uncertainty resulting from multiple NaN values, considerable scatter, possible local concrete cracks, variations in cross-sectional area, and pile stiffness is too significant to utilize the FOSC for anything beyond confirming the trend observed from the VWSG.

Thus, Rayleigh based FOSC can provide continuous strain profiling that enables identification of local defects that can affect the pile capacity by quantifying local strain variations with great accuracy, but also at the same time can lead to erroneous interpretation of strain data in terms of soil-pile interface behaviour, if not fully understood.

10.2 Residual stresses

In the literature review (refer to section 2.1.2), three methods, namely Method 1: Simplified method, Method 2: Pennington (1995), and Method 3: Siegel and McGillivray (2009), were identified to interpret residual stresses in bored piles. These methods rely on data from vibrating wire strain gauges (VWSG) measured during the casting of the bored pile until the initiation of the pile loading test.

Previous investigations by Flynn et al. (2012) and Flynn and McCabe (2022b) focused on driven cast-in-situ piles in mixed ground conditions, and they found that the method proposed by Siegel and McGillivray (2009) produced the most realistic results in terms of derived residual loads. However, a comparative analysis of the three interpretation methods for bored piles could not be found in the existing literature.

To enhance understanding and improve the interpretation of residual stresses in bored piles, all three methods were applied to test piles 4 and 8 at the Hinge test site. Unfortunately, these methods were found to be inadequate for rectifying residual stresses in the test piles. The primary challenge stems from accurately quantifying and distinguishing internal pile strains resulting from concrete setting

and curing, from mechanical strains generated by external forces acting on the pile shaft (such as down drag).

This study introduced a new method for analysing field test results concerning residual stresses, which focuses on documenting residual stresses based on post pile loading test data. Unlike the methods found in the literature review that rely on data measurements from the casting of the bored pile until the initiation of the pile loading test, this new method does not require supplementary, long-term measurements.

In this new method, the remaining unit shaft resistance is evaluated after unloading the test piles. It assumes that the shaft resistance is fully mobilised along the length of the test piles during the failure stage of the pile loading test and considers the pile to be "stress-free" after unloading. It is important to note that this assumption may not be entirely accurate, as residual forces may still exist after unloading due to differences in elastic pile strains and soil stiffnesses along the pile length.

Most likely the distribution of residual stresses after unloading is governed by the small downward pile movement relative to the soil from the elastic rebound of the pile after the static pile loading test in tension. This induce negative unit shaft resistance along the upper length of the pile that is resisted by positive unit shaft resistance along the lower length of the pile. At the test site in Hinge, the elastic rebound is determined cf. section 5.6 to be between 0.3 and 0.4 mm for test piles 1-8. By analysing the mobilised unit shaft resistance curves provided in section 6.3.4, it becomes evident that the maximum error, when assuming a stress-free state after unloading, remains below 10 kPa for all soil layers. This minor error is considered to be a representation of the uncertainties associated with the utilization of the new method.

For simplicity, a linear elastic behaviour during pile unloading after failure, with a shear stiffness equivalent to the initial linear elastic shear stiffness of the observed load transfer curve, is assumed. While this assumption is an approximation, it has been found to be reasonably accurate (refer to section 6.2.7).

Residual stresses play a crucial role, despite the challenges in demonstrating their influence on pile loading test data, particularly for bored piles. Quantifying the effects of these residual stresses is even more difficult. These residual stresses can result in fully mobilised negative or positive unit shaft resistance, leading the observed load transfer curve to either depict the ultimate unit shaft resistance twice or create an impression that there is no mobilised unit shaft resistance along the pile length.

In the case of the Hinge test site, the determined residual stresses had accumulated between 73% positive and 27% negative of the "true" ultimate unit shaft resistance. As a result, the observed load transfer curves display ultimate mobilised unit shaft resistance values ranging from 27% to 127% of the ultimate mobilised unit shaft resistance derived from the "true" load transfer curves. Specifically,

in the upper sand layer, the values range from 27% to 80%, in the lower sand layer from 94% to 123%, in the upper clay layer from 76% to 119%, and in the lower clay layer from 71% to 117%.

At first, the residual loads, F_{res}, for test piles 2-8 appear to exhibit random variations. However, when compared to the residual loads determined from Method 1: Simplified method, Method 2: Pennington (1995), and Method 3: Siegel and McGillivray (2009) for test piles 4 and 8, it becomes evident that the residual loads determined by the new method are of similar magnitudes, despite variations along the length of the test piles. Refer to Figure 142 in section 8.1.5 for visual representation.

Test piles 2, 4, 5, and 6 exhibit a behaviour where positive induced residual stresses are observed along the upper length of the piles, while negative induced residual stresses are observed along the lower length of the piles. This behaviour can be attributed to down drag effects caused by the compression of loosely built sand in the top 3.4 m of the test piles due to rainwater seepage and/or the replacement of sand and base course with gravel in the upper 0.4 m before conducting pile loading tests. Refer to Figure 143 (a) in section 8.1.5 for visual representation.

On the other hand, test piles 3, 7, and 8 display a different pattern where positive induced residual stresses are observed along both the upper and lower length of the piles, with negative induced residual stresses in between. This behaviour could be attributed to internal strains within the piles resulting from concrete setting and curing, causing swelling in the sand layer at the upper section of the test pile and shrinkage in the low permeable, high plasticity Eocene clay (Søvind Marl) at the lower section. Refer to Figure 143 (b) in section 8.1.5 for visual representation.

It is important to note that these residual stresses do not affect the overall value of shaft resistance in the test piles (proof test). However, they are critical in determining the distribution of shaft resistance along the pile length, particularly when extrapolating the findings to longer or shorter piles or piles with different diameters.

10.3 Development of axial pile capacity with time

The impact of time on the pile capacity for bored piles was investigated using the empirical relationship presented by Skov and Denver (1988), which was originally developed for the second phase of set-up for driven piles (refer to section 2.4.2). The objective of this study was to examine whether the empirical relationship proposed by Skov and Denver (1988) can also be applied to characterize the development of bearing capacity for bored piles. This investigation was centred around test pile 2-8 from the Hinge test site, along with available data on bored piles installed in stiff, high plasticity clay obtained from the literature review on time effects in section 2.4.

The analysis focused on the second phase of set-up characterized by linear dissipation of excess porewater pressure, and the third phase known as ageing. The transition from phase two to phase three was expected to occur gradually and therefore, it is assumed that the same log-linear evolution of pile capacity can be applied during this transition.

Thus, the normalized log-linear relationship for the development of axial pile capacity with respect to time, Q_t, can be expressed as follows:

$$\frac{Q_t}{Q_0} = 1 + \mathrm{A}_t \cdot log_{10}\left(\frac{t}{t_0}\right) \tag{97}$$

Here, Q_t is the axial pile capacity at time t after installation, Q_0 is the axial pile capacity at time t_0, A_t is a rate coefficient depending on soil type and t_0 is an empirical initial time value.

The development of axial pile capacity over time was assessed for bored piles installed in stiff, high plasticity clay. This analysis incorporated the findings from test piles 1-8 at the Hinge test site, as well as bored piles in London clay (Whitaker and Cooke, 1966) and Danish Eocene clay at Fehmern (Morrison et al., 2012). Tension tests were conducted on the bored piles, demonstrating the increase in shaft resistance over time. A total of 15 data points were collected, with the bored piles being tested at various intervals after installation, ranging from 30 to 1044 days.

The axial pile capacity, Q_0, after one month (t_0=30 days) was specifically chosen for bored piles, as freshly cast concrete typically requires around one month to achieve the necessary strength prior to conducting pile loading tests. The axial pile capacity increases with approximately 11 % per log change in time ($\mathrm{A}_t = 0.11$), which is slightly lower than the axial pile capacity increase of 14 % per log change in time (t_0=30 days) determined by Augustesen et al. (2006) for driven piles in a wide range of fine-grained soils. However, the trend is weak with an R^2 value of 0.34.

In light of the weak trend observed in the previous analysis, the development of pile capacity with respect to time, Q_t, utilized by the empirical relationship introduced by Skov and Denver (1988) is not ideal to use combined over presumably the second and third phase of set-up of bored piles in high plasticity clay. Thus, additional data at various intervals after installation is required to improve the ability to predict the time evolution of pile capacity.

This also enables the determination of whether the observed decrease or cessation in the logarithmic rate of pile increase after the initial 100-200 days is a result of the transition from the second phase, characterized by linear dissipation of excess porewater pressure, to the third phase, known as ageing (refer to Figure 152 in section 8.3.3).

10.4 Determination of empirical adhesion coefficient using the field vane strength

The mobilised unit shaft resistance, r_s, is connected to the undrained shear strength, c_u, through the empirical adhesion coefficient, α, as discussed in section 2.2. The selection of a reference value for undrained shear strength, c_u, is often influenced by national geotechnical engineering traditions and personal experience in practical applications. However, this choice becomes particularly critical when dealing with fissured and slicken-sided structured clays, such as the Søvind Marl. In such cases, the undrained shear strength, c_u^{CIU}, obtained from isotropic consolidated undrained triaxial compression

(CIU) test, is significantly lower compared to other measurements like the intact field vane strength, c_{fv}, determined through Danish field vane tests. This divergence can be attributed to differences in failure mechanisms.

In general, the Danish field vane test (shown in Figure 154 (a) in section 8.4.1) induces failure along the vane's edge during rotation, representing the intact undrained shear strength, $c_{u,intact}$, if $c_{fv} = c_{u,intact}$ is assumed. On the other hand, an isotropic consolidated undrained triaxial compression (CIU) test on a soil mass exhibits a barrel-shaped failure mode (shown in Figure 154 (b) in section 8.4.1), representing the intact undrained shear strength , $c_{u,intact}$, if $c_u^{CIU} = c_{u,intact}$ is assumed.

However, in the case of the Søvind Marl, which is fissured and slicken-sided, an isotropic consolidated undrained triaxial compression (CIU) test will predominantly induce failure along a fissure (as shown in Figure 154 (c) in section 8.4.1). This failure mode represents a fissured undrained shear strength, $c_{u,fissured}$, if $c_u^{CIU} = c_{u,fissured}$ is assumed.

For bored piles, the capacity is primarily derived from shaft friction, with base resistance not significantly mobilised under working loads. Shaft failure occurs when shearing takes place across a substantial soil volume along the length of the bored piles and such large, interconnected fracture systems are unrealistic. Therefore, it is more favourable to consider the intact undrained shear strength, $c_{u,intact}$, rather than the fissured undrained shear strength, $c_{u,fissured}$, as the representative value for shaft failure.

Furthermore, the field vane test is relatively straightforward and cost-effective, making it a commonly employed practice in practical geotechnical engineering in Denmark. By using this widely accepted reference, a substantial amount of data can be accumulated in the near future, further advancing the knowledge of the α-c_u relationship. Thus, the empirical adhesion coefficient, α, is determined by using the field vane strength, c_{fv}, as a reference for the undrained shear strength, c_u.

For the Søvind Marl at the Hinge test site, the empirical adhesion coefficient, α_{cfv}, is computed based on data from test piles 2-8. In the upper clay layer (at strain gauge level 3-4), α_{cfv} ranges between 0.28 and 0.38, while in the lower clay layer (at strain gauge level 4-5), it varies between 0.31 and 0.40. Comparatively, the empirical adhesion coefficient, α_{cfv}, for the Søvind Marl is 2.3 to 3.3 times higher than the empirical adhesion coefficient ($\alpha = 0.12$) specified for bored piles in Denmark, as mentioned in section 2.2.2.

Furthermore, a best fit, lower bound, and upper bound envelope for the α-c_u relationship was established for both fine grained soils in general and specifically for high plasticity clay. To determine these envelopes for fine-grained soils and high plasticity clay, relevant databases from the literature were included, including those pertaining to fine-grained soils in general, as well as specific soils such as London clay and Danish Eocene clay. Considering the minor discrepancies arising from a

reduced number of data points, the best fit, lower bound, and upper bound envelope for the α-c_u relationship provided for fine-grained soils in general is preferred.

Equation (98) represents the best-fit envelope, while equations (99) and (100) correspond to the upper and lower bound envelopes of the α-c_u relationship for fine-grained soils in general.

Best fit:

$$\alpha_{intact} = 6.65 * {c_{u,intact}}^{-0.59} \quad (98)$$

Upper bound (95th percentile):

$$\alpha_{intact} = 8.12 * {c_{u,intact}}^{-0.56} \quad (99)$$

Lower bound (5th percentile):

$$\alpha_{intact} = 4.04 * {c_{u,intact}}^{-0.57} \quad (100)$$

Even the lower bound envelope exceeds the empirical adhesion coefficient $\alpha = 0.12$, as specified in the Danish National Annex to Eurocode 7, Annex L (DS/EN_1997-1_DK_NA, 2021). For instance, the lower limit envelope surpasses the empirical adhesion coefficient $\alpha = 0.12$ specified for bored piles in Denmark by 2.4 times when the undrained shear strength is 100 kPa. Similarly, it exceeds the empirical adhesion coefficient $\alpha = 0.12$ by 1.6 times for an undrained shear strength of 200 kPa. This Danish specification, described in section 2.2.2, pertains to an undrained shear strength c_u of 500 kPa or lower.

10.5 Hyperbolic non-linear loading models

In this study, two analytical models were formulated for bored piles in stiff clays, employing the load transfer method. The load transfer method is an iterative technique that solves a set of differential equations, which represents the pile behaviour using the finite-difference approach. To automate the process of solving these differential equations iteratively, Spyder IDE 5.4.3 (Python 3.8.10 64-bit | Qt 5.15.2 | PyQt5 5.15.9 | Windows 10) is utilized. The construction of the model is illustrated in Figure 160 in section 9.1.

In this study, two analytical models were developed: a hyperbolic non-linear loading model (HN model) and a hyperbolic non-linear loading model including residual stresses (HNr model). Both models exhibit an excellent fit to the measured data from the Hinge test site for axial forces, F, with accuracy values of 0.9958 and 0.9983, respectively. This high level of accuracy is expected as the models are based on back-calculated data. The slight difference in accuracy indicates that the HN model in section 9.2 is incapable of accurately predicting the ultimate values obtained during the constant rate of uplift portion of the static pile loading test for test piles 3, 6, and 8 at the Hinge test site.

Both hyperbolic non-linear loading models (HN model and HNr model) are capable of modelling the vertical displacements, $\delta_{pile,soil}$, between the pile and the soil. The ratio between the vertical displacement determined by the hyperbolic non-linear loading models, δ_{model}, and the corresponding measured data, $\delta_{measured}$, were determined along the length of test piles 2-8 for each applied load step on the virgin load curves and for the peak value from the constant rate of uplift portion of the pile loading test. The hyperbolic non-linear loading model (HN model) exhibits an average vertical displacement ratio between 0.44 and 1.73. Similarly, the hyperbolic non-linear loading model including residual stresses (HNr model) exhibits an average vertical displacement ratio between 0.20 and 1.56.

10.6 Prediction of load transfer curves

In everyday geotechnical engineering practice, it is valuable to have an initial estimation of load transfer curves based on limited information, which is often the case at the beginning of a new project. Typically, the available information includes the field vane strength, c_{fv}, obtained from the Danish field vane test. For predicting load transfer curves, the strain-softening load transfer function proposed by Vijayvergiya (1977) is utilized. This function was also used for back analysis of static pile loading test results in the upper and lower clay layers of the Søvind Marl at the Hinge test site. The load transfer function is presented below, specifically applicable to fine-grained soils

$$\frac{r_s}{r_{peak}} = 2 \cdot \sqrt{\frac{\delta_{pile,soil}}{\delta_{peak}}} - \frac{\delta_{pile,soil}}{\delta_{peak}} \tag{101}$$

Here, r_s is the mobilised unit shaft resistance, $\delta_{pile,soil}$ is the displacement paired with, r_{peak} is the ultimate unit shaft resistance, δ_{peak} is the displacement paired with r_{peak}.

The displacement, δ_{peak}, corresponding to the ultimate unit shaft resistance, r_{peak}, is anticipated to fall within the range of 5-10 mm (Vijayvergiya, 1977, Kulhawy, 1985). In cases where no previous knowledge of pile load tests under similar ground conditions and pile dimensions is available, it is recommended to utilize the mean value of the displacement, δ_{peak} within the provided range.

For the test piles installed in Søvind marl at the Hinge test site, the displacement, δ_{peak}, paired with ultimate unit shaft resistance $r_{s,peak}$ was determined to 8.7 mm, which aligns well with the recommendation provided above.

The determination of the ultimate unit shaft resistance, r_{peak}, follows the α method explained in section 2.2.1. It assumes that the undrained shear strength, c_u, is equivalent to the field vane strength, c_{fv}, at the middle of the considered soil layer, as described in equation (56) in section 3.10 (where $c_{fv} = 96.7 + 17.1 \cdot z_d$). The empirical adhesion factor, $\alpha_{c_{fv}}$, is obtained from the best-fit envelope

for the α-c_u relationship mentioned in equation (81) in section 8.4.3, representing fine-grained soils in general ($\alpha_{c_{fv}} = 6.65 * {c_{u,c_{fv}}}^{-0.59}$).

A similar approach is employed for high plasticity clay, using the best-fit envelope given by equation (84) in section 8.4.3 ($\alpha_{c_{fv}} = 9.88 * {c_{u,c_{fv}}}^{-0.67}$). However, considering the minor discrepancies arising from a reduced number of data points, the best-fit envelope provided for fine-grained soils in general is preferred.

The predicted load transfer functions based on the Vijayvergia function can predict the mobilised unit shaft resistance within a satisfactory ±30 % bound up till the peak value. It is important to note that the predicted load transfer functions have only been applied to a limited number of test piles in the Søvind Marl at the Hinge test site. The undrained shear strength, c_u, is assumed to be equal to the field vane strength, c_{fv}, with values of 174 in the middle of the upper clay layer (4.5 m below ground level) and 208 kPa in the middle of the lower clay layer (6.5 m below ground level). Therefore, further validation of these load transfer functions is required by testing multiple piles in various types of fine-grained soils, considering different undrained shear strengths, c_u. This validation process will help ensure the reliability and applicability of the predicted load transfer functions in a broader range of scenarios.

10.7 Future works

Below are some recommendations for future research on the intricate interaction between soil and bored piles along the length of the piles, specifically focusing on shaft resistance:

- Additional research is required to address the issue of mechanical strain influencing the measurements obtained from fibre optic temperature cables (FOTC) in test piles. Currently, the temperatures measured by the FOTC are considered invalid and unsuitable for accurately correcting strain data collected by the fibre optic strain cables (FOSC). It is crucial to investigate methods to utilize FOTC effectively. One potential approach is to conduct tests exploring techniques that can make the FOTC immune to mechanical strains. For instance, installing the FOTC within a small tube or protecting it with a flexible material might shield it from strain-related influences. These investigations will help develop a viable solution to ensure the accuracy and reliability of strain data obtained from FOTC, thus improving the overall assessment of the pile's performance.
- To improve the estimation of the fitted power laws for the best fit, upper bound, and lower bound envelopes for the α-c_u relationship, there is a need for additional high-quality test data obtained from pile loading tests conducted in fine-grained soils. This data should focus on determining the empirical adhesion factor, α, especially for high values of undrained shear strength, c_u, exceeding 500kPa. Currently, there are limited data points available for this specific range, and obtaining more data in this category would greatly enhance the accuracy of the estimations.

- An area of research worth pursuing is the further development of the hyperbolic non-linear loading models discussed in sections 9.2 and 9.3. These models should be enhanced to incorporate static pile loading tests in compression, as well as the subsequent reloading curves back to tension meaning that models should be modified as t-z models that can predict the effect of load reversals on the stiffness response (i.e. using a tangent stiffness method rather than a secant stiffness). By doing so, the models would have the ability to accurately capture and simulate large residual compressive loads.
- To validate and compare the hyperbolic non-linear loading models presented in sections 9.2 and 9.3, it would be beneficial to conduct numerical finite element calculations using Plaxis software. Specifically, a 2D axi-symmetric analysis can be performed to simulate the behaviour and response of the soil-pile system. By comparing the numerical results with the predictions of the non-linear loading models, a comprehensive evaluation of their accuracy and applicability can be established.
- An avenue for further development is the transformation of the hyperbolic non-linear loading models into commercially available software. By creating dedicated software that incorporates these models, users will have the convenience of an accessible and user-friendly tool for analysing and simulating pile loading scenarios. This would enable engineers and researchers to easily apply the hyperbolic non-linear loading models in their design and analysis processes, enhancing the practicality and widespread adoption of these models.
- For a more comprehensive validation, it is recommended to conduct additional pile loading tests in various types of fine-grained soils. The objective would be to verify the accuracy and reliability of the method presented in section 9.4 for predicting load transfer functions. Alternatively, the obtained test data can be compared with existing data from the literature, providing further validation and strengthening the credibility of the load transfer function predictions.
- To enhance the confirmation of pile capacity, it is recommended to conduct additional tests using a flat jack applied at the pile base. By conducting this test, the pile's shaft resistance can be verified using a different pile loading test method. Furthermore, the distribution of displacements and forces along the shaft of bored piles can be determined and compared to the distribution of displacements and forces along the shaft of bored piles from the static pile loading test conducted in tension. Furthermore, this test should include post-construction stressing to engage the base resistance of the pile. The purpose is to limit settlement or compact loose/remoulded material at the pile base.

Bibliography

AKAI, K. 1960. De strukturellen eigenschaften von schluft mitteilugen. *Die Technische Hochschule Aachen*.

ALBERDI-PAGOLA, M. 2018. *Design and performance of energy pile foundations.* PhD thesis, Aalborg University.

ASTM_D3689/D3689M 2013. Standard Test Methods for Deep Foundations Under Static Axial Tensile Loas.

AUGUSTESEN, A., ANDERSEN, L. & SØRENSEN, C. S. 2006. Assessment of time functions for piles driven in clay.

AXELSON, G. 2002. A Conceptual Model of Pile Set-Up for Driven Piles in Non-Cohesive Soil. *Deep Foundations 2002.*

BACH, D. & VAN GELDER, P. 2014. Incorporating set-up into LRFD method for drilled shafts. *Georisk: Assessment and Management of Risk for Engineered Systems and Geohazards,* 8**,** 81-91.

BALSTRUP, T. 1972. Farum. Motorvejsbro. Borede pæles bæreevne i moræneler. Geoteknisk Institut.

BECKER, D., CROOKS, J., BEEN, K. & JEFFERIES, M. 1987. Work as a criterion for determining in situ and yield stresses in clays. *Canadian Geotechnical Journal,* 24**,** 549-564.

BENNICK, K. G. 1975. Borede pæles bæreevne i moræneler. *Nordisk Geoteknikermøde.* København: Polyteknisk forlag.

BERSAN, S., BERGAMO, O., PALMIERI, L., SCHENATO, L. & SIMONINI, P. 2018. Distributed strain measurements in a CFA pile using high spatial resolution fibre optic sensors. *Engineering structures,* 160**,** 554-565.

BISHOP, A. W., GREEN, G. E., GARGA, V. K., ANDRESEN, A. & BROWN, J. D. 1971. A New Ring Shear Apparatus and Its Application to the Measurement of Residual Strength. *Géotechnique,* 21**,** 273-328.

BISHOP, A. W., WEBB, D. L. & LEWIN, P. I. 1965. Undisturbed Samples of London Clay from the Ashford Common Shaft: Strength–Effective Stress Relationships. *Géotechnique,* 15**,** 1-31.

BULLOCK, P. J., SCHMERTMANN, J. H., MCVAY, M. C. & TOWNSEND, F. C. 2005a. Side Shear Setup. I: Test Piles Driven in Florida. *Journal of geotechnical and geoenvironmental engineering,* 131**,** 292-300.

BULLOCK, P. J., SCHMERTMANN, J. H., MCVAY, M. C. & TOWNSEND, F. C. 2005b. Side Shear Setup. II: Results From Florida Test Piles. *Journal of geotechnical and geoenvironmental engineering,* 131**,** 301-310.

BURLAND, J. 1990. On the compressibility and shear strength of natural clays. *Géotechnique,* 40**,** 329-378.

BURLAND, J. & TWINE, D. The shaft friction of bored piles in terms of effective strength. Proceeding of 1st international conference on Deep Foundations on Bored and Augered Piles, 1988 Balkema, Rotterdam. 411-420.

BURLAND, J. B. 1973. Shaft friction of piles in clay - A simple fundamental approach. *Ground Engineering,* 6**,** 30-42.

BUSTAMANTE, M. & GIANESELLI, L. Pile bearing capacity prediction by means of static penetrometer CPT. Proceedings of the 2nd European symposium on penetration testing, 1982. Balkema, Amsterdam, the Netherlands, 493-500.

CAMP, W. M. & PARMAR, H. S. 1999. Characterization of Pile Capacity with Time in the Cooper Marl: Study of Applicability of a Past Approach To Predict Long-Term Pile Capacity. *Transportation research record,* 1663**,** 16-24.

CASAGRANDE, A. 1932. Research on the Atterberg Limits of soils. Public Roads.

CASAGRANDE, A. The determination of the pre-consolidation load and its practical significance. Procedings of the First International Conference on Soil Mechanics and Foundation Engineering, 1936 Cambridge. 60-64.

CHEN, Y.-J. & KULHAWY, F. H. 1993. Undrained strength interrelationships among CIUC, UU, and UC tests. *Journal of Geotechnical Engineering,* 119**,** 1732-1750.

CHEN, Y.-J., LIN, S.-S., CHANG, H.-W. & MARCOS, M. C. 2011. Evaluation of side resistance capacity for drilled shafts. *Journal of marine science and technology,* 19.

CHEN, Y. & KULHAWY, F. 1994. Case history evaluation of the behavior of drilled shafts under axial and lateral loading.: Electric Power Research Inst., Palo Alto, CA (United States); Cornell Univ., Ithaca, NY (United States). Geotechnical Engineering Group.

CHENG, S., ZHANG, Q.-Q., LI, S.-C., LI, L.-P., ZHANG, S.-M. & WANG, K. 2018. Nonlinear analysis of the response of a single pile subjected to tension load using a hyperbolic model. *European Journal of Environmental and Civil Engineering,* 22**,** 181-191.

CHRISTENSEN, N. H. & HANSEN, B. 1959. *Shear strength properties of skive septarian clay*.

CIRIA_REPORT_PG7 1980. Pile load testing procedures. *In:* WELTMAN, A. J. (ed.).

CLAUSEN, C. J. F. & AAS, P. M. 2000. Bearing capacity of driven piles in clays. *NGI-report.* Norwegian Geotechnical Institute.

CLAYTON, C. R. I. & MILITITSKY, J. 1983. Installation effects and the performance of bored piles in stiff clay. *Ground Engineering,* 16**,** 17-22.

COWI 2023. Unpublished COWI case files from Aarhus Harbour.

COYLE, H. M. & REESE, L. C. 1966. Load transfer for axially loaded piles in clay. *Journal of the soil mechanics and foundations division,* 92**,** 1-26.

CUI, C.-Y., WANG, S.-J., LIU, Q. & ZHANG, Y.-L. 2020. An approach for response prediction of a single pile subjected to tension load considering modulus degradation of soil. *Geotechnical and Geological Engineering,* 38**,** 1195-1203.

CULSHAW, B. & KERSEY, A. 2008. Fiber-optic sensing: A historical perspective. *Journal of Lightwave Technology,* 26**,** 1064-1078.

D'ONOFRIO, A., SILVESTRI, F. & VINALE, F. 1999. Strain rate dependent behaviour of a natural stiff clay. *Soils and Foundations,* 39**,** 69-82.

DARENDELI, M. B. 2001. *Development of a new family of normalized modulus reduction and material damping curves.* PhD PhD Thesis, The university of Texas at Austin.

DE BATTISTA, N., KECHAVARZI, C., SEO, H., SOGA, K. & PENNINGTON, S. 2016b. Distributed fibre optic sensors for measuring strain and temperature of cast-in-situ concrete test piles. *International Conference on Smart Infrastructure and Construction.* Cambridge, United Kingdom: ICE Publishing.

DE BATTISTA, N., KECHAVARZI, C. & SOGA, K. Distributed fiber optic sensors for monitoring reinforced concrete piles using Brillouin scattering. 2016a. SPIE, 99160U-99160U-4.

DS/EN_1991-1-5 2007. Eurocode 1: Actions on structures - Part 1-5: General actions - Thermal actions. Danish Standard.

DS/EN_1991-1-5_DK_NA 2012. National Annex to Eurocode 1: Actions on structures - Part 1-5: General actions - Thermal actions. Danish Standard.

DS/EN_1997-1 2007. Eurocode 7: Geotechnical design - Part 1: General rules. Danish Standard.

DS/EN_1997-1_DK_NA 2021. National Annex to Eurocode 7: Geotechnical design - Part 1: General rules. Danish Standard.

DS/EN_14199 2015. Execution of special geotechnical works - Micropiles. Danish Standard.

DS/EN_ISO_17892-9 2018. Geotechnical investigation and testing – Laboratory testing of soil – Part 9: Consolidated triaxial compression tests on water saturated soils. Danish Standard.

DS/EN_ISO_22477-1 2018. Geotechnical investigation and testing – Testing of geotechnical structures – Part 1: Testing of piles: static compression load testing. Danish Standard.

FELLENIUS, B. 2023. *Basics of foundation design*, www.Fellenius.net.

FELLENIUS, B. H. 1989. Tangent modulus of piles determined from strain data. *In:* KULHAWY, F. H. (ed.) *The American Society of Civil Engineers, ASCE, Geotechnical Engineering Division, 1989 Foundation Congress.*

FELLENIUS, B. H. 2002a. Determining the True Distributions of Load in Instrumented Piles. *International Deep Foundation Congress* Orlando, Florida: ASCE.

FELLENIUS, B. H. 2002b. Determining the Resistance Distribution in Piles. Part 1: Notes on Shift of No-Load Reading and Residual Load. *Geotechnical News Magazine,* 20**,** 35-38.

FELLENIUS, B. H. 2002c. Determining the Resistance Distribution in Piles. Part 2: Method for Determining the Residual Load. *Geotechnical News Magazine,* 20**,** 25-29.

FELLENIUS, B. H. 2015. Static tests on instrumented piles affected by residual load. *DFI Journal - The Journal of the Deep Foundations Institute,* 9**,** 11-20.

FELLENIUS, B. H. & RAHMAN, M. M. 2019. Load-movment responce by t-z and q-z functions. *Geotechnical Engineering Journal of the SEAGS & AGSSEA,* 50**,** 11-19.

FLEMING, W. 1992. A new method for signle pile settlement prediction and analysis. *Geotechnique,* 42**,** 411-425.

FLEMING, W. G. K., WELTMAN, A. J., RANDOLPH, M. F. & ELSON, W. K. 2009. *Piling Engineering,* New York, USA, Wiley.

FLYNN, K., MCCABE, B. & EGAN, D. 2012. Residual load development in cast in place piles - a review and a new case history. *9th International Conference on Testing and Design Methods for Deep Foundations.* Kanazawa, Japan.

FLYNN, K. N. & MCCABE, B. A. 2022a. Instrumented concrete pile tests – part 1: a review of instrumentation and procedures. *Proceedings of the Institution of Civil Engineers - Geotechnical Engineering,* 175**,** 86-111.

FLYNN, K. N. & MCCABE, B. A. 2022b. Instrumented concrete pile tests – part 2: strain interpretation. *Proceedings of the Institution of Civil Engineers - Geotechnical Engineering,* 175**,** 112-135.

FOCHT, J. A. & VIJAYVERGIYA, V. N. A New Way to Predict Capacity of Piles in Clay. Offshore Technology Conference, 1972 Houston, Texas.

GALSGAARD, J., FREDERICIA, J., FREDERIKSEN, J., JAKOBSEN, L., OKKELS, N., STOCKMARR, P. & SØRENSEN, J. 2021. *A guide to engineering geological soil description*, Danish Geotechnical Society.

GASPARRE, A., NISHIMURA, S., COOP, M. R. & JARDINE, R. J. 2007. The influence of structure on the behaviour of London Clay. *Géotechnique,* 57**,** 19-31.

GEO 2021. Notat | National Test Site Hinge - Geoteknisk felt arbejde. *In:* SIMONSEN, T. R. (ed.).

GILLIBRAND, C. 2020. *Influence of structure on high plasticity eocene clay.* Master, Aarhus University.

GOH, A. T., KULHAWY, F. H. & CHUA, C. 2005. Bayesian neural network analysis of undrained side resistance of drilled shafts. *Journal of Geotechnical and Geoenvironmental Engineering,* 131**,** 84-93.

GRØNBECH, G. L. 2015. *Søvind Marl - Behaviour of a plastic fissured Eucene clay.* PhD PhD thesis, Aalborg University.

GRØNBECH, G. L., NIELSEN, B. N. & IBSEN, L. B. Comparison of liquid limit of highly plastic clay by means of Casagrande and Fall Cone Apparatus. 14th Pan-American Conference on Soil Mechanics and Geotechnical Engineering (PCSMGE), the 64th Canadian Geotechnical Conference (CGC) and the 5th Pan-American Conference on Teaching and Learning of Geotechnical Engineering (PCTLGE), 2011 Toronto, Canada.

GRØNBECH, G. L., NIELSEN, B. N., IBSEN, L. B. & STOCKMARR, P. 2015. Geotechnical properties of Søvind Marl—a plastic Eocene clay. *Canadian Geotechnical Journal,* 52**,** 469-478.

GWIZDALA, K. & JACOBSEN, M. 1992. *Bearing capacity and settlements of piles*.

HANNA, T. H. & TAN, R. H. S. 1973. The Behavior of Long Piles Under Compressive Loads in Sand. *Canadian Geotechnical Journal,* 10**,** 311-340.

HANSEN, J. B. 1963. Discussion of "Hyperbolic Stress-Strain Response: Cohesive Soils". *Journal of the Soil Mechanics and Foundations Division,* 89**,** 241-242.

HAYES, J. & SIMMONDS, T. Interpreting strain measurements from load tests in bored piles. Proceedings of the Ninth International Conference on Piling and Deep Foundations, 2002.

HEILMANN-CLAUSEN, C. 2022. *RE: Lector emeritus, Geological Institute, Aarhus University. E-mail correspondance.*

HEILMANN-CLAUSEN, C., NIELSEN, O. B. & GERSNER, F. 1985. Lithostratigraphy and depositional environments in the Upper Paleocene and Eocene of Denmark. *Bulletin of the Geological Society of Denmark,* 33**,** 287-323.

HEILMANN-CLAUSEN, C. & RASMUSSEN, E. S. 2010. Danmarks geologiske udvikling fra 65 til 2,6 mio år før nu. *Geoviden.* Geocenter Danmark.

HIRANY, A. & KULHAWY, F. 1988. Conduct and interpretation of load tests on drilled shaft foundations:. Electric Power Research Inst., Palo Alto, CA (United States); Cornell Univ., Ithaca, NY (United States). Geotechnical Engineering Group.

HIRANY, A. & KULHAWY, F. H. Interpretation of load tests on drilled shafts—Part 1: Axial compression. *In:* KULHAWY, F. H., ed. Foundation engineering: Current principles and practices, 1989 New York. ASCE, 1132-1149.

HIRANY, A. & KULHAWY, F. H. On the interpretation of drilled foundation load test results. *In:* O'NEILL, M. W. & TOWNSEND, F. C., eds. Deep foundations 2002: An international perspective on theory, design, construction, and performance, 2002 Orlando, Florida, USA. 1018-1028.

HOLLOWAY, D. M., CLOUGH, G. W. & VESIC, A. S. The Effects Of Residual Driving Stresses On Pile Performance Under Axial Loads. 1978. Offshore Technology Conference.

HOLTZ, R. D. & KOVACS, W. D. 1981. *An introduction to geotechnical engineering,* Englewood Cliffs, New Jersey, Prentice-Hall, Inc.

HUNTER, A. H., DAVISSON, M. T., LUNDGREN, R. & D'APPOLONIA, E. 1969. Measurements of Pile Load Transfer. *Performance of Deep Foundations.* ASTM International.

ICE 2017. Specification for Piling and Embedded Retaining Walls.

JANBU, N., TOKHEIM, O. & SENNESET, K. 1981. Consolidation tests with continuous loading. *Proc 10th International Conference on Soil Mechanics and Foundation Engineering,* . Stockholm, Sweden.

KANIA, J. & SØRENSEN, K. K. A static pile load test on a bored pile instrumented with Distributed Fibre Optic Sensors. 10th International Symposium on Field Measurements in Geomechanics, Rio de Janeiro. In printing, 2018.

KANIA, J. G., SORENSEN, K. K. & FELLENIUS, B. H. 2020. Application of distributed fibre optic cables in piles. *Geotechnical Engineering,* 51**,** 94-102.

KARLSRUD, K., CLAUSEN, C. & AAS, P. Bearing capacity of driven piles in clay, the NGI approach. International symposium on frontiers in offshore geotechnics, 19-21 september 2005 2005 Perth, WA, Australia. 775-782.

KECHAVARZI, C., PELECANOS, L., DE BATTISTA, N. & SOGA, K. 2019. Distributed fibre optic sensing for monitoring reinforced concrete piles. *Geotechnical Engineering Journal of the SEAGS & AGSSEA,* 50**,** 43-51.

KECHAVARZI, C., SOGA, K. B., BATTISTA, N. D., PELECANOS, L., ELSHAFIE, M. Z. E. B. & MAIR, R. J. 2016. *Distributed Fibre Optic Strain Sensing for Monitoring Civil Infrastructure - A practical guide,* London, UK, ICE publishing.

KIM, M., CAVUSOGLU, E., O'NEILL, M., ROBERTS, T. & YIN, S. 2004. Residual load development in ACIP piles in a bridge foundation. *GeoSupport 2004.*

KIM, S., CHUNG, S. & FELLENIUS, B. H. 2011. Distribution of residual load and true shaft resistance for a driven instrumented test pile. *Canadian Geotechnical Journal,* 48**,** 583-598.

KLAR, A., BENNETT, P. J., SOGA, K., MAIR, R. J., TESTER, P., FERNIE, R., JOHN, H. D. S. & TORP-PETERSON, G. 2006. Distributed strain measurement for pile foundations. *Proceedings of the Institution of Civil Engineers - Geotechnical Engineering,* 159**,** 135-144.

KNAPPETT, J. & CRAIG, R. F. 2012. *Craig's soil mechanics. 8th edition*, Spon Press.

KNUDSEN, B. Undated. Beregning af borede pæles bæreevne. Geoteknisk Institut.

KNUDSEN, J., SØRENSEN, K. K., STEENFELT, J. S. & TRANKJÆR, H. 2019. Design of bored piles in Denmark - a historical perspective. *XVII European Conference on Soil Mechanics and Geotechnical Engineering.* Reykjavik.

KOLK, H. J. & DER VELDE, E. A Reliable Method to Determine Friction Capacity of Piles Driven into Clays. Offshore Technology Conference, 1996 Houston, Texas.

KOMURKA, V. E., WAGNER, A. B. & EDIL, T. B. 2003. A rewiew of pile set-up. *51st Annual Geotechnical Engineering Conference.* University of Minnesota, St. Paul, Minnesota.

KONDNER, R. L. 1963. Hyperbolic Stress-Strain Response: Cohesive Soils. *Journal of the Soil Mechanics and Foundations Division,* 89**,** 115-143.

KREGER, S. T., GIFFORD, D. K., FROGGATT, M. E., SOLLER, B. J. & WOLFE, M. S. High Resolution Distributed Strain or Temperature Measurements in Single-and Multi-mode Fiber Using Swept-Wavelength Interferometry. Optical Fiber Sensors, 2006/10/23 2006 Cancun. Optica Publishing Group, ThE42.

KROGSBØLL, A., HEDEDAL, O. & FOGED, N. Deformation properties of highly plastic fissured Palaeogene clay–Lack of stress memory. Nordic Geotechnical Meeting (NGM), 2012 Copenhagen, Denmark. 133-140.

KULHAWY, F. & CHEN, Y. 2003. Evaluation of undrained side and tip resistances for drilled shafts. *In:* CULLIGAN, P. J., EINSTEIN, H. H. & WHITTLE, A. J. (eds.) *Soil and Rock America 2003: 12th Panamerican Conference on Soil Mechanics and Geotechnical Engineering.* Cambridge, Massachusetts, USA.

KULHAWY, F. H. Drained uplift capacity of drilled shafts. 11th International Conference on Soil Mechanics and Foundation Engineering, 1985 Rotterdam, The Netherlands. 1549-1552.

KULHAWY, F. H. 2008. Discussion of "Reliability approach for the side resistance of piles by means of the total stress analysis (α Method)"Appears in Canadian Geotechnical Journal, 44(11): 1378–1390. *Canadian Geotechnical Journal,* 45**,** 1646-1647.

KULHAWY, F. H. & JACKSON, C. S. Some observations on undrained side resistance of drilled shafts. Foundation Engineering: Current principles and practices, 1989. ASCE, 1011-1025.

KULHAWY, F. H. & PHOON, K.-K. Drilled shaft side resistance in clay soil to rock. Design and performance of deep foundations: Piles and piers in soil and soft rock, 1993. ASCE, 172-183.

LEROUEIL, S. & VAUGHAN, P. 1990. The general and congruent effects of structure in natural soils and weak rocks. *Géotechnique,* 40**,** 467-488.

LI, L., CHEN, S. & ZHANG, Z. 2019. A Numerical Study on Installation Effects and Long-Term Shaft Resistance of Pre-Bored Piles in Cohesive Soils. *Transportation Research Record,* 2673**,** 494-505.

LO PRESTI, D., JAMIOLKOWSKI, M., PALLARA, O., CAVALLARO, A. & PEDRONI, S. 1997. Shear modulus and damping of soils. *Géotechnique,* 47**,** 603-617.

LODAHL, M. R. 2017. *Influence of smectite content on the deformation behaviour of clay.* PhD, Aarhus University.

LUKOSE, A. & THIYYAKKANDI, S. Predicting Residual Stress State Around Bored Cast-In-Situ Piles Utilizing Cavity Contraction and Expansion Solutions. *In:* SATYANARAYANA REDDY, C. N. V., MUTHUKKUMARAN, K., SATYAM, N. & VAIDYA, R., eds. Ground Characterization and Foundations, 2022// 2022 Singapore. Springer Singapore, 627-638.

LUNA, I. 2014. Distributed Fiber Optic Sensing: Temperature Compensation of Strain Measurement. internal Report.

LUNA, I. 2017. ODiSI B. Data Sheet.

LUNNE, T., ROBERTSON, P. K. & POWELL, J. J. M. 2002. *Cone penetration testing in geotechnical practice*.

LYSE, C., CHRISTOFFERSEN, A. G. & CHRISTENSEN, R. 2020. A reflection on the capacity and service responce of large diameter cast-in-place bored piles installed in fissured and highly plastic Eocene clay at the port of Aarhus, Denmark. Unpublished: Rambøll.

MADSEN, M. G. & CHRISTOFFERSEN, A. G. 2018. *Undrained response of very high plasticity clays during CU triaxial tests and pile driving.* Master, Aarhus University.

MARSLAND, A. 1972. Clays subjected to in situ load tests. *Ground Engineering,* 5**,** 24-31.

MASCARUCCI, Y., MANDOLINI, A. & MILIZIANO, S. 2013. Effects of residual stresses on shaft friction of bored cast in situ piles in sand. *Journal of Geo-Engineering Sciences,* 1**,** 37-51.

MAYNE, P. W., KULHAWY, F. H. & KAY, J. N. 1990. Observations on the development of pore-water stresses during piezocone penetration in clays. *Canadian Geotechnical Journal,* 27**,** 418-428.

MEYERHOF, G. G. 1976. Bearing capacity and settlement of pile foundations. *Journal of the Geotechnical Engineering Division,* 102**,** 195-228.

MEYERHOF, G. G. & MURDOCK, L. J. 1953. An investigation of the bearing capacity of some bored and driven piles in london clay. *Geotechnique,* 3**,** 267-282.

MIKKELSEN, A. R. & NIELSEN, V. K. H. 2023. *Influence of structure on the rate dependent behaviour of clays.* Master, Aarhus University.

MOHAMAD, H., SOGA, K. & BENNETT, P. Fibre optic installation techniques for pile instrumentation. Proceedings of the 17th International Conference on Soil Mechanics and Geotechnical Engineering, 2009. IOS Press, 1873-1876.

MOHAMAD, H., TEE, B., CHONG, M. & ANG, K. Investigation of shaft friction mechanisms of bored piles through distributed optical fibre strain sensing'. 19th International Conference on Soil Mechanics and Geotechnical Engineering, 2017.

MOHAN, D. & CHANDRA, S. 1961. Frictional Resistance of Bored Piles in Expansive Clays. *Geotechnique,* 11**,** 294-301.

MORRISON, P., HAMMAMI, R., HANSEN, G. L. & BAILIE, P. Fehmarnbelt Fixed Link-Installation and testing of driven steel tube piles and bored cast-in-place concrete piles. Nordic Geotechnical Meeting 2012, 2012 Copenhagen, Denmark. dgf-Bulletin 27, 507-514.

NEVILLE, A. M. & BROOKS, J. J. 1987. *Concrete technology,* Harlec, UK, Longman Scientific & Technical England.

NIAZI, F. S. & MAYNE, P. W. Modeling of shear stiffness reduction from database of axial load tests on pile foundations. 7th International Symposium on Deformation Characteristics of Geomaterials, 2019 Glasgow. E3S Web Conf.

O'NEIL, M. W. & REESE, L. C. 1999. Drilled shafts: Construction procedures and design methods. United States. Federal Highway Administration. Office of Infrastructure.

OKKELS, N. & HANSEN, P. Swell pressure and yield stresses in Danish, highly overconsolidated, Palaeogene clays of extreme plasticity. 17th Nordic Geotechnical Meeting, 2016 Reykjavik, Iceland. 367-376.

OKKELS, N. & JUUL, K. 2008. Søvindmergel. *Nordic Geotechnical Meeting (NGM).* Sandefjord, Norway.

OUYANG, Y., BROADBENT, K., BELL, A., PELECANOS, L. & SOGA, K. 2015. The use of fibre optic instrumentation to monitor the O-Cell load test on a single working pile in London. *XVI European Conference on Spol Mechanics and Geotechnical Engineering.* Edingburg, United Kingdom.

PALMIERI, L. & SCHENATO, L. 2013. Distributed optical fiber sensing based on Rayleigh scattering. *The Open Optics Journal,* 7**,** 104-127.

PEI, H., YIN, J. & WANG, Z. 2019. Monitoring and analysis of cast-in-place concrete bored piles adjacent to deep excavation by using BOTDA sensing technology. *Journal of modern optics,* 66**,** 703-709.

PELECANOS, L., SOGA, K., CHUNGE, M. P., OUYANG, Y., KWAN, V., KECHAVARZI, C. & NICHOLSON, D. 2017. Distributed fibre-optic monitoring of an Osterberg-cell pile test in London. *Géotechnique Letters,* 7**,** 152-160.

PELECANOS, L., SOGA, K., ELSHAFIE, M., DE BATTISTA, N., KECHAVARZI, C., GUE, C. Y., OUYANG, Y. & SEO, H.-J. 2018. Distributed fiber optic sensing of axially loaded bored piles. *Journal of Geotechnical and Geoenvironmental Engineering,* 144**,** 1-16.

PELECANOS, L., SOGA, K., HARDY, S., BLAIR, A., CARTER, K. & PATEL, D. 2016. Distributed fibre-optic monitoring of tension piles under a basement excavation at the V&A Museum in London. *International Conference on Smart Infrastructure and Construction.* Cambridge, United Kingdom: ICE Publishing.

PENNINGTON, D. 1995. Cracked? Exploring post-construction evidence in the interpretation of trial pile data. *Proceedings of the Institution of Civil Engineers - Geotechnical Engineering,* 113**,** 132-143.

RANDOLPH, M. & WROTH, C. 1979. *A simple approach to pile design and the evaluation of pile tests*, ASTM International.

RANDOLPH, M. F. 2003. RATZ manual version 4-2: Load transfer of axially loaded piles. *RATZ software manual.*

RANDOLPH, M. F., CARTER, J. P. & WROTH, C. P. 1979. Driven piles in clay—the effects of installation and subsequent consolidation. *Géotechnique,* 29**,** 361-393.

RANDOLPH, M. F. & MURPHY, B. S. Shaft Capacity of Driven Piles in Clay. Offshore Technology Conference, 1985 Houston, Texas.

RANDOLPH, M. F. & WROTH, C. P. 1978. Analysis of deformation of vertically loaded piles. *Journal of the geotechnical engineering division,* 104**,** 1465-1488.

REESE, L. C. Load versus settlement for an axially loaded pile. Symposium On Bearing Capacity of Piles, 1964 United States. 18-38.

SAND-JENSEN, K. & BINDERUP, M. 2006. *Naturen i Danmark. Bind 2: Geologien*, Gyldendal A/S.

SCHMERTMANN, J. H. 1991. The Mechanical Aging of Soils. *Journal of Geotechnical Engineering,* 117**,** 1288-1330.

SCHOFIELD, A. N. & WROTH, P. 1968. Coulomb's failure equation and the choise of strength parameters. *Critical State Soil Mechanics.* Cambridge University.

SEED, H. B. & REESE, L. C. 1957. The action of soft clay along friction piles. *Transactions of the American Society of Civil Engineers,* 122**,** 731-754.

SIEGEL, T. & MCGILLIVRAY, A. Interpreted residual load in an augered cast-in-place pile. Proceedings of the Deep Foundations Institute 34th annual conference on deep foundations, 2009 Kansas City, MO.

SIMONSEN, T. R. 2018. *Pore water pressure response and heave of Palaeogene clays in connection with deep excavation and pile driving.* PhD, Aarhus University.

SKEMPTON, A. W. 1959. Cast in-situ bored piles in london clay. *Geotechnique,* 9**,** 153-173.

SKEMPTON, A. W. Horizontal stresses in overconsolidated Eocene clay. 5th International Conference on Soil Mechanics and Foundation Engineering, 1961 Paris, France. 351-367.

SKEMPTON, A. W., SCHUSTER, R. L. & PETLEY, D. J. 1969. Joints and Fissures in the London Clay at Wraysbury and Edgware. *Géotechnique,* 19**,** 205-217.

SKOV, R. & DENVER, H. Time-dependence of bearing capacity of piles. 3rd International Conference on the Application of Stress-Wave Theory to Piles. , 1988 Ottawa. 879-889.

SORENSEN, K. & OKKELS, N. Correlation between drained shear strength and plasticity index of undisturbed overconsolidated clays. Proceedings of the 18th International Conference on Soil Mechanics and Geotechnical Engineering, Paris, 2013. 423-428.

STANTON, K., MOTAMED, R., ELFASS, S. & ELLISON, K. An evaluation of tz analysis methods. 40th annual conference on deep foundations, 12-15 October 2015 2015 Oakland, CA, USA.

SVINKIN, M. R. & SKOV, R. Set-up effect of cohesive soils in pile capacity. 6th International Conference on Application of Stress Waves to Piles, 2000 Sao Paulo, Brazil. Balkema, 107-111.

TERZAGHI, K. 1943. Bearing Capacity. *Theoretical Soil Mechanics.* John Wiley and Sons, Onc.

THOMSEN, E. 2022. *RE: Lector emeritus, Geological Institute, Aarhus University. E-mail correspondance.*

TOMLINSON, M. J. & WOODWARD, J. 2015. *Pile design and construction practice,* Boca Raton, CRC Press.

VARDANEGA, P. & BOLTON, M. Practical methods to estimate the non-linear shear stiffness of fine grained soils. 5th International Symposium on Deformation Characteristics of Geomaterials, 2011a Seoul, South Korea. 372-379.

VARDANEGA, P. & BOLTON, M. 2011b. Strength mobilization in clays and silts. *Canadian Geotechnical Journal,* 48**,** 1485-1503.

VARDANEGA, P. J. & BOLTON, M. Predicting shear strength mobilization of London clay. 15th European conference on soil mechanics and geotechnical engineering, 2011c. 487-492.

VARDANEGA, P. J., WILLIAMSON, M. G. & BOLTON, M. D. 2012b. Bored pile design in stiff clay II: Mechanisms and uncertainty. *Proceedings of the Institution of Civil Engineers: Geotechnical Engineering,* 165**,** 233-246.

VIJAYVERGIYA, V. N. Load-movement characteristics of piles. 4th Annual Symposium of Waterway, Port, Coastal and Occean Division of ASCE, 9-11 March 1977 1977 Long Beach, California. ASCE, 269-284.

WHITAKER, T. & COOKE, R. W. 1966. An investigation of the shaft and base resistances of large bored piles in London Clay. *Large bored piles.* Thomas Telford Publishing.

XU, D.-S., YIN, J.-H. & LIU, H.-B. 2018. A new measurement approach for deflection monitoring of large-scale bored piles using distributed fiber sensing technology. *Measurement : journal of the International Measurement Confederation,* 117**,** 444-454.

ZHANG, J., ANDRUS, R. D. & JUANG, C. H. 2005. Normalized shear modulus and material damping ratio relationships. *Journal of geotechnical and geoenvironmental engineering,* 131**,** 453-464.

ZHANG, Q.-Q., LI, S.-C., ZHANG, Q., LI, L.-P. & ZHANG, B. 2015. Analysis on Response of a Single Pile Subjected to Tension Load Using a Softening Model and a Hyperbolic Model. *Marine Georesources & Geotechnology,* 33**,** 167-176.

ZHANG, Q.-Q. & ZHANG, Z.-M. 2012. A simplified nonlinear approach for single pile settlement analysis. *Canadian Geotechnical Journal,* 49**,** 1256-1266.

Published papers

Tension tests on bored instrumented piles installed in marine Eocene clay

J Knudsen[1,2], K K Sørensen[1], J S Steenfelt[3] and H Trankjær[2]

[1] Department of Engineering, Aarhus University, Inge Lehmannsgade 10, 8000 Aarhus C, Denmark
[2] COWI Aarhus, Jens Chr. Skous Vej 9, 8000 Aarhus, Denmark
[3] COWI Lyngby, Parallelvej 2, 2800 Lyngby, Denmark

Jahs@cowi.com

Abstract. This paper presents parts of the results from two full-scale loading tests (tension) on bored cast-in-place piles installed in high plasticity marine Eocene clay at a test site in Hinge, central Jutland, Denmark. Testing was carried out to investigate the development and distribution of shaft resistance on the test piles. Each test pile was instrumented with distributed fiber-optic strain and temperature cables, in addition to traditional vibrating wire strain gauges and tell tales. Selected examples of retrieved data are presented. The measured shaft resistance is compared to an analytical method based on the Danish National Annex to Eurocode 7, part 1 which represents a conservative estimate for the shaft resistance of bored piles. The results from the two full-scale loading tests (tension) on bored cast-in-place piles in marine Eocene clay show that the Danish code-requirement, concerning shaft resistance, is too conservative.

1. Introduction

This paper presents the preliminary results from the first two full-scale loading (tension) tests from a test program consisting of 8 full-scale bored test piles installed in a high plasticity marine Eocene clay. The purpose of the test program is to determine the development and the distribution of the shaft resistance along the length of the pile as the pile is gradually being loaded to a failure condition. In addition, by testing the piles in pairs at different times after installation (1.5 months, 6 months and 12 months) the full test program will also investigate possible ageing effects on the shaft resistance (results are to be published at later time). To achieve detailed measurements of the distribution of shaft resistance each test pile was instrumented with distributed fibre-optic strain and temperature cables in addition to traditional vibrating wire strain gauges and tell tales. The results are compared to an analytical method based on the Danish National Annex to Eurocode 7, part 1 [1] The code-requirement limits the shaft resistance for a bored pile to 30 per cent of the shaft resistance of the corresponding driven pile unless recognised documentation to show otherwise is available.

1.1. Back ground

The development and magnitude of shaft resistance on bored piles in fine grained soils is controlled by various mechanisms and highly depend on the chosen execution methods. Stresses will gradually build up after installation of the pile and shaft resistance during static pile load test will depend on the degree of swelling and softening taking place in the clay during installation.

Content from this work may be used under the terms of the Creative Commons Attribution 3.0 licence. Any further distribution of this work must maintain attribution to the author(s) and the title of the work, journal citation and DOI.
Published under licence by IOP Publishing Ltd

Major shear distortion from pile installation is confined to a relative thin zone around the pile shaft [2-3] making it practically impossible to measure the detailed effects of the governing mechanism in terms of normal and shear stresses, their distribution along the pile shaft as well as excess pore pressure in the adjacent clay. Hence, using the effective stress analysis, also known as the β-method, is not practically possible for determination of shaft resistance for bored piles.

Determination of shaft resistance for bored piles in clay is therefore conventionally based on an empirical approach, where a reduction factor is applied to the undisturbed undrained shear strength c_u of the clay layers which the pile penetrates. This is also known as the α method:

$$R_{s,cal} = \sum \alpha \cdot c_u \cdot A_s \quad (1)$$

where $R_{s,cal}$ is the shaft resistance, α is an empirical adhesion coefficient and A_S is the shaft surface area.

Experience from pile load tests in similar ground conditions is required to determine the α-value. Uncertainties in the α-value and the variation of the undrained shear strength of the soil adjacent to the pile means that the α-method only gives an estimate of the total shaft resistance. Hence, the distribution of shaft resistance along the pile shaft is unknown.

The distribution of shaft resistance along the pile length during load testing can be determined from the measured displacements and strains inside the piles at selected predetermined locations by using tell tales and strain gauges [4-5]. However, the conversion from strains to normal stresses in the pile and finding the actual stresses acting on the pile shaft is not a simple matter. This requires knowledge of the variation in pile stiffness along the length of the pile and the change in stiffness with increasing strains. In addition, the possible existence of locked-in residual forces acting on the pile after concrete curing and prior to pile testing can be hard to estimate [6].

1.2. Shaft resistance of bored piles based on the Danish National Annex to Eurocode 7, part 1

The results from the conducted pile load tests are compared to an analytical method based on the Danish National Annex to Eurocode 7, part 1 [1], where realistic strength parameters (best estimate) are applied. According to [1] the shaft resistance $R_{s,cal}$ of a bored pile can be estimated from:

$$R_{s,cal} = \sum \alpha \cdot c_u \cdot A_s = \sum (0.3 \cdot m \cdot \mathrm{r}) \cdot c_u \cdot A_s \quad (2)$$

where m is a material factor, r is a regeneration factor, c_u is the undrained shear strength and A_S is the shaft surface area. The factor 0.3 is the 30 per cent reduction of the shaft resistance of the corresponding driven pile.

The material factor considers the ratio of adhesion to undrained shear strength. For concrete piles a material factor of 1.0 is generally used. The regeneration factor considers the strength reduction of the clay due to remoulding during pile driving and also considers the subsequent strength gain over time due to dissipation of excess pore water pressure [7]. It is usual practice in Denmark to assume a regeneration factor of 0.4 (i.e. 60 % reduction of the intact undrained shear strength) for driven piles 28 days after pile installation if $c_u < 500$ kPa. In Denmark the empirical α-factor used is applied to the intact undisturbed undrained shear strength determined from in-situ tests (e.g. from field vane tests, where the field vane strength, c_{fv} can be assumed equal to c_u) [1].

The empirical α-factors used for driven and bored concrete piles in Denmark are therefore equal to $\alpha = 0.4$ and $\alpha = 0.12$ respectively. The α-factor used for bored piles is based on the results from a low number (7 documented cases) of in-situ pile loading tests carried out in Denmark in the 1970´s, consisting of different pile types and execution methods, primarily established in clay till cf. [8]. In addition, it is likely that experience was drawn upon from abroad, where especially pile testing in stiff over consolidated London Clay was considered relevant as it bears resemblance to the stiff over consolidated Danish Palaeogene clays. In this respect, it should be noted that in the UK the α-factor is traditionally derived from a comparison of pile test results with the results of undrained triaxial compression tests on undisturbed specimens. This implies that the α-factor will be highly affected by the presence of fissures, and the values reported in the literature for stiff fissured clays like London clay

are therefore often not directly comparable without careful consideration and knowledge of the fissure strength in relation to the intact strength. Hence, for stiff fissures clays it would generally seem better to derive the α-factor based on the intact undisturbed undrained shear strength determined from in-situ testing.

Today's pile types, execution methods and installation time has changed and together with more challenging ground conditions, this has created a need for a revision of the empirical α-factor in Denmark.

2. Ground conditions and test methods

2.1. Ground conditions

Testing was carried out at a dedicated test site located in Hinge, central Jutland, Denmark. The location provides opportunity to work undisturbed for the duration of the entire full-scale test program and provides uniform ground conditions (very high plasticity clay) only approximately 3 m below ground.

Three geotechnical boreholes (B1-A, B2-A and B3-A) with field vane tests and four Cone Penetration Tests (CPT1-CPT4) were performed. Intact samples were collected in A-tubes (Shelby type) from six adjacent boreholes (B1-B&C, B2- B&C and B3- B&C). The locations of boreholes and CPT tests in relation to the test piles are illustrated in figure 1a.

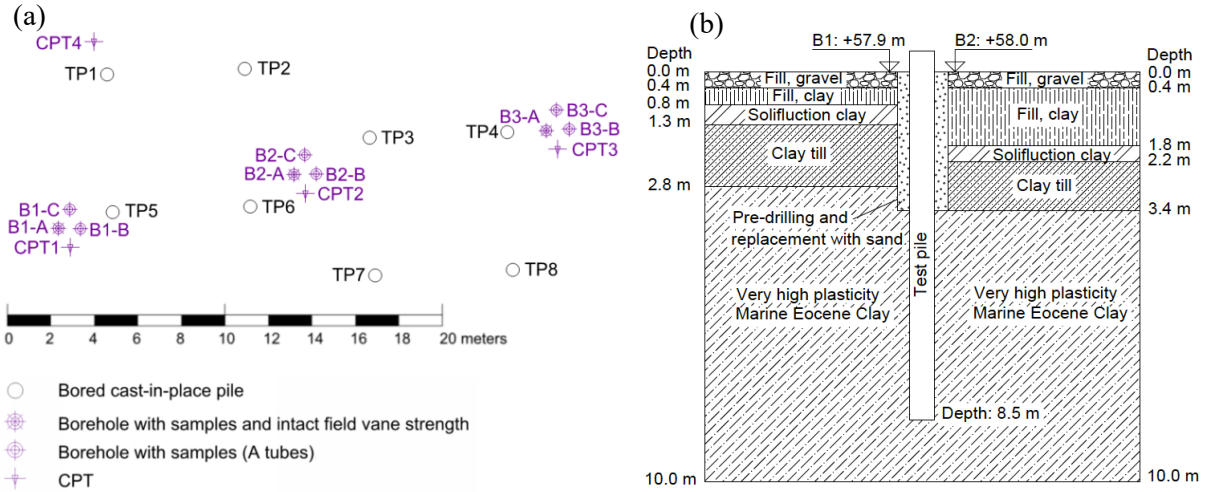

Figure 1. (a) Overview of geotechnical investigations and bored cast-in-place piles; (b) Representative soil profiles (B1-A and B2-A) around the test piles.

The top of the geotechnical boreholes B1-A and B2-A indicate 0.8 to 1.8 m clay fill. This is underlain by 0.4 to 0.5 m late glacial deposits of solifluction clay and 1.2 to 1.5 m glacial deposit of clay till down to the top of the glacially disturbed marine Eocene clay 2.8 to 3.4 m below ground, see figure 1(b). The ground level is approximately at +58.0 m above mean sea level (Danish Vertical Reference 1990).

Prior to installation of the bored cast-in-place piles the uppermost 0.4 m of soil was replaced by base course and steel mats to create a stable working platform for the piling rig, and subsequently replaced by gravel around the test setup to minimize settlement in the upper layers during load testing.

At each pile location the top 3.4 m of soil was predrilled (Ø1000 mm diameter) and replaced by sand (poorly graded medium sand). This was done to minimize contributions from the upper soil layers to the shaft resistance, thereby making it easier to deduce the contributions from the underlying layers of marine Eocene clays, see figure 1(b).

The clay till varies from low plasticity in the top of the layer to high plasticity in the bottom of the layer due to the underlying marine Eocene clay. The marine Eocene clay is a very high plasticity clay with an intact undrained shear strength (assumed equal to the field vane strength) between 100 and 350

kPa with an average value of 210 kPa (over the depth of the piles). The natural water content ranges between 41- 68 % and the unit weight ranges between 16.0 - 17.2 kN/m³. See figure 2.

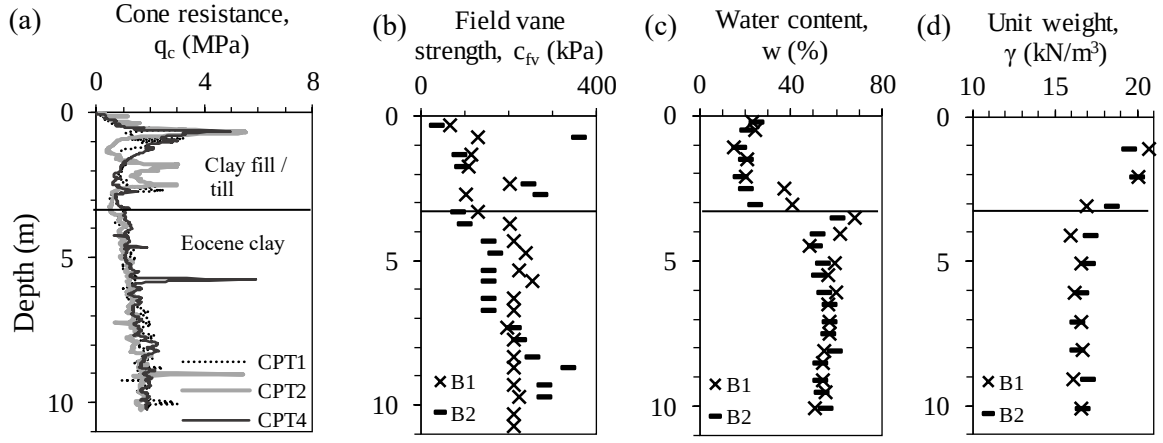

Figure 2. Cone resistance (a); Field vane strength (b); Water content (c); Unit weight (d).

Atterberg limits and calcite content for the marine Eocene clay at test site Hinge are given in Table 1 cf. [9].

Table 1. Atterberg limits and calcite content for marine Eocene clay at test site Hinge.

Water content (%)	Liquid limit (%)	Plastic limit (%)	Plasticity index (%)	Calcite (%)
44 - 62	160 - 233	11 - 44	86 - 202	13 - 36

The groundwater level at the site is varying between 0.5 and 1.5 m below ground level with a hydrostatic pressure distribution. Seasonal variations can be expected in the upper layers.

2.2. Test piles and pile instrumentation

The full-scale test program consists of eight instrumented full-scale bored cast-in-place piles. The test piles are 0.62 m in diameter and have a length of 8.5 m + 0.5 m (0.5 m above ground level). The reinforcement cage consists of eight Y32 bars with Y14/190 shear reinforcement in each pile. The concrete used was A35 MPa, and a pair of Ø63.5 mm GEWI PLUS bars were installed 6 m into the test pile to transfer the force from the hydraulic jacks to the test pile during pile load testing.

The reinforcement cage of each test pile was instrumented with 2 distributed fibre-optic strain cables, 1 distributed fibre-optic temperature cable, 10 vibrating wire strain gauges (one pair at 5 different levels) and 4 tell tales. All monitoring equipment was installed in pairs within the reinforcement cage on diametrically opposite sides to separate bending moments from axial loads, see figure 3.

Selected examples of the distribution of shaft resistance from vibrating wire strain gauges are presented in this paper, while the detailed measurement results will be presented and analysed in a future paper.

Installation of the test piles commenced three days after predrilling and replacement of the upper 3.4 m with sand, and the test piles were drilled as cased Kelly piles. No water was used in the borehole during drilling and cleaning. The casing was always kept 1 m above ground to ensure against contamination by debris, and the reinforcement cage was lowered into the borehole before concreting.

The piles were concreted from the bottom up with a tremie pipe, and the tip was kept below the surface of the concrete to avoid mixture and separation. The GEWI bars for the static loading test (tension) were installed manually after concreting of the piles.

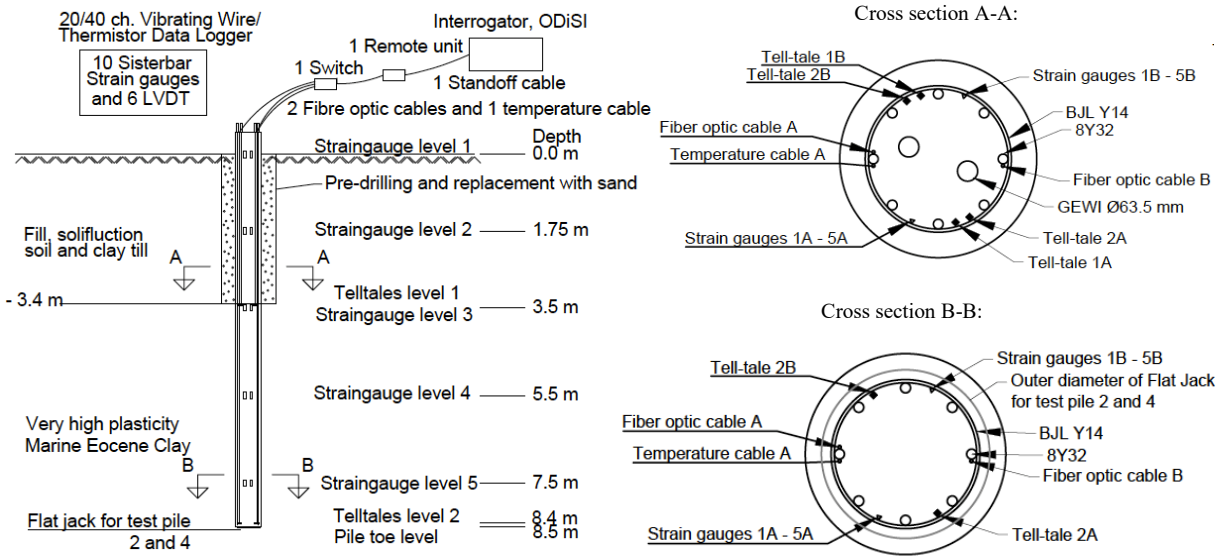

Figure 3. Details of test pile instrumentation. Levels relative to ground level.

2.3. Pile load tests and test setup

The first two static pile loading tests (tension), which are dealt with in this paper, were completed 48 days (test pile 7) and 51 days (test pile 1) after pile installation, respectively. Figure 4 shows the steel traverse system that was used to provide the reaction force for the pile load tests. The steel traverse system consists of two steel mats located with a clearance of approximately 2.5 m on both sides of the test piles. A pair of 4 m long HE300B load distribution beams were placed on top of the steel mats with two HE800B main beams on top. Finally, two pairs of HE400B beams with a length of 4 m were located crosswise above the centre of the test piles to distribute the load on both main beams and to stabilize the load application system. The test load was applied by four hydraulic jacks located central to the pile axis. Each hydraulic jack had a capacity of 300 t and a stroke of 250 mm. The load was measured by 3 MN load cells.

Figure 4. Steel traverse system for static pile load test (tension).

The reference beams (yellow beams at ground level) were 6 m long and mounted on wooden beams at the ends to ensure that the measurements of the pile displacement were independent from the test setup and any movements thereof. The reference beams were measured with surveyor's level at two points to check for possible movements.

The test piles were loaded to failure in two load cycles. In the 1st load cycle the load was applied in 5 steps of 100 kN, which corresponds to a total of 500 kN or 60 % of the expected failure load. The

holding time at each load step was 30 min. The pile was then unloaded in steps of 100 kN with a holding time of 5 minutes at each load step, and a holding time of min. 30 minutes before the 2nd load cycle commenced. In the 2nd load cycle the load was applied in steps of 125 kN and then reduced to steps of 50 kN when the test pile showed sign of imminent failure. The holding time at each load step was 30 min. The actual time-load curves for test pile 1 and test pile 7 is presented in figure 5.

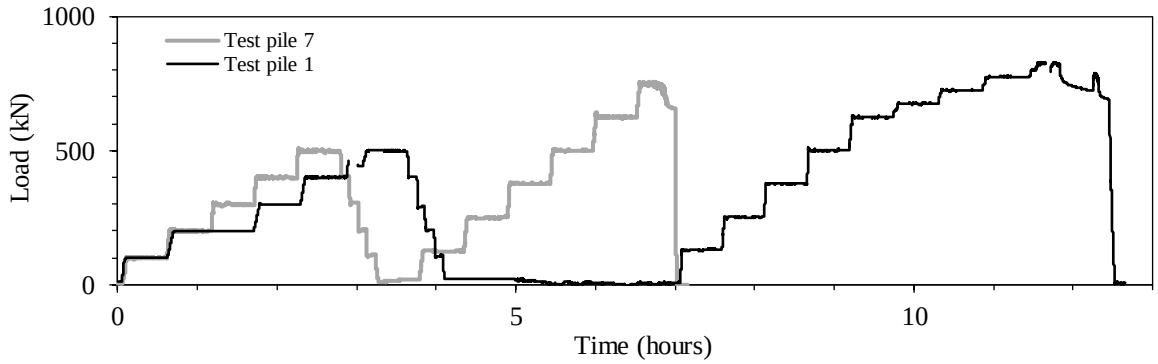

Figure 5. Loading procedure for test pile 1 and test pile 7.

For each new load step, the load was increased or decreased continuously over a time period of approximately 3 minutes to avoid shocks and vibrations. The load was held as constant as possible during each load step. For test pile 1 the power was lost twice during the static pile load test, which resulted in minor data losses between load step 4 (400 kN) and load step 5 (500 kN), and at the final load step (825 kN). Furthermore, the hydraulic system for test pile 1 had a leak, which was discovered at load step 2 (200 kN) and repaired between the 1st and 2nd load cycle. Therefore, the holding time was extended to approximately one hour for load step 2 and three hours for load step 10 (between 1st and 2nd load cycle).

3. Results

3.1. Load-displacement curves and mobilized pile capacities

The load-displacement curves for the static pile load tests (tension) on test piles 1 and 7 are shown in figure 6. The results are based on data from the displacement transducers on pile top, and no correction were made relative to the surveyor's level.

The overall behaviour of the shaft resistance response is seen from figure 6 to be strain hardening. The magnitude of creep displacement is seen to increase with increasing load level. This highlight the rate dependent behaviour of the load-displacement response and the mobilised shaft resistance. Test pile 1 is seen to experience creep failure at a sustained load of 825 kN, while test pile 7 fails at 750 kN. The initial almost vertical straight-line portion of the load-displacement curves during the first and second unloading highlight that the elastic lengthening and rebound of the pile is insignificant – this is furthermore confirmed by the measured very small internal strains shown in figure 8. The following sections will focus on the results from the tension load test on test pile 7.

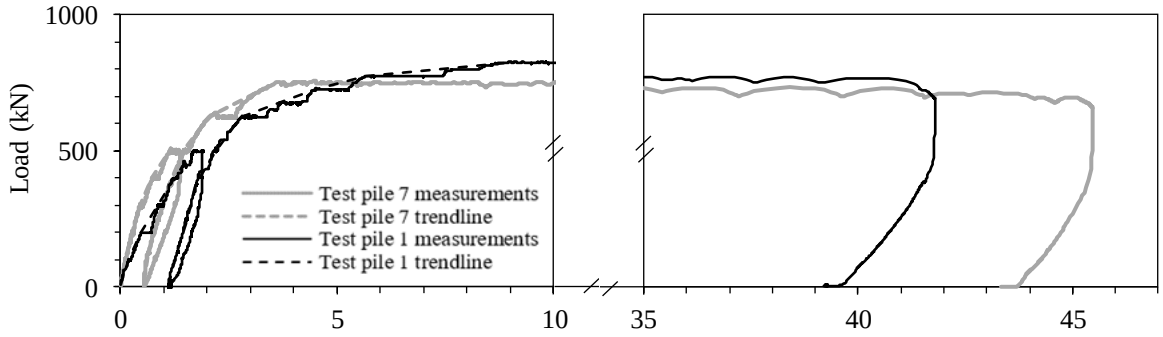

Figure 6. Load-displacement curves for test pile 1 and test pile 7.

3.2. Rate of creep and shaft resistance

The shaft resistance of the test piles equals the total bearing capacity from the static pile load test, as the performed static pile load tests were tension tests. However, the test piles were loaded incrementally to failure and therefore the log time-displacement/load curves and the corresponding rate of creep were investigated for the last two load steps to document in more detail the influence of creep rate on the shaft resistance of the test piles.

Figure 7(a) and figure 7(b) show the displacement per log time and creep displacement rate against time respectively for the last two load steps (625 kN and 750 kN) for test pile 7. The rate of creep per log cycle of time (trendline) is determined to be 0.18 mm/lct and 67.91 mm/lct at the end of each load step. In the last load step at 750 kN the creep displacement rate is initially seen to reduce and then after reaching a rate of approximately 0.005 mm/sec the creep displacement rate is seen to accelerate and the pile experiences creep failure. In the previous load step at 625 kN the creep displacement rate is found to reduce approximately linearly with time and there are no signs of eminent failure.

Test pile 1 shows similar behaviour in the last to load steps (775 kN and 825 kN) to what is seen for test pile 7. However, considering the magnitude of rate effects highlighted from the load-displacement curves in figure 6 and the small difference in load of only 50 kN between the two last load steps, it is likely that if enough creep time had been allowed, then the pile would eventually also experience creep failure at 775 kN.

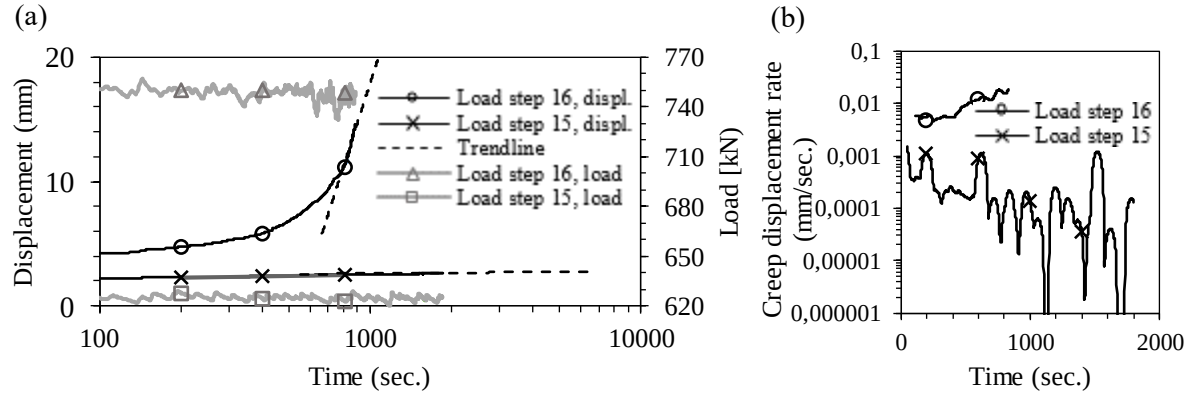

Figure 7. Log time-displacement and load curve for test pile 7 (a);
Time-creep displacement rate curve for test pile 7, average over 100 readings (b).

3.3. Internal strain profile of the test pile

The results from the vibrating wire strain gauges have been used to determine the distribution of shaft resistance. In the following section examples from the vibrating wire strain gauges level 1 through 5 is presented for test pile 7. For vibrating wire strain gauges the notation SG-1 through SG-5 has been used.

All displayed data are mean values from the pairs installed on diametrically opposite sides to separate bending moments from axial loads. Furthermore, an average value over the period of the maintained load step has been used. Figure 8(a) shows the load-micro strain curves at each gauge level for the 2nd load cycle (reloading until 500 kN) for test pile 7, while figure 8(b) shows the corresponding variation in tangent stiffness E_tA with increasing micro-strain at each gauge level.

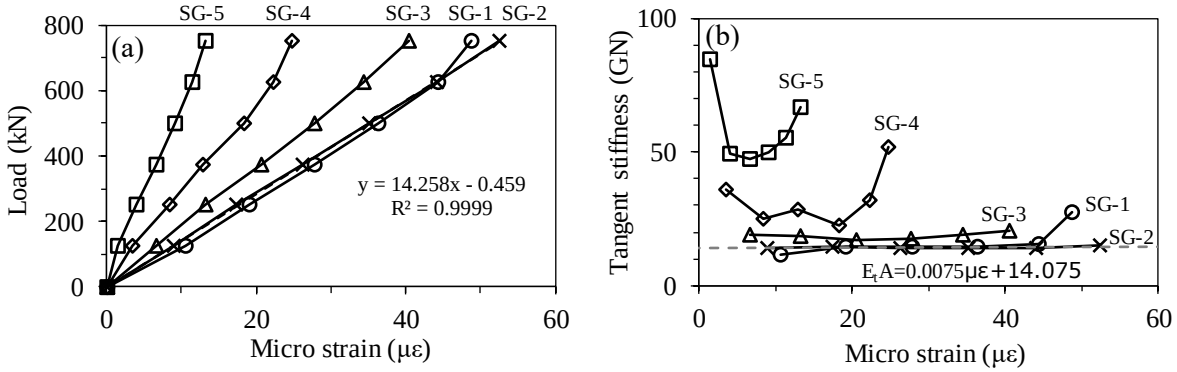

Figure 8. Test pile 7 – Applied load-micro strain curve for strain gauges level 1 through 5 (a); Tangent stiffness-micro strain curve for strain gauges level 1 through 5 (b).

From figure 8(a) is can be seen that the there is a close agreement between the load-micro strain curves for SG-1 (located at ground level) and SG-2 (located 1.75 m below ground level). This indicates that only minor shaft resistance is mobilised within the upper sand fill. Hence, the slope of the straight part of the load-micro strain lines SG-1 and SG-2 represent an approximate value of the pile stiffness (around 14 GN). However, at the maximum load the load-micro strain curve for SG-1 is seen to unexpectedly drop, indicating a false increase in pile stiffness. This can possibly be explained by the development of small tension cracks at the pile top at higher tension loads. These will lead to the tension load not being fully transferred to the pile before SG-2, because of the application of the tension load through GEWI bars concreted 6 m into the test pile.

If the applied load on the test pile is transferred along the pile shaft by gradual mobilisation of the shaft resistance down the pile, then it would be expected that the load-micro strain curves shown in figure 8(a) for the lower strain gauge levels would first rise and then become parallel with the upper strain gauge lines. This is however not seen to be the case, as can also be seen from the variation in tangent stiffness with increasing micro strain in figure 8(b). The tangent stiffness for SG-3 to SG-5 is on the other hand seen to initially reduce and then increase with increasing load level and micro strain. This is an indication, that the pile stiffness is significantly larger than the soil stiffness, and therefore the shaft resistance is activated simultaneously along the length of the pile. The tangent method therefore cannot be applied for the lower strain gauge levels despite full mobilisation of the shaft resistance above. Generally, the tangent method can only be expected to be applicable in compression testing where mobilisation of the base resistance is much slower than the mobilisation of shaft resistance.

Nonetheless, the pile tangent stiffness can be estimated based on SG-1 and SG-2. The E-modulus is often not a constant and can be expected to reduce linearly with increasing strain. From figure 8(b) it can however be seen that the tangent stiffness E_tA of the pile can be considered constant within the limited strain range (up to around 50 $\mu\varepsilon$) with a value of around 14 GN, hence the tangent stiffness E_tA and secant stiffness E_sA can be considered equal.

3.4. Load distribution in test pile and mobilisation of unit shaft resistance

The load distribution for all load steps applied to test pile 7 in the 2nd load cycle (reloading up to 500 kN) is shown in figure 9a. The load distribution is converted from the measured strains using the previous determined secant stiffness and assuming that it is valid for the entire length of the pile (the

reduction in pile stiffness of around 1.3 GN at the bottom 2.5 m of the pile due to the lack of the GEWI bars is not considered, as it has only little influence).

The load distribution lines between SG-2 and SG-5 are seen to be approximately linear and rotate gradually with increasing load. This indicates that the mobilised unit shaft resistance is approximately constant with depth and is mobilised simultaneously along the pile below SG-2, as was also indicated from the tangent stiffness in figure 8(b).

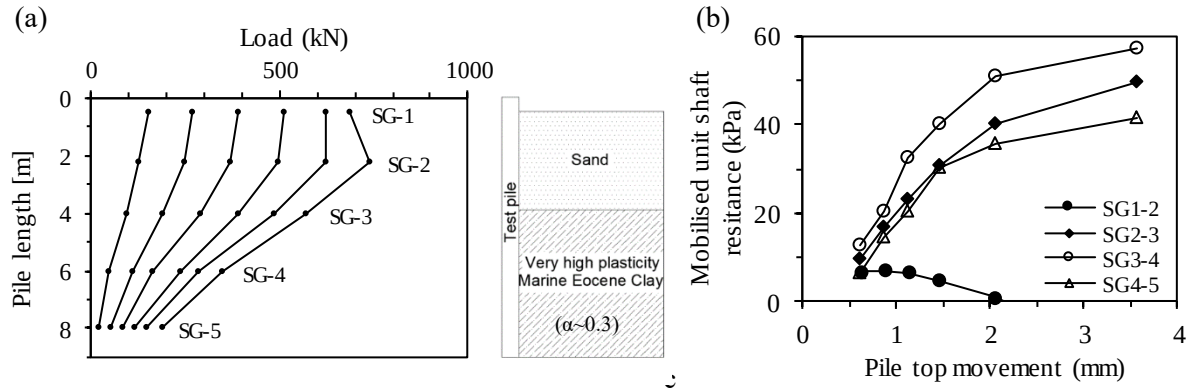

Figure 9. Test pile 7 - Back-calculated load distributions (a);
Mobilisation of unit shaft resistance in-between gauge levels (b)

The mobilised unit shaft resistance in-between each gauge level is plotted in figure 9(b) against the pile top movement which can be expected to be similar the relative movement between the pile and the soil. From figure 9(b) the unit shaft resistance below SG-2 is seen to increase gradually as the pile is moving upwards (relative to the soil) reaching ultimate values of around 41 kPa to 57 kPa in the marine Eocene clay (SG-3 to SG-5). Strain hardening behaviour is seen within the plotted range of movement. Surprisingly high mobilised unit shaft resistance is also indicated in the lower sand layer (between SG-2 and SG-3). If the average ultimate mobilised unit shaft resistance in the marine Eocene clay (49 kPa) is compared to an estimated average intact undrained strength of around 160 kPa from boring B2, an α-value of around 0.3 is achieved.

In figure 10 the measured total shaft resistances from the two full-scale loading tests (tension) on test pile 1 and test pile 7 are compared to the analytically calculated shaft resistance of the corresponding driven pile (equivalent diameter) using the intact undrained shear strength profile from borings B1 and B2 respectively and applying an α-value of 0.4 in clay as given by the equations according to [1]. The contribution from the sand represent less than five per cent of the analytically calculated shaft resistance of the corresponding driven pile and is thus omitted in the following. In the figure the assumed relationship between the shaft resistances for bored (α=0.12) and driven piles (α=0.4) in clays as given by [1] is also shown.

The derived value of shaft resistance for test pile 1 was 825 kN for a displacement rate of 0.005 mm/sec. This corresponds to an empirical adhesion coefficient α=0.37 which is close to the values used for driven piles and around 208 % greater than given by [1] for at bored pile. For test pile 7, the derived value of shaft resistance was 750 kN for a displacement rate of 0.005 mm/sec. This corresponds to an empirical adhesion coefficient α=0.42 which again is close to the values used for driven piles and around 250 % greater than given by [1] for at bored pile. The deviation between the adhesion coefficient α= 0.3 for the marine Eocene clay estimated from the unit shaft resistance and the analytical back calculated empirical adhesion coefficient α= 0.42 based on the total shaft resistance for test pile 7 is likely to be due to the observed mobilised shaft resistance in the lower sand layer.

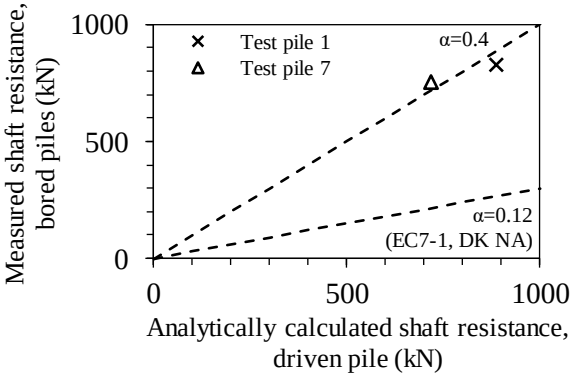

Figure 10. Comparison of measured total shaft resistance and analytically calculated shaft resistance for an equivalent driven pile.

4. Conclusions

The results from the tension load tests directly gives a measure of the total mobilised shaft resistance of the test piles. Distribution of load in the test piles and hence mobilised unit shaft resistance along the length of the pile has been derived assuming a constant pile stiffness derived from the two uppermost gauges levels in the pile. The results from the load tests indicate that the mobilised unit shaft resistance is approximately constant with depth and is mobilised simultaneously along the pile in the marine Eocene clay. α-values ranging from around 0.3 to 0.4 are back-calculated based on the two load tests. Hence, the results from the two full-scale loading tests (tension) clearly show that the Danish code-requirement, limiting the shaft resistance to 30 per cent of the corresponding driven pile (i.e. $\alpha = 0.12$), is too conservative.

Acknowledgements

The authors would like to thank COWIfonden, Innovation Fund Denmark and Per Aarsleff A/S for providing funding for this study. Furthermore, Per Aarsleff A/S for geotechnical investigations and installation of the instrumented test piles, DMT Gründungstechnik, GmbH, for pile load testing and Saint-Gobain Weber A/S for access to the test site.

References

[1] *DS/EN 1997-1 DK NA (2015): National Annex to Eurocode 7: Geotechnical design - Part 1: General rules: Danish Standard*

[2] Meyerhoff G G and Murdock L J 1953 An investigation of the bearing capacity of some bored and driven piles in london clay *Geotechnique* **3** 267-282

[3] Clayton C R I and Militsky J 1983 Installation effects and the performance of bored piles in stiff clay *Ground Engineering* **16** 17-22

[4] Dunnicliff J 1993 *Geotechnical instrumentation for monitoring field performance (*John Wiley & Sons) Chapter 5, pp 26-29

[5] Chen W F and Liew J Y R 2002 *The civil engineering handbook* 2nd edition (CRC Press) Section III, pp 28-16 – 28-18

[6] Fellenius B H 2017 *Best practice for performing static loading tests. Examples of test results with relevance to design* (3rd Bolivian Int. Conf. on Deep Foundations) pp 63-73

[7] Skov R and Denver H 1988 *Time-dependence of bearing capacity of piles* (Ottawa, Proc. 3rd Int. Conf. on the Application of Stress-Wave Theory to Piles) pp 879-889

[8] Knudsen J, Sørensen K K, Steenfelt J S and Trankjær H 2019 *Design of bored piles in Denmark - a historical perspective* (Reykjavik, XVII ECSMGE) pp 1-8

[9] Simonsen T R 2018 *Pore water pressure response and heave of palaeogene clays in connection with deep excavation and pile driving* (Aarhus University, PhD Thesis)

Appendixes

Soil-pile interaction for bored cast-in-situ piles in stiff clays

Jannie Knudsen

Soil-pile interaction for bored cast-in-situ piles in stiff clays

Appendixes

Jannie Knudsen

November 2024

Thesis submitted:	November 2024
PhD Supervisor:	Professor (Docent) Kenny Kataoka Sørensen Department of Civil and Architectural Engineering, Aarhus University
Company main supervisor:	Technical Director, Professor Jørgen S. Steenfelt Department 7104.008**,** COWI A/S, Kgs. Lyngby
Company co. supervisor:	Leading specialist Helle Trankjær Department 7104.002**,** COWI A/S, Aarhus
PhD Committee:	Professor Ken Gavin Department of Geoscience and Engineering, TU Delft
	Paul Morrison Director, Arup
	Associate professor Min Wu Department of Civil and Architectural Engineering, Aarhus University
PhD Series:	Faculty of Technical Sciences, Aarhus University

© 2024 Copyright by Jannie Knudsen

CONTENTS

A Borehole profiles 1

B Laboratory tests 8

B.1 Procedures for laboratory tests ... 8
B.2 Water content ... 10
B.3 Unit weight ... 12
B.4 Atterberg limit ... 13
B.5 Calcite content ... 22
B.6 Particle density ... 23
B.7 Oedometer tests ... 24
B.8 Triaxial tests ... 33

C Procedures for field tests 73

C.1 Instrumentation of test piles ... 73
C.2 Test pile installation ... 76
C.3 Conduction of static pile load tests ... 80
C.4 Flat Jack test ... 84

D Specification of test piles 85

D.1 Static documentation ... 85
D.2 Axial pile stiffness ... 91

E Static pile loading tests 93

E.1 Deviations observed during the static pile loading tests ... 93
E.2 Maintained load ... 94
E.3 Time-load curves ... 102
E.4 Time-displacement and load curves ... 106
E.5 Rate of creep ... 122
E.6 Shear stiffness degeneration curves ... 130
E.7 Average unloading-reloading stiffness ... 134

F Temperature data 137

F.1 Temperature development with time ... 138

F.2 Temperature development during static pile loading test 140
F.3 Temperature observations from strain free piles 149
F.4 Temperature observations from piles influenced by strain 153
F.5 Temperature variation over cross-sectional area 162

G Tell-tale measurements 170

G.1 Displacement-load curves 172

H Strain gauges measurements 180

H.1 Time-strain curves (Raw data) 180
H.2 Time-strain curves (Thermal influence) 188
H.3 Time-strain curves 196
H.4 Strain-pile length curves 200
H.5 Axial stiffness determined by direct secant method 208
H.6 Mobilised unit shaft resistance-pile top movement 211
H.7 Shear stiffness degradation curves 214

I Fibre optic strain measurements 217

I.1 HD strain sensor 2 217
I.2 Pre-tension 219
I.3 Confirmation of no creep 227
I.4 Internal strain profiles 232
I.5 Non-uniform pile stiffness 240

J Residual stresses 242

J.1 Load distribution along the length of test piles 242
J.2 Interpretation of residual stresses cf. Method 1, 2 and 3 246

K Accuracy of analytical models 248

K.1 HN model 248
K.2 HNr model 251
K.3 Examples of Python scripts 254

A Borehole profiles

LEGEND FOR BOREHOLE LOGS

Soil Signature

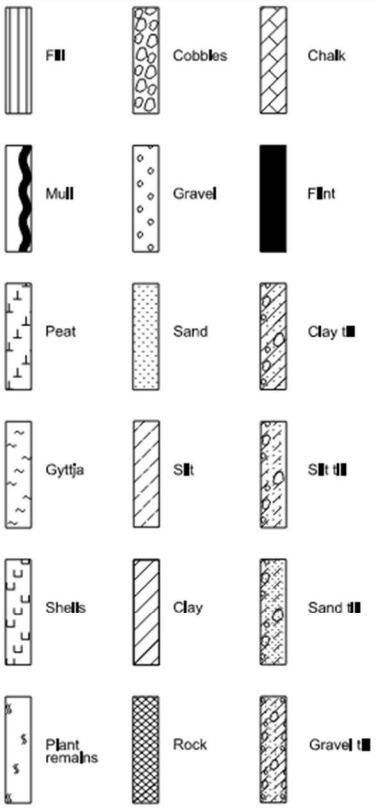

Till deposits can be expected to contain cobbles and boulders (not apparent in boreholes).

CPT log

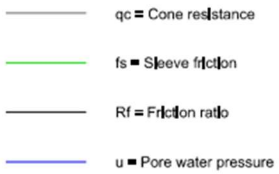

Borehole log

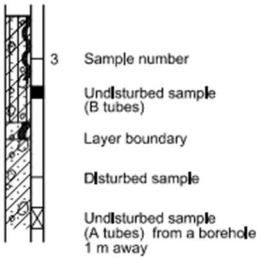

Geological abbreviations

Environment :

Fw	Freshwater deposit
Ss	Solifluction soil
Fl	Fill
Gl	Glacier deposit
Ma	Marine deposit
Wd	Washdown deposit
Ts	Topsoil
Ls	Landslide deposit
Mw	Meltwater deposit
Ae	Aeolian (wind) deposit
Br	Brackish water deposit

Age :

Re	Recent
Pg	Postglacial
Lg	Late Glacial
Gc	Glacial
Ig	Interglacial
Te	Tertiary
Ct	Cretaceous
Da	Danian
Mi	Miocene
Eo	Eocene
Ol	Oligocene

Stand pipe

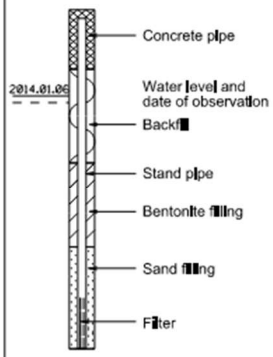

Definitions

Signature	Parameter	Sym.	Unit	Definition
▽- - - -▽	Water content	w	%	Weight of water in percent of solid matter
⊣	Liquid limit	w_L	%	Water content at yield point
⊢	Plastic limit	w_P	%	Water content at plastic limit
⊢⊣	Plastic index	I_P	%	$w_L - w_P$
X	Unit weight	Y	kN/m³	Ratio between total weight and total volume
+	Loss on ignition	gl	%	Weight loss of combustion in percent of solid matter
+	Reduced loss on ignition	gl_{red}	%	gl - ka
	Carbonate content	ka	%	Weight of $CaCO^3$ in percent of solid matter
-/(+)/+/++	Carbonate content	-		Reaction w. hydrochoric acid: - = no lime; (+) = low content of lime; + = limy; ++ = high content of lime
●—●	Shear strength	c_{fv}	kN/m²	Shear strength measured with a vane test in undisturbed soil
○—○	Shear strength, remoulded	c_{vr}	kN/m²	Shear strength measured with a vane test in disturbed soil
	CPT	q_c, f_s, u	MPa	Cone resistance, sleeve friction resistance, pore water pressure
		Rf	%	Friction ratio
	Sounding resistance SPT-probe, closed/open	N	N_{300}	No. of strokes pr. 300 mm penetration

Date	Prepared	Checked	Approved	Rev. 1.0	Page 1 of 1
06.06.2019	LNJE / JAHS	JAHS	JAHS		

AARHUS UNIVERSITY

Industrial PhD project:
Soil-pile interaction for bored cast-in-place piles in stiff clays and soft rocks

COWI

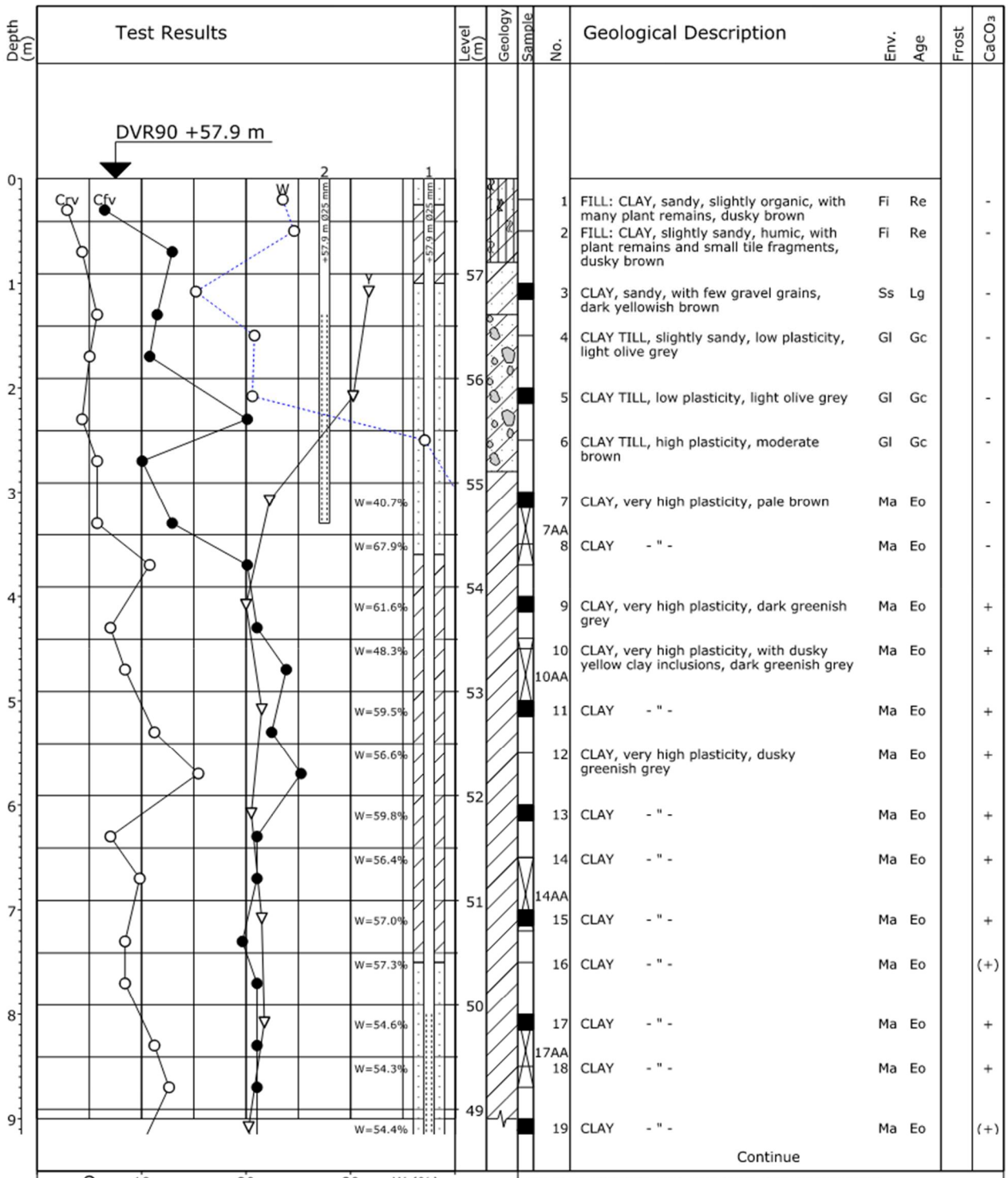

Sample 3: Slightly layered. Sample 5 and 6: Tertiary printed
Sample 7-21: Lillebælt clay. Sample 7 and 8: L6. Sample 9-21: L5
The Marine Eocene sequence is glacial disturbed. A tubes taken December 2019

Method: 6" auger with casing
Projection: UTM32E89
X: 564821 (m) Y: 6249509 (m) Plan:

Project: A113120 Soil-pile interaction for bored cast-in-place piles in stiff clays. Test site Hinge

Drilled by: PAA / JJ Date: 2019.05.06 Geologist: LCX Public No.: Borehole: TSH.B1-A

Prepared by: LNJE Checked by: JAHS Approved by: JAHS Date: 2021.05.11 Encl. No.: P. 1/2

COWI

GeoGIS2020 20.03.36 PSTR 11-05-2021 12:59:19

Borehole Log

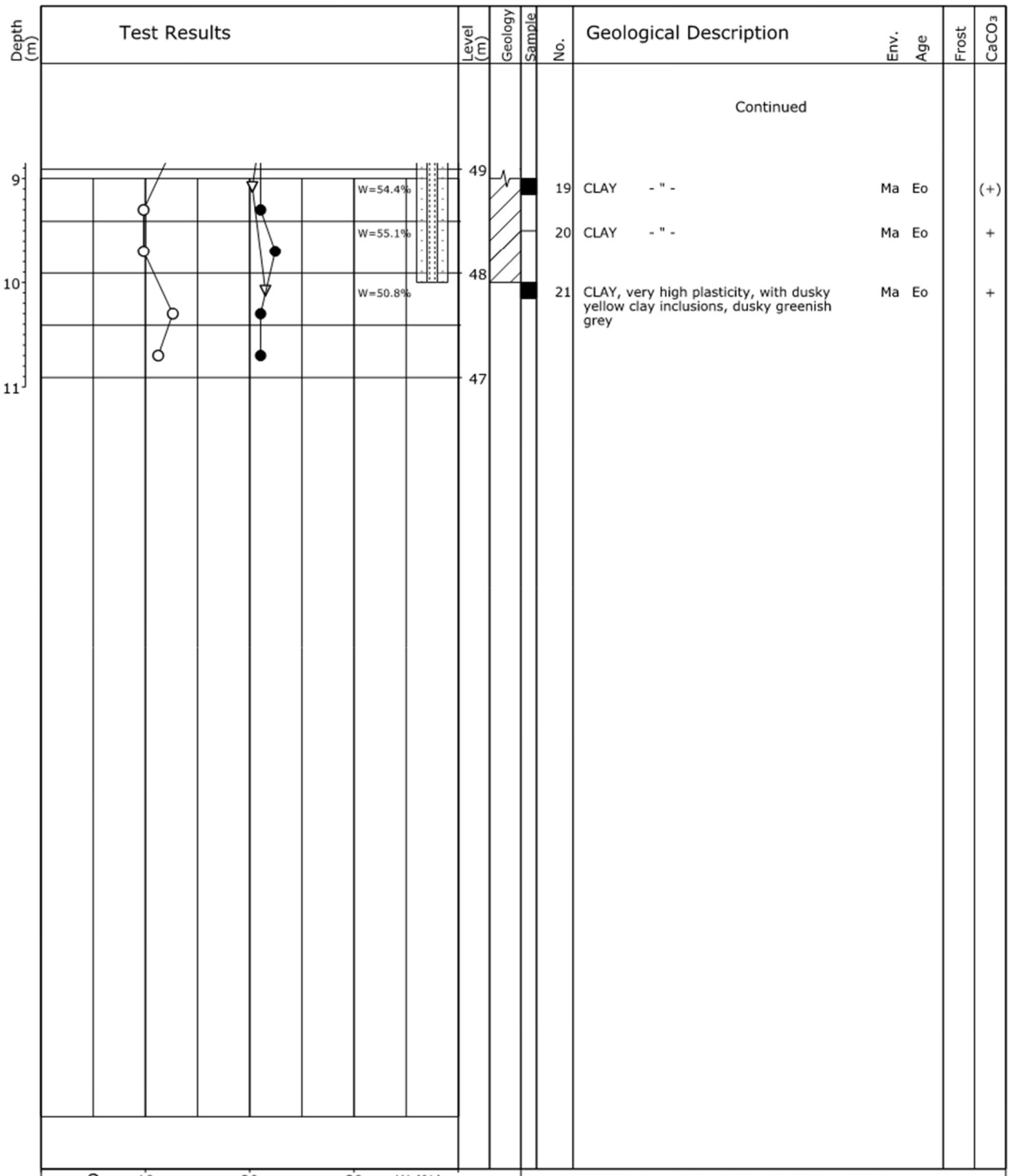

Sample 3: Slightly layered. Sample 5 and 6: Tertiary printed
Sample 7-21: Lillebælt clay. Sample 7 and 8: L6. Sample 9-21: L5
The Marine Eocene sequence is glacial disturbed. A tubes taken December 2019

Method: 6'' auger with casing
Projection: UTM32E89
X: 564821 (m) Y: 6249509 (m) Plan:

Project: A113120 Soil-pile interaction for bored cast-in-place piles in stiff clays. Test site Hinge

Drilled by: PAA / JJ Date: 2019.05.06 Geologist: LCX Public No.: Borehole: TSH.B1-A

Prepared by: LNJE Checked by: JAHS Approved by: JAHS Date: 2021.05.11 Encl. No.: P. 2/2

COWI

Borehole Log

GeoGIS2020 20.03.36 PSTR 11-05-2021 12:59:19

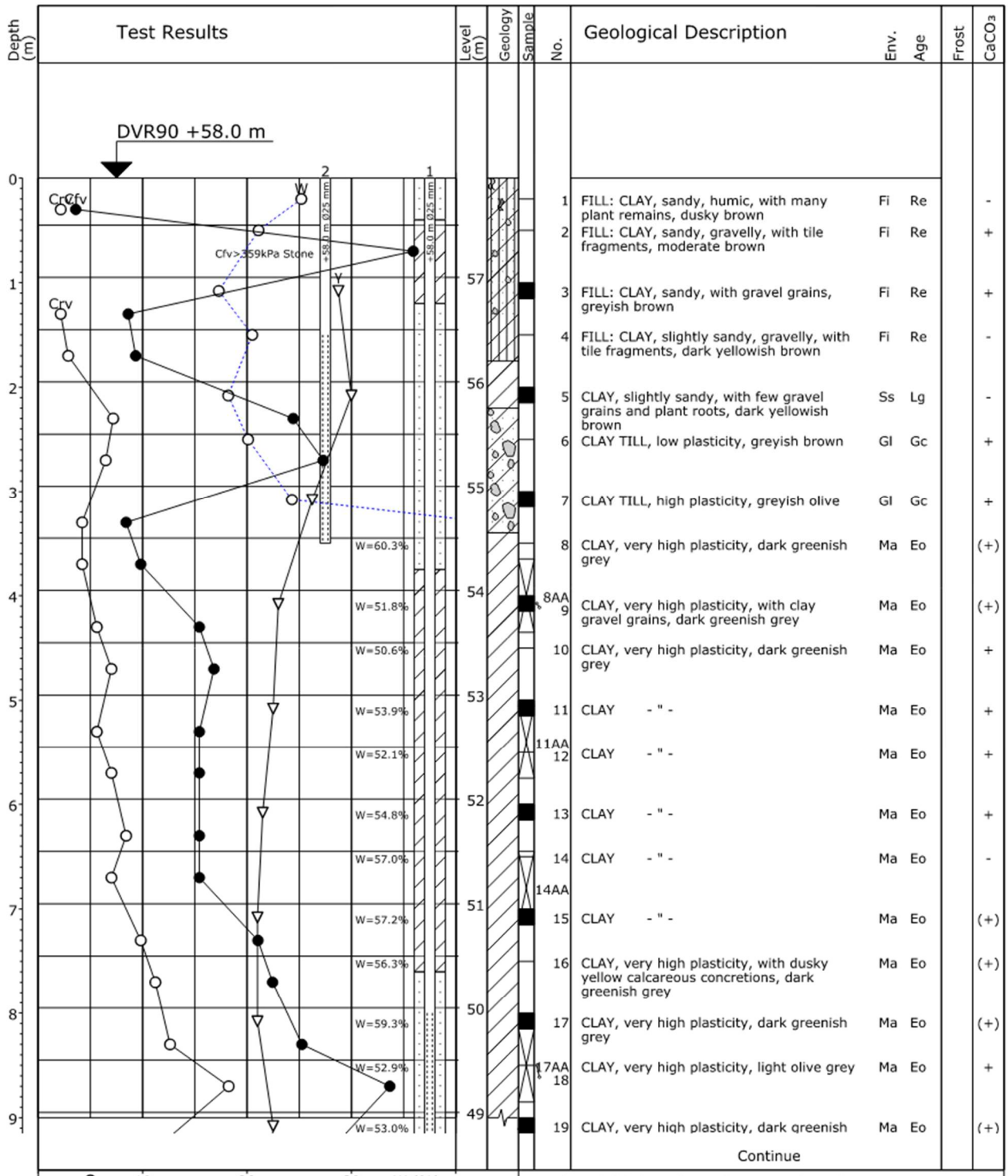

Sample 5: Slightly layered. Sample 7:Tertiary layered
Sample 8-21: Lillebælt clay. Sample 8-16: L6. Sample 17-21: L5
The Marine Eocene sequence is glacial disturbed. A tubes taken December 2019

Method: 6" auger with casing
Projection: UTM32E89
X: 564829 (m) Y: 6249516 (m) Plan:

Project: A113120 Soil-pile interaction for bored cast-in-place piles in stiff clays. Test site Hinge

Drilled by: PAA / JJ Date: 2019.05.06 Geologist: LCX Public No.: Borehole: TSH.B2-A

Prepared by: LNJE Checked by: JAHS Approved by: JAHS Date: 2021.05.11 Encl. No.: P. 1/2

COWI

Borehole Log

GeoGIS2020 20.03.36 PSTR 11-05-2021 12:58:52

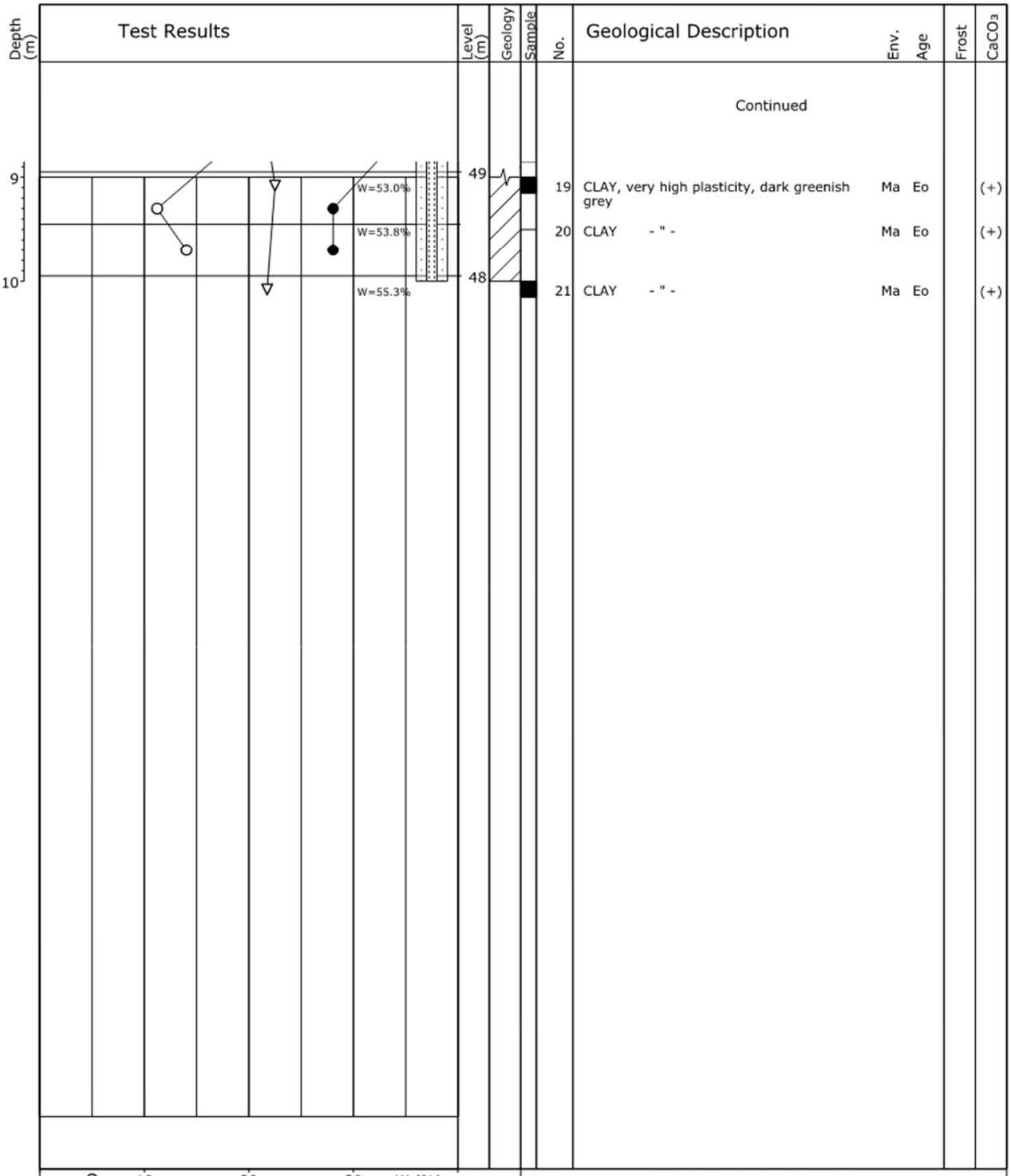

Sample 5: Slightly layered. Sample 7:Tertiary layered
Sample 8-21: Lillebælt clay. Sample 8-16: L6. Sample 17-21: L5
The Marine Eocene sequence is glacial disturbed. A tubes taken December 2019

Method: 6'' auger with casing
Projection: UTM32E89
X: 564829 (m) Y: 6249516 (m) Plan:

Project: A113120 Soil-pile interaction for bored cast-in-place piles in stiff clays. Test site Hinge

Drilled by: PAA / JJ Date: 2019.05.06 Geologist: LCX Public No.: Borehole: TSH.B2-A

Prepared by: LNJE Checked by: JAHS Approved by: JAHS Date: 2021.05.11 Encl. No.: P. 2/2

COWI

Borehole Log

GeoGIS2020 20.03.36 PSTR 11-05-2021 12:58:52

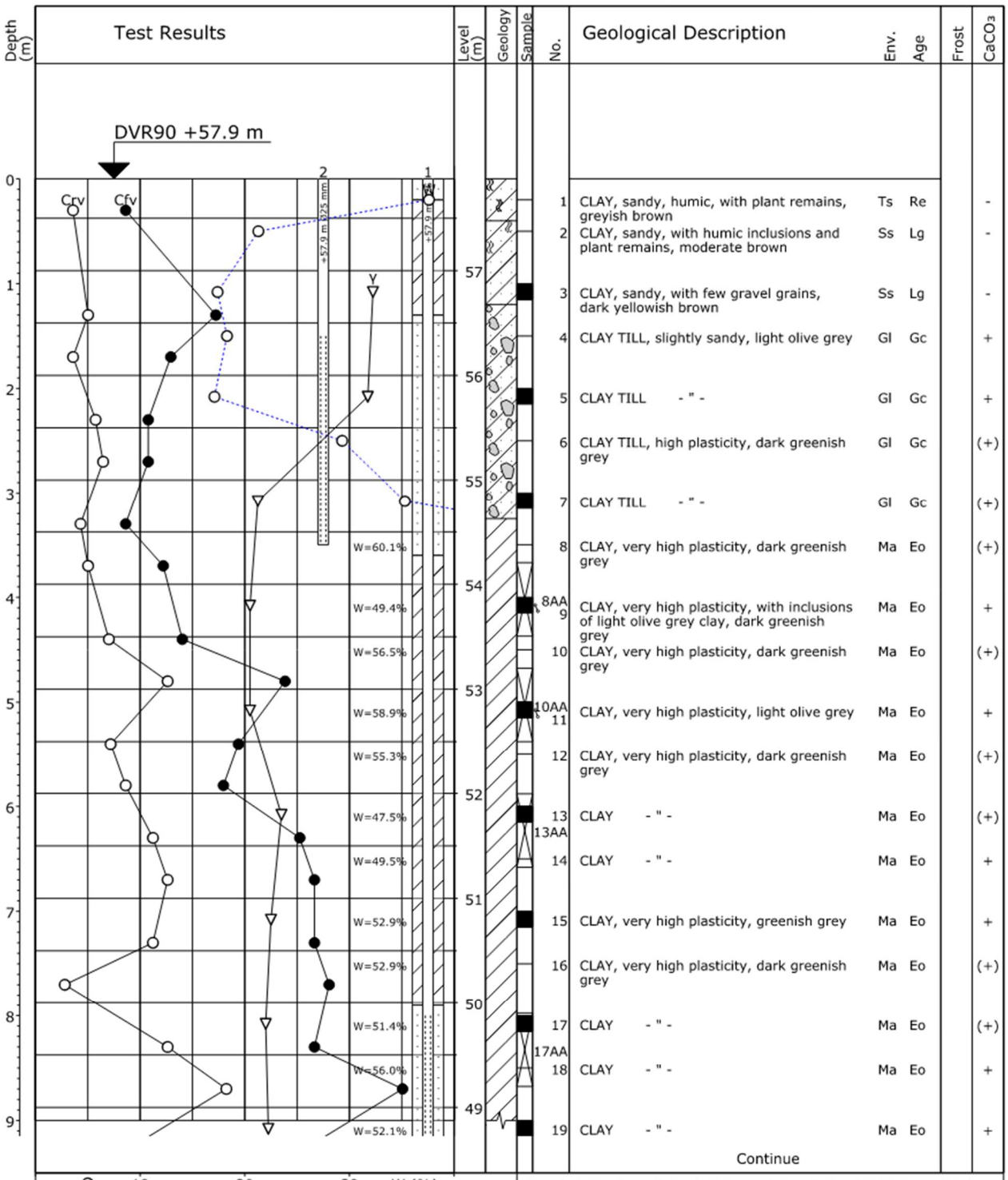

Sample 1: Meadow soil. Samle 3: Layered. Sample 6 and 7: Tertiary printed
Sample 8-21: Lillebælt clay. Sample 8 and 9: L6. Sample 10-21: L5
The Marine Eocene sequence is glacial disturbed. A tubes taken December 2019

Method: 6" auger with casing
Projection: UTM32E89
X: 564839 (m) Y: 6249523 (m) Plan:

Project: A113120 Soil-pile interaction for bored cast-in-place piles in stiff clays. Test site Hinge

Drilled by: PAA / JJ Date: 2019.05.08 Geologist: LCX Public No.: Borehole: TSH.B3-A

Prepared by: LNJE Checked by: JAHS Approved by: JAHS Date: 2021.05.11 Encl. No.: P. 1/2

COWI

Borehole Log

GeoGIS2020 20.03.36 PSTR 11-05-2021 12:58:32

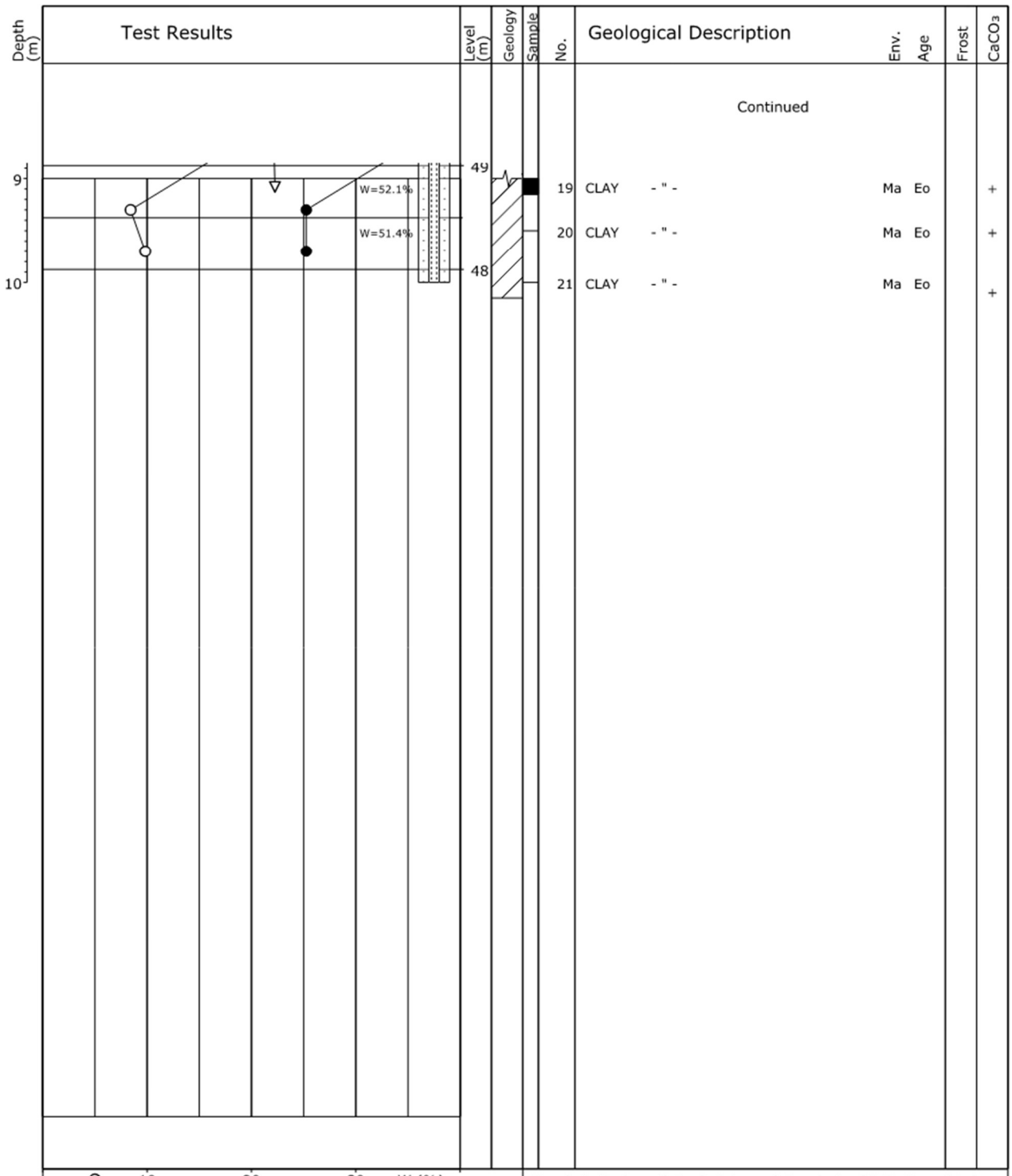

Sample 1: Meadow soil. Samle 3: Layered. Sample 6 and 7: Tertiary printed
Sample 8-21: Lillebælt clay. Sample 8 and 9: L6. Sample 10-21: L5
The Marine Eocene sequence is glacial disturbed. A tubes taken December 2019

Method: 6'' auger with casing
Projection: UTM32E89
X: 564839 (m) Y: 6249523 (m) Plan:

Project: A113120 Soil-pile interaction for bored cast-in-place piles in stiff clays. Test site Hinge

Drilled by: PAA / JJ Date: 2019.05.08 Geologist: LCX Public No.: Borehole: TSH.B3-A

Prepared by: LNJE Checked by: JAHS Approved by: JAHS Date: 2021.05.11 Encl. No.: P. 2/2

COWI

Borehole Log

GeoGIS2020 20.03.36 PSTR 11-05-2021 12:58:32

B Laboratory tests

B.1 Procedures for laboratory tests

This section describes the methods applied for the laboratory tests performed on intact A- and B-tubes extracted from the three geotechnical boreholes (B1-A, B2-A and B3-A) at the test site in Hinge.

B.1.1 Water content

The mass of an empty water container tin is measured and subsequently, a sample of soil is placed in the water container tin, after which the mass is measured again. The soil sample is then dried in the oven for 24 hours at 110°C. The mass of the dry sample is measured, and the natural water content (w_{nat}) is determined as the ratio of the amount of water to the amount of dry soils:

$$w_{nat} = \frac{M_w}{M_s} \tag{1}$$

Here w_{nat} is the natural water content, M_w is the mass of water and M_s is the mass of solids.

The mass of water (M_w) is determined as the mass of the soil sample subtracted the mass of the dry soil sample, while the mass of the solids (M_s) is determined as the mass of dry soil sample subtracted the mass of the empty water container tin.

B.1.2 Unit weight

The mass of a B-tube including soil sample is measured and subsequently, the sample of soil is extracted from the B-tube and the mass of the empty B-tube is measured. The inner diameter of the B-tube and the height of the extracted soil sample is measured. The natural in situ weight of the soil (also known as bulk unit weight) is determined as its weight per unit volume:

$$\gamma = \frac{W}{V} \tag{2}$$

Here γ is the unit weight (bulk unit weight), W is the weight of the soil sample and V is the volume of the soil sample.

The weight of the soil sample (W) is determined as the mass of the soil sample subtracted the mass of the dry soil sample multiplied by the gravitational acceleration, while the volume of the soil sample (V) is determined from inner diameter of the B-tube and the height of the extracted soil sample.

B.1.3 Atterberg limits

Atterberg limits are performed according to DS/EN 17892-12:2018 – Fall-Cone Method.

B.1.4 Calcite content

Carbonate contents are performed according to DGF Bulletin 15.

B.1.5 Particle density

Particle density tests are performed according to DS/EN 17892-3:2015.

B.1.6 Oedometer tests

Oedometer tests are performed according to principles in DS/EN 17892-5:2017.

B.1.7 Triaxial tests

Triaxial compression tests (CIU) are performed according to principles in 17892-9:2018.

B.2 Water content

For results of water content determination, see the tables below and the borehole profiles in Appendix A.

Borehole no. TSH.B1-A **Oven temperature** 110°C **Duration:** 24 hours

Depth [m]	Bowl number [-]	Bowl weight [g]	Bowl + wet sample [g]	Bowl + dry sample [g]	Wet sample weight [g]	Dry sample weight [g]	Water in sample [g]	Water content [%]
0,2	1	42,48	83,29	75,52	40,81	33,04	7,77	23,52
0,5	2	39,83	80,72	72,66	40,89	32,83	8,06	24,55
1,0	61	93,20	261,86	239,59	168,66	146,39	22,27	15,21
1,5	3	42,08	92,45	83,77	50,37	41,69	8,68	20,82
2,0	40	96,78	208,75	189,64	111,97	92,86	19,11	20,58
2,5	4	34,73	78,07	66,35	43,34	31,62	11,72	37,07
3,0	106	96,08	245,86	202,55	149,78	106,47	43,31	40,68
3,5	5	42,97	83,59	67,17	40,62	24,20	16,42	67,85
4,0	109	97,96	184,81	151,69	86,85	53,73	33,12	61,64
4,5	6	41,60	86,22	71,69	44,62	30,09	14,53	48,29
5,0	105	97,89	176,67	147,29	78,78	49,40	29,38	59,47
5,5	7	42,82	82,51	68,17	39,69	25,35	14,34	56,57
6,0	36	96,88	182,86	150,69	85,98	53,81	32,17	59,78
6,5	8	42,15	83,84	68,80	41,69	26,65	15,04	56,44
7,0	45	97,81	213,31	171,36	115,50	73,55	41,95	57,04
7,5	9	41,89	83,44	68,30	41,55	26,41	15,14	57,33
8,0	15	78,17	192,24	151,98	114,07	73,81	40,26	54,55
8,5	10	40,18	89,18	71,94	49,00	31,76	17,24	54,28
9,0	59	93,75	215,25	172,46	121,50	78,71	42,79	54,36
9,5	11	41,10	83,76	68,60	42,66	27,50	15,16	55,13
10,0	100	95,40	225,32	181,56	129,92	86,16	43,76	50,79

Borehole no. TSH.B2-A **Oven temperature** 110°C **Duration:** 24 hours

Depth [m]	Bowl number [-]	Bowl weight [g]	Bowl + wet sample [g]	Bowl + dry sample [g]	Wet sample weight [g]	Dry sample weight [g]	Water in sample [g]	Water content [%]
0,2	12	42,95	92,51	82,54	49,56	39,59	9,97	25,18
0,5	13	38,89	80,57	73,30	41,68	34,41	7,27	21,13
1,0	11	78,25	239,90	216,04	161,65	137,79	23,86	17,32
1,5	14	38,89	82,07	74,72	43,18	35,83	7,35	20,51
2,0	34	76,50	164,43	150,90	87,93	74,40	13,53	18,19
2,5	15	41,79	82,51	75,69	40,72	33,90	6,82	20,12
3,0	48	96,50	217,57	193,89	121,07	97,39	23,68	24,31
3,5	16	34,91	76,43	60,81	41,52	25,90	15,62	60,31
4,0	104	96,69	176,08	148,98	79,39	52,29	27,10	51,83
4,5	17	36,38	77,15	63,46	40,77	27,08	13,69	50,55
5,0	56	96,57	232,25	184,71	135,68	88,14	47,54	53,94
5,5	18	42,04	86,42	71,22	44,38	29,18	15,20	52,09
6,0	44	96,73	219,94	176,32	123,21	79,59	43,62	54,81
6,5	19	37,66	82,17	66,01	44,51	28,35	16,16	57,00
7,0	19	96,09	213,87	171,01	117,78	74,92	42,86	57,21
7,5	20	37,02	79,20	64,01	42,18	26,99	15,19	56,28
8,0	13	96,30	192,11	156,46	95,81	60,16	35,65	59,26
8,5	21	25,74	67,41	52,99	41,67	27,25	14,42	52,92
9,0	101	95,85	175,75	148,07	79,90	52,22	27,68	53,01
9,5	22	37,52	78,98	64,47	41,46	26,95	14,51	53,84
10,0	96	94,06	221,13	175,89	127,07	81,83	45,24	55,29

Borehole no. TSH.B3-A **Oven temperature** 110°C **Duration:** 24 hours

Depth [m]	Bowl number [-]	Bowl weight [g]	Bowl + wet sample [g]	Bowl + dry sample [g]	Wet sample weight [g]	Dry sample weight [g]	Water in sample [g]	Water content [%]
0,2	23	25,96	66,33	55,30	40,37	29,34	11,03	37,59
0,5	24	27,75	75,12	66,80	47,37	39,05	8,32	21,31
1,0	99	95,92	203,14	187,23	107,22	91,31	15,91	17,42
1,5	25	26,22	70,03	63,24	43,81	37,02	6,79	18,34
2,0	63	94,37	206,85	190,41	112,48	96,04	16,44	17,12
2,5	26	25,59	66,29	57,08	40,70	31,49	9,21	29,25
3,0	32	76,42	194,41	163,64	117,99	87,22	30,77	35,28
3,5	27	23,88	63,90	48,88	40,02	25,00	15,02	60,08
4,0	42	96,97	189,95	159,21	92,98	62,24	30,74	49,39
4,5	28	24,17	65,37	50,49	41,20	26,32	14,88	56,53
5,0	110	98,79	209,68	168,58	110,89	69,79	41,10	58,89
5,5	29	27,00	70,16	54,80	43,16	27,80	15,36	55,25
6,0	29	77,24	167,95	138,75	90,71	61,51	29,20	47,47
6,5	30	27,19	67,88	54,41	40,69	27,22	13,47	49,49
7,0	98	96,63	230,48	184,19	133,85	87,56	46,29	52,87
7,5	31	24,98	68,19	53,25	43,21	28,27	14,94	52,85
8,0	39	96,03	198,24	163,56	102,21	67,53	34,68	51,35
8,5	32	24,68	66,13	51,25	41,45	26,57	14,88	56,00
9,0	57	96,18	200,75	164,93	104,57	68,75	35,82	52,10
9,5	33	24,93	72,42	56,29	47,49	31,36	16,13	51,43

B.3 Unit weight

For results of unit weight determination, see the tables below and the borehole profiles in Appendix A.

Borehole no. TSH.B1-A

Depth [m]	Height, total [cm]	Height, empty [cm]	Diameter, inner [cm]	B-tube + sample [g]	B-tube weight [g]	Sample weight [g]	Height, sample [cm]	Volume [cm^3]	Density [g/cm^3]	Unit weight [kN/m^3]
1,0	14,0	1,8	4,2	604	249	356	12,2	169	2,1	20,7
2,0	14,0	2,5	4,2	575	249	326	11,5	159	2,0	20,1
3,0*			4,2			122	5,1	71	1,7	16,9
4,0	14,0	0,0	4,2	565	248	317	14,0	194	1,6	16,0
5,0	14,0	3,1	4,2	590	334	256	10,9	151	1,7	16,6
6,0	14,0	0,0	4,2	572	252	321	14,0	194	1,7	16,2
7,0	14,0	2,1	4,2	613	335	279	11,9	165	1,7	16,6
8,0	14,0	0,8	4,2	646	336	310	13,2	183	1,7	16,7
9,0	14,0	1,1	4,2	541	249	293	12,9	179	1,6	16,1
10,0	14,0	1,7	4,2	535	247	288	12,3	170	1,7	16,6

* The soil is measured and weighted after removal from the B tube.

Borehole no. TSH.B2-A

Depth [m]	Height, total [cm]	Height, empty [cm]	Diameter, inner [cm]	B-tube + sample [g]	B-tube weight [g]	Sample weight [g]	Height, sample [cm]	Volume [cm^3]	Density [g/cm^3]	Unit weight [kN/m^3]
1,0	14,0	1,0	4,2	609	250	358	13,0	180	2,0	19,5
2,0	14,0	4,0	4,2	532	249	283	10,0	139	2,0	20,0
3,0*	14,0	8,7	4,2	473	335	139	5,3	73	1,9	18,5
4,0	14,0	2,1	4,2	623	335	288	11,9	165	1,7	17,2
5,0	14,0	2,5	4,2	526	250	276	11,5	159	1,7	17,0
6,0	14,0	0,0	4,2	577	249	328	14,0	194	1,7	16,6
7,0	14,0	1,2	4,2	549	252	297	12,8	177	1,7	16,4
8,0	14,0	0,0	4,2	575	251	324	14,0	194	1,7	16,4
9,0	14,0	2,1	4,2	535	249	286	11,9	165	1,7	17,0
10,0	14,0	0,0	4,2	578	249	329	14,0	194	1,7	16,7

* The B tube were not full upon delievery.

Borehole no. TSH.B3-A

Depth [m]	Height, total [cm]	Height, empty [cm]	Diameter, inner [cm]	B-tube + sample [g]	B-tube weight [g]	Sample weight [g]	Height, sample [cm]	Volume [cm^3]	Density [g/cm^3]	Unit weight [kN/m^3]
1,0*			4,2			250	8,5	118	2,1	20,9
2,0	14,0	1,7	4,2	695	335	359	12,3	170	2,1	20,7
3,0	14,0	2,4	4,2	517	247	270	11,6	161	1,7	16,5
4,0	14,0	1,0	4,2	495	198	298	13,0	180	1,7	16,2
5,0	14,0	2,2	4,2	519	248	270	11,8	163	1,7	16,2
6,0	14,0	1,3	4,2	562	249	313	12,7	176	1,8	17,4
7,0	14,0	2,9	4,2	515	248	267	11,1	154	1,7	17,0
8,0	14,0	0,0	4,2	583	251	332	14,0	194	1,7	16,8
9,0	14,0	0,0	4,2	585	250	334	14,0	194	1,7	16,9

* The soil is measured and weighted after removal from the B tube.

B.4 Atterberg limit

Liquid Limit, Plastic Limit and Plasticity Index of Soils - Fall-Cone Method

Identification		Geological description
Borehole	TSH.B1	CLAY, very high plasticity, fissured with slickensides, sl. calcareous, brownish-grey
Specimen no.	7AA	
Depth [m]	3.5	

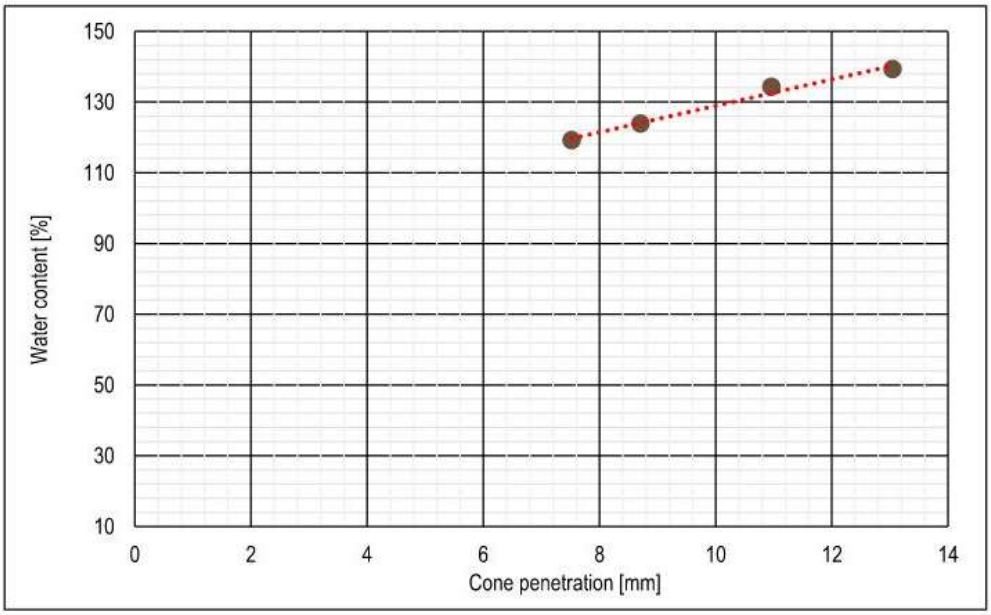

Results

Initial water content	$w_{initial}$	[%]	58.3
Liquid limit	w_L	[%]	128.9
Plastic limit	w_P	[%]	43.5
Plasticity Index	I_P	[%]	85.5
Particles >0.425 mm	-	[%]	0.0

Notes

Standard

Testing is carried out in accordance with DS/CEN ISO 17892-12:2018 - Fall-Cone Method.

Prepared :	NJO	Date :	2023-02-21	Project :	207165 Hinge
Checked :	NJO	Date :	2023-02-22	Report :	1
Approved :	LAB	Date :	2023-03-08	Subject :	Plasticity Index

Encl. no.: 1.1.1

Geo Copenhagen +45 4588 4444
Geo Aarhus +45 8627 3111

Rev: 0

Page 1/1

Liquid Limit, Plastic Limit and Plasticity Index of Soils - Fall-Cone Method

Identification		Geological description
Borehole	TSH.B1	CLAY, very high plasticity, calcareous, w. silt streaks, olive - light yellowish brown.
Specimen no.	10AA	
Depth [m]	4.9	

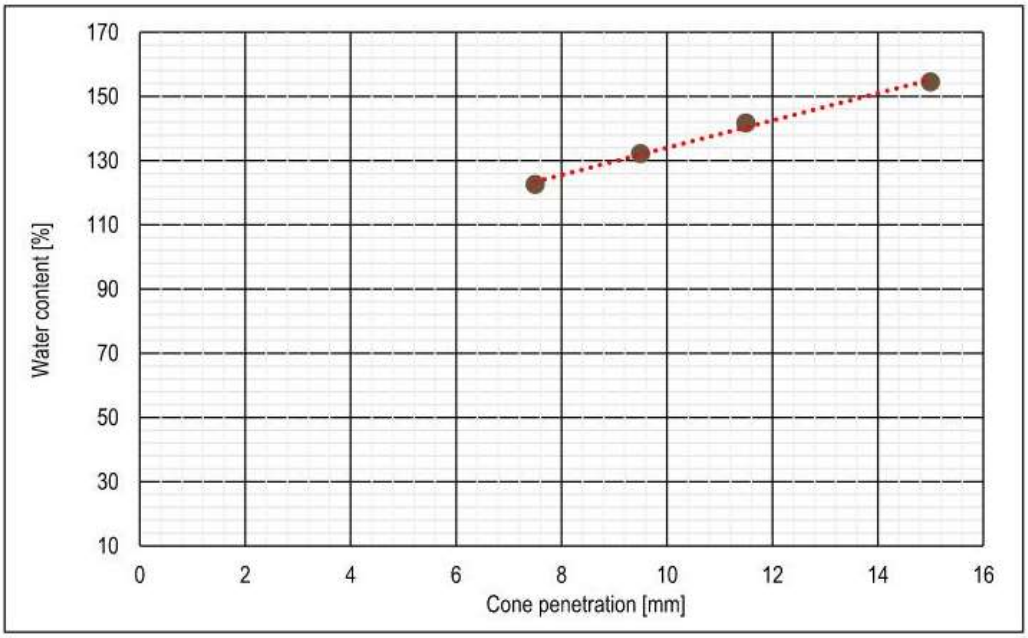

Results

Initial water content	$w_{initial}$	[%]	52.3
Liquid limit	w_L	[%]	134.0
Plastic limit	w_P	[%]	30.6
Plasticity Index	I_P	[%]	103.4
Particles >0.425 mm	-	[%]	0.0

Notes

Standard

Testing is carried out in accordance with DS/CEN ISO 17892-12:2018 - Fall-Cone Method.

Prepared :	RIM	Date :	2023-03-23	Project :	207165 Hinge
Checked :	VIJ	Date :	2023-03-24	Report :	1
Approved :	VIJ	Date :	2023-03-24	Subject :	Plasticity Index

Encl. no.: 1.1.6

Geo Copenhagen +45 4588 4444
Geo Aarhus +45 8627 3111

Liquid Limit, Plastic Limit and Plasticity Index of Soils - Fall-Cone Method

Identification		Geological description
Borehole	TSH.B1	CLAY, very high plasticity, fissured with slickensides, calcareous, grey
Specimen no.	14AA	
Depth [m]	7.0	

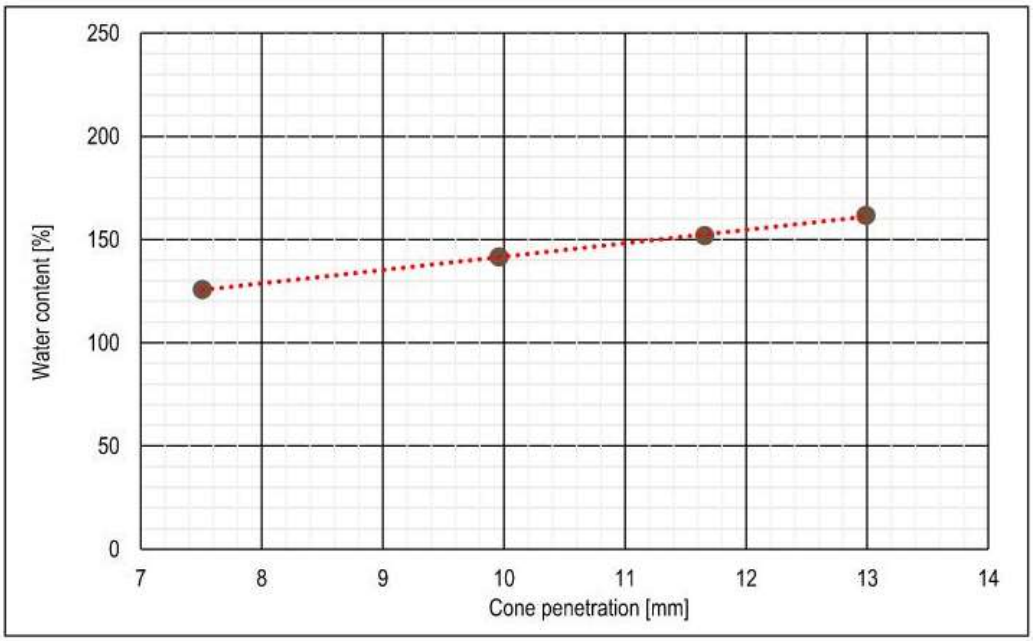

Results

Initial water content	$w_{initial}$	[%]	53.8
Liquid limit	w_L	[%]	141.7
Plastic limit	w_P	[%]	39.9
Plasticity Index	I_P	[%]	101.8
Particles >0.425 mm	-	[%]	0.0

Notes

Standard

Testing is carried out in accordance with DS/CEN ISO 17892-12:2018 - Fall-Cone Method.

Prepared :	NJO	Date :	2023-02-15	Project :	207165 Hinge	
Checked :	NJO	Date :	2023-02-17	Report :	-	Encl. no.: 1.1.2
Approved :	LAB	Date :	2023-03-08	Subject :	Plasticity Index	

Liquid Limit, Plastic Limit and Plasticity Index of Soils - Fall-Cone Method

Identification		Geological description
Borehole	TSH.B1	CLAY, very high plasticity, calcareous, grey
Specimen no.	17AA	
Depth [m]	8.5	

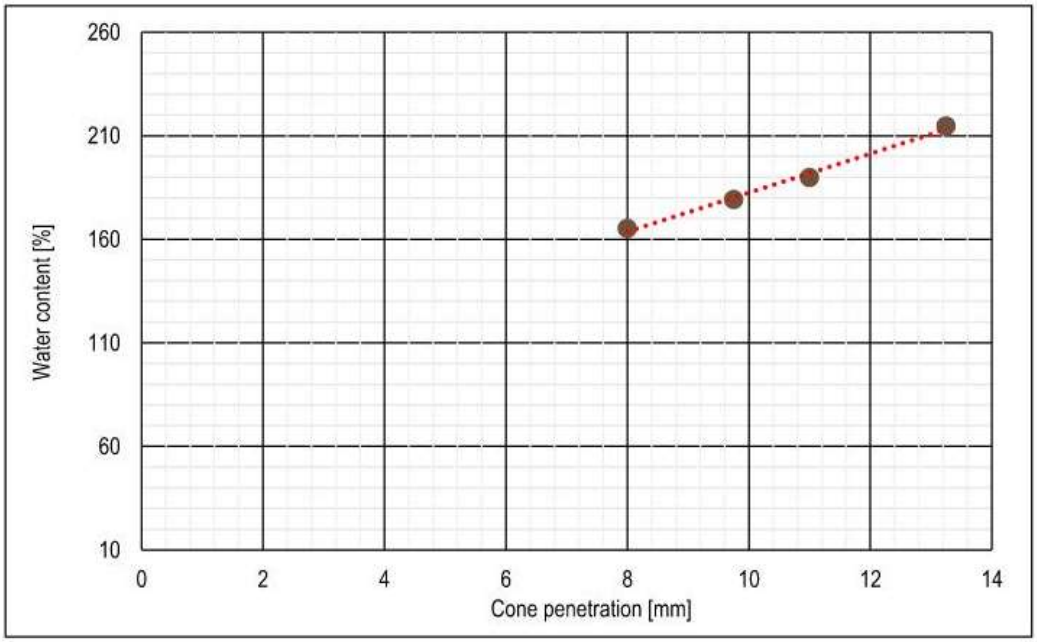

Results

Initial water content	$w_{initial}$	[%]	49.2
Liquid limit	w_L	[%]	182.5
Plastic limit	w_P	[%]	29.5
Plasticity Index	I_P	[%]	153.0
Particles >0.425 mm	-	[%]	0.0

Notes

Standard

Testing is carried out in accordance with DS/CEN ISO 17892-12:2018 - Fall-Cone Method.

Prepared :	RIM	Date :	2023-03-23	Project :	207165 Hinge	
Checked :	VIJ	Date :	2023-03-24	Report :	1	Encl. no.: 1.1.7
Approved :	VIJ	Date :	2023-03-24	Subject :	Plasticity Index	

Liquid Limit, Plastic Limit and Plasticity Index of Soils - Fall-Cone Method

Identification		Geological description
Borehole	TSH.B2	CLAY, very high plasticity, calcareous, olive grey
Specimen no.	17AA	
Depth [m]	8.5	

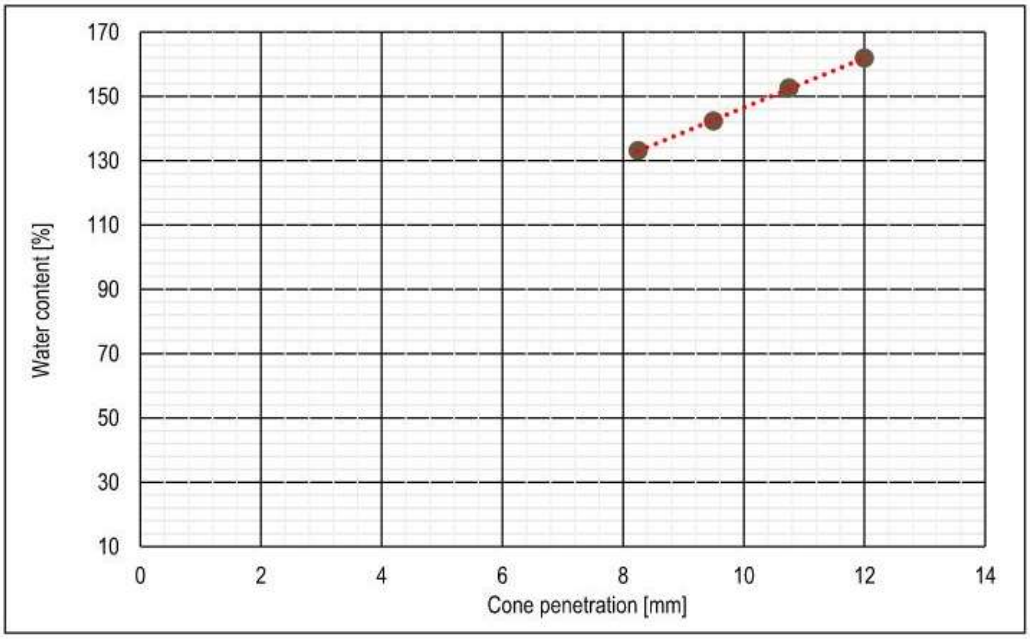

Results

Initial water content	$w_{initial}$	[%]	56.0
Liquid limit	w_L	[%]	146.5
Plastic limit	w_P	[%]	25.4
Plasticity Index	I_P	[%]	121.1
Particles >0.425 mm	-	[%]	0.6

Notes

Standard

Testing is carried out in accordance with DS/CEN ISO 17892-12:2018 - Fall-Cone Method.

Prepared :	EMJ	Date :	2023-03-24	Project :	207165 Hinge
Checked :	SAS	Date :	2023-03-27	Report :	1
Approved :	JSK	Date :	2023-03-27	Subject :	Plasticity Index

Encl. no.: 1.1.8

Liquid Limit, Plastic Limit and Plasticity Index of Soils - Fall-Cone Method

Identification		Geological description
Borehole	TSH.B2	CLAY, very high plasticity, fissured with slickensides, calcareous, grey
Specimen no.	17AA	
Depth [m]	8.6	

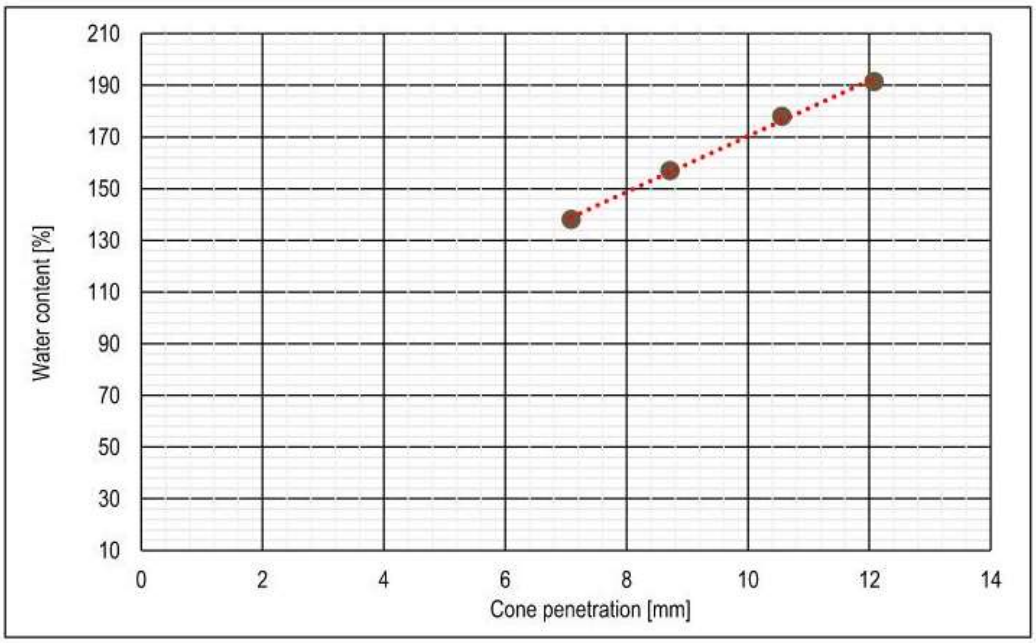

Results

Initial water content	$w_{initial}$	[%]	57.6
Liquid limit	w_L	[%]	170.3
Plastic limit	w_P	[%]	40.2
Plasticity Index	I_P	[%]	130.1
Particles >0.425 mm	-	[%]	0.0

Notes

Standard

Testing is carried out in accordance with DS/CEN ISO 17892-12:2018 - Fall-Cone Method.

Prepared :	NJO	Date :	2023-02-21	Project :	207165 Hinge	
Checked :	NJO	Date :	2023-02-22	Report :	1	Encl. no.: 1.1.3
Approved :	LAB	Date :	2023-03-08	Subject :	Plasticity Index	

Geo Copenhagen +45 4588 4444
Geo Aarhus +45 8627 3111

Liquid Limit, Plastic Limit and Plasticity Index of Soils - Fall-Cone Method

Identification		Geological description
Borehole	TSH.B3	CLAY, very high plasticity, calcareous, w. ochre specks, grey
Specimen no.	10AA	
Depth [m]	5.1	

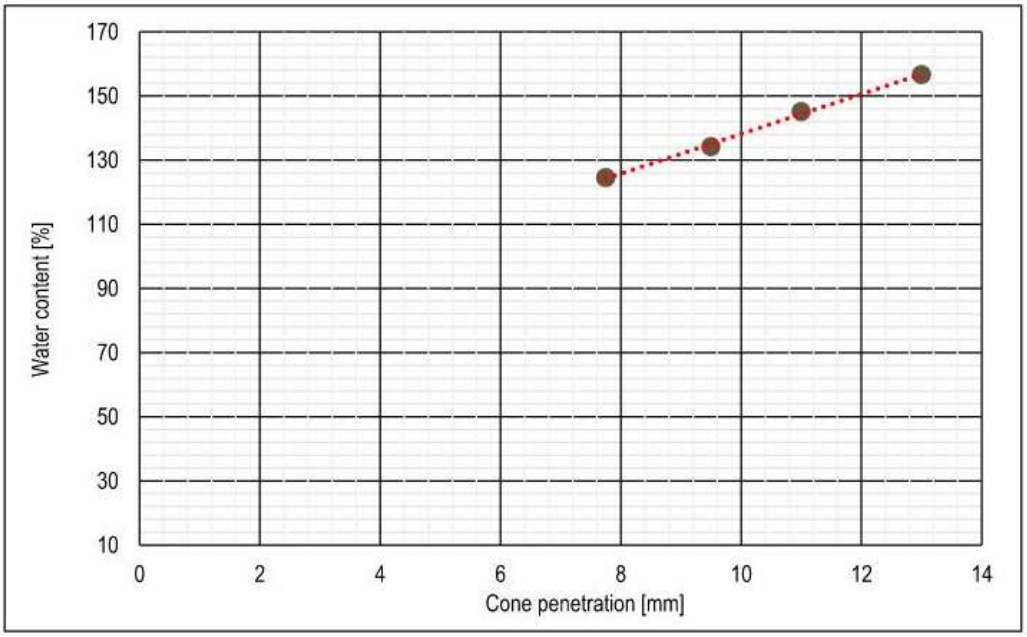

Results

Initial water content	$w_{initial}$	[%]	50.1
Liquid limit	w_L	[%]	138.2
Plastic limit	w_P	[%]	32.7
Plasticity Index	I_P	[%]	105.4
Particles >0.425 mm	-	[%]	0.0

Notes

Standard

Testing is carried out in accordance with DS/CEN ISO 17892-12:2018 - Fall-Cone Method.

Prepared :	RIM	Date : 2023-03-03	Project :	207165 Hinge	
Checked :	JSK	Date : 2023-03-03	Report :	1	Encl. no.: 1.1.4
Approved :	JSK	Date : 2023-03-03	Subject :	Plasticity Index	

Geo Copenhagen +45 4588 4444
Geo Aarhus +45 8627 3111

Liquid Limit, Plastic Limit and Plasticity Index of Soils - Fall-Cone Method

Identification		Geological description
Borehole	TSH.B3	CLAY, very high plasticity, calcareous, w. few silt streaks, dark greyish brown.
Specimen no.	13AA	
Depth [m]	6.3	

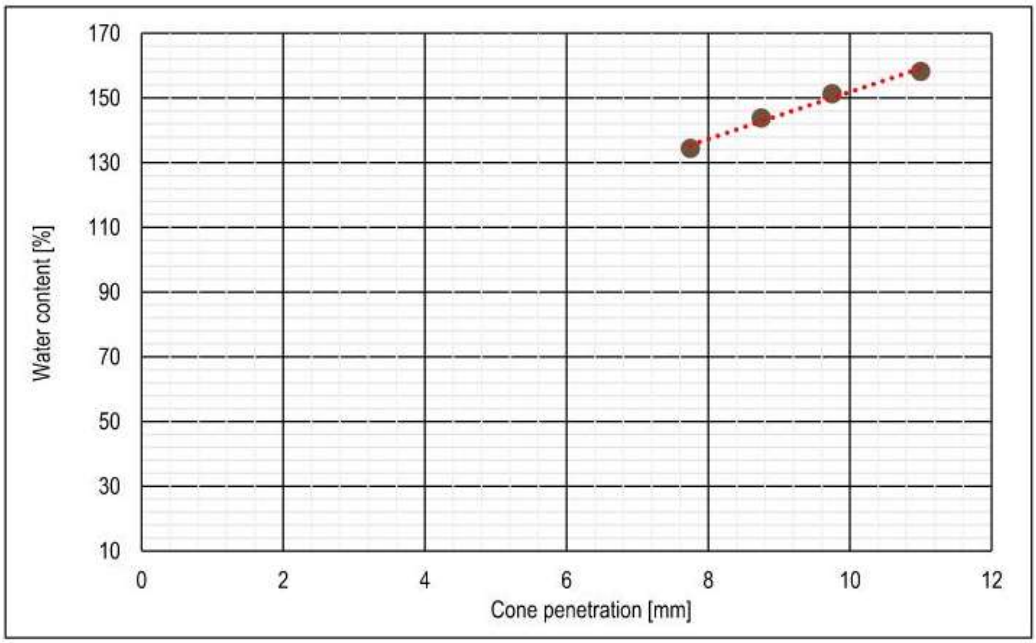

Results

Initial water content	$w_{initial}$	[%]	51.9
Liquid limit	w_L	[%]	151.9
Plastic limit	w_P	[%]	26.5
Plasticity Index	I_P	[%]	125.3
Particles >0.425 mm	-	[%]	0.0

Notes

Standard

Testing is carried out in accordance with DS/CEN ISO 17892-12:2018 - Fall-Cone Method.

Prepared :	EMJ	Date :	2023-03-24	Project :	207165 Hinge
Checked :	SAS	Date :	2023-03-27	Report :	1
Approved :	JSK	Date :	2023-03-27	Subject :	Plasticity Index

Encl. no.: 1.1.9

Liquid Limit, Plastic Limit and Plasticity Index of Soils - Fall-Cone Method

Identification		Geological description
Borehole	TSH.B3	CLAY, very high plasticity, very calcareous, grey
Specimen no.	17AA	
Depth [m]	8.4	

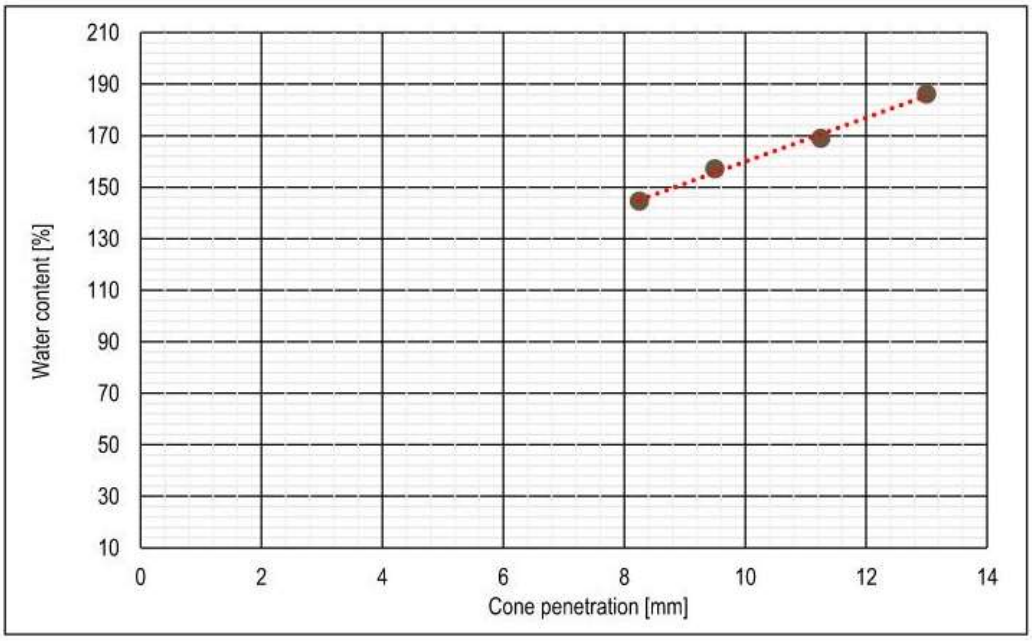

Results

Initial water content	$w_{initial}$	[%]	46.7
Liquid limit	w_L	[%]	159.9
Plastic limit	w_P	[%]	31.1
Plasticity Index	I_P	[%]	128.8
Particles >0.425 mm	-	[%]	0.1

Notes

Standard

Testing is carried out in accordance with DS/CEN ISO 17892-12:2018 - Fall-Cone Method.

Prepared :	RIM	Date :	2023-03-03	Project :	207165 Hinge	
Checked :	JSK	Date :	2023-03-03	Report :	1	Encl. no.: 1.1.5
Approved :	JSK	Date :	2023-03-03	Subject :	Plasticity Index	

B.5 Calcite content

Carbonate content								
Bor. No.	TSH.B1	TSH.B1	TSH.B2	TSH.B3	TSH.B3			
Sample no.	7AA	14AA	17AA	10AA	17AA			
Flask no.	49	22	1	708	787			
Dry sample g	5,39	5,006	5,698	6,786	7,415			
HCL (1,0) mL	50	75	75	100	100			
NaOH (1,0) mL	45,4	56,8	52,5	83,3	58,7			
Carb. Cont. %	4,27	18,18	19,74	12,30	27,85			

Carbonate content								
Bor. No.	TSH.B1	TSH.B1	TSH.B2	TSH.B3				
Sample no.	10AA	17AA	17AA	13AA				
Flask no.	317	R34	FC38	R56				
Dry sample g	6,559	5,987	5,663	5,887				
HCL (1,0) mL	100	100	100	100				
NaOH (1,0) mL	74,1	73,4	75,4	77,1				
Carb. Cont. %	19,74	22,21	21,72	19,45				

Carbonate content								
Bor. No.								
Sample no.								
Flask no.								
Dry sample g								
HCL (1,0) mL								
NaOH (1,0) mL								
Carb. Cont. %								

Testing according to:	DGF Bulletin 15

Comment:

Job : 207165 Hinge
Prepared : NJO Date : 2023-02-22
Checked : NJO Date : 2023-02-23
Approved : LAB Date : 2023-03-28 Report : 1 Encl. No. : 1.2.1 Page 1 / 1

Sødalsparken 12, DK-8220 Brabrand
Phone.: +45 8627 3111, www.geo.dk

Carbonate Content

B.6 Particle density

Particle Density

Sample no.	Depth [m]	Particle Density	Soil description
7AA_PD_TSH.B1	3.45-3.60	2,77	CLAY, medium to high plasticity, sandy, calcareous, w. sand smears, olive
17AA_PD_TSH.B3	8.39-8.47	2,78	CLAY, very high plasticity, very calcareous, grey

Standard

Paticle Density is performed according to DS/EN ISO 17892-3:2015

Prepared:	SAS	Date:	2023-02-28	Project :	207165 Hinge	
Checked:	JSK	Date:	2023-03-01	Report:	1	Enclosure no.: 1.5.1
Approved:	JSK	Date:	2023-03-01	Subject:	Particle Density	

B.7 Oedometer tests

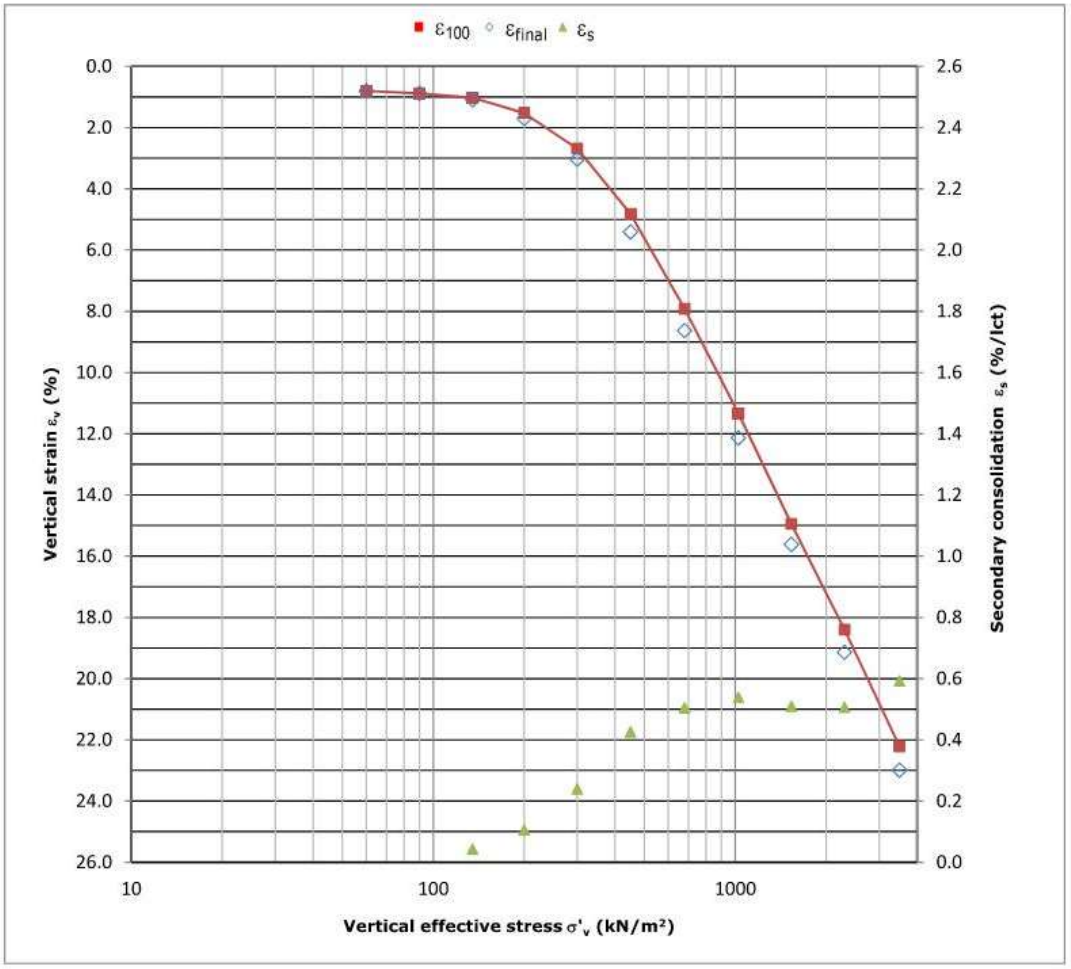

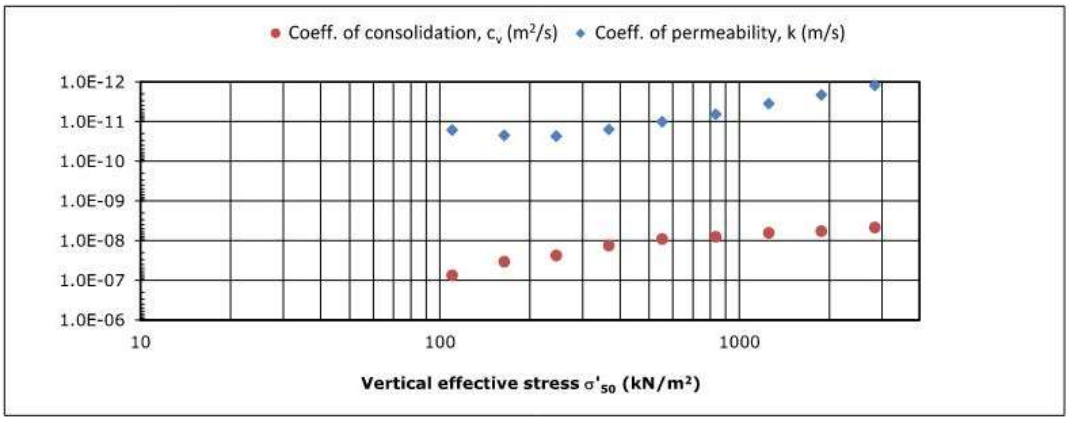

Geology: CLAY, very high plasticity, fissured with slickensides, calcareous, grey

Plasticity index, I_P	101.8	%
Carbonate content, Ka	18.2	%

GEO	Sødalsparken 12, 8220 Brabrand Phone: 8627 3111, www.geo.dk		Project:	207165 Hinge		
Performed	: LAB	Date : 2023-02-23	Subject:	Oedometer test	Boring no.	TSH.B1
Checked	:	Date :			Lab no.	14AA
Approved	: TRT	Date : 2023-02-23	Report	1	Enc. 1.3.1	Page 1/3

Test parameters

	σ'_v kN/m^2	ε_{final} %	ε_{100} %	ε_s %/lct	σ'_{50} kN/m^2	c_v m^2/s	k m/s
*	60	0.80	0.80				
**	90	0.88	0.88				
	135	1.09	1.03	0.043	110	7.5E-08	1.6E-11
	200	1.70	1.53	0.106	164	3.4E-08	2.2E-11
	300	3.03	2.69	0.240	245	2.4E-08	2.3E-11
	450	5.41	4.82	0.426	367	1.3E-08	1.6E-11
	680	8.63	7.92	0.505	553	9.1E-09	1.0E-11
	1025	12.14	11.33	0.539	835	8.0E-09	6.5E-12
	1535	15.62	14.95	0.510	1254	6.4E-09	3.6E-12
	2300	19.14	18.40	0.507	1879	5.8E-09	2.1E-12
	3500	22.99	22.22	0.593	2837	4.7E-09	1.2E-12

*adding water - tendency to swell;next load step applied, $\varepsilon_{100} = \varepsilon_{final}$
**tendency to swell; next load step applied, $\varepsilon_{100} = \varepsilon_{final}$

Bor. No.	TSH.B1		Depth:	7.0	m
Lab. No.	14AA		Level:		m DVR90
Area	28.27	cm^2	c_{fv}	210	kN/m^2
Height	24.0	mm	σ'_0	58	kN/m^2
e_0	1.51		σ'_{pc}	400-500	kN/m^2
ρ_0	1.70	g/cm^3	$Q_{C(2300-3500)}$	20.9	(%/lcs)
w_0	53.8	%	$Q_{C(-)}$		(%/lcs)
Sr	99	%	$Q_{S(-)}$	-	(%/lcs)
$\rho_{s,\ estimate}$	2.77	g/cm^3	σ'_{pc}/σ'_0	-	OCR
Equipment	GDS		Temperature	22	°C

Method: Oedometer-test with incremental loading
Procedure: According to DS/CEN ISO/TS 17892-5 Part 5
Water in cell: Tap water
Type of cell: Fixed ring at initial loadning and floating ring during unloading/reloading.
$Q_c=\delta\varepsilon_{100}/\delta\log\sigma'_v$: Compression ratio. $Q_s=\delta\varepsilon_{100}/\delta\log\sigma'_{vS}$: Swelling ratio
c_v determined by sqrt(t)
The values of k and c_v is calculated at the average temperature in the laboratory as listed above.
σ'_{pc} is estimated with assistance from the methods Casagrande, Akai, Becker and Janbu.
Geological description is carried out by Geo.

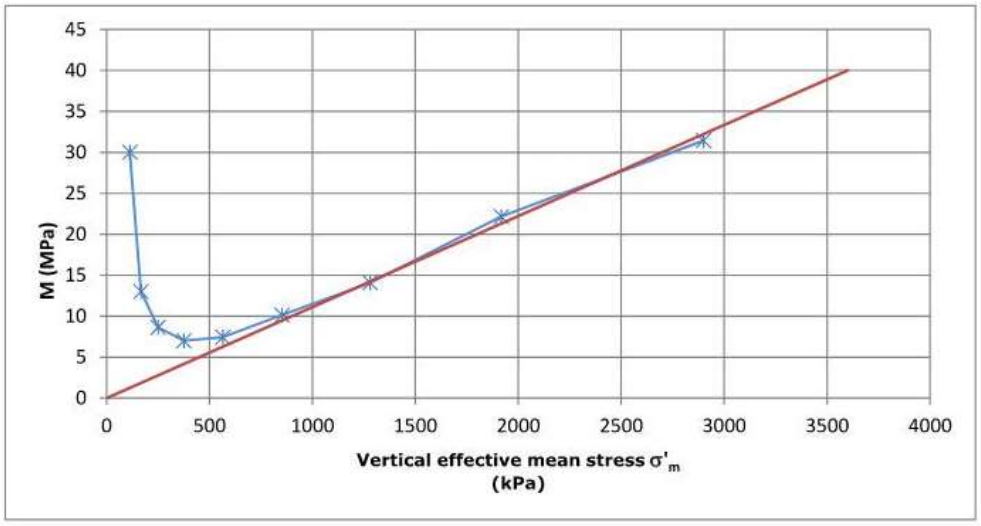

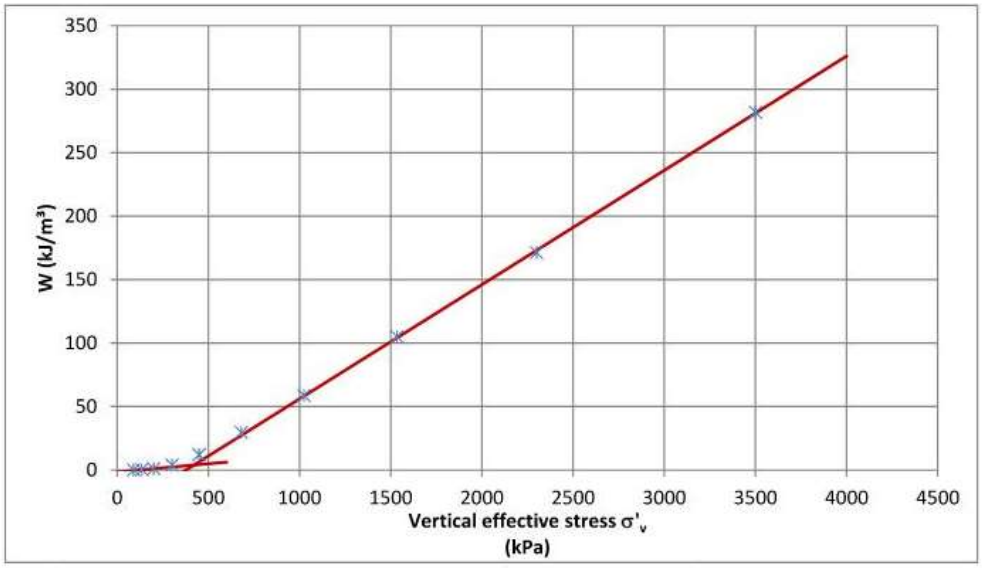

σ'_v kN/m²	ε_{100} %	W kJ/m³	σ'_m kN/m²	M MPa
60	0.80	-	-	-
90	0.88	0.1	75	38
135	1.03	0.2	113	30
200	1.53	1.1	168	13
300	2.69	4.0	250	9
450	4.82	12.0	375	7
680	7.92	29.5	565	7
1025	11.33	58.6	853	10
1535	14.95	104.8	1280	14
2300	18.40	171.1	1918	22
3500	22.22	281.7	2900	31

Note: determination of W og M are only based on loadsteps higher then $\sigma'_{o\ estimate}$

Geo Sødalsparken 12, 8220 Brabrand
Phone: 8627 3111, www.geo.dk

Project: 207165 Hinge

Performed	: LAB	Date : 2023-02-23	Subject:	Oedometer test	Boring no.	TSH.B1
Checked	:	Date :			Lab no.	14AA
Approved	: TRT	Date : 2023-02-23	Report	1	Enc. 1.3.1	Page: 3/3

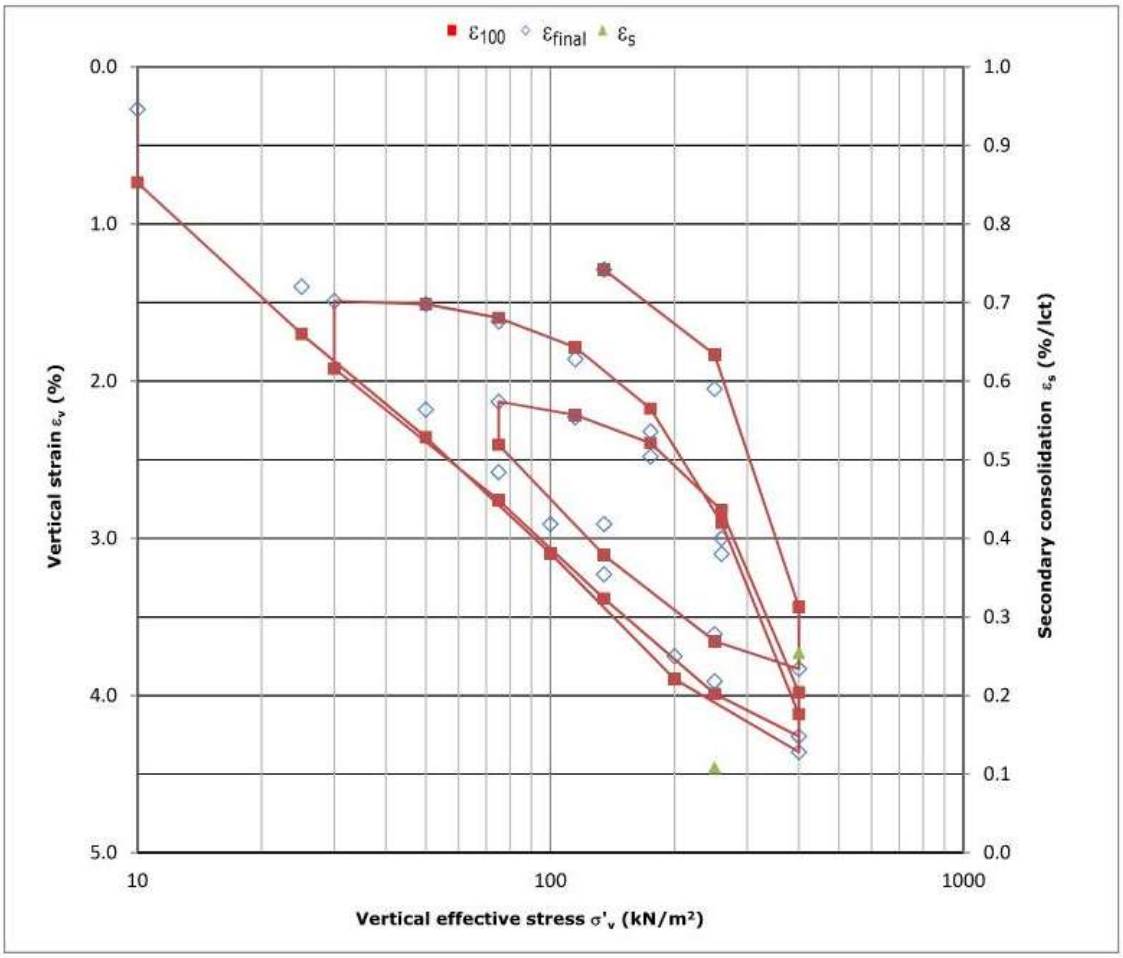

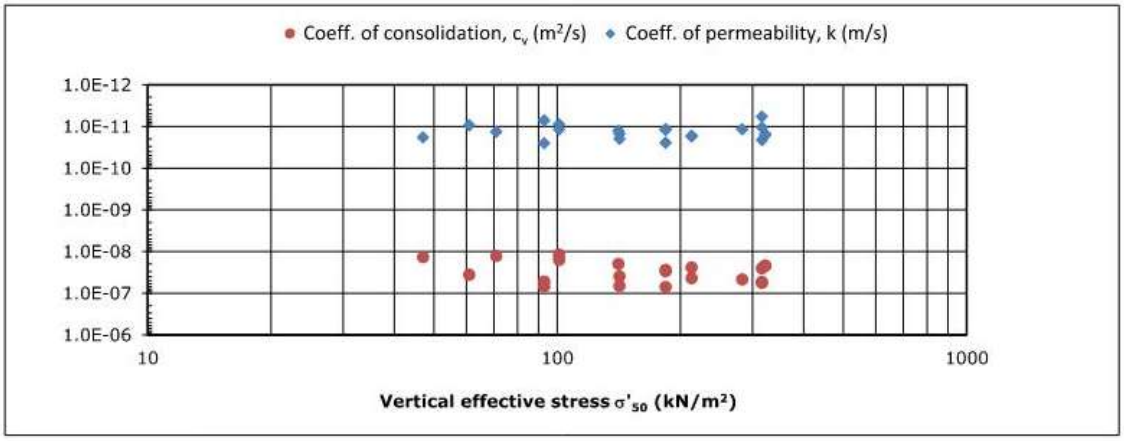

Geology: CLAY, very high plasticity, fissured with slickensides, calcareous, grey

Plasticity index, I_P	101.8	%
Carbonate content, Ka	18.2	%

Sødalsparken 12, 8220 Brabrand
Phone: 8627 3111, www.geo.dk

Project: 207165 Hinge

Performed	: LAB	Date : 2023-04-14	Subject:	Oedometer test	Boring no.	TSH.B1	
Checked	:	Date :			Lab no.	14AA	
Approved	: TRT	Date : 2023-0419	Report	1	Enc. 1.3.2	Page	1/3

Test parameters

	σ'_v kN/m^2	ε_{final} %	ε_{100} %	ε_s %/lct	σ'_{50} kN/m^2	c_v m^2/s	k m/s
*	135	1.29	1.29				
	250	2.05	1.83	0.108	184	7.1E-08	2.5E-11
	400	3.83	3.44	0.254	316	2.5E-08	2.1E-11
	250	3.61	3.65		316	5.5E-08	5.8E-12
	135	2.91	3.11		184	3.0E-08	1.2E-11
	75	2.13	2.41		101	1.2E-08	9.0E-12
	115	2.23	2.22		93	5.3E-08	7.2E-12
	175	2.48	2.39		142	6.7E-08	1.5E-11
	260	3.00	2.82		213	4.3E-08	1.7E-11
	400	4.26	3.98		322	2.2E-08	1.5E-11
	250	3.91	3.99		316	5.7E-08	1.1E-11
	135	3.23	3.38		184	2.7E-08	1.2E-11
	75	2.58	2.76		101	1.6E-08	1.2E-11
	30	1.49	1.92		47	1.4E-08	1.8E-11
**	50	1.51	1.51				
	75	1.62	1.60		61	3.6E-08	9.4E-12
	115	1.86	1.78		93	7.0E-08	2.5E-11
	175	2.32	2.17		142	4.0E-08	2.0E-11
	260	3.10	2.90		213	2.4E-08	1.7E-11
	400	4.36	4.12		322	2.2E-08	1.6E-11
	200	3.75	3.89		283	4.7E-08	1.2E-11
	100	2.91	3.09		141	2.0E-08	1.3E-11
	50	2.18	2.36		71	1.3E-08	1.4E-11
	25	1.40	1.70		35	1.1E-08	1.9E-11
	10	0.27	0.74		16	6.0E-09	2.3E-11

*adding water - timecurve not possible to interpret; $\varepsilon_{100} = \varepsilon_{final}$
**timecurve not possible to interpret

Bor. No.	TSH.B1		Depth:	6.9	m
Lab. No.	14AA		Level:		m DVR90
Area	28.27	cm^2	c_{fv}	210	kN/m^2
Height	24.0	mm	σ'_0	58	kN/m^2
e_0	1.47		σ'_{pc}		kN/m^2
ρ_0	1.71	g/cm^3	$Q_{C(-)}$		(%/lcs)
w_0	52.9	%	$Q_{S(25-10)}$	2.4	(%/lcs)
Sr	100	%	σ'_{pc}/σ'_0		OCR
$\rho_{s,\ estimate}$	2.77	g/cm^3	Temperature	22	°C
Equipment	GDS				

Method: Oedometer-test with incremental loading
Procedure: According to DS/CEN ISO/TS 17892-5 Part 5
Water in cell: Tap water
Type of cell: Fixed ring at initial loadning and floating ring during unloading/reloading.
$Q_c=\delta\varepsilon_{100}/\delta\log\sigma'_v$: Compression ratio. $Q_s=\delta\varepsilon_{100}/\delta\log\sigma'_{vs}$: Swelling ratio
c_v determined by sqrt(t)
The values of k and c_v is calculated at the average temperature in the laboratory as listed above.
Geological description is carried out by Geo

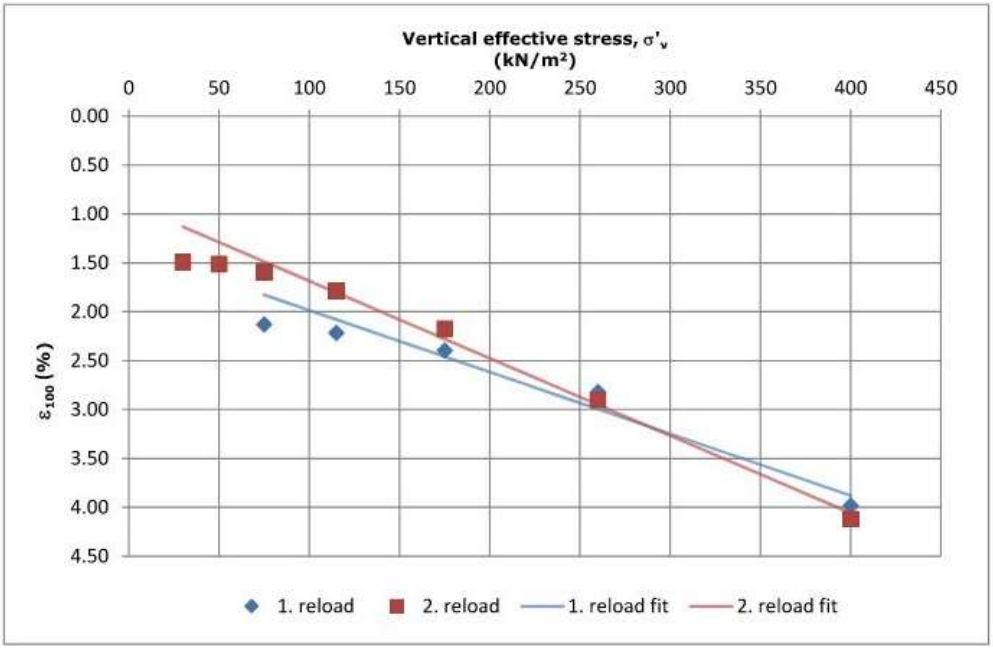

Data:

	σ'_a kN/m²	E_{oed} kN/m²		
1. reload.	75	15,800		
2. reload.	30	12,600		
3. reload.				

E_{oed} is determined from the reloading curves.

Linear fit is used for the reloading curves. The first point on the reloading curves is disregarded (this point is plotted as ε_{final}).

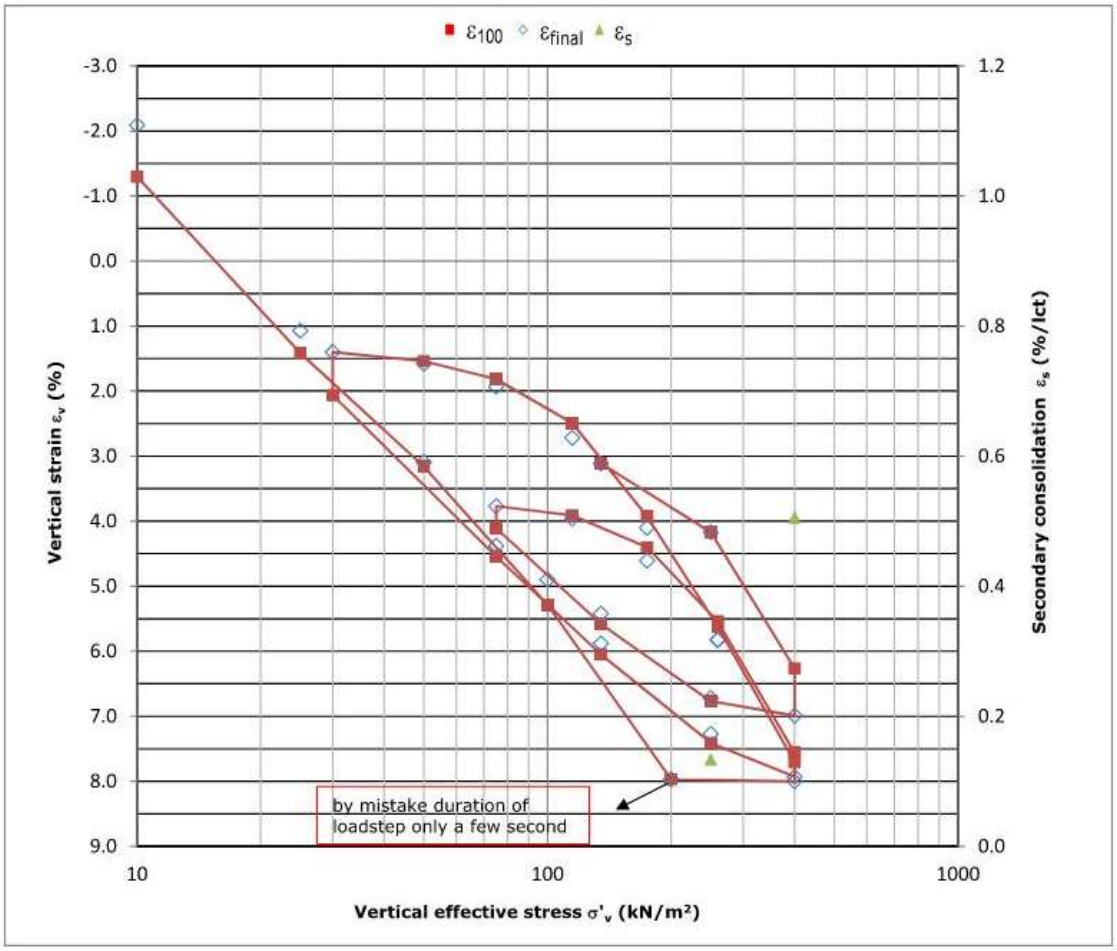

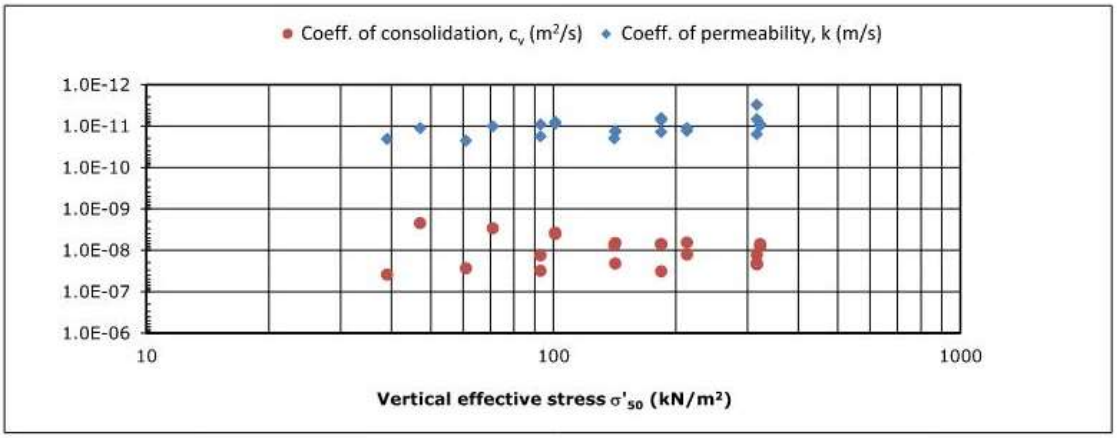

Geology: CLAY, very high plasticity, fissured with slickensides, calcareous, grey

Plasticity index, I_p	130.1	%
Carbonate content, Ka	19.7	%

Geo
Sødalsparken 12, 8220 Brabrand
Phone: 8627 3111, www.geo.dk

Project: 207165 Hinge

Performed	: LAB	Date : 2023-04-14	Subject:	Oedometer test		Boring no.	TSH.B2
Checked	:	Date :				Lab no.	17AA
Approved	: TRT	Date : 2023-04-19	Report	1		Enc. 1.3.3	Page 1/3

Test parameters

	σ'_v kN/m^2	ε_{final} %	ε_{100} %	ε_s %/lct	σ'_{50} kN/m^2	c_v m^2/s	k m/s
*	135	3.11	3.11				
	250	4.17	4.17	0.134	184	3.2E-08	1.4E-11
	400	6.99	6.27	0.506	316	1.3E-08	1.6E-11
	250	6.72	6.77		316	2.1E-08	3.1E-12
	135	5.42	5.58		184	7.2E-09	6.5E-12
	75	3.77	4.11		101	3.8E-09	7.9E-12
	115	3.96	3.91		93	3.1E-08	9.2E-12
	175	4.61	4.40		142	2.1E-08	1.4E-11
	260	5.82	5.54		213	1.3E-08	1.3E-11
	400	7.93	7.56		322	8.1E-09	9.6E-12
	250	7.27	7.41		316	2.2E-08	7.0E-12
	135	5.88	6.05		184	7.2E-09	7.2E-12
	75	4.38	4.55		101	4.1E-09	8.8E-12
	30	1.40	2.06		47	2.2E-09	1.1E-11
	50	1.58	1.54		39	3.9E-08	2.0E-11
	75	1.93	1.82		61	2.7E-08	2.3E-11
	115	2.72	2.50		93	1.3E-08	1.8E-11
	175	4.10	3.93		142	6.7E-09	1.3E-11
	260	5.83	5.62		213	6.5E-09	1.1E-11
	400	8.00	7.70		322	7.0E-09	9.2E-12
**	200	7.97	7.97				
	100	4.90	5.29		141	7.6E-09	2.0E-11
	50	3.09	3.16		71	3.0E-09	1.0E-11
	25	1.07	1.41		35	2.3E-09	1.5E-11
	10	-2.09	-1.30		16	1.3E-09	2.0E-11

*adding water - timecurve not possible to interpret; $\varepsilon_{100} = \varepsilon_{final}$
**by mistake duration of loadstep only a few seconds

Bor. No.	TSH.B2		Depth:	8.6	m
Lab. No.	17AA		Level:		m DVR90
Area	28.27	cm^2	c_{fv}	330	kN/m^2
Height	24.0	mm	σ'_0	71	kN/m^2
e_0	1.61		σ'_{pc}		kN/m^2
ρ_0	1.67	g/cm^3	$Q_{C(\cdot)}$		(%/lcs)
w_0	57.6	%	$Q_{S(25\text{-}10)}$	6.8	(%/lcs)
Sr	99	%	σ'_{pc}/σ'_0		OCR
$\rho_{s,\ estimate}$	2.77	g/cm^3	Temperature	22	°C
Equipment	GDS				

Method: Oedometer-test with incremental loading
Procedure: According to DS/CEN ISO/TS 17892-5 Part 5
Water in cell: Tap water
Type of cell: Fixed ring at initial loadning and floating ring during unloading/reloading.
$Q_c=\delta\varepsilon_{100}/\delta\log\sigma'_v$: Compression ratio. $Q_s=\delta\varepsilon_{100}/\delta\log\sigma'_{vS}$: Swelling ratio
c_v determined by sqrt(t)
The values of k and c_v is calculated at the average temperature in the laboratory as listed above.
Geological description is carried out by Geo

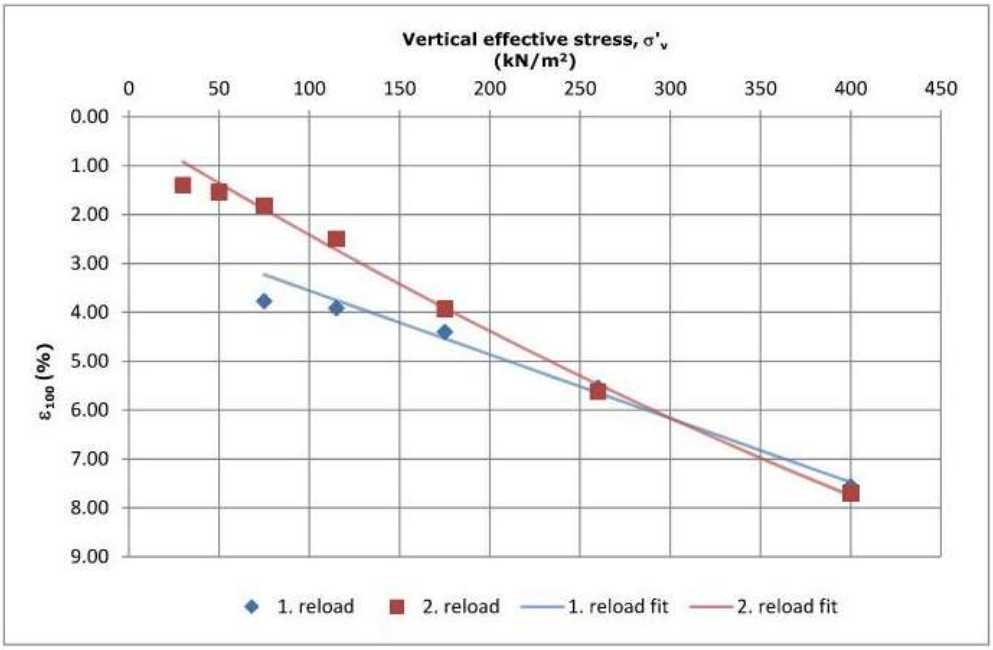

Data:

	σ'_a kN/m²	$E_{oed, \Delta 50\ kPa}$ kN/m²	$E_{oed, \Delta 100\ kPa}$ kN/m²	$E_{oed, \Delta 200\ kPa}$ kN/m²
1. reload.	75	7,700	7,700	7,700
2. reload.	30	4,600	4,800	5,000
3. reload.				

E_{oed} is determined from the reloading curves for an additional stress of 50, 100 and 200 kPa respectively

Polynomial fit is used for the reloading curve from 30 kPa while linear fit is used for the reloading curve from 75 kPa. The first point on the reloading curves is disregarded (this point is plotted as ε_{final}).

B.8 Triaxial tests

Consolidated Isotropically Undrained Triaxial Compression Test with Measurement of Pore Pressure

Identification		Geological description
Borehole	TSH.B1	CLAY, medium to very high plasticity, sandy, calcareous, w. sand smears, olive
Specimen no.	7AA	
Depth [m]	3.5	

Specimen dimensions, classification parameters and in-situ conditions

H	70	mm	$p'_{v0,\ est.}$	62	kPa	e	1.608	-
D	70	mm	$p'_{pc,\ est.}$	240	kPa	ρ_{bulk}	1.66	g/cm^3
V	269	cm^3	S_r	96.7	%	ρ_{dry}	1.06	g/cm^3
$w_{initial}$	56.1	%	w_{after}	54.5	%	$\rho_{s,\ est.}$	2.77	g/cm^3

Test setup and test conditions

Pore water	De-aired tap water	Temperature	20.3	°C
Cell water	Tap water	Back pressure	600	kPa
End pistons	Smooth	Skempton B-value	0.99	-
Drainage conditions	Dry side drains and filters	Specimen condition	Intact	

Chronological presentation of test sequence

Test phases	σ'_A [kPa]	σ'_R [kPa]	ε_A [%]	ε_{sA} [%]	ε_V [%]	σ'_R/σ'_A [-]	Rate
1) Initial loading, LVDT zeroed	18	17	0.0	-	-	0.94	200 kPa/hr
2) Saturation w. back pressure	59	57	0.8	-	-	0.97	100 kPa/hr
3) Consolidation, isotropic	239	242	3.8	-	7.0	1.01	1000 kPa/hr
4) Unloading and time curve	66	63	3.0	-	3.7	0.95	1000 kPa/hr
5a) Shear failure at 10 % add. strain	257	52	12.7	10.0	3.8	0.20	0.29 %/hr
5b) Shear failure at max $\sigma_A - \sigma_R$	257	51	12.5	9.9	3.8	0.20	0.29 %/hr

Results and interpretations

c_u at 5a)	[kPa]	103
c_u at 5b)	[kPa]	103
φ'	[°]	-
c'	[kPa]	-

Sketch of failure mode

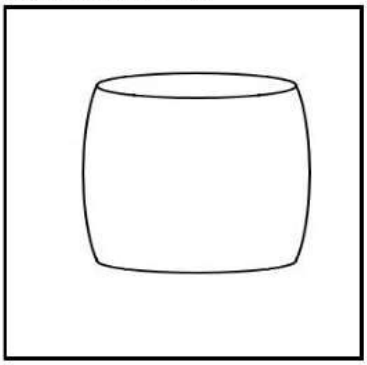

Notes

Testing is carried out in accordance with DS/EN ISO 17892-9:2018.

The standard prescribes a height:diameter ratio of 2:1 and not 1:1 as used here.

Consolidated Isotropically Undrained Triaxial Compression Test with Measurement of Pore Pressure

Identification		Geological description
Borehole	TSH.B1	CLAY, medium to very high plasticity, sandy, calcareous, w. sand smears, olive
Specimen no.	7AA	
Depth [m]	3.46	

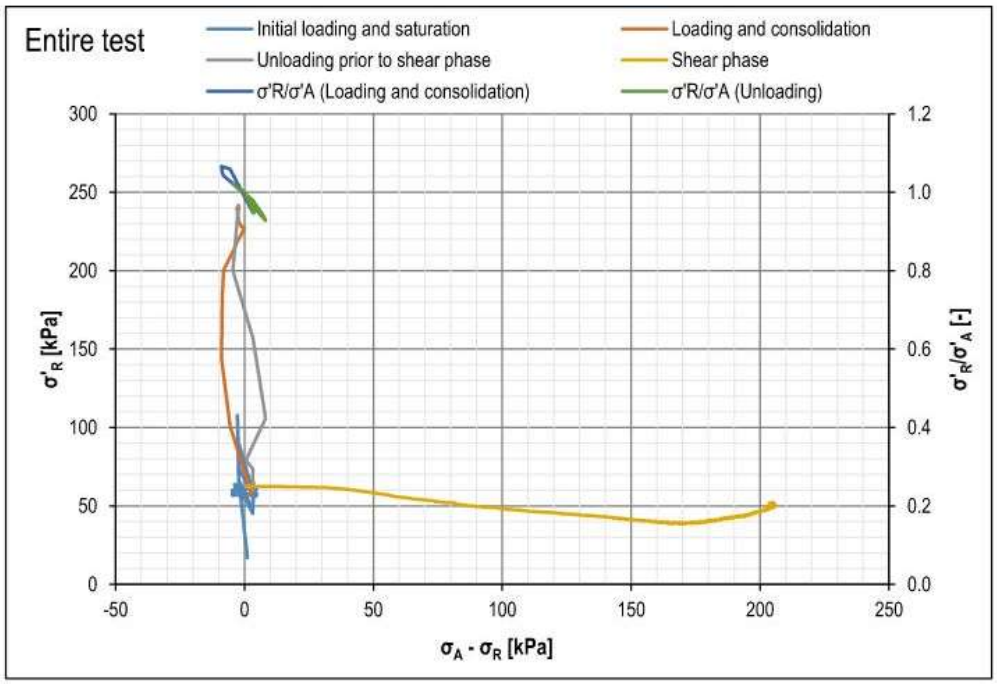

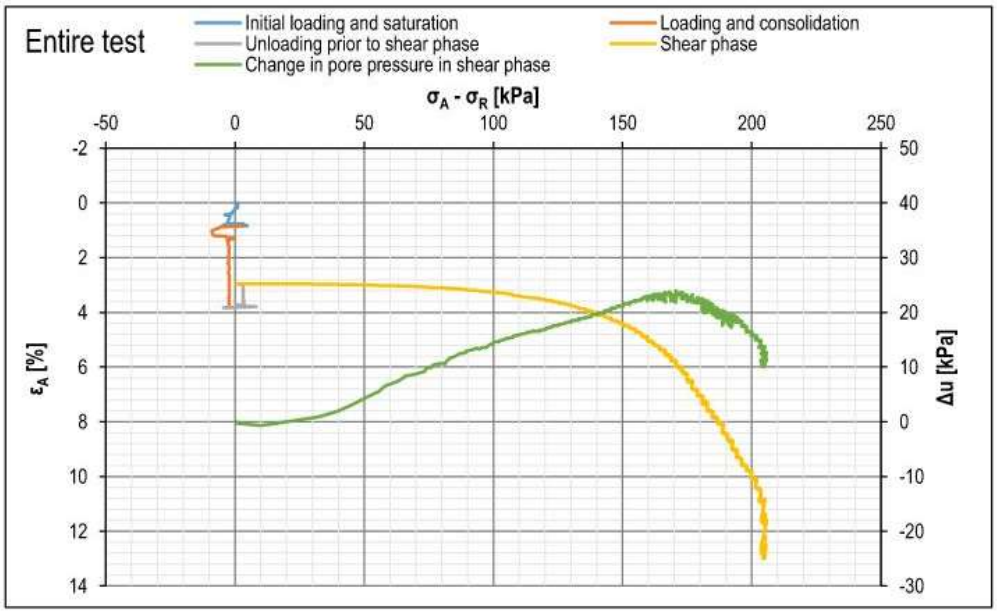

Prepared :	AMB	Date :	08-03-2023	Project : 207165 Hinge	
Checked :	JBR	Date :	10-03-2023	Report : 1	Encl. no.: 1.4.1
Approved :	SPL	Date :	14-03-2023	Subject : Triaxial test, CIUc	

Consolidated Isotropically Undrained Triaxial Compression Test with Measurement of Pore Pressure

Identification		Geological description
Borehole	TSH.B1	CLAY, medium to very high plasticity, sandy, calcareous, w. sand smears, olive
Specimen no.	7AA	
Depth [m]	3.46	

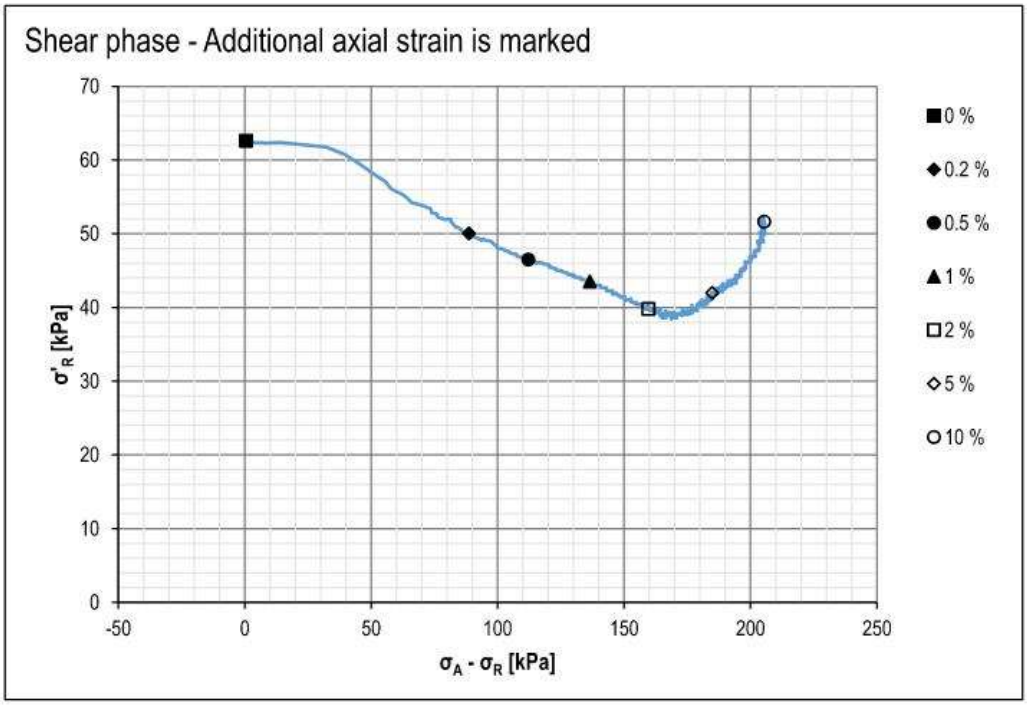

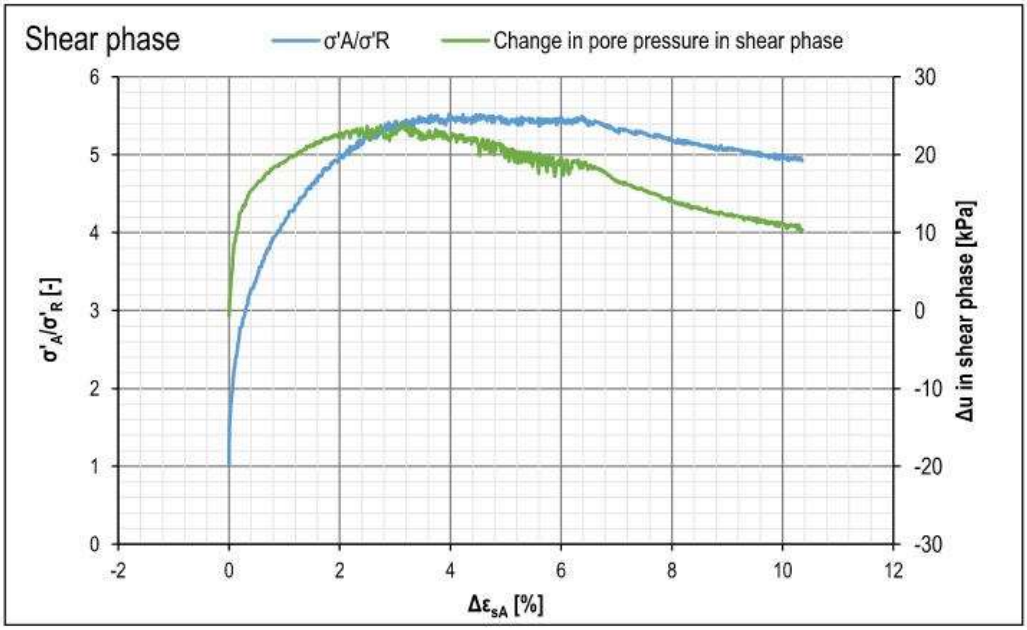

Prepared :	AMB	Date :	08-03-2023	Project : 207165 Hinge	
Checked :	JBR	Date :	10-03-2023	Report : 1	Encl. 1.4.1
Approved :	SPL	Date :	14-03-2023	Subject : Triaxial test, CIUc	
Geo		Geo Copenhagen		+45 4588 4444	Rev: 0
		Geo Aarhus		+45 8627 3111	Page 3/5

Consolidated Isotropically Undrained Triaxial Compression Test with Measurement of Pore Pressure

Identification		Geological description
Borehole	TSH.B1	CLAY, medium to very high plasticity, sandy, calcareous, w. sand smears, olive
Specimen no.	7AA	
Depth [m]	3.46	

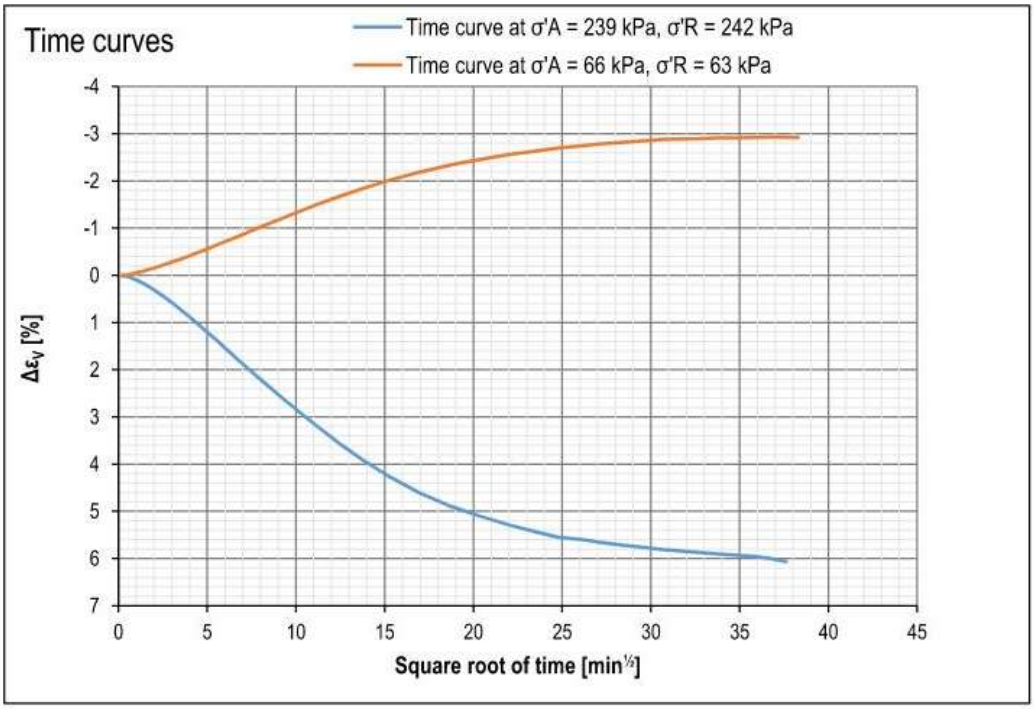

Prepared :	AMB	Date :	08-03-2023	Project : 207165 Hinge	
Checked :	JBR	Date :	10-03-2023	Report : 1	Encl. no.: 1.4.1
Approved :	SPL	Date :	14-03-2023	Subject : Triaxial test, CIUc	
Geo		Geo Copenhagen		+45 4588 4444	Rev: 0
		Geo Aarhus		+45 8627 3111	Page 4/5

Consolidated Isotropically Undrained Triaxial Compression Test with Measurement of Pore Pressure

Identification		Geological description
Borehole	TSH.B1	CLAY, medium to very high plasticity, sandy, calcareous, w. sand smears, olive
Specimen no.	7AA	
Depth [m]	3.46	

Photo before testing

Photo after testing

Prepared :	AMB	Date :	08-03-2023	Project : 207165 Hinge	
Checked :	JBR	Date :	10-03-2023	Report : 1	Encl. no.: 1.4.1
Approved :	SPL	Date :	14-03-2023	Subject : Triaxial test, CIUc	
GEO		Geo Copenhagen		+45 4588 4444	Rev: 0
		Geo Aarhus		+45 8627 3111	Page 5/5

Consolidated Isotropically Undrained Triaxial Compression Test with Measurement of Pore Pressure

Identification		Geological description
Borehole	TSH.B1	CLAY, very high plasticity, calcareous, w. silt streaks, olive - light yellowish brown
Specimen no.	10AA	
Depth [m]	4.9	

Specimen dimensions, classification parameters and in-situ conditions

H	70	mm	$\sigma'_{v0,\ est.}$	75	kPa	e	1.532	-
D	70	mm	$\sigma'_{pc,\ est.}$	240	kPa	ρ_{bulk}	1.68	g/cm^3
V	269	cm^3	S_r	97.2	%	ρ_{dry}	1.09	g/cm^3
$w_{initial}$	53.7	%	w_{after}	54.7	%	$\rho_{s,\ measured}$	2.77	g/cm^3

Test setup and test conditions

Pore water	De-aired tap water	Temperature	21.8	°C
Cell water	Tap water	Back pressure	697	kPa
End pistons	Smooth	Skempton B-value	0.95	-
Drainage conditions	Dry side drains and filters	Specimen condition	Intact	

Chronological presentation of test sequence

Test phases	σ'_A [kPa]	σ'_R [kPa]	ε_A [%]	ε_{sA} [%]	ε_V [%]	σ'_R/σ'_A [-]	Rate
1) Initial loading, LVDT zeroed	19	18	0.0	-	-	0.94	200 kPa/hr
2) Saturation w. back pressure	77	76	0.7	-	-	0.99	100 kPa/hr
3) Consolidation, isotropic	238	241	2.6	-	4.0	1.01	1000 kPa/hr
4) Unloading and time curve	77	76	1.4	-	0.9	0.98	1000 kPa/hr
5a) Shear failure at 10 % add. strain	256	73	11.3	10.0	0.7	0.29	0.33 %/hr
5b) Shear failure at max σ_A - σ_R	258	73	11.4	10.1	0.7	0.28	0.33 %/hr

Results and interpretations

c_u at 5a)	[kPa]	92
c_u at 5b)	[kPa]	92
φ'	[°]	-
c'	[kPa]	-

Sketch of failure mode

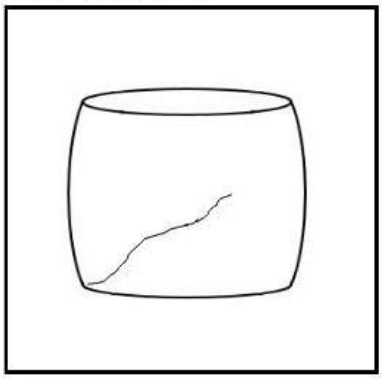

Notes

Testing is carried out in accordance with DS/EN ISO 17892-9:2018.

The standard prescribes a height:diameter ratio of 2:1 and not 1:1 as used here.

Consolidated Isotropically Undrained Triaxial Compression Test with Measurement of Pore Pressure

Identification		Geological description
Borehole	TSH.B1	CLAY, very high plasticity, calcareous, w. silt streaks, olive - light yellowish brown
Specimen no.	10AA	
Depth [m]	4.9	

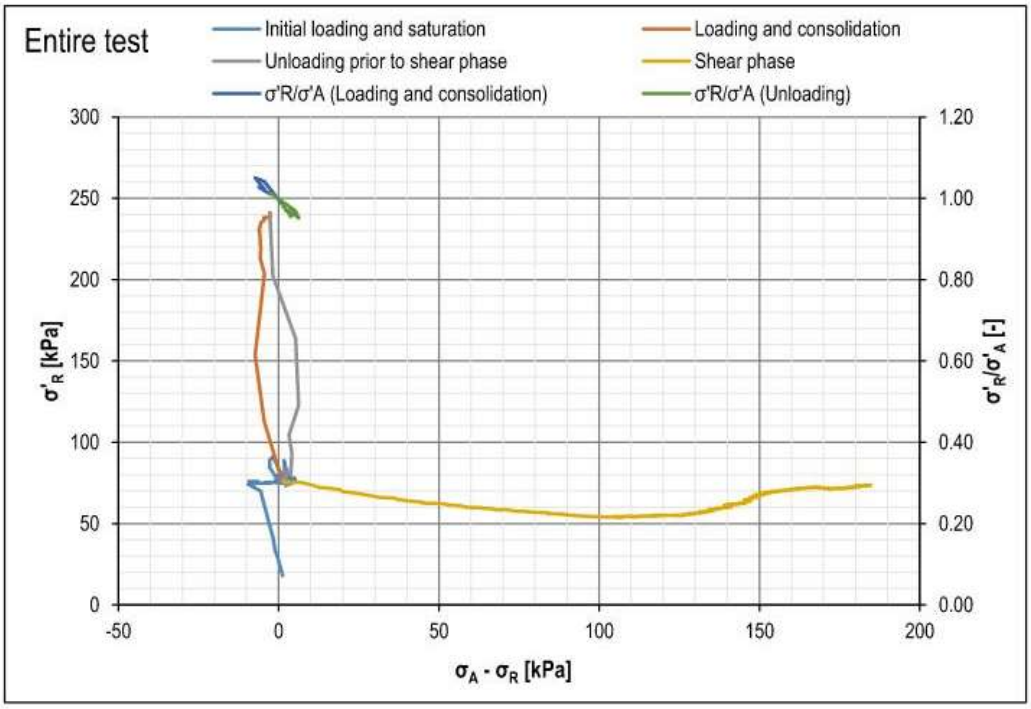

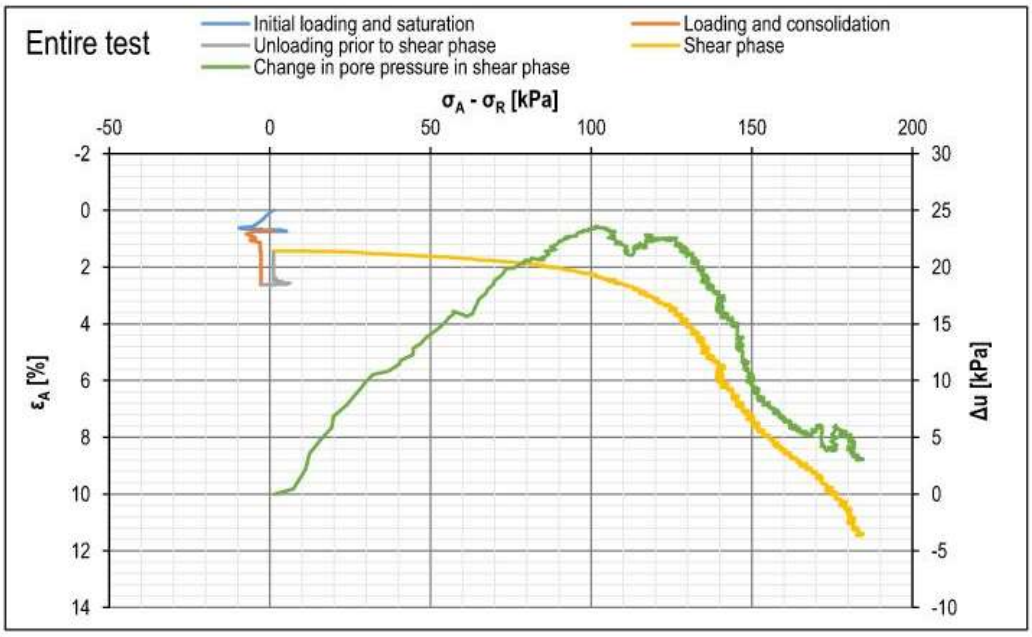

Prepared :	AMB	Date :	29-03-2023	Project : 207165 Hinge	
Checked :	JBR	Date :	13-04-2023	Report : 1	Encl. no.: 1.4.5
Approved :	SPL	Date :	13-04-2023	Subject : Triaxial test, CIUc	
		Geo Copenhagen		+45 4588 4444	Rev: 0
		Geo Aarhus		+45 8627 3111	Page 2/5

Consolidated Isotropically Undrained Triaxial Compression Test with Measurement of Pore Pressure

Identification		Geological description
Borehole	TSH.B1	CLAY, very high plasticity, calcareous, w. silt streaks, olive - light yellowish brown
Specimen no.	10AA	
Depth [m]	4.9	

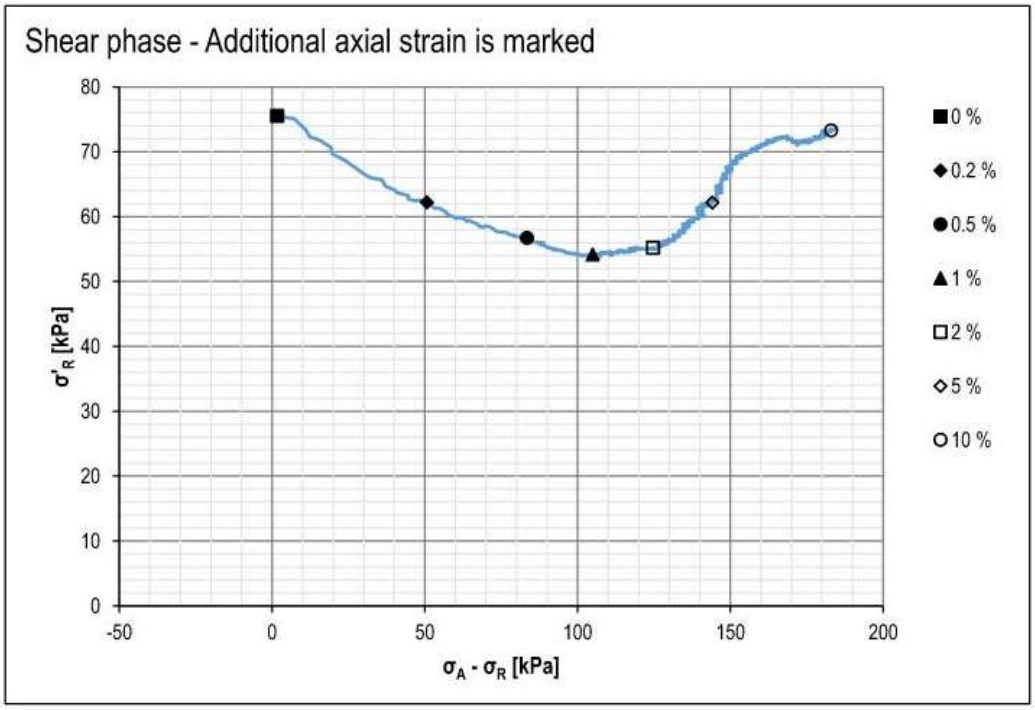

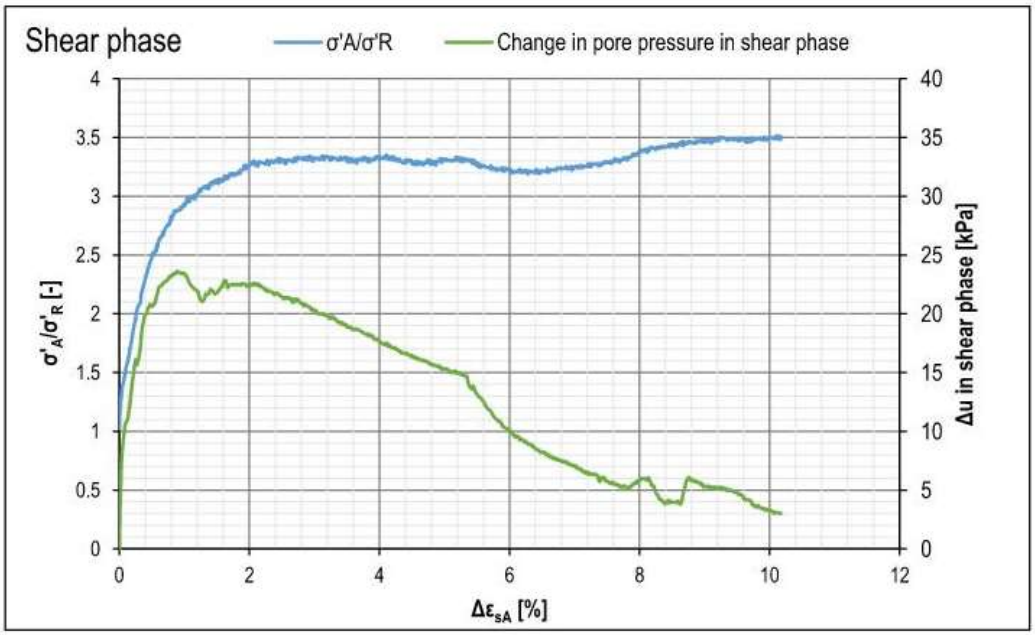

Prepared :	AMB	Date :	29-03-2023	Project : 207165 Hinge	
Checked :	JBR	Date :	13-04-2023	Report : 1	Encl. no.: 1.4.5
Approved :	SPL	Date :	13-04-2023	Subject : Triaxial test, CIUc	
Geo		Geo Copenhagen		+45 4588 4444	Rev: 0
		Geo Aarhus		+45 8627 3111	Page 3/5

Consolidated Isotropically Undrained Triaxial Compression Test with Measurement of Pore Pressure

Identification		Geological description
Borehole	TSH.B1	CLAY, very high plasticity, calcareous, w. silt streaks, olive - light yellowish brown
Specimen no.	10AA	
Depth [m]	4.9	

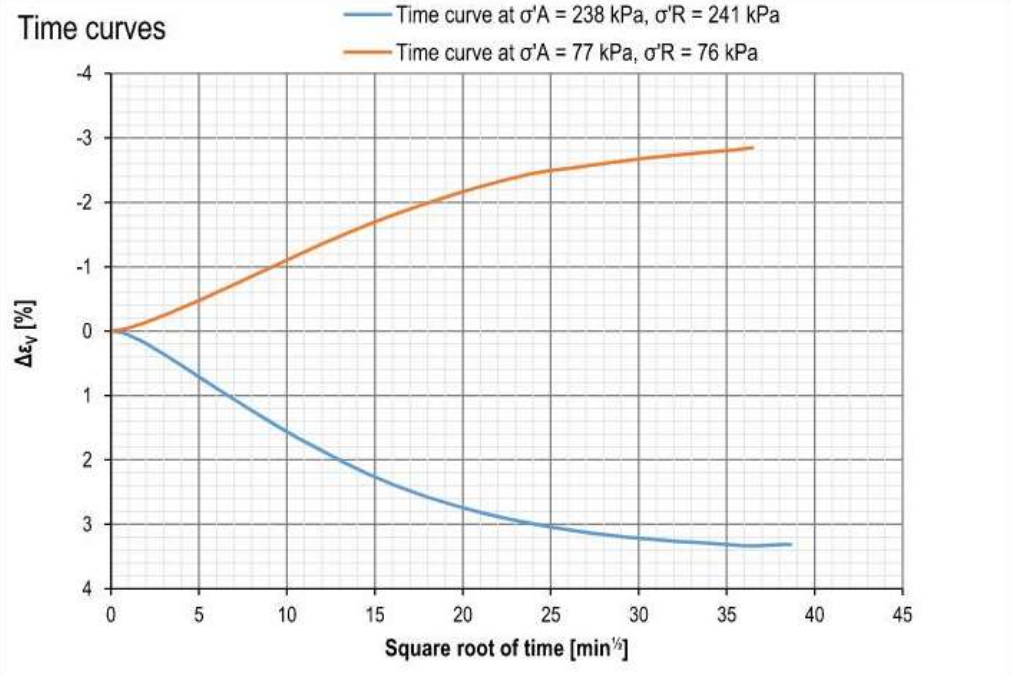

Consolidated Isotropically Undrained Triaxial Compression Test with Measurement of Pore Pressure

Identification		Geological description
Borehole	TSH.B1	CLAY, very high plasticity, calcareous, w. silt streaks, olive - light yellowish brown
Specimen no.	10AA	
Depth [m]	4.9	

Photo before testing

Photo after testing

Consolidated Isotropically Undrained Triaxial Compression Test with Measurement of Pore Pressure

Identification		Geological description
Borehole	TSH.B1	CLAY, medium to very high plasticity, sandy, calcareous, greenish grey
Specimen no.	14AA	
Depth [m]	6.8	

Specimen dimensions, classification parameters and in-situ conditions

H	70	mm	$p'_{v0,\ est.}$	97	kPa	e	1.601	-
D	70	mm	$p'_{pc,\ est.}$	240	kPa	ρ_{bulk}	1.64	g/cm^3
V	269	cm^3	S_r	93.7	%	ρ_{dry}	1.07	g/cm^3
$w_{initial}$	54.1	%	w_{after}	56.6	%	$\rho_{s,\ est.}$	2.77	g/cm^3

Test setup and test conditions

Pore water	De-aired tap water	Temperature	20.6	°C
Cell water	Tap water	Back pressure	598	kPa
End pistons	Smooth	Skempton B-value	0.95	-
Drainage conditions	Dry side drains and filters	Specimen condition	Intact	

Chronological presentation of test sequence

Test phases	σ'_A [kPa]	σ'_R [kPa]	ε_A [%]	ε_{sA} [%]	ε_V [%]	σ'_R/σ'_A [-]	Rate
1) Initial loading, LVDT zeroed	23	20	0.0	-	-	0.86	200 kPa/hr
2) Saturation w. back pressure	114	114	1.5	-	-	1.01	100 kPa/hr
3) Consolidation, isotropic	238	239	2.6	-	3.1	1.01	1000 kPa/hr
4) Unloading and time curve	121	119	2.1	-	1.2	0.99	1000 kPa/hr
5a) Shear failure at 10 % add. strain	294	85	11.9	10.0	1.3	0.29	0.33 %/hr
5b) Shear failure at max σ_A - σ_R	297	86	12.1	10.3	1.3	0.29	0.33 %/hr

Results and interpretations

c_u at 5a)	[kPa]	104
c_u at 5b)	[kPa]	106
φ'	[°]	-
c'	[kPa]	-

Sketch of failure mode

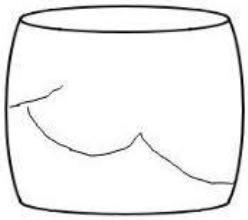

Notes

Testing is carried out in accordance with DS/EN ISO 17892-9:2018.

The standard prescribes a height:diameter ratio of 2:1 and not 1:1 as used here.

Consolidated Isotropically Undrained Triaxial Compression Test with Measurement of Pore Pressure

Identification		Geological description
Borehole	TSH.B1	CLAY, medium to very high plasticity, sandy, calcareous, greenish grey
Specimen no.	14AA	
Depth [m]	6.80	

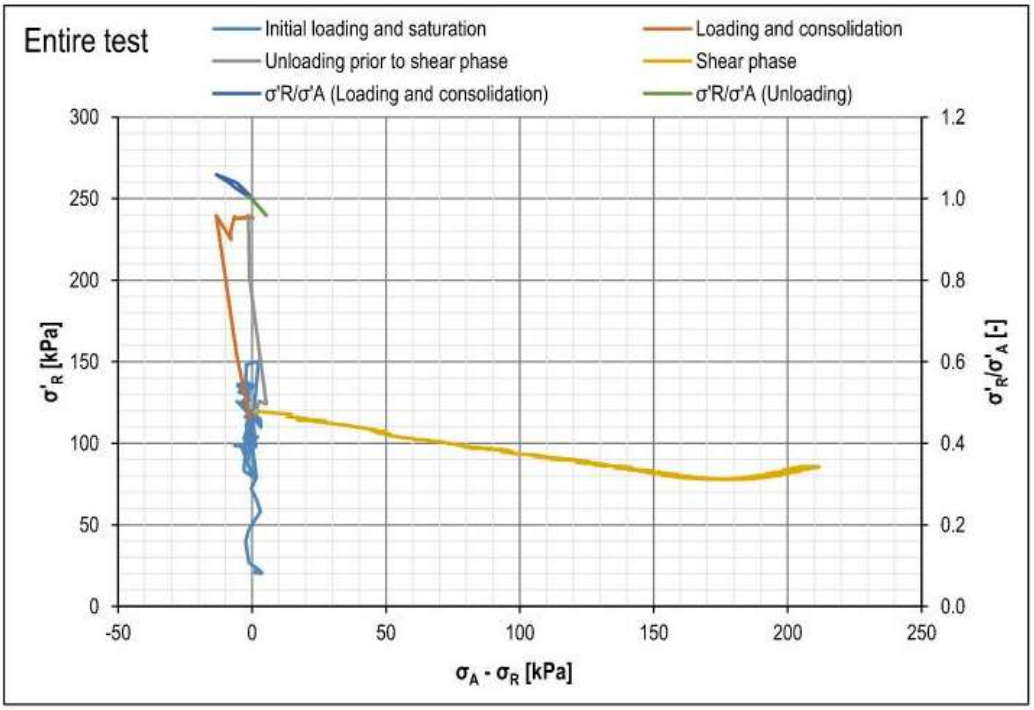

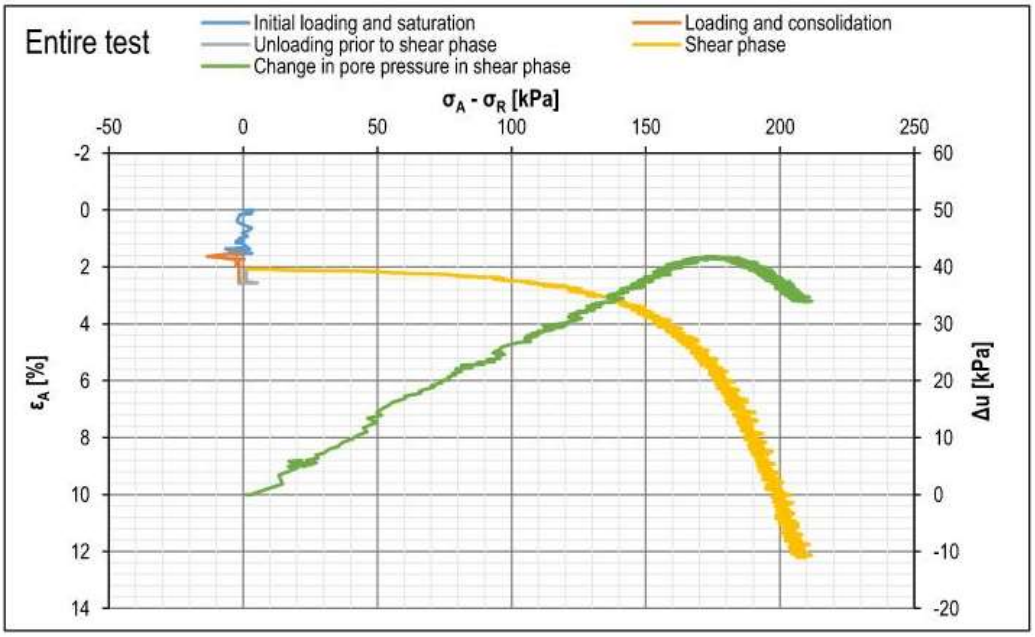

Prepared :	AMB	Date :	08-03-2023	Project :	207165 Hinge
Checked :	JBR	Date :	10-03-2023	Report :	1
Approved :	SPL	Date :	14-03-2023	Subject :	Triaxial test, CIUc

Consolidated Isotropically Undrained Triaxial Compression Test with Measurement of Pore Pressure

Identification		Geological description
Borehole	TSH.B1	CLAY, medium to very high plasticity, sandy, calcareous, greenish grey
Specimen no.	14AA	
Depth [m]	6.80	

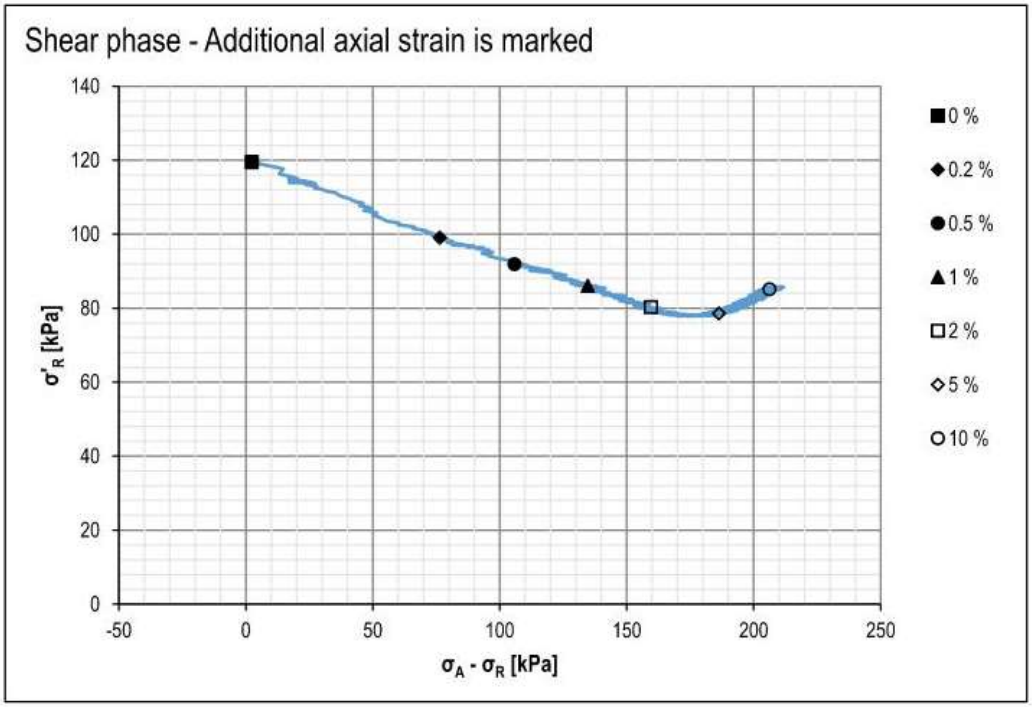

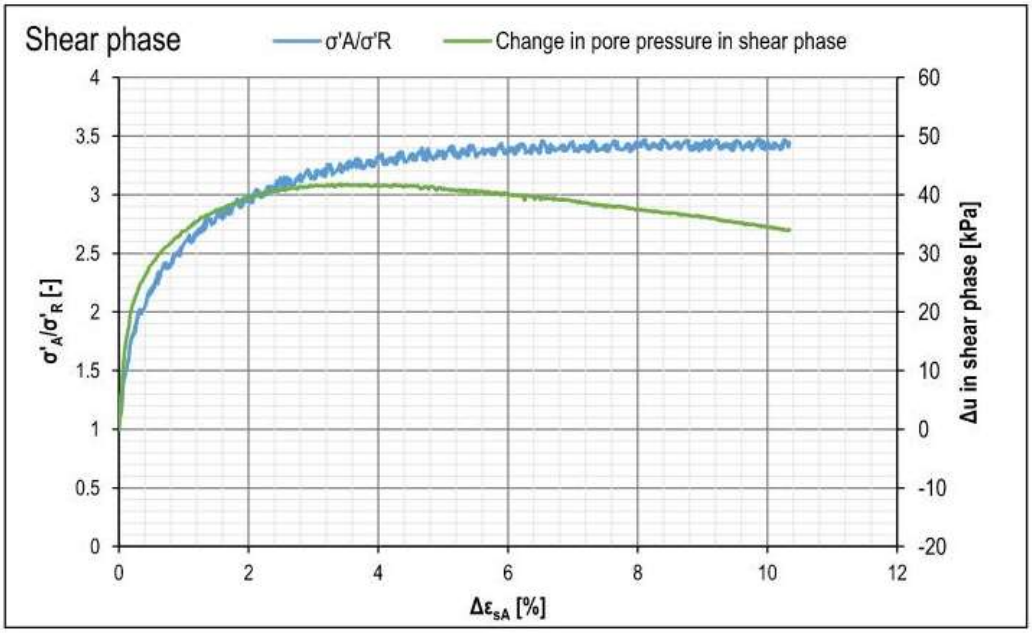

Prepared :	AMB	Date :	08-03-2023	Project : 207165 Hinge	
Checked :	JBR	Date :	10-03-2023	Report : 1	Encl. no.: 1.4.2
Approved :	SPL	Date :	14-03-2023	Subject : Triaxial test, CIUc	
Geo		Geo Copenhagen		+45 4588 4444	Rev: 0
		Geo Aarhus		+45 8627 3111	Page 3/5

Consolidated Isotropically Undrained Triaxial Compression Test with Measurement of Pore Pressure

Identification		Geological description
Borehole	TSH.B1	CLAY, medium to very high plasticity, sandy, calcareous, greenish grey
Specimen no.	14AA	
Depth [m]	6.80	

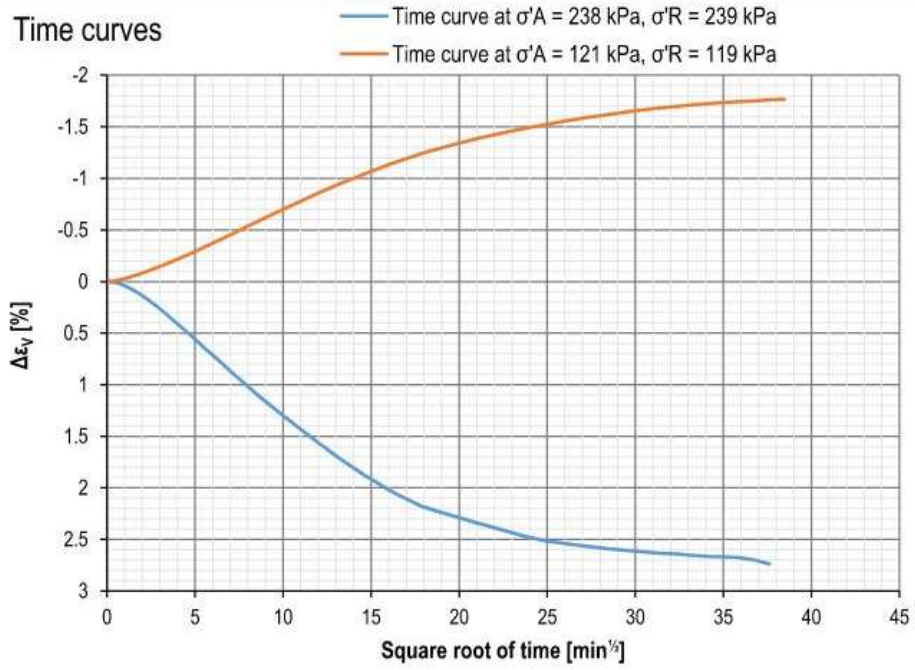

Prepared :	AMB	Date :	08-03-2023	Project : 207165 Hinge	
Checked :	JBR	Date :	10-03-2023	Report : 1	Encl. no.: 1.4.2
Approved :	SPL	Date :	14-03-2023	Subject : Triaxial test, CIUc	
Geo		Geo Copenhagen		+45 4588 4444	Rev: 0
		Geo Aarhus		+45 8627 3111	Page 4/5

Consolidated Isotropically Undrained Triaxial Compression Test with Measurement of Pore Pressure

Identification		Geological description
Borehole	TSH.B1	CLAY, medium to very high plasticity, sandy, calcareous, greenish grey
Specimen no.	14AA	
Depth [m]	6.80	

Photo before testing

Photo after testing

Prepared :	AMB	Date :	08-03-2023	Project : 207165 Hinge	
Checked :	JBR	Date :	10-03-2023	Report : 1	Encl. no.:1.4.2
Approved :	SPL	Date :	14-03-2023	Subject : Triaxial test, CIUc	
Geo		Geo Copenhagen		+45 4588 4444	Rev: 0
		Geo Aarhus		+45 8627 3111	Page 5/5

Consolidated Isotropically Undrained Triaxial Compression Test with Measurement of Pore Pressure

Identification		Geological description
Borehole	TSH.B1	CLAY, very high plasticity, calcareous, grey
Specimen no.	17AA	
Depth [m]	8.5	

Specimen dimensions, classification parameters and in-situ conditions

H	70	mm	$\sigma'_{v0,\,est.}$	113	kPa	e	1.490	-
D	69	mm	$\sigma'_{pc,\,est.}$	240	kPa	ρ_{bulk}	1.69	g/cm^3
V	262	cm^3	S_r	~100	%	ρ_{dry}	1.08	g/cm^3
$w_{initial}$	57.1	%	w_{after}	54.8	%	$\rho_{s,\,est.}$	2.68	g/cm^3

Test setup and test conditions

Pore water	De-aired tap water	Temperature	22.2	°C
Cell water	Tap water	Back pressure	594	kPa
End pistons	Smooth	Skempton B-value	1.00	-
Drainage conditions	Dry side drains and filteres	Specimen condition	Intact	

Chronological presentation of test sequence

Test phases	σ'_A [kPa]	σ'_R [kPa]	ε_A [%]	ε_{sA} [%]	ε_V [%]	σ'_R/σ'_A [-]	Rate
1) Initial loading, LVDT zeroed	22	20	0.0	-	-	0.89	200 kPa/hr
2) Saturation w. back pressure	153	157	1.3	-	-	1.02	100 kPa/hr
3) Consolidation, isotropic	239	243	2.1	-	1.9	1.02	1000 kPa/hr
4) Unloading and time curve	164	163	1.8	-	1.0	1.00	1000 kPa/hr
5a) Shear failure at 10 % add. strain	367	114	11.6	10.0	0.8	0.31	0.29 %/hr
5b) Shear failure at max $\sigma_A - \sigma_R$	376	114	11.8	10.2	0.8	0.30	0.29 %/hr

Results and interpretations

c_u at 5a)	[kPa]	127
c_u at 5b)	[kPa]	131
φ'	[°]	-
c'	[kPa]	-

Sketch of failure mode

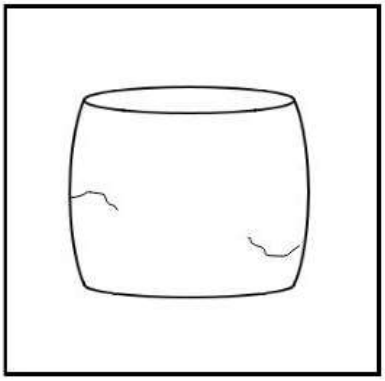

Notes

Testing is carried out in accordance with DS/EN ISO 17892-9:2018.

The standard prescribes a height:diameter ratio of 2:1 and not 1:1 as used here.

Swell observed in initial loading. Isotropic stresses were ramped to first 138 kPa then 158 kPa.

Consolidated Isotropically Undrained Triaxial Compression Test with Measurement of Pore Pressure

Identification		Geological description
Borehole	TSH.B1	CLAY, very high plasticity, calcareous, grey
Specimen no.	17AA	
Depth [m]	8.5	

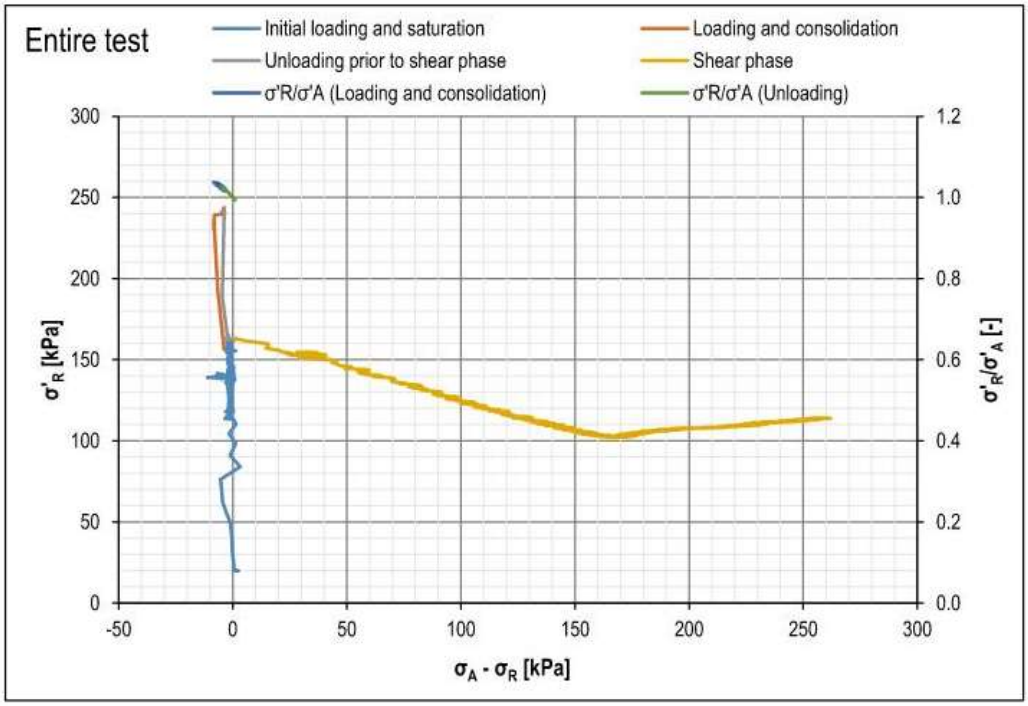

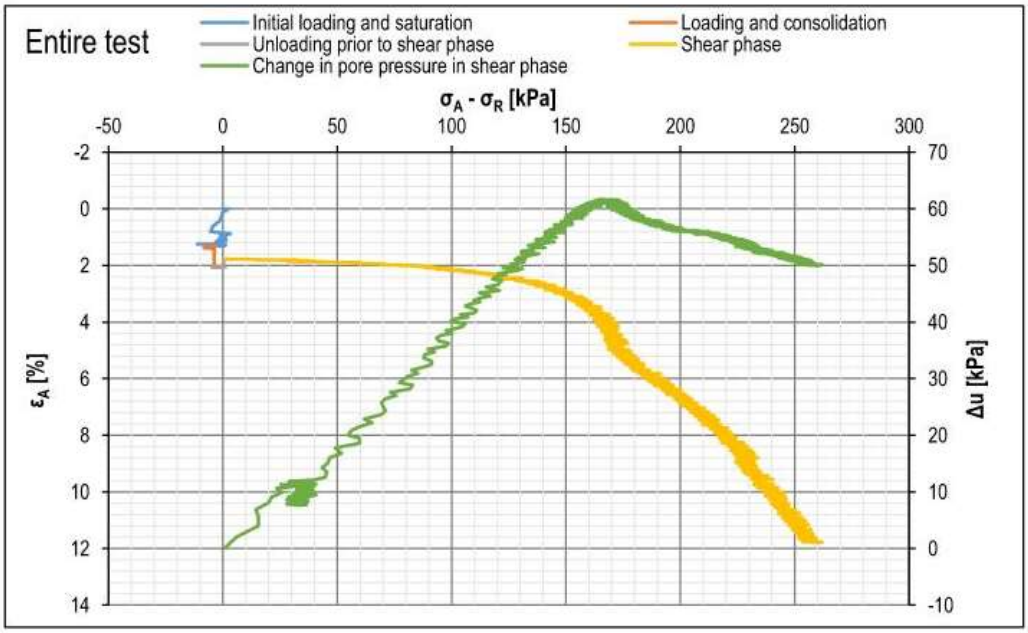

Prepared :	AMB	Date :	30-03-2023	Project : 207165 Hinge	
Checked :	JBR	Date :	13-04-2023	Report : 1	Encl. no.: 1.4.6
Approved :	SPL	Date :	13-04-2023	Subject : Triaxial test, CIUc	
Geo		Geo Copenhagen		+45 4588 4444	Rev: 0
		Geo Aarhus		+45 8627 3111	Page 2/5

Consolidated Isotropically Undrained Triaxial Compression Test with Measurement of Pore Pressure

Identification		Geological description
Borehole	TSH.B1	CLAY, very high plasticity, calcareous, grey
Specimen no.	17AA	
Depth [m]	8.5	

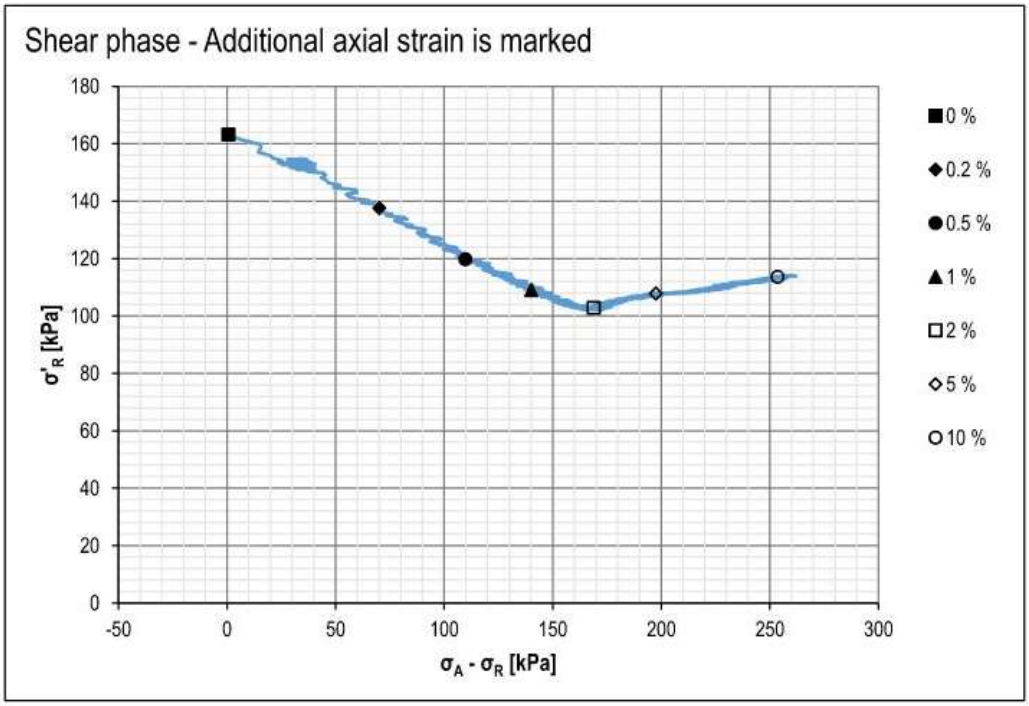

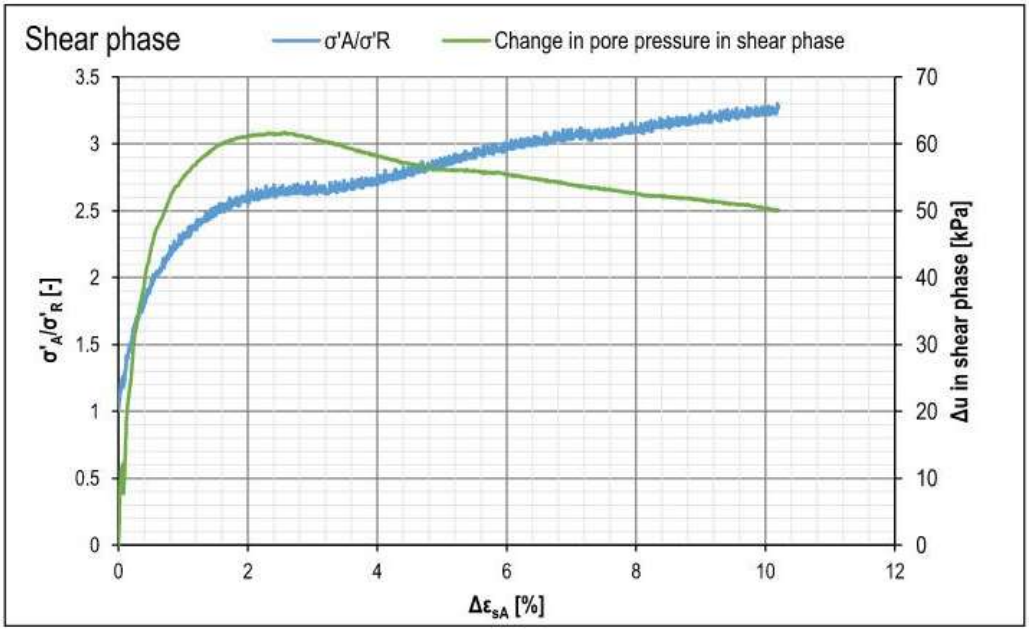

Prepared :	AMB	Date :	30-03-2023	Project : 207165 Hinge	
Checked :	JBR	Date :	13-04-2023	Report : 1	Encl. no.: 1.4.6
Approved :	SPL	Date :	13-04-2023	Subject : Triaxial test, CIUc	
Geo		Geo Copenhagen		+45 4588 4444	Rev: 0
		Geo Aarhus		+45 8627 3111	Page 3/5

Consolidated Isotropically Undrained Triaxial Compression Test with Measurement of Pore Pressure

Identification		Geological description
Borehole	TSH.B1	CLAY, very high plasticity, calcareous, grey
Specimen no.	17AA	
Depth [m]	8.5	

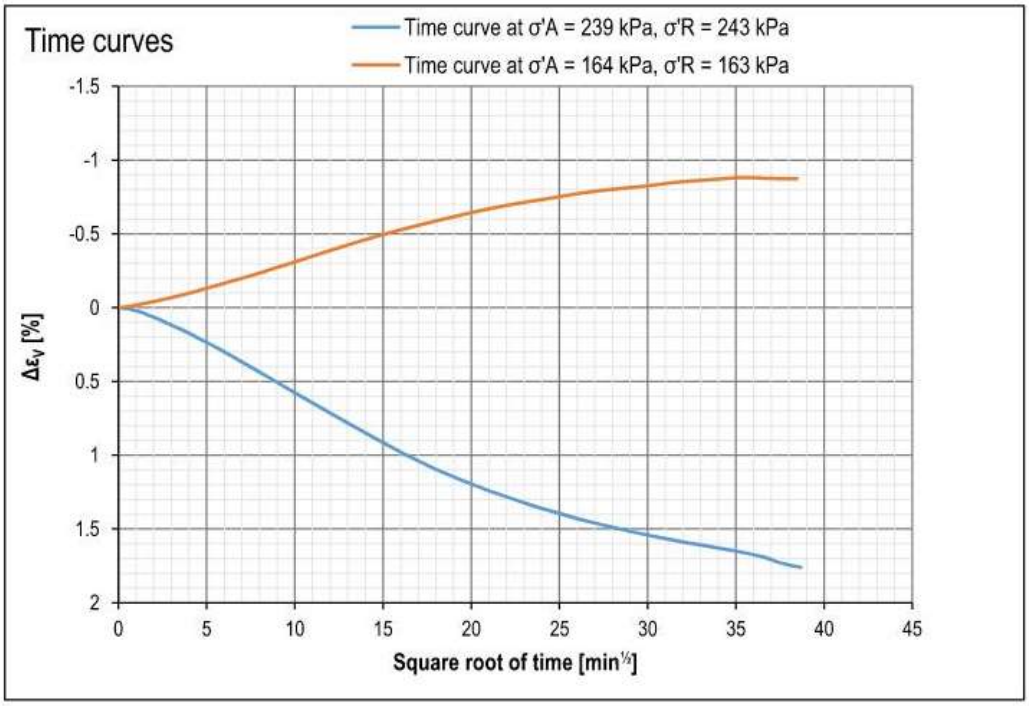

Consolidated Isotropically Undrained Triaxial Compression Test with Measurement of Pore Pressure

Identification		Geological description
Borehole	TSH.B1	CLAY, very high plasticity, calcareous, grey
Specimen no.	17AA	
Depth [m]	8.5	

Photo before testing

Photo after testing

Prepared :	AMB	Date :	30-03-2023	Project : 207165 Hinge	
Checked :	JBR	Date :	13-04-2023	Report : 1	Encl. no.: 1.4.6
Approved :	SPL	Date :	13-04-2023	Subject : Triaxial test, CIUc	
GEO		Geo Copenhagen		+45 4588 4444	Rev: 0
		Geo Aarhus		+45 8627 3111	Page 5/5

Consolidated Isotropically Undrained Triaxial Compression Test with Measurement of Pore Pressure

Identification		Geological description
Borehole	TSH.B2	CLAY, very high plasticity, calcareous, olive grey
Specimen no.	17AA	
Depth [m]	8.5	

Specimen dimensions, classification parameters and in-situ conditions

H	70	mm	$\sigma'_{v0,\ est.}$	118	kPa	e	1.681	-
D	69	mm	$\sigma'_{pc,\ est.}$	240	kPa	ρ_{bulk}	1.65	g/cm^3
V	262	cm^3	S_r	104.1	%	ρ_{dry}	1.00	g/cm^3
$w_{initial}$	65.3	%	w_{after}	59.7	%	$\rho_{s,\ est.}$	2.68	g/cm^3

Test setup and test conditions

Pore water	De-aired tap water	Temperature	22	°C
Cell water	Tap water	Back pressure	595	kPa
End pistons	Smooth	Skempton B-value	1.00	-
Drainage conditions	Dry side drains and filters	Specimen condition	Intact	

Chronological presentation of test sequence

Test phases	σ'_A [kPa]	σ'_R [kPa]	ε_A [%]	ε_{sA} [%]	ε_V [%]	σ'_R/σ'_A [-]	Rate
1) Initial loading, LVDT zeroed	18	16	0.0	-	-	0.88	200 kPa/hr
2) Saturation w. back pressure	111	110	2.1	-	-	1.00	100 kPa/hr
3) Consolidation, isotropic	243	245	4.2	-	5.3	1.01	1000 kPa/hr
4) Unloading and time curve	119	118	3.4	-	3.0	1.00	1000 kPa/hr
5a) Shear failure at 10 % add. strain	211	88	13.1	10.0	2.8	0.42	0.16 %/hr
5b) Shear failure at max $\sigma_A - \sigma_R$	220	89	8.2	4.9	3.0	0.40	0.16 %/hr

Results and interpretations

c_u at 5a)	[kPa]	62
c_u at 5b)	[kPa]	66
φ'	[°]	-
c'	[kPa]	-

Sketch of failure mode

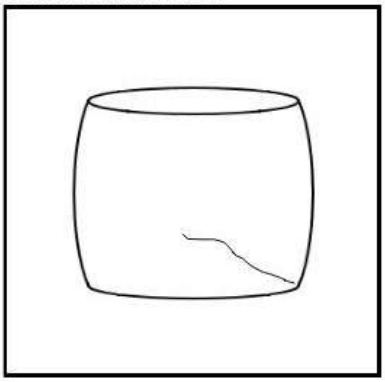

Notes

Testing is carried out in accordance with DS/EN ISO 17892-9:2018.

The standard prescribes a height:diameter ratio of 2:1 and not 1:1 as used here.

Consolidated Isotropically Undrained Triaxial Compression Test with Measurement of Pore Pressure

Identification		Geological description
Borehole	TSH.B2	CLAY, very high plasticity, calcareous, olive grey
Specimen no.	17AA	
Depth [m]	8.5	

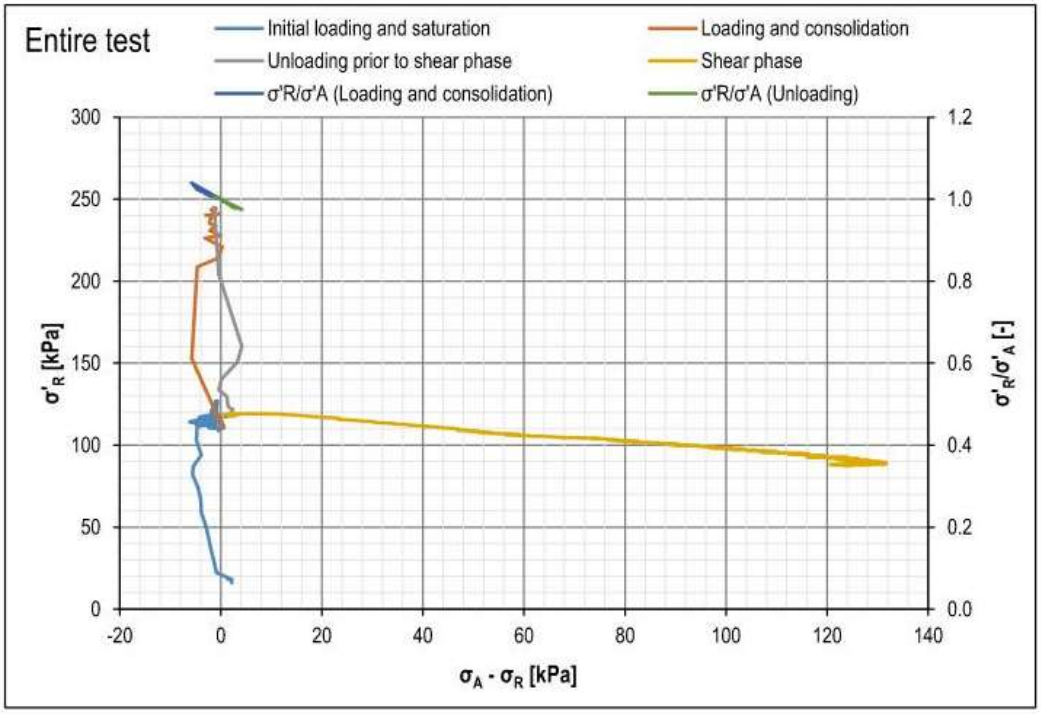

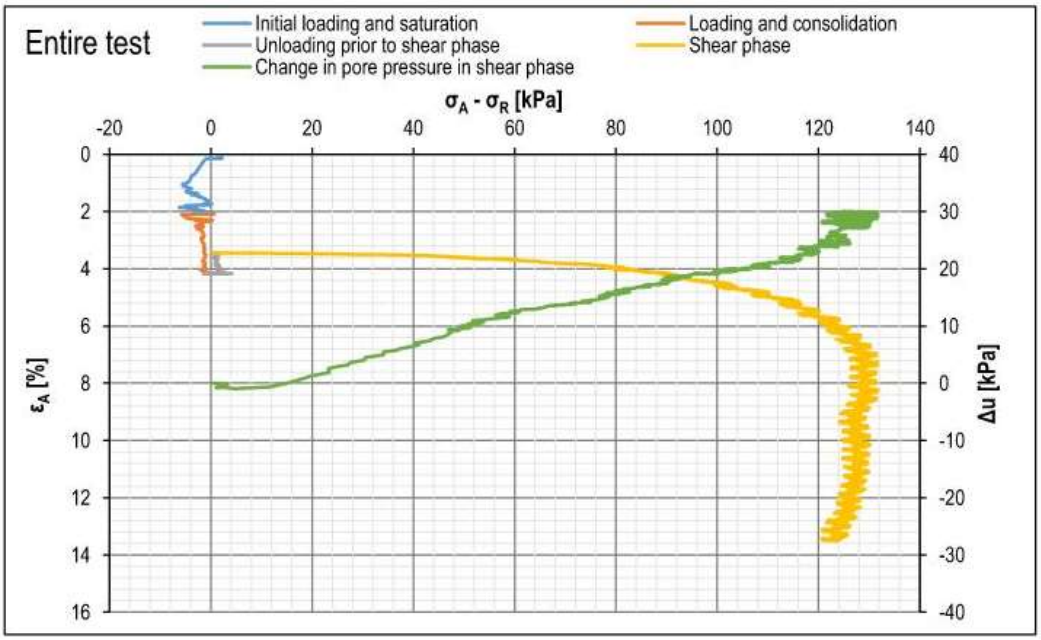

Prepared :	AMB	Date :	30-03-2023	Project : 207165 Hinge	
Checked :	JBR	Date :	13-04-2023	Report : 1	Encl. no.: 1.4.7
Approved :	SPL	Date :	13-04-2023	Subject : Triaxial test, CIUc	
Geo		Geo Copenhagen		+45 4588 4444	Rev: 0
		Geo Aarhus		+45 8627 3111	Page 2/5

Consolidated Isotropically Undrained Triaxial Compression Test with Measurement of Pore Pressure

Identification		Geological description
Borehole	TSH.B2	CLAY, very high plasticity, calcareous, olive grey
Specimen no.	17AA	
Depth [m]	8.5	

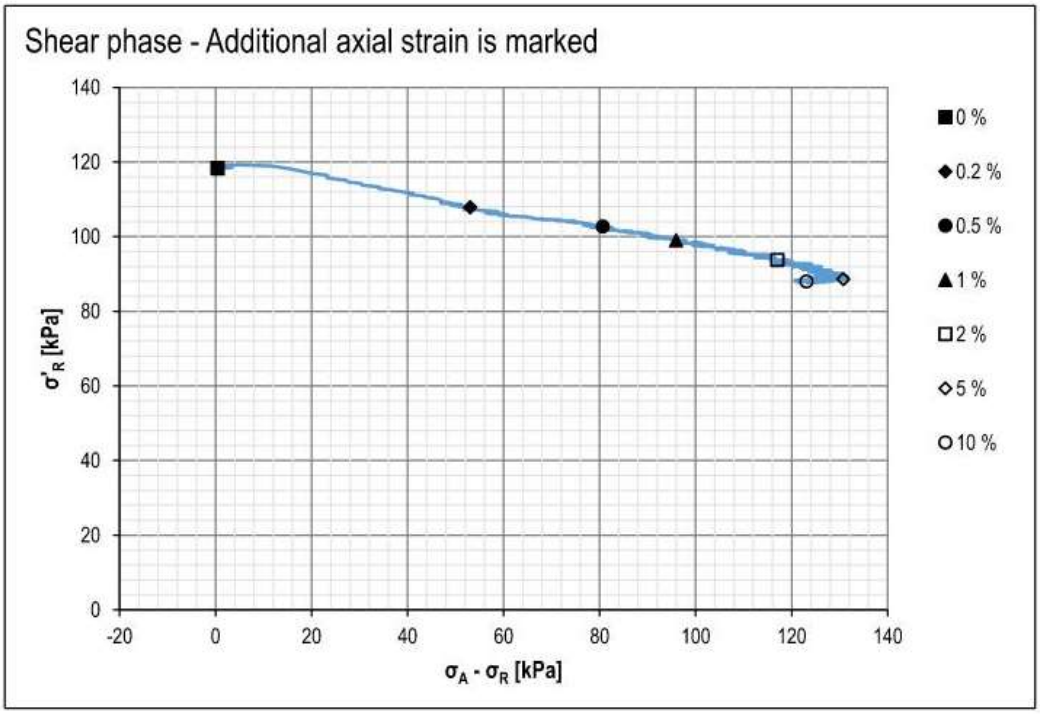

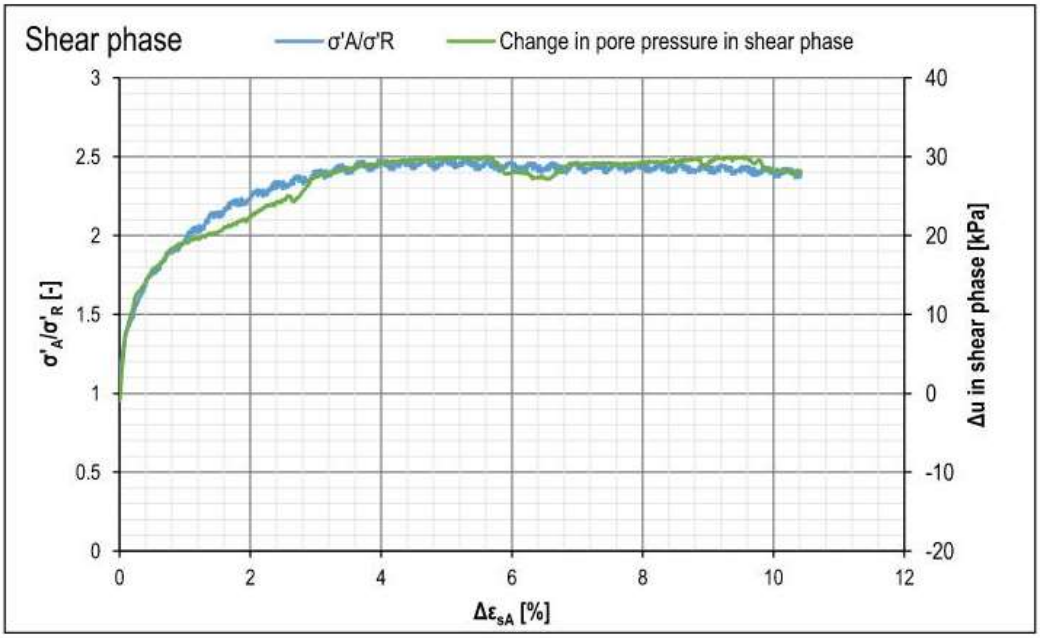

Prepared :	AMB	Date :	30-03-2023	Project : 207165 Hinge	
Checked :	JBR	Date :	13-04-2023	Report : 1	Encl. no.: 1.4.7
Approved :	SPL	Date :	13-04-2023	Subject : Triaxial test, CIUc	
		Geo Copenhagen		+45 4588 4444	Rev: 0
		Geo Aarhus		+45 8627 3111	Page 3/5

Consolidated Isotropically Undrained Triaxial Compression Test with Measurement of Pore Pressure

Identification		Geological description
Borehole	TSH.B2	CLAY, very high plasticity, calcareous, olive grey
Specimen no.	17AA	
Depth [m]	8.5	

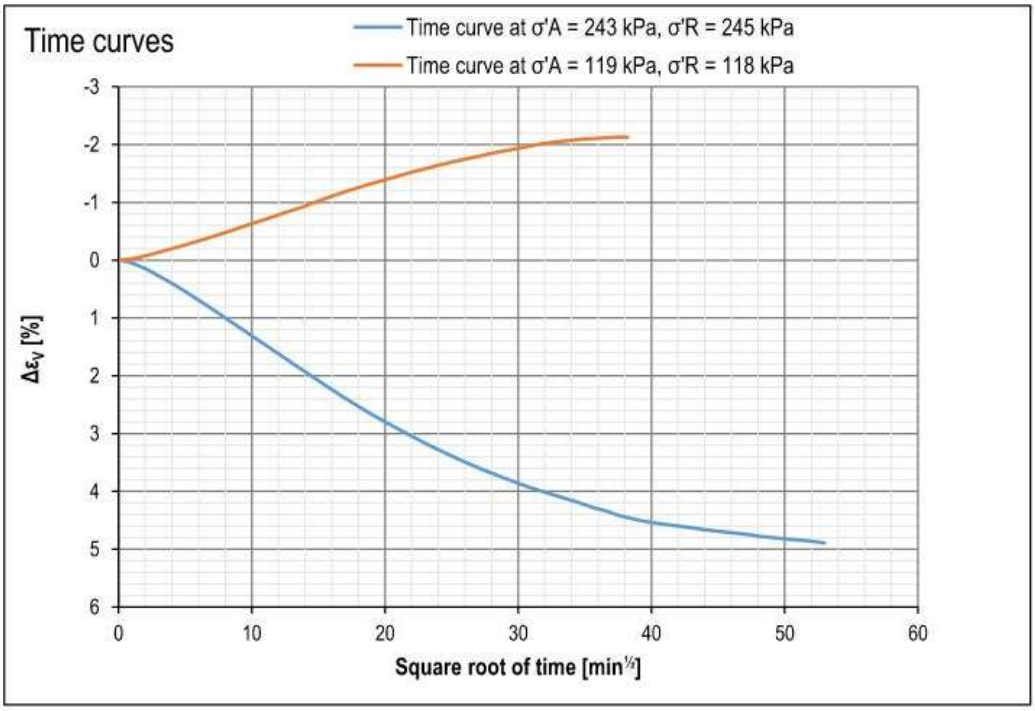

Prepared :	AMB	Date :	30-03-2023	Project : 207165 Hinge	
Checked :	JBR	Date :	13-04-2023	Report : 1	Encl. no.: 1.4.7
Approved :	SPL	Date :	13-04-2023	Subject : Triaxial test, CIUc	
Geo		Geo Copenhagen		+45 4588 4444	Rev: 0
		Geo Aarhus		+45 8627 3111	Page 4/5

Consolidated Isotropically Undrained Triaxial Compression Test with Measurement of Pore Pressure

Identification		Geological description
Borehole	TSH.B2	CLAY, very high plasticity, calcareous, olive grey
Specimen no.	17AA	
Depth [m]	8.5	

Photo before testing

Photo after testing

Consolidated Isotropically Undrained Triaxial Compression Test with Measurement of Pore Pressure

Identification		Geological description
Borehole	TSH.B3	CLAY, very high plasticity ,calcareous, w. ochre specks, grey
Specimen no.	10AA	
Depth [m]	5.1	

Specimen dimensions, classification parameters and in-situ conditions

H	70	mm	$p'_{v0,\ est.}$	80	kPa	e	1.587	-
D	70	mm	$p'_{pc,\ est.}$	240	kPa	ρ_{bulk}	1.67	g/cm^3
V	269	cm^3	S_r	97.2	%	ρ_{dry}	1.07	g/cm^3
$w_{initial}$	55.5	%	w_{after}	55.4	%	$\rho_{s,\ est.}$	2.78	g/cm^3

Test setup and test conditions

Pore water	De-aired tap water	Temperature	20.8	°C
Cell water	Tap water	Back pressure	594	kPa
End pistons	Smooth	Skempton B-value	0.97	-
Drainage conditions	Dry side drains and filters	Specimen condition	Intact	

Chronological presentation of test sequence

Test phases	σ'_A [kPa]	σ'_R [kPa]	ε_A [%]	ε_{sA} [%]	ε_V [%]	σ'_R/σ'_A [-]	Rate
1) Initial loading, LVDT zeroed	19	18	0.0	-	-	0.97	200 kPa/hr
2) Saturation w. back pressure	98	100	1.1	-	-	1.02	100 kPa/hr
3) Consolidation, isotropic	239	241	3.0	-	4.1	1.01	1000 kPa/hr
4) Unloading and time curve	108	106	2.1	-	1.8	0.98	1000 kPa/hr
5a) Shear failure at 10 % add. strain	236	79	11.9	10.0	1.8	0.34	0.25 %/hr
5b) Shear failure at max $\sigma_A - \sigma_R$	236	78	11.2	9.3	1.8	0.33	0.25 %/hr

Results and interpretations

c_u at 5a)	[kPa]	78
c_u at 5b)	[kPa]	79
φ'	[°]	-
c'	[kPa]	-

Sketch of failure mode

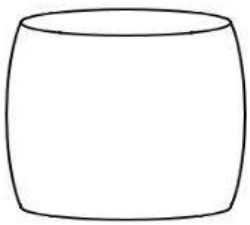

Notes

Testing is carried out in accordance with DS/EN ISO 17892-9:2018.

The standard prescribes a height:diameter ratio of 2:1 and not 1:1 as used here.

Consolidated Isotropically Undrained Triaxial Compression Test with Measurement of Pore Pressure

Identification		Geological description
Borehole	TSH.B3	CLAY, very high plasticity ,calcareous, w. ochre specks, grey
Specimen no.	10AA	
Depth [m]	5.1	

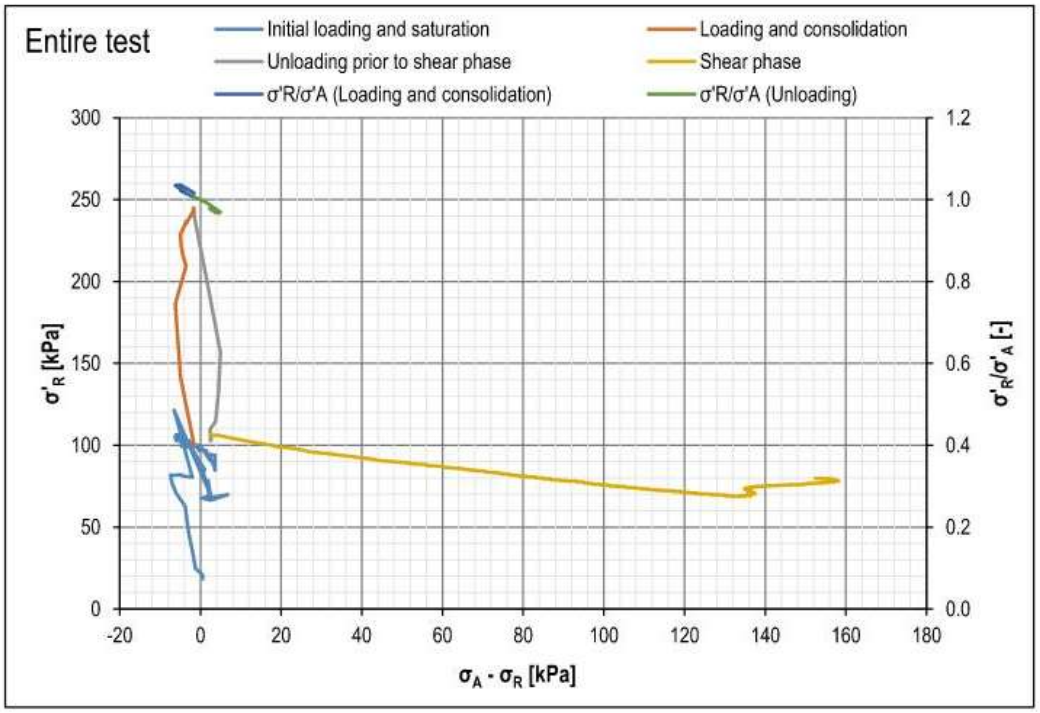

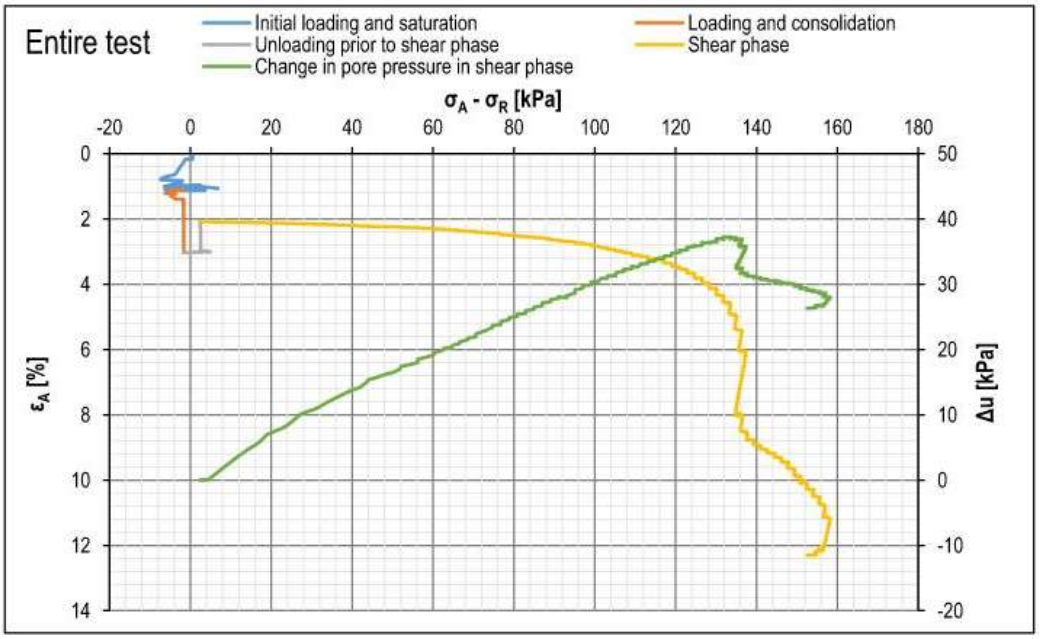

Prepared :	AMB	Date :	08-03-2023	Project : 207165 Hinge	
Checked :	JBR	Date :	10-03-2023	Report : 1	Encl. no.: 1.4.3
Approved :	SPL	Date :	14-03-2023	Subject : Triaxial test, CIUc	
		Geo Copenhagen		+45 4588 4444	Rev: 0
		Geo Aarhus		+45 8627 3111	Page 2/5

Consolidated Isotropically Undrained Triaxial Compression Test with Measurement of Pore Pressure

Identification		Geological description
Borehole	TSH.B3	CLAY, very high plasticity ,calcareous, w. ochre specks, grey
Specimen no.	10AA	
Depth [m]	5.1	

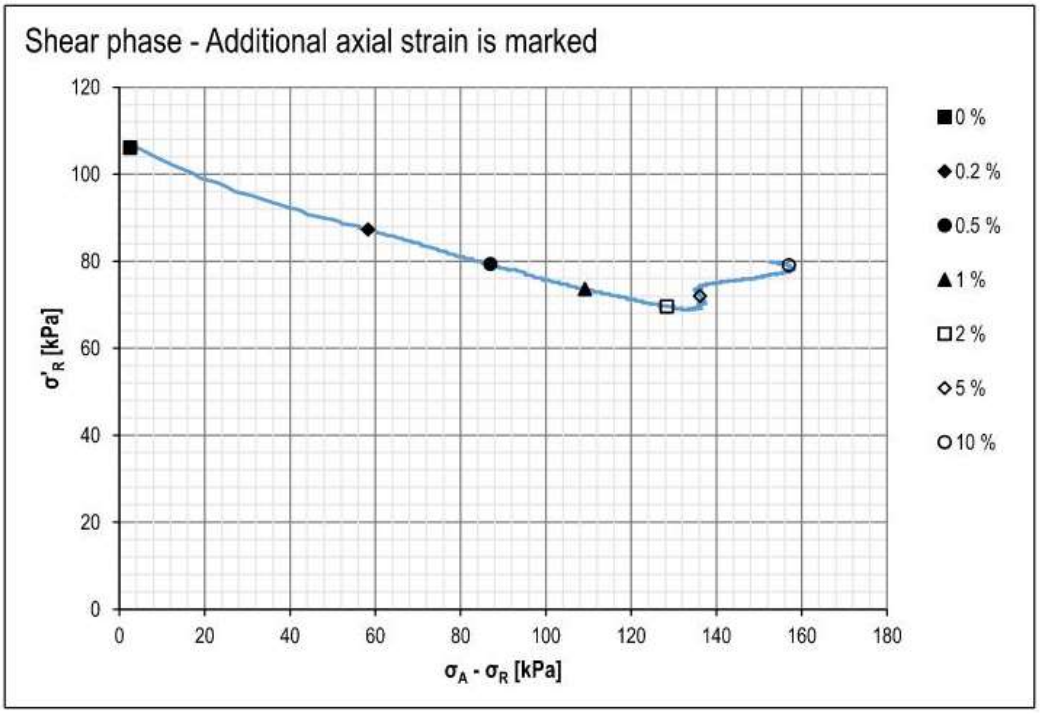

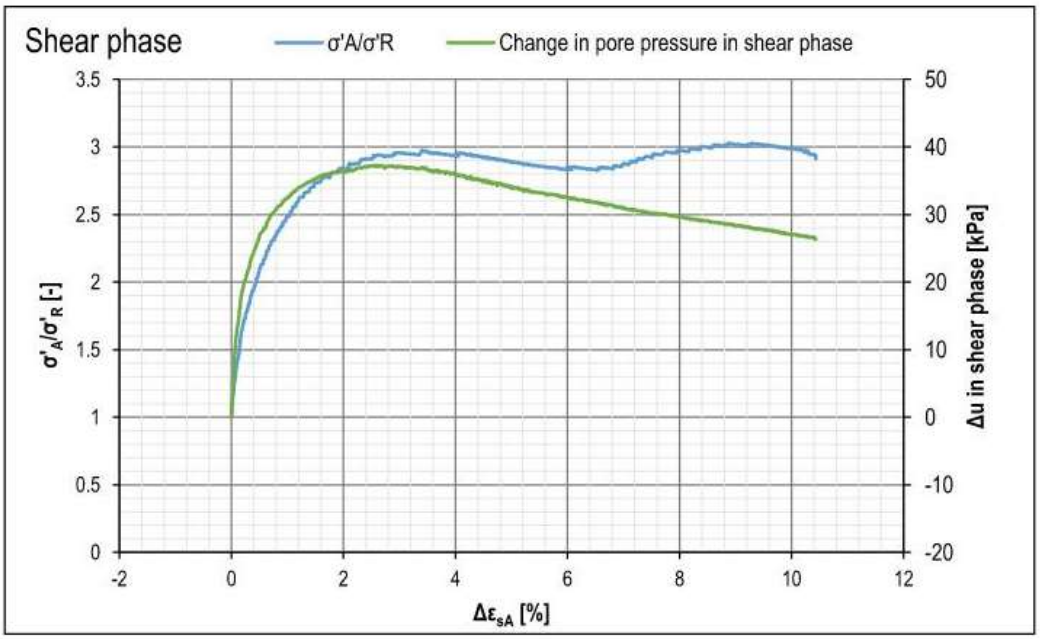

Prepared :	AMB	Date :	08-03-2023	Project : 207165 Hinge	
Checked :	JBR	Date :	10-03-2023	Report : 1	Encl. no.: 1.4.3
Approved :	SPL	Date :	14-03-2023	Subject : Triaxial test, CIUc	
		Geo Copenhagen		+45 4588 4444	Rev: 0
		Geo Aarhus		+45 8627 3111	Page 3/5

Consolidated Isotropically Undrained Triaxial Compression Test with Measurement of Pore Pressure

Identification		Geological description
Borehole	TSH.B3	CLAY, very high plasticity ,calcareous, w. ochre specks, grey
Specimen no.	10AA	
Depth [m]	5.1	

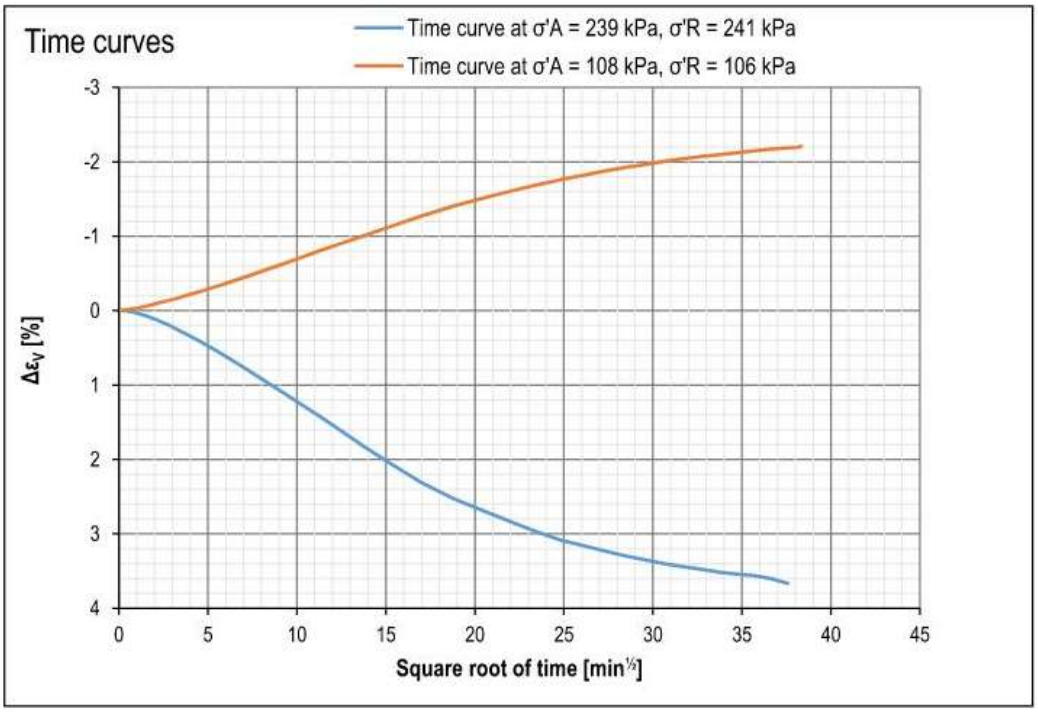

Consolidated Isotropically Undrained Triaxial Compression Test with Measurement of Pore Pressure

Identification		Geological description
Borehole	TSH.B3	CLAY, very high plasticity ,calcareous, w. ochre specks, grey
Specimen no.	10AA	
Depth [m]	5.1	

Photo before testing

Photo after testing

Prepared :	AMB	Date :	08-03-2023	Project : 207165 Hinge	
Checked :	JBR	Date :	10-03-2023	Report : 1	Encl. no.: 1.4.3
Approved :	SPL	Date :	14-03-2023	Subject : Triaxial test, CIUc	
GEO		Geo Copenhagen		+45 4588 4444	Rev: 0
		Geo Aarhus		+45 8627 3111	Page 5/5

Consolidated Isotropically Undrained Triaxial Compression Test with Measurement of Pore Pressure

Identification		Geological description
Borehole	TSH.B3	CLAY, very high plasticity, calcareous, w. few silt streaks, dark greyish brown
Specimen no.	13AA	
Depth [m]	6.3	

Specimen dimensions, classification parameters and in-situ conditions

H	70	mm	$\sigma'_{v0,\,est.}$	93	kPa	e	1.507	-
D	69	mm	$\sigma'_{pc,\,est.}$	240	kPa	ρ_{bulk}	1.71	g/cm^3
V	262	cm^3	S_r	~100	%	ρ_{dry}	1.11	g/cm^3
$w_{initial}$	54.4	%	w_{after}	52.7	%	$\rho_{s,\,measured}$	2.78	g/cm^3

Test setup and test conditions

Pore water	De-aired tap water	Temperature	21.5	°C
Cell water	Tap water	Back pressure	597	kPa
End pistons	Smooth	Skempton B-value	0.98	-
Drainage conditions	Dry side drains and filters	Specimen condition	Intact	

Chronological presentation of test sequence

Test phases	σ'_A [kPa]	σ'_R [kPa]	ε_A [%]	ε_{sA} [%]	ε_V [%]	σ'_R/σ'_A [-]	Rate
1) Initial loading, LVDT zeroed	24	21	0.0	-	-	0.87	200 kPa/hr
2) Saturation w. back pressure	92	91	1.2	-	-	0.99	100 kPa/hr
3) Consolidation, isotropic	239	241	2.6	-	3.9	1.01	1000 kPa/hr
4) Unloading and time curve	98	95	1.9	-	1.8	0.97	1000 kPa/hr
5a) Shear failure at 10 % add. strain	190	74	11.7	10.0	1.6	0.39	0.29 %/hr
5b) Shear failure at max σ_A - σ_R	194	71	6.7	4.9	1.6	0.37	0.29 %/hr

Results and interpretations

c_u at 5a)	[kPa]	58
c_u at 5b)	[kPa]	62
φ'	[°]	-
c'	[kPa]	-

Sketch of failure mode

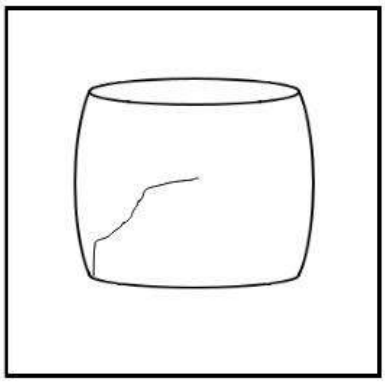

Notes

Testing is carried out in accordance with DS/EN ISO 17892-9:2018.

The standard prescribes a height:diameter ratio of 2:1 and not 1:1 as used here.

Consolidated Isotropically Undrained Triaxial Compression Test with Measurement of Pore Pressure

Identification		Geological description
Borehole	TSH.B3	CLAY, very high plasticity, calcareous, w. few silt streaks, dark greyish brown
Specimen no.	13AA	
Depth [m]	6.3	

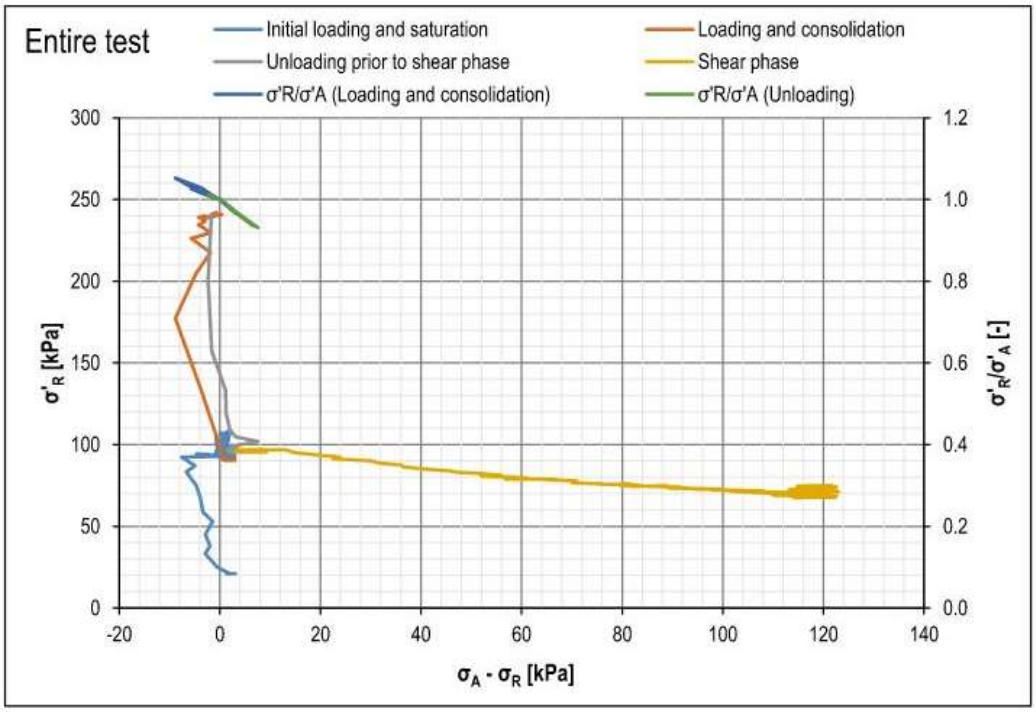

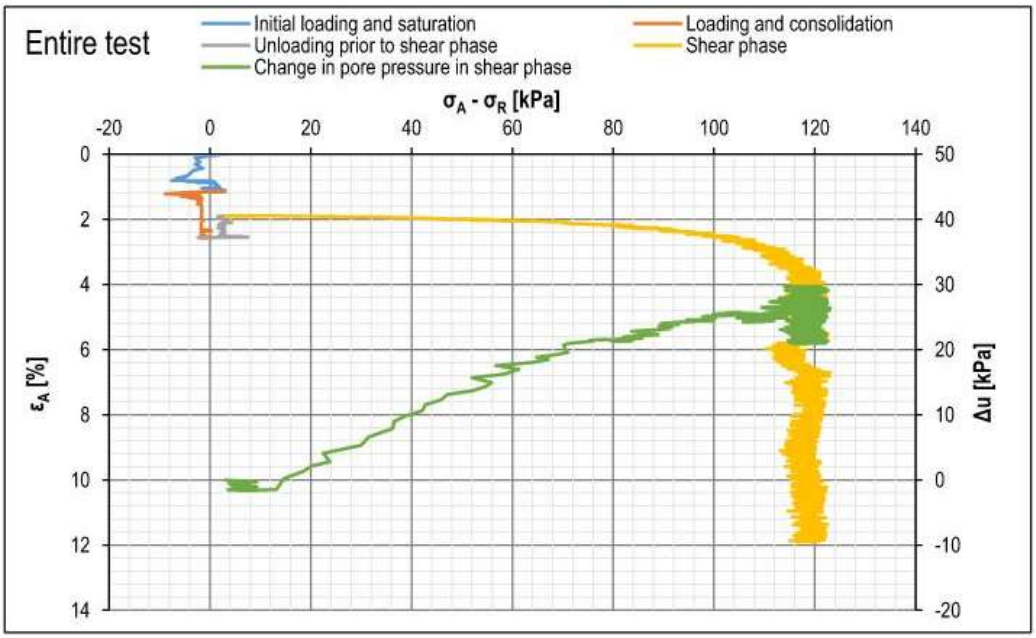

Prepared :	AMB	Date :	30-03-2023	Project : 207165 Hinge	
Checked :	JBR	Date :	13-04-2023	Report : 1	Encl. no.: 1.4.8
Approved :	SPL	Date :	13-04-2023	Subject : Triaxial test, CIUc	
Geo		Geo Copenhagen		+45 4588 4444	Rev: 0
		Geo Aarhus		+45 8627 3111	Page 2/5

Consolidated Isotropically Undrained Triaxial Compression Test with Measurement of Pore Pressure

Identification		Geological description
Borehole	TSH.B3	CLAY, very high plasticity, calcareous, w. few silt streaks, dark greyish brown
Specimen no.	13AA	
Depth [m]	6.3	

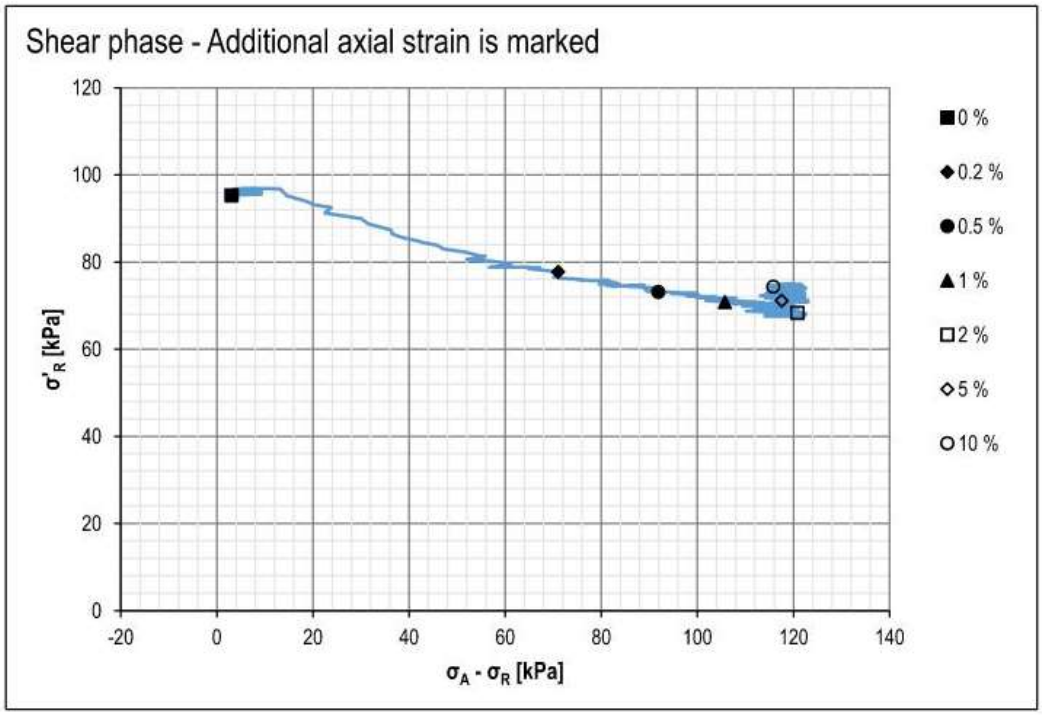

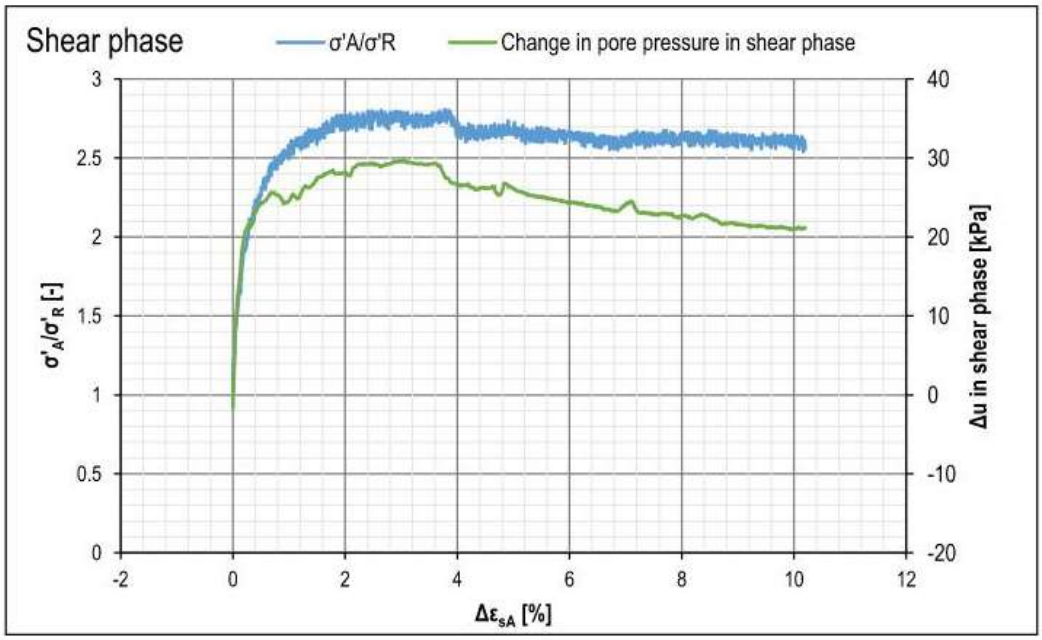

Prepared :	AMB	Date :	30-03-2023	Project : 207165 Hinge	
Checked :	JBR	Date :	13-04-2023	Report : 1	Encl. no.: 1.4.8
Approved :	SPL	Date :	13-04-2023	Subject : Triaxial test, CIUc	
		Geo Copenhagen		+45 4588 4444	Rev: 0
		Geo Aarhus		+45 8627 3111	Page 3/5

Consolidated Isotropically Undrained Triaxial Compression Test with Measurement of Pore Pressure

Identification		Geological description
Borehole	TSH.B3	CLAY, very high plasticity, calcareous, w. few silt streaks, dark greyish brown
Specimen no.	13AA	
Depth [m]	6.3	

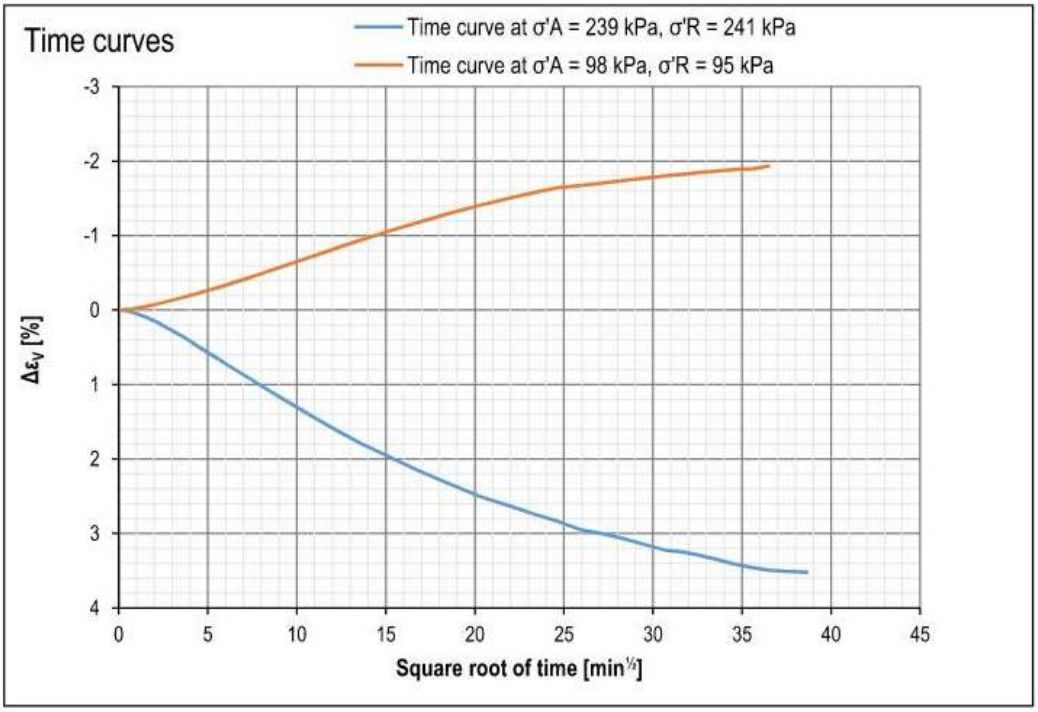

Consolidated Isotropically Undrained Triaxial Compression Test with Measurement of Pore Pressure

Identification		Geological description
Borehole	TSH.B3	CLAY, very high plasticity, calcareous, w. few silt streaks, dark greyish brown
Specimen no.	13AA	
Depth [m]	6.3	

Photo before testing

Photo after testing

Prepared :	AMB	Date :	30-03-2023	Project : 207165 Hinge	
Checked :	JBR	Date :	13-04-2023	Report : 1	Encl. no.: 1.4.8
Approved :	SPL	Date :	13-04-2023	Subject : Triaxial test, CIUc	
Geo		Geo Copenhagen		+45 4588 4444	Rev: 0
		Geo Aarhus		+45 8627 3111	Page 5/5

Consolidated Isotropically Undrained Triaxial Compression Test with Measurement of Pore Pressure

Identification		Geological description
Borehole	TSH.B3	CLAY, very high plasticity, very calcareous, grey
Specimen no.	17AA	
Depth [m]	8.4	

Specimen dimensions, classification parameters and in-situ conditions

H	70	mm	$p'_{v0, est.}$	118	kPa	e	1.476	-
D	70	mm	$p'_{pc, est.}$	240	kPa	ρ_{bulk}	1.67	g/cm^3
V	269	cm^3	S_r	92.4	%	ρ_{dry}	1.12	g/cm^3
$w_{initial}$	49.0	%	w_{after}	52.3	%	$\rho_{s, est.}$	2.78	g/cm^3

Test setup and test conditions

Pore water	De-aired tap water	Temperature	22.0	°C
Cell water	Tap water	Back pressure	598	kPa
End pistons	Smooth	Skempton B-value	0.96	-
Drainage conditions	Dry side drains and filters	Specimen condition	Intact	

Chronological presentation of test sequence

Test phases	σ'_A [kPa]	σ'_R [kPa]	ε_A [%]	ε_{sA} [%]	ε_V [%]	σ'_R/σ'_A [-]	Rate
1) Initial loading, LVDT zeroed	19	16	0.0	-	-	0.88	200 kPa/hr
2) Saturation w. back pressure	114	115	1.7	-	-	1.01	100 kPa/hr
3) Consolidation, isotropic	240	241	3.0	-	2.7	1.00	1000 kPa/hr
4) Unloading and time curve	119	119	2.3	-	0.9	1.00	1000 kPa/hr
5a) Shear failure at 10 % add. strain	243	80	12.1	10.0	0.9	0.33	0.43 %/hr
5b) Shear failure at max $\sigma_A - \sigma_R$	245	80	12.4	10.4	0.9	0.33	0.43 %/hr

Results and interpretations

c_u at 5a)	[kPa]	81
c_u at 5b)	[kPa]	82
φ'	[°]	-
c'	[kPa]	-

Sketch of failure mode

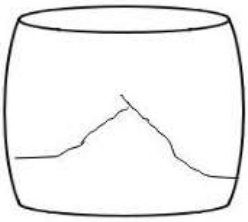

Notes

Testing is carried out in accordance with DS/EN ISO 17892-9:2018.

The standard prescribes a height:diameter ratio of 2:1 and not 1:1 as used here.

Consolidated Isotropically Undrained Triaxial Compression Test with Measurement of Pore Pressure

Identification		Geological description
Borehole	TSH.B3	CLAY, very high plasticity, very calcareous, grey
Specimen no.	17AA	
Depth [m]	8.4	

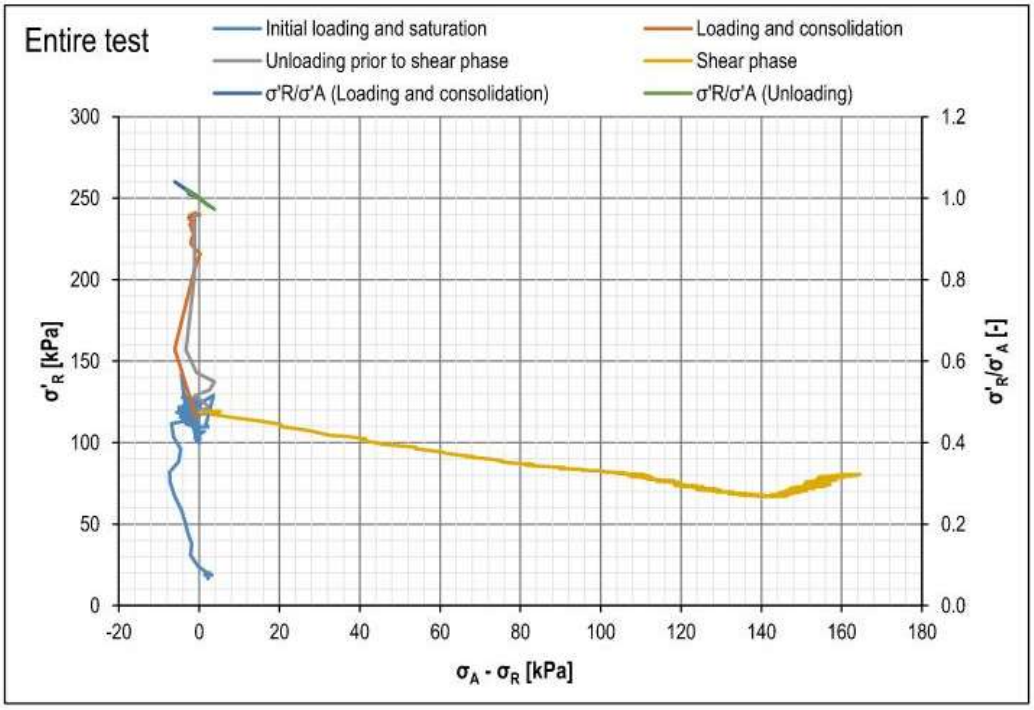

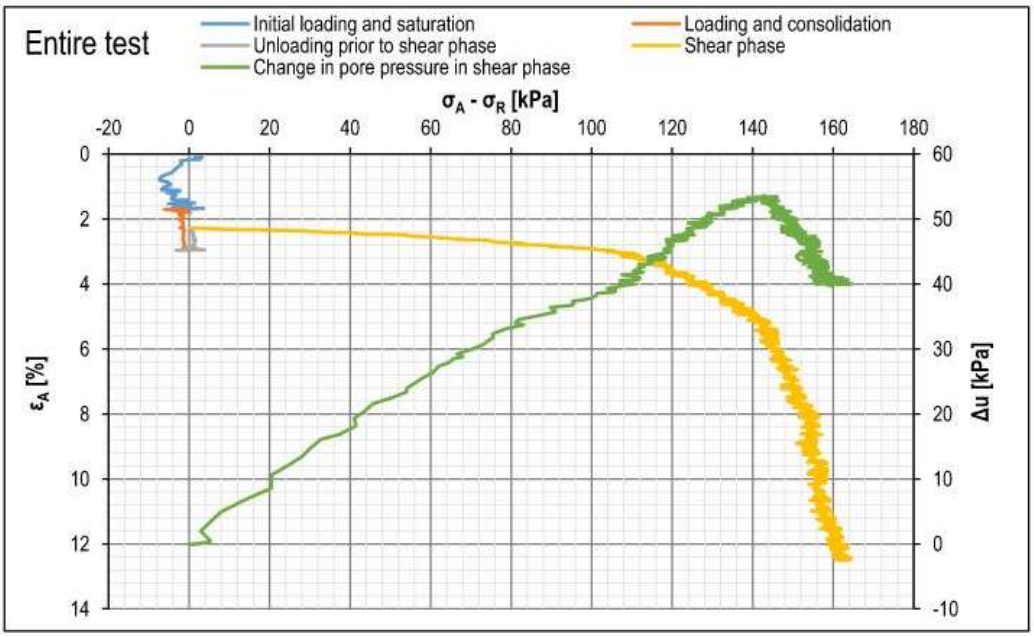

Prepared :	AMB	Date :	08-03-2023	Project : 207165 Hinge	
Checked :	JBR	Date :	10-03-2023	Report : 1	Encl. no.: 1.4.4
Approved :	SPL	Date :	14-03-2023	Subject : Triaxial test, CIUc	
Geo		Geo Copenhagen		+45 4588 4444	Rev: 0
		Geo Aarhus		+45 8627 3111	Page 2/5

Consolidated Isotropically Undrained Triaxial Compression Test with Measurement of Pore Pressure

Identification		Geological description
Borehole	TSH.B3	CLAY, very high plasticity, very calcareous, grey
Specimen no.	17AA	
Depth [m]	8.4	

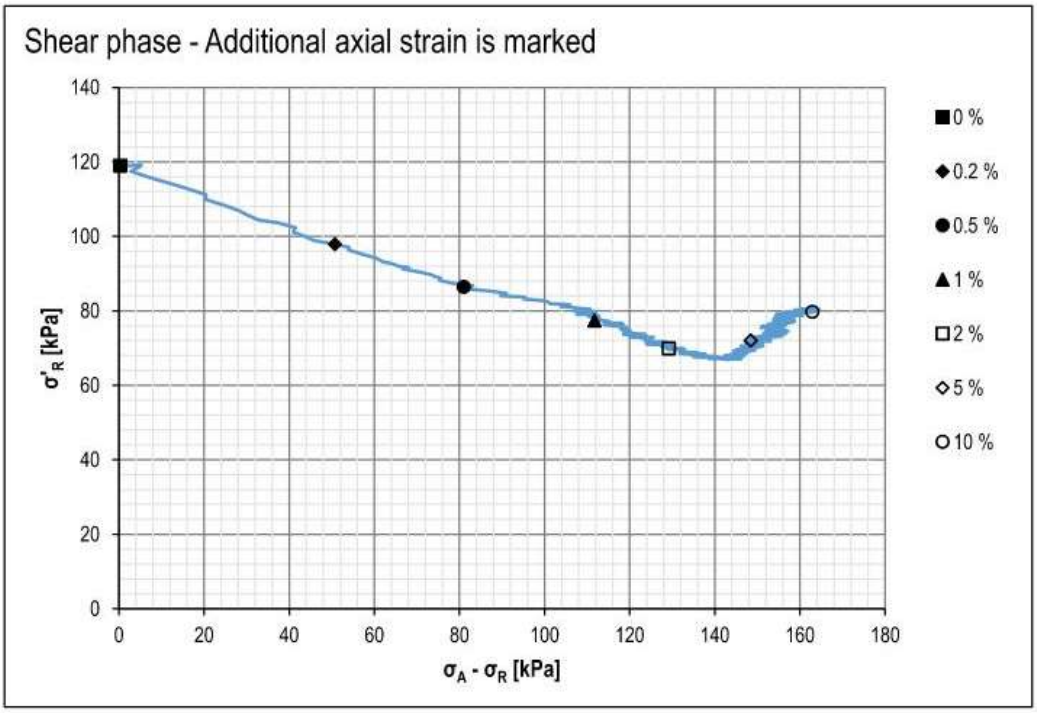

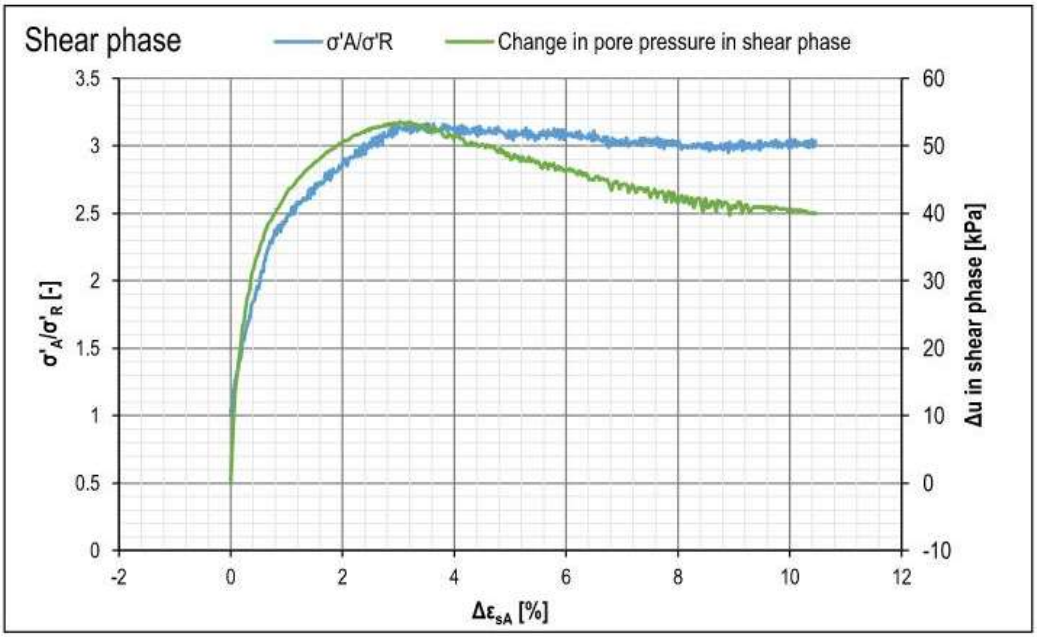

Prepared :	AMB	Date :	08-03-2023	Project : 207165 Hinge	
Checked :	JBR	Date :	10-03-2023	Report : 1	Encl. no.: 1.4.4
Approved :	SPL	Date :	14-03-2023	Subject : Triaxial test, CIUc	
		Geo Copenhagen		+45 4588 4444	Rev: 0
		Geo Aarhus		+45 8627 3111	Page 3/5

Consolidated Isotropically Undrained Triaxial Compression Test with Measurement of Pore Pressure

Identification		Geological description
Borehole	TSH.B3	CLAY, very high plasticity, very calcareous, grey
Specimen no.	17AA	
Depth [m]	8.4	

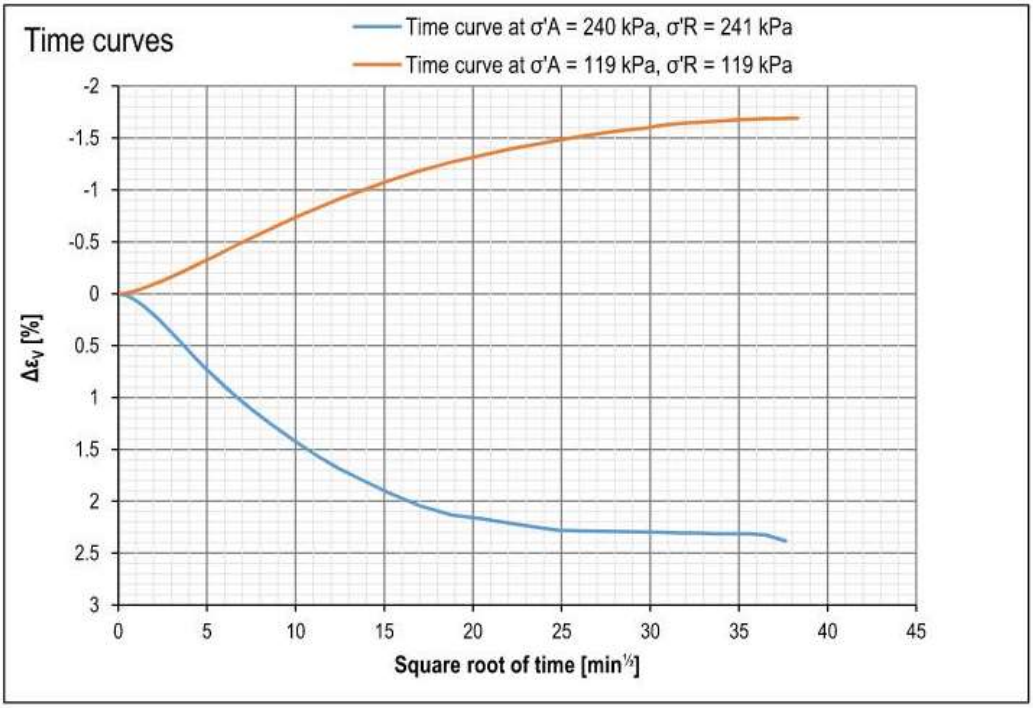

Consolidated Isotropically Undrained Triaxial Compression Test with Measurement of Pore Pressure

Identification		Geological description
Borehole	TSH.B3	CLAY, very high plasticity, very calcareous, grey
Specimen no.	17AA	
Depth [m]	8.4	

Photo before testing

Photo after testing

Prepared :	AMB	Date :	08-03-2023	Project : 207165 Hinge	
Checked :	JBR	Date :	10-03-2023	Report : 1	Encl. no.: 1.4.4
Approved :	SPL	Date :	14-03-2023	Subject : Triaxial test, CIUc	
		Geo Copenhagen		+45 4588 4444	Rev: 0
		Geo Aarhus		+45 8627 3111	Page 5/5

C Procedures for field tests

This section presents the applied methods for performing eight full-scale test piles and the subsequent pile loading tests. The test piles were installed as bored cast-in-situ piles at the Hinge test site. Prior to installation, each reinforcement cage was instrumented with distributed fibre optic strain and temperature cables (FOSC and FOTC), traditional vibrating wire strain gauges (VWSG) and tell-tales (TT). Static pile load tests were conducted as tension tests at three different times after installation (∼1.5 months, ∼7.5 months and ∼3 years). Data obtained during pile load testing were post-processed subsequently.

C.1 Instrumentation of test piles

The PhD student instrumented the test piles with measuring equipment from Friday the 16th of august 2019 till Monday the 19th of august 2019 at Aarsleff's workshop in Hasselager. Each reinforcement cage was instrumented with 2 FOSC, 1 FOTC, 10 VWSG (one pair. at 5 different levels) and 4 TT, see Figure 1.

Figure 1: Instrumentation of reinforcement cages in Aarsleff's workshop.

C.1.1 Fibre optic strain cables (FOSC)

The Rayleigh based FOSC (BRUsens V9 strain cables from BRUGG cables) were installed initially as a gauge length installation, where the sensing section of the strain cables was attached only at two discrete points (top and bottom of reinforcement cage). Hereby mimicking a long-strain gauge sensor with the strain in the cable being the average strain between the two attachment points. For gauge length installations the strain cable cannot measure strain if there is a slack in the cable and therefore needs to be pre-tensioned. Once the strain cables are embedded in concrete, they can measure the true distributed strain profile along the embedded length (with sampling resolution of 2.6 mm based on a spatial resolution of 5.2 mm).

The FOSC were attached to the reinforcement bar by initially dressing a sanding pad with turbo tack over the individual cables at the bottom of reinforcement cage (first attachment point). Subsequently the cables were clamped to the rebar using cable ties, see Figure 2.

Figure 2: Left, sanding pad with turbo tack. Right, cable-tying and clamping to the rebar.

After the turbo tack had solidified the FOSC were pre-tensioned to approximately 1000 με and then attached to the top of the reinforcement cage (second attachment point). The same procedure was followed except the turbo tack was omitted to avoid slippage of the FOSC in the period until solidification. The strain cables were subsequently cable-tied loosely to the rebar between the two attachment points to avoid displacement of the strain cable during concrete pouring, see Figure 3.

Figure 3: Left, fibre optic spectrum analyser (FOSA) and fibre optic switch (FOS). Right, loosely cable-tied fibre optic strain cable (FOSC).

C.1.2 Fibre optic temperature cables (FOTC)

The Rayleigh based FOTC (commercially available BRUsens temperature 85 °C cables from BRUGG cables) were also installed as gauge length installation, where the temperature cables were loosely attached at two discrete points (top and bottom of reinforcement cage) to avoid slippage during installation. The FOTC were attached loosely without pre-tension to function independently

of the strain in the construction and can measure the temperature changes with a spatial resolution of 2.6 mm.

The FOTC were attached at two attachment point using only cable-ties, as the loose tube inside the temperature cable is sufficiently strong to protect the optical fibre. The FOTC were subsequently cable-tied loosely to the rebar between the two attachment points to avoid displacement of the temperature cable during concrete pouring, see Figure 4.

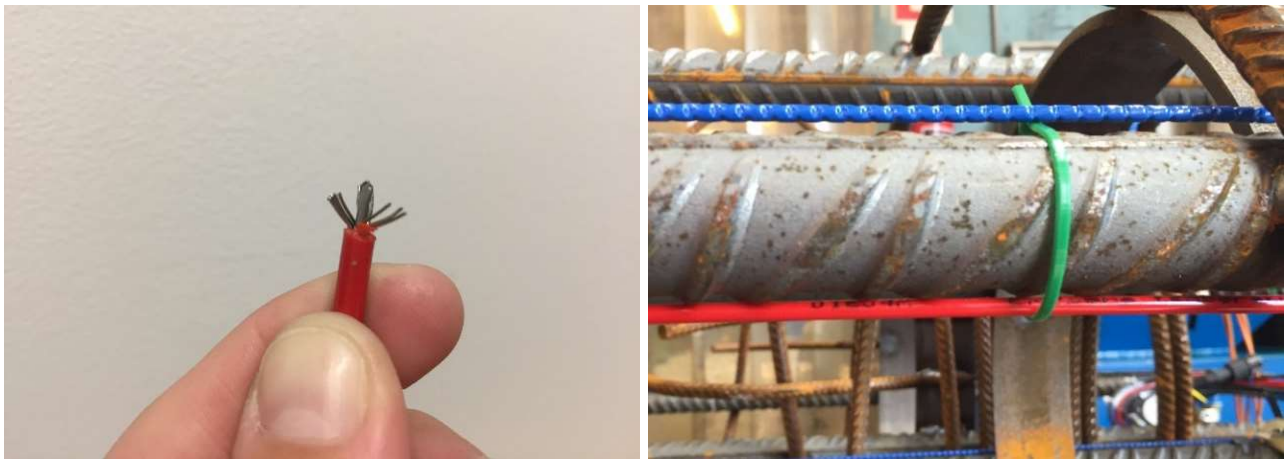

Figure 4: Left, loose tube inside fibre optic temperature cable (FOTC). Right, loosely cable-tied fibre optic temperature cable (FOTC).

C.1.3 Vibrating wire strain gauges (VWSG)

Geosense VWS-4000 VWSG on sister bars with a diameter of 16 mm were used, see Figure 5.

Figure 5: Vibrating wire strain gauges (VWSG) mounted on sister bar in reinforcement cage.

To ensure measurements of strain in the concrete, the sister bars with VWSG were cable-tied to the reinforcement cage and not fixed in such a way (e.g. welded) that they would measure strain in the reinforcement bar, see Figure 6.

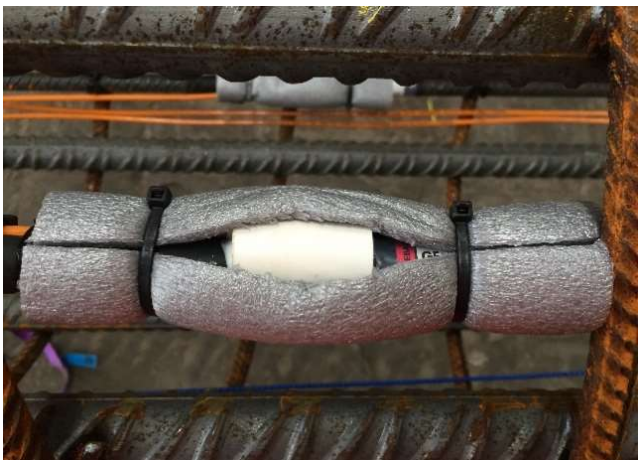

Figure 6: Left, cable-tied sister bar for the vibrating wire strain gauge (VWSG). Right, vibrating wire strain gauge (VWSG) mounted on sister bar.

C.1.4 Tell-tales (TT)

TT were lowered into one-inch diameter tubes after concreting of the pile and before initiating the actual tests on the piles. To serve as basis for displacement transducers a small steel plate was welded on top of the TT.

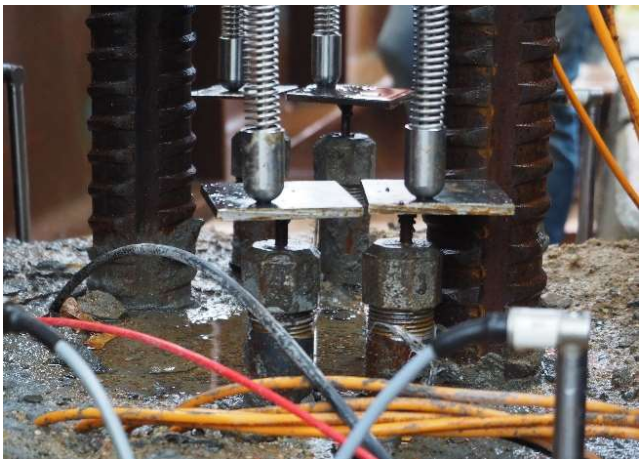

Figure 7: Left, welding of steel plate on tell-tales (TT). Right, displacement transducers on tell-tales (TT).

C.2 Test pile installation

The test piles (bored cast-in-situ piles) were installed by Aarsleff under supervision of the Industrial PhD student. The piles were installed according to "DS/EN 1536:2010+A1:2015, Execution of special geotechnical work – Bored piles" and DS/EN 1992-1-1, Eurocode 2: Design of concrete structures – Part 1-1: General rules and rules for buildings.

C.2.1 Installation method

The equipment used for installation of the test piles was a Bauer drilling rig (BG 36 H) that provides Kelly drilling, see Figure 8.

BAUER Maschinen GmbH
BAUER-Str.1, 86529 Schrobenhausen, Deutschland

Spezialtiefbaugerät, Gerätetyp *Special foundation equipment, Type*			BG 36 H
Baujahr *Year of manufacture*	2018	Trägergerät *Base carrier*	BS 95.6.3033
Fabrik Nr. *Serial No.*	3796	Gesamtgewicht *Total weight*	101000 kg
Motorleistung *Engine power*	403 kW	Arbeitsspannung *Working voltage*	24 V
Inventurnummer *Inventory number*		Rückzugskraft *Pulling force*	400 kN
Betriebsdruck *Working pressure*	350 bar	Vorschubkraft *Pushing force*	400 kN
Hauptwinde Hakenregellast / Ausnahmelast *Main winch normal / exeption*			287 kN
Hilfswinde Hakenregellast / Ausnahmelast *Auxiliary winch normal / exeption*			80 kN

Figure 8: Left, Bauer drilling rig (BG 36 H). Right, Data sheet on Bauer drilling rig.

Pre-drilling (Ø1000 mm diameter) to 3.4 m below ground for replacement with sand prior to pile installation commenced on Saturday the 17th of August 2019. Subsequently the eight test piles were installed with a Ø620 mm diameter casing from Tuesday the 20th of august to Friday the 23rd of august 2019. The accurate installation periods of the test piles are given according to Table 1.

Table 1: Installation periods for the eight test piles at the test site in Hinge.

Test pile [No.]	Date [dd-mm-yyyy]	Drilling [hh:mm]	Concreting [hh:mm]
5	20-08-2019	07:30 – 09:30	11:51 – 12:50
1	20-08-2019	13:30 – 14:30	15:25 – 15:53
7	21-08-2019	07:15 – 08:10	10:25 – 11:06
2	21-08-2019	11:00 – 12:10	15:11 – 15:43
6	22-08-2019	07:30 – 08:10	10:03 – 11:17
3	22-08-2019	12:00 – 13:00	15:00 – 15:37
4	23-08-2019	07:15 – 08:30	09:19 – 09:52
8	23-08-2019	11:10 – 12:00	13:41 – 14:29

The casing was lowered simultaneous with the drilling equipment and kept at a depth that allowed drilling inside the casing. An auger was used for drilling inside the casing and a bucket was used to clean the bottom of the borehole before concreting. No water was used in the borehole during drilling and cleaning. The casing was always kept 1 m above ground to ensure against contamination by debris, and the reinforcement cage was lowered into the borehole before concreting, see Figure 9.

Figure 9: Left, auger for drilling inside casing. Middle, bucket for cleaning of the bottom. Right, lowering of reinforcement cage into borehole.

The PhD student attached dataloggers to the VWSG on each reinforcement cage prior to lifting and lowering into the borehole to monitor the strain development during installation. Furthermore, the PhD student took manual readings of the FOSC and FOTC when each reinforcement cage was located flat on the ground as well as hanging vertically from the drilling rig just prior to and immediately after touching the bottom of the borehole and immediate after concreting of the test piles. Likewise, these readings are used to monitor the strain development during installation and to validate the results. See Figure 10.

Figure 10: Left, collection of data from dataloggers. Right, readings of fibre optic cables.

The bored cast-in-situ piles were concreted from the bottom up with a tremie pipe, and the tip was kept below the surface of the concrete to avoid mixture and separation. The attached dataloggers were protected inside a plastic bag during concreting and attached to the drilling rig during withdrawal of the casing, see Figure 11.

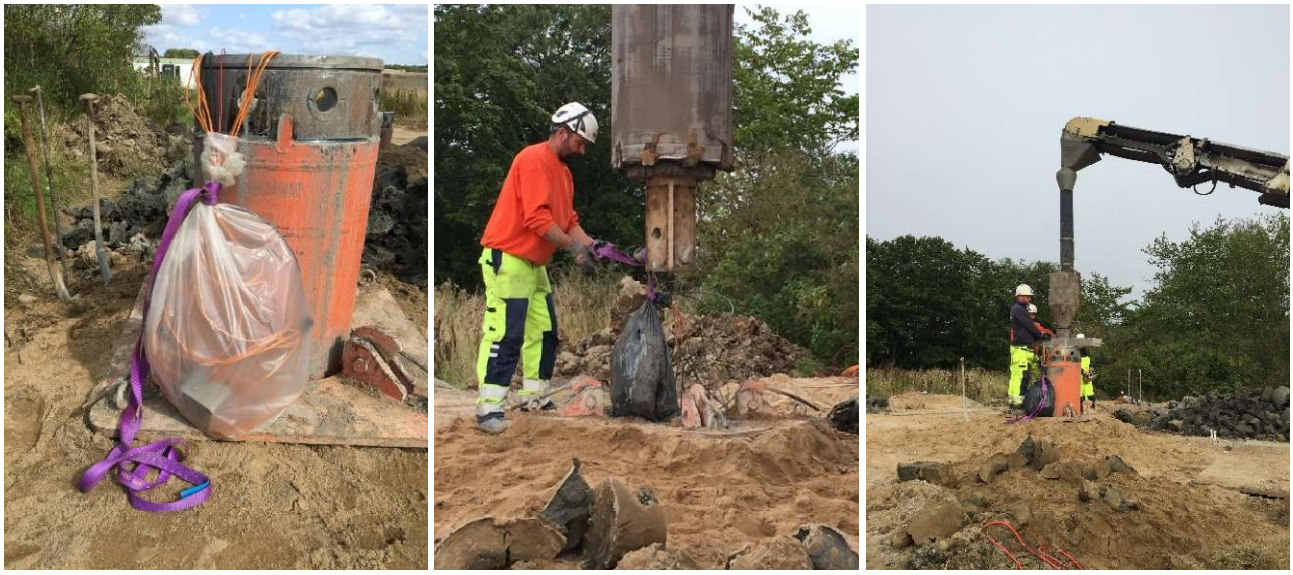

Figure 11: Left, protection of dataloggers. Middle; attachment of plastic bag to drilling rig. Right, concreting of pile with tremie pipe.

The GEWI bars for the pile test were installed manually after concreting of the piles, see Figure 12.

Figure 12: Left, Manual installation of GEWI bars after concreting. Right, Installed GEWI bars.

C.2.2 Deviations in the field

The bottom of the boreholes varies from 5 cm too low to 3 cm too high for test pile 1 – test pile 8.

The reinforcement cages generally fit tight in the casing and is hammered into place and is therefore possibly not hanging free during lowering into the borehole. This was pronounced for test pile 1 and test pile 2.

For test pile 2 and 4, there was poured a little concrete in the borehole prior to installation of the reinforcement cage due to the attached flat jack at the bottom.

For test pile 3 the reinforcement cage followed the casing up during withdrawal of the casing and was pushed back down after final concreting.

For test pile 4 there were approximately 10 cm of water at the bottom of the borehole before concreting. The water came in from the side of the casing, not from below the pile. Furthermore, the measurements with fibre optic and temperature cables were discarded for the reinforcement cage hanging in the borehole and standing on the bottom of the borehole due to noise. After concreting, the fibre optic cables were working again.

C.3 Conduction of static pile load tests

Static pile load tests for the eight test piles were conducted as tension tests by DMT. The PhD student supervised the static pile load tests and collected data from the distributed FOSC and FOTC, traditional VWSG and TT. The piles were tested in groups at three different times after installation (∼1.5 months, ∼7.5 months and ∼3 years).

Test round 1

First test round includes test pile 1 and test pile 7 approximately 1.5 months after pile installation. Test pile 7 was tested on Tuesday the 8th of October 2019 and test pile 1 was tested on Thursday the 10th of October 2019 after 48 and 51 days of rest, respectively.

Test round 2

Second test round applied test pile 3, test pile 5 and test pile 8 approximately 7.5 months after pile installation. Test pile 5 was tested on Tuesday the 31st of March 2020, test pile 3 was tested on Thursday the 2nd of April 2020 and test pile 8 was tested on Saturday the 4th of April 2020 after 224, 224 and 225 days of rest, respectively.

Test round 3

Third test round applied test pile 2, test pile 4 and test pile 6 approximately 3 years after pile installation. Test pile 2 was tested on Tuesday the 28th of June 2022, test pile 6 was tested on Thursday the 30th of June 2022 and test pile 4 was tested on Saturday the 2nd of Juli 2022 after 1042, 1044 and 1043 days of rest, respectively.

C.3.1 Steel traverse system

The steel traverse system was built around each test pile one day prior to the static pile loading test in tension. Cribbing was used on both sides of the test pile with a clearance of approximately 2.5 m from the test pile. A pair of 4 m long HE300B load distribution beams were placed on top of each cribbing as support for the two HE800B main beams with a length of 10 m. Above, two pairs of HE400B beams with a length of 4 m were located crosswise above the centre of the test piles to distribute the load on both main beams and to support the load application system, see Figure 13 and Figure 14.

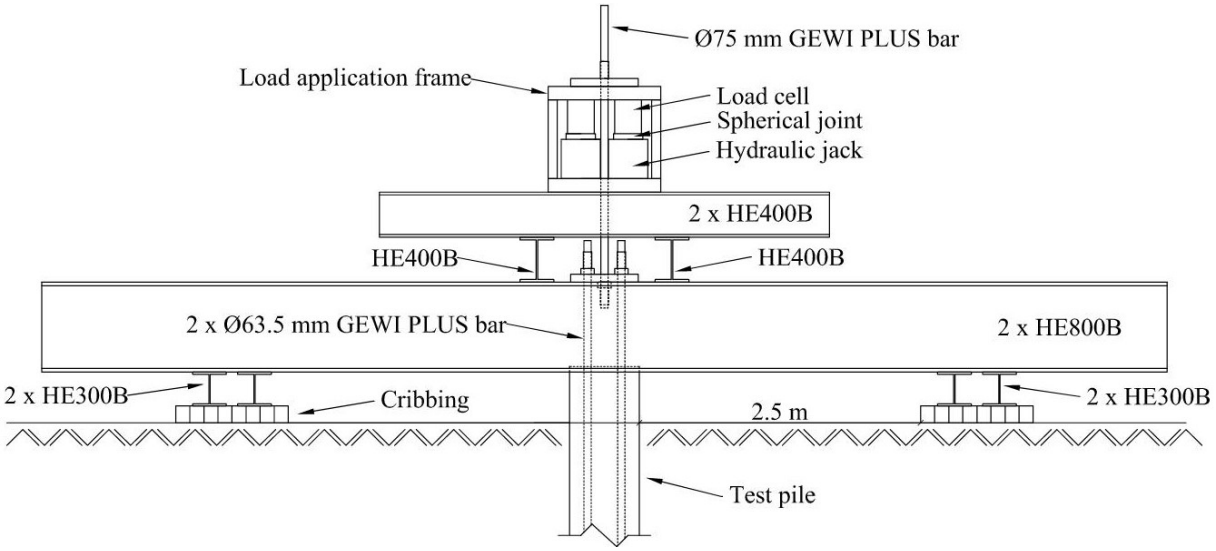

Figure 13: Illustration of steel traverse system for static pile loading test in tension seen from the side.

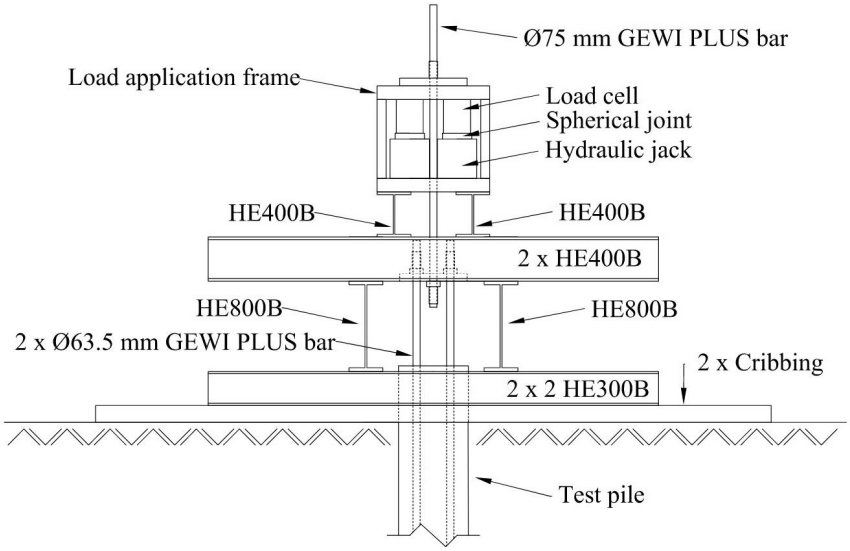

Figure 14: Illustration of steel traverse system for static pile loading test (tension) seen from the end.

C.3.2 Load Application system

The load application system consisted of a load application frame with four hydraulic jacks. The load frame was located central to the pile axis and each hydraulic jack had a capacity of 300 t and a stroke of 250 mm. The load was measured by 3 MN load cells on top of each hydraulic jack. A coupler steel plate with a GEWI PLUS 75 mm bar was attached to the two GEWI PLUS 63.5 mm bars anchored into each test pile to transfer the force from the load application system to the test pile. See Figure 15.

Figure 15: Left, installation of load frame. Middle, load frame for static pile load test (tension). Right, connection to test pile.

C.3.3 Reference system

Four displacements transducers measured the vertical displacement of the test piles (pile top) against independent reference beams. Two additional displacements transducers were used to measure any horizontal displacements of the pile top during test. The latter were mounted horizontally with an internal angle of 90 degrees. The reference beams (yellow) were 6 m long and mounted on square woods at the ends to ensure independent measurements of pile displacement from test setup and any movements thereof. Possible elevations of the reference beams were measured with surveyors' level at two selected points. See Figure 16.

Figure 16: Left, surveyors' level. Right, reference beams (yellow).

Moreover, four displacement transducers measured the vertical displacement of TT against an independent reference system. For test pile 1 the reference system was a beam mounted on a steel box in one end, and square wood in the other end and for test pile 7 the reference system was a beam

mounted on Hoffmann blocks on top of square wood. See Figure 17. For test piles 2-6 and 8 a developed steel frame attached to the yellow reference beams made up the reference system.

Figure 17: Left, reference system for measuring tell-tales (TT) displacements, Middle (two pictures), reference system for test pile 1. Right, reference system for test pile 7.

C.3.4 Instrumentation

Loads were measured by Implenia 3 MN circular load cells, and the load system (4 Implenia load cells) can measure loads of 0-12 MN with an accuracy of ≤1 kN. Readings were carried out with 0.1 kN precision, and a resolution of 15 significant digits. Data acquisition was performed using HBM QuantumX MX80 amplifiers using Catman AP software. Data acquisition was performed with a frequency of 1 Hz.

Displacement transducers for pile top and TT movement were HBM WA100-T displacement transducers with 100 mm range and an accuracy ≤ 0.001 mm. Readings were carried out with 0.01 mm precision, and a resolution of 15 significant digits. Data acquisition was performed using HBM QuantumX MX-840 amplifiers using Catman AP software. Data acquisition was performed with a frequency of 1 Hz.

For test pile 1 and 7 however, the displacement transducers for TT movement were vibrating wire displacement transducers, model VWDT 6000, with 75 mm range and an accuracy ± 0.1 % FSO. Readings were carried out with a resolution of 0.025% FS. Data acquisition was performed using RST Instruments vibrating wire / thermistor data logger using DT Logger Host software. Data acquisition was performed with a frequency of 1/60 Hz.

VWSG were Geosense VWS-4000 series vibrating wire sister bars with 3000 με range and an accuracy ± 0.25 % FS. Readings were carried out with a resolution of 0.4 με. Temperatures were measured by thermistors (3k ohms at 25°C). Data acquisition was performed using the RST Instruments vibrating wire / thermistor data logger using DT Logger Host software. Data acquisition was performed with a frequency of 1/60 Hz.

FOSC and FOTC were BRUsens V9 strain cables (blue) and BRUsens temperature 85 °C cables (red) from BRUGG cables. Readings were carried out with a resolution of 0.01 με for FOSC and 0.0001 °C for FOTC. Data acquisition was performed using the LUNA fibre optic switch (FOS), a remote module, a standoff cable and the LUNA optical distributed sensor interrogator, model ODiSI-B using the ODiSI-B software, where a spatial and sampling resolutions of 5.2 mm and 2.6 mm, respectively, was used. Data acquisition was performed manually.

C.4 Flat Jack test

Aarsleff performed a flat jack test for test pile 2 on Wednesday the 16th of October 2019 and for test pile 4 on Thursday the 17th of October 2019 after 56 and 55 days of rest, respectively. Unfortunately, the Flat Jack test failed, and all pressure was lost at 19 bar for both test piles. It was not possible to reapply the pressure and analysis of the results were therefore omitted. However, subsequently test pile 2 and test pile 4 were subjected to a static pile load test (tension) and post-processing of the retrieved data.

No pictures or detailed information about the Flat Jack device is provided in agreement with Aarsleff.

D Specification of test piles

D.1 Static documentation

COWI

JULI 2019

ADRESSE COWI A/S
Jens Chr. Skous Vej 9
8000 Aarhus C
Danmark

TLF +45 56 40 00 00
FAX +45 56 40 99 99
WWW cowi.dk

Borede pæle, forsøg

Statisk dokumentation

INDHOLD

1 Introduktion

2 Grundlag og forudsætninger

3 Kontrol af armeringsgrad

4 Eftervisninger

5 Konklusion

BILAG

1 Armeringsgrad og revnevidde
2 Trykkapacitet, søjlebetragtning
3 DYWIDAG reinforcement systems, GEWI PLUS
4 GEWI PLUS accessories
5 GEWI PLUS
6 Mail

REFERENCER

/BCJ/ Betonkonstruktioner efter DS/EN 1992-1-1
/KM/ Kaj Madsen, note om forankring af kabler
/EC2/ DS/EN 1992-1-1, 2008

PROJEKTNR.	A113120
DOKUMENTNR.	KON-TEK-100
VERSION	1.0
UDGIVELSESDATO	JULI 2019
UDARBEJDET	AHML
KONTROLLERET	FANA
GODKENDT	JAHS

1 Introduktion

Nærværende dokument indeholder en statisk dokumentation af betonpæle, som skal anvendes til hhv. træk- og trykforsøg til Jannie Knudsens erhvervs ph.d. Pælene funderes i en dybde på 8m, hvor 1m pæl er over terræn.

2 Grundlag og forudsætninger

2.1 Geometri for pæle

Diameter $d := 620mm$

Længde $l := 9m$

Dæklag $c := 85mm$

Areal pæl $A_c := \pi \cdot \frac{d^2}{4}$ $A_c = 301907.05 \cdot mm^2$

2.2 Forudsætninger for flatjack, som anvendes til trykforsøg

Det er oplyst, at flatjacken's areal udgør 53% af pælens areal. dermed er flatjackens diameter

Diameter $d_{fj} := \sqrt{\left(\frac{d}{2}\right)^2 \cdot 0.53 \cdot 2}$ $d_{fj} = 451.37 \cdot mm$

Areal $A_{fj} := \pi \cdot \frac{d_{fj}^2}{4}$ $A_{fj} = 160010.74 \cdot mm^2$

Kontrol $A_{fj} = 0.53 A_c$ $\frac{A_{fj}}{A_c} = 0.53$

Maksimalt tryk $p_{max} := 100bar$ $p_{max} = 10000 \cdot \frac{kN}{m^2}$

Maksimal kraft $P_{max} := p_{max} \cdot A_{fj}$ $P_{max} = 1600.11 \cdot kN$

2.3 Belastninger

For at mindske risikoen for, at det ikke bliver armeringen eller betonen som bryder under forsøgene, regnes der med en trykkraft på 2000 kN. Derudover forudsættes det, at pælene skal kunne modstå en trækkraft på ca. 3000 kN.

Trækkraft $P_t := 3000kN$

Trykkraft $P_c := 2000kN$

2.4 Materialeparametre

Beton:

Trykstyrke, 5% fraktil $f_{ck} := 35MPa$

Partialkoefficient for tryk $\gamma_c := 1.45$

$$f_{cd} := \frac{f_{ck}}{\gamma_c} = 24.14 \cdot MPa \qquad f_{cd} = 24.14 \cdot MPa$$

Trækstyrke, 5% fraktil $f_{ctk} := 2.2MPa$

Partialkoefficient for træk $\gamma_c := 1.7$

$$f_{ctd} := \frac{f_{ctk}}{\gamma_c} \qquad f_{ctd} = 1.29 \cdot MPa$$

Stål $f_{yk} := 550MPa$

$\gamma_s := 1.2$

$$f_{yd} := \frac{f_{yk}}{\gamma_s} \qquad f_{yd} = 458.33 \cdot MPa$$

Tilladelig spænding til spalte-armering, jf /KM/ $\sigma_{s.till} := 200MPa$

2.5 Armering:

Langsgående

Diameter $d_s := 32mm$ $d_s = 32 \cdot mm$

Antal stænger $n_s := 8$ $n_s = 8$

Armeringsareal $A_s := \frac{d_s^2}{4} \cdot \pi \cdot n_s$ $A_s = 6433.98 \cdot mm^2$

Tværgående

Diameter $d_{st} := 10mm$ $d_{st} = 10 \cdot mm$

Afstand $c_{st} := 200mm$ $c_{st} = 0.2\,m$

Antal bøjler i ethvert snit $n_{st} := 2$ $n_{st} = 2$

3 Kontrol af armeringsgrad

3.1 Langsgående armering

Armeringsgraden er kontrolleret ved brug af et COWI best practice dokument, se bilag 1. Dokumentet anvendes til kontrol af armeringsgraden, samt til beregning af revnevidder i afsnit 4. Derfor skal der ses bort fra øvrige advarsler i dokumentet.

Bemærk at tværsnittet i dokumentet er rektangulært, hvorfor nominelle værdier for bredde og højde af tværsnittet er fundet her.

Given

$A_c = b^2$

$b_c := \text{Find}(b) \rightarrow (310 \cdot \sqrt{\pi} \cdot mm \quad -310 \cdot \sqrt{\pi} \cdot mm)$ $b_c = (549.46 \quad -549.46) \cdot mm$

Derudover er der ilagt 8Y32 svarende til den faktiske armering, og det ses at tværsnittet er normaltarmeret.

3.2 Tværarmering

Den maksimale afstand mellem tværarmeringen findes ved EC2 afsnit 9.5.3(3), og det kontrolleres at øvrige krav i 9.5.3 overholdes.

Maksimal afstand $s_{cl.t.max} := \min(20 \cdot d_s, d, 400mm)$ $s_{cl.t.max} = 400 \cdot mm$

4 Eftervisninger

4.1 Trykkapacitet

Jvf. EC7 afsnit 7.8(5), skal der ikke laves kontrol for søjlevirkning, såfremt pælene er i jordlag med en karakteristisk, udrænet forskydningsstyrke cu på over 10 kPa. Det forudsættes at pælene funderes i jordlag der overholder dette krav, hvorfor der ikke tjekkes for søjlevirkning i de nederste 7 meter af pælene.

Pælene er ca. 1m over jorden, hvorfor der for denne del skal tjekkes søjlevirkning. Konservativt betragtes de øverste 2m, og eftersom det betragtes som en indspændt søjle, er den frie søjlelængde 4m.

Trykbelastningen er beskrevet i afsnit 2.3. Det antages at eccentriciteten for denne trykbelastning, maksimalt vil være 50mm. Eftervisningen af pælens trykkapacitet er eftervist i bilag 2. Af bilag 2, ses det, at kapaciteten er tilstrækkelig.

4.2 Trækkapacitet

$$P_{t.Rd} := A_s \cdot f_{yd} \qquad P_{t.Rd} = 2948.91 \cdot kN$$

Bæreevnen på over 2900kN vurderes tilstrækkelig.

4.3 Revnevidder

Revnevidden er beregnet ved brug af bilag 1. Her er normalkraften påsat, som den eneste belastning, og er påsat som en trækkraft. Dermed findes revnevidden for pælen, og det ses at revnevidden bliver ca. end 0.12mm

4.4 Lokalt tryk i bunden

Grundet flatjacken i bunden, antages det at trykket fordeles over 53% at tværsnittet, se afsnit 2.2. Derfor tjekkes der for lokalt tryk i bunden af pælen, samt armeringsbehovet til det tværgående træk.

Lokal trykbæreevne, uden hensyn til styrkeforøgelse. $N_{Rd.l} := A_{fj} \cdot f_{cd} = 3862.33 \cdot kN$ $N_{Rd.l} = 3862.33 \cdot kN$

$$krav_{tryk} := if\left(\frac{P_c}{N_{Rd.l}} \le 1, "OK", "NB"\right) \qquad krav_{tryk} = "OK"$$

Tværgående træk $F_{Ed} := 0.25 \cdot P_c \cdot \left(1 - \frac{d_{fj}}{d}\right) = 135.99 \cdot kN$

Armeringen der ilægges for at modsvare dette tværgående træk, skal fordeles over en afstand svarende til søjlens bredde, d. Ved den valgte armering, hvor afstanden mellem tværarmeringen lokalt reduceres til 100mm fås:

Afstand $c_{st.l} := 100mm$ $c_{st.l} = 0.1\,m$

Antal bøjler $n_l := round\left(\frac{d}{c_{st.l}}\right)$ $n_l = 6$

Kapacitet $F_{Rd} := \frac{d_{st}^2}{4} \cdot \pi \cdot n_{st} \cdot \eta_1 \cdot \sigma_{s.till}$ $F_{Rd} = 188.5 \cdot kN$

$krav_{Fed} := if\left(\frac{F_{Ed}}{F_{Rd}} \le 1, "OK", "NB"\right)$ $krav_{Fed} = "OK"$

4.5 Ankerstang til trækforsøg

Til trækforsøget anvendes GEWI PLUS ankre, som indstøbes i betonen.
Flydestyrken fremgår af figur 0.

Flydestyrke $f_{yk.a} := 670MPa$ $f_{yk.a} = 670 \cdot MPa$

$f_{yd.a} := \frac{f_{yk.a}}{1.2}$ $f_{yd.a} = 558.33 \cdot MPa$

Nødvendigt antal stænger og diameter.

Nødvendigt areal $A_{a.req} := \frac{P_t}{f_{yd.a}}$ $A_{a.req} = 5373.13 \cdot mm^2$

Af bilag 2 ses det på side 2, at arealet af en Ø75 stang ikke er tilstrækkeligt, hvorfor der anvendes to Ø63.5 stænger.

steel grade	yield strength [N/mm²]	tensile strength [N/mm²]	nominal diameter [mm]	cross sectional area [mm²]	weight per metre [kg/m]	load at yield [kN]	ultimate load [kN]
GEWI®Plus	670	800	30	707	5.55	475	565
GEWI®Plus	670	800	35	962	7.55	640	770
GEWI®Plus	670	800	43	1,466	11.51	980	1,170
GEWI®Plus	670	800	57.5	2,597	20.38	1,740	2,080
GEWI®Plus	670	800	63.5	3,167	24.86	2,120	2,540
GEWI®Plus	670	800	75	4,418	34.68	2,960	3,535

Figur 0: Udsnit af bilag 2

Diameter $d_a := 63.5mm$

Afstand mellem stænger (center) $a_a := 200mm$

Dæklag stænger $c_a := \frac{d - a_a - d_a}{2}$ $c_a = 178.25 \cdot mm$

Areal 1 Ø63,5 $A_a := \frac{d_a^2}{4} \cdot \pi$ $A_a = 3166.92 \cdot mm^2$

Samlet areal $A_{a.total} := A_a \cdot 2$ $A_{a.total} = 6333.84 \cdot mm^2$

4.6 Forankring af GEWI PLUS stænger

Forankringen antages at blive optaget via forskydning langs ankerstængerne, hvor det skal sikres at der er tilstrækkelig forankringslængde. Dette er valgt, da der ikke er plads til spaltearmering og ankerplader under støbning.

Forankringsstyrke :

Faktor mht armeringsforhold, konservativt antages "ikke gode forhold" $\eta_1 := 0.7$

Faktor mht. diameter $\eta_2 := \frac{\left(132 - \frac{d_a}{mm}\right)}{100}$ $\eta_2 = 0.69$

Forankringsstyrke $f_{bd} := 2.25 \cdot \eta_1 \cdot \eta_2 \cdot f_{ctd}$ $f_{bd} = 1.4 \cdot MPa$

Forankringslængde :

Basisforankringslængde $l_{b.rqd} := \frac{d_a}{4} \cdot \frac{f_{yd.a} \cdot \frac{A_{a.req}}{A_{a.total}}}{f_{bd}}$ $l_{b.rqd} = 5.39\,m$

Dette antages også at være den regnignsmæssige. Trækkraften i ankerstængerne skal overføres til den generelle længdearmering, hvorfor disse skal kunne aktiveres. Forholdene for den generelle længdearmering er bedre end for ankerstænger, da de både har mindre diameter, men også er under gode forankringsforhold. Derfor vil forankringslængden for disse være væsentligt mindre, og vil ikke blive eftervist. Da spændingerne skal spredes ud til den generelle armering, rundes forankringslængden op til 6m, for at sikre tilstrækkelig overførsel.

Forankringslængde $l_{bd} := 6m$

5 Konklusion

Det vurderes ud fra ovenstående beregninger, at der er tilstrækkelig kapacitet i betonpælen til de tiltænkte forsøg, hvor følgende eftervisninger er gennemført:

- Armeringsgrad
- Trykkapacitet hvor de øverste 2m af pælen betragtes som en søjle
- Trækkapacitet, hvor der er en kapacitet på 2948kN
- Revnevidder, hvor den største revne teoretisk er 0,12mm
- Lokalt tryk i bunden, hvor der anvendes flatjacks
- GEWI PLUS ankerstænger, herunder:
    - Størrelse og antal for tilstrækkelig trækkapacitet. 2 stk. Ø63,5mm GEWI PLUS
    - Forankringlængde 6m

Mht. forankring af ankerstænger. Det er oplyst, se bilag 6, at forankringslængden for GEWI PLUS Ø63,5 stænger er 3,8m under gode forankringsforhold. Dermed anses den beregnede forankringslængde for at være konservativ.

D.2 Axial pile stiffness

Urevnet tværsnit

Det antages at der ved lave spændinger forekommer træk i betonen såvel som armeringen.

Forudsætninger beton

Materiale

Betonens E-modul ved træk, antages at være lig begyndelseselasticitetsmodulet. I det følgende regnes begyndelseselasticitetsmodulet efter /BCJ/ formel 1.2 samt /EC2/ tabel 3.1, baseret på middelbetonstyrken og tøjningen ved $\sigma_c = 0$

Middelbetonstyrke	f_{cm}	60	N/mm²
Middeltrækstyrke	f_{ctm}	4,35	N/mm²
Sekantelasticitetsmodul	E_{cm}	37659	N/mm²
Tryktøjning i beton ved højeste spænding	ε_{c1}	2,49	promille
k-faktor	k	1641	-
Tøjning	ε_c	0	promille
Begyndelseselasticitetsmodul	E_c	39542	N/mm²

Geometri

Diameter	d_c	620	mm
Areal	A_c	301907	mm²
Længde pæl	L	9000	mm

Forudsætninger armering

Materiale

E-modul	E_s	200000	N/mm²

Geometri

Diameter armeringsstang	d_s	32	mm
Antal armeringsstænger	n_s	8	-
Armeringsareal	A_s	12768	mm²

Ved et element af to materialer, transformeres det ene materiale til det andet, baseret på elasticitetsmodulerne.

Transformationsfaktor $\alpha = \frac{E_S}{E_C}$ 5,06 -

Stivhed

E-modul	E	39542	N/mm²
Transformeret areal	A_t	366486	mm²
Stivhed	$E A_t$	1,4492E+10	N

Urevnet tværsnit

Det antages at der ved lave spændinger forekommer træk i betonen såvel som armeringen.

Forudsætninger beton

Materiale

Betonens E-modul ved træk, antages at være lig begyndelseselasticitetsmodulet. I det følgende regnes begyndelseselasticitetsmodulet efter /BCJ/ formel 1.2 samt /EC2/ tabel 3.1, baseret på middelbetonstyrken og tøjningen ved $\sigma_c = 0$

Middelbetonstyrke	f_{cm}	60	N/mm²
Middeltrækstyrke	f_{ctm}	4,35	N/mm²
Sekantelasticitetsmodul	E_{cm}	37659	N/mm²
Tryktøjning i beton ved højeste spænding	ε_{c1}	2,49	promille
k-faktor	k	1641	-
Tøjning	ε_c	0	promille
Begyndelseselasticitetsmodul	E_c	39542	N/mm²

Geometri

Diameter	d_c	620	mm
Areal	A_c	301907	mm²
Længde pæl	L	9000	mm

Forudsætninger armering

Materiale

E-modul	E_s	200000	N/mm²

Geometri

Diameter armeringsstang	d_s	32	mm
Antal armeringsstænger	n_s	8	-
Armeringsareal	A_s	6434	mm²

Ved et element af to materialer, transformeres det ene materiale til det andet, baseret på elasticitetsmodulerne.

Transformationsfaktor $\alpha = \frac{E_s}{E_c}$ 5,06 -

Stivhed

E-modul	E	39542	N/mm²
Transformeret areal	A_t	334450	mm²
Stivhed	E A_t	1,3225E+10	N

E Static pile loading tests

E.1 Deviations observed during the static pile loading tests

Maintained load (ML) test

For test pile 1 the power was lost twice during the static pile load test, which resulted in minor data losses after approximately 3 hours and 11 hours, 40 minutes. Furthermore, the hydraulic system for test pile 1 had a leak, which was discovered at load step 2 (200 kN) and repaired between the 1st and 2nd load cycle. Therefore, the time of sustained load was extended to approximately one hour for load step 2 and three hours for load step 10 (between 1st and 2nd load cycle).

Constant rate of uplift (CRU) test

For test pile 2, the rate of the initial part of the reloading path with a constant rate of uplift (CRU) of 20 mm/h was unstable (rate significantly lower) up till approximately 150 kN.

For test pile 3 the laptop charger failed during the static pile load test, which resulted in approximately 31 minutes of data loss between the 1st and 2nd load cycle. The static pile load test continued immediately after the laptop was replaced.

For test pile 4, the measurements from one of the four displacement transducers for pile top movement were jumping and thus unreliable. Therefore, two of the remaining three functioning displacement transducers installed in diametrically opposite sides of the test pile (to ensure the bending moments are separated from the axial loads) was used.

For test pile 5 the laptop charger failed during the static pile load test, which resulted in approximately 1 hour and 39 minutes of data loss at load step 13 (750 kN). The static pile load test continued immediately after the laptop charger was replaced. Furthermore, an interruption occurred during the constant rate of uplift (CRU) part of the test, which resulted in a minor data loss of approximately 2 min.

E.2 Maintained load

Test pile 1

Table 2: Deviations from target load for test pile 1.

Test pile 1	Applied load		
Load step no.	Target (kN)	Average (kN)	Deviation (%)
1	100	100	-0.20
2	200	200	-0.19
3	300	299	-0.21
4	400	400	-0.05
5	500	500	-0.08
6	400	402	0.43
7	300	291	-3.10
8	200	203	1.42
9	100	106	6.41
10	0	10	-
11	125	129	3.39
12	250	252	0.68
13	375	377	0.45
14	500	501	0.19
15	625	625	0.03
16	675	675	0.02
17	725	725	0.02
18	775	775	0.01
19	825	824	-0.13

Table 3: Deviations from average value to the determined maximum and minimum load for test pile 1.

Test pile 1	Applied load				
Load step no.	Average (kN)	Maximum (kN)	Deviation (%)	Minimum (kN)	Deviation (%)
1	100	101	1.2	98	-1.5
2	200	201	0.6	198	-1.0
3	299	301	0.7	297	-0.8
4	400	402	0.6	396	-1.0
5	500	501	0.3	498	-0.4
6	402	402	0.1	399	-0.6
7	291	293	0.6	285	-2.0
8	203	204	0.8	198	-2.3
9	106	109	2.3	101	-4.9
10	10	23	-	-5	-
11	129	133	3.1	124	-4.0
12	252	255	1.5	246	-2.4
13	377	380	0.9	373	-0.9
14	501	512	2.2	497	-0.9
15	625	631	0.9	620	-0.8
16	675	679	0.5	669	-1.0
17	725	731	0.8	721	-0.6
18	775	778	0.3	772	-0.4
19	824	830	0.7	815	-1.1

Test pile 2

Table 4: Deviations from target load for test pile 2.

Test pile 2	Applied load		
Load step no.	Target (kN)	Average (kN)	Deviation (%)
1	100	100	-0.07
2	200	200	-0.07
3	100	101	0.83
4	0	11	-
5	100	100	-0.13
6	200	200	-0.05
7	300	300	0.00
8	400	400	-0.02
9	500	500	0.04
10	600	600	-0.03
11	650	650	-0.02
12	700	700	-0.05
13	750	750	-0.01
14	800	800	-0.01

Table 5: Deviations from average value to the determined maximum and minimum load for test pile 2.

Test pile 2	Applied load				
Load step no.	Average (kN)	Maximum (kN)	Deviation (%)	Minimum (kN)	Deviation (%)
1	100	101	1.1	98	-1.7
2	200	201	0.7	197	-1.6
3	101	102	1.1	99	-2.1
4	11	13		10	
5	100	101	1.1	99	-1.2
6	200	202	1.1	199	-0.5
7	300	301	0.5	297	-0.9
8	400	404	0.9	397	-0.6
9	500	503	0.5	496	-0.8
10	600	604	1	596	-0.7
11	650	651	0.2	647	-0.5
12	700	703	0.5	697	-0.4
13	750	752	0.3	747	-0.4
14	800	802	0.3	796	-0.5

Test pile 3

Table 6: Deviations from target load for test pile 3.

Test pile 3	Applied load		
Load step no.	Target (kN)	Average (kN)	Deviation (%)
1	100	102	2.35
2	200	202	1.19
3	100	106	5.79
4	0	12	-
5	100	104	4.33
6	200	206	2.98
7	300	302	0.58
8	400	402	0.40
9	500	501	0.19
10	600	600	0.08
11	650	651	0.15
12	700	700	0.06
13	750	751	0.07
14	800	800	0.06

Table 7: Deviations from average value to the determined maximum and minimum load for test pile 3.

Test pile 3	Applied load				
Load step no.	Average (kN)	Maximum (kN)	Deviation (%)	Minimum (kN)	Deviation (%)
1	102	107	4.1	98	-4.1
2	202	208	2.6	198	-2.2
3	106	107	0.9	103	-2.4
4	12	15	-	2	-
5	104	107	2.6	100	-4.5
6	206	209	1.7	201	-2.3
7	302	306	1.4	296	-1.8
8	402	407	1.3	399	-0.7
9	501	504	0.6	495	-1.2
10	600	606	1.0	594	-1.1
11	651	654	0.5	646	-0.8
12	700	704	0.5	697	-0.5
13	751	755	0.5	746	-0.6
14	800	805	0.5	797	-0.5

Test pile 4

Table 8: Deviations from target load for test pile 4.

Test pile 4	Applied load		
Load step no.	Target (kN)	Average (kN)	Deviation (%)
1	100	100	-0.05
2	200	200	0.11
3	100	99	-1.43
4	0	16	-
5	100	100	0.05
6	200	200	-0.11
7	300	300	-0.01
8	400	400	-0.02
9	500	500	-0.08
10	600	599	-0.08
11	650	650	-0.02
12	700	699	-0.08
13	750	750	0.00
14	800	800	-0.04

Table 9: Deviations from average value to the determined maximum and minimum load for test pile 4.

Test pile 4	Applied load				
Load step no.	Average (kN)	Maximum (kN)	Deviation (%)	Minimum (kN)	Deviation (%)
1	100	103	3.0	96	-3.6
2	200	203	1.3	196	-2.2
3	99	106	7.1	95	-3.3
4	16	17		14	
5	100	101	0.9	99	-1.3
6	200	205	2.9	195	-2.4
7	300	304	1.2	297	-1.0
8	400	403	0.9	395	-1.1
9	500	502	0.6	493	-1.2
10	599	604	1	592	-1.2
11	650	654	0.6	645	-0.7
12	699	703	0.6	695	-0.7
13	750	754	0.5	746	-0.5
14	800	803	0.4	796	-0.4

Test pile 5

Table 10: Deviations from target load for test pile 5.

Test pile 5	Applied load		
Load step no.	Target (kN)	Average (kN)	Deviation (%)
1	100	104	4.21
2	200	204	1.93
3	100	107	6.66
4	0	16	-
5	100	106	5.66
6	200	204	2.17
7	300	304	1.28
8	400	405	1.34
9	500	504	0.88
10	600	604	0.67
11	650	654	0.61
12	700	704	0.56
13	750	751	0.10
14	800	803	0.35

Table 11: Deviations from average value to the determined maximum and minimum load for test pile 5.

Test pile 5	Applied load				
Load step no.	Average (kN)	Maximum (kN)	Deviation (%)	Minimum (kN)	Deviation (%)
1	104	107	2.3	100	-3.6
2	204	207	1.6	198	-3.1
3	107	112	4.6	101	-5.2
4	16	21	-	9	-
5	106	111	4.8	100	-5.3
6	204	207	1.5	201	-1.8
7	304	309	1.8	298	-1.9
8	405	414	2.1	398	-1.8
9	504	509	0.8	498	-1.3
10	604	609	1.0	598	-1.1
11	654	658	0.7	650	-0.7
12	704	709	0.7	699	-0.6
13	751	755	0.7	747	-0.5
14	803	810	0.9	797	-0.7

Test pile 6

Table 12: Deviations from target load for test pile 6.

Test pile 6	Applied load		
Load step no.	Target (kN)	Average (kN)	Deviation (%)
1	100	100	-0.05
2	200	200	-0.03
3	100	100	-0.43
4	0	10	-
5	100	105	5.00
6	200	200	-0.01
7	300	300	-0.05
8	400	400	0.03
9	500	500	0.06
10	600	600	0.04
11	650	650	-0.07
12	700	700	-0.04
13	750	750	-0.02
14	800	800	-0.02

Table 13: Deviations from average value to the determined maximum and minimum load for test pile 6.

Test pile 6	Applied load				
Load step no.	Average (kN)	Maximum (kN)	Deviation (%)	Minimum (kN)	Deviation (%)
1	100	101	1.4	96	-3.5
2	200	202	1.1	197	-1.6
3	100	101	1.7	98	-1.4
4	10	14		9	
5	105	106	0.9	101	-4.2
6	200	202	1.0	198	-0.7
7	300	302	0.6	296	-1.3
8	400	403	0.8	397	-0.7
9	500	503	0.5	496	-0.8
10	600	607	1.2	597	-0.5
11	650	652	0.4	643	-0.9
12	700	703	0.4	696	-0.5
13	750	755	0.7	747	-0.4
14	800	802	0.3	798	-0.3

Test pile 7

Table 14: Deviations from target load for test pile 7.

Test pile 7	Applied load		
Load step no.	Target (kN)	Average (kN)	Deviation (%)
1	100	100	-0.39
2	200	200	-0.16
3	300	299	-0.46
4	400	399	-0.16
5	500	498	-0.30
6	400	405	1.15
7	300	306	1.85
8	200	204	1.88
9	100	109	8.62
10	0	15	-
11	125	125	-0.19
12	250	249	-0.24
13	375	376	0.39
14	500	500	-0.05
15	625	625	0.01
16	750	748	-0.28

Table 15: Deviations from average value to the determined maximum and minimum load for test pile 7.

Test pile 7	Applied load				
Load step no.	Average (kN)	Maximum (kN)	Deviation (%)	Minimum (kN)	Deviation (%)
1	100	105	5.4	94	-5.9
2	200	208	4.4	194	-3.1
3	299	306	2.5	292	-2.3
4	399	406	1.7	395	-1.1
5	498	509	2.2	492	-1.4
6	405	406	0.5	401	-1.0
7	306	308	0.9	298	-2.6
8	204	207	1.6	196	-3.9
9	109	111	2.3	101	-6.6
10	15	20	-	6	-
11	125	129	3.4	115	-7.5
12	249	255	2.1	247	-0.9
13	376	381	1.3	373	-1.0
14	500	506	1.2	497	-0.6
15	625	642	2.7	620	-0.7
16	748	757	1.2	732	-2.1

Test pile 8

Table 16: Deviations from target load for test pile 8.

Test pile 8	Applied load		
Load step no.	Target (kN)	Average (kN)	Deviation (%)
1	100	103	3.05
2	200	202	1.23
3	100	104	4.31
4	0	21	-
5	100	104	4.20
6	200	203	1.63
7	300	302	0.70
8	400	402	0.62
9	500	502	0.32
10	600	601	0.12
11	650	650	0.07
12	700	701	0.12
13	750	751	0.14
14	800	801	0.11

Table 17: Deviations from average value to the determined maximum and minimum load for test pile 8.

Test pile 8	Applied load				
Load step no.	Average (kN)	Maximum (kN)	Deviation (%)	Minimum (kN)	Deviation (%)
1	103	105	2.3	100	-2.6
2	202	206	2.0	199	-1.7
3	104	106	1.8	101	-3.4
4	21	26	-	19	-
5	104	106	1.4	100	-4.3
6	203	207	2.0	200	-1.5
7	302	307	1.8	299	-1.0
8	402	409	1.6	399	-1.0
9	502	509	1.5	496	-1.1
10	601	604	1.0	597	-0.6
11	650	657	1.0	646	-0.8
12	701	704	0.4	697	-0.5
13	751	756	0.7	747	-0.5
14	801	805	0.5	797	-0.5

E.3 Time-load curves

Maintained load (ML) test

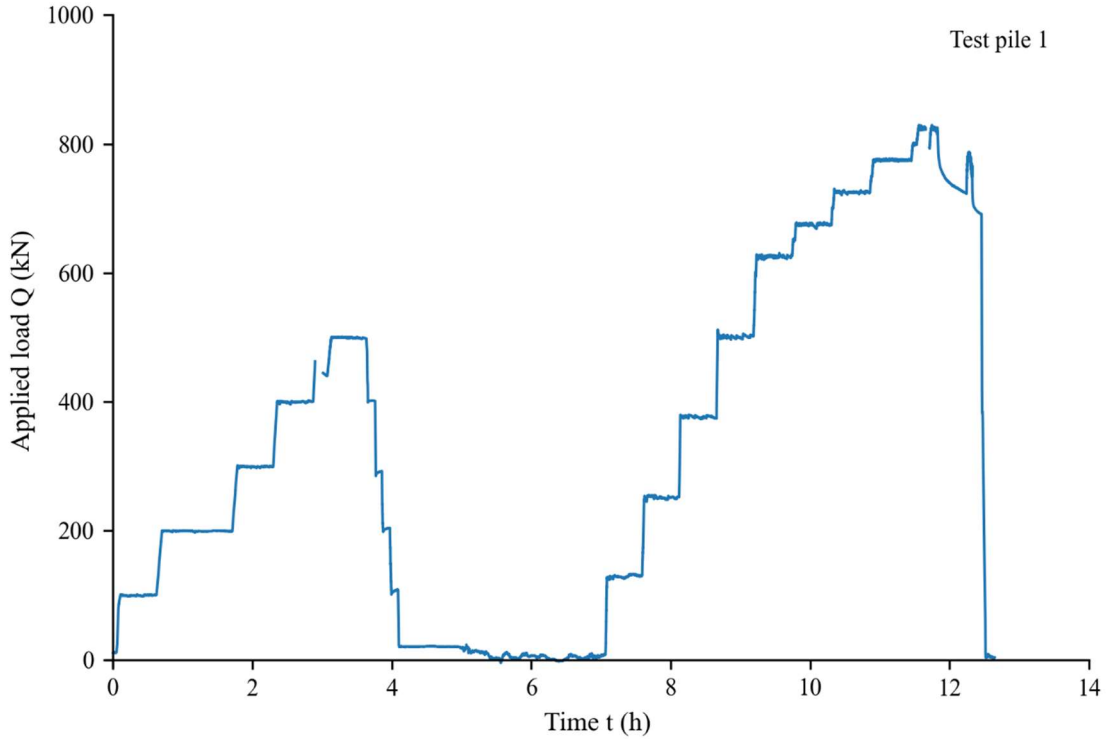

Figure 18: Actual loading of test pile 1 during the maintained load (ML) test.

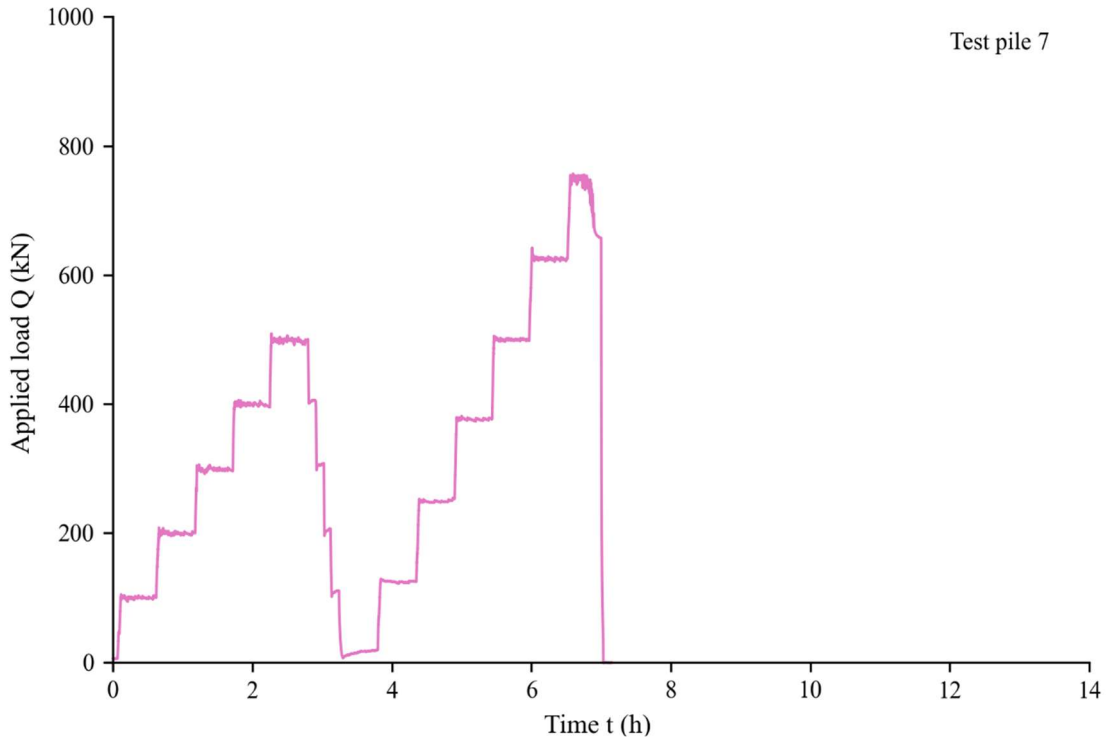

Figure 19: Actual loading of test pile 7 during the maintained load (ML) test.

Constant rate of uplift (CRU) test

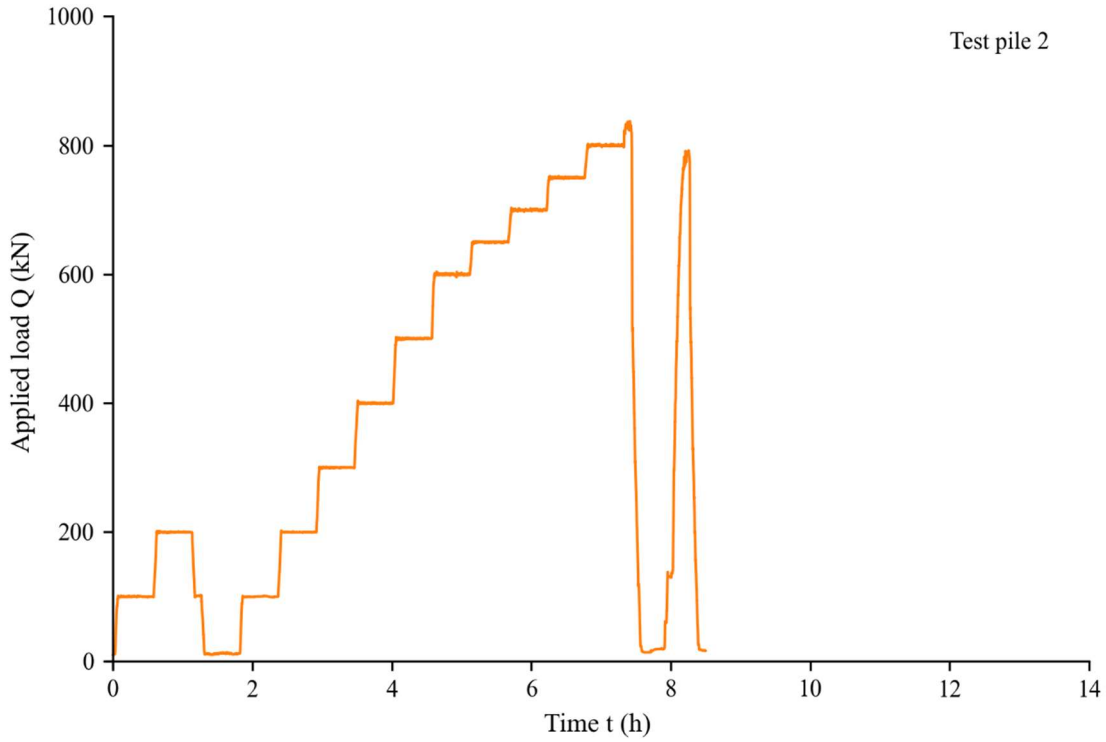

Figure 20: Actual loading of test pile 2 during the constant rate of uplift (CRU) test.

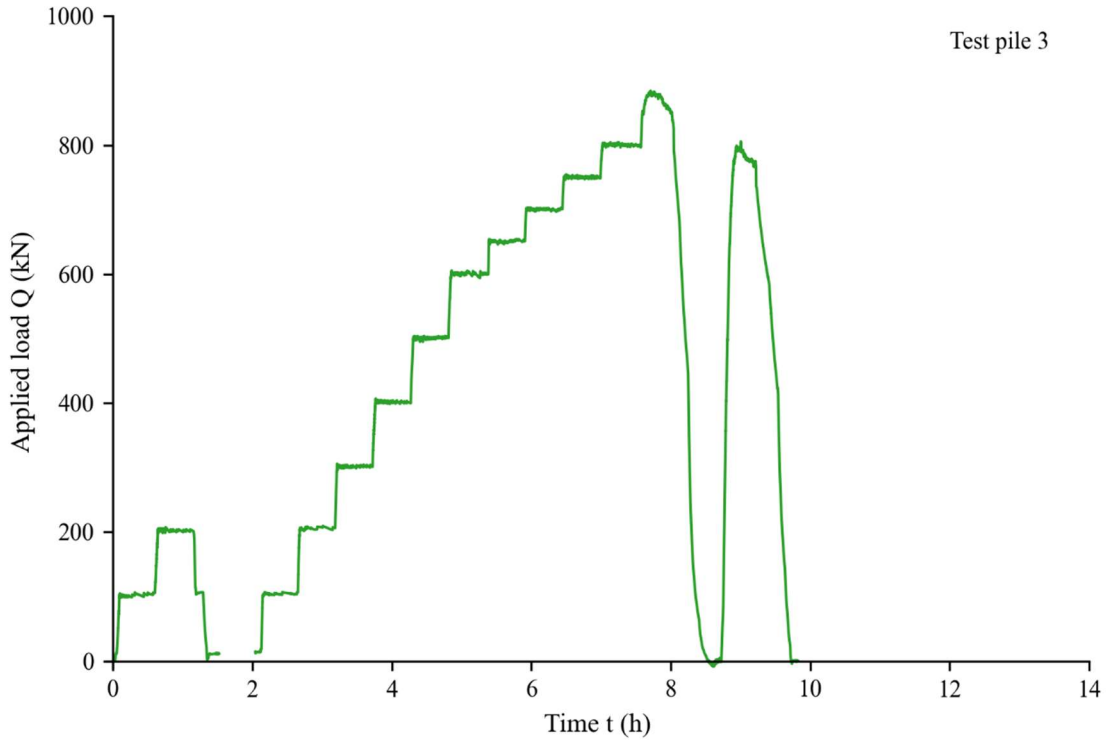

Figure 21: Actual loading of test pile 3 during the constant rate of uplift (CRU) test.

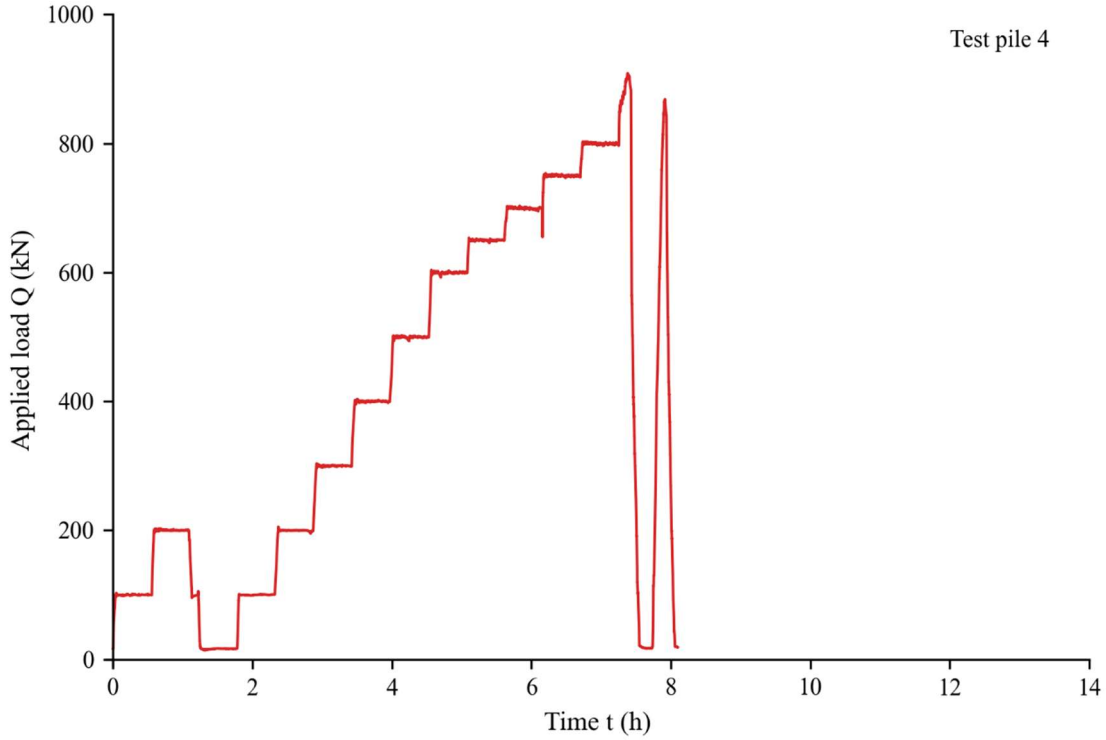

Figure 22: Actual loading of test pile 4 during the constant rate of uplift (CRU) test.

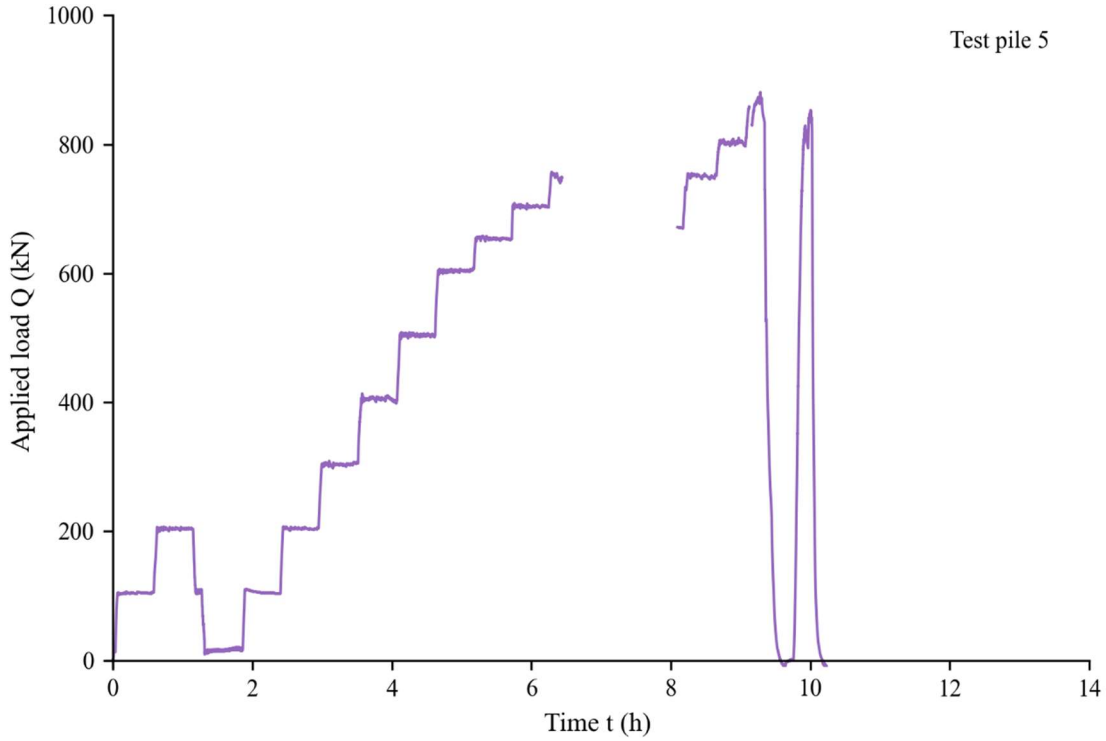

Figure 23: Actual loading of test pile 5 during the constant rate of uplift (CRU) test.

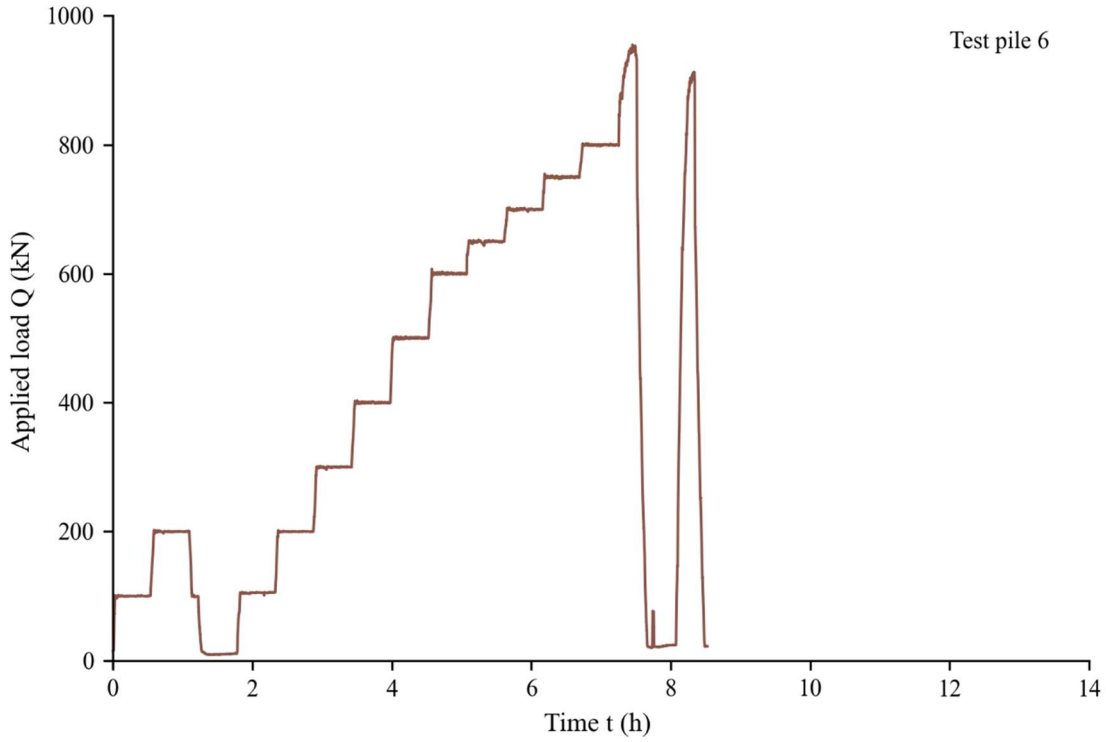

Figure 24: Actual loading of test pile 6 during the constant rate of uplift (CRU) test.

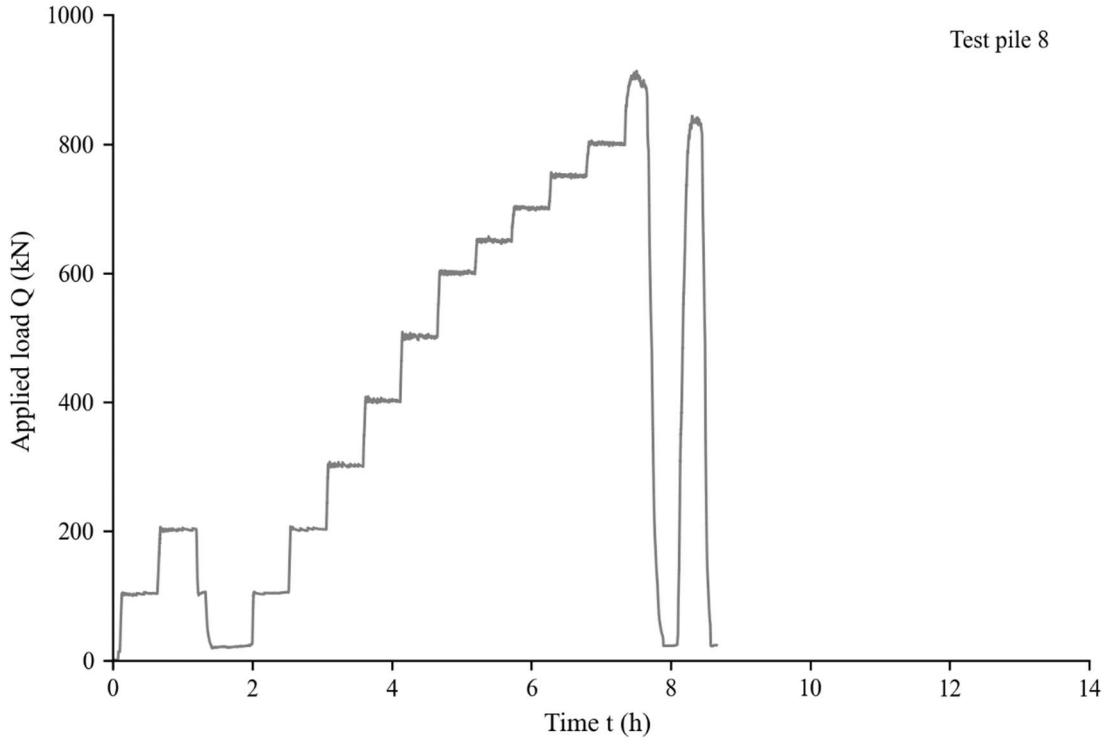

Figure 25: Actual loading of test pile 8 during the constant rate of uplift (CRU) test.

E.4 Time-displacement and load curves

Maintained load (ML) test

Test pile 1

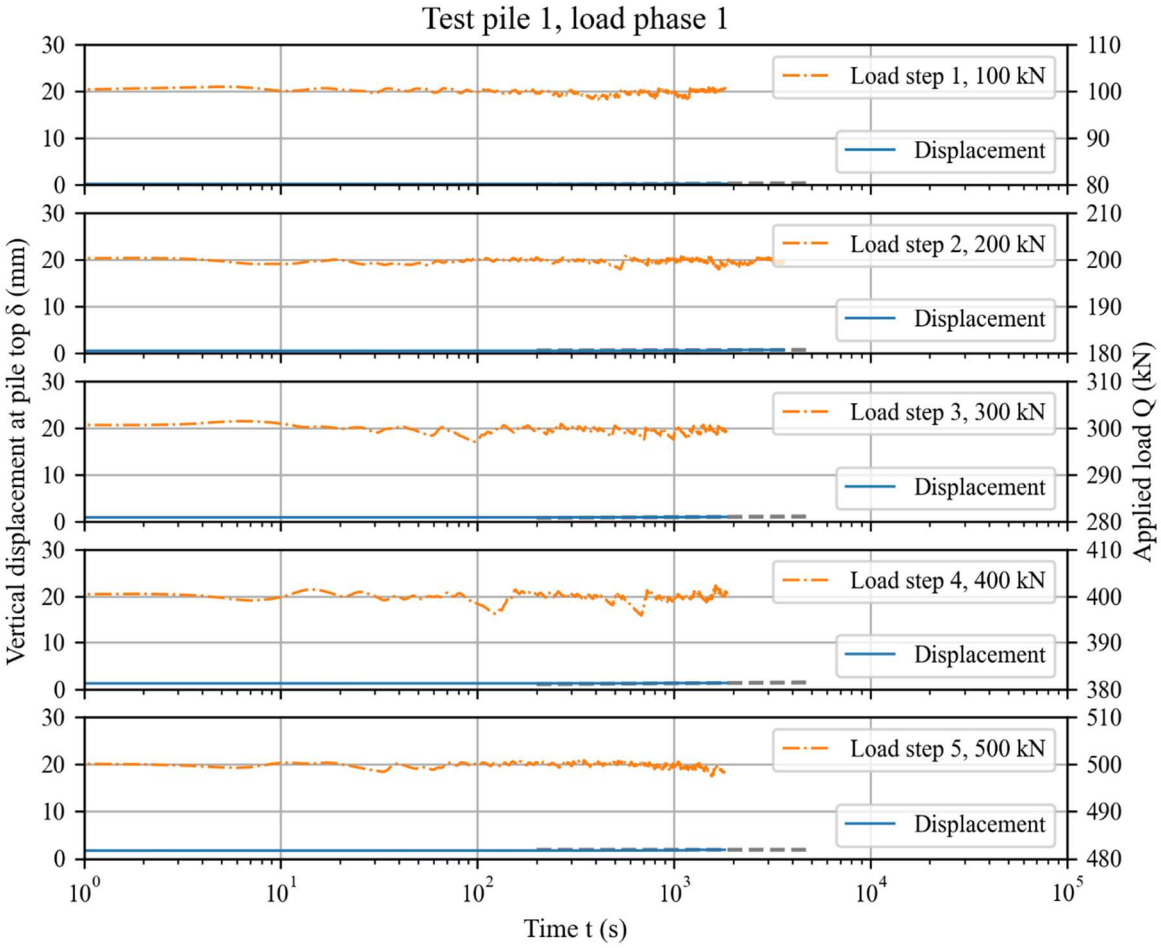

Figure 26: Load variation, displacement, and rate of creep for test pile 1, load phase 1.

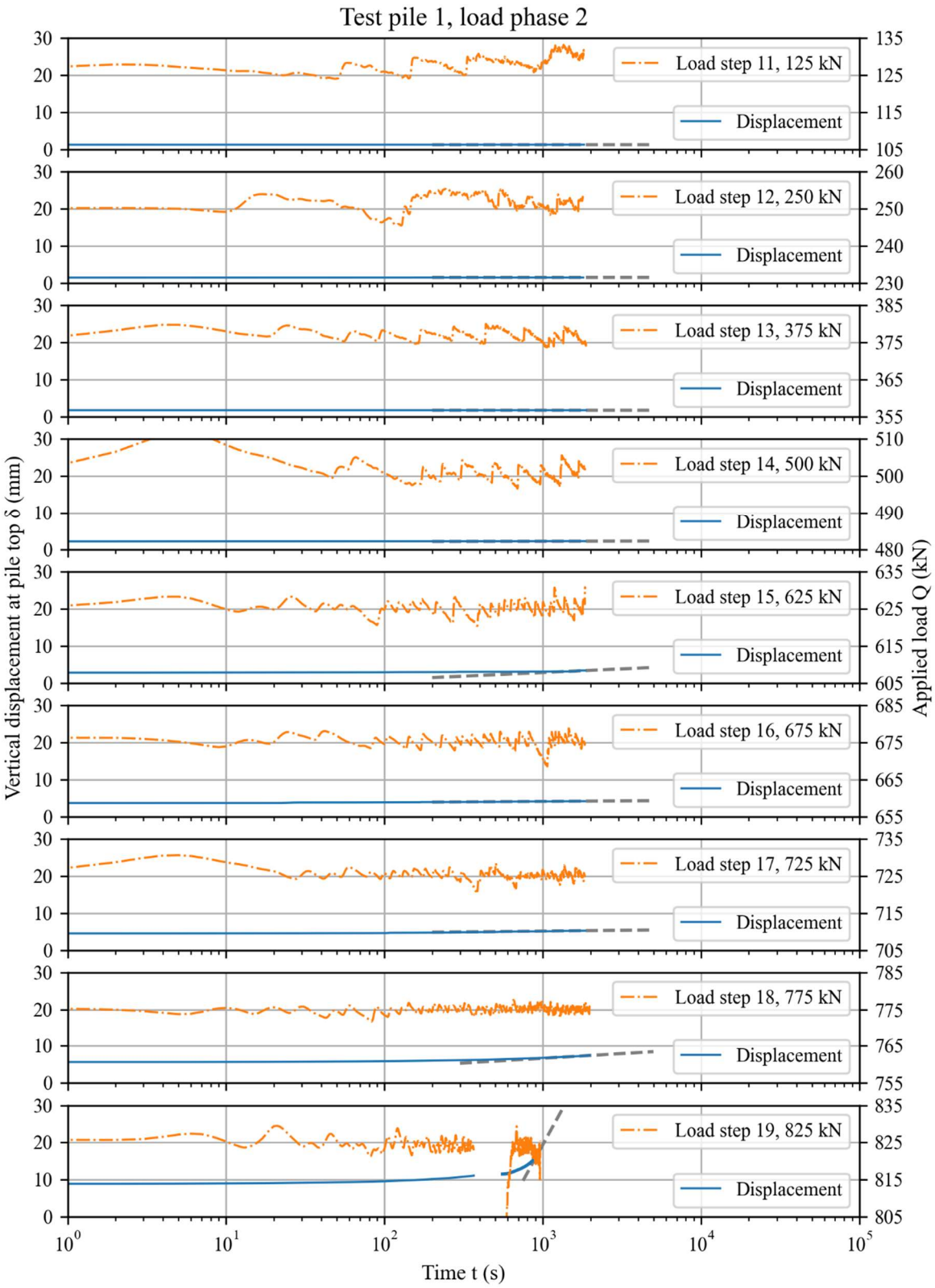

Figure 27: Load variation, displacement, and rate of creep for test pile 1, load phase 2.

Test pile 7

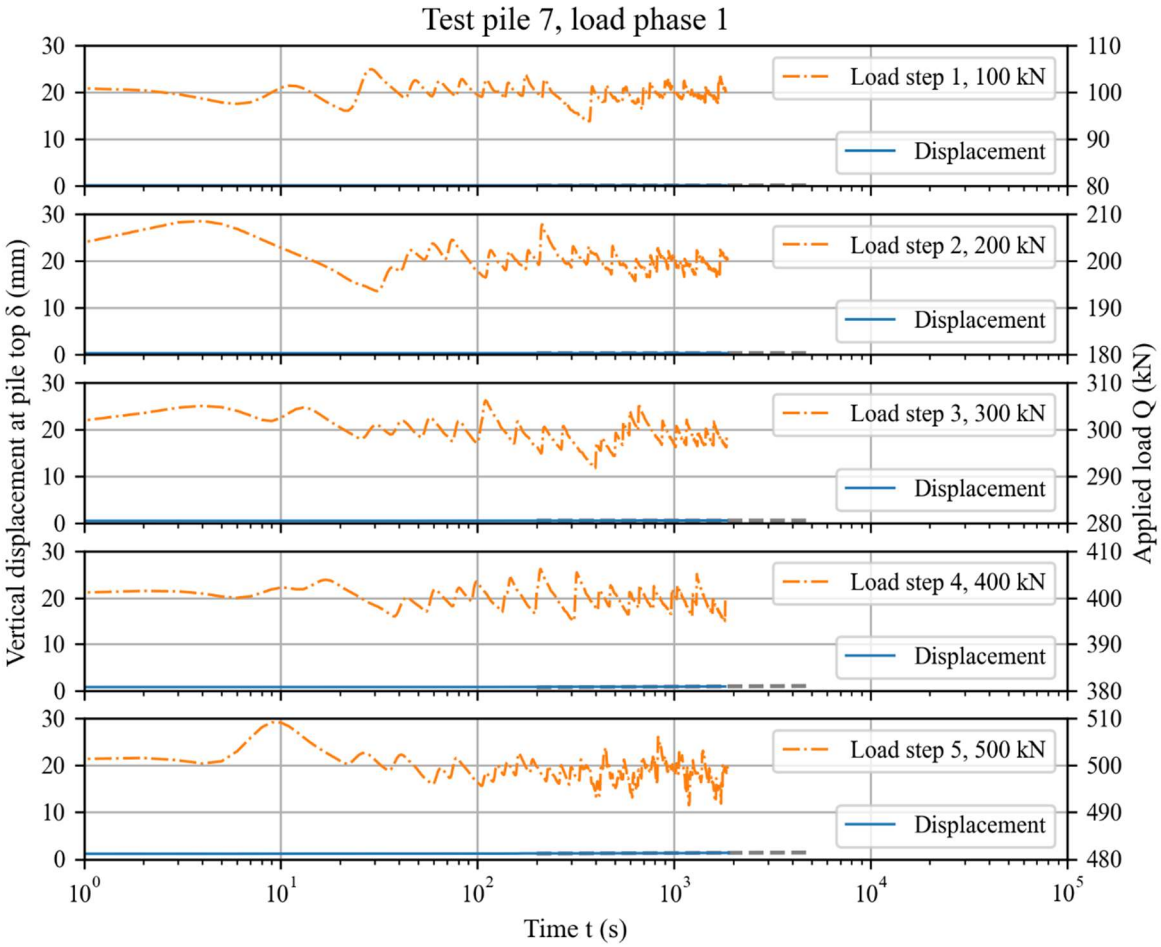

Figure 28: Load variation, displacement, and rate of creep for test pile 7, load phase 1.

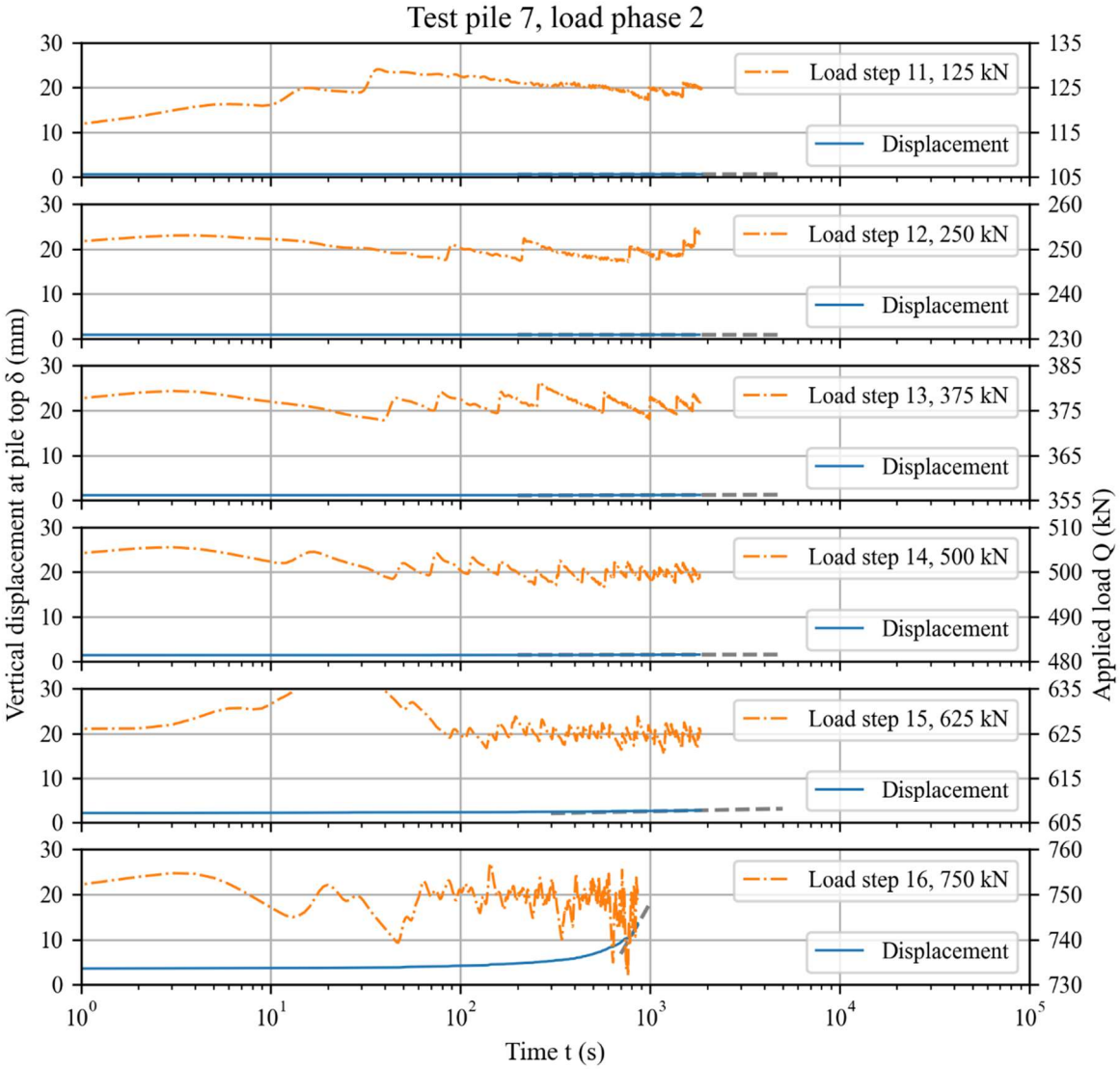

Figure 29: Load variation, displacement, and rate of creep for test pile 7, load phase 2.

Constant rate of uplift (CRU) test

Test pile 2

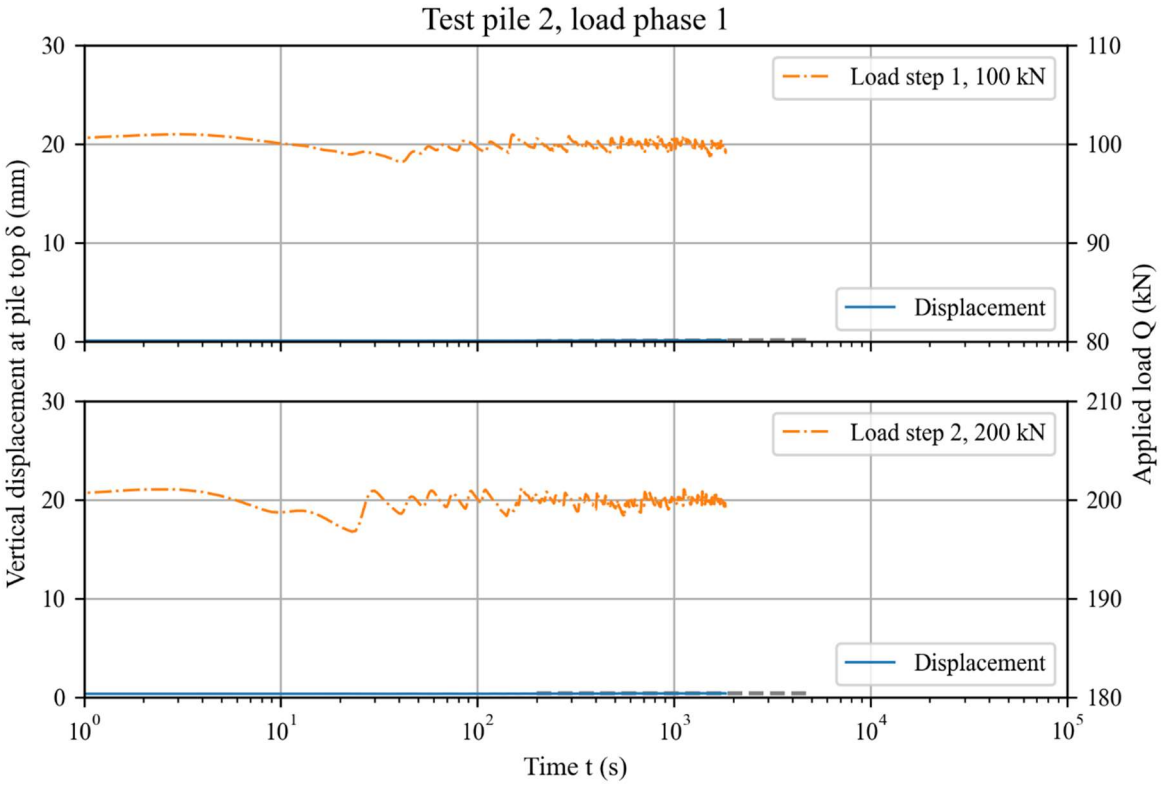

Figure 30: Load variation, displacement, and rate of creep for test pile 2, load phase 1.

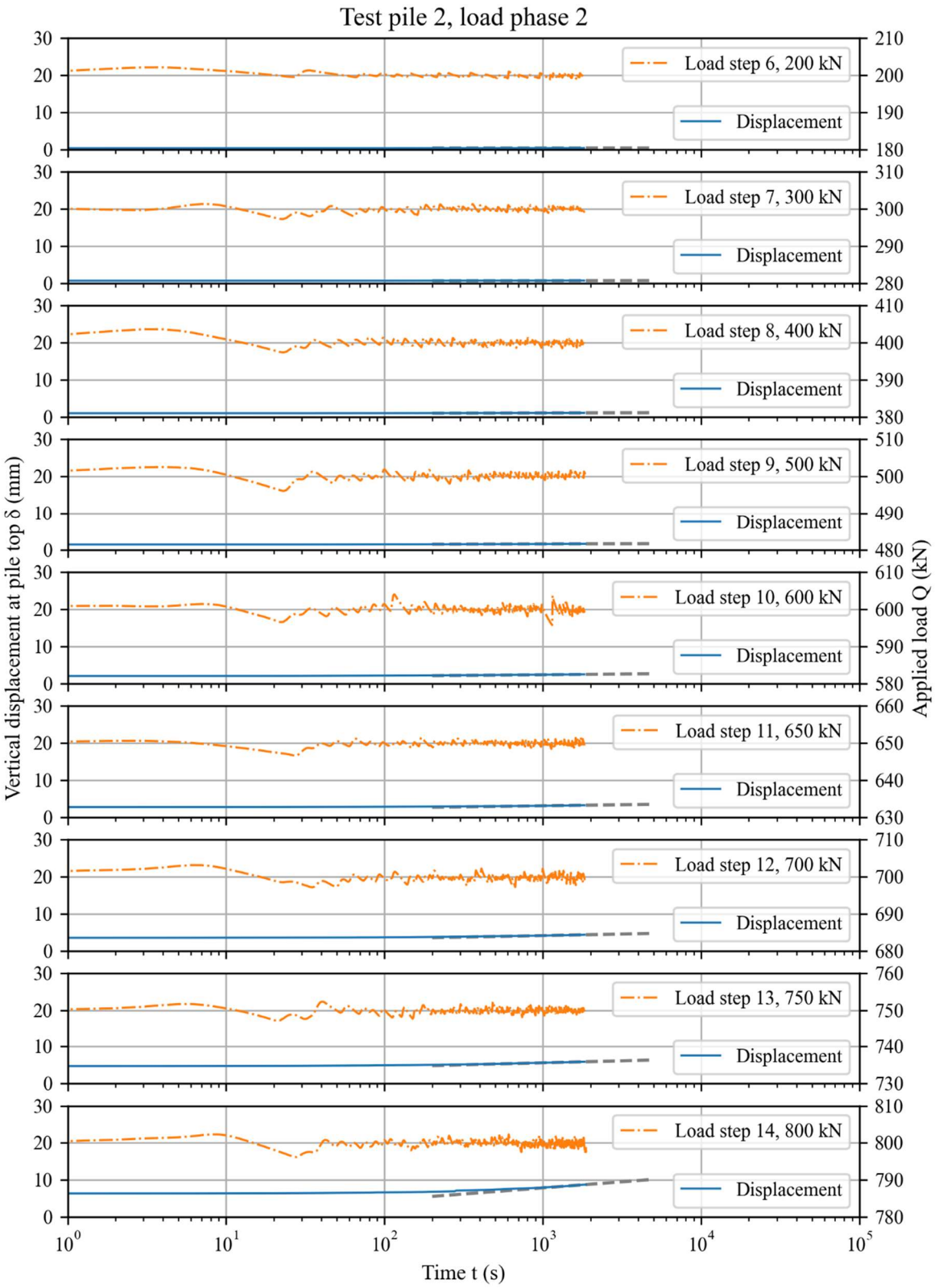

Figure 31: Load variation, displacement, and rate of creep for test pile 2, load phase 2.

Test pile 3

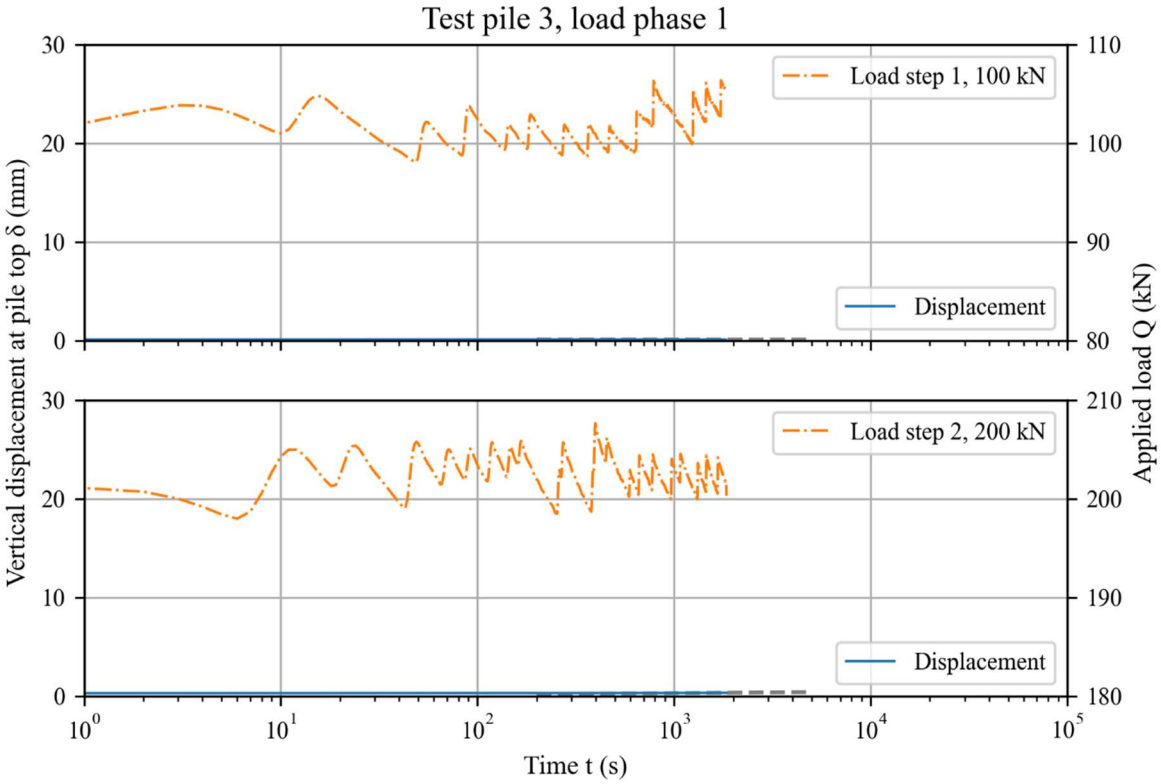

Figure 32: Load variation, displacement, and rate of creep for test pile 3, load phase 1.

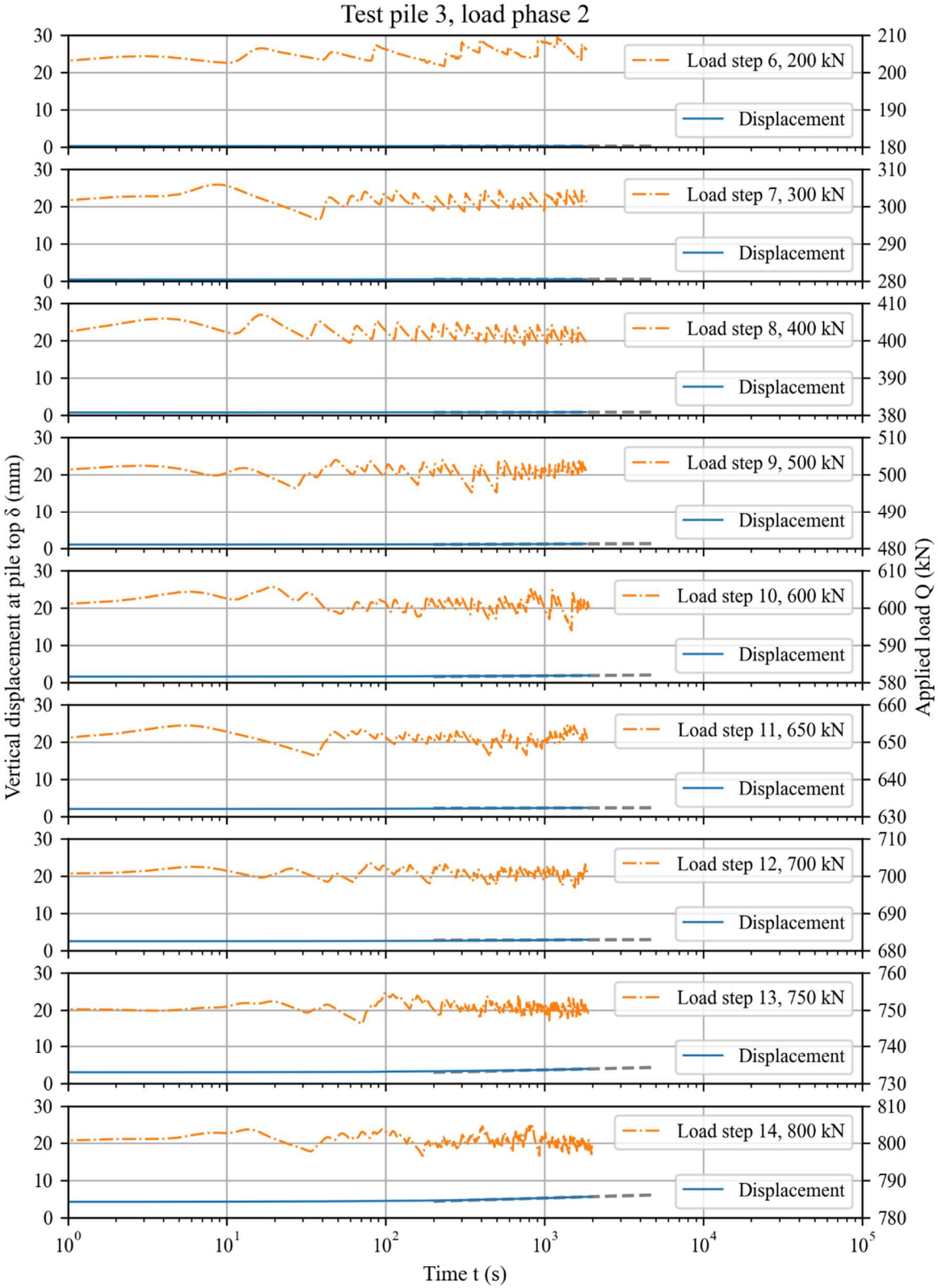

Figure 33: Load variation, displacement, and rate of creep for test pile 3, load phase 2.

Test pile 4

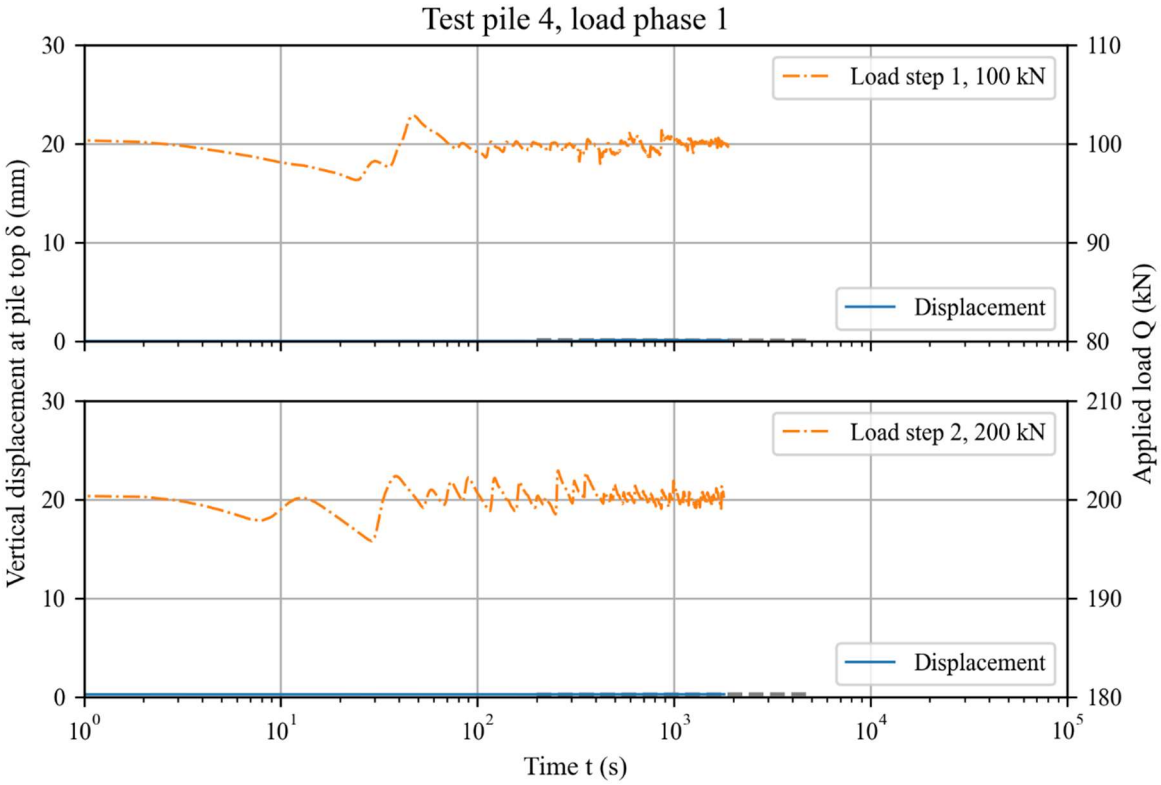

Figure 34: Load variation, displacement, and rate of creep for test pile 4, load phase 1.

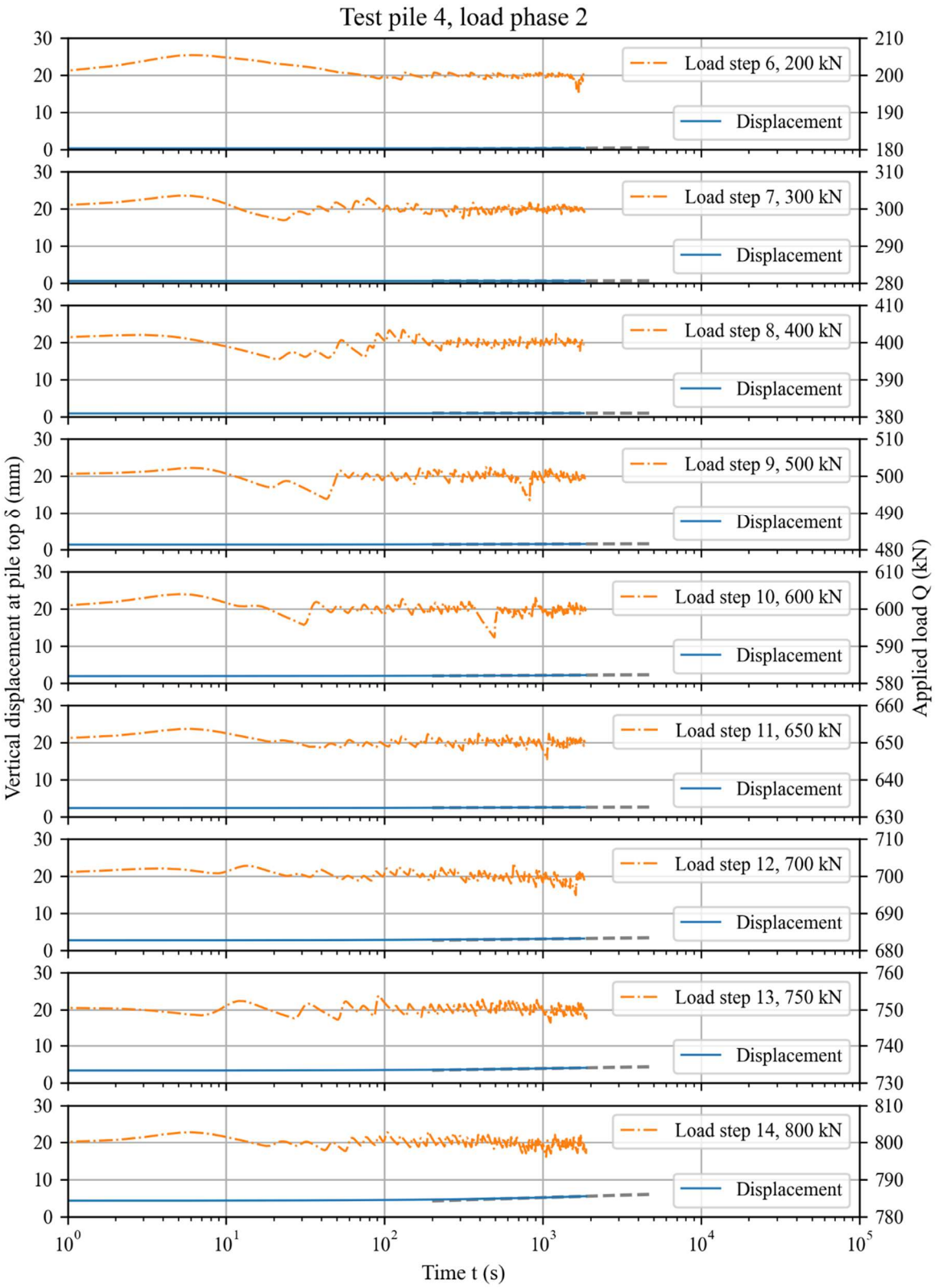

Figure 35: Load variation, displacement, and rate of creep for test pile 4, load phase 2.

Test pile 5

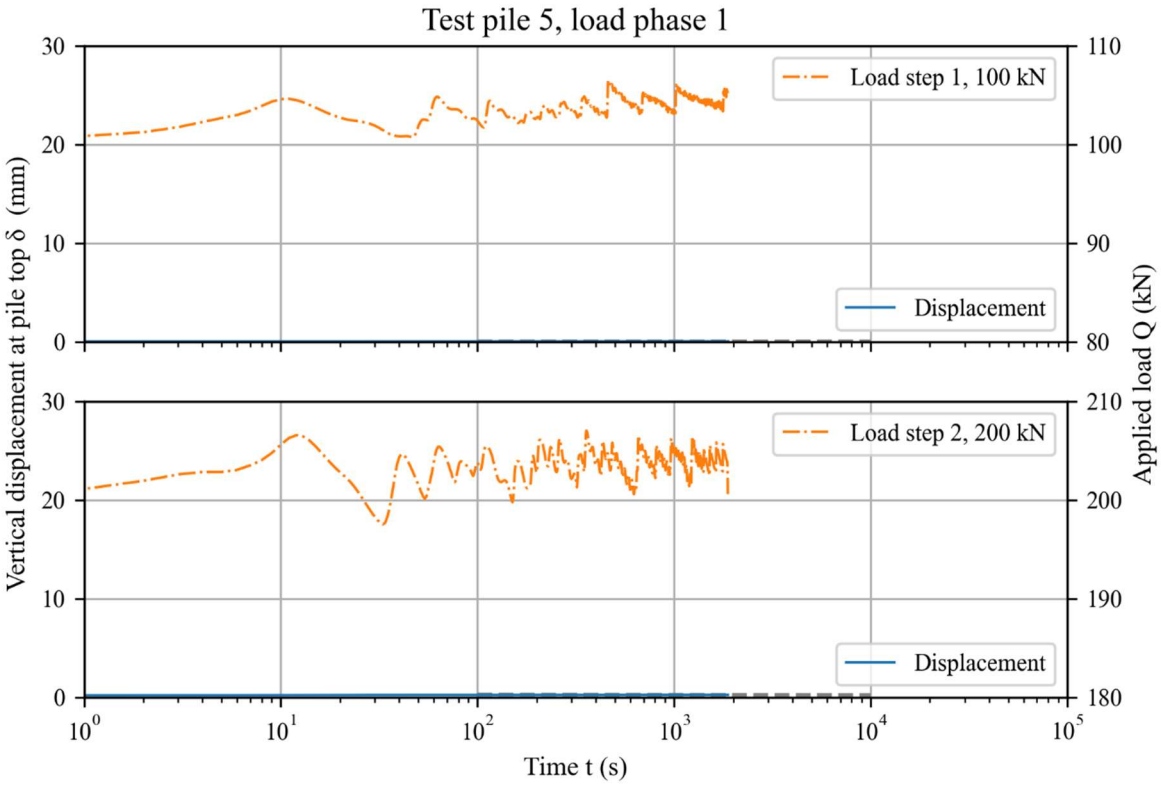

Figure 36: Load variation, displacement, and rate of creep for test pile 5, load phase 1.

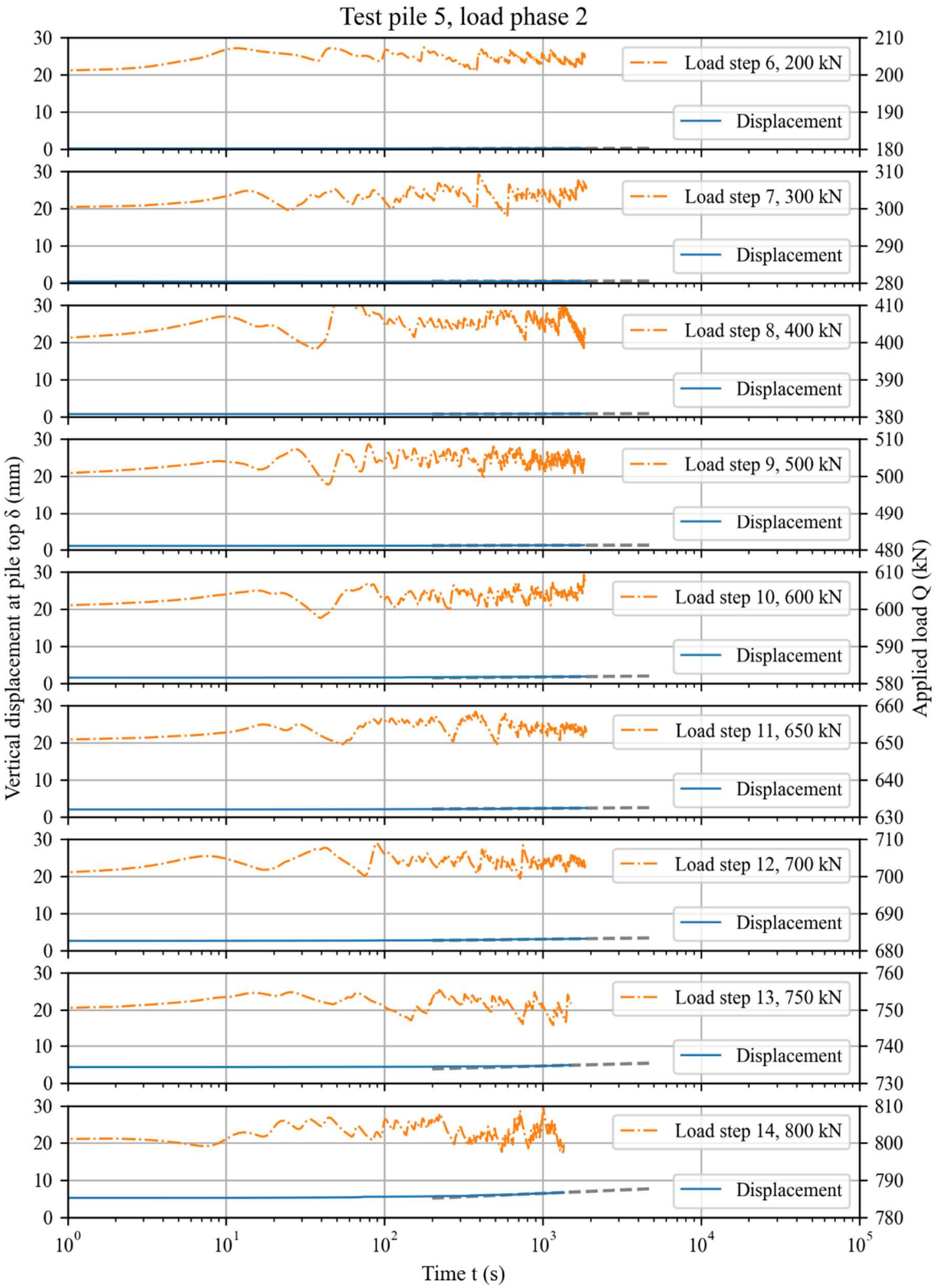

Figure 37: Load variation, displacement, and rate of creep for test pile 5, load phase 2.

Test pile 6

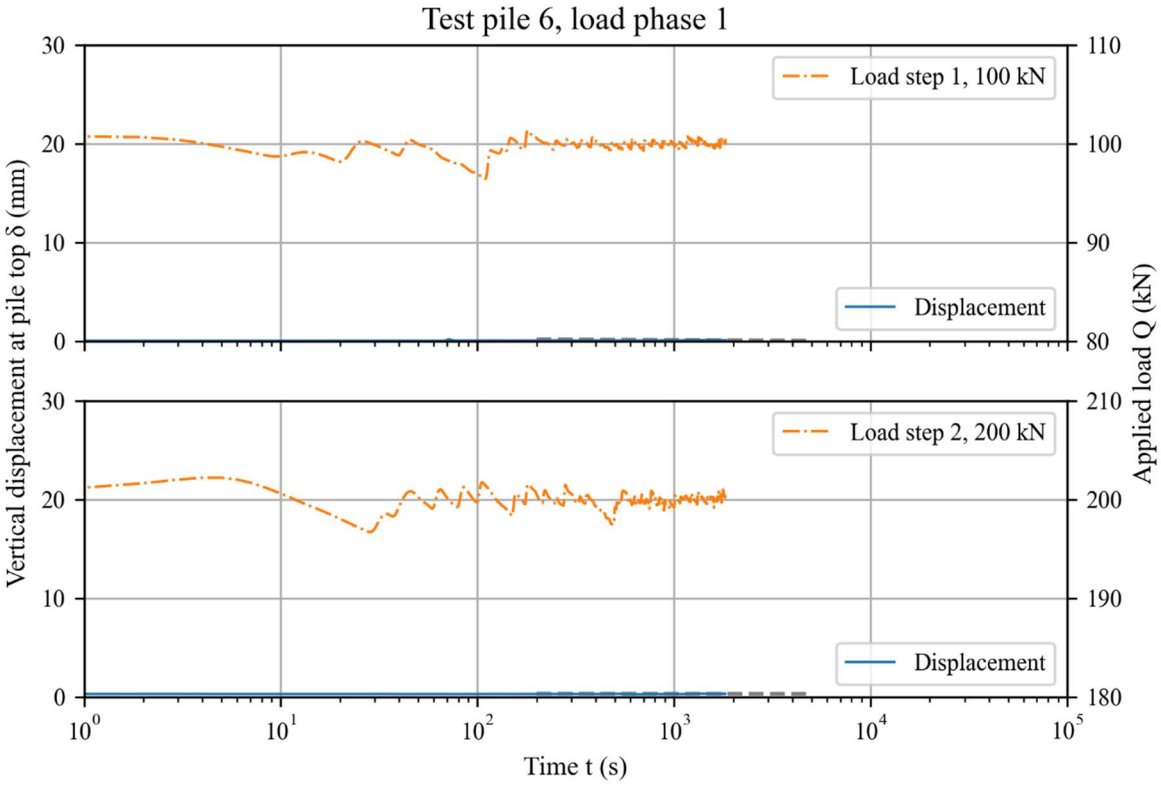

Figure 38: Load variation, displacement, and rate of creep for test pile 6, load phase 1.

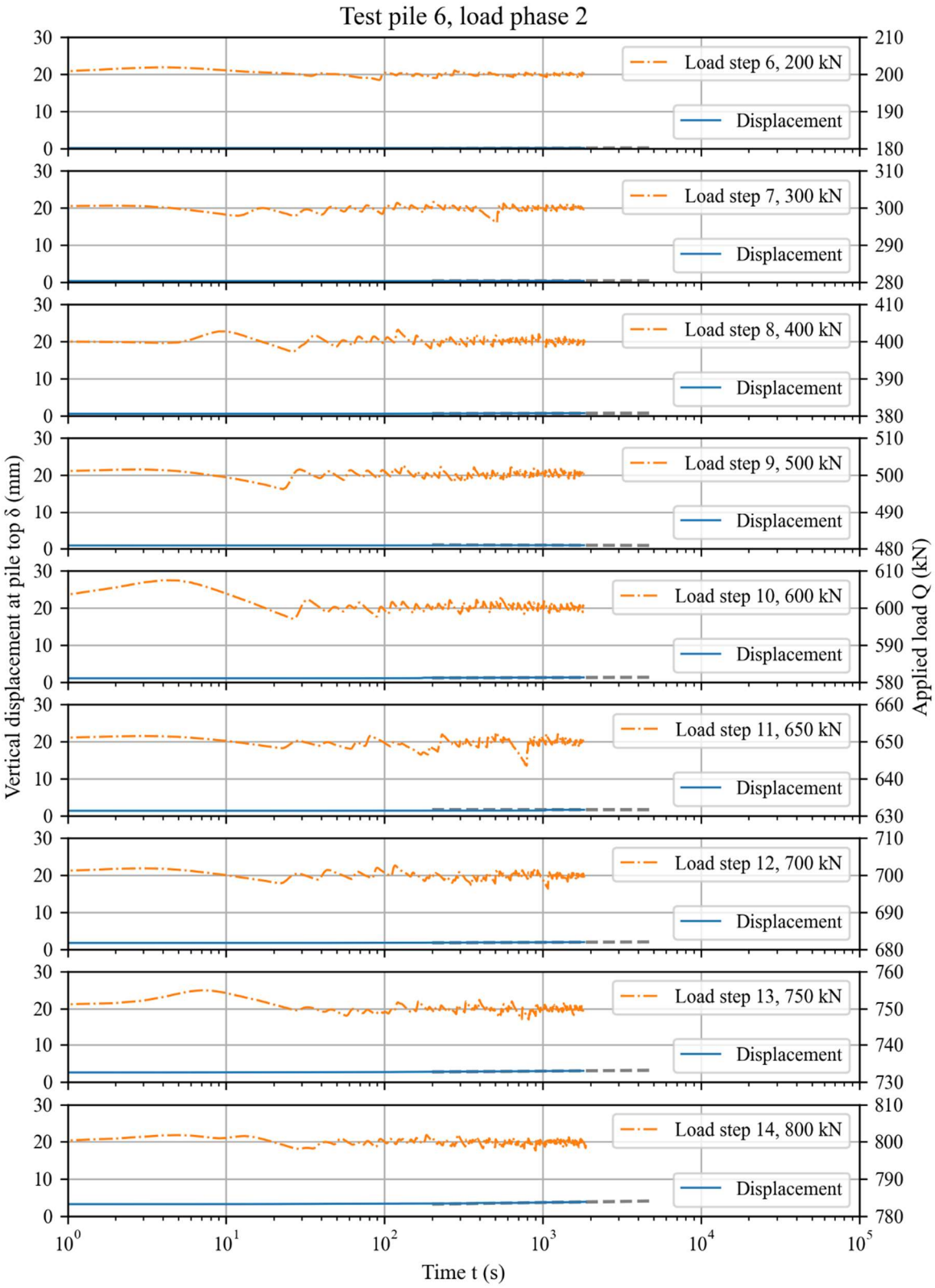

Figure 39: Load variation, displacement, and rate of creep for test pile 6, load phase 2.

Test pile 8

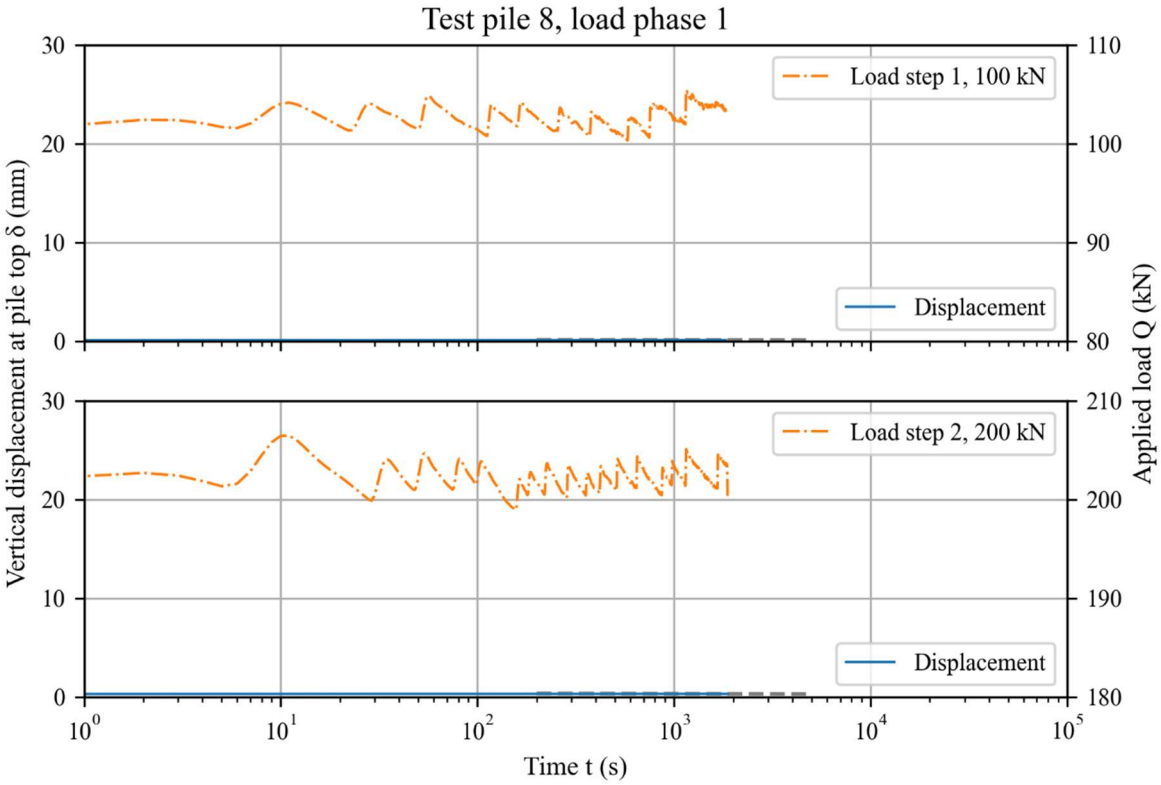

Figure 40: Load variation, displacement, and rate of creep for test pile 8, load phase 1.

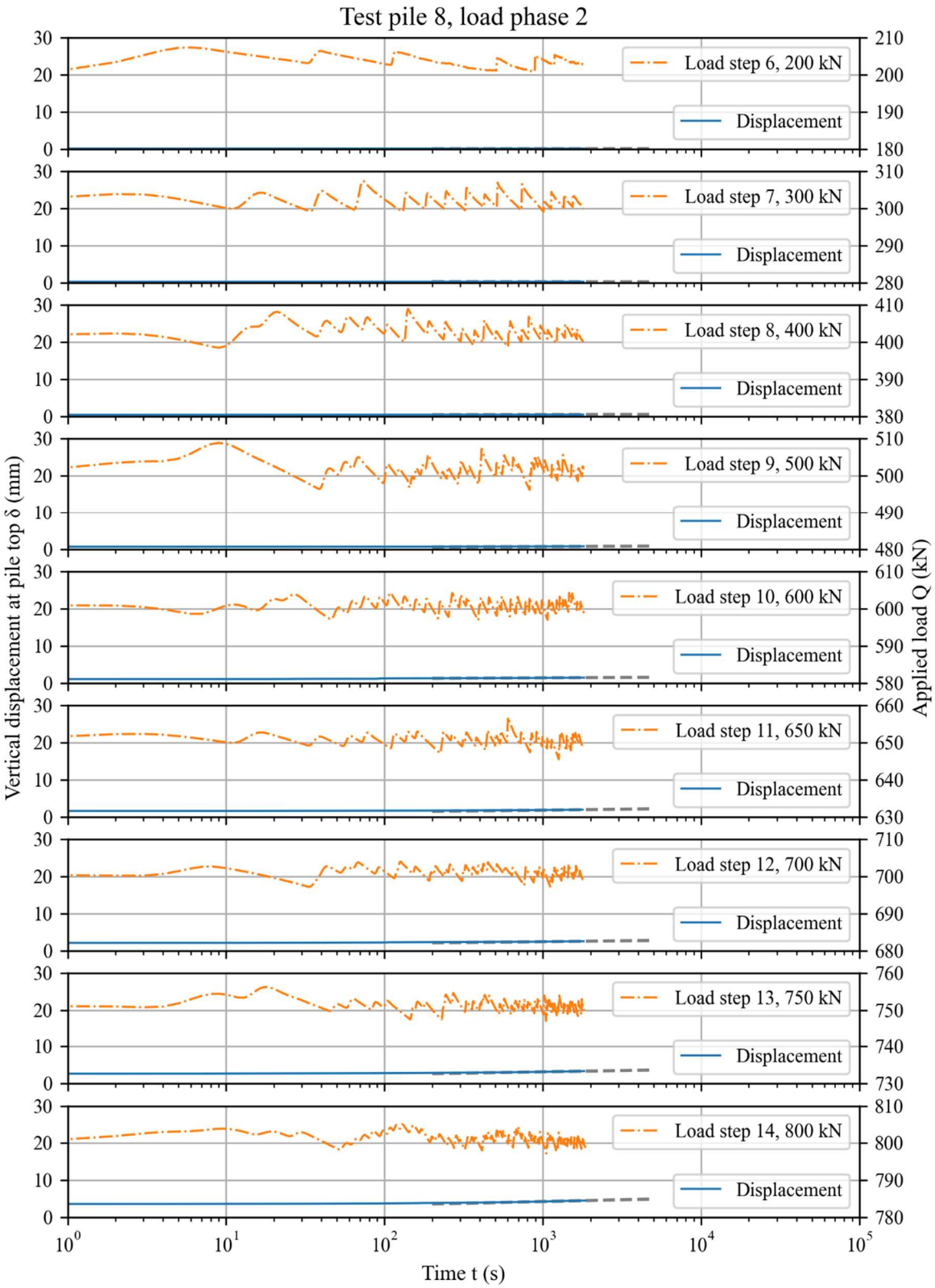

Figure 41: Load variation, displacement, and rate of creep for test pile 8, load phase 2.

E.5 Rate of creep

Maintained load (ML) test

Test pile 1

Table 18: Rate of creep overview for test pile 1.

Test pile 1	Load / Reload [kN]	Trendline equation Spyder (python) [-]	Rate of creep [mm/lct]
Load phase 1			
Load step 1	100	$y = 0.072 \cdot \ln(x) - 0.29$	**0.17**
Load step 2	200	$y = 0.037 \cdot \ln(x) + 0.39$	**0.09**
Load step 3	300	$y = 0.101 \cdot \ln(x) + 0.22$	**0.23**
Load step 4	400	$y = 0.105 \cdot \ln(x) + 0.52$	**0.24**
Load step 5	500	$y = 0.001 \cdot \ln(x) + 1.88$	**0.00**
Load phase 2			
Load step 11	125	$y = 0.005 \cdot \ln(x) + 1.28$	**0.01**
Load step 12	250	$y = -0.000 \cdot \ln(x) + 1.53$	**-0.00**
Load step 13	375	$y = 0.001 \cdot \ln(x) + 1.74$	**0.00**
Load step 14	500	$y = 0.043 \cdot \ln(x) + 1.92$	**0.10**
Load step 15	625	$y = 0.852 \cdot \ln(x) - 3.05$	**1.96**
Load step 16	675	$y = 0.113 \cdot \ln(x) + 3.32$	**0.26**
Load step 17	725	$y = 0.183 \cdot \ln(x) + 3.88$	**0.42**
Load step 18	775	$y = 1.104 \cdot \ln(x) - 0.96$	**2.54**
Load step 19	825	$y = 33.682 \cdot \ln(x) - 213.22$	**77.55**

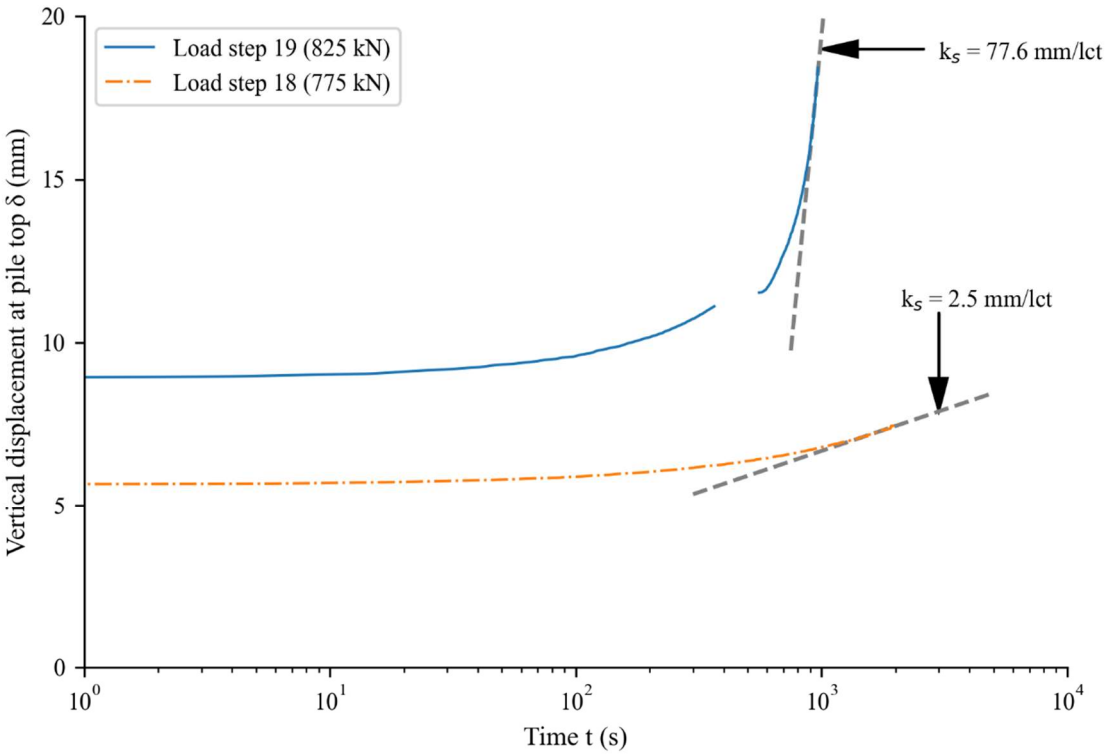

Figure 42: Rate of creep for the final two load steps for test pile 1.

Test pile 7

Table 19: Rate of creep overview for test pile 7.

Test pile 7	Load / Reload [kN]	Trendline equation Spyder (python) [-]	Rate of creep [mm/lct]
Load phase 1			
Load step 1	100	$y = 0.017 \cdot \ln(x) - 0.00$	**0.04**
Load step 2	200	$y = 0.004 \cdot \ln(x) + 0.26$	**0.01**
Load step 3	300	$y = -0.001 \cdot \ln(x) + 0.52$	**-0.00**
Load step 4	400	$y = 0.090 \cdot \ln(x) + 0.21$	**0.21**
Load step 5	500	$y = 0.063 \cdot \ln(x) + 0.88$	**0.14**
Load phase 2			
Load step 11	125	$y = 0.018 \cdot \ln(x) + 0.52$	**0.04**
Load step 12	250	$y = -0.011 \cdot \ln(x) + 0.96$	**-0.02**
Load step 13	375	$y = 0.061 \cdot \ln(x) + 0.71$	**0.14**
Load step 14	500	$y = 0.028 \cdot \ln(x) + 1.36$	**0.07**
Load step 15	625	$y = 0.361 \cdot \ln(x) - 0.04$	**0.83**
Load step 16	750	$y = 31.687 \cdot \ln(x) - 200.77$	**72.96**

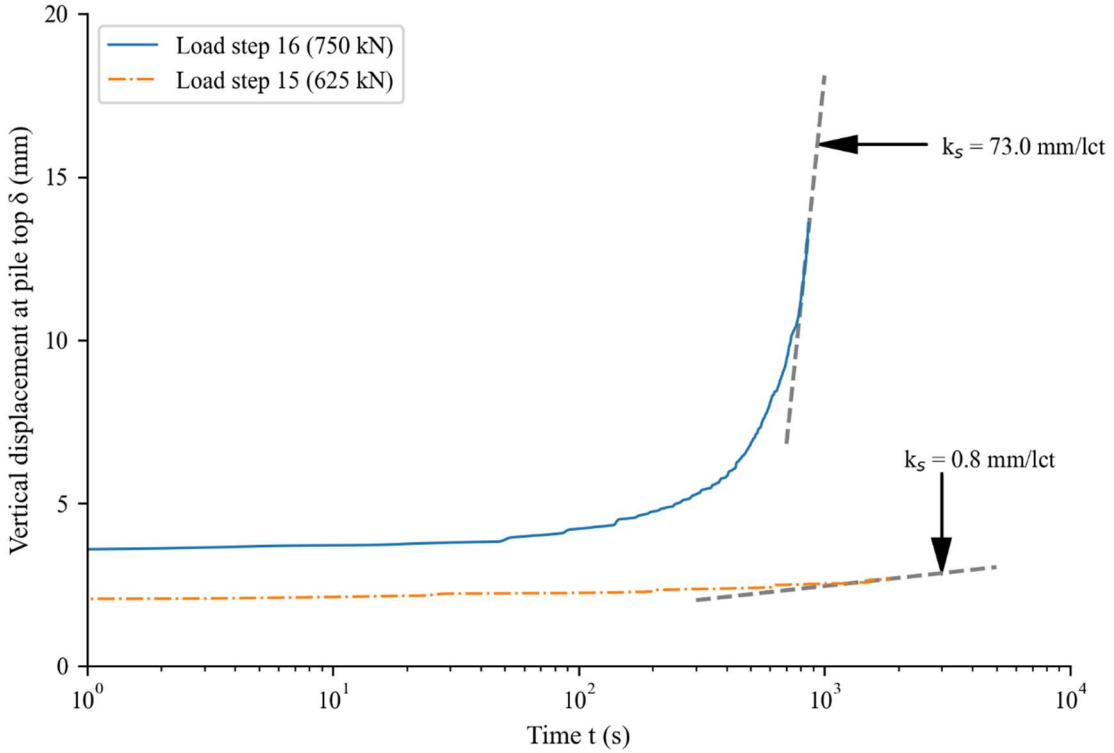

Figure 43: Rate of creep for the final two load steps for test pile 7.

Constant rate of uplift (CRU) test

Test pile 2

Table 20: Rate of creep overview for test pile 2.

Test pile 2	Load / Reload [kN]	Trendline equation Spyder (python) [-]	Rate of creep [mm/lct]
Load phase 1			
Load step 1	100	$y = 0.028 \cdot \ln(x) - 0.06$	**0.06**
Load step 2	200	$y = -0.001 \cdot \ln(x) + 0.40$	**-0.00**
Load phase 2			
Load step 5	100	$y = -0.046 \cdot \ln(x) + 0.55$	**-0.10**
Load step 6	200	$y = 0.001 \cdot \ln(x) + 0.43$	**0.00**
Load step 7	300	$y = 0.016 \cdot \ln(x) + 0.60$	**0.04**
Load step 8	400	$y = 0.045 \cdot \ln(x) + 0.77$	**0.10**
Load step 9	500	$y = 0.047 \cdot \ln(x) + 1.26$	**0.11**
Load step 10	600	$y = 0.162 \cdot \ln(x) + 1.24$	**0.37**
Load step 11	650	$y = 0.248 \cdot \ln(x) + 1.35$	**0.57**
Load step 12	700	$y = 0.361 \cdot \ln(x) + 1.61$	**0.83**
Load step 13	750	$y = 0.469 \cdot \ln(x) + 2.37$	**1.08**
Load step 14	800	$y = 1.427 \cdot \ln(x) - 1.97$	**3.29**

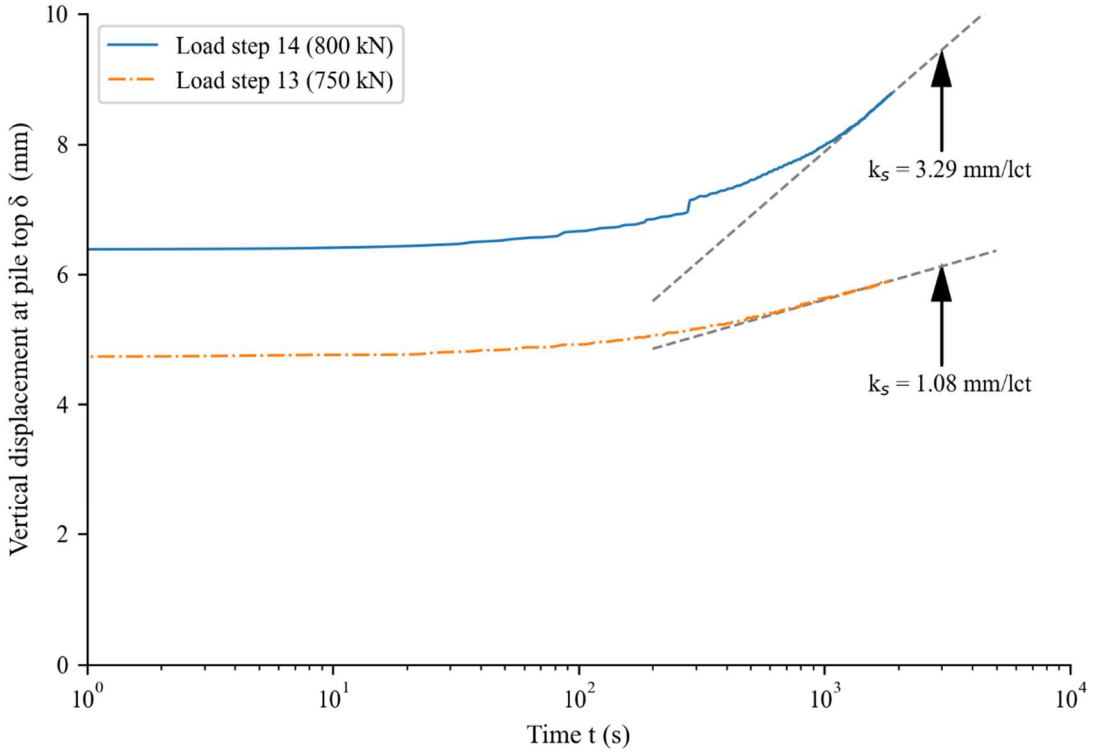

Figure 44: Rate of creep for the final two load steps for test pile 2.

Test pile 3

Table 21: Rate of creep overview for test pile 3.

Test pile 3	Load / Reload [kN]	Trendline equation Spyder (python) [-]	Rate of creep [mm/lct]
Load phase 1			
Load step 1	100	$y = 0.000 \cdot \ln(x) + 0.14$	**0.00**
Load step 2	200	$y = 0.060 \cdot \ln(x) - 0.11$	**0.14**
Load phase 2			
Load step 5	100	$y = 0.016 \cdot \ln(x) - 0.03$	**0.04**
Load step 6	200	$y = 0.017 \cdot \ln(x) + 0.14$	**0.04**
Load step 7	300	$y = 0.001 \cdot \ln(x) + 0.47$	**0.00**
Load step 8	400	$y = 0.016 \cdot \ln(x) + 0.66$	**0.04**
Load step 9	500	$y = 0.083 \cdot \ln(x) + 0.58$	**0.19**
Load step 10	600	$y = 0.135 \cdot \ln(x) + 0.82$	**0.31**
Load step 11	650	$y = 0.041 \cdot \ln(x) + 1.96$	**0.10**
Load step 12	700	$y = 0.068 \cdot \ln(x) + 2.33$	**0.16**
Load step 13	750	$y = 0.411 \cdot \ln(x) + 0.85$	**0.95**
Load step 14	800	$y = 0.535 \cdot \ln(x) + 1.62$	**1.23**

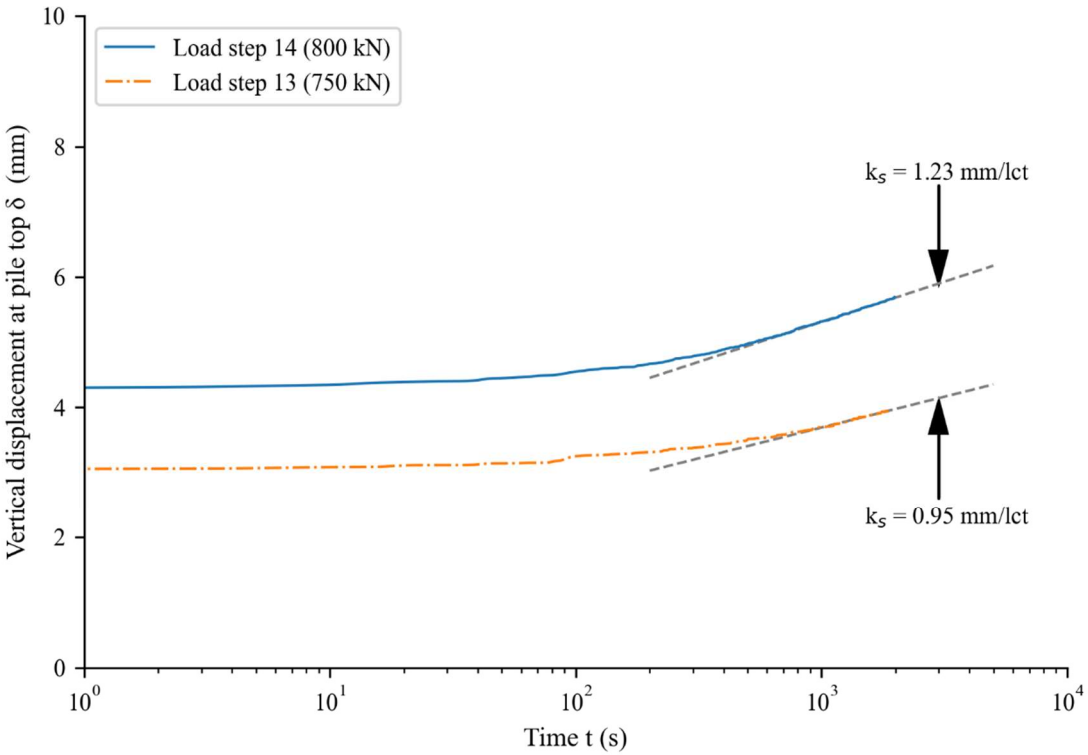

Figure 45: Rate of creep for the final two load steps for test pile 3.

Test pile 4

Table 22: Rate of creep overview for test pile 4.

Test pile 4	Load / Reload [kN]	Trendline equation Spyder (python) [-]	Rate of creep [mm/lct]
Load phase 1			
Load step 1	100	$y = -0.013 \cdot \ln(x) + 0.22$	**-0.03**
Load step 2	200	$y = 0.010 \cdot \ln(x) + 0.20$	**0.02**
Load phase 2			
Load step 5	100	$y = -0.014 \cdot \ln(x) + 0.25$	**-0.03**
Load step 6	200	$y = 0.077 \cdot \ln(x) - 0.22$	**0.18**
Load step 7	300	$y = 0.019 \cdot \ln(x) + 0.46$	**0.04**
Load step 8	400	$y = -0.011 \cdot \ln(x) + 1.01$	**-0.02**
Load step 9	500	$y = 0.050 \cdot \ln(x) + 1.11$	**0.12**
Load step 10	600	$y = 0.096 \cdot \ln(x) + 1.42$	**0.22**
Load step 11	650	$y = 0.046 \cdot \ln(x) + 2.16$	**0.11**
Load step 12	700	$y = 0.208 \cdot \ln(x) + 1.58$	**0.48**
Load step 13	750	$y = 0.287 \cdot \ln(x) + 1.94$	**0.66**
Load step 14	800	$y = 0.557 \cdot \ln(x) + 1.37$	**1.28**

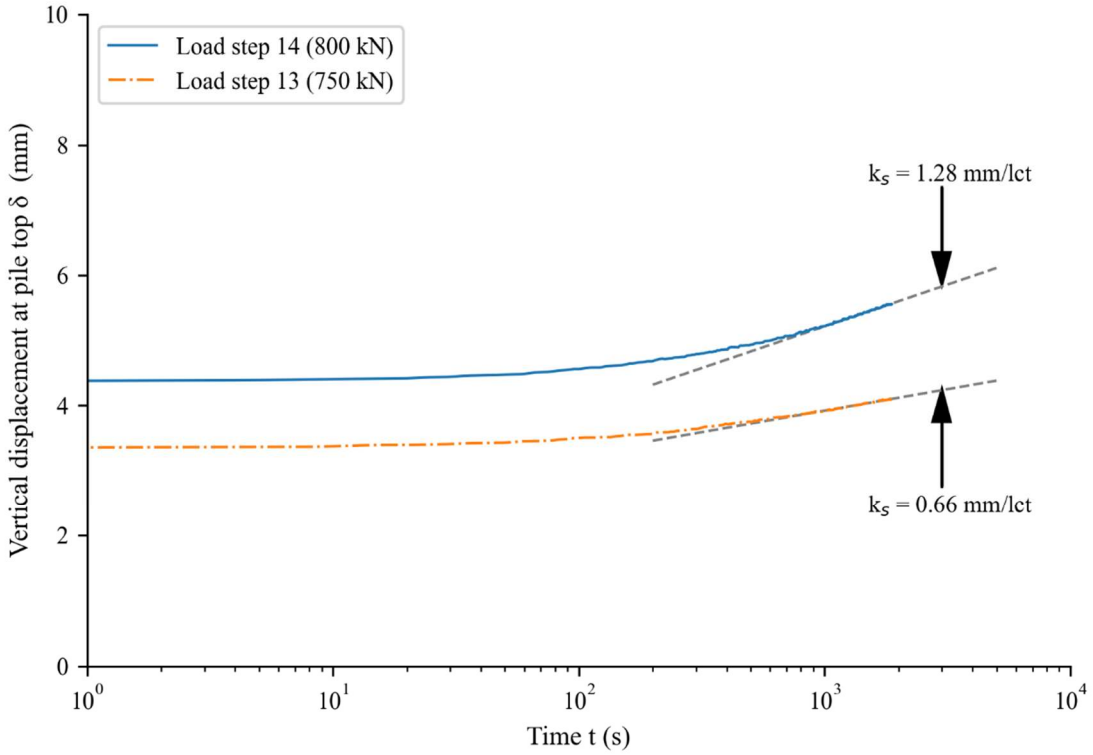

Figure 46: Rate of creep for the final two load steps for test pile 4.

Test pile 5

Table 23: Rate of creep overview for test pile 5.

Test pile 5	Load / Reload [kN]	Trendline equation Spyder (python) [-]	Rate of creep [mm/lct]
Load phase 1			
Load step 1	100	$y = -0.001 \cdot \ln(x) + 0.09$	**-0.00**
Load step 2	200	$y = -0.014 \cdot \ln(x) + 0.35$	**-0.03**
Load phase 2			
Load step 5	100	$y = 0.001 \cdot \ln(x) + 0.02$	**0.00**
Load step 6	200	$y = 0.032 \cdot \ln(x) + 0.01$	**0.07**
Load step 7	300	$y = 0.015 \cdot \ln(x) + 0.39$	**0.03**
Load step 8	400	$y = 0.030 \cdot \ln(x) + 0.59$	**0.07**
Load step 9	500	$y = 0.040 \cdot \ln(x) + 0.91$	**0.09**
Load step 10	600	$y = 0.164 \cdot \ln(x) + 0.57$	**0.38**
Load step 11	650	$y = 0.117 \cdot \ln(x) + 1.48$	**0.27**
Load step 12	700	$y = 0.214 \cdot \ln(x) + 1.54$	**0.49**
Load step 13	750	$y = 0.478 \cdot \ln(x) + 1.38$	**1.10**
Load step 14	800	$y = 0.793 \cdot \ln(x) + 1.04$	**1.83**

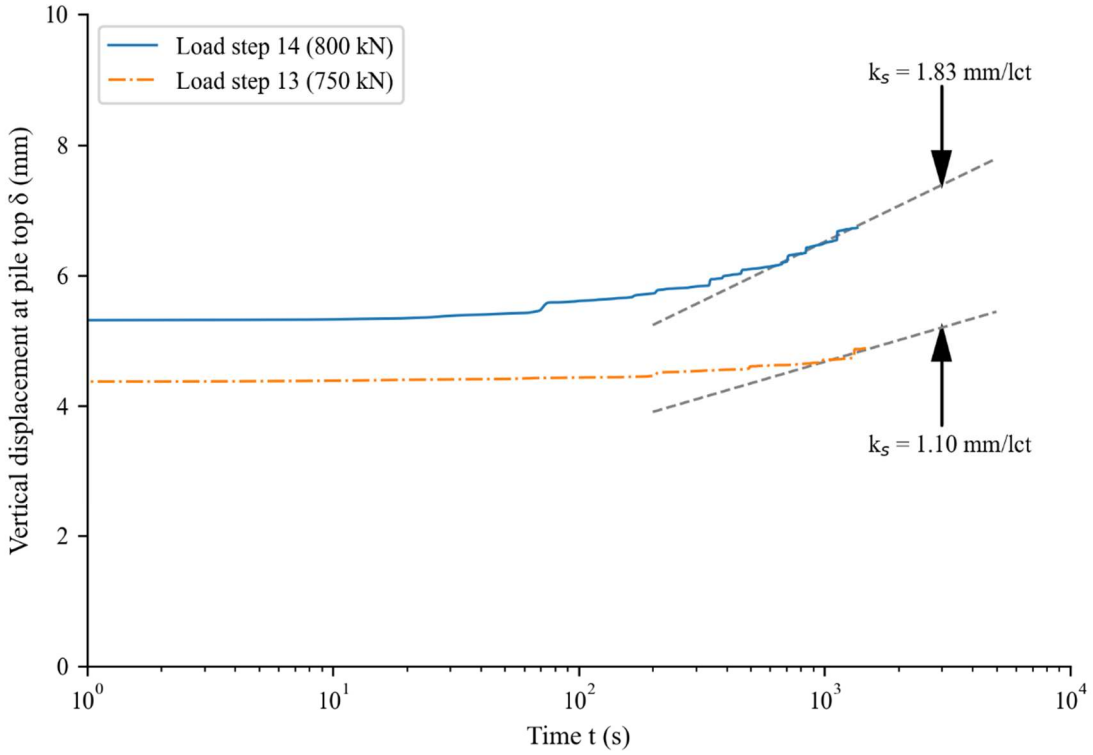

Figure 47: Rate of creep for the final two load steps for test pile 5.

Test pile 6

Table 24: Rate of creep overview for test pile 6.

Test pile 6	Load / Reload [kN]	Trendline equation Spyder (python) [-]	Rate of creep [mm/lct]
Load phase 1			
Load step 1	100	$y = -0.038 \cdot \ln(x) + 0.42$	**-0.09**
Load step 2	200	$y = -0.005 \cdot \ln(x) + 0.36$	**-0.01**
Load phase 2			
Load step 5	100	$y = -0.033 \cdot \ln(x) + 0.27$	**-0.08**
Load step 6	200	$y = 0.051 \cdot \ln(x) - 0.22$	**0.12**
Load step 7	300	$y = 0.007 \cdot \ln(x) + 0.33$	**0.02**
Load step 8	400	$y = 0.045 \cdot \ln(x) + 0.34$	**0.10**
Load step 9	500	$y = -0.049 \cdot \ln(x) + 1.25$	**-0.11**
Load step 10	600	$y = 0.060 \cdot \ln(x) + 0.80$	**0.14**
Load step 11	650	$y = -0.003 \cdot \ln(x) + 1.62$	**-0.01**
Load step 12	700	$y = 0.077 \cdot \ln(x) + 1.32$	**0.18**
Load step 13	750	$y = 0.134 \cdot \ln(x) + 2.06$	**0.31**
Load step 14	800	$y = 0.261 \cdot \ln(x) + 1.93$	**0.60**

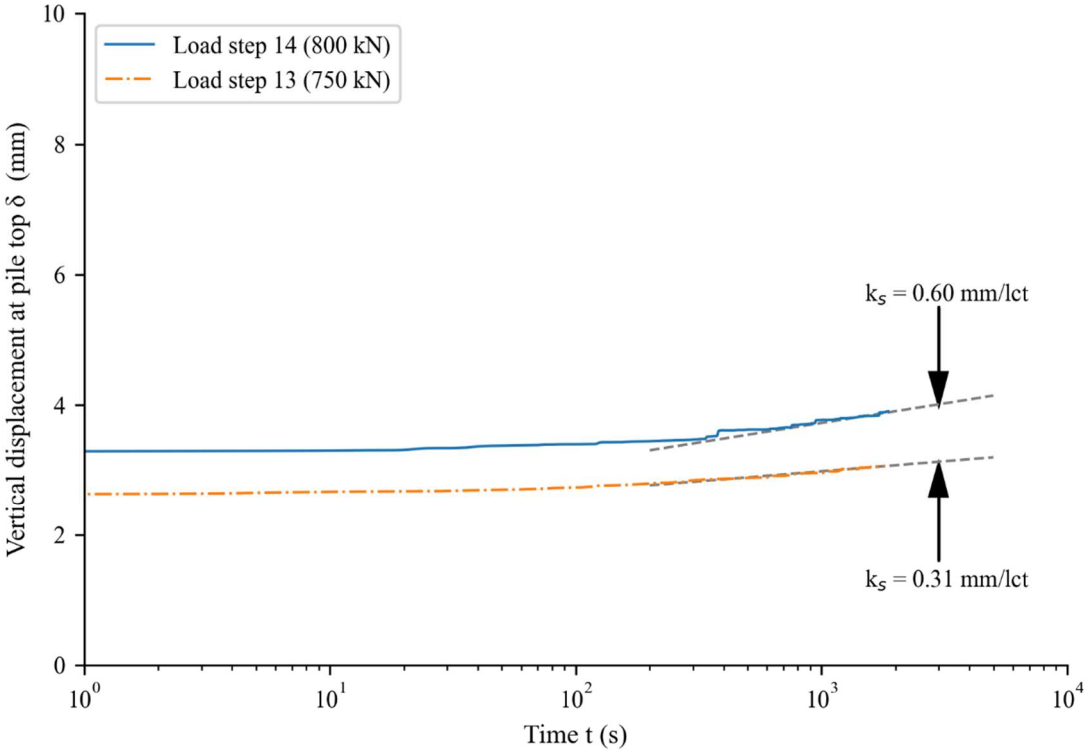

Figure 48: Rate of creep for the final two load steps for test pile 6.

Test pile 8

Table 25: Rate of creep overview for test pile 8.

Test pile 8	Load / Reload [kN]	Trendline equation Spyder (python) [-]	Rate of creep [mm/lct]
Load phase 1			
Load step 1	100	$y = -0.007 \cdot \ln(x) + 0.20$	**-0.02**
Load step 2	200	$y = -0.014 \cdot \ln(x) + 0.42$	**-0.03**
Load phase 2			
Load step 5	100	$y = -0.002 \cdot \ln(x) + 0.03$	**-0.00**
Load step 6	200	$y = 0.004 \cdot \ln(x) + 0.11$	**0.01**
Load step 7	300	$y = -0.011 \cdot \ln(x) + 0.36$	**-0.02**
Load step 8	400	$y = 0.019 \cdot \ln(x) + 0.34$	**0.04**
Load step 9	500	$y = 0.081 \cdot \ln(x) + 0.16$	**0.19**
Load step 10	600	$y = 0.080 \cdot \ln(x) + 0.85$	**0.19**
Load step 11	650	$y = 0.210 \cdot \ln(x) + 0.35$	**0.48**
Load step 12	700	$y = 0.194 \cdot \ln(x) + 1.07$	**0.45**
Load step 13	750	$y = 0.297 \cdot \ln(x) + 1.13$	**0.68**
Load step 14	800	$y = 0.415 \cdot \ln(x) + 1.43$	**0.95**

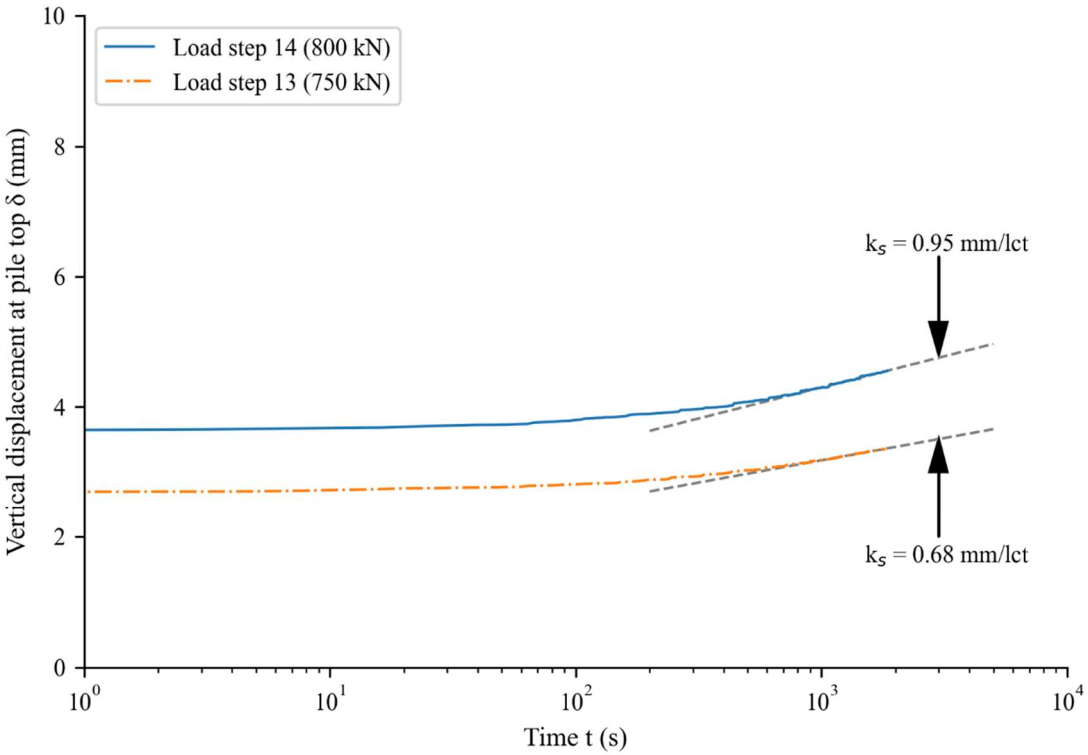

Figure 49: Rate of creep for the final two load steps for test pile 8.

E.6 Shear stiffness degeneration curves

Maintained load (ML) test

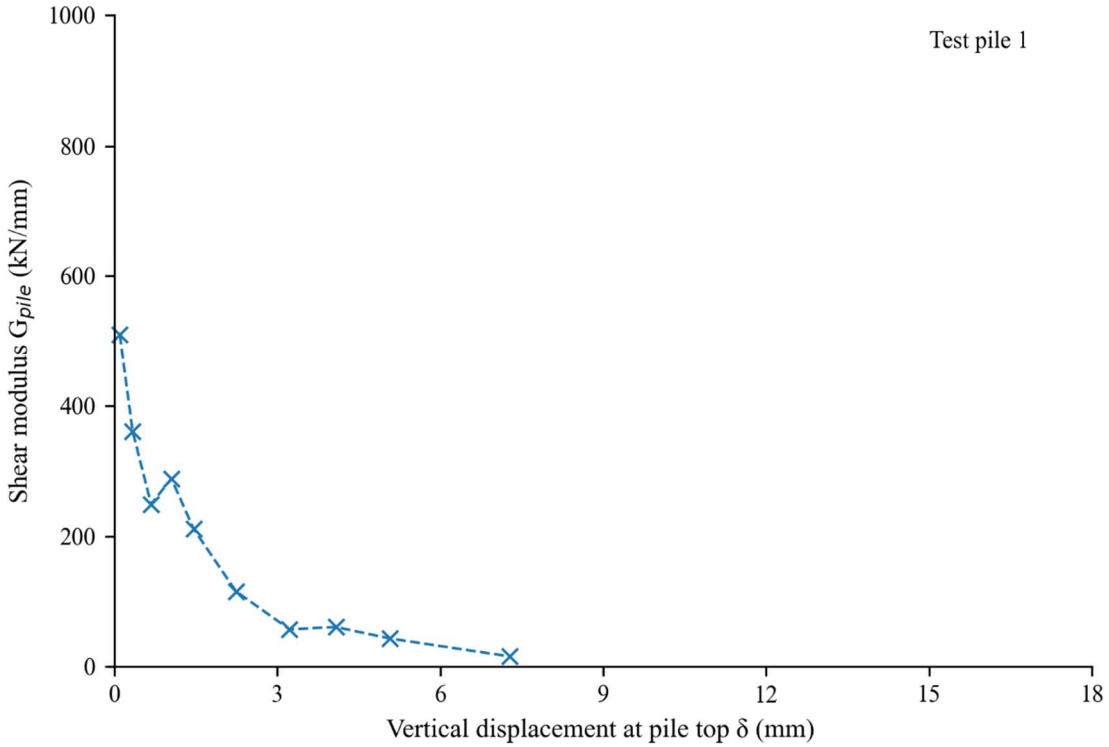

Figure 50: Shear stiffness degeneration curve for test pile 1 during the maintained load (ML) test.

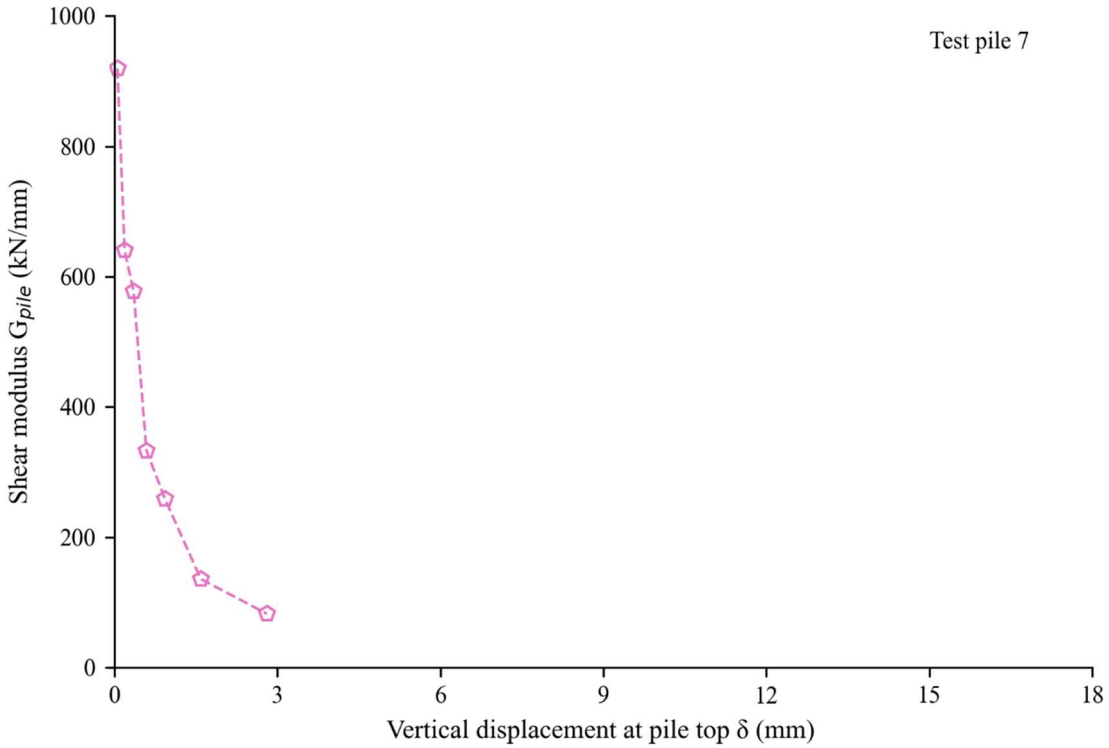

Figure 51: Shear stiffness degeneration curve for test pile 7 during the maintained load (ML) test.

Constant rate of uplift (CRU) test

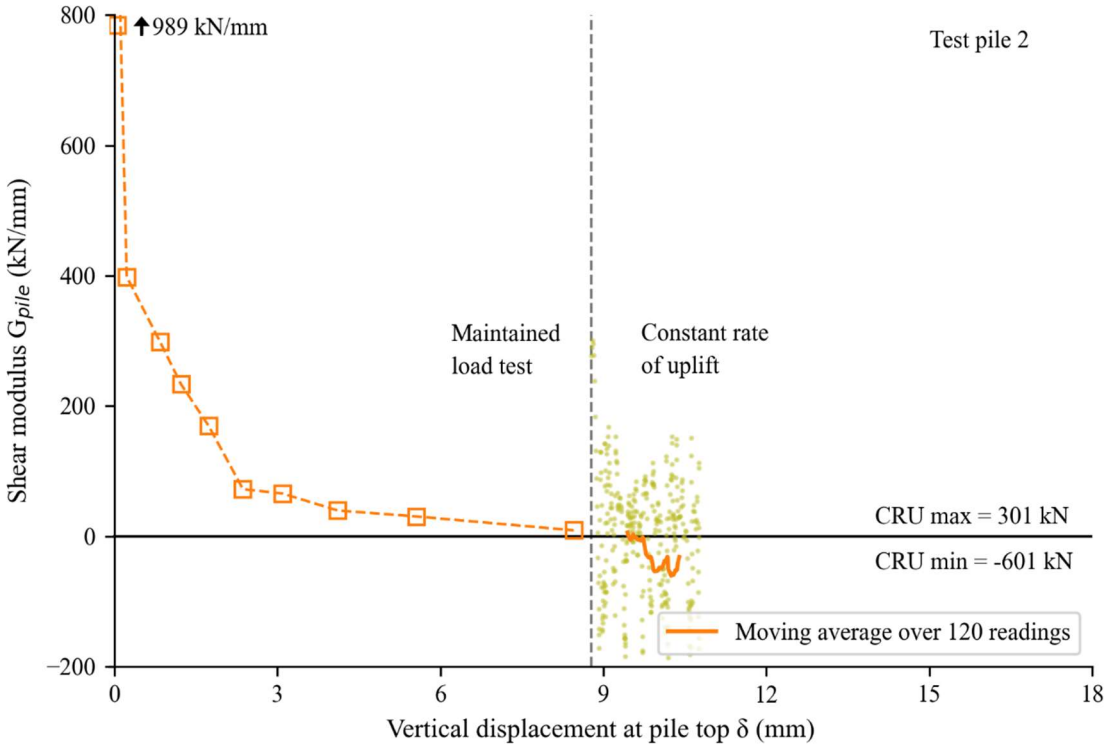

Figure 52: Shear stiffness degeneration curve for test pile 2 during the constant rate of uplift (CRU) test.

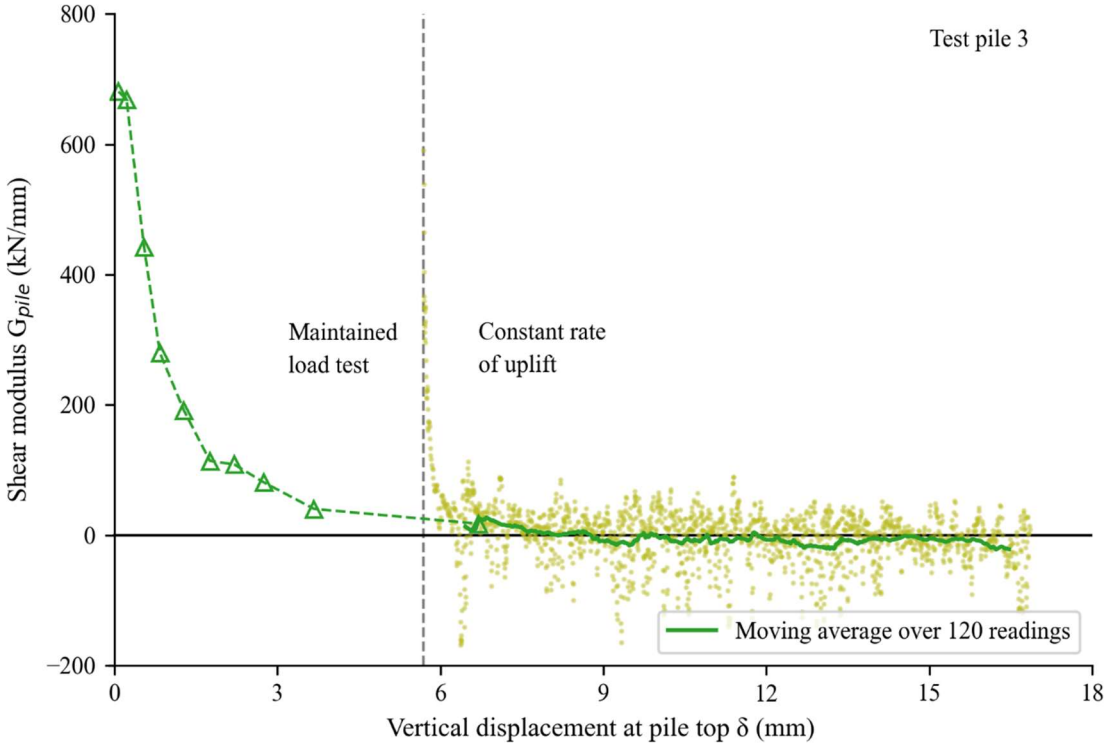

Figure 53: Shear stiffness degeneration curve for test pile 3 during the constant rate of uplift (CRU) test.

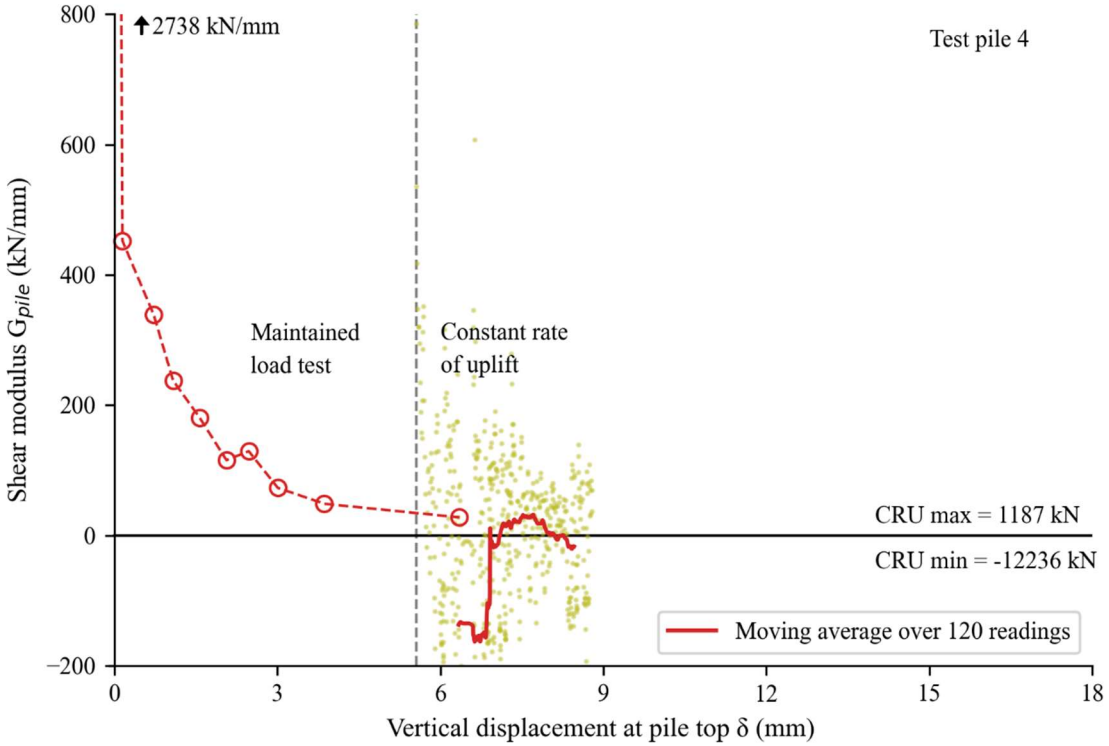

Figure 54: Shear stiffness degeneration curve for test pile 4 during the constant rate of uplift (CRU) test.

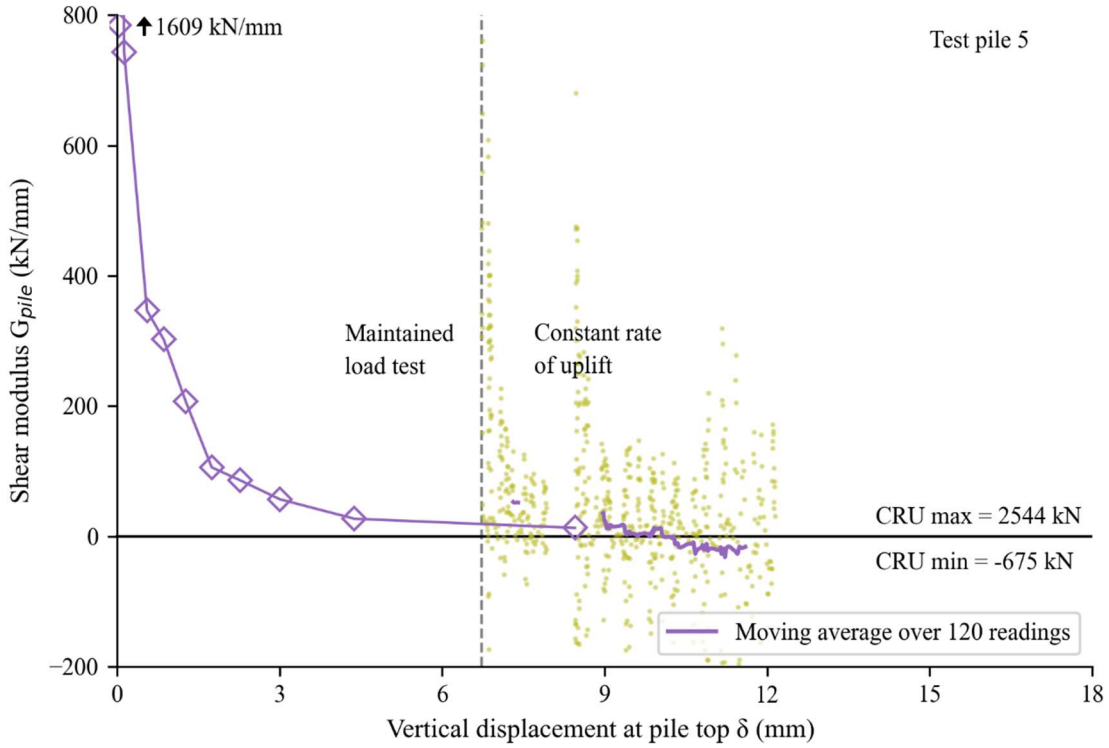

Figure 55: Shear stiffness degeneration curve for test pile 5 during the constant rate of uplift (CRU) test.

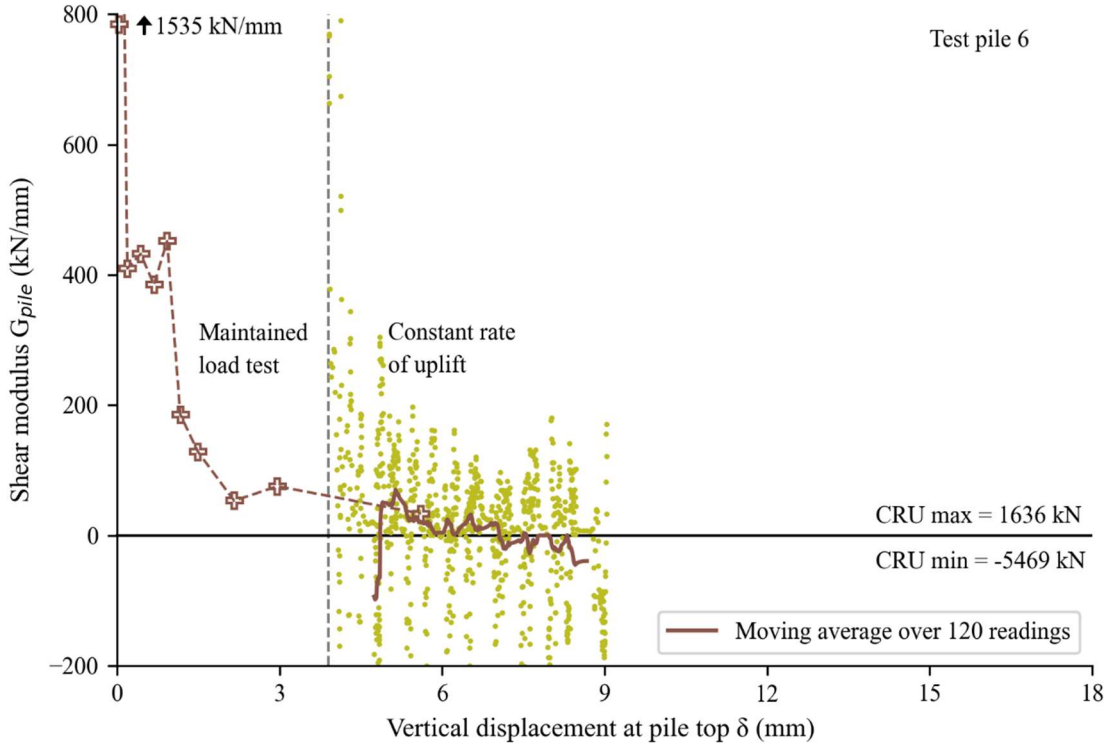

Figure 56: Shear stiffness degeneration curve for test pile 6 during the constant rate of uplift (CRU) test.

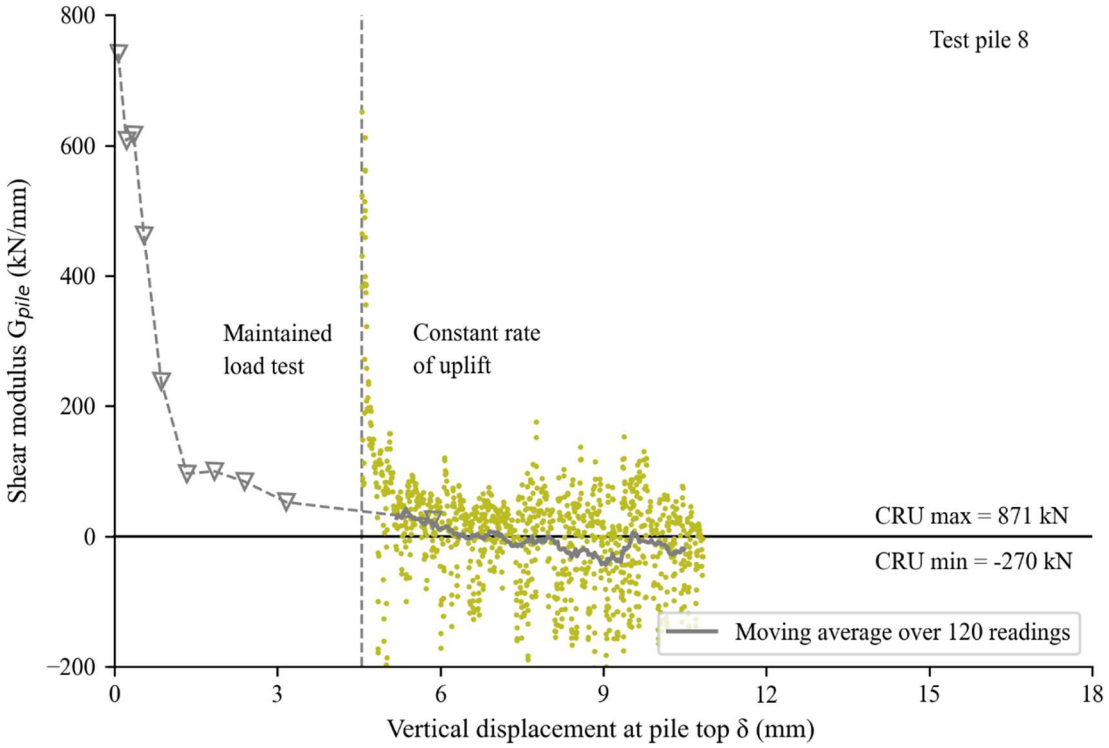

Figure 57: Shear stiffness degeneration curve for test pile 8 during the constant rate of uplift (CRU) test.

E.7 Average unloading-reloading stiffness

Constant rate of uplift (CRU) test

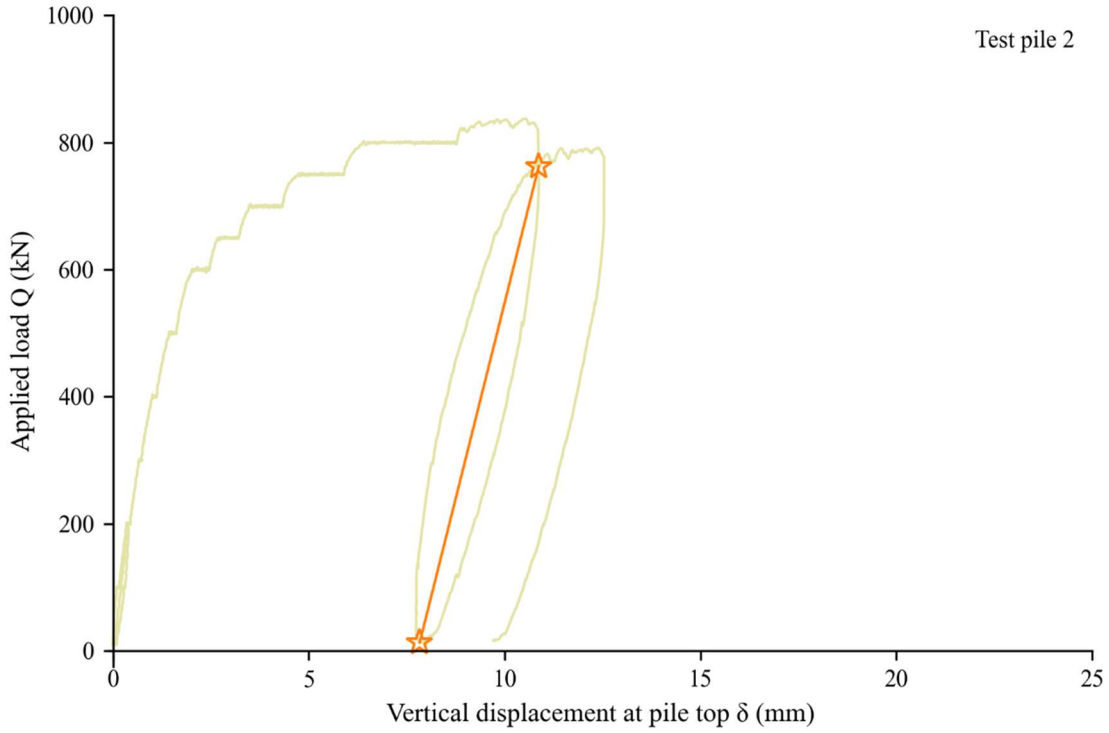

Figure 58: Determination of the shear modulus, G_{pile}, as the average value of the inclination of the unloading-reloading hysteresis for test pile 2.

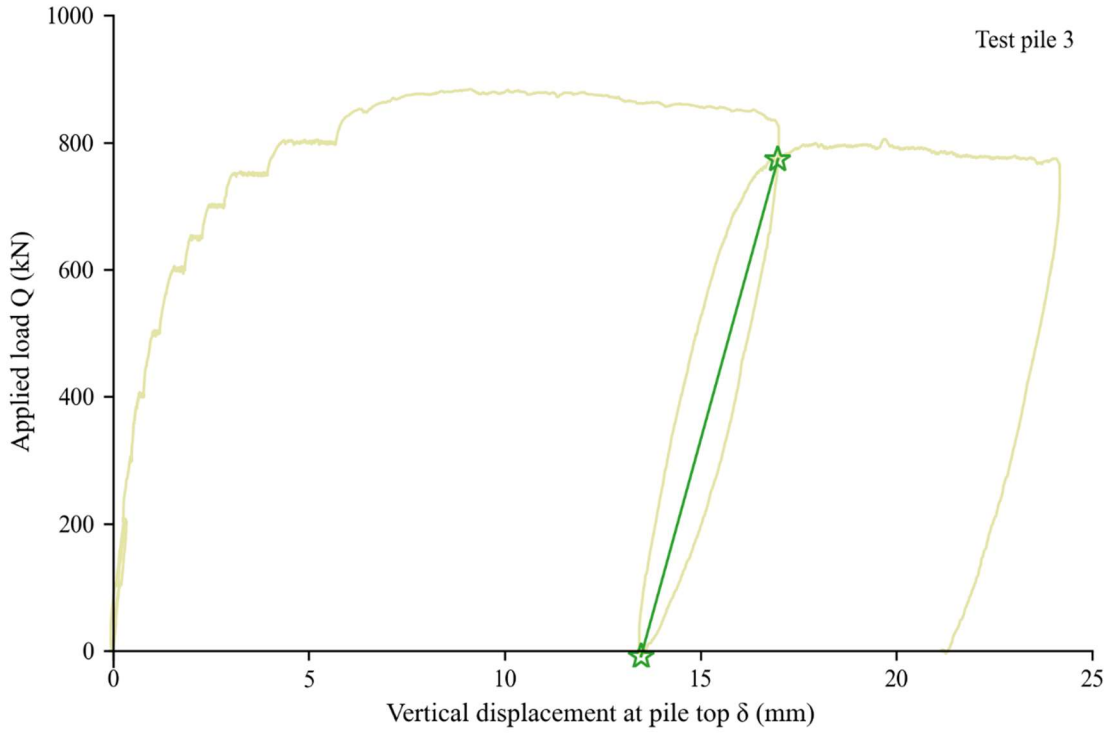

Figure 59: Determination of the shear modulus, G_{pile}, as the average value of the inclination of the unloading-reloading hysteresis for test pile 3.

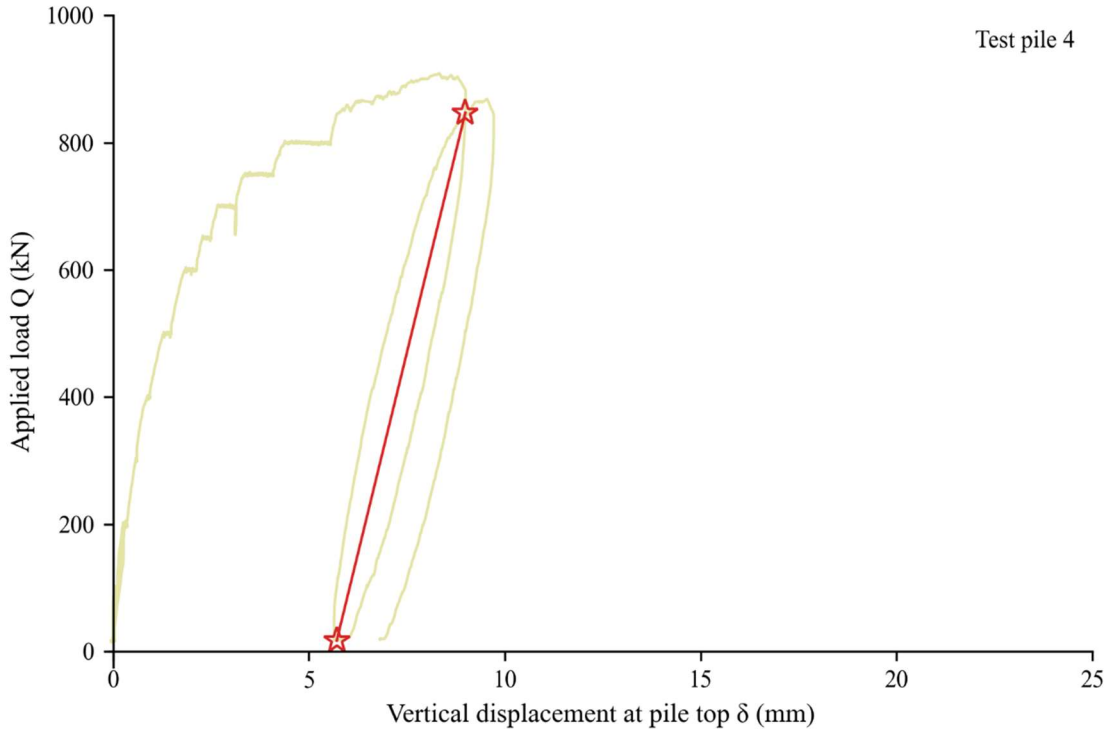

Figure 60: Determination of the shear modulus, G_{pile}, as the average value of the inclination of the unloading-reloading hysteresis for test pile 4.

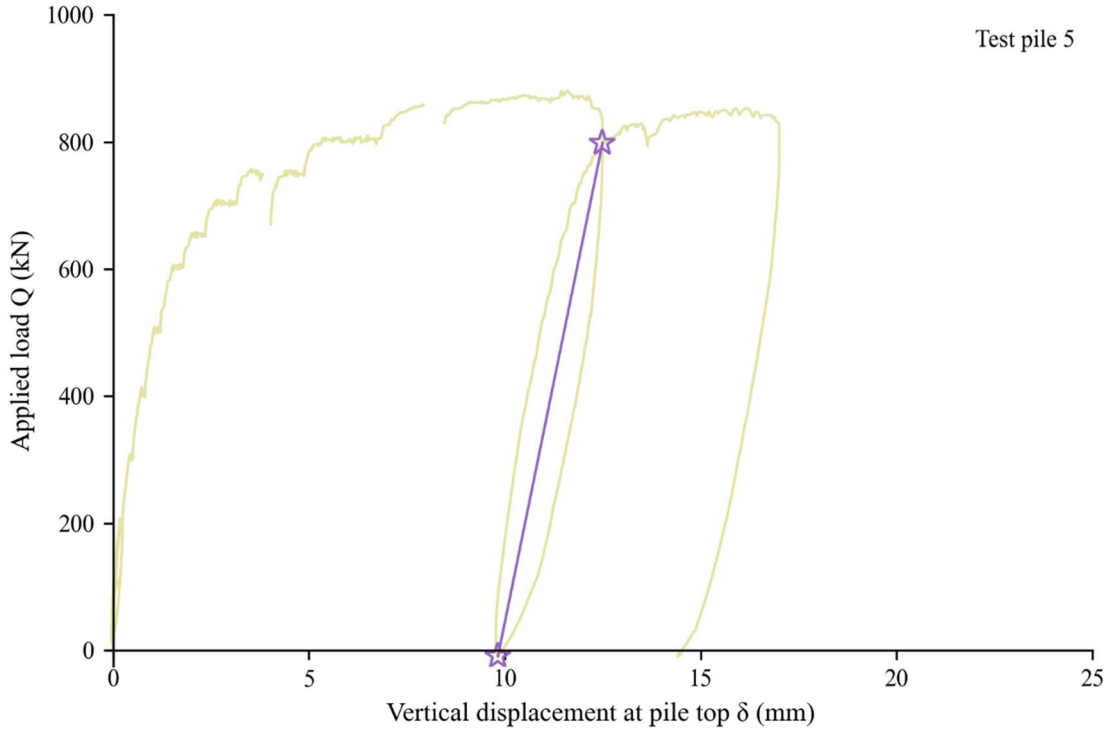

Figure 61: Determination of the shear modulus, G_{pile}, as the average value of the inclination of the unloading-reloading hysteresis for test pile 5.

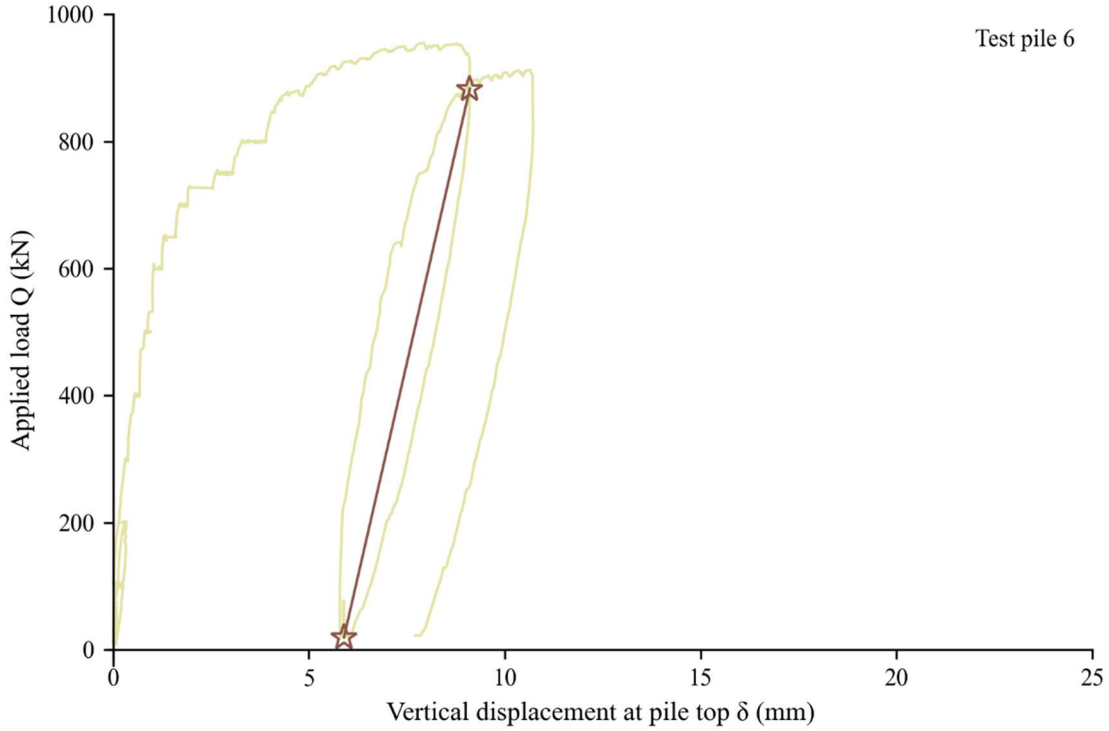

Figure 62: Determination of the shear modulus, G_{pile}, as the average value of the inclination of the unloading-reloading hysteresis for test pile 6.

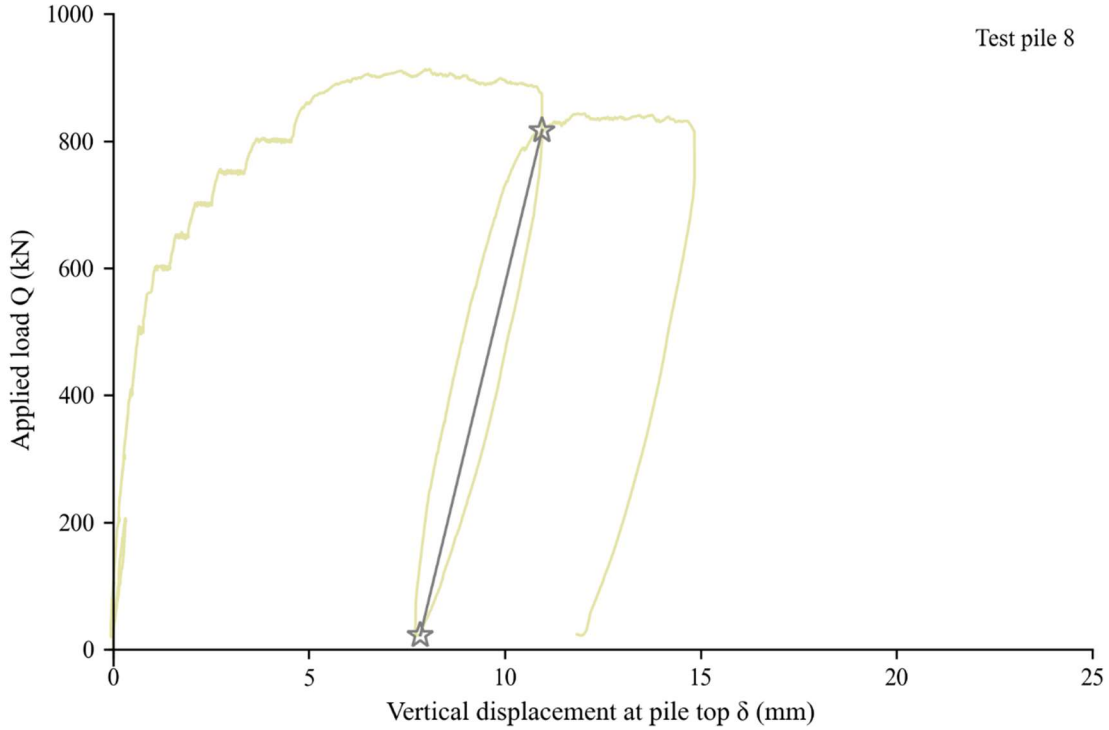

Figure 63: Determination of the shear modulus, G_{pile}, as the average value of the inclination of the unloading-reloading hysteresis for test pile 8.

F Temperature data

F.1 Temperature development with time

Test pile 4

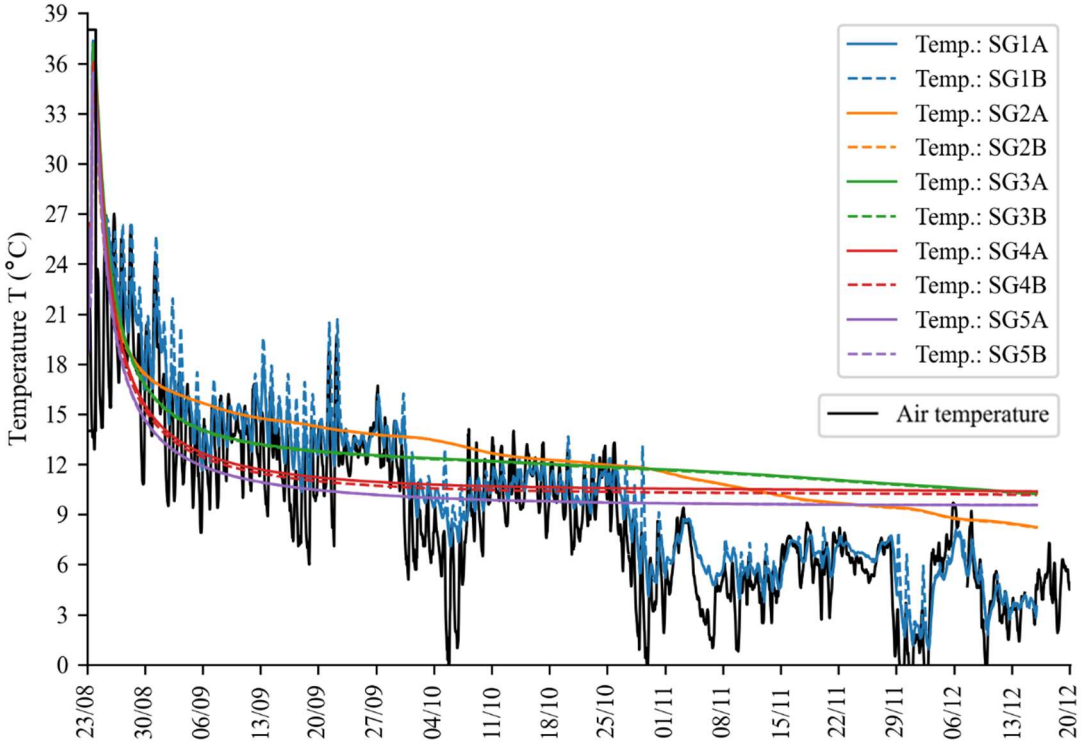

Figure 64: Measured temperatures in test pile 4 from installation of the test pile on the 23rd of August 2019 and throughout the following 116 days (~4 months).

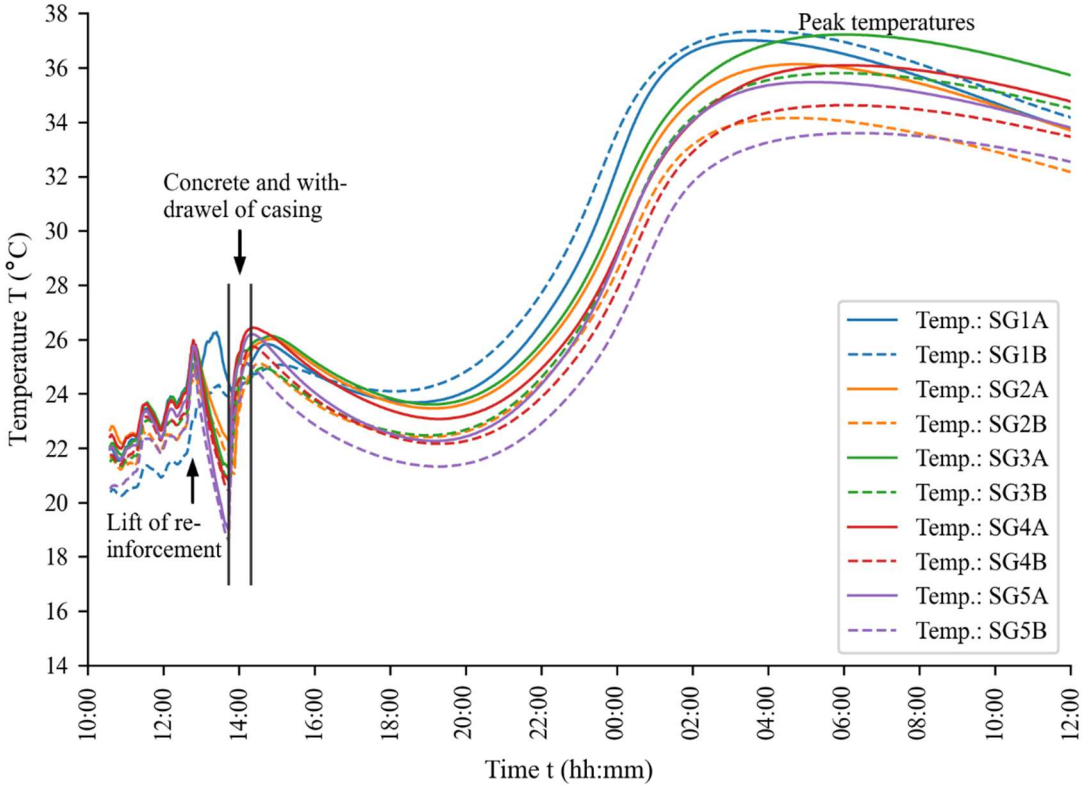

Figure 65: Measured temperatures in test pile 4 during installation of the test pile on the 23rd of August 2019 through the 24th of August 2019.

Test pile 8

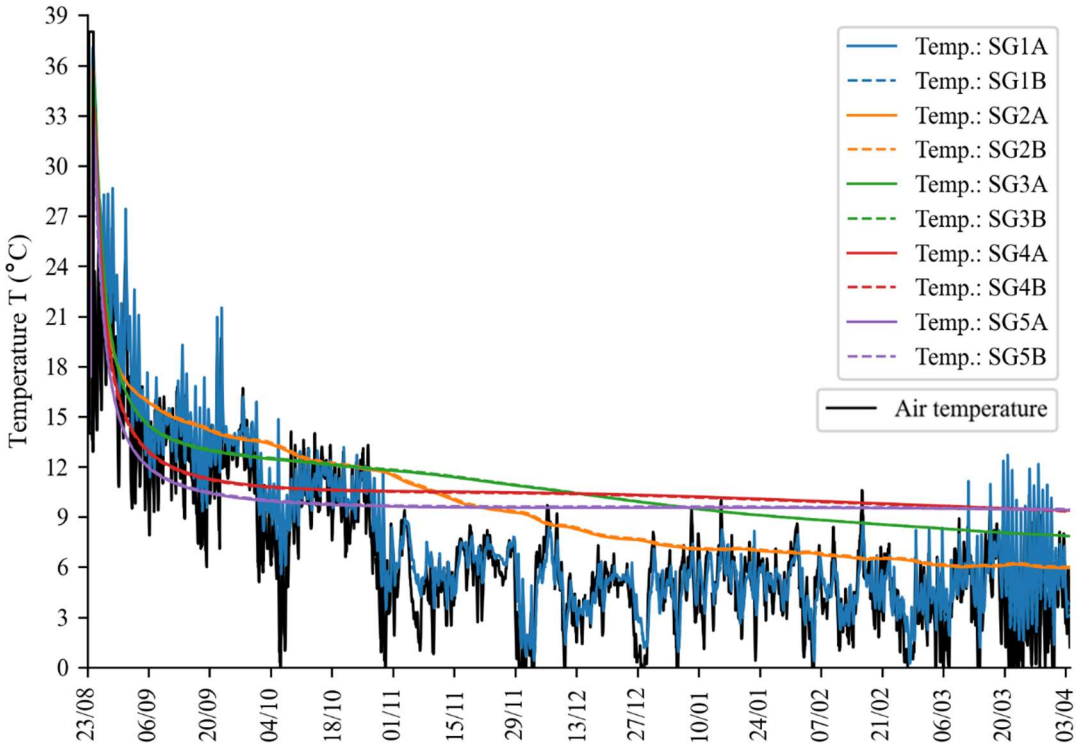

Figure 66: Measured temperatures in test pile 8 from installation of the test pile on the 23rd of August 2019 and throughout the following 225 days (~7½ months).

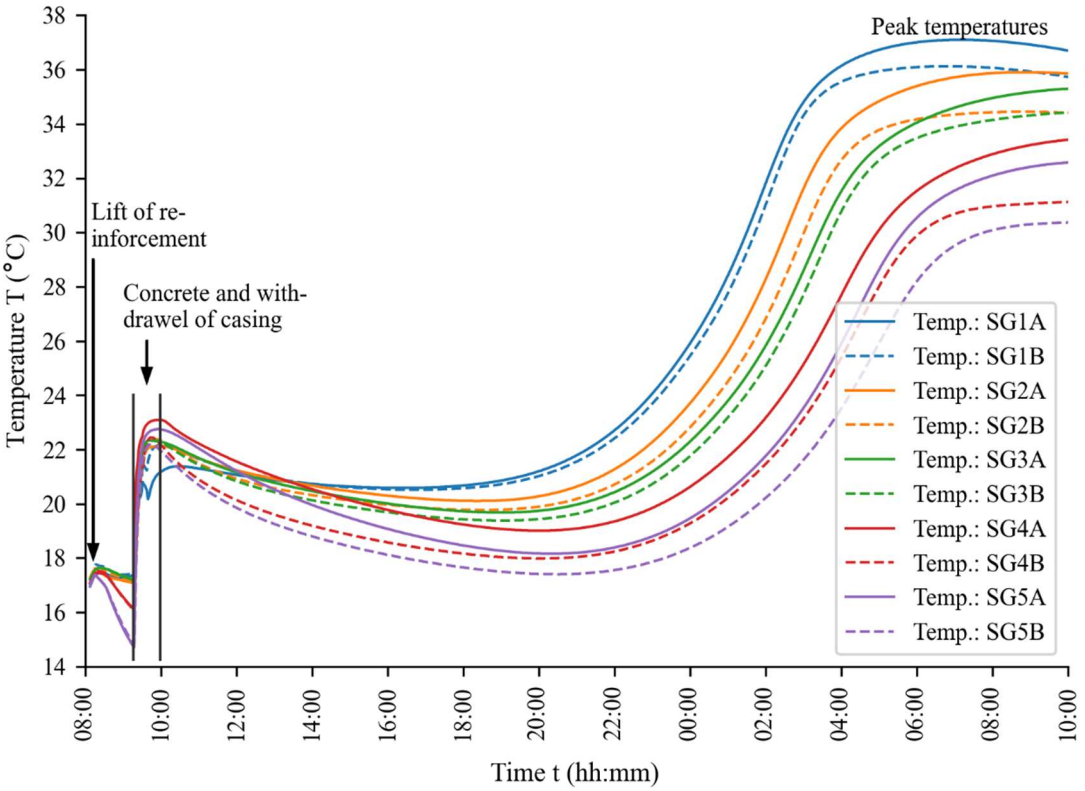

Figure 67: Measured temperatures in test pile 8 during installation of the test pile on the 23rd of August 2019 through the 24th of August 2019.

F.2 Temperature development during static pile loading test

Test pile 1

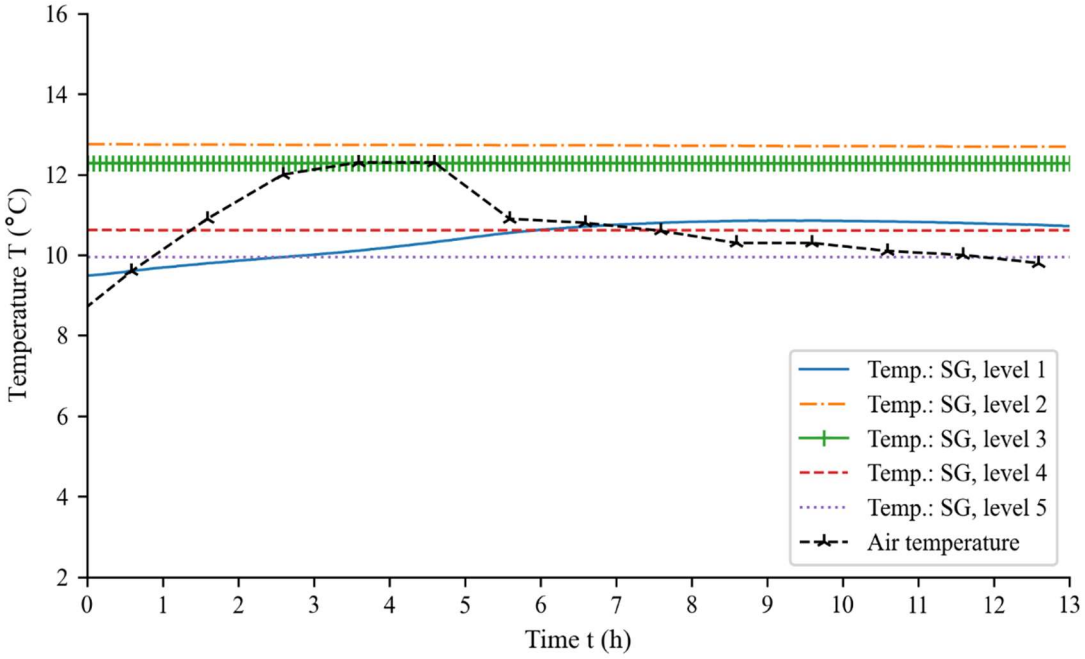

Figure 68: Temperatures at each strain gauge level for test pile 1 during static pile loading test. The air temperature in Randers (nearest measuring point) from DMI weather archive added.

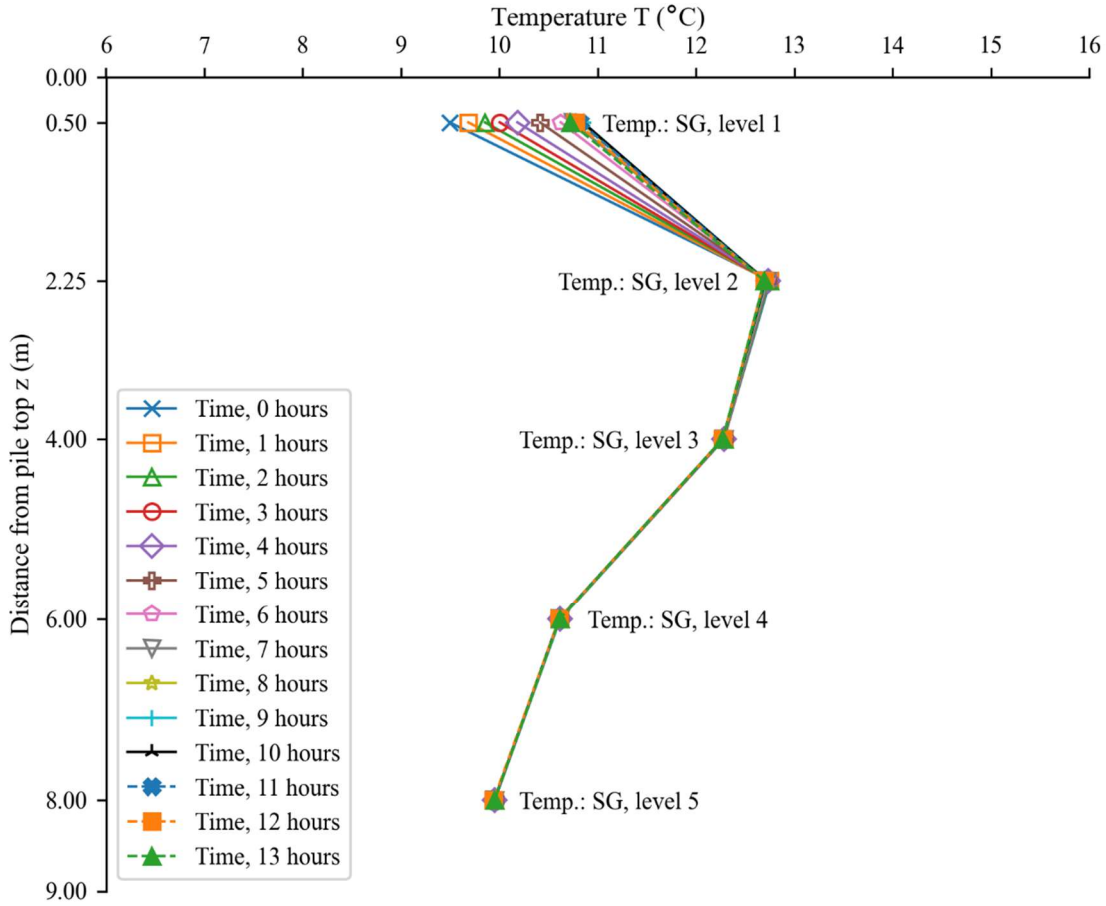

Figure 69: Temperature development along the length of test pile 1 during static pile loading test. The time indications are established as zero at the beginning of the static pile loading tests. Solid lines represent increasing temperatures, and dotted lines represent decreasing temperatures.

Test pile 2

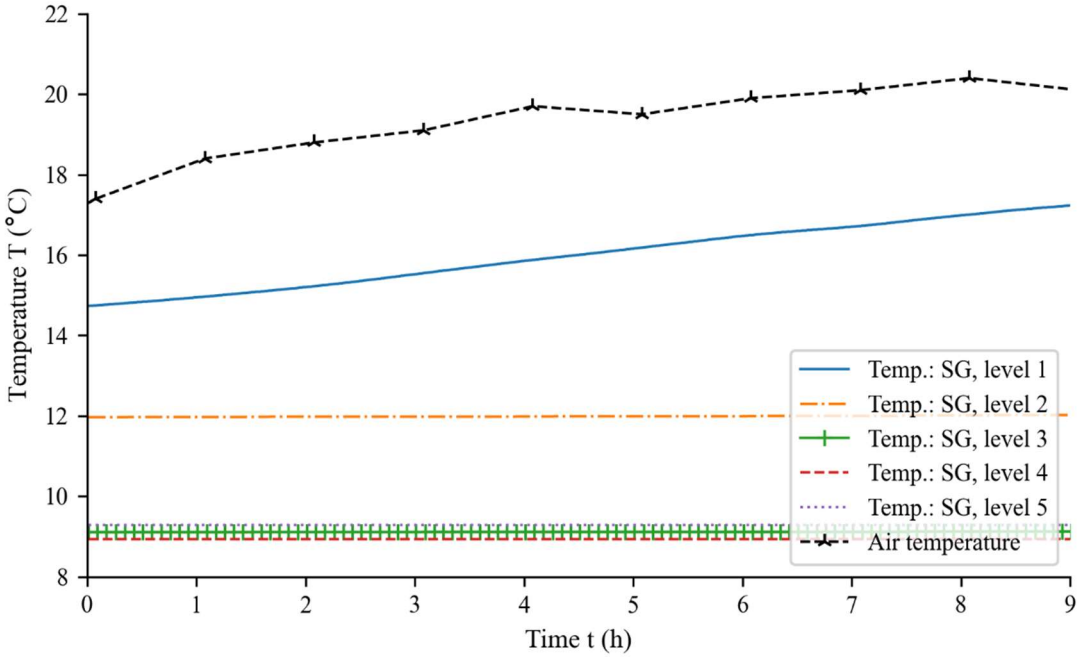

Figure 70: Temperatures at each strain gauge level for test pile 2 during static pile loading test. The air temperature in Randers (nearest measuring point) from DMI weather archive added.

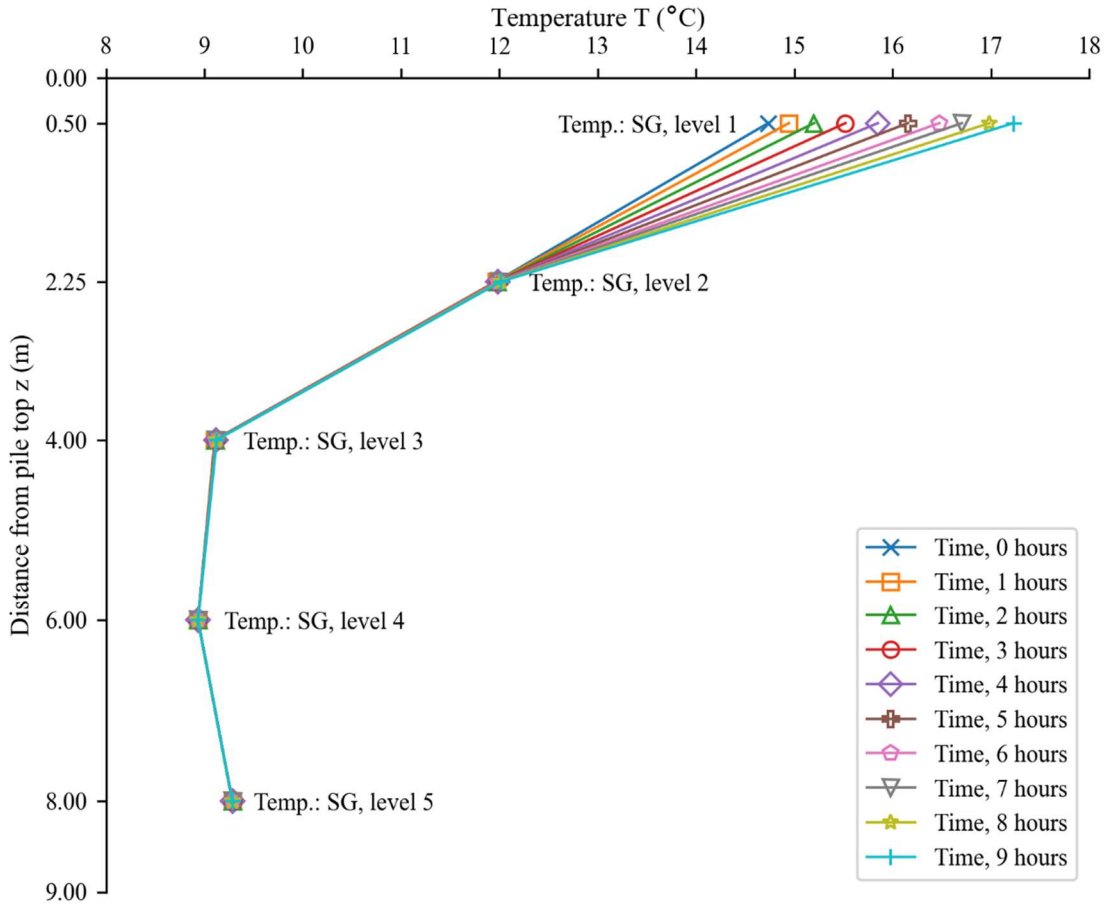

Figure 71: Temperature development along the length of test pile 2 during static pile loading test. The time indications are established as zero at the beginning of the static pile loading tests. Only the upper strain gauge level was affected by temperature changes during the static pile loading tests.

Test pile 3

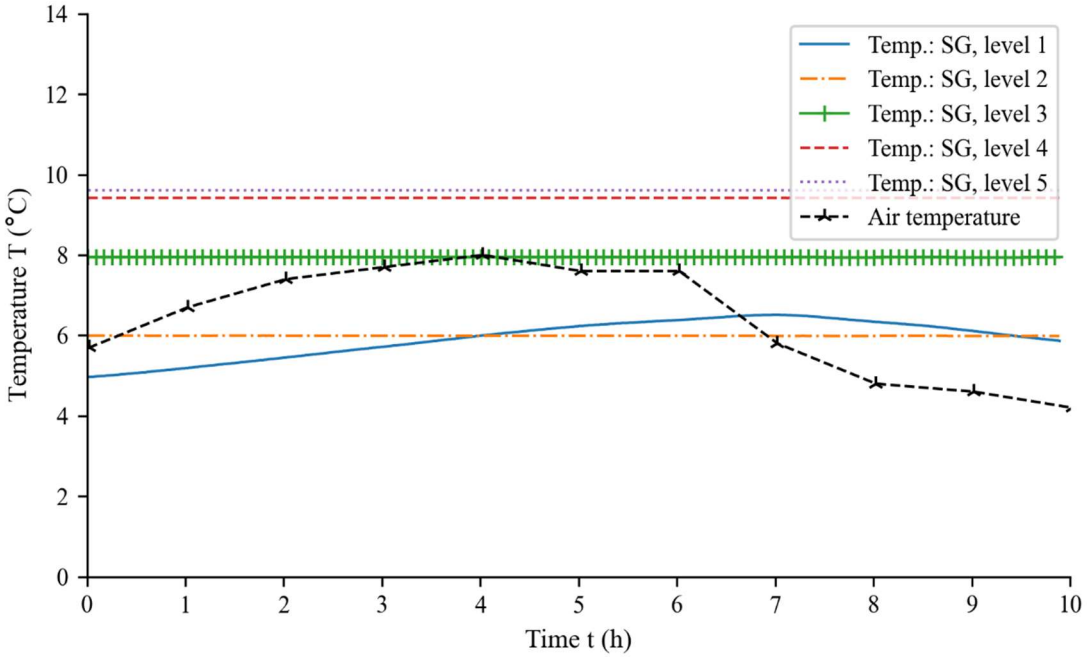

Figure 72: Temperatures at each strain gauge level for test pile 3 during static pile loading test. The air temperature in Randers (nearest measuring point) from DMI weather archive added.

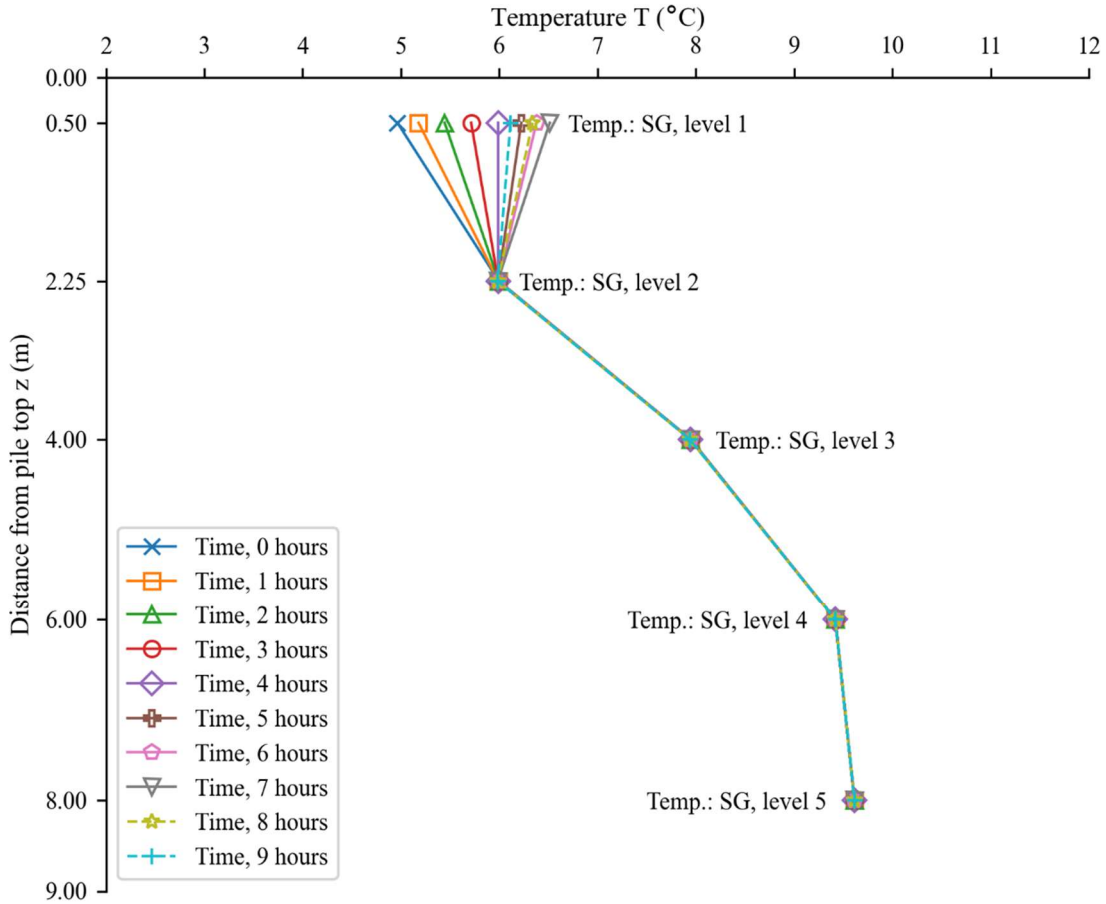

Figure 73: Temperature development along the length of test pile 3 during static pile loading test. The time indications are established as zero at the beginning of the static pile loading tests. Solid lines represent increasing temperatures, and dotted lines represent decreasing temperatures.

Test pile 4

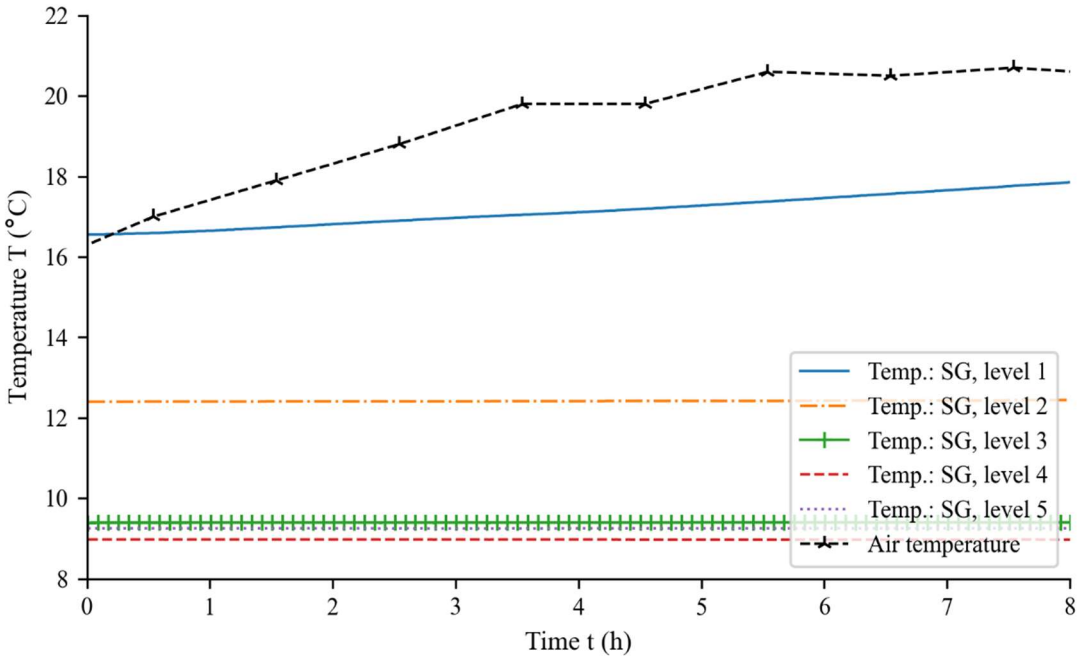

Figure 74: Temperatures at each strain gauge level for test pile 4 during static pile loading test. The air temperature in Randers (nearest measuring point) from DMI weather archive added.

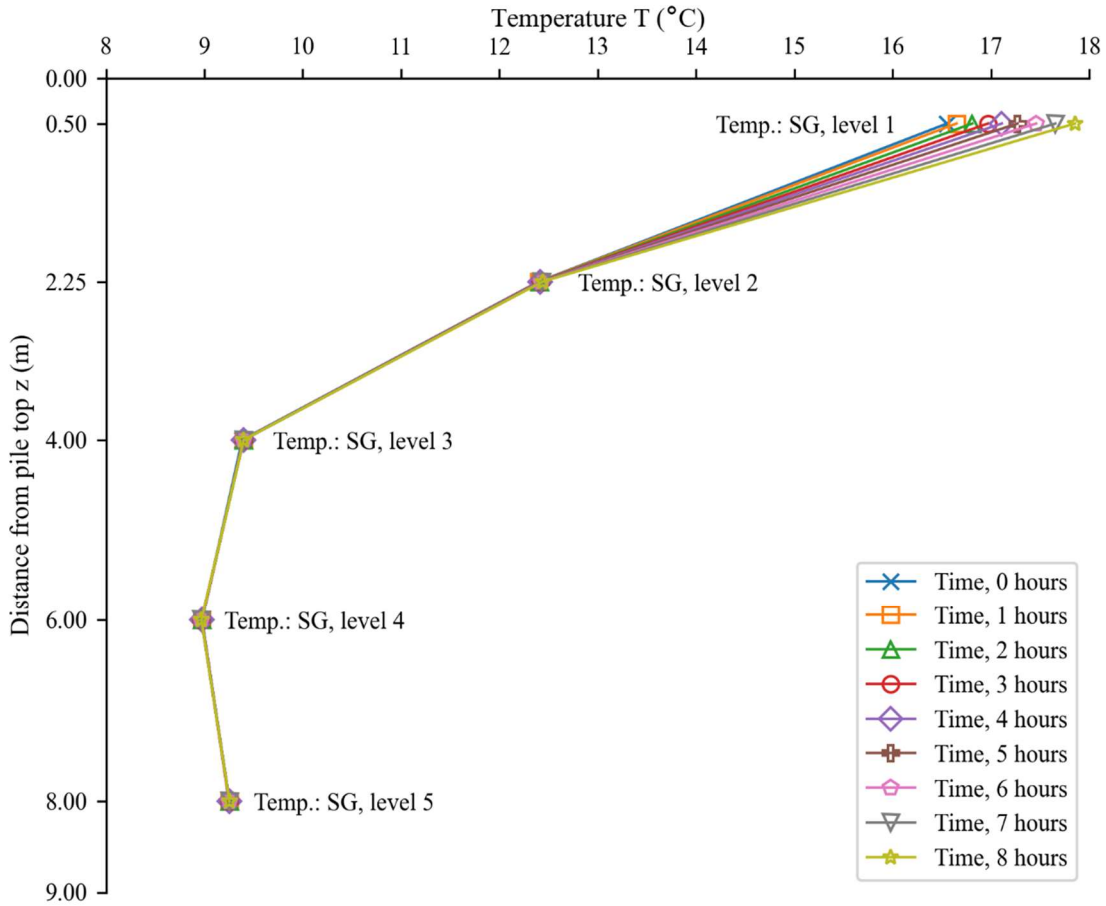

Figure 75: Temperature development along the length of test pile 4 during static pile loading test. The time indications are established as zero at the beginning of the static pile loading tests. Only the upper strain gauge level was affected by temperature changes during the static pile loading tests.

Test pile 5

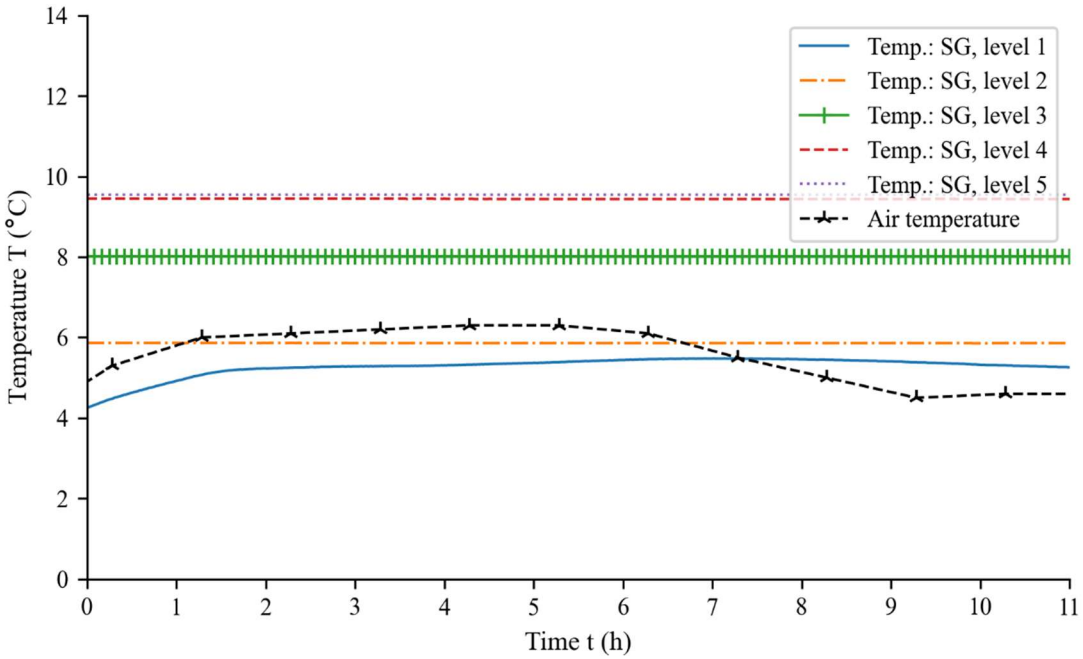

Figure 76: Temperatures at each strain gauge level for test pile 5 during static pile loading test. The air temperature in Randers (nearest measuring point) from DMI weather archive added.

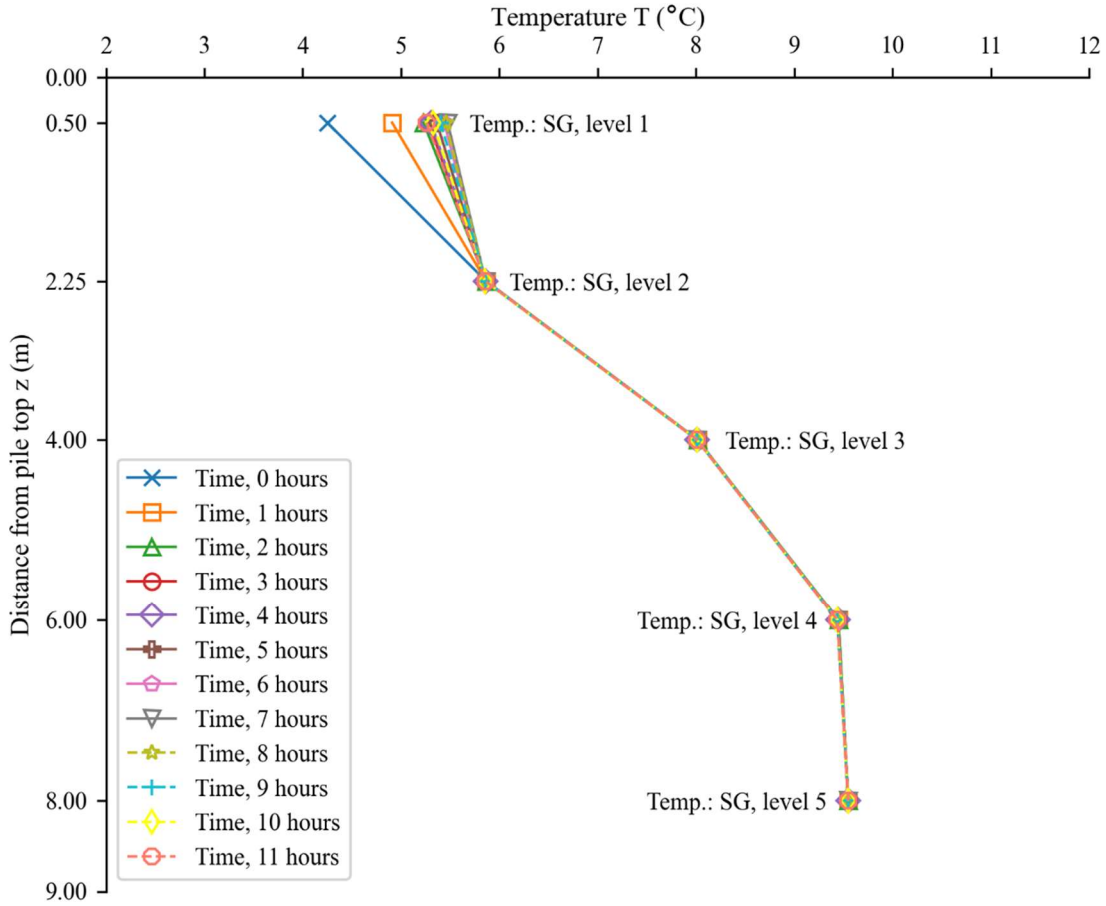

Figure 77: Temperature development along the length of test pile 5 during static pile loading test. The time indications are established as zero at the beginning of the static pile loading tests. Solid lines represent increasing temperatures, and dotted lines represent decreasing temperatures.

Test pile 6

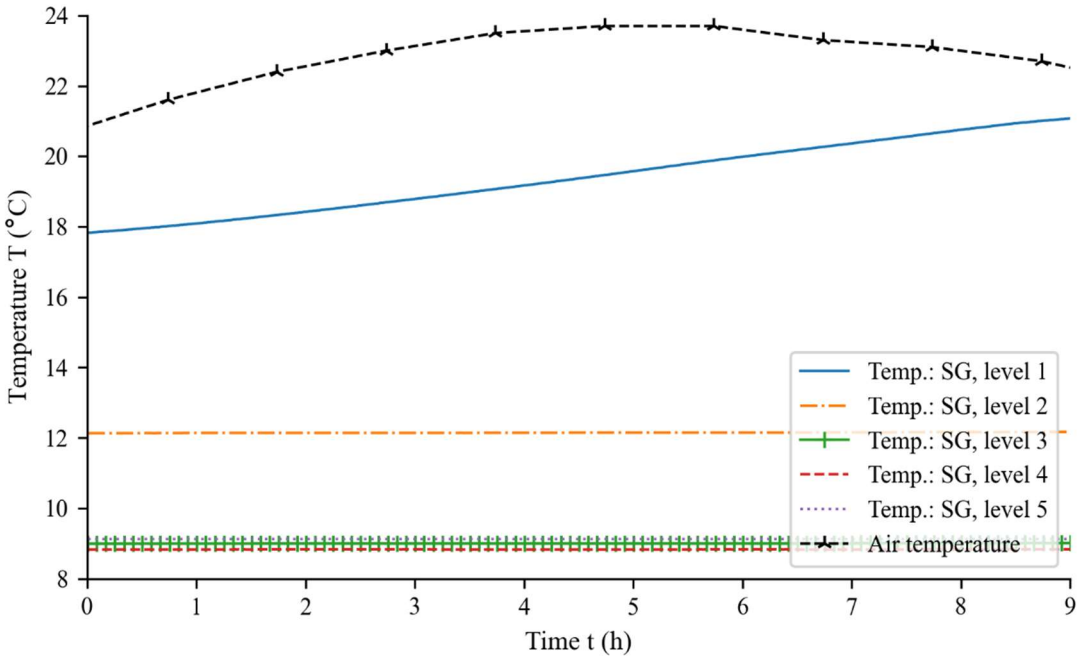

Figure 78: Temperatures at each strain gauge level for test pile 6 during static pile loading test. The air temperature in Randers (nearest measuring point) from DMI weather archive added.

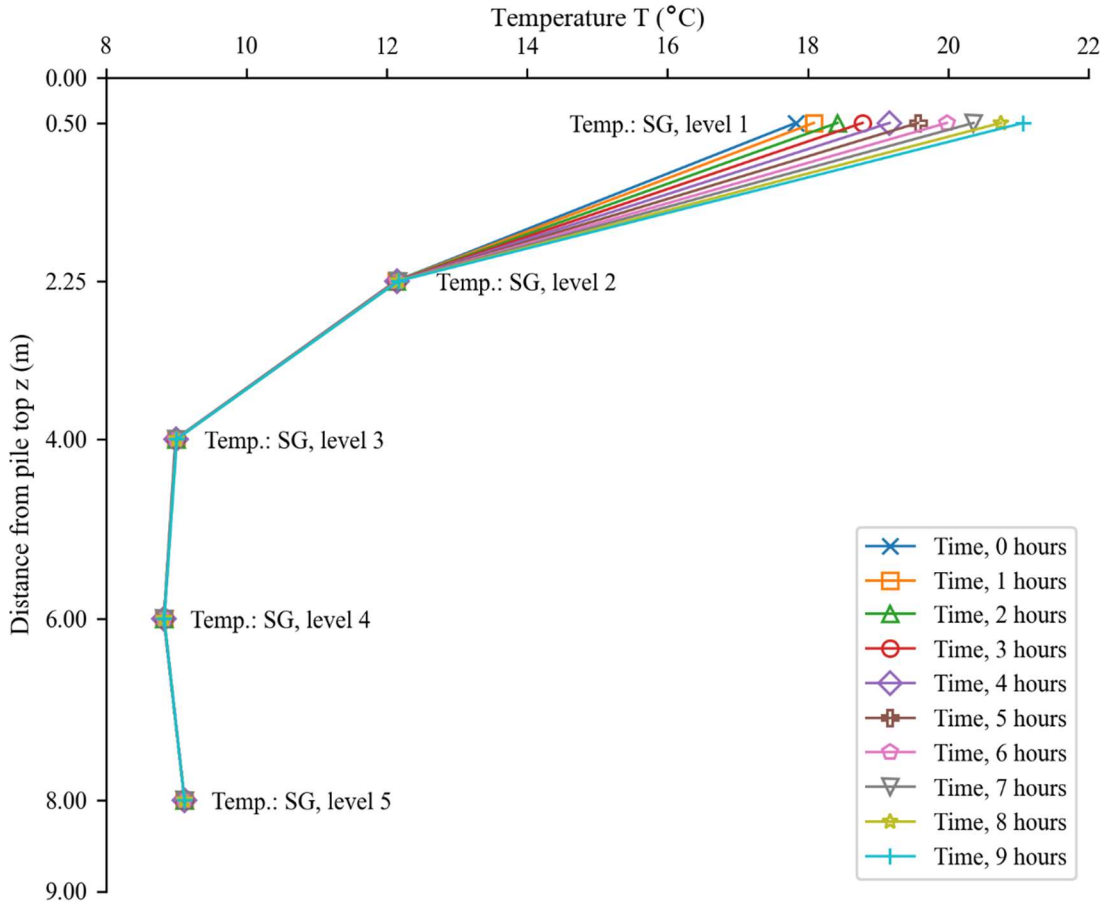

Figure 79: Temperature development along the length of test pile 6 during static pile loading test. The time indications are established as zero at the beginning of the static pile loading tests. Only the upper strain gauge level was affected by temperature changes during the static pile loading tests.

Test pile 7

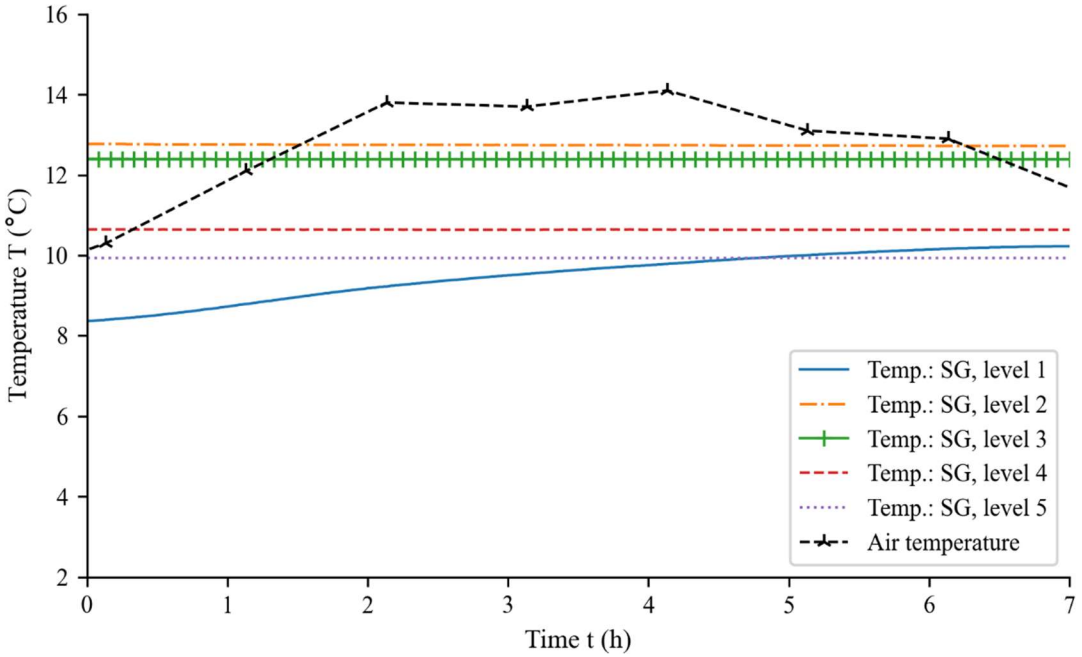

Figure 80: Temperatures at each strain gauge level for test pile 7 during static pile loading test. The air temperature in Randers (nearest measuring point) from DMI weather archive added.

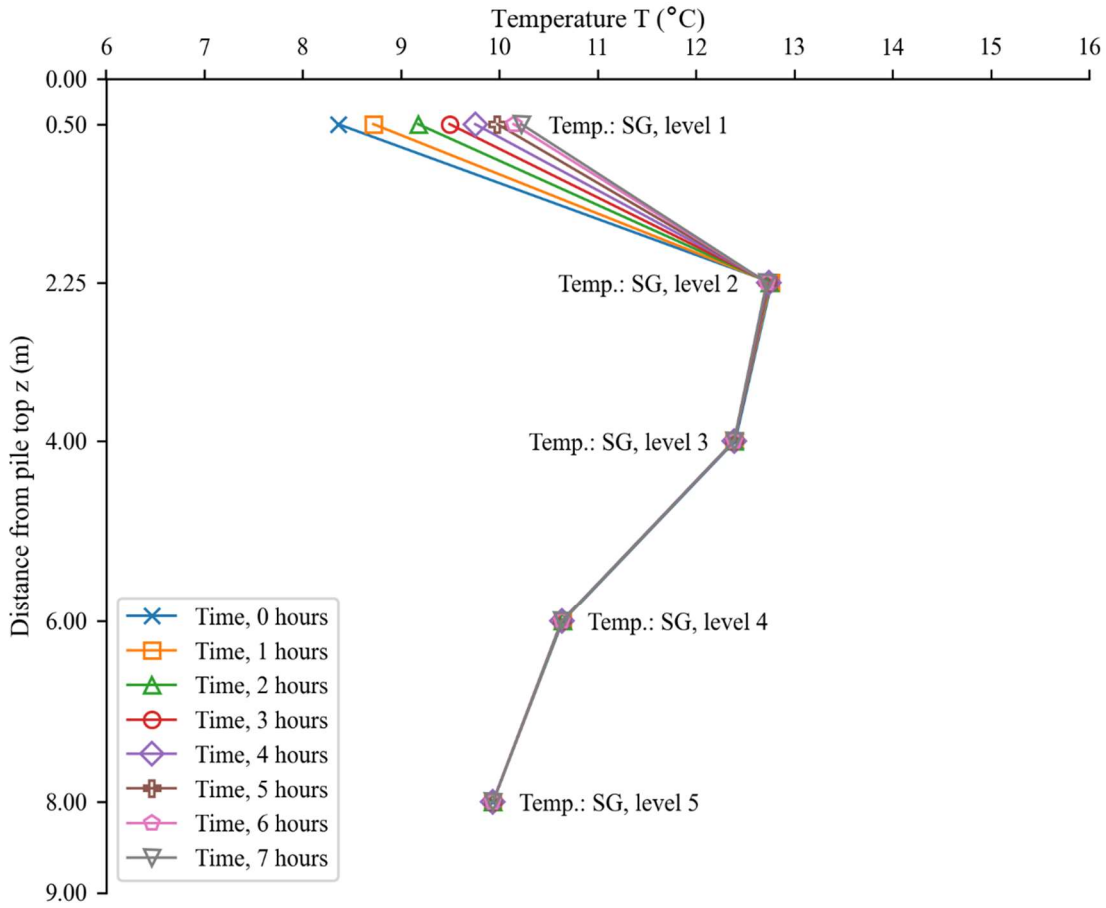

Figure 81: Temperature development along the length of test pile 7 during static pile loading test. The time indications are established as zero at the beginning of the static pile loading tests. Only the upper strain gauge level was affected by temperature changes during the static pile loading tests.

Test pile 8

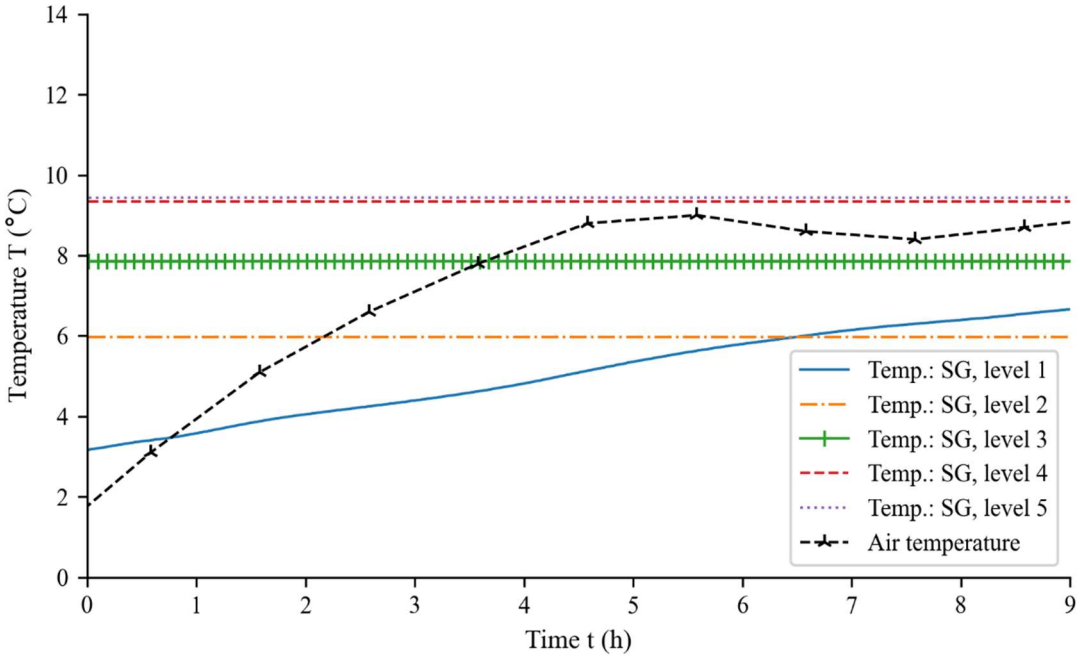

Figure 82: Temperatures at each strain gauge level for test pile 8 during static pile loading test. The air temperature in Randers (nearest measuring point) from DMI weather archive added.

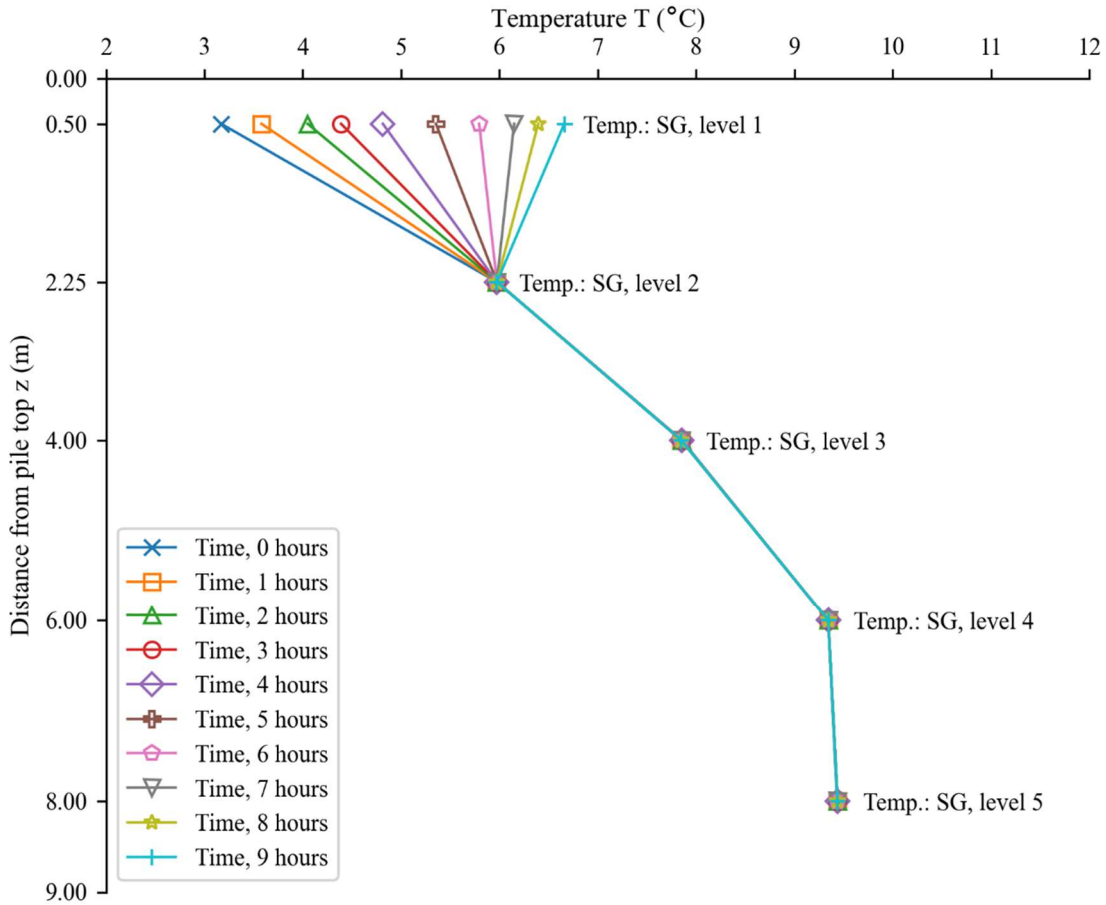

Figure 83: Temperature development along the length of test pile 8 during static pile loading test. The time indications are established as zero at the beginning of the static pile loading tests. Only the upper strain gauge level was affected by temperature changes during the static pile loading tests.

F.3 Temperature observations from strain free piles

Test pile 1

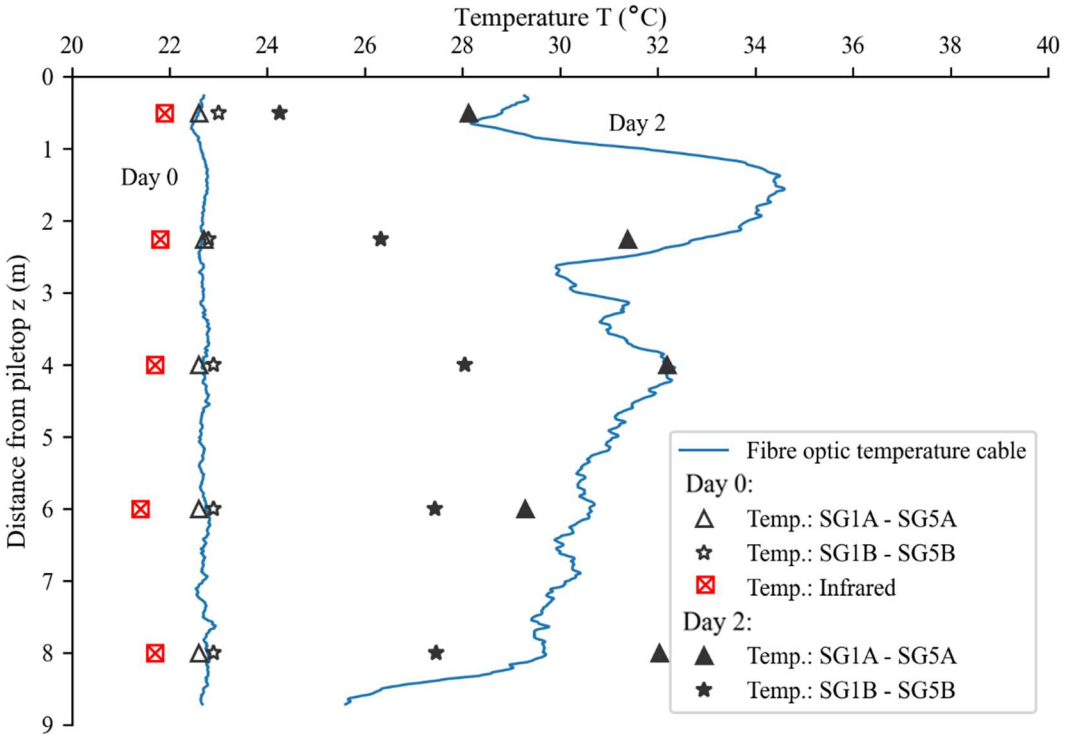

Figure 84: Temperature measurements collected along the reinforcement cage connected to test pile 1 for Day 0 and Day 2. Blue lines represent the fibre optic temperature cables (FOTC), and symbols represent the thermistors in the vibrating wire strain gauges (VWSG thermistor).

Test pile 2

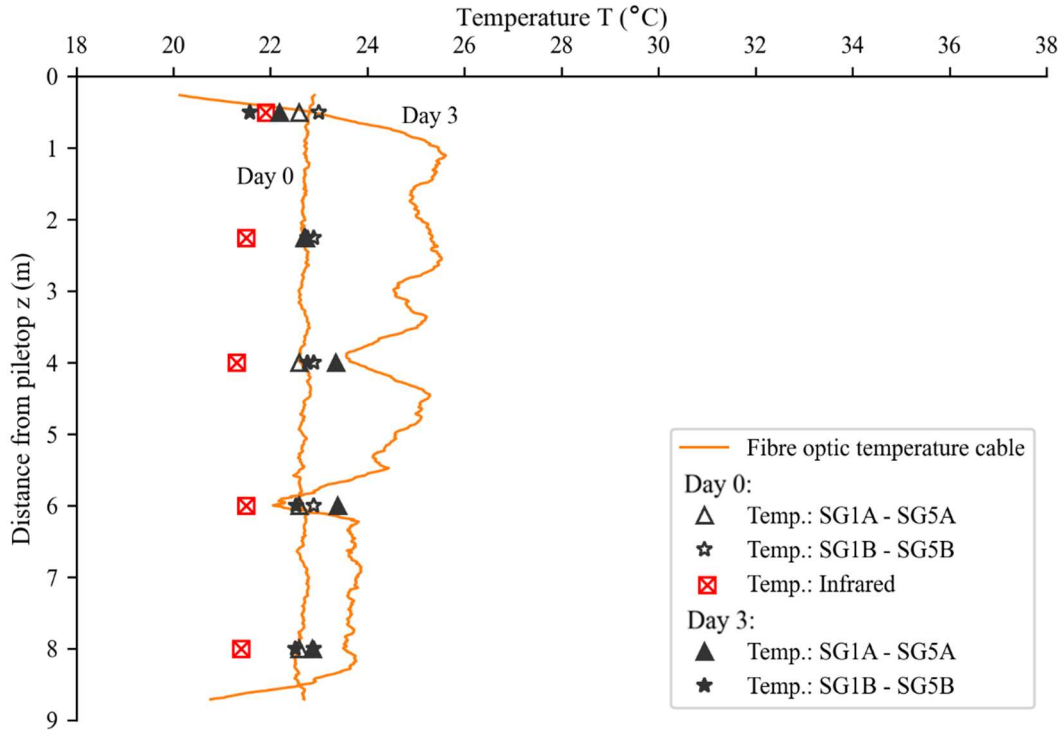

Figure 85: Temperature measurements collected along the reinforcement cage connected to test pile 2 for Day 0 and Day 3. Orange lines represent the fibre optic temperature cables (FOTC), and symbols represent the thermistors in the vibrating wire strain gauges (VWSG thermistor).

Test pile 3

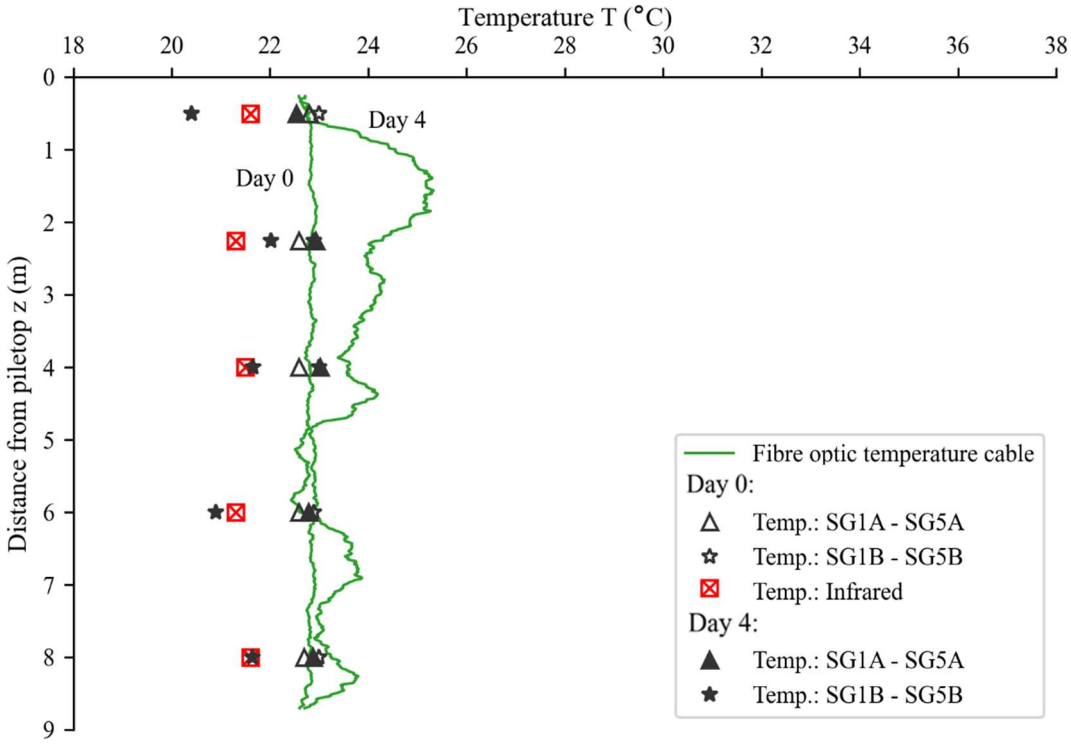

Figure 86: Temperature measurements collected along the reinforcement cage connected to test pile 3 for Day 0 and Day 4. Green lines represent the fibre optic temperature cables (FOTC), and symbols represent the thermistors in the vibrating wire strain gauges (VWSG thermistor).

Test pile 4

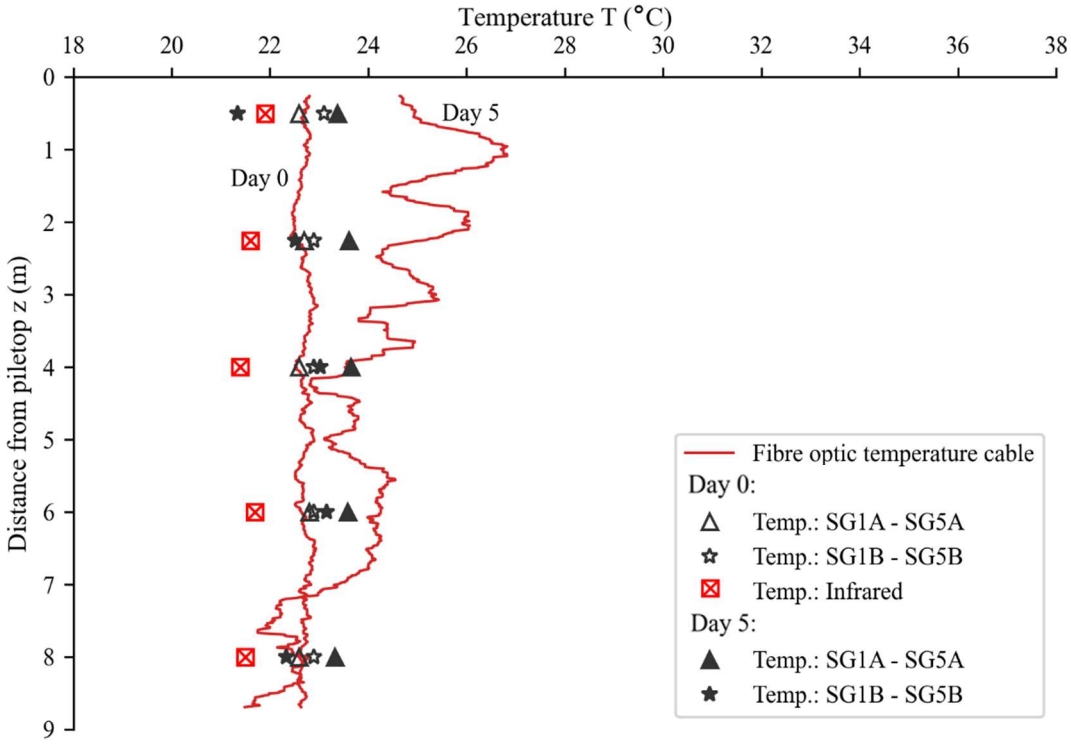

Figure 87: Temperature measurements collected along the reinforcement cage connected to test pile 4 for Day 0 and Day 5. Red lines represent the fibre optic temperature cables (FOTC), and symbols represent the thermistors in the vibrating wire strain gauges (VWSG thermistor).

Test pile 5

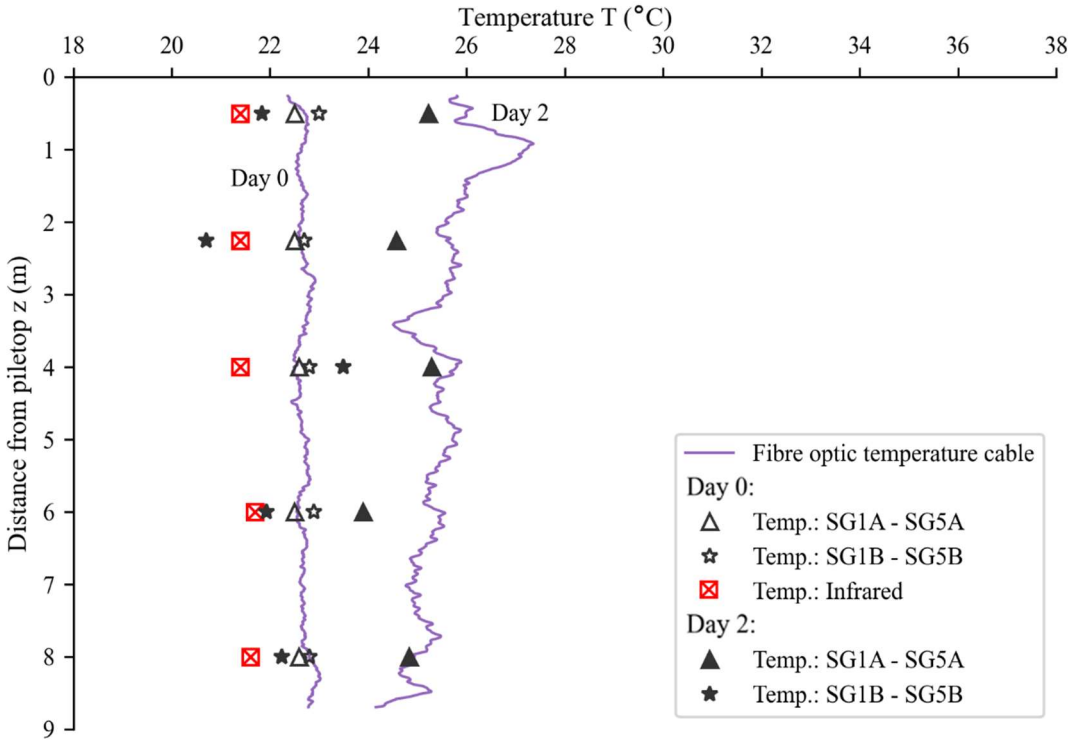

Figure 88: Temperature measurements collected along the reinforcement cage connected to test pile 5 for Day 0 and Day 2. Purple lines represent the fibre optic temperature cables (FOTC), and symbols represent the thermistors in the vibrating wire strain gauges (VWSG thermistor).

Test pile 6

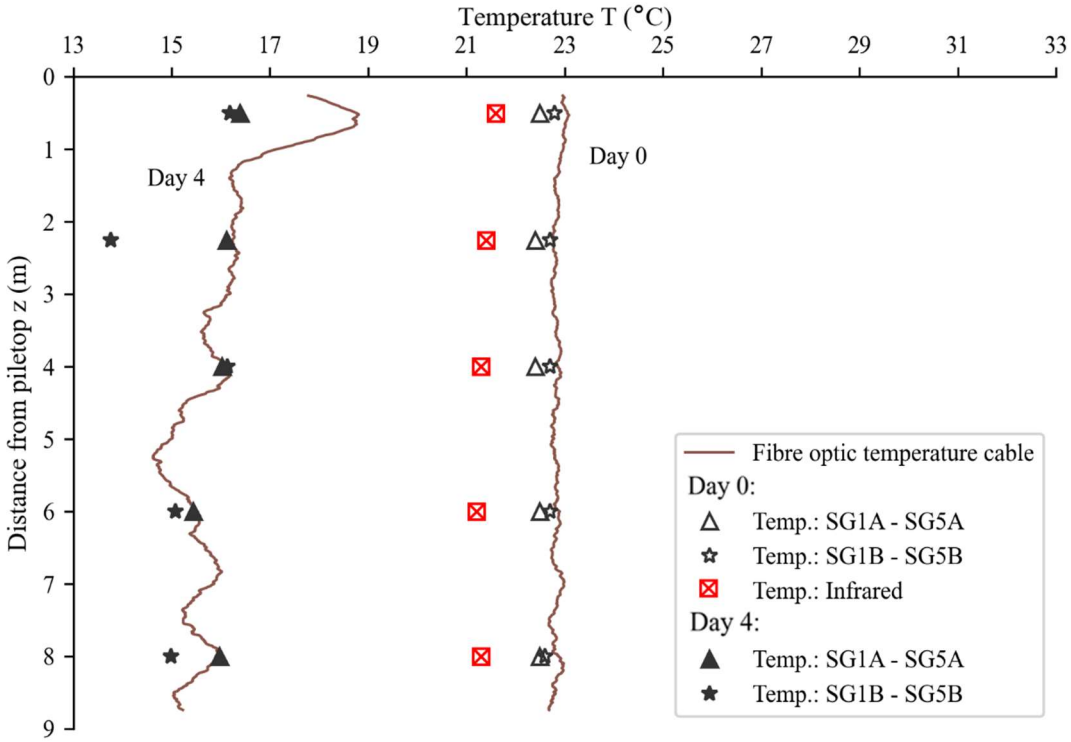

Figure 89: Temperature measurements collected along the reinforcement cage connected to test pile 6 for Day 0 and Day 4. Brown lines represent the fibre optic temperature cables (FOTC), and symbols represent the thermistors in the vibrating wire strain gauges (VWSG thermistor).

Test pile 7

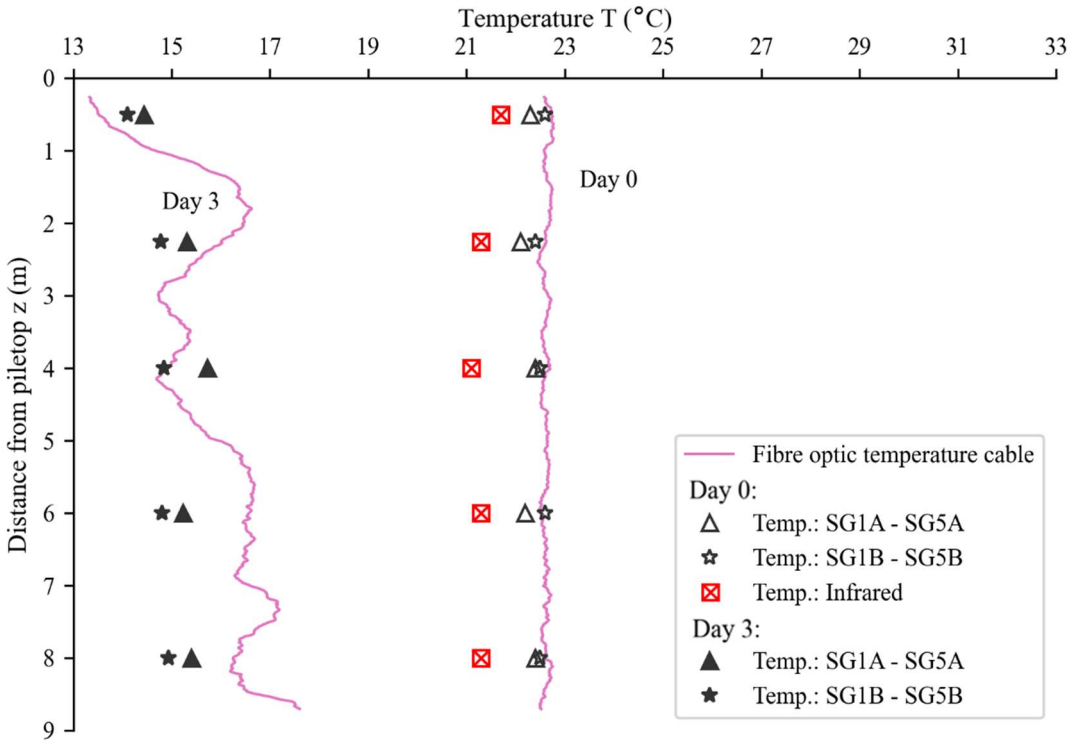

Figure 90: Temperature measurements collected along the reinforcement cage connected to test pile 7 for Day 0 and Day 3. Pink lines represent the fibre optic temperature cables (FOTC), and symbols represent the thermistors in the vibrating wire strain gauges (VWSG thermistor).

Test pile 8

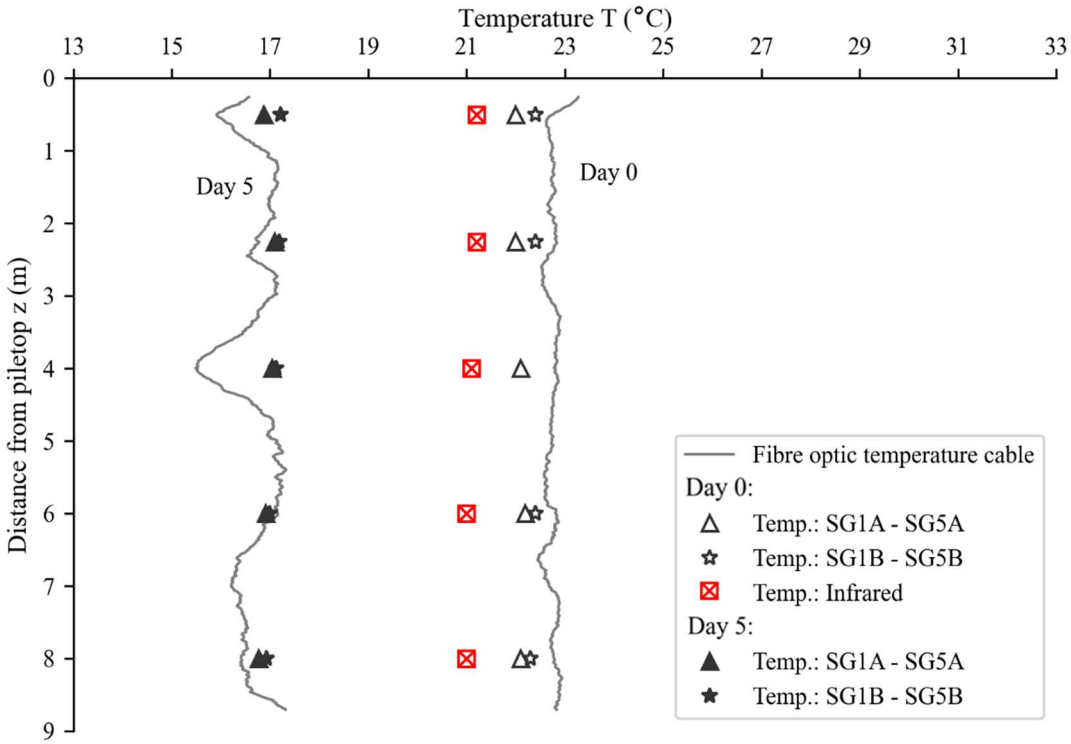

Figure 91: Temperature measurements collected along the reinforcement cage connected to test pile 8 for Day 0 and Day 5. Grey lines represent the fibre optic temperature cables (FOTC), and symbols represent the thermistors in the vibrating wire strain gauges (VWSG thermistor).

F.4 Temperature observations from piles influenced by strain

Test pile 1

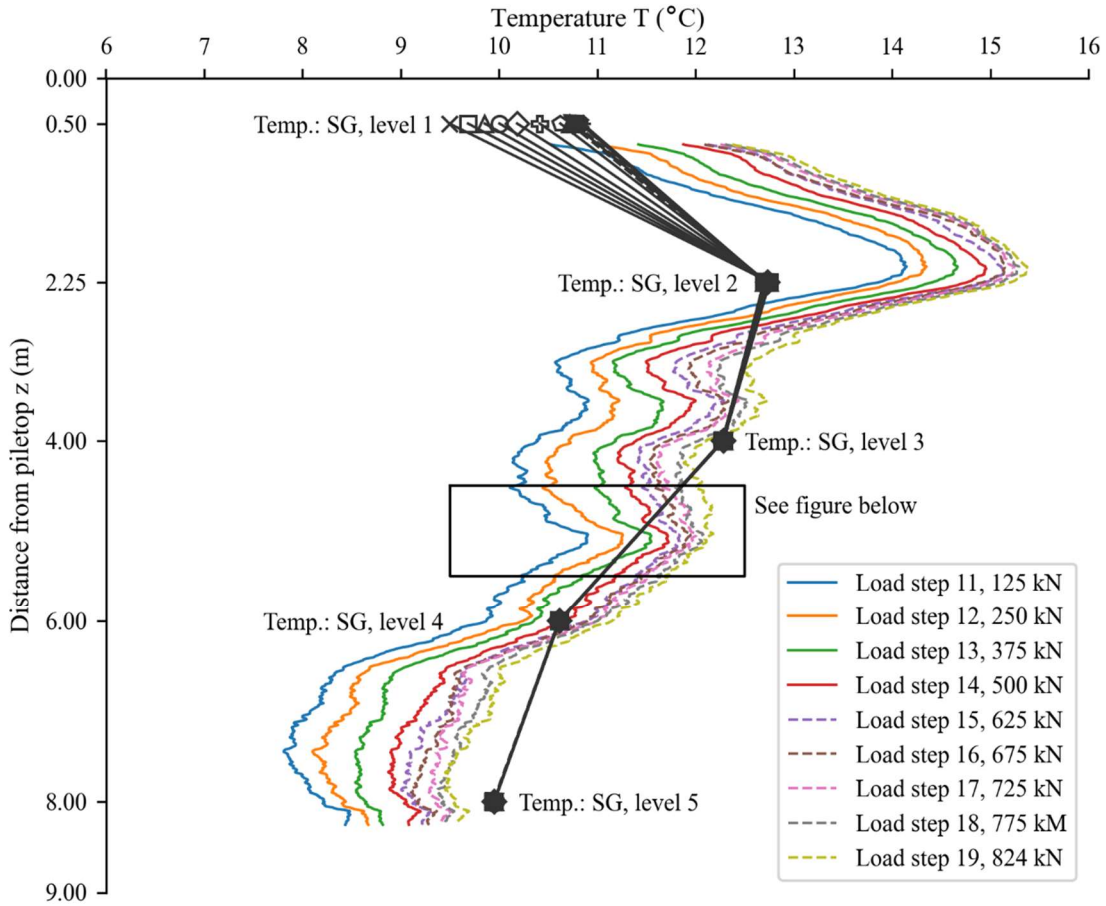

Figure 92: Temperature development along the length of test pile 1 at the inception of each load step during the static pile loading test, focusing on the data obtained from the fibre optic temperature cables (FOTC). Load phase 1 is not shown due to a faulty standoff cable that was replaced between 1st and 2nd load phase. Load phase 2 is shown with solid lines, smaller load steps in phase 2 is shown with dotted lines. Additionally, the temperature development recorded by the thermistors in the vibrating wire strain gauges (VWSG thermistors) is represented by the black lines.

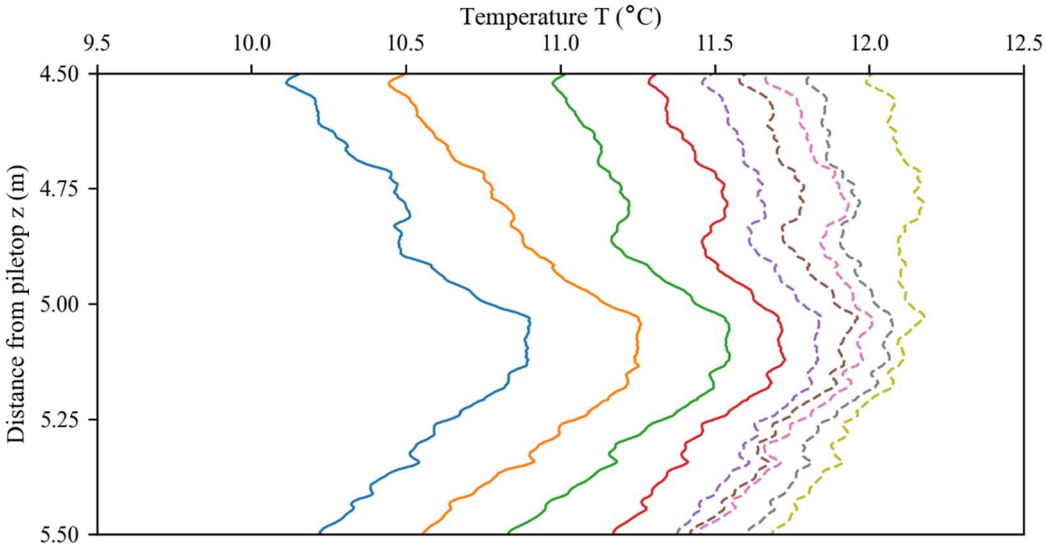

Figure 93: Zoom of temperature development along the length of test pile 1 from fibre optic cables. The temperature rises with increasing load in load phase 2 (load step 11-19) and thus, indicating the temperature measurements are affected by mechanical strain in the test pile.

Test pile 2

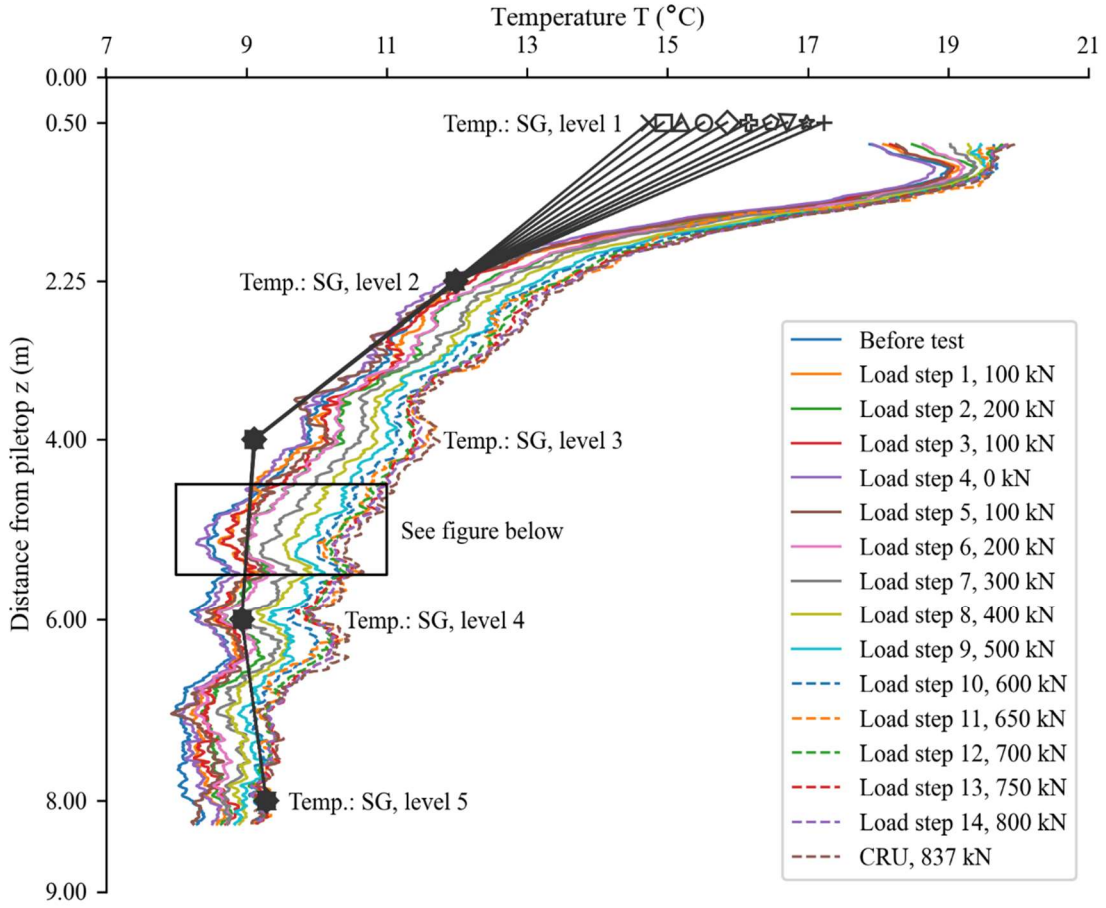

Figure 94: Temperature development along the length of test pile 2 at the inception of each load step during the static pile loading test, focusing on the data obtained from the fibre optic temperature cables (FOTC). Load phase 1 and 2 is shown with solid lines, smaller load steps in phase 2 is shown with dotted lines. Additionally, the temperature development recorded by the thermistors in the vibrating wire strain gauges (VWSG thermistors) is represented by the black lines.

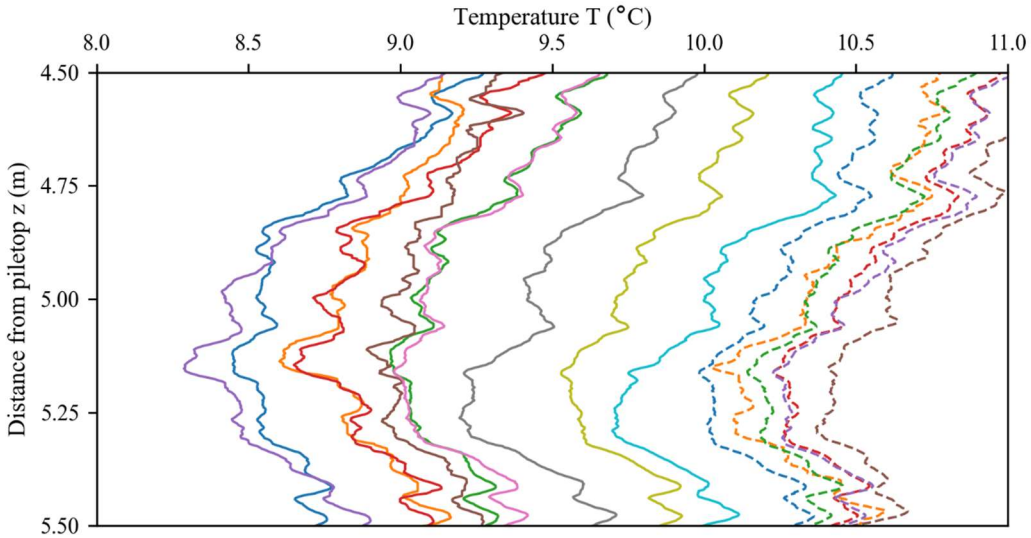

Figure 95: Zoom of temperature development along the length of test pile 2 from fibre optic cables. The temperature rises with increasing load in load phase 1 (load step 0-2), falls with decreasing load during unloading of load phase 1 (load step 2-4) and rises with increasing load in load phase 2 (load step 4-14 and CRU) and thus, indicating the temperature measurements are affected by mechanical strain in the test pile.

Test pile 3

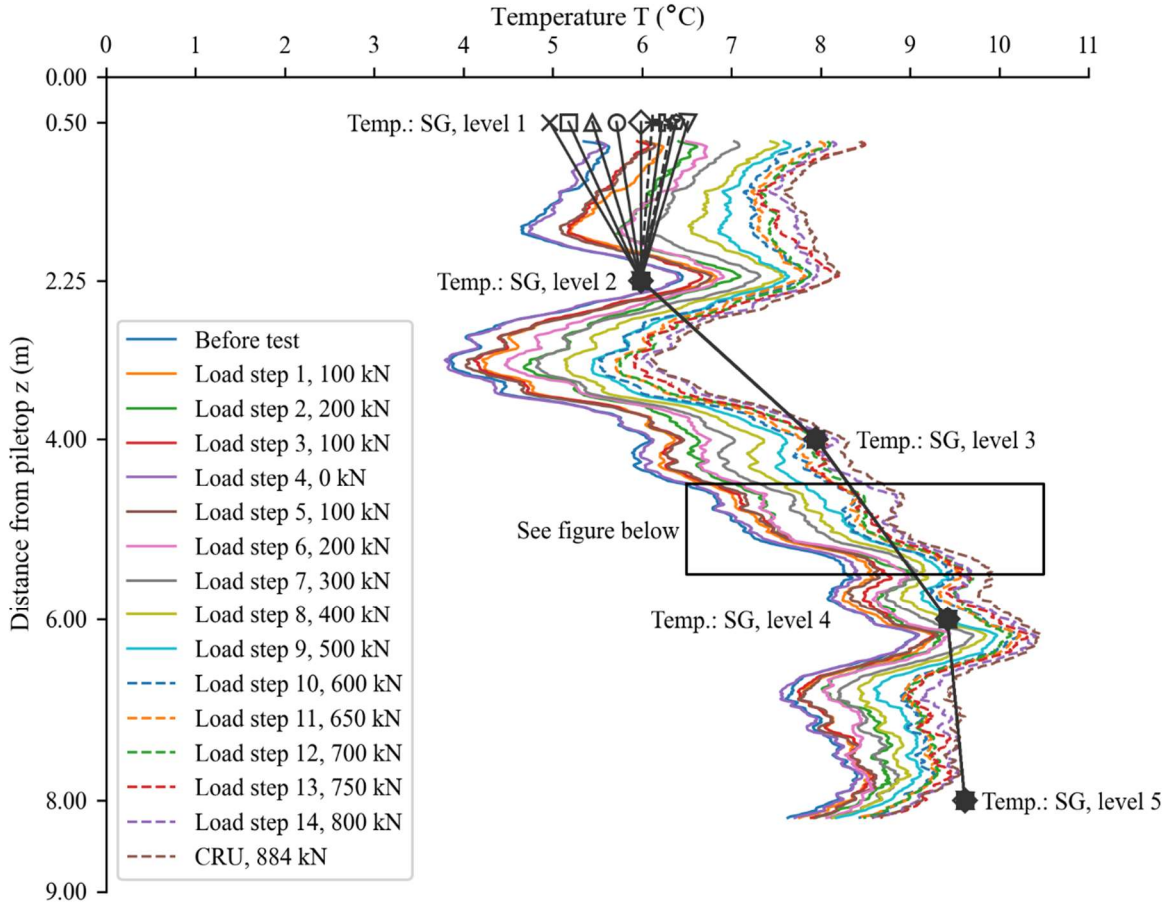

Figure 96: Temperature development along the length of test pile 3 at the inception of each load step during the static pile loading test, focusing on the data obtained from the fibre optic temperature cables (FOTC). Load phase 1 and 2 is shown with solid lines, smaller load steps in phase 2 is shown with dotted lines. Additionally, the temperature development recorded by the thermistors in the vibrating wire strain gauges (VWSG thermistors) is represented by the black lines.

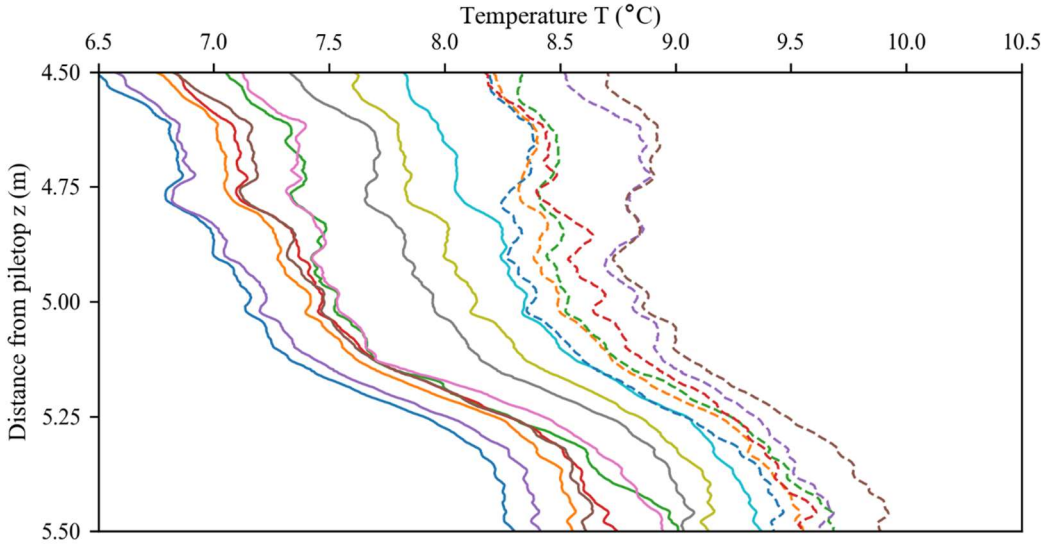

Figure 97: Zoom of temperature development along the length of test pile 3 from fibre optic cables. The temperature rises with increasing load in load phase 1 (load step 0-2), falls with decreasing load during unloading of load phase 1 (load step 2-4) and rises with increasing load in load phase 2 (load step 4-14 and CRU) and thus, indicating the temperature measurements are affected by mechanical strain in the test pile.

Test pile 4

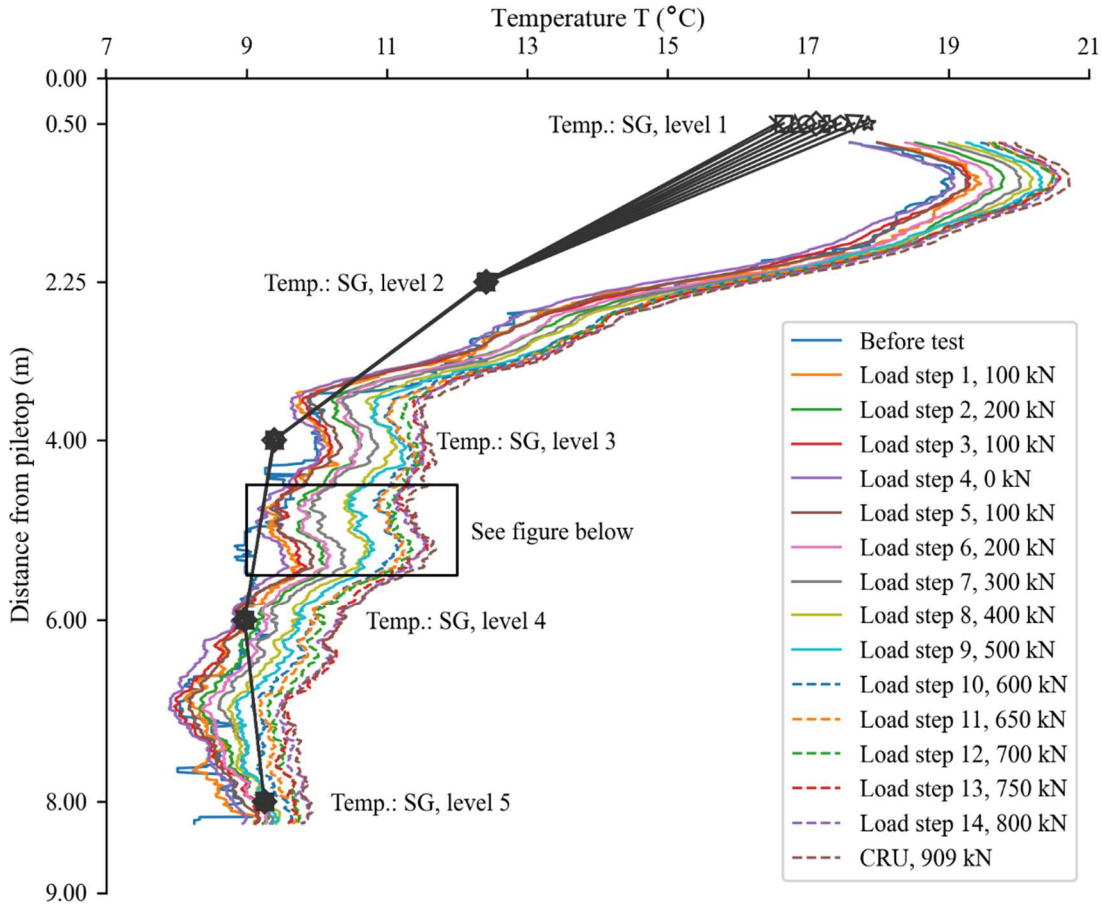

Figure 98: Temperature development along the length of test pile 4 at the inception of each load step during the static pile loading test, focusing on the data obtained from the fibre optic temperature cables (FOTC). Load phase 1 and 2 is shown with solid lines, smaller load steps in phase 2 is shown with dotted lines. Temperature data from "before test" is affected by unexpected jumps due to a high number of NAN points. Additionally, the temperature development recorded by the thermistors in the vibrating wire strain gauges (VWSG thermistors) is represented by the black lines.

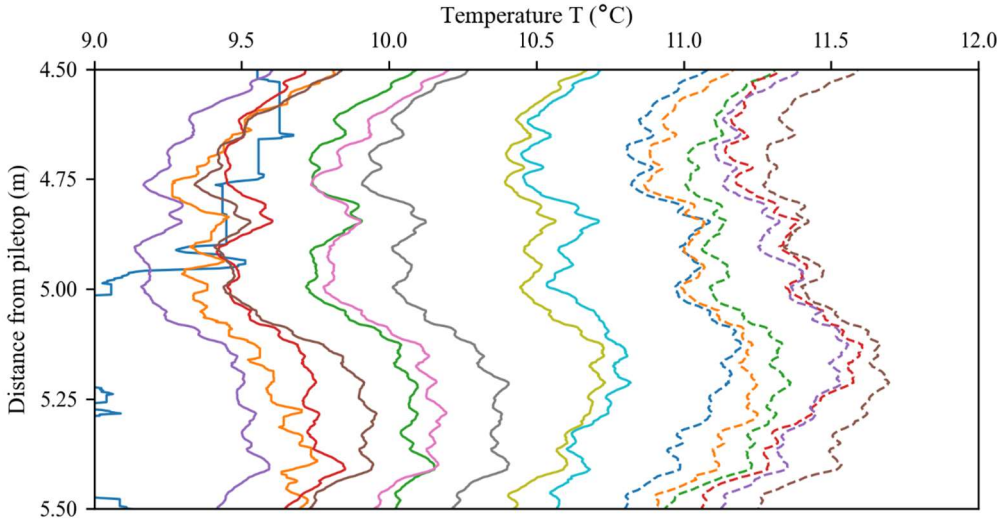

Figure 99: Zoom of temperature development along the length of test pile 4 from fibre optic cables. The temperature rises with increasing load in load phase 1 (load step 0-2), falls with decreasing load during unloading of load phase 1 (load step 2-4) and rises with increasing load in load phase 2 (load step 4-14 and CRU) and thus, indicating the temperature measurements are affected by mechanical strain in the test pile.

Test pile 5

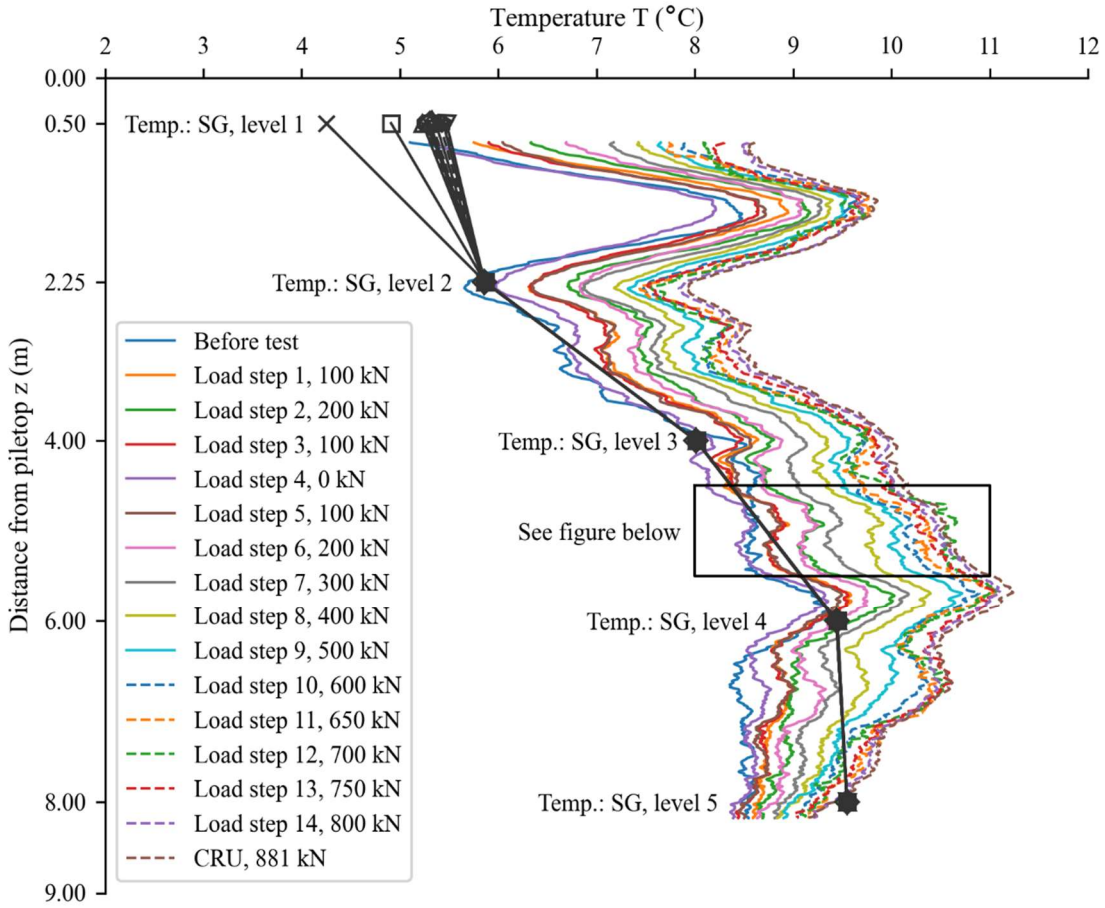

Figure 100: Temperature development along the length of test pile 5 at the inception of each load step during the static pile loading test, focusing on the data obtained from the fibre optic temperature cables (FOTC). Load phase 1 and 2 is shown with solid lines, smaller load steps in phase 2 is shown with dotted lines. Additionally, the temperature development recorded by the thermistors in the vibrating wire strain gauges (VWSG thermistors) is represented by the black lines.

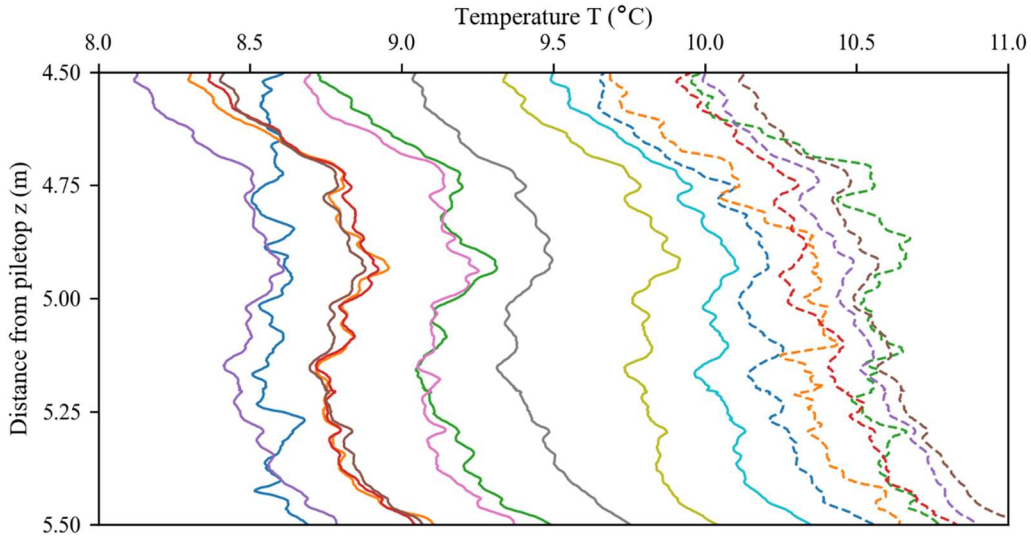

Figure 101: Zoom of temperature development along the length of test pile 5 from fibre optic cables. The temperature rises with increasing load in load phase 1 (load step 0-2), falls with decreasing load during unloading of load phase 1 (load step 2-4) and rises with increasing load in load phase 2 (load step 4-14 and CRU) and thus, indicating the temperature measurements are affected by mechanical strain in the test pile.

Test pile 6

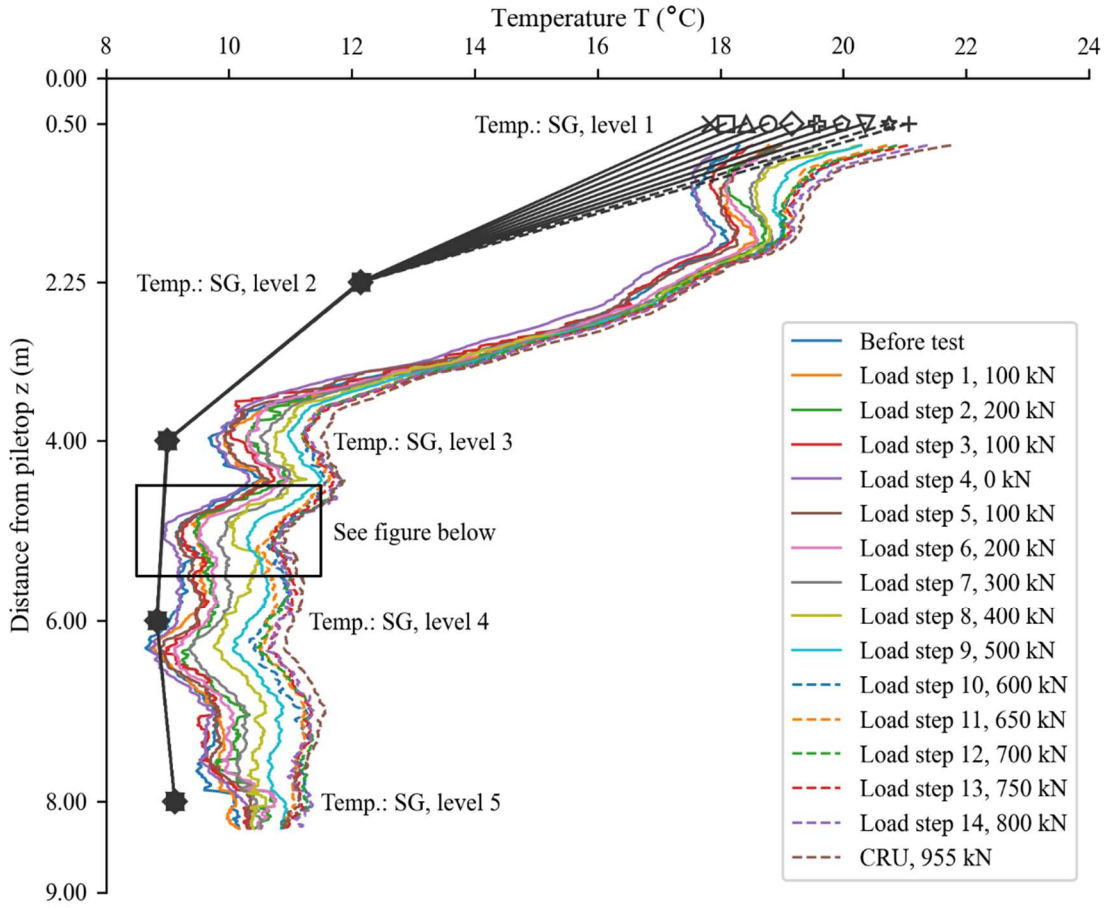

Figure 102: Temperature development along the length of test pile 6 at the inception of each load step during the static pile loading test, focusing on the data obtained from the fibre optic temperature cables (FOTC). Load phase 1 and 2 is shown with solid lines, smaller load steps in phase 2 is shown with dotted lines. Additionally, the temperature development recorded by the thermistors in the vibrating wire strain gauges (VWSG thermistors) is represented by the black lines.

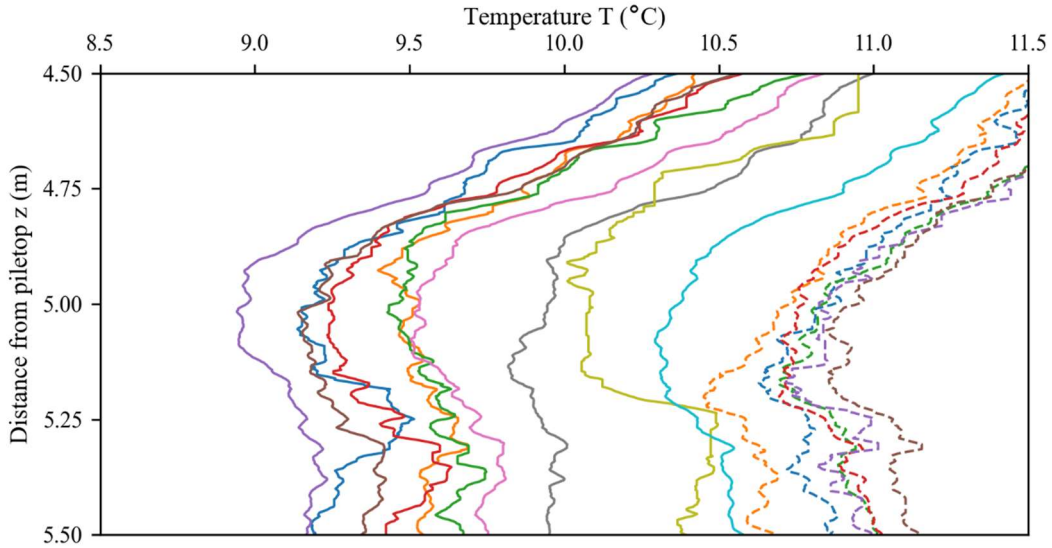

Figure 103: Zoom of temperature development along the length of test pile 6 from fibre optic cables. The temperature rises with increasing load in load phase 1 (load step 0-2), falls with decreasing load during unloading of load phase 1 (load step 2-4) and rises with increasing load in load phase 2 (load step 4-14 and CRU) and thus, indicating the temperature measurements are affected by mechanical strain in the test pile.

Test pile 7

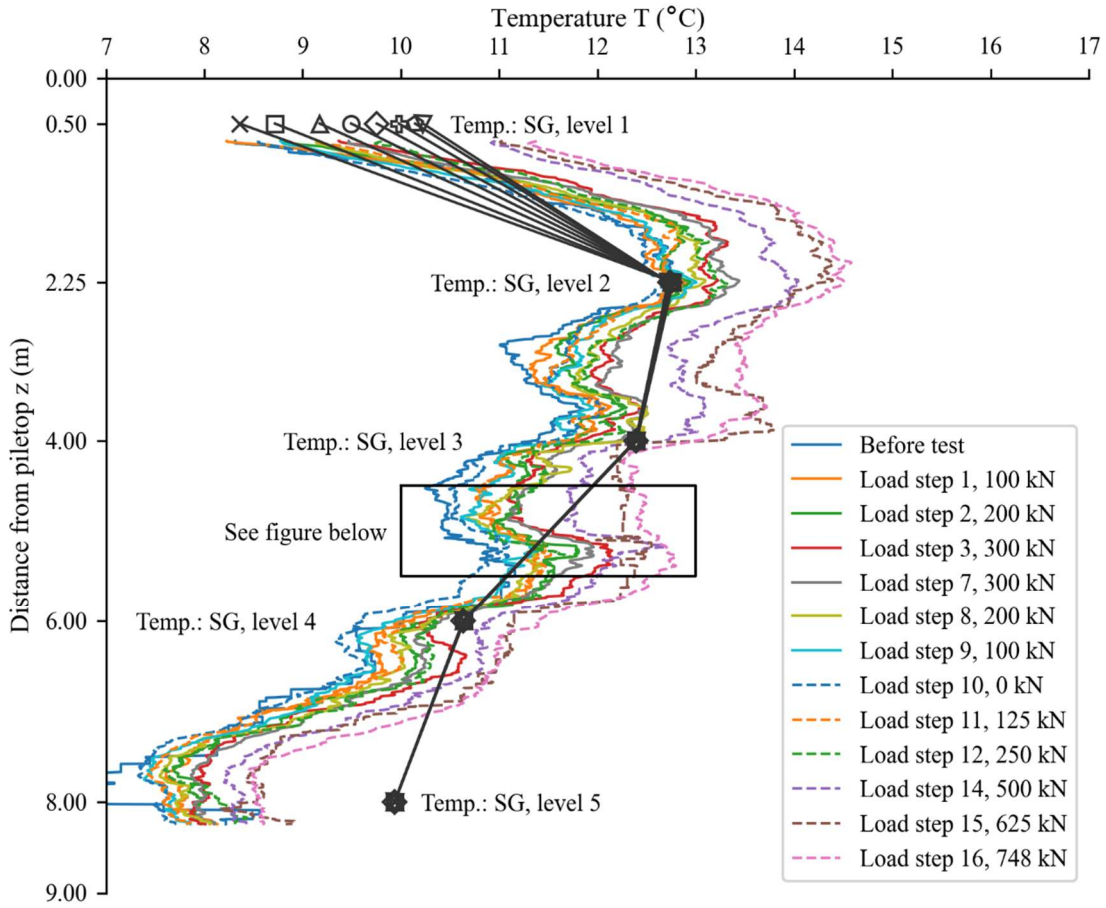

Figure 104: Temperature development along the length of test pile 7 at the inception of each load step during the static pile loading test, focusing on the data obtained from the fibre optic temperature cables (FOTC). Load phase 1 and 2 is shown with solid lines, smaller load steps in phase 2 is shown with dotted lines. Temperature data from load step 4, 5, 6 and 13 is excluded due to an extremely high number of NAN data points. Additionally, the temperature development recorded by the thermistors in the vibrating wire strain gauges (VWSG thermistors) is represented by the black lines

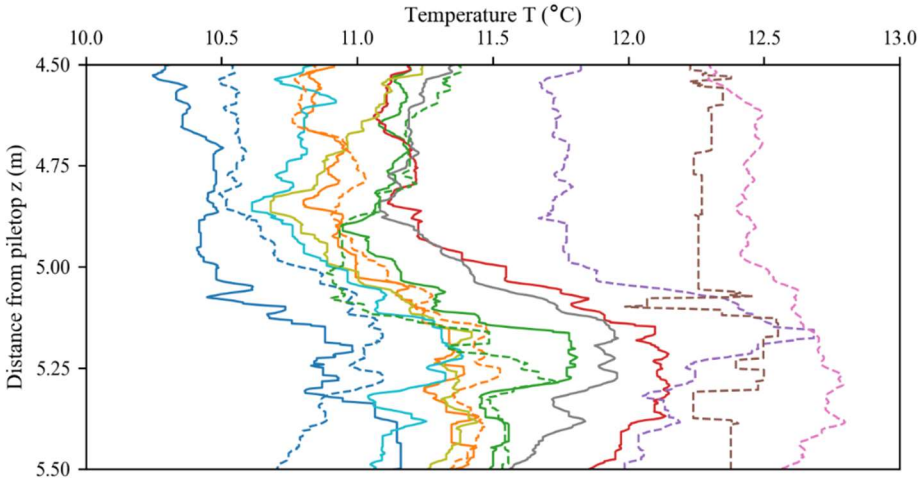

Figure 105: Zoom of temperature development along the length of test pile 7 from fibre optic cables. The temperature rises with increasing load in load phase 1 (load step 0-5), falls with decreasing load during unloading of load phase 1 (load step 5-10) and rises with increasing load in load phase 2 (load step 10-16) and thus, indicating the temperature measurements are affected by mechanical strain in the test pile. Temperature data is generally affected by unexpected jumps due to a high number of NAN data points.

Test pile 8

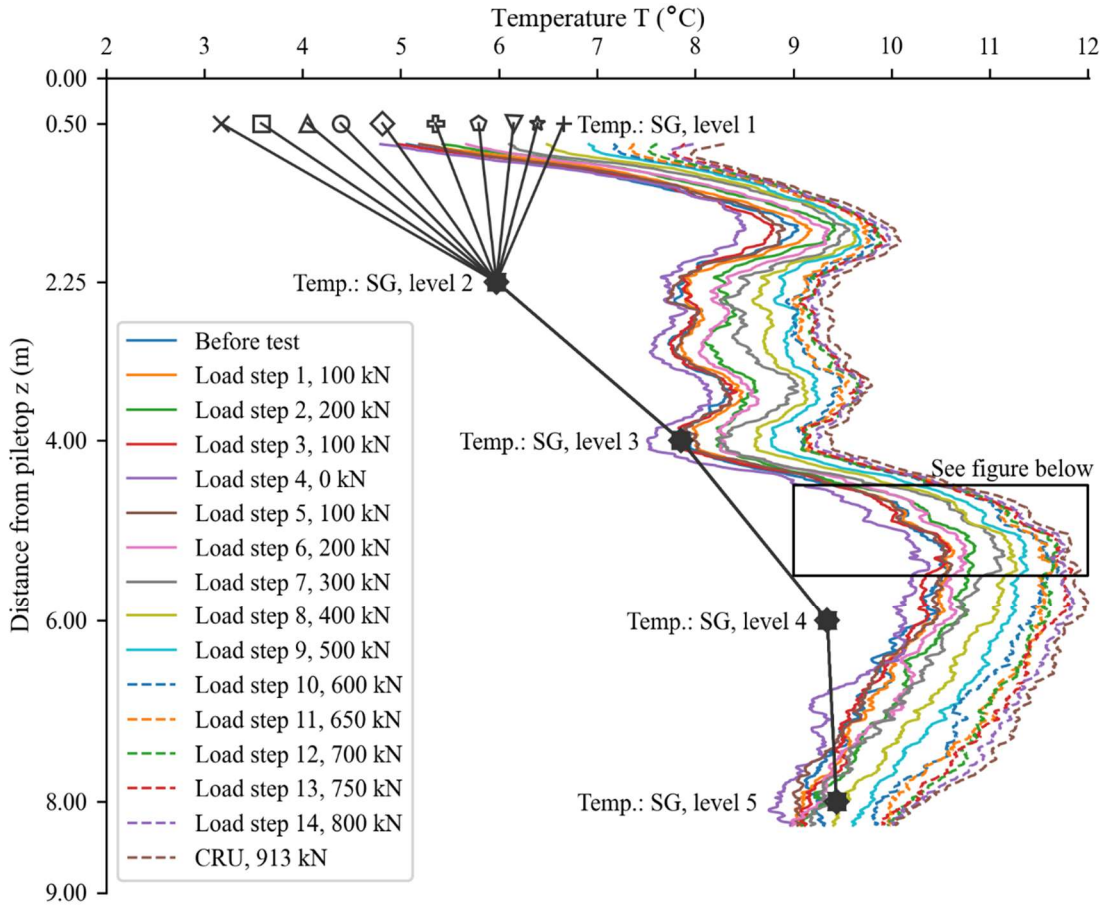

Figure 106: Temperature development along the length of test pile 8 at the inception of each load step during the static pile loading test, focusing on the data obtained from the fibre optic temperature cables (FOTC). Load phase 1 and 2 is shown with solid lines, smaller load steps in phase 2 is shown with dotted lines. Additionally, the temperature development recorded by the thermistors in the vibrating wire strain gauges (VWSG thermistors) is represented by the black lines.

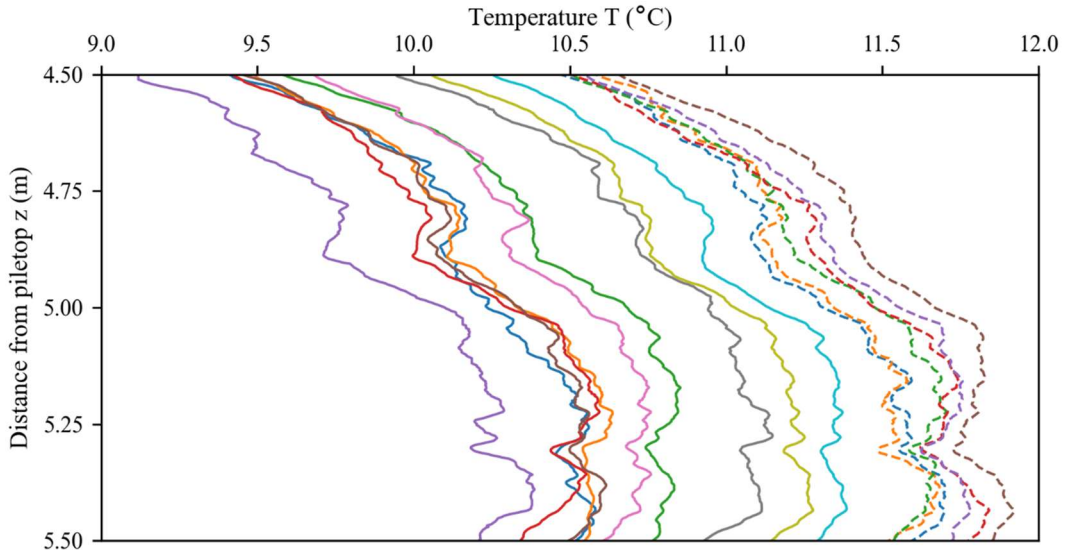

Figure 107: Zoom of temperature development along the length of test pile 8 from fibre optic cables. The temperature rises with increasing load in load phase 1 (load step 0-2), falls with decreasing load during unloading of load phase 1 (load step 2-4) and rises with increasing load in load phase 2 (load step 4-14 and CRU) and thus, indicating the temperature measurements are affected by mechanical strain in the test pile.

F.5 Temperature variation over cross-sectional area

Test pile 1

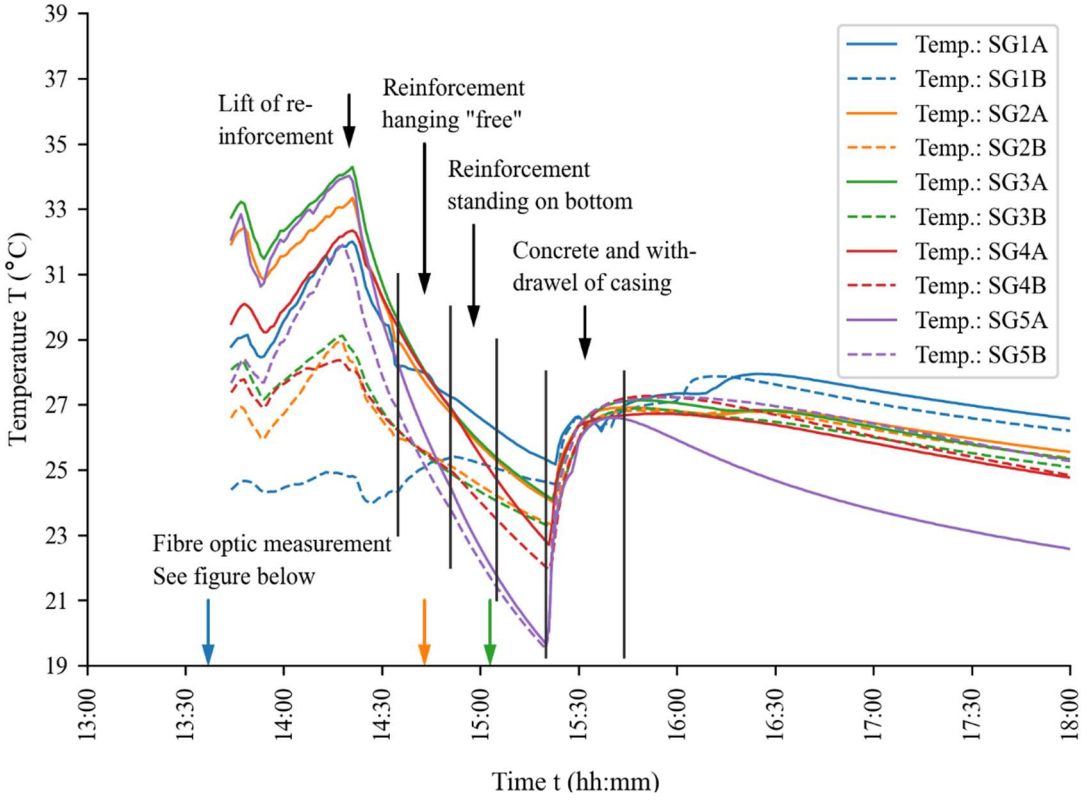

Figure 108: Temperatures recorded by the thermistors in the vibrating wire strain gauges (VWSG thermistors) during the installation of the reinforcement cage in the borehole for test pile 1 on the 20th of August 2019.

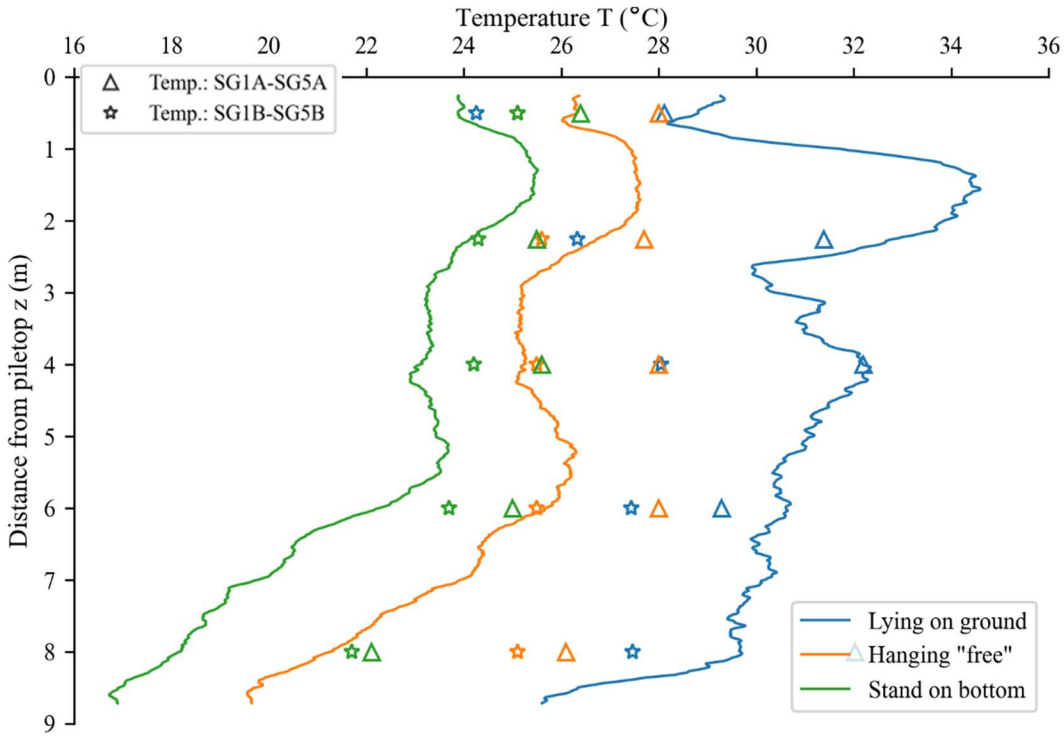

Figure 109: Measurements of temperatures for test pile 1 on the 20th of August 2019. Solid lines (blue, orange and green) represent the fibre optic temperature cable (FOTC), and symbols represent the thermistors in the vibrating wire strain gauges (VWSG thermistor).

Test pile 2

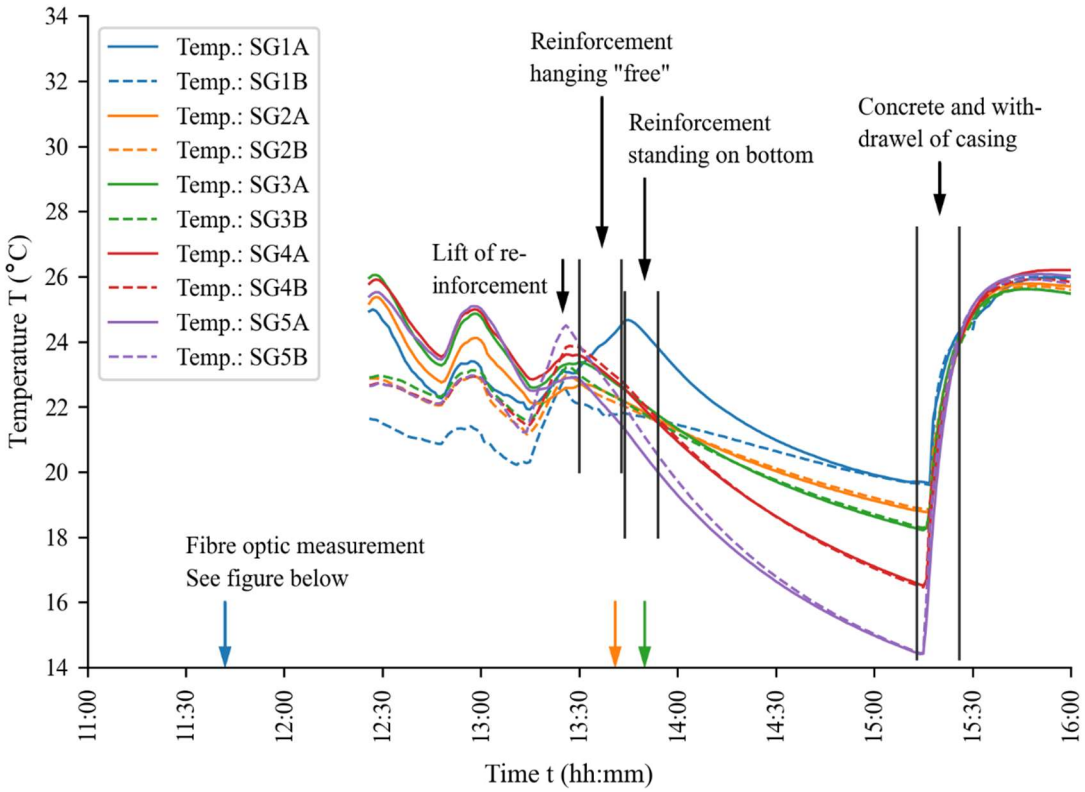

Figure 110: Temperatures recorded by the thermistors in the vibrating wire strain gauges (VWSG thermistors) during the installation of the reinforcement cage in the borehole for test pile 2 on the 21st of August 2019.

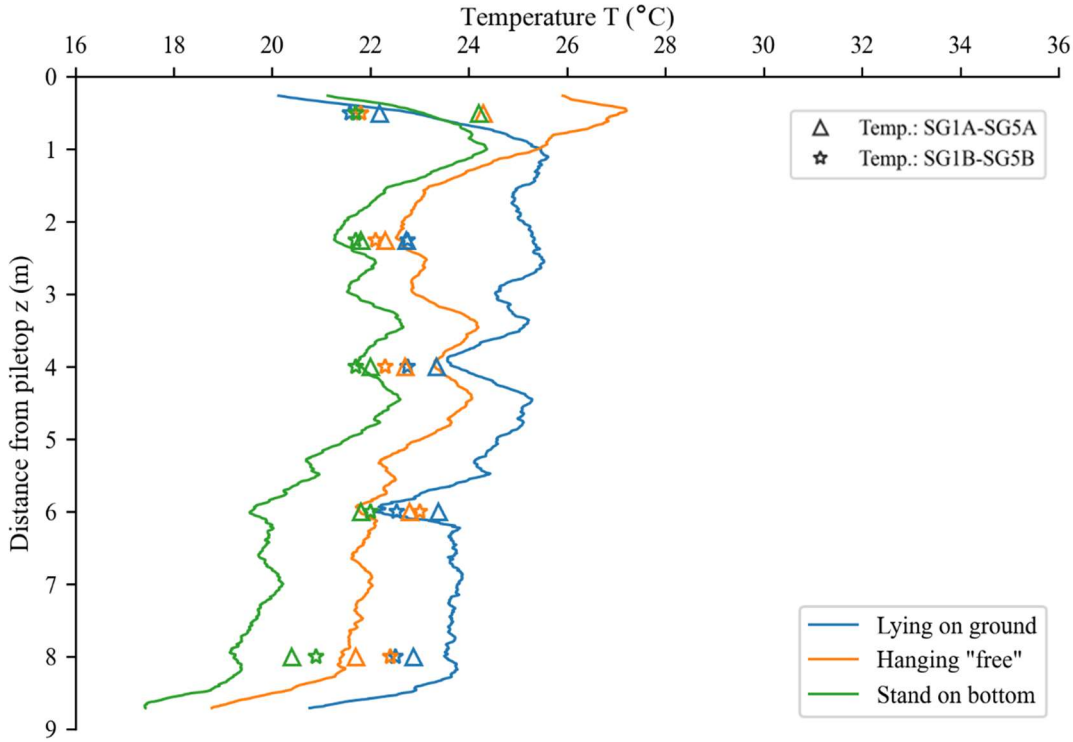

Figure 111: Measurements of temperatures for test pile 2 on the 21st of August 2019. Solid lines (blue, orange and green) represent the fibre optic temperature cable (FOTC), and symbols represent the thermistors in the vibrating wire strain gauges (VWSG thermistor).

Test pile 3

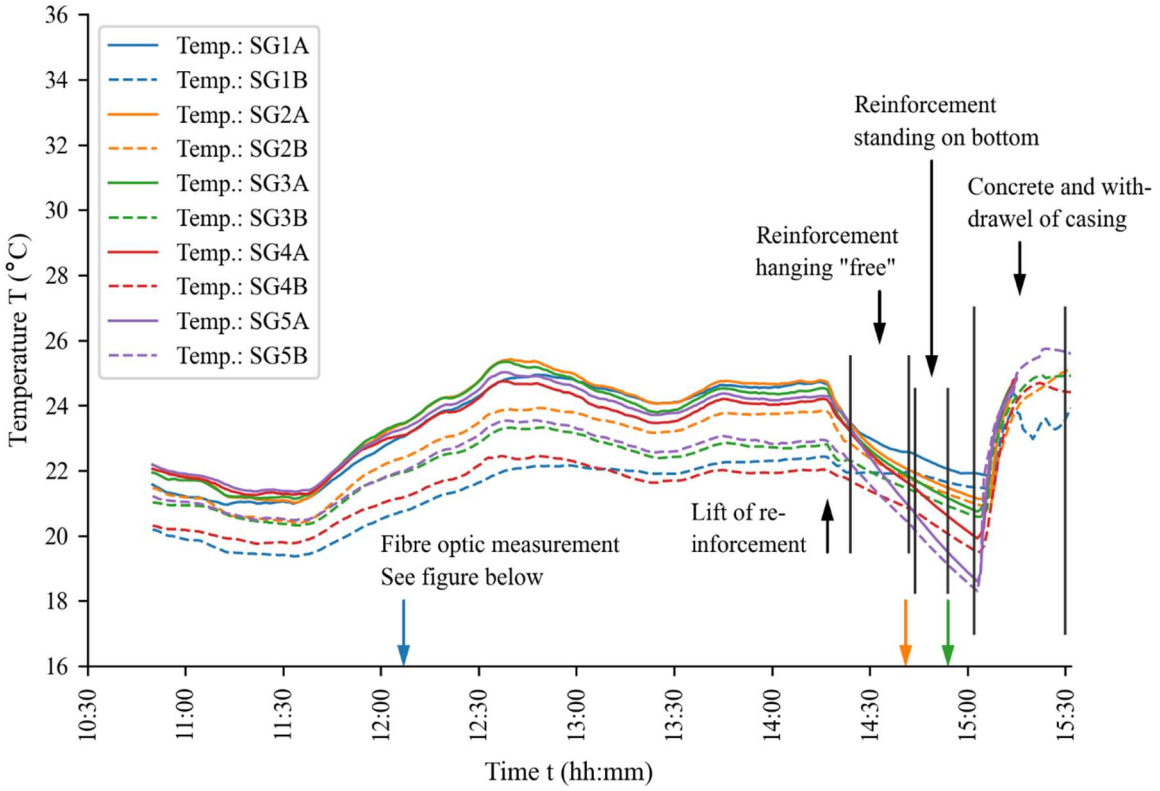

Figure 112: Temperatures recorded by the thermistors in the vibrating wire strain gauges (VWSG thermistors) during the installation of the reinforcement cage in the borehole for test pile 3 on the 22nd of August 2019.

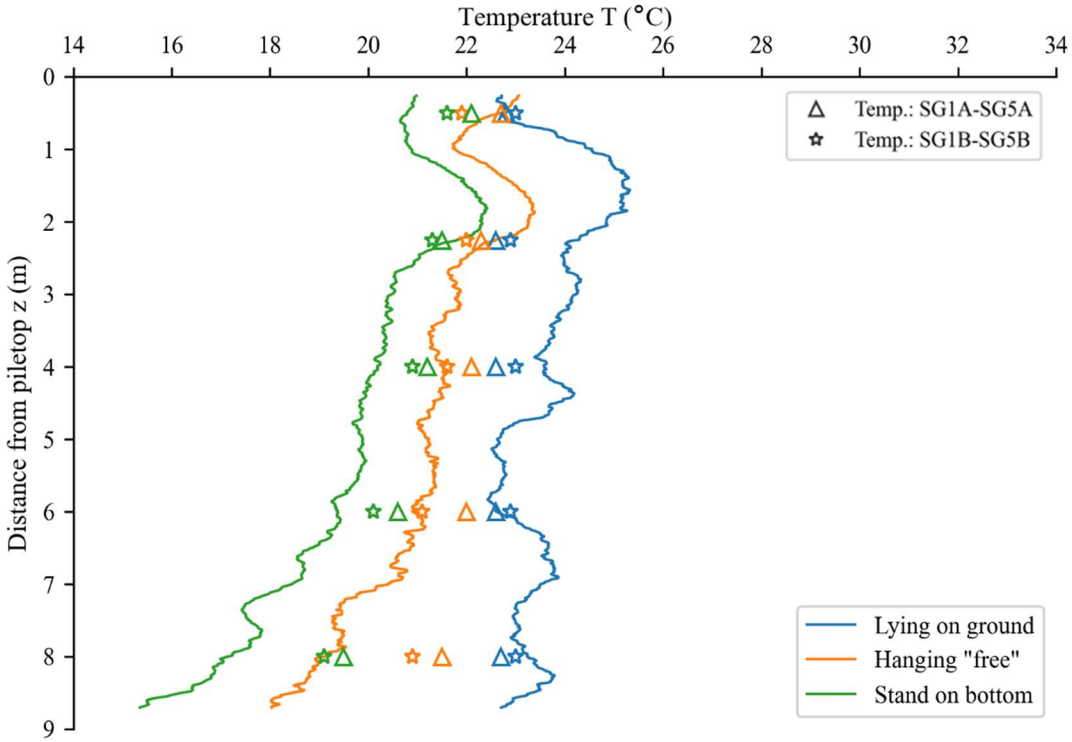

Figure 113: Measurements of temperatures for test pile 3 on the 22nd of August 2019. Solid lines (blue, orange and green) represent the fibre optic temperature cable (FOTC), and symbols represent the thermistors in the vibrating wire strain gauges (VWSG thermistor).

Test pile 4

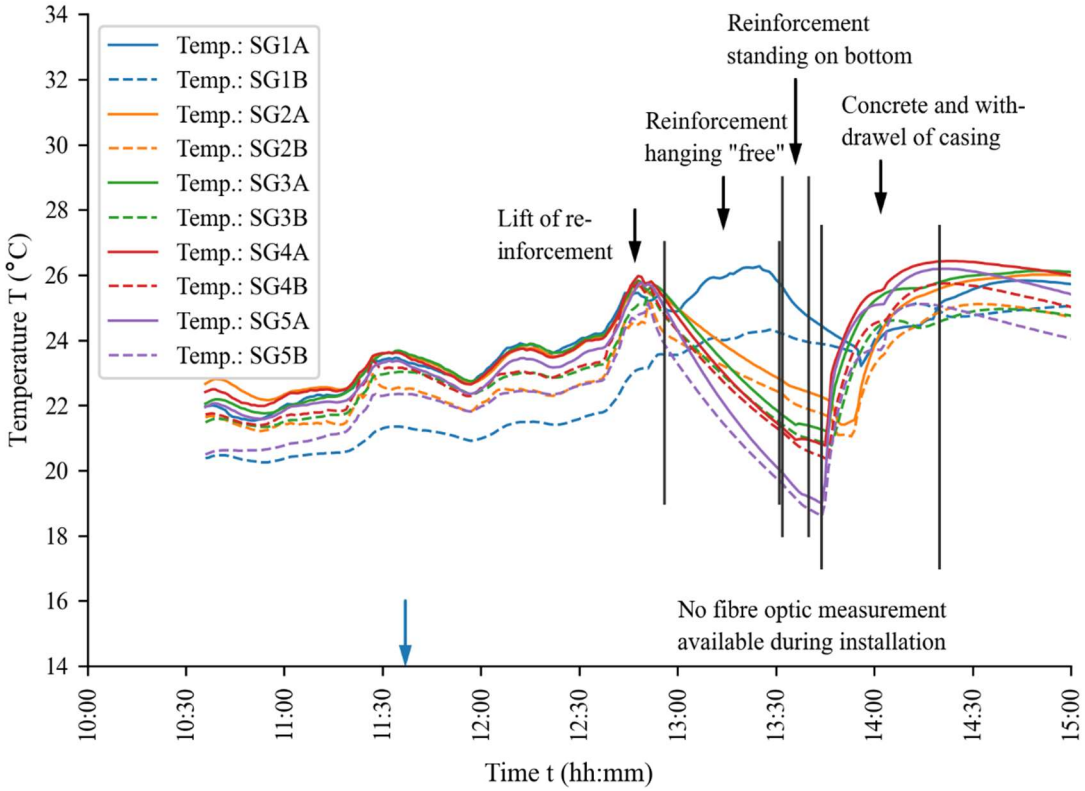

Figure 114: Temperatures recorded by the thermistors in the vibrating wire strain gauges (VWSG thermistors) during the installation of the reinforcement cage in the borehole for for test pile 4 on the 23rd of August 2019.

Test pile 5

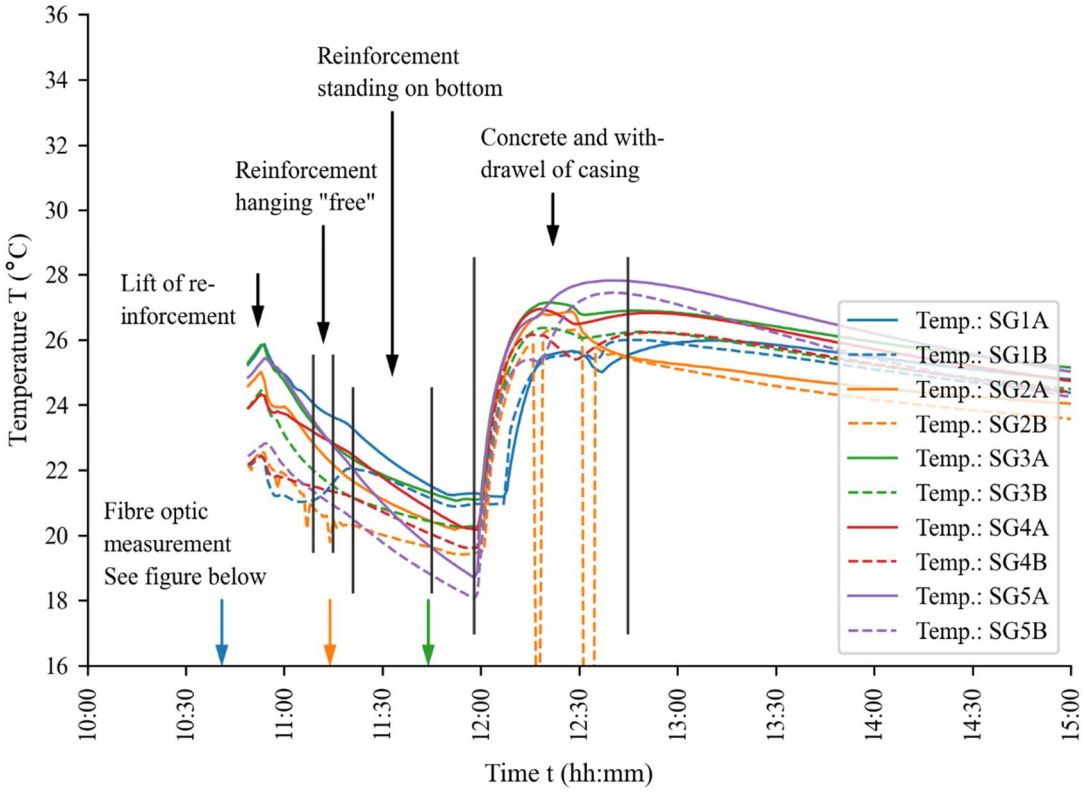

Figure 115: Temperatures recorded by the thermistors in the vibrating wire strain gauges (VWSG thermistors) during the installation of the reinforcement cage in the borehole for test pile 5 on the 20th of August 2019.

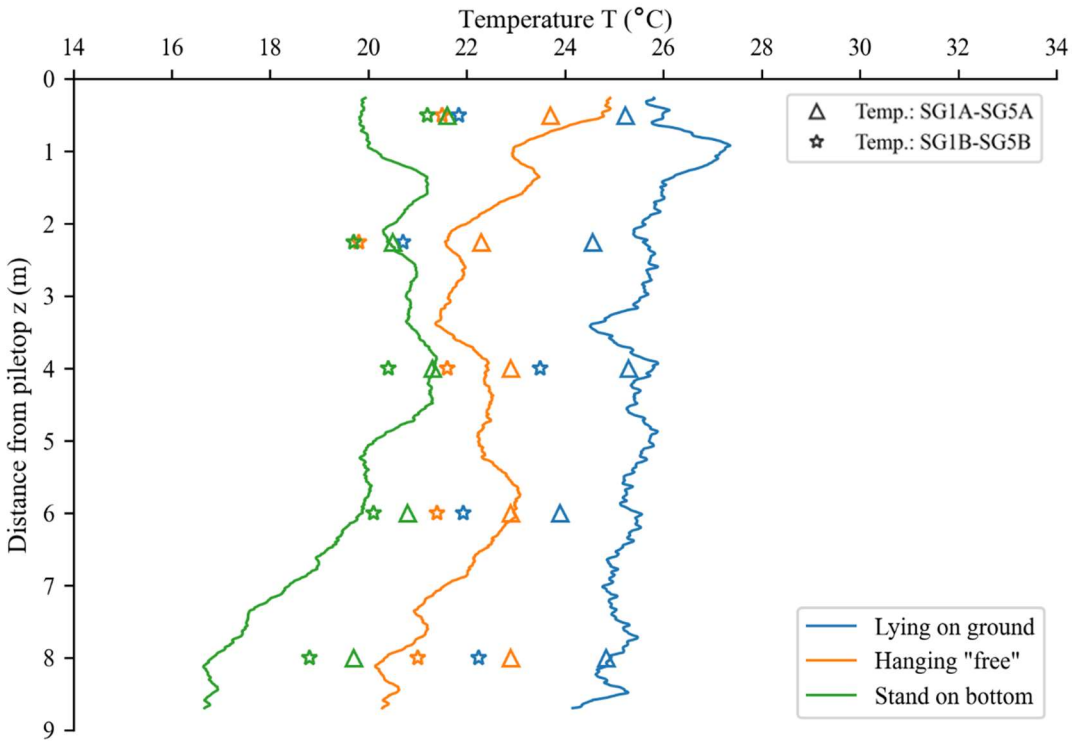

Figure 116: Measurements of temperatures for test pile 5 on the 20th of August 2019. Solid lines (blue, orange and green) represent the fibre optic temperature cable (FOTC), and symbols represent the thermistors in the vibrating wire strain gauges (VWSG thermistor).

Test pile 6

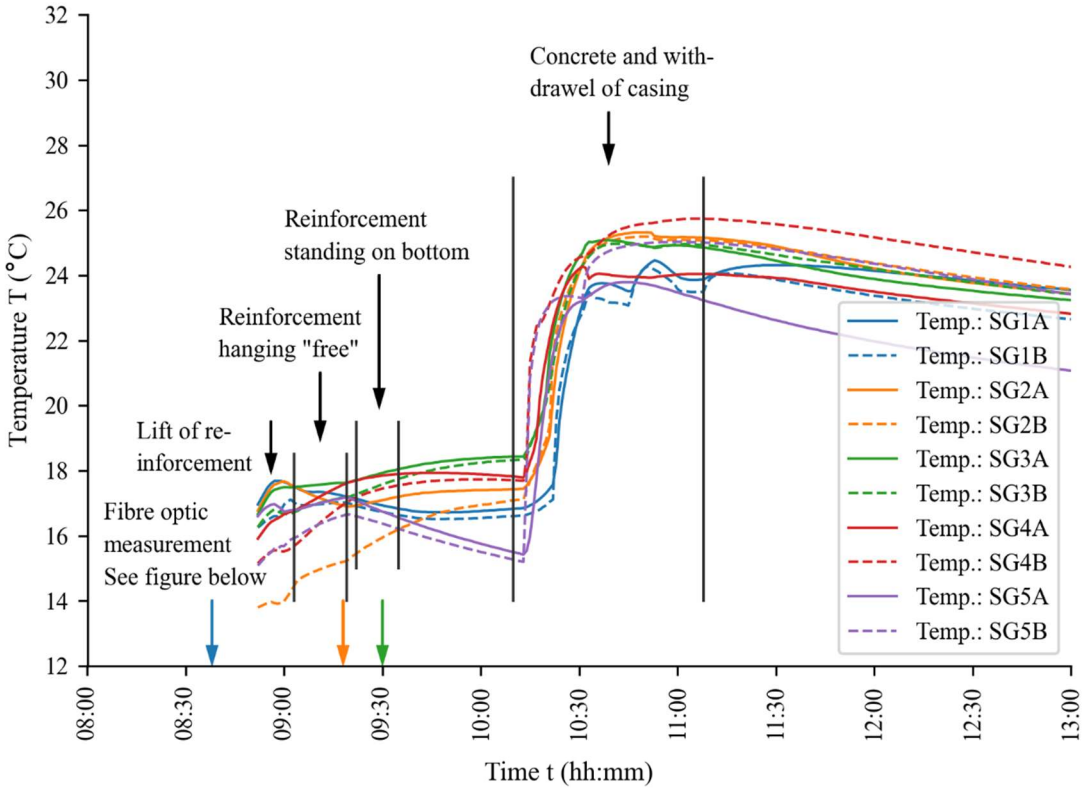

Figure 117: Temperatures recorded by the thermistors in the vibrating wire strain gauges (VWSG thermistors) during the installation of the reinforcement cage in the borehole for test pile 6 on the 22nd of August 2019.

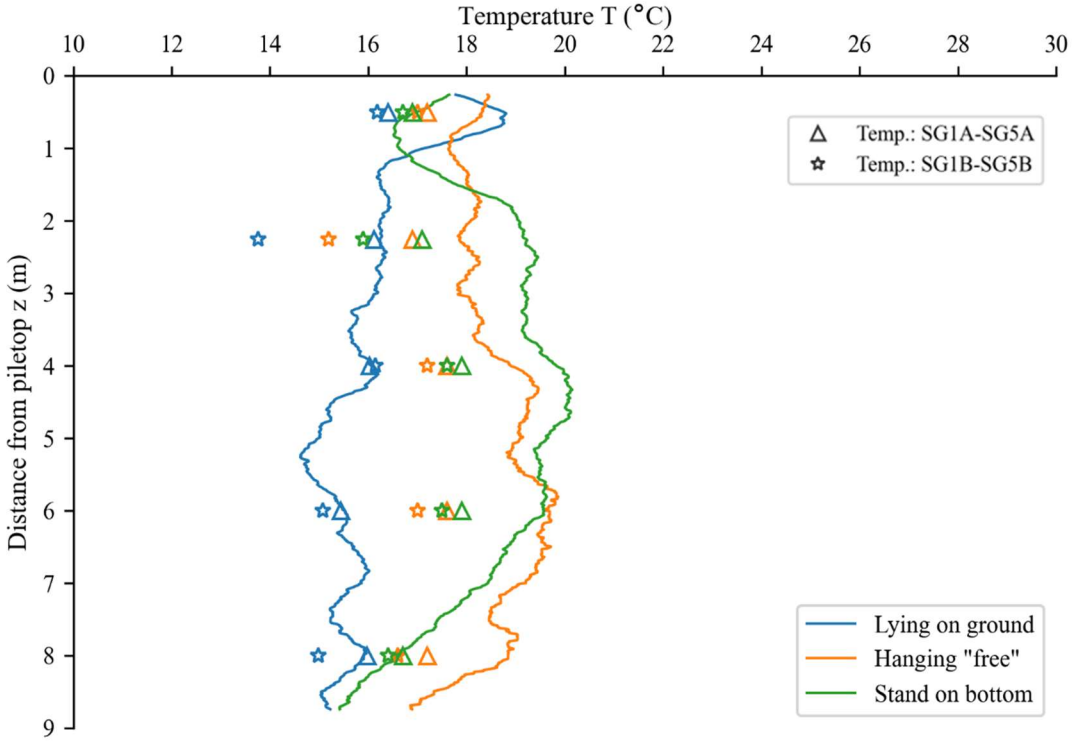

Figure 118: Measurements of temperatures for for test pile 6 on the 22nd of August 2019. Solid lines (blue, orange and green) represent the fibre optic temperature cable (FOTC), and symbols represent the thermistors in the vibrating wire strain gauges (VWSG thermistor).

Test pile 7

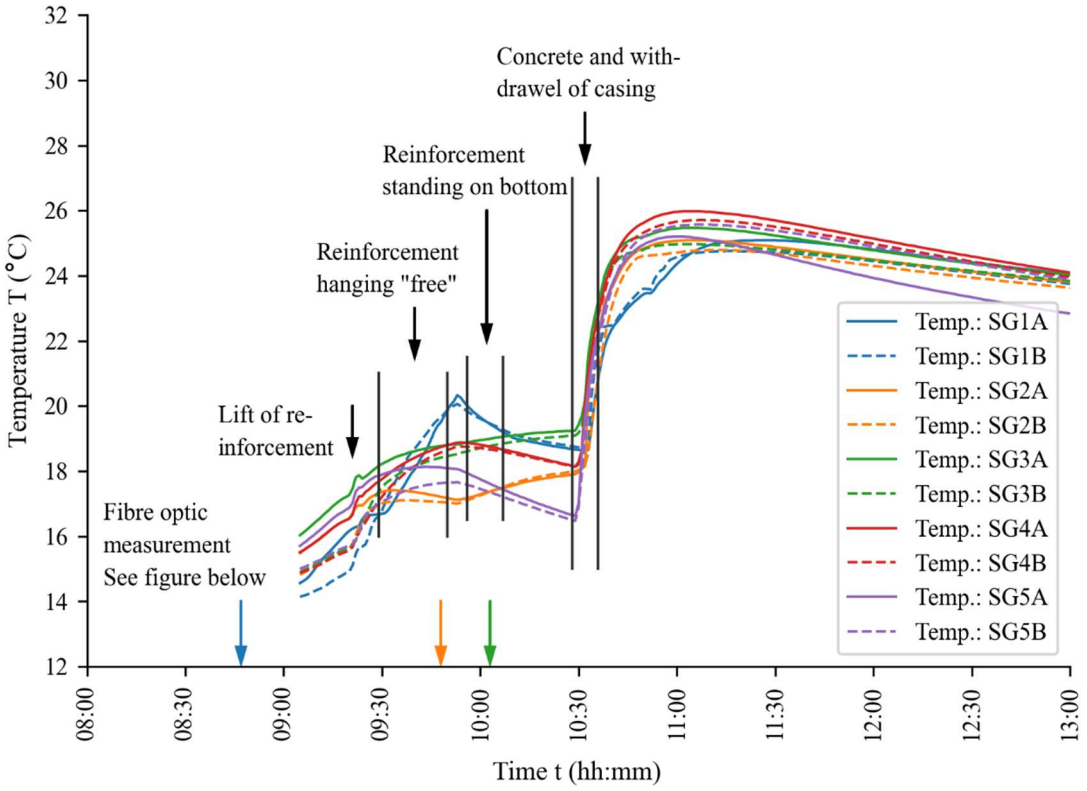

Figure 119: Temperatures recorded by the thermistors in the vibrating wire strain gauges (VWSG thermistors) during the installation of the reinforcement cage in the borehole for test pile 7 on the 21st of August 2019.

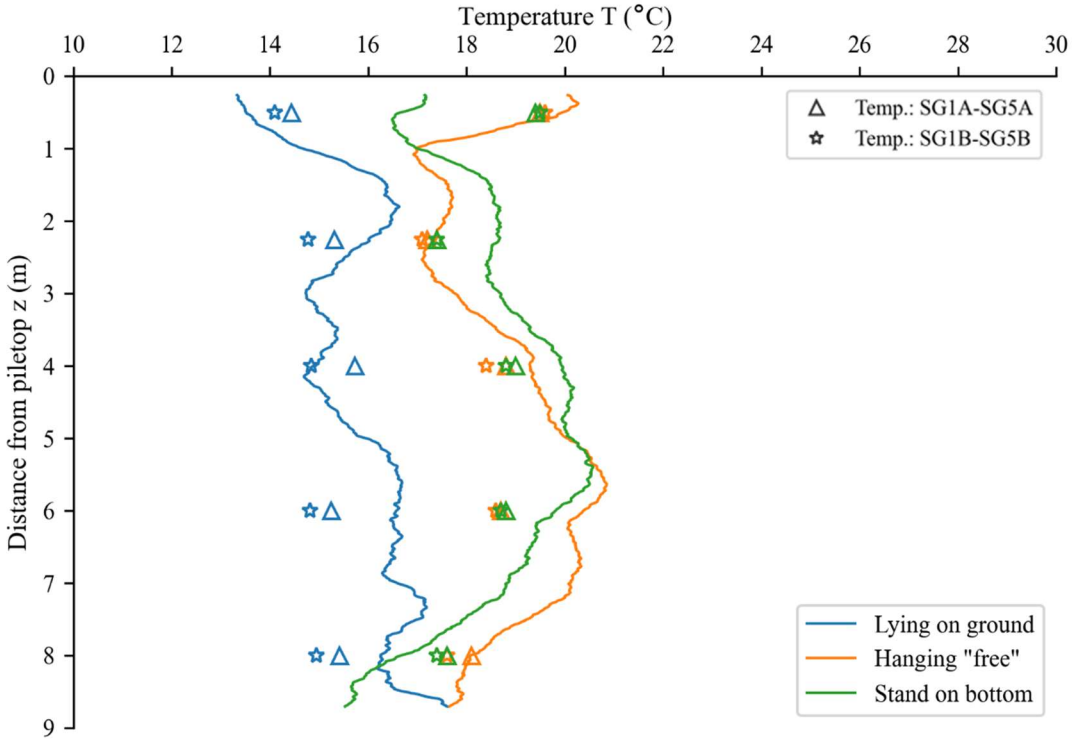

Figure 120: Measurements of temperatures for test pile 7 on the 21st of August 2019. Solid lines (blue, orange and green) represent the fibre optic temperature cable (FOTC), and symbols represent the thermistors in the vibrating wire strain gauges (VWSG thermistor).

Test pile 8

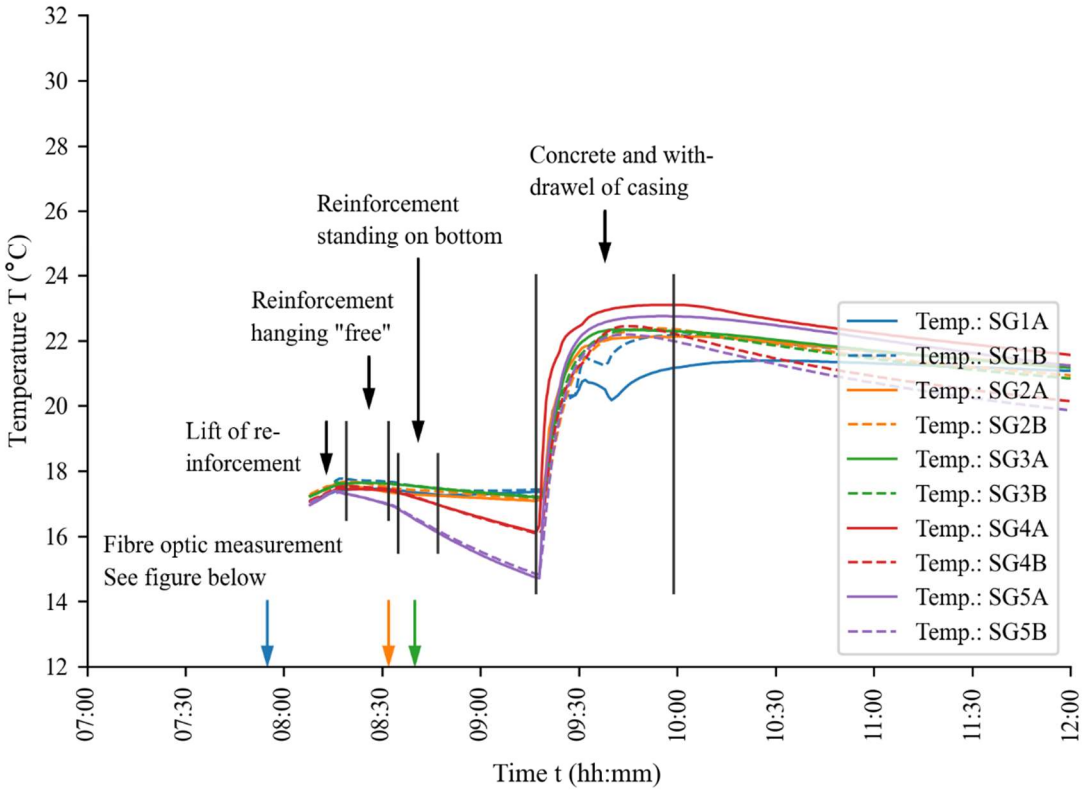

Figure 121: Temperatures recorded by the thermistors in the vibrating wire strain gauges (VWSG thermistors) during the installation of the reinforcement cage in the borehole for test pile 8 on the 23rd of August 2019.

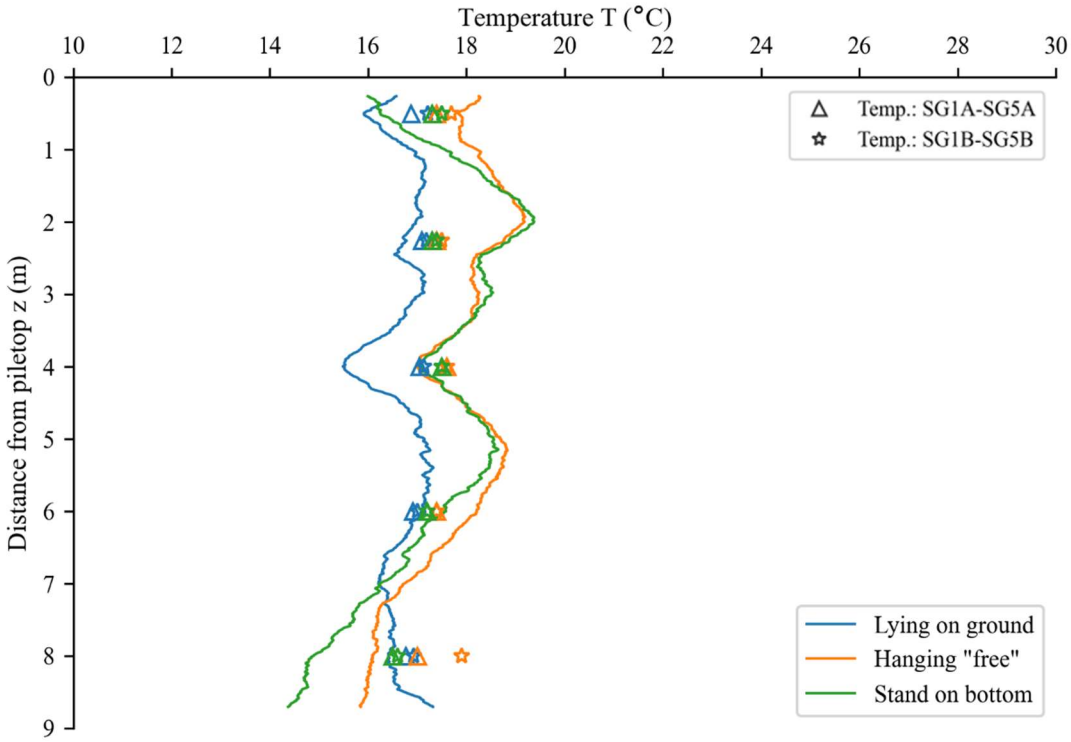

Figure 122: Measurements of temperatures for test pile 8 on the 23rd of August 2019. Solid lines (blue, orange and green) represent the fibre optic temperature cable (FOTC), and symbols represent the thermistors in the vibrating wire strain gauges (VWSG thermistor).

G Tell-tale measurements

Unfortunately, the vertical displacement measurements obtained from tell-tales are considered unreliable for this particular PhD project, despite their general reputation for trustworthiness. Below, the observed discrepancies are presented along with a possible explanation.

During the maintained load (ML) test conducted on test piles 1 and 7, the vertical displacement measured at the two tell-tale levels appears significantly lower compared to the measurements taken at the pile top. Figure 123 to Figure 127 in Appendix G.1 illustrate this observation, where the displacement-load curves from the tell-tale levels are noticeably shifted to the left when compared to the curve from the pile top.

To provide an example, for test pile 7 at an applied load of 600 kN, the measured vertical displacement is 1.92 mm at the pile top level, while the corresponding measurements at the two tell-tale levels are 1.11 mm and 0.87 mm, respectively. Considering the distance between the pile top level and the tell-tales at the sand/clay interface as 3.5 m, and between the tell-tales at the sand/clay interface and the tell-tales at the pile base as 4 m, the average strain values can be calculated. These calculations yield an average strain of 231 $\mu\varepsilon$ between the pile top level and the tell-tales at the sand/clay interface, and 60 $\mu\varepsilon$ between the tell-tales at the sand/clay interface and the tell-tales at the pile base.

Comparatively, the average strain value of 231 $\mu\varepsilon$ between the pile top level and the tell-tales at the sand/clay interface is roughly 2.5 times greater than the maximum strain of 90 $\mu\varepsilon$ measured by the vibrating wire strain gauges at the upper strain gauge level in test pile 1 (refer to Appendix H.3).

This inconsistency could be attributed to differences in the displacement transducers used for vertical displacement measurement. Test piles 1 and 7 utilized vibrating wire displacement transducers (model VWDT 6000) at the two tell-tale levels, while HBM WA100-T displacement transducers were employed for vertical displacement measurements at the pile top. Additionally, it is important to note that these transducers were mounted on two distinct and independent reference systems.

Consequently, for the static pile loading tests conducted on the remaining test piles (piles 2-6 and 8), the same displacement transducers used for vertical displacement at the pile top (HBM WA100-T displacement transducers) were also employed for vertical displacement measurement at the two tell-tale levels. To ensure consistency, a steel frame was developed and affixed to the reference beams, which formed the reference system for the displacement transducers used at the two tell-tale levels (refer to Appendix C.3.3).

However, during the constant rate of uplift (CRU) test performed on test piles 2-6 and 8, a new observation emerged. The measured vertical displacement at the two tell-tale levels now appeared to be greater than the displacement measured at the pile top (see Figure 127 to Figure 138 in Appendix

G.1). Consequently, the displacement-load curves from the two tell-tale levels were positioned to the right of the curve obtained from the pile top.

This discrepancy is contradictory to what is expected in reality, as vertical displacement during the static pile loading test in tension should be highest at the pile top and decrease along the length of the test piles, moving from the pile top to the pile base.

It is believed that this inconsistency stems from the previous use of the tell-tales, which resulted in slight bending and rusting. Additionally, the relocation of the tell-tales from one test pile to another exposed some loosened connections and caused the small steel plates welded on top of the tell-tales (to serve as a basis for the displacement transducers) to become slightly tilted. Consequently, despite their general perceived trustworthiness, the vertical displacement measurements obtained from the tell-tales are deemed useless for this PhD project.

G.1 Displacement-load curves

Maintained load (ML) test

Test pile 1

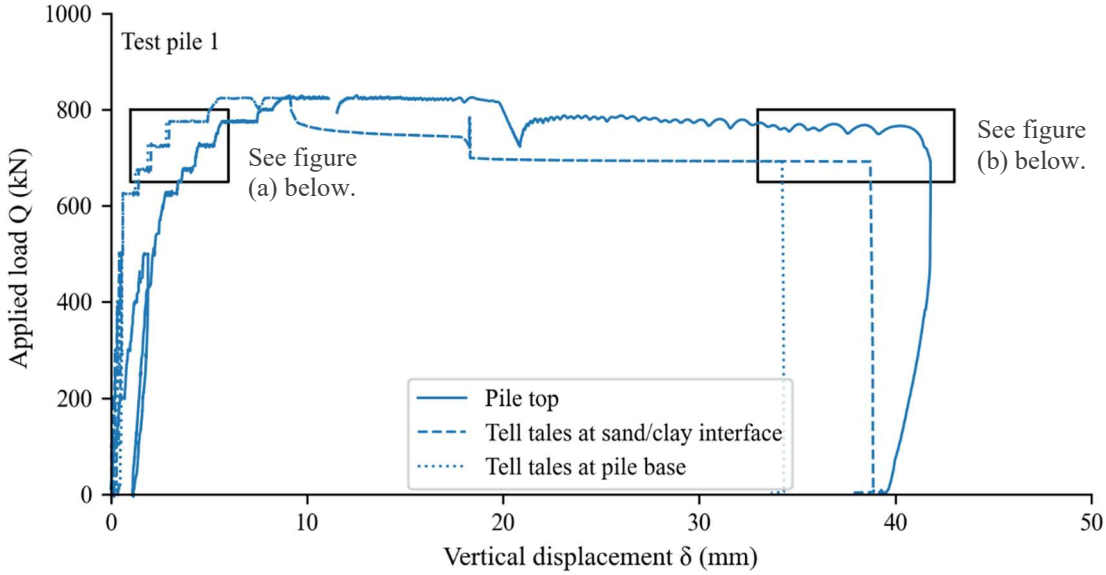

Figure 123: Load-displacements curves from the maintained load (ML) test for test pile 1 displaying the vertical displacement recorded from pile top, tell-tales at sand/clay interface, and tell-tales at pile base.

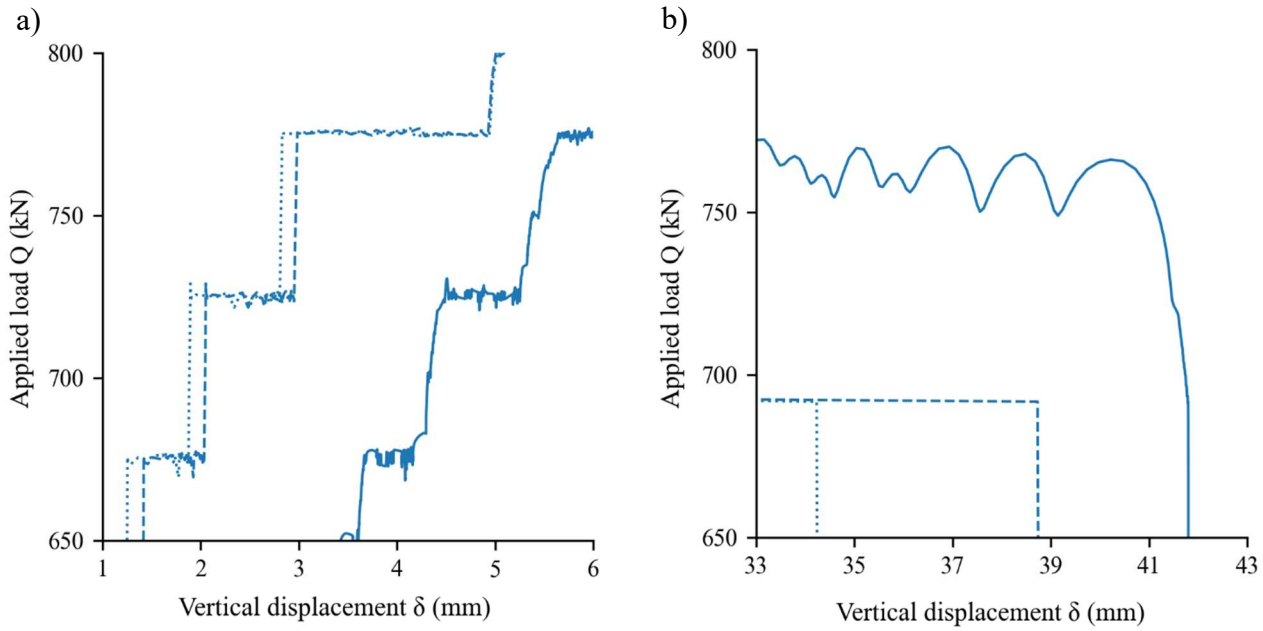

Figure 124: Zoom of vertical displacement relative to each other for pile top level, tell-tales at sand/clay interface, and tell-tales at pile base. The difference between two levels represents the extension of test pile 1 between these two specific levels and hence, can be used to determine an average strain value.

Test pile 7

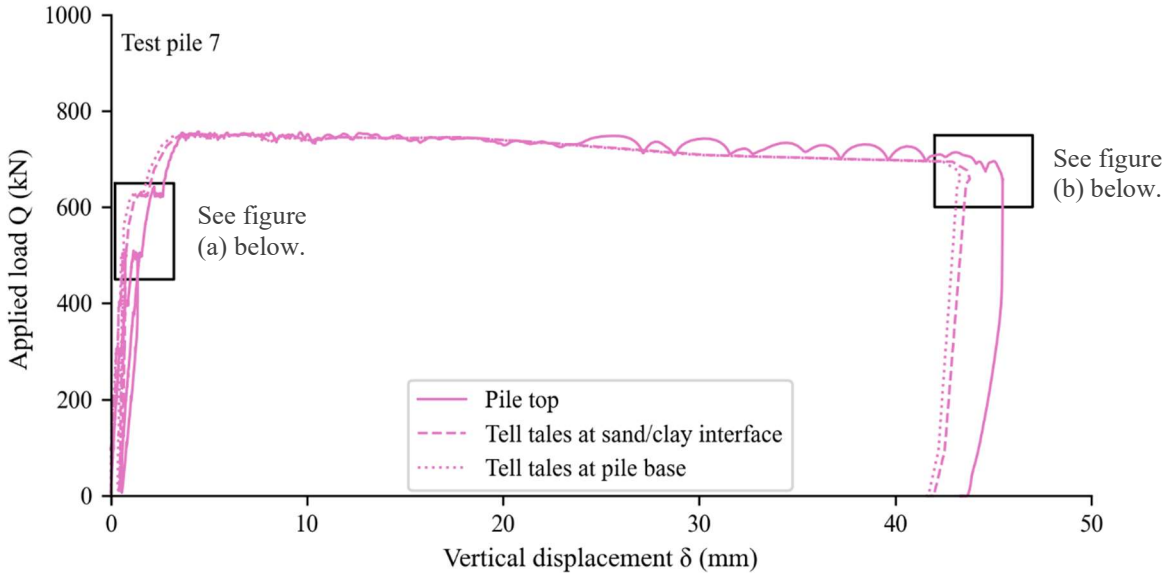

Figure 125: Load-displacements curves from the maintained load (ML) test for test pile 7 displaying the vertical displacement recorded from pile top, tell-tales at sand/clay interface, and tell-tales at pile base.

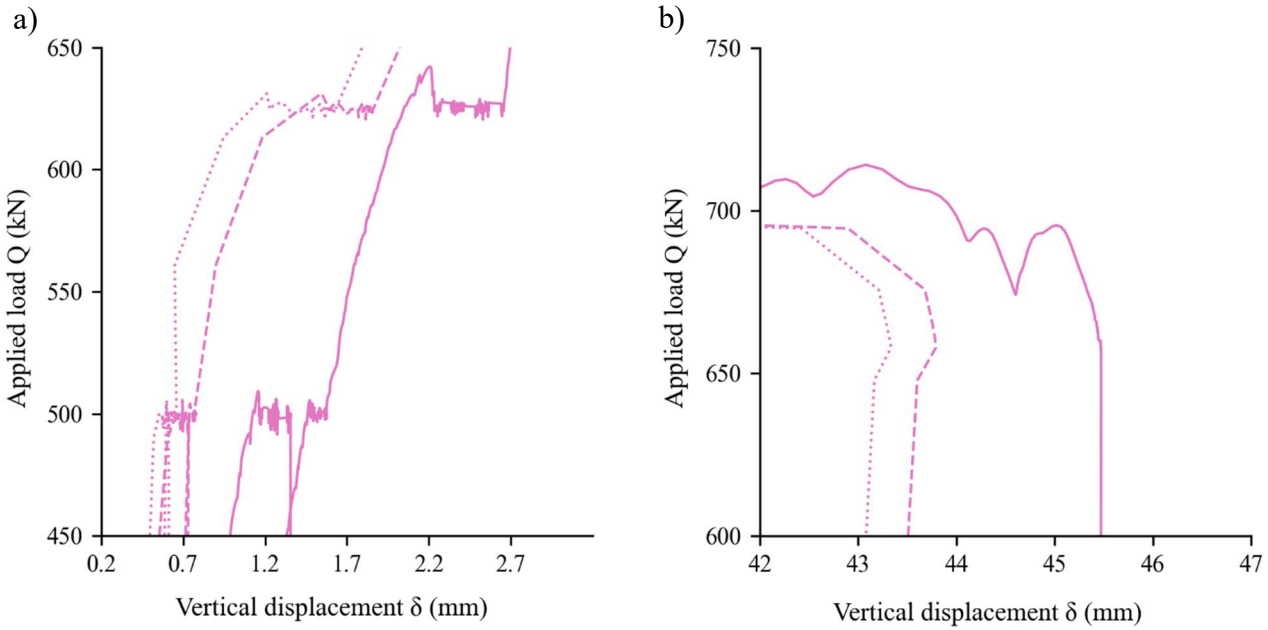

Figure 126: Zoom of vertical displacement relative to each other for pile top level, tell-tales at sand/clay interface, and tell-tales at pile base. The difference between two levels represents the extension of test pile 7 between these two specific levels and hence, can be used to determine an average strain value.

Constant rate of uplift (CRU) test

Test pile 2

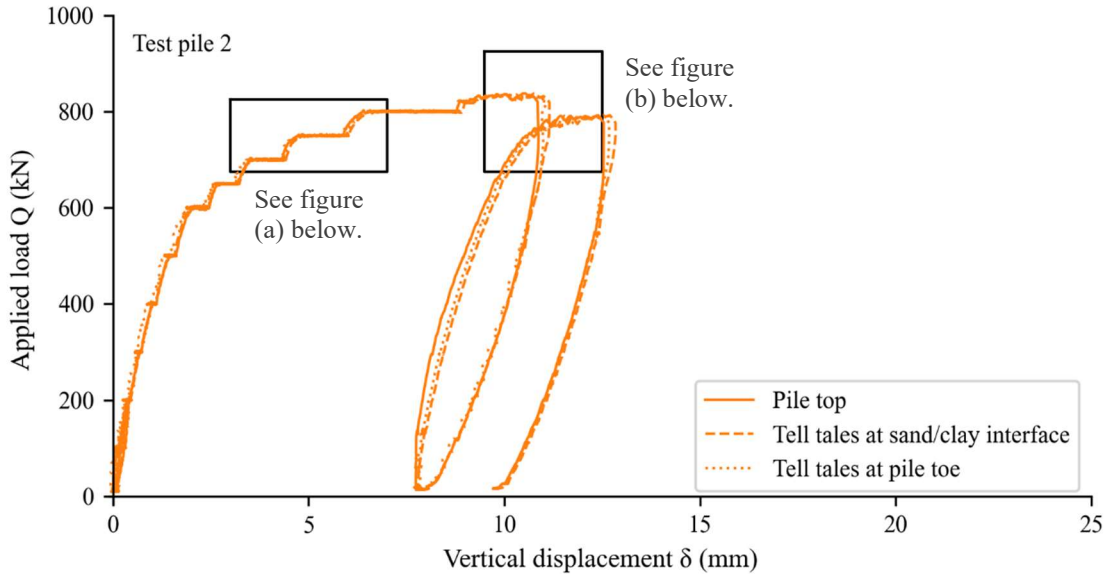

Figure 127: Load-displacements curves from the constant rate of uplift (CRU) test for test pile 2 displaying the vertical displacement recorded from pile top, tell-tales at sand/clay interface, and tell-tales at pile base.

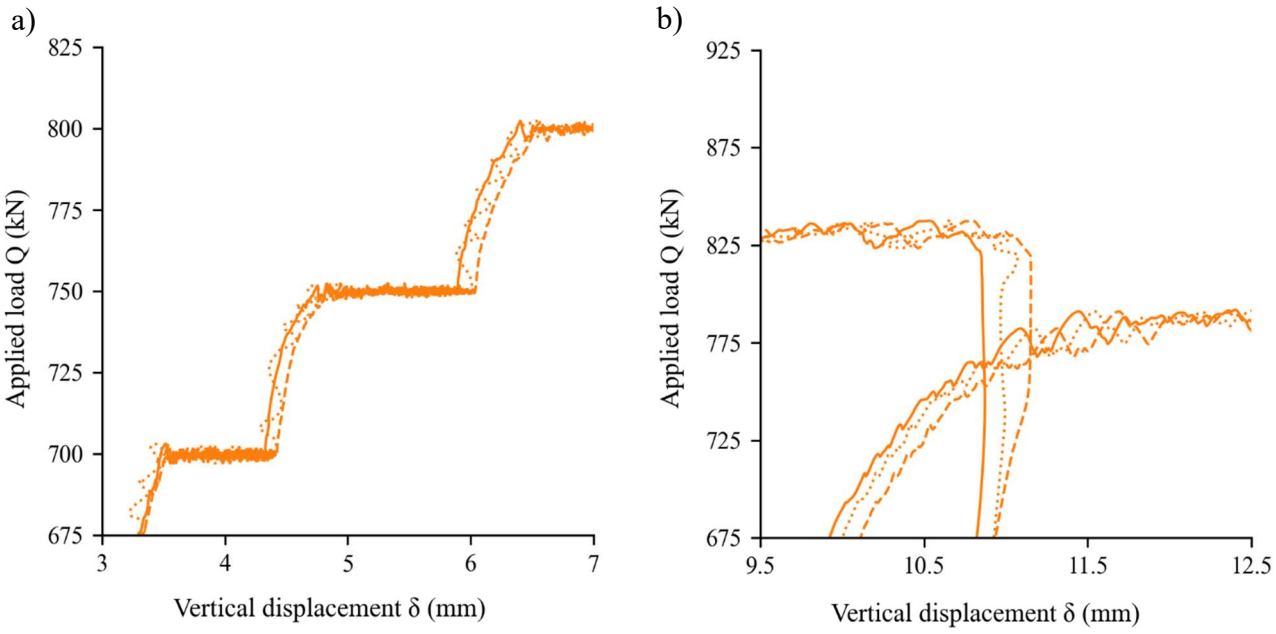

Figure 128: Zoom of vertical displacement relative to each other for pile top level, tell-tales at sand/clay interface, and tell-tales at pile base. The difference between two levels represents the extension of test pile 2 between these two specific levels and hence, can be used to determine an average strain value.

Test pile 3

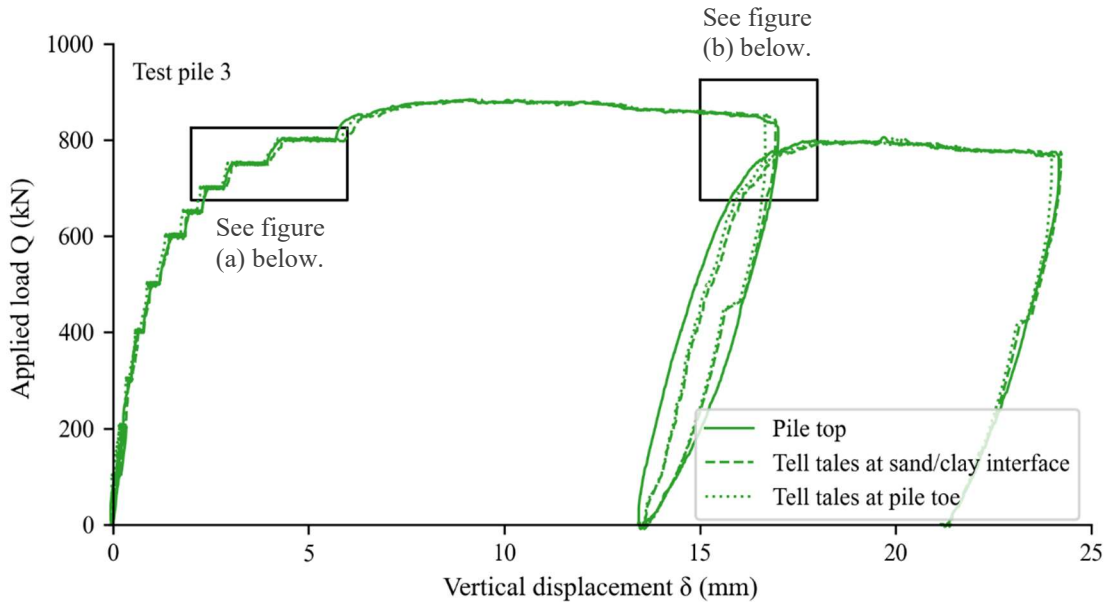

Figure 129: Load-displacements curves from the constant rate of uplift (CRU) test for test pile 3 displaying the vertical displacement recorded from pile top, tell-tales at sand/clay interface, and tell-tales at pile base.

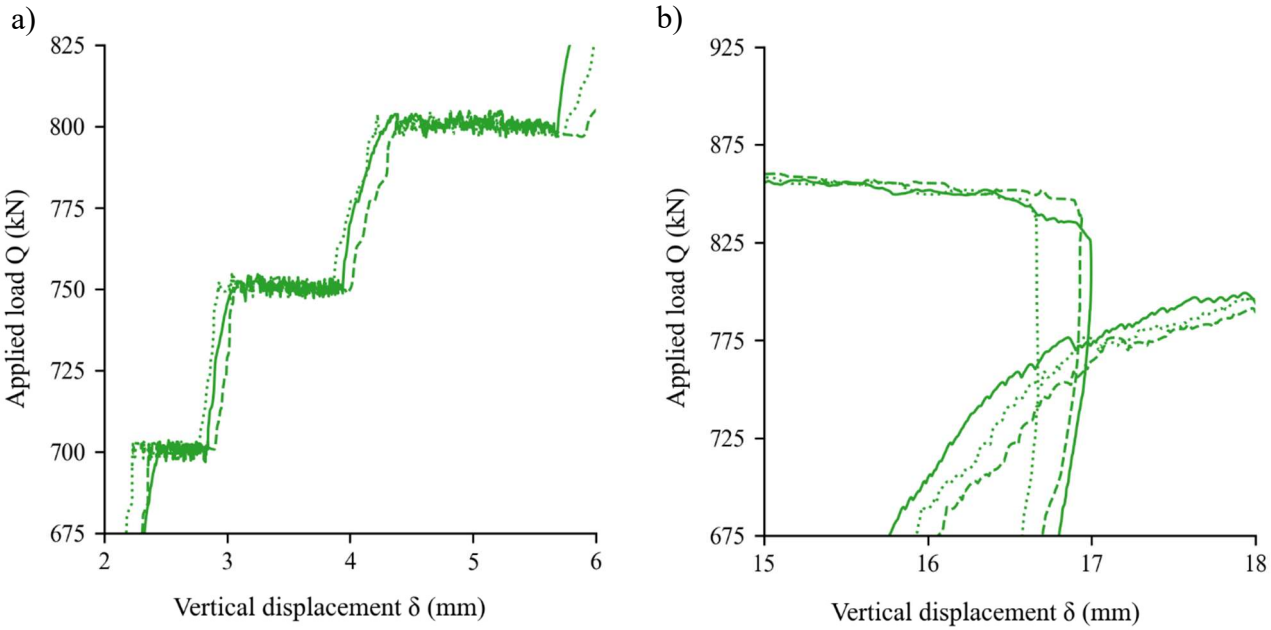

Figure 130: Zoom of vertical displacement relative to each other for pile top level, tell-tales at sand/clay interface, and tell-tales at pile base. The difference between two levels represents the extension of test pile 3 between these two specific levels and hence, can be used to determine an average strain value.

Test pile 4

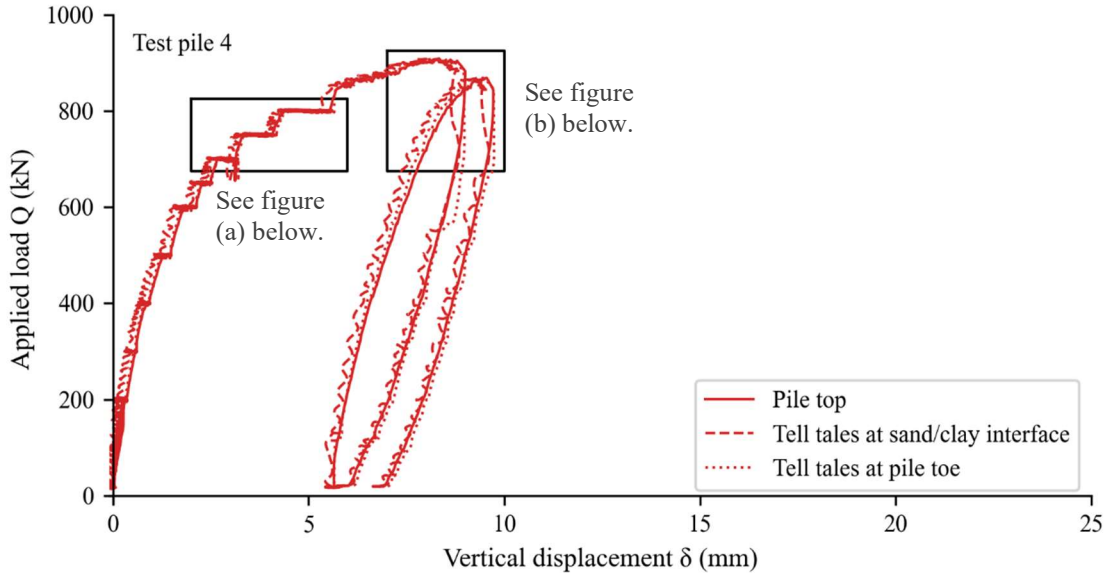

Figure 131: Load-displacements curves from the constant rate of uplift (CRU) test for test pile 4 displaying the vertical displacement recorded from pile top, tell-tales at sand/clay interface, and tell-tales at pile base.

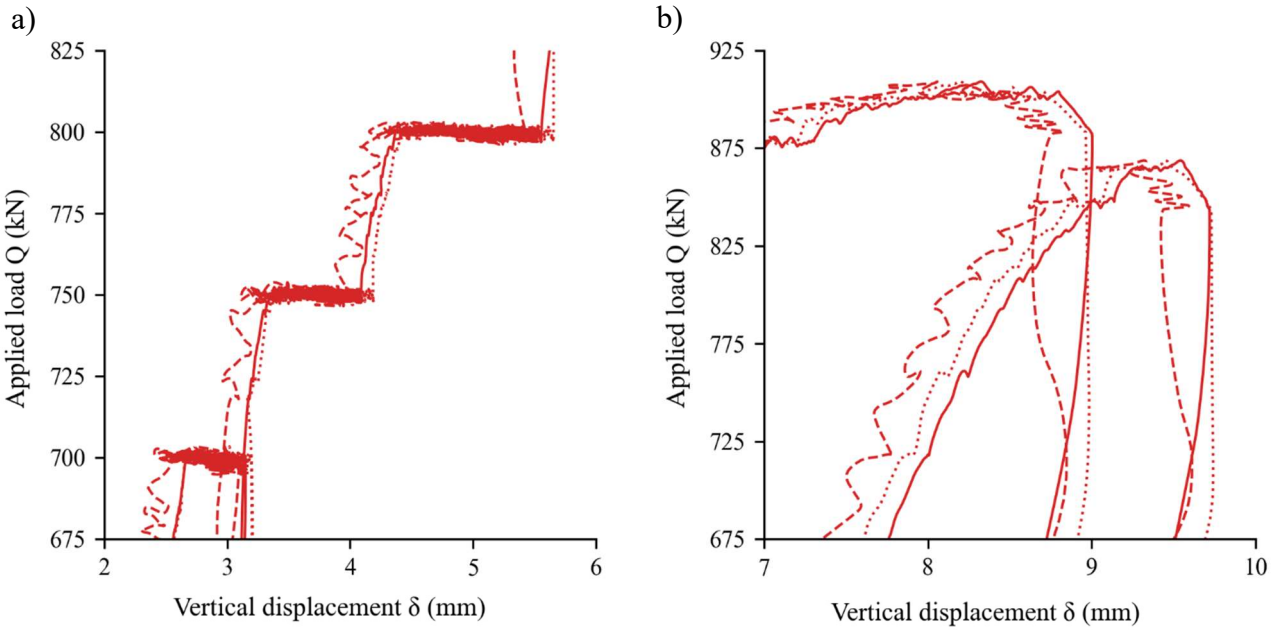

Figure 132: Zoom of vertical displacement relative to each other for pile top level, tell-tales at sand/clay interface, and tell-tales at pile base. The difference between two levels represents the extension of test pile 4 between these two specific levels and hence, can be used to determine an average strain value.

Test pile 5

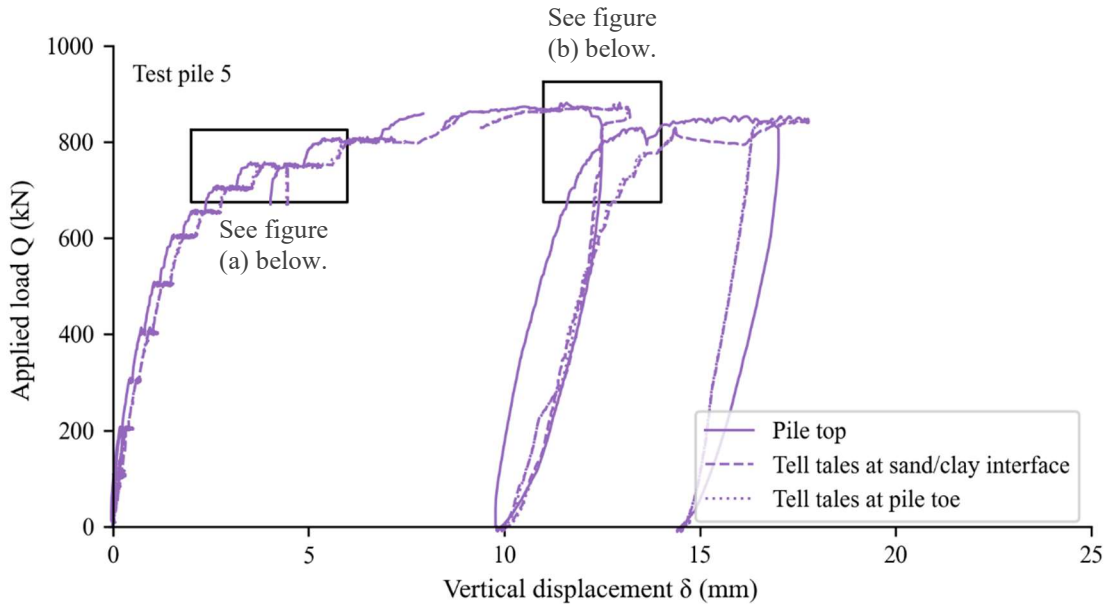

Figure 133: Load-displacements curves from the constant rate of uplift (CRU) test for test pile 5 displaying the vertical displacement recorded from pile top, tell-tales at sand/clay interface, and tell-tales at pile base.

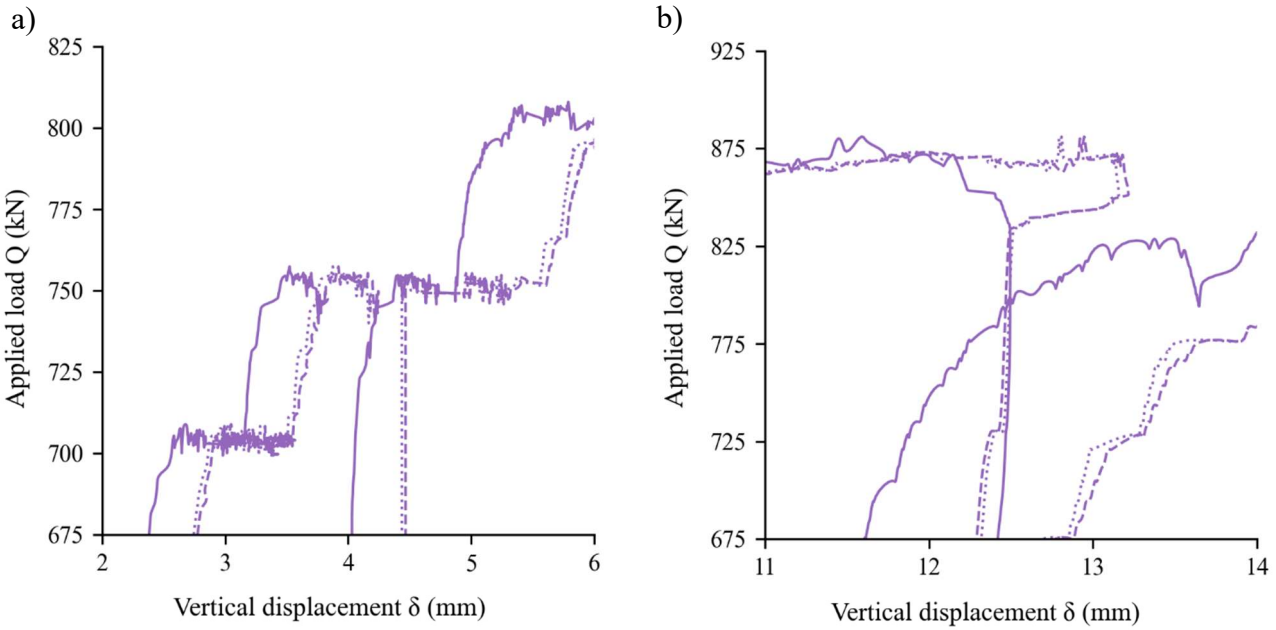

Figure 134: Zoom of vertical displacement relative to each other for pile top level, tell-tales at sand/clay interface, and tell-tales at pile base. The difference between two levels represents the extension of test pile 5 between these two specific levels and hence, can be used to determine an average strain value.

Test pile 6

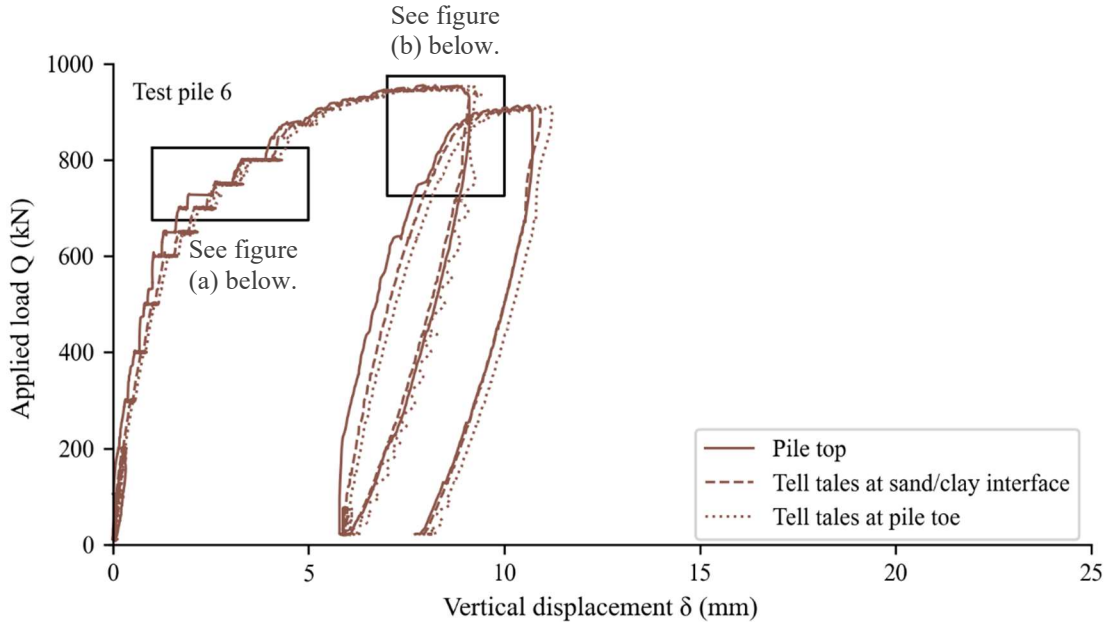

Figure 135: Load-displacements curves from the constant rate of uplift (CRU) test for test pile 6 displaying the vertical displacement recorded from pile top, tell-tales at sand/clay interface, and tell-tales at pile base.

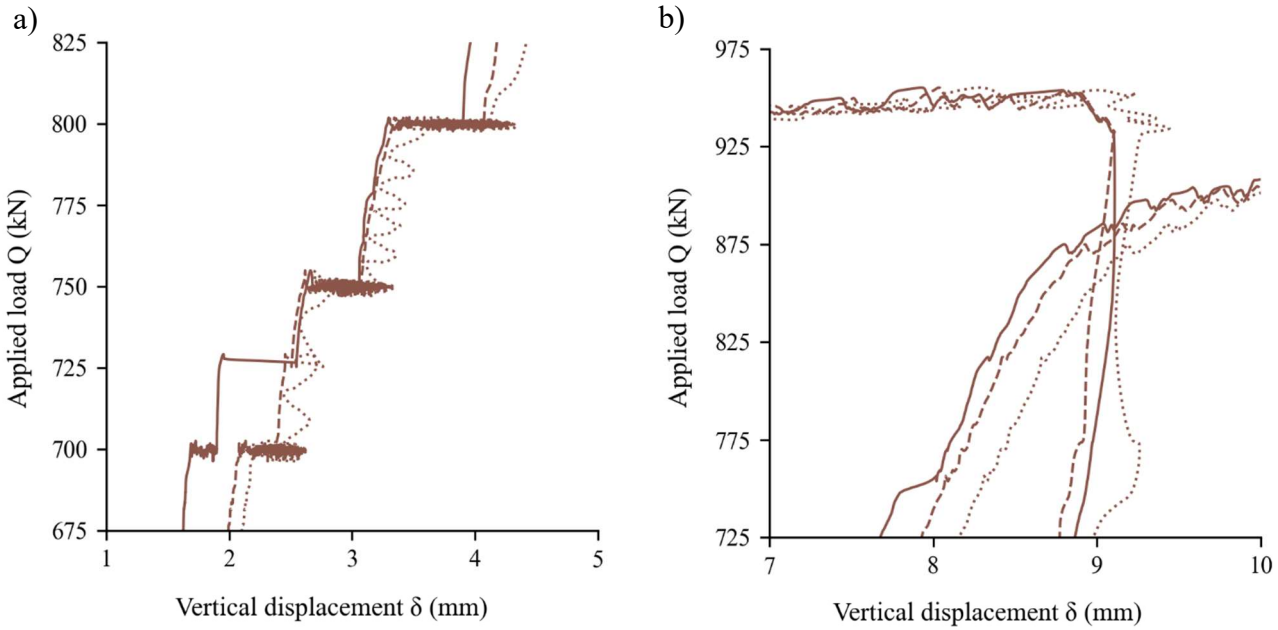

Figure 136: Zoom of vertical displacement relative to each other for pile top level, tell-tales at sand/clay interface, and tell-tales at pile base. The difference between two levels represents the extension of test pile 6 between these two specific levels and hence, can be used to determine an average strain value.

Test pile 8

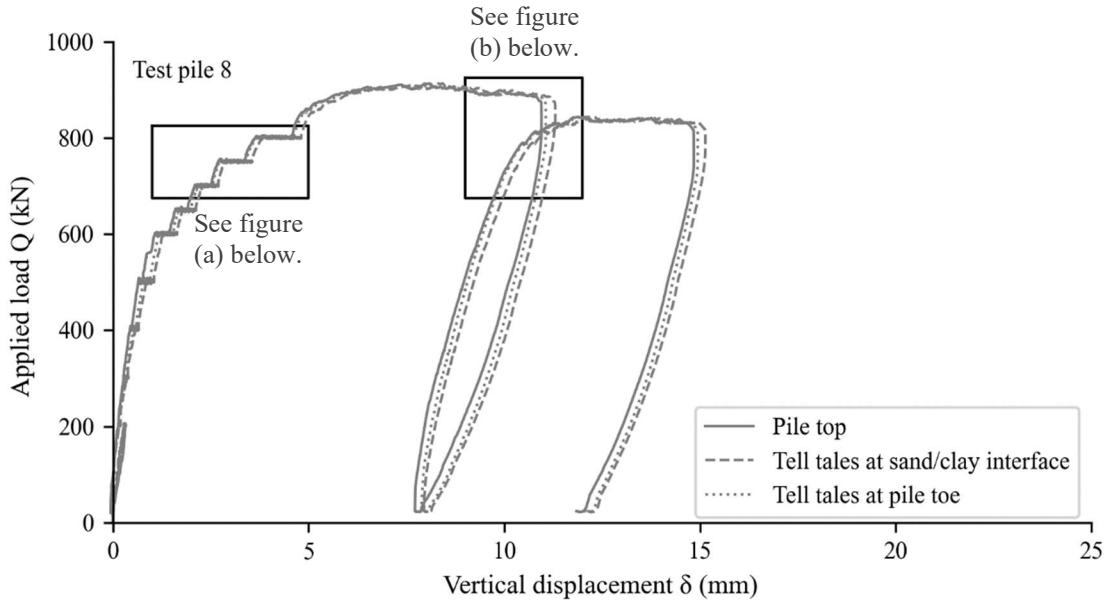

Figure 137: Load-displacements curves from the constant rate of uplift (CRU) test for test pile 8 displaying the vertical displacement recorded from pile top, tell-tales at sand/clay interface, and tell-tales at pile base.

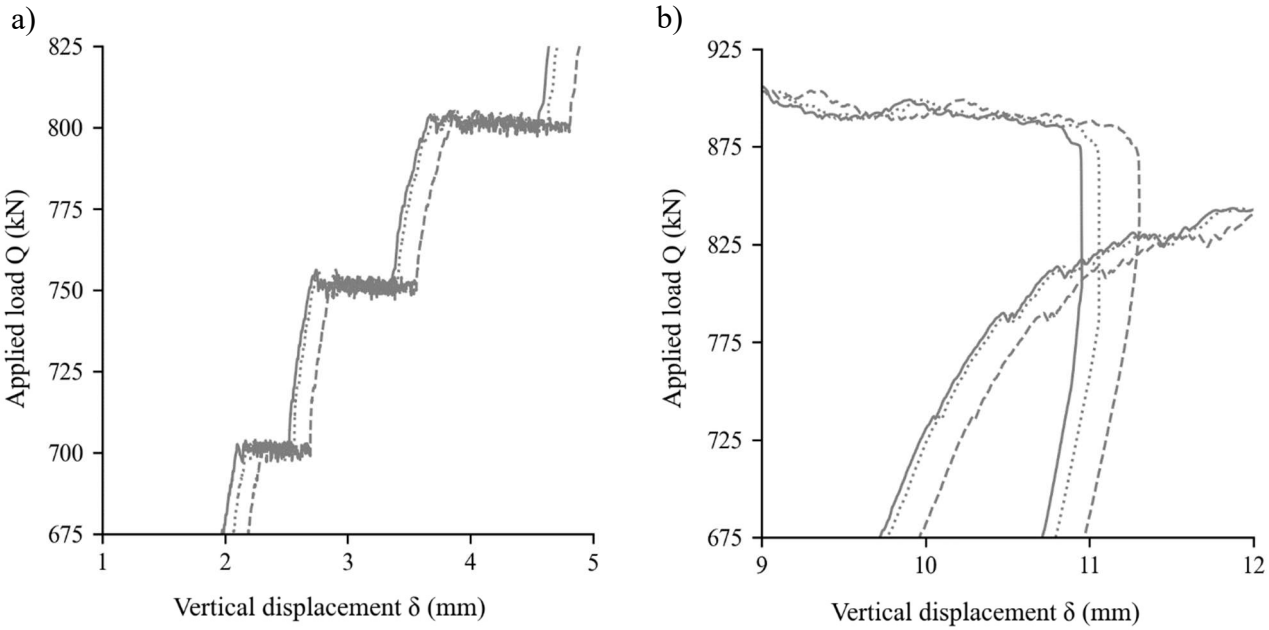

Figure 138: Zoom of vertical displacement relative to each other for pile top level, tell-tales at sand/clay interface, and tell-tales at pile base. The difference between two levels represents the extension of test pile 8 between these two specific levels and hence, can be used to determine an average strain value.

H Strain gauges measurements

H.1 Time-strain curves (Raw data)

Maintained load (ML) test

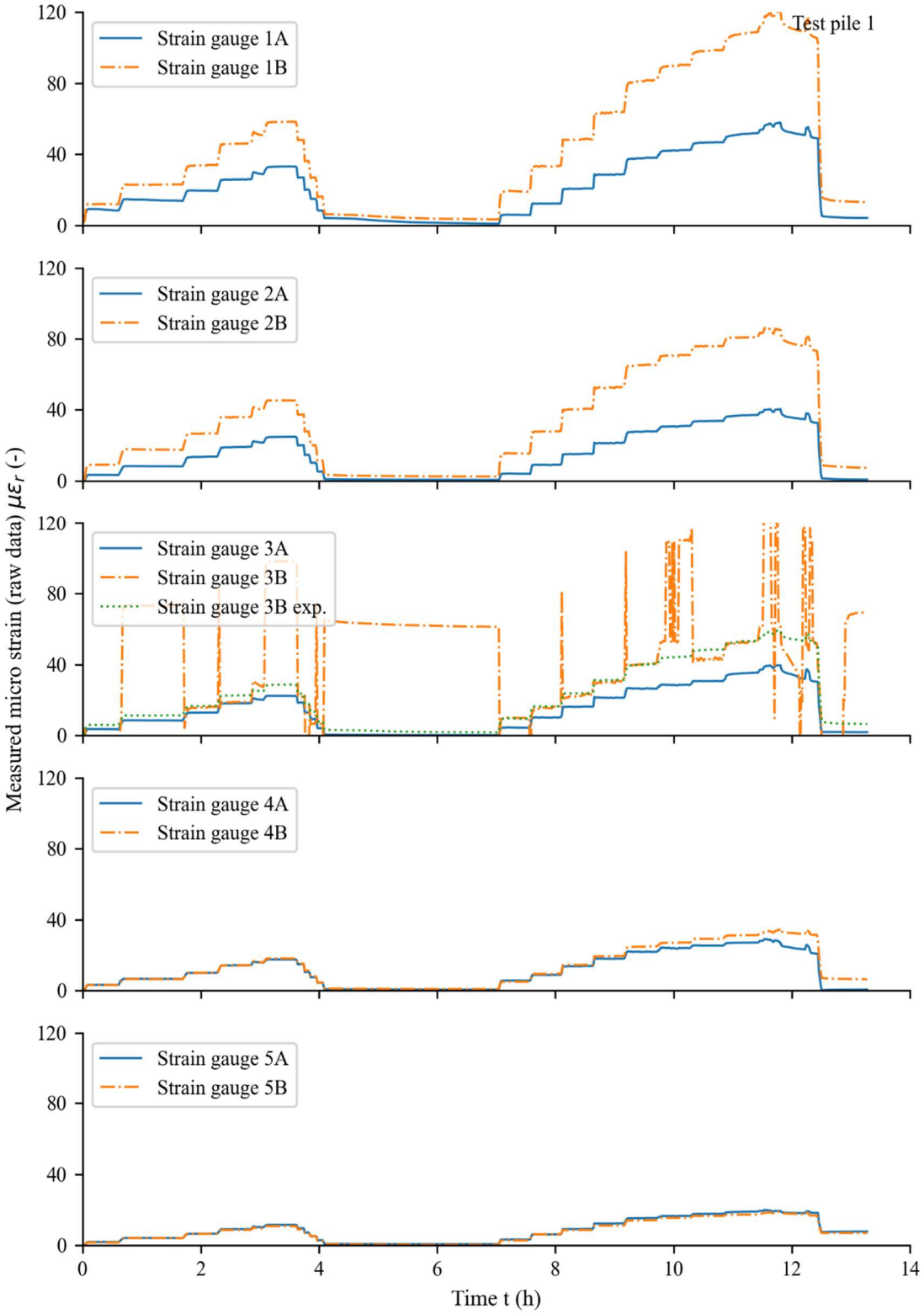

Figure 139: Development of measured strains (raw data) with time for test pile 1.

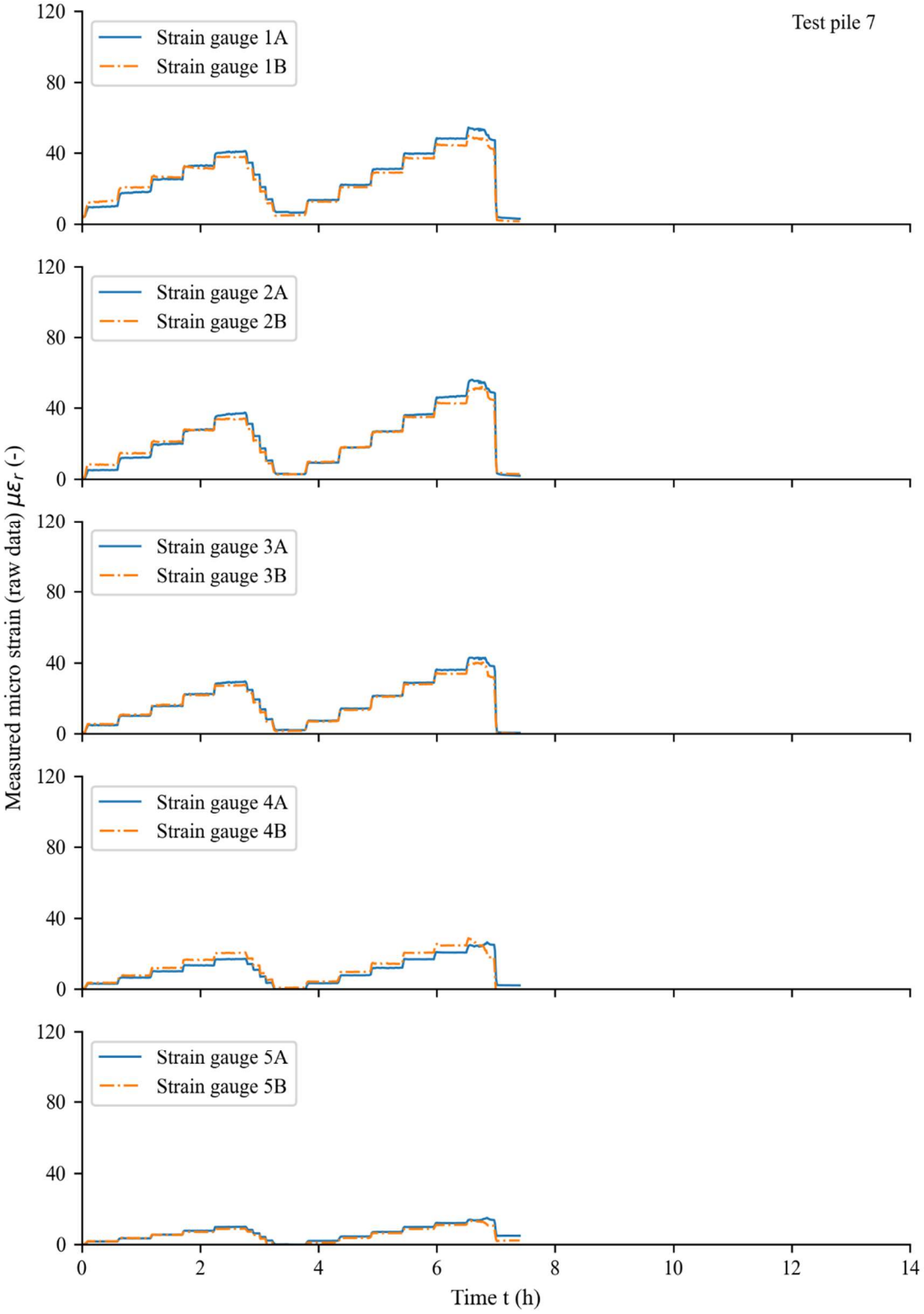

Figure 140: Development of measured strains (raw data) with time for test pile 7.

Constant rate of uplift (CRU) test

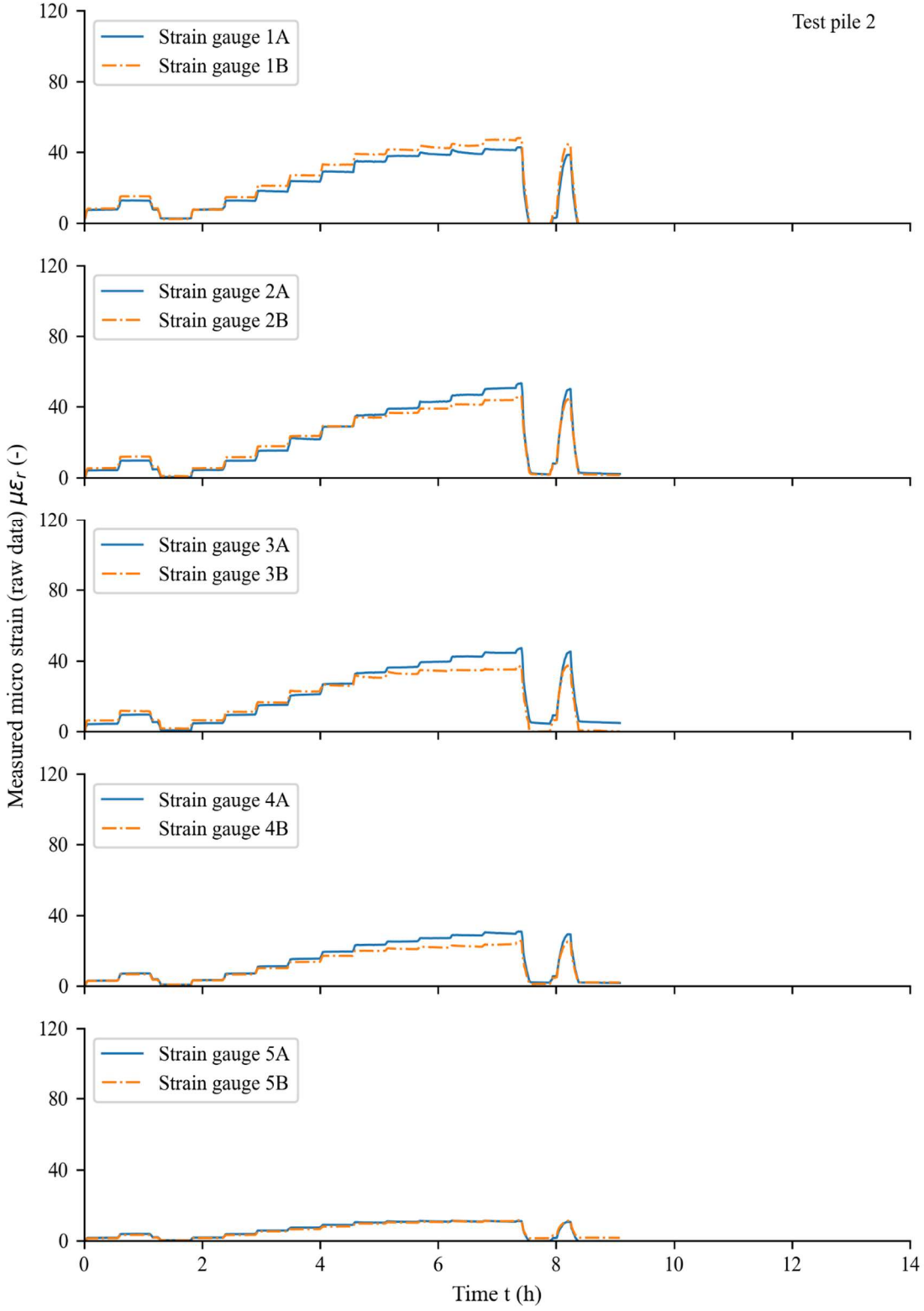

Figure 141: Development of measured strains (raw data) with time for test pile 2.

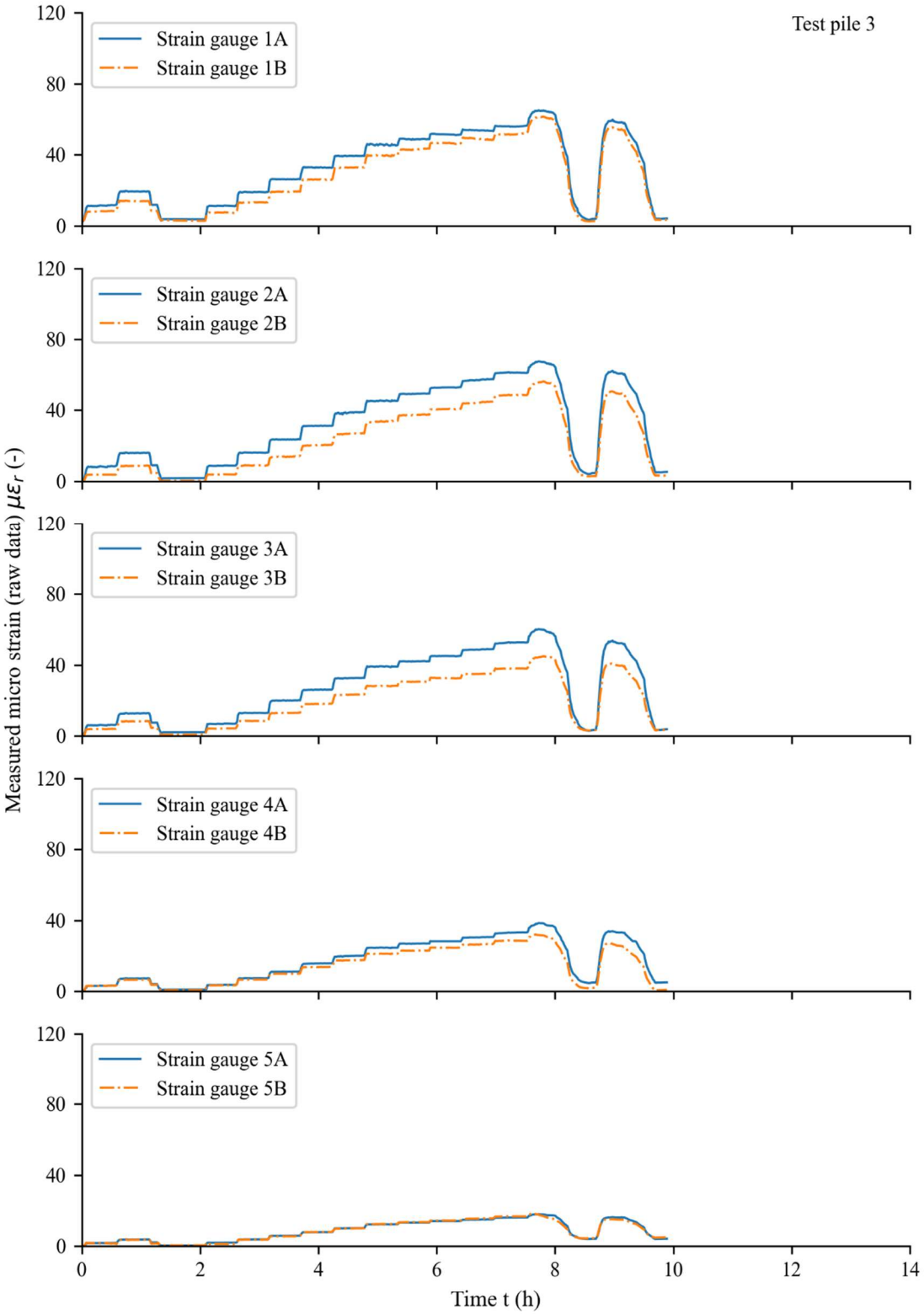

Figure 142: Development of measured strains (raw data) with time for test pile 3.

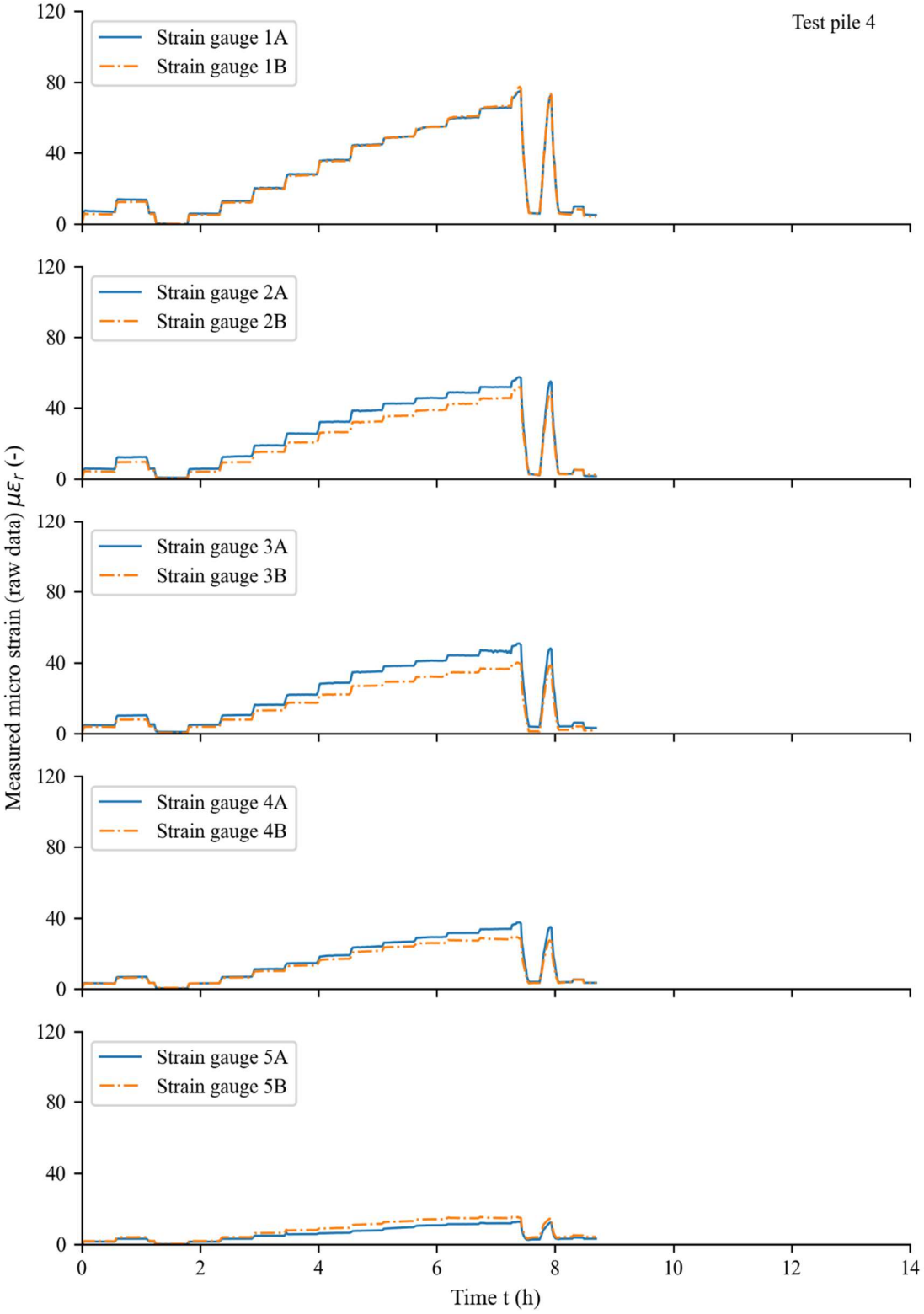

Figure 143: Development of measured strains (raw data) with time for test pile 4.

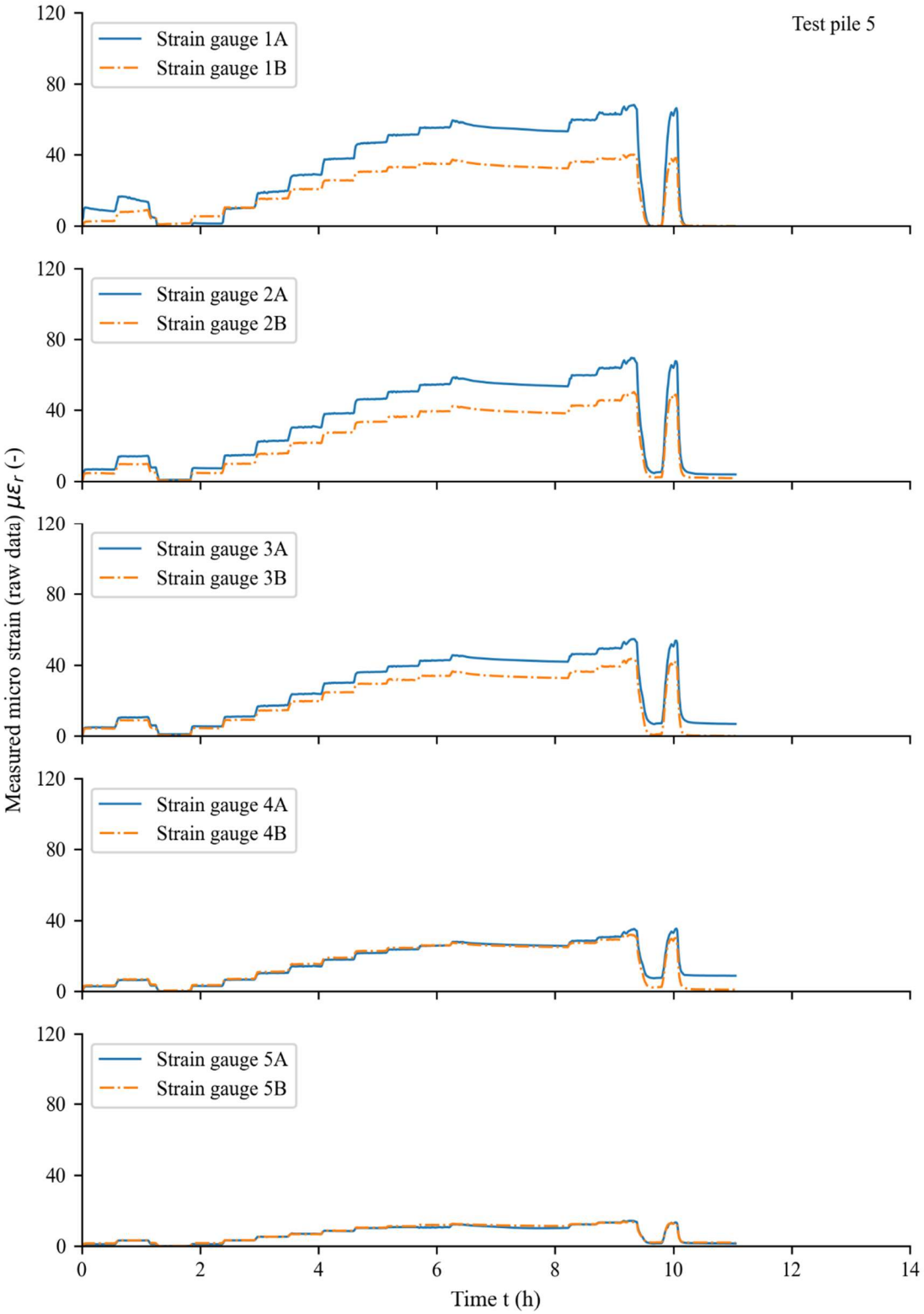

Figure 144: Development of measured strains (raw data) with time for test pile 5.

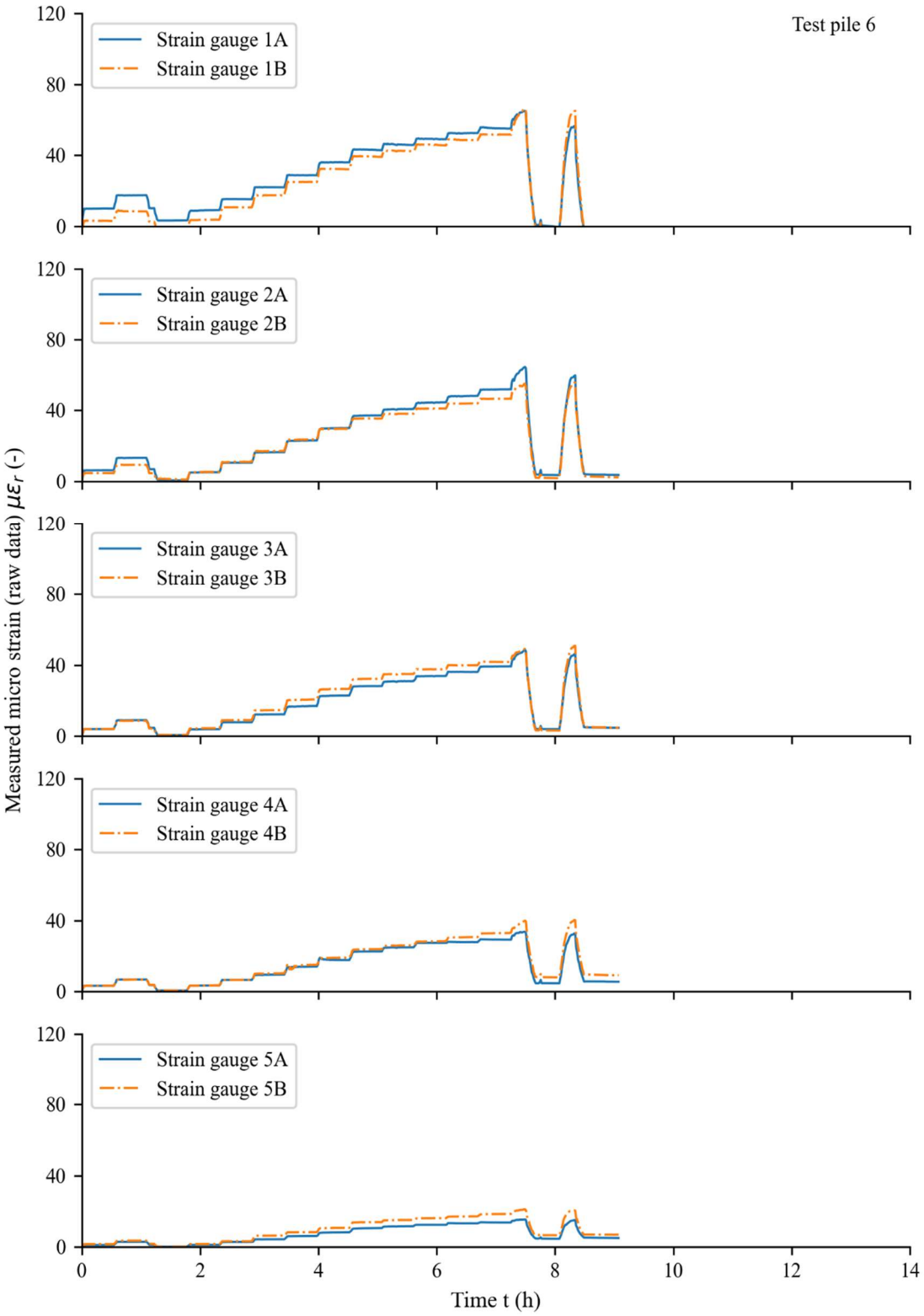

Figure 145: Development of measured strains (raw data) with time for test pile 6.

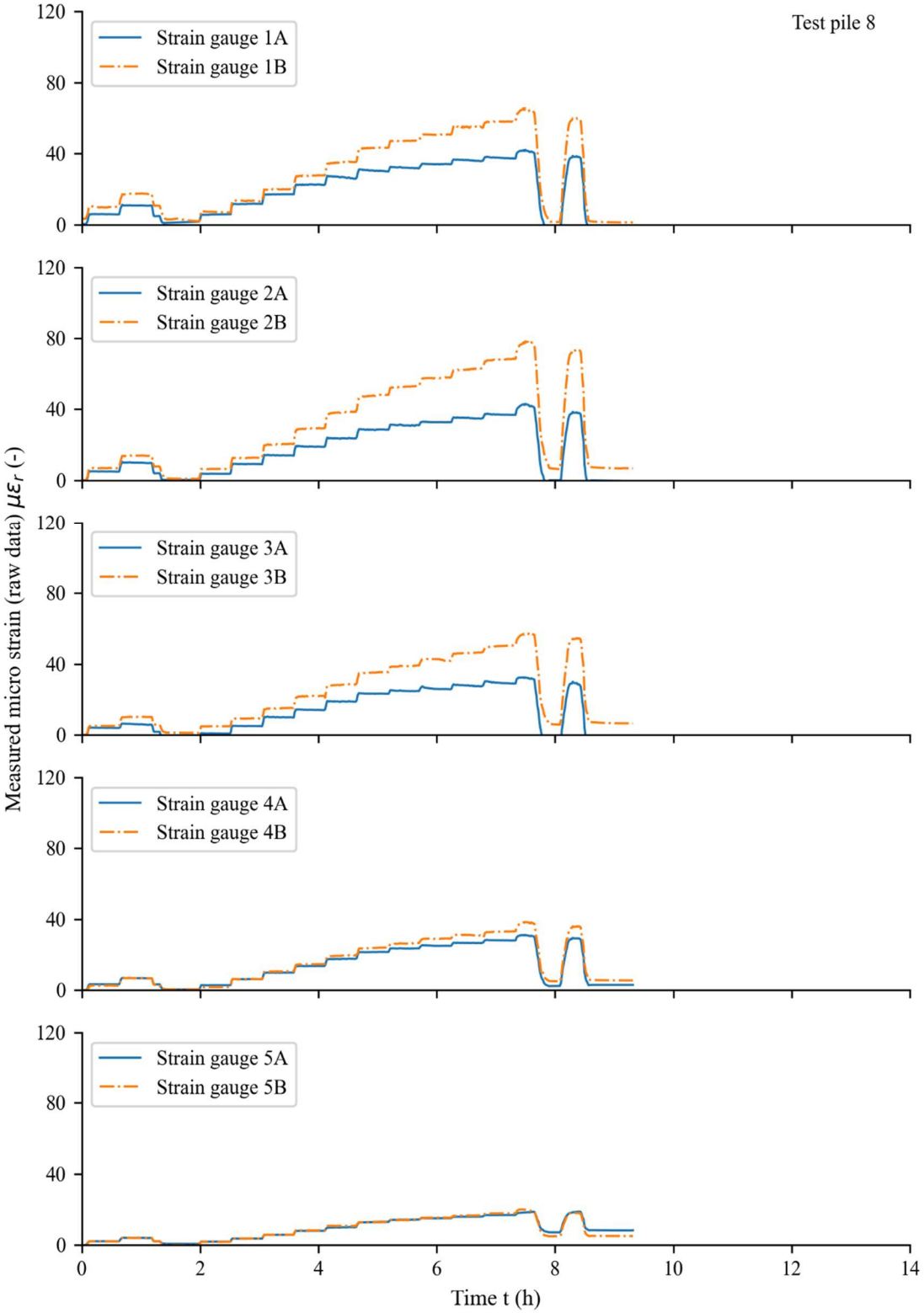

Figure 146: Development of measured strains (raw data) with time for test pile 8.

H.2 Time-strain curves (Thermal influence)

Maintained load (ML) test

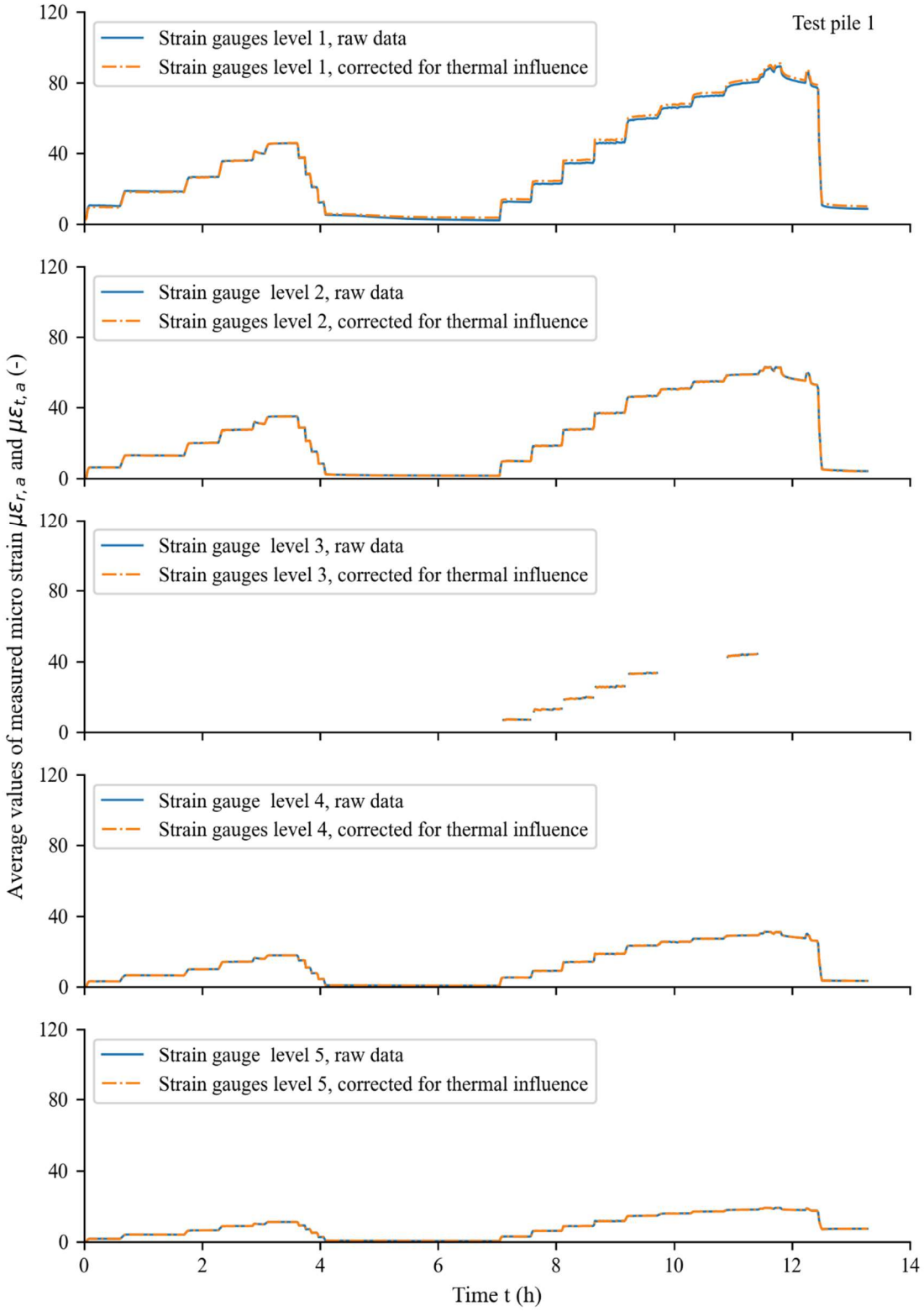

Figure 147: Average values of measured strains (raw data) and average values of measured strains corrected for thermal influence for test pile 1.

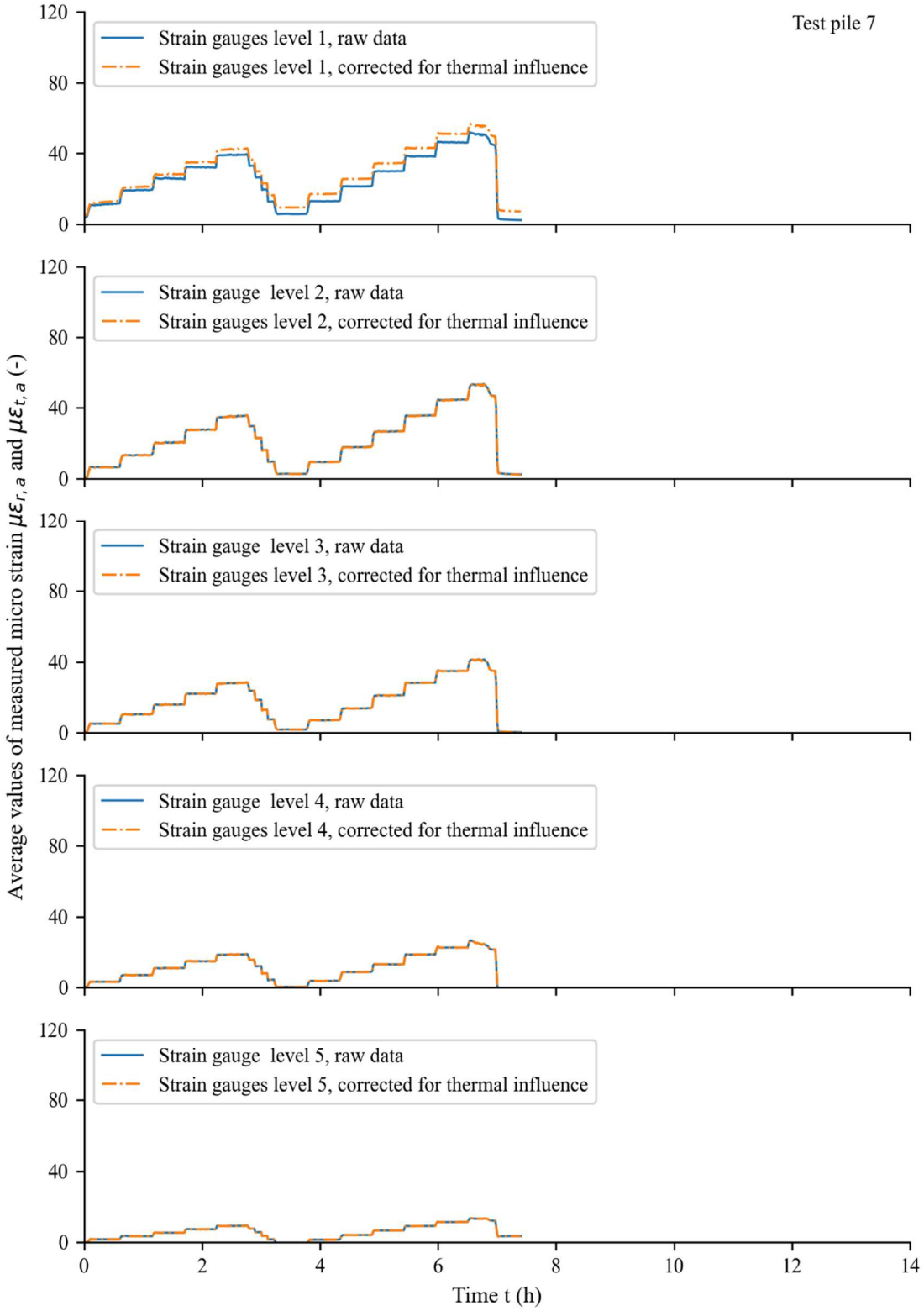

Figure 148: Average values of measured strains (raw data) and average values of measured strains corrected for thermal influence for test pile 7.

Constant rate of uplift (CRU) test

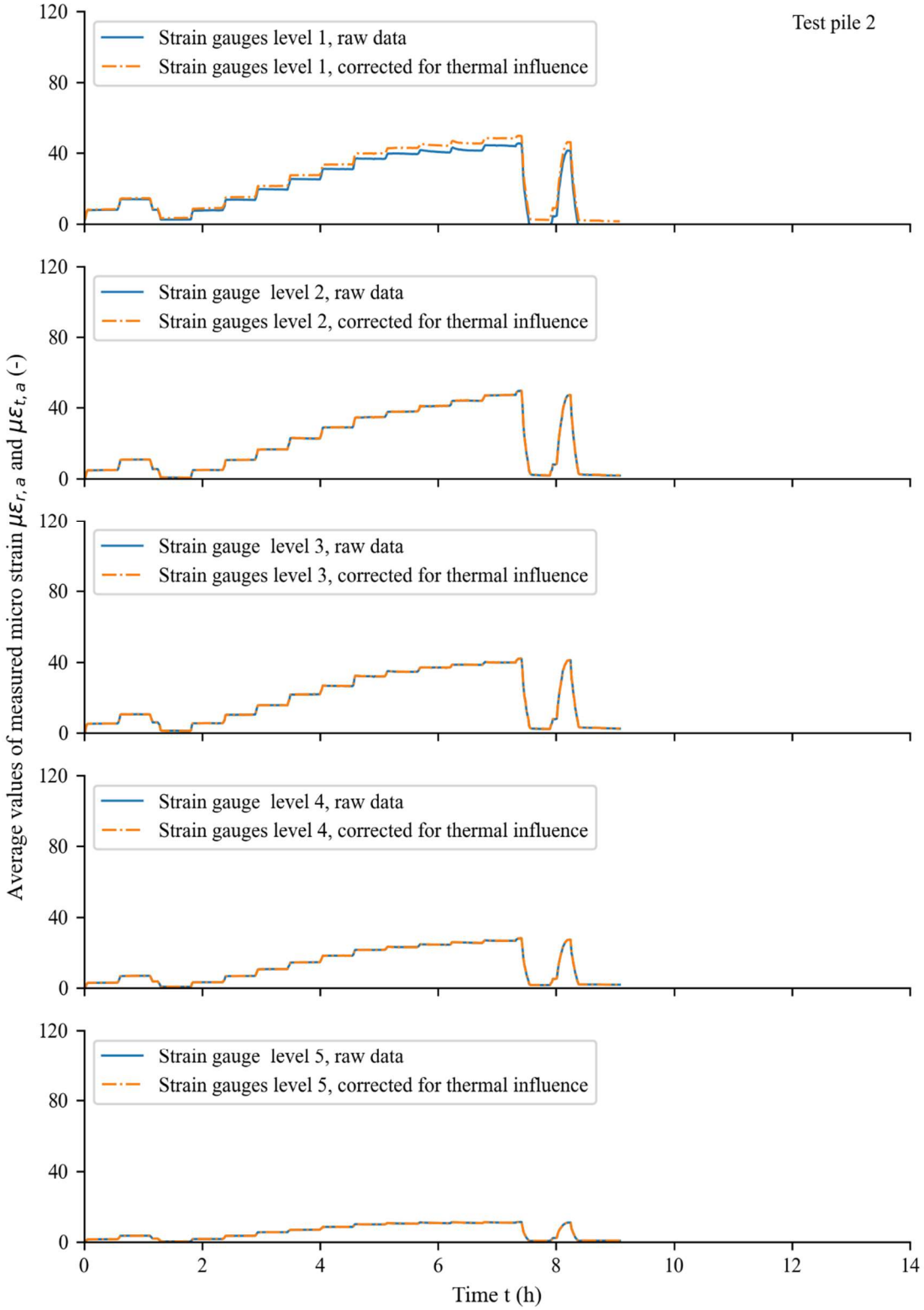

Figure 149: Average values of measured strains (raw data) and average values of measured strains corrected for thermal influence for test pile 2.

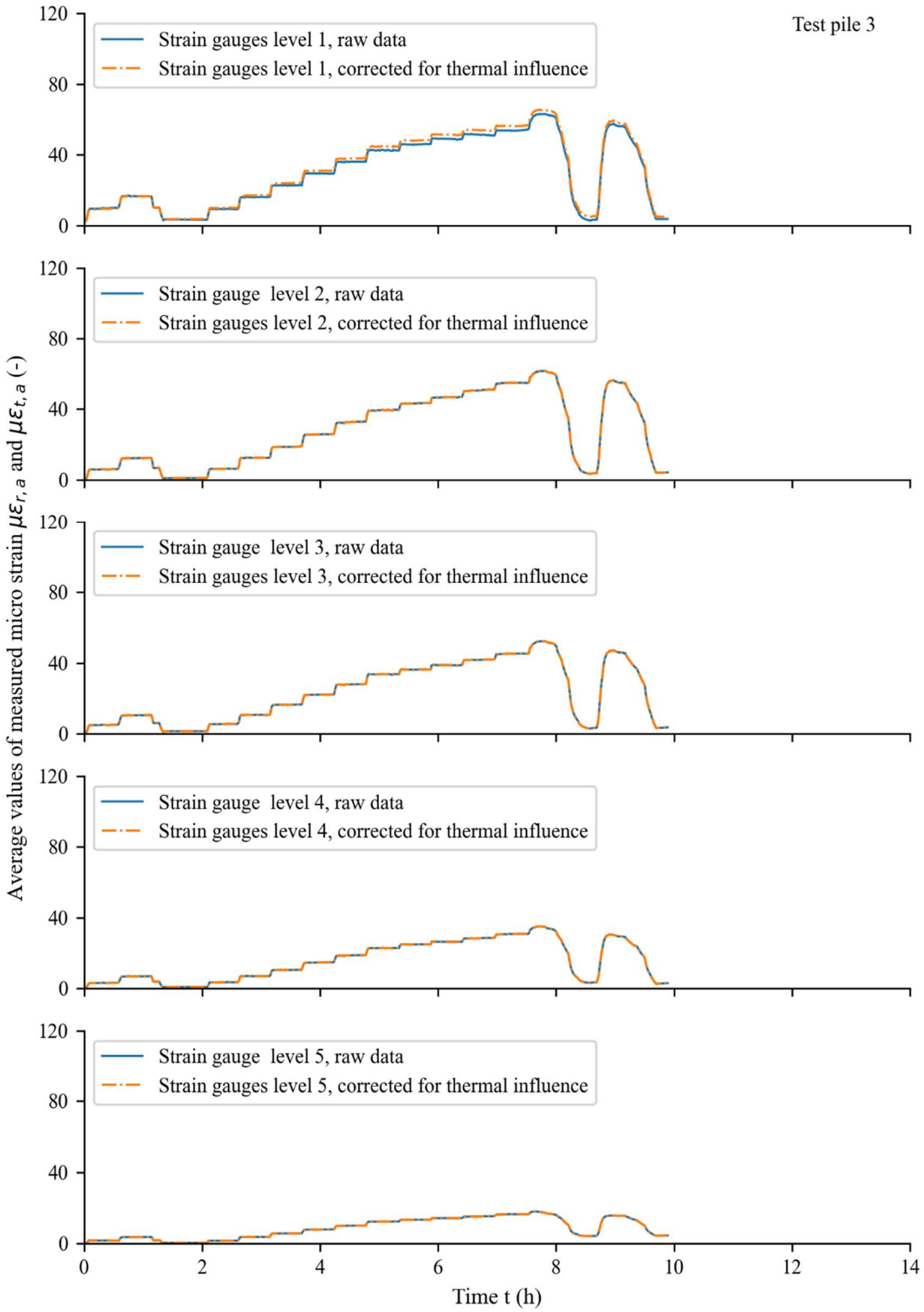

Figure 150: Average values of measured strains (raw data) and average values of measured strains corrected for thermal influence for test pile 3.

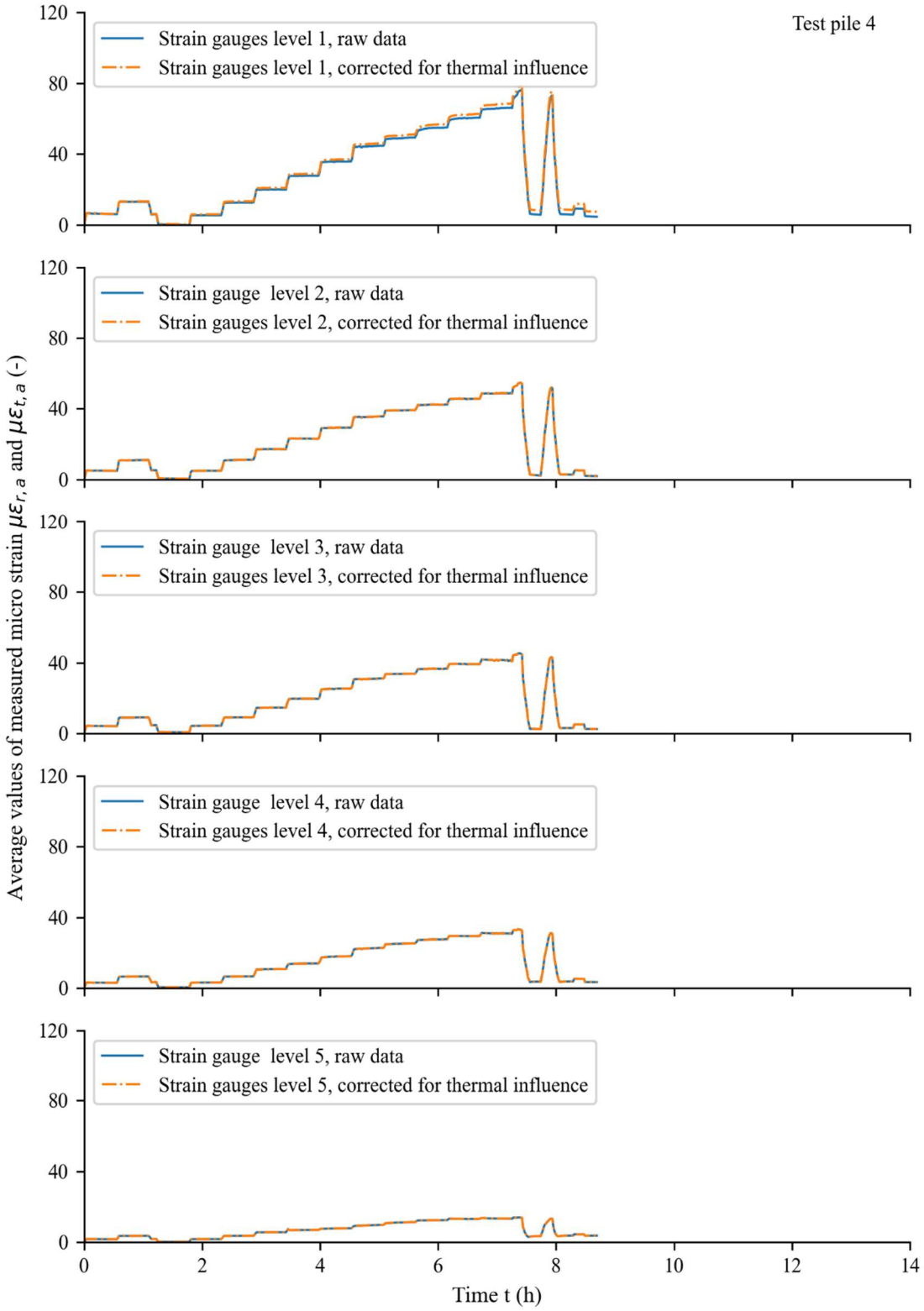

Figure 151: Average values of measured strains (raw data) and average values of measured strains corrected for thermal influence for test pile 4.

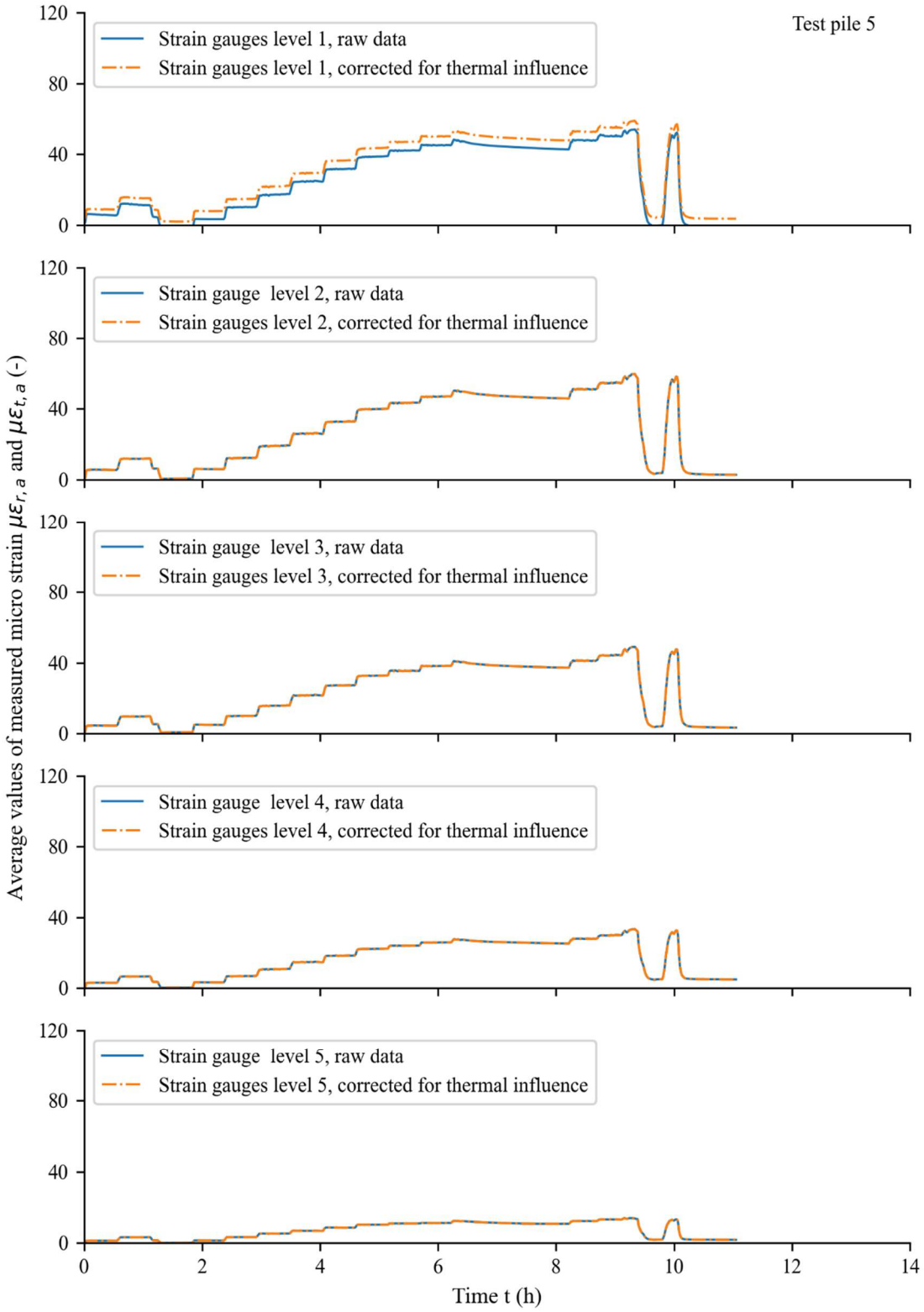

Figure 152: Average values of measured strains (raw data) and average values of measured strains corrected for thermal influence for test pile 5.

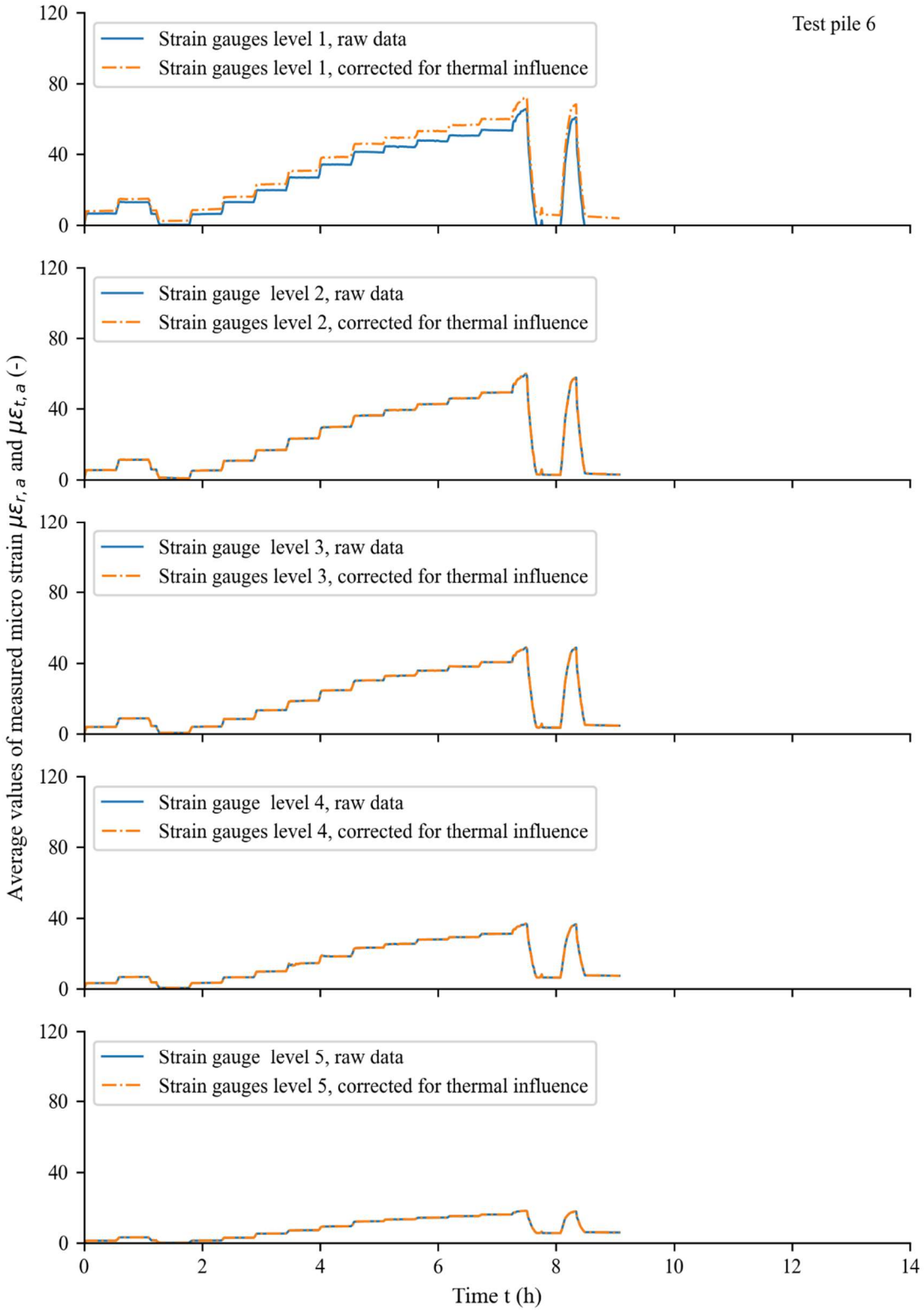

Figure 153: Average values of measured strains (raw data) and average values of measured strains corrected for thermal influence for test pile 6.

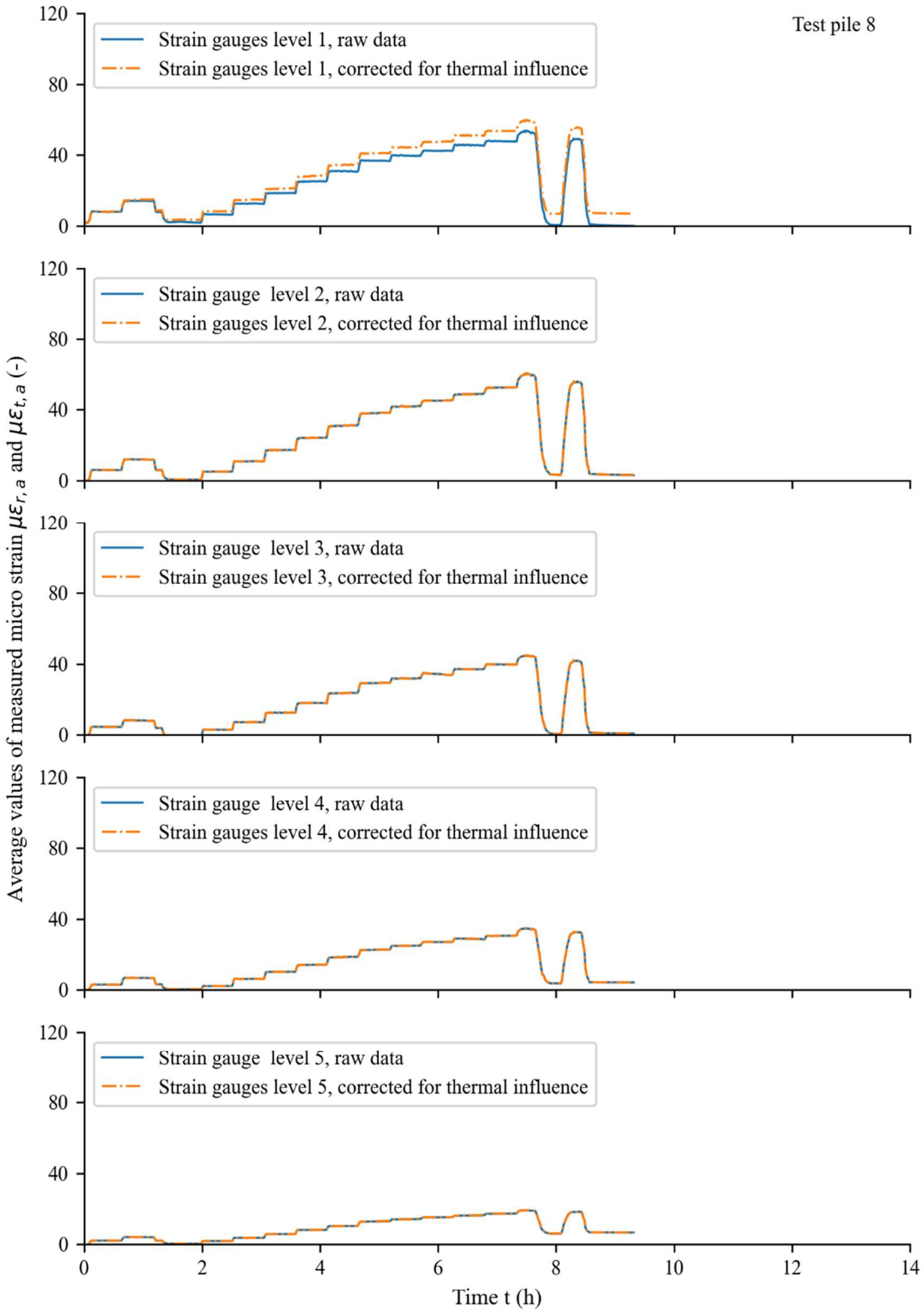

Figure 154: Average values of measured strains (raw data) and average values of measured strains corrected for thermal influence for test pile 8.

H.3 Time-strain curves

Maintained load (ML) test

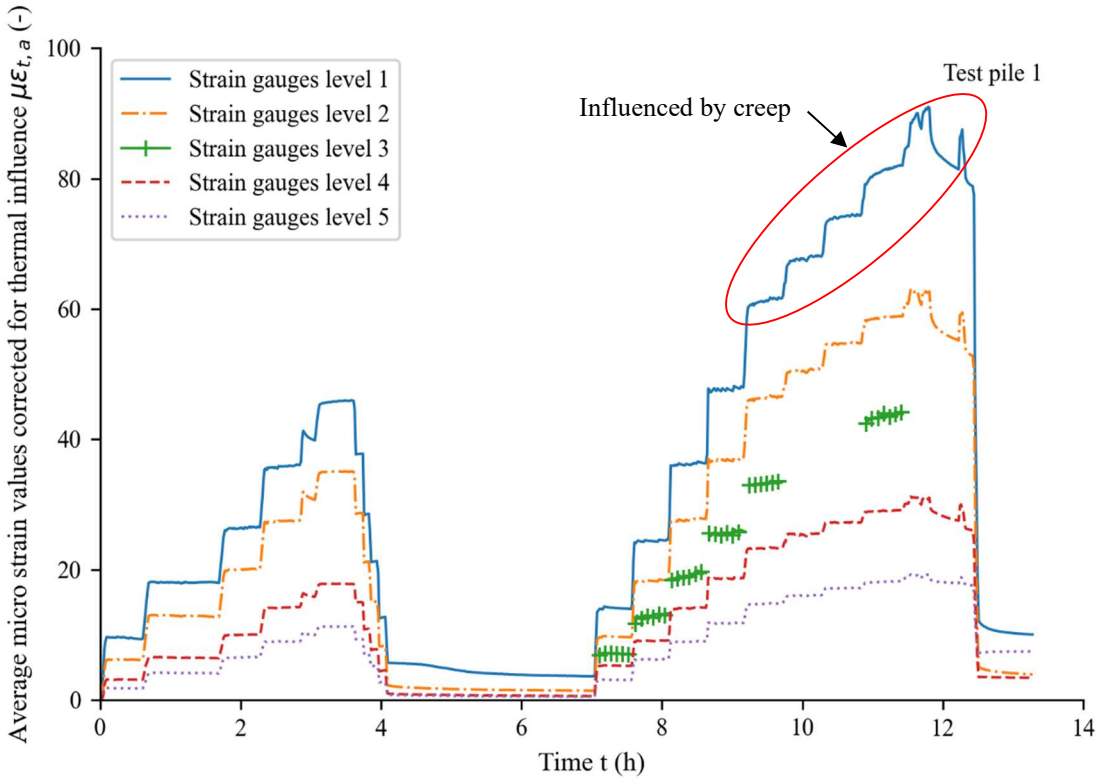

Figure 155: Average values of measured strains corrected for thermal influence for test pile 1.

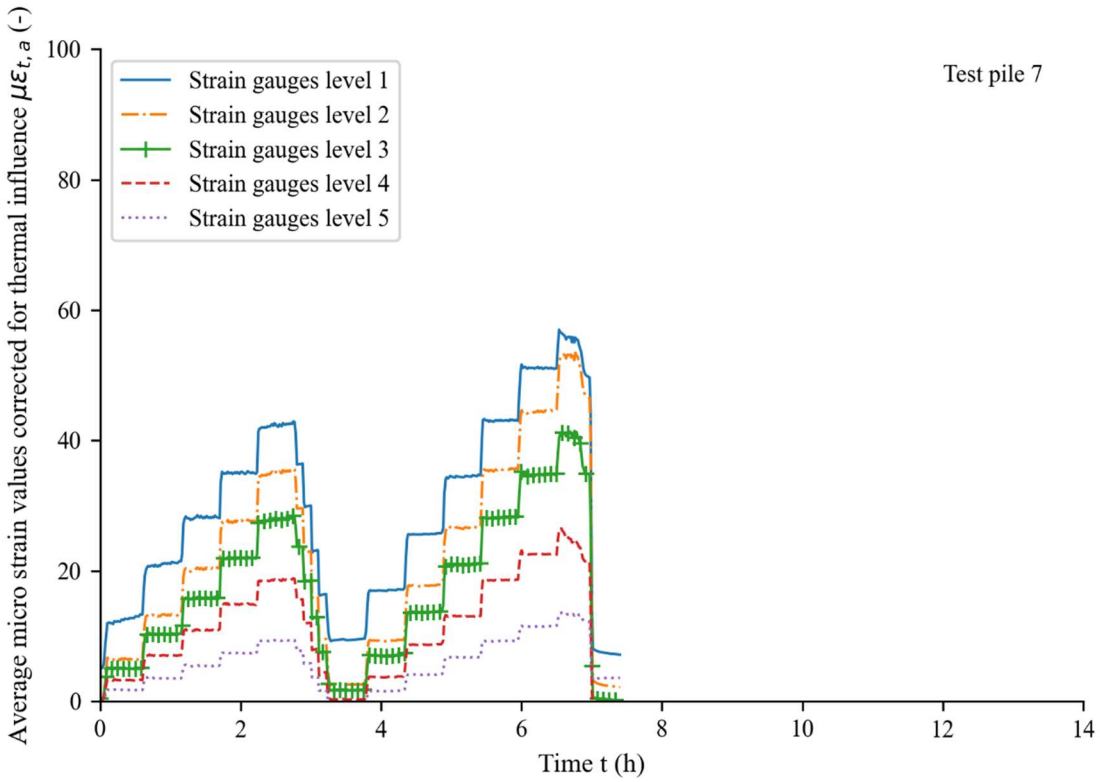

Figure 156: Average values of measured strains corrected for thermal influence for test pile 7.

Constant rate of uplift (CRU) test

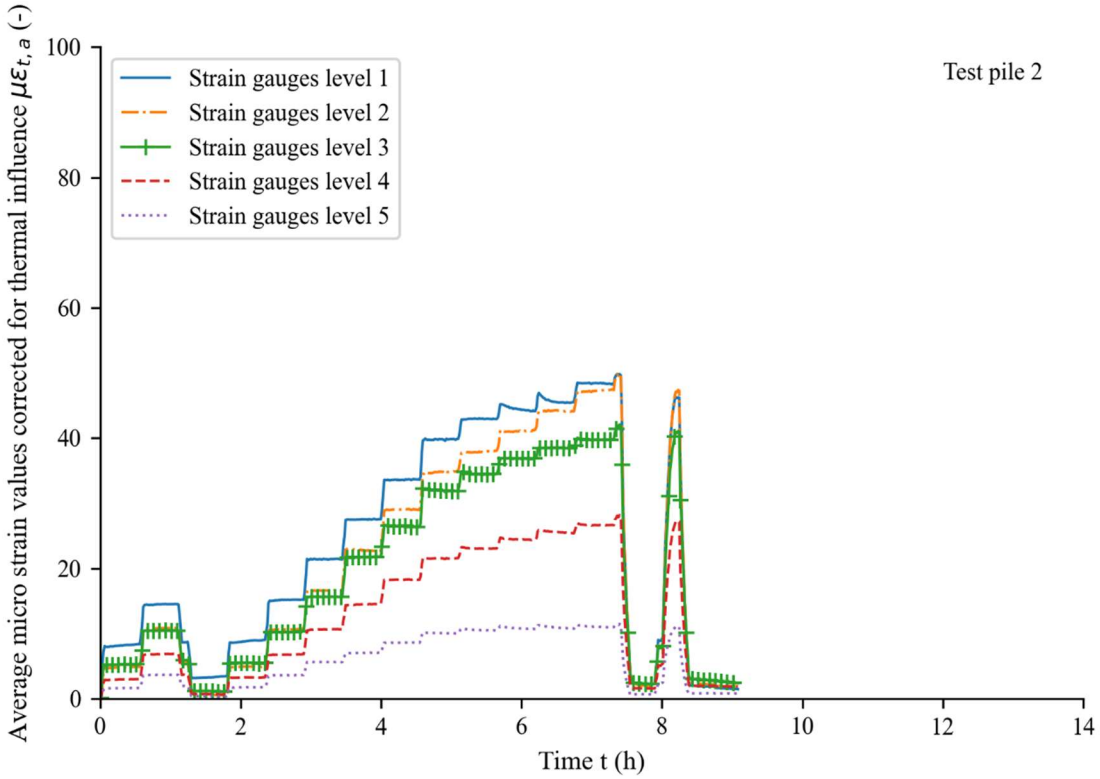

Figure 157: Average values of measured strains corrected for thermal influence for test pile 2.

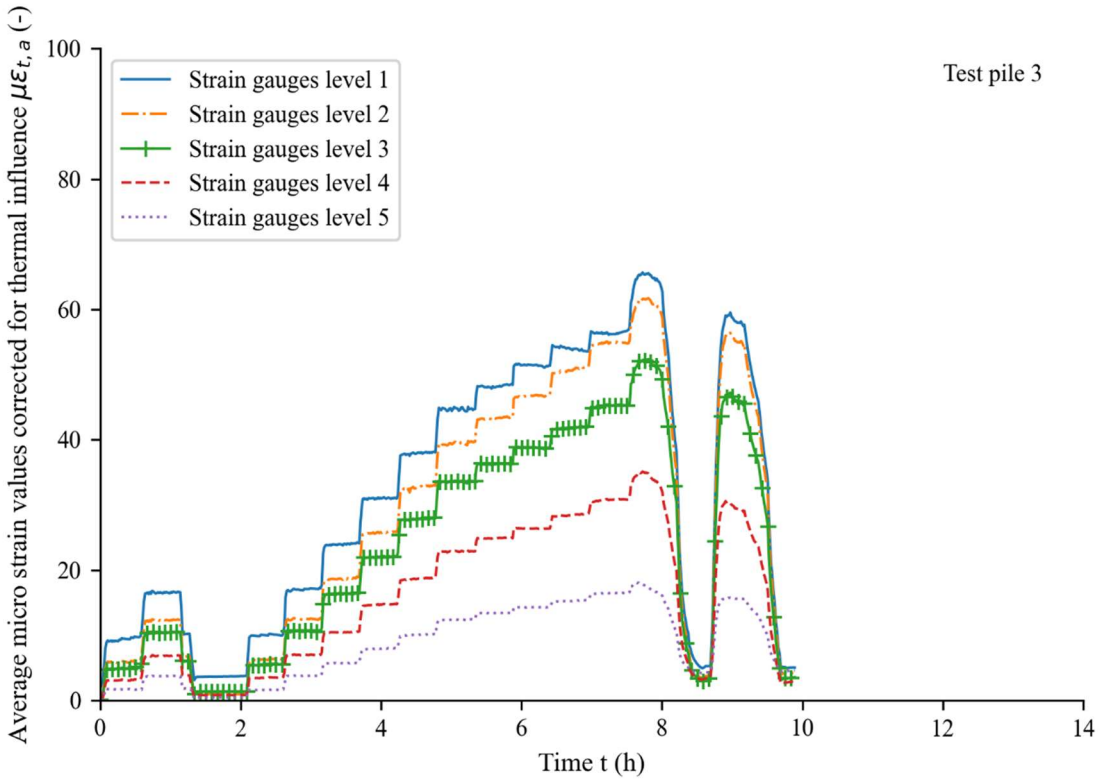

Figure 158: Average values of measured strains corrected for thermal influence for test pile 3.

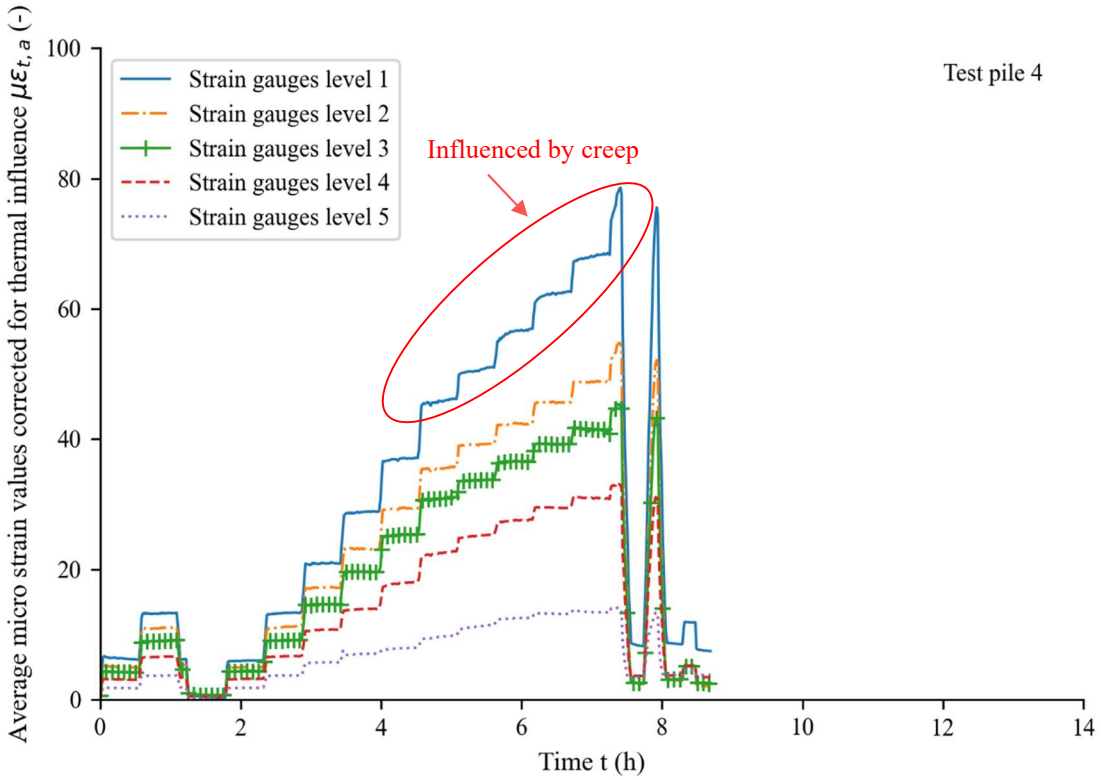

Figure 159: Average values of measured strains corrected for thermal influence for test pile 4.

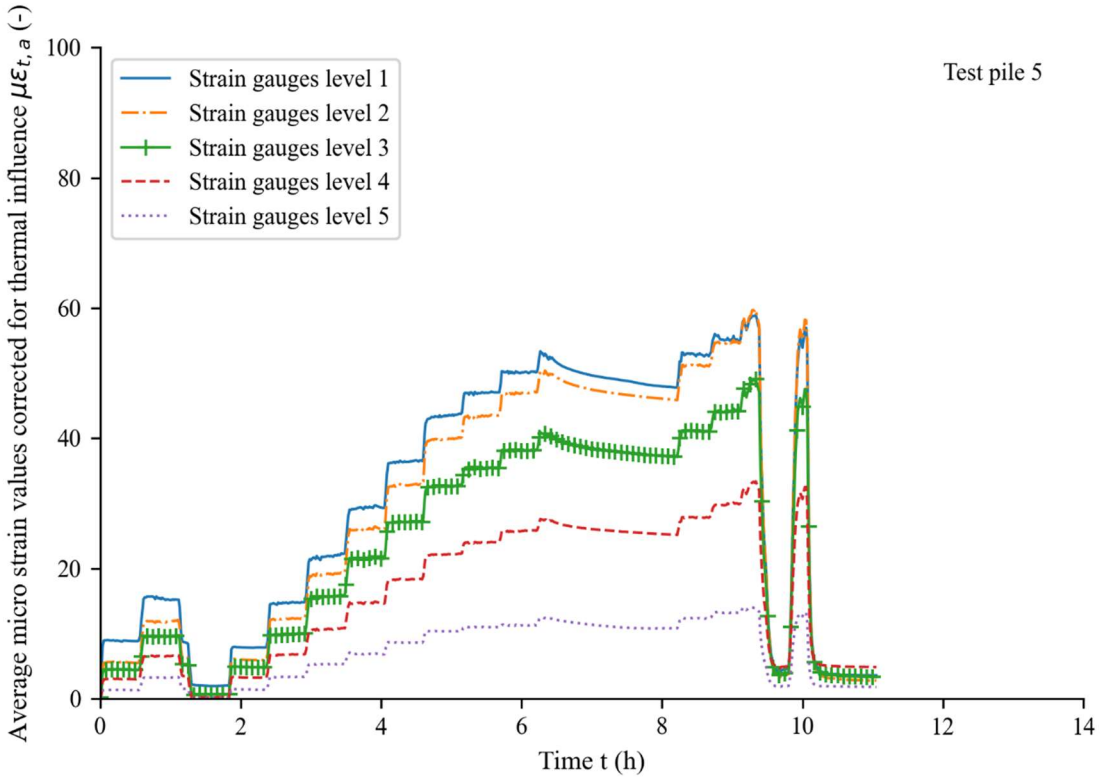

Figure 160: Average values of measured strains corrected for thermal influence for test pile 5.

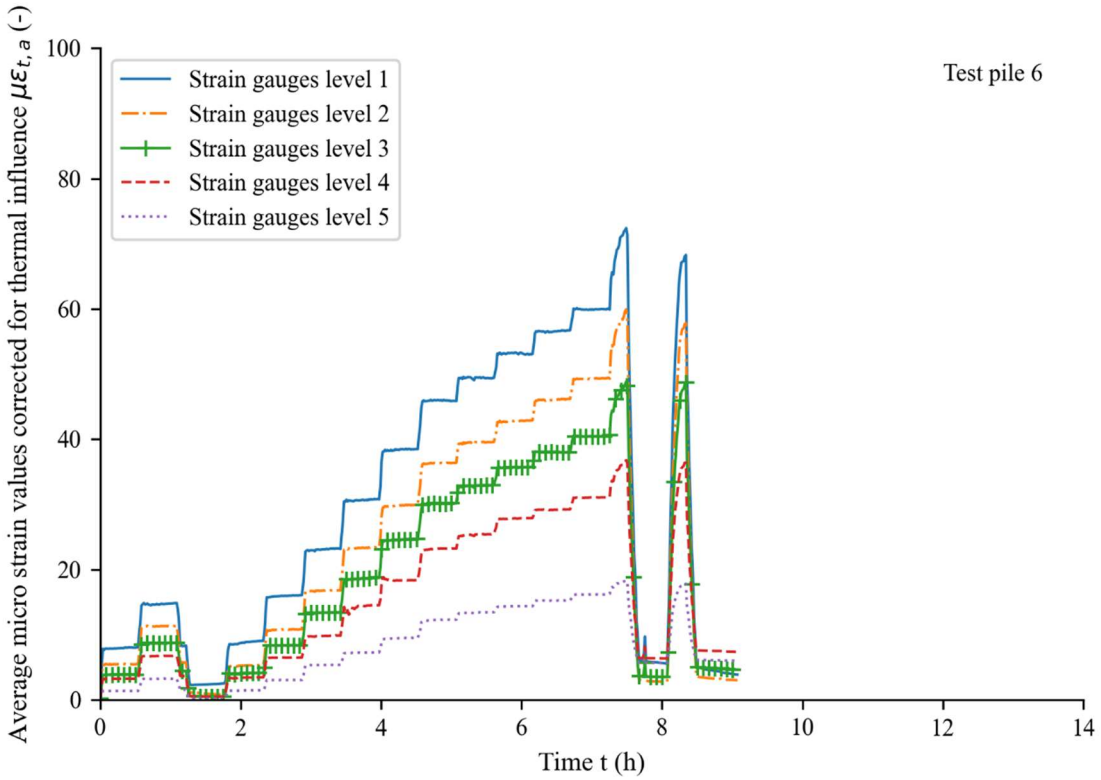

Figure 161: Average values of measured strains corrected for thermal influence for test pile 6.

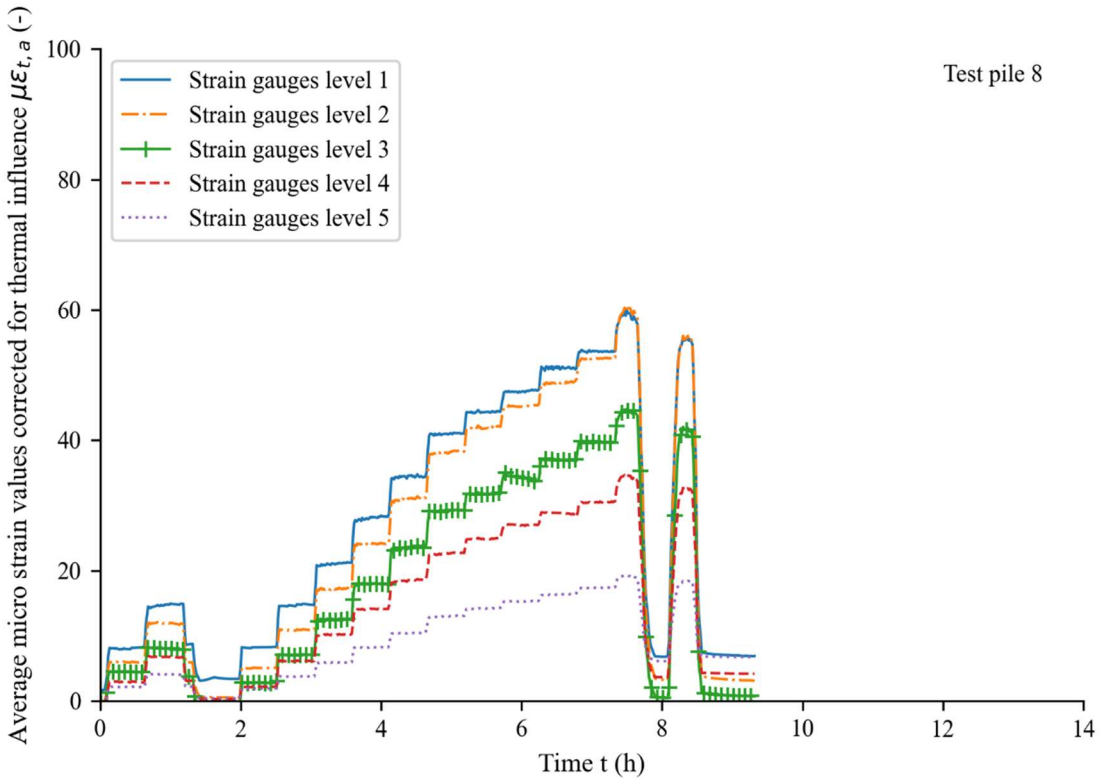

Figure 162: Average values of measured strains corrected for thermal influence for test pile 8.

H.4 Strain-pile length curves

Maintained load (ML) test

Test pile 1

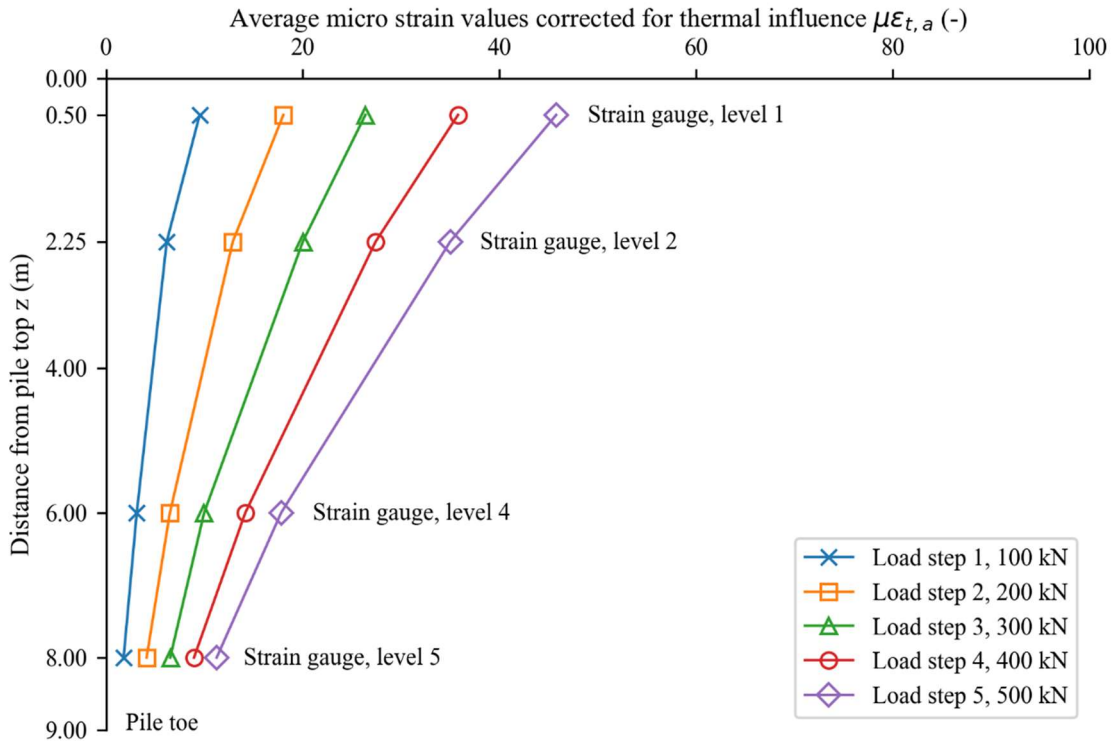

Figure 163: Strain development along the length of test pile 1 in load phase 1.

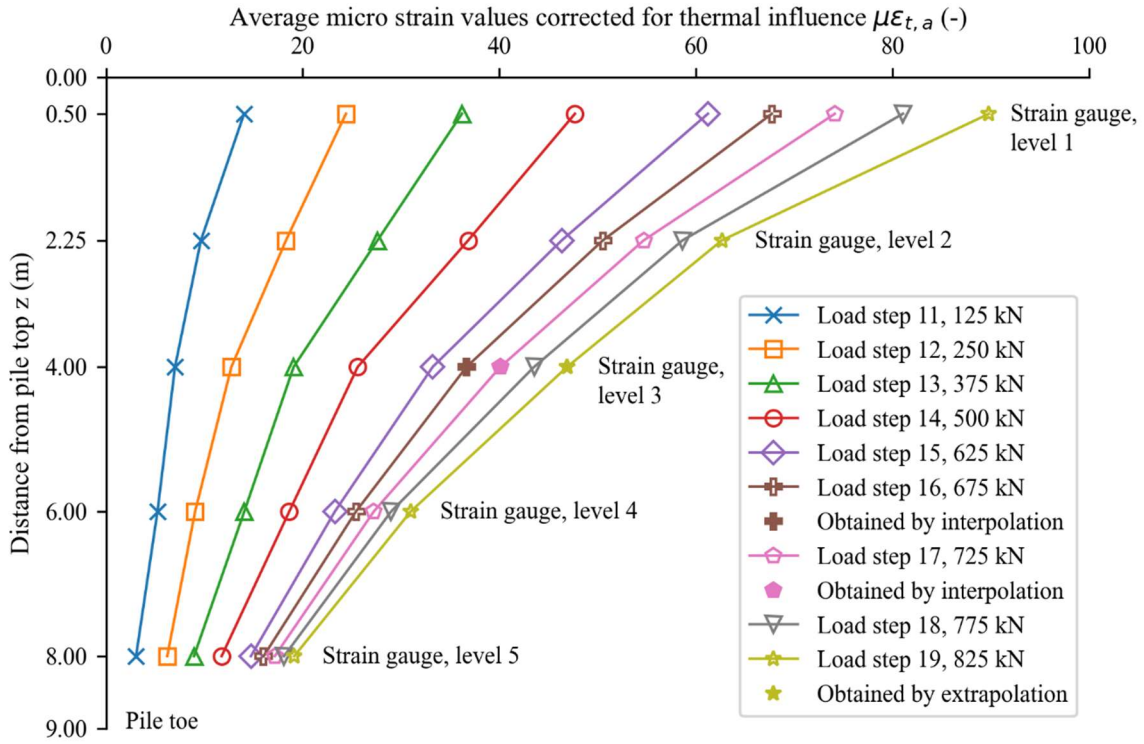

Figure 164: Strain development along the length of test pile 1 in load phase 2.

Test pile 7

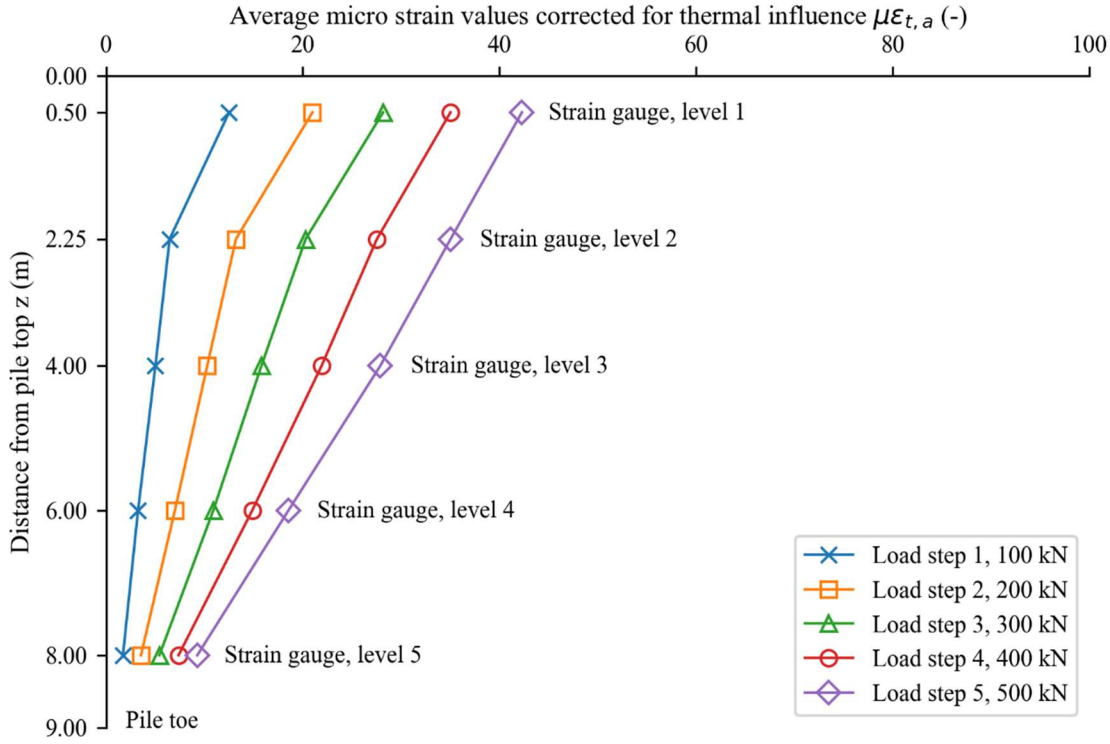

Figure 165: Strain development along the length of test pile 7 in load phase 1.

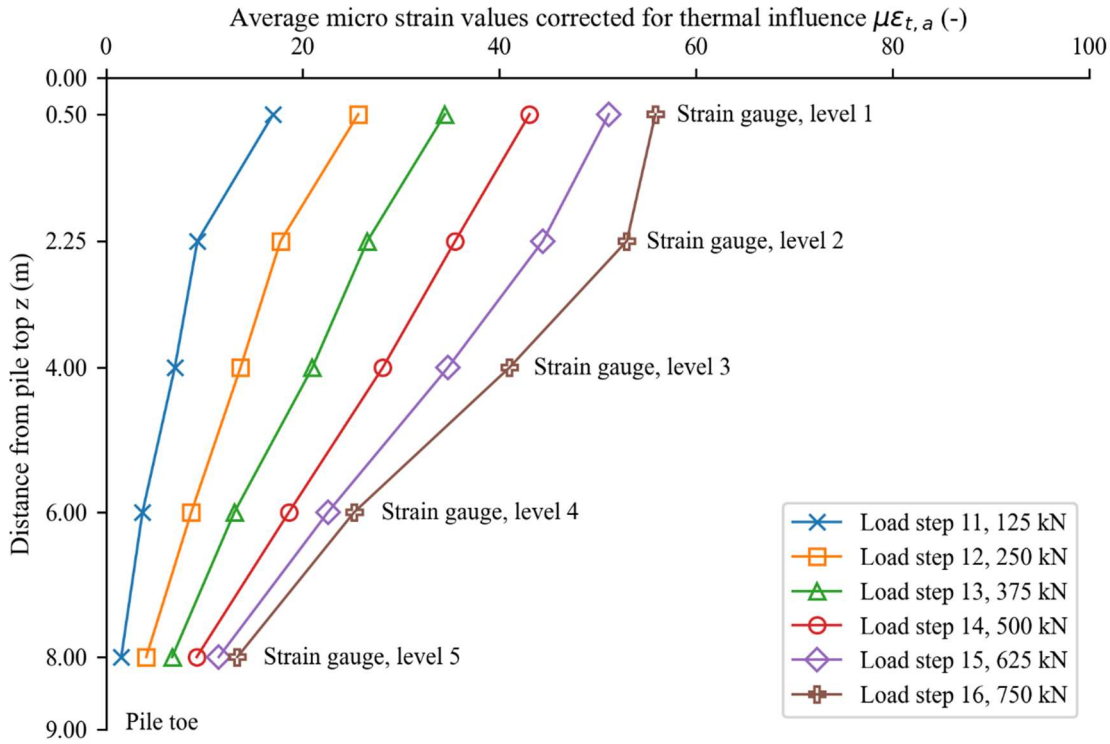

Figure 166: Strain development along the length of test pile 7 in load phase 2.

Constant rate of uplift (CRU) test

Test pile 2

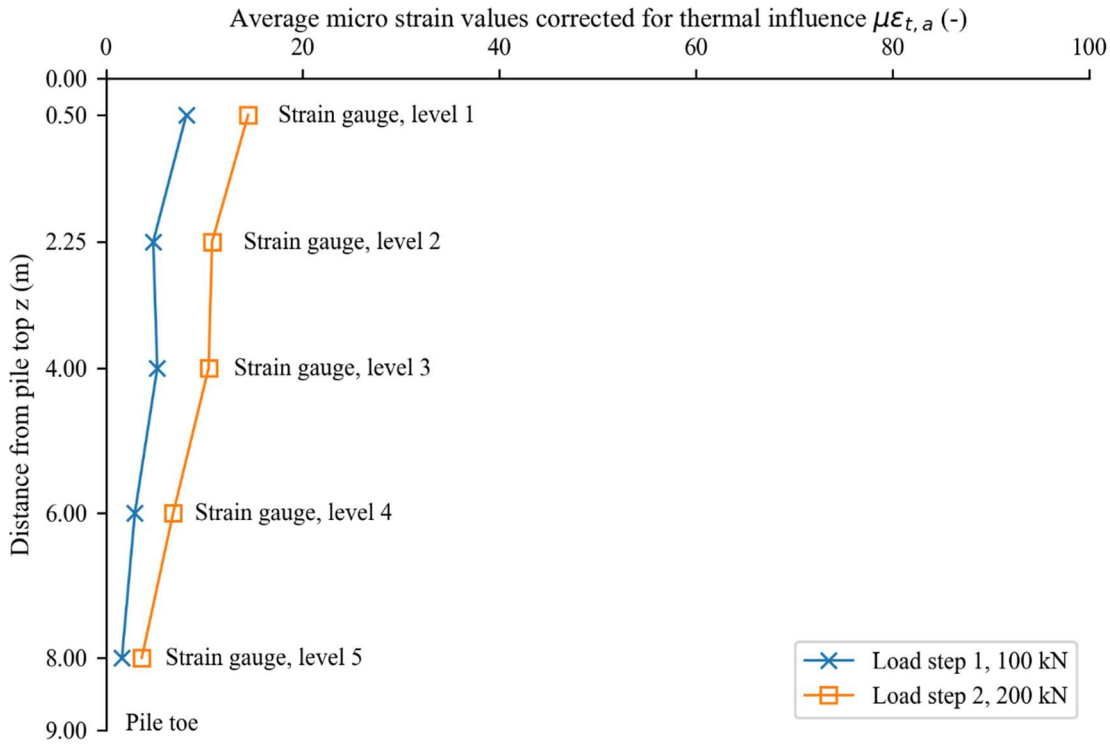

Figure 167: Strain development along the length of test pile 2 in load phase 1.

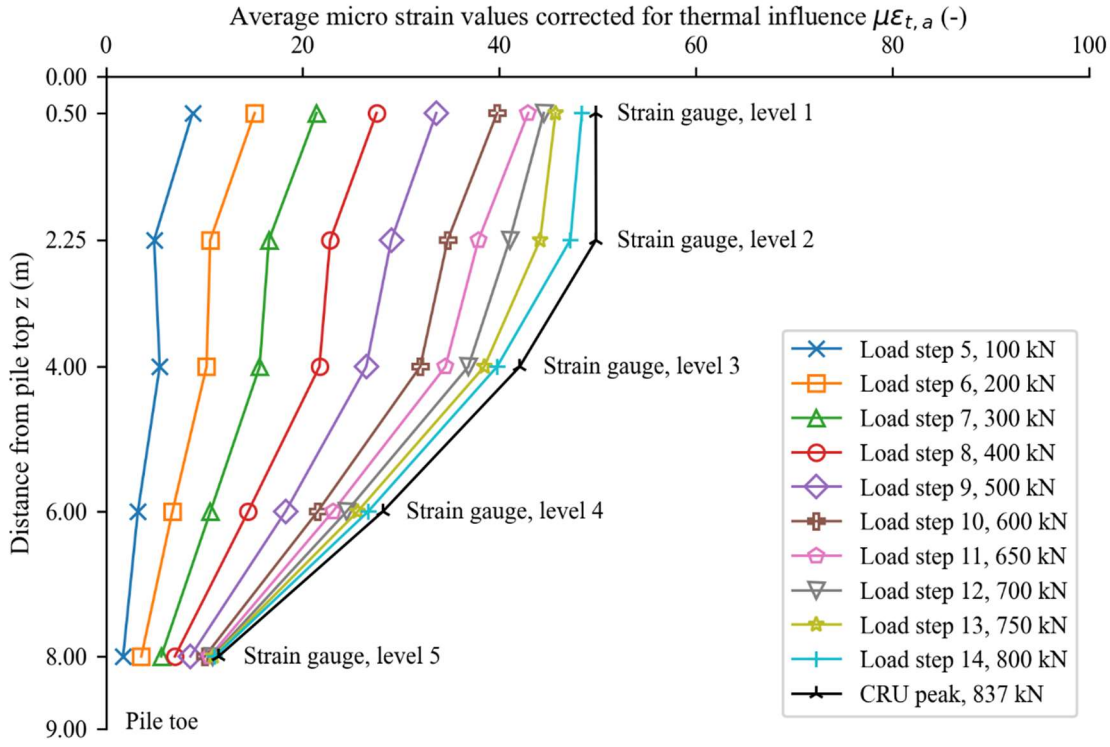

Figure 168: Strain development along the length of test pile 2 in load phase 2.

Test pile 3

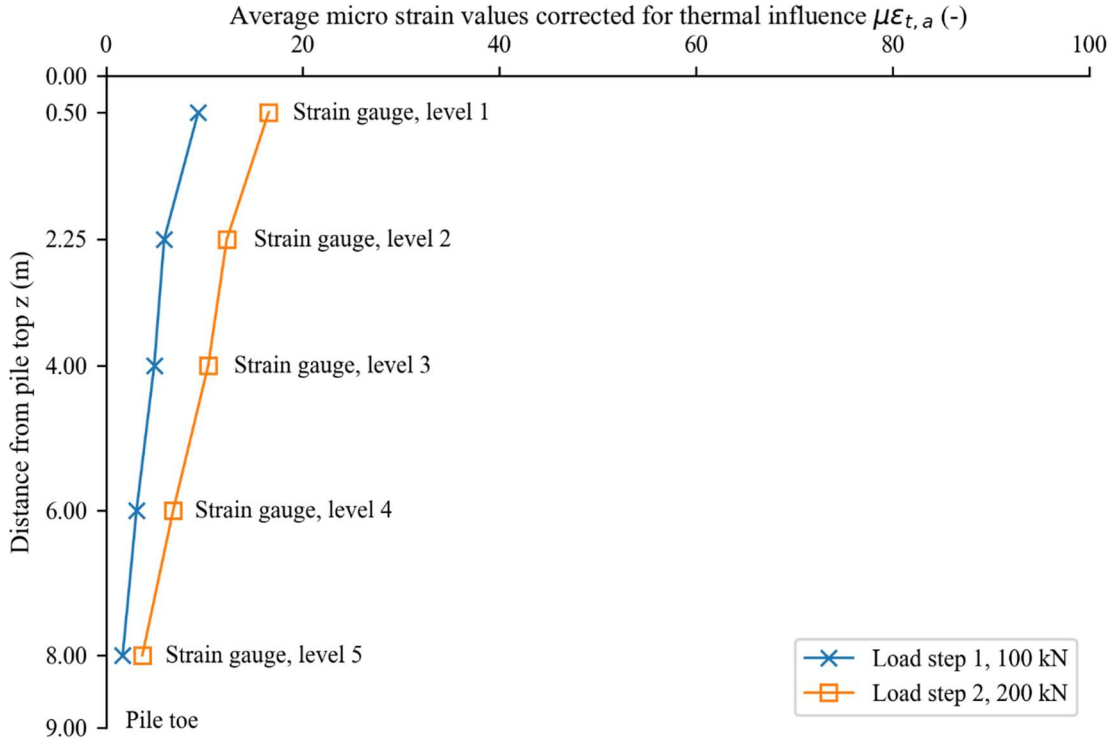

Figure 169: Strain development along the length of test pile 3 in load phase 1.

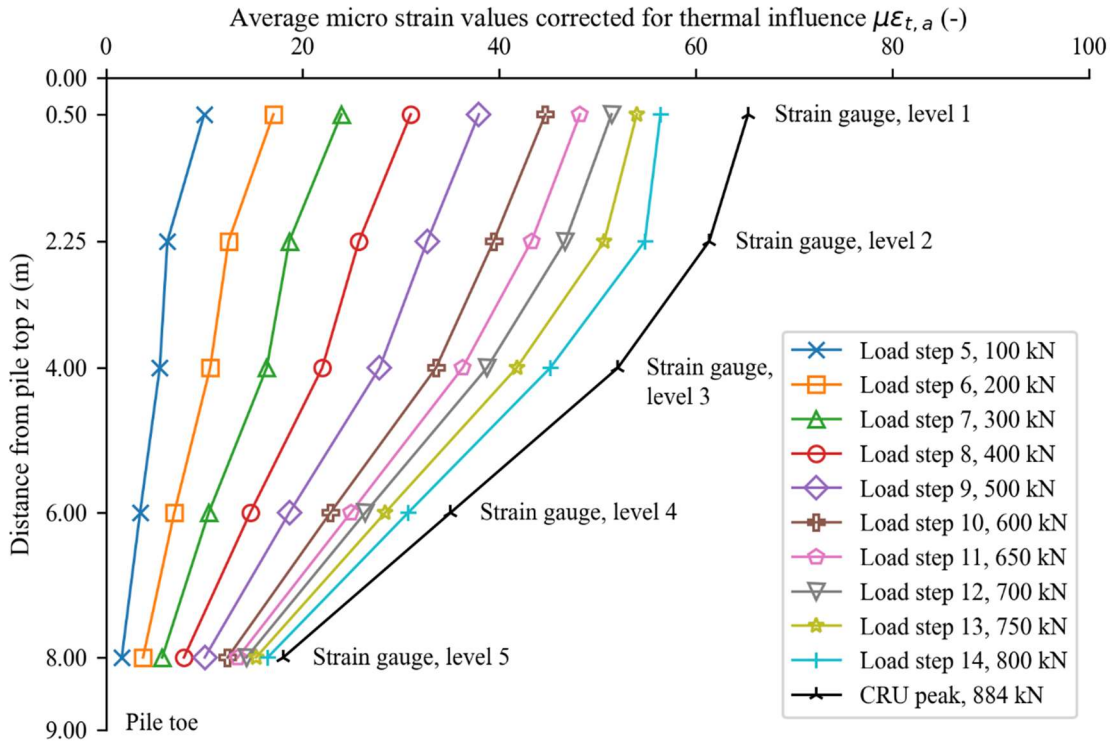

Figure 170: Strain development along the length of test pile 3 in load phase 2.

Test pile 4

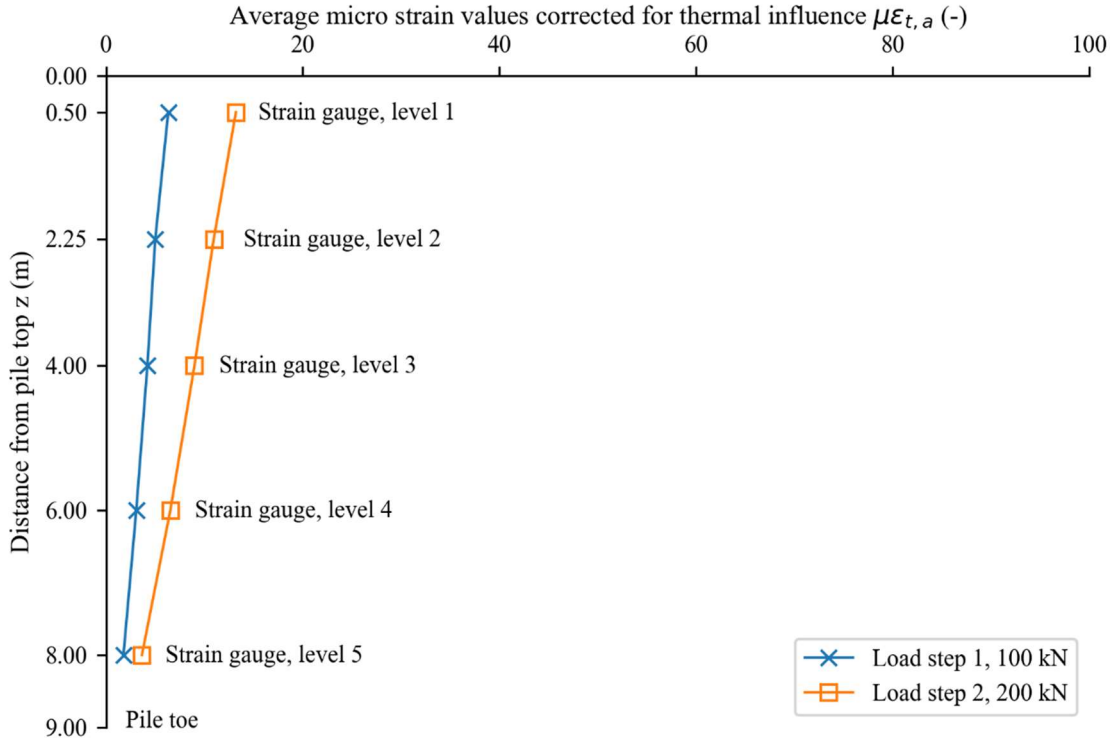

Figure 171: Strain development along the length of test pile 4 in load phase 1.

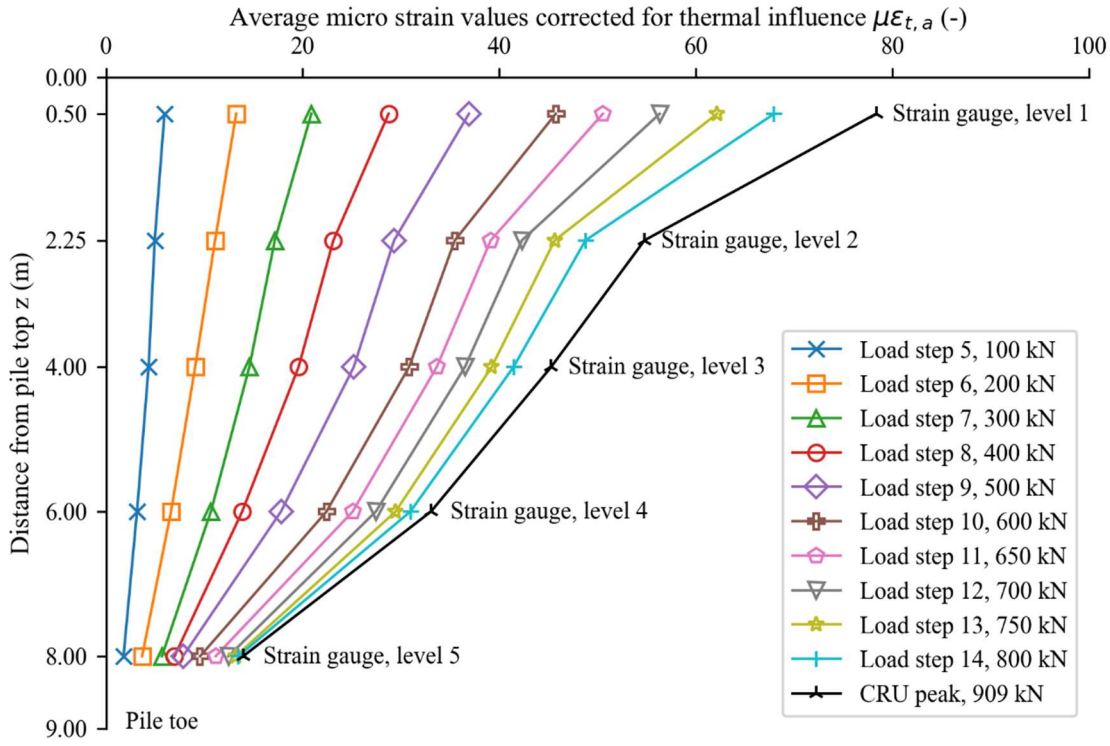

Figure 172: Strain development along the length of test pile 4 in load phase 2

Test pile 5

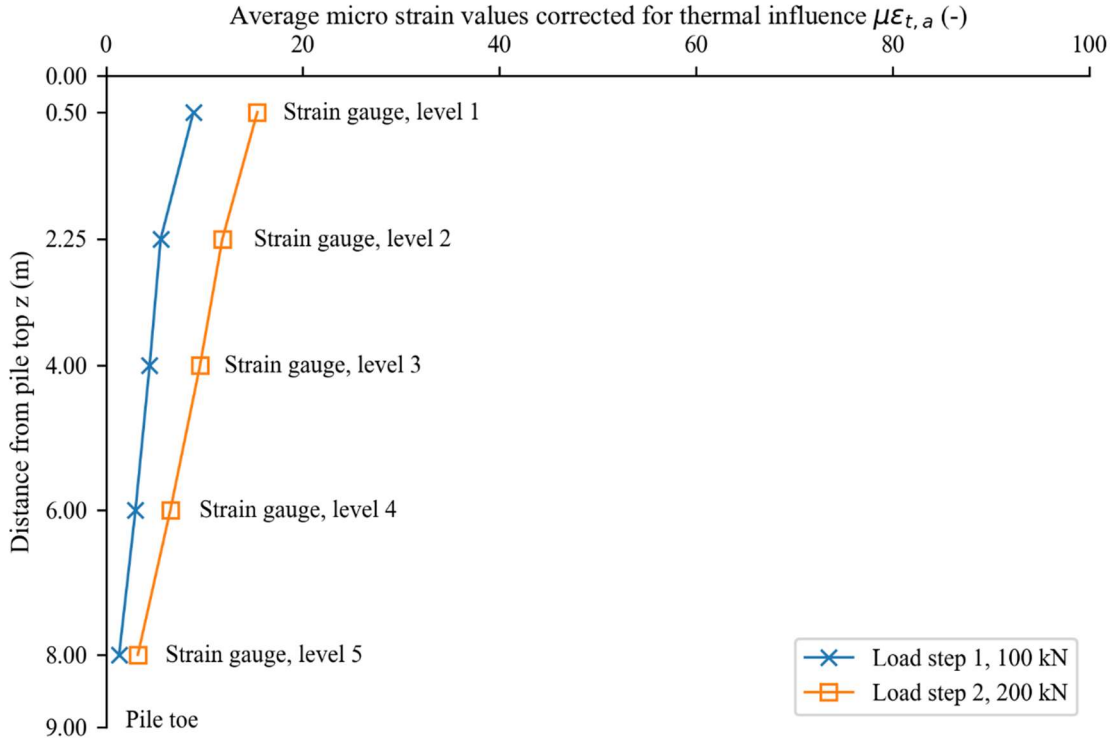

Figure 173: Strain development along the length of test pile 5 in load phase 1.

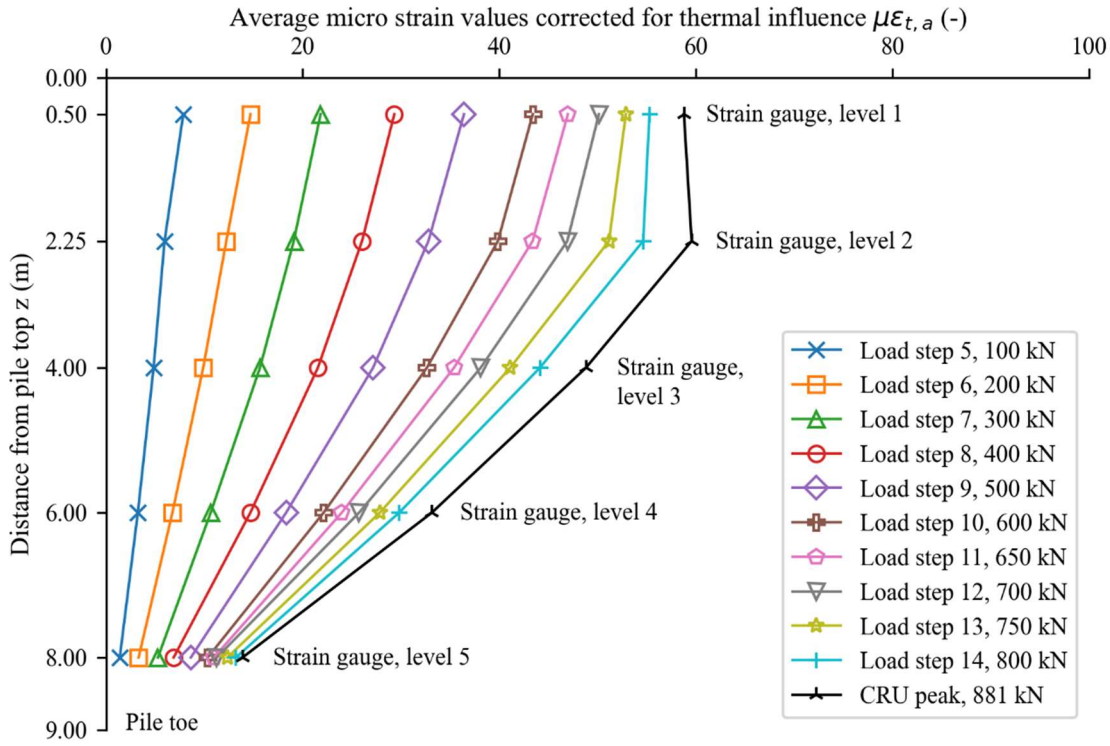

Figure 174: Strain development along the length of test pile 5 in load phase 2.

Test pile 6

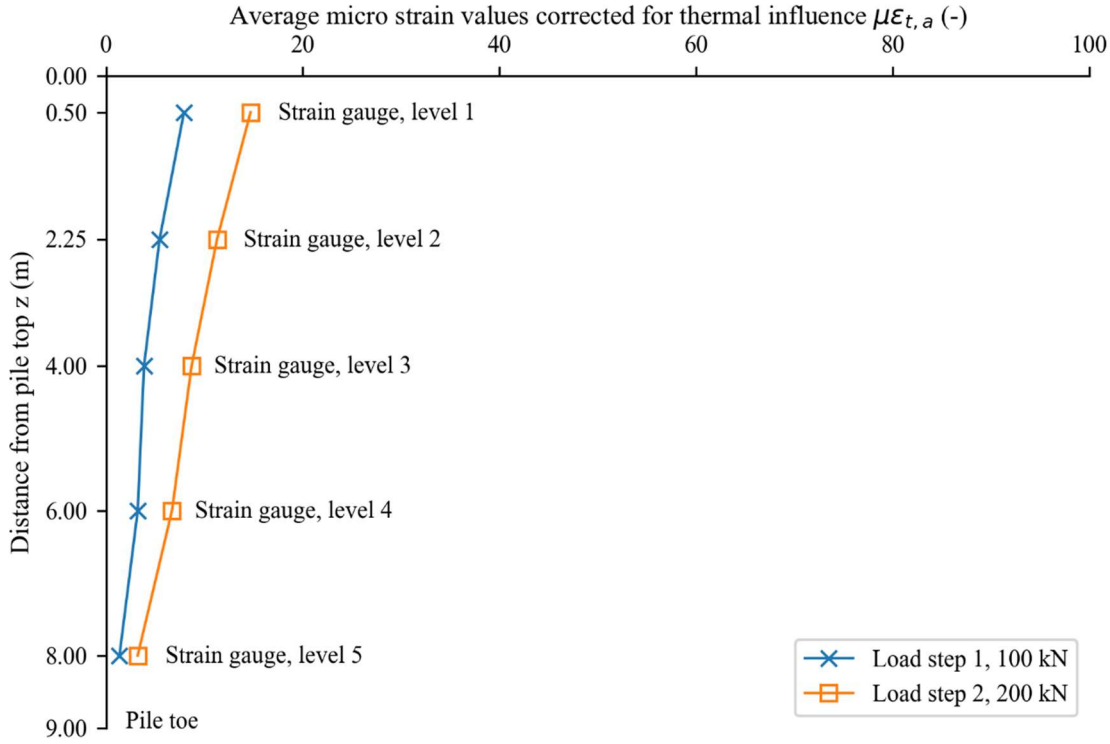

Figure 175: Strain development along the length of test pile 6 in load phase 1.

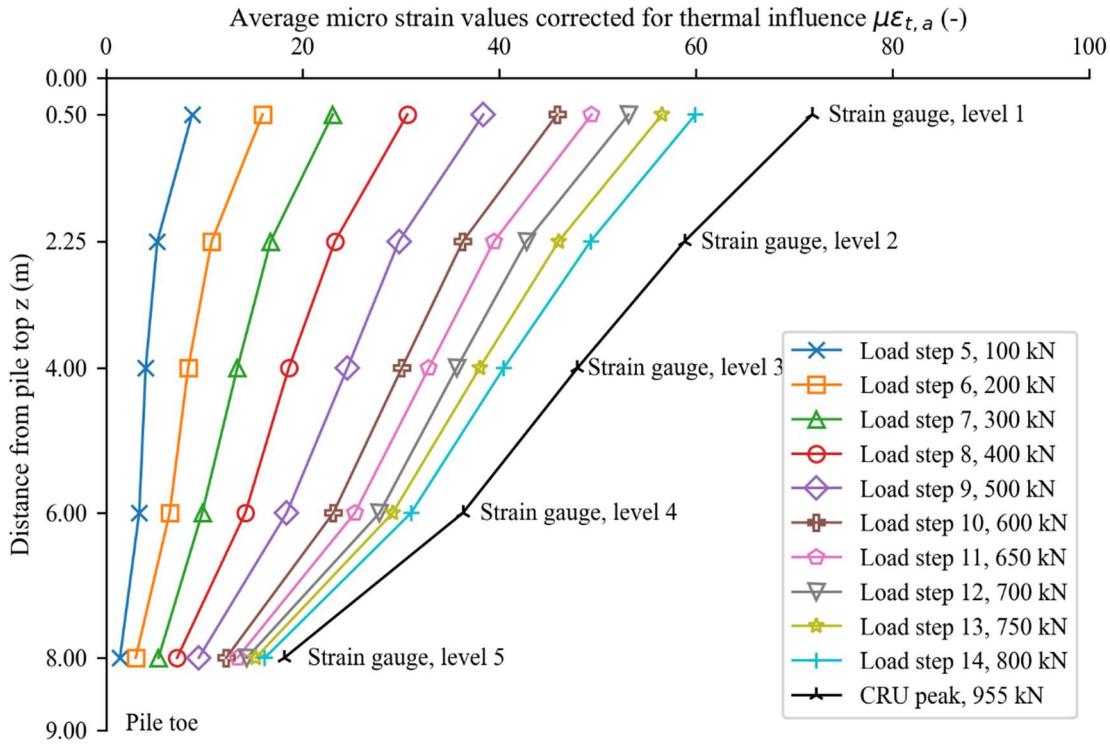

Figure 176: Strain development along the length of test pile 6 in load phase 2.

Test pile 8

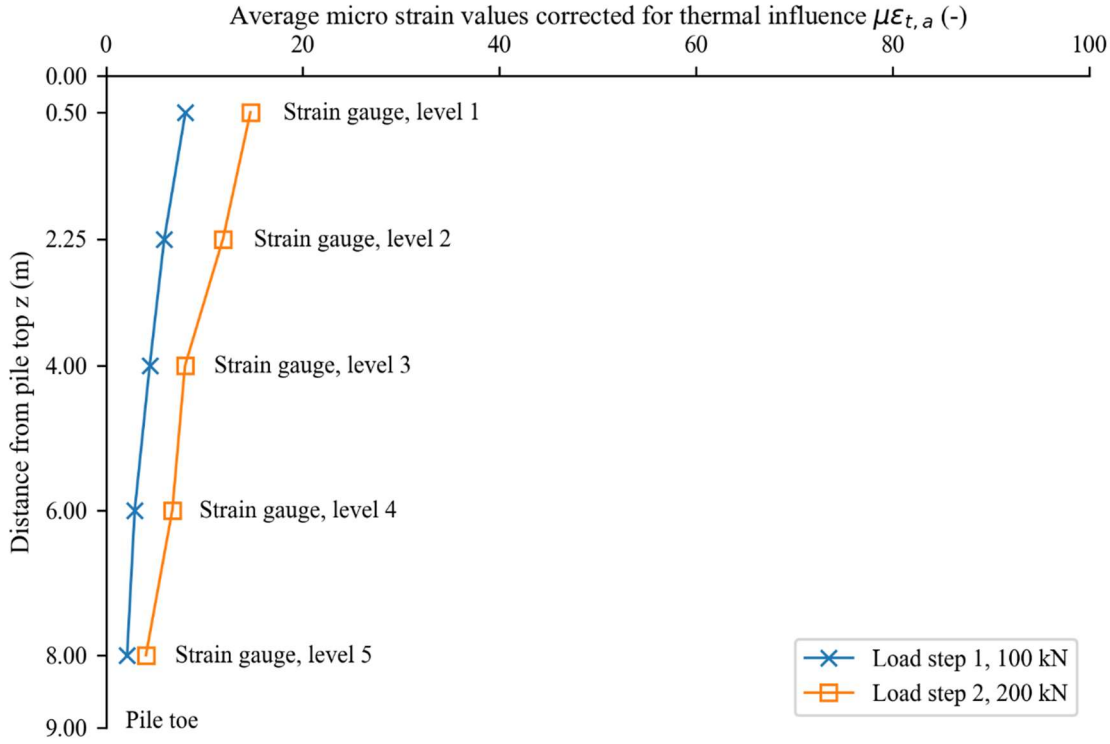

Figure 177: Strain development along the length of test pile 8 in load phase 1.

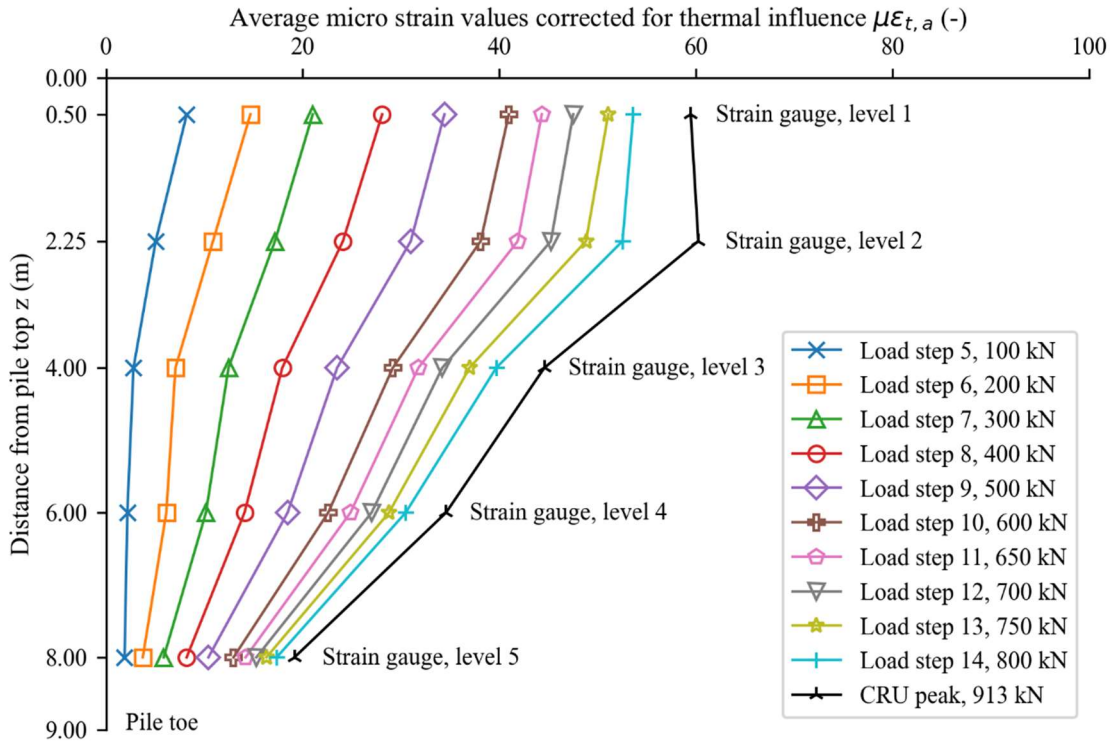

Figure 178: Strain development along the length of test pile 8 in load phase 2.

H.5 Axial stiffness determined by direct secant method

Maintained load (ML) test

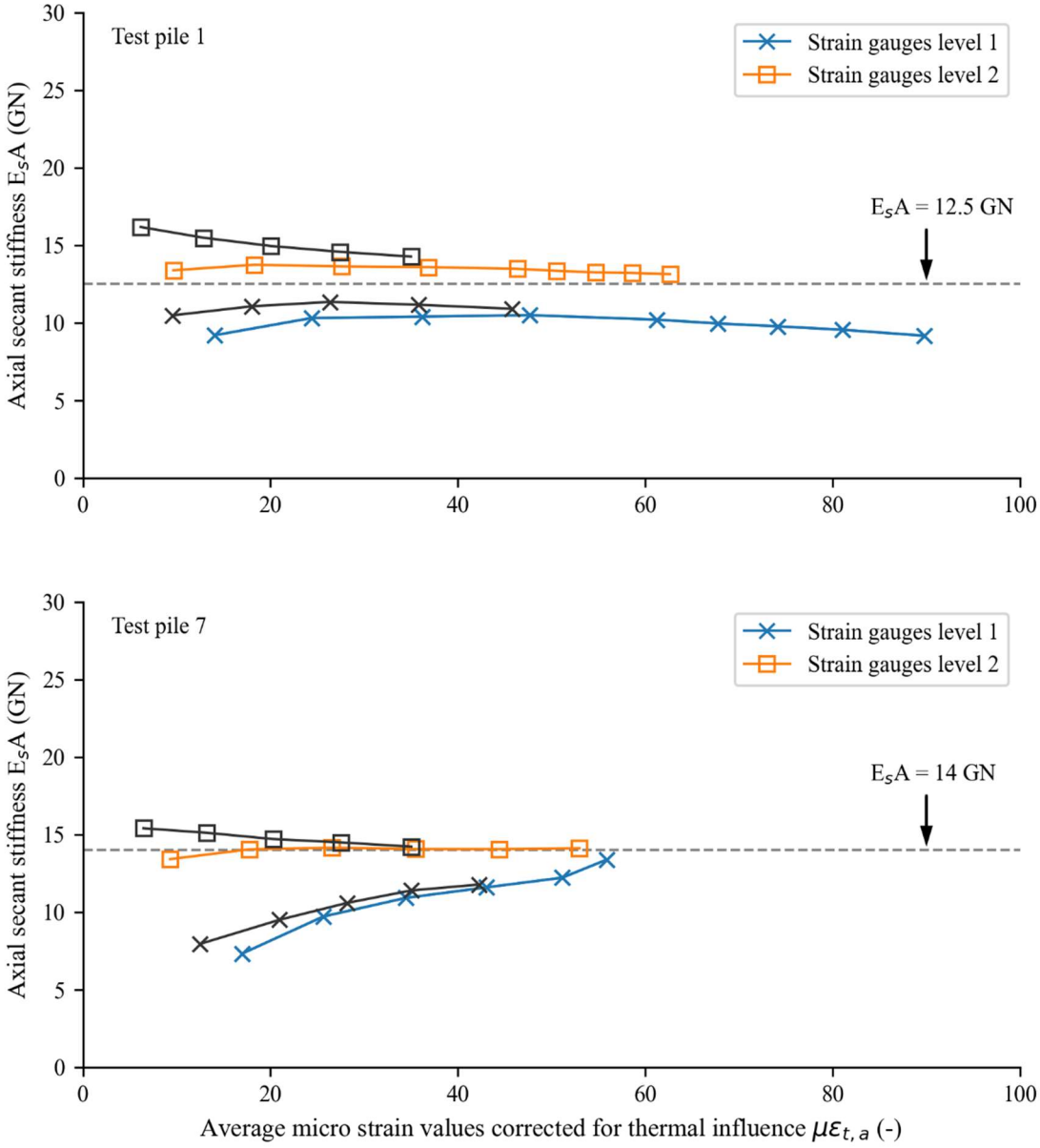

Figure 179: Axial stiffness determined by direct secant method for strain gauge level 1-2 in test pile 1 and 7. Load phase 1 is presented *in black.*

Constant rate of uplift (CRU) test

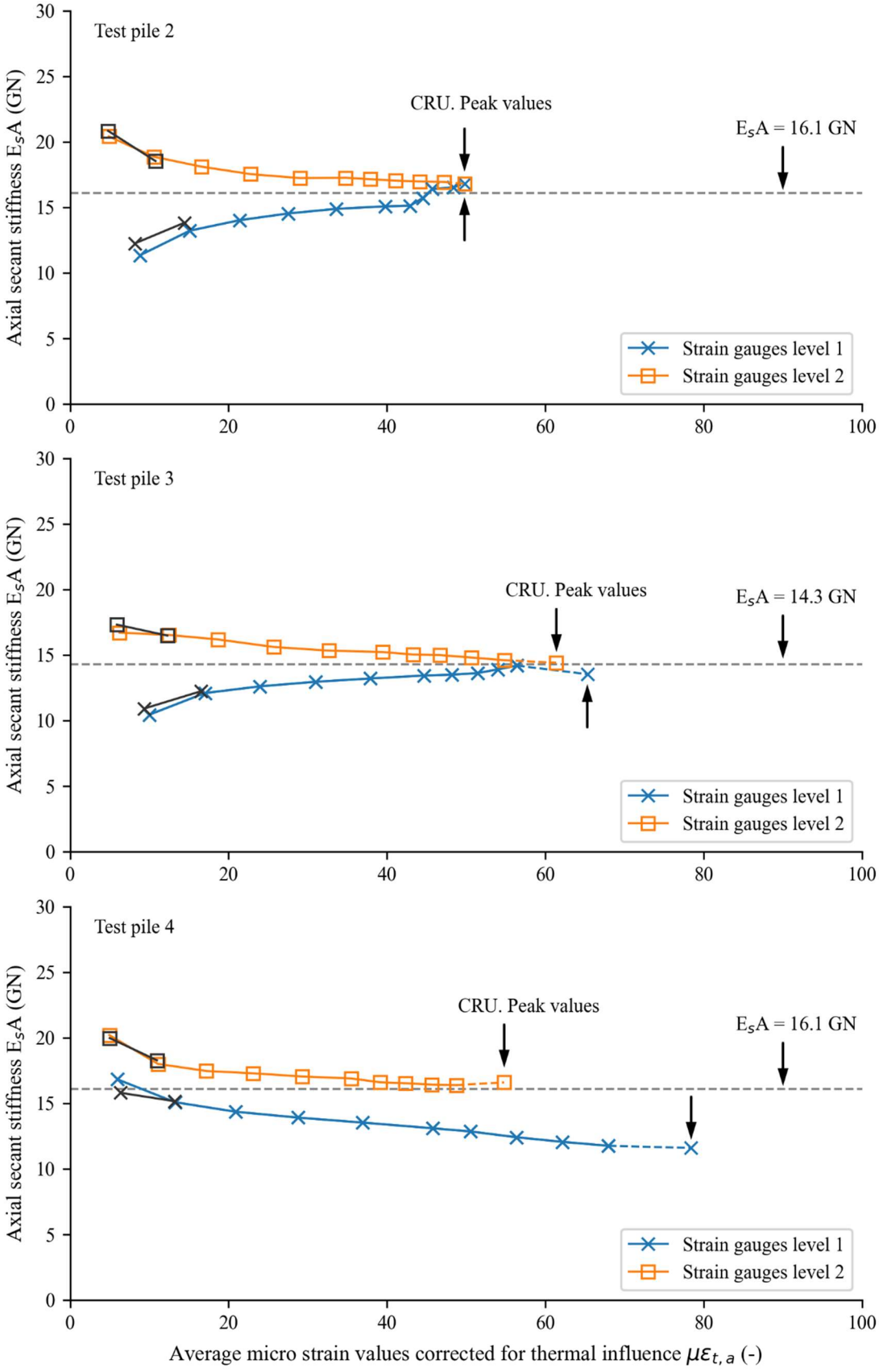

Figure 180: Axial stiffness determined by direct secant method for strain gauge level 1-2 in test pile 2-4. Load phase 1 is presented *in black.*

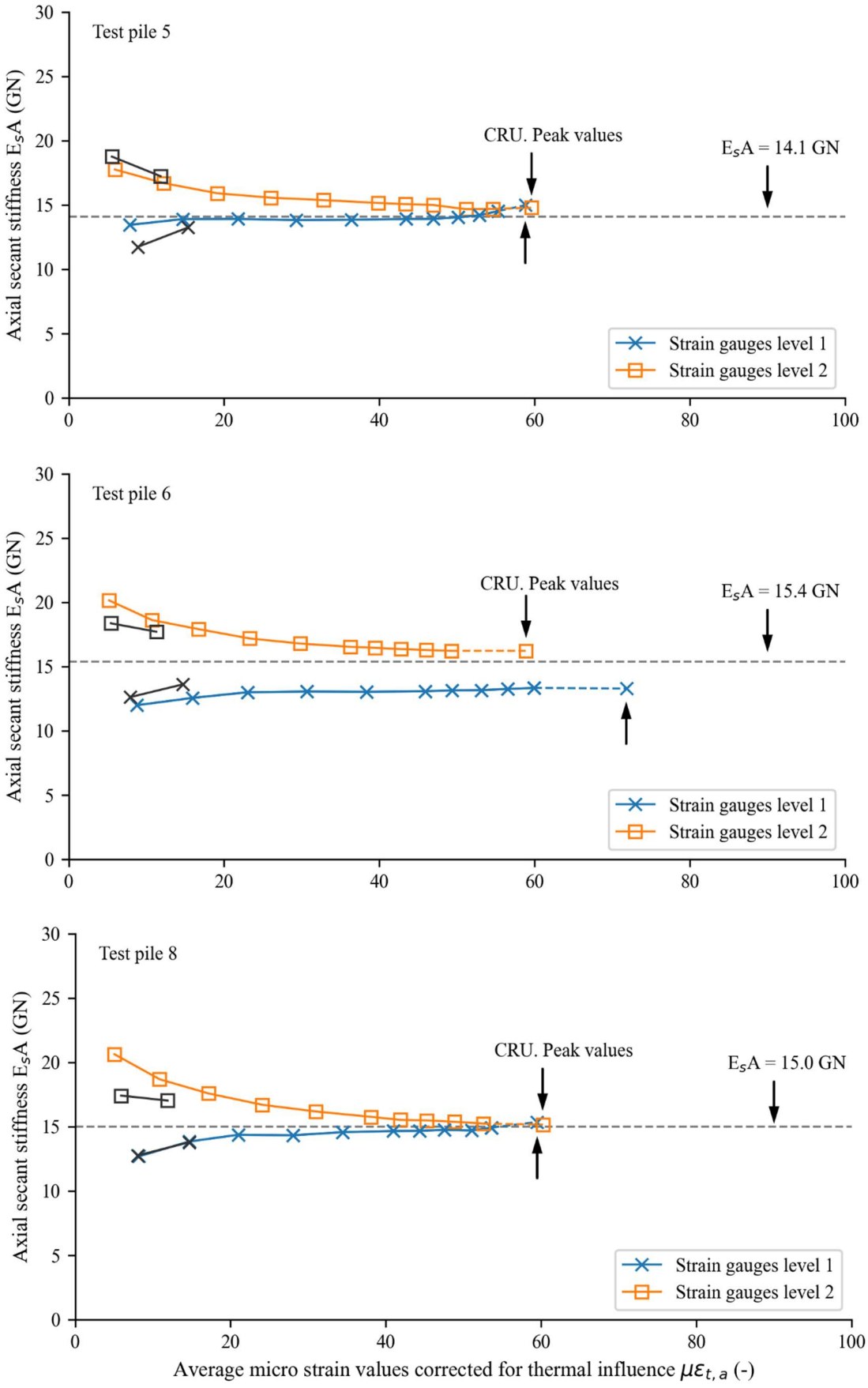

Figure 181*: Axial stiffness determined by direct secant method for strain gauge level 1-2 in test pile 5-6 and 8. Load phase 1 is presented in black.*

H.6 Mobilised unit shaft resistance-pile top movement

Maintained load (ML) test

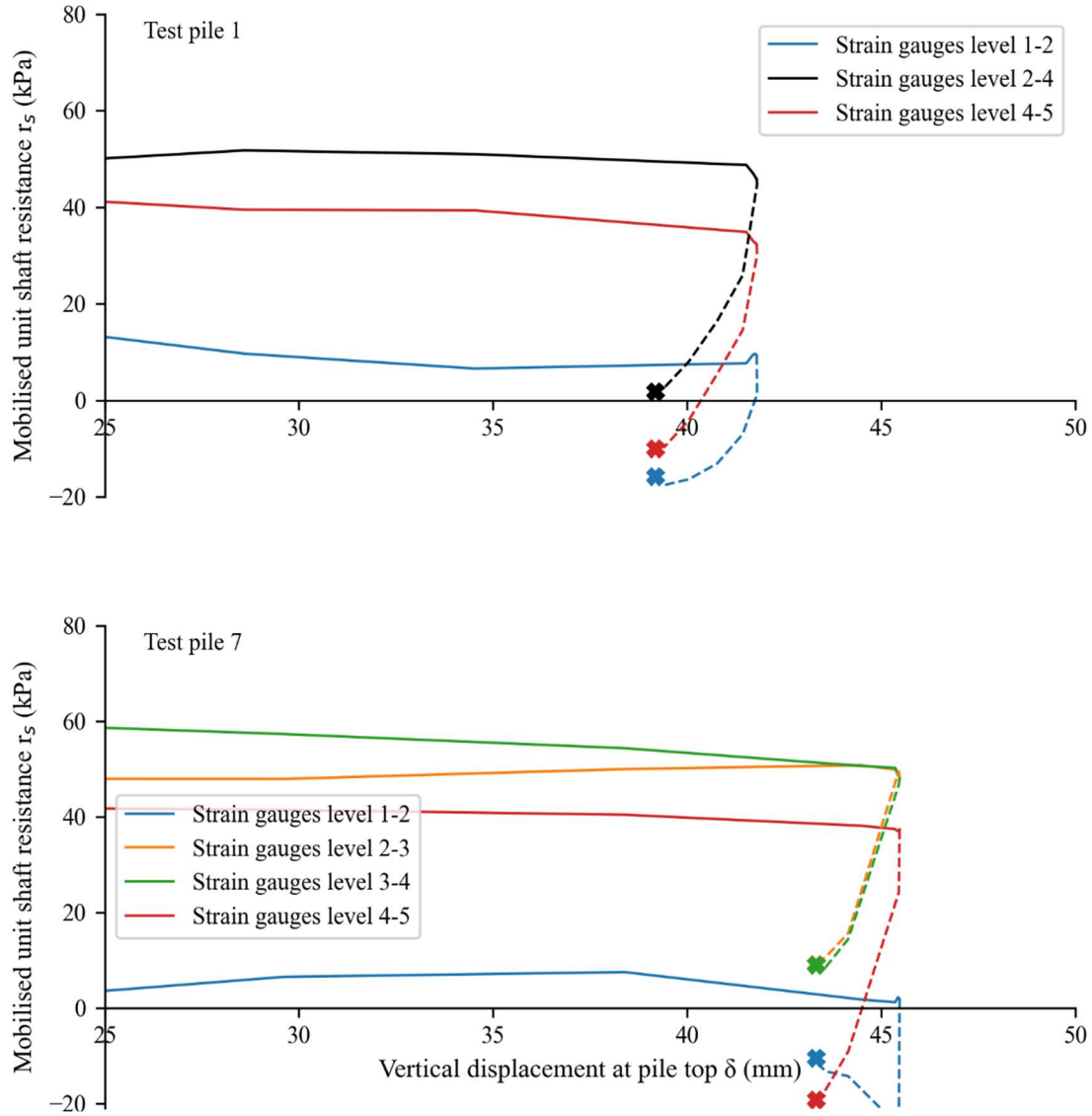

Figure 182: Mobilised unit shaft resistance for test piles 1 and 7. Residual stresses marked with a cross.

Constant rate of uplift (CRU) test

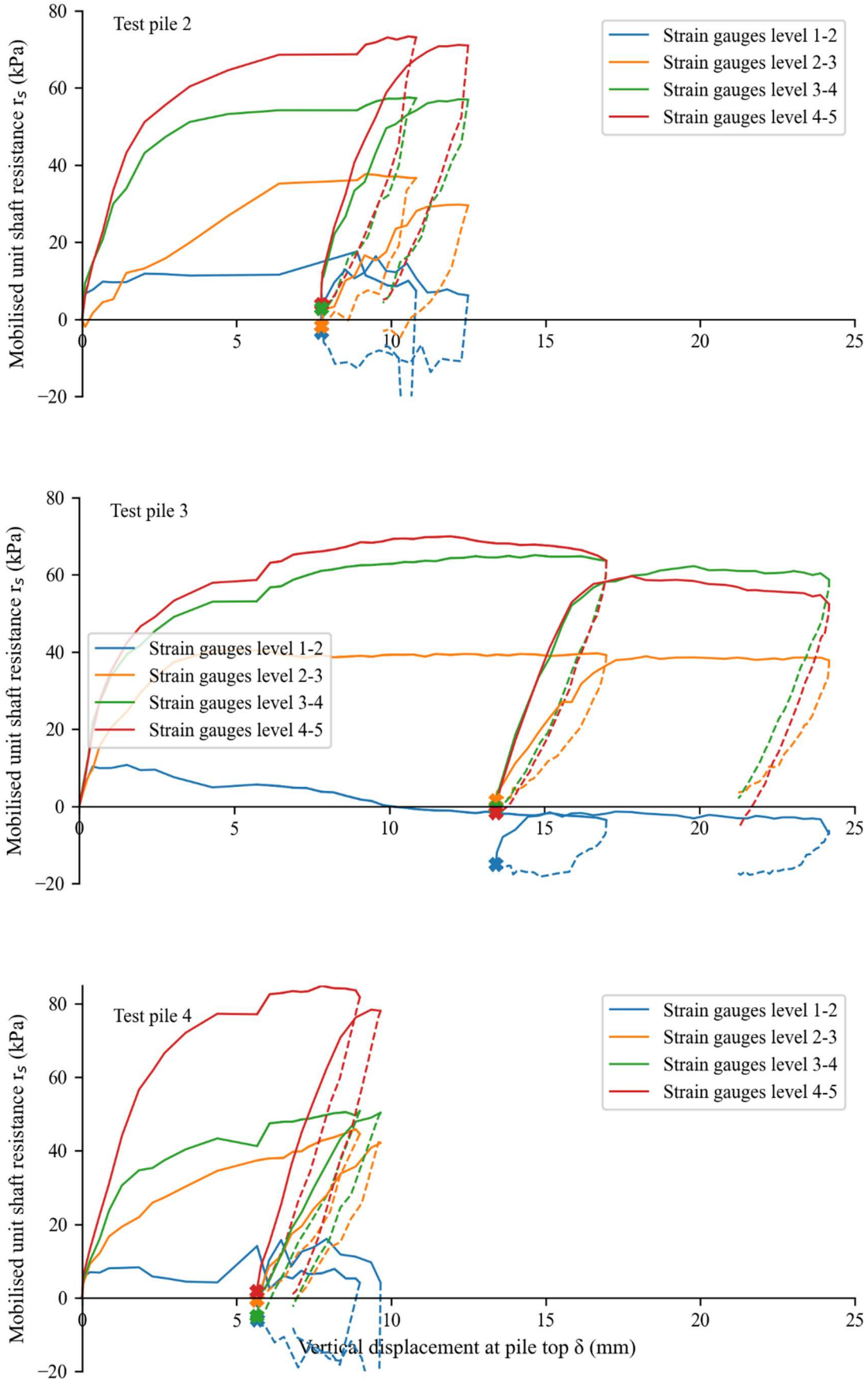

Figure 183: Mobilised unit shaft resistance for test piles 2-4. Residual stresses marked with a cross.

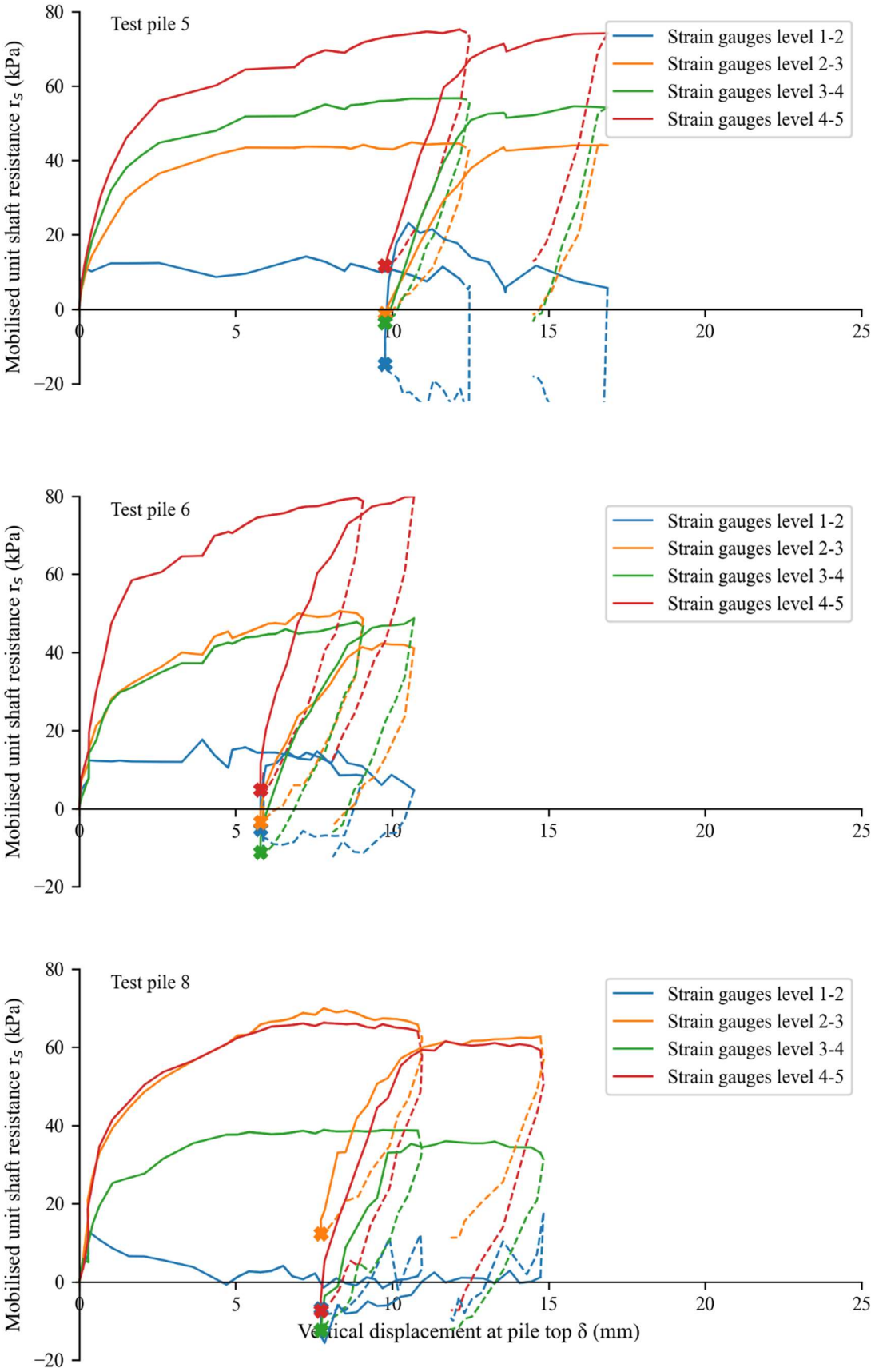

Figure 184: Mobilised unit shaft resistance for test piles 5-6 and 8. Residual stresses marked with a cross.

H.7 Shear stiffness degradation curves

Maintained load (ML) test

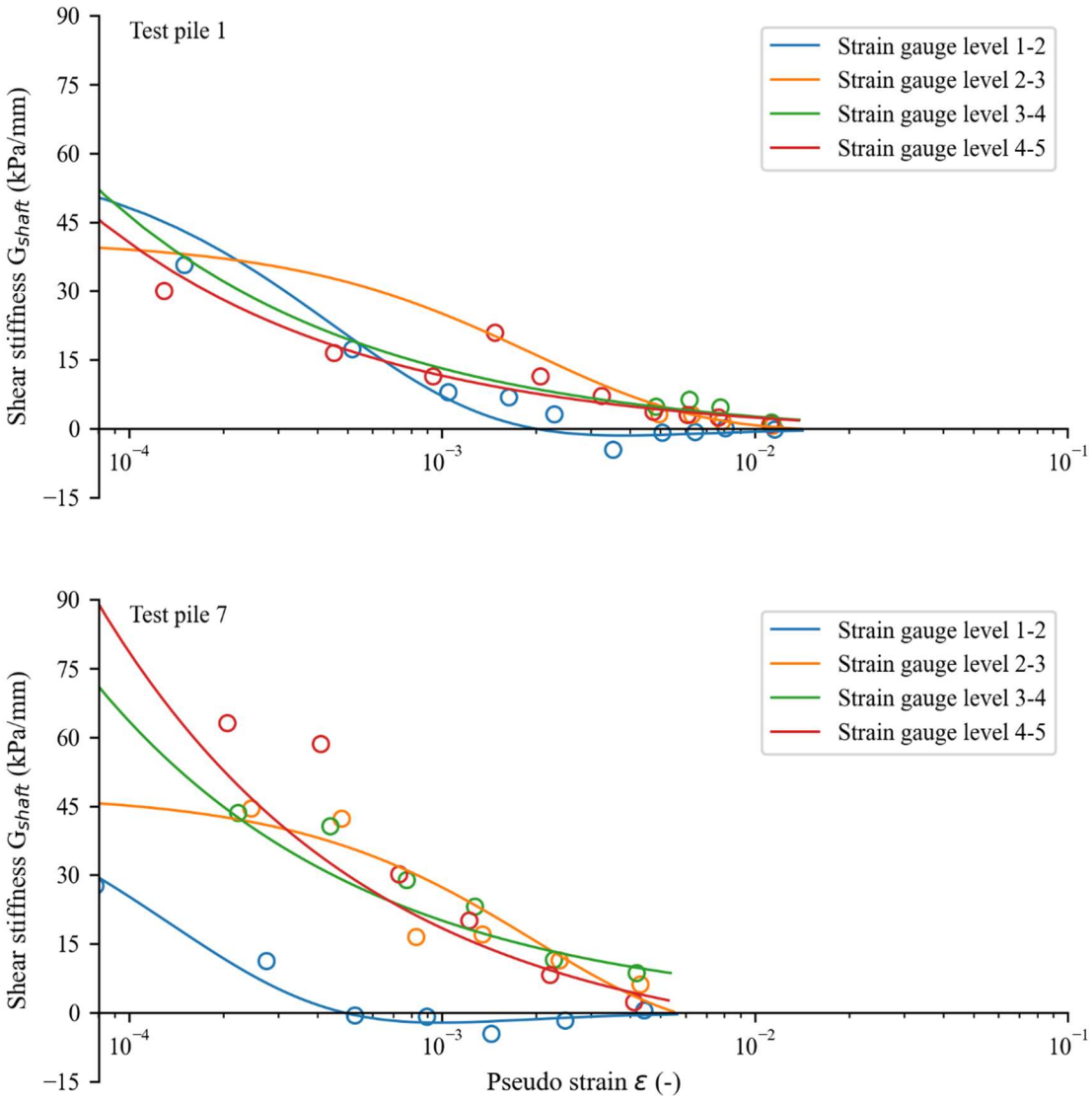

Figure 185: Shear stiffness degradation curves for test pile 1 and 7.

Constant rate of uplift (CRU) test

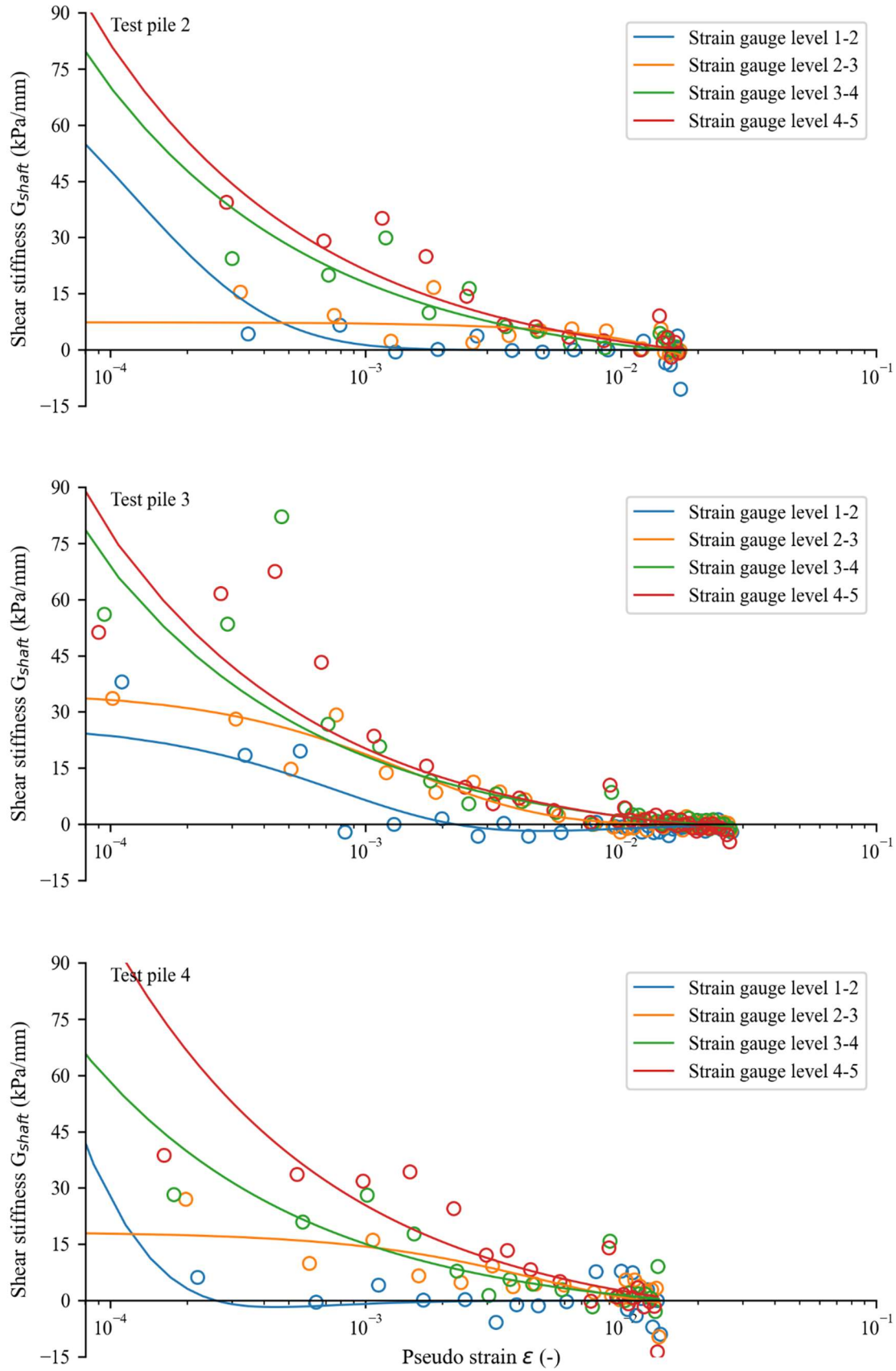

Figure 186: Shear stiffness degradation curves for test pile 2-4.

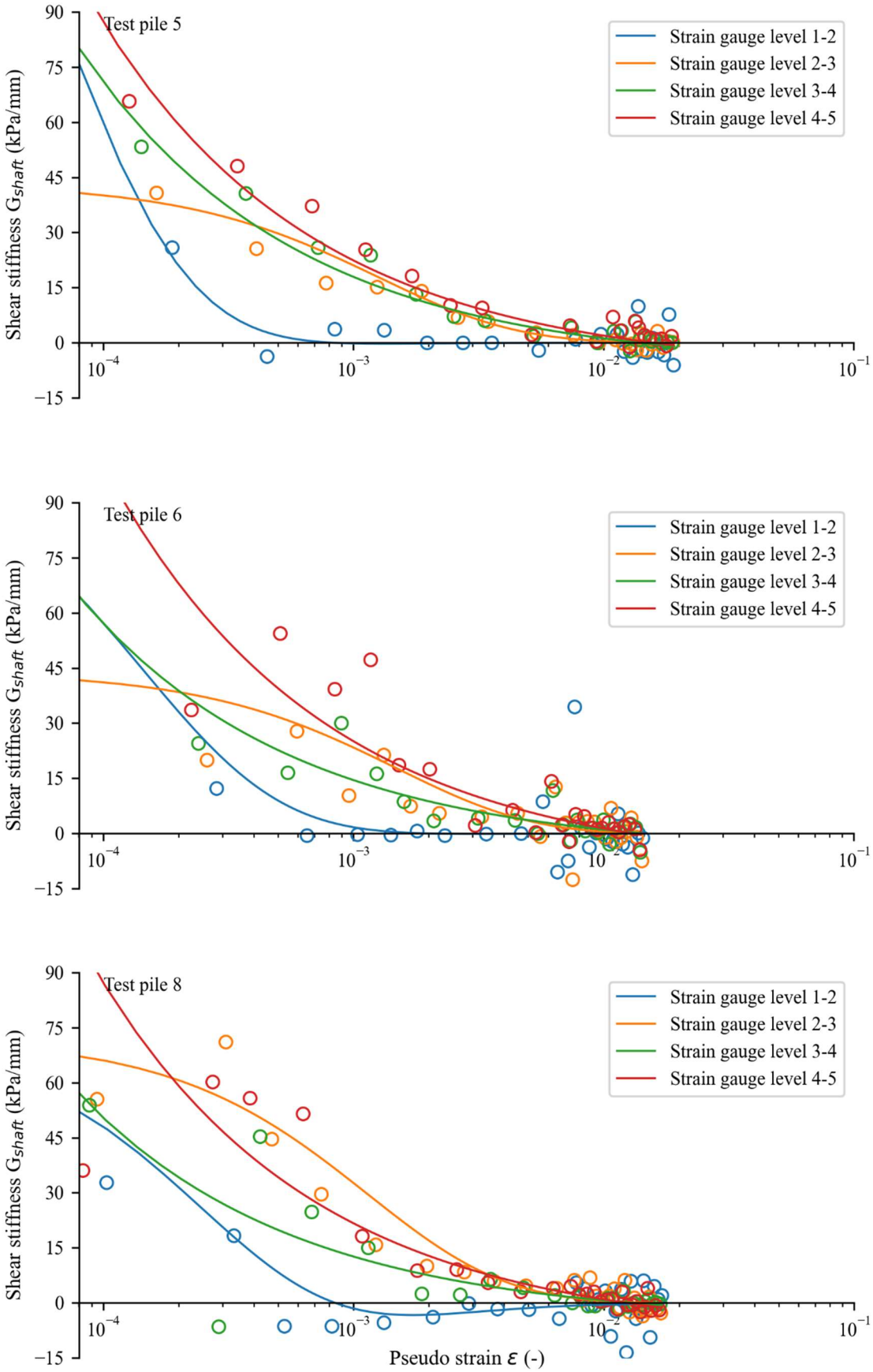

Figure 187: Shear stiffness degradation curves for test pile 5-6 and 8.

I Fibre optic strain measurements

I.1 HD strain sensor 2

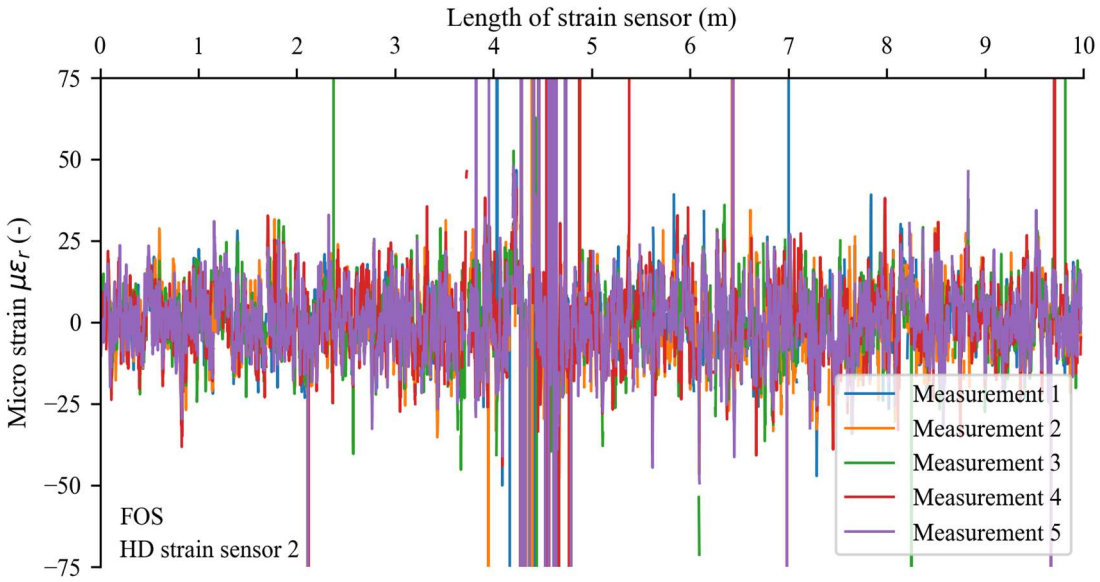

Figure 188: Development of strain along the length of high-definition (HD) strain sensor 2 using the fibre optic switch (FOS).

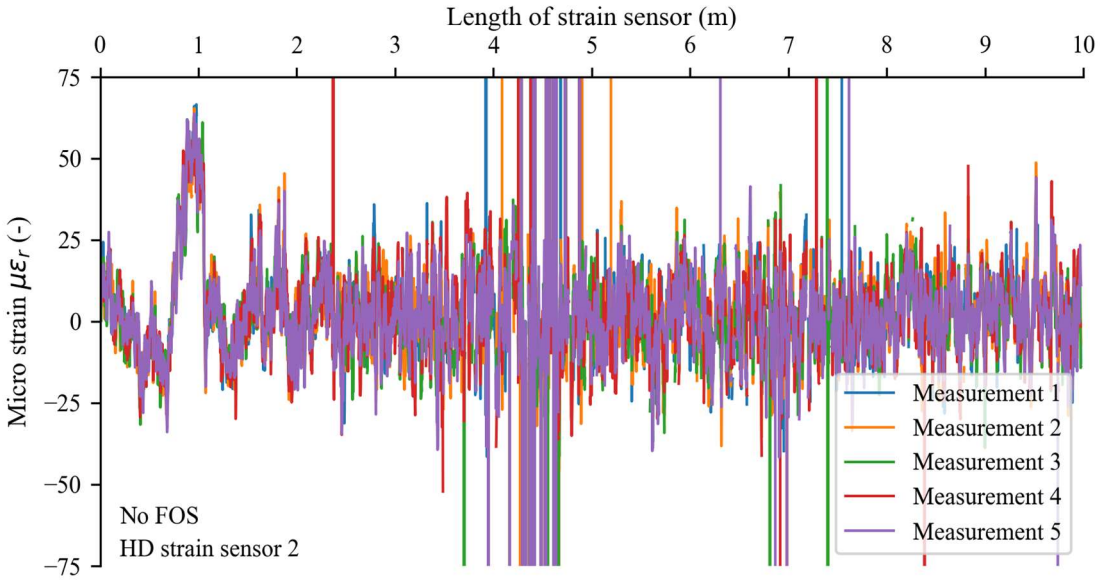

Figure 189: Development of strain along the length of high-definition (HD) strain sensor 2 without using the fibre optic switch (FOS).

Table 26: HD strain sensor 2: Mean (arithmetic), 5th percentile, 95th percentile and standard deviation.

HD strain sensor 2	Mean [$\mu\varepsilon$]	5th percentile [$\mu\varepsilon$]	95th percentile [$\mu\varepsilon$]	Standard deviation [$\mu\varepsilon$]
FOS				
Measurement 1	-12.71	-16.58	18.16	1119
Measurement 2	-26.60	-18.19	17.75	1213
Measurement 3	-50.85	-18.60	17.78	1169
Measurement 4	-47.57	-17.94	18.88	1126
Measurement 5	-19.21	-17.40	17.24	1223
No FOS				
Measurement 1	-24.90	-18.07	23.79	1194
Measurement 2	-40.65	-18.30	24.26	1198
Measurement 3	-47.75	-17.20	23.81	1155
Measurement 4	-25.55	-18.80	25.32	1067
Measurement 5	-36.69	-17.05	23.45	1100

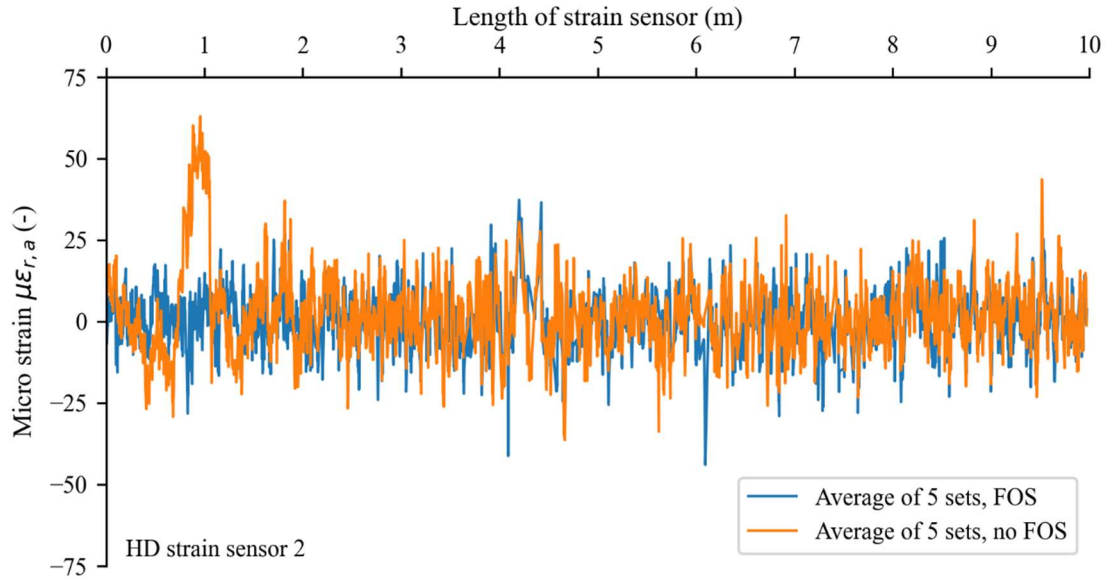

Figure 190: Development of strain along the length of high-definition (HD) strain sensor 2 for an average value of 5 measurements with and without the use of fibre optic switch (FOS).

Table 27: HD strain sensor 2: mean (arithmetic), 5th percentile, 95th percentile and standard deviation.

HD strain sensor 2	Mean [$\mu\varepsilon$]	5th percentile [$\mu\varepsilon$]	95th percentile [$\mu\varepsilon$]	Standard deviation [$\mu\varepsilon$]
FOS	0.44	-14.79	15.28	9.3
No FOS	2.32	-15.51	20.77	12.3

I.2 Pre-tension

Test pile 1

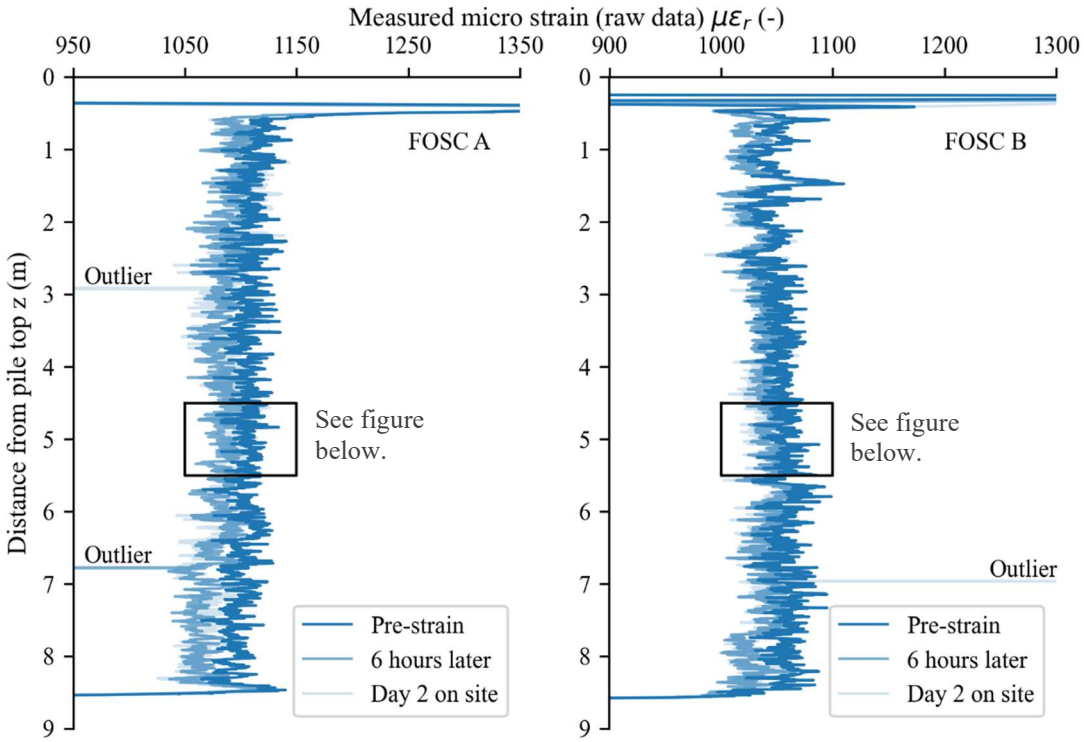

Figure 191: Development of pre-tensioning within the first 6 hours at the indoor storage facility as well as with the reinforcement cage on the ground at the test site in Hinge (day 2 on site).

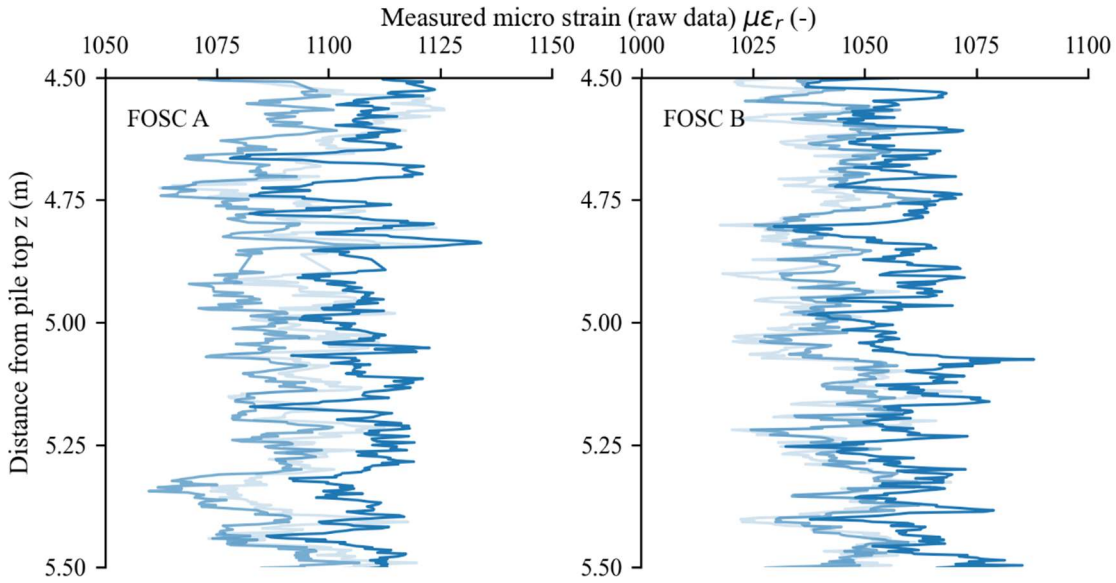

Figure 192: Zoom of the development of strain along the length of test pile 1 from fibre optic cables. The pre- tensioning is slightly loosening over the first hours after which the strain measurements are affected by uneven temperature changes over the cross section and along the length of test pile 1 due to exposure to direct sunlight and partial shading by tufts of grass.

Test pile 2

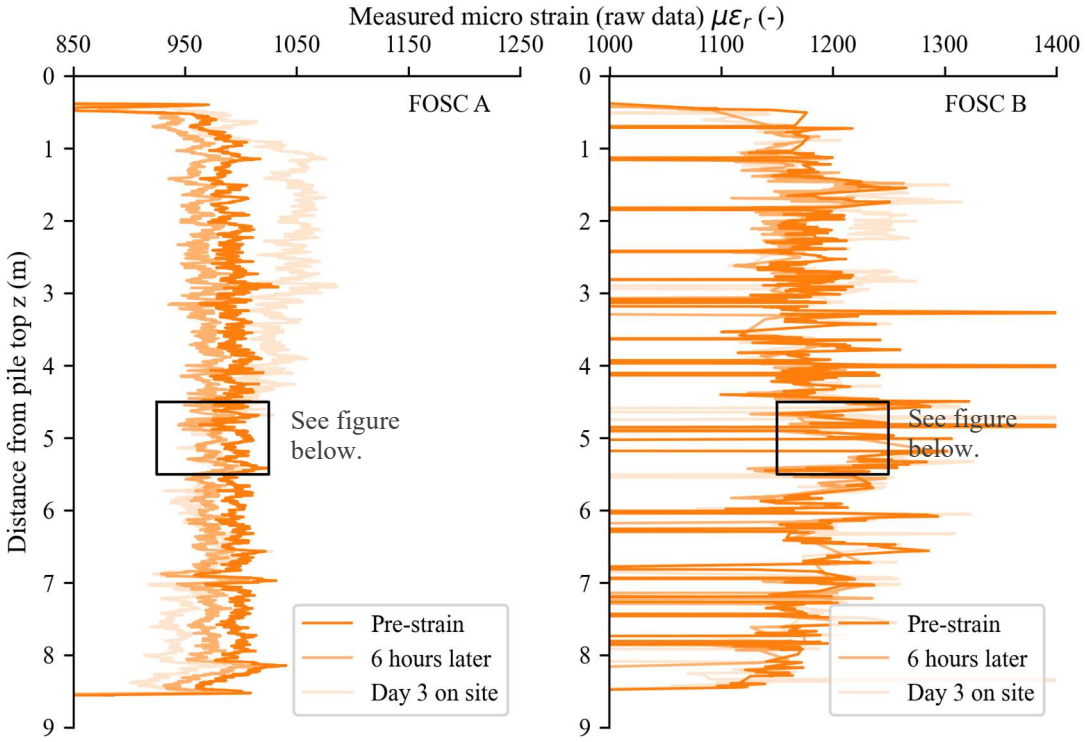

Figure 193: Development of pre-tensioning within the first 6 hours at the indoor storage facility as well as with the reinforcement cage on the ground at the test site in Hinge (day 3 on site). However, large amounts of noise (outliers) are found for fibre optic cable B in general and only a single reading is presented (and not an average over 5 readings) from the test site in Hinge (day 3) due to noise.

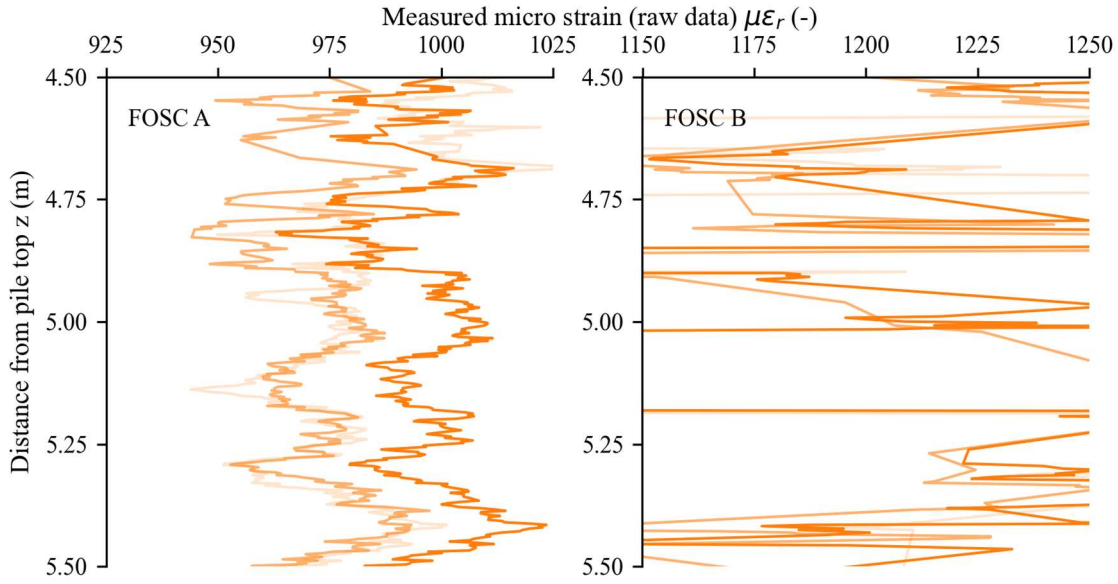

Figure 194: Zoom of the development of strain along the length of test pile 2 from fibre optic cables. The pre- tensioning is slightly loosening over the first hours after which the strain measurements are affected by uneven temperature changes over the cross section and along the length of test pile 2 due to exposure to direct sunlight and partial shading by tufts of grass.

Test pile 3

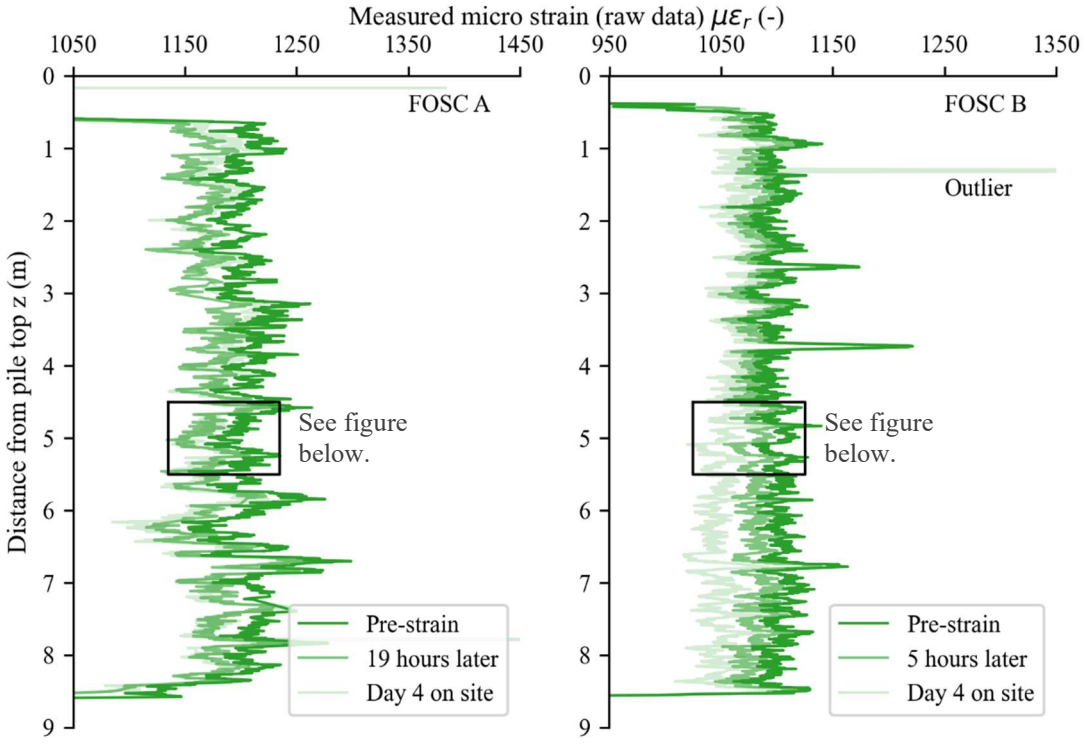

Figure 195: Development of pre-tensioning within the first either 19 or 5 hours at the indoor storage facility as well as with the reinforcement cage on the ground at the test site in Hinge (day 4 on site).

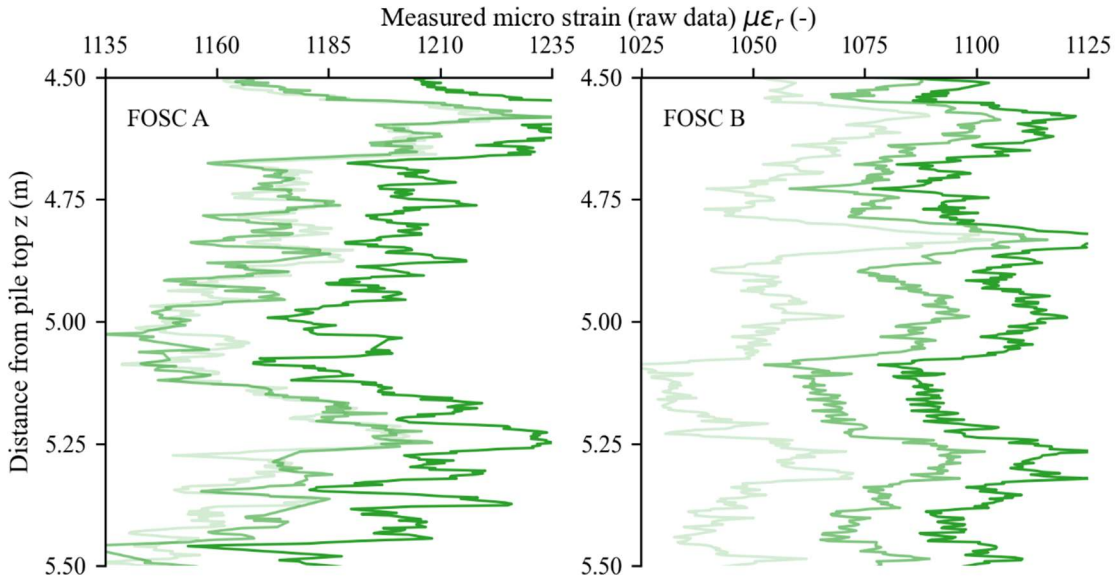

Figure 196: Zoom of the development of strain along the length of test pile 3 from fibre optic cables. The pre- tensioning is slightly loosening over the first hours after which the strain measurements are affected by uneven temperature changes over the cross section and along the length of test pile 3 due to exposure to direct sunlight and partial shading by tufts of grass.

Test pile 4

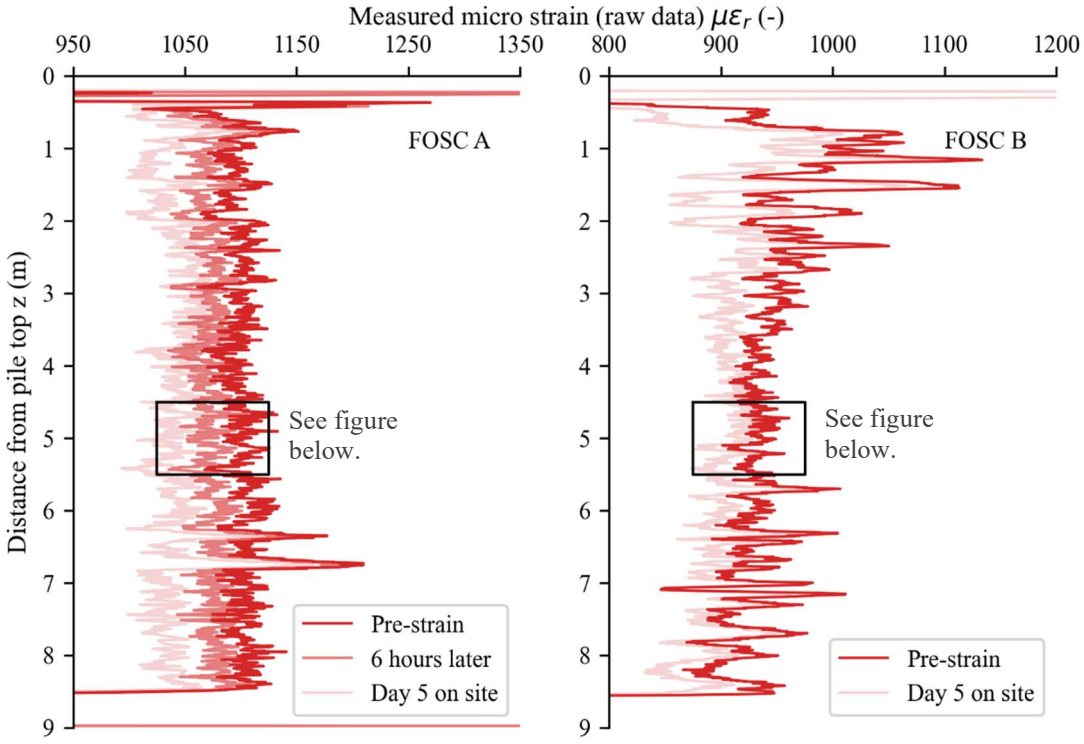

Figure 197: Development of pre-tensioning within the first 6 hours at the indoor storage facility as well as with the reinforcement cage on the ground at the test site in Hinge (day 5 on site). For fibre optic cable B the pre-tensioning was performed one day later, as the original fibre optic cable malfunctioned during the measurements 6 hours later.

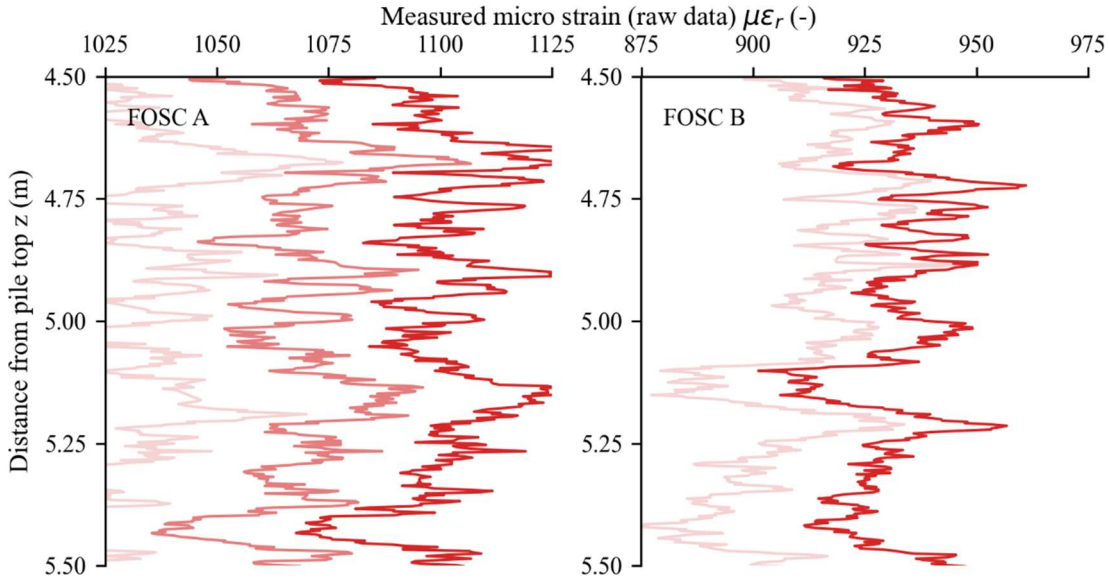

Figure 198: Zoom of the development of strain along the length of test pile 4 from fibre optic cables. The pre- tensioning is slightly loosening over the first hours after which the strain measurements are affected by uneven temperature changes over the cross section and along the length of test pile 4 due to exposure to direct sunlight and partial shading by tufts of grass.

Test pile 5

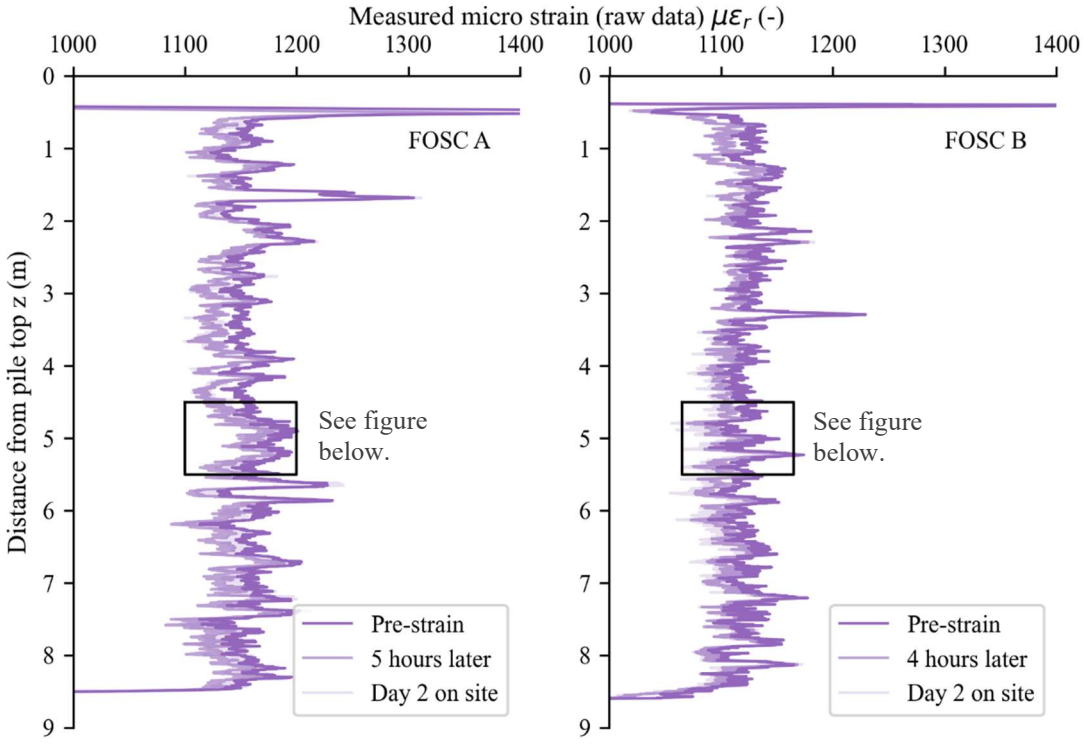

Figure 199: Development of pre-tensioning within the first either 5 or 4 hours at the indoor storage facility as well as with the reinforcement cage on the ground at the test site in Hinge (day 2 on site)

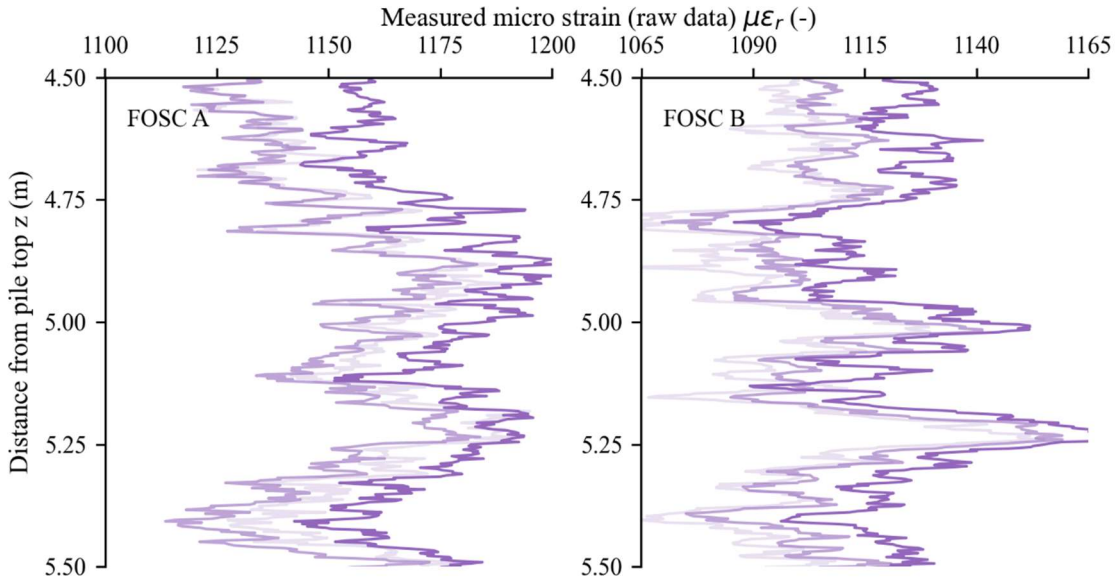

Figure 200: Zoom of the development of strain along the length of test pile 5 from fibre optic cables. The pre- tensioning is slightly loosening over the first hours after which the strain measurements are affected by uneven temperature changes over the cross section and along the length of test pile 5 due to exposure to direct sunlight and partial shading by tufts of grass.

Test pile 6

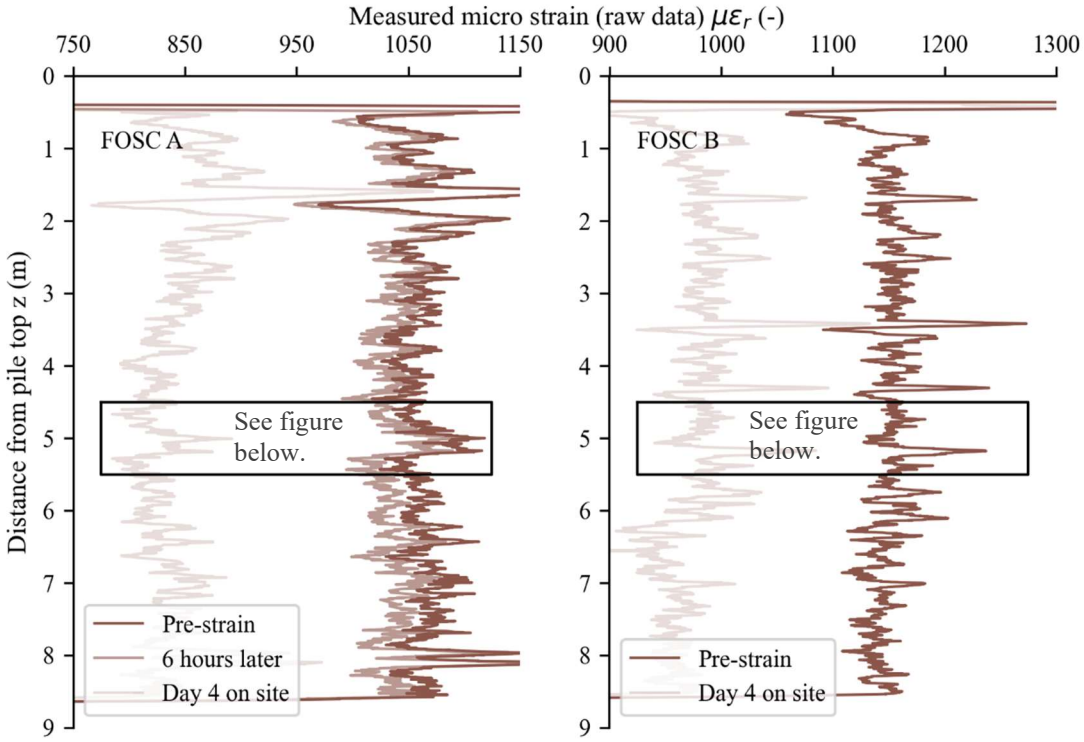

Figure 201: Development of pre-tensioning within the first 6 hours at the indoor storage facility as well as with the reinforcement cage on the ground at the test site in Hinge (day 4 on site). For fibre optic cable B the pre- tensioning was performed when the original fibre optic cable malfunctioned during the measurements 6 hours later.

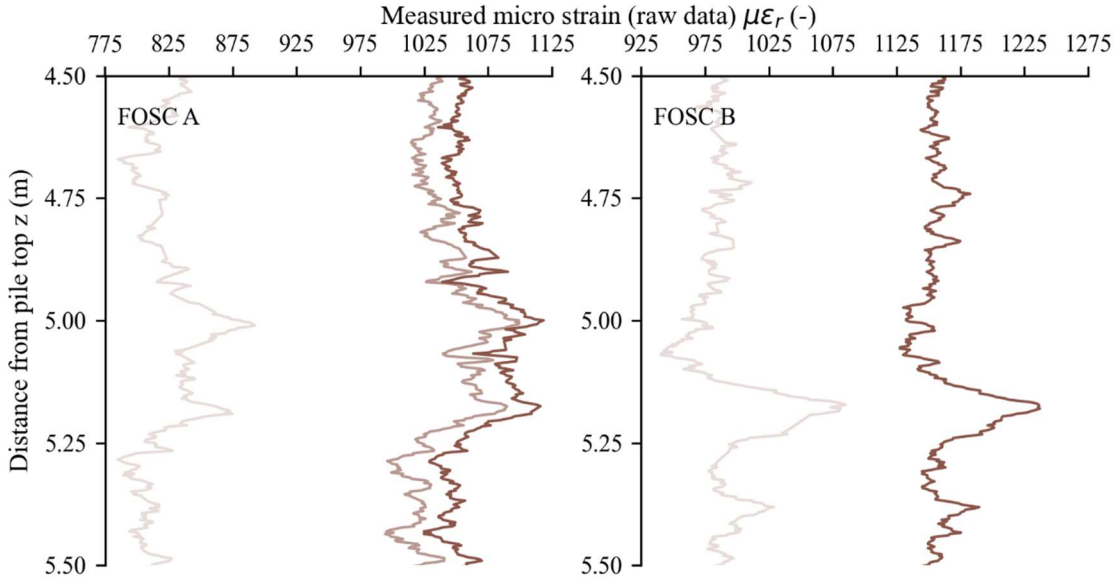

Figure 202: Zoom of the development of strain along the length of test pile 6 from fibre optic cables. The pre- tensioning is slightly loosening over the first hours after which the strain measurements are affected by a temperature drop of approximately 7-8 degrees Celsius.

Test pile 7

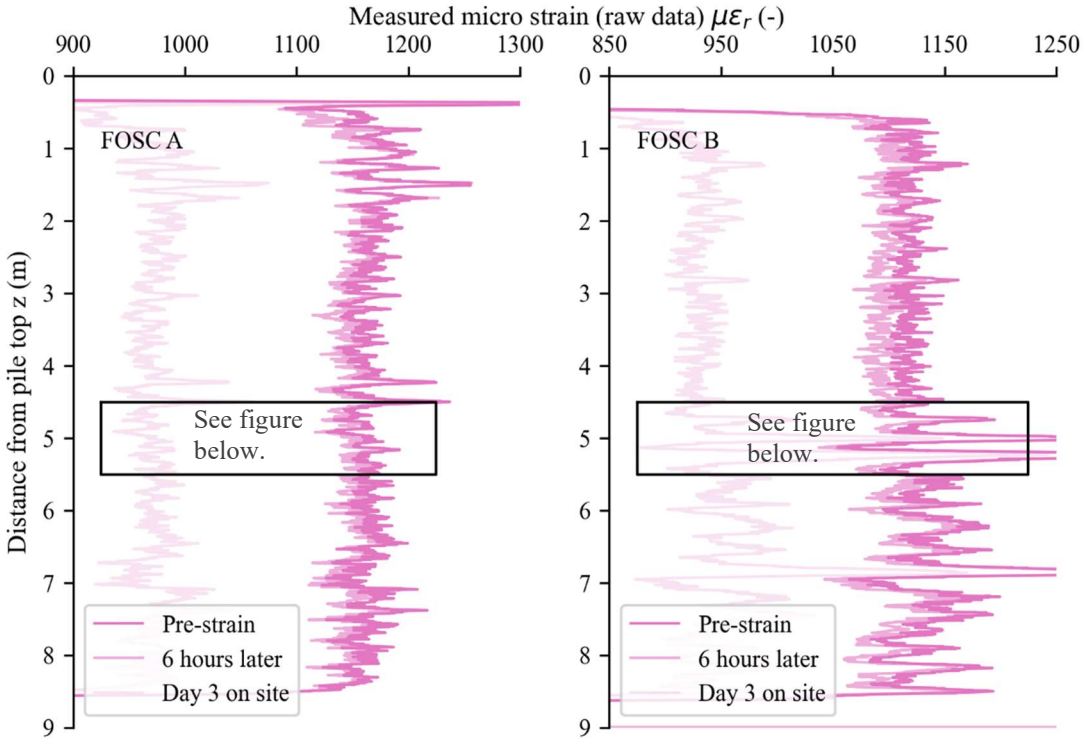

Figure 203: Development of pre-tensioning within the first 6 hours at the indoor storage facility as well as with the reinforcement cage on the ground at the test site in Hinge (day 3 on site). The lower half of fibre optic cable B is livelier than expected.

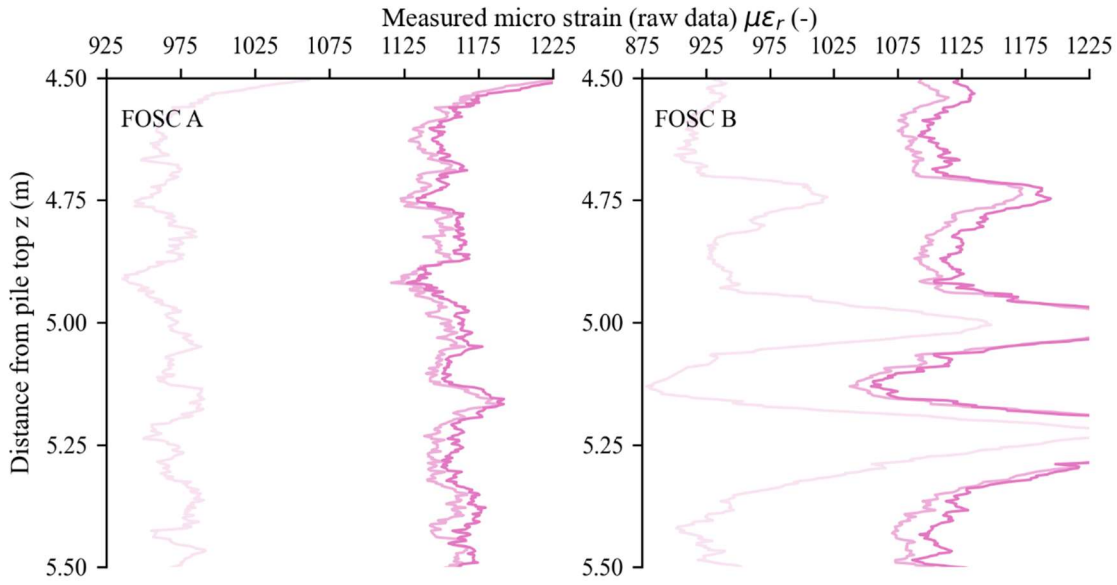

Figure 204: Zoom of the development of strain along the length of test pile 7 from fibre optic cables. The pre- tensioning is slightly loosening over the first hours after which the strain measurements are affected by a temperature drop of approximately 7-8 degrees Celsius.

Test pile 8

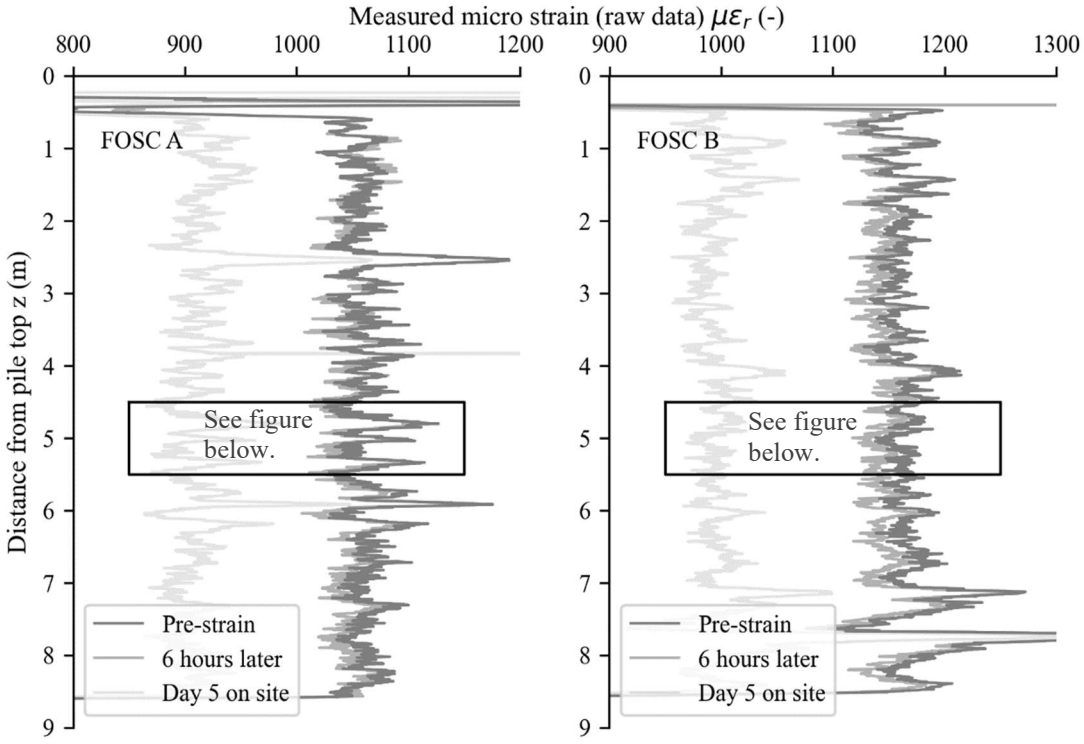

Figure 205: Development of pre-tensioning within the first 6 hours at the indoor storage facility as well as with the reinforcement cage on the ground at the test site in Hinge (day 5 on site).

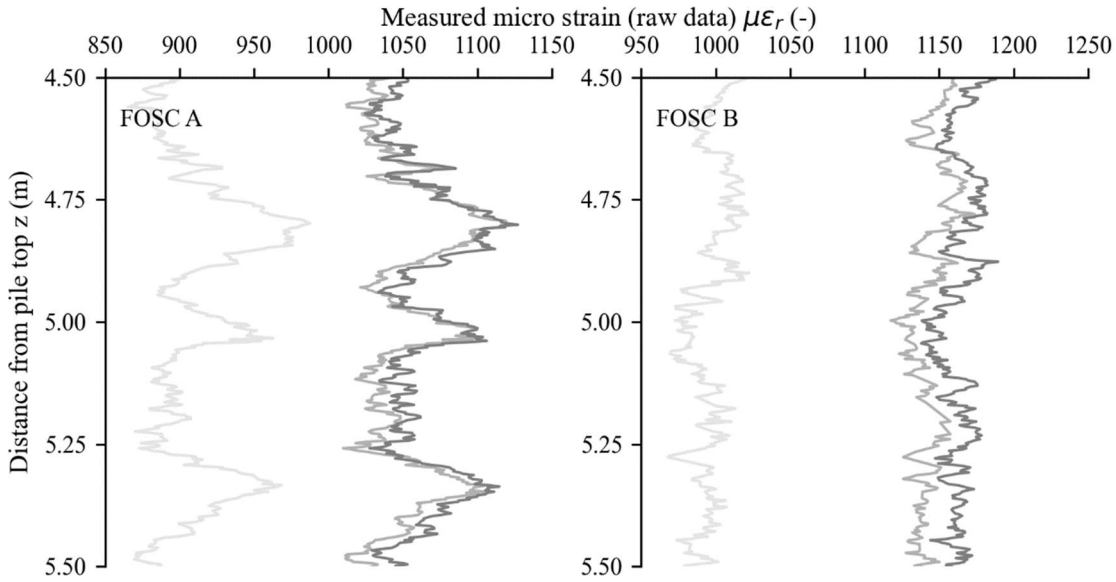

Figure 206: Zoom of the development of strain along the length of test pile 8 from fibre optic cables. The pre- tensioning is slightly loosening over the first hours after which the strain measurements are affected by a temperature drop of approximately 6-7 degrees Celsius.

I.3 Confirmation of no creep

Creep is only observed at the upper strain gauge level (SG, level 1) for VWSG in test pile 1 and 4 and is therefore also not expected for the FOSC. This is confirmed for the final maintained load step during static pile loading tests. However, the second to last load step was used for test pile 1 as a partially defect strain gauge caused the strain data in the final load step to partially be extrapolated.

The internal strain profiles are given subsequently for test pile 1-3, 5, 7 and 8 immediately after reaching the maintained load step (solid line), 10 min after reaching the maintained load step (dashed line) and 20 min. after reaching the maintained load step (dotted line), see Figure 207 - Figure 209.

Maintained load (ML) test

Test pile 1 and 7

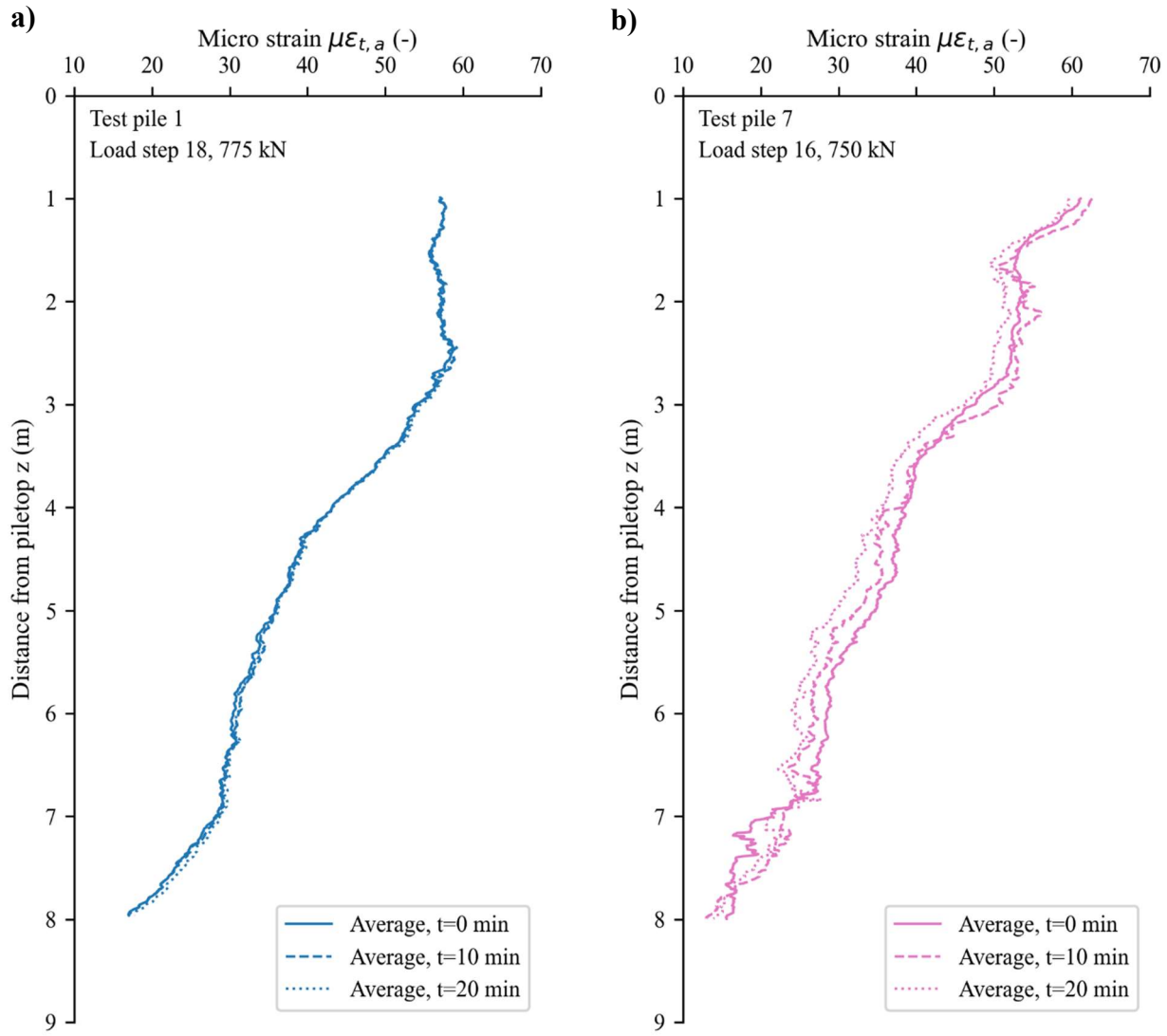

Figure 207: Strain development along the length of (a) test pile 1 and (b) test pile 7 immediately after reaching the maintained load step (solid lines), 10 min after reaching the maintained load step (dashed lines) and 20 min. after reaching the maintained load step (dotted lines).

Constant rate of uplift (CRU) test

Test pile 2 and 3

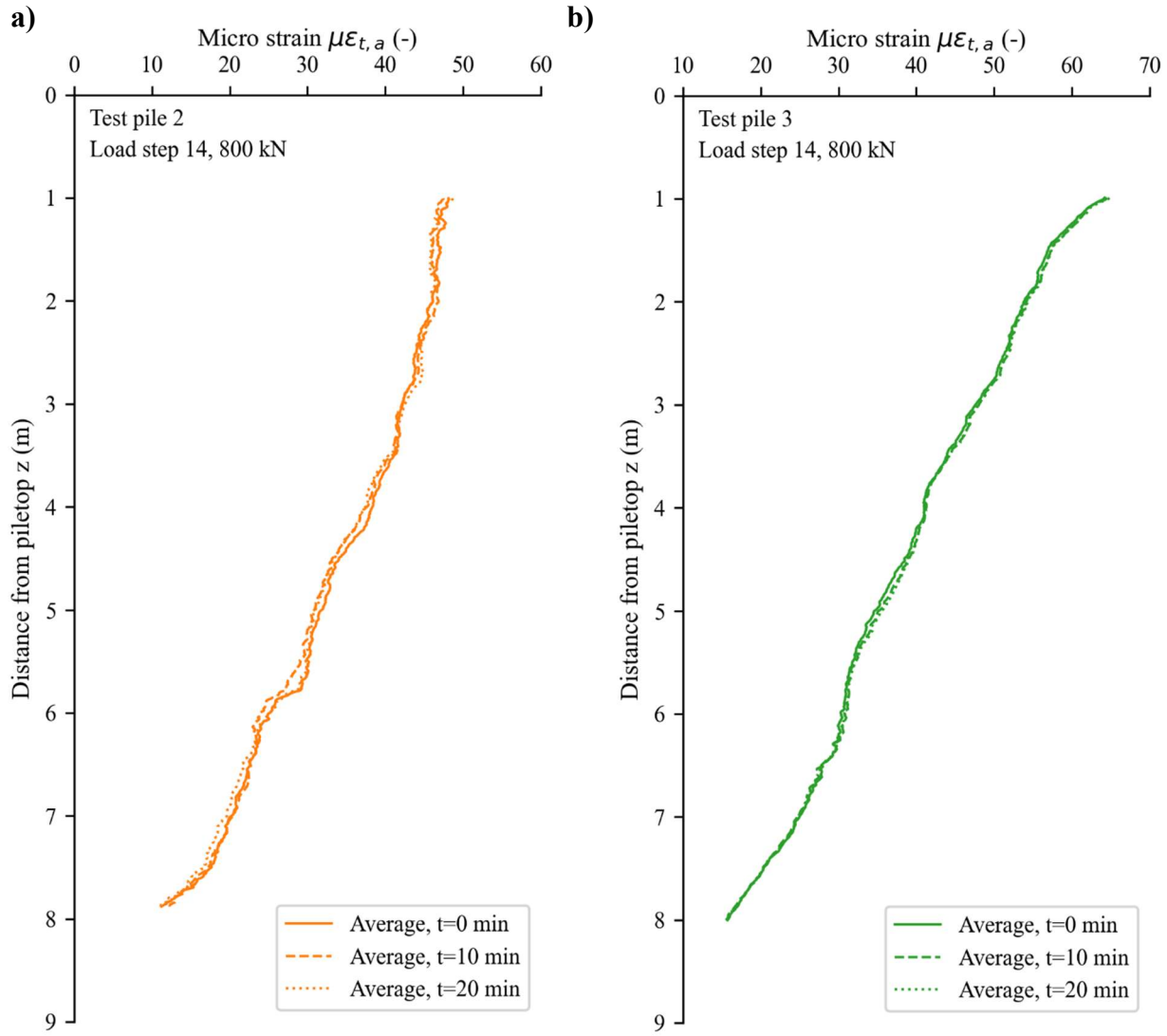

Figure 208: Strain development along the length of (a) test pile 21 and (b) test pile 3 immediately after reaching the maintained load step (solid lines), 10 min after reaching the maintained load step (dashed lines) and 20 min. after reaching the maintained load step (dotted lines).

Test pile 5 and 8

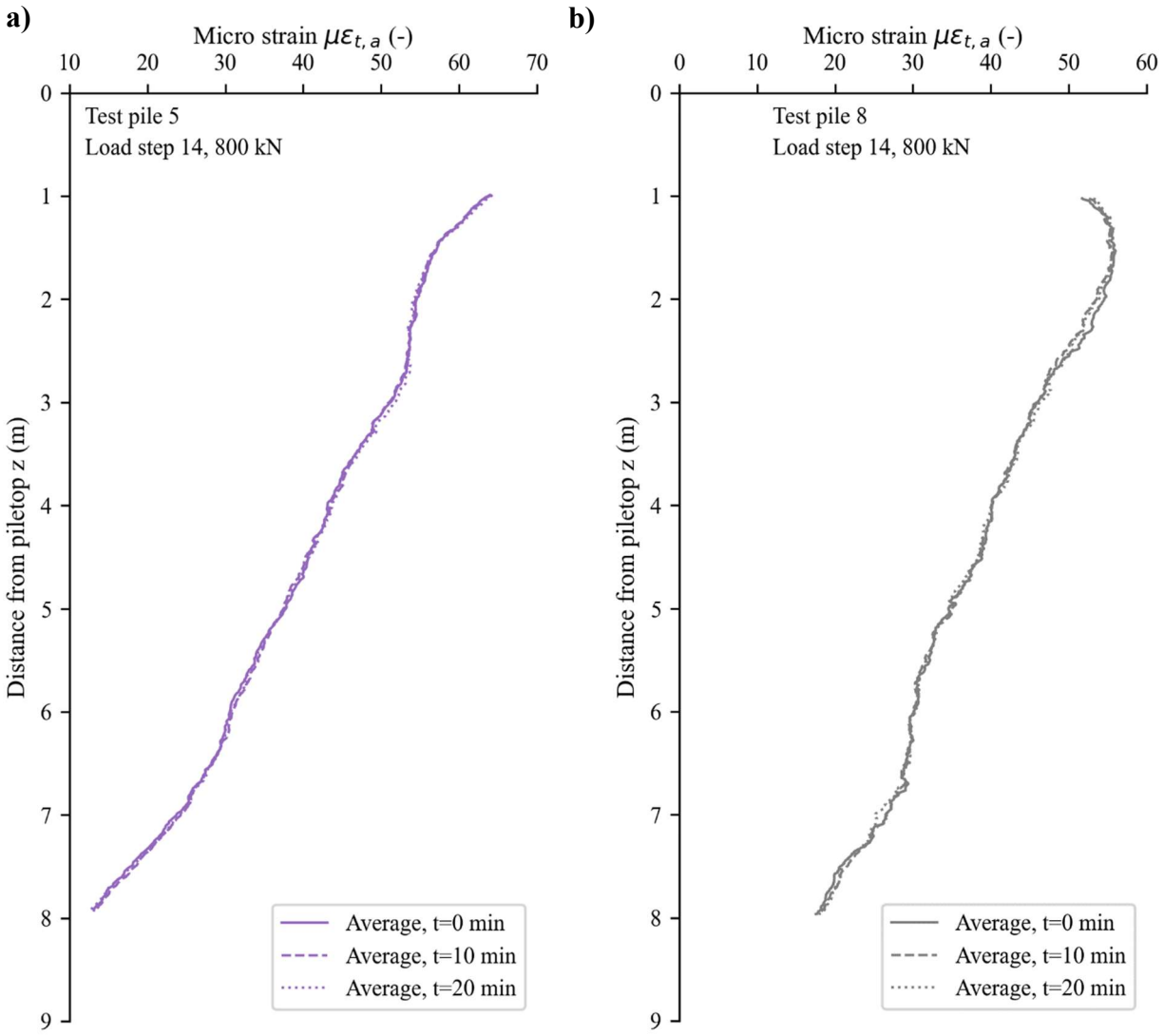

Figure 209: Strain development along the length of (a) test pile 5 and (b) test pile 8 immediately after reaching the maintained load step (solid lines), 10 min after reaching the maintained load step (dashed lines) and 20 min. after reaching the maintained load step (dotted lines).

It is seen from Figure 207 - Figure 209, that the internal strain profiles immediately after reaching the maintained load step (solid line), 10 min after reaching the maintained load step (dashed line) and 20 min. after reaching the maintained load step (dotted line) are very similar and alike. Hence, there is no develop of the internal strain profiles with time along the maintained load steps (no creep observed).

However, for test pile 7, the stand-off cable was damaged due to wear and tear resulting in strain measurements from the fibre optic strain cables with high amounts of scatter, making the internal strain profiles for test pile 7 immediately after reaching the maintained load step (solid line), 10 min after reaching the maintained load step (dashed line) and 20 min. after reaching the maintained load step (dotted line) slightly different.

An overall assessment of the internal strain profiles immediately after reaching the maintained load step (solid line) relative to 10 min after reaching the maintained load step (dashed line) and 20 min. after reaching the maintained load step (dotted line) are presented in Figure 210 and Figure 211.

Maintained load (ML) test

Test pile 1 and 7

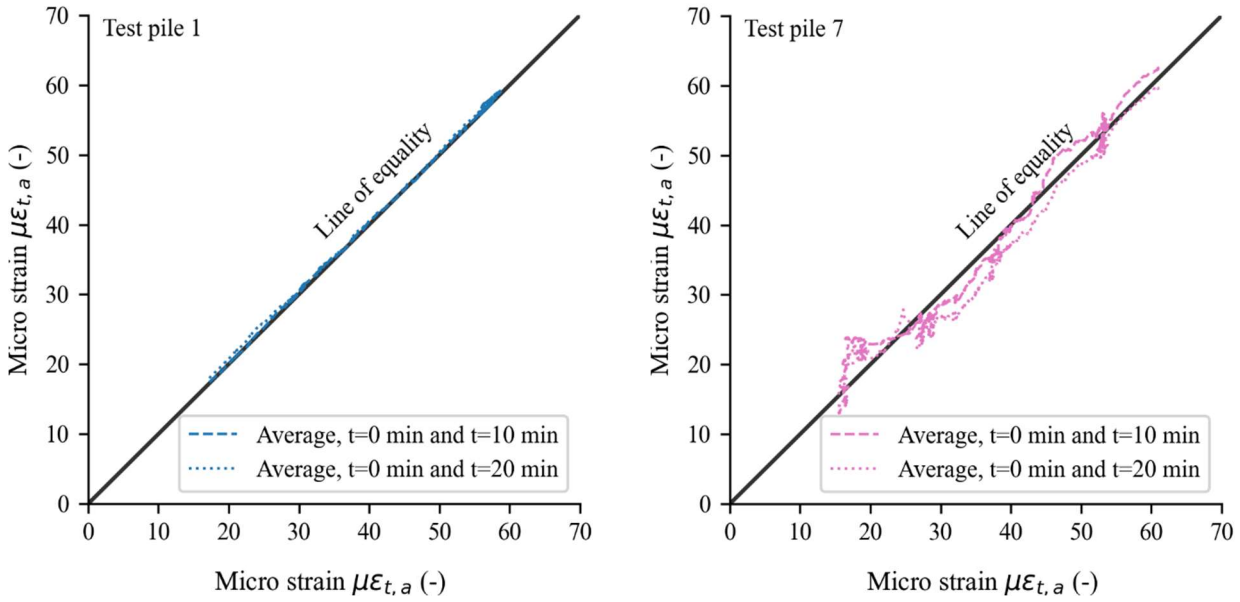

Figure 210: Internal strain profiles immediately after reaching the maintained load step (solid line) relative to 10 min after reaching the maintained load step (dashed line) and 20 min. after reaching the maintained load step (dotted line) for test pile 1 and 7.

Constant rate of uplift (CRU) test

Test pile 2, 3, 5 and 8

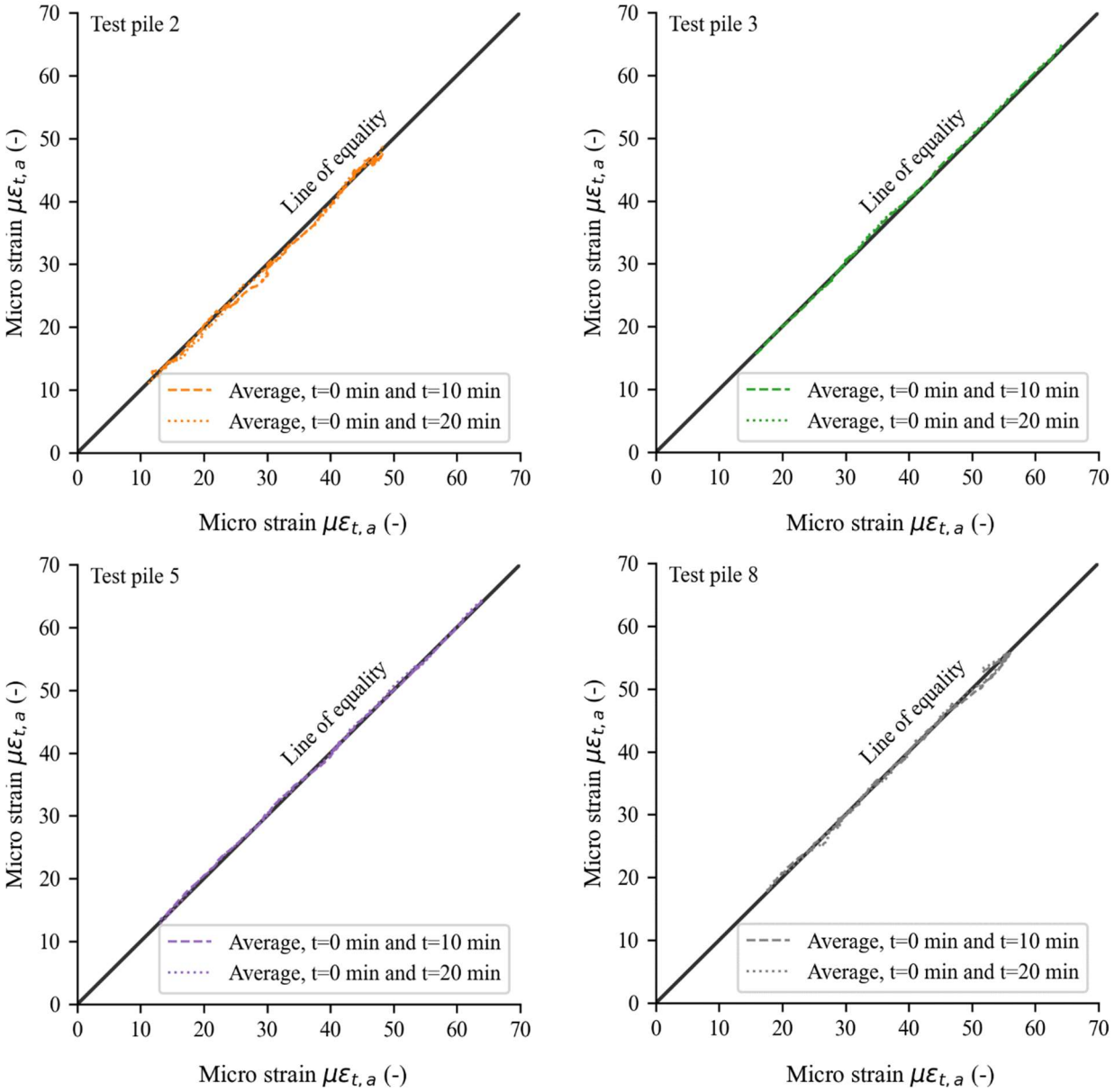

Figure 211: Internal strain profiles immediately after reaching the maintained load step (solid line) relative to 10 min after reaching the maintained load step (dashed line) and 20 min. after reaching the maintained load step (dotted line) for test piles 2, 3, 5 and 8.

It is seen from Figure 210 and Figure 211, that the internal strain profiles immediately after reaching the maintained load step (solid line) relative to 10 min after reaching the maintained load step (dashed line) and 20 min. after reaching the maintained load step (dotted line) falls almost perfectly to the line of equality (except for test pile 7 with the large amount of scatter). Hence, it is reasonable to compare the average value at each strain gauge level (strain gauge level 1-5) over the period of each maintained load step for the vibrating wire strain gauges with the measurements immediately after reaching each maintained load step for the Rayleigh based fibre optic cables.

I.4 Internal strain profiles

Maintained load (ML) test

Test pile 1

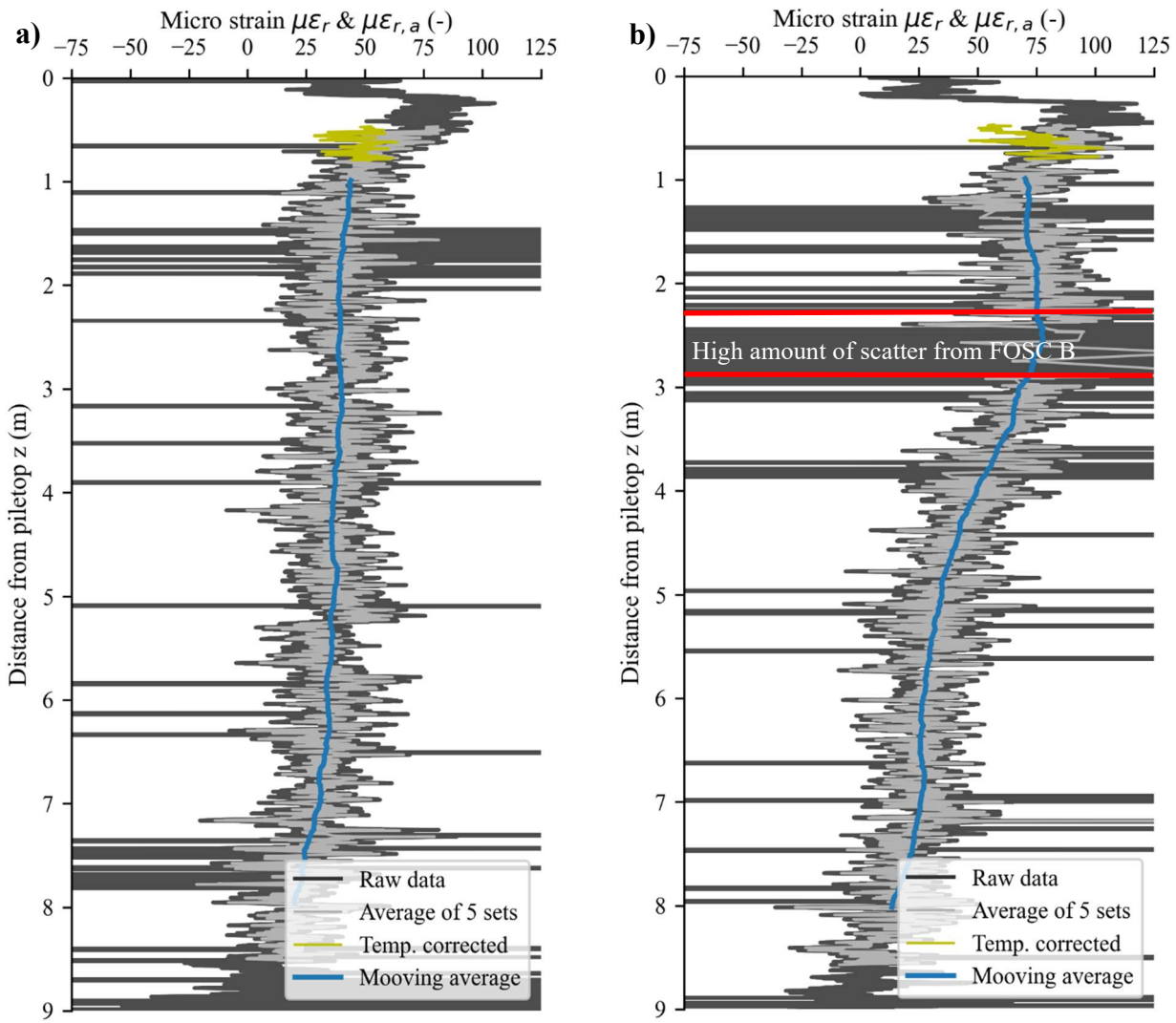

Figure 212: Strain development along the length of test pile 1 in load step 18 for (a) FOSC A and (b) FOSC B with high amount of scatter between 2.3 and 2.9 (red lines). The moving average is influenced 0.5 m above and below the section with high amount of scatter.

Test pile 7

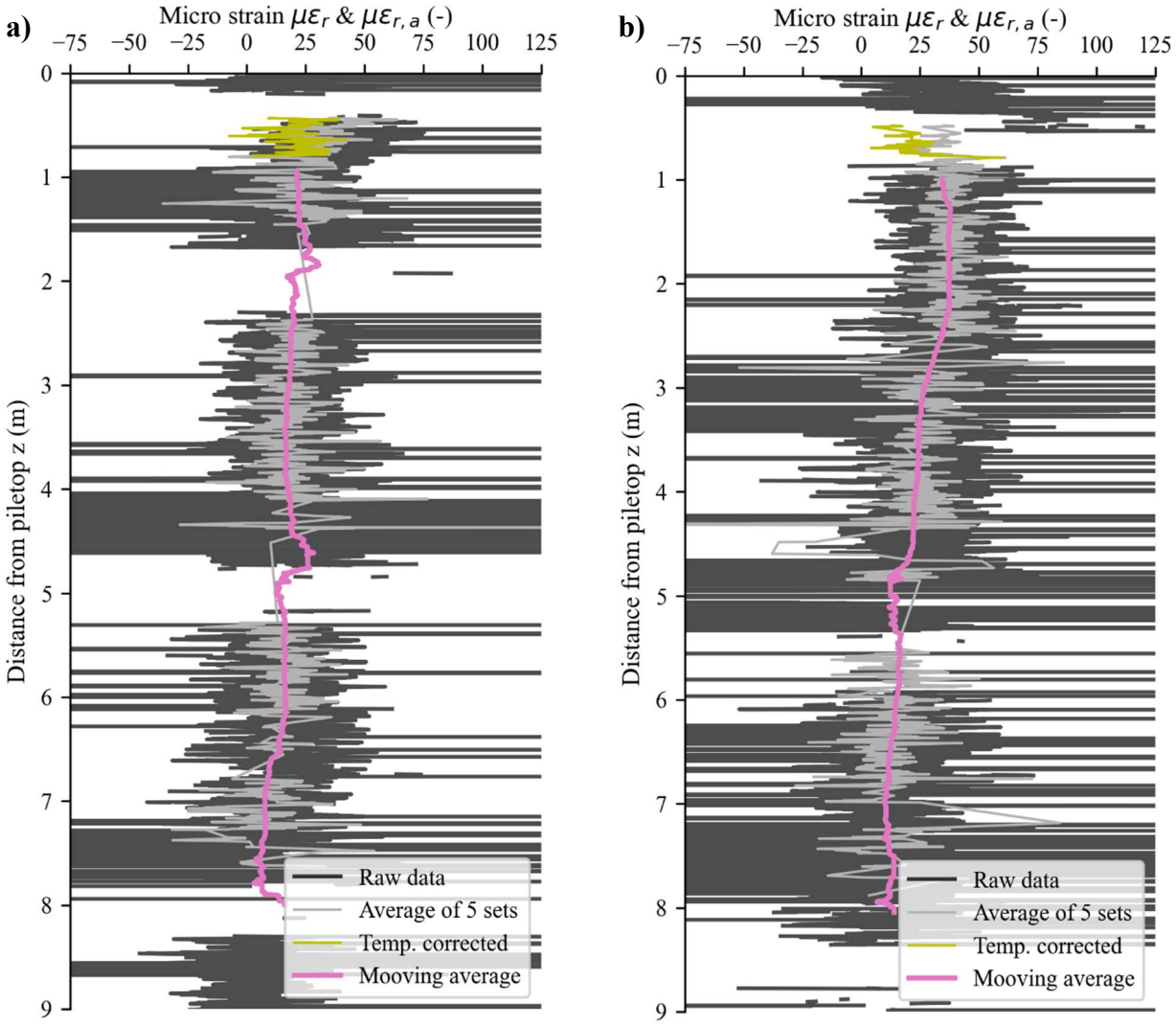

Figure 213: Strain development along the length of test pile 8 in load step 11 for (a)FOSC A and (b) FOSC B with high amount of scatter and multiple NaN values along the length of the test pile.

Constant rate of uplift (CRU) test

Test pile 2

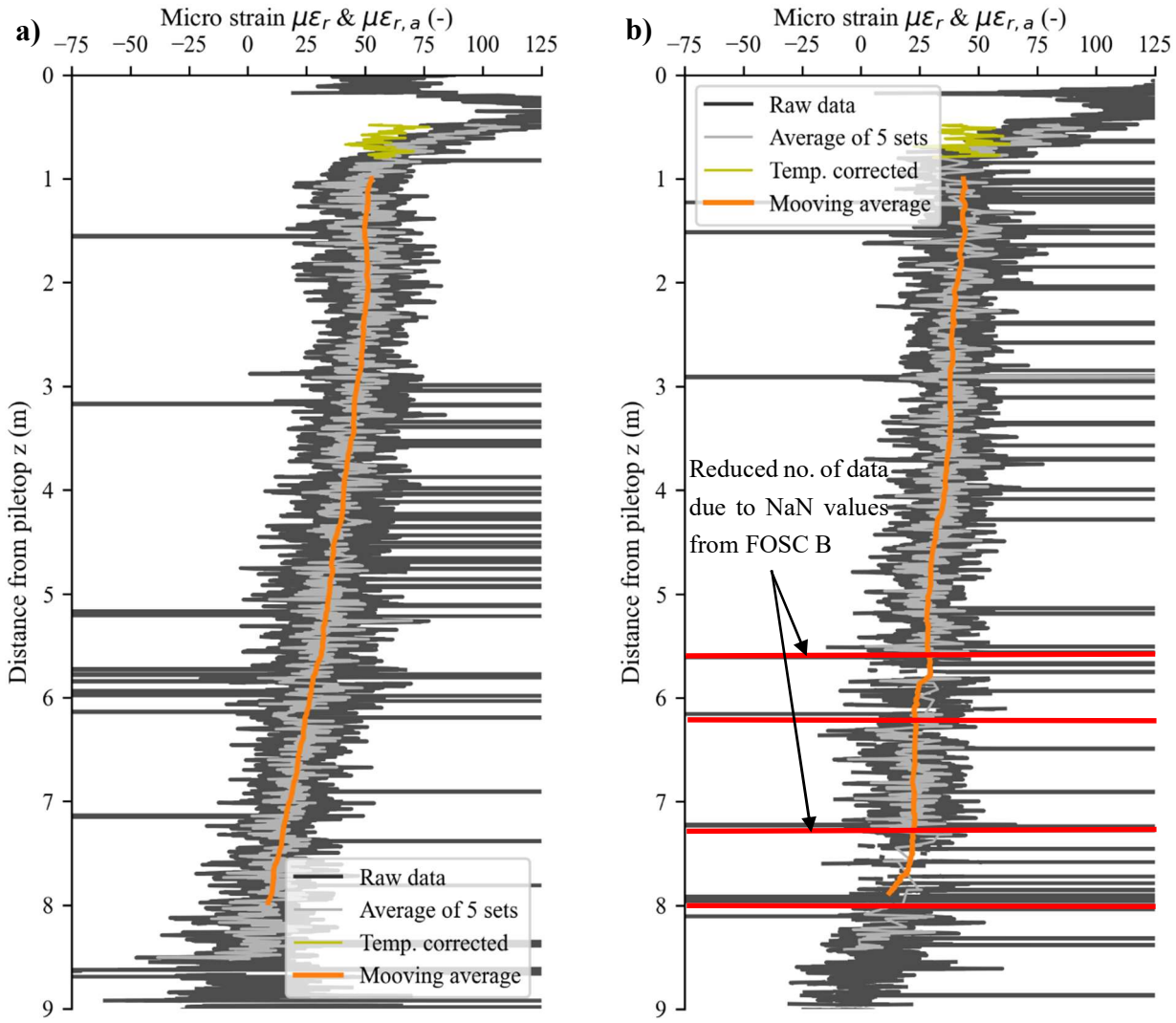

Figure 214: Strain development along the length of test pile 2 in load step 14 for (a) FOSC A and (b) FOSC B with multiple NaN values between 5.6 and 6.2 as well as between 7.3 and 8.0 (red lines). The moving average is influenced 0.5 m above and below the section with multiple NaN values.

Test pile 3

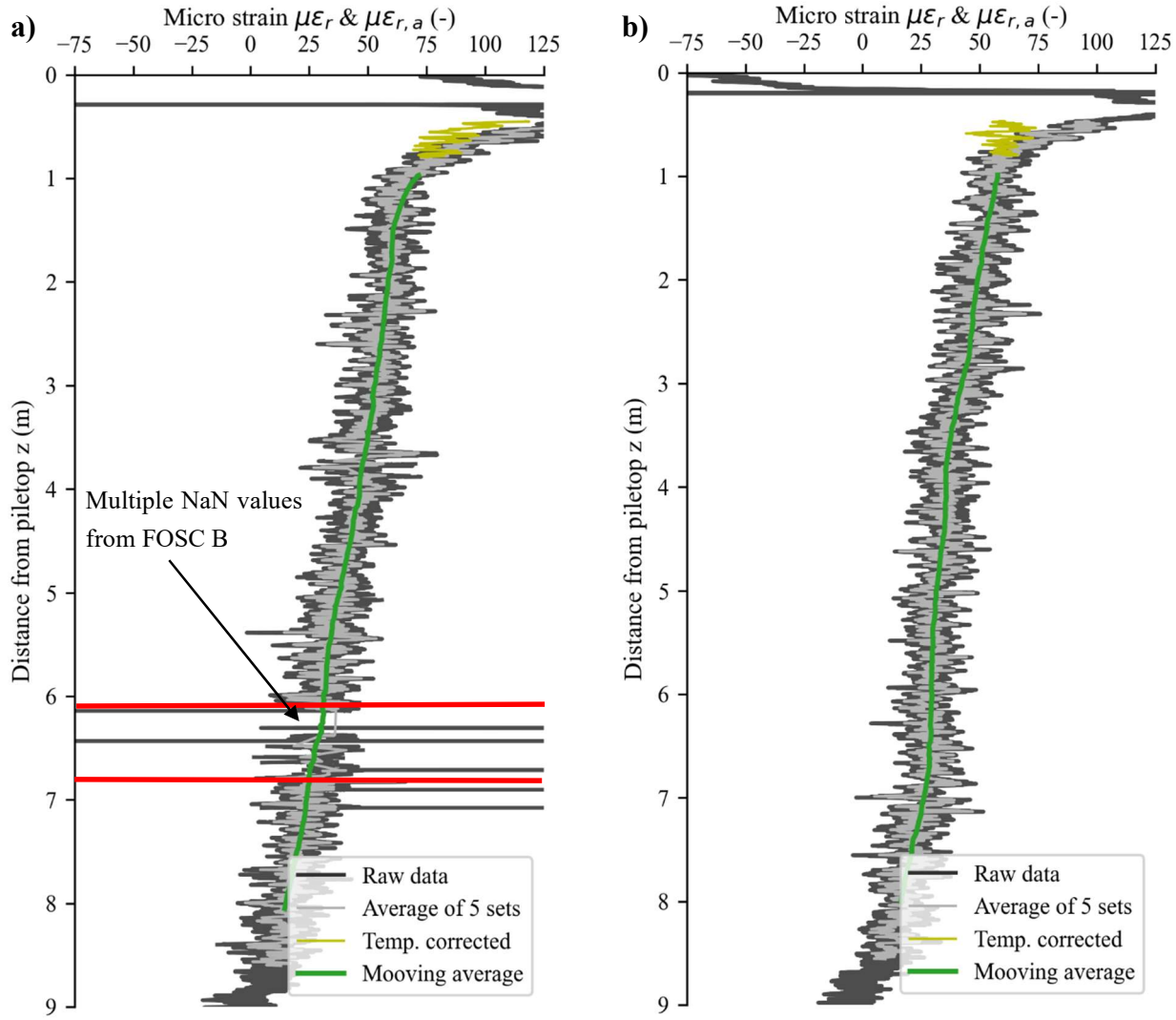

Figure 215: Strain development along the length of test pile 3 in load step 14 for (a) FOSC A with multiple NaN values between 6.1 and 6.8 (red lines) and (b) FOSC B. The moving average is influenced 0.5 m above and below the section with multiple NaN values.

Test pile 4

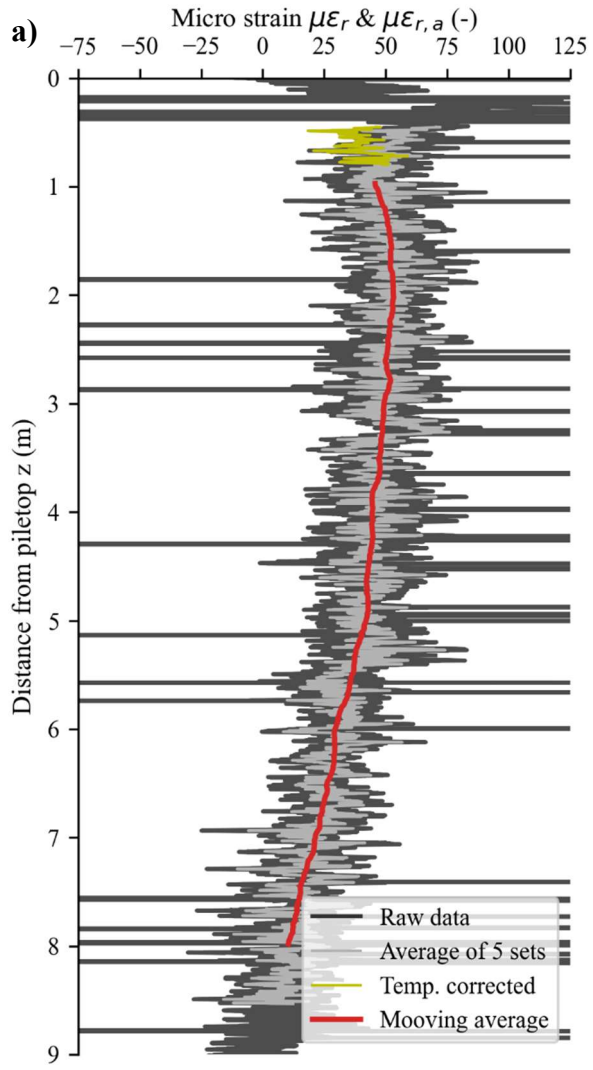

Figure 216: Strain development along the length of test pile 4 in load step 14 for only (a) FOSC A, because FOSC B is not working.

Test pile 5

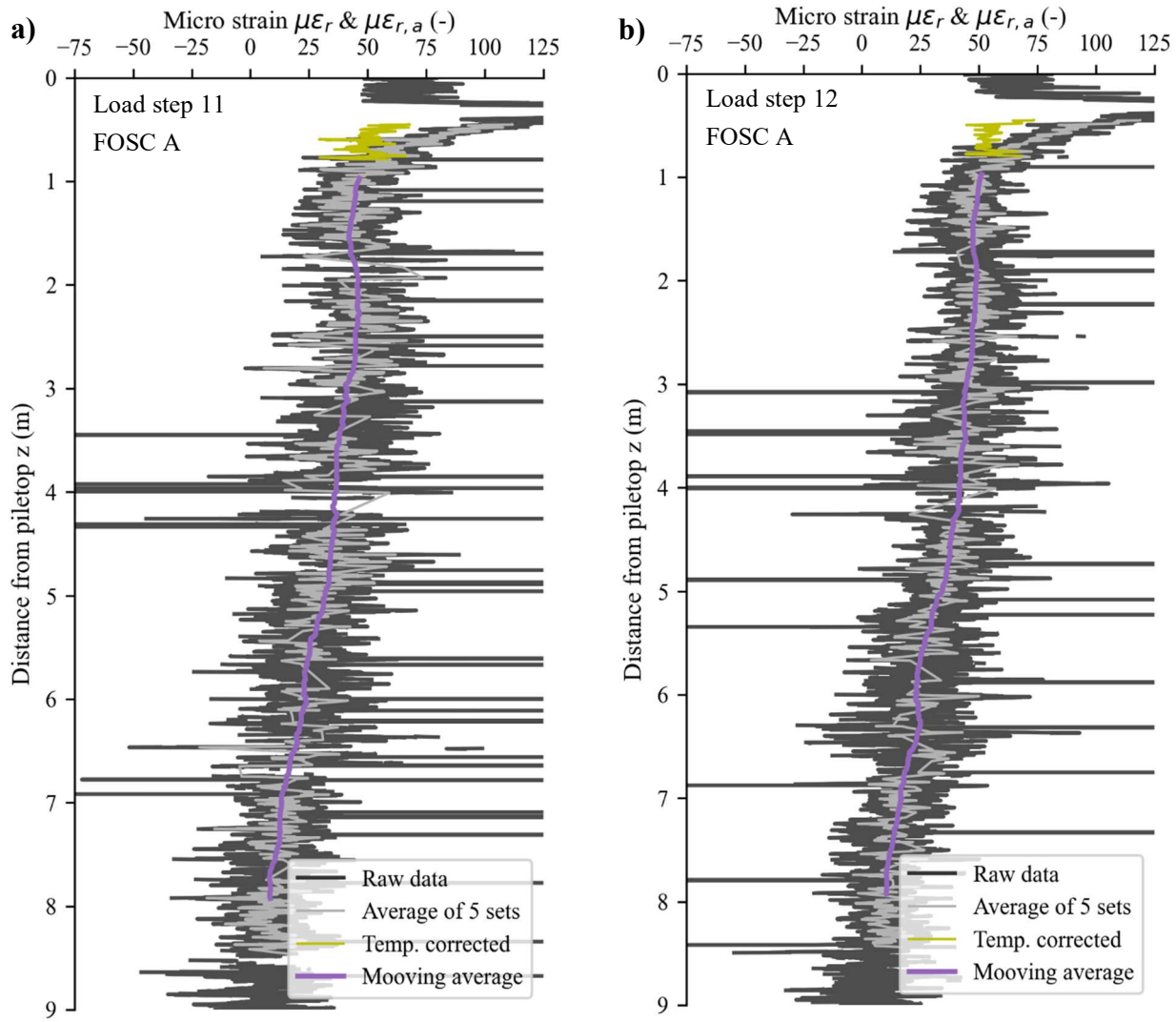

Figure 217: Strain development along the length of test pile 5 in load step (a)11 and (b) 12 for FOSC A with multiple NaN values along the length of the test pile.

Test pile 6

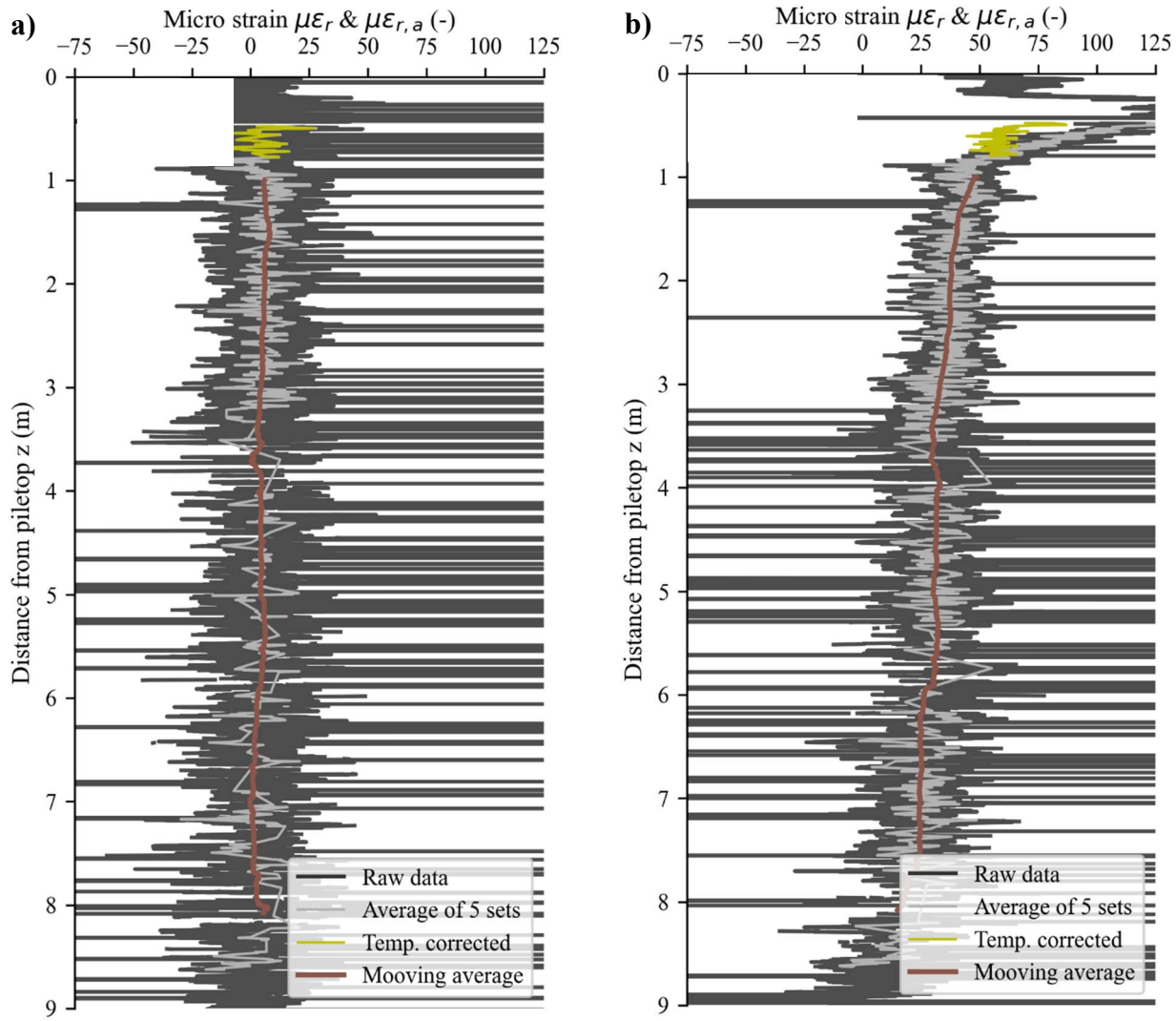

Figure 218: Strain development along the length of test pile 6 in load step (a)1 and (b) 14 for FOSC A with high amount of scatter along the length of the test pile.

Test pile 8

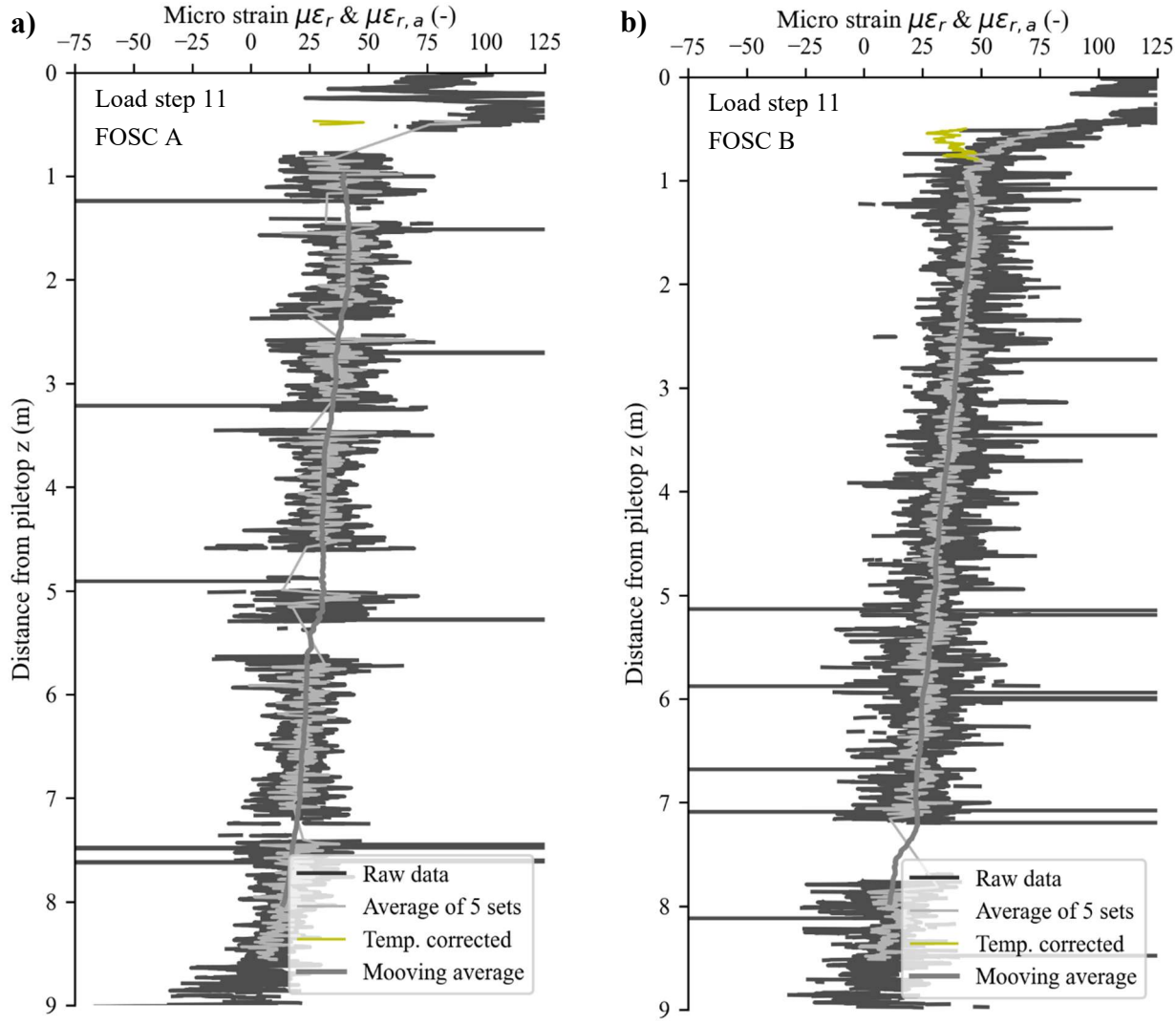

Figure 219: Strain development along the length of test pile 8 in load step 11 for (a)FOSC A and (b) FOSC B with multiple NaN values along the length of the test pile.

I.5 Non-uniform pile stiffness

Maintained load (ML) test

Test pile 7

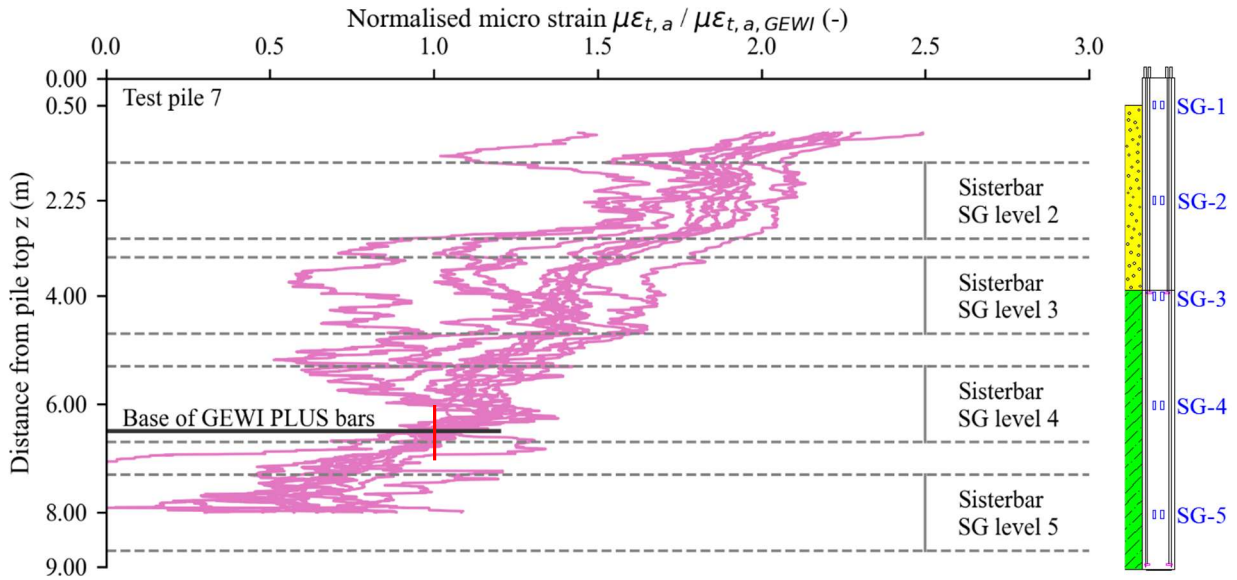

Figure 220: Influence of non-uniform pile stiffness on test pile 7 Dashed, grey lines indicate top and base of the approximately 1.4 m long sister bars used for the vibrating wire strain gauges (VWSG) measurements. Black line indicates base of the GEWI PLUS bars employed for transferring the force from the hydraulic jacks to the test piles during the static pile loading tests.

Constant rate of uplift (CRU) test

Test pile 2

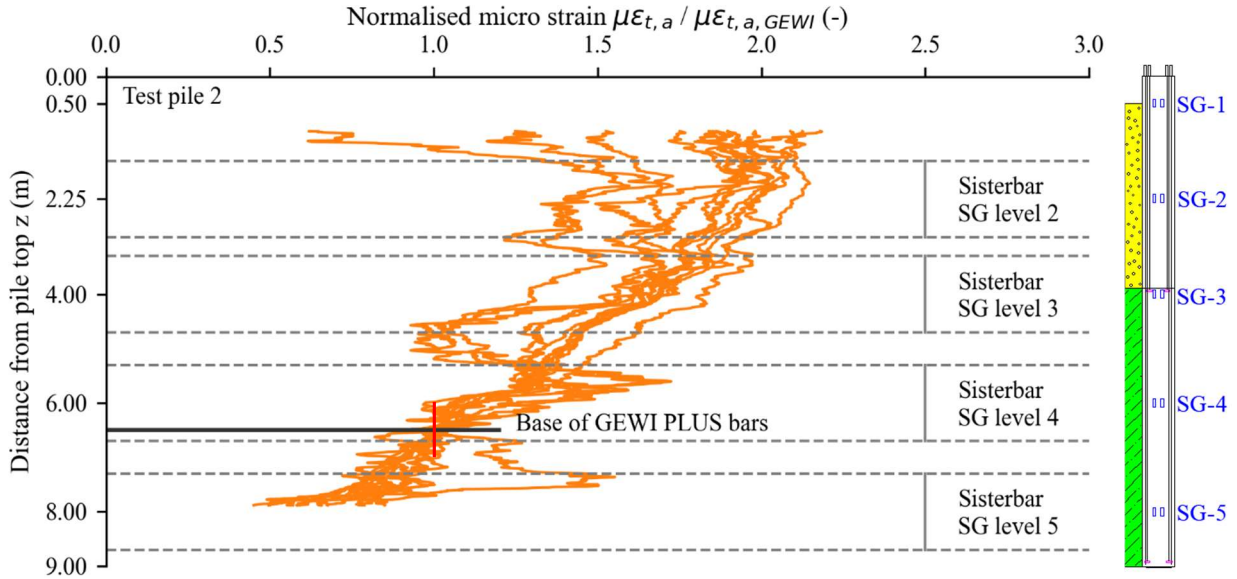

Figure 221: Influence of non-uniform pile stiffness on test pile 2. Dashed, grey lines indicate top and base of the approximately 1.4 m long sister bars used for the vibrating wire strain gauges (VWSG) measurements. Black line indicates base of the GEWI PLUS bars employed for transferring the force from the hydraulic jacks to the test piles during the static pile loading tests.

Test pile 3

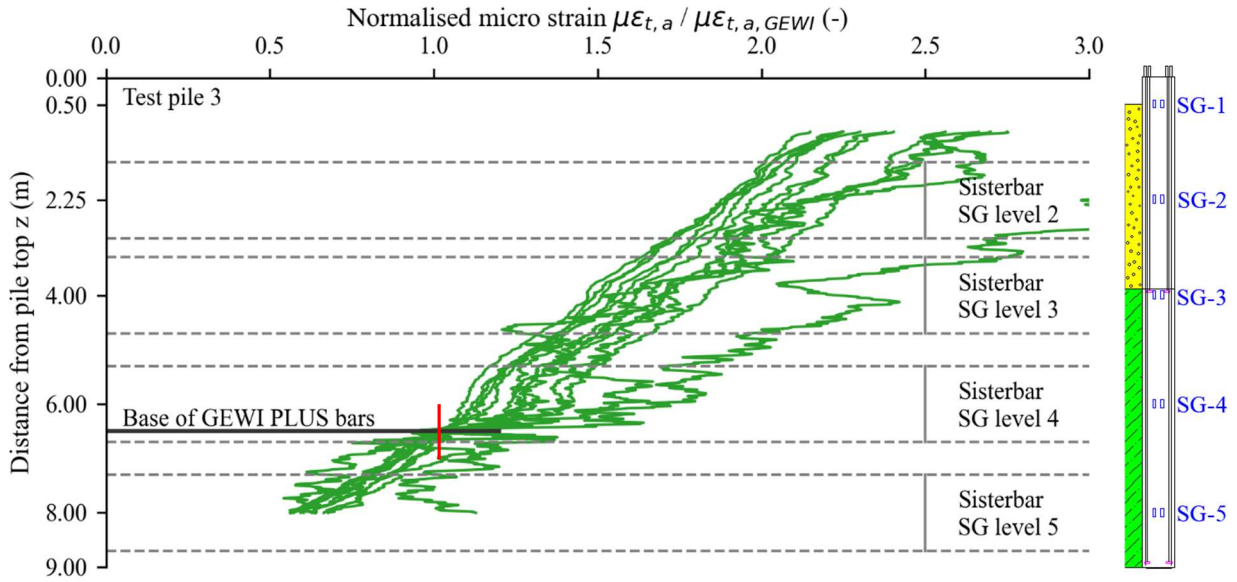

Figure 222: Influence of non-uniform pile stiffness on test pile 3. Dashed, grey lines indicate top and base of the approximately 1.4 m long sister bars used for the vibrating wire strain gauges (VWSG) measurements. Black line indicates base of the GEWI PLUS bars employed for transferring the force from the hydraulic jacks to the test piles during the static pile loading tests.

J Residual stresses

J.1 Load distribution along the length of test piles

Test pile 2

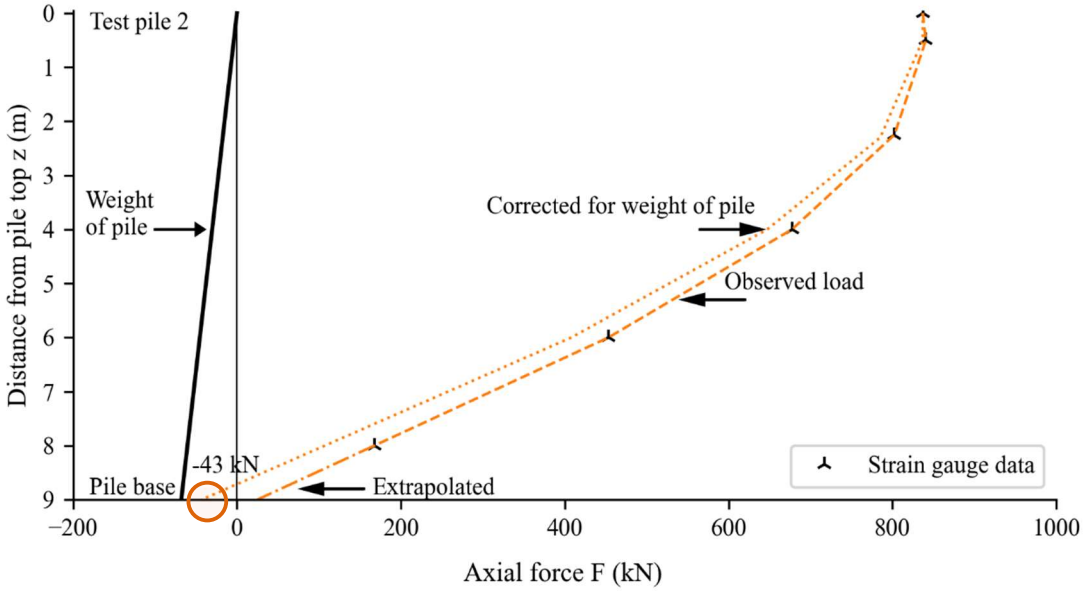

Figure 223: Axial load distribution along the length of test pile 2 based on vibrating wire strain gauge (VWSG) data, which corrected for weight of the test pile has -43 kN in compressive force at pile toe.

Test pile 3

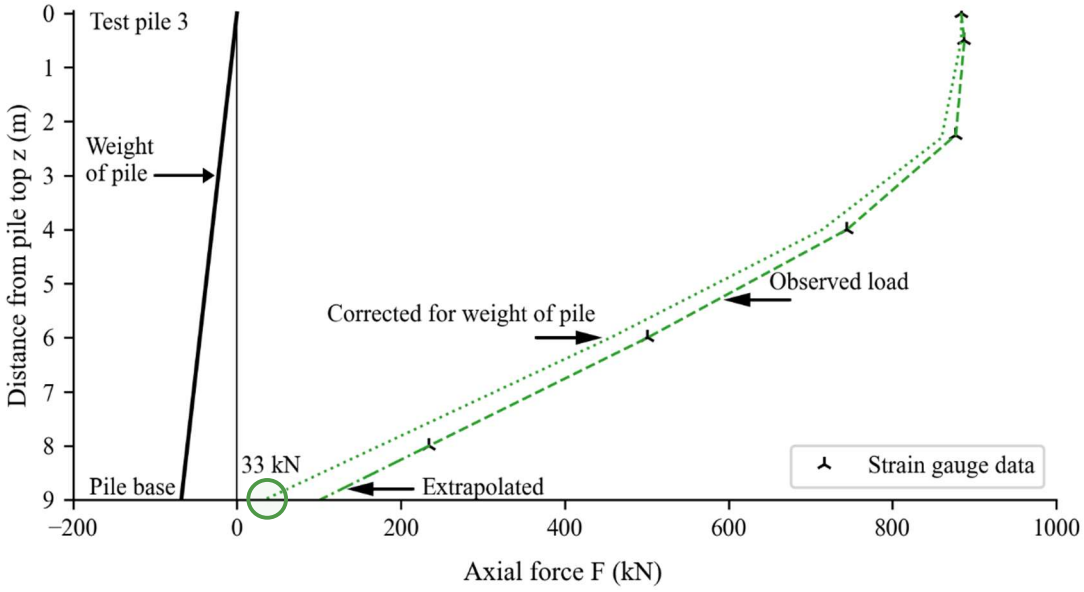

Figure 224: Axial load distribution along the length of test pile 3 based on vibrating wire strain gauge (VWSG) data, which corrected for weight of the test pile has 33 kN in tension at pile toe.

Test pile 4

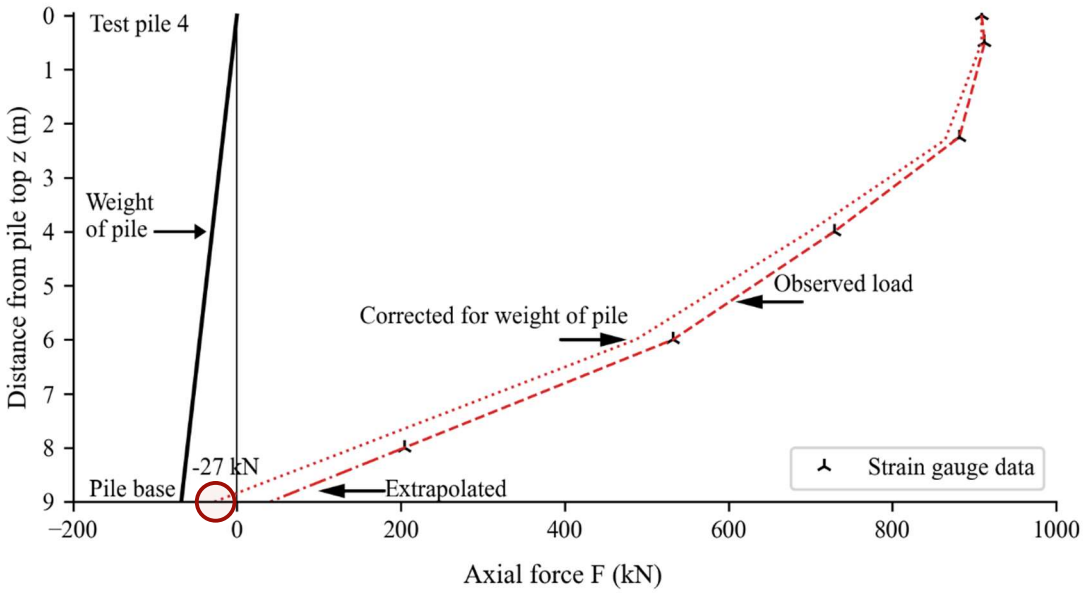

Figure 225: Axial load distribution along the length of test pile 4 based on vibrating wire strain gauge (VWSG) data, which corrected for weight of the test pile has -27 kN in compressive force at pile toe.

Test pile 5

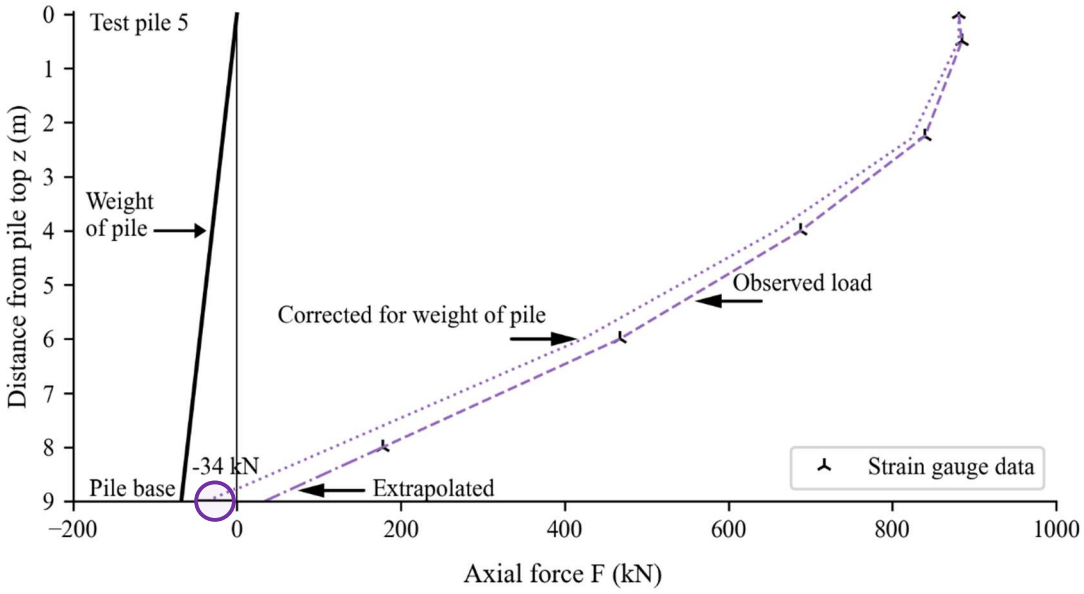

Figure 226: Axial load distribution along the length of test pile 5 based on vibrating wire strain gauge (VWSG) data, which corrected for weight of the test pile has -34 kN in compressive force at pile toe.

Test pile 6

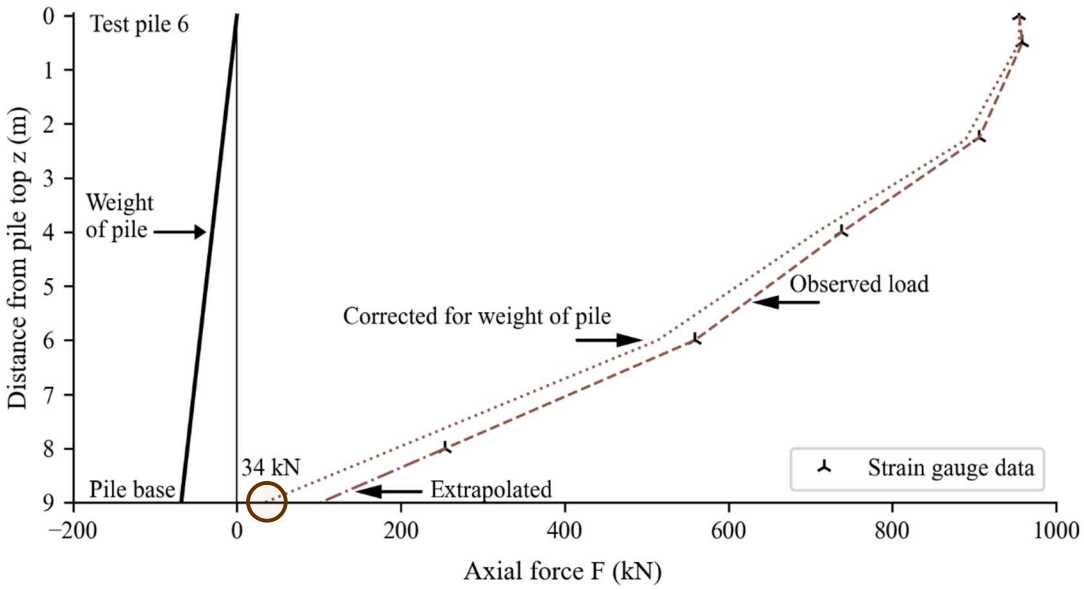

Figure 227: Axial load distribution along the length of test pile 6 based on vibrating wire strain gauge (VWSG) data, which corrected for weight of the test pile has 34 kN in tension at pile toe.

Test pile 7

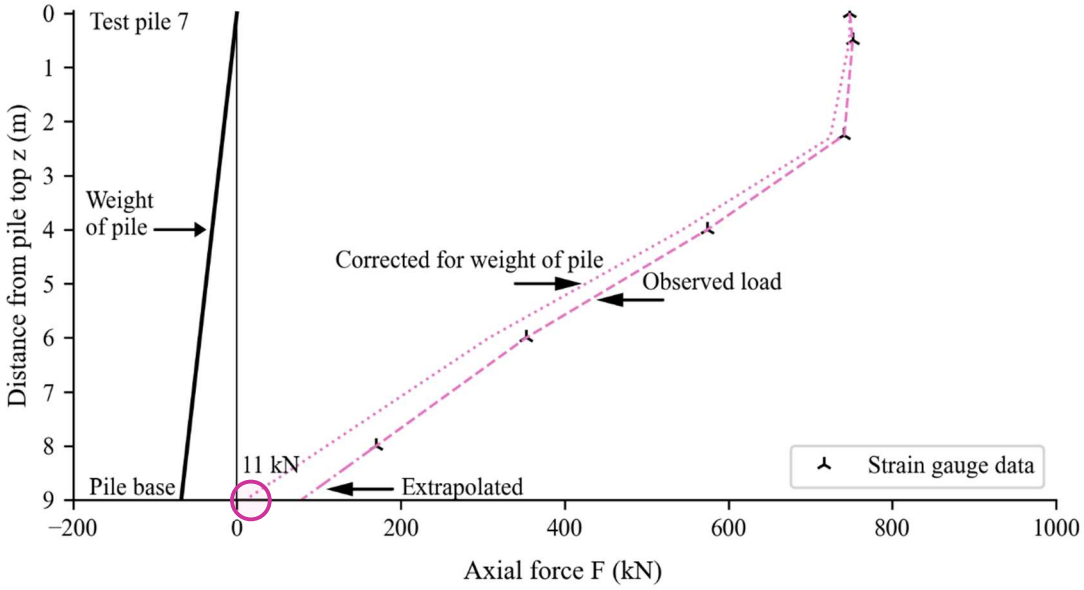

Figure 228: Axial load distribution along the length of test pile 7 based on vibrating wire strain gauge (VWSG) data, which corrected for weight of the test pile has 11 kN in tension at pile toe.

Test pile 8

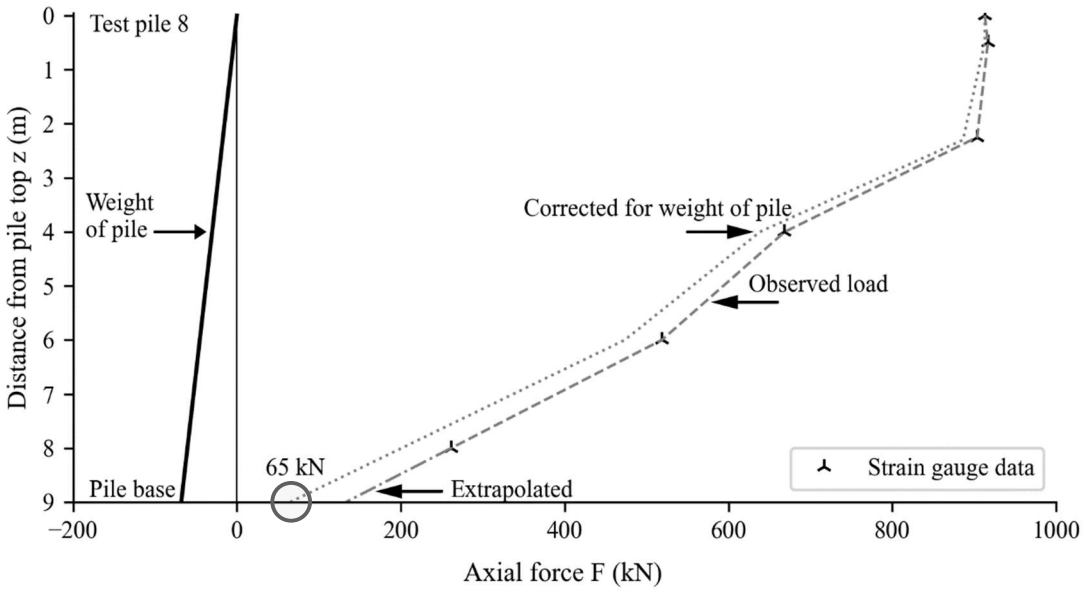

Figure 229: Axial load distribution along the length of test pile 8 based on vibrating wire strain gauge (VWSG) data, which corrected for weight of the test pile has 65 kN in tension at pile toe.

J.2 Interpretation of residual stresses cf. Method 1, 2 and 3

Test pile 4

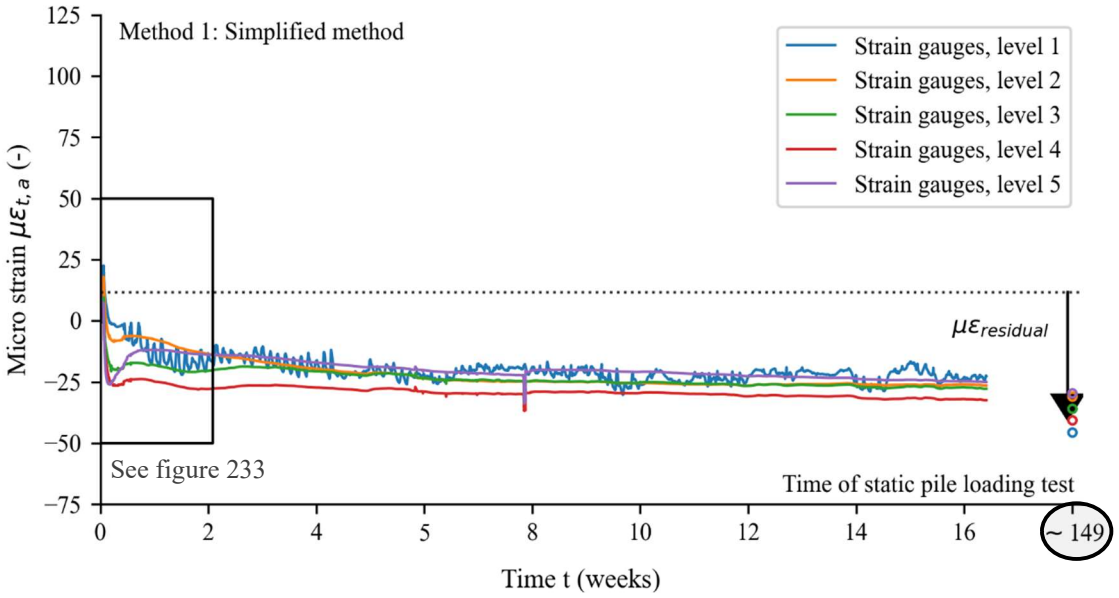

Figure 230: Interpretation of residual strains cf. Method 1; Simplified method for test pile 4.

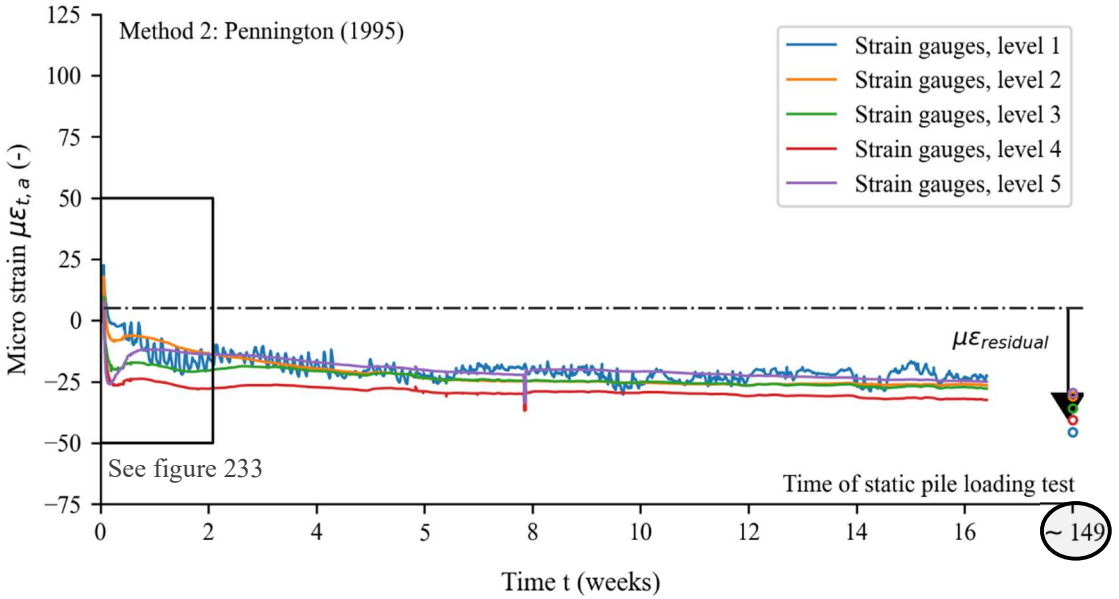

Figure 231: Interpretation of residual strains cf. Method 2; Pennington (1995) for test pile 4.

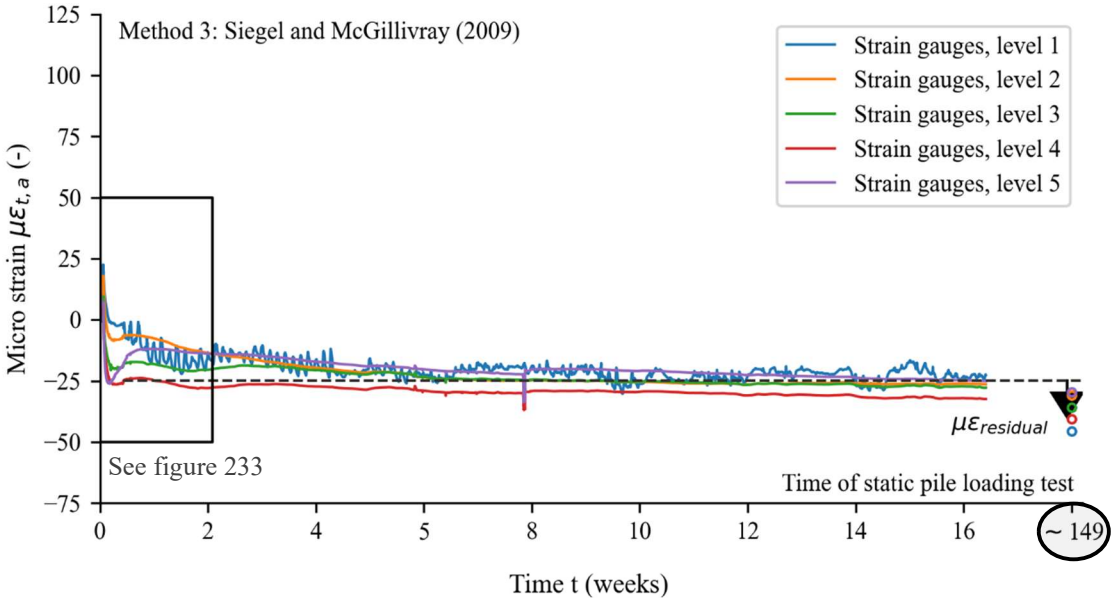

Figure 232: Interpretation of residual strains cf. Method 3; Siegel and McGillivray (2009) for test pile 4.

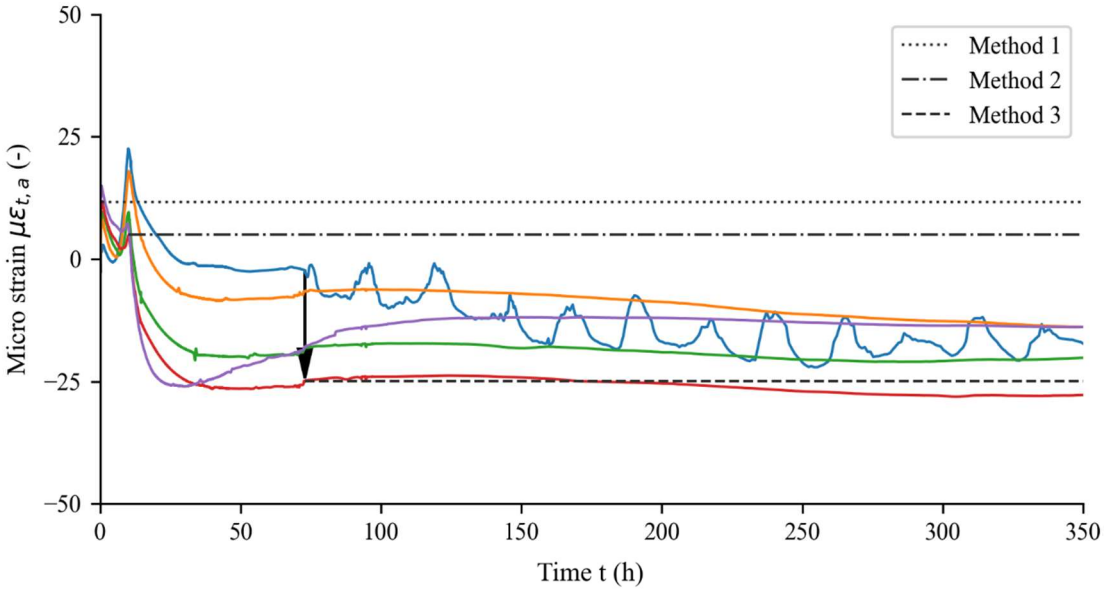

Figure 233: Development of residual stresses in the initial 350 hours after installation of test pile 4 cf. Method 1; Simplified method; Method 2; Pennington (1995) and Method 3; Siegel and McGillivray (2009).

K Accuracy of analytical models

K.1 HN model

Maintained load (ML) test

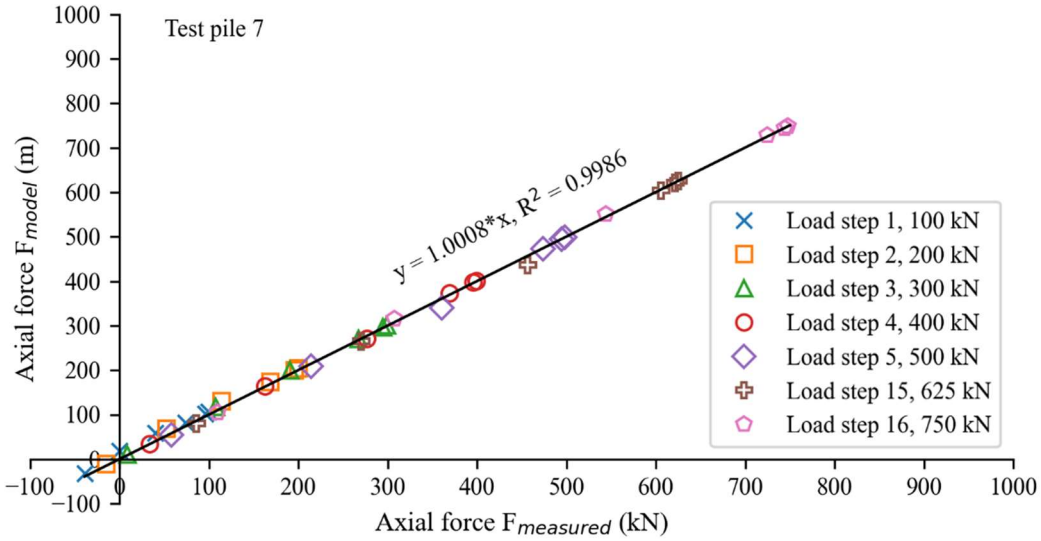

Figure 234: Measured data vs. HN model values of axial forces for test piles 7 at the Hinge test site.

Constant rate of uplift (CRU) test

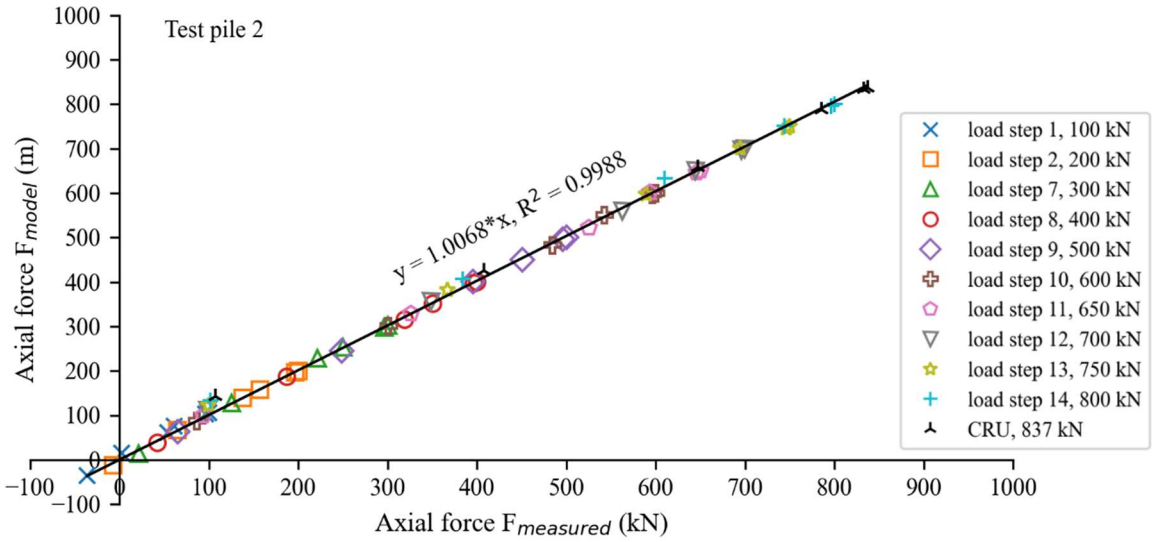

Figure 235: Measured data vs. HN model values of axial forces for test piles 2 at the Hinge test site.

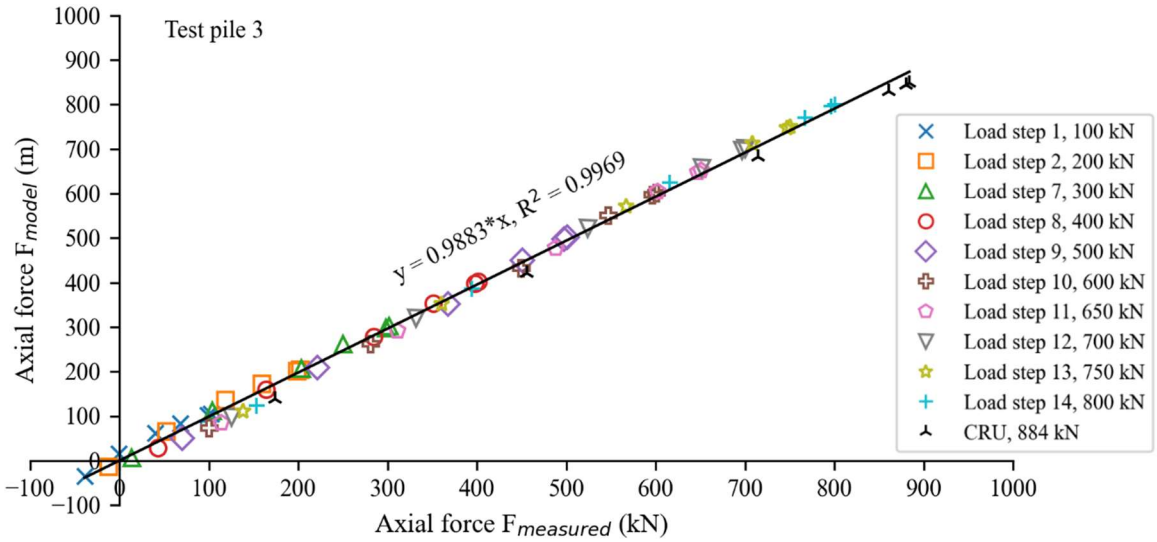

Figure 236: Measured data vs. HN model values of axial forces for test piles 3 at the Hinge test site.

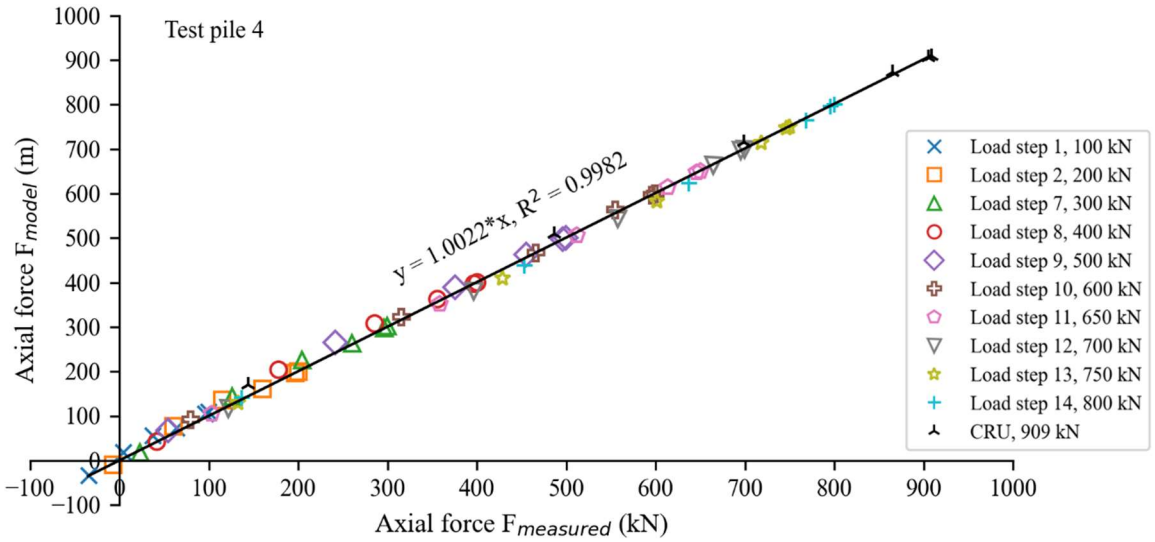

Figure 237: Measured data vs. HN model values of axial forces for test piles 4 at the Hinge test site.

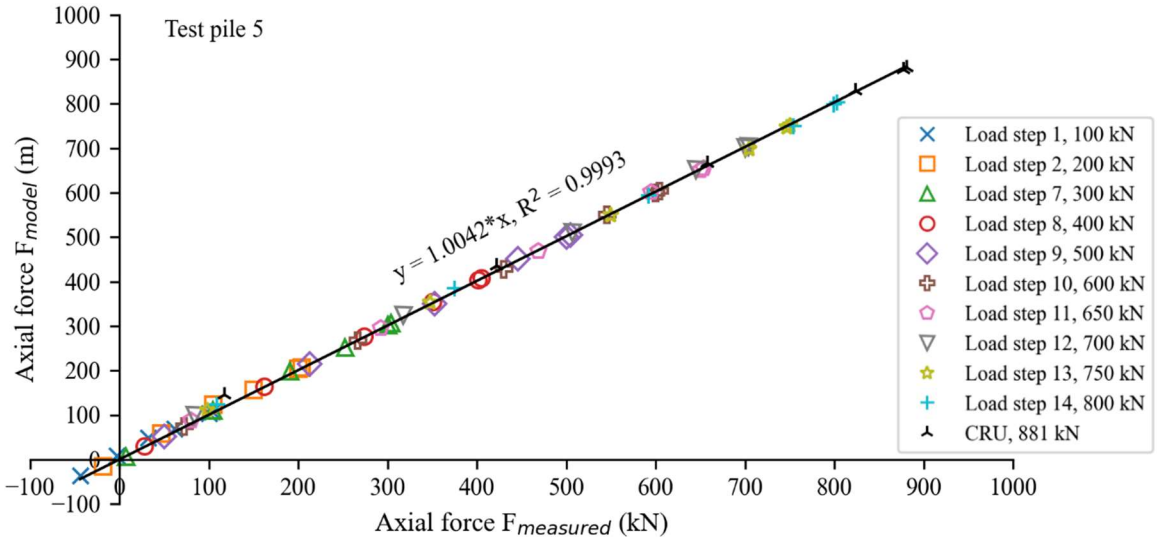

Figure 238: Measured data vs. HN model values of axial forces for test piles 5 at the Hinge test site.

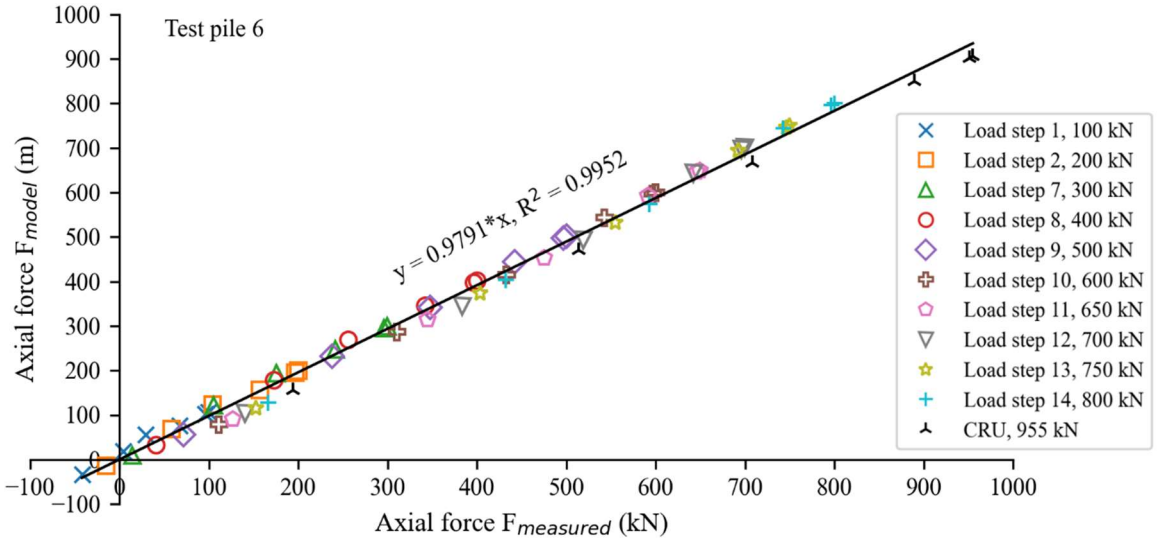

Figure 239: Measured data vs. HN model values of axial forces for test piles 6 at the Hinge test site.

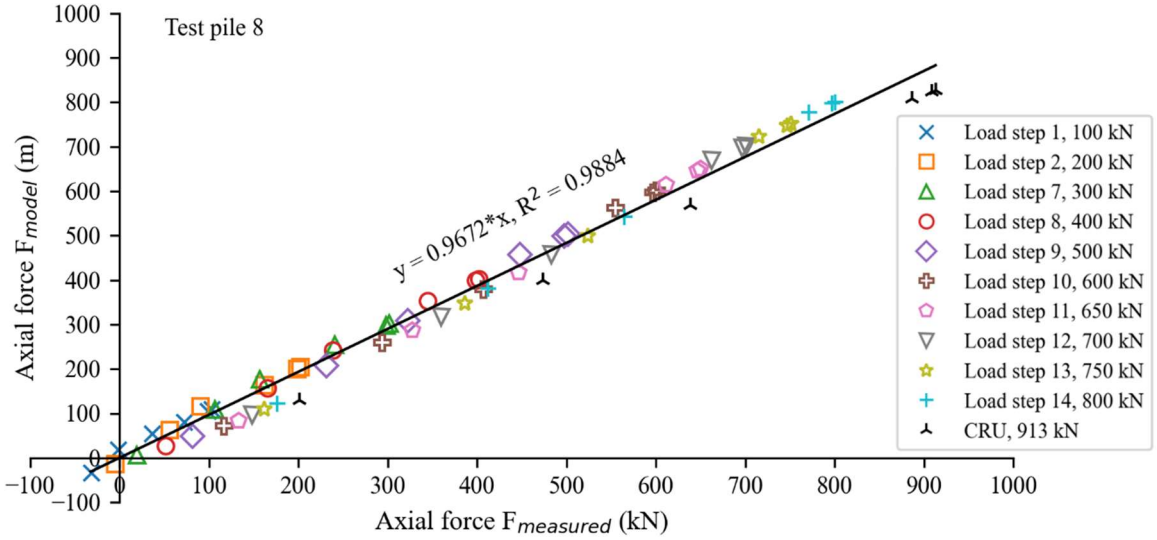

Figure 240: Measured data vs. HN model values of axial forces for test piles 8 at the Hinge test site.

K.2 HNr model

Maintained load (ML) test

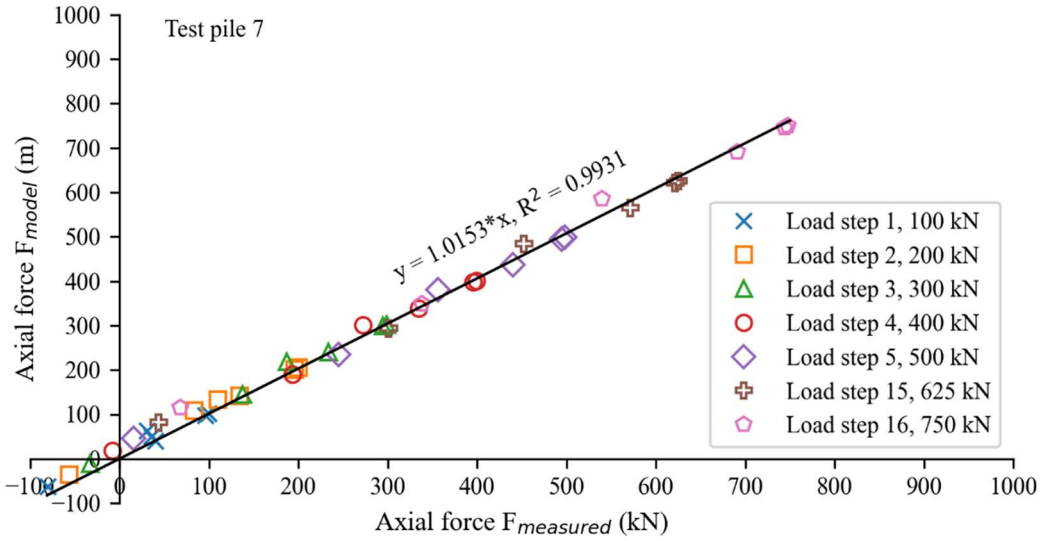

Figure 241: Measured data vs. HNr model values of axial forces for test piles 7.

Constant rate of uplift (CRU) test

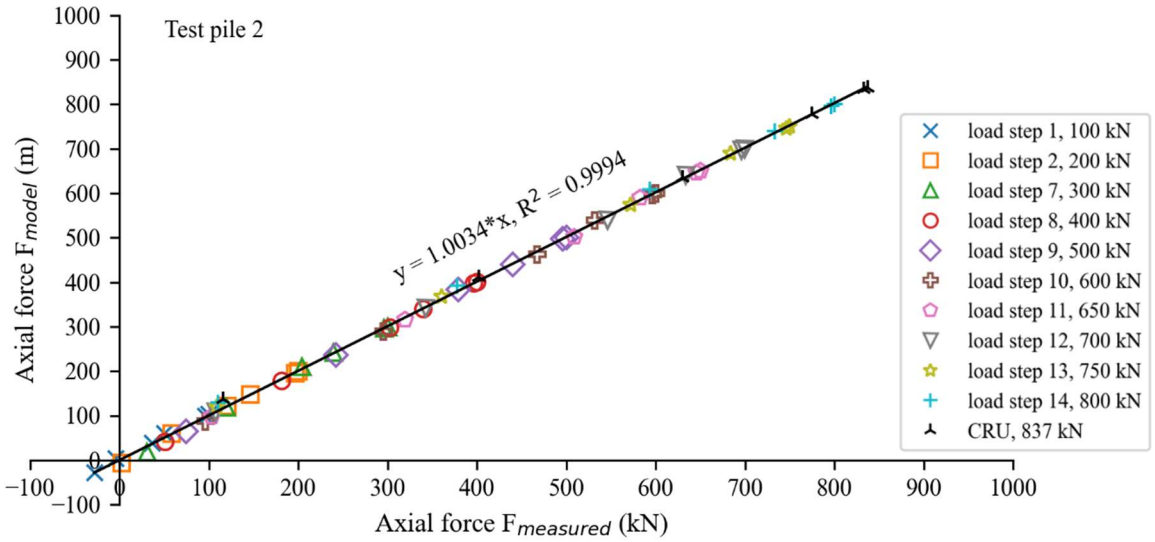

Figure 242: Measured data vs. HNr model values of axial forces for test piles 2.

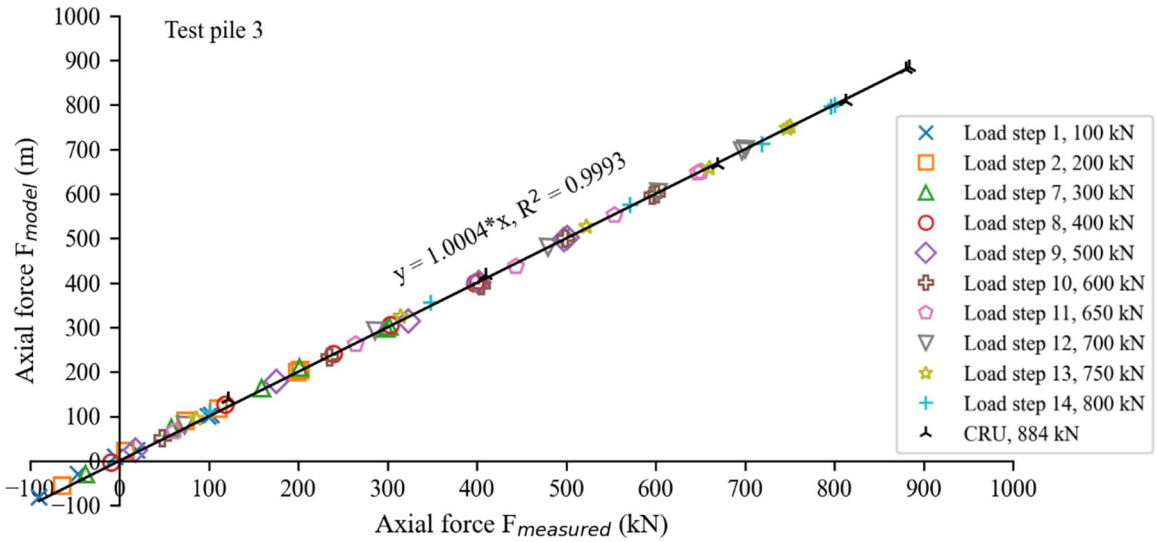

Figure 243: Measured data vs. HNr model values of axial forces for test piles 3.

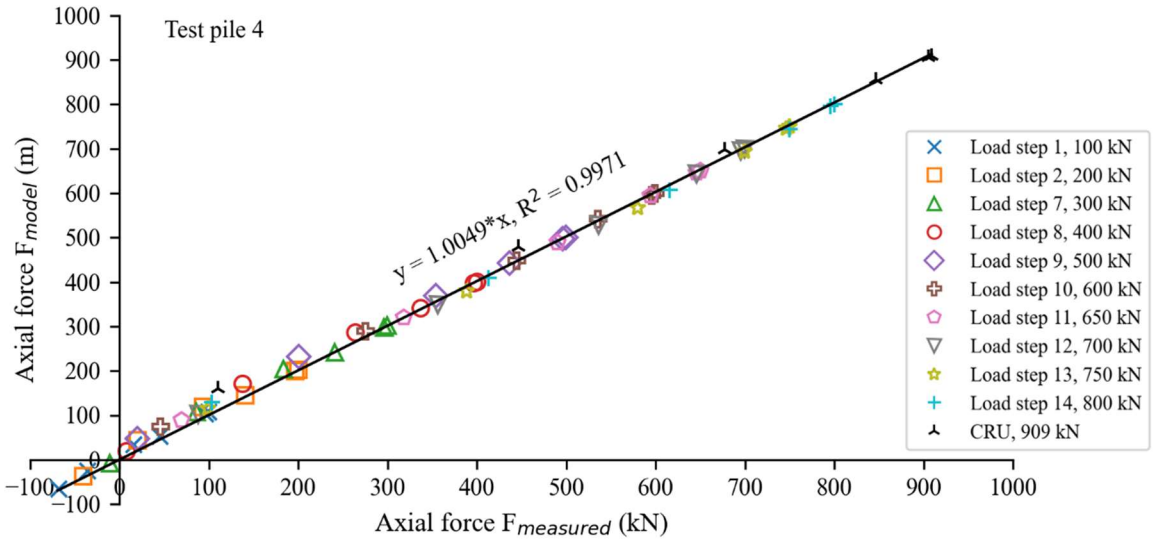

Figure 244: Measured data vs. HNr model values of axial forces for test piles 4.

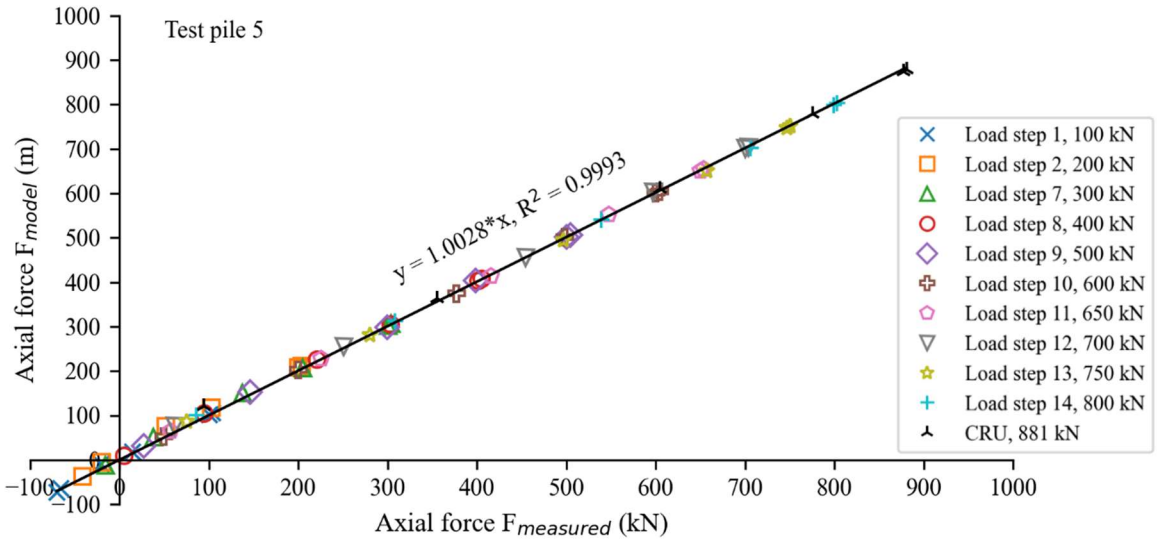

Figure 245: Measured data vs. HNr model values of axial forces for test piles 5.

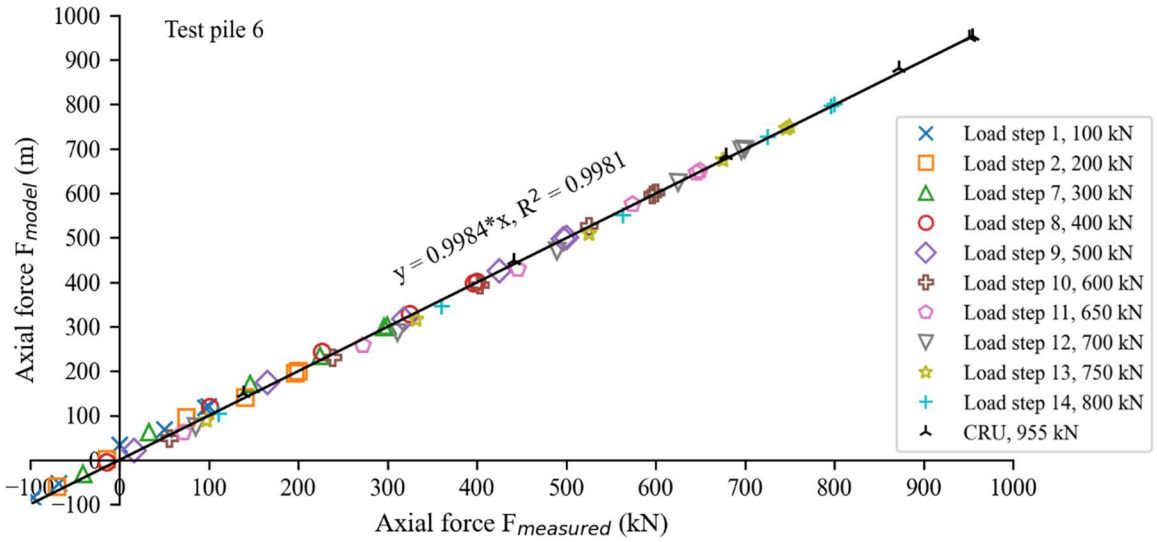

Figure 246: Measured data vs. HNr model values of axial forces for test piles 6.

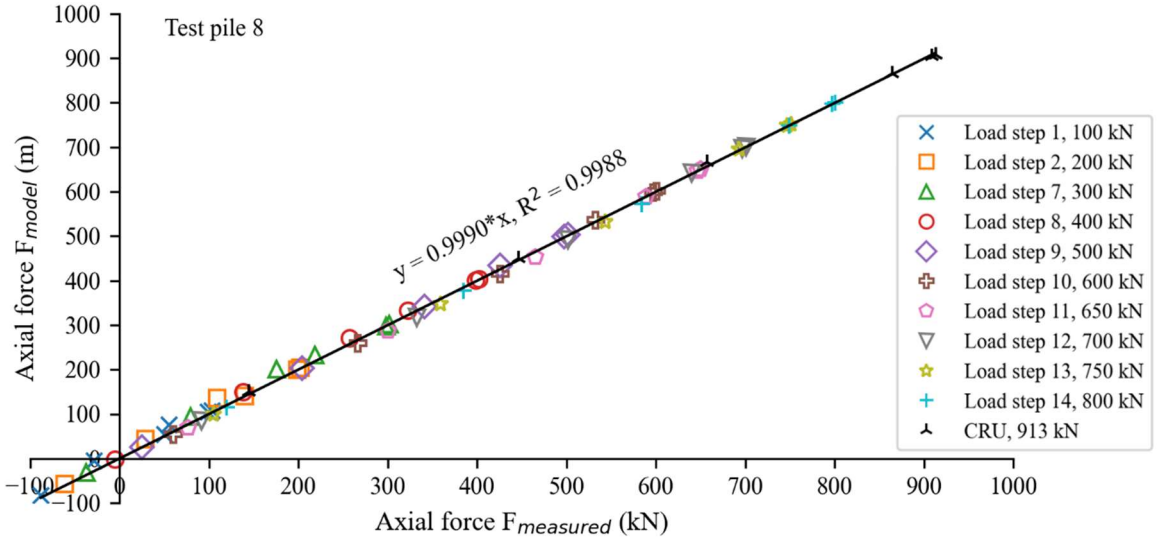

Figure 247: Measured data vs. HNr model values of axial forces for test piles 8.

K.3 Examples of Python scripts

Script from hyperbolic non-linear loading model (HN model)

```
"""
TZ model korrigeret for egenvægt af pælen
"""
#T-Z model (Corrected for dead weight of pile)

#Inddeling af pælen i elementer
Ls_self=Ls   #Længden af hvert enkelt delelement (m)

#Angiv start værdier til iterationsprocessen
Zinitial=0.02   #Startværdi af flytning (mm), som anvendes i den efterfølgende iterationsproces (må ikke være 0 pga. iterationsproblemer)
Step=0.01   #Skridtlængden som anvendes under iterationsprocessen
Ztotal_self=np.array([]) #Oprettelse af et tomt array til opsamling af flytningsserier
Zs=np.zeros(element+1) #Oprettelse af et array med element (f.eks. 100) x nul som startværdier

Fs=-G   #Oprettelse af et array med start værdier svarende til egenvægt af pælen
Fs=np.append(0,Fs[1::])
Ftotal_self=np.array([]) #Oprettelse af et tomt array til opsamling af lastserier
Fstopvalues=np.array([loadlc1[0],loadlc1[1],loadlc1[2],loadlc2[3],loadlc2[4],loadlc2[5],loadlc2[6],loadlc2[7],loadlc2[8],loadlc2[9],loadlc2[10],848])   #Oprettelse af et array med stopværdier


for x in range(0,len(Fstopvalues)):
    Fstop=Fstopvalues[x]


    while Fs[0]<Fstop:   #Zinitial<np.amax(Soil_virgin_SG1_2): #Soil_virgin_SG2_3[len(Soil_virgin_SG2_3)-1]:

        Zinitial=Zinitial+Step
        Ftoe=(Fstopvalues[x]/884)*G[len(G)-1]-G[len(G)-1]   #Bestemmelse af værdier ved pælespids, lineær fordeling antaget

        Ds_self=np.array([]) #Oprettelse af et tomt array til bestemmlse af dybde under pæletop
        NyD=0

        for l in range(0,element):
            DeltaD=NyD+Ls_self*l
            Ds_self=np.append(Ds_self,DeltaD)

       Ds_self=np.append(Ds_self,Ls_self*element)


       for k in range(0,10):

           MS=np.array([]) #Oprettelse af et tomt array til bestemmlse af mobiliseret overflademodstand
           Zs=np.array([]) #Oprettelse af et tomt array til bestemmelse af flytning langs pælen
           NyZ=Zinitial
           MS_initial=0

           for i in range(0,element):
               DeltaZ=(Ls_self/(EsA*1000000))*0.5*(Fs[i]+Fs[i+1])   #Omregning fra GN til kN
               NyZ=NyZ-(DeltaZ*1000)   #Omregning fra m til mm
               Zs=np.append(Zs,NyZ)
               Depth=Ls_self*(i+1)
               if Depth<=0.5:
                   mus_curve=0
               elif Depth>0.5 and Depth<=2.25:
                   mus_curve=(NyZ*(a_virgin_SG1_2+c_virgin_SG1_2*NyZ)/((a_virgin_SG1_2+b_virgin_SG1_2*NyZ)**2))   #Bestemmelse af mobiliseret enhedsoverflademodstand i den aktuelle dybde
               elif Depth>2.25 and Depth<=4.0:
                   mus_curve=(NyZ*(a_virgin_SG2_3+c_virgin_SG2_3*NyZ)/((a_virgin_SG2_3+b_virgin_SG2_3*NyZ)**2))   #Bestemmelse af mobiliseret enhedsoverflademodstand i den aktuelle dybde
               elif Depth>4.0 and Depth<=6.0:
                   mus_curve=((a_poly_SG3_4*t_vija_SG3_4**2+b_poly_SG3_4*t_vija_SG3_4+c_poly_SG3_4)*(V_virgin_SG3_4*np.sqrt(NyZ/t_vija_SG3_4)-(V_virgin_SG3_4-1)*(NyZ/t_vija_SG3_4)))
               else:
                   mus_curve=((a_poly_SG4_5*t_vija_SG4_5**2+b_poly_SG4_5*t_vija_SG4_5+c_poly_SG4_5)*(V_virgin_SG4_5*np.sqrt(NyZ/t_vija_SG4_5)-(V_virgin_SG4_5-1)*(NyZ/t_vija_SG4_5)))

               NyMS=Pile_circumfer*Ls_self*mus_curve
               MS=np.append(MS,NyMS)

           Zs=np.append(Zinitial,Zs)
           MS=np.append(MS_initial,MS)

           Fs=np.array([]) #Oprettelse af et tomt array til bestemmelse af last langs pælen
           NyF=Ftoe

           for j in range(0,element):
               NyF=NyF+0.5*(MS[element-(j+1)]+MS[element-(j)])+Pile_area*Ls_self*Econ
               Fs=np.append(NyF,Fs)

           Fs=np.append(Fs,Ftoe)


    Ftotal_self=np.append(Ftotal_self,Fs)
    Ztotal_self=np.append(Ztotal_self,Zs)

Ftotal_self=np.reshape(Ftotal_self, newshape=(x+1,len(Fs)))
Ztotal_self=np.reshape(Ztotal_self, newshape=(x+1,len(Zs)))
```

Script from hyperbolic non-linear loading model incl. residual stresses (HNr model)

```
"""
TZ model korrigeret for egenvægt af pælen samt residual værdier
"""
#T-Z model (True distribution of axial force)

#Inddeling af pælen i elementer
Ls_cor=Ls   #Længden af hvert enkelt delelement (m)

#Angiv start værdier til iterationsprocessen
Zinitial=0.02   #Startværdi af flytning (mm), som anvendes i den efterfølgende iterationsproces
Step=0.01   #Skridtlængden som anvendes under iterationsprocessen
Ztotal_cor=np.array([]) #Oprettelse af et tomt array til opsamling af flytningsserier
Zs=np.zeros(element+1) #Oprettelse af et array med element (f.eks. 100) x nul som startværdier

Fs=-Fs_res   #Oprettelse af et array med start værdier svarende til residual værdier samt egenvægten af pælen
Fs=np.append(0,Fs[1::])
Ftotal_cor=np.array([]) #Oprettelse af et tomt array til opsamling af lastserier
Fstopvalues=np.array([loadlc1[0],loadlc1[1],loadlc1[2],loadlc2[3],loadlc2[4],loadlc2[5],loadlc2[6],loadlc2[7], loadlc2[8],loadlc2[9],loadlc2[10],884])   #Oprettelse af et array med stopværdier


for x in range(0,len(Fstopvalues)):
    Fstop=Fstopvalues[x]


    while Fs[0]<Fstop:   #Zinitial<np.amax(Soil_virgin_SG1_2): #Soil_virgin_SG2_3[len(Soil_virgin_SG2_3)-1]:

        Zinitial=Zinitial+Step
        Ftoe=(Fstopvalues[x]/884)*Fs_res[len(Fs_res)-1]-Fs_res[len(Fs_res)-1]   #Bestemmelse af værdier ved pælespids, lineær fordeling antaget

        Ds_cor=np.array([]) #Oprettelse af et tomt array til bestemmlse af dybde under pæletop
        NyD=0


        for l in range(0,element):
            DeltaD=NyD+Ls_cor*1
            Ds_cor=np.append(Ds_cor,DeltaD)

        Ds_cor=np.append(Ds_cor,Ls_cor*element)


        for k in range(0,10):

            MS=np.array([]) #Oprettelse af et tomt array til bestemmlse af mobiliseret overflademodstand
            Zs=np.array([]) #Oprettelse af et tomt array til bestemmelse af flytning langs pælen
            NyZ=Zinitial
            MS_initial=0

            for i in range(0,element):
                DeltaZ=(Ls_cor/(EsA*1000000))*0.5*(Fs[i]+Fs[i+1])   #Omregning fra GN til kN
                NyZ=NyZ-(DeltaZ*1000)   #Omregning fra m til mm
                Zs=np.append(Zs,NyZ)
                Depth=Ls_cor*(i+1)
                if Depth<=0.5:
                    mus_curve=0
                elif Depth>0.5 and Depth<=2.25:
                    NyZZ=NyZ-(MUSreloading[0,0]/y_stiffness_SG1_2_cor)
                    if NyZZ<0:
                        mus_curve=NyZZ*y_stiffness_SG1_2_cor
                    else:
                        mus_curve=(NyZZ*(a_virgin_SG1_2_cor+c_virgin_SG1_2_cor*NyZZ)/((a_virgin_SG1_2_cor+b_virgin_SG1_2_cor*NyZZ)**2))   #

                elif Depth>2.25 and Depth<=4.0:
                    NyZZ=NyZ-(MUSreloading[1,0]/y_stiffness_SG2_3_cor)
                    if NyZZ<0:
                        mus_curve=NyZZ*y_stiffness_SG2_3_cor
                    else:
                        mus_curve=(NyZZ*(a_virgin_SG2_3_cor+c_virgin_SG2_3_cor*NyZZ)/((a_virgin_SG2_3_cor+b_virgin_SG2_3_cor*NyZZ)**2))   #Bestemmelse af mobiliseret enhedsoverflademodstand i den aktuelle dybde
                elif Depth>4.0 and Depth<=6.0:
                    NyZZ=NyZ-(MUSreloading[2,0]/y_stiffness_SG3_4_cor)
                    if NyZZ<0:
                        mus_curve=NyZZ*y_stiffness_SG3_4_cor
                    else:
                        mus_curve=((a_poly_SG3_4_cor*t_vija_SG3_4_cor**2+b_poly_SG3_4_cor*t_vija_SG3_4_cor+c_poly_SG3_4_cor)*(V_virgin_SG3_4_cor*np.sqrt(NyZZ/t_vija_SG3_4_cor)-(V_virgin_SG3_4_cor-1)*(NyZZ/t_vija_SG3_4_cor)))
                else:
                    NyZZ=NyZ-(MUSreloading[3,0]/y_stiffness_SG4_5_cor)
                    if NyZZ<0:
                        mus_curve=NyZZ*y_stiffness_SG4_5_cor
                    else:
                        mus_curve=((a_poly_SG4_5_cor*t_vija_SG4_5_cor**2+b_poly_SG4_5_cor*t_vija_SG4_5_cor+c_poly_SG4_5_cor)*(V_virgin_SG4_5_cor*np.sqrt(NyZZ/t_vija_SG4_5_cor)-(V_virgin_SG4_5_cor-1)*(NyZZ/t_vija_SG4_5_cor)))

                NyMS=Pile_circumfer*Ls_cor*mus_curve
                MS=np.append(MS,NyMS)

            Zs=np.append(Zinitial,Zs)
            MS=np.append(MS_initial,MS)

            Fs=np.array([]) #Oprettelse af et tomt array til bestemmelse af last langs pælen
            NyF=Ftoe

            for j in range(0,element):
                NyF=NyF+0.5*(MS[element-(j+1)]+MS[element-(j)])+Pile_area*Ls_cor*Econ
                Fs=np.append(NyF,Fs)

            Fs=np.append(Fs,Ftoe)


    Ftotal_cor=np.append(Ftotal_cor,Fs)
    Ztotal_cor=np.append(Ztotal_cor,Zs)

Ftotal_cor=np.reshape(Ftotal_cor, newshape=(x+1,len(Fs)))
Ztotal_cor=np.reshape(Ztotal_cor, newshape=(x+1,len(Zs)))
```